

INVITED TALKS
OPENING PLENARY SESSION
(OPS)

RATIONAL POLYMERASE CHAIN REACTOR DESIGN

Dr. Marc Jozef Madou

Distinguished Professor, Instituto Tecnológico y de Estudios Superiores de Monterrey (Tec), N.L.,
Mexico

Distinguished Professor Emeritus, UC Irvine, MEA
Entrepreneur in Residence at AMDI
NAI Fellow, Academia Mexicana de Ciencias

ABSTRACT

Limit of detection (LOD), speed and cost for some of the most important diagnostics tools for COVID-19 i.e., lateral flow assays (LFA), enzyme-linked immunosorbent assay (ELISA) and Polymerase Chain Reaction (PCR) all benefitted from both the financial and regulatory support brought about by the pandemic. Before COVID-19, LFA was the fastest and least expensive but came with the poorest limit of detection (LOD). The slowest, most expensive but with the best (lowest) LOD was PCR. In between those two extremes, in terms of cost, LOD and speed, was an ELISA. Today, through the “COVID-19 accelerator effect” there are point of care (POC) reverse transcriptase quantitative PCR (i.e., RT-qPCR) COVID-19 tests on the market that provide sample to answer in under 20 minutes, while retaining the same very low LOD but at a lower cost [1]. There are even POC PCR tests under development that come in at less than 10 minutes: beating both LFA and ELISAs in terms of time and LOD [2]. Although RT-qPCR has gained the most in overall performance, signal-amplified POC LFAs are possible now with an LOD that rivals that of an ELISA.

However, implementing the next generation PCR equipment in point-of-care settings, remains very challenging because of difficulties in reaching a 10 minute or below sample to answer time, instrument complexity and cost. In this work, we discuss the engineering challenges involved in the development of high-speed microfluidic PCR equipment. To guide this review/comparison of PCR advances we introduce three parameters. The first one is the overall sample to answer time (t), the second is called lambda (λ) and is a measure of the degree to which stochastic effects interfere with obtaining analytical results and thereby setting the minimal number of copies required per volume. The third parameter gamma (γ), introduced first by Dong et al [3], is the ratio of thermal cycling time (in min) to the heat cycled sample volume (in mL). It describes the trade-off between the speed of the PCR system and the desired level of sensitivity. It can be interpreted as a system efficiency: the most efficient system heat cycles the largest amount of sample in the smallest amount of time.

With these three criteria in mind, we set out to suggest designs for an optimized POC reverse transcriptase (rt) quantitative qPCR or rt-qPCR system. Applications of RT-qPCR include quantifying gene expression levels, and detecting pathogens such as viruses. The aim of this specific POC RT-qPCR system is to provide sample to answer in ten minutes or less for a respiratory pathogens panel, with an LOD of 500 copies/mL and the capability to multiplex (8 chambers) while remaining portable and low cost.

References

- [1] Tsang, Hin Fung, Wai Ming Stanley Leung, Lawrence Wing Chi Chan, William Chi Shing Cho, and Sze Chuen Cesar Wong. *Performance Comparison of the Cobas® Liat® and Cepheid® GeneXpert® Systems on SARS-CoV-2 Detection in Nasopharyngeal Swab and Posterior Oropharyngeal Saliva*. Expert Review of Molecular Diagnostics **21**(5) (2021) 515–18.
- [2] Buckland, Justin, Tom Jellicoe, Alex Stokoe, And Amaru Araya-Williams. *Variable temperature reactor, heater and control circuit for the same*. Patent Application, (2020).
- [3] Dong, Xiaobin, Luyao Liu, Yunping Tu, Jing Zhang, Guijun Miao, Lulu Zhang, Shengxiang Ge, Ningshao Xia, Duli Yu, and Xianbo Qiu. *Rapid PCR Powered by Microfluidics: A Quick Review under the Background of COVID-19 Pandemic*. Trends in Analytical Chemistry **143** (2021) 116377.

BIOGRAPHY



Before joining Tec de Monterrey (Tec) (<https://tec.mx/en/our-faculty/eic/marc-j-madou>) as a Distinguished Professor and part time Entrepreneur in Residence at Autonomous Medical Incorporated (AMDI) (<https://amdilabs.com/team/>), Marc Madou was a Distinguished Professor and Chancellor's Professor in Mechanical and Aerospace Engineering (MEA) at UC Irvine (where he is a Distinguished Professor Emeritus now) before that he was Vice President of Advanced Technology at Nanogen in San Diego. He specializes in the application of miniaturization technology to chemical and biological problems (BIO-MEMS). He is the author of several books in this burgeoning field he helped pioneer both in Academia and in Industry. He founded several micromachining companies and has been on the board of many more.

Dr. Madou has worked with research teams in Mexico, India, Malaysia, South-Korea, Canada, and Germany. Many of his students became well known in academia and through successful MEMS start-ups. Madou was the founder of the SRI International's Microsensor Department, founder, and President of Teknekron Sensor Development Corporation (TSDC), Visiting Miller Professor at UC Berkeley and Endowed Chair at the Ohio State University (Professor in Chemistry and Materials Science and Engineering). He is the author of the three editions of "Fundamentals of Microfabrication," an introduction to MEMS and NEMS. The books have become known as the "bible" of micromachining. Madou has more than 350 peer-reviewed journal papers and conference proceedings, more than 200 plenary/invited talks in the last 10 years, 8 books, 25 book chapters and 27 patents. Dr. Madou has an h-index of 91 (as of October 2, 2023) and is considered the pioneer of two research fields that are now being pursued worldwide i.e., Carbon Micro- and Nanofabrication (C-MEMS and C-NEMS) and Compact Disc Fluidics (CD-Fluidics) for Molecular Diagnostics. Madou is among the few top contributors to chemical/biomedical applications of micro and nanofabrication ranging from novel sensors to CD-based microfluidic systems. The CD technology has resulted in at least 4 commercial companies (including GenePoc, Samsung-Nexus, Sensor Kinesis Corporation now AMDI and POC Medical Systems), the Carbon-MEMS technology he also pioneered, today has resulted in two companies (Enevate and Cence - both founded by Madou). The largest company he founded is Enevate Corporation that employs over eighty people, raised more than 200 Million dollars and is profitable today. Enevate Corporation is a leading advanced Lithium-ion (Li-ion) battery company with its global headquarters in Irvine, CA.

Distinguished Professor
Instituto Tecnológico y de Estudios Superiores de Monterrey (Tec)
Av. Eugenio Garza Sada 2501 Sur, Tecnológico, 64849 Monterrey, N.L., Mexico
Direct: 949 981 5672 (mobile)
E-mail: mmadou@tec.mx
<https://tec.mx/en>

Entrepreneur in Residence
Autonomous Medical Devices Inc.
3511 W Sunflower Avenue
Santa Ana, CA 92704
Direct: 949-981-5672
E-mail: marcmadou@amdilabs.com
www.amdilabs.com

Distinguished Emeritus Professor, UC Irvine, Department of Mechanical and Aerospace Engineering
NAI Fellow
Academia Mexicana de Ciencias
Direct: 949 981 5672 (mobile)
E-mail: mmadou@uci.edu
<https://uci.edu/>

THERMAL SCANNING PROBE LITHOGRAPHY (T-SPL): GRAYSCALE NANOENGINEERING APPLIED TO 2D MATERIALS.

Juergen Brugger, Berke Erbas, Xia Liu, Giovanni Boero

Microsystems Laboratory, Institute of Micro and Electrical Engineering School of Engineering, Ecole Polytechnique Fédérale de Lausanne (EPFL), 1015 Lausanne, Switzerland
Email: juergen.brugger@epfl.ch

ABSTRACT

While nanolithography has historically focused on downscaling, there is now a growing interest in grayscale nanolithography for introducing or enhancing functionality in micro- and nanodevices through the creation of micro- and nanoscale grayscale topographies with multiple depth levels. Interference lithography and grayscale electron beam lithography are commonly used techniques to produce complex surface topographies, but have spatial resolutions limited to tens of nanometers due to diffraction and electron scattering limitations. As an emerging technique, single-digit nanometer spatial resolution and sub-nanometer depth control for grayscale nanofabrication are achieved by thermal scanning probe lithography (t-SPL), but it is limited to shallow depths [1]. t-SPL has been successfully implemented for sub-10 nm silicon nanopatterning [2], nanofluidic devices for precise particle separation [3], and sinusoidal gratings for enhanced optical diffraction [4]. However, the performance and efficiency of devices are constrained by the limited depths and aspect ratios achievable with scanning probes. Charge-free writing on non-conventional substrates is another asset of t-SPL. Recently, we have shown the use of thermo-mechanical indentation of heated nanotip to strain 2D materials (2DMs) placed on top of a PPA layer [5]. This approach enables deterministic strain engineering of 2DMs, allowing for the modification of their electrical and optical properties and enhancing the performance of integrated devices. However, achievable strain in this approach is limited by the depths of indentations (up to 0.06) and underlying PPA, which could degrade over time, is not robust enough for use in devices such as field effect transistors and sensors.

Here, we combine t-SPL with dry etching to overcome the limitation in patterning depth, resulting in a significant increase in the aspect ratio of grayscale nanopatterns created on thermally-sensitive polyphthalaldehyde (PPA) resist when transferred into SiO₂ layers (Fig. 1a). First, we create rectangular and sinusoidal nanopatterns by t-SPL on PPA. Then, the aspect ratios of the “shallow” polymer patterns are amplified up to 10 times in a dry etch process when transferred into the underlying SiO₂ dielectric layer using CHF₃/SF₆ plasma (50/10 sccm), without causing additional surface roughness. The highest SiO₂ to PPA etch selectivity, which is 3.3:1, is reported for binary patterns using C₄F₈/He/H₂ plasma, but this resulted in a 7.7-fold increase in RMS surface roughness [6]. After dry etching process presented in this work, the surface roughness of the grayscale nanostructures undergoes the same level of amplification as the structures themselves (Fig. 1b). This aspect ratio amplification is achieved without any distortion of the original shapes, such as sinusoidal patterns, in processes providing up to 5 times amplification in depth profiles. Deformations in the sinusoidal shapes begin to appear for pattern transfer resulting in amplifications larger than 5 times (See Fourier transforms of the measured topographies in Fig. 1c). As shown in Fig. 2, surface topography characterization on PPA and SiO₂ confirms 5 times amplification in depth profiles of rectangular and sinusoidal nanostructures (400 nm pitch with 10, 20 and 30 nm depths). We intend to use these structured dielectric surfaces as a platform to induce local strain in atomically thin 2DMs to be reported at the conference. As increased aspect ratios in sinusoidal patterns result in higher strain [5], we aim to achieve increased and deterministic local straining of 2DMs with precise nanolithography. This technique for the fabrication of the high aspect ratio and smooth grayscale dielectric nanostructures presented in this work has the potential to open new opportunities in photonic and nanoelectronics applications.

Keywords: scanning probes, nanopatterning, grayscale, 2D material, strain engineering

References

- [1] A. W. Knoll et al., *Advanced Materials* **22** (2010) 3361-3365.
- [2] Y. K. Ryu Cho et al. *ACS Nano* **11** (2017) 11890–11897.
- [3] M. J. Skaug et al., *Science* **359** (2018) 1505–1508.
- [4] N. Lassaline et al., *Nature* **582** (2020) 506–510.
- [5] X. Liu et al., *Nano Letters* **20** (2020) 8250-8257.
- [6] Y. Lisunova et al. *Microelectronic Engineering* **180** (2017) 20–24.
- [7] B. Erbas et al. *ChemRxiv* (2023)

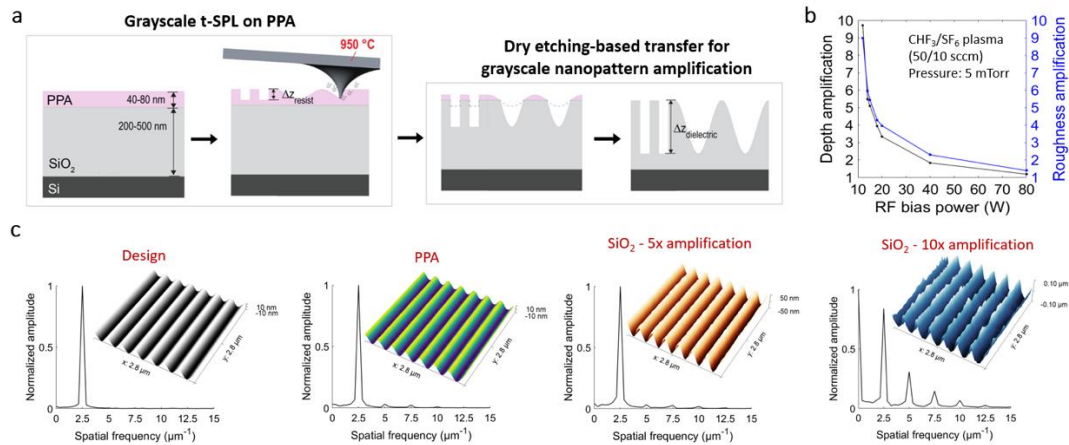


Figure 1. (a) Cross-sectional illustration of aspect ratio amplification for grayscale nanopatterns. The vertical amplification ($\Delta z_{\text{dielectric}}/\Delta z_{\text{resist}}$) results from the difference of etch rates between the PPA resist and SiO₂ in CHF₃/SF₆ plasma. Images are not to scale. (b) Effect of RF bias power in the reactive ion etching process on depth amplification and the corresponding surface roughness amplification after dry etching. (c) Fourier transforms of grayscale design, the measured topographies on PPA and on SiO₂ dielectric layers after 5 times and 10 times depth amplifications. Fourier transforms are obtained along 140 lines on sinusoidal nanopatterns and then averaged.

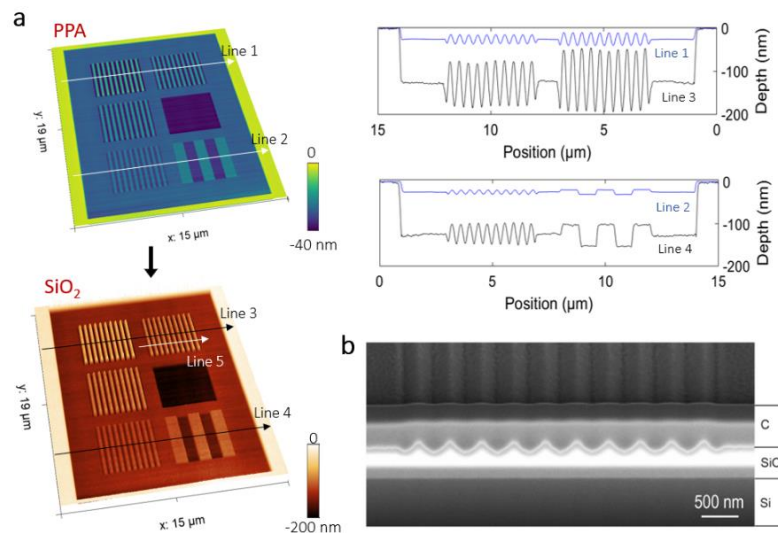


Figure 2. (a) AFM images and surface profile comparison of the nanostructures on PPA after t-SPL and SiO₂ after dry etching resulting in 5 times amplification in depth profiles. (b) FIB milled cross-sectional SEM image of sinusoidal nanostructures fabricated on SiO₂, corresponding to Line 5. 54° tilt corrected image.

BIOGRAPHY



Juergen Brugger is a Professor of Microengineering at the Swiss Federal Institute of Technology Lausanne (EPFL). Previously he was at the MESA Research Institute of Nanotechnology, University of Twente, The Netherlands, at IBM Zurich Research Laboratory, and at Hitachi Central Research Laboratory, in Tokyo, Japan, where he mainly worked on parallel scanning probe systems. He received a M.Sc. in Physical-Electronics and a Ph.D. degree from Neuchâtel University, Switzerland. Research in his laboratory focuses on various aspects of MEMS, nanotechnology, printing and self-assembly. Juergen Brugger is Fellow of the IEEE and the 2022 MNE Fellow. In 2017 he was awarded an ERC AdvG in the field of advanced micro-manufacturing.

Molecular Simulation of Conduction in Nanocomposite Insulator Interfaces

Nick Quirke

Department of Chemistry, Imperial College

301G Molecular Sciences Research Hub, London, W12 OBZ, UK

State Key Laboratory of Electrical Insulation and Power Equipment, Xi'an Jiaotong University,

28 Xianning West Road, Xi'an 710049, Shaanxi, China

ABSTRACT

Molecular Dynamics (MD), Monte Carlo, Lanczos and Density Functional methods (DFT), here called Molecular Simulation (MS), provide insight into electrical insulation and dielectric phenomena that cannot be obtained from other sources. While experiment is vital to electrical engineering, MS offers information at a molecular level, providing a window onto fundamental process which underlie laboratory work. The work of my group has elucidated the connections between fundamental properties such as electron affinity, band gaps, molecular structure and voids and observables such as electron trapping and heat conduction and the resultant I(V) characteristics and thermal transport, providing experimentalists with a better understanding of insulation and dielectric phenomena.

1. INTRODUCTION

In many branches of science and engineering, molecular simulation techniques are an integral part of modern research programmes. They can provide a theoretical basis upon which to interpret experimental results as well as a tool for discovery in their own right. For example, computer simulations can explore the properties of 'perfect' materials free from chemical and morphological contamination to establish a best case scenario [1]. Once the relationship between the simulated and experimental systems is established, the simulation can be used to explore the effects of changing both external (pressure, temperature, density, etc.) and internal (composition, morphology, defect structure, etc.) variables. Detailed reviews can be found in our previous work [1,2] and that of others [3,4,5]

2.1. ALL ELECTRON METHODS FOR ELECTRON TRAPPING

In this subsection we discuss the use of DFT methods to describe electron trapping in PE and at interfaces relevant to nanocomposite materials. Following validation [6] of DFT methods we employed the LUMO to study interfaces relevant to composite materials based on PE [7]. We have used ab initio molecular dynamics and density-functional theory calculations at the B3LYP/6-31G** level of theory to evaluate the energy and localisation of excess electrons at a number of

representative interfaces of polymer nanocomposites. These modelled interfaces are made by combining liquid water and amorphous slabs of polyethylene and silica. The walls of the amorphous silica slabs are built with two surface chemistries: Q4 or fully-dehydroxylated and Q3/Q4 or partially hydroxylated with a silanol content between 1.62 and 6.86 groups per nm². Our results indicate that in silica/polyethylene systems an excess electron would sit at the interface with energies between -1.75 eV with no hydroxylation and -0.99 eV with the highest silanol content. However, in the presence of a free water film, the chemistry of the silica surface has a negligible influence on the behaviour of the excess electron. The electron sits preferentially at the water/vapour interface with an energy of minus a few tenths of an eV (figure 1), moving from an initial site in the silica interface after 7 ps. Note the variation of the LUMO with time, especially after 7 ps, when the electron sits in its final position, the LUMO varies between -1 and +0.5. Clearly the moisture content in a wet polymer nanocomposite has a profound influence on the electron trapping behaviour as it produces much lower trapping energies and a higher excess-electron mobility compared to the dry material. In addition to freeing otherwise trapped electrons, there is the contribution (at least at room temperature) of the natural self-ionisation of water [8].

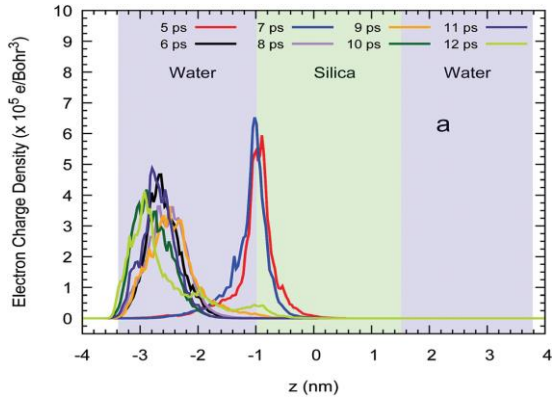


Figure 1a: Average profile of the LUMO charge density across the z direction [7]

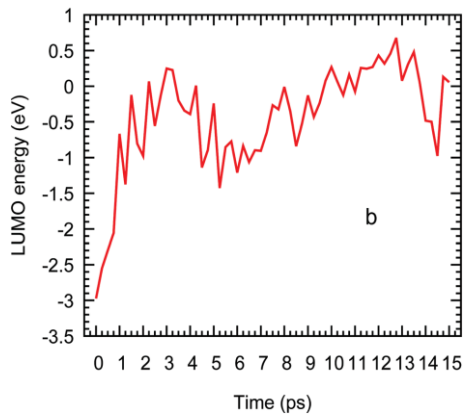


Figure 1b: The energy of this orbital vs. the ab initio simulation time [29]

2.2. TWO-TEMPERATURE NONEQUILIBRIUM MOLECULAR DYNAMICS FOR HEAT CONDUCTIVITY [9]

Thermal transport through model copper-polyethylene interfaces was studied using two-temperature nonequilibrium molecular dynamics. This approach treats electronic and phonon contributions to the thermal transport in the metallic region (Copper), but only phonon mediated transport is assumed in the polymer (PE). Results are compared with nonequilibrium molecular dynamics simulations of heat transport in which only phonon contributions are incorporated. The influence of the phase of the polyethylene component (crystalline, amorphous, and lamella) and, where relevant, its orientation relative to the metallic interface structure was explored. These computational studies suggest that the thermal conductivity of the metal-polymer interface can be more than 40 times greater when the polymer chains of the lamella are oriented perpendicular to the interface than the situation when the interface is formed by an

amorphous polymer or a crystalline polymer phase in which the chains orient parallel to the interface

Table

PE structure	$(G_{ep}\kappa_p)^{-1/2}$	R_{ep}	R_{pp}	κ_I	κ_I^{MD}
Lam- \perp	0.77×10^{-3}	0.62×10^{-3}	3.35×10^{-3}	252	316
Amo	0.74×10^{-3}	0.67×10^{-3}	5.52×10^{-3}	162	200
Xtl- \parallel	1.0×10^{-3}	0.74×10^{-3}	5.4×10^{-3}	163	204

Table: Components of the interface or Kapitza resistance, $RI = R_{ep} + R_{pp}$, in $m^2K(MW)^{-1}$, interface conductance, $\kappa_I = 1/RI$, in $MWm^{-2}K^{-1}$. [9].

From the results summarized in the table, the interface resistance is dominated by the contribution to energy transfer due to phonon-phonon interactions, R_{pp} , across the interface.

It is interesting to note that the calculated interface conductances reported in the table suggest that the phonon-only result, κ_I^{MD} , is some 25% larger than the interface conductance, κ_I , computed incorporating the influence of electron-phonon coupling using the TTM-MD approach. This arises due to the finite, approximately constant, electron-phonon thermal interface resistance.

3. CONCLUSION

Introducing interfaces such as hydroxylated silica/PE leads to major changes in the electron trapping behavior with free electrons localising at the silica /vacuum interface for zero silanols at the surface of the silica, but with increasing silanol concentration they move to the silica/pe interface with trapping energies between +1.75 eV for zero silanol concentration to +0.99 eV for a surface silanol concentration of 6.86 nm^{-2} . These are very deep traps with very long lifetimes. The situation changes radically however in the presence of water. For a model silica/water interface, the chemistry spontaneously produces a silanol concentration of 1.62 nm^{-2} in the first 7 ps which causes the electron to move to the water phase and sit in the interface (figure 3a) with a fluctuating trap energy of $0.27 \pm 0.53 \text{ eV}$ (figure 3b) taken over 4ps to 15 ps. This behavior is very similar to an excess electron at a water/vacuum interface which leads us to conclude that in the presence of water the detailed chemistry of the silica interface has little influence on an excess electron. Given that the fluctuations in the trap energy are so large, including times when the trap energy is

negative we must expect that this electron would be very mobile on a timescale of ps. In conclusion, any excess electrons trapped in silica or at a silica/pe interface would be released in the presence of water. The TTMD simulations of the Cu/PE interface suggest that the phonon contribution to the thermal conductivity of the copper region can be increased by as much as a factor of three when coupling between the electrons and phonons in the metal region is incorporated. This, combined with the explicit inclusion of the purely electronic component of the thermal transport in the metal region, can lead to a substantial increase in the heat flux promoted by the interface while maintaining a constant temperature drop.

These simulation results have important implications for designing materials that have excellent electrical insulation properties but can also be highly effective in heat conduction.

ACKNOWLEDGMENT

I would like to acknowledge the contribution of my students, postdocs and colleagues to this work.

REFERENCES

- [1] K. E. Gubbins and N. Quirke, *Industrial Applications of Molecular Modeling*, Gordon and Breach, London, UK, (1996).
- [2] Y. Wang, K Wu, D. Cubero, and N. Quirke, *Molecular Modeling and Electron Transport in Polyethylene*, IEEE Transactions on Dielectrics and Electrical Insulation, **21**(4) (2014) 1726-1734.
- [3] D Frenkel and B. Smit, *Understanding Molecular Simulation: From Algorithms to Applications*, Academic Press, London, UK, (2002).
- [4] M. P. Allen and D. J. Tildesley, *Computer Simulation of Liquids*, Oxford Science, Bristol, UK, (1994)
- [5] R. M. Martin, *Electronic Structure: Basic Theory and Practical Methods*, Cambridge University Press, UK, (2004).
- [6] Fernan Saiz, David Cubero and Nick Quirke, *The excess electron at polyethylene interfaces*, Phys.Chem.Chem.Phys., **20** (2018) 25186.
- [7] Fernan Saiz, Nick Quirke, *The excess electron in polymer nanocomposites*, Physical Chemistry Chemical Physics, **20** (2018) 27528
- [8] I Hosier, A Vaughan, N Quirke, *Electrical Conductivity of Waxes as Model Systems for Polyethylene: Role of Water*, J. Appl. Polym. Sci., **137** (2019) 48765
- [9] Yuanyang Ren, Kai Wu, David F. Coker, and Nick Quirke, *Thermal transport in model copper-polyethylene Interfaces*, J. Chem. Phys. **151** (2019) 174708.

BIOGRAPHY



Nick Quirke is Professor of Chemical Physics at **Imperial College**, London. His group conducts theoretical research in the general area of nanomaterials with particular interest in their interaction with biological interfaces and with polymeric insulators. This fundamental research finds application in toxicology and in power engineering. He is a Fellow of the Royal Society of Chemistry, Editor-in-Chief of the international Journals, *Molecular Simulation*, and the *Journal of Experimental Nanoscience*. He received the 1998 Royal Society of Chemistry Medal for Thermodynamics and was Royal Society / Kan Tong Po Professor at the University of Hong Kong for 2003/2004. He was awarded the 2006 NSTI Fellow Award for Outstanding Contributions in Advancing Nanotechnology and in 2013 a Yangtze river professorship ship at Xi'an Jiaotong university and was appointed adjunct professor at BUCT. His career has included leadership positions in both academia and industry. He was Principal Research Associate at BP. From 2006 to 2011 he was Vice President and Principal of engineering and science, University College Dublin.

ADVANCED NEW SYSTEMS & DEVICES FOR SOLAR ENERGY CONVERSION

Lionel Vayssieres

International Research Center for Renewable Energy (IRCRES), Xi'an Jiaotong University, Xi'an, China
lionelv@xjtu.edu.cn

ABSTRACT

This decade is witnessing the widest consequences of man-made activities with worldwide environmental disasters at a record high. It is thus crucial to transition to novel societies where environmental, energy, and economic policies are no longer based on endless-growth financial models and fossil fuel technologies to decrease our environmental footprint and health impacts. The origin of this strong imbalance between human activities and the environment could be found in the endless-growth economic system in place in major countries worldwide as it inherently requires the use of endless cheap energy to be sustained, hence the massive use of coal and fossil fuels as energy sources for a more profitable energy return on energy invested, which might be good for the economy but not for our environment, health, and sustainable future. Technological innovations have always helped boost the economy numerous times throughout civilizations yet it must involve large-scale, clean, and cost-effective fabrication techniques and be based on efficient earth-abundant and easily recyclable materials. The transition to hydrogen-based energy and economy would be ideal as it produces zero carbon emission and hydrogen fuel cell powered cars and public transportations are now available worldwide. However, most of the hydrogen produced still comes from nonrenewable sources, made by steam reforming of methane which produces large amount of carbon dioxide. The most natural, cleanest and sustainable way to produce hydrogen at large scale is by solar water splitting^[1].

Our strategy is to fabricate earth-abundant and non-toxic devices consisting of oriented arrays of quantum rods/dots of high purity synthesized by aqueous chemical growth at low temperature without surfactant and with controlled dimensionalities and surface chemistry^[2] with intermediate bands for high visible-light conversion, band-structure edges optimized for stability against photocorrosion and operation conditions at neutral pH, low bias and no sacrificial agent.

Such characteristics, combined with the in-depth investigation of their size-dependent and interfacial electronic structure^[3] and electrical properties^[4] provide better fundamental understanding and structure-efficiency relationships for a cost-effective and sustainable generation of hydrogen from the two most abundant and geographically-balanced free resources available, the sun and seawater. An overview of the outcome of such a strategy is presented for oxides, nitrides, sulfides and semiconductor-molecular catalysts hybrids^[5], their physical characterization, photogenerated charge dynamics, dopant segregation and thermal processing effects^[1].

References

- [1] K.C. Bedin et al *J. Am. Ceram. Soc.* **106** (2023) 79; I. Rodriguez-Gutierrez et al *ECS J. Solid State Sci. Tech.* **11** (2022) 043001; J. B. Souza Jr et al *Appl. Phys. Lett.*, **119** (2021) 200501; Y. Chen et al *J. Mater. Chem. C*, **9** (2021) 3726; A. Tofanello et al *J. Appl. Phys.*, **128** (2020) 063103; A. Tofanello et al *APL Mater.*, **8** (2020) 040905; Y. Wei et al *Sol. Energy Mater. Sol. Cells*, **201** (2019) 110083; X. Guan et al *ACS Energy Lett.*, **3** (2018) 2230; X. Guan et al *J. Phys. Chem. C*, **122** (2018) 13797; J. Su et al *J. Phys. Chem. Lett.*, **8** (2017) 5228; J. Su et al *ACS Energy Lett.*, **1** (2016) 121; Y. Tachibana et al *Nat. Photon.*, **6** (2012) 511; C.X. Kronawitter et al *Energy Environ. Sci.*, **4** (2011) 3889
- [2] L.Vayssieres, *Adv. Mater.*, **15** (2003) 464; L.Vayssieres, *Int. J. Nanotechnol.*, **1** (2004) 1; L.Vayssieres, *Int. J. Nanotechnol.*, **2** (2005) 411; L.Vayssieres, *J. Phys. Chem. C*, **113** (2009) 4733; J. Lützenkirchen et al *Colloids Interfaces*, **4** (2020)39 ;
- [3] L.Vayssieres et al *Appl. Phys. Lett.* **99** (2011) 183101; *Adv. Mater.*, **17**, 2320; C.X. Kronawitter et al *Phys. Rev. B* **85** (2012) 125109; *Energy Environ. Sci.*, **7** (2014) 3100; *Nano Lett.* **11** (2011) 3855; *J. Phys. Chem. C* **116** (2012) 22780; *PhysChemChemPhys* **15** (2013) 13483; M.G. Kibria et al *Adv. Mater.* **28** (2016) 8388; K. Nie et al *Nano Energy* **53** (2018) 493; C.L. Dong et al *Chem. Eur. J.* **24** (2018) 18356.

- [4] J. Wang et al ACS Appl. Mater. Interfaces **11** (2019) 2031; J. Engel et al Adv. Func. Mater. **24** (2014) 4952; I. Rodriguez-Gutierrez et al Electrochim. Acta **308** (2019) 317; Appl. Phys. Lett. **119** (2021) 071602; K. C. Bedin et al Chin. J. Catal. **43** (2022) 1247
[5] T. Benko et al Catal. Sci. Technol. **11** (2021) 6411; Y. Wei et al Nano Res. **9** (2016) 156.

BIOGRAPHY



1995 PhD in Chemistry, Pierre et Marie Curie University, Paris, France.
Visiting scientists (Sweden, South Africa, USA, Switzerland, UK, Australia, Singapore, Japan, Germany, Brazil). Since 2012, full time High Talent Global Expert professor IRCRE co-founder and scientific director, Xi'an Jiaotong University, China
2014 Sanqin- & 2016 National Chinese Government Friendship Awards.
2016 American Ceramic Society Global Ambassador
2014-2022 Most cited Chinese researcher in Materials Science & Engineering
2020-2022 Top 2% World Scientists ranking (Top 0.18% in Nanoscience)

INVITED TALKS
***FUNDAMENTALS OF
NANOTECHNOLOGY***
(FON)

Density Functional Theory Analysis of H₂S Adsorption on Nitrogen-Doped Graphene

Takaya Fujisaki¹, Kei Ikeda², Aleksandar Tsekov Staykov³, Hendrik Setiawan⁴ and Yusuke Shiratori⁵

¹Faculty of Materials for Energy, Shimane University, Shimane 690-0823, Japan

²Institute for Materials Chemistry and Engineering and Integrated Research Consortium on Chemical Science (IRCCS), Kyushu University, 744 Motooka, Nishi-ku, Fukuoka, Japan

³International Institute for Carbon-neutral Energy Research(WPI-I2CNER), Kyushu University, 744 Motooka, Nishi-ku, Fukuoka, Japan

⁴Hydrogen Energy Systems, Graduate School of Engineering, Kyushu University, 744 Motooka, Nishi-ku, Fukuoka, Japan

⁵Department of Mechanical Science and Engineering, School of Advanced Engineering, Kogakuin University, 2665-1 Nakano-machi, Hachioji, Tokyo

Email: takaya.fujisaki@mat.shimane-u.ac.jp

ABSTRACT

Concerns about the depletion of fossil fuels and climate change caused by their consumption have created a need for alternative energy sources that are not dependent on fossil fuels. A power generation system combining biomass and fuel cells is expected not only to promote food production, but also to decarbonize economic activity. Methane produced from biomass through methane fermentation is used to generate electricity with solid oxide fuel cells (SOFCs). H₂S is produced during the methane fermentation process, and it is known that even a few ppm of H₂S reduce the power generation efficiency of SOFCs. These days, graphene-based structures known as pyridinic N and oxidized N have attract attention because they are in some biomass and can remove H₂S. This study analyzes their adsorption properties by density functional theory (DFT) to clarify which material is better for H₂S removal.

Fig. 1 indicates the analysis results by density functional theory, and the adsorption energy of pyridinic N is smaller than that of oxidized N, showing that pyridinic N is a better material for adsorbing H₂S than oxidized N[1].

Keywords: Fibers, carbon nanotubes, nanocomposite (less than 5 keywords)

Acknowledgements

This work was supported by JSPS KAKENHI (20KK0248).

[1] T. Fujisaki, K. Ikeda, A.T. Staykov, H. Setiawan, Y. Shiratori, RSC advances **12**(31) 19955-19964.

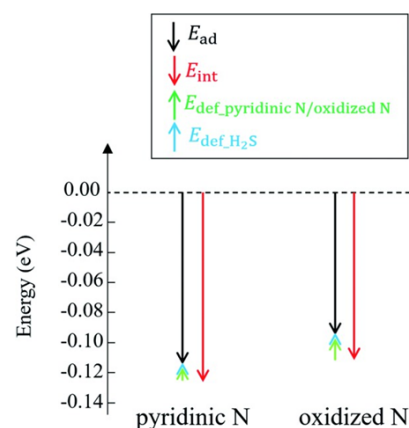


Fig. 1 Adsorption energy (E_{ads}) and interaction energy (E_{int}) between H₂S and pyridinic N/oxidized N. The deformation energies of pyridinic N ($E_{def_pyridinic\ N}$), oxidized N ($E_{def_oxidized\ N}$), and H₂S are also shown.

BIOGRAPHY



2019: Graduated from Kyushu University
 2021: Post-doc at Tohoku University
 2023: Assistant Prof. in Shimane University

MATERIALS STRUCTURE SEARCH USING DATA SCIENTIFIC TECHNIQUES

Ryo Maezono¹,

¹ School of Information Science, JAIST, Asahidai 1-1, Nomi, Ishikawa 923-1292, Japan.

Email: rmaezono@mac.com

ABSTRACT

The properties of a material originate from its atomic geometry. Therefore, the pursuit for novel materials properties reduces to the exploration of new geometries such as crystal structures. Given the structure of a material as input data, one can evaluate its properties through *ab initio* calculations [2]. Hence, the idea is to vary the trial input structure and search for novel structures that realize novel properties. This began with the initial efforts of randomly altering the input structure [1], but in recent years, techniques to update the input structure using data science methods to enhance search efficiency have been intensively studied. Implementations employing genetic algorithms to update input data have made significant progress. We are applying this technique to predict new crystal structures in ternary hydrides that achieve high T_c superconductors [3-6]. Using the same method, we collaborate with experimental researchers to predict new crystal structures under high pressure [7], and we have succeeded in synthesizing entirely new compounds that were predicted [8]. Parallel to the genetic algorithm, there is the particle swarm algorithm, by which we successfully predicted a new crystal phase with unknown hydrogen crystal structures under high pressure [9].

Keywords: *Ab initio*, crystal structure, superconductors, genetic algorithm, particle swarm algorithm

References

- [1] C.J. Pickard, R.J. Needs, Phys. Rev. Lett. **97** (2006) 045504.
- [2] R. Maezono, *Ab initio Calculation Tutorial: For Materials Analysis, Informatics and Design*, Springer Nature, (2023)
- [3] P. Song, H. Zhufeng, P.B. de Castro, K. Nakano, K. Hongo, Y. Takano, R. Maezono, Chem. Mater. **33** (2021) 9501.
- [4] P. Song, H. Zhufeng, P.B. de Castro, K. Nakano, Y. Takano, R. Maezono, K. Hongo, Adv. Theory Simul, (2022) 2100364:1-10.
- [5] P. Song, H. Zhufeng, K. Nakano, K. Hongo, R. Maezono, Mater. Today Phys. **28** (2022) 100873.
- [6] P. Song, H. Zhufeng, P.B. de Castro, K. Nakano, K. Hongo, Y. Takano, R. Maezono, J. Phys. Chem. C, **126** (2022) 2747.
- [7] P. Song, M. Khawaguch, Y. Masubuchi, K. Nakano, R. Maezono, K. Hongo, Comput. Mater. Sci. **226** (2023) 112202.
- [8] D. Kato, P. Song, H. Ubukata, H. Taguro, C. Tassel, K. Miyazaki, T. Abe, K. Nakano, K. Hongo, R. Maezono, H. Kageyama, Angew. Chem. Int. Ed. **62** (2023) e202301416:1-7.
- [9] T. Ichibha, Y. Zhang, K. Hongo, R. Maezono, F.A. Reboredo, Phys. Rev. B, **104** (2021) 214111.

BIOGRAPHY



Dr. Ryo Maezono (PhD/Applied Physics) is a full Professor at JAIST (Japan Advanced Institute of Science and Technology), school of Information Science, working on Simulation Science Research area. He got his BSc (1995) and PhD (2000) in Applied Physics at Tokyo University, majoring condensed matter theory working on the phase diagrams of magnetic oxides. He was a JSPS fellow (Tokyo University/1999-2000), working on the magnetic properties of oxides. He got a postdoctoral position at Cavendish Laboratory, Cambridge University (EPSRC fellow/2000-2002), and moved to NIMS (National Institute of Materials Science, Japan), as a tenure researcher (2001-2007). In 2007, he moved to JAIST and now a tenure faculty there. Since his postdoc in Cambridge, he has worked on Diffusion

Monte Carlo (DMC) electronic structure calculations using massive parallel computations. He has published several DMC works using world top class huge parallel calculations, exploring cutting-edge of numerical quantum many-body problem. As an expert of DMC method, he has given several lectures on many-body problems at Osaka University, Yokohama National University Kanazawa University etc., outside of JAIST. As a computer scientist, he has contributed also to the education of simulation science for high school students, which contents are published in his books (ISBN:978-4627818217, 978-4627170315, 978-9819909186, 978-4627170322). As a researcher of computational materials science, he leads several industrial collaborations with companies (Toyota-Motor/Sumitomo-Mining/Shin-Etsu Chemicals/Asahi grass Inc./Denso Inc./Morita Chemical Inc.), as well as those with experimental synthesis community in inorganic Chemistry.

THE EVOLUTION IN CHARACTERISTICS OF GERMANENE UPON HYDROGENATION

Hanh Thi-Thu Tran^{*1}, Hoang Huy Mai¹, Chien Mau Dang²

¹Laboratory of Computational Physics, Faculty of Applied Science, Ho Chi Minh City University of Technology (HCMUT), VNU-HCM, Ho Chi Minh City, Vietnam

²Institute for Nanotechnology, Vietnam National University, Ho Chi Minh City, Vietnam

Email: thuhanhsp@hcmut.edu.vn, hoang.mai159w@hcmut.edu.vn, dmchien@vnuhcm.edu.vn

ABSTRACT

The hydrogenation of the two-dimensional Ge system is studied based on density functional theory. Hydrogen atoms adsorbed onto the two-dimensional Ge surface were recorded to exist at the high warp peak (T1), and the low warp peak (T2) positions. Model optimization is obtained at point k with (5x5x1) MP. When releasing all hydrogen onto the T1 and T2 peak positions, the adsorption energies of all system are calculated. The adsorption site T2 is shown to be the site with the least stable binding ability and the easiest to escape from the 2D Ge surface.

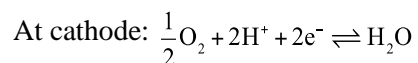
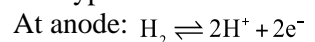
Keywords: Germanene, hydrogenation, adsorption energy, density functional theory.

INTRODUCTION

The continuous increase in world population and economic growth in developing countries is one of the many causes of increased energy demand as well as increased greenhouse gas emissions. Current technological challenges are how to ensure an adequate supply of energy needs while still keeping greenhouse gas emissions such as CH₄, N₂O, especially CO₂ low enough not to affect the natural environment. The main cause of global climate change is believed to be CO₂ gas, which is a direct product emitted by the use of fossil energy in industry, mechanics, and vehicles [1, 2]. In the early years of the 20th century, the concentration of CO₂ in the air reached 280 ppm and in 2005 that number was 370 ppm. The growth rate of CO₂ concentration in the environment over a decade (1995-2005) is about 1.9 ppm per year, the highest in any decade in the past 200 years [3]. Currently, the new energy source that can satisfy energy needs without affecting the world's environment is hydrogen.

Fuel cells can be used as an alternative energy source to fossil fuels because they produce oxygen and water as by-products. There is a lot of research on manufacturing and developing models of fuel cells, but one thing is inevitable: these fuel cells mostly need hydrogen for fuel. Storing hydrogen for fuel cells is not easy. It is a challenge to put fuel cells to use safely and effectively. In fuel cells, the hydrogen

combustion reaction is divided into the following two types of reactions:



Hydrogen, discovered in 1776 by Henry Cavendish, is the most common element in the universe but does not occur in air, being 14.4 times lighter than air [4]. The highest thermal efficiency of hydrogen is 141.8 KJ/g, much higher than other fuels such as gasoline (47.5 KJ/g), diesel (47.5 KJ/g), and methane (55.5 KJ/g) [5]. This means that the same amount of hydrogen produces more heat and energy than other fuels of the same mass, for example, 1 kg of hydrogen produces the same amount of energy as 2.1 kg of natural gas. fuel or 2.8 kg of gasoline [5]. At low temperatures hydrogen solidifies at -262 °C and has a density of 70.6 kg/m³ and in gas form has a density of 0.089 kg/m³ at 0 °C and a pressure of 1 bar.

It can be seen that hydrogen is very sensitive to changes in temperature and pressure, with constant pressure the density of hydrogen increases when the temperature decreases, and vice versa with constant temperature the density increases when pressure decreases. Hydrogen storage simply reduces the huge volume of hydrogen gas, 1 kg of hydrogen gas at room temperature, and atmospheric pressure takes up about 11 m³ of volume, to increase the density, it is necessary to compress the hydrogen, reducing

the heat. hydrogen concentration below the critical point or by other storage methods [6].

Besides the problem of finding how to produce hydrogen in the most efficient and economical way, transportation and storage are important issues of concern. Hydrogen storage known today is divided into two large categories: physical storage methods and chemical storage methods. In chemical adsorption, hydrogen molecules split into two independent atoms, then move into the material and form a chemical bond with that material. In this study, we study the adsorption of hydrogen onto 2D germanene material.

Germanene was first synthesized by M.E. Dávila and colleagues in 2015 on Ag(111) substrate [7]. Like graphene, germanene consists of Ge atoms arranged in a flat, hexagonal honeycomb-shaped sheet. Germanene has a similar structure to silicene but has a larger distance between two atoms and has higher buckling. The length between two Ge atoms is 2.43 Å, the warping is about 0.68 Å [8].

There have been several published studies on the study of hydrogenation on germanene material, the first is by Sasfan Arman Wella [9] on the energy band structure of the hydrogen drop model, the second is by Lei Liu [10] on phonon spectra. The common point of these two research papers is that they use a change in the lattice constants for each H/Ge model system, showing that their germanene model is a free model. For this article, the Ge models have fixed lattice constants, although the Ge atoms are still flexible, leading to different results between this work and two previous studies on hydrogen adsorption ability and structure.

CALCULATION METHOD

SIESTA calculation

Strong developments in computer science in recent years have allowed us to simulate materials at the nanoscale, with the study of materials at the subatomic level. There are two commonly used quantum simulations: first principles and semi-empirical methods [11, 12]. Density functional theory (DFT) is a part of first principles, a first principle method of solving the Schrödinger equation for many-particle systems, this method does not require experimental data but only needs to rely on elements in the chemistry table [11]. This method allows accurate calculations of electronic structures and properties.

SIESTA, Spanish Initiative for Electronic Simulations with Thousands of Atoms, is a computer implementation program that performs electronic structure calculations and molecular dynamics simulations in first principles. SIESTA is a first-principle simulation calculation software for materials. Using self-consistent field loops to solve the Kohn – Sham equation, commands are available using molecular dynamics methods to check the stability of the model. The software uses norm-preserving pseudopotentials, local density approximation, and generalized gradient approximation. SIESTA calculates the Brillouin zone discretization of Monkhorst – Pack, and uses atomic orbital basis sets such as DZ, SZP, and DZP. The study uses this software mainly because it is open source, free, and has been used by many reputable studies worldwide [13, 14].

Mesh-cutoff energy and k-point optimization methods

Optimizing the two k-point values and mesh-cutoff energy is absolutely necessary. The optimal run indicates that it is not necessary to use a large number of these two parameters for use. According to theoretical calculations, more k-points and mesh-cutoff energy will increase the accuracy of the system. But when a point of total energy convergence is reached, the k-point and mesh-cutoff energy values after this convergence point will show results that are very little different from those at the convergence point. Therefore, there is no need to use too many k-points and mesh-cutoff energy. Using many k-points and mesh-cutoff energy also makes the simulation process difficult, because the more it is, the more resources it takes up the computer to run, making the simulation time unnecessarily long. The process of optimizing the two parameters k point and cutting energy does not need to be sequential. In this study, k-point optimization was conducted when the mesh-cutoff energy was at 150 Ry (Figure 1). After finding the optimal k-point, this k-point value is used to optimize mesh-cutoff energy.

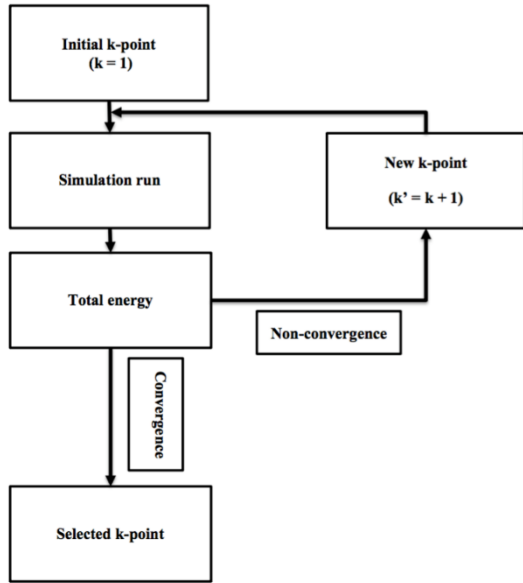


Figure 1. The k-point optimization procedure by converging the total energy.

Adsorption energy calculation

The adsorption energy was investigated to calculate the adsorption capacity of as much hydrogen as possible onto germanene. The adsorption energy of hydrogen onto the germanene surface is based on the following formula:

$$E_{\text{ads}} = E_{\text{germanene-nH}} - E_{\text{germanene}} - n_{\text{H}} E_{\text{H}}$$

where E_{ads} is the adsorption energy of hydrogen on the germanene surface, n_{H} is the number of hydrogen adsorbed, $E_{\text{germanene-nH}}$ is the total energy of the H/Ge system, $E_{\text{germanene}}$ is the energy of germanene surface, and E_{H} is the energy of one hydrogen atom.

Ge and H/Ge structure construction methods

The germanene model consists of 72 Ge atoms, with an initial unit cell containing 2 Ge atoms (a (6x6) supercell forming 72 atoms). Germanene has a structure similar to the two-dimensional graphene structure in the $P6_3mc$ hexagonal crystal system (Figure 2). This two-dimensional structure consists of one surface of Ge atoms placed in the (0,0,1) direction. Ge atoms are bonded together into a triangle with a non-planar structure, which means that between two Ge atoms, there is a buckling equal to $\Delta Z = 0.77 \text{ \AA}$, and the distance between two Ge atoms is $d(\text{Ge-Ge}) = 2.44 \text{ \AA}$ [15, 16]. The model was created in a vacuum with a periodic boundary, and the surface layer was separated from its periodic image by 30.8 \AA to avoid unnecessary interactions between the two Ge layers.

The lattice vector after being stabilized with the optimized k-point and mesh-cutoff energy parameters is:

$$\begin{pmatrix} 24.478880448 & -0.000045899 & 0.000032290 \\ -12.239482796 & 21.199307387 & -0.000033237 \\ 0.000014617 & -0.000008934 & 30.808766064 \end{pmatrix}$$

Hydrogen atoms are then dropped on the 2D Ge surface based on this lattice vector, with the distance between H and Ge atoms being $\Delta(\text{h-ge}) = 1.5 \text{ \AA}$ (Figure 3).

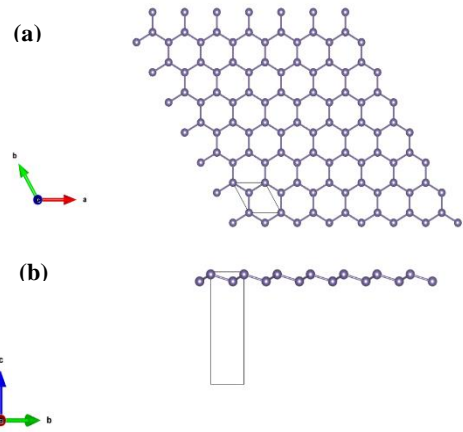


Figure 2. Germanene structure: (a) top view of the honeycomb structure, (b) side view of the buckling structure.

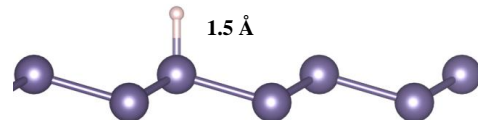


Figure 3. Bond length between hydrogen and germanene.

RESULT AND DISCUSSION

The hydrogen molecule is rechecked by SIESTA simulation. The result shows that the distance between two hydrogen atoms in molecule is 0.75 \AA , which is consistent with the experimental value [17].

The optimized k-point after converging the total energy for the germanene model is (5x5x1) (see Figure 4). Because the germanene system is a 2D surface, there is no need to discretely integrate the k-point on the z-axis to reduce the consumption of computer resources.

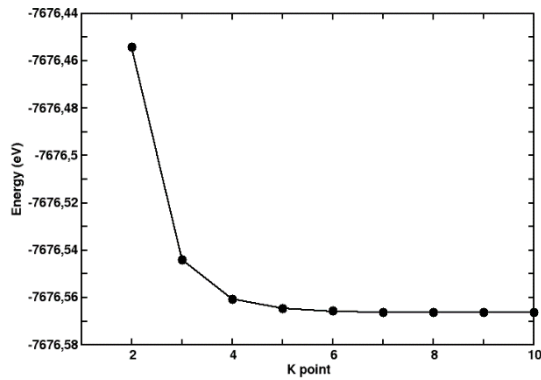


Figure 4. Optimize point k by converging the total energy.

For the configuration of hydrogen adsorption on the 2D germanene, the k -point parameter and the mesh-cutoff energy found in the germanene model are used. The H/Ge configuration is shown in Figure 5. After optimizing the Ge and H/Ge models, parameters such as bond length $d(\text{Ge-Ge})$, the angle between three Ge atoms (Ge-Ge-Ge), the bond length between Ge and hydrogen $d(\text{Ge-H})$, the angle between two Ge atoms and hydrogen atoms (Ge-H-Ge), the buckling ΔZ , and lattice constant (α) are determined and shown in Table 1.

Table 1. Lattice constant (α), bond length (d), buckling (Δ), and bond angle of the optimized model of germanene and its hydrogen adsorption.

	Ge model	H/Ge model
$d(\text{Ge-Ge}) \text{ \AA}$	2.46469	2.57014
$d(\text{Ge-H}) \text{ \AA}$		1.58736 (Top1) 1.69198 (Top2)
$\angle(\text{Ge-Ge-Ge})^\circ$	111.71580	105.06330
$\angle(\text{Ge-H-Ge})^\circ$		70.83560
$\Delta Z \text{ \AA}$	0.72556	1.02829
$\alpha \text{ \AA}$	24.47888	24.47888

The results show that when H is adsorbed on the Ge surface, the structure of 2D Ge is changed. Specifically, when H is adsorbed, the buckling increases and the distance between Ge atoms in the crystal lattice also becomes longer, while the angle between Ge atoms decreases. This proves that when there is adsorption of H, the properties of the 2D Ge model have changed.

CONCLUSION

Using density functional theory, the hydrogen adsorption on the 2D Ge is studied. The optimized k -point value of $5 \times 5 \times 1$ MP is found by

converging the total energy. When hydrogen is adsorbed onto the 2D Ge surface, the distance between Ge atoms is 2.57 \AA , the buckling is 1.03 \AA . The properties of the adsorption model are being further studied.

Acknowledges

We acknowledge Ho Chi Minh City University of Technology (HCMUT), VNU-HCM for supporting this study.

References

- [1] A. Bostrom, M. G. Morgan, B. Fischhoff, and D. Read, *What do people know about global climate change? 1. Mental models*, Risk Analysis, **14-6** (1994) 959-970.
- [2] R. J. Bord, R. E. O'connor, and A. Fisher, 'In what sense does the public need to understand global climate change', Public understanding of science, **9-3** (2000) 205-218.
- [3] M. J. Ring, D. Lindner, E. F. Cross, and M. E. Schlesinger, *Causes of the global warming observed since the 19th century*, Atmospheric and Climate sciences, **2-4** (2012) 401-415.
- [4] H. Cavendish, *XII. An account of some attempts to imitate the effects of the torpedo by electricity*, Philosophical Transactions of the Royal Society of London, **66** (1776) 196-225.
- [5] D. R. Lide, *CRC handbook of chemistry and physics*, CRC press, **85** (2004).
- [6] A. Züttel, *Hydrogen storage methods*, Naturwissenschaften, **91** (2004) 157-172.
- [7] M. E. Dávila, L. Xian, S. Cahangirov, A. Rubio, and G. Le Lay, *Germanene: a novel two-dimensional germanium allotrope akin to graphene and silicene*, New Journal of Physics, **16-9** (2014) 095002.
- [8] A. Jain, S. P. Ong, G. Hautier, W. Chen, W. D. Richards, S. Dacek, ... and K. A. Persson, *Commentary: The Materials Project: A materials genome approach to accelerating materials innovation*, APL materials, **1-1** (2013).
- [9] S. A. Wella, and Suprijadi *First principle calculation on electronic and magnetic properties of hydrogenated germanene*, Journal of Engineering and Applied Sciences, **10-18** (2015) 8250.
- [10] L. Liu, Y. Ji, and L. Liu, *First principles calculation of electronic, phonon and thermal properties of hydrogenated germanene*,

- Bulletin of Materials Science, **42-4** (2019) 157.
- [11] C. Fonseca Guerra, J. G. Snijders, G. T. Te Velde, and E. J. Baerends, *Towards an order-N DFT method*, Theoretical Chemistry Accounts, **99** (1998) 391-403.
- [12] G. Zhang, and C. B. Musgrave, *Comparison of DFT methods for molecular orbital eigenvalue calculations*, The journal of physical chemistry A, **111-8** (2007) 1554-1561.
- [13] P. Ordejón, E. Artacho, and J. M. Soler, *Self-consistent order-N density-functional calculations for very large systems*, Physical review B, **53-16** (1996) R10441.
- [14] J. M. Soler, E. Artacho, J. D. Gale, A. García, J. Junquera, P. Ordejón, and D. Sánchez-Portal, *The SIESTA method for ab initio order-N materials simulation*, Journal of Physics: Condensed Matter, **14-11** (2002) 2745.
- [15] A. Jain, S. P. Ong, G. Hautier, W. Chen, W. D. Richards, S. Dacek,... and K. A. Persson, *Commentary: The Materials Project: A materials genome approach to accelerating materials innovation*, APL materials, **1-1** (2013).
- [16] M. Ashton, J. Paul, S. B. Sinnott, and R. G. Hennig, *Topology-scaling identification of layered solids and stable exfoliated 2D materials*, Physical review letters, **118-10** (2017) 106101.
- [17] N. Furuya, and S. Koide, *Hydrogen adsorption on iridium single-crystal surfaces*, Surface Science, **226-3** (1990) 221-225.

BIOGRAPHY



Tran Thi Thu Hanh is a lecturer at the Ho Chi Minh City University of Technology (HCMUT), Vietnam National University, Ho Chi Minh City, Vietnam. She graduated with bachelor's and master's degrees from Voronezh State University-Russia, and a doctorate from Tokyo University-Japan. Her main area of research is computational physics using molecular dynamics and density functional theory methods. She focuses on studying the interaction, the hydrogen storage of fuel cells, and the electronic properties, structural deformation of 2D, 3D materials.

IMPROVING LENS-FREE MICROSCOPY IMAGE RECONSTRUCTION BY USING ALTERNATION OF INVERSE PROBLEM APPROACH AND DEEP LEARNING

R. Campagnolo, L. Hervé, D. C. Kraemer, O. Cioni, O. Mandula, M. Menneteau, S. Morales, C. Allier
CEA, LETI, MINATEC Campus, Technologies for Healthcare and Biology division, University.
Grenoble Alpes, F-38000 Grenoble, France
Email: raymond.campagnolo@cea.fr

ABSTRACT

A lens-free microscope is a minimalist setup performing in-line holographic measurements. Due to the absence of focusing optics, a reconstruction algorithm is needed to retrieve the sample image by solving the inverse problem. Usually, relying on gradient computation, an optimization method is used. However, the presence of local minima leads to unsatisfactory convergence when phase wrapping errors occur. To date, the occurrence of phase wrapping errors in the holographic reconstruction limits the application of lens-free imaging microscopy in live cell imaging. To overcome this issue, we propose a novel approach in which the reconstruction alternates between two processes, an inverse problem optimization and deep learning. We demonstrate the applicability of this approach in solving phase wrapping problem occurring with cells in suspension at large densities.

Keywords: lens-free microscopy, holographic reconstruction, deep learning

BIOGRAPHY



Raymond CAMPAGNOLO

70 years old, born on January 23rd 1953 in Sannois (Val d'Oise, France)
Married, two children.



CEA Grenoble
LETI/DTBS-DIR
17 rue des Martyrs
38054 Grenoble CEDEX 9
France

Education

In **1976**, **Engineer** graduated from Ecole Nationale Supérieure d'Electronique et Radio Electricité de Grenoble (France)

In **1980**, **Ph. D. degree of Doctor** from the Institut National Polytechnique de Grenoble (France)

Positions

1980-1989: research engineer on algorithms, hardware architecture and software design for Positron Emission Tomography Scanners for medical imaging at CEA-LETI. Principal scientist in image reconstruction and test software for first and second generation PET cameras. Field maintenance engineer of the scanners.

1989 - 1994: project manager of the 3D X-Ray imaging device, MORPHOMETRE project at CEA-LETI, using cone-beam image reconstruction from digital subtracted angiograms in collaboration with General Electric Medical Systems. Head of the support team for the two prototypes of 3D cameras.

1994 - 1998: project manager of Digital X-Ray Imaging System for Mammography and Full Field general purpose Radiography at CEA-LETI, he designed and developed a full field imaging device (40 cm x 40 cm) using scintillating screen and high-performance cooled CCD camera.

1998 - 2001: lab manager of the Electronic & Biology Laboratory at CEA-LETI, his team studied and developed dedicated instrumentation for fluorescent measurements in the field of DNA biochip and Lab-On-Chip using detection technologies for micro-capillaries.

2001 - 2006: associated manager of the joined team between CEA-LETI and the French company bioMérieux (World leader of microbiology bacterial identification and antimicrobial susceptibility testing system), the team applies micro-technology skills to Nucleic Acid amplification, detection and screening systems.

2006 - 2012: Program Manager in the field of Implantable Medical Devices at CEA-LETI in the **Microtechnologies for Biology and Healthcare Department (DTBS)**

2012 - 2015: Chief Scientist Officer at CEA-LETI in the **Microtechnologies for Biology and Healthcare Department (DTBS)**

2015 – 2023: Scientific Advisor at CEA-LETI in the **Microtechnologies for Biology and Healthcare Department (DTBS)** in the field of wearable medical devices

He holds 25 patents in the field of fluorescent detection technology (DNA chip and Lab-On-Chip), control of micro-systems for local drug delivery and molecular information in vivo capture.

Award

In 1982, he received the George Von HEVESY Prize for Nuclear Medicine for its contribution to the Time Of Flight Information to Positron Tomographic Imaging.

MATERIALS SCIENCE FOR COMPUTING DEVICES

Christophe Wyon

Univ. Grenoble Alpes, CEA-Leti, 38054, Grenoble,
FranceEmail: cwyon@cea.fr

ABSTRACT

This paper will highlight the paramount importance of materials science and engineering for the development of computing devices. It will address the deployment of logic integrated circuits from the conventional bulk CMOS to Gate-All-Around (GAA) architectures through FinFET and FD-SOI from a material scientist point of view. It will present the recent paradigm shifts in computing for reducing the power/energy consumption of computing systems through the deployment of novel concepts such as near-memory and in-memory computing. The later technology would require the development of new non-volatile memories such as ReRAM, PCRAM, MRAM, FeRAM, and ECRAM, which are all based on the peculiar properties of various thin and/or ultrathin films.

Keywords: Processors, Random Access Memories (RAM), Nano-electronics, In-memory computing

BIOGRAPHY



After a PhD thesis on the development of carbon thin films for solar photo-thermal energy conversion, Dr. Christophe Wyon has worked for CEA-Leti since 1984. He was firstly involved in the crystal growth of semiconductor, laser and scintillator materials. He managed laboratories dedicated to the development of FEOL CMOS processes, to physical characterization and failure analyses of microelectronic devices, and to the research of novel OLED microdisplays. Then, he worked for the French Ministry of Industry/Economy on preparing and launching very large national and European programs for the development of nanoelectronic devices. He is currently mainly involved in setting-up technology roadmaps for the European Components and Systems community.

INVITED TALKS
NANOFABRICATION TECHNIQUES
(NFT)

3D-BIOPRINTING TECHNIQUES FOR DEVELOPING THE BIOCHIP DNA SENSORS

Majid Monajjemi^{1,2,*}, Dung My Thi Dang^{1,2}, Fatemeh Mollaamin³, Chien Mau Dang^{1,2,*}

¹Institute for Nanotechnology, Community 6, Linh Trung Ward, Thu Duc City, Ho Chi Minh City, Vietnam;

²Vietnam National University Ho Chi Minh City, Ho Chi Minh City, Vietnam

³Department of Biology, Faculty of Science, Kastamonu University, Kastamonu, Turkey

ABSTRACT

Recently, the activity for tissue-chip (TC) model has gained great attention from scientists in the world. Powerful instruments for biomedical engineering researches including disease modeling, drug designing and nano-drug delivering, have been extremely investigated by researchers. This review highlights the important points and background of biochip development. Herein, we concentrate on applications of Lab Chips (LCs) instruments as a versatile tool for point of health care (PHC) applications. We also review current progress in various platforms towards biochip DNA sensors as an alternative to the general bio electrochemical sensors. The fundamental of optical sensing is generally based on the intercalation between glasses surfaces consisting of DNA with any kind of light such as absorption, fluorescence or reflectance that depends on the optical characteristics of the chemical agents of the matrix used. Recently, the situation of novel techniques employing optical fiber has progressed significantly, and we suggest highlighted remarks and future perspectives of these kinds of platforms for PHC applications.

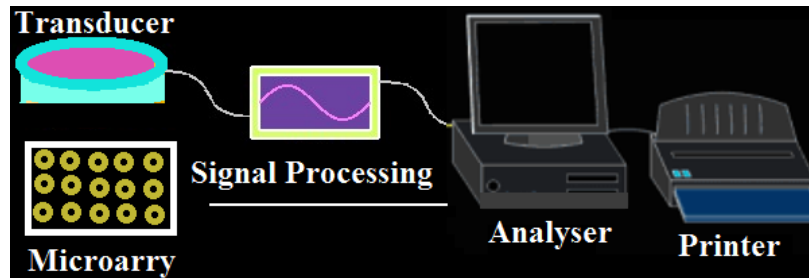
Keywords: Microfluidics; Biochips; System-on-chip; Point of health care; Lab Chips; DNA sensors; Ink-Jet

INTRODUCTION

1.1. Biochips as miniaturized laboratories

In cellular biochemistry, biochips use as miniaturized labs that are able to host a large amount of biological reactions. One of the most targets of using the biochips in human tissues is their effective and efficient screen of biological analyses with high applications from cancer diagnosis to detection of bio disease roots [1-4]. As instance, microfluidic biochips (MFB) with digital format are under designing for using in biomedical research [1, 5]. MFB consist of a collection of neighbor cells that are able to regulate for working as storage, operations and transporting droplets continuously. Microfluidic devices which are manufactured under Bio micro-electro-mechanical systems (BMEMS) are similar to DNA and protein arrays, without any electrical or mechanical parts [6]. Platforms of tissues chips or microfluidic cell culture instruments, potentially mimic tissue physiology, and recently have been spread in several departments of biochemical engineering or related subjects [4, 7]. These advanced and

targeted platforms are important for medicine knowledge and understanding the biochemistry phenomenon in human organs and tissue physiology and consequently offer the essential biomedical tools for cancer diagnosis [8], pharmaceutical studies [5], and medicinal laboratory [2, 9]. Scheme 1 exhibits the simple structure of a general biochip platform. Any kind of transduction in this system must be translated a real sensing event such as DNA binding, oxidation, and DNA repairing into a template understandable through differences voltage, light intensity and electrical current (for producing a final human-readable output). Therefore, biochips are a platform that require both microarray technology transduction and also signal processing technologies to output the information of sensing experiments. The word biochip arises from the main fabrication methods in computer microchips manufacturing and causes us to control surface features sizes on the nanometer scale [10, 11].



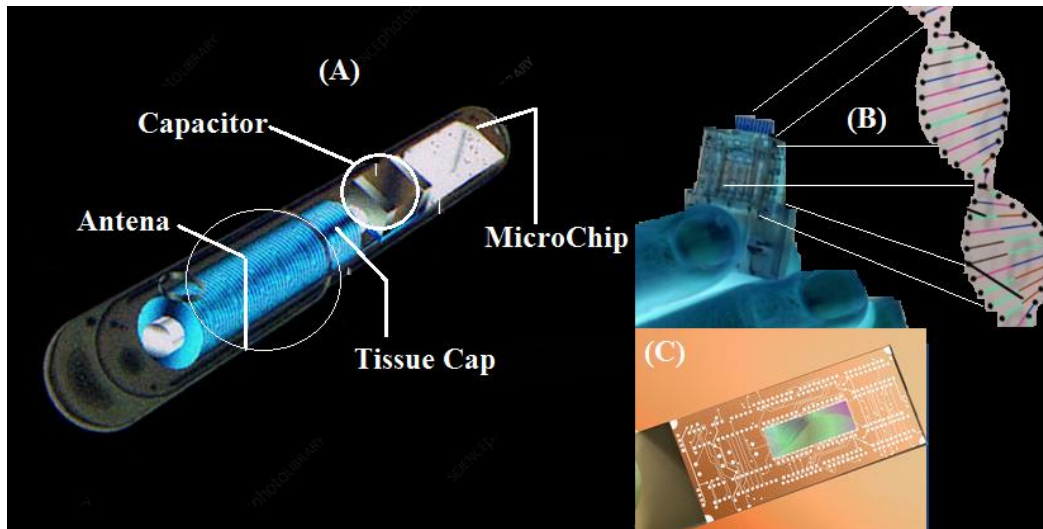
Scheme 1. Platform of microarray transduction including analyzer printer

This review concentrates on technologies progress of "Lab Chip" (LC) towards: Tissue Chip" (TC) knowledge from their initial backgrounds up to now. Therefore, the LC devices must be explained by details for further application in point of health care (PHC). We also consider the previous activities and evaluate the present progress in two approaches of LC and TC and then introduce several researchers of the major pioneers in this medical technology. Consequently by analyzing the specifications of LC and TC, we offer some comments for future perspectives in the development of TC platforms for drug discovery and PHC applications.

1.2. Microarray fabrication

The microarray structure contains two-dimensional grid of biosensors with a critical part of a biochip platform. Generally, the biochips are located on a flat foundation, which can be prepared by a passive surface such as silicon or glass or provided by an active surface such as electronics devices or micromechanical instruments to control signal transduction. The theory and concepts of thermodynamic for surface chemistry can be considered to simulate the molecular sensor system on the substrate area. Although the fabrication of microarrays, economically and technologically are easy, there are various hurdles that may finally confirm or refuse the success of future biochip platforms. In other words, the main challenge is the way of locating each biochip at a certain position on the Cartesian network on the substrate sheet [12]. Although several ways has been designed to control the mechanism of biochips placement,

usually the robotic micro-pipetting [13] or micro-printing [14] devices are considered for placing tiny spots of sensor material on the chip surface. It is notable only a few spots can be placed at a time because each sensor has unique situation for related place, so the low-potential of this process causes the manufacturing costs increase. Fodor investigated an especial fabrication process in which a collection of microlithography phases is applied for synthesizing around one million of single-stranded DNA biochips on substrate nucleotide simultaneity [15]. It is considerable that one phase of lithography is needed for each nucleotide base type such as adenine, so for cytosine, guanine, thymine and adenine, as a total of four phases are necessary for single stranded DNA. Although this procedure is a strong technique due to placing of million sensors simultaneously, in recent technologies cannot be used widely and only applied for providing small DNA strands (5–10 codons). In addition, numerous numbers of microarrays consist of a Cartesian grid of biochips that can be used mainly for coding the coordinate of each sensor to its application. Biochips in these arrays generally obey from fluorescence technique, so each of their coordinates is only a unique character. Using random encoding in biochip fabrication is another method that saves time for enabling and coding self-assembly techniques. In this procedure, large categories of unique sensors can be prepared and then the chips from each category are composed into an array (Scheme 2).



Scheme 2. (A): A simple structure of microchip; (B): DNA Chip; (C): numerous numbers of microarrays consist of a Cartesian grid of biochips.

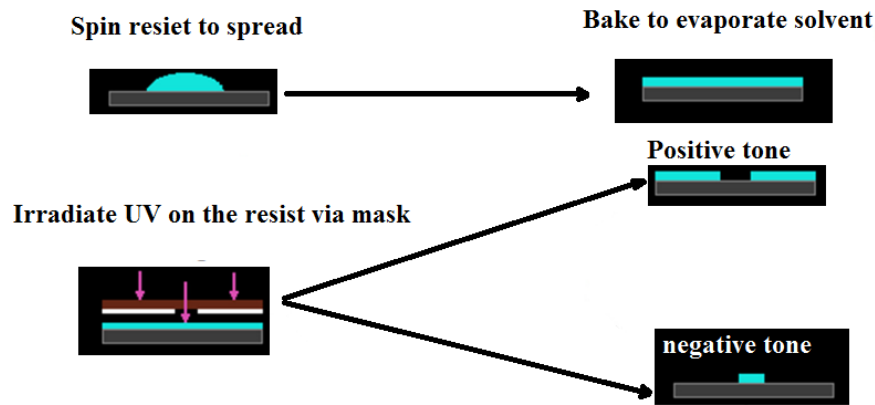
2. Micro technology

2.1. Bio micro electro mechanical systems (BMEMS)

After developing the micro technology, quickly the planar substrate technique was replaced into the microelectronics approaches [16, 17]. Consequently, via orders of photolithography and thin-film deposition phases of a micro/nano structure on planar substrates was achieved. As it can be seen in scheme 3, the fundamental of the photolithography process is based on spinning the photoresist through fixed speed for keeping the certain thickness of biomaterial on the substrate. Although the photoresist is better to be irradiated with UV light while passed through a photo mask, sometimes the curing of the photoresist is not needed [18-20]. In the past 3 decades, scientists such as Manz and Harrison, progressed the mechanism of using planar fluidic instruments for running small volumes of liquid in preparation for liquid chips through chemical analysis system [21, 22]. As a result, based on their invention the electrophoretic segregation of amino acids that are fluorescently coded were provided to microchip evaluating [23, 24]. Since BMEMS instruments have progressed, the focus in microsystems as novel tools for biomedical engineering has extremely increased [16]. Due to small size of chips, ability to react under physiologically and these kind tools provide

suitable platforms that are interesting for biological applications [25].

Bio micro electro mechanical system (Figure1-a), is a subunit of electro mechanical systems that has the biomedical engineering applications and providing of these devices originated from knowledge of micro fabrication devices. In other words, processing, manipulation, analysis and construction of biological samples were accomplished in these micro-devices [26]. Now decades, interests to these systems such as diagnostics in DNA and bio macromolecules micro-arrays, microfluidics, DNA repairing, cell membrane sensing, trans membrane proteins, protein signaling, biosensors, drug designing, stimulating neural implants, retinal implants for therapy of blind patients and micro needles of biomedical engineering, are increasing quickly [27, 28]. The matching of these subjects with the recent genomics/proteomics and tissue technologies, provide important situations for inventing various tools in medical activities. BMEMS for antibodies detection, bacterial detection, and viral detection, and antibiotic susceptibility, diagnostics cancer and cell culture are some of the available applications in micro techniques [26-29]. In addition, these tools have a significant function in the future of biomedical engineering knowledge [30].



Scheme 3. Photolithography, including spinning, irradiates with UV light, positive/negative tone, and adaptation of reference [1]

Four types system of materials can be applied for invention of BMEMS based tools in biomedical engineering [1]. The first one includes glass of silicon for electronics tools in the MEMS instruments. The second category is plastic and polymers, which have low cost, high electrical conductivities, low thermal, easiness of fabrication, rapid sampling and easiness of surface modification are excellence suited for fabrication of BMEMS [29–31]. For any further information, we refer the readers to references of [32–35] for polymer-based devices. The third category includes biological materials such as sell membrane, DNA, proteins, and tissues that can be applied in BMEMS technologies. The fourth category consists of disease materials including, viruses, cancer tumors and abnormal tissues. Although applies of biological materials are new, these groups of materials offer interesting occasions in biomedical subject in TC technologies [36]. This kind of small platform or LC can gather the whole laboratory activities into a chip format. The idea of LC has been developed after discovering the micro total systems to analytical purposes. Based on this definition, LC devices also are sub units of BMEMS. In fact, LC platforms are knowledge of manipulation of extremely small volumes of liquids with integrated microfluidics platforms to perform multiple laboratory processes in our biological bodies instead of in vitro labs. In the following part, we will overview microfluidic chips and their applications in the tissue engineering.

2.2. Microfluidic biochips (MFB)

Now days, MFB for biomedical activities are receiving much attractive [37-40]. These chips, also known as LC or BMEMS, offer several advantages over usual laboratory procedures.

They are able to handle low amounts, around Nano liters of the bio liquids to provide supersensitive detection at lower time and costs than traditional manners in a smaller laboratory space. Microfluidics technologies present exciting abilities in the area of enzymology, DNA analysis including PCR, proteomics, toxicity assays, and immune monitoring. An important usage of MFBs is point-of-health care (PHC) diagnosis of diseases and they are ready for a real-time testing of specimen for toxins, pandemic, and other dangerous infection disease. The most MFBs are containing micro-pump, micro-valve, and micro-channel, and also their activities are based on the continuous fluid flow [41, 42]. The alternative antcipant for manipulating separated droplets is based on producing digital microfluidics (DMFs). In contrast to continuous-micro flow biochips, DMFs biochips present a 2-D array system over identical cells. In addition, the digital systems have dynamic structural capability in a microfluidic array for changing their position during the concurrent set of bioassays. This ability of restructuring is suitable for inventing DMFs biochips platform for DNA analyzing and quick detection. There are two different classes of MFBs, namely continuous-flow biochips (CFB) and droplet- microfluidic biochips (DMB)[43]. Among the invented tools, electro wetting-on-dielectric (EWOD) has looked at considerable attention in recent years (Figure1-a & b). The main core of EWOD contains of two equal glass plates, as shown in Figure1-b. The bottom sheet includes an array of individually controllable electrodes, and the top palate is coated with a continuous ground electrode. All electrodes are covered by Indium tin oxide (ITO) and a

dielectric separator might be prepared by hydrophobic Teflon. The detailed fabrication process is described in papers of Pollack works [44, 45]. It is notable based on FAIR, and KHLYSTOV works, silicone oil is the most suitable material as the filler medium has been selected for reducing contamination and consequently for facilitating microfluidic biochip reuses [46, 47]. By changing the voltage, the movement of droplet can be controlled and voltage changing between two electrodes adjacent at the same time causes the electrode just under the droplet is deactivated. Via the EWOD mechanism, a surface tension gradient along the split between the adjacent electrodes causes the transportation of the droplet. The speed of the droplets set-out by voltages among ten to ninety volts that the droplets can be moved at speeds around 20-25 cm/s through these voltages [44, 45]. Consequently, by this theory and approach, the DMFs biochips can be made from well-characterized cells for sample introduction, sample movement, temporarily sample preservation, and the mixing of different samples. The set upping of the microfluidic and the way of droplets move can be used through the voltages of electrodes in the array. These characters of DMFs allow us to handle all steps of biochemical analysis on-chip, from sampling, sample-processing, mixing, and detection to waste handling. A general microfluidic array platform or basic DMFs biochips contain a few storages that produce the droplets of samples and reagents by optical detection system of LEDs technologies (Figure 1.c). Silicon substrate is also suitable for fabricating a droplet-based biochip that is fixed around one million digits on 25 μm by 25 μm electrode area. By using separate droplets, a microfluidic can be converted to a set of basic operations, that is, random moving one droplet over one electrode length that known as digitization. In other words, digitization is a series group of micro droplet-based bioassay programs that might be used to digital MFBs. Digitization in total contains several steps,

including, 1- Distribution sample droplets over the microfluidic array, 2- putting the droplets on especial place on the array of substrate that has several sub steps including mixing, detection and dilution, 3- transporting the wastes droplets out of the array. Figure 1.d exhibits a photo of fabricated DMFs applied for biomedical testing; this chip has been fabricated in Duke University's laboratory by Srinivasan et al. [48-51]. Another item of DMFs contains a chip detection of explosives such as commercial TNT or trinitrotoluene by Pamula et al [52], automated on-chip measurement of airborne particulate matter by Fair et al. [46, 47]. DMFs are also being fabricated for several systems such as gene sequencing [53], protein crystallization, integrated hematology, pathology, cytology, microbiology, and serology. By using separate droplets, a microfluidic can be converted to a set of basic operations, that is, random moving one droplet over one electrode length that known as digitization. In other words, digitization is a series group of micro droplet-based bioassay programs that might be used to digital MFBs. Digitization in total contains several steps, including, 1- Distribution sample droplets over the microfluidic array, 2- putting the droplets on especial place on the array of substrate that has several sub steps including mixing, detection and dilution, 3- transporting the wastes droplets out of the array. Figure 1.d exhibits a photo of fabricated DMFs applied for biomedical testing; this chip has been fabricated in Duke University's laboratory by Srinivasan et al. [48-51]. Another item of DMFs contains a chip detection of explosives such as commercial TNT or trinitrotoluene by Pamula et al [52], automated on-chip measurement of airborne particulate matter by Fair et al. [46, 47]. DMFs are also being fabricated for several systems such as gene sequencing [53], protein crystallization, integrated hematology, pathology, cytology, and microbiology.

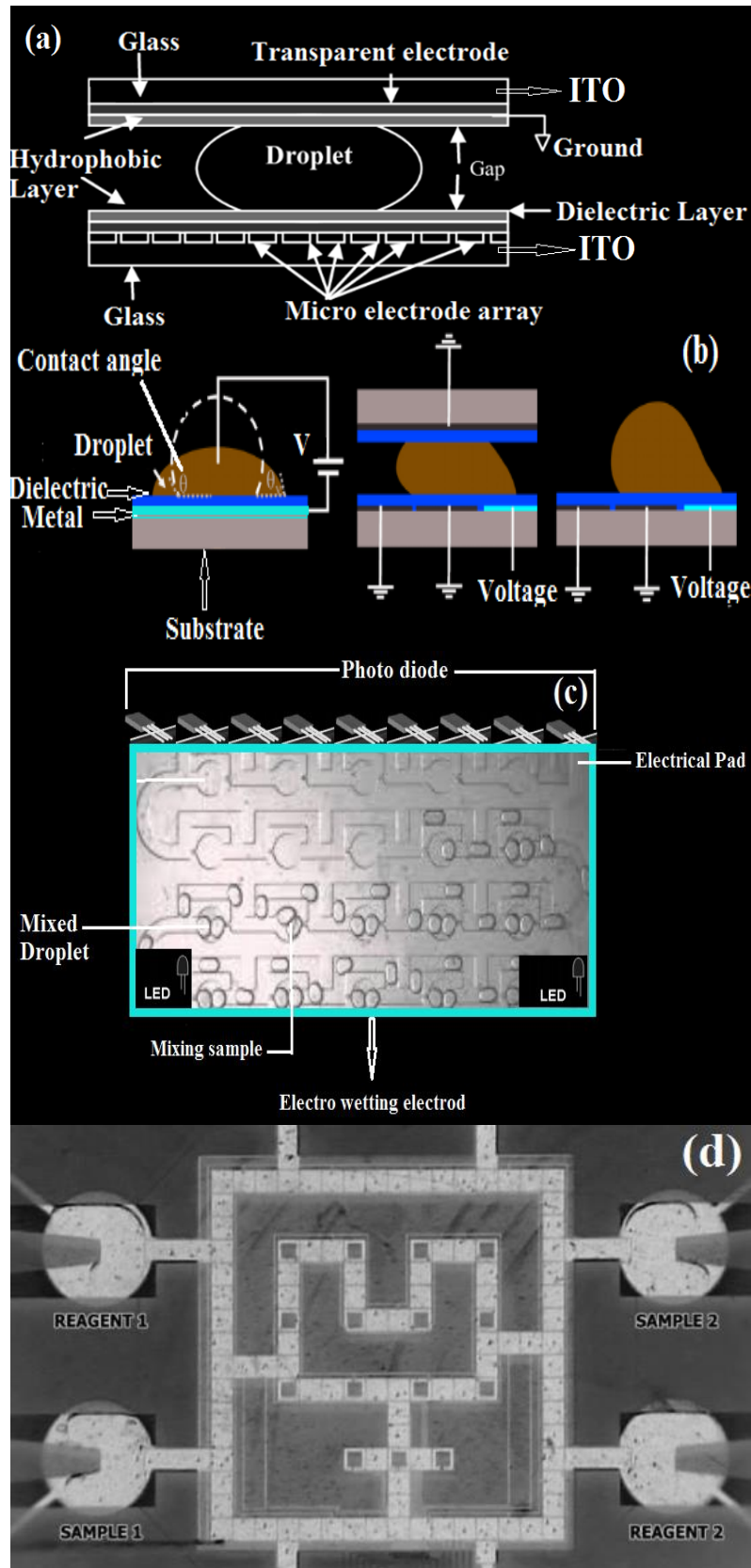


Figure 1. (a): Architecture of droplet digital microfluidic biochips (DMFs); (b): electro wetting-on-dielectric (EWOD); (c): Droplet trapping in MFBS; (d): Fabricated microfluidic array used in multiplexed biomedical assays [49].

3. In vitro chips

3.1. Point of health care (PHC)

Point of health care (PHC) platforms is medical instruments that produce important data rapidly [54]. This diagnostic disease can be accomplished by the patient both at home or clinic. By growing technology, necessities for the rapid diagnostic of dangerous diseases such as infarction, cancer, diabetes and heart attacking for home care monitoring in patients, have grown the interest to develop PHC systems. The large ratios of surface over volume of these kind systems in microfluidic systems yield a suitable decrease in the time of analysis in LC for PHC testing [55] and also increase the chance for fast diagnosis and treatment at the point of care. In addition, patients can easily work with these testers and extract the experimental results with these PHC devices. Lateral experiments with paper strips tester that have been applied since the 1965s [56], are the main categories of PHC systems where use a paper strip for corroborating the positive or negative answers of the goal testing such as various antibodies or pathogen antigens. By adding a little bit of liquid sample , same as blood , the capillary phenomenon will appear and the liquid moves across the channel passing through the paper strips where include the antibodies or pathogens Figure2.a). If the targeted problem is available in the liquid sample, it will be attached to labels and the results will be positive for the related disease. As the liquid droplets move ahead, the reagents where are placed on the paper strips will be binded to the targeted molecules at the test line to read out clearly the colored section, or looked at digitally

in the related instruments by the user [57,58]. These kind medical instruments are cheap, easy to work, popular for people, and available in any drug store with sensitive biomarkers and can be used for proteins detection, nucleic acids detection, cell problems and metabolite diseases such as high blood glucose, urea nitrogen toxic and also measuring the lactate in blood [58]. Membrane paper strips are used widely for detection of infectious diseases, syphilis and HIV, pneumonia, various influenza viruses or recently for corona viruses are some of the items of tests in PHC. In under developing countries such as African countries, due to the low degree of hospital centers, the death rate from infectious disease is high [59], so, POC systems by fast detection of infectious diseases significantly help to increase patient survival rate [60]. The membrane strips testers for checking glucose-level [61], or glycemic motoring immunoassay [62], as well as home pregnancy (Figure2.b) are some of the PHC application which currently are presented to bazar. The first pregnancy test was populated in the 1975s [63]. When the pregnancies urine is defined inside the sample layer through the device's inlet, it is transported by capillary forces. In the conjugate layer, where the antibodies have been fixed, binding between antibodies and pregnancy antigens will occur. The positive or negative answer of hCG (pregnancy hormone) in the liquid sample will be confirmed by the boundary line. Within seconds, the answer appears in detection section indicating whether or not hCG hormone has occurred in the sample [64].

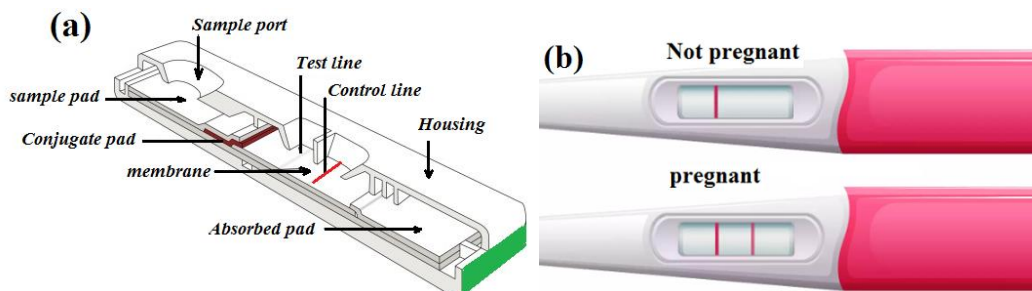


Figure 2. (a): Structure of tester strip; (b): Home pregnancy test.

PHC diagnostic instrument has significant impacts in public health of under developing countries. Although low energy consumption, low cost, popular using, frequent individual

testing, automated test, ability to test whole blood, and several other advantages being highly user-facilities, provide interpreted results rapidly and less challenges in view point of public

transportation and traffic. Several usual microfluidics devices that produce commercialized LHC diagnostic instruments are listed in Table 1.

3.2. Tissue Chip (TC)

Microfluidic cell culture platforms are accomplished through a dynamic physiological micro-environment. Cell culture techniques mostly focus to rely on monoculture cell and cell-

cell interaction. In addition, cellular activities in three dimensional directions of the tissue levels have significant impacts on cellular interaction to environment [65]. Mechanical tension, structural properties, and biochemical microsystem that cells feel in a living organ [66] are affected by static 3D cell-culture models such as bioreactors, spheroid and gel based cell culture techniques.

Table 1. Several microfluidic companies for manufacturing PHC diagnostic instruments adapted from Reference [54].

Commercial corporation	Manufacturing materials	Applications	Analytes	Sample Types	Measuring & Signal Detection	PHC Technology
Micronics (Sony)	Polymer cartridge	Cardiac, hormones	DNA, proteins	Whole blood, saliva	Fluorescent Optic	Handheld digital with magnetic nanoparticles
Alere (formerly inverness Medical)	Polymer elastically Deformable materials	HIV/AIDS, clotting time	Proteins, cells	Whole blood	Fluorescence	Disposable cartridge, immune hematology test
Daktari Diagnostics	Plastic cartridge	HIV/AIDS	Cells	Whole blood	Electrochemical (impedance spectroscopy)	Handheld instrument, electrochemical sensing
Biosite (Alere)	Strip with textured microstructures	Cardiovascular drugs of abuse	proteins	Whole blood, plasma	Fluorescence	Portable reader, disposable capillary
Philips	Plastic cartridge	Cardiac damage, hormones	Nucleic acids, proteins	Whole blood, saliva	Optical (frustrated total internal reflectance)	Handheld reader with magnetic nanoparticles
Epocal (Alere)	Film, epoxy laminates	Blood chemistries	Small molecules	Whole blood	Electrochemical	Self-contained cards, electrodes sensing
HandyLab (BD)	Disposable cartridges	drug susceptibility Bacterial infections	Nucleic acids	Vaginal, rectal, nasal swabs	Fluorescence with molecular beacons	Disposable cards with integrated heating
Abaxis	Polymer disc	Small molecules, proteins	Blood Metabolites	Whole blood	Absorbance	Compact analyzer, injection-molded,
i-STAT Corp (Abbott)	Polymer cartridge silicon microchip	Blood, cardiac markers	Small molecules	Whole blood, urine	Electrochemical potentiometric	Portable analyzer, thin-film electrodes

Acknowledgment

The authors highly appreciate the financial support of Vietnam National University Ho Chi Minh City for this research under the grant number TX2023-32-01.

References

- [1] Convery, N.; Gadegaard, N. *30 years of microfluidics*. *Micro Nano Eng.* **2** (2019) 76–91.
- [2] Astolfi, M.; Péant, B.; Lateef, M.; Rousset, N.; Kendall-Dupont, J.; Carmona, E.; Monet, F.; Saad, F.; Provencher, D.; Mes-Masson, A.-M. *Micro-dissected tumor tissues on chip: An ex vivo method for drug testing and*

- personalized therapy*. *Lab Chip* **16** (2016) 312–325.
- [3] Sun, W.; Luo, Z.; Lee, J.; Kim, H.J.; Lee, K.; Tebon, P.; Feng, Y.; Dokmeci, M.R.; Sengupta, S.; Khademhosseini, A. *Organ-on-a-Chip for Cancer and Immune Organs Modeling*. *Adv. Healthc. Mater.* **8** (2019) 1801363.
- [4] Ahadian, S.; Civitarese, R.; Bannerman, D.; Mohammadi, M.H.; Lu, R.; Wang, E.; Davenport-Huyer, L.; Lai, B.; Zhang, B.; Zhao, Y. *Organ-On-A-Chip Platforms: A Convergence of Advanced Materials, Cells, and Microscale Technologies*. *Adv. Healthc. Mater.* **7** (2018) 1700506.
- [5] Liu, W.; Sun, M.; Lu, B.; Yan, M.; Han, K.; Wang, J. *A microfluidic platform for multi-size 3D tumor culture, monitoring and drug resistance testing*. *Sens. Actuators B Chem.*, **292** (2019) 111–120.
- [6] Grayson, A.C.R.; Shawgo, R.S.; Johnson, A.M.; Flynn, N.T.; Li, Y.; Cima, M.J.; Langer, R. *A BioMEMS review: MEMS technology for physiologically integrated devices*. *Proc. IEEE*, **92** (2004) 6–21.
- [7] Bhise, N.S.; Ribas, J.; Manoharan, V.; Zhang, Y.S.; Polini, A.; Massa, S.; Dokmeci, M.R.; Khademhosseini, A. *Organ-on-a-chip platforms for studying drug delivery systems*. *J. Control. Release*, **190** (2014) 82–93.
- [8] Zhang, Y.S.; Zhang, Y.-N.; Zhang, W. *Cancer-on-a-chip systems at the frontier of nanomedicine*. *Drug Discov. Today*, **22** (2017) 1392–1399.
- [9] Bhatia, S.N.; Ingber, D.E. *Microfluidic organs-on-chips*. *Nat. Biotechnol.* **32** (2014) 760–772.
- [10] Bhatia, S.N.; Chen, C.S. *Tissue engineering at the micro-scale*. *Biomed. Microdevices*, **2** (1999) 131–144.
- [11] Chin, C.D.; Linder, V.; Sia, S.K. *Lab-on-a-chip devices for global health: Past studies and future opportunities*. *Lab Chip*, **7** (2007) 41–57.
- [12] Cheng, J.; KrickaL.J.; *Technology Options and Applications of DNA Microarrays*, Harwood Academic Publishers, Philadelphia **2001** (2001) 185–216.
- [13] Schena, M.; Shalon, D.; Davis, R.W.; Brown, P.O. *Quantitative monitoring of gene expression patterns with a complementary DNA microarray*, *Science* , **270** (1995) 467–470.
- [14] MacBeath, G.; Koehler, A.N.; Schreiber, S.L.; *Printing small molecules as microarrays and detecting protein-ligand interactions en masse*, *J. Am. Chem. Soc.* **121** (1999) 7967–7968.
- [15] Fodor, S.P.; Read, J.L.; Pirrung, M.C.; Stryer, L.; Lu, A.T.; Solas, D.; *Light-directed, spatially addressable parallel chemical analysis*, *Science* , **251** (1991) 767–773.
- [16] Abgrall, P.; Gue, A. *Lab-on-chip technologies: Making a microfluidic network and coupling it into a complete microsystem—A review*. *J. Micromech. Microeng.*, **17** (2007) R15.
- [17] Temiz, Y.; Lovchik, R.D.; Kaigala, G.V.; Delamarche, E. *Lab-on-a-chip devices: How to close and plug the lab?* *Microelectron. Eng.*, **132** (2015) 156–175
- [18] Kovacs, G.T.; Maluf, N.I.; Petersen, K.E. *Bulk micromachining of silicon*. *Proc. IEEE*, **86** (1998) 1536–1551.
- [19] Bustillo, J.M.; Howe, R.T.; Muller, R.S. *Surface micromachining for microelectromechanical systems*. *Proc. IEEE*, **86** (1998) 1552–1574.
- [20] Schmidt, M.A. *Wafer-to-wafer bonding for microstructure formation*. *Proc. IEEE* **86** (1998) 1575–1585
- [21] Manz, A.; Graber, N.; Widmer, H.Á. *Miniaturized total chemical analysis systems: A novel concept for chemical sensing*. *Sens. Actuators B Chem.*, **1** (1990) 244–248.
- [22] Manz, A.; Harrison, D.J.; Verpoorte, E.M.; Fetting, J.C.; Paulus, A.; Lüdi, H.; Widmer, H.M. *Planar chips technology for miniaturization and integration of separation techniques into monitoring systems: Capillary electrophoresis on a chip*. *J. Chromatogr. A*, **593** (1992) 253–258.
- [23] Jacobson, S.C.; Hergenroder, R.; Koutny, L.B.; Ramsey, J.M. *High-speed separations on a microchip*. *Anal. Chem.*, **66** (1994) 1114–1118.
- [24] Harrison, D.J.; Fluri, K.; Seiler, K.; Fan, Z.; Effenhauser, C.S.; Manz, A. *Micromachining a miniaturized capillary electrophoresis-based chemical analysis system on a chip*. *Science*, **261** (1993) 895–897.
- [25] Puleo, C.M.; Yeh, H.-C.; Wang, T.-H. *Applications of MEMS technologies in tissue*

- engineering. *Tissue Eng.*, **13** (2007) 2839–2854.
- [26] Bashir, R. *BioMEMS: State-of-the-art in detection, opportunities and prospects*. *Adv. Drug Deliv. Rev.*, **56** (2004) 1565–1586.
- [27] Polla, D.L.; Erdman, A.G.; Robbins, W.P.; Markus, D.T.; Diaz-Diaz, J.; Rizq, R.; Nam, Y.; Brickner, H.T.; Wang, A.; Krulevitch, P. *Microdevices in medicine*. *Annu. Rev. Biomed. Eng.*, **2** (2000) 551–576.
- [28] Dittrich, P.S.; Manz, A. *Lab-on-a-chip: Microfluidics in drug discovery*. *Nat. Rev. Drug Discov.*, **5** (2006) 210.
- [29] Quake, S.R.; Scherer, A. *From micro-to nanofabrication with soft materials*. *Science*, **290** (2000) 1536–1540.
- [30] Huh, D.; Kim, H.J.; Fraser, J.P.; Shea, D.E.; Khan, M.; Bahinski, A.; Hamilton, G.A.; Ingber, D.E. *Microfabrication of human organs-on-chips*. *Nat. Protoc.*, **8** (2013) 2135–2157.
- [31] Zhang, B.; Radisic, M. *Organ-on-a-chip devices advance to market*. *Lab Chip*, **17** (2017) 2395–2420.
- [32] Tsao, C.-W. *Polymer microfluidics: Simple, low-cost fabrication process bridging academic lab research to commercialized production*. *Micromachines*, **7** (2016) 225.
- [33] Becker, H.; Gärtner, C. *Polymer microfabrication technologies for microfluidic systems*. *Anal. Bioanal. Chem.*, **390** (2008) 89–111.
- [34] Giboz, J.; Copponnex, T.; Mélé, P. *Microinjection molding of thermoplastic polymers: A review*. *J. Micromech. Microeng.*, **17** (2007) R96.
- [35] Kim, B.J.; Meng, E. *Review of polymer MEMS micromachining*. *J. Micromech. Microeng.*, **26** (2015) 013001.
- [36] Voldman, J. *BioMEMS: Building with cells*. *Nat. Mater.*, **2** (2003) 433
- [37] Su, F. And Chakrabarty, K. . *Module placement for fault-tolerant microfluidics-based biochips*. *ACM Trans. Des. Automat. Elect. Syst.* **11** (2006) 682–710.
- [38] Su, F., Chakrabarty, K., Fair, R. B. *Microfluidics-based biochips: technology issues, implementation platforms, and design automation challenges*. *IEEE Trans. Comput.-Aid. Des. Integr. Circ. Syst.*, **25** (2006) 211–223.
- [39] Su, F., Hwang, W. Chakrabarty, K. , *Droplet routing in the synthesis of digital microfluidic biochips*. In *Proceedings of the Design, Automation and Test in Europe (DATE) Conference.*, (2006) 323–328.
- [40] Su, F.; Ozev, S., Chakrabarty, K. *Ensuring the operational health of droplet-based microelectrofluidic biosensor systems*. *IEEE Sensors*, **5** (2005) 763–773.
- [41] Venkatesh, S.; Memish , Z. A. *Bioterrorism: A new challenge for public health*. *Int. J. Antimicrobial Agents*, **21** (2003) 200–206.
- [42] Thorsen, T., Maerkl, S., Quake, S. *Microfluidic large-scale integration*. *Science*, **298** (2002) 580–584.
- [43] Jones, T. B., Gunji, M., Washizu, M., Feldman, M. J.. *Dielectrophoretic liquid actuation and nanodroplet formation*. *J. Appl. Phys.* **89** (2001) 1441–1448.
- [44] Pollack, M. G., Fair, R. B., Shenderov, A. D.. *Electrowetting-based actuation of liquid droplets for microfluidic applications*. *Appl. Phys. Lett.*, **77** (2000) 1725–1726.
- [45] Pollack, M. G., Shenderov, A. D., Fair, R. B. *Electrowetting-based actuation of droplets for integrated microfluidics.*, *Lab on a Chip* **2** (2002) 96–101.
- [46] Fair, R. B., Khlystov, A., Srinivasan, V., Pamula, V. K., Weaver, K. N. 2004. *Integrated chemical/biochemical sample collection, pre-concentration, and analysis on a digital microfluidic lab-on-a-chip platform*. In *Proceedings of the SPIE Lab-on-a-Chip: Platforms, Devices, and Applications*. L. A. Smith and D. Sobek, Eds., **5591** (2004) 113–124.
- [47] Fair, R. B., Srinivasan, V., Paik, P., Ren, H., Pamula, V. K. . *Electrowetting-based onchip sample processing for integrated microfluidics*. In *Proceedings of the IEEE International Electronic Devices Meeting (IEDM).*, (2003) 32.5.1–32.5.4.
- [48] Srinivas, M. Patnaik, L. M. *Genetic algorithms: a survey.*, *IEEE Comput.* **27** (1994) 17–26.
- [49] Srinivasan, V., Pamula, V. K., Fair, R. B. . *An integrated digital microfluidic lab-on-a-chip for clinical diagnostics on human physiological fluids*. *Lab on a Chip*, (2004), 310–315.
- [50] Srinivasan, V., Pamula, V. K., Paik, P., Fair, R. B. . *Protein stamping for MALDI mass spectrometry using an electrowetting-based microfluidic platform*. In *Proceedings of the SPIE*. **5591** (2004) 26–32.

- [51] Srinivasan, V., Pamula, V. K., Pollack, M. G., Fair, R. B. . *Clinical diagnostics on human whole blood, plasma, serum, urine, saliva, sweat, and tears on a digital microfluidic platform*. In Proceedings of the International Conference on Micro Total Analysis Systems. (2003) 1287–1290.
- [52] Pamula, K., Srinivasan, V., Chakrapani, H., Fair, R. B., Toone, E. J. *A droplet-based lab-on-a-chip for colorimetric detection of nitroaromatic explosives*. In Proceedings of the IEEE Conference on Micro-Electro-Mechanical Systems. (2005) 722–725.
- [53] Fair, R. B., Khlystov, A., Taylor, T. D., Ivanov, V., Kvas, R. D., Srinivasan, A., Pamola, V. K., Pollock, M. G., Griffin, P. B., Zhou, J. *Chemical and biological applications of digital microfluidic devices*. IEEE Des. Test Comput. **24** (2006) 10–24.
- [54] Chin, C.D.; Linder, V.; Sia, S.K. *Commercialization of microfluidic point-of-care diagnostic devices*. Lab Chip, **12** (2012) 2118–2134.
- [55] Jung, W.; Han, J.; Choi, J.-W.; Ahn, C.H. *Point-of-care testing (POCT) diagnostic systems using microfluidic lab-on-a-chip technologies*. Microelectron. Eng., **132** (2015) 46–57.
- [56] Haeberle, S.; Zengerle, R. *Microfluidic platforms for lab-on-a-chip applications*. Lab Chip, **7** (2007) 1094–1110.
- [57] Jung, W.; Han, J.; Choi, J.-W.; Ahn, C.H. *Point-of-care testing (POCT) diagnostic systems using microfluidic lab-on-a-chip technologies*. Microelectron. Eng., **132** (2015) 46–57.
- [58] St John, A.; Price, C.P. *Existing and emerging technologies for point-of-care testing*. Clin. Biochem. Rev., **35** (2014) 155.
- [59] Schito, M.L.; Patricia D’Souza, M.; Michele Owen, S.; Busch, M.P. *Challenges for rapid molecular HIV diagnostics*. J. Infect. Dis., **201** (2010) S1–S6.
- [60] Weigl, B.; Domingo, G.; LaBarre, P.; Gerlach, J. *Towards non-and minimally instrumented, microfluidics-based diagnostic devices*. Lab Chip, **8** (2008) 1999–2014
- [61] Heller, A.; Feldman, B. *Electrochemical glucose sensors and their applications in diabetes management*. Chem. Rev., **108** (2008) 2482–2505.
- [62] Liu, L.; Peng, C.; Jin, Z.; Xu, C. *Development and evaluation of a rapid lateral flow immunochromatographic strip assay for screening 19-nortestosterone*. Biomed. Chromatogr., **21** (2007) 861– 866.
- [63] Leavitt, S.A. *A private little revolution: The home pregnancy test in American culture*. Bull. Hist. Med., **80** (2006) 317–345.
- [64] Posthuma-Trumpie, G.A.; Korf, J.; van Amerongen, A. *Lateral flow (immuno) assay: Its strengths, weaknesses, opportunities and threats. A literature survey*. Anal. Bioanal. Chem., **393** (2009) 569–582.
- [65] Young, E.W. *Cells, tissues, and organs on chips: Challenges and opportunities for the cancer tumor microenvironment*. Integr. Biol., **5** (2013) 1096–1109.

BIOGRAPHY



He was born in 21 of March 1957 in Mashhad, a big city in the north eastern of Iran. He received his B. Sc. in Chemistry from Kharazemi University in Tehran in 1981 and his Ph.D. from Islamic Azad University of Tehran in 1994. He was the dean of science faculty in Islamic Azad University of Tehran from 2000 to 2006 and director of Interdisciplinary Science and Research Center from 2006 to 2008. He has been collaborating with several universities worldwide; including his collaborations with Professor James E. Boggs in the Institute of Theoretical Chemistry in University of Texas Austin, Texas, USA (working on molecular modeling and computational calculations of nano-molecules), and so on. He is a professor in the field of Computational Chemistry in Science and Research Branch of Islamic Azad University in Tehran. His research interests are in the area of interdisciplinary sciences, mainly in molecular modeling and QM/MM calculations of macro-biomolecules, electronic structure calculations of nano-biomolecules, non-bonded electronic structure of BnNn rings, NMR contour maps, and quantum investigations of non-bonded interactions. He designed a nano- molecular motor structure which can be used for detecting the biological molecules. He is focusing for understanding the root of some human behaviors for instance the role of microtubules in the human's conscious or what is the biophysical chemistry role in the telepathy which is interdisciplinary subjects among chemistry, biology, quantum theory and calculations. Currently, he started collaboration with INT center in Vietnam, Ho Chi Minh City on the Lithium Ion Batteries (LIBTs) both theoretically and experimentally with Professor Chien Mau Dang and his groups.

TITLE: OPTICAL CHEMICAL WAVEGUIDE SENSOR ELABORATED BY SOL-GEL TECHNIQUE

David Riassetto*, Ibtihel Marzouk, and Michel Langlet

Grenoble INP-PHELMA

Laboratory of Physical Engineering and Material Science (LMGP) FRANCE

Email: David.Riassetto@grenoble-inp.fr

ABSTRACT

We present a fluorescent wave-guiding micro-structured sensor on glass entirely elaborated by sol-gel processing. This architecture is composed of a channel waveguide doped with an oxygen sensitive fluorophore (Rudpp) and endowed with diffraction gratings. It particularly takes advantage of a high refractive index titanium oxide based sol-gel photoresist that can be imprinted through a single photolithography step. The gratings enable to inject the blue excitation signal in the axis of the waveguide core and to extract the red signal emitted by Rudpp toward a photodetector. We firstly present the multi-step elaboration process leading to this architecture. Opto-geometrical properties of the channel waveguide and diffraction gratings are assessed and optimized on the basis of optical and AFM characterizations. According to these properties, best injection and extraction geometry of the excitation and emission signals have been determined and correlated to simulation. Then, we present fluorescence measurements performed in wave-guiding configuration using a specifically designed optical bench. These measurements demonstrate that the waveguide enables efficient propagation of light at the excitation and emission wavelengths of the fluorophore and that the diffraction gratings are compatible with efficient injection and extraction of the excitation and emission signals. This work constitutes a promising first step towards a new class of oxygen sensors based on the well-known principle of oxygen driven extinction of the Rudpp fluorescence.

BIOGRAPHY



Dr. David Riassetto is an Associate professor of Material Science. He got a Master of Science degree in physics and energy with honors in 2005 at University Joseph Fourier of Grenoble and a Ph.D. at Grenoble Institute of Technology in 2009. Between 2009 and 2011 he was a postdoctoral researcher at the University of Utah. Since 2011, he is an associate professor at Grenoble Institute of Technology and doing his researches in the LMGP laboratory (Laboratory of Materials and Physical Engineering) has a member of the Thin Films, Nanomaterials and Nanostructures team, and more precisely of the Wet Chemistry & Surface Functionalization group. Currently Dr. David Riassetto's researches focus on the surface functionalization at the nanometer scale, using wet-chemistry methods (e.g. sol-gel, photochemistry, ...).

SELF-ALIGNED FABRICATION OF NANOMECHANICAL AND NANO-ELECTRONIC DEVICES BY CONVEX CORNER LITHOGRAPHY ON SILICON WEDGES

Céline Steenge¹, Lucas Kooijman¹, Chris van Kampen¹, Bjorn Borgelink¹, Yves Janssens¹, Yasser Pordeli¹, Roald Tiggelaar², Erwin Berenschot¹, and Niels Tas¹

¹Mesoscale Chemical Systems, Faculty of Science and Technology, University of Twente, The Netherlands.

²NanoLab, MESA+ Institute, Faculty of Electrical Engineering, Mathematics and Computer Science, University of Twente, The Netherlands.

Email: n.r.tas@utwente.nl, c.steenge@utwente.nl

ABSTRACT

This paper explains how the so-called convex corner lithography can be integrated in complete process flows and examples will be given of functional devices that have been realized [1,2]. These include nanomechanical check valves as well as confined, curved tunnel junctions. A perspective will be given on the possible realization of full 3D networks of electronic devices through the application of self-aligned fabrication strategies.

Keywords: Self-aligned patterning, corner lithography, silicon nanomachining, nanomechanics, nanoelectronics

INTRODUCTION

Self-aligned nano patterning is widely employed to create device features with dimensions smaller than the resolution of the typical photolithography used. In particular edge lithography is part of mainstream CMOS process flows and is often referred to as self-aligned double patterning (SADP) or self-aligned quadruple patterning (SAQP) [3]-[6]. This technique makes use of standard lithography with the combination of chemical vapor deposition (CVD) as first published in 1983 by Flanders and Efremow [7].

In recent years, our group focused on self-aligned techniques that can be employed in full 3D, including retraction edge lithography [8] and corner lithography [9], [10]. While corner lithography was initially developed for concave corners, a variant has been introduced that can selectively open a hard mask on convex corners of silicon structures [11], [12], referred to as convex corner lithography (CvCL). Miniaturization of nanoelectromechanical systems (NEMS) and semiconductor electronics are great candidates for employing CvCL, as will be discussed here.

FABRICATION OF WEDGES

The process starts with the development of waferscale V-grooves with the help of the Vängbo

process [13] and Displacement Talbot Lithography (DTL) [14].

The Vängbo process is used to determine the crystallographic orientation. The alignment to the crystallographic orientation is crucial for the crystallographic etching.

A 13 nm Si_3N_4 hardmask is deposited using low pressure chemical vapor deposition (LPCVD) after which a 190 nm thick bottom anti-reflective coating (BARC) and 200 nm thick photoresist (PR) layer are spin-coated on the surface. DTL aligned to the Si orientation is used to pattern the linear grating into the PR, where the period of the linear grating can be altered by choosing the appropriate mask. The BARC/PR pattern is transferred into the Si_3N_4 using capacitively coupled plasma reactive ion etching (CCP-RIE)

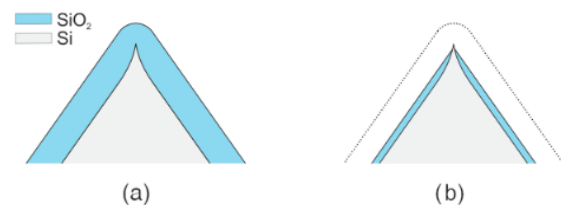


Figure 1: convex corner lithography process. From the wedge structures a low temperature thermal oxidation step (a) after which isotropic thinning (b) is applied. Figure obtained from [11] with permission.

plasma etching. An anisotropic etch in 20% KOH at 20 °C creates the first set of V-grooves, where the Si<111> planes are again protected using local oxidation of silicon (LOCOS). The second set of V-grooves can be generated by removing the Si₃N₄ hardmask in 85% H₃PO₄ at 140 °C and etching the Si in 25% TMAH at 75 °C. The duty-cycle of the V-grooves can be altered based on the etch time and can be checked with the help of the Scanning Electron Microscope (SEM). It is therefore important that the etch rate is determined before etching and should be constant during the process.

The remaining SiO₂ is removed using 1% HF at 20 °C. CvCL is performed using low temperature, typically below 950 °C [15]-[17], thermal oxidation (Figure 1a). The thermal oxidation sharpens the structures, creating a thinner oxide layer on and near the apex of the structures. By isotropic thinning of the silicon dioxide in 1% HF at 20 °C, the convex corner can be selectively exposed and further processed (Figure 1b). Due to the thinner oxide, the thicker oxide on the Si<111> planes will remain. The newly created nanogap can now be used for further processing of the device. As Berenschot et al [11] discussed in their paper, the dimensions of wedges can be decreased to sub-10 nm scale details creating great possibilities for device dimensions not possible with conventional lithography.

NANOMECHANICAL CHECK VALVES

Chris van Kampen et al [1] demonstrated in their paper the fabrication of a parallel NEMS flow restriction nano-slit array on a wafer scale utilizing CvCL. The exposed convex corners are used as nanogaps to create nanopore arrays for flow-through applications such as water filtration, DNA sequencing and chemical detection. CvCL addressed the limitations of existing fabrication techniques in terms of size reduction, scalability, and pore distribution, enabling the creation of wafer-scale nanopores. Furthermore, through the elastic nature of the inclined, free standing sides of the created nozzles, mechanical check valves can be formed with ultra-fast response times.

The process starts with a silicon on insulator (SOI) wafer where V-grooves are fabricated in (Figure 2a). The low temperature oxidation step of the CvCL is applied next, after which a new Si₃N₄ layer is deposited. A second DTL step is applied to define the nano support structure (Figure 2b) oriented at 90 ° with respect to the original DTL

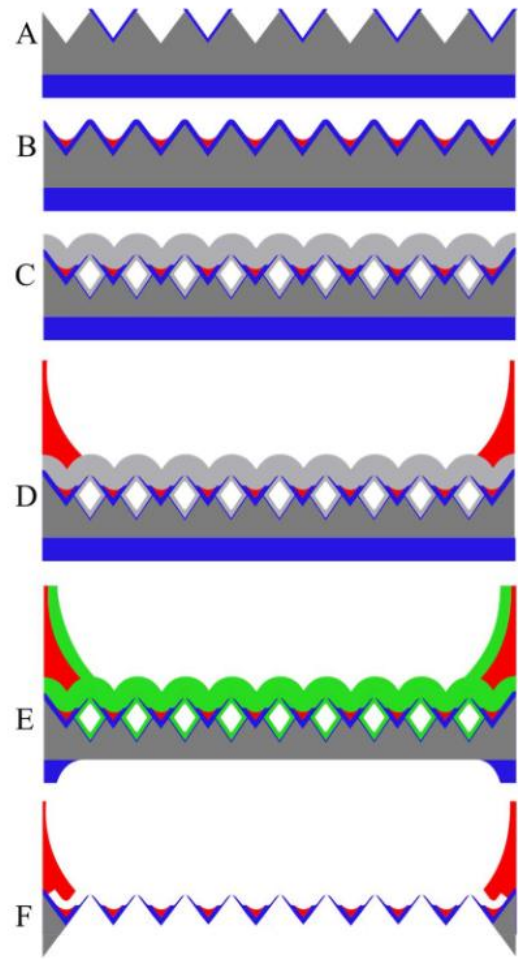


Figure 2: nanomechanical check valves of [1], where (light) grey represents Si, blue SiO₂, red Si₃N₄ and green PR. A) V-grooves formation. B) CvCL and silicon nitride protection and support grid formation. C) cavity formation and a-Si deposition. D) Micro support formation E) BOX layer etching. F) final device formed.. Figure obtained from [1] with permission.

defined structures. The next step is to remove the SiO₂ from the CvCL apex, creating the nanogap. The nano gaps and the cavities are protected by an a-Si stopping layer (Figure 2c). The a-Si is selectively removed from the backside of the wafer and thick silicon-rich silicon nitride is deposited. At the backside it acts as a mask for etching the handle wafer until the buried oxide (BOX) layer. At the front side it is patterned such that it acts as a micro support array (Figure 2d). The a-Si is removed using 25% TMAH at 70 °C and photoresist is spun on the front side for protection. The BOX layer is then etched in HF solution (Figuree), after which the PR is stripped in acetone and the remaining silicon in TMAH.

The removal of the protective oxide in the cavities (by much diluted HF solution) is the last step in the creation of the valves (Figure 2f).

The structure is supported using a dedicated mechanical design consisting of support beams allowing for robust operation even under high differential pressures.

The device's performance was characterized using a combination of molecular and viscous flow models, demonstrating a substantial mass flow rate of 25 $\mu\text{g/s}$ at 4 bar differential pressure. Moreover, the device exhibited pressures up to 6.5 bar without experiencing failure.

CURVED TUNNEL JUNCTIONS

In his master's thesis [2], Bjorn Borgelink demonstrated the utility of CvCL in the production of asymmetric curved tunnel junctions. Asymmetric tunnel junctions are considered as candidates for fast responding diodes, if a relatively low junction capacitance and resistance can be implemented [18]-[22]. The novel approach for creating asymmetric tunnel junctions involves an array of out-of-plane oriented silicon wedges, which serve as wafer scale template.

The exposed convex corners in the fabrication process form the location of the tunnel junction. A new thin barrier oxide is grown on the exposed apex after the CvCL is applied. Figure 3 shows a schematic cross section of typical fabricated devices, where the junction is confined to about 20 nm across in one direction. Measured tunnel currents show expected current densities, which scale proportional to the active device area. This is indicative for high yield fabrication of the confined tunnel junctions.

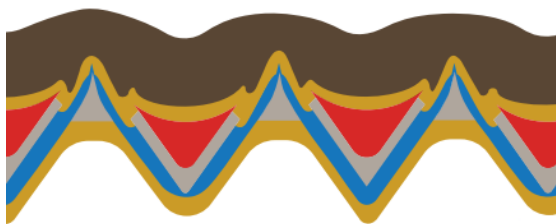


Figure 3: cross section of geometrically asymmetric MIS junction of [2] where grey represents (poly-)Si, blue SiO₂, red low-stress SiRN, light brown metal and dark brown parlylene. Figure obtained from [2] with permission.

CONCLUSION AND OUTLOOK

The nanomechanical check valves and the curved tunnel junctions already show how CvCL can be of great value in fabricating nanoscale devices on wafer scale. CvCL relies essentially on isotropic processing. Therefore, the intriguing possibility to apply it in the self-aligned fabrication of full 3D systems will be further explored.

Acknowledgment

The authors gratefully acknowledge the extensive support by the MESA+ NanoLab staff.

References

- [1] C. P. van Kampen *et al.*, *Massive Parallel NEMS Flow Restriction Fabricated Using Self-Aligned 3D-Crystallographic Nanolithography*, in 2020 IEEE 33rd Int. Conf. Micro Electro Mech. Syst., IEEE, (2020) 1106–1109.
- [2] B. T. H. Borgelink, *Fabrication and characterization of a geometrical asymmetric tunneling junction*, University of Twente, (2017).
- [3] A. Vanleenhove and D. Van Steenwinckel, *A litho-only approach to double patterning*, in Proc. SPIE 6520, Opt. Microlithogr. XX, 65202F, D. G. Flagello, Ed., SPIE, (2007) 65202F.
- [4] C. Bencher, Y. Chen, H. Dai, W. Montgomery, and L. Huli, *22nm half-pitch patterning by CVD spacer self alignment double patterning (SADP)*, in Proc. SPIE 6924, Opt. Microlithogr. XXI, 69244E, SPIE, 2008.
- [5] E. Liu, S. Thibaut, A. Ko, and P. Biolsi, *Integrated self-aligned quadruple patterning*, *Generation of <50 nm period gratings using edge defined techniques*, J. Vac. Sci. Technol. B Microelectron. Process. Phenom., **1**(4) (1983) 1105–1108.
- [8] Y. Zhao, E. Berenschot, H. Jansen, N. Tas, J. Huskens, and M. Elwenspoek, *Multi-silicon ridge nanofabrication by repeated edge lithography*, *Nanotechnology*, **20** (2009) 7.
- [9] E. Berenschot, N. R. Tas, H. V. Jansen, and M. Elwenspoek, *3D-Nanomachining using corner lithography*, 3rd IEEE Int. Conf. Nano/Micro Eng. Mol. Syst. NEMS, (2008).
- [10] E. J. W. Berenschot *et al.*, *3D Nanofabrication of Fluidic Components by Corner Lithography*, *Small*, **8**(24) (2012) 3823–3831.
- [11] E. Berenschot *et al.*, *Self-Aligned Crystallographic Multiplication of Nanoscale Silicon Wedges for High-Density Fabrication of 3D Nanodevices*, *ACS Appl. Nano Mater.*, **5**(10) (2022) 15847–15854.
- [12] E. Berenschot, C. Deenen, R. Tiggelaar, H. Gardeniers, and N. Tas, *Wafer scale fabrication of nanogaps by convex corner lithography*, in Proc.

- 6th Int. Work. Nanotechn. Appl., Phan Thiet, Vietnam, (2017).
- [13] M. Vangbo and Y. Bläcklund, *Precise mask alignment to the crystallographic orientation of silicon wafers using wet anisotropic etching*, *J. Micromechanics Microengineering*, **6**(2) (1996) 279.
- [14] H. H. Solak, C. Dais, and F. Clube, *Displacement Talbot lithography: a new method for high-resolution patterning of large areas*, *Opt. Express*, **19**(11) (2011) 10686.
- [15] E. P. EerNisse, *Stress in thermal SiO₂ during growth*, *Appl. Phys. Lett.*, **35**(1) (1979) 8–10.
- [16] R. B. Marcus, T. T. Sheng, and P. Lin, *Polysilicon/SiO₂ Interface Microtexture and Dielectric Breakdown*, *J. Electrochem. Soc.*, **129**(6) (1982) 1282–1289.
- [17] Dah-Bin Kao, J. P. McVittie, W. D. Nix, and K. C. Saraswat, *Two-dimensional thermal oxidation of silicon—I. Experiments*, *IEEE Trans. Electron Devices*, **34**(5) (1987) 1008–1017.
- [18] K. Choi *et al.*, *A focused asymmetric metal-insulator-metal tunneling diode: Fabrication, DC characteristics and RF rectification analysis*, *IEEE Trans. Electron Devices*, **58**(10) (2011) 3519–3528
- [19] N. M. Miskovsky *et al.*, *Nanoscale Devices for Rectification of High Frequency Radiation from the Infrared through the Visible: A New Approach*, *J. Nanotechnol.*, **2012** (2012) 1–19.
- [20] S. Joshi, Z. Zhu, S. Grover, and G. Moddel, *Infrared optical response of geometric diode rectenna solar cells*, in 2012 38th IEEE Photovolt. Spec. Conf., IEEE (2012) 002976–002978.
- [21] S. Hemour and K. Wu, *Radio-Frequency Rectifier for Electromagnetic Energy Harvesting: Development Path and Future Outlook*, *Proc. IEEE*, **102**(11) (2014) 1667–1691.
- [22] A. Sharma, V. Singh, T. L. Bougher, and B. A. Cola, *A carbon nanotube optical rectenna*, *Nat. Nanotechnol.*, **10**(12) (2015) 1027–1032.

BIOGRAPHY



Niels Tas received his Ph.D. degree from the University of Twente (UT) in April 2000 on the topic of MEMS linear electrostatic motors, employing walking motion and mechanical leverage. His thesis project was carried out in close collaboration with Philips Research. From 2000 – 2004 he was a post-doctoral fellow in the BIOS lab-on-a-chip group, UT, working on surface tension effects in nanochannels, like capillary negative pressure and dynamics of capillary filling. In 2004 he was appointed as assistant professor, and in 2010 as associate professor. In 2008 Niels Tas was awarded a Vidi-grant which he used to further develop self-aligned 3D-nanofabrication techniques for application in advanced scanning probe microscopy. Currently, he is focusing on design and fabrication of 3D integrated nanosystems, combining nanofluidic, nanomechanical, nano-photonic and nano-electronic domains. Niels Tas is a contributing PI to the International Max Planck Research School for Science and Technology of Nano-Systems.

LATERAL AND VERTICAL SPIN VALVE DEVICES USING MOLECULAR BEAM EPITAXIAL GROWN MNAS/INAS HYBRID STRUCTURES

Md. Tauhidul Islam, Van Thuan Pham, Yingshu Ma, Masashi Akabori

Center for Nano Materials and Technology (CNMT),
Japan Advanced Institute of Science and Technology (JAIST),
Asahidai 1-1, Nomi, Ishikawa 923-1292, Japan
akabori@jaist.ac.jp

ABSTRACT

Ferromagnetic/semiconductor hybrid structures have been paid much attention because they are applicable to spintronic devices such as spin field effect transistors [1]. We focus on hexagonal MnAs, which are ferromagnetic metals at room temperature and can be formed on III-V semiconductors such as GaAs and InAs. Especially, the growth on (111)B surfaces is hopeful because c-axis of hexagonal MnAs tends to be aligned perpendicular to III-V semiconductors [2]. Moreover, we also focus on InAs, which is a narrow bandgap III-V semiconductor and has relatively large spin-orbit coupling in conduction band electrons. By using a conventional molecular beam epitaxy, we study MnAs/InAs hybrid structures on GaAs (111)B substrates for spintronic device applications [3]. We have developed lateral spin valve devices for spin injection/detection evaluation [4]. Figures 1(a) and 1(b) show an optical micrograph and signal of a lateral spin valve device, respectively. Using difference of MnAs sizes (0.5 μm and 3 μm), antiparallel state was realized around ± 140 mT. From the signals and their dependence on channel length, the spin injection efficiency and the spin diffusion length can be estimated. Recently, we have studied MnAs/InAs/ MnAs stacking by low temperature growth for vertical spintronic device applications [5]. Figures 2(a) and 2(b) show a backscattering electron image and elemental line profile taken by energy dispersive X-ray spectroscopy. We have successfully obtained MnAs/InAs/MnAs hybrid structure. Using the structure and combination of a dry etching and a digital wet etching techniques [6], in near future, we would like to fabricate a vertical spin valve device as shown in Fig. 2(c).

Keywords: spin-valve, MnAs/InAs, MBE

References

- [1] S. Datta and B. Das, Appl. Phys. Lett. **56** (1990) 665.
- [2] Y. Morishita et al., Jpn. J. Appl. Phys. **36** (1997) L1100.
- [3] Md. E. Islam, M. Akabori., J. Crystal Growth **463**, (2017) 86.
- [4] Md. E. Islam et al., AIP Advances, **9** (2019) 115215.
- [5] Md. T. Islam, M. Akabori, EM-NANO **2023** (2023) PB-48.
- [6] Y. Ma and M. Akabori, EM-NANO **2023** (2023) PB-16.

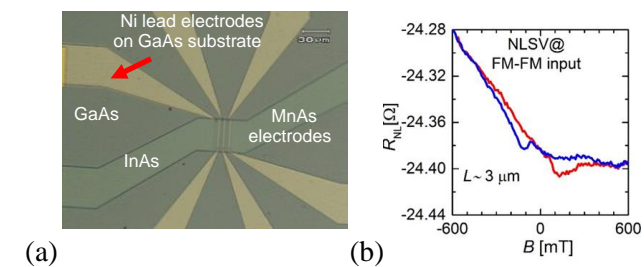


Figure 1. (a) Lateral spin valve device using MnAs/GaAs/InAs on GaAs (111)B. (b) Non-local spin valve signal.

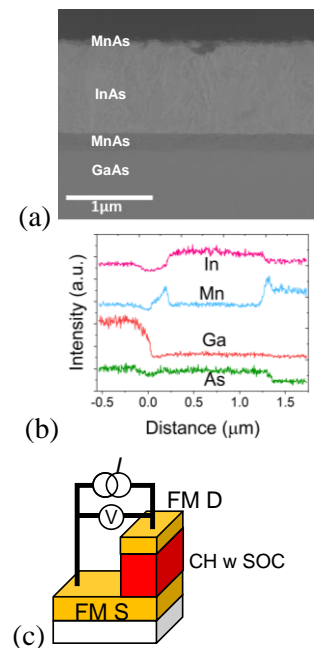


Figure 2. (a) Cross-section of MnAs/InAs/MnAs/GaAs(111)B. (b) Elemental line profile in vertical direction. (c) Schematic of a vertical spin valve device.

BIOGRAPHY



Dr. Masashi Akabori is currently Associate Professor of Center for Nano Materials and Technology (CNMT), Japan Advanced Institute of Science and Technology (JAIST). He received the B.E., M.E. and Ph.D. degrees in Electronics and Information Engineering from Hokkaido University, Japan, in 1995, 1997 and 2000, respectively. He was also adopted as Research Fellow DC1 and PD of Japan Society for the Promotion of Science (JSPS) from 1997 to 2000 and from 2000 to 2002, respectively. From 1995 to 2000, he worked on GaAs-based lateral superlattice structures formed by metal-organic vapor phase epitaxy (MOVPE) on vicinal surfaces. From 2000 to 2002, he worked on photonic crystal structures formed by selective-area MOVPE on (111)B surfaces. In 2002, he joined CNMT, JAIST as Assistant Professor, and started to work on electronic and spintronic devices and materials based on narrow bandgap III-V semiconductors. From 2007 to 2009, he was adopted as Overseas Research Fellow of JSPS, and worked at Research Center Juelich, Germany. At that time, he conducted III-V semiconductor nanowire works. In 2013, he was promoted Associate Professor of CNMT, JAIST. He also belongs to School of Materials Science, and Research Center for Empathetic and Symbiotic Technology with Nature. From 2021, he is a part-time lecturer in Iwate University. He is currently working on semiconductor spintronics research. He is a member of the Japan Society of Applied Physics (JSAP), the Physical Society of Japan (JPS), and the Institute of Electronics, Information and Communication Engineers (IEICE).

ELECTROSPINNING OF POLY(VINYL ALCOHOL)/CHITOSAN AND PEG 400 ALONG WITH MANGIFERA EXTRACT ENHANCED BY ARGON PLASMA JET TREATMENT

Pongphun Sukum*, Pipath Poramapijitwat, and Dheerawan Boonyawan

¹ Plasma and Beam Physics Research Facility, Department of Physics and Materials Science, Faculty of Science, Chiang Mai University, Chiang Mai 50200, Thailand;
Email: pongphun_su@cmu.ac.th

ABSTRACT

The electrospinning technique is used to fabricate nanofiber wound dressing with highly porous nanofibers and a large surface area, similar to the extracellular environment promoting wound healing. However, this technique relies on various forces such as rheological behavior, conductivity, and surface tension. Treatment with an atmospheric pressure plasma jet can enhance the electrospinning process by inducing chemical changes in the solution and improving its polarity. This treatment can cause chemical changes in the solution, enhancing solvent polarity and consequently improving the ability to electrospin the polymer solution. Various medicinal plants are extensively utilized in traditional wound treatments worldwide, indicating their potential for wound healing. These plants are believed to contain phytochemicals such as phenolic compounds, terpenoids, and alkaloids, which possess antimicrobial properties. The leaves of the mango plant contain a range of phenolic compounds that possess analgesic properties, exhibit anti-inflammatory and antibacterial effects, and serve as antioxidants. Furthermore, mango leaves have been shown to support the immune system and aid in wound healing. Therefore, this study aimed to investigate the effect of plasma treatment on PVA, CS, and PEG polymer solutions and to fabricate nanofiber wound dressings using electrospinning.

The results showed that plasma treatment increased the viscosity and conductivity of the polymer solution, as well as the diameter of the nanofibers. Adding 1% mangiferin extract to the solution reduced fiber diameter compared to electrospun nanofibers without extract. The CS/PVA-based nanofiber membrane promoted faster wound closure, indicating its antimicrobial properties.

Keywords: Argon Plasma Jet; *Mangifera indica* extraction; electrospun nanofibrous membrane; HDFa cells

BIOGRAPHY

Author's Name Pongphun Sukum



Education:

2018 PhD student in Nanoscience and Nanotechnology, Faculty of Science, Chiang Mai University, Thailand

2015 Master of Science Program in Toxicology, Faculty of Medicine, Chiang Mai University, Thailand

2007 Bachelor of Pharmacy, Chiang Mai University, Thailand

Scientific presentation Pongphun Sukum and Dheerawan Boonyawan, "Argon plasma jet treatment on poly(vinyl alcohol)/chitosan and polyethylene glycol 400 with Mangifera extract (ME) solution for electrospun nanofiber membrane fabrication", 18th Siam Physics Congress (SPC2023), Empress Convention Centre, Chiang Mai, Thailand, 14-16 June 2023, Acceptance date 28 April 2023.

Pongphun Sukum, Winita Punyodom, Somsak Dangtip, and Dheerawan Boonyawan, “Affectation of Plasma Treatment on Poly (Vinyl Alcohol)/Chitosan and Polyethylene Glycol 400 Solution”, The 4th International Conference on Radiation and Emission in Materials, Acceptance date 24 March 2022.

Pongphun Sukum, and Dheerawan Boonyawan, “EFFECT OF PLASMA TREATMENT ON POLY(VINYL ALCOHOL)/CHITOSAN AND POLY ETHELENE GLYCOL 400 NANOFIBROUS MEMBRANE”, The 3rd International Conference on Radiation and Emission in Materials, Acceptance date 28 October 2020.

Scientific publication

Sukum P, Punyodom W, Dangtip S, Poramapijitwat P, Daranarong D, Jenvoraphot T, Nisoa M, Kuensaen C, Boonyawan D. “Argon Plasma Jet-Treated Poly (Vinyl Alcohol)/Chitosan and PEG 400 Plus *Mangifera indica* Leaf Extract for Electrospun Nanofiber Membranes: In Vitro Study”. *Polymers*. 2023; 15(11):2559.

Poramapijitwat P, Thana P, Sukum P, Liangdeng Y, Kuensaen C, Boonyawan D. Selective Cytotoxicity of Lung Cancer Cells—A549 and H1299—Induced by Ringer's Lactate Solution Activated by a Non-thermal Air Plasma Jet Device, Nightingale®. *Plasma Chemistry and Plasma Processing*. 2023:1-26.

DIAMOND-LIKE CARBON COATINGS USING REACTIVE MAGNETRON SPUTTERING

Phitsanu Poolcharuansin¹

¹ Department of Physics, Faculty of Science, Mahasarakham University, Maha Sarakham, Thailand
Email: phitsanu.p@msu.ac.th

ABSTRACT

Diamond-like carbon (DLC) films exhibit superior mechanical attributes such as elevated hardness, minimal friction, and chemical stability. Nonetheless, their poor adhesion to substrates, attributed to high internal stress, remains a significant limitation. To improve this issue, DLC films incorporating a multi-layered Ti/TiC/Ti-DLC structure were fabricated via reactive magnetron sputtering, employing a titanium target within an argon-acetylene gas mixture. Results demonstrate that the presence of acetylene markedly influences the sputtering kinetics at the target surface, plasma emissions, and the ultimate properties of the resultant films. Specifically, carbon film formation at the target surface diminishes the exposed titanium area, leading to a substantial reduction in average target current and the intensity of Ti I emission lines. The study further reveals that the attributes of the deposited films are intricately related to process parameters, including the average target current and target-to-substrate distance. These observations can be explained by the boundary-layer concept, delineating the zones dominated by titanium and acetylene plasmas.

Keywords: ion energy, ion distribution function, ion energy analyzer, magnetron sputtering,

BIOGRAPHY



Dr. Phitsanu Poolcharansin currently holds the role of Assistant Professor at the Department of Physics, Faculty of Science, Mahasarakham University, Thailand. With a Ph.D. in Electrical Engineering & Electronics from the University of Liverpool, UK, obtained in 2012, Dr. Poolcharansin has established a comprehensive research portfolio centered around three core areas including technological plasma physics and plasma diagnostics and magnetron sputtering for thin film deposition. With a commendable record of 35 peer-reviewed publications, Dr. Poolcharansin's scholarly contributions are both extensive and impactful. Notably, a chapter on "Synthesis of Novel DLC Films" was contributed to the book "Diamond-Like Carbon Coatings Technologies and Applications," further establishing domain expertise.

THE EFFECT OF REDUCTION TIME FOR SYNTHESIS OF THERMALLY REDUCED GRAPHENE OXIDE

Junaid Khan¹ and Mariatti Jaafar²

¹ School of Materials and Mineral Resources Engineering,
Universiti Sains Malaysia, Nibong Tebal Penang, 14300, Malaysia;
Email: mariatti@usm.my

ABSTRACT

Graphene is emerging as the most widely studied material due to its amazing properties and versatile applications. The synthesis of graphene via reduction of graphene oxide (GO) is the most feasible method for large-scale production. GO reduction can be carried out using various chemical reductants as well as by high-temperature thermal annealing. Thermal reduction is considered more eco-friendly since it eliminates the use of toxic chemical reductants. The reduction time will significantly influence the properties of reduced graphene oxide (rGO) synthesized. In this study, the GO synthesized using modified Hummer's method was thermally reduced for different time duration such as 60, 120 and 180 mins at constant thermal annealing of 200 °C temperature to determine the most optimum time duration for rGO synthesis. The synthesized rGO was characterized for functional group, morphological, structural and conductivity analysis using FTIR, FESEM, XRD and resistance measurement respectively. The results indicated that 120 mins is optimum for oxygen termination since there was only marginal difference in electrical conductivity as well as structural and functional groups when reduction was carried out for 180 mins.

Keywords: Graphene oxide, Thermal reduction, Reduction time.

BIOGRAPHY



Mariatti Jaafar is a Professor at the School of Materials and Mineral Resources Engineering, Universiti Sains Malaysia. She completed her PhD in Polymer Composite from Universiti Sains Malaysia in 2002. Her multidisciplinary research includes nanocomposites for electronic applications, conductive ink, Polymer Matrix Composites (PMC) and nanocomposites.

NONLINEAR OPTICS ON-A-CHIP WITH LITHIUM NIOBATE AND BARIUM TITANATE

Aaron Danner¹, **Hong-Lin Lin**¹, **Guanyu Chen**¹ and **Cao Yu**¹

¹ Dept. of Electrical and Computer Engineering, National University of Singapore,
4 Engineering Drive 3, Singapore;
Email: adanner@nus.edu.sg

ABSTRACT

Certain transparent crystals which have a strong light-matter interaction, such as lithium niobate, are highly important because they are used to fabricate high speed fiber optic modulators (and are thus critical to the functioning of the Internet). A strong nonlinear light-matter interaction is also useful for on-chip quantum optics, and is a key requirement of photonic quantum computing or cryptography schemes, such as in parametric down-conversion single photon sources. But traditionally, lithium niobate has been difficult to process and miniaturization of many optical components has proven troublesome. However, with development of relevant cleanroom fabrication procedures in recent years, our research group has been able to demonstrate low loss lithium niobate waveguides, modulators, switches, and couplers. Furthermore, with pulse laser deposition, we have also fabricated high quality single crystal barium titanate, a material which has a stronger Pockels parameter than lithium niobate and may therefore prove important in the next generation of optical devices.

Keywords: Pulse laser deposition, optical materials, modulators (less than 5 keywords)

BIOGRAPHY



Dr. Aaron Danner is with the Department of Electrical and Computer Engineering at the National University of Singapore (NUS). He is also deputy director of the Centre for the Development of Teaching and Learning at NUS.

<https://danner.group>

REVIEW ON RECENT DEVELOPMENTS IN METALORGANIC CHEMICAL VAPOR PHASE (MOCVD) TECHNOLOGY

Prof. Dr. M. Heuken¹

¹ AIXTRON SE, Dornkaulstrasse 2, 52134 Herzogenrath, Germany
Email: m.heuken@aixtron.com

ABSTRACT

This talk presents a summary on recent progress in Metal-Organic Chemical Vapor Deposition (MOCVD) production technology. Today MOCVD is a key deposition technique for compound semiconductors and other materials including 2D materials for applications in opto- and power electronic. We discuss notable advancements in MOCVD, including improved film quality, growth uniformity, automation, and simulation. Key factors driving progress include novel advanced reactor designs, automation, and optimized process parameters on even larger wafer. The abstract also highlights the expanding applications of MOCVD, such as in the fabrication of high-performance electronic and optoelectronic devices, as well as advanced 2D materials for upcoming quantum applications. This presentation provides a concise overview of the latest developments in MOCVD production technology and its broadening impact.

Keywords: MOCVD, Optoelectronic, Nanoelectronic, III-V Compound Semiconductor

BIOGRAPHY



Prof. Dr. Michael Heuken was born in Oberhausen, Germany on November 17, 1961. He received the Diplom Ingenieur degree and the Dr. Ing. degree in Electrical Engineering from Duisburg University in 1985 and 1989, respectively. He joined the Institut für Halbleitertechnik at RWTH Aachen as senior engineer and has been working in the field of metalorganic vapor phase epitaxy for electronic and optoelectronic devices. In 1994 he finished his habilitation in semiconductor technology and devices with a thesis on MOCVD technology for optoelectronic devices. Since then and still at present he has been lecturer for semiconductor

technology and devices as well as circuits for communication systems at RWTH. In 1997 he joined AIXTRON AG in Aachen/Germany where he is now Vice President Advanced Technologies. In 1999 he was honored as Professor at RWTH Aachen. His main experience is in the fields of semiconductor growth by MOVPE, Nanotechnology, electronic and optoelectronic devices and circuits.

Prof. Heuken is author and co-author of more than 650 publications in international journals and several invited papers at international conferences. He was President of DGKK (German Crystal Growth Association), he is elected Executive Committee member of the IOCG (International Organization of Crystal Growth), member of VDE/ITG and was board member of OptechNet e.V. He acts as referee for international Journals. He has been granted several patents in the field of semiconductor technology. More than 150 publicly funded projects were successfully managed by Professor Heuken.

RADIATION PROCESSING TECHNOLOGY FOR PREPARATION OF NANOMATERIALS

Hien Quoc Nguyen

Vietnam Atomic Energy Institute, 59 Ly Thuong Kiet, Hoan Kiem District, Hanoi city, Vietnam

Email: hien7240238@yahoo.com

ABSTRACT

Radiation processing technology is to apply ionizing radiation (X ray, gamma ray and electron beam) as an energy source in industrial processes. Radiation technology has been applied on industrial scale for sterilization of medical devices, crosslinking wires and cables and rubber tires, surface curing of coating, food irradiation. In this report, the irradiation facilities (X ray, gamma Co-60 ray, electron beam) for industrial applications and for preparation of nanomaterials (Ag, Au, Pt, Se, Ag/SiO₂, Ag/TiO₂,...) are briefly outlined. Compared with other methods, radiation technology has been considered as an effective method with several advantages such as: 1) the reaction is carried out at room temperature, 2) yield of nanomaterials is high, (3) nanomaterials can be purely prepared without contamination of excessive chemical reductant and precursor ions residue, (4) the size of nanomaterials is fairly controlled by varying precursor ions concentrations or seed enlargement approaches, 5) mass production can be favorably carried out and 6) processing is satisfied to the requirements of clean production. Typically, large-scale production of colloidal solution of silver nanoparticles (1000 liters/batch) by gamma Co-60 ray irradiation is described. In addition, nanomaterial powders (Au, Se, Ag/SiO₂, Ag/TiO₂,...) of high purity without contamination of by-products are favorably prepared for convenient storage, transportation and applications. Nanomaterial products prepared by irradiation method for application in various fields are also presented.

Keywords: Radiation, gamma Co-60, electron beam, nanomaterials

References

- [1] B.D. Du, ..., N. Q. Hien, J. Exp. Nanosci. **3**(3) (2008) 207-213.
- [2] N.T. Anh, D.V. Phu, N.N. Duy, B.D., N.Q. Hien, Radiat. Phys. Chem. **79** (2010) 405-408.
- [3] N.Q. Hien, D.V. Phu, N. N. Duy, L.A. Quoc, Carbohydr. Polym. **89** (2012) 537-541.
- [4] T.K.L. Nguyen, T.A.T. Nguyen, V.P. Dang, N.D. Nguyen, A.Q. Le, Q. H. Nguyen, Adv. Nat. Sci.: Nanosci. Nanotechnol. **4** (2013) 045004.
- [5] N.N. Duy, D.X. Du, D.V. Phu, L.A. Quoc, B.D. Du, N.Q. Hien, Colloids Surf. A Physicochem. Eng. Asp. **436** (2013) 633-638.
- [6] T.A.T. Nguyen, V.P. Dang, N.D. Nguyen, A.Q. Le, D.T. Nguyen, Q.H. Nguyen, Adv. Nat. Sci.: Nanosci. Nanotechnol. **5** (2014) 035001.
- [7] D.V. Phu, L.A. Quoc, N.N. Duy, N.T.K. Lan, B.D. Du, L.Q. Luan, N. Q. Hien, Nanoscale Res. Lett. **9**(162) (2014).
- [8] T.T. Hanh, N.T. Thu, L.A. Quoc, N.Q. Hien, Radiat. Phys. Chem. **139** (2017) 141-146.
- [9] P.H.N. Diem, ..., N.Q. Hien, J. Chem. **2017** (2017) 6836375.
- [10] P.V. Viet, T.T. Sang, N.Q. Hien, C.M. Thi, L.V. Hieu, Nucl. Inst. Meth. Phys. Res. B, **429** (2018) 14-18.
- [11] N.Q. Hien et al., Mater. Chem. Phys. **205** (2018) 29-34.
- [12] H.T. Truong, T.D. Nguyen, H.Q. Nguyen, Aquac. Rep. **16** (2020) 100286.

BIOGRAPHY



Dr. Quoc Hien Nguyen is a full Professor at Vietnam Atomic Energy Institute (VAEC) working on radiation technology for modification of polymer materials and for preparation of nanomaterials. He got his BSc (1977) at Hanoi University and PhD (1996) in Physical Chemistry at University of Science-VNUHCM. From 1979 to 2001, he worked at Nuclear Research Institute (Dalat city), Head of Radiation Technology Department. From 2002 to 2020, he worked at Research and Development Center for Radiation Technology (Ho Chi Minh city), Head of R&D Department (2007-2016), Senior Researcher (2017). From 2021 to now, he works at Vietnam Atomic Energy Institute, Hanoi city. Thus far, he has published over

150 papers in peer reviewed journals with more than 1400 citations, and with H-index of 22.

INVITED TALKS

NANOMATERIALS AND NANODEVICES
(NMD)

POSSIBILITY OF STRAINED CHANNEL FOR DEVICES FDSOI 10NM AND BEYOND

Nguyet Phuong TRAN

CEA, LETI, Univ.grenoble Alpes, 38000 Grenoble, France

Email: Nguyet-phuong.TRAN@cea.fr

ABSTRACT

Driven by the adoption of ever more electronic components in end products, the semiconductor industry is facing a new era in which device scaling and cost reduction will no longer continue as fast as before. In order to satisfy market demands, the industry is looking for technology solutions to bridge the gap and improve cost/performance while at the same time adding more functionality through integration. The new generation FDSOI needs more performance boosters to increase the mobility in the channels where electron mobility is improved with tensile strain for NMOS and hole mobility is improved with compressive strain for PMOS.

In this talk, we focus on a review of possibilities to obtain the strained channels responding to boost the motility of NMOS and PMOS as known more mechanical constraints in channels so more performance. The chosen techniques here are near to the flow of FDSOI 10nm generation and beyond.

Keywords: FDSOI scaling, tensile strain, compressive strain, mobility enhancement

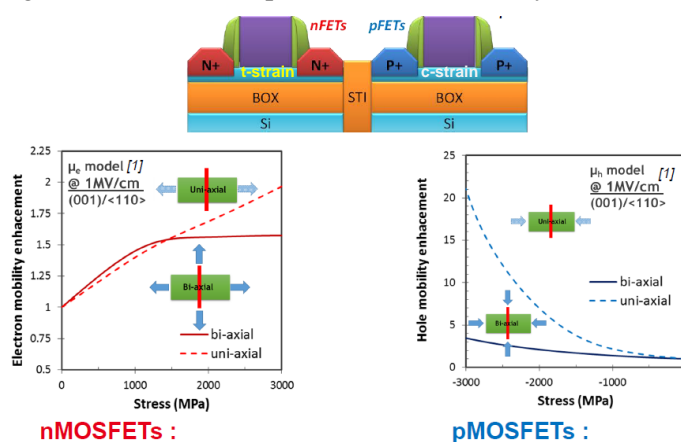


Figure: Carrier mobility gains as a function of the stress (uni-axial or bi-axial) induced in the channel of n and pMOSFETs

BIOGRAPHY



Dr. Nguyet Phuong TRAN received the Dr.Sci. degree in Process Engineering from the Grenoble Institute of Technology, France, in 1993. In 2002, she joined SOITEC, Grenoble, France, as a R&D engineer of different types of Substrate on Insulator (SOI, sSOI, XsSOI, SOQ, SOS,...). Her research interests also include semiconductor device physics on these substrates. Since 2009, she has worked on technology development for the fabrication of multiple gate nanowires and channel strain engineering for n and pFETs. In 2017, she joined CEA-Leti Grenoble France as a R&D integration engineer on Phase Change Memory (PCM) and since 2022 she participate in the NEXTGEN (project aims to develop the future of FD-SOI chips, with nodes beyond 10 nm and a new generation non-volatile onboard memory).

NANOMATERIALS FOR HYDROGEN ENERGY: RECENT ADVANCES AT IMS-VAST

Doan Dinh Phuong

Institute of Materials Science (IMS), Vietnam Academy of Science and Technology (VAST),
18 Hoang Quoc Viet, Hanoi, Vietnam
Email: phuongdd@ims.vast.ac.vn

ABSTRACT

Green hydrogen, hailed as the fuel of the future for its environmental friendliness, remarkable efficiency, and renewable potential, holds the key to a sustainable energy landscape. Unlocking the full potential of hydrogen energy relies on advancements in three pivotal technologies: hydrogen production, storage, and conversion, each imposing specific and unique requirements that can be met through the utilization of nanomaterials. In our constant pursuit of solutions to address global warming, we present the latest research results on nanomaterials for hydrogen energy at the Institute of Materials Science – Vietnam Academy of Science and Technology. Our presentation showcases cutting-edge research capabilities and novel results in the development of nanomaterials for water-splitting/fuel-cell catalysts and hydrogen storage. We also discuss the potential trajectory of nanomaterials for hydrogen energy, guiding us towards the realization of a sustainable "Hydrogen Economy".

Keywords: water-splitting catalysts, hydrogen storage, fuel cell, hydrogen energy

BIOGRAPHY



Prof. Doan Dinh Phuong currently serves as the Director of IMS-VAST. He earned his engineering degree in metallurgy from Slovakia in 1987 and his doctoral degree from Hanoi University of Science and Technology in 2007. In 2008, he was appointed as the Vice Director of IMS, and in 2017, he assumed the role of Director. He published over 100 papers in international journals and conference proceedings and holds 8 patents both domestically and internationally. Currently, he is leading a project on hydrogen energy at VAST.

LASER INDUCED HYDROGEN GENERATION FROM METHANOL VAPOR ASSISTED BY DC ELECTRIC FIELD

Wieslaw Strek, Przemyslaw Wiewiorski, Robert Tomala, Mariusz Stefanski

Institute of Low Temperature and Structure Research,
Polish Academy of Sciences, Okolna 2, Wroclaw, Poland
Email: w.strek@intibs.pl

ABSTRACT

The generation of hydrogen from methanol vapor was investigated under the simultaneous application of laser-induced and electric field ionization of methanol molecules. The process was performed using graphene aerogel both as an electrode and optical target for the generation of hot electrons. The generation of hydrogen was very efficient occurred with no CO₂ and a limited amount of CH₄ emissions.

Keywords: hydrogen, graphene, laser induced phenomena

INTRODUCTION

Recently we have presented the laser-induced hydrogen generation from methanol vapor [1], methanol as a liquid [2], ethanol [3] and water [4] solutions by using graphene aerogel as a target and CW infrared laser diode irradiation. In the present work we report a new concept of efficient generation of hydrogen from methanol vapor by using two combined processes contributing simultaneously to the ionization of methanol particles: laser-induced ionization (LII) and graphene aerogel as optical target and the electric field ionization (EFI) contributing to direct dissociation of methanol particles in vapor.

EXPERIMENTAL

The compacted graphene aerogel particles formed the aerogel (Graphene Aerogel-GA) applied as the optical and electrode target in different DC electrical configurations. Second electrode was a tungsten spike-type electrode near the GA. The ionization region formed between two electrodes configuration (see supplementary as anode (the positive potential) and cathode (negative potential). The emission spectra of laser-induced ionization of methanol in argon vapor were measured using the CW laser diode 980 nm.

The hybrid hydrogen generator was based on simultaneous electro-optical excitation of graphene electrodes as a target using an original quartz photocatalytic reactor attached to the reference catalysis stand of the AutoChem II 2920 system.

RESULTS AND DISCUSSION

The LI emission spectra of graphene aerogel in methanol vapor subjected to pre-ionization measured in argon atmosphere are presented in Fig. 1. They consist of the sharp narrow lines attributed to ionized argon and methanol vapor and the broadband emission of graphene cathode centered at 630 nm.

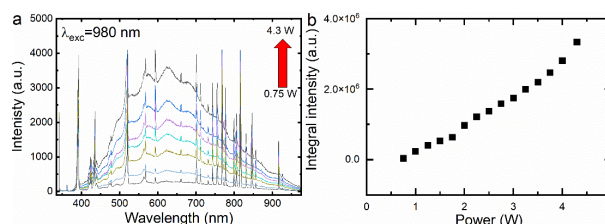


Figure 1. The dependence of emission spectra of graphene aerogel (cathode) in argon and methanol vapor measured in the hybrid (EFI+LII) process for different excitation laser powers (a). The power dependence of LII emission intensity on excitation power (b).

The dependence of emission spectra of methanol in argon gas vapor on excitation laser power is shown in Fig. 1a. The white broadband emission centered at 630 nm is prescribed to the emission of graphene. The sharp and narrow lines are related to the ionization of argon gas. The power dependence of LII emission intensity on excitation power is shown in Fig. 1b.

The results of the electrically assisted laser-induced hydrogen generation as a function of laser power are presented in the Table 1.

The conversion of methanol into hydrogen in the presence of an electric field was significantly enhanced (more than double). The final result of the EFI+LII hybrid process is characterized by a

rapid growth of hydrogen content but at the cost of the reduction of H₂/CO ratio compared to laser-only operation.

The variability of methanol conversion into hydrogen for the EFI, LII, and the hybrid EFI+LII process is presented in Fig. 2.

Methanol Concentration [%]	Process	H ₂ [%]	CO [%]	CH ₄ [%]	Methanol Conversion [%]
0.9	EFI	0.47	0.31	0.02	68.0
	LII	0.27	0.14	0	7.40
	EFI+LII	1.04	0.63	0.03	77.8
3.5	EFI	1.10	0.75	0.06	60.0
	LII	1.00	0.54	0	19.3
	LII+EFI	2.41	1.55	0.08	79.8
8.3	EFI	2.30	1.59	0.21	41.1
	LII	3.10	1.75	0	39.0
	LII+EFI	5.70	3.50	0.39	91.7
12.1	EFI	2.69	1.87	0.32	26.5
	LII	3.78	2.20	0	49.2
	LII+EFI	7.43	5.18	0.55	90.3
14.9	EFI	2.82	2.01	0.38	17.4
	LII	4.37	2.57	0	59.0
	LII+EFI	8.14	5.62	0.56	87.2

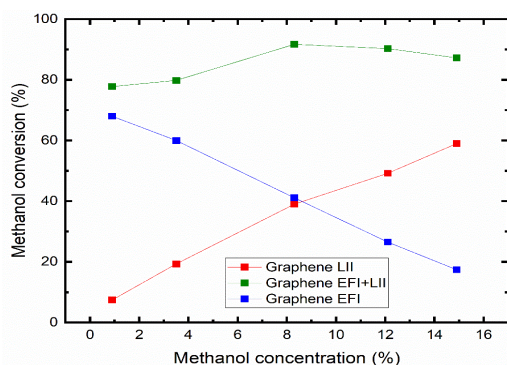


Figure 2. Variability of methanol conversion to H₂ in a course of EFI, LII and hybrid EFI+LII processes.

CONCLUSION

In this work, we have reported the laser-induced generation of hydrogen from ionized methanol vapor assisted by the applied DC electric field. The process has taken place by using the graphene aerogel as the optical target and electrode (cathode) simultaneously. It was shown that the produced syngas consisted of a predominant degree of hydrogen and carbon oxide. Moreover, it was found that for the LII process, no methane emission was observed. The efficiency of methanol conversion was very stable in a large range of methanol concentrations reaching almost 90%. The hybrid mechanism is a new sustainable pathway to produce efficiently almost green hydrogen from methanol vapor.

Acknowledgment

The authors would like to thank the National Science Centre, Poland for financial support (grant no. 2020/37/B/ST5/02399).

References

- [1] W. Strek, P. Wiewiórski, W. Miśta, R. Tomala, M. Stefanski, *Laser-induced generation of hydrogen from methanol vapor*, Int. J. Hydrogen Energy 47 (2022) 27032.
- [2] W. Strek, P. Wiewiórski, W. Mista, T. Hanulia, R. Tomala, *Laser-Induced Hydrogen Generation from Methanol with Graphene Aerogel as the Target*, ACS Omega 6 (2021) 3711.
- [3] W. Strek, W. Mista, P. Wiewiorski, R. Tomala, *Laser induced hydrogen emission from ethanol with dispersed graphene particles*, Chem. Phys. Lett. 775 (2021) 138649.
- [4] W. Strek, P. Wiewiórski, W. Miśta, R. Tomala, M. Stefanski, *Laser-Induced Generation of Hydrogen in Water by Using Graphene Target*, Molecules 27 (2022) 718.

BIOGRAPHY



Prof. Dr hab. Wieslaw Streck (1948) is employed at the Institute of Low Temperature and Structure Research of Polish Academy of Sciences in Wroclaw, Poland since 1971.

His research activity includes optical studies of rare earth and transition metal ions in crystal, glasses and nanostructures, laser spectroscopy, optical sensors, laser materials and graphene applications. He has participated in many national and international research projects. Author and co-author of more than 800 scientific publications (13.500 citations, Hirsch index - 57). Member of editorial boards of Journal of Alloys and Compounds, (Elsevier), Rare Earth Journal (Elsevier), Results in Physics (Elsevier), Polish Materials Science, Materials (MDPI). He is a member of European Society of Art, Literature and Science.

He has completed scientific internships in Denmark many times, multiple research stays in Brazil, Belarus, France, Finland, Israel, Germany, China, Japan, Italy, Russia, Vietnam, USA,

He was a member of organizing committees of International Conference of f-elements, International Conference on Luminescence (ICL), Rare Earth Spectroscopy (RES), Excited States of Transition Elements (ESTE), International Conference on Sol-Gel Materials and a supervisor of 15 doctoral thesis.

He was co-creator more than 30 patents and patent applications in counterfeiting materials, nanotechnology, sol-gel technology, thermal insulation porous materials, graphene technologies, luminescent materials, lighting, hydrogen generation, cryo-medicine and laser therapy,

DEFECT-ENGINEERING TOWARDS ENHANCED ACTIVITY IN PHOTOCATALYSIS

Chuanyi Wang*

School of Environmental Science and Engineering, Shaanxi University of Science and Technology, Xi'an 710021, P. R. China

Email: wangchuanyi@sust.edu.cn

ABSTRACT

Photocatalysis has gained increasing attention due to their wide applications in many fields, especially in addressing the global challenges caused by energy crisis and environmental pollution problems. However, its practical application is impeded by two intrinsic “bottlenecks”, i.e., limited light absorption and rapid recombination of photogenerated charge carriers. Generally, photocatalytic reactions preferentially occur on the surface of photocatalytic materials, and defects play an important role in modifying their surface and electronic structures, and consequently their photocatalytic activities. From this prospect, we explored the correlation of $\text{CaCu}_3\text{T}_{14}\text{O}_{12}$ synthesized by a molten salt method between its morphology-defect-crystal structure and photocatalytic performance. Furthermore, we observed that the piezoelectric coefficient and potential of $\text{SrBi}_4\text{Ti}_4\text{O}_{15}$ prepared by a molten salt method (SBT-850) was improved by 4.9 and 2.7 times compared to that of its counterpart prepared by a solid-state reaction (SBT-SSR), respectively. As a result, synergistic stimulation of piezo and photo promotes the generation of photocatalytic reactive oxygen species, which play an important role in the photocatalytic oxidation of tetracycline. In addition, our work shows that defect engineering could be coupled with plamonic effect, which plays a significant role in developing full spectrum response photocatalys for environmental remediation such as DeNO_x . Overall, through our work, the concept of defect chemistry is emphasized, which provides a theoretical basis for exploring new photocatalytic nanomaterials with excellent performance. This work was supported by the National Natural Science Foundation of China (52161145409, 21976116).

Keywords: Environmental Photocatalysis, Surface Chemistry, Defect Engineering, Light Response, Charge Transfer.

BIOGRAPHY



Dr. Chuanyi Wang, Fellow of Royal Society of Chemistry, is a distinguished professor and academic dean at School of Environmental Science and Engineering, Shaanxi University of Science & Technology (SUST), China. Before moving to SUST in 2017, he was a distinguished professor of Chinese Academy of Sciences (CAS), serving as Director of Laboratory of Environmental Science & Technology of Xinjiang Technical Institute of Physics & Chemistry, CAS (2010-2017). He obtained his Ph.D. degree with honor from Institute of Photographic Chemistry of CAS in 1998, worked in Germany as an Alexander von Humboldt research fellow from 1999 to 2000, and then worked in

USA (Tufts University and Missouri University-Kansas City) from 2000 to 2010. Currently, Dr. Wang also serves as an associate editor of *Environmental Chemistry Letters* (IF15.7) and editorial board member for number of international journals. Dr. Wang's research interest covers catalysis and photo-/electro-catalysis at nanostructured materials with focus on applications in energy conversion and environmental remediation. By far, he has published over 300 papers in peer reviewed journals with more than 17700 times of citations with an H-index of 76 (from Google Scholar). In addition, he edited one English monograph and licensed more than 60 Chinese invention patents.

ORGANIC ADLAYERS ASSISTED GRAPHENE SURFACE MODIFICATIONS

Thanh Hai Phan

Faculty of Natural Sciences, Quy Nhon University

Email: phanthanhhai@qnu.edu.vn

ABSTRACT

Graphene, a single layer of graphite, has raised extensive interest due to its extraordinary thermal, mechanical, electrical and other properties. However, most electronic applications are handicapped by the absence of a semiconducting gap in the pristine graphene. Herein, such approaches for controllable tuning of its electronic properties by using organic adlayers are presented. The molecular adlayers in-situ generated on graphene surface are expected to alter both the band-gap and electron mobility of graphene. The efficiency of our approaches is demonstrated by combined cyclic voltammetry (CV), atomic force microscopy (AFM), ambient scanning tunneling microscopy (STM), Kelvin probe force microscopy (KPFM) and Raman spectroscopy. Our resultant findings open a way to further develop and design new graphene material based nano-optoelectronic devices.

BIOGRAPHY



Dr. Thanh Hai Phan is Vice-Dean of the Faculty of Natural Sciences, Quy Nhon University, responsible for postgraduate and scientific research sections. After receiving PhD degree at Bonn University under supervision of Prof. Klaus Wandelt (Germany, 2012), he completed postdoctoral stays with Prof. Steven De Feyter (KU Leuven, Belgium, 2013-2017) and Dr. Magali Lingenfelder (EPFL, Switzerland, 2017-2018).

Dr. Thanh Hai Phan has published over 20 papers in international peer-reviewed journals, which have attracted over 600 citations. Particularly, two of his papers have been highlighted on Nature and Science journals. His current research interests are at the interface between physics and chemistry and focus on the functionalization of 2-dimensional materials toward nano-electronics and energy conversion applications.

ENHANCING THE SENSING CAPABILITIES OF RESISTIVE-TYPE GAS SENSORS BY SURFACE MODIFICATION

Hyoun Woo Kim¹ and Sang Sub Kim²

¹ Division of Materials Science and Engineering, Hanyang University, Seoul 04763, Republic of Korea;

² Department of Materials Science and Engineering, Inha University, Incheon 22212, Republic of Korea

Email: sangsub@inha.ac.kr

ABSTRACT

The reliable and early-stage detection of hazardous gases has become gradually important in modern society since the 4th industrial revolution. The aim includes safety both in industry and at home, health care, defense of terror and chemical warfare, and environment monitoring. There are a variety of gas sensors, which can be classified according to material, sensing principles, etc. Resistive-type gas sensors have been extensively investigated, due to its merits such as easy fabrication, low cost, adaptability to nanostructures, and potential possibility of attaining extremely high sensing performances. In order to improve sensing performances, significant efforts have been made. In this presentation, we introduce the recent results on modification of sensor surfaces to enhance the sensing performances. Here, various beam-irradiation techniques, in terms of electron beam, helium ion-beam, xenon ion beam, proton beam, laser beam are introduced and discussed.

Keywords: Nanomaterials, Chemiresistive sensor, Gas sensor, Surface modification

BIOGRAPHY



Sang Sub Kim joined the Department of Materials Science and Engineering, Inha University, in 2007 as a full professor. He received his B.S. degree from Seoul National University and his M.S and Ph.D. degrees from Pohang University of Science and Technology (POSTECH) in Material Science and Engineering in 1987, 1990, and 1994, respectively. He was a visiting researcher at the National Research in Inorganic Materials (currently NIMS), Japan for 2 years each in 1995 and in 2000. In 2006, he was a visiting professor at Department of Chemistry, University of Alberta, Canada. In 2010, he also served as a cooperative professor at Nagaoka University of Technology, Japan. His research interests include the synthesis and applications of nanomaterials such as nanowires and nanofibers, functional thin films, and surface and interfacial characterizations. He published more than 400 scientific papers. Currently, he is serving as Editorial Board Members for the following journals: Scientific Reports, Sensors, Applied Sciences, Journal of Sensors, and Electronic Materials Letters. He is Fellow of The Korean Academy of Science & Technology, and General Member of The National Academy of Engineering of Korea. And he was former (2022) President of Materials Research Society of Korea.

SELECTED LANTHANIDE-DOPED NANOLUMINOPHORS FOR SENSING APPLICATIONS

Stefan Lis¹, **Natalia Stopikowska**¹, **Zhen Teng**^{1,2}, **Małgorzata Skwierczyńska**¹, **Venkata N. K. B. Adusumalli**^{1,3}, **Marcin Runowski**¹, **Piotr Kulpinski**⁴

¹ Department of Rare Earths, Faculty of Chemistry, Adam Mickiewicz University in Poznań, Uniwersytetu Poznańskiego 8, 61-614 Poznań, Poland;

² School of Physical Science and Technology Ningbo University, Ningbo, Zhejiang 315211, China;

³ School of Chemical Engineering, Chonnam National University, 77 Yongbong-ro, Buk-gu, Gwangju 61186, Republic of Korea;

⁴ Department of Mechanical Engineering, Informatics and Chemistry of Polymer Materials, Faculty of Material Technologies and Textile Design, Lodz University of Technology, Zeromskiego 116 90-924 Lodz, Poland

Email: stefan.lis@amu.edu.pl

ABSTRACT

Selected nanomaterials based on inorganic matrices (e.g.: fluorides, vanadates, borates, phosphates, silicates, etc.) doped with luminescent lanthanide (Ln) ions, characterized by efficient emission properties, are shown as excellent materials for sensing applications. Such materials should show high crystallinity, phase purity and homogeneity, small particle size and particle size distribution, and should not be agglomerated. Examples of effective nanoluminophors (NL) and up-converting nanoluminophors (UCNL) doped with Ln³⁺ (or Ln²⁺) ions, and their surface functionalized by coating with organic compounds, hybrid systems for sensing applications are discussed in detail. In the lecture I will present examples of selected Ln-doped NLs and UCNLs that can be successfully used as optical sensors, capable of measuring changes of pressure and temperature in nanothermometry and/or nanomanometry. NLs and UCNLs and their functionalized systems have proven to be excellent and useful materials for protection (e.g. important documents, branded textile) against counterfeiting, and for biomedical and analytical purposes. Innovative luminescent and luminescent-magnetic cellulose microfibers, based on Ln³⁺-doped luminescent and luminescent-magnetic NLs used as nanomodifiers of the fibers are presented. We have developed new highly sensitive and exceedingly selective fluorescence methods based on energy transfer from the analyte ion to the Tb³⁺ ion, or Eu³⁺ ion NPs for the (sensing) determination of metal species (e.g. Cu²⁺, Al³⁺) in water. The methods were successfully tested for the metal species determination in real water samples taken from a tap, lake, and river.

Keywords: Lanthanide; nanoluminophors; functional materials; optical sensors.

INTRODUCTION

In the past and nowadays rare-earth ions had been and are an important part in development of science and technology and our life, from material sciences, bio-chemical and medical applications to advances in green technology and sustainable chemistry. Due to the unique features of the intra-configurational 4f-4f transitions, Ln³⁺ ions have been applied as effective and irreplaceable dopants, endowing the host matrices various optical, electronic, and magnetic properties [1,2]. Currently, Ln based luminescent materials are used in many fields, including optical fibres for optical sensing techniques of temperature and pressure [3-5], other sensing techniques, and

protection of materials against counterfeiting [6]. The pressure and temperature have a significant influence on the physicochemical features of materials. The precise determination of temperature and pressure is very important in not only scientific research, but also for industrial manufacturers. The carefully designed host matrices combined with selected Ln ions enable the design of a luminescent manometer and an optical thermometer with excellent sensing performances. The choice of the matrix host should ensure the high chemical stability of the composition structure in a given temperature and pressure range. The implementation of high pressure, HP, in scientific research based on the compression of materials has found wide

application in the study of pressure-triggered variations in the structural, magnetic and spectroscopic properties of substances, phase transformations and the formation of new materials under extreme conditions, as well as in-depth insight into the intriguing and conclusive mechanisms that have made great progress in solid-state physics and chemistry, material science, spectroscopic and structural change of the chemical compounds, etc. [7] Selected inorganic Ln-doped NLs and UCNs synthesized with different methods can be used as optical sensors for nanothermometry and/or nanomanometry. The NLs and UCNs including luminescent-magnetic core/shell [8] type materials used as modifiers for the cellulose fibers functionalization were prepared by a spinning method [6,9]. The fibers modified in this way can be successfully used to produce threads and fabrics to protect valuable materials (payment cards, important documents, branded textiles, etc) against counterfeiting. Strong red of Eu^{3+} or green of Tb^{3+} emission in organic molecules capped nanocrystals as a result of energy transfer from the organic ligand to Ln ions, were used for sensing of Cu^{2+} [10] and Al^{3+} metal species, and applied as a very sensitive and selective spectrofluorimetric method for the determination of trace amounts of Cu^{2+} and Al^{3+} determination in real water samples.

EXPERIMENTAL

Luminescence properties of Ln based NLs are size dependent. By selecting appropriate synthesis methods (e.g. sol-gel, hydrothermal, solid state), one can perfectly control the size, morphology and level of agglomeration, and thus design the expected characteristics of the final product with high crystallinity [1, 2]. Such methods open up more possibilities for the synthesis of efficient NLs or UCNs with small grain sizes, and high crystallinity. The obtained materials were examined in terms of structure, morphology and composition using XRD, TEM, SEM and SEM-EDX, respectively. Depending on the type of the material, they were studied using luminescence spectroscopy (at ambient conditions and/or as a function of pressure or temperature), absorption and IR spectroscopy, and SQUID in the case of magnetic properties.

The excitation and emission spectra, as well as emission lifetimes, band intensity ratio, energy alterations of the radiative transitions and luminescence intensity as variations in a function of increasing pressure were measured using the

experimental setup of high-pressure spectroscopy as shown in Fig. 1a, and for spectroscopic measurements under changing temperature Fig. 1b.

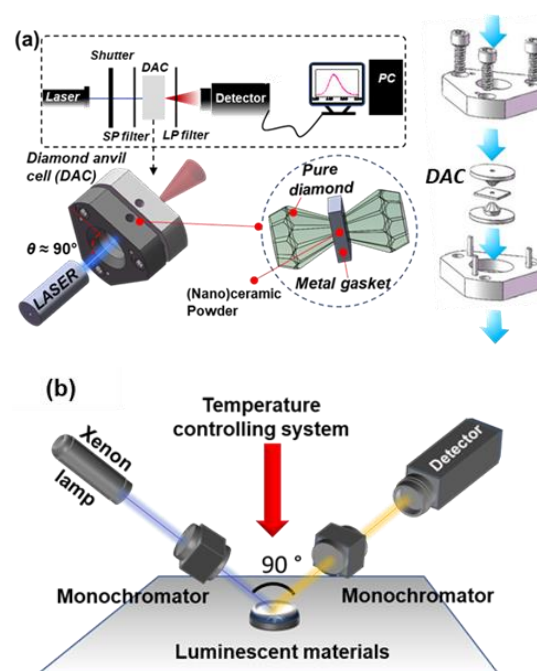


Fig. 1. experimental setup for (a) the HP, (b) DAC presentation and (c) high temperature PL measurements for luminescent materials.

RESULTS AND DISCUSSION

In this lecture, I selected several examples from a large group of inorganic (fluorides, vanadates, borates, phosphates, silicates) NL and UCNL based on lanthanide ions, characterized by excellent luminescence intensity, high stability, insolubility in water, highly stable colloidal systems and also high resistance to different pH conditions. The selection of this group of compounds was motivated by their high potential in sensing applications. Excellent luminescence efficiency of such phosphors was achieved thanks to sensitization processes, i.e. energy transfer ET and charge transfer, np. ET in fluorides (LnF_3 co-doped with Ce^{3+} , Gd^{3+} , Eu^{3+}) [11] and CT in matrices containing electron-donate atoms (e.g. from oxygen to Ln^{3+} in vanadate $\text{GdVO}_4:\text{Eu}^{3+}$) [12].

Optical noncontact pressure sensor are based on the spectroscopic variations as a function of pressure or temperature in optically active materials doped with Ln (Ln^{3+} or Ln^{2+}) ions. As the pressure or temperature varies the following changes can be observed: emission band intensity

ratio, bandwidth, luminescence lifetimes, or the morphology and structure of the material analysed.

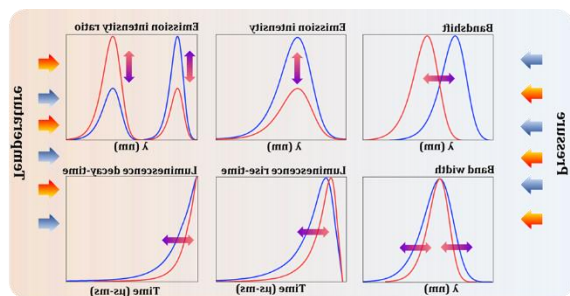


Fig. 2. Presentation of the concept of the pressure- and temperature-induced luminescence properties of Ln-doped materials for the luminescent manometry and thermometry

High-pressure luminescence nanomanometry of up-converting Ln-doped $\text{SrF}_2:\text{Yb}^{3+}, \text{Er}^{3+}$ NCs [7] showed fully reversible interdependence between the luminescence lifetime and pressure. The pressure dependence of the luminescence lifetime was very strong, we have applied the measurements of the luminescence lifetime for ultra-sensitive calibration of high pressure (alternative to ruby). Another example of a material with outstanding pressure sensing properties is the Ce^{3+} -activated $\text{Ca}_2\text{Gd}_8\text{Si}_6\text{O}_{26}$ luminophore with outstanding pressure sensing properties [13]. It is a promising candidate for ultrasensitive manometry (pressure sensing to ~ 10 GPa and enormous red-shift of the Ce^{3+} emission band of 3.00 nm/GPa). An example of the use of Ln^{2+} ions as a pressure sensor is the luminophore $\text{SrB}_4\text{O}_7:\text{Sm}^{2+}, \text{Eu}^{2+}$. In this case due to ET from Eu^{2+} to Sm^{2+} huge enhancement (~ 60 times) in emission intensity of the $^5\text{D}_0 \rightarrow ^7\text{F}_0$ emission line of Sm^{2+} was observed and correlated with pressure up to ~ 58 GPa [14]. The most commonly developed luminescent sensors of temperature are based on lanthanide ions, such as $\text{Yb}^{3+}, \text{Er}^{3+}, \text{Tm}^{3+}, \text{Ho}^{3+},$ and Nd^{3+} embedded in various matrices (e.g. $\text{YF}_3, \text{YVO}_4,$ and NaYF_4). The upconverting nanomaterial based on $\beta\text{-NaYF}_4:\text{Yb}^{3+}-\text{Er}^{3+}@\text{SiO}_2$ was proven to be excellent contactless sensors of temperature, exhibiting a bright dual-center emission ($\lambda_{\text{ex}} = 975$ nm) i.e. UCL of Er^{3+} and down-shifting emission of Yb^{3+} , located in I-BW and II-BW (biological windows) of the spectral range [6].

Luminescent-magnetic core/shell type NLs (or UCNLs), based on Ln-doped fluorides and

magnetite were used as nanomodifiers of the fibers. Luminescent-magnetic cellulose fibers modified with $\text{Fe}_3\text{O}_4/\text{SiO}_2/\text{NH}_2/\text{PAA}/\text{LnF}_3:\text{Eu}^{3+},$ or Tb^{3+} NPs, after successful incorporation of the bifunctional nanomodifiers into the cellulose structure, the functionalized fibers exhibited superior properties, that is, multicolor emission (red of Eu^{3+} and green of Tb^{3+}) under UV light and strong magnetic response [15]. Luminescence intensity ratios (ratiometric) upconversion temperature sensor based on cellulose fibers modified with $\text{YF}_3:\text{Yb}^{3+}, \text{Er}^{3+}$ NPs was used to produce a knitted fabric that was successfully applied to determine human skin temperature [7]. The application demonstrated potential in the field of wearable health monitoring devices and providing a promising alternative to thermometers based on conductive materials that are sensitive to electromagnetic fields.

Lanthanide NLs capped with organic molecules were successfully used for analytical applications. For example, nanocrystals of dipicolinic acid (DPA)-capped- $\text{LaF}_3:\text{Eu}^{3+},$ and furoic acid (FA)-capped $\text{LaF}_3:\text{Tb}^{3+},$ in which, as a result of energy transfer from the organic ligand to Ln ions, were used for sensing of Cu^{2+} [10] and Al^{3+} metal ions. Very sensitive and selective spectrofluorimetric methods have been developed to determine trace amounts of these ions in real water samples

CONCLUSION

The results presented show that the Ln based nanocrystals can be satisfactorily used as effective NLs and functional materials: core/shell, hybrid structures. Optical, contactless nanosensors of pressure and temperature based on lanthanide ions (in NLs and UCNLs) can be successfully used as promising ultrasensitive nanomanometers and nanothermometers. Functionalized fibers with bifunctional luminescence-magnetic properties proved to be excellent advanced materials for multifunctional protection (e.g. textiles, valuable documents, prints, payment cards) against counterfeiting.

Lanthanide NLs capped with organic molecules were also used for analytical applications. We have developed and successfully applied new, very sensitive and selective spectrofluorimetric methods for the determination of trace amounts of metal Cu^{2+} and Al^{3+} ions in real water.

References

- [1] J. Zhang, J. Shi, J. Tan, X. Wang, M. Gong, *CrystEngComm*. **12** (2010) 1079–1085.
- [2] C. D. S. Brites, A. Millán, L. D. Carlos, Elsevier, Amsterdam, Editors: J-C Bünzli, V. K. Pecharsky, *Handbook on the Physics and Chemistry of Rare Earths*, **49** (2016) 239-427.
- [3] N. Stopikowska, M. Runowski, M. Skwierczyńska, S. Lis, *Nanoscale* **13** (2021) 14139-14146.
- [4] T. Zheng, M. Sójka, P. Woźny, I. R. Martín, V. Lavin, E. Zych S. Lis, P. Du, L. Lou, M. Runowski, *Adv. Opt. Mater.* **10** (2022) 2201055.
- [5] M. Runowski, N. Stopikowska, D. Szeremeta, S. Goderski, M. Skwierczyńska, S. Lis, *ACS Appl. Mater. Interfaces* **11** (2019) 13389–13396.
- [6] M. Skwierczyńska, N. Stopikowska, P. Kulpiński, M. Kłównska, S. Lis, M. Runowski, *Nanomaterials* **12** (2022) 1926.
- [7] M. Runowski, J. Marciniak, T. Grzyb, D. Przybylska, A. Shyichuk, B. Barszcz A. Katrusiak, S. Lis, *Nanoscale* **11** (2019) 8718-8726.
- [8] S. Balabhadra, M. Runowski, S. Lis, *J Rare Earths*, **32** (2014) 232-237.
- [9] P. Kulpiński, A. Erdman, T. Grzyb, S. Lis, *Polymer Composites* **37** (2016) 15-160.
- [10] J. V. N. K. B. Adusumalli, S. Lis, Y. I. Park, *J. Mater. Chem. C* **10** (2022) 17494
- [11] M. Runowski, S. Lis, *J. Alloys Compds*, **597** (2014) 63–71.
- [12] A. Szczeszak, T. Grzyb, Z. Sniadecki, N. Andrzejewska, S. Lis, M. Matczak, G. Nowaczyk, S. Jurga, B. Idzikowski, *Inorg. Chem.*, **53** (2014) 12243–12252.
- [13] T. Zheng, L. Luo, P. Du, S. Lis, U. R. Rodríguez-Mendoza, V. Lavin, I. R. Martín, M. Runowski, *Chem. Eng. J.* **443** (2022) 136414.
- [14] T. Zheng, M. Runowski, P. Wozny, S. Lis, V. Lavin, *J. Mater. Chem. C*, **8** (2020) 4810-4817.
- [15] M. Skwierczyńska, M. Runowski, S. Goderski, J. Szczytko, J. Rybusiński, P. Kulpiński, S. Lis, *ACS Omega*, **3** (2019) 10383-10390.

BIOGRAPHY



Stefan Lis received his Ph.D. (1986) and D.Sc. (1995) degrees in inorganic and analytical chemistry from Adam Mickiewicz University in Poznan, Poland, where he has been a full professor since 2003. He had conducted scientific research in the Florida State University (1989-1991, and 1993-1995). He was a research fellow or visiting professor at research centers in Japan: Japan Atomic Energy Research Institute, (2000), and Tokyo University of Science (2004 and 2006); in the Czech Republic, Germany, Belgium, Spain, China and Brazil. He conducts basic and application research in the field of various group of complexes and nanomaterials based on rare earths. His research concerns emission processes, structural and photophysical studies of lanthanide (Ln) systems, including: development of new analytical methods for the determination of substances of biochemical importance based on Ln luminescence; physicochemical characterization of multifunctional nanostructures; core/shell nanoparticles doped with Ln ions and their surface functionalized systems; application in chemistry, biology: nanomanometry, nanothermometry, anti-counterfeiting systems, medicinal and analytical chemistry, etc. He supervised 15 doctoral theses. Is the author/co-author: ~300 scientific papers, 2 books, several book chapters, 9 patents; [citations: ~7500, index H = 46 (Google Scholar), over 6300, index H = 42 (Scopus)], delivered over 100 invited (15 plenary) lectures at scientific conferences and congresses, was the chairman or member of many scientific international committees; and PI of 11 research projects.

REALIZATION OF TRANSFER-FREE, HIGH-QUALITY, LARGE-AREA GRAPHENE AND N-DOPED GRAPHENE FIELD-EFFECT TRANSISTORS FOR DIGITAL APPLICATIONS

Soon-Gil Yoon*, Jang-Su Jung, Venkatraju Jella, and Swathi Ippili

Department of Materials Science and Engineering, Chungnam National University, Daeduk Science Town, 34134, Daejeon, Republic of Korea
Email: sgyoon@cnu.ac.kr

ABSTRACT

Although graphene has been studied as wonder materials for electronics due to its outstanding charge transport properties, its lack of an electronic bandgap has hindered its application to large-scale field-effect transistor (FET) circuits, thereby making bandgap opening a key priority. Further, the fabrication of graphene devices to date conventionally requires the transfer of graphene from its growth substrate to a target substrate, which introduces defects and negatively impacts the device performance. Overcoming these challenges, we demonstrate a transfer-free approach for the low-temperature growth (~ 100 °C) and *in-situ* doping of monolayer graphene, which enables FETs with cutting-edge performance and stability. With a focus on nitrogen-doped graphene, we realize *n*-channel FETs with an *on-off* ratio of $\sim 2 \times 10^8$, a mobility of $\sim 1,500$ $\text{cm}^2\text{V}^{-1}\text{s}^{-1}$, and a subthreshold swing of ~ 90 mVdec^{-1} . Such devices are highly reproducible and exhibit high wafer-scale uniformity and thermal and bias-stress stability. Further, our approach is highly versatile, for instance also allowing the fabrication of *p*-channel FETs with a mobility of ~ 470 $\text{cm}^2\text{V}^{-1}\text{s}^{-1}$ and an *on-off* ratio of 2×10^5 . In this presentation, various applications using transfer-free graphene will be demonstrated.

Keywords: Transfer-free graphene, N-doped graphene FETs, High-quality, Large-area graphene

BIOGRAPHY



Prof. Soon-Gil Yoon received his Ph.D. from Korea Advanced Institute of Science and Technology (KAIST), Korea in 1988. He is currently a distinguished professor in Department of Materials Science and Engineering, Chungnam National University, Republic of Korea. His current research interests are Thin film capacitor, Fusion technology of Solar cell, Thermoelectric, and Piezoelectric using one material and one structure, Flexoelectric properties using Zn-Al: LDH nanosheets. Mechanical energy harvesting and storage via lithium-battery. Photodetector applications using inorganic/organic perovskite thin films such as MAPbI_3 , MASnI_3 , MAPbCl_3 , lead-free $\text{MA}_3\text{Bi}_2\text{I}_9$ thin films by CVD. He also studied the antibacterial activity, antireflective, and hydrophobicity using the ZnO-based thin films deposited on smart-phone panel. He had published SCI papers of about 405 including Nano Letters, Advanced Materials, ACS Nano, Nano Energy, J. Mater. Chem. A, and Chemical Engineering Journal etc.

A STUDY OF CELL ENCAPSULATED MICROFLUIDICS SYSTEM FOR APPLICATION OF SINGLE CELL ANALYSIS

Hoang Anh Phan¹, Tan Duong Van¹, Nguyen Pham Dang¹, Cuong Nguyen Nhu¹, Loc Do Quang¹, Trung Vu Ngoc², Tung Thanh Bui¹, Chun-Ping Jen³, Hoang Hai Nguyen¹, Trinh Chu Duc^{1*}

¹ Vietnam National University, Hanoi, Vietnam

² Hanoi University of Public Health, Hanoi, Vietnam

³ National Chung Cheng University, Chia-Yi, Taiwan, ROC

*Email: trinhcd@vnu.edu.vn

ABSTRACT

Single-cell analysis is a robust method for investigating cellular diversity, particularly in gaining insights into genetic factors and facilitating early diagnosis, especially in cancer. In this study, a droplet microfluidic channel system capable of creating stable and customizable droplets was proposed and investigated. The droplet generation channel was experimented with for its ability to encapsulate individual beads into droplets and separate them from the bead-containing solution. A YOLOv5 model was used to detect and enumerate the number of beads within each droplet to identify droplets containing a single bead, a crucial prerequisite for downstream droplet sorting techniques. The potential for real-time application by the model is demonstrated, with processing conducted with high accuracy. The experimental results also demonstrated the potential of the proposed approach for single-cell sorting based on cell enumeration, which enables the isolation of rare cell populations for further analysis.

Keywords: single-cell, deep learning, microfluidic, droplet.

INTRODUCTION

Single-cell analysis allows for studying individual cells within a population, providing insights into cellular diversity, identifying rare cell subpopulations, studying cellular dynamics, identifying new cell types and markers, and advancing drug discovery, personalized medicine, and gene therapy [1–3]. Single-cell analysis can be applied to many types of cells, including blood, cancer, stem, and neural cells. It is widely used in several fields, such as genomics, epigenetics, transcriptomics, and proteomics, to understand cell cellular diversity and heterogeneity [4]. Therefore, studies on single-cell isolation are receiving significant attention, particularly microfluidics technology, attracting many researchers due to its promise of delivering more efficient and precise sorting methods [5].

Droplet-based microfluidic platforms are a single-cell sorting method that uses microfluidic structures to generate and manipulate droplets containing individual cells[6]. Droplet generation in microfluidics refers to the process of creating tiny droplets of liquid within a continuous fluid stream by controlling the flow rate and pressure of the liquids [7].

The utilization of droplet-based microfluidics in single-cell sorting applications exhibits several advantages over other single-cell sorting methods[8]. One of the main advantages is its high throughput, which allows for sorting large numbers of cells in parallel. Additionally, droplet-based microfluidics provides precise control over droplet size, which can be essential for sorting cells based on size or volume. A droplet containing single-cell can be classified by several methods, such as flow cytometry, optical sorting, and Machine Learning (ML) algorithms[9–12]. Recent advances in the field, like ML algorithms and integrating multiplexing techniques, are promising to improve classification accuracy and efficiency.

Classifying single-cell coated droplets using ML can be challenging for several reasons. One difficulty is that the data used for training the models may be limited and not represent the full range of droplet variations[12–14]. Additionally, the images of the droplets may be affected by noise and other factors that can make it difficult to classify the droplets accurately. The challenge of analyzing droplet coat cell images arises when cells adhere to the droplet edge or aggregate with other cells, as it becomes challenging to detect

and quantify the individual cells accurately. This difficulty is due to the overlapping and occlusion of cells, which can lead to inaccuracies in cell counting and size measurements. Therefore, developing effective methods to detect and analyze these challenging cases is essential in droplet-based microfluidics.

In this study, a microfluidic channel system was proposed and investigated to produce stable and customizable droplets. The droplet generation channel was evaluated for its ability to encapsulate individual beads into droplets and separate them from the bead-containing solution. Polystyrene beads were utilized with dimensions, morphology, and physical properties equivalent to a cell's to examine the encapsulation capability. Then, an ML model was developed to detect and count the number of beads within each droplet, enabling the identification of droplets containing a single bead, a crucial prerequisite for downstream droplet sorting techniques. The results indicate that Machine learning-based bead enumeration within droplets has the potential to enhance the accuracy and throughput of single-cell sorting applications significantly.

MATERIALS AND METHODS

Encapsulation of Beads in a Microfluidic Droplet Generation Device

A microfluidic device is designed to generate droplets using a Y-shaped geometry. The device is fabricated using conventional soft lithography techniques. It has two 50- μm wide sheath

channels running parallel to each other and a 100- μm wide central channel connecting the two sheath channels at the "Y" intersection. The system uses two liquids, oils in the sheath channels and water in the central channel (Fig. 1).

The flow rate and the geometry of the channels were controlled using a dual-channel syringe pump (KDS Gemini 88 Plus) to control the size of the droplets and the number of beads per droplet. In this study, 8- μm polystyrene beads were used in water as the droplet-generating fluid in the central channel of the microfluidic device. The utilization of beads of the specified dimensions can be attributed to their resemblance to the size and shape of a singular cell. This approach lets us precisely control the flow rate and droplet size for single-cell encapsulation and droplet-based assays. The proposed microfluidic setup is equipped with a micro camera, which is used with a 10x microscope objective lens to capture high-resolution images of the droplets as they flow through the designated window of the microfluidic channel. This configuration allows us to analyze droplet size, shape, and encapsulation efficiency and monitor the behavior of cells or other particles inside the droplets.

Droplet acquisition for computer vision model

This study actively engaged an automated sampling process to create a comprehensive dataset for the ML model. This process involved capturing a video recording of the microfluidic droplet generation system and utilizing advanced

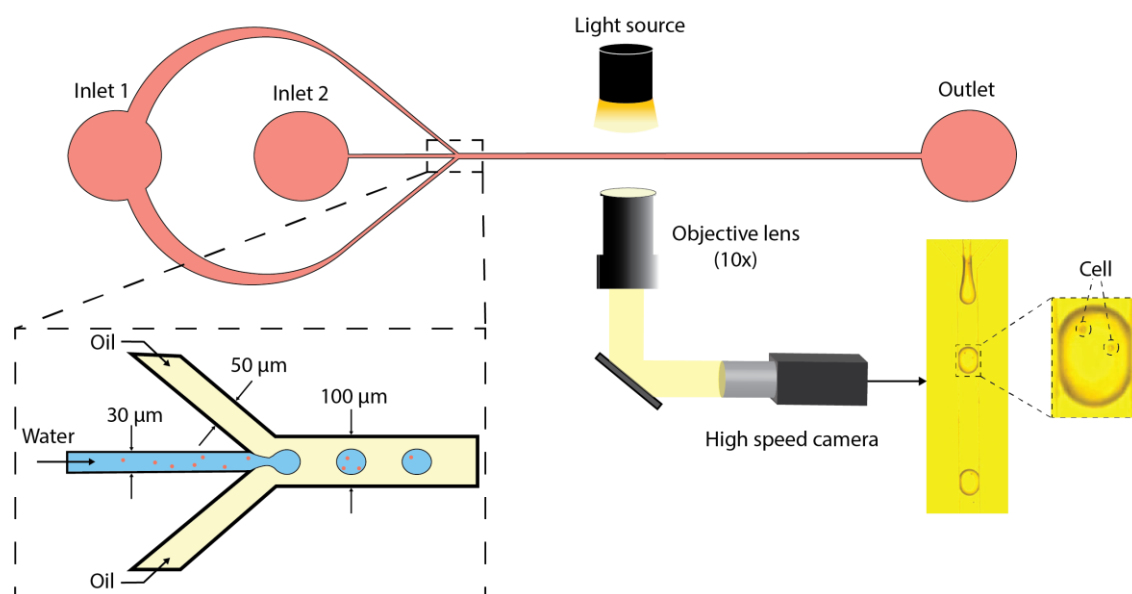


Figure 1. Schematic of the microfluidic platform for cell encapsulation in droplet and droplet classification based on real-time object detection.

image processing techniques to detect and crop images of the droplets. The video was recorded at a high frame rate of 30 frames per second and had a WXGA resolution of 1280x800 pixels per frame. In order to detect the droplets in the image frames, the process was initiated by converting the frames into grayscale. Subsequently, Gaussian Blur was applied to eliminate artifacts, such as stains and channel walls, which could affect result accuracy. The Canny edge detection algorithm was then employed to delineate the droplets' boundaries accurately. Morphological operations were applied to remove any irregular noise within the contour and contouring image.

Machine-learning based Object detection for bead enumeration

In this study, two different types of ML models were utilized: (1) an object detection model to detect individual droplets in the ensemble, referred to as the droplet model, and (2) an object detection model to detect the beads inside the droplets referred to as the cell model. YOLOv5 was a superior choice for the ML model due to its exceptional accuracy in detecting and locating small objects within an image[15]. This is especially critical in bead enumeration studies, where the objects of interest are often small and tightly packed together.

EXPERIMENT RESULTS

This study aimed to develop a machine learning-based approach for precise bead enumeration within droplets, particularly for single-cell sorting applications. Leveraging the YOLO-v5 model, this challenge was tackled by employing convolutional neural networks (CNNs) to analyze high-resolution images of

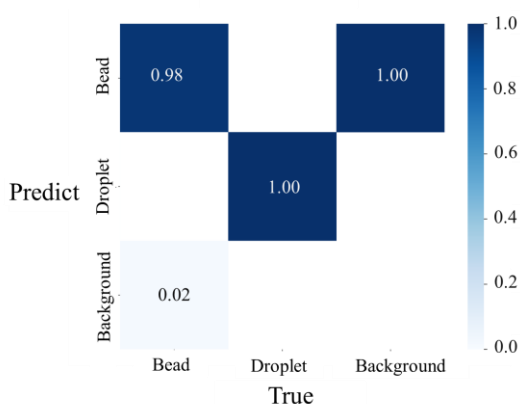


Figure 2. The Confusion matrix for the droplet model test set

droplets. The primary objective was to fine-tune the model to enhance its accuracy, especially in uncertain scenarios, and to illustrate its potential for sorting droplets based on bead quantity. The model demonstrated a robust ability to detect two distinct objects within the data, namely, droplets and beads, achieving a high reliability of up to 80% per frame.

The confusion matrix is a vital tool for assessing the predictive accuracy of a model. In this work, the confusion matrix was employed to gauge the precision of the proposed model's predictions regarding bead quantities within droplets (Fig. 2). The results demonstrate an outstanding accuracy level, with 100% precision in droplet prediction and 98% in bead detection. The remarkably high accuracy score underscores the efficacy of the proposed machine learning-based approach in the precise enumeration of beads within droplets.

A comprehensive set of metrics beyond the traditional accuracy rate was employed to evaluate the detection task's performance on the dataset. In particular, Precision and Recall were utilized, in addition to the accuracy rate, to ensure a fair and thorough assessment of the detection outcomes. The Precision and Recall curves enable the selection of an appropriate threshold that balances both the accuracy of detection and the rate of False Positives and False Negatives. The threshold value decreases as Recall decreases from 1 to 0. The classification performance for both object classes is highly effective, with an average value at a threshold of 0.5 reaching 98.3% (Fig. 3). Regarding the bead object under study, the Precision and Recall values are 97.3% and 99.3%, respectively, at the threshold of 0.5. These values demonstrate a highly effective classification ability for the particle object.

CONCLUSION

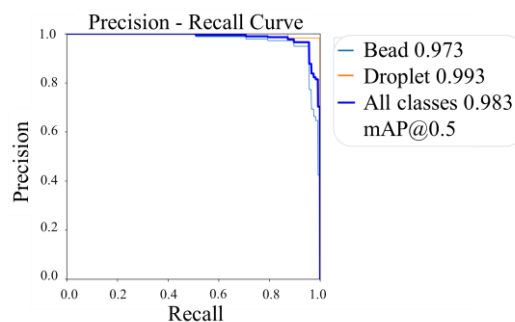


Figure 3. The Precision – Recall Curve for droplet model test set

In this investigation, a droplet microfluidic channel system designed for the controlled generation of stable and customizable droplets was proposed and investigated. The proposed strategy harnessed a YOLOv5 model for precisely detecting and enumerating beads within each droplet, a crucial prerequisite for downstream droplet sorting techniques. The experimental results underscored the prospective utility of the proposed methodology for single-cell sorting predicated on cell enumeration. This capability paves the way for isolating rare cell populations, facilitating their subsequent in-depth analysis.

Acknowledgements

This work was funded by the Vietnam Ministry of Science and Technology under Grant ĐTĐL.CN-40/23.

References

- [1] H. Lu, O. Caen, J. Vrignon, E. Zonta, Z. El Harrak, P. Nizard, J.C. Baret, V. Taly, *High throughput single cell counting in droplet-based microfluidics*, Scientific Reports 2017 7:1. **7** (2017) 1–9.
- [2] A. Arjun, R.R. Ajith, S. Kumar Ranjith AFFILIATIONS, *Mixing characterization of binary-coalesced droplets in microchannels using deep neural network*, Biomicrofluidics. **14** (2020) 34111.
- [3] A. Chu, D. Nguyen, S.S. Talathi, A.C. Wilson, C. Ye, W.L. Smith, A.D. Kaplan, E.B. Duoss, J.K. Stolaroff, B. Giera, *Automated detection and sorting of microencapsulation via machine learning*, Lab Chip. **19** (2019) 1808–1817.
- [4] A. Arjun, R.R. Ajith, S. Kumar Ranjith, *Mixing characterization of binary-coalesced droplets in microchannels using deep neural network*, Biomicrofluidics. **14** (2020).
- [5] L. Mazutis, J. Gilbert, W.L. Ung, D.A. Weitz, A.D. Griffiths, J.A. Heyman, *Single-cell analysis and sorting using droplet-based microfluidics*, Nat Protoc. **8** (2013) 870–891.
- [6] M. Sesen, G. Whyte, *Image-Based Single Cell Sorting Automation in Droplet Microfluidics*, Sci Rep. **10** (2020).
- [7] K. Matuła, F. Rivello, W.T.S. Huck, *Single-Cell Analysis Using Droplet Microfluidics*, Adv Biosyst. **4** (2020).
- [8] M. Sesen, G. Whyte, *Image-Based Single Cell Sorting Automation in Droplet Microfluidics*, Sci Rep. **10** (2020).
- [9] H. Hashemzadeh, S. Shojaeilangari, A. Allahverdi, M. Rothbauer, P. Ertl, H. Naderi-Manesh, *A combined microfluidic deep learning approach for lung cancer cell high throughput screening toward automatic cancer screening applications*, Sci Rep. **11** (2021).
- [10] S. Srikanth, S.K. Dubey, A. Javed, S. Goel, *Droplet based microfluidics integrated with machine learning*, Sens Actuators A Phys. **332** (2021).
- [11] P. Hadikhani, N. Borhani, S.M. H. Hashemi, D. Psaltis, *Learning from droplet flows in microfluidic channels using deep neural networks*, Sci Rep. **9** (2019).
- [12] F. Anagnostidis, Vasileios; Sherlock, Benjamin; Metz, Jeremy; Mair, Philip; Hollfelder, Florian; Gielen, *Deep learning guided image-based droplet sorting for on-demand selection and analysis of single cells and 3D cell cultures*, Lab Chip. (2014) 1037–1043.
- [13] S. Vanapalli, W. Li, K. Gardner, M. Uddin, L. Tran, T. Pham, *Deep learning detector for high precision monitoring of cell encapsulation statistics in microfluidic droplets*, **22** (2022) 4067.
- [14] X. Niu, M. Zhang, S. Peng, W. Wen, P. Sheng, *Real-time detection, control, and sorting of microfluidic droplets*, Biomicrofluidics. **1** (2007).
- [15] T. Pham, S. Vanapalli, W. Li, K. Gardner, M. Uddin, L. Tran, *Deep learning detector for high precision monitoring of cell encapsulation statistics in microfluidic droplets Lab on a Chip Devices and applications at the micro-and nanoscale Deep learning detector for high precision monitoring of cell encapsulation statistics in microfluidic droplets Deep learning detector for high precision monitoring of cell encapsulation statistics in microfluidic droplets*, **22** (2022) 4067

BIOGRAPHY



Chu Duc Trinh is a full professor with the Faculty of Electronics and Telecommunications (FET), VNU-UET. He obtained his B.Sc. degree in physics from VNU University of Science, Vietnam in 1998, followed by an M.Sc. degree in electrical engineering from VNU-UET in 2002, and a Ph.D. in microelectromechanical systems from Delft University of Technology, the Netherlands in 2007.

Prof. Dr. Trinh Chu Duc currently serves as the Rector at the University of Engineering and Technology, Vietnam National University (VNU-UET), Vietnam. Before assuming the position of Rector of the University of Engineering Technology, he has experienced various positions such as Vice

Dean of FET, VNU-UET; Head of Electronics and Telecommunications Practice Room, FET, VNU-UET; Vice Rector of VNU-UET.

Since 2015 Prof. Dr. Trinh Chu Duc has held the position of Head of the Department of Microelectromechanical Systems and Microsystems (MEMS). Currently, his research primary focuses on semiconductor manufacturing, microfabrication, integrated circuit design, MEMS sensors, polymeric actuators, sensing microgrippers, and microsystems technology, especially microfluidics systems for various biomedical applications. He is the author of over 150 journal and conference papers and holds several patented inventions.

EMBEDDED NON-VOLATILE MEMORY FOR FUTURE EDGE COMPUTING

F. Andrieu

CEA-Leti, Grenoble Alpes University, 17 rue des Martyrs, 38054 GRENOBLE, FRANCE

Email: francois.andrieu@cea.fr

ABSTRACT

Embedded Non-Volatile Memory (eNVM) is a key solid-state device for low-power computing at the edge. It enables to store the code and the data in micro-controllers or micro-processors. Historically, NOR flash technology relies on the storage of electrons in a nitride layer embedded in the gate stack. However, since the 28nm node, dielectrics of high permittivity (high-k) and metal gates were introduced, which made the co-integration of the traditional e-flash more difficult. At the same time, Resistive Random Access Memories (RRAM) appeared as a promising alternative because of the full Back-End-Of-Line (BEOL) integration as well as a reduced operating voltage and power consumption. In RRAM, the information is no longer encoded by the amounts of charges but by different resistance values of a material. There are many flavors of emerging RAM: Magnetic (MRAM), Oxide (OxRAM) or Phase Change Memory (PCM). Hafnium oxide based Ferroelectric memory (FeRAM / FeFET) is another emerging device, leveraging the electrical polarization of a dielectric. At CEA Leti, we are working on all of these devices, their process integration, as well as the relative circuit designs.

On OxRAM, we integrated these devices in 28nm node [1]. Low raw BER approaching 10^{-5} without Error Correction Code (ECC) or redundancy was achieved, along with 10^6 cycles endurance. We reported stable memory window after 15h bake at 210°C and 10kcycles, which is one of the best results reported so far to our knowledge. Technology passed basic (3x reflow) and extended (9 cycles) SMT tests with zero failures. Optimized forming protocols were developed to increase memory yield over cycling. Program and verify algorithms allowed to insure no overlap between high and low resistive states on 1Mb arrays. All of these results make this technology very attractive for low-cost micro-controllers.

As far as the PCM is concerned, this technology was demonstrated in 28nm node with a bipolar transistor selector, a cell size as small as $0.019\mu\text{m}^2$, in a macro-cell as large as 16MB [2]. It fulfills all of the requirement for automotive grade 0. At CEA-Leti, we are exploring the integration of a full Back-End-Of-Line (BEOL) selector in order to gain even more in terms of density. Functional GeSbSeN switches as small as $60*80\text{ nm}^2$ were fabricated and directly co-integrated with GeSbTe PCM memories to evaluate the interest of this solution for embedded applications.

FeRAM technology is very attractive for energy efficient systems, as the reading is charge-based and not current-based (like for OxRAM or PCM). We integrated 7nm thin HfZrO materials as ferroelectric layers and demonstrated Bit Error Rates down to 10^{-5} for $0.24\mu\text{m}^2$ capacitors and at 2.8V programming voltage. Functionality was even highlighted down to 1.8V.

All of these device flavors are not only attractive for data/code storage application but also for Artificial Intelligence based on In-Memory-Computing.

Keywords: Non-Volatile-Memory, Resistive Memory

References

- [1] Molas, G., Piccolboni, G., Bricalli, A., Verdy, A., Naot, I., Cohen, Y., & Grenouillet, L. *High temperature stability embedded ReRAM for 2x nm node and beyond*. In 2022 IEEE International Memory Workshop (IMW), (2022) 1-4.
- [2] Disegni, F., Ventre, A., Molgora, A., Cappelletti, P., Badalamenti, R., Ferreira, P., & Peri, M. *16MB High Density Embedded PCM macrocell for automotive-grade microcontroller in 28nm FD-SOI, featuring extension to 24MB for Over-The-Air software update*. In 2021 Symposium on VLSI Circuits, (2021) 1-2.

- [3] Bourgeois, G., Meli, V., Antonelli, R., Socquet-Clerc, C., Magis, T., Laulagnet, F., & Navarro, G. *Crossbar Arrays based on “Wall” Phase-Change Memory (PCM) and Ovonic-Threshold Switching (OTS) Selector: a Device Integration Challenge Towards New Computing Paradigms in Embedded Applications*. In 2023 7th IEEE Electron Devices Technology & Manufacturing Conference (EDTM), (2023) 1-3.
- [4] L. Grenouillet et al., NVMTS’2023

BIOGRAPHY



Dr. François Andrieu is CEA fellow and the head of Laboratory “Nano-devices for Memory and Computing” at CEA-Leti, Grenoble, France.

His fields of interest are: NVM Resistive-RAM and In-Memory-Computing, advanced CMOS transistors, stacked nanowires, 3D-sequential integration. He has been strongly involved in the development of the Fully-Depleted-Silicon-OnInsulator (FDSOI) CMOS technology at Leti and with STMicroelectronics, where he was assigned between 2012-2015 in the process-integration and technology-todesign groups.

More widely, he is the author or co-author of more than 34 patents, 240 conference abstracts or refereed journal articles, 11 invited papers and 3 book chapters. He has served in many conference TPCs (IEDM, VLSI-TSA, EDTM, ESSDERC, SSDM...) and is currently in the steering committee of ESSDERC-ESSCIRC. He received the IEEE senior grade in 2018, the IEEE/SEE Brillouin award in 2018 and the European ERC consolidator grant in 2019.

AN ANTI-GLARE AUTOMOTIVE LIGHTING SYSTEM USING POLARIZING FILTERS AND FLIP PLATE

Minh Ngoc Phan², **Nghia Phan Trong Nguyen**¹, **Duc Anh To**³, **Anh Van Thi Nguyen**¹, **Thuy Thi Bui**¹, and **Thang Hung Bui**¹

¹ Institute of Materials Science, Vietnam Academy of Science Technology, Hanoi, Vietnam

² Graduate School of Science and Technology, Vietnam Academy of Science Technology, Hanoi, Vietnam

³ Vietnam National Space Center, Vietnam Academy of Science Technology, Hanoi, Vietnam

Email: thangbh@ims.vast.ac.vn

ABSTRACT

In the past, polarizing filters were used to reduce glare coming for other vehicles. However, the filters absorbed a significant amount of light from the headlights and hindered the driver's vision. Along with overheating issues and numerous technical and logistical limitations, polarized automotive lighting systems have not become standardized. In this research, we propose using a polarized LED lighting system to improve drivers' visibility. Our results demonstrated an illuminance reduction of up to 97.5% when using a polarized headlight filter and flip plate. Furthermore, our system's lower operating temperatures increases the operating life of the filters by approximately 120 times compared to a conventional halogen lighting system.

Keywords: Polarization, anti-glare, traffic vehicles, lifespan.

BIOGRAPHY



Prof. Phan Ngoc Minh completed his PhD of solid state physics at Institute of Physics, Vietnam Academy of Science and Technology (VAST) in 1996; PhD of Engineering at Tohoku University, Japan in 2001. From 2001-2004 he worked as a Post-Doctoral and then Assistant Professor at Tohoku University, Japan in the field of Nanotechnology. He became Associate Professor and Professor of Physics in 2007 and 2016, respectively. From 2016 - 2021, he was Vice President of Vietnam Academy of Science and Technology, Rector of the Graduate University of Science and Technology. Now, he is a Professor and a Senior Researcher at Graduate University of Science and Technology; Laboratory of Carbon nanomaterials, Center of Application & Development of Technology, Institute of Materials Science;

Center of Advanced Materials, Center of High Technology Development of the Academy.

MATERIALIZING COGNITION: INFORMATION PROCESSING IN COGNITIVE MATTER

Wilfred G. van der Wiel^{1,2}

¹ BRAINS Center for Brain-Inspired Nano Systems, University of Twente,
PO Box 217, 7500 AE, Enschede, The Netherlands;

²Institute of Physics, University of Münster, 48149 Münster, Germany
Email: W.G.vanderWiel@utwente.nl

ABSTRACT

Throughout history, man has exploited matter to carry out tasks well beyond his biological constraints. Starting from primitive tools with functionality solely derived from shape and structure, we have moved on to responsive matter that can change its properties upon external stimulus and even further to adaptive matter that can change its response depending on the environment. One of the grand scientific and intellectual challenges is to make matter that can actually *learn*. Such matter's behavior would not only depend on the here and now, but also on its past. It would have memory, and ultimately autonomously interact with its environment and self-regulate its action. We may call such matter 'cognitive' or even 'intelligent'^{1,2}.

Here we introduce a number of experiments on disordered nanomaterial systems, where we make use of "material learning" to realize functionality. We have shown that a 'designless' network of gold nanoparticles can be configured into Boolean logic gates using artificial evolution³. We further demonstrated that this principle is generic and can be transferred to other material systems. By exploiting the nonlinearity of a nanoscale network of dopants in silicon, referred to as a dopant network processing unit (DNPU), we can significantly facilitate handwritten digit classification⁴. An alternative material-learning approach is followed by first mapping our DNPU on a deep-neural-network model, which allows for applying standard machine-learning techniques in finding functionality⁵. We give examples how simulated multi-DNPU networks can solve more complex tasks than individual DNPUs^{6,7}. Finally, we show that our devices are not only suitable for solving static problems but can also be applied in highly efficient real-time processing of time-dependent signals.

References

- [1] C. Kaspar et al., *Nature* **594** (2021) 345.
- [2] H. Jaeger et al., *Nat. Commun.* **14** (2023) 4911.
- [3] S.K. Bose, C.P. Lawrence et al., *Nature Nanotechnol.* **10** (2015) 1048.
- [4] T. Chen et al., *Nature* **577** (2020) 341.
- [5] H.-C. Ruiz Euler et al., *Nat. Nanotechnol.* **15** (2020) 992.
- [6] H.-C. Ruiz Euler et al., *Neuromorph. Comput. Eng.* **1** (2021) 024002.
- [7] B. van de Ven et al., *Front. Nanotechnol.* **5** (2023) 1055527.

BIOGRAPHY



Wilfred G. van der Wiel (Gouda, 1975) is full professor of Nanoelectronics and director of the BRAINS Center for Brain-Inspired Nano Systems at the University of Twente, The Netherlands. He holds a second professorship at the Institute of Physics of the University of Münster, Germany. His research focuses on unconventional electronics for efficient information processing. Van der Wiel is a pioneer in Material Learning at the nanoscale, realizing computational functionality and artificial intelligence in designless nanomaterial substrates through principles analogous to Machine Learning. He is author of more than 125 journal articles receiving over 8,500 citations.

DETECTION OF LOW CONCENTRATION OF BIOMARKERS WITH A SANDWICH TYPE IMMUNOSENSOR INTEGRATED BY METASURFACE AND UPCONVERSION NANOPARTICLES

Chia-Chen Hsu¹, Yu-Chung Chiu¹, Yen-Ta Tseng^{1,2}, Van Dai Pham¹, Wen-Hsuan Wu¹, Thanh Thu Le Vu¹, Lai-Kwan Chau², Shiao-Wei Kuo³, Michael WY Chan⁴, Hung-Chih Kan¹, Jiunn-Yuan Lin¹,

¹ Department of Physics, National Chung Cheng University, Ming-Hsiung, Chia-Yi, 621, Taiwan;

² Department of Chemistry and Biochemistry National Chung Cheng University, Chia-Yi, 621, Taiwan;

³ Department of Materials and Optoelectronic Science, National Sun Yat Sen University, Kaohsiung, 804, Taiwan;

⁴ Department of Biomedical Science, National Chung Cheng University, Chia-Yi, 621, Taiwan

Email: phycch@ccu.edu.tw

ABSTRACT

A sandwich type immunosensor in a 3x3 well array format based on the integration of metasurface and upconversion nanoparticles (UCNPs) is presented in this work for the detection of low concentration of biomarkers in blood. UCNPs are used to label target biomarkers captured by capture antibodies immobilized on the surface of the metasurface, and the metasurface is used to enhance the upconversion luminescence (UCL) of UCNPs through excitation resonance. The limit of detection (LOD) of the immunosensor is greatly reduced due to the increased UCL of UCNPs and the reduction of nonspecific adsorption of detection antibody-conjugated UCNP on the metasurface. The immunosensor exhibited an extremely low LOD (0.24 fg/mL (9.1 aM)) and wide detection range (1 fg/mL to 100 pg/mL) in the detection of cardiac troponin I (cTnI). Having higher number of wells in such an array-based biosensor, the sensor can be developed as a high-throughput diagnostic tool for clinically important biomarkers.

Keywords: Upconversion nanoparticle, upconversion luminescence, cardiac troponin I, sandwich-type immunoassay, metasurface, excitation resonance.

BIOGRAPHY



Chia Chen Hsu

Department of Physics, National Chung Cheng University (CCU)

168 University Road, Ming-Hsiung, Chia-Yi County, 62102 Taiwan

Phone : 886-5-2720411-66305, Fax :886-5-2720587, Email: phycch@ccu.edu.tw

Education

Ph.D., Physics, University of Arizona, 1991.

Master, Optical Sciences, National Central University 1984.

B.S., Physics, National Central University, 1981.

Work Experience

Distinguished Professor, Department of Physics, CCU, Taiwan, 2016/01-present.

Professor, Department of Physics, CCU, Taiwan, 2001/08-2015/12.

Invited Professor, Laboratoire de photonique quantique et moléculaire, École normale supérieure de Cachan, France, 2015/09-2016/01.

Dean, College of Science, CCU, Taiwan, 2009/08-2012/07.

Visiting Professor, Department of Physics and Astronomy, University of British Columbia, Canada, 2006/05-2006/08.

Director, Graduate Institute of Opto-Mechatronics, CCU, Taiwan, 2002/08-2005/07.

Associate Professor, Department of Physics, CCU, Taiwan, 1991/08-2001/07.

Awards

2009, Outstanding research award, National Chung Cheng University

2016, Distinguished Professor, National Chung Cheng University

Research Interests

Nanophotonics, Nonlinear Optics, Nano Materials, Biosensing.

Selected publications

1. V. N. Nguyen, Y. H. Lee, T. T. Le-Vu, J. Y. Lin*, H. C. Kan, and **C. C. Hsu***, 2022 “Impact of excitation intensity-dependent fluorescence intensity ratio of upconversion nanoparticles on wide-field thermal imaging” *ACS Applied Nano Materials*, **5**, 15172. 5.

2. D. T. Vu, Y. C. Tsai, Q. M. Le, S. W. Kuo, N. D. Lai, H. Benisty, J. Y. Lin, H. C. Kan, and **C. C. Hsu***, 2021 “A synergy approach to enhance upconversion luminescence emission of rare earth nanophosphors with million-fold enhancement factor” *Crystals*, **11**, 1187.

3. D. T. Vu, H. W. Chiu, R. Nababan, Q. M. Le, S. W. Kuo, L. K. Chau, C. C. Ting, H. C. Kan, and **C. C. Hsu***, 2018 “Enhancing upconversion luminescence emission of rare earth nanophosphors in aqueous solution with thousands fold enhancement factor by low refractive index resonant waveguide grating” *ACS Photonics*, **5**, 3263.

4. A. T. Nguyen, W. C. Lai, B. D. To, D. D. Nguyen, Y. P. Hsieh, M. Hofmann, H. C. Kan, and **C. C. Hsu***, 2017 “Layer control of tubular graphene for corrosion inhibition of nickel wires” *ACS Applied Materials and Interfaces*, **9**, 22911.

5. J. H. Lin, H. Y. Liou, C. D. Wang, C. Y. Tseng, C. T. Lee, C. C. Ting, H. C. Kan*, and **C. C. Hsu***, 2015.” Giant enhancement of upconversion fluorescence NaYF₄:Yb³⁺,Tm³⁺ nanocrystals with resonant waveguide grating substrate”, *ACS Photonics*, **2**, 530.

AUTO-CHARGING OF MICROSPRAYS AND APPLICATIONS

Cees JM van Rijn¹, and Stefan Kooij² 1

Van der Waals-Zeeman Institute, University of Amsterdam, Science Park 904, Amsterdam, Netherlands;

Email: c.j.m.vanrijn@uva.nl

ABSTRACT

We show that the spray plume dynamics and maximum travelled distance of a microspray depends on the level of charging of the individual droplets forming the spray. The charging of the droplets makes them repel each other, thereby preventing droplet coalescence and leading to strongly curved trajectories. In this work we focus on laminar jets created by ultrashort channels, and quantify the amount of charging as a function of the ionic strength of the liquid relevant for different applications.

Keywords: spray plume, charged droplets, ionic strength

INTRODUCTION

Spray plume dynamics is important for many applications such as drug delivery [1,2], coatings, but also in the spreading of pathogens such as SARS-CoV-2 [3,4]. When poorly conducting liquids are used, interaction of the flow with the nozzle can lead to auto-charging. If droplets are large, this effect can often be ignored. For fine sprays however, the droplets are small enough such that the electric charges can have a significant impact on the shape and travelled distance of the spray plume (Fig. 1).

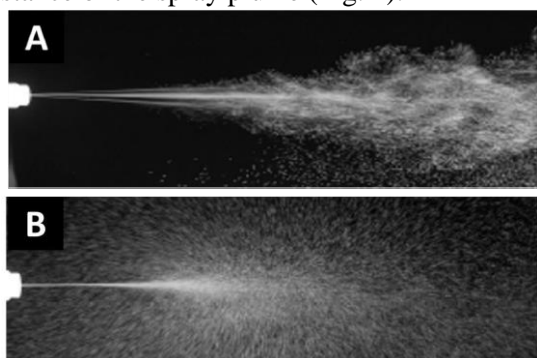


Fig 1. Spray plumes without (A) and with charging (B) using a $2\ \mu\text{m}$ nozzle. In (B) the droplet trajectories are curved due to droplet repulsion.

Charge separation due to liquid flow has been widely studied in various context, such as energy production [5,6], sliding droplets [7], erosion due to liquid flow [8], and risks of fire and explosion in the transport of hydrocarbons through metallic

pipes [9–11]. The phenomena of charging of poorly conducting liquids flowing through pipes and orifices is therefore wellknown, and as a consequence a number of theories has been developed [11,12].

Models for electrokinetic charging are generally based on the fact that when a material comes into contact with a liquid, it will release or absorb some ions, leaving behind a charged surface. With counter-ions moving towards the surface an electrical double layer is formed [13].

EXPERIMENTAL

The amount of auto-charging depends on the spray exit velocity and the ionic strength or salt concentration of the liquid. A higher exit velocity induces a larger friction with the nozzle wall, resulting in a larger charge per droplet. The ionic strength determines the amount of reflow of charge from the jets back to the bulk.

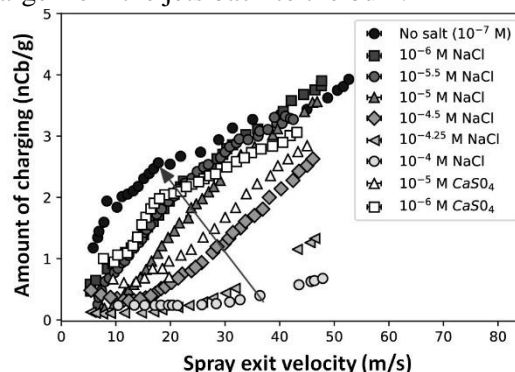


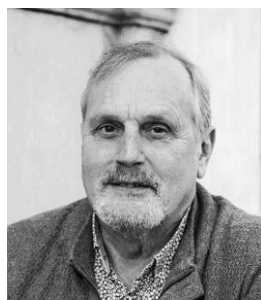
Fig. 2. Charging efficiency for different salt concentrations in water as a function of the spray exit velocity.

The arrow in fig. 2 indicates a decreasing salt concentration, showing that for salt concentrations higher than 10^{-4} M, charging becomes substantially less.

References

- [1] D. D'Angelo, S. Kooij, F. Verhoeven, F. Sonvico, and C. van Rijn, *Fluorescence-enabled evaluation of nasal tract deposition using an innovative spray device*, Journal of Advanced Research (2022).
- [2] M. Y. Foo, Y.-S. Cheng, W.-C. Su, and M. D. Donovan, *The influence of spray properties on intranasal deposition*, Journal of Aerosol Medicine **20** (2007) 495.
- [3] M. Jayaweera, H. Perera, B. Gunawardana, and J. Man-atunge, *Transmission of covid-19 virus by droplets and aerosols: Environmental research* **188** (2020) 109819.
- [4] Z. P. Tan, L. Silwal, S. P. Bhatt, and V. Raghav, *Experimental characterization of speech aerosol dispersion dynamics*, Scientific reports **11** (2021) 1.
- [5] M. Duffin and R. J. Saykally, *Electrokinetic hydrogen generation from liquid water microjets*, The Journal of Physical Chemistry C **111** (2007) 12031.
- [6] M. Duffin and R. J. Saykally, *Electro kinetic power generation from liquid water microjets*, The Journal of Physical Chemistry C **112** (2008) 17018.
- [7] Z. Stetten, D. S. Golovko, S. A. Weber, and H.-J. Butt, *Slide electrification: charging of surfaces by moving water drops*, Soft Matter **15** (2019) 8667.
- [8] D. Lis, E. H. Backus, J. Hunger, S. H. Parekh, and M. Bonn, *Liquid flow along a solid surface reversibly alters interfacial chemistry*, Science **344** (2014) 1138.
- [9] P. M. Hirsch, *Electrostatic charge generation in hydrocarbon liquids*, Ph.D. thesis, Massachusetts Institute of Technology (1979).
- [10] J. Van der Minne and A. Klinkenberg, *Electrostatics in the Petroleum Industry*.
- [11] J. Davies and E. Rideal, *Interfacial phenomena*. Chapter.
- [12] Boumans, *Streaming currents in turbulent flows and metal capillaries: I. theory (1). distribution of charge in the liquid*, Physica **23**, 1007 (1957).
- [13] D. C. Grahame, *The electrical double layer and the theory of electrocapillarity.*, Chemical reviews **41**, 441 (1947).

BIOGRAPHY



Prof. Dr. Cees van Rijn graduated from the Vrije Universiteit of Amsterdam in 1982 on Condensed Matter Physics. He received Ph.D at University of Leiden on ‘Nuclear Magnetic Relaxation of Polyelectrolyte Solutions’. He has worked at Philips Eindhoven and gained expertise in semiconductor technology during the ‘Megachip’ project (1986-1991). In the early nineties he founded Aquamarijn Micro Filtration (www.aquamarijn.nl) and initiated research on micro filtration membranes made with semiconductor technology at the MESA Research Institute. He is founding father of Medspray (www.medspray.com) in 2002, Nanomi (www.nanomi.com) in 2004, Nanosens (www.nanosens.nl) in 2006, and Vycap (www.vycap.com) in 2011. He is author and co-author of more than 144 scientific publications. He published a book ‘Nano and Micro Engineered Membrane Technology’, Elsevier Amsterdam (2004) ISBN 0.444-51489-9. The book covers a broad spectrum of membrane science and technology, such as micro and nano filtration, biosensors, photonics, microbiology, controlled drug delivery, nanopatterning, micro contact printing, emulsification and atomisation. In 2006 he holds a chair at University of Wageningen on Micro and Nanotechnology, and since 2020 he holds a chair at University of Amsterdam on nanotechnology and microfluidics.

THERMOELECTRIC MODULE BASED In and Ga CO-DOPED ZnO THIN FILMS

Athorn Vora-ud^{a,b,*1}, Anh Tuan Thanh Pham^{c,d,e,1}, Dai Cao Truong^{d,e}, Somporn Thoawankeaw^b, Hoa Thi Lai^{d,e}, Thu Bao Nguyen Le^{e,f}, Nhat Quang Minh Tran^{d,e}, Mekhala Insawang^a, Pennapa Muthitamongkol^g, Mati Horprathum^h, Manish Kumarⁱ, Sungkyun Park^j, Gerald Jeffrey Snyder^k, Tosawat Seetawan^{a,b,} and Thang Bach Phan^{d,e,***}**

^a Program of Physics, Faculty of Science and Technology, Sakon Nakhon Rajabhat University, Thailand

^b Thin Film Laboratory, Center of Excellence on Alternative Energy, Research and Development Institution, Sakon Nakhon Rajabhat University, Thailand

^c Laboratory of Advanced Materials, University of Science, Ho Chi Minh City, Vietnam

^d Center for Innovative Materials and Architectures, Ho Chi Minh City, Vietnam

^e Vietnam National University, Ho Chi Minh City, 700000, Vietnam

^f Department of Mathematics and Physics, University of Information Technology, Ho Chi Minh City, Vietnam

^g National Metal and Materials Technology Center, National Science and Technology Development Agency, Pathumthani 12120, Thailand

^h National Electronics and Computer Technology Center, 114 Thailand Science Park, Thailand

ⁱ Centre for Advanced Materials, Organisation for Science Innovations and Research, RS Science Park, Bah 283104, India

^j Department of Physics, Pusan National University, Busan 46241, Republic of Korea

^k Department of Materials Science and Engineering, Northwestern University, Evanston, IL, 60208, United States

Email: pbthang@inomar.edu.vn

ABSTRACT

Here, we report the thermoelectric properties of dual Ga and In doped ZnO films (IGZO) deposited on a polyimide substrate with post-thermal treatment in vacuum along with fabricating 4-unileg flexible IGZO thermoelectric devices. All the as-deposited and annealed IGZO films are the preferred (002) orientation and under tensile stress. Among the films, the IGZO film annealed at 250°C has the best power factor of $16.9 \mu\text{Wm}^{-1}\text{K}^{-2}$ with the largest crystal size, lowest tensile stress, highest carrier concentration, and lowest density-of-state effective mass. The practical application of flexible IGZO films was also reported via a 4-unileg-IGZO films thermoelectric module, which achieved an output power about 3.2 nW at $\Delta T = 120$ K.

Keywords: ZnO thin films, flexible-transparent thermoelectric, Seebeck coefficient; thermopower factor

BIOGRAPHY



Thang Bach Phan

Senior lecturer, Professor

Center for Innovatives Materials and Architectures, Vietnam National University HoChiMinh City (VNU-HCM)

Email: pbthang@inomar.edu.vn

Tel: +84 079 790 7700

<http://inomar.edu.vn>

<https://scholar.google.com.vn/citations?user=EjMB36MAAAAJ&hl=en>.

Professor Thang Bach Phan received the Bachelor degree in Applied Physics from University of Science, Vietnam National University HoChiMinh City (VNU-HCM) in 2001 and Ph.D. degree from School of Advanced Materials and Engineering, Sungkyunkwan University, South Korea in 2009. Currently, he is the Director of Center for Innovative Materials and Architectures (INOMAR, VNU-HCM).

His research interests are synthesis and applications of nano structural materials for thermoelectric conversion, drug delivery, biosensors. He have been holding a Principal investigator (PI) of more than 10 key projects funded from Ministry of Science and Technology (MOST), National Foundation for Science and Technology Development (NAFOSTED), VNU-HCM. Currently, he is leading the VNU-HCM Key Research Group (2019-2024) in Physics Materials which is focusing on new materials applied in Clean Energy (thermoelectric), Health care (biosensor, drug delivery,). In addition, his group is also funded as the NAFOSTED Key Research group for the period 2022 – 2025 in Clean Energy (Thermoelectric conversion materials and Devices).

He is also a Standing committee (2019-2024) of Vietnam Materials Research Society (V-MRS), Scientific committees member of NAFOSTED – Physics division (2017 - present), Standing committee and Vice President (2017-present) of Vietnam Magnetic Society, Council members (2017 - present) of The Asian Union of Magnetism Societies (AUMS). To his credit, he has published about 150 papers in reputed peer-reviewed International Journals, 1 Book, 1 Book chapter and 01 US patent, $H_{index} = 25$.

INTEGRATING METAL OXIDE SEMICONDUCTOR FIELD EFFECT TRANSISTOR SENSORS WITH MICROFLUIDIC TOWARDS POINT-OF-CARE TESTING FOR PREECLAMPSIA

Duy P. Tran, Edward Cheah, Mohamed T. Amen, Benjamin Thierry

Future Industries Institute, University of South Australia, Adelaide 5000

Email: Benjamin.thierry@unisa.edu.au

ABSTRACT

Advancement in affinity-based nanoscale field-effect-transistor (FET) biosensors paves the way to the feasibility of ultra-sensitive measurement of diagnostic biomarkers in complex biological matrices such as blood and saliva and in the point-of-care format, with the potential to match the analytical performance of centralized testing. However, real-life implementation remains faced with several challenge, including the scale-up manufacture of high-performance FET sensors and their integration within disposable test cartridges. In addition, mitigating the issues of non-specific fouling of affinity-biosensors and their shelf-life remains challenging.

This presentation will illustrate these challenges and discuss potential solutions in the context of point-of-care testing for preeclampsia blood biomarkers. Accurate and timely diagnosis of preeclampsia is necessary to administer the appropriate care and prevent the potentially dramatic complications of the condition for both mothers and their babies. The current gold standard preeclampsia assessment based on angiogenic biomarkers requires centralized bioanalytical facilities, and therefore biomarker testing cannot be implemented in remote/low-resource areas.

Towards addressing the need for better preeclampsia testing in primary care, we are developing a fully integrated biodiagnostic platform based on nanoscale indium oxide field effect transistor (FET) sensors integrated within autonomous 3D printed blood processing cartridges and handheld readers. High-performance nanosensors with a steep subthreshold swing of 80 mV per decade are achieved through a combination of high-quality fabrication, stringent quality assessment, and the choice of a suitable device operation point that mitigates the issue of device-to-device performance variation. The 3D-printed blood processing cartridges are driven by hydrostatic pressure to automatically dispense plasma from finger-pricked blood and deliver washing/measurement buffer to the nanosensors without the need for operator intervention during the assay. Within 40 minutes and from 30 μ L of blood, the nanosensor platform could reliably measure PlGF with a limit of detection of 0.06 pg/mL and a five order magnitudes dynamic range. Pilot clinical validation in four preeclamptic pregnancies confirmed the accuracy and reliability of the platform, paving the way for further development of a much-needed point-of-care preeclampsia technology.

Keywords: Biosensors, Nanofabrication, Point of Care, Biomarker.

BIOGRAPHY



Prof Benjamin Thierry is the UniSA Professor of Bioengineering and a NHMRC Investigator Fellow (2021-2025). He obtained his PhD in 2004 in Biomedical Engineering at McGill University. Prof Thierry is currently a Research Leader at the Future Industries Institute where he leads a cross-disciplinary research team of ~15 PhD students and ECRs focussed on the development and translation of biodiagnostic technologies. His has received continuous funding from the NHMRC since 2008 and served as the Head of the South Australian node of the ARC Centre of Excellence for Convergent Bio and Nano Science. He also serves as a scientific advisor to Ferronova, the precision cancer diagnostic company he co-founded, and presently oversees the development of FerroTrace-FAPi, a second generation theranostic agent designed for image-guided cancer treatment. Ferronova recently completed a Au\$8M capital raise to fund its ongoing clinical program and R&D activities.

ODOR SENSORS – FROM PLASMONIC-BASED DEVICE TO AN ARRAY OF MACH-ZEHNDER INTERFEROMETERS

Thierry LIVACHE

CEA Research Director,

Univ. Grenoble Alpes, CNRS, CEA, IRIG, SyMMES, F-38000 Grenoble, France,

Former Scientific Director of Aryballe

ABSTRACT

Beyond the classical lock/key-recognition-based approach used in the bio-analytical field, an electronic nose device is an assembly of non-specific sensors working in gas phase. Following a long story around the imaging of biological interactions of biomolecules by Surface Plasmon Resonance Imaging, we recently extended this approach to the non-specific interactions studies in gas phase giving rise to a new optical-nose generation. The signals resulting from the binding of VOCs on an array of bioinspired receptors can be seen as 3D continuous dynamic images or movies. Finally, complex data obtained from odors are analyzed as simple images via a specific database. This flexible and straightforward approach allowed a downscaling of the device and a new miniaturized portable and generic opto-nose Neose was recently launched also based on silicon integrated photonic technologies (Mach-Zehnder interferometers array). The new device involves an array of 64 MZI functionalized by different peptides. In this case, the signal is generated as a phase shift, that is translated into a more classical sensogram. This approach allows for a real miniaturization of the sensor and opens you doors for the construction of systems that could help patients suffering from anosmia (European project ROSE).

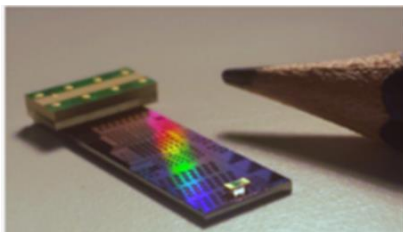


Figure miniaturized integrated photonic chip and the new Neose instrument.

Reference

Laplatine et al. Silicon photonic olfactory sensor based on an array of 64 biofunctionalized Mach-Zehnder interferometers. *Optics Express*, 19, 33955-33968 (2022)

BIOGRAPHY



Dr. Thierry Livache, (PharmD, Hab.) is a Research Director at CEA IRIG. He had been a senior R&D scientist in a pharmaceutical company, CIS-bio, for 10 years (1990-2000) where he had developed microsystems for biological analyses, pioneering the domain of the use of silicon chips for in vitro bio-analyses. In 2000, he came back to basic researches at CEA where he constructed and led the CREAB group within the joined unit Symmes (CEA, CNRS, University of Grenoble). In 2014, he was appointed CEA “*Directeur de Recherche*” and co-founded Aryballe where he had been the Scientific Director (CSO) from 2016 to 2022. He recently came back to the CEA-Grenoble to start a new project dealing with bacteria detection and quantification for clinical applications.

His expertise includes the development of micro-bioanalytical tools at the interface of physics, chemistry and biology and their clinical applications. His work in plasmonics and photonics coupled with combinatorial chemistry led to the development of a new photonic e-nose approach and to the launching of Aryballe Technologies dealing with the construction of devices devoted to odour analysis.

He cofounded three companies Genoptics (SPR imaging now included in the Horiba Scientific Group) in 2002, PrestoDiag in 2012 (plasmonic-based bacteria detection), and Aryballe in 2014. He is the author of more than 120 peer-reviewed publications ~60 invited conferences and ~40 families of patents. Hfactor 44 (Google Scholar).

DEVELOPMENT OF NANOMEDICINE BASED ON SELF-ASSEMBLED POLY(AMINO ACID) FOR BIOMEDICAL APPLICATIONS

Long Binh Vong^{1,2}

¹ School of Biomedical Engineering, International University, Ho Chi Minh, Vietnam, Community 6, Linh Trung Ward, Thu Duc City, Ho Chi Minh City, Vietnam;

² Vietnam National University Ho Chi Minh, Vietnam Community 6, Linh Trung Ward, Thu Duc City, Ho Chi Minh City, Vietnam

Email: yblong@hcmiu.edu.vn

ABSTRACT

Amino acids have attracted considerable attention in drug development because they play important roles in many physiological and pathological processes. In the past several decades, various amino acid supplementations have been reported to have potential therapeutic efficacy for the treatment of many disorders in clinical trials. However, their effectiveness is controversially reported, which may be explained by poor pharmacokinetic properties of such low-molecular-weight (LMW) agents. The nanoparticle-based drug delivery systems (nano-DDS) have attracted considerable attention for the last several decades as an innovative medical technology, since these systems alter the biodistribution of the therapeutic agent with the controlled release manner at the target tissues, resulting in a significant therapeutic drug effect. Merely simple encapsulation of the conventional LMW amino acid in nano-DDS can not be stable enough and cannot control the release properly. In this presentation, we have discussed the current therapeutic applications of certain amino acids, and have introduced our approach of using amino acid-based self-assembled nanostructures as novel therapeutic agents.¹ Using animal disease models, poly(ornithine)-based nanoparticle was designed for treatment of hyperammonia in liver acute injury,² poly(dopamin)-based nanoparticle was used in treating the Parkinson's disease,³ and poly(arginine)-based nanogel was used in treatment of myocardial infarction.⁴ By covalently introducing a substrate into the nanosystem, amino acid-based self-assembled macromolecules could overcome the aforementioned drawbacks by improving the pharmacokinetic profile and accumulation of specific molecules at target sites to enhance the therapeutic effect (**Figure 1**). As the results, the therapeutic efficacies have been significantly improved, which is anticipated to open the future development of an emerging and novel concept of self-assembled macromolecule-based therapeutic approach.

Keywords: self-assembly nanoparticle, nanomedicine, poly(aminoacid), drug delivery.

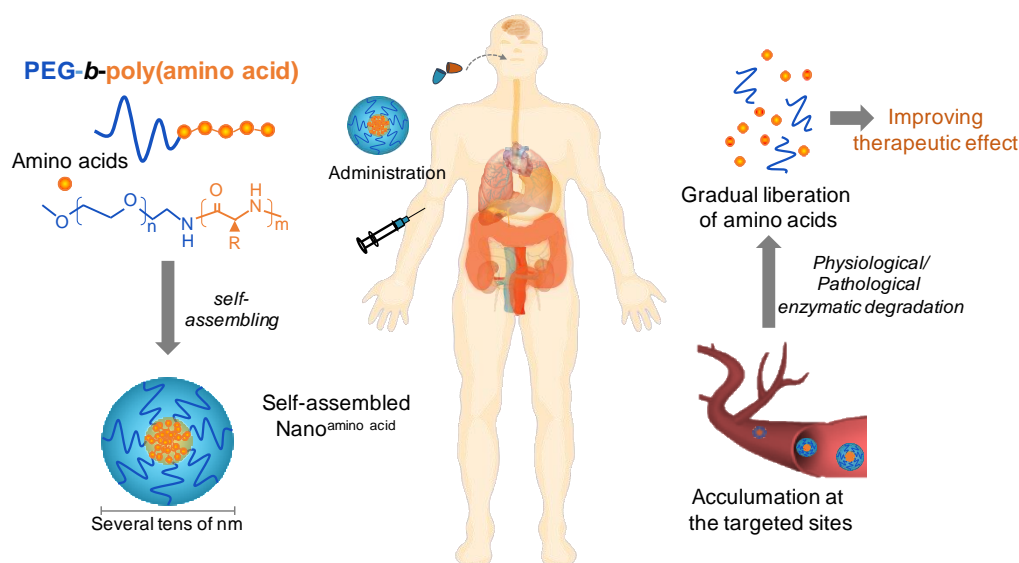


Figure 1: The concept of self-assembling amino acid based-drugs

Acknowledgments

This research is funded by Ministry of Education, Culture, Sports, Science and Technology (MEXT), Japan, and Vietnam National University Ho Chi (VNU-HCM) under grant number NCM2020-28-01. Authors would like to express sincere appreciation to Prof. Nagasaki Yukio (University of Tsukuba, Japan) for the collaborations.

References

- [1] LB Vong, NT Trinh, Y Nagasaki, *Design of amino acid-based self-assembled nano-drugs for therapeutic applications*, Journal of Controlled Release 326 (2020) 140-149.
- [2] L.B. Vong, Y. Ibayashi, Y. Lee, D.N. Ngo, Y. Nishikawa, Y. Nagasaki, *Poly(ornithine)-based self-assembling drug for recovery of hyperammonemia and damage in acute liver injury*, Journal of Controlled Release 310 (2019) 74–81.
- [3] L.B. Vong, Y. Sato, P. Chonpathompikunlert, S.Tanasawet, P. Hutamekalin, Y. Nagasaki, *Self-assembled polydopamine nanoparticles improve treatment in Parkinson's disease model mice and suppress dopamine-induced dyskinesia*, Acta Biomaterialia 109 (2020), 220–228.
- [4] L.B. Vong, T.Q. Bui, T. Tomita, H. Sakamoto, Y. Hiramatsu, Y. Nagasaki, *Novel angiogenesis therapeutics by redox injectable hydrogel - Regulation of local nitric oxide generation for effective cardiovascular therapy*, Biomaterials, 167 (2018) 143–152.
- [5] QN Nguyen-Trinh, KXT Trinh, NT Trinh, N Li, Y Nagasaki, LB Vong. *A silica-based antioxidant nanoparticle for oral delivery of Camptothecin which reduces intestinal side effects while improving drug efficacy for colon cancer treatment*, Acta Biomaterialia, 143(2022) 459-470.

BIOGRAPHY



Associate Professor Long Binh Vong received the fellowship of Japan Society for the Promotion of Science (JSPS) and got the Ph.D. Degree in Department of Materials Science, Graduate School of Pure and Applied Sciences, University of Tsukuba in 2015; later then, he worked as postdoctoral fellow. In 2018, he was selected as top 10 outstanding young scientists in Vietnam. He is currently Vice Dean, School of Biomedical Engineering, International University, Vietnam National University Ho Chi Minh city. His research activities focus on the development of innovative biomaterials for biomedical applications, particularly smart nanomedicine and drug delivery systems. Recently, he has developed the oral nanomedicine for treatment of oxidative stress-induced diseases in gastrointestinal tract, especially ulcerative colitis and intestinal cancer. Targeted delivery and controlled drug release using designed biopolymers and nanomedicine apply to various animal disease models. These works were published prominent scientific journals such as *Gastroenterology*, *Biomaterials*, *Journal Controlled Release*, *Nano Today*, *Molecular Pharmaceutics*, *Journal of Chemical Engineering*...and presented in more hundred national and international conferences worldwide where he received many excellent presentation awards.

ULTRAFAST CARRIER DYNAMICS AND LAYER-DEPENDENT CARRIER RECOMBINATION RATE IN InSe

Ting-Hsuan Wu, Hao-Yu Cheng, Wei-Chiao Lai, Raman Sankar,
Kung-Hsuan Lin and Chia-Seng Chang

ABSTRACT

InSe layered semiconductors with high mobility have advantages over transition-metal dichalcogenides in certain device applications. Understanding the dynamics of carriers, especially around the major bandgaps, is not only of fundamental interest but also important for improving the performance of devices. We investigated ultrafast carrier dynamics in exfoliated InSe near the bandgap and found that the presence of photocarriers led to shrinkage in the optical bandgap. In addition, we observed that the carrier recombination rate increased when the thickness of the InSe nanoflakes was reduced and the process was dominated by surface recombination. For the same flakes, the recombination rate became lower after the freshly exfoliated InSe was exposed to air and oxidized. Using a free carrier diffusion model, layer-dependent surface recombination velocities were obtained. Our investigation reveals that the surface condition and the thickness of few-layer InSe play important roles in carrier lifetimes.

Keywords: InSe, layered semiconductor, carrier dynamics, recombination rate

BIOGRAPHY



Dr. Jason C. S. Chang graduated from National Tsing-Hua University in 1978 and obtained his Ph.D in Physics from Arizona State University (ASU), USA in 1988 and had also his postdoctoral career with ASU till 1991. He joined the Institute of Physics (IoP), Academia Sinica in late 1991 as an assistant research fellow. In the year of 2000, he was promoted to research fellow and later served as the convener of quantum materials physics group in the Institute. He was appointed as one of the Deputy Directors of IoP in 2016 and Director in 2018.

He has been actively involved in surface sciences and nanotechnology research for over 30 years, most notably on novel scanning probe microscopy development, atomic manipulation, quantum size effects in metallic thin films, and physical properties of carbon nanotubes. He has published over 150 technical and review papers in these fields. Dr. Chang is also currently an adjunct professor in the Department of Physics at National Taiwan University. He is a Fellow of the Physical Society of Taiwan (2009), American Physical Society (2012), and American Vacuum Society (2017).

Dr. Chang has been PI and co-PI for several National projects and Thematic projects of Academia Sinica. Previously, he served as the Editor-in-Chief of the Chinese Journal of Physics (2004-2006), and the convener of Physics Division Panel of National Science Council (2007-2009), for which he helped establish Taiwan Consortium of Emergent Crystalline Materials (TCECM). He also sit on the Executive Council of the Physical Society of Taiwan (TPS) overseeing the publication department (2008-2009). From the year of 2009 to 2018, he directed the Nano Science and Technology Program of Taiwan International Graduate Program of Academia Sinica. Internationally, he was the Taiwan representative to European M-ERA.net Program from 2018 to 2020 and currently is one of Secretaries for the Asia Nano Forum.

Dr. Chang's homepage: <https://www.phys.sinica.edu.tw/~nano/>

DEVELOPMENT OF ELECTRICALLY ACTIVABLE LAYER TO EFFICIENTLY STRUGGLE BACTERIAL INFECTIONS

Jean-Manuel Raimundo

Aix Marseille Université, CNRS, CINaM 7325, 163 Ave de Luminy Case 913, 13009 Marseille France

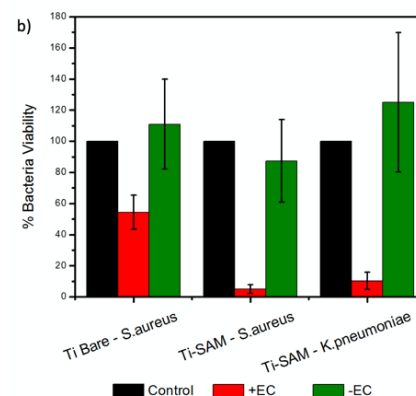
Email: jean-manuel.raimundo@univ-amu.fr

ABSTRACT

Bacterial infections are one of the major threats to public health, food safety and development today which makes it urgent to combat by developing materials or strategies limiting or preventing these bacterial proliferations and biofilm infections.[1] Although, medical implants have led to dramatic improvement in patient's health and well-being, there are often drawbacks that include surgical risks during placement or removal, implant failure and more specifically microbial infections. These implant-associated infections are mainly caused by the bacterial biofilm formation in which bacteria are more recalcitrant towards treatments. Indeed, implant surfaces are non-vascularized abiotic materials rendering the common strategies inappropriate and ineffective.[2]

In this context we have designed and developed innovative and smart interfaces based on phosphonium SAMs¹ that can be electrically activated on-demand for eradicating bacterial infections on solid surfaces. Hence, upon electroactivation, using a low potential of 0.2V for 1 hour, a successful stamping out of Gram-positive and Gram-negative bacteria strains has been clearly highlighted on SAM-modified titanium surfaces. Subsequently, using these conditions, *Staphylococcus aureus* and *Klebsiella pneumoniae* were killed up to 95% and 90% respectively and full eradication if time is prolonged (Fig. 1). More importantly, no harmful activity has been observed towards eukaryotic cells which clearly demonstrates the biocompatible character of these novel surfaces for further implementation.

Keywords: responsive surfaces, self-assembled monolayers, electroactivation, biocidal effect.



- [1] Tacconelli, E.; Carrara, E.; Savoldi, A.; Harbarth, S.; Mendelson, M.; Monnet, D. L.; Pulcini, C.; Kahlmeter, G.; Kluytmans, J.; Carmeli, Y.; Ouellette, M.; Outtersson, K.; Patel, J.; Cavalieri, M.; Cox, E. M.; Houchens, C. R.; Grayson, M. L.; Hansen, P.; Singh, N.; Theuretzbacher, U.; Magrini, N. *Lancet Infect. Dis.* 18 (2018) 318-327.
- [2] a) Brunel, F.; Lautard, C.; Giorgio, S.; Garzino, F.; Raimundo, J. M.; Bolla, J. M.; Camplo, M. (2018) *Bioorg. Med. Chem. Lett.* 28, 926-929; b) Brunel, F.; Lautard, C.; Garzino, F.; Raimundo, J. M.; Bolla, J. M.; Camplo, M. (2020) *Bioorg. Med. Chem. Lett.* 30, 127389; c) Raimundo, J.-M.; Camplo, M.; Bolla, J.-M.; Brunel, F.; Lautard, C.; PCT Int. Appl. (2020) WO 2020008000 A1 20200109; d) Carrara, S.; Rouvier, F.; Auditto, S.; Brunel, F.; Janneau, C.; Camplo, M.; Sergent, M.; About, I.; Bolla, J.-M.; Raimundo, J.-M.) *Int. J. Mol. Sci.*, 2(4) (2022) 2183.

BIOGRAPHY



Jean-Manuel Raimundo, is full professor at CINaM (UMR 7325) and at Materials' Department of Polytech'Marseille (Aix-Marseille University). He obtained a B.S. in Biochemistry (Univ. of Rennes) and a PhD at the Univ. of Angers (J. Roncali). Thereafter, he was consecutively postdoctoral researcher at ETH- Zürich (F. Diederich), ATER at the Univ. of Angers and postdoctoral researcher (in coll. TotalFina Elf) before being appointed assistant professor at the Univ. of Nice. In 2012, he was invited researcher at NIMS-MANA (Tsukuba Japan, Ariga's group). His main activity is devoted to (supra)-molecular engineering of novel π -conjugated chromophores for optoelectronics and biomedical, surface science engineering and (bio)sensors applications.

MEMS NOZZLE for DRY-CAPTURING HUNDRED-LEVEL LILY POLLENS IN ARRAY AND FIXING ON CULTURE MEDIA FOR PLASMA BIO-APPLICATIONS

Minoru Sasaki

Toyota Technological Institute,
2-12-1 Hisakata, Tenpaku-ku, Nagoya, 468-8511, Japan
Email: mnr-sasaki@toyota-ti.ac.jp

ABSTRACT

A nozzle device featuring a micro-electromechanical system (MEMS) was developed to realize a series of advanced micromanipulation steps for capturing pollens from flower stamen and fixing them in arrays on culture media without cell damage. The MEMS nozzle, which has an array of through-holes with counterbores, was fabricated by the photolithography and Si etching. During the manipulation, the pollen in the air was captured in the counterbores due to the negative pressure applied from the nozzle backside. When the device with the captured pollen was moved into the liquid culture media of the gelatin, the liquid was sucked into each counterbore, so that the captured pollen was covered. By cooling the culture media down and switching off negative pressure, the controlled release of sucked cells without damage and the fixation in array on solid culture media were achieved. Through experiments implemented by the nozzle, the positive effect of plasma-treated water on the pollen growth was verified. The microarray strategy presented in this work will make the cell experiments and their result analysis more effective, especially for the plasma bio-applications.

Keywords: MEMS nozzle, dry-capturing cells in array and fixing, Plasma bio-application

INTRODUCTION

Microarray of cells has been successfully used in basic scientific studies, drug discovery, and diagnostic purposes. Microarrays usually bases on the microfluid using the suspension cells in liquid[1]. There are few microarray techniques for handling the cells in air (e.g., seeds), which are important sample in plasma bio applications. In this study, new MEMS nozzle is introduced for handling the pollen.

EXPERIMENTAL

MEMS nozzle is fabricated by etching 200 μm -thick Si substrate from top and bottom sides. The through holes are arrayed in 12x12 matrix with 500 μm pitch. The inset photo of Fig. 1 is the micrograph of the nozzle. Each 42 μm -through hole has 150, 110, or 78 μm -diameter counterbore. Its surface is coated using water/oil-repellent agent. The vacuum evacuation through the nozzle attracts the lily pollen in counterbore. The lily pollen having about 100 μm size is trapped inside.

Figure 1 shows the setup for fixing the pollen on the culture media. The nozzle is placed in the petri dish with the melted gelatin media, the gelatin solution is introduced inside the hole. Then, the gelatin is hardened by cooling the shale

using Peltier stage at 4 $^{\circ}\text{C}$. The petri dish is removed with the gelatin including the pollen.

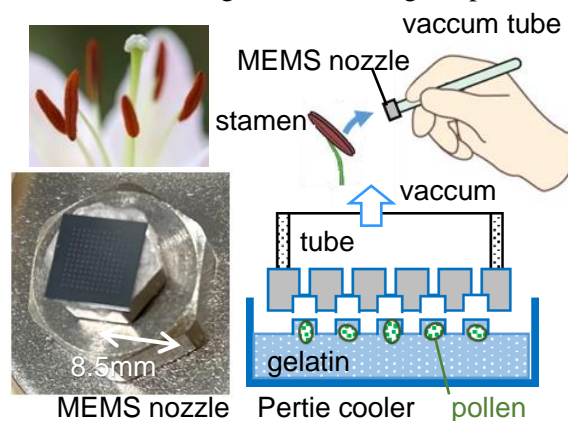


Fig. 1 Setup for arraying / fixing lily pollens using MEMS nozzle. Pollens are fixed in gelatin pillars after cooling.

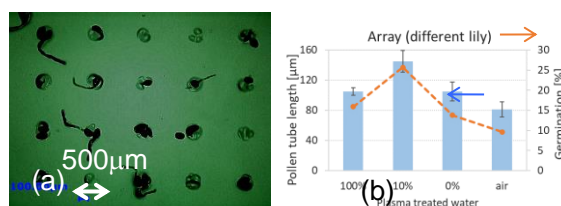


Fig. 2 (a) Lily pollens with tube on gelatin. (b) Pollen tube length and germination ratio against plasma treatments.

RESULTS AND DISCUSSION

The lily pollens are fixed on gelatin in array. In many sites, there are a few pollens. The size mismatch between the pollen and the hole may be the reason. The pollen cell is considered to deform when evacuated inside the hole. These pollens stay at room temperature over one night and the tube grows. Figure 2(a) shows the result. The array pitch 500 μm is the appropriate distance for observing the tubes. This fact indicates the handling using the nozzle does not give the serious damage to the pollens.

The plasma treated water (PTW) is placed by about 10 μl . This PTW is prepared irradiating the atmospheric pressure Ar plasma for 5 min at the distance about 13 mm from the plasma source to water surface. Figure 2(b) shows the pollen tube length and the germination rate after one night's culture. Both the germination rate and the length of pollen tubes show larger values in the order of 10%, 100%, and 0% PTW. The least effect is air (as is). The exception is the subtle difference of the tube length between 100% and 0% PTW. In experiments, the 10% plasma-treated water shows the best effect for promoting the growth among four conditions, which indicates the importance of the moderate concentration of the active species. Some middle concentration between 10 and 100% plasma-treated water will be examined in future.

CONCLUSION

A MEMS nozzle with an array of the through-holes realizes the advanced array fixation strategy on culture media. In the air, the device can capture about 100 pollens in array through the negative pressure. This method does not rely on the liquid flow, important for manipulating cells sensitive to water. By solidifying the gelatin inside the nozzle, the pollens could be precisely fixed on gelatin in array simultaneously without cell damage. 10% deionized plasma-treated water has better effect on the growth of pollen than original 100% pure plasma-treated water, pure water, and air. The proposed array strategy obviously enhances the analysis efficiency of experimental results, and has further potential applications in fields such as biological sample handling, micro-assembly, and bio-medicine.

Acknowledgment

The water/oil-repellent agent (Fluoro SurfTM) is supplied from Fluoro Technology. This work is supported by the grants from the joint usage/research program of center for Low-temperature Plasma Science, Nagoya University, with the cooperation of Research Center for Smart Photons and Materials, Toyota Technological Institute, Japan.

References

- [1] W.-H. Tan, S. Takeuchi: PNAS **104** (2007) 1146-1151.

BIOGRAPHY



Minoru Sasaki received the M. S. and Dr. Eng. degrees from Nagoya University in 1993 and 1995, respectively. In 1995, he is a Research Fellow of the Japan Society for the Promotion of Science. Since 1996, he is an assistant professor in Tohoku University. Since 2007, he has been a professor in Toyota Technological Institute, Nagoya, Japan. His current research interests include MEMS, plasma, and 3D microfabrication. The followings are some selected activities including the schedule.

2013.8.19-22 General Chair of IEEE International Conference on Optical MEMS and Nanophotonics (Kanazawa, Japan). 2021.6.20 Tutorial lecturer, "Lithography on non-flat 3-D surface", The 21st International Conference on Solid-State Sensors, Actuators and Microsystems. 2023.6.30-7.1 Chair of domestic annual conference for joint research groups in Sensors and Micromachines Society in Institute of Electrical Engineers of Japan. 2023.4.1-2025.3.31 Vice president of Sensors and Micromachines Society in Institute of Electrical Engineers of Japan. 2025.3.2-6 General chair of the International Symposium on Advanced Plasma Science and its Applications for Nitrides and Nanomaterials.

AgInS₂ NANOCRYSTALS COATED WITH THE GaS_x SINGLE-SHELL OR GaS_x/ZnS DOUBLE-SHELL FOR EMITTING STRONG AND NARROW EXCITONIC LUMINESCENCE

Ung Thi Dieu Thuy, Tran Thu Huong, Nguyen Thu Loan and Nguyen Quang Liem

Institute of Materials Science, Vietnam Academy of Science and Technology,

18 Hoang Quoc Viet, Cau Giay, Hanoi, Vietnam

Email: liemnq@vast.vn

ABSTRACT

The systematic synthesis of AgInS₂ (AIS) nanocrystals (NCs) with different sizes of 2.6 – 6.8 nm just by controlling only the reaction temperature was carried out in 2 steps: (i) synthesis of Ag₂S NCs and then (ii) partial exchange of Ag⁺ with In³⁺ in the template Ag₂S NCs. For step (i), Ag₂S NCs of different sizes were synthesized by reaction of the Ag and S precursors at different temperatures of 30 °C to 130 °C, for the same reaction time of 30 min. In step (ii), AIS NCs were created by the exchange of Ag⁺ with In³⁺ at 120 °C for 60 min. Finally, GaS_x was shelled on AIS core NCs producing the AgInS₂/GaS_x core/shell structures. The synthesized AIS/GaS_x NCs demonstrate the clear excitonic absorptions and strong, narrow excitonic luminescence peaking at 530 – 606 nm depending correspondingly on the size of AIS core NCs mentioned above. AIS NCs could also be synthesized using the solvothermal method at 200 °C by reaction of all three precursors. This higher-temperature chemical reaction could make the NCs more stable; however, it was necessary to adjust the precursor ratios and reaction time to obtain NCs that emit luminescence at the required wavelength. To further improve the excitonic luminescence properties and also the photochemical stability of AIS/GaS_x NCs, the second outermost ZnS shell was added. An example is shown for the AgInS₂/GaS_x/ZnS core/double-shell NCs, which were prepared via three steps: (i) synthesis of AgInS₂ core NCs by solvothermal method at 200 °C for 30 min, (ii) shelling GaS_x on AgInS₂ core NCs at 280 °C for 60 min to produce the AgInS₂/GaS_x core/shell structure, and (iii) the outermost ZnS shelling at 140 °C for 10 min. The luminescence evolution of the synthesized NCs is as follows: from the broad spectrum (peaking at 756 nm) of the AgInS₂ core NCs to become the narrow excitonic emission (at 575 nm) prominent beside the broad one after shelling with GaS_x, then only the bright excitonic luminescence (at 575 nm) without broad emission after double-shelling with GaS_x/ZnS. The double-shell has made the AgInS₂/GaS_x/ZnS NCs not only remarkably enhance their luminescence quantum yield (QY) up to ~60% but also maintain the narrow excitonic emission stably for a long-term storage over 12 months. The outermost ZnS shell is reasonably considered to play a key role in enhancing QY and protecting AgInS₂ and AgInS₂/GaS_x from certain damage.

Keywords: AgInS₂, AgInS₂/GaS_x, AgInS₂/GaS_x/ZnS, nanocrystals, exciton

BIOGRAPHY



Prof. Nguyen Quang Liem is serving at the Institute of Materials Science, Vietnam Academy of Science and Technology (VAST). He currently holds several positions, including Chairman of the National Program on Application and Development of Materials Technology in Vietnam, Chairman of the Scientific Council for the Materials Science Direction at VAST, and Editor-in-Chief of *Advances in Natural Sciences: Nanoscience and Nanotechnology*, an international journal jointly published by VAST and IOP Publishing. He has been working for many years in the field of optoelectronic materials in various structures. He has authored and co-authored over a hundred articles, one book and two book chapters, and holds three patents.

THE STUDY OF THERMOELECTRIC GENERATOR (TEGs) WITH A HIGH INTEGRATION DENSITY FOR PORTABLE AND IoT SENSOR SYSTEM IN THE AQUAPONIC FARM.

Nguyen Van Hieu^{1,2,*}, Nguyen Hoang Quan¹, Bui The Anh¹, Mai Thanh Tan Cuong¹, Nguyen Van An¹, Ho Thanh Huy¹, Nguyen Chi Nhan¹, Nguyen Van Toan³ and Takahito Ono³

¹BiSAE Laboratory, Dept. of Physics and Electronic Engineering, Faculty of Physics – Engineering Physics, VNUHCM- University of Science

227 Nguyen Van Cu Str., Dist. 5, Hochiminh city, Vietnam;

²Dept. of Science and Technology, Vietnam National University Hochiminh city (VNUHCM)

Linh Trung Ward, Thu Duc City, Hochiminh city, Vietnam;

³Ono-Nguyen-Tada Laboratory, Graduate School of Engineering, Tohoku University

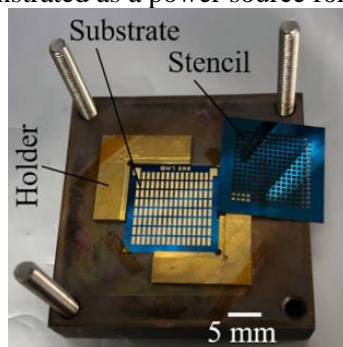
2 Chome-1-1 Katahira, Aoba Ward, Sendai, Miyagi 980-8577, Japan.

*E-mail: hieunv@vnuhcm.edu.vn

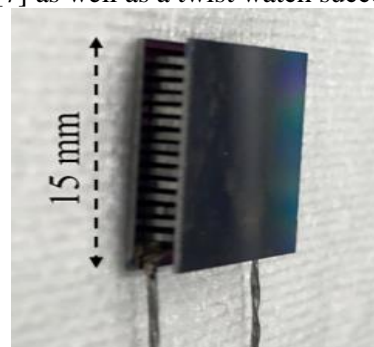
ABSTRACT

Thermoelectric generators (TEGs) could be used in power plants and factories to convert waste heat into additional electrical power. TEGs are usually employed where the Seebeck effect can be observed. TEGs have been well developed in recent years which can convert thermal energy continually as long as a temperature difference across the TEG is supplied. Generally, the output power of TEGs is small because of low conversion efficiency and small sizing. We also think the optimal design of heat sink efficiency will strongly effected the TEG output power density. The wearable electronic devices is the power supply issue Therefore, electronic devices can continue to operate by collecting energy in the working environment without an external energy supply. Some natural energy sources available in the environment for portable and wearable electronic devices, including mechanical energy [1], solar energy [2], and thermal energy [3-6], could readily be captured.

In this work, TEGs for portable and wearable self-powered electronic devices, including low and high integrated number of thermoelectric elements, employing a high performance thermoelectric material fabricated by an assembly technology. The TEG device #1 consists of 17 pairs of thermoelectric elements with their dimensions of 1 mm × 1 mm × 2 mm which was fabricated on the Si substrate of 15 mm × 15 mm. Maximum output powers for devices #1 are obtained as 43μW and 10.1 mW at temperature difference ΔT of 5 °C and 75 °C respectively. Moreover, the harvested energy from the fabricated TEG can be stored in a rechargeable battery via a DC-DC converter. The output of the DC-DC converter reaches 2.8 V and 4 V at $\Delta T = 2$ °C and 8 °C, respectively, which corresponds to the DC-DC electronic conversion efficiency η_{DC-DC} is 8.1% and 23.3%, respectively. These TEG has been demonstrated as a power source for a calculator recently [7] as well as a twist watch successfully.



(a)



(b)

Fig. 1. The fabricated TEG device #1: (a) Device fabrication setup including holders, substrate, and stencil wafer; And (b) Completely fabricated device.

Moreover, the TEG device #2 also consists of 17 pairs with their dimensions of $1.3 \text{ mm} \times 1.3 \text{ mm} \times 1.5 \text{ mm}$ and its Si substrate of $40 \text{ mm} \times 40 \text{ mm}$ also studied output powers of TEG with several kinds of heat sink ($40 \text{ mm} \times 40 \text{ mm}$, 50mm high) for the applications with IoT sensors system in Aquaponic farm. The simulating data from COMSOL for out put power are compared to measuring results that seem to be in good agreement.

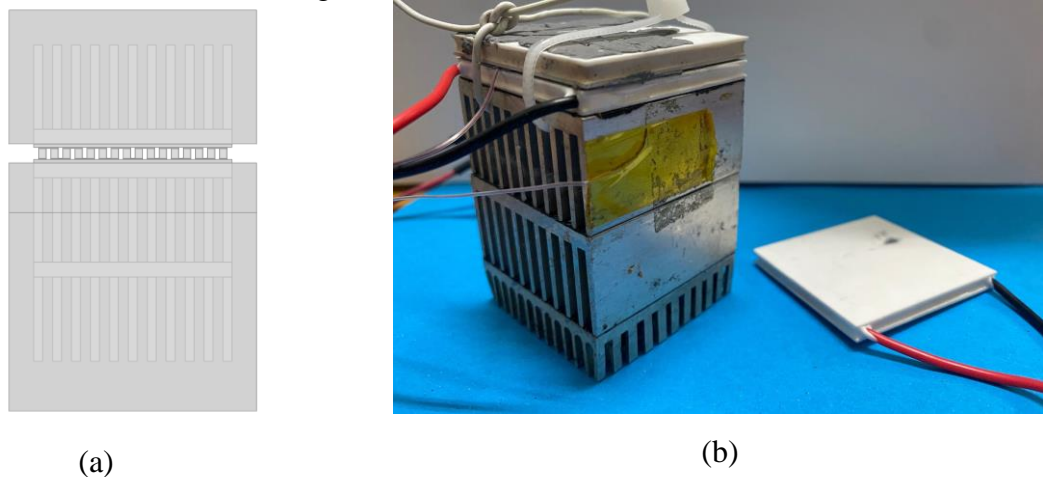


Fig. 2. The TEG device #2: (a) COMSOL simulating structure and (b) Its checking output power for the application of aquaponic farm.

The output powers of this TEG can reached the maximum of power is 3564,60 mW at temperature difference ΔT of $13.7 \text{ }^\circ\text{C}$ and the maximum of 63,77mW when its temperature difference ΔT is $0.8 \text{ }^\circ\text{C}$. However, at temperature difference of $5.4 \text{ }^\circ\text{C}$, the out put power also get high value of 502 mW. Therefore, the bigger dimensions of TEG is the higher out put power. TEG device #2 will be better in using for IoT sensors system with the DC-DC converter circuits in aquaponic system.

Keywords: Thermoelectric generator, Out put power, DC-DC converter, Portable and wearable self-powered electronic devices, Aquaponic system.

References

- [1] Liu Y, Zheng Y, Wu Z, Zhang L, Sun W, Li T, et al. *Conductive elastic sponge-based triboelectric nanogenerator (TEG) for effective random mechanical energy harvesting and ammonia sensing*. Nano Energy; **79** (2021) 105422.
- [2] Chang S-Y, Cheng P, Li G, Yang Y. *Transparent polymer photovoltaics for solar energy harvesting and beyond*. Joule **2**(6) (2018) 1039–54.
- [3] Toan NV, Hasana MMIM, Udagawa D, Inomata N, Toda M, Said SM, et al. *Thermoelectric generator battery using 10 nm diameter of Al_2O_3 nanochannels for low-grade waste heat energy harvesting*. Energy Convers Manage; **199** (2019) 111979.
- [4] Ono T, Nguyen TH, Samat KF, Li J, Toan NV. *Nanoengineered thermoelectric energy devices for IoT sensing applications*. ECS Trans **92** (2019) 163–8.
- [5] Zhang Y, Phuong PTT, Roake E, Khanbareh H, Wang Y, Dunn S, et al. *Thermal energy harvesting using pyroelectric-electrochemical coupling in ferroelectric materials*. Joule **4**(2) (2020) 301–9.
- [6] Tuoi TTK, Toan NV, Ono T. *Theoretical and experimental investigation of a thermoelectric generator (TEG) integrated with a phase change material (PCM) for harvesting energy from ambient temperature changes*. Energy Rep **6** (2020) 2022–9.
- [7]. Nguyen Van Toan, Truong Thi Kim Tuoi, Nguyen Van Hieu and Takahito Ono. *ThermoElectric Generator with a high integration density for portable and wearable self-powered electronic devices*. Energy Conversion and Management **245** (2021) 114575.

BIOGRAPHY



Full name: Nguyen Van HIEU

Academic title: PhD., Associate Professor, Senior Lecturer.

The current position:

Deputy Director, Department of Science and Technology, Vietnam National University Hochiminh city, Vietnam.

Inviting senior lecture, Biosensors and Applied Electronic Laboratory (BiSAE), Department of physics and Electronic Engineering, Faculty of Physic – Engineering Physics, VNUHCM- University of Science, Hochiminh city, Vietnam.

Former head (2007-2022), Department of physics and Electronic Engineering, Faculty of Physic – Engineering Physics, VNUHCM- University of Science, Hochiminh city, Vietnam.

The contact information:

. Email: hieunv@vnuhcm.edu.vn.

. Handphone: (+84) 903.629704

The education: Mr. Hieu obtained his bachelor degree (1994) and mater degrees (2000) in Physic from University of Hochiminh City and VNUHCM-University of Science in 1994 and 2000, respectively.

In 2007, he received his Ph.D. degree in Physics from Graduate School of Science, Osaka University (Osaka, Japan).

The administrating experience: A headof Department of Physics and Electronic Engineering (from Apr 2007-2022); A dean of Faculty of Electronics and Telecommunications (Dec 2008 to Sep 2010); A head Office of International Relations-Projects Management in VNUHCM-US (Dec 2011-Mar 2019). Since Sep 2020, he has appointed a deputy director, Dept. of Science and Technology in VNUHCM.

The expert experience: A visiting researcher for the research field of UVLEDs in Ritsumeikan University- Japan (2011-2012); An inviting researcher in Lab of Semiconducting Technology (Saigon Hi-Tech Park) for microelectronic projects (2014-2017); A visiting associate professor in Sofia University (Tokyo, Japan) for semiconducting device project (April to June 2017).

Dr. He is also a member of some academic units: Institute of Electrical and Electronic Engineering in Japan (IEEJ), The editor board of Korean Institution of Electrical and Electronic Engineer (KIEEE); Physics Society of Vietnam, Microelectronics program in Hochiminh City, Scientific council of Saigon Hi-Tech Park,...

He also had a chance to take the International Dean Course ‘s South East Asian which organized by DAAD (Germany). He became an alumnus and co-coordinator of DAAD for education program in Hochiminh City. He was also a guest of the 2nd Roundtable under the European Union- Asian Higher education Platform, Organizatio by EUA & DAAD (Belgium; July 2009). He was also an alumnus of Osaka University as JUACH, JAV, ... in Vietnam.

The scientific achievements: Dr. Hieu had may invited talk in ASPA2013 (in SHTP), 4S international Conference 2010, 2012, SHTP Annual Conference2014, STT41 (Thailand), SHTP Annual Conference2016, MRS (Thailand2017), IKEEE conference (2017, 2018), 7th&8th Benjamitra Conference (2016, 2018, Thailand), 38th Sensor Micromachines and Applied Systems" Symposium (online, Japan 2021), IWNA2009-2023, ODF2020, ISET2021(online), OPTIC2022 (Taiwan), ISET2023.

Yearly, he has many lectures for students in universities other institutes. Since 2000, he was scientific supervisors for more than 50 bachelors, 15 master and Ph.D. theses. He had more than 32 talks in domestic and international conferences. His research group had around 40 Journal papers and proceeding of international conferences in the field of physics Engineering, semiconducting devices, MEMS, microelectronics,

Dr. Hieu was a program chair or member of program committee of many seminars, international workshops, conferences: VJSE2005, VJSE2006 (Japan),4SForum (2012, SHTP), IWTDMT2013, 1stVCWRE2015 (VNU-Vietnam and CNU-Korea), IWNA (2009,2011,2013,2015, 2017),...Co-general chair of 3rd IWEMA2022.

DEVELOPMENT OF CLOCK-BASED AUTOMATIC FLOW CONTROL METHODS FOR COMPACT MICROFLUIDIC ANALYTICAL SYSTEMS

Yoshiaki Ukita¹

¹ Graduate Faculty of Interdisciplinary Research, University of Yamanashi,
4-3-11 Takeda, Kofu, Yamanashi, 400-8511, Japan;
Email: yukita@yamanashi.ac.jp

ABSTRACT

In this presentation, I will introduce our original flow control technology for microfluidic systems. This is a centrifugal microfluidic device, which operates multistep and complex flow control semi-autonomously based on a water clock that operates passively under centrifugal force, and which we call Control of Liquid Operation Centrifugal hydroKinetic (CLOCK). In this talk, I will explain the basic principle of CLOCK and introduce the immune analysis technology based on CLOCK. In addition, the multi-parameter analysis, which is important for improving the accuracy of CLOCK, will also be introduced. Since pretreatment of blood samples is important from the viewpoint of clinical application. Therefore, we are also working on the development of a blood cell separation mechanism. The results of these studies will also be presented. We are also developing an injection molding method to improve the productivity of the device for industrial applications. In the talk, we will also report the latest results of our research and development.

Keywords: Microfluidics, centrifugal microfluidics, flow control, bio-analysis, microsystems

BIOGRAPHY



Yoshiaki Ukita was born in 4th Mar 1982 in Japan. He received Dr. degree from University of Hyogo in 2009 and became research fellow of Laboratory of Advanced Science and Technology for Industry (LASTI), University of Hyogo and Japan Society for Promotion of Science (JSPS). He became assistant professor of Japan Advanced Institute of Science and Technology (JAIST) in 2010. He moved to University of Yamanashi and have his laboratory as a principle investor from 2014. He became associate professor of University of Yamanashi in 2019. His research interest is development of microsystems and biomolecular sensing system.

PULSED PHOTONIC PROCESSING FOR PRINTABLE FLEXIBLE ELECTRONICS & APPLICATIONS

M. Bolduc

Universite du Quebec a Trois-Rivieres, Trois-Rivieres, Quebec, Canada

Email: ddctin@vnuhcm.edu.vn

ABSTRACT

Photonic processing has importance for future high-speed manufacturing of printable materials and sensors. This technology may enable the development of low-cost, eco-friendly, and flexible sensors. Photonic Laser and Intense Pulsed Light sintering processes involve the use of high-power nanosecond or microsecond pulse light to heat the functional ink layer in milliseconds beyond the maximum working temperature of the flexible polymer or paper substrate. The thermal penetration from a nanosecond laser irradiation is in the micrometer range estimated using COMSOL simulation. This process allows for the rapid and intense thermal penetration waves to occur, which leads to the sintering of nanoparticles and grains growth in the crystalline structure. In a first step the heat applied during photon irradiation volatilizes vehicle components in the printable ink formulation, then followed functional nanoparticles to contact each other. This technology is advantageous for flexible substrates having a low glass transition temperature. The study also highlights the potential of photonic technologies integration onto high-speed printing systems, which can potentially transform the field of microelectronics.

BIOGRAPHY



Dr. Martin Bolduc: Professor in Mechanical Engineering at UQTR, Canada since 2021. He holds a Research Chair in Intelligent Manufacturing under a NSERC Canada Early Career Researcher Grant. Prior to joining UQTR (2009-2021), he first was postdoc at State University of New York (SUNY-Albany) and at Massachusetts Institute of Technology (MIT), USA working on nanotechnology for microelectronics. Then he worked in the industry on the microfabrication of infrared and terahertz cameras at the National Optics Institute (INO), Canada. In 2012, he started research activities on printable optoelectronic sensors using high-resolution laser processing. He is a scientific committee member of the Canadian IntelliFLEX Alliance and the author/co-author of more than 70 publications/patents with 2 technology transfers to startup companies.

DETERMINING BY RAMAN SPECTROSCOPY THE AVERAGE THICKNESS AND N-LAYER-SPECIFIC SURFACE COVERAGES OF MoS₂ THIN FILMS WITH DOMAINS MUCH SMALLER THAN SPOT SIZE

Matthieu Paillet¹, Felipe Wasem Klein¹, Jean-Roch Huntzinger¹, Vincent Astié², Damien Voiry³, Houssin Makhlouf¹, Sandrine Juillaguet¹, Jean-Manuel Decams¹, Sylvie Contreras², Périne Landois², Ahmed-Azmi Zahab¹ and Jean-Louis Sauvajol¹

¹Laboratoire Charles Coulomb, Université de Montpellier, CNRS, F-34095, Montpellier, France ;

²Annealsys, 139 Rue des Walkyries, 34000 Montpellier, France ;

³Institut Européen des Membranes, IEM, UMR 5635, Université Montpellier, ENSCM, CNRS, Montpellier, France

Email: matthieu.paillet@umontpellier.fr

ABSTRACT

Molybdenum disulfide, MoS₂, is of particular interest in optoelectronic applications due to its transition to a direct bandgap semiconductor when thinned down to a monolayer. Because the properties of MoS₂ flakes are firstly a function of their thickness, or layer number (N), it is of a primary importance to determine the N of MoS₂ samples prepared by different routes.

Raman spectroscopy is a widely used technique to characterize nanomaterials due to its convenience, non-destructiveness, and sensitivity to materials change. The primary purpose of this work is to determine using Raman spectroscopy the average thickness of MoS₂ thin films synthesized by direct liquid injection pulsed-pressure chemical vapor deposition (DLI-PP-CVD). Such samples are constituted of nanoflakes (with a lateral size of typically 50 nm, *i.e.* well below laser spot size), with possibly a distribution of thicknesses and twist angles between adjacent layers of multilayer domains. As an essential preliminary, we reassess first the domains and limits of application of different Raman criteria which allow determining the thicknesses of MoS₂ flakes from measurements performed on reference samples, namely well characterized mechanically exfoliated and standard chemical vapor deposition MoS₂ large flakes deposited on 90 (±6) nm SiO₂ on Si substrates. Then, we discuss their application for significantly different DLI-PP-CVD MoS₂ samples with average thicknesses ranging from sub-monolayer up to three layers. Finally, an original procedure based of the measurement of the intensity of the layer breathing modes is proposed to evaluate the surface coverage for each N (*i.e.* the ratio of the surface covered by exactly N layers and the total surface) in DLI-PP-CVD MoS₂ samples.

Keywords: Raman spectroscopy, Molybdenum disulfide, number of layers

BIOGRAPHY



M. Paillet was born in 1978. He received his Ph.D. degree in materials science from the University of Montpellier in 2005. He is currently holding a full-time CNRS researcher position at the Laboratoire Charles Coulomb (University of Montpellier). His research interests are focused on carbon nanotube, graphene and other 2D materials physical properties.

Co₃O₄ HOLLOW SPHERES AS HIGH-PERFORMANCE SUPERCAPACITOR MATERIAL

Hang T. T. Le and Thanh-Tung Mai

The School of Chemical and Life Science, Hanoi University of Science and Technology, 1 Dai Co Viet road, Hai Ba Trung district. Hanoi 100000, Vietnam

Email: tung.maithanh@hust.edu.vn

ABSTRACT

Cobalt oxide (Co₃O₄) is well-known as a promising material for various applications, especially, in electrical energy storage systems. Unfortunately, its practical application remains limited due to small surface area and high electrical resistance. In this study, Co₃O₄ hollow spheres were prepared by using the incipient wetness impregnation method, wherein carbon spheres were used as supporting material. The as-prepared product was characterized by powder X-ray diffraction (XRD), field-emission scanning electron microscope (FE-SEM), nitrogen adsorption-desorption isotherm (BET). The application potential of the Co₃O₄ hollow spheres for supercapacitors was evaluated at different temperatures using the cyclic voltammetry (CV) and galvanostatic charge-discharge (GCD) techniques. The obtained Co₃O₄ hollow spheres exhibited excellent specific capacitance performance of 1300 F g⁻¹ at the specific current of 2.0 A g⁻¹ in 4 M KOH electrolyte solution. The Co₃O₄ electrode was tested long-term cyclability for 1000 cycles of consecutive charge-discharge. The obtained result shows an excellent capacitance retention (95%) after 1000 cycles suggesting high chemical stability because of the hollow structure of the Co₃O₄ spheres. In addition, to verify the outstanding performance of the as-prepared Co₃O₄ in the present work, the supercapacitive performance of the commercial Co₃O₄ was evaluated and compared. The experimental result demonstrated that the prepared Co₃O₄ in the present work pose the superior electrochemical performance to the commercial one.

Keywords: Supercapacitors, cobalt oxide, hollow spheres

BIOGRAPHY



Mai Thanh Tung, PhD
Full Professor
The School of Chemical and Life Science
Hanoi University of Science and Technology (HUST)
Office 214, C4 building, No.1 Dai Co Viet Road, Hanoi, Vietnam
Tel: +84 2348680070, HP: +84 912316363, Fax: +84 248680070
Email: tung.maithanh@hust.edu.vn
Vice Presidency of Vietnam Corrosion Association (VICORRA)

Professor Mai Thanh Tung had been educated in Hanoi University of Science and Technology (HUST), receiving his Engineer degree of Chemical Engineering with the specialized major of Electrochemistry and Corrosion Protection in 1995. Then, in 1998 he received Master degree of Materials Science and Engineering at Chalmers University of Technology (Sweden). After that, he started participating a Doctoral program at Heinrich- Heine- University Duesseldorf (Germany) and graduated with a doctorate degree in Physical Chemistry and Electrochemistry in 2003. As soon as he had received the PhD degree, he returned Vietnam and joined Department of Electrochemistry and Corrosion Protection, School of Chemical Engineering (now it changes into the School of Chemical and Life Science), HUST, where he initiated his independent academic career. Since starting his research career, he has contributed to building and reinforcing the department and enhancing the ranking of the university as well. Currently, he has been teaching some courses for undergraduate and graduate students.

Professor Mai has achieved recognition as a full professor with various roles such as:

- Principal Investigator (PI)
- Overall project management, guidance, direction and leadership to project team and project manager in relation to various issues, risks, and approach.
- Lead advocacy activities, networking, and build relationships with partners.
- Lead the activity relating to policy recommendation and Policy dialog on for wastewater recycling and water circulation

Professor Mai is also an famous expert in several fields for example:

- Batteries and power sources (Lithium ion batteries, supercapacities) for EV, BESS
- Batteries materials (Carbon systems for anodes, cathode materials)
- Surface Engineering and Electrochemical Engineering

In general, professor Mai is a scientist in the area of electrochemistry, energy storage and materials science. With his achievements, he has been served as the Vice Presidency of Vietnam Corrosion Association. Currently, he has worked as a peer reviewer for national and international journals such as *Electrochimica Acta*, *Journal of Electrochemical Science and Technology*, *Metals and Materials International*... Besides, Professor Mai has published a large number of scientific papers (~100 papers) including ISI papers, national papers and conference papers. He also published 3 books for undergraduate and graduate students. His researches almost focus on development of electrode active materials for batteries, surface engineering and electrochemical engineering. Especially, his work is very close to Batteries Industries (Hai Phong Batteries, VINFAST, VNPT, EVN...) and Governments (MOIT, MOST...). In addition, so far Professor Mai have been working as PI and Co-PI of 15 projects including domestic projects and international cooperation projects.

INVITED TALKS
***APPLICATIONS OF MICRO-
NANOTECHNOLOGY***
(AMN)

ACTIVITIES for REALIZING NEXT-GENERATION SHRIMP FARMING WITH BIOGAS-FUELED SOFC and IoT

**Yusuke Shiratori¹, Tu Hoan Phuc¹, Tin Chanh Duc Doan^{2,3}, Akira Kurihara⁴, Takeo Yamakawa⁵,
Le Quoc Viet⁶, Tran Sy Nam⁷, Kazuhiro Shibagaki⁸, Motoki Sakurai⁸,
Ryuji Nakayama⁹, and Toshihide Sugawara⁹**

¹ Department of Mechanical Science and Engineering, School of Advanced Engineering, Kogakuin University, 2665-1 Nakano-machi, Hachioji, Tokyo 192-0015, Japan;

² Institute for Nanotechnology, Community 6, Linh Trung Ward, Thu Duc City, Ho Chi Minh City, Vietnam;

³ Vietnam National University Ho Chi Minh City, Ho Chi Minh City, Vietnam;

⁴ Aqua-Bioresource Innovation Center, Faculty of Agriculture, Kyushu University, 744 Motoooka, Nishiku, Fukuoka 819-0395, Japan;

⁵ Department of Agricultural Science and Technology, Faculty of Agriculture, Setsunan University, 45-1 Nagaotoge-cho, Hirakata, Osaka 573-0101, Japan;

⁶ Faculty of Marine Science and Technology, College of Aquaculture and Fisheries, Campus II, Can Tho University, 3/2 Street, Xuan Khanh Ward, Ninh Kieu District Can Tho City, Viet Nam;

⁷ Department of Environmental Sciences, Campus II, Can Tho University, 3/2 Street, Xuan Khanh Ward, Ninh Kieu District Can Tho City, Viet Nam;

⁸ Mitsubishi Research Institute, Inc., 10-3 Nagata-cho, 2-Chome, Chiyoda-Ku, Tokyo 100-8141, Japan;

⁹ Yuko Keiso Co., Ltd., 2-8-8 Chuo-cho, Meguro-ku, Tokyo 152-0001, Japan

Email: shiratori@cc.kogakuin.ac.jp

ABSTRACT

Fuel cell based on electrochemical process can convert chemical energy of a fuel directly into electricity, resulting in elevated efficiency. Among various types of fuel cells, solid oxide fuel cells (SOFCs) composed of ceramic materials operated at high temperature (600-900°C) exhibit highest power generation efficiency (η_e) over 50% even with small output power range less than 10 kW due to its rapid reaction kinetics. Here, fundamental research activities on the biogas-fueled SOFC aiming at the spread of SOFC technology, such as desulfurizer made from rice husk and catalyst for hydrogen production from biogas, will be presented. In addition, the concept of the next-generation shrimp farming with biogas-fueled SOFC controlled by IoT (A pilot plant is now being constructed by Japanese team in Tien Giang province.) for the sustainable development of Mekong Delta will be introduced.

Keywords: Solid oxide fuel cell, biogas, shrimp farming, IoT, resource circulation

BIOGRAPHY



Yusuke Shiratori earned his Ph.D. in the field of electrochemistry (Modeling and performance simulation of solid oxide fuel cell (SOFC)) at Tokyo Institute of Technology in 2002. He, then, engaged in the development of electrolyte material for SOFC at Forschungszentrum Jülich (Germany) as a postdoctoral fellow. After his stay in Germany, he has been working for Department of Mechanical Engineering, Faculty of Engineering, Kyushu University as an Assistant Professor to study fuel cell anodes with enhanced catalytic activity for hydrocarbon reforming. In 2011, he became an Associate Professor of this department, and his research created a novel structured-catalyst material to realize direct internal reforming SOFC. From 2015, he started Vietnam-Japan international joint research project as a leader of Japan side to develop and demonstrate a fuel cell-incorporated energy circulation system using regional biomasses as energy resources to contribute to the sustainable development of Mekong Delta region. In April 2022, he launched education and research activities in Department of Mechanical Science and Engineering, School of Advanced Engineering, Kogakuin University as a Professor.

ARTIFICIAL SENSORY RECEPTORS FOR NEUROMORPHIC PERCEPTION

Seokju Hong¹, Yurim Lee¹, M. Junaid Sultan¹, Hamna Haq Chouhdry², Hung Quang Hyunh¹,
Tran Quang Trung¹, Atanu Bag² and Nae-Eung Lee^{1,2,3},

¹School of Advanced Materials Science & Engineering, ²SKKU Advanced Institute of Nanotechnology (SAINT), ³Biomedical Institute for Convergence at SKKU (BICS), and Samsung Advanced Institute for Health Sciences and Technology (SAIHST), Sungkyunkwan University, Suwon, Gyeonggi-do 16419, Korea

Email: nelee@skku.edu

ABSTRACT

Neuromorphic perception is a field of research and development focused on creating artificial systems that can perceive and interpret sensory information in a manner similar to biological organisms. Inspired by the efficiency and adaptability of the human brain, researchers aim to replicate these qualities in artificial systems. To achieve artificial neuromorphic perception, specialized hardware called neuromorphic hardware is required. This hardware is designed to emulate the neural architecture of the brain, including sensors. By emulating the brain's signal processing capabilities, neuromorphic systems can perform computations faster and more energy-efficiently, making them suitable for real-time applications and environments with limited resources. Efficiently inputting sensory data into neuromorphic perception systems is crucial. One interesting approach involves emulating biological receptors found in somatosensory neuronal systems. These biological sensory receptors have the ability to preprocess signals, adapt to changing conditions, and store information before encoding and transmitting the signal to the brain. By replicating these functionalities, artificial systems can enhance their ability to process and interpret sensory input.

In this presentation, In the forthcoming presentation, I will share our latest advancements in the realm of artificial sensory synapses, encompassing their materials, design, and operational intricacies. These remarkable synapses have the unique capacity to not only detect and retain signals but also emulate the remarkable functionalities exhibited by biological mechanoreceptors, chemoreceptors, and photoreceptors. Our innovative sensory synapses have proven their proficiency in discerning and categorizing a diverse array of attributes. These encompass variances in textures, distinctions between gases, and even responses to varying light stimuli. Such versatility underscores their potential in various future perception applications. Furthermore, our discourse will delve into the pivotal role of these sensory receptors in shaping the landscape of future neuromorphic perception systems. The symbiotic fusion of biology-inspired design and cutting-edge technology holds promise for the continued evolution of these systems.

Keywords: sensor, synapse, neuromorphic, perception

BIOGRAPHY



Nae-Eung Lee received BS and MS degrees from Seoul National University (SNU), Korea and Ph.D. degree in Materials Science and Engineering from University of Illinois at Urbana-Champaign in 1996. He had worked as a senior process engineer at Lam Research Corp., USA for two years from 1996. Then, he joined Sungkyunkwan University (SKKU) in 1998 and is currently Professor in the Department of Materials Science and Engineering at SKKU, Korea. He is also holding adjunct professorships in SKKU Advanced Institute of Nanotechnology (SAINT) and Samsung Advanced Institute for Health Sciences and Technology (SAIHST). He was an awardee of SKKU fellowship (2018) and is now a member of The National Academy of Engineering of Korea. He served as the dean of SKKU College of Engineering from 2021 to 2022. His research interests include neuromorphic sensors, flexible/stretchable electronics and biosensor-integrate systems.

ENERGY CONVERSION OF BIOFUEL REFORMING CATALYST AND SOLID OXIDE FUEL CELL COMBINED DEVICE

Yuya Tachikawa¹

¹ Department of Mechanical Engineering, Faculty of Engineering, Kyushu University, 744, Motoooka, Nishi-ku, Fukuoka, 819-0395, Japan
Email: tachikawa.yuya.657@m.kyushu-u.ac.jp

ABSTRACT

The performance of biofuel reforming module using nickel-based catalyst combined with solid oxide fuel cell (SOFC) is evaluated using heat and mass balance simulation. The prototype SOFC device was simulated to evaluate the influence of biofuel conversion due to reforming catalyst and device operating condition on the SOFC performance. When the catalytic activity of reforming catalyst was dropped, the electrical and net efficiencies also decreased due to the increase of waste heat. The biofuel conversion efficiency change on the reforming module directly leads device performance drop. However, flexible operating condition control was able to reduce the influence on performance drop.

Keywords: biofuel, solid oxide fuel cell, reforming catalyst,

BIOGRAPHY



Yuya Tachikawa is an associate professor of mechanical engineering at Kyushu University. His major research field is the thermal and computational engineering. His work now focuses on the electrochemical energy conversion using solid oxide material device and the development of carbon neutral energy applications. He promotes several regional model demonstration projects for hydrogen society in Japan.

PLANT BIOMASS-DERIVED HYBRIDS CARBON NANOMATERIALS COMPOSITES FOR ADVANCED ENERGY STORAGE APPLICATIONS

Balla D Ngom

Laboratoire de Photonique Quantique, d'Energie et de Nano-Fabrication, Departement de Physique, Faculté des Sciences et Techniques, Université Cheikh Anta Diop de Dakar (UCAD) B.P. 5005 Dakar-Fann Dakar, Sénégal

Email: balla.ngom@ucad.edu.sn or bdngom@gmail.com

ABSTRACT

Energy as a commodity is facing a global crisis due to its high demand and consumption in all areas, overuse of fossil fuels is also causing environmental problems such as global warming and depletion of the ozone layer. To solve this problem, researchers have been interested on developing efficient, sustainable, and clean energy storage systems to boost the use of renewable energy. We report on green and ecofriendly biomass derived devices for energy storage applications. From our results on activated carbon nanostructures from peanut shell waste using different porosity-enhancing agents, an asymmetric supercapacitor device was assembled in a neutral electrolyte (2.5 M KNO₃) at a cell voltage of 1.8 V, which yielded 224.3 F g⁻¹ specific capacitance at a specific current of 1 A g⁻¹ with a corresponding specific energy of 25.2 W h kg⁻¹ and 0.9 kW kg⁻¹ of specific power. To enhance the performance of the device, ex-situ nitrogen-doped porous carbon was synthesized and investigated in the same electrolyte. The fabricated device exhibited a 251.2 F g⁻¹ of specific capacitance at a gravimetric current of 1 A g⁻¹ at a wide cell voltage of 2.0 V. A specific energy of 35 Wh kg⁻¹ with a corresponding specific power of 1 kW kg⁻¹ at 1 A g⁻¹ was obtained. For future development of environmentally friendly and sustainable electrode materials, we developed sustainable binary vanadium pentoxide carbon graphene foam composites (V₂O₅@C-R₂HS/GF) using a green method. The device showed high specific energy and specific power values of 55 W h kg⁻¹ and 707 W kg⁻¹, respectively, at a specific current of 1 A g⁻¹. The device presented a good stability test showing 99% capacity retention up to 10000 cycles confirmed by the floating time up to 150 h with specific energy an increase of 23.6% after the first 10 h.

Keywords: Biomass, Energy Storage, Supercapacitors, Energy and Power densities

BIOGRAPHY



Balla Diop Ngom is a Professor of Nanomaterials Physics originally trained in solid state physics at the University Cheikh Anta Diop of Dakar (UCAD) in Dakar, Senegal. His keen interest led him to complete doctoral studies in Physics at the same university. His scientific curiosity led him to pursue a second PhD in nanomaterials physics at the University of the Western Cape (UWC), Cape Town, South Africa. Building on this high-level training, excellent academic record and uncommon motivation and dedication, he returned to Senegal to embark on an academic career of high promise, already delivering spectacular results and outcomes. As a result of these distinguished academic achievements, Prof Balla has gained some twelve years of in-depth knowledge and experience in the multi-disciplinary field of nanoscience, focusing on energy and smart nanomaterials. He has co-authored more than 80 ISI scientific publications, given more than 50 invited lectures at national and international conferences, universities and research institutions including ten lectures at multinational companies. In addition to his outstanding research and training of young scientists, Prof. Ngom is also actively involved in the promotion of science, technology and education motors of development in Africa and the global South, for example via website and social media platforms. Prof Balla is the President of the African Materials research Society (AMRS) and the Chairman of the NanoSciences African Network (NanoAfnet).

SOLAR PHOTOVOLTAIC INTEGRATION TO GRIDS: IMPACTS AND SOLUTIONS

Quoc Tuan Tran

CEA-Liten

Le Bourget du Lac, France

Email: quoctuan.tran@cea.fr

ABSTRACT

Increasing integration of solar energy along with electrification and decarbonisation challenges the existing grid infrastructures due to their intermittent characteristics with high levels of uncertainty and complexity. Several impacts on the grid operation include voltage variations, frequency variation, voltage unbalance, stability, protection and challenges for managing... These impacts are even more complicated for islanded or weak grid areas. A better knowledge, analysis and evaluation methods of the induced constraints become necessary in order to determine the hosting capacity, to assess impacts of solar photovoltaic generation on the distribution network and to assess technical and economic opportunities provided by solar photovoltaic generation. This keynote presents analyses of the impacts provided by solar photovoltaic integration into grid. Solutions by intelligent control and energy management in order to reduce these impacts, to maximize the ancillary services contributed by solar photovoltaics and to maintain the grid stability are discussed. Solutions associated with energy storage and the development of micro-grid technologies will be presented to address mentioned grid challenges.

Keywords: Solar photovoltaic, Impacts, Solutions, Control, Energy management

BIOGRAPHY



Prof. Quoc Tuan TRAN received his Ph.D. degree in Electrical Engineering and his “Habilitation à Diriger des Recherches” degree (Dr. Habil.) from the Grenoble Institute of Technology, France, in 1993 and 2000, respectively. He is actually a Professor at the National Institute for Nuclear Science and Technology/Paris-Saclay University, Director of Research, Fellow Scientist and International Expert at the CEA (French Alternative Energies and Atomic Energy Commission), Scientific Manager for smart grid at the CEA-Liten/INES (French National Institute for Solar Energy) and Teacher at the INSTN and the Grenoble Institute of Technology, the

Grenoble Alpes University (UGA) and the ENSTA (Paris Polytechnic Institute).

His research interests are in the fields of smart grid, microgrid, power system analysis, operations and protection, electromagnetic transients, real-time and co-simulation, renewable energy (solar energy & wind energy), power electronic, MV/HVDC, electric vehicle, energy storage, smart building, energy management and control. He has realized and piloted more than 50 projects, such as European, industrial, Ademe, ANR projects... He holds 12 patents, is the (co)author of seven books, and has published more than 350 publications in journals and conference proceedings. He has supervised 50 PhD theses. He is an IEEE senior member and CIGRE member and General Chair of IEEE EEE-AM conference, Hanoi, from 13th to 15th November 2023 (<https://eeeam.net/>).

BIOSENSORS: THE GAME-CHANGING REVOLUTION IN HEALTHCARE

Prof Ir Dr Fatimah Ibrahim

Centre for innovation in Medical Engineering, FAC. of Engineering, Universiti Malaya

Email: fatimah@um.edu.my

ABSTRACT

The healthcare industry has experienced rapid technological advancements that have brought about innovative breakthroughs. This discussion will delve into the latest developments in biosensors and flexible electronics, and their profound impact on healthcare. The speaker will highlight how biosensors can detect and analyze biological information, providing extensive opportunities for early disease detection, patient health monitoring, and personalized healthcare. Flexible electronic systems can seamlessly work with biosensors, enhancing their capabilities and allowing for real-time data collection and monitoring. By combining these technologies, we can significantly improve diagnostics and patient care. Lastly, the speaker will emphasize the crucial role of green electronics in shaping the future of healthcare.

BIOGRAPHY



Professor Ir. Dr. Fatimah Ibrahim received her B.Sc.E.E. from Marquette University, USA in 1989. She obtained her M.Sc. Electronics (Medical Systems) from University of Hertfordshire, UK in 1994 and Ph.D. in Biomedical Engineering from University of Malaya (UM), Malaysia in 2005. She is a Professor of Biomedical Engineering, UM, the head of Centre for Innovation in Medical Engineering (CIME), and advisor for the Center of Printable Electronics, UM. She is the senior member of IEEE, fellow of Institute of Engineer Malaysia (IEM), and fellow of Academy Science Malaysia (ASM). She is a Professional Engineer with Practising Certificate (PEPC) registered under Board of Engineer Malaysia. Her

research interests are in physiological measurement and modeling, biosensors, BioMEMS, bioinstrumentation, and artificial intelligence in medicine. She owned 16 patents including 3 commercialised patents. In recognition of her research innovations, she has received 9 top awards (Gold medal/best award/special award), 3 Silver Medals, and 2 bronze medals at various international and national invention exhibitions. She has been awarded the Top Research Scientist Malaysia (TRSM 2019) by the Academy of Sciences Malaysia (ASM) and the world's top 2% scientist in 2022 reported by Stanford University. She received the IFMBE Laura Bassi Award 2022, an award attributed to a female biomedical engineer for her outstanding research contributions in the field of medical and biological engineering by the International Federation of Medical and Biological Engineering (IFMBE), USA.

Affiliation: HEAD, CENTRE FOR INNOVATION IN MEDICAL ENGINEERING, FAC. OF ENGINEERING, UNIVERSITI MALAYA

Email Address: fatimah@um.edu.my

Nationality: MALAYSIA

Education:

2005 Ph.D. Biomedical Engineering, Universiti Malaya, Malaysia.

1994 MScEE Medical Systems, University of Herfordshire, UK.

1989 BScEE (Hons) Electrical Engineering, Marquette University, USA.

Present Positions:

- PROFESSOR, DEPARTMENT OF BIOMEDICAL ENGINEERING, FACULTY OF ENGINEERING, UNIVERSITI MALAYA
- HEAD, CENTRE FOR INNOVATION IN MEDICAL ENGINEERING, UNIVERSITI MALAYA

Research Interests:

- Detection and monitoring of infectious diseases and foodborne pathogens, carbon MEMS/NEMS biosensing, diagnostics, bioinstrumentation, artificial intelligence and Internet of Things (IoT) integration in medicine as well as physiological measurement and modelling.

Achievements (latest):

- World's Top 2% Scientist 2022
- 2nd Place, Selangor R&D and Innovation Expo 2022.
- IFMBE Laura Bassi 2022 Award by The International Federation for Medical and Biological Engineering
- Gold Award and Special Prize Award by Korea Institute of Patent Information in Korea International Women's Invention Exposition 2021 (KIWIE)
- EMBS Academic Achievement Award, IEEE-EMBS Malaysia Chapter, 2020, (National) (2020)
- Top Research Scientist Malaysia (TRSM) from the Academy of Sciences Malaysia (2019)

GRAPHITE FELT MODIFIED WITH ATOMIC LAYER DEPOSITED ULTRATHIN TITANIUM DIOXIDE NANOCOATING AS HIGH EFFICIENT ELECTRODE FOR ALL-VANADIUM REDOX FLOW BATTERY

Wen-Jen Lee^{1,*}, **Yu-Shan Gao**¹ and **Chi-Chang Chen**^{2,*}

¹ Department of Applied Physics, National Pingtung University, Taiwan

² Green Energy and Environment Research Lab., Industrial Technology Research Institute, Taiwan

*Email: wenjenlee@mail.nptu.edu.tw (WJ Lee); cc_chen@itri.org.tw (CC Chen)

ABSTRACT

Graphite felt (GF) is widely used as an electrode for all-vanadium redox flow batteries (VRFBs) due to its high conductivity, excellent acidic corrosion resistance, and three-dimensional structure with high porosity. However, due to the inherent hydrophobicity of GF, surface modification treatment must be carried out to obtain GF electrodes with high electrochemical activity and performance. Although various methods have been used to surface modify GF, there are some shortcomings, such as little improvement in efficiency, poor stability, or complex processes, making them unsuitable for practical applications. In this work, a simple and effective method for GF surface modification is reported, which is ultrathin (only 5 nm) titanium dioxide (TiO₂) film coated on the surface of GF by atomic layer deposition (ALD). The ALD-TiO₂ nanocoating modified GF exhibits excellent hydrophilicity and electrochemical activity. Furthermore, the VRFB based on ALD-TiO₂/GF electrodes demonstrates high efficiency and long-term durability. The maximum operating current density (250mA/cm²) of ALD-TiO₂/GF is five times that of the original GF (50mA/cm²). The energy efficiency (87.3%) of ALD-TiO₂/GF operated at 50mA/cm² is 22% higher than the energy efficiency of the original GF (65.3%). Besides, the energy efficiency of ALD-TiO₂/GF at the current density of 100, 150, 200, and 250 mA/cm² is 83.6, 79.1, 73.9, and 67.9 %, respectively. In addition, as the result of the 200 charge-discharge cycling test at a high current density of 250mA/cm², the ALD-TiO₂/GF demonstrates excellent long-term durability (its energy efficiency has no attenuation at all). This study successfully utilized atomic layer deposition with titanium dioxide nanocoatings to greatly improve the performance of GF, and the ALD-TiO₂/GF demonstrated commercialization potential. This work was mainly supported by the National Science and Technology Council of Taiwan (No.: NSTC 111-2221-E-153-002 and 112-2221-E-153-001-MY3), partially supported by National Pingtung University (No.: NPTU-111-012) and the Bureau of Energy, Ministry of Economic Affairs of Taiwan (No.: BOE-112-D0113).

Keywords: Atomic layer deposition, graphite felt, surface modification, redox flow battery

BIOGRAPHY



Dr. Wen-Jen Lee obtained his PhD degree in Materials Science and Engineering at National Chen Kung University, Taiwan. He is currently an associate professor and head of the Department of Applied Physics, National Pingtung University. Prof. Lee has been engaged in the growth and application of functional thin film materials using atomic layer deposition (ALD) for 20 years. Recently, Prof. Lee's research interests mainly focused on developing surface modification techniques for carbon-based electrodes and applying them to vanadium redox flow batteries (VRFBs).

BIOMASS-DERIVED CARBON AEROGEL FOR OIL ADSORPTION AND ENERGY STORAGE

Phan Minh Tu^{1,2,3}, Tran Do Dat^{1,2,3}, Truong Thien Vinh An^{1,2,3}, Ta Kien Thanh^{1,2,3},
Nguyen Thi Hanh^{1,2,3}, Nguyen Thi Ngoc Hieu^{1,2,3}, Dang Thanh Phong^{1,2,3},
Dang Thanh Cong Minh^{1,2,3}, Ta Dang Khoa^{2,3}, Nguyen Truong Son^{2,3}, Huynh Khanh Duy^{2,3},
Tong Thanh Danh^{2,3}, Huynh Ky Phuong Ha^{2,3}, Doan Thi Yen Oanh⁴, Ngo Van Tuyen^{1,2,3},
Mai Thanh Phong^{1,2,3}, and Nguyen Huu Hieu^{1,2,3*}

¹VNU-HCM, Key Laboratory of Chemical Engineering and Petroleum Processing (Key CEPP Lab), Ho Chi Minh City University of Technology (HCMUT), 268 Ly Thuong Kiet Street, District 10, Ho Chi Minh City, Vietnam

²Faculty of Chemical Engineering, Ho Chi Minh City University of Technology (HCMUT), 268 Ly Thuong Kiet Street, District 10, Ho Chi Minh City, Vietnam

³Vietnam National University Ho Chi Minh City (VNU-HCM), Linh Trung Ward, Thu Duc City, Ho Chi Minh City, Vietnam

Email: nhhieubk@hcmut.edu.vn

ABSTRACT

As the inspiration in the developing tendency of green synthesis, in this article, *Pachyrhizus erosus*-derived carbon aerogel (BS-CA) was synthesized through a simple and green process: hydrothermal, freeze-drying, and pyrolysis. The impact of pyrolysis temperature on the characterization of the BS-CA was investigated through modern analytical methods, including scanning electron microscope, energy dispersive X-ray, X-ray diffraction analysis, Raman spectroscopy, and nitrogen adsorption-desorption isotherm. Due to its porous structure and high specific surface area, the BS-CA possesses potential applications in oil adsorption and storage energy. Indeed, the oil adsorption capacity of the BS-CA was assessed by the weight difference method, resulting in the capacity is more than 20 times the weight of the material. Furthermore, the BS-CA also has the potential to replace electrode materials with a specific capacitance up to 150 F/g at 10 mV/s.

Keywords: Biomass waste, carbon aerogel, oil adsorption, storage energy, supercapacitor

INTRODUCTION

Nowadays, biomass has been studied as an abundant and potential raw material in the field of science with multiple applications. The major component of biomass is carbohydrates, which consist of C and O elements, and can be converted into biochar, which is an environmentally friendly source of materials [1,2]. Besides, among this biomass, yam bean (YB) has not been studied widely. Most of the previous studies on YB only focused on studying and extracting some compounds in YB. Therefore, the green synthesis of yam bean-derived carbon aerogel (YB-CA) was investigated. YB is scientifically known as *Pachyrhizus erosus* (L.).

Carbon aerogel (CA) exhibits a 3D structure, highly porous structure, large surface area, and low density. Previously, CA was often synthesized from chemical precursors such as resorcinol, formaldehyde, carbon nanotube, etc.

by complex synthesis processes, thus the scope of the practical application of CA is limited. However, according to the trend of sustainable development, biomass-derived materials can replace previous chemical precursors [3–5].

In this study, yam bean-derived carbon aerogel (YB-CA) was synthesized through green methods: Hydrothermal, freeze-drying combined with pyrolysis. The effect of pyrolysis temperature on the characteristics of YB-CA was specifically studied through modern materials analysis methods: Scanning electron microscope (SEM), Raman spectroscopy, X-ray diffraction analysis (XRD), energy dispersive X-ray (EDX), and Fourier transform infrared spectroscopy (FTIR). With the characteristics of pores and three-dimensional structure, YB-CA was investigated for its ability to adsorb oil and organic solvents. Additionally, the electrochemical properties of YB-CA were characterized through cyclic voltammetry (CV),

electrochemical impedance spectroscopy (EIS), and galvanometer charge-discharge (GCD) in the three-electrode system [6].

EXPERIMENTAL

Yam bean-derived CA was synthesized by the green process through freeze-drying and pyrolysis. YB was pretreated to remove the horny layer and the middle sponge was peeled, then cut into pieces ($3 \times 3 \times 1 \text{ cm}^3$). After that, the sample was immersed in alcohol to remove impurities. It was placed into the hydrothermal autoclave reactor at 180°C for 12 h to gain biochar before being frozen at -4°C to ensure a porous structure. Finally, YB-derived aerogel (YB-A) was produced by freeze-drying the material at -80°C for 48 h. Then, YB-A was pyrolyzed at $600\text{-}800^\circ\text{C}$ to get YB-CA-600, YB-CA-700, and YB-CA-800, respectively, as shown in Figure 1.

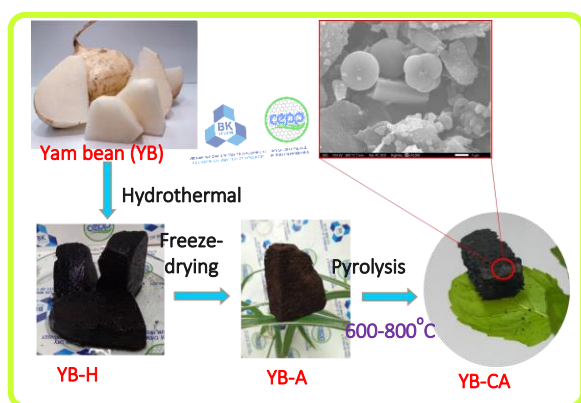


Figure 1. Schematic of synthesis of YB-CA

RESULTS AND DISCUSSION

The surface morphology of YB-CA-600, YB-CA-700, and YB-CA-800 are shown by SEM results in Figure 2. From there, it can be seen that the pyrolysis temperature has a great influence on the morphology of YB-CA. In Figure 1, the SEM images of YB-CA are shown at different magnifications from 10 μm , which can show the general morphology of the material and when increasing the magnification at 5 and 1 μm to see details of morphology. YB was originally composed of carbohydrates such as starch, cellulose, etc. has a block structure, with many interlocking panels. When hydrothermal and pyrolysis, the components of carbon hydrates convert to carbon slowly [7,8]. Thanks to the diverse existence of YB, it creates a 3D

framework and a diverse structure of components, so that YB-CA can adsorb oil and become a potential material for fabricating supercapacitor electrodes.

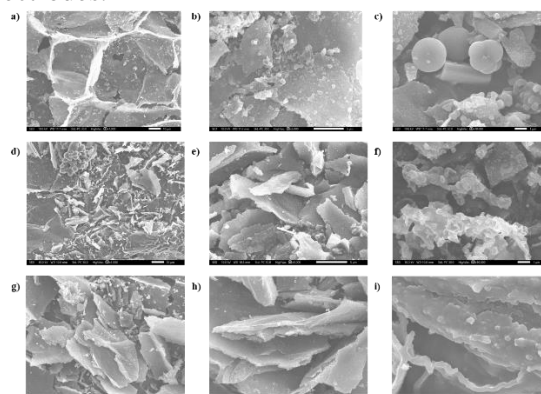


Figure 2. SEM images of YB-CA in differences scale (a-c) YB-CA-600; (d-f) YB-CA-700; and (g-i) YB-CA-800

The results of oil and organic solvents adsorption by using YB-CA, are shown in Figure 3. For used diesel oil, YB-CA has the highest adsorption capacity of 31 g/g (YB-CA-700), adsorbing an amount of oil 31 times the weight of the material. YB-CA-600 and YB-CA-800 achieved the used oil adsorption amount of 28.4 and 15.9 g/g, respectively. The effect of pyrolysis temperature on the characteristics of the material is clearly shown in SEM images, whereby YB-CA-600 has diverse morphology but large pores, not densely packed. Therefore, the oil adsorption capacity of YB-CA-600 is the lowest. As for YB-CA-800, there are signs of 3D structural collapse, reducing the ability of YB-CA-800 to adsorb oil particles.

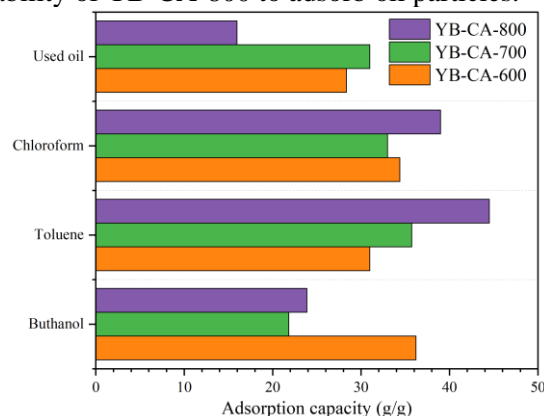


Figure 3. Adsorption capacity of YB-CA

Figure 4 shows the CV curves of YB-CA at 50 mV/s and the obtained specific capacitance values of YB-CA-600, YB-CA-700, and

YB-CA-800 are 233.0, 349.9, and 199.3 F/g, respectively. YB-CA-700 has the highest obtained CV curve area as well as specific capacitance.

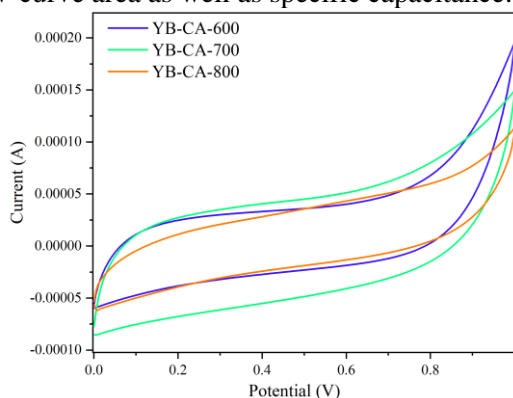


Figure 4. CV curves of YB-CA at 50 mV/s

Besides, Nyquist plot results (Figure 5) also shown consistency with the resistance of YB-CA-700. The resistance of YB-CA was determined through Nyquist plots from EIS results, when changing the sweep frequency range from 1 Hz to 1 MHz based on the correlation of Z' and Z'' , a small half-circle curve was created. From that, the relative resistance of YB-CA is predicted, the resistance of YB-CA-600, YB-CA-700, and YB-CA-800 are 215.3, 205.5, and 212.0 Ohm, respectively.

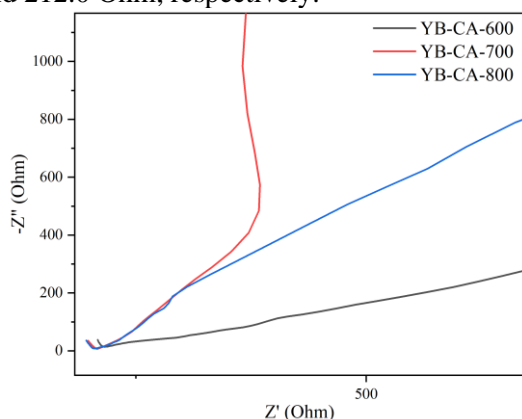


Figure 5. Nyquist plots of YB-CA

CONCLUSION

In this study, yam bean-derived carbon aerogel (YB-CA) was successfully synthesized with diversity in structure and size pores when investigating the material at different pyrolysis temperatures (600-800°C, N_2). For 600°C pyrolysis YB-CA (YB-CA-600), the structure is in the form of thin sheets, folded into polygons like the petals of *Clerodendrum thomsoniae* flowers. When the pyrolysis temperature was

increased to 700 (YB-CA-700) and 800°C (YB-CA-800), the broken plate structure produced spherical particles, small layered plates. Therefore, YB-CA has the ability to absorb oil up to 31 times the weight of the material (YB-CA-700). Furthermore, YB-CA has the ability to adsorb chloroform, toluene, and butanol with adsorption capacities of 39.0, 44.5, and 36.2 g/g, respectively. In addition, YB-CA has the potential to replace supercapacitor materials with a specific capacitance of nearly 350 F/g at a scanning speed of 50 mV/s. In particular, the study used yam bean as a precursor with a 3D block structure, from which YB-CA was synthesized through green methods (hydrothermal, freeze-drying combined with pyrolysis), almost without using chemicals, contributing to a green, low-cost, and simple, easy to industrialize synthesis of carbon aerogel process.

Acknowledgment

We acknowledge the support of time and facilities from Ho Chi Minh City University of Technology (HCMUT), VNU-HCM for this study.

References

- [1] Wei G, Zhang J, Usuelli M, Zhang X, Liu B, Mezzenga R. *Biomass vs inorganic and plastic-based aerogels: Structural design, functional tailoring, resource-efficient applications and sustainability analysis*. *Prog Mater Sci*. **125** (2022)100915.
- [2] Xiao X, Chen B, Chen Z, Zhu L, Schnoor JL. *Insight into Multiple and Multilevel Structures of Biochars and Their Potential Environmental Applications: A Critical Review*. *Environ Sci Technol* **52** (2018) 5027–47.
- [3] Zhao S, Li C, Zhou Y, Wang S, Su F, Cui J, et al. *A multifunctional hydrogel based on heterostructured hybrids of single-walled carbon nanotubes and clay nanoplatelets*. *Carbon N Y* **77** (2014) 846–56.
- [4] Qian Z, Wang Z, Zhao N, Xu J. *Aerogels Derived from Polymer Nanofibers and Their Applications*. *Macromol Rapid Commun*. **39** (2018) 1700724.
- [5] Qian Y, Ismail IM, Stein A. *Ultralight, high-surface-area, multifunctional graphene-based aerogels from self-assembly of graphene oxide and resol*. *Carbon N Y* **68** (2014) 221–31.

- [6] Hao P, Zhao Z, Tian J, Li H, Sang Y, Yu G, et al. *Hierarchical porous carbon aerogel derived from bagasse for high performance supercapacitor electrode*. *Nanoscale* **6** (2014) 12120–9.
- [7] Sakdaronnarong C, Pipathworapoom W, Vichitsrikamol T, Sema T, Posoknistakul P, Koo-amornpattana W, et al. *Integrative process for a sugarcane bagasse biorefinery to produce glucose, bio-oil and carbon microspheres*. *Process Safety and Environmental Protection* **116** (2018) 1–13.
- [8] Ma X-X, He X-Q, Asefa T. *Hierarchically Porous Co₃C/Co-N-C/G Modified Graphitic Carbon: A Trifunctional Corrosion-Resistant Electrode for Oxygen Reduction, Hydrogen Evolution and Oxygen Evolution Reactions*. *Electrochim Acta* **257** (2017) 40–8.

Biography



Nguyen Huu Hieu received his doctoral degree from Chonbuk National University, Korea, in 2012. He is currently an Associate Professor in Chemical engineering in Ho Chi Minh University of Technology, Viet Nam National University Ho Chi Minh City. His current research interests include graphene aerogel, adsorption materials, and photodegradation materials.

SINGEL PARTICLE SENSOR BASED ON BIONANOSPHERICAL PROBE TO LABEL CANCER CELL AND TRACK BY FLUORESCENT HIGH RESOLUTION MICROSCOPY

Le Quoc Minh^{1,4,5}

Tran Kim Anh¹, Nguyen Thanh Huong^{1,4}, Do Thi Thao²,
Nguyen Trong Nghia³, Nguyễn Văn Nghĩa⁶ and Pham Thi Lien^{1,4}

1. Institute of Materials Science, Vietnam Academy of Science and Technology, 18 Hoang Quoc Viet Road, Hanoi 100000, Vietnam
2. Institute of Biotechnology, Vietnam Academy of Science and Technology VAST, 18 Hoang Quoc Viet Road Hanoi 100000, Vietnam
3. Institute of Physics, Vietnam Academy of Science and Technology, 18 Hoang Quoc Viet Road, Hanoi 100000, Vietnam
4. Graduate University of Science and Technology, Vietnam Academy of Science and Technology, 18 Hoang Quoc Viet Road, Hanoi 100000, Vietnam
5. Institute of Technology, Environment and Green Energy CMN, Vietnam Union of Science and Technique Association VUSTA, Bld A2, 18 Hoang Quoc Viet, Cau Giay, Hanoi, Vietnam
6. Thuy Loi University, Hanoi, Vietnam

ABSTRACT

Rare Earth nanoparticles are promising sensors of chemical, mechanical, and temperature changes. At present the almost sensing processes have focused on using stimuli probe from an ensemble of plenty of nanoparticle. This ensemble of nanoparticle, usually, consist of at least several ten until hundred thousand nanoparticles (species). Therefore the ensemble drive sensors raise high restriction of physical specisity, of position in nanoscal, of effective sensitivity and of weight- ability of great materials amount and created big sensor device dimension.

To overcome these disadvantages a novel strategy seem to be very perspective is development of a sensor based on a single nanoparticle. It is able one of the key direction of Nano sensor science, technology and industrial production in period from 2020 to 2030 plus...

Here we present for the first time the investigation toward to a single particle biosensor from design, nanomaterial synthesis, bio probe construction, imaging label and track by a fluorescent high resolution microscopy. The nanomaterial was high-mohomogeneous Nano sphere $Gd_2O_3: Yb^{3+}, Er^{3+}$, which fabricated by synergic method.

The probe $Gd_2O_3: Yb^{3+}, Er^{3+}/Silica/NH/mAb^{CD133}$ [BNSP] was constructed by consequent engineering from Nano coating, functionalization and conjugation between Nano sphere and monoclonal antibody. And the target cell for label test was NTERA-2 cancer stem cells. The fluorescent Nano pictures tracked in using the STORM microscopy by mode of fluorescence.

The basic investigation revealed that this bionanospherical probe was highly specific for precise detection and identification of cancer stem cell NTERA-2. The BNSP could be also a useful tool for cancer cellular biomedicine and may serve as a probe platform for develop single particle sensor for tracking chemical and temperature changes. The BNSP is also modified to a drug delivery system for multifunctionalization in using theranostic treatment of cancer in biomedicine.

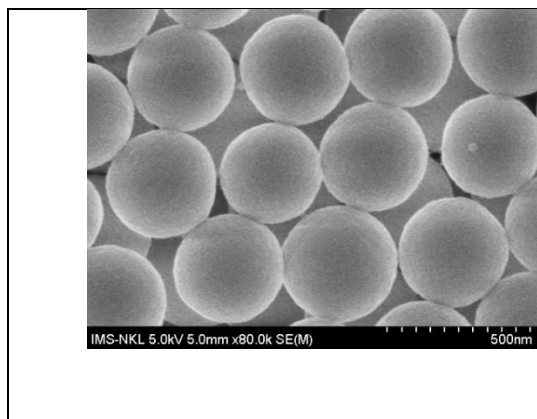


Fig1. Nano sphere GdOYbEr around 200nm

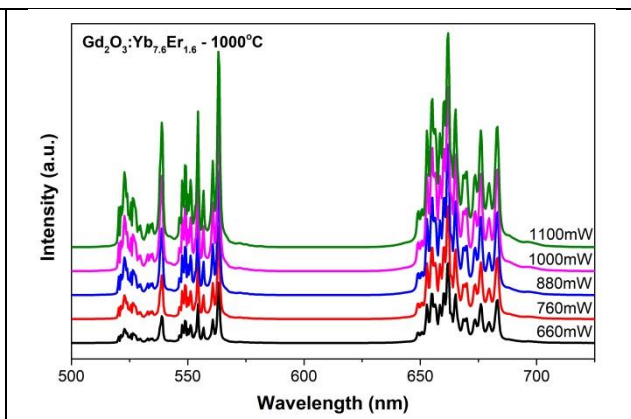
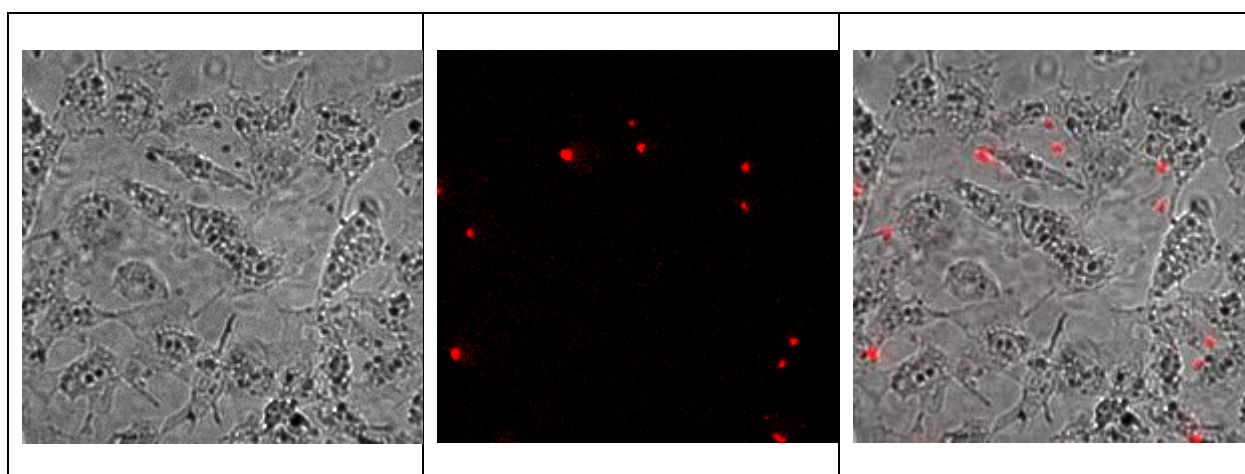


Fig 2. UCL spectra of GdOYbEr with excitation at 975nm



Images of labeling cancer stem cell NTERA-2 by BNSP probe. These pictures obtained in using fluorescence mode of a STORM microscopy.

Reference

- [1] R. C. Jason, A. M. Claire, S. Chris and A. D. Jennifer, *Lanthanide based Nano sensors: refining nanoparticle responsiveness for single particle imaging of stimuli*, ACS Photonics **8** (2021) 3.
- [2] Nguyen Thanh Huong, Do Thi Thao, Nguyen Trong Nghia, Nguyen Thi Nga, Pham Thi Lien, Ha Thi Phuong, Nguyen Van Nghia, Vu Duong, Tran Thu Huong, Tran Kim Anh and Le Quoc Minh. *Optic bionanospherical probe from Gd₂O₃: Yb, Er upconverting nanosphere and mAb^{CD133} antibody for precise imaging label of cancer stem cell NTERA-2*, Communication in Physics, **33**(3) (2023) 253-264.

BIOGRAPHY



Full Professor Le Quoc Minh received Dr. Rer. Nat. at the Academy of Science, Berlin, in Optic and Spectroscopy
 Director of Research, Vietnamese Academy of Science and Technology (VAST)., Institute of Physics (1969–1993) Institute of Materials Science (1993–2016),
 Laboratory of Photochemistry, Imaging and Photonic (1986–today), Graduated University of Science and Technology (2015-today)
 Director of Corporation of Inovative Materials and Aparatus Group (IMAG) (1986–2008). Administrative Advisor of IMAG Corp.(2008–today)

President of Institution Council, Institute Technology, Environment, Green Energy CMN, Vietnamese Union of Science and Technique Association VUSTA (2019–today)

Fellow member of International Committee on Imaging Science ICIS (1986– today)

Vice President (2003–today), Secretary General (2003–2019) of Vietnam- Materials Resaerch Society (V-MRS)

300 Publications, 3 books and sponshorship 9 PhD thesis, Cordinator of over 20 International and State Projects,

Organization Committee Members of Conference ICCE, IWAMSN, SPMS and IWNA

Interest include: Photoresponsive, Optoelectronic, Nano-Materials, Luminescence, Inorganic-Organic Hybrid, Laser spectroscopy and NanoTechnology, Rare Earth Luminophor, Graphene, Digital Imaging, micro-nano Composite for Infrastrutures and NanoMat&Tech Application for Biology and Medicine

BIOINSPIRED INNOVATIONS IN NANOTECHNOLOGY AND THEIR PRACTICAL APPLICATIONS

Kishore M Paknikar^{1,2}

¹ Department of Chemistry, Indian Institute of Technology Bombay, Powai, Mumbai 400076, India

² Centre for Nanobioscience, Agharkar Research Institute, G.G. Agarkar Road, Pune 411004, India

Email: kpaknikar@gmail.com

ABSTRACT

Nanotechnology provides unique nanostructures such as metallic, semiconductor or magnetic nanoparticles, nanowires or nanotubes, exhibiting unique, size-controlled, electronic, optical and catalytic properties. In addition, unique microscopy tools for imaging nanostructures on surfaces, patterning of surfaces, and manipulating surfaces at the molecular level are available.

The study of the synthesis, exotic properties, assembly/packaging and potential commercial application of nanomaterials is an extremely important topic of research that is expected to have far-reaching global impact. Recognizing that some of the most exquisite and highly functional nanomaterials are grown by biological systems, many researchers have focused attention on understanding how inorganic materials are made by biological systems and attempting to replicate such processes in the laboratory.

The biomolecule–nanoparticle hybrid systems are the key elements of the rapidly developing research area of nanobiotechnology. Numerous applications of biomolecule–nanoparticle hybrids are envisaged, such as the tailoring of electronic or optical biosensors, the synthesis of nanocircuitry and nanoelectronic networks, the fabrication of nanoscale devices, such as transistors, and the development of new therapeutic materials and drug delivery systems.

In an effort to seek an answer to a rather unpretentious question ‘do metal-interacting microbes synthesize nanoparticles?’, we pioneered a new approach for ‘Microbially-assisted nanotechnology’. Eventually concerted efforts were made to develop a strong research program focusing on bioinspired methods of nanomaterials synthesis and assembly as well as developing commercially important products and processes. The talk will take an overview of these diverse, yet exciting research activities specifically focusing on work on treatment of burns, wounds, diabetes and cancers; development of rapid diagnostic methods, etc. Several of these recent developments are already at advanced phases of commercialization.

Keywords: Bioinspired, Nanobiotechnology, Nanomedicine, Nanomaterials

BIOGRAPHY



Dr. Kishore M. Paknikar obtained a doctorate in Microbiology from the University of Pune, India. He received post-doctoral training in the field of biohydrometallurgy at the Institute of Microbiology, Russian Academy of Sciences, Moscow, Russia and St. Andrews University, UK.

In 1984, he joined Agharkar Research Institute, an Institute under the Department of Science and Technology (DST), Government of India at Pune. He was the Director of this Institute from May 2013-February 2019. He currently holds the position of Distinguished Visiting Professor at Indian Institute of Technology Bombay, Mumbai and Visiting / Adjunct appointments at Nitte University, Mangalore and Institute of Chemical Technology, Mumbai.

Dr. Paknikar has been a Visiting Professor at the University of Strasbourg, France and Wayne State University, School of Medicine, Detroit, USA. He was also an Advisor at the National Nanotechnology Centre, Bangkok, Thailand and Marico Industries Visiting Fellow at the University Institute of Chemical Technology, Mumbai. He served on the Board of Directors of a start-up company, Nano Cutting Edge Technology Pvt. Ltd., Mumbai. He has been a Chair and expert member of various committees of national importance in the Government of India such as Niti Ayog (Planning Commission), Department of Biotechnology (DBT), Department of Science and Technology (DST), Defence Research and Development Organization (DRDO) and Indian Council of Agricultural Research (ICAR).

Dr. Paknikar is an elected Fellow of the National Academy of Sciences India, National Academy of Agricultural Sciences, Academy of Microbiological Sciences, Biotech Research Society of India and Maharashtra Academy of Sciences.

Dr. Paknikar has published >150 research papers in internationally reputed journals, received >12800 citations with an 'h' index of 49. He has edited one book, contributed 30 book chapters and has 36 granted international and national patents to his credit. Dr. Paknikar was involved in several successful transfer of technologies to the industries. So far, 39 students have completed PhD under the guidance of Dr. Paknikar.

AN A-SI:H/C-SI HETEROJUNCTION SOLAR CELLS – ADVANCED TECHNOLOGIES FOR HIGH EFFICIENCY OF 23.1%

Vinh Ai Dao^{1,*}, Thanh Thuy Trinh^{2,3}, Heondo Kim⁴, Changkyun Park⁴, Kiduck Kim⁴, Kyoungjin Lim⁴, Jeongho Seo⁴, Hoang An Quoc¹, and Junsin Yi^{5,*}

¹ HCMC University of Technology and Education, Ho Chi Minh City 700000, Vietnam;

² Department of Physics, International University, Block 6, Linh Trung Ward, Thu Duc City, Ho Chi Minh City 700000, Vietnam;

³ Vietnam National University, Ho Chi Minh City, Vietnam;

⁴ Solar R&D division, JUSUNG Engineering Co., Ltd.240, Opo-ro, Opo-Eup, Gwangju-Si, Gyeonggi-do, 12773, Republic of Korea;

⁵ College of Information and Communication Engineering, Sungkyunkwan University, Suwon, 440-746, Republic of Korea.

Email: daovinhai@hcmute.edu.vn

ABSTRACT

Wafer bowing and breakage as a result of high-temperature processes in the metal back contact are of concern due to the current industry trend toward thinner solar-cell wafers. An a-Si:H/c-Si heterojunction (HJ) solar cell is a good solution to these problems since it can be produced with low-temperature processes, while obtaining high conversion efficiency. Doing so limits the thermal budget and allows inexpensive, low-quality materials to be used as base materials. In recent years, a considerable number of studies have focused on a-Si:H/c-Si HJ solar cells. Among them, SKKU-JUSUNG-SPKT's a-Si:H/c-Si HJ solar cells based on n-type c-Si wafers exhibit the efficiency of 23.1%. In this presentation, we discuss the state-of-art process for HJ solar cells and describe recent advances in our technology.

Keywords: Silicon heterojunction, Advantaged technologies, High efficiencies

ACKNOWLEDGMENTS

This work was supported by Ho Chi Minh City Department of Science and Technology under Grant No. 171/QĐ-SKHCHN.

BIOGRAPHY



Vinh-Ai Dao is an associate professor in Faculty of Applied Sciences, HCMC University of Technology and Education, Vietnam. He received his MS in applied physics from the University of Science, Vietnam in 2005, and his Ph.D in Electronic and Electrical Engineering from Sungkyunkwan University. His main work has been concerning solar cells, which includes HIT solar cells, crystalline silicon solar cells, thin-film silicon solar cells, and transparent solar cells.

OPTIMIZATION OF LARGE-SCALE GOLD ELECTRODEPOSITION FOR BIOINSPIRED ANTIMICROBIAL NANOSTRUCTURES

Marion Stalet^{1,2,3}, Laurence Convert^{1,2}, Loïc Leroy³, Michael Canva^{1,2} and Yoann Roupioz³

¹Laboratoire Nanotechnologies Nanosystèmes (LN2 – IRL 3463), CNRS, Université de Sherbrooke, Sherbrooke, QC J1K OA5, Canada

²Institut Interdisciplinaire d'Innovation Technologique (3IT), Sherbrooke, QC J1K OA5, Canada

³Univ. Grenoble Alpes, CEA, CNRS, IRIG-SyMMES, 38000 Grenoble, France.

Email: michael.canva@usherbrooke.ca, yoann.roupioz@cea.fr

ABSTRACT

Bioinspired nanostructured surfaces have been studied in recent years due to passive antimicrobial properties they may have. While most structuration studies are made using substrates fabricated using costly and time-consuming methods that are often not-scalable, electrodeposition (ED) has the advantage, among others, of being cost-effective and scalable. In this study, we assessed the ED of gold, and nanostructure formation on surfaces up to 13 cm² in less than a minute. The ED parameters such as deposition time and electrolyte concentration were investigated, and we demonstrated that the homogeneous nanostructuring was possible using concentrations from 50 to 100 mM of HAuCl₄. Various morphological parameters of the nanopikes generated were obtained by changing deposition time and potential, such as heights ranging from 125 to 480 nm and rugosity up to 120 nm. The surface area of the sample was more than doubled compared to bare Au. The antimicrobial properties of the nanostructured surfaces were assessed and showed interesting first results with the prevention of bacteria clusters formation. This study layers the groundwork for future investigations of large-scale homogeneous nanostructuring with potential antimicrobial application.

Keywords: Electrodeposition, gold nanostructuring, antimicrobial surface.

INTRODUCTION

Microbial proliferation poses a significant public health challenge, inflicting substantial economic and social repercussions across various sectors. These concerns are aggravated by the prevalence of antibiotic resistance, marked by a shortage of innovative antibiotic agents. In response, it is imperative to engineer surfaces capable of inhibiting the initial adhesion and proliferation of microorganisms. Over the past decade, there has been a growing interest in bioinspired antimicrobial micro- and nanostructured surfaces. [1, 2] The initial exploration of the passive mechanical interactions between bacteria and nanopillars can be attributed to the pioneering work of Ivanova *et al.* in 2012. [3] This work opened the door to investigations into various naturally microbicidal surfaces, including the wings of cicadas and dragonflies, gecko skin, and lotus leaves. [4] In response to these findings, numerous biomimetic surfaces were developed to emulate the effects of their natural counterparts and to try to understand the factors that influence the effectiveness of nanostructures against microorganisms. Most

studies relied on established structuring techniques to fabricate synthetic antimicrobial surfaces, such as e-beam lithography, nanoimprint, reactive-ion etching, plasma etching, anodization, and laser interference. These methods predominantly use materials like silicon, metals such as titanium, and various polymers. However, they are not designed for large-scale applications, which highlight the need to develop of high-throughput nanostructuring processes. Electrodeposition (ED) stands out as a quick and

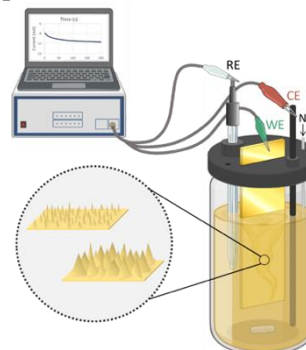


Figure 1 – ED set-up composed of a potentiostat and electrochemical cell with HAuCl₄/Pb(CH₃COO)₂ electrolyte.

cost-effective method for nanostructuring surfaces. It's versatile, compatible with various metals, including the readily available and biocompatible gold. The primary aim of this study is to investigate the impact of deposition parameters on nanostructure morphology and uniformity. By doing so, we aim to address the scalability of the ED process and improve our ability to predict nanostructure morphologies based on deposition conditions.

EXPERIMENTAL

Reagents: Tetrachloroauric (III) Acid Trihydrate ($\text{HAuCl}_4 \cdot 3\text{H}_2\text{O}$) and lead (II) acetate trihydrate ($\text{Pb}(\text{CH}_3\text{COO})_2 \cdot 3\text{H}_2\text{O}$) were purchased from Fischer Scientific and used as received. Acetone ($(\text{CH}_3)_2\text{CO}$ from HoneyWell), Hydrochloric acid 37% (HCl from Regent), OptiClear™ (from Life Science Product), 2-propanol, ($(\text{CH}_3)_2\text{CHOH}$ from High Purity Products) and sulfuric acid, 98% (wt./wt.) (H_2SO_4 from Sigma-Aldrich) were also used. All the solutions were prepared using Milli-Q (18 $\text{M}\Omega/\text{cm}$) deionized water. Before each step of the fabrication, the substrates are thoroughly washed in consecutive 5-minutes ultrasound baths of OptiClear™, acetone, 2-propanol and finally deionized water.

Au substrates preparation: 75 x 25 mm microscope glass slides from Fischerfinest (Fisherbrand) were washed as previously described and deposited via e-beam evaporation with a 3 nm titanium (Ti) adhesion layer and a of 30 nm gold (Au) layer.

Nanostructures fabrication and electrochemical characterization: Gold nanospikes were fabricated using an ED process, previously described in various protocols. [5] Before ED, the substrates were washed as previously described and then inserted as the working electrode (WE) in a three-electrodes adaptable set-up, allowing reproducible positioning of the substrates (Fig. 1). They were electrodeposited with gold nanostructures using a CH Instruments CHI604C potentiostat and different concentration of $\text{HAuCl}_4/\text{Pb}(\text{CH}_3\text{COO})_2$ electrolyte. A silver-silver chloride electrode (Ag/AgCl , 3M KCl from BASi®) was used as the reference electrode (RE) and a 12 inches graphite rod of 6mm \varnothing (from Northern Materials Innovations ltd) as the counter electrode (CE). The substrate was placed to deposit around 2/3 of the total sample surface ($\sim 11.5 \text{ cm}^2$). The ED parameters were set and controlled using the CH604c user interface with the

chronoamperometry technic and the current during ED was recorded live at a sensitivity of 0.1 A/V. The ED was performed at 0.05 V with an agitation of 1000 rpm and various deposition time.

Cyclic Voltammetry (CV) was used to calculate the electrochemical surface before and after each ED. A platinum CE (from BASi®) was used. Each time, the three-electrodes cell was dipped in 0.5 M H_2SO_4 solution under agitation at 600 rpm and three cycles from 0 to 1.6 V at a speed of 0.1 V/s with a sensitivity of 10 mA/V were recorded. The electro-active surface was calculated by integrating the oxidation peak of the CV and using the charge density of a monolayer of gold oxide. [6] After CV, the samples were rinsed thoroughly with deionized water. Prior to any electrochemical measurement (CV and ED), the solution was degassed with nitrogen (N_2) using an inlet tube for 10 min. During ED, the N_2 flow was maintained over the solution. After the ED, the sample were once again washed using the described procedure.

Morphological characterization: Nanostructures morphologies were assessed using electron microscopy (SEM) and atomic force microscopy (AFM). SEM micrographs were acquired using the Axia™ ChemiSEM™ instrument at tilts of 0° and 45°. The working distance was up to 8 mm, with a magnification of 15000, an acquisition time of 1 μs , an intensity of 12 pA and a voltage of 30 kV. To assess the homogeneity of the nanostructured surface, at least 4 micrographs at different spacing from the sample center were taken. The AFM images were acquired using the Dimension Icon Scanasyt (Veeco, Bruker) in Tapping mode with ScanAssist-Air probes. The scan rate was set to 0.5 Hz and at least 3 images/sample of 25 μm^2 (512 x 512 lines) were acquired.

AFM and SEM analysis: AFM and SEM images were analyzed using Fiji ImageJ and Gwyddion.

Antimicrobial preliminary testing: viability of *Escherichia coli* (ATCC 11775) was tested via fluorescence imaging using the LIVE/DEAD™ BacLight™ kit from Invitrogen, according to the constructor recommendations. Assays were carried according to Parreira's *et al.* protocol [7].

RESULTS AND DISCUSSION

In the first series of experiments, we examined the widely used 6.5 mM HAuCl_4 concentration, a standard in the literature. We explored different deposition times, potentials, and Pb^{2+}

concentrations. Deposition times ranged from 60 seconds to 930 seconds, including a benchmark time of 540 seconds as reported in the literature. We also tested three potential values: 0.05 V, 0.01 V, and 0.1 V. Additionally, we investigated two Pb^{2+} concentrations: 0.5 mM and 1 mM. To determine the electroactive surface areas of samples, we employed the formula $S_a = \frac{A_h}{q}$. Here, A_h represents the total charge of the oxidation layer, calculated by integrating the reduction peak following CV measurements. The charge density of a monolayer of gold oxide, equal to 3.90 C/m^2 , was used for the value of q . [6] We quantified the increase in surface area from the formation of nanostructures by calculating the ratio between S_a before and after ED.

For the 6.5 mM $HAuCl_4$ concentration, SEM micrographs revealed an overall increase in surface roughness across the entire sample. However, nanostructures were predominantly observed within a few micrometers of sample edges (Fig 2 – left). This trend was consistent even with extended deposition times, and the surface ratio of all samples remained below 1.8. As a result, we explored higher concentrations of gold salt, specifically 50 mM and 100 mM. When using concentrations of 50 mM and 100 mM, the samples exhibited a more uniform surface structuring (Fig 2 – right) with well-defined nanopikes.

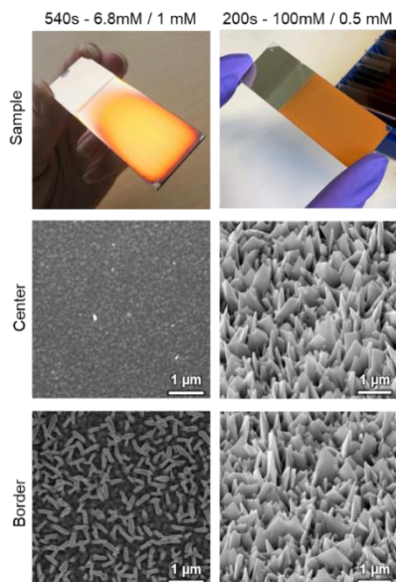


Figure 2 - SEM

micrographs of the homogeneity of the surface for different deposition conditions.

We explored different deposition times and potentials at these concentrations to achieve a

variety of nanostructure morphologies. From these investigations, we selected four sets of deposition conditions for further large-scale production, and antimicrobial testing:

(A) – $[Au] = 100 \text{ mM}$, $[Pb]=0.5 \text{ mM}$, time = 300s;
 (B) – $[Au] = 100 \text{ mM}$, $[Pb]=0.5 \text{ mM}$, time = 100s;
 (C) – $[Au] = 100 \text{ mM}$, $[Pb]=1 \text{ mM}$, time = 300s;
 (D) – $[Au] = 50 \text{ mM}$, $[Pb]=0.5 \text{ mM}$, time = 300s.
 These groups were considered to have significantly different morphologies. The surface ratio calculated from CV revealed a minimum 2.3-fold increase linearly correlated with deposition time. Notably, homogenous surfaces were achieved within 100 s at 100 mM $HAuCl_4$. Key characteristics of the sample are summarized in Table 1. Atomic Force Microscopy (AFM) imaging over a $5 \times 5 \mu\text{m}$ area confirmed the height and density of nanopikes, while Scanning Electron Microscopy (SEM) micrographs validated their sharpness and orientation (Fig 3).

Table 1 – Quantification of the morphological aspects of nanostructures

Sample	Height (nm)	RMS (nm)	Density (μm^{-1})	Ratio S_a
A	439 ± 16	115 ± 6	7 ± 1	3.8 ± 0.1
B	156 ± 11	43.6 ± 3	21 ± 2	2.9 ± 0.1
C	425 ± 49	113 ± 16	12 ± 2	3.7 ± 0.3
D	198 ± 10	60 ± 5	40 ± 5	2.8 ± 0.1

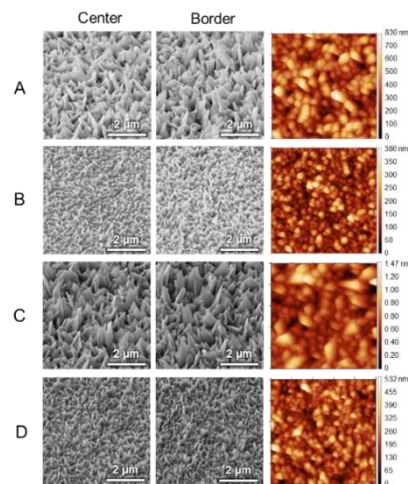


Figure 3 - SEM micrographs and AFM imaging of the four deposition conditions after ED.

From all the experimental results, the charge density was extracted from the current data during the ED process and a linear relation with the rugosity of the obtained samples was highlighted. Finally, the potential bactericidal effect on *Escherichia coli* of the nanostructures from the A group was tested using a process inspired from

Parreira *et al.* [7]. The surfaces were incubated with 10^5 CFU/mL of bacteria in PBS at 150 rpm and 37°C and after 2h the adhered bacteria on the surface were put in contact with fresh TSB to study re-proliferation and colonies development. After 4h the viability of the bacteria was assessed by fluorescence microscopy. Compared to bare gold (Fig 4 - left), bacteria were not able to create clusters on the nanostructured surfaces and displayed a greater mortality rate (Fig 4 - right). These preliminary results are promising for future biological characterization and nanostructuring usage as antibacterial surfaces.

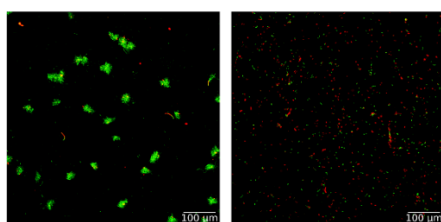


Figure 1 - Fluorescence microscopy imaging of *Escherichia coli* on bare (left) and structured surface (right).

CONCLUSION

In this study, we examined the potential for upscaling a cost-effective and straightforward nanostructuring process using gold electrodeposition (ED). To achieve a uniform surface structuring, it was found that higher concentrations of gold were required compared to conventional usages in existing literature. Four distinct types of nanostructures were successfully fabricated. These preliminary findings pave the way to a more extensive study that will explore the impact of ED parameters on antimicrobial efficiency, further enhancing our understanding of the intricate relationship between these parameters.

Acknowledgment

Authors gratefully acknowledge the financial funding of the Biosurf Project by the CNRS 80|Prime, by Labex ARCANE and by CBH-EUR-GS (Grant ANR-17-EURE0003).

References

[1] M.-S. Lee, H. R. Hussein, S.-W. Chang, C.-Y. Chang, Y.-Y. Lin, Y. Chien, Y.-P. Yang, L.-V. Kiew, C.-Y. Chen, et al., *Nature-Inspired Surface Structures Design for Antimicrobial Applications*, 2, Int. J. Mol. Sci., **24** (2023) 1348.

[2] T. E. Catley, R. M. Corrigan and A. J. Parnell, *Designing Effective Antimicrobial Nanostructured Surfaces: Highlighting the Lack of Consensus in the Literature*, ACS Omega, **8** (2023) 14873–14883.

[3] E. P. Ivanova, J. Hasan, H. K. Webb, V. K. Truong, G. S. Watson, J. A. Watson, V. A. Baulin, S. Pogodin, J. Y. Wang, et al., *Natural Bactericidal Surfaces: Mechanical Rupture of Pseudomonas aeruginosa Cells by Cicada Wings*, Small, **8** (2012) 2489-2494.

[4] Y. Cai, W. Bing, X. Xu, Y. Zhang, Z. Chen and Z. Gu, *Topographical nanostructures for physical sterilization*, Drug Deliv. Transl. Res., (2021).

[1] M.-S. Lee, H. R. Hussein, S.-W. Chang, C.-Y. Chang, Y.-Y. Lin, Y. Chien, Y.-P. Yang, L.-V. Kiew, C.-Y. Chen, et al., *Nature-Inspired Surface Structures Design for Antimicrobial Applications*, 2, Int. J. Mol. Sci., **24** (2023) 1348.

[2] T. E. Catley, R. M. Corrigan and A. J. Parnell, *Designing Effective Antimicrobial Nanostructured Surfaces: Highlighting the Lack of Consensus in the Literature*, ACS Omega, **8** (2023) 14873–14883.

[3] E. P. Ivanova, J. Hasan, H. K. Webb, V. K. Truong, G. S. Watson, J. A. Watson, V. A. Baulin, S. Pogodin, J. Y. Wang, et al., *Natural Bactericidal Surfaces: Mechanical Rupture of Pseudomonas aeruginosa Cells by Cicada Wings*, Small, **8** (2012) 2489-2494.

[4] Y. Cai, W. Bing, X. Xu, Y. Zhang, Z. Chen and Z. Gu, *Topographical nanostructures for physical sterilization*, Drug Deliv. Transl. Res., (2021).

[5] B. Plowman, S. J. Ippolito, V. Bansal, Y. M. Sabri, A. P. O'Mullane and S. K. Bhargava, *Gold nanospikes formed through a simple electrochemical route with high electrocatalytic and surface enhanced Raman scattering activity*, Chem. Commun., (2009) 5039–5041.

[6] S. Trasatti and O. A. Petrii, *Real surface area measurements in electrochemistry*, Pure Appl. Chem., **63** (1991) 711-734.

[7] P. Parreira, C. Monteiro, V. Graça, J. Gomes, S. Maia, P. Gomes, I. C. Gonçalves and M. C. L. Martins, *Surface Grafted MSI-78A Antimicrobial Peptide has High Potential for Gastric Infection Management*, Sci. Rep., **9** (2019) 18212.

BIOGRAPHY



Yoann Roupioz graduated in Chemistry/Bio-chemistry both in France at the University of Grenoble Alpes and at the University of Montréal, Canada. After completing his PhD degree on the design of synthetic DNA strands for enzymatic assays in 2001 in France, he moved to the University of British Columbia, Vancouver, Canada, in the group of David Perrin to develop engineered DNAzymes. Since 2005, Yoann Roupioz is PI for the French National Scientific Research Center (CNRS) and is developing bio-active surfaces and biosensors for Health at the SyMMES laboratory in Grenoble, France. He is expert in the design of engineered bio-molecules and surface functionalization to target biomarkers, nanometric objects or prokaryotic and eucaryotic cells. In 2011, he received the Masao Horiba International Award in Kyoto, Japan. Since 2014, he is also Deputy Head of the SyMMES laboratory in Grenoble, France. He is currently co-leading several national (GDR Interfaces Bio-engineering) and international networks (NanoAndes) dedicated to surface micro- and nano-engineering for health. He published more than 50 papers in peer-reviewed journals and filed a dozen of patents.

ORAL SESSIONS
***FUNDAMENTALS OF
NANOTECHNOLOGY***
(FON)

STUDY OF SLIP SYSTEM ACTIVITIES IN ZINC SINGLE CRYSTALS UNDER THE NANOINDENTATION TEST AND CRYSTAL PLASTICITY MODEL

Pham The Nhan Nguyen, Duc Hanh Dinh, Tran Anh Vo, Minh Sang Tran, Van Trung Pham, Xuan Thuy Dang

Faculty of Mechanical Engineering, The University of Danang, University of Science and Technology, Danang City, Vietnam.

Email: nptnhan@dut.udn.vn

ABSTRACT

Studying the microscale deformation mechanism of the metal crystal structure to better understand its mechanical properties, is one of the basic factors for a good prediction of the deformation behavior in the whole metal. To observe the deformation mechanism at the microscopic scale of the metal crystal structure, it is possible to use experimental tests [1] or the crystal plasticity model based on the finite element method [2-4]. However, due to the variety of shapes and types of material crystals, it is still a challenge to study the exact mechanical properties of single crystals.

In this study, a crystal plasticity model is developed in the finite element code Abaqus using a user material subroutine to simulate the nanoindentation test on zinc grains with different orientations. The accuracy of the model is evaluated through comparison between experimental and numerical results in terms of load-penetration depth curves and indent imprint profiles, which show good agreement. An analysis of slip system activity is given to understand more about the micromechanical behavior of pure zinc crystals. We can notice that the shear strain of the basal glide is small but activated as the primary slip system, followed by the prismatic glide and/or secondary slip systems provided by the pyramidal $\langle c+a \rangle$. Besides, different slip systems are activated for the different grain orientations.

Keywords: Crystal plasticity, Nanoindentation, Zinc, HCP, Finite element analysis.

INTRODUCTION

The investigations of the mechanical properties of the coatings are difficult as the traditional compression and tensile tests are unable to apply well at very small scales. Based on the capacity to probe at small volumes, the nanoindentation test, which is interpreted by Oliver and Pharr [5], can be used for a wide range of applications, for example: (i) The measurement of mechanical properties of coke as used in the minerals processing industry [6]; (ii) Application of nanoindentation tests to study surface coatings and thin films [7]; (iii) Nano/micro-electromechanical systems and single crystal plasticity [8]. Owing to the development of new sensors and actuator a veritable revolution has occurred in indentation testing, allowing instrumented indentations to be routinely performed on submicron scales. The resulting technique, termed nanoindentation, or instrumented indentation technique, has now become a powerful technique for mechanical property measurements such as the hardness,

dislocation motion, and Young's modulus at nano/microscale [9].

Besides the development of experimental methods, the Crystal Plasticity Finite Element Method (CPFEM) has implemented into an extremely competent tool for describing the mechanical response of crystalline materials on all length scales from single crystals to engineering parts. The first introduction of the CPFE method was presented by Peirce et al. in 1982 [10] to simulate two symmetric slip systems in order to study the tensile behavior of single crystals. Huang [11] and Marin [12] promoted ABAQUS finite element programs of user-material subroutine for cubic system. Along with the increase in computational power, an ever-increasing number of CPFE simulations has been performed to mature into a whole family of constitutive and numerical formulations as the overview of Roters [13].

Zinc metal has several characteristics that make it a well-suited corrosion protective coating for iron and steel products. Besides, zinc is also

commonly used in battery industry. Zinc crystals have a hexagonal close-packed structure (HCP). Compared to other HCP metals such as titanium or magnesium, zinc is characterized by a high c/a lattice ratio (Zn: $c/a= 1.856$) and exhibits a strong anisotropic behavior.

EXPERIMENTAL

The material used in this work is a high-purity (99.99%) polycrystalline zinc, provided by Goodfellow (Lille, France). Made by cold rolling without recrystallization annealing, it is in the form of sheets of one millimeter of thickness. Figure 1 illustrates the EBSD mapping obtained on a sample taken from the central zone of the zinc sheet and the shape of the selected grains for the experiment. We selected grains #11, #16, and #18, corresponding to different crystallographic orientations provided in Table 1 [4].

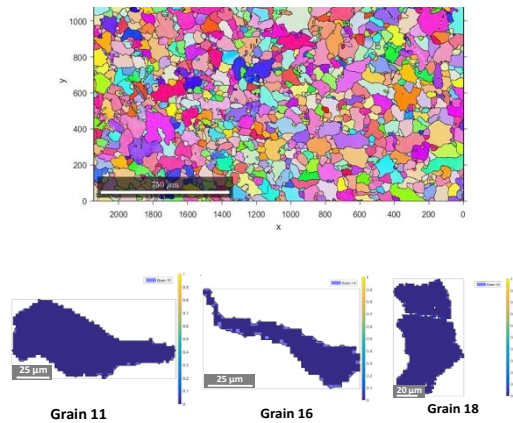


Figure 1.(a) EBSD mapping of the selected area, (b) the shape of the selected grains.

Table 1. Crystalline orientation of the selected grains.

Grain #	Crystalline Orientation	Bunge Angles (°)		
		ϕ_1	ϕ	ϕ_2
11	Prismatic	3.89	107.01	214.74
16	Pyramidal	158.75	72.58	184.56
18	Basal	0.04	137.10	233.02

Nanoindentation tests were performed using a 90° cono-spherical diamond indenter with tip radius of 1 μm , mounted in an NHT-2 nanoindenter (CSM Instruments). Indentations were carried out in load-control mode. The indentation strain rate in the loading stage of this study was controlled to be 0.05 s^{-1} . In practice, the applied load, P , on the indenter is accurately controlled, while the penetration depth, h , is simultaneously measured by recording the indenter's displacement into the grain surface. To

avoid grain boundary influence, all the indents were in the mid-zone of individual grains.

CRYSTAL PLASTICITY FINITE ELEMENT SIMULATION

Three-dimensional finite element simulations of the nanoindentation experiments were performed using the commercial software ABAQUS. The zinc grain has been modelled as a cylinder of 20 μm diameter and 20 μm height, was discretized using 13,860 eight-node linear hexahedral elements with a reduced integration scheme (C3D8R), and the smallest element size was 60 nm. To keep the simulations computationally tractable, the mesh density was progressively coarsened away from the contact zone. The cono-spherical indenter was modelled as a fully rigid body, with a tip radius of 1 μm and a half apex angle of 45° (Figure 2). The indenter was only allowed to move in the indentation direction. A friction coefficient of 0.1 was assumed between the indenter and the substrate [4,8].

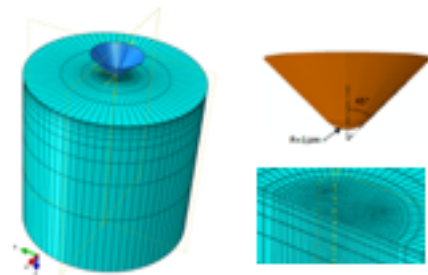


Figure 2. Finite element mesh and indenter geometry.

To perform numerical simulations for nanoindentation experiments on single crystals zinc grains, we used the crystal plasticity model, which was initially developed by Marin for cubic system [12]. In this work, the plastic shear strain is assumed to occur only on each of the 12 HCP slip systems (3 basal systems, 3 prismatic systems, and 6 pyramidal π_2 systems) [14-15], no twinning was observed in the nanoindentation experiments we have carried out, therefore the compression twin system is not considered.

We have modified crystal plasticity finite element method (CPFEM) Abaqus UMAT subroutines available in the literature to perform nanoindentation simulations for an HCP crystal. The crystals (grains) are discretized by the finite elements and balance laws are applied to the level of individual crystals. The numerical solution for the equilibrium equations then distributes the

deformation between the single crystals. With the known applied deformation on each single crystal, the crystal state is evolved by numerically integrating the constitutive equations of the single crystal. The single crystal state then defines directly the anisotropic material behavior at each computational point of the finite element model [4].

RESULTS AND DISCUSSION

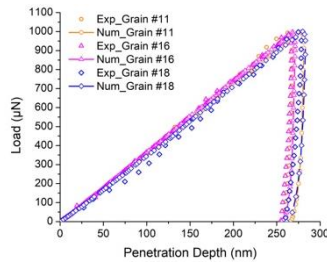


Figure 3. Experimental and numerical P-h curves for Grains #11, #16, and #18.

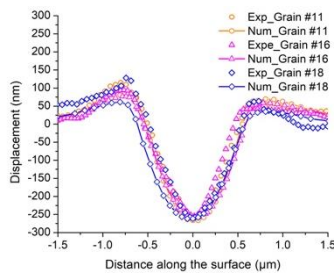


Figure 4. Experimental and numerical penetration depth profiles after unloading for Grains #11, #16, and #18.

The crystal plasticity model parameters of pure zinc was identified with the method described in

the previous study using the load vs. penetration curve and residual imprint [4]. The simulation for Grains #11, #16, and #18 were performed. We can see a good agreement between the experimental data and the simulated responses for load-penetration depth curve (P-h curve), and the penetration depth profiles, depicted in Figures 3 and 4.

The activity of slip systems in the area underneath the indenter of Grains #11, #16, and #18 is analysed. The evolution of shear strain on all slip systems are plotted in Figure 5, 6, and 7, respectively.

We can notice that, with grain #11 in the crystalline orientation of prismatic and grain #16 in the crystalline orientation of pyramidal, all three systems of basal glide were activated at small shear strains (less than 0.019) and saturated at very small penetration depth (less than 60 nm) (Fig. 5a, 6a). However, with grain #18, which is in the crystalline orientation of basal, the basal glide was the most active with the highest shear strains (greater than 0.35 of basal system $\{0001\}\langle 11-20 \rangle$) and the saturation was not observed in the penetration depth range of 0 to 275 nm (for basal systems $\{0001\}\langle 1-210 \rangle$ and $\{0001\}\langle 2-1-10 \rangle$) (Fig. 7a). On the contrary, in grain #18, the small shear strains were achieved with prismatic glide and saturated at an early deformation stage (less than 50 nm) (Fig. 7b). While the shear strains were higher with prismatic glide in grains #11 and #16 (≈ 0.16) (Fig. 5b and 6b). With the second-order pyramidal glide, the six systems were activated at high shear strains in all three grains (≈ 0.4 in grains #11 and #16, ≈ 0.18 in grains #18) (Fig. 5c, 6c and 7c).

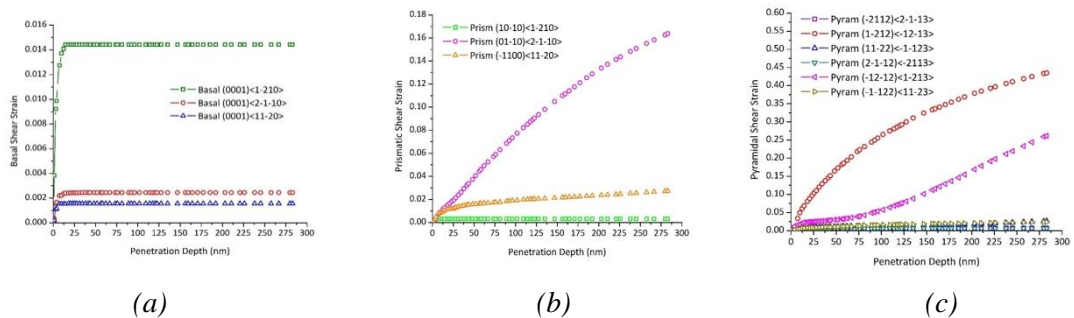


Figure 5. Evolution of slip activity $\gamma^{(\alpha)}$ in a point underneath the indenter for Grain #11.

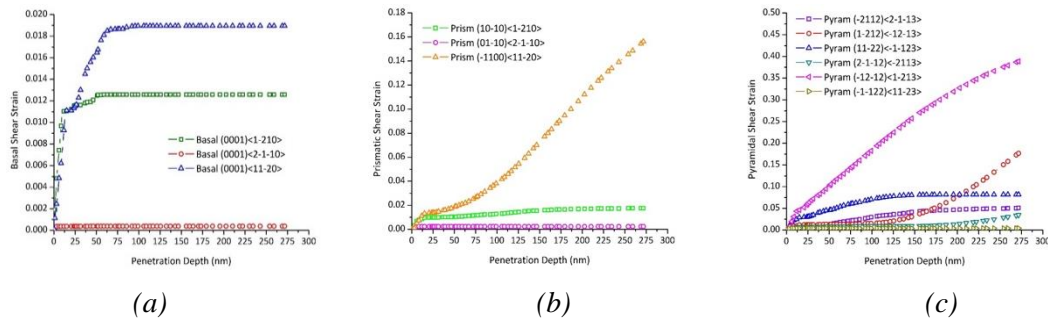


Figure 6. Evolution of slip activity $\gamma^{(\alpha)}$ in a point underneath the indenter for Grain #16.

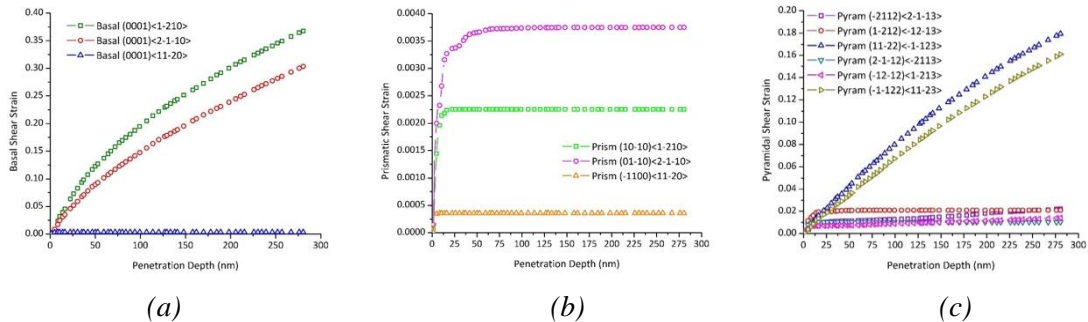


Figure 7. Evolution of slip activity $\gamma^{(\alpha)}$ in a point underneath the indenter for Grain #18.

CONCLUSION

This work concerns the characterization and modeling of the mechanical behavior of a high-purity polycrystalline zinc using nanoindentation tests and CPFEM. The model is relatively accurate when simulated on grains of different crystalline orientations with good agreement between experimental data and numerical simulation results of the load-penetration depth curves and the penetration depth profiles. The deformation mechanism of zinc was observed by simulation of the nanoindentation test. We notice that different slip systems are activated for the different grain orientations.

Acknowledgment

This work was supported by The University of Danang, University of Science and Technology, code number of Project: B2022-DN02-15.

References

[1] Yoo, M. H., *Slip, Twinning, and Fracture in Hexagonal Close-Packed Metals*, Metallurgical Transactions A **12A** (1981) 409-18.
 [2] J.J. Funderberger, M.J. Philippe, F. Wagner, C. Esling, *Modelling and prediction properties for materials with hexagonal symmetry (Zinc, Titanium and Zirconium*

alloys), Acta Materialia **45** (1997) 4041-4055.

[3] J.H. Yoon, O. Cazacu, R.K. Mishra, *Constitutive modeling of AZ31 sheet alloy with application to axial crushing*, Mater. Sci. Eng. A **565** (2014) 203-212.
 [4] Nguyen P.T.N., F. Abbès, J. S. Lecomte, C. Schuman and B. Abbès, *Inverse Identification of Single-Crystal Plasticity Parameters of HCP Zinc from Nanoindentation Curves and Residual Topographies*, Nanomaterials **12** (2022) 300.
 [5] Oliver, W. C. and G. M. Pharr., *An Improved Technique for Determining Hardness and Elastic Modulus Using Load and Displacement Sensing Indentation Experiments*, Journal of Materials Research **7**(6) (1992)1564-83.
 [6] Mallikarjunachari, G., Trivikram Nallamilli, Parag Ravindran, and Madivala G. Basavaraj, *Nanoindentation of Clay Colloidosomes*, Colloids and Surfaces A: Physicochemical and Engineering Aspects **550** (2018) 167-75.
 [7] Rodriguez, J., A. Rico, E. Otero, and W. M. Rainforth, *Indentation Properties of Plasma Sprayed Al₂O₃-13% TiO₂ Nanocoatings*, Acta Materialia **57**(11) (2009) 3148-56.
 [8] Nguyen, P. T. N., F. Abbes, B. Abbes, J. S. Lecomte, and C. Schuman, *Experimental Characterisation and Numerical Modelling*

- of the Effect of Cold Rolling on the Nanoindentation Response of Pure Zinc Grains*, IOP Conference Series: Materials Science and Engineering **540**(1) (2019) 1-8.
- [9] Kushch, V. I., S. N. Dub, and P. M. Litvin, Determination of the Young Modulus from Elastic Section of the Berkovich Indenter Loading Curve, *Journal of Superhard Materials* **29**(4) (2007) 228-34.
- [10] Peirce, D., R. J. Asaro, and A. Needleman, *An Analysis of Nonuniform and Localized Deformation in Ductile Single Crystals*, Acta Metallurgica **30**(6) (1982) 1087-1119.
- [11] Huang, Y., *A user-material subroutine incorporating single crystal plasticity in the abaqus finite element program*, Harvard University MECH Report (1991).
- [12] Marin, E.B., Dawson, P.R., *Elastoplastic Finite Element Analyses of Metal Deformations Using Polycrystal Constitutive Models*, Comput. Methods Appl. Mech. Eng **165** (1998), 23-41.
- [13] Roters, F., P. Eisenlohr, T. R. Bieler, and D. Raabe, *Crystal Plasticity Finite Element Methods in Materials Science and Engineering*, WILEY-VCH Verlag GmbH & Co., Weinheim (2010).
- [14] Bell R.L., Cahn R.W., *The Dynamics of Twinning and the Interrelation of Slip and Twinning in Zinc Crystals*, Proc. R. Soc. A Math. Phys. Sci **239** (1957) 494-521.
- [15] Philippe M.J., Wagner F., Mellab F.E., Esling C., Wegria J., *Modelling of texture evolution for materials of hexagonal symmetry-I. Application to zinc alloys*, Acta Metall. Et Mater **42**(1994) 239-250.

SERS-BASED SENSOR USING SUB-NANOMETRIC COPPER-SILVER MIXED CLUSTERS $Ag_{8-n}-Cu_n$ (N=0-8): A THEORETICAL STUDY FOR PYRIDINE

Duy Quang Dao^{1,2,*}, Dinh Hieu Truong^{1,2}, Thi Chinh Ngo^{1,2}, Thi Le Anh Nguyen^{1,2}

¹Institute of Research and Development, Duy Tan University, Da Nang 550000, Viet Nam;

²Faculty of Natural Science, Duy Tan University, Da Nang 550000, Viet Nam

Email: daoduyquang@duytan.edu.vn

ABSTRACT

In this work, we evaluated the SERS spectra of pyridine (Py) adsorbed on the copper-silver mixed clusters $Ag_{8-n}-Cu_n$ ($n=0-8$) using Density functional theory (DFT). Geometrical and electronic structures of the mixed clusters, as well as Py adsorption configuration on these clusters, were computed. Calculated SERS spectra then revealed the influence of the Ag/Cu mixing ratio on the SERS enhancement. As a result, the substituted copper atoms on the silver cluster turns out to be a favorable adsorption sites for Py. Interestingly, when the number of Cu atoms increases from 0 (pure Ag_8 cluster) to 5 (Ag_3Cu_5 cluster), the ring stretching peak (1590 cm^{-1}) of Py significantly increases from 20 to 120 a.u. and then saturates around this value despite increasing the Cu atom number to 8 (pure Cu_8 cluster). The obtained results hopefully provide helpful information for further design of the analytical sensors with lower cost.

Keywords: Surface-enhanced Raman spectroscopy, sensor, copper, silver, Density functional theory.

INTRODUCTION

Surface-enhanced Raman spectroscopy (SERS) is a trendy analytical technique in which the incident light scattered by a molecule is largely enhanced when the molecule is adsorbed on the rough surface of a noble metal nanoparticles (NPs).[1] The SERS enhancement mechanisms combines electromagnetic enhancement (EM), which involves plasmon excitation in the metal nanoparticles, and chemical enhancement (CE), a phenomenon resulted from electron transfer between the adsorbate molecule and the metal NPs in both ground and excited states. An overall enhancement factor (EF) up to $\sim 10^8$ can be achieved. While the EM mechanism has been well defined, the CE is a highly complex process that depends on chemical nature of adsorbate or its adsorption orientation on the metal surface.

Using a small metallic cluster model to replace the nanoparticle is a common strategy that has been used to analyze SERS properties of organic compounds.[2] For example, Nguyen *et al.* recently evaluated adsorption behavior and SERS spectra of the 5-fluorouracil on Au clusters involving 6, 8, and 20 Au atoms employing density functional theory (DFT).[3] Vo *et al.* analyzed SERS properties of sulfathiazole antibiotic using DFT on the Au_{20} pyramidal

cluster model.[4] Interestingly, Dao *et al.* investigated the SERS spectra of 2,4,5-trichlorophenoxyacetic acid (2,4,5-T),[5] and chlorpyrifos pesticide,[6] all adsorbed on Ag_{20} cluster model. An excellent agreement between experimental and modeling SERS spectra was reported for these molecules.

Although Cu is easily oxidized in air, its SERS enhancement is more remarkable than that of Au or Ag metals.[7] Indeed, SERS chemical enhancement of thiram by Cu_{20} cluster is about 2 - 6 times of those obtained from Ag_{20} and Au_{20} clusters, respectively.[7] Therefore, mixing Au or Ag clusters with Cu element hopefully can provide better air stability and higher SERS enhancement. For example, Le *et al.* compared the chemical enhancement of 2,4,5-T adsorbed on bimetallic clusters $Au_{20-x}M_x$ (M: Ag, Cu; x : 1, 3, 10) in which the mixed atoms (Ag and Cu) were placed at the sublayers of the Au cluster and the analyst molecule was always adsorbed on the Au layer [9]. However, with this particular design, mixed Ag/Cu atoms into a pyramidal Au_{20} cluster slightly reduces SERS activities.[8] Al-Otaibi *et al.* studied SERS spectra of pyrrole adsorbed on the silver mixed with Au, Ni, and Cu, Ag_x-M_y ($x = 4, 5$; $y = 2, 1$ and $M = Au, Ni, Cu$) and found that the characteristic Raman spectra of pyrrole in the 500-

1500 cm⁻¹ zone are strongly enhanced when it was adsorbed on the Ag₅M₁ or Ag₄M₂ clusters.[9]

The SERS properties of pyridine (Py) adsorbed on different metals, including Ag,[10] Au,[11] and Cu[12] were investigated. Recently, Seuret-Hernández *et al.* theoretically analyzed in detail the SERS spectra of Py adsorbed on the Ag₁₀Cu₁₀ tetrahedral (Td) clusters *via* two binding positions: vertex (V) and surface (S).[13] As a result, the static SERS response for Cu–Py–V complexes is 5 to 10 times greater than Ag–Py–V EF and up to 28 times greater than Py–S complexes. The Raman spectra of the Ag–Py–V or -S bimetallic clusters are enhanced compared with monometallic clusters, indicating that the SERS enhancement of Ag₂₀ Td cluster can be improved by adding Cu atoms. An exciting work related to interaction mechanism and SERS enhancement of Py adsorbed on diatomic coinage cluster model, *i.e.*, Au-Ag, Au-Cu, and Ag-Cu, was performed. The obtained data showed that SERS intensities of the complexes depend on the nature of adsorbed metallic atoms. Indeed, the most significant peak enhancements were observed with the Au-Cu-Py and Ag-Cu-Py complexes, in which the Py molecule interacts with the Cu atom of these bimetallic clusters.

This work aims to understand better the SERS enhancement of Py adsorbed on the bimetallic Ag/Cu clusters, allowing further analytical sensing applications to detect the six-membered nitrogen-containing heterocyclic compounds. We used the smallest magic Ag cluster containing eight atoms with a T_d symmetry point group. The geometrical and electronic structures of all possible mixed AgCu clusters were optimized using DFT approaches. The enhancement mechanism was studied by investigating the binding energy, Raman, and SERS spectra of Py adsorbed on the most stable clusters.

COMPUTATIONAL METHODS

All DFT calculations were performed using Gaussian 16 Rev.C.01.[14] The PBE functional[15] was combined with the cc-pVDZ-PP basis set[16] for Ag and Cu, and the cc-pVDZ[17] other atoms. The most stable isomer of a magic silver cluster (Ag₈) with a T_d symmetry point group was chosen as the Ag cluster model.[18] The Ag₈ cluster was then doped with 1 to 8 Cu atoms at different Ag positions. Binding energy, dipole moment, orbital energies, and energy gaps, were analyzed for the most stable structure of the mixed clusters. We modeled all

possible interaction configurations of pyridine (Py) on the mixed AgCu clusters.

The following equations computed the binding energy (BE) per atom:[13]

$$BE = \frac{1}{m+n} [E_{m+n} - mE_{Ag} - nE_{Cu}]$$

The E_a represents the energy of a metallic atom, N is the total number of atoms, and *m* and *n* are the number of Ag and Cu atoms.

HOMO and LUMO distributions for the cluster-Py complexes were carried out. Finally, the static surface-enhanced Raman spectroscopy (SERS) spectra of the complexes were analyzed.

RESULTS AND DISCUSSION

1. Optimized structure of mono- and bimetallic AgCu clusters

The optimized geometries of the bare Ag₈ and Cu₈ cluster and all lowest energy mixing configurations with 1 – 7 Cu atoms are presented in *Figure 1*. Binding energy (BE) per atom is also shown in the parentheses.

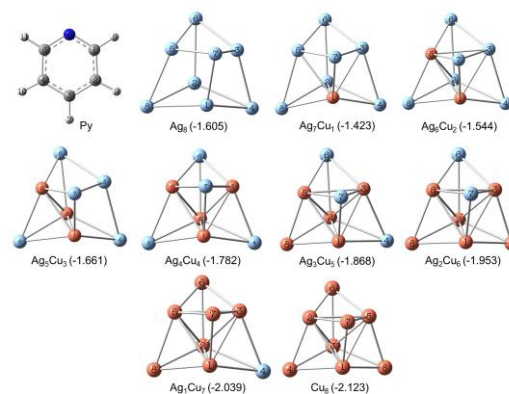


Figure 1. Optimized geometries for pyridine (Py) and the most stable Ag_(8-n)Cu_n (n=0-8) clusters. Values in parentheses correspond to absolute binding free energies (BE, eV). Ag: baby blue, Cu: orange.

The lowest BE of the smallest magic Ag cluster (Ag₈) is found -1.605 eV. Generally, increasing number of Cu atoms leads to lower BE values. The BE values lower up to -2.039 eV (Ag₁Cu₇ cluster), which is close to the one of the bare Cu₈ cluster (-2.123 eV).

2. Interactions of Py and AgCu clusters

It is widely accepted that the Py coordinates with the metallic cluster *via* the N atom of the pyridine ring, which possesses one electron pair free for donating to the vacant *d*-orbital of the metallic atom. On the other hand, the Ag₈ Td cluster has two types of Ag sites: (i) the site with 3-coordination numbers (Ag₄, Ag₆, Ag₇, and

Ag8 atom), and (ii) the site with 4-coordination numbers (Ag1, Ag2, Ag3, and Ag5 atom) (**Figure 1**). A metallic atom with lower coordination number is more active in the interaction with the ligand. Thus, the most stable complex of Py to Ag8 is formed at Ag1 position. A similar phenomenon is observed for the bare Cu8 cluster. Regarding the interaction of Py with Cu/Ag clusters, it is observed that the lowest energy complex is always formed at Cu position. For example, the lowest interaction energy of Py with the Ag7Cu1 cluster is found at the Cu1 atom with the distance N-Cu of 2.05 Å compared to N-Ag being 2.30 – 2.34 Å. A similar observation is also recognized for the other AgCu clusters with higher Cu/Ag mixing ratios. Moreover, the interaction at the Cu atom with a lower coordination number also leads to lower energy complexes. For example, the complex obtained at the Cu8 site (coordination 3) possesses lower enthalpy than the one at the Cu3 atom (coordination 4). As expected, the N-Cu8 distance (1.97 Å) is shorter than the N-Cu3 one (2.03 Å).

It can be seen in **Table 1** that the free Py possesses a low HOMO energy (E_H , -5.706 eV) and a high LUMO energy (E_L , -1.627 eV) tending to a large band gap (ΔE_{L-H} , 4.078 eV). On the other hand, the bare Ag8 or Cu8 cluster has smaller energy gap of 2.30-2.05 eV. The higher the mixing ratio Cu/Ag, the narrower the gap of energies of the mixed AgCu clusters. Indeed, the ΔE_{L-H} value decreases from 2.23 to 2.01 eV in increasing the number of Cu atoms (from 1 to 7) in the mixed clusters. For the complexes, the gaps are strongly reduced by elevating the E_H and lowering the E_L energy. The ΔE_{L-H} value decreases from 1.57 to 1.14 eV corresponding to Cu atoms from 1 to 7. Thus, the higher the Cu/Ag mixing ratio, the better the electron transfer between the frontier orbitals of the Py ligand and the clusters, and the tighter the interaction between the Py and the metallic clusters. It is demonstrated that mixing 5 Cu atoms in the silver Ag8 cluster may be the most effective choice for designing the mixed AgCu nanocluster.

Table 1. Energies of HOMO and LUMO (E_H and E_L) and band gap energies (ΔE_{L-H}) for all the studied clusters and complexes.

Clusters/Complex	E_H , eV	E_L , eV	ΔE_{L-H} , eV
Cu8/PyCu8	-4.80/-3.97	-2.75/-2.85	2.05/1.13
Ag1Cu7/PyAg1Cu7	-4.82/-3.99	-2.81/-2.85	2.01/1.14

Ag2Cu6/PyAg2Cu6	-4.83/-4.01	-2.84/-2.85	2.00/1.16
Ag3Cu5/PyAg2Cu6	-4.86/-4.04	-2.86/-2.85	2.00/1.18
Ag4Cu4/PyAg4Cu4	-4.90/-4.09	-2.88/-2.63	2.02/1.45
Ag5Cu3/PyAg5Cu3	-4.94/-4.12	-2.85/-2.63	2.08/1.49
Ag6Cu2/PyAg6Cu2	-4.97/-4.16	-2.81/-2.64	2.15/1.53
Ag7Cu1/PyAg7Cu1	-5.03/-4.21	-2.80/-2.64	2.23/1.57
Ag8/PyAg8	-5.11/-4.40	-2.81/-2.78	2.30/1.62
Py	-5.706	-1.627	4.078

3. Raman and SERS spectra.

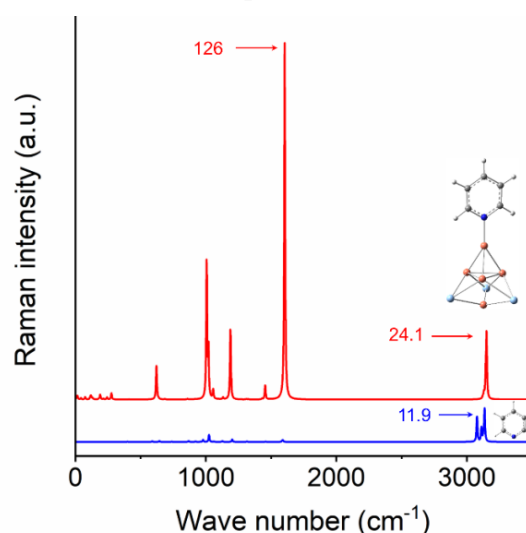


Figure 2. SERS of Ag3Cu5 (red) and Raman spectrum of pyridine (blue).

Figure 2 displays the computed Raman spectra of Py in comparison with the SERS one of Py adsorbed on all the studied Ag3Cu5 clusters. The most characteristic peak at 1590 cm⁻¹ representing the ring stretching sharply increases to 17 fold. The doping of 5 Cu atoms in the Ag8 cluster shows best enhancement, which may be due to a narrower band gap of the formed Py-cluster complex as well as the highest electron density transfer between the Py and the cluster. The higher Cu/Ag mixing ratio does not enhance peak intensity but can cause a higher oxidation risk of the metallic nanocluster due to the presence of copper atoms.

CONCLUSIONS

This work has achieved detailed analysis of the atomic, electronic, and surface-enhanced Raman scattering properties for pyridine (Py) adsorbed on bimetallic Ag_{8-n}-Cu_n (n=0-8) clusters by employing the Density functional theory. The results showed that mixing up to 5 Cu atoms into the magic Ag8 Td cluster maximizes the Raman peak intensity of Py

adsorbate with a 17-fold increase. Thus, the Ag₃Cu₅ formulation is recommended as the promising mixed nanocluster for analytical SERS-based sensor applications.

References

- [1] J. Langer et al., *Present and Future of Surface-Enhanced Raman Scattering*, ACS Nano, **14** (2020) 28-117.
- [2] N. V. Trang, D. Q. Dao, P. V. Nhat et al., *A Cluster Model for Interpretation of Surface-Enhanced Raman Scattering of Organic Compounds Interacting with Silver Nanoparticles*, in Practical Aspects of Computational Chemistry V, Springer International Publishing, (2022) 255-285.
- [3] N. T. Si, P. V. Nhat, and M. T. Nguyen, *Binding mechanism and SERS spectra of 5-fluorouracil on gold clusters*, Front. Chem, **10** (2022).
- [4] K. Q. Vo et al., *Controlled synthesis of spinous gold nanoparticles and their use for surface-enhanced Raman scattering (SERS) detection of the antibiotic sulfathiazole*, New J. Chem, **47** (2023) 6833-6843.
- [5] D. Q. Dao et al., *SERS Chemical Enhancement of 2,4,5-Trichlorophenoxyacetic Acid Adsorbed on Silver Substrate*, J. Phys. Chem. A, **125** (2021) 8529-8541.
- [6] T. C. Ngo et al., *SERS Spectra of the Pesticide Chlorpyrifos Adsorbed on Silver Nanosurface: The Ag 20 Cluster Model*, J. Phys. Chem. C, **124** (2020) 21702-21716.
- [7] T. D. Hieu et al., *SERS chemical enhancement by copper - nanostructures: Theoretical study of Thiram pesticide adsorbed on Cu20 cluster*, Vietnam J. Chem, **8**.
- [8] D. Q. Dao et al., *SERS chemical enhancement of 2,4,5-trichlorophenoxyacetic acid absorbed on Au20, its Au-Ag and Au-Cu bimetallic clusters: a DFT study*, V. J. Sci. Technol., **60** (2022) 641-651.
- [9] J. S. Al-Otaibi et al., *Evidence of cluster formation of pyrrole with mixed silver metal clusters, Ag_x-M_y (x = 4,5, y = 2/1 and M = Au/Ni/Cu) using DFT/SERS analysis*, Comput. Theor. Chem, **1208** (2022) 113569.
- [10] Zhao, L. Jensen, and G. C. Schatz, *Pyridine–Ag₂₀ Cluster: A Model System for Studying Surface-Enhanced Raman Scattering*, J. Am. Chem. Soc, **128** (2006) 2911-2919.
- [11] C. M. Aikens and G. C. Schatz, *TDDFT Studies of Absorption and SERS Spectra of Pyridine Interacting with Au₂₀*, J. Phys. Chem. A, **110** (2006) 13317-13324.
- [12] J. D. Amador-Martínez et al., *Experimental and DFT studies of copper nanoparticles as SERS substrates*, Appl. Phys. A, **129** (2023) 254.
- [13] H. Y. Seuret-Hernández et al., *DFT Study of the Adsorption and SERS of Pyridine on M₁₀N₁₀ (M, N = Cu, Ag) Tetrahedral Clusters*, J. Phys. Chem. A, **127**, (2023), 6697-6710.
- [14] M. J. Frisch et al., Gaussian 16 Rev. C.01. Wallingford, CT, 2016.
- [15] Y. Zhao and D. G. Truhlar, *The M06 suite of density functionals for main group thermochemistry, thermochemical kinetics, noncovalent interactions, excited states, and transition elements: two new functionals and systematic testing of four M06-class functionals and 12 other functionals*, Theor. Chem. Acc., vol. **120** (2008) 215-241.
- [16] K. A. Peterson et al., *Systematically convergent basis sets for transition metals. II. Pseudopotential-based correlation consistent basis sets for the group 11 (Cu, Ag, Au) and 12 (Zn, Cd, Hg) elements*, Theor. Chem. Acc, **114** (2005) 283-296.
- [17] T. H. Dunning, *Gaussian basis sets for use in correlated molecular calculations. I. The atoms boron through neon and hydrogen*, J. Chem. Phys, **90** (1989) 1007-1023.
- [18] P. V. Nhat, N. T. Si, and M. T. Nguyen, *Elucidation of the molecular and electronic structures of some magic silver clusters Ag_n (n = 8, 18, 20)*, J. Mol. Model, **24** (2018) 209.

A COMBINATION APPROACH STUDIES THE INTRINSIC SPIN HALL CONDUCTIVITY OF β -W BASED ALLOYS

Nguyen Huynh Tuan Anh, Ho Van Binh, Hua Thi Hoang Yen, and Do Duc Cuong*

Faculty of Physics and Engineering Physics, University of Science, VNU-HCM, Ho Chi Minh City, 70000, Vietnam

*Email: ddcuong@hcmus.edu.vn

ABSTRACT

In this work, spin Hall conductivity of $W_{0.875}Ta_{0.125}$ alloy has been theoretically studied by the combination of the first principles calculation with the tight binding method. Both two possible configurations of Ta in W sites are considered and contribution of each configuration to average SHC is estimated using Boltzmann transport distribution. We find that SHC of $W_{0.875}Ta_{0.125}$ alloy when Ta is in the body centered cubic site is much enhanced but gives less contribution to the thermodynamic average of SHC due to the large difference in total energy of the two configurations.

Keywords: spin Hall conductivity, ab initio, tight binding, β -W, alloys

INTRODUCTION

Recently, A15 structure β -W had been extensively studied as a potential spin Hall material due to its large spin Hall efficiency (so called spin Hall angle - SHA). It is reported that SHA of β -W is up to -0.5, which makes it become one of the largest SHA materials [1-9]. Previous theoretical predictions showed that alloys of β -W with Ta are even much more improved SHC [10,11]. X. Sui *et al.* showed that SHC of $W_{0.875}Ta_{0.125}$ when Ta substituting in body centered (bcc) site of W atom can enhance up to 41% compared with that of the pristine one [10]. However, recent experiments showed that the SHC efficiency of $W_{0.875}Ta_{0.125}$ alloy is reduced [12]. In this study, we revisited studying the alloy $W_{0.875}Ta_{0.125}$ by using a combination approach of the first principles calculations and the tight binding method. We find that although SHC of the alloy when Ta in the bcc site is much enhanced like previous reports [10], but thermo-dynamical average SHC of $W_{0.875}Ta_{0.125}$ alloy is reduced compared with SHC of pristine β -W, which are very good agreement with with recent experiments [12].

METHODOLOGY

In the current combination method, first principles calculations have been carried out to obtain the ground state electronic structure and Bloch states of material [13-14]. Those Bloch states are then used to convert into a set of the maximally localized Wannier functions and from that an effective tight binding Hamiltonian is

constructed [15-17]. Finally, a simple tight binding method is used to calculate SHC.

The SHC can be calculated using the linear-response Kubo formula approach [18-20]

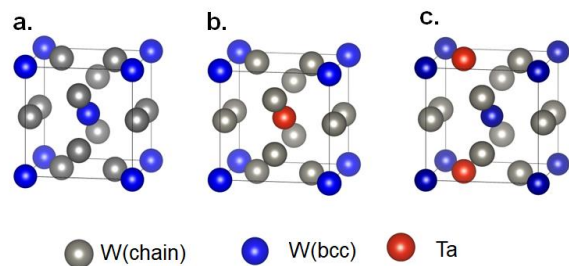
$$\sigma_{xy}^z = \frac{e}{\hbar} \sum_k \sum_n f_{nk} \Omega_{n,xy}^z(k) \quad (1)$$

Where $\Omega_{n,xy}^z(k)$ is spin Berry curvature defined by:

$$\Omega_{n,xy}^z(k) = \sum_{m \neq n} \frac{2Im[\langle nk | \hat{j}_x | mk \rangle \langle mk | \hat{v}_y | nk \rangle]}{(\varepsilon_{nk} - \varepsilon_{mk})^2} \quad (2)$$

With f_{nk} is the Fermi-Dirac distribution, ε_n and ε_m are eigenvalues corresponding to eigenvectors $|nk\rangle$ and $|mk\rangle$, respectively, $v_\alpha = \frac{1}{\hbar} \frac{\partial H(k)}{\partial k_\alpha}$ defines velocity operator along α direction with α is Cartesian axes (x,y,z) , and $\hat{j}_x = \frac{\hbar}{4} \{ \hat{\sigma}_z, \hat{v}_x \}$ is spin current density operator. However, due to Fermi distribution, the spin Hall conductivity given in Eq. (2) is limited to the occupied band. Therefore, $\Omega_{n,xy}^z(k)$ is large when Fermi level lies between gapped Dirac crossings [11].

RESULTS AND DISCUSSION



The structure of β -W belongs to the A15 type structure which is illustrated in Fig.1(a). Its structure is composed of eight W atoms, in which two W atoms occupy the bcc sites, forming the bcc sub-lattice, and six others occupy the linear chain sites, forming a one-dimensional chain along three orthogonal directions. The calculated lattice constant of β -W is 5.06 Å, which is consistent with the experimental lattice constant (5.03 ~ 5.04 Å). To study the alloy of Ta with β -W, we substitute one W atom by one Ta atom giving the stoichiometric of alloy is $W_{1-x}Ta_x$ with $x = 0.125$ is a concentration of the substituted atom (Ta). The lattice constant of alloy, $a_0(W_{1-x}Ta_x)$ is estimated using the Vegard's law for the intermetallic compound, given by:

$$a_0(W_{1-x}Ta_x) = (1 - x) a_0(\beta\text{-W}) + x a_0(\beta\text{-Ta}) \quad (1)$$

where $a_0(\beta\text{-W})$ and $a_0(\beta\text{-Ta})$ are the theoretical lattice constants of β -W and β -Ta in the cubic A15 structure, respectively. One Ta substituting into W will generate two possible configurations as depicted in Fig. 1(b) and Fig. 1(c), in which Ta_c and Ta_b denote the substitution of Ta into either chain or bcc site.

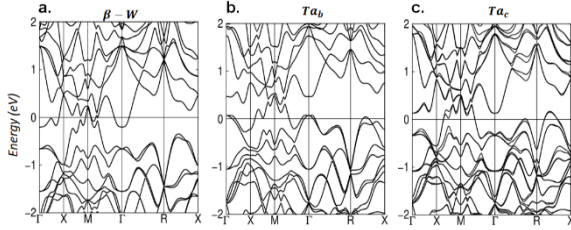


FIG. 2: The band structures of (a) Pristine W; (b) Ta in the chain site (Ta_b); and (c) Ta in the bcc site (Ta_c) in $W_{0.875}Ta_{0.125}$ alloy

In Fig. 2 (a), we show fully relativistic band structure of pristine β -W. In pristine β -W band structure, we observed many gapped Dirac crossings in the energy range from -0.7 to 0.1 eV. The existence of the gapped Dirac crossings had been reported to provide a large contribution to SHC of A15 class [11]. Our calculated SHC of β -W at $E_F = 0.00$ eV is -817 \hbar/e S/cm.

The band structures of two configurations are shown in Fig. 2 (b) and (c). We find that the band structures of $W_{0.875}Ta_{0.125}$ are modified compared with that of pristine β -W, but the fundamental Dirac crossings are still conserved due to the symmetry. The Fermi levels of both alloys shift down as compared with that of the pristine β -W as expected because the Ta has one electron less than W. More importantly, the Fermi level of Ta_b configuration is still located in between the

gapped Dirac crossing and therefore, SHC is expected to be large in this configuration. On the other hand, the Fermi level of Ta_c configuration moves away from the gapped crossing levels. As a result, the SHC of Ta_b is much enhanced up to -1394 \hbar/e S/cm [10], while the SHC of Ta_c is reduced to -745 \hbar/e S/cm. We note that the total energy of Ta_c is found to be lower than that of Ta_b , amount of $\Delta E_{tot} = E_{tot}(Ta_b) - E_{tot}(Ta_c) = 0.35$ eV, indicating that the Ta_c configuration is more stable than Ta_b configuration. Because of the existence of two different configurations, it is necessary to estimate the thermal-dynamical average SHC, $\sigma_{xy}^z(x)$, of both configurations using the Boltzmann distribution function given by:

$$\sigma_{xy}^z = \frac{\sum_i \sigma_{xy}^z(i) e^{\frac{E_i}{k_B T}}}{\sum_i \frac{E_i}{k_B T}} \quad (3)$$

where E_i and $\sigma_{xy}^z(i)$ are the total energy and SHC of i th configuration, respectively. The Boltzmann factor, $e^{\frac{E_i}{k_B T}}$, defines the probability of i th configuration. Although SHC of Ta_b is much enhanced compared with that of pristine β -W, probability of Ta_b in the contribution of this configuration to thermodynamic average SHC, σ_{xy}^z , is very small (only 0.01%) while that of Ta_c is up to 99.99%. As a result, σ_{xy}^z of $W_{0.875}Ta_{0.125}$ is only -745 \hbar/e S/cm, smaller than SHC of pristine β -W. Interestingly, this thermodynamic average value is found to be in good agreement with the recent experiment [12].

CONCLUSION

In this study, SHCs of β -W and its alloys with Ta have been theoretically studied by the combination of the first principles calculation with the tight binding method. The thermodynamic average SHC of the alloys is estimated to consider the contribution of two possible configurations. We found that although SHC of Ta_b configuration is much enhanced as same as previous reports [10,11], but the thermodynamic average SHC of the alloys is reduced compared with that of pristine β -W, which are in good agreement with the previous experiments [12].

Acknowledgment

This research is funded by Vietnam National University, Ho Chi Minh City (VNU-HCM) under grant number C2021-18-16

References

- [1] J. Sinova, S. Murakami, S.-Q. Shen, and M.-S. Choi, *Spin-Hall effect: Back to the beginning at a higher level*, Solid. Stat. Comm. 138 (2006) 214.
- [2] J. Sinova, S. O. Valenzuela, J. Wunderlich, C. H. Back, and T. Jungwirth, *Spin Hall effects*, Rev. Mod. Phys. 87 (2015) 1213.
- [3] Mohsin Z Minhas, Avanindra K Pandeya, Bharat Grover, Alessandro Fumarola, Ilya Kostanovskiy, Binoy K Hazra, Wolfgang Hoppe, Georg Woltersdorf, Amilcar Bedoya-Pinto, Stuart S P Parkin, *Doping-induced spin Hall ratio enhancement in A15-phase, Ta-doped β -W thin films*, J. Phys. Mater. 3 (2020) 044001.
- [4] K.-U. Demasius, T. Phung, W. Zhang, B. P. Hughes, S.-H. Yang, A. Kellock, W. Han, A. Pushp, and S. S. P. Parkin, *Enhanced spin-orbit torques by oxygen incorporation in tungsten films*, Nat. Comm. 7 (2016) 10644.
- [5] Q. Hao, W. Chen, and G. Xiao, *Beta (β) tungsten thin films: Structure, electron transport, and giant spin Hall effect*, Appl. Phys. Lett. 106 (2015) 182403.
- [6] L. Liu, C.-F. Pai, Y. Li, H. W. Tseng, D. C. Ralph, and R. A. Buhrman, *Spin-Torque Switching with the Giant Spin Hall Effect of Tantalum*, Science 336 (2012) 555.
- [7] L. Zhu, D. C. Ralph, and R. A. Buhrman, *Highly Efficient Spin-Current Generation by the Spin Hall Effect in $Au_{1-x}Pt_x$* , Phys. Rev. Appl. 10 (2018) 031001.
- [8] R. Bansal, G. Nirala, A. Kumar, S. Chaudhary, and P. K. Muduli, *Large Spin Hall Angle in β -W Thin Films Grown on CoFeB without Oxygen Plasma*, SPIN 08 (2018) 1850018.
- [9] L. Wang, K. Shi, S. Peng, K. Cao, H. Yang, J. Gao, W. Zhao, and C. Zhao, *Large spin Hall effect of perpendicularly magnetized β -W/CoFeB/MgO layers with high thermal stability*, Jpn. J. Appl. Phys. 58 (2019) 050903.
- [10] X. Sui, C. Wang, J. Kim, J. Wang, S. H. Rhim, W. Duan, and N. Kioussis, *Giant enhancement of the intrinsic spin Hall conductivity in β -tungsten via substitutional doping*, Phys. Rev. B **96** (2017) 241105.
- [11] E. Derunova, Y. Sun, C. Felser, S. S. P. Parkin, B. Yan, and M. N. Ali, *Giant intrinsic spin Hall effect in W_3Ta and other A15 superconductors*, Sci. Adv. 5 (2019) aav8575.
- [12] G. W. Kim*, D. D. Cuong*, Y. J. Kim, I. H. Cha, T. Kim, M. Lee, O. Lee, S.C. Hong, S..H. Rhim, and Y. K. Kim, *Spin-orbit torque engineering in β -W/CoFeB heterostructures with W-Ta or W-V alloy layers between β -W and CoFeB*, NPG Asia Materials 13 (2021)60.
- [13] P. E. Blöchl, *Projector augmented-wave method*, Phys. Rev. B 50 (1994), 17953. [14] G. Kresse and J. Hafner, *Ab initio molecular dynamics for liquid metals*, Phys. Rev. B 47 (1993) 558.
- [15] X. Wang, J. R. Yates, I. Souza, and D. Vanderbilt, *Ab initio calculation of the anomalous Hall conductivity by Wannier interpolation*, Phys. Rev. B 74(2006) 195118.
- [16] G. H. Wannier, *The Structure of Electronic Excitation Levels in Insulating Crystals*, Phys. Rev. 52 (1937) 191.
- [17] I. Souza, N. Marzari, and D. Vanderbilt, *maximally localized Wannier functions for entangled energy bands*, Phys. Rev. B 65 (2001) 035109.
- [18] J. Qiao, J. Zhou, Z. Yuan, and W. Zhao, *Calculation of intrinsic spin Hall conductivity by Wannier interpolation*, Phys. Rev. B **98** (2018) 214402.
- [19] G. Y. Guo, S. Murakami, T.-W. Chen, and N. Nagaosa, *Intrinsic Spin Hall Effect in Platinum: First-Principles Calculations*, Phys. Rev. Lett. **100** (2008) 096401.
- [20] G. Y. Guo, *Ab initio calculation of intrinsic spin Hall conductivity of Pd and Au*, J. Appl. Phys. **105**(2009) 07C701.

ORAL SESSIONS
NANOFABRICATION TECHNIQUES
(NFT)

STUDY ON THE PREPARATION OF BIMETALIC SILVER COPPER NANOPARTICLES BY ELECTRON BEAM IRRADIATION METHOD

Nguyen Thi Kim Lan, Dang Van Phu, Nguyen Chi Thuan, Le Anh Quoc, Cao Van Chung, Phan Phuoc Thang, Nguyen Ngoc Duy*

Research and Development Center for Radiation Technology, Vietnam Atomic Energy Institute, 202A, Street 11, Linh Xuan Ward, Thu Duc District, Ho Chi Minh City, Vietnam

Email: ngocduy158@gmail.com

ABSTRACT

Silver and copper nanoparticles are well-known as good antimicrobial agents. The size of the nanoparticles plays a crucial role in enhancing their antimicrobial activity. In this study, we successfully prepared and characterized silver-copper nanoparticles (Ag-CuNPs) using the electron beam (EB) irradiation reduction method. Chitosan (CTS) was used as a stabilizer agent. The obtained Ag-Cu NPs were characterized using powder X-ray diffraction (XRD), transmission electron microscopy (TEM), UV-vis spectrophotometry and EDX spectroscopy. The influence of the different concentration of $\text{Ag}^+/\text{Cu}^{2+}$ ions at the ratio $[\text{Ag}^+]:[\text{Cu}^{2+}] = 1:1$ was investigated. Based on the TEM results, the average size of the Ag-CuNPs ranged from 11.02 to 13.73 nm when the total concentration of $\text{Ag}^+/\text{Cu}^{2+}$ ions varied from 250 to 1000 mg/l, respectively.

Keywords: Ag/Cu nanoparticles, bimetallic, core-shell structure, electron beam irradiation

INTRODUCTION

Nanomaterials applied in agriculture have the potential to reduce the use of traditional chemical products, which contribute to drug resistance, impact human health, and cause environmental pollution. Nanoscale metallic materials, particularly nano alloys, have gained research interest for their high activity against bacteria and fungi [1, 2]. Silver nanoparticles (AgNPs) have been extensively studied and applied due to their non-toxic nature, high electrical and thermal conductivity, and anti oxidizing properties. However, their commercial use of AgNPs is still costly. As an alternative, research on the application of copper nanoparticles (CuNPs) has shown promising results, with a lower cost and almost similar antibacterial and antifungal activity [3]. However, CuNPs are easily oxidized during storage, so many studies have been conducted to fabricate silver/copper bimetallic nanoparticles (Ag-CuNPs) with superior properties compared to single AgNPs and CuNPs. Some studies have reported that the antibacterial and antifungal effectiveness of Ag-CuNPs is higher than that of individual AgNPs or CuNPs at the same concentration [4, 5]. This is attributed to the surface properties of Ag-CuNPs, which play a role in all proposed antimicrobial mechanisms. Additionally, the alloy form helps prevent the oxidation of CuNPs into copper ions,

thereby increasing their bactericidal and fungicidal effectiveness. For instance, in the study by Hong et al., polyester fabrics coated with a mixture of Ag-CuNPs particles demonstrated significantly enhanced antibacterial properties compared to fabrics treated with AgNPs alone [5]. Another study comparing AgNPs, CuNPs, AgNPs mixture, CuNPs, and Ag-CuNPs bimetallics found that the antimicrobial activity of Ag-CuNPs bimetallics was much higher than that of the other three [6]. Likewise, in the study of Wang et al., Ag-CuNPs bimetallics exhibited stronger inhibitory activity against the growth of Gram-negative bacteria *E. coli* and Gram-positive *S. aureus* compared to AgNPs or CuNPs when the Ag:Cu ratio was 1:1 [7].

However, manufacturing Ag-CuNPs materials with small size, high uniformity, and good stability remains a challenge. Currently, popular methods used to manufacture Ag-CuNPs include chemical reduction, thermal decomposition, polyol, laser irradiation, and biology [8]. So far as we know research on manufacturing of Ag-CuNPs bimetallic nanocolloids using electron beam (EB) irradiation method is still a new, both nationally and globally. In this study, we aim to fabricate Ag-CuNPs bimetallic nanoparticles using the EB irradiation method. This study offers advantages such as conducting the reaction and fabrication

process under normal conditions, resulting in a nano colloidal solution. The obtained bimetallic exhibits high purity, small grain size, meets clean production requirements, and enables industrial-scale production at competitive prices. Moreover, there is an urgent need for a new generation of nano products with small particle size, high stability, safety, and high bactericidal and fungicidal efficiency for prevention and treatment applications. Treating plant diseases in agriculture aims to limit the use of toxic pesticides that contribute to protecting the environment, and develop a safe and sustainable agriculture.

EXPERIMENTAL

Copper (II) sunfate ($\text{CuSO}_4 \cdot 5\text{H}_2\text{O}$), silver nitrat (AgNO_3), lactic acid ($\text{C}_3\text{H}_6\text{O}_3$) used in this study were purchased from Shanghai Chemical Co., China. Chitosan (CTS) with a molecular weight of 600.000 g/mol and a deacetylation degree greater than 90% was supplied by the Center for Radiation Technology Research and Development (VINAGAMMA), Vietnam. Distilled water was used in all experiments.

To prepare the CTS solution, dissolve 2% CTS into 2% lactic acid solution and stir for 30 minutes. Filter the chitosan solution using a 100-mesh stainless steel to obtain CTS solution. Dissolve AgNO_3 and CuSO_4 salts in water and add them to CTS solution. the mixture was stirred well on a magnetic stirrer for 30 minutes. The resulting $\text{Ag}^+/\text{Cu}^{2+}/\text{CTS}$ solution was placed in a zip bag and irradiated on an electron beam at VINAGAMMA Center to obtain the Ag-CuNPs solution.

For UV-Vis spectrometry, the Ag-CuNPs solution was diluted in distilled water to a 20 ppm solution, calculated based on the $\text{Ag}^+/\text{Cu}^{2+}$ concentration. The absorbance of the solution was recorded using a UV-Vis spectrophotometer (UV-2401PC, Shimadzu, Japan).

Transmission electron microscope (TEM) photography was used to determine the size of the Ag-CuNPs. TEM images were taken using the TEM model JEM-1400 from JEOL, Japan. The grain size on the TEM images was measured using Photoshop CS2 software.

XRD spectrometry was performed using a diffractometer (D2 - Phaser, Bruker, Germany) with $\text{CuK}\alpha$ radiation. X-ray diffraction patterns of the Ag-CuNPs samples were recorded in the 2θ range of $10\text{-}80^\circ$.

FTIR spectrometry was conducted using a Jasco FTIR - 4700 spectrometer from Easten, MA, USA. The sample measurement range was from $4000 - 400 \text{ cm}^{-1}$, with a resolution mode of 4.00 cm^{-1} .

For EDX Spectroscopy, the 1000ppm Ag-CuNPs sample was dried at 60°C for 3 days and then crushed using a ball mill (Fritsch, Germany). Measurements were conducted using an EDS-Quantax EDS-Bruker machine, which was combined with a SEM TM4000Plus device (Hitachi, Japan).

RESULTS AND DISCUSSION

The results of Figure 1 demonstrate that the optical density (OD) gradually decreases from 100 ppm to 1000 ppm at the peak of AgNPs, with λ_{max} remaining nearly constant. Meanwhile, OD increases from 100 ppm to 1000 ppm at the copper peak and λ_{max} shifts toward higher wavelengths. The UV-Vis spectrum of Ag-CuNPs exhibits two absorption peaks, with characteristic wavelengths ranging from 380-420 nm for AgNPs and from 570-600 nm for CuNPs. This indicates the presence of silver-copper bimetallic nanoparticles in the solution.

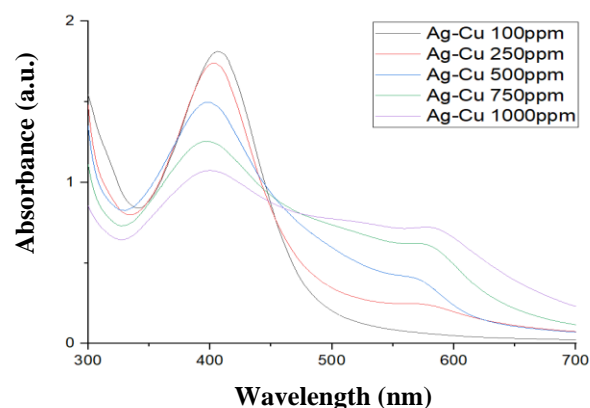


Figure 1. UV-Vis spectra of Ag-CuNPs solution at different $\text{Ag}^+/\text{Cu}^{2+}$

Based on the UV-Vis spectroscopy results, it can be inferred that for solutions with a low initial total $\text{Ag}^+/\text{Cu}^{2+}$ concentration (100 ppm), the average particle size is small and the particle size distribution is narrow. Conversely, for solutions with a high total $\text{Ag}^+/\text{Cu}^{2+}$ concentration (1000 ppm), the average particle size is large and the particle size distribution is wide. This can be attributed to the need for a larger amount of reducing agent (e_{aq}^- , H^\cdot) to completely reduce Ag^+ ions to Ag^0 and further reduce Cu^{2+} to Cu^0 at higher $\text{Ag}^+/\text{Cu}^{2+}$ concentrations. The effect of

total $\text{Ag}^+/\text{Cu}^{2+}$ concentration on the size of Ag-CuNPs particles is also evident in the TEM images.

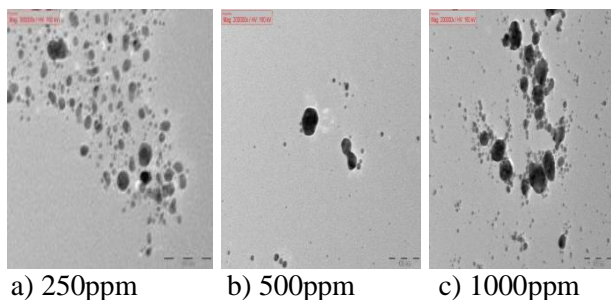


Figure 2. TEM image of Ag-CuNPs solution at different $\text{Ag}^+/\text{Cu}^{2+}$ concentrations

The Figure 2 showed that the particle size of Ag-CuNPs increases with the increase concentration of $\text{Ag}^+/\text{Cu}^{2+}$. Specifically, at an initial concentration of $\text{Ag}^+/\text{Cu}^{2+}$ of 250 ppm, the average particle size of Ag-CuNPs is 11.02 nm. However, when the $\text{Ag}^+/\text{Cu}^{2+}$ concentration is increased to 500 and 1000 ppm, the average Ag-CuNPs particle size increases to 12.55 nm and 13.73 nm, respectively. These TEM results align with the findings of Zain et al [9], which state that the size of Ag-CuNPs/CTS increases with an increase in the initial concentration of Ag^+ and Cu^{2+} .

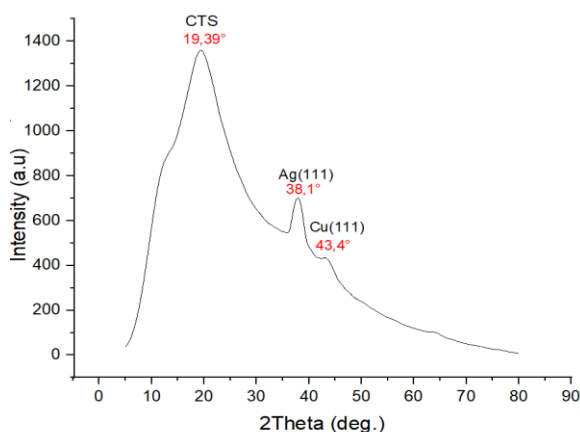


Figure 3. XRD pattern of Ag-CuNPs material

Figure 3 shows the XRD pattern of the Ag-CuNPs bimetallic material. The pattern exhibits characteristic crystal peaks that match the standard spectrum of copper at a 2θ position of 43.4° ($d_{111} = 2.087 \text{ \AA}$), corresponding to the (111) face in the face-centered cubic structure of Cu metal [10]. Additionally, a characteristic crystal peak of silver is observed at a position of $2\theta = 38.1^\circ$ ($d_{111} = 2.360 \text{ \AA}$), corresponding to the (111) plane in the face-centered cubic structure of Ag metal [11]. These parameters indicate the

formation of silver and copper crystals in the solution after electron beam irradiation. The XRD pattern also displays a peak at $2\theta = 19.39^\circ$, indicating the presence of CTS particles.

The FTIR spectrum of Ag-CuNPs/CTS shown in Figure 4 also exhibits characteristic peaks similar to CTS [12]. However, there are changes in intensity and wave number at specific absorption peaks. For example, the absorption intensity of the -OH group in the Ag-CuNPs solution is smaller than in the CTS solution, and there is a shift in wavelength from 3350 cm^{-1} (CTS) to 3277 cm^{-1} (Ag-CuNPs/CTS). The change in absorption intensity and wavelength shift can be explained by the participation of Ag-CuNPs particles in coordinating bond formation with oxygen and nitrogen atoms on the CTS chain. The free electron pair of oxygen and nitrogen atoms on the CTS chain is strongly attracted to Ag^+ or Cu^{2+} ions in solution, leading to deformation of the original bond. This bonding helps stabilize the Ag-CuNPs particles, preventing flocculation and demonstrating the protective mechanism of CTS as a stabilizer for Ag-CuNPs particles.

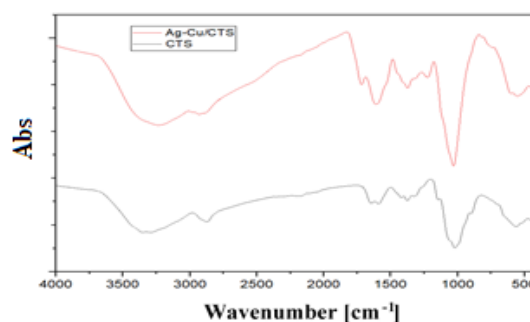


Figure 4. FTIR spectra of CTS and Ag-CuNPs/CTS samples

The EDX spectrum in Figure 5 displays peaks corresponding to the main elements C and O, which account for 66.31% and 31.71% of the mass of the material sample, respectively. This can be explained by the dominance of O and C in the CTS molecular structure. Additionally, the EDX spectrum detected two other elements, Ag and Cu, with proportions of 1.12% and 0.60% of the mass of the synthesized material sample, respectively. Therefore, it can be concluded that the synthesized Ag-CuNPs/CTS nano powder exhibits high purity, consisting solely of Ag-CuNPs and CTS components.

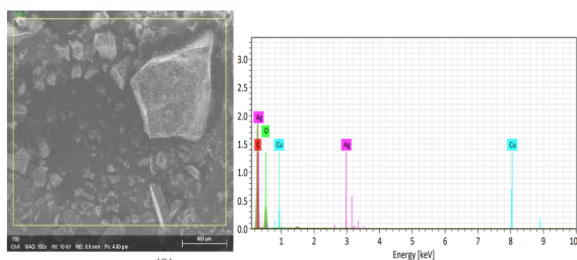


Figure 5. (a) SEM image (b) EDX spectrum of Ag-CuNPs material

CONCLUSION

The study on the influence of different Ag⁺/Cu²⁺ concentration on Ag-CuNPs particle size reveals that the size of Ag-CuNPs increases from 11.02 to 13.73 nm, corresponding with the increase of the Ag⁺/Cu²⁺ concentration is increased from 250 to 1000 ppm.

Acknowledgment

The authors would like to acknowledge the financial support for this research provided by the Vietnam Atomic Energy Institute, Ministry of Science and Technology, Government of Vietnam.

References

- [1] H.J. Lee, S.H. Jeong, *Bacteriostasis and Skin Innoxiousness of Nanosize Silver Colloids on Textile Fabrics*, Textile Research Journal, **75**(7) (2005) 551-556.
- [2] V. Saharan, G. Sharma, M. Yadav, M. K. Choudhary, S.S. Sharma, A. Pal, R. Raliya, P. Biswas, *Synthesis and in vitro antifungal efficacy of Cu-chitosan nanoparticles against pathogenic fungi of tomato*, International Journal of Biological Macromolecules, **75** (2015) 346-353.
- [3] T.M.D. Dang, T.T.T. Le, E. Fribourg-Blanc, M.C. Dang, *The influence of solvents and surfactants on the preparation of copper nanoparticles by a chemical reduction method*, Advances in Natural Sciences: Nanoscience and Nanotechnology, **2**(2) (2011).
- [4] M. Reyes-Blas, N.M. Maldonado-Luna, C.M. Rivera-Quiñones, A.L. Vega-Avila, F.R. Roman-Velázquez, O.J. Perales-Perez, *Single step microwave assisted synthesis and antimicrobial activity of silver, copper and silver-copper nanoparticles*, Journal of Materials Science and Chemical Engineering, **8**(8) (2020) 13-29.
- [5] H.R. Hong, J. Kim, C.H. Park, *Facile fabrication of multifunctional fabrics: use of copper and silver nanoparticles for antibacterial, superhydrophobic, conductive fabrics*, RSC Advances, **73** (2018) 41782-41794.
- [6] N.M. Zain, A.G.F. Stapley, G. Shama, *Green synthesis of silver and copper nanoparticles using ascorbic acid and chitosan for antimicrobial applications*, Carbohydrate Polymers, **112**(4) (2014) 195-202.
- [7] X. Wang, R. Li, Z. Li, R. Xiao, X.-B.Chen, T. Zhang, *Design and preparation of nanoporous Ag-Cu alloys by dealloying Mg-(Ag,Cu)-Y metallic glasses for antibacterial applications*, Journal Materials Chemistry B, **26** (2019) 4169-417.
- [8] D. Chattopadhyay, B.H. Patel, *Improvement in physical and dyeing properties of natural fibres through pre-treatment with silver nanoparticles*, Indian Journal of Fibre and Textile Research, **34**(4) (2009) 368-373.
- [9] N. M. Zain, A. G. F. Stapley, and G. Shama, *Green synthesis of silver and copper nanoparticles using ascorbic acid and chitosan for antimicrobial applications*, Carbohydrate Polymers, **112** (2014) 195-202.
- [10] K. Giannousi, G. Sarafidis, S. Mourdikoudis, A. Pantazaki, and C. Dendrinou-Samara, *Selective synthesis of Cu₂O and Cu/Cu₂O NPs: antifungal activity to yeast Saccharomyces cerevisiae and DNA interaction*, Inorganic Chemistry, **53**(18) (2014) 9657-9666.
- [11] X. Jiang, Q. Zeng, and A. Yu, *Thiol-frozen shape evolution of triangular silver nanoplates*, Langmuir, **23**(4) (2007) 2218-2223.
- [12] M. Venkatesham, D. Ayodhya, A. Madhusudhan, N. Veera Babu, and G. Veerabhadram, *A novel green one-step synthesis of silver nanoparticles using chitosan: catalytic activity and antimicrobial studies*, Applied Nanoscience, **4**(1) (2014) 113-119.

GREEN SYNTHESIS OF SILVER NANOPARTICLES USING GUAVA (*PSIDIUM GUAJAVA LINN.*) LEAF EXTRACT, PREPARED BY ULTRASONIC-ASSISTED EXTRACTION, AS REDUCING AGENT

Minh Quang Tran¹, Tran Ngoc Thi Tran¹, Nhan Chi Thuc Ha¹ and Ngoc Ha-Thu Le¹

¹ Faculty of Materials Science and Technology, University of Science, VNU-HCM, 227 Nguyen Van Cu Street, Ward 4, District 5, Ho Chi Minh City, 700000, Viet Nam.

Email: tqminh@hcmus.edu.vn

ABSTRACT

In this study, guava (*P. guajava L.*) leaf extract, which is prepared by ultrasonic method, is used as green reducing agent for silver nanoparticles synthesis. Ultrasonic-assisted extraction provides not only a shortened process at low temperature but also a higher amount of reducing agents, compared to magnetic stirring method in same condition. A highly efficient radical scavenging activity of guava leaf extract, prepared by sonication, possesses the 50% inhibitory concentration (IC₅₀) of 43.293 µg/mL (DPPH), whereas ascorbic acid is 25.689 µg/mL. The synthesized silver nanoparticles (AgNPs) were confirmed by UV-vis spectrophotometry at 405 nm and X-ray diffraction (XRD). Field emission scanning electron microscopy (FESEM) and dynamic light scattering (DLS) showed that the average sizes of the AgNPs were 20 – 40 nm and 27.3 nm, respectively. Guava leaf extract also acts as stabilizer for AgNPs. Zeta potential measurements (−56.5 mV) showed that the synthesized AgNPs had reasonably good stability. Antimicrobial activity assays of the AgNPs showed inhibition against selected bacteria, *E. coli*. This study revealed that the low-cost, fast and environmentally friendly synthesis of AgNPs, which can be used as antimicrobial agent in nanobiotechnology field.

Keywords: Ultrasonic-assisted extraction, silver nanoparticles synthesis, guava (*Psidium Guajava Linn.*) leaf extract.

INTRODUCTION

Ultrasound-assisted extraction (UAE) has been extensively used for the plant's extraction due to increasing extraction rate and reduced processing time compared to traditional heating magnetic stirring method [1]. Though UAE is a fast, effective extraction method for isolating plant material, this method affects many parameters such as sonication intensity, extraction time, solvent to solid ratio which need to be further investigated.

Plant extracts are currently being employed as reducing reagents in the green synthesis of silver nanoparticles (AgNPs). Plant extracts are a good technique to not only generate benign and stable nanoparticles, but also to reduce the need of harmful compounds or powerful reductants [2].

P. guajava L. is widely cultivated in Vietnam. Many studies indicate that *P. guajava L.* leaf extract contains a great number of bioactive compounds, such as flavonoids, polyphenol, polysaccharides, ascorbic acid, which may be considered as good reducing agent and stabilier of nano particles [3].

In this study, *P. guajava L.* leaf extract prepared by sonication was used as reductants to reduce silver ions to rapidly form silver nanoparticles at room temperature. The obtained silver nanoparticles were analyzed using various techniques (UV-vis, FTIR, XRD, SEM, DLS, zeta potential). To the best of our knowledge, this is the first report to synthesize and characterize AgNPs at room temperature using *P. guajava L.* leaf extracts prepared by sonication.

EXPERIMENTAL

Preparation of *P. guajava L.* leaf extracts

First, the fresh leaves collected from Tien Giang province (Vietnam) were cleaned with deionized water to remove any dirt and dust, dried for 24 h at 60 °C, and ground into fine powder. Then, 10 g of *P. guajava L.* leaves were mixed with 150 mL deionized water and placed in ultrasonic bath (Elmasonic S60H, 37 kHz, 150W) for different times (5, 10, 15, 20, 25 mins). The pale brown extract was filtrated to remove contaminants. Finally, the obtained extraction

was freeze-dried to remove H₂O and stored in a freezer at -20 °C for further experiments.

Preparation of AgNPs from AgNO₃ using *P. guajava* L. leaf extracts as reducing agent

P. guajava L. leaf extracts (50 mL) were added into solution of AgNO₃ 0.07 % (50 mL). This mixture was stirred and then slowly dropped NaOH 1 M until pH = 9. After stirring for 2 hours, dark brown solution was obtained and cool centrifuged in 10 mins to get AgNPs. AgNPs were dried in 50 °C to use for characterizations.

RESULTS AND DISCUSSION

Preparation of *Psidium guajava* L. leaf aqueous extracts

The aqueous extracts of *P. guajava* L. leaves were obtained by sonication in different time (from 5 to 25 mins). Fig. 1 shows the UV-vis spectrum of the *P. guajava* L. extract in various sonication time (solid line). The results showed a strong absorption peak at 275 nm with increasing of intensity from 5 to 15 mins and slightly decreasing from 15 to 25 mins. It means that the longer sonication time, the more time it takes to crack the cell walls and reveal the cell contents. However, prolonged extraction time may give a negative result due to increasing the chances of decomposition of bioactive compound in samples and motivating the reabsorption which lowers the yield [4]. In addition, Fig. 1 also shows the UV-vis spectrum of the *P. guajava* L. extract from magnetic stirring at room temperature in 15 mins and 120 mins (dotted line). The results indicate that the amount of extraction from magnetic stirring method in same condition is much lower than that induced by ultrasound wave.

Synthesis of silver nanoparticles with *Psidium guajava* L. leaf aqueous extracts

Silver nanoparticles were rapidly synthesized from Ag⁺ ion using the prepared aqueous extracts of *P. guajava* L. leaves as reducing agent. The UV-vis spectrum in Fig. 2 shows a strong absorption peak at 405 nm which is the characteristics for surface plasmon resonance band of silver nanoparticles. At 405 nm, the intensity of absorption peak increases when using the *P. guajava* L. leaf extracts with longer sonication time. The highest intensity when using the *P. guajava* L. leaf extracts with 15 mins sonication indicates that the largest amount of reducing agent included. This result is consistent with reported data shown in Fig. 1.

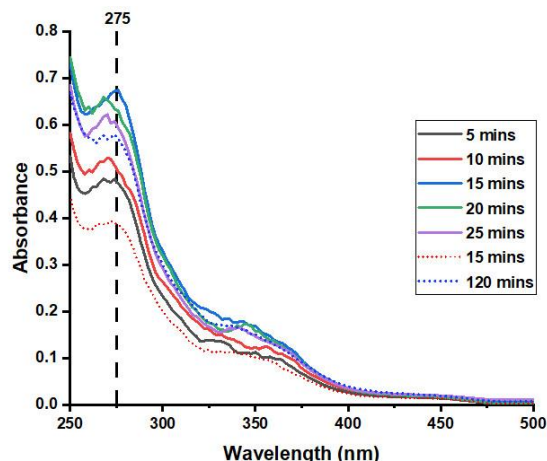


Fig. 1. UV-vis spectra of *P. guajava* L. leaf extracts prepared by ultrasound-assisted extraction from 5 to 25 mins (solid line) and heating magnetic stirring method from 15 mins to 120 mins (dotted line) in the range of 250–500 nm.

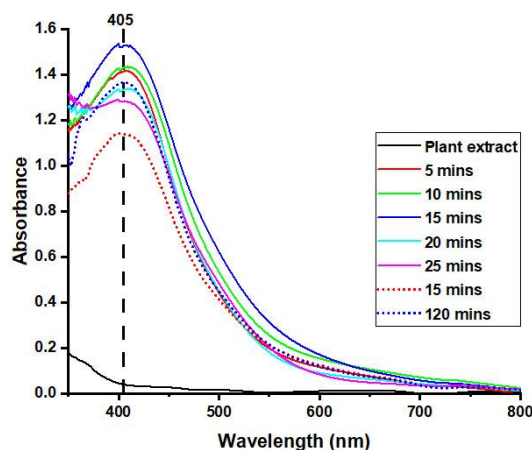


Fig. 2. UV-vis spectra of colloidal AgNPs in *P. guajava* L. leaf extracts prepared by ultrasound-assisted extraction from 5 to 25 mins (solid line) and magnetic stirring at room temperature from 15 mins to 120 mins (dotted line) in the range of 350–800 nm.

Characteristics of AgNPs

X-ray diffraction (XRD)

As shown by the XRD pattern of the AgNPs (Fig. 3), the analyzed sample has strong diffraction peaks at $2\theta = 38.24^\circ; 44.22^\circ; 64.52^\circ; 77.52^\circ; 81.67^\circ$ is clearly defined. Those diffraction peaks are characteristic of the (111), (020), (022), (131) and (222) lattice surfaces. This is the face-centered cubic (FCC) structure of Ag metal. This allows us to confirm the formation of silver crystals in the solution after the reaction. The

AgNPs crystallite size using Scherrer equation is 13.9 nm.

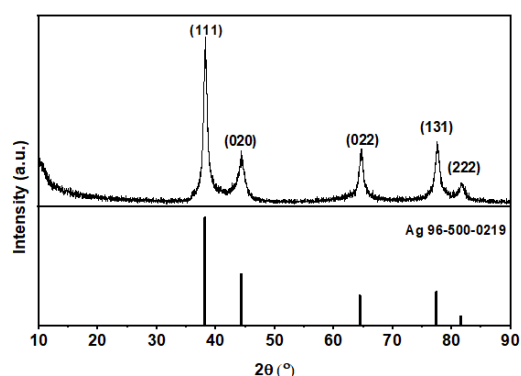


Fig. 3 XRD patterns of AgNPs.

Microscopic structure of AgNPs

The shape, morphology, and dispersal characteristics of the nanoparticles were analyzed by a FE-SEM analysis technique. Fig. 4 shows FE-SEM images of AgNPs showing that a thin organic shell is covered on each individual silver nanoparticle, which may be responsible for reducing Ag^+ ions to Ag^0 and helping to stable AgNPs. Most AgNPs are spherical and have sizes in the range of 20-40 nm showing polydispersity.

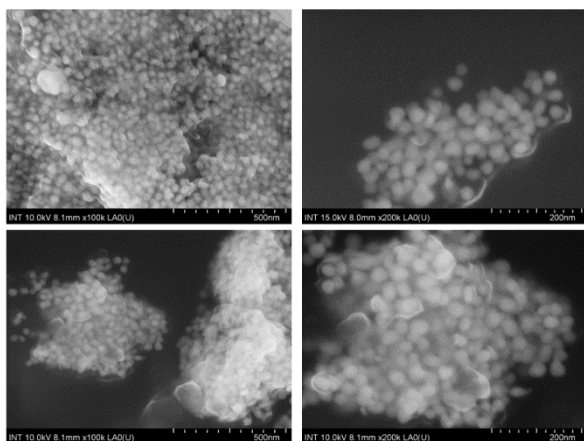


Fig. 4. FE-SEM image of AgNPs

Fourier transform infrared spectrometer (FTIR)

The probable bioactive compounds responsible for the reduction of silver ions and capping of the reduced P-AgNPs produced using *P. guajava L.* leaf extracts were identified using FTIR analysis (Fig. 5). The strong band at 1640 cm^{-1} corresponds to the -C=C stretching vibration, the strongest peak 594 cm^{-1} and other peaks at 1375 cm^{-1} , 1065 cm^{-1} , 599 cm^{-1} are signals corresponding to heterocyclic compounds in extract, such as flavonoids and polyphenols. The peak at 2926 cm^{-1} corresponds to the C-H stretching vibration of the polyphenolic group.

The strong peak at 3385 cm^{-1} corresponds to O-H, C=O or N-H stretching vibrations for AgNPs using guava extract as reducing agent.

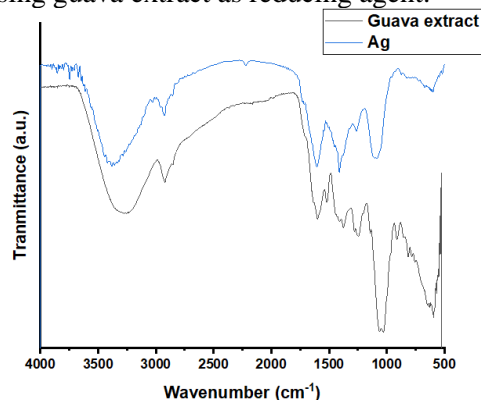


Fig. 5. FTIR absorption spectra of AgNPs and *P. guajava L.* leaf extracts.

Dispersion stability

The zeta potential of a sample is often used as an index of dispersion stability. Large zeta potential predicts more stable dispersion and vice versa. The zeta potential value for AgNPs reduced by guava leaf extract on the first day was -56.5 mV (Fig. 6a), which shows that the synthesized AgNPs are quite stable and well dispersed. The average particle size recorded through DLS results is 27.3 nm . Moreover, the zeta potential and DLS synthesized AgNPs sample after 30 days are -22.7 mV and 55.3 nm , respectively (Fig. 6b). This shows that AgNPs clusters still maintain their nanostructure and relatively high stability. It has been proven that guava leaf extract, in addition to being a reducing agent, also acts as a good stabilizer for AgNPs.

Antioxidant activity

Antioxidant activity was expressed through DPPH measurement. The results recorded that the IC_{50} index of guava leaf extract after 15 minutes of ultrasound was $43.293\text{ }\mu\text{g/mL}$ compared to the positive control ascorbic acid which was $25.689\text{ }\mu\text{g/mL}$. This shows the antioxidant capacity of guava leaf extract. This extracted sample, after being reduced to Ag, still maintained its antioxidation ability, IC_{50} index is measured at AgNPs concentration of $39.370\text{ }\mu\text{g/mL}$. This proves that AgNPs-reduced by *Psidium guajava L.* leaf aqueous extract not only formed successfully but also remains advantage of the antioxidant properties of natural guava leaf extract.

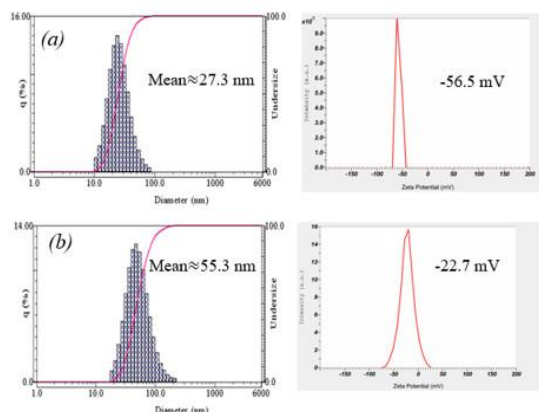


Fig. 6. DLS (left) and zeta potential (right) of AgNPs. (a) Day 1; (b) Day 30.

Antimicrobial activity

The Gram-negative bacteria - *Escherichia coli* was used to evaluate the antibacterial ability of the AgNPs sample. All AgNPs samples appear antibacterial circles (Fig. 7), with an average diameter of 13.6 ± 0.7 nm. This shows that the antibacterial ability of AgNPs against *E. coli*

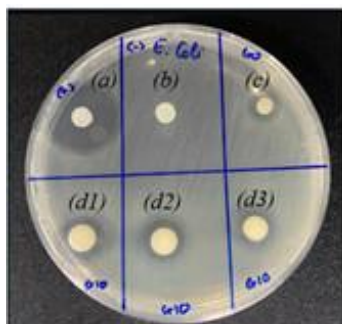


Fig. 7. Antimicrobial activity of AgNPs against *E. Coli* depicting zones of inhibition of (a) positive control-gentamicin, (b) negative control-water, (c) pure guava leaf extract, (d) AgNPs ($30 \mu\text{g/mL}$)

Toxicity

In vitro testing on the L929 cell line showed the toxicity ability of the AgNPs sample. The result was that the percentage of living cell of the AgNPs sample was 91.5% compared to the negative control sample. This result is assessed as the formed Ag is not toxic to cells, according to ISO 10995-5 standards.

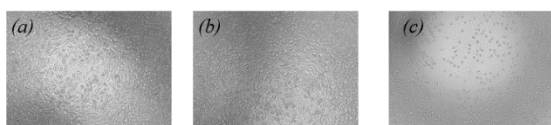


Fig. 8. Toxicity activity of (a) AgNPs ($30 \mu\text{g/mL}$), (b) negative control-culture and (c)

positive control-culture and 20% DMSO on L929 cell line.

CONCLUSION

AgNPs were successfully green synthesized using *Psidium guajava L.* leaf aqueous extract prepared by sonication in short time (15 mins), which acts as both a reducing agent and a stabilizer. The AgNPs maintained their stability and nanostructure for up to 30 days. XRD spectra showed that AgNPs were formed with a single phase of Ag and had a nanostructure. FE-SEM images show that the particles have a uniform size, distributed from 20 - 40 nm and AgNPs are covered by a thin organic shell, which can give durability to the particles. AgNPs show good antibacterial ability against Gram-negative bacteria *E. coli* and do not cause toxicity to L929 cells.

Acknowledgment

This research is funded by University of Science, VNU-HCM under grant number T2023 – 154

References

- [1] A. Carreira-Casais, P. Otero, P. Garcia-Perez, P. Garcia-Oliveira, A. G. Pereira, M. Carpena, A. Soria-Lopez, J. Simal-Gandara, M. A. Prieto, *Benefits and Drawbacks of Ultrasound-Assisted Extraction for the Recovery of Bioactive Compounds from Marine Algae*, Int J. Environ. Res. Public Health. **18**(17) (2021) 9153-9178.
- [2] A. Saravanakumar, M. M. Peng, M. Ganesh, J. Jayaprakash, M. Mohankumar, H. T. Jang, *Low-cost and eco-friendly green synthesis of silver nanoparticles using Prunus japonica (Rosaceae) leaf extract and their antibacterial, antioxidant properties*, Artif. Cell. Blood, Sub **45**(6) (2017) 1165–1171.
- [3] L. Wang, W. Wei, X. Tian, K. Shi, Z. Wu, *Improving bioactivities of polyphenol extracts from Psidium guajava L. leaves through co-fermentation of Monascus anka GIM 3.592 and Saccharomyces cerevisiae GIM 2.139*, Ind. Crop. Prod. **94** (2016) 206–215.
- [4] M. M. H. Shah Buddin, M. Z. Amat Rithuan, M. S. Aiman Surni, N. H. Mhd Jamal, M. F. Faiznur, *Ultrasonic assisted extraction (UAE) of Moringa oleifera Seed Oil: Kinetic study*. ASM Science Journal, **11**(3) (2018) 158–166.

USING COLD ATMOSPHERIC PLASMA TECHNIQUE TO CREATE COVALENT BINDING ON THE MICROFLUIDIC CHIP SURFACE FOR FABRICATION SWEAT GLUCOSE WEARABLE COLORIMETRIC SENSOR

Giang Dau Huong¹, Nam Luyen Van¹, Yoshiaki Ukita², Truong TN Lien^{1*}

¹ Convergence Technology Division, Vietnam-Korea Institute of Science and Technology Hoa Lac High-tech Park, Km29 Thang Long Boulevard, Hanoi 100000, Vietnam

² University of Yamanashi, Japan

Email: ttlien@most.gov.vn

ABSTRACT

The quality of a biosensor significantly increased when there is a suitable bioreceptor immobilization technique, allowing them to be securely and orientationally mounted on the electrode surface without affecting its biological activity. Recently, cold atmospheric plasma technology has been strongly developed to modify the electrode surface for the covalent immobilization of functional biomolecules without the using chemicals. This study proposed a wearable colorimetric sensor based on microfluidic chips to realize non-invasive in situ analysis of epidermal sweat. A simple microfluidic chip design using PDMS as fabrication material with air venting allows sweat to be easily collected into the reaction chamber. The surface of the reaction chamber is denatured by cold plasma flow for direct immobilization of two enzymes Glucose Oxidase (GOx) and Horseradish Peroxidase (HRP), and 3,3',5,5'-tetramethylbenzidine (TMB) as color reagent. Glucose in sweat will react with GOx enzyme that decomposes glucose. The product of this reaction is H₂O₂ - under the decomposition effect of HRP enzyme will react with TMB to show blue color. The intensity of the color shown will be linearly proportional to a given concentration range of glucose present in the sample. This microfluidic chip also enables four simultaneous detections to be performed based on an isolated separation design between the reaction chambers, providing reliability with high efficiency. The application potential of this device is considerable with its simple structure and convenient in design and usage.

Keywords: cold plasma, microfluidic chip, biosensor, colorimetric sensor .

INTRODUCTION

Developing new and faster biosensor manufacturing technologies is a major challenge for science and industry today. The sensitivity and selectivity of the sensor strongly depend on the technique of attaching the biological receiver to the electrode surface. Recently, a technology has emerged that allows attaching biological receivers to solid electrode surfaces quickly, effectively and at lower production costs, which is cold plasma technology. Applications of plasma technology have a long history in electronics, semiconductor industry and materials science such as plasma polymerization, surface structuring [1, 2]. In recent decades, cold atmospheric pressure plasma (CAP) technology has been actively used in several industrial sectors, because it is suitable for surface treatment of various materials such as metal,

wood, paper, glass, polymer, ceramic, non-woven fabric, etc., without losing material properties [3, 4]. CAP is an innovative, powerful, and effective tool that offers the potential for widespread application. In this study, we aim to apply cold plasma technology to modify the electrode surface of a wearable sensor with functional groups that allow the biological receivers to be fixed to the surface to measure Glucose concentration in sweat. In fact, blood Glucose concentration testing systems are gradually being commercialized and becoming very popular in life. However, controlling in this way shows a major disadvantage: it is painful, in addition, taking samples by invasive methods multiple times will cause discomfort for patients when they need to be tested many times in one day. There have been many research efforts to develop personal Glucose sensors using painless and non-invasive methods like testing sugar

concentration in sweat samples, but the practical application is not much because there are still limitations in many aspects such as retention time and poor reading of results.

Here we create a wearable biochip, with the goal of improving these limitations. The polydimethyl siloxane (PDMS) based chip was modified with nonionic surfactants to ensure good hydrophilicity for the automatic collection of sweat. Besides, a simple, reliable, and low-cost paper-based sensor was prepared for the sensing of Glucose concentration.

EXPERIMENTAL

A. Chemicals and Materials

PDMS and curing agent from Dow Corning Corporation, D-Glucose (D-Glc), Glucose Oxidase (GOx), Horseradish Peroxidase (HRP), 3,3',5,5'-tetramethylbenzidine (TMB), hydrogen peroxide (H₂O₂) from Sigma Aldrich, Deion water.

➤ Preparation of reaction solutions

1. TMB solution: mix 10 mg/mL TMB in DMSO.
2. AuNPs/TMB solution: use 480 μ L of AuNPs stock solution, centrifuge to remove all water, then mix with 480 μ L of TMB (10 mg/mL in DMSO).
3. HRP: mix HRP solution at the concentration of 1 mg/mL in PBS.
4. GOx: mix GOx solution with a concentration of 2 mg/mL in PBS.
5. H₂O₂: used 30% H₂O₂ solution.
6. D-Glucose: mix a solution of 1 mg/mL concentration in H₂O, leave stable at 24h conditions, 4°C.

B. Experimental

1. Fabricating microfluidic chip

1.1. Sample preparation

The microfluidic chip has a channel structure as shown in **Figure 1**, with a chip thickness of 3 mm, a channel depth of 200 μ m and a reaction chamber volume of about 3 μ L with 4 independent reaction chambers. The details are arranged in a circular mold with a diameter of 3 cm. The two ends of the channel are designed to be perforated with outside air to help balance the pressure in the reaction chamber, making it easy for the solution to be transported from the input into the reaction chamber.

To fabricate the microfluidic chip, PDMS monomer was mixed with the catalyst in a 10:1

ratio and poured onto the mold with a thickness of 0.5 mm. Incubate PDMS at 75°C for 90 minutes and separate the microfluidic chip structure from the mold at high temperature. Stabilize the chip structure by incubation for 2 hours at 80°C. Using 1 mm and 1.5 mm diameter punches to punch through the thickness of the PDMS block to create inlets and outlets. After punching holes, the PDMS microfluidic chip is cleaned by ultrasonic vibration in ethanol and water.

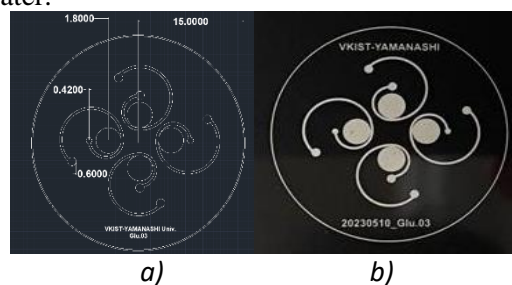


Figure 1. a) Microfluidic system design and b) the photomask after fabrication

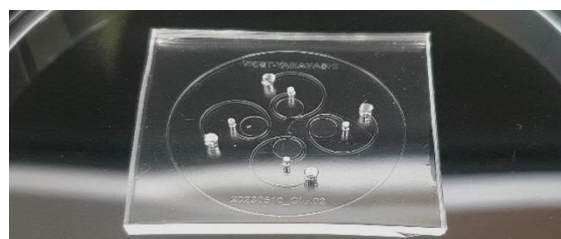


Figure 2. Microfluidic chip after fabricated.

1.2. Plasma treatment



Figure 3. Surface modification of PDMS chip with cold plasma.

The process of modifying the microfluidic chip surface structure was performed with an RF power source with a frequency of 13.56 MHz to excite the plasma under a pressure of 100 μ bar. The oxygen flow rate used is 20 sccm. The

voltage to create the plasma current is about 0.45 A and is used to denature the chip surface for 90 seconds.

2. Paper-based colorimetric biosensor fabrication

2.1. Mechanism of operation of the colorimetric sensor for Glucose detection.

The color reaction will go through 3 stages. First, β -D-Glucose, under the influence of the enzyme GOx, is oxidized to produce H_2O_2 . Then, the HRP enzyme decomposes H_2O_2 from stage 1, creating atomic Oxygen. Finally, the atomic oxygen oxidizes the color indicator, changing the reaction color. The color intensity is proportional to the Glucose concentration in the sample. We choose TMB as a color indicator, the solution gives a blue color immediately after the reaction.



Figure 4. Reaction of TMB with HRP and H_2O_2 gives blue color.

Recently, the use of gold nanoparticles (AuNPs) to replace HRP enzyme has been studied and shown many good results with equivalent color display efficiency. In this study, we will also test the effect of the presence of these two factors during the reaction process, thereby evaluating the effect of AuNPs.

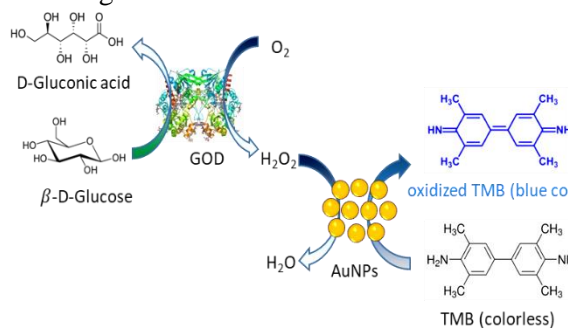


Figure 5. Schematic diagram of the GOx – AuNPs – TMB reaction system.

2.2. Paper-based colorimetric biosensor fabrication.

We used Glass Fiber paper as the material to manufacture colorimetric sensors based on paper electrodes. The surface of glass fiber was modified with cold plasma after each step to attach the reactive components to its surface. Dropping 5 μ L of AuNPs/TMB solution onto the paper and dry at 37°C for 90 minutes. Then add 5 μ L of GOx/HRP enzyme mixture (1/1, v/v) and react

with 10 μ L of D-Glc solution with different concentrations. The experiment was performed in parallel with the comparison reaction without using AuNPs particle solution. The reaction between the two enzymes GOx and HRP with D-Glc solution to change the color of TMB is a common reaction, also known and used in many studies.

RESULTS AND DISCUSSION

1. Cold plasma treatment

The surface of the PDMS sheet is dotted with fluorescent solution after being modified with cold plasma (on the left half in Fig 6). Comparison with the unmodified right half shows that the PDMS surface is restructured by the action of plasma rays, transforming into a radical (-COOH), thereby changing its hydrophobic properties to hydrophilic.



Figure 6. PDMS surface with luminescent solution drops

The behavior of the microfluidic chip before and after denaturation with cold plasma was tested with a fluorescent solution (Fig 7). Before surface modification, the chip is more difficult to collect samples, the solution has difficulty entering the channels and cannot completely fill the chambers.



Figure 7. Solution filled into the chambers of the chip a) before and b) after denaturation with cold plasma.

After being surface modified with cold plasma, the microfluidic chip collects solution samples more easily, because denaturation with cold plasma has the effect of creating a hydrophilic radical to bring the sweat sample solution into the reaction chamber.

2. Paper-based colorimetric biosensor fabrication

The paper-based sensor is made of glass fiber. After the reaction components are attached to the

surface, it is attached to the chamber of the microfluidic chip using cold plasma. From reference documents on Glucose concentration in test samples from patients and normal people, we investigated the response of paper electrodes with a range of Glucose concentrations in the sample from 0.1 mg/mL to 1 mg/mL. The color intensity index after the reaction is read through processing software on the phone to provide accurate results to the user. The color intensity and result graph are shown in Fig. 8 and 9.

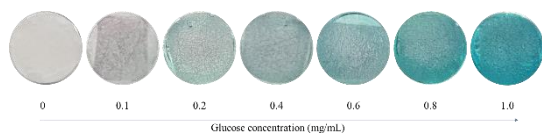


Figure 8. Color reaction at different Glucose concentrations

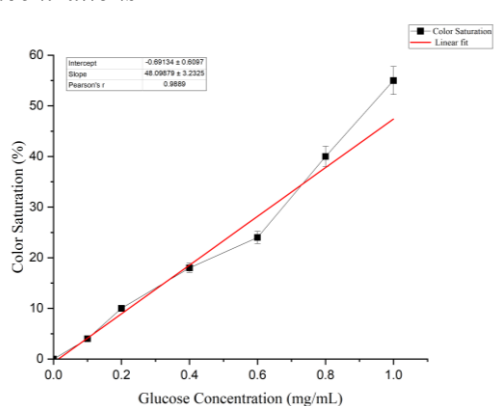


Figure 9. Graph of color intensity versus Glucose concentration

Figure 10 below is the results of the experiment comparing using and not using AuNPs. AuNPs particles help stabilize and preserve color. When not using AuNPs, the color of the reaction quickly changed from blue to yellow when tested at low Glucose concentrations. When additional AuNPs were used, test experiments showed that the color intensity value could be read after 1 hour of reaction without changing the results. Thanks to that, AuNPs bring great advantages by helping users be more flexible in the process of using and reading test results.

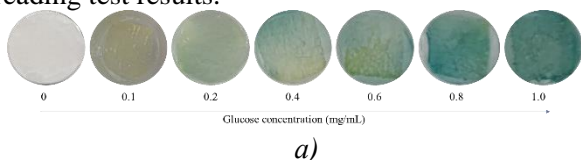


Figure 10. Color reaction at different Glucose concentrations without AuNPs

CONCLUSION

We have created a microfluidic chip device with a structure that can passively collect sweat by applying it to locations on the skin. This microfluidic chip is combined with a paper electrode as a colorimetric sensor used to identify Glucose in sweat samples with a concentration range of 0 - 1.0 mg/mL. The biggest advantage of this device is good sensitivity, stable operation, low price, ease of use and safety for users because it only uses biological ingredients and only contacts the skin surface during the process. Non-invasive testing (using sweat samples) will not bring pain to the patient during the sample collection process. Fast reaction time and clear, long-lasting display colors help patients easily monitor results, which is also a great advantage compared to other non-invasive testing devices. The isolated structure of the reaction chambers also helps test many other factors in the sweat sample at the same time, bringing a lot of potential to exploit and develop the device's application for many other purposes in the future.

Acknowledgement

All authors are grateful for the financial support from ministry-project level 01.M04.2022.

References

- [1] P. Tichá, et al., *Fiber reinforced concrete: Residual flexure strength enhancement using surface modified fibers*. In *Special Concrete and Composites 2020: 17th International Conference*, AIP Publishing: College Park, MD, USA, **2322** (2021) 020-030.
- [2] M. Steinerova, et al., *Human osteoblast-like SAOS-2 cells on submicron-scale fibers coated with nanocrystalline diamond films*, *Mater. Sci. Eng. C* **121** (2021) 111792.
- [3] M. Domonkos, P. Demo, A. Kromka, *Nanosphere Lithography for Structuring Polycrystalline Diamond Films*, *Crystals* **10** (2020) 118.
- [4] V. Medvecká, et al., *Preparation and characterization of alumina submicron fibers by plasma assisted calcination*, *Ceram. Int.* **46** (2020) 22774–22780.

THE NOVEL PHOTOLITHOGRAPHY TECHNOLOGY USING UVLED FOR FABRICATING ELECTRONIC COMPONENTS AND MEMS PROCESS

**Nguyen Hoang Quan^{1,*}, Tran Quoc Thanh¹, Truong Hai Yen¹, Huynh Hoang Trung²,
Nguyen Phan Minh Nguyet¹, Ho Thanh Huy¹, Nguyen Van Toan³ and Nguyen Van Hieu¹**

¹ BiSAE Lab, Dept. of Physics and Electronic Engineering, Faculty of Physics – Engineering Physics, VNUHCM- University of Science, Hochiminh City, Vietnam;

² Material Sciences lab, Faculty of Fundamental Science, HCM City University of Education and Technology, Hochiminh City, Vietnam;

³ Ono and Toda lab, Graduate School of Engineering, Tohoku University, Sendai, Japan

*Corresponding author email: nhquan@hcmus.edu.vn

ABSTRACT

In this work, using the photolithography with UVLED for fabricating process of electronic components and MEMS that can be confirmed one of the effective technical solutions. The manufactured a computer-controlled mini photolithography cabinet with a resolution of less than 50 μ m and radiation of 365nm UVLED was used in the fabricating process for over 100 samples of nMOS electrodes and UVLED electrodes to determine the optimal photolithography parameters.

The optimal parameter for fabricating process of these nMOS electrodes were clarified and determined as well as: irradiation time (tex) 45 seconds, rinsing time (tdev) 55 seconds, distance between emission source and mask (h) 10 cm, intensity for UV LED emission (I) 50 mA and irradiation angle (θ) 0 degree. The shapes of electrodes are verified through SEM imaging indicated that the achieving high definition with the smallest size of 8 μ m for the structure of nMOS. We also succeeded in designing and fabricating UVLED electrodes with the smallest dimensional material size reaching 120 μ m by SEM measurement [4]. Moreover, the fabricating TEGs was carried out as well as their testing of portable electronic devices ‘s application [5]. This uvled photolithography technology will be used for the fabrication of electrodes in future biosensors and MEMS collaborative projects.

Keywords: Photolithography, UVLED, nMOS, Electrodes, MEMS.

INTRODUCTION

Fabrication of thin film layers, photolithography and etching processes are very important steps that determine the quality of performance of chips, sensors, electronic components, and MEMS as IC designed from the researchers and their efficiency of fabrication in industry [1-3]. Therefore, photolithography process must be done as a patterning process that uses light to transfer a pattern from a mask to a photosensitive polymer layer. Then, patterns can either be etched into the underlying surface or used to define the patterning of a layer deposited onto the masked surface. However, we must understand that two-dimensional process can be repeated numerous times to fabricate various structures and devices. Moreover, if we try to fabricate even smaller features, the fabricating process also must developed such as electron

beam lithography, focused ion beam lithography, and nanoimprint lithography,...

MEMS was developed in the middle of the 20th century that using for built-in acceleration sensors or gyroscopes in smart phones and other devices.

As a movable semiconductor, MEMS technology is used in a wide range of fields such as vehicles / automatic driving, big data, AI, robotics, health care, environment and energy, and the latest relevant technologies emerge in endlessly. It is realizing that a wide range of application-aware product development, such as smart phones upgrades, Internet of things, automatic driving, virtual reality, augmented reality and 5G communications. MEMS market includes areas in sensors (inertia, pressure, microphone, environment, optics, etc.), actuators (ink-jet print heads, microfluidic and RF, etc.), automobiles, household appliances, defense, health care,

communication, aerospace and others. Nowadays, LED and UVLED have been widely used not only in the field of lighting, electronic display devices, but also in the fields of farming, disinfecting surgical equipment, printing confidential documents, and checking mineral composition. , bank ATM card services,... very diverse, convenient and safe. Finally, the photolithography and etching processes are very important steps to getting high quality of performance of chips, sensors and electronic components.

In this work, using the photolithography with UVLED for fabricating process of electronic components and MEMS that can be confirmed one of the effective technical solutions. The manufactured a computer-controlled mini photolithography cabinet with a resolution of less than $50\mu\text{m}$ and radiation of 365nm UVLED was used in the fabricating process for over 100 samples of nMOS electrodes and UVLED electrodes to determine the optimal photolithography parameters.

Here, the following contents were carried out:

(1) Design masks with minimum sizes from $48\mu\text{m}$ down to $1\mu\text{m}$ for nMOS electrode photolithography process.

(2) Using computer-controlled UV LED irradiation lithography technology to perform irradiation from 20 seconds to 60 seconds and rinsing time from 20 seconds to 70 seconds to determine 2 optimal times for nMOS photolithography process.

(3) Perform over 100 nMOS and UVLED samples for photolithography, coating, etching processes and check electrode shape quality through microscope and SEM to evaluate and determine optimal photolithography parameters.

(4) Fabrication of UVLED electrodes on wafers with UVLED structure, cutting, wire bonding, packaging and PL measurement for emission wavelength, emission stability through IV curves.

EXPERIMENTAL

1.The design of mask parttens

For nMOS electrodes, 03 types of masks were designed for the electrode fabrication process with designed dimensions and simulated nMOS structure (which the research team had previously made using Layout Editor software. Shape mask and mask size parameters are shown in Fig. 1 and Table 1.

For Mask#1 with pairs of length (a) and width (b) dimensions as shown in table 1: (48,40),

(24,20), (12,10) and (6,5) with units is μm . Similarly for Mask #2 with 03 parameters (a, b, c). For mask #3 only a parameter.

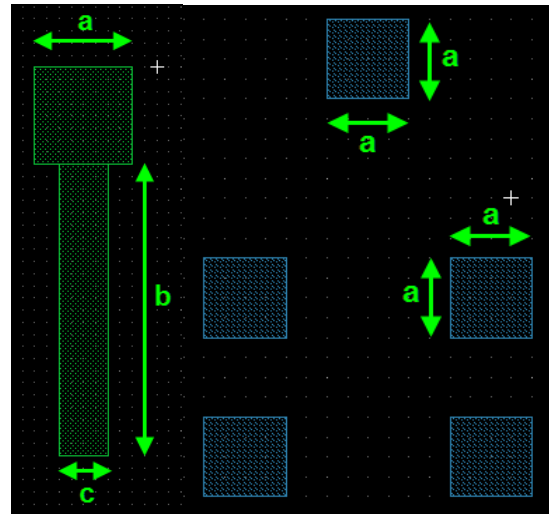


Fig. 1. Two in 3 designed masks (#2,#3) for nMOS electrodes.

The Table 1 shows the dimensions for mask#1, mask#2 and mask#3 with their unit of μm for a,b,c dimensions.

Table 1. The dimensions for Mask#1, Mask#2 and Mask#3.

Type of mask	Dimension a (μm)	Dimension b (μm)	Dimension c (μm)
Mask #1	48	40	none
	24	20	
	12	10	
	6	5	
Mask #2	16	48	8
	8	24	4
	4	12	2
	2	6	1
	1	5	0.5
Mask #3	8	none	none
	4		
	2		
	1		

In the case study for the mask for UVLED electrodes, it includes many masks for one fabrication on the wafer according to the determined size and structure (see Fig. 2).

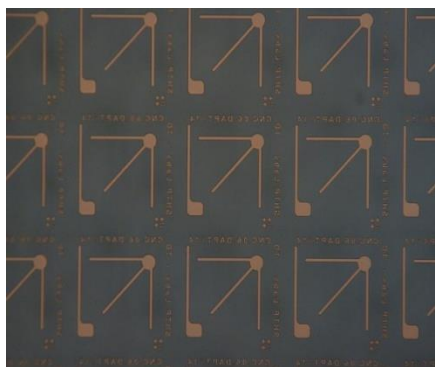


Fig. 2. The designed electrodes of UVLED 385nm for photolithography process.

2. Photolithography process



Fig. 3. The mini photolithography device at BiSAE lab (VNUHCM - University of Science, VNUHCM) for the mask aligner.

For the advantages of UVLED compared to UV lamp, this study used 18 UVLEDs with 02 types of 1W and 5 epiled LED chips of 3W type with the same wavelength of 365 nm. The UVLEDs are arranged close and in a certain order so that the light intensity is evenly distributed when irradiated. The mini photolithography device at BiSAE lab was controlled for the lighting time and the number of illuminated UVLEDs input via the computer connection interface. The 3 real masks for photolithography process of nMOS electrodes are in Fig.4.



Fig. 4. Three real kind of masks for nMOS electrodes.

The photos of fabricated electrodes of nMOS and UVLED 385nm using the photolithography with UVLED for fabricating process of electronic components and MEMS that can be shown in the next part.

RESULTS AND DISCUSSION

In this section, we experiment to determine the optimal irradiation time and rinsing time for the nMOS process. The time of irradiation on the sample affects the radiation energy irradiated on the sample. We investigated the irradiation process with 1cmx1cm silicon substrate samples coated with copper material, and coated with a positive photoresist layer at a high speed of 4000rpm/50s from a spin coating machine as well as a soft bake process. sample for 60s at 100°C.

With the same irradiation conditions of the radiation source, the radiation energy projected onto the sample is proportional to the irradiation time. Experiment with a rinsing time of 60 seconds, set the input parameters for UV LED irradiation time from 20 seconds to 60 seconds (as Table 2) to investigate the photolithography quality of 8 samples for Mask 2. Reason Do not choose Mask 1 as large size, Mask 3 as small size and both have simple square shapes. Mask 2 has 3 important size parameters that need to be investigated to choose optimal conditions when manufacturing.

Conditions for investigating the irradiation time of samples are as follows: Distance between UV source and substrate sample: $h = 10$ cm; Incident angle of the irradiated ray to the sample: $\theta = 0^\circ$; The current through the UV emitter is $I=50$ mA. The irradiation time of sample T01 to T08 are shown in Table 2.

Table 2. The irradiation time, t_{ex} (second) of 8 samples for nMOS electrodes.

Type of sample	The irradiation time, t_{ex} (second)
T01	20
T02	30
T03	35
T04	40
T05	45
T06	50
T07	55
T08	60

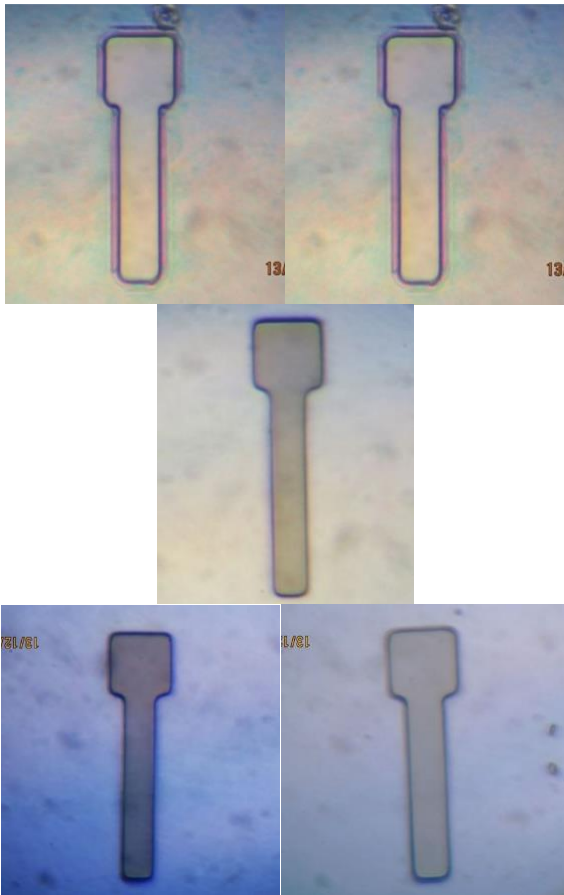


Fig. 5. The SEM of nMOS electrodes by photolithography UVLED for 20, 30,40,50 and 60 seconds irradiation time (mask#2), respectively.

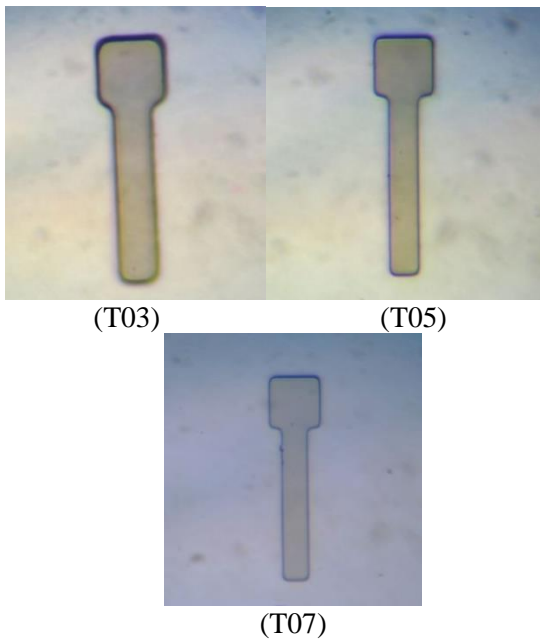


Fig. 6. The SEM of nMOS electrodes by photolithography UVLED for 35, 45 and 55 seconds irradiation time (mask#2) as T03, T05 and T07.

Observing the microscope (Fig.5 and Fig.6), sample T01 still has photoresist, samples T02 to T04 have not sharp edges, indicating that there is a gradient between the photoresist and the wafer, samples T06, T07 and T08 have exposed structures beyond the limit. should be deeply penetrated into the structure. Meanwhile, model T05 has the sharpest quality. Performing a total of 60 successful samples for evaluation, an irradiation time of 45 seconds is good for photolithography.

Next, the rinsing time for the nMOS process also studied for 10 sample of electrodes as sample T09 to sample T18.

Continuing the experiment when irradiating UV LED for 45 seconds, how long will the rinsing time be optimal for photolithographic nMOS electrode sample sizes. Finding the appropriate rinsing time for each sample with different thickness and irradiation time is essential for samples in the photolithography process. Survey the sample rinsing time for masks #2 with UV irradiation time of 45 seconds as shown in Table 3.

Table 3. The survey rinsing time for masks #2 for 10 samples of nMOS electrodes.

Type of sample	The rinsing time for masks #2 (s) t_{dev}
T09	20
T10	30
T11	35
T12	40
T13	45
T14	50
T15	55
T16	60
T19	65
T18	70

Photo of the washing results of sample of fabricated nMOS electrodes with irradiation time (tax) of 45s and rinsing time (tdev) of 20s, 30s, 35s, 40s, 45s, 50s, 55s, 60s, 65s, 70s using Photolithography equipment with UVLED 365nm (see Fig. 7 in below).

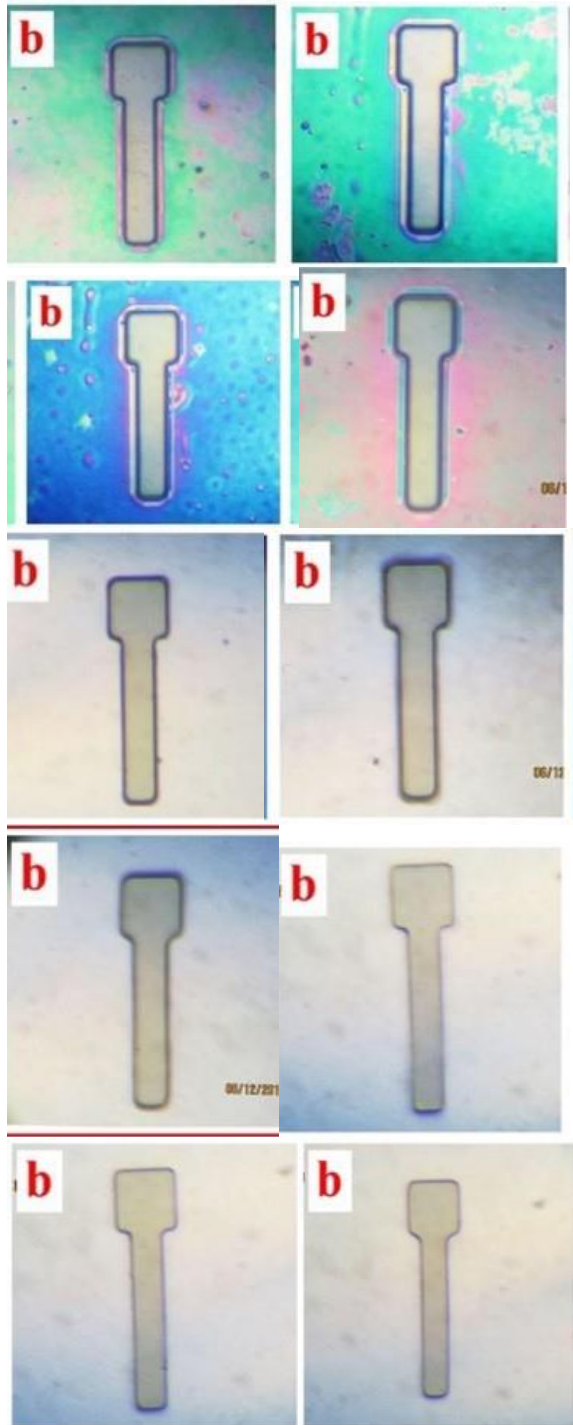


Fig. 7. The shape of the nMOS electrode was photoetched and etched with 10 samples of UV light irradiation for 45 seconds and variable washing time (from 20 seconds to 70 seconds) mask type #2.

Survey of 80 images for 10 samples (T09 to T18) of nMOS electrodes are shown in Fig.7 in below:

(1) Corresponding to samples with rinsing time from 20s to 70s, there is a change in speed.

The later samples are cleaner of the photosensitizer. The structure of the details becomes clearer; (2) The parts that need to be manufactured have different sizes and shapes, so the rinsing time is also different. For large parts such as sample a (with size set 16 μ m; 48 μ m; 8 μ m) and sample b (with size set 8 μ m; 24 μ m; 4 μ m), if the soaking time is a little longer, the part will be corroded by rinsing agent is negligible, the time for clear images is from 40s to 65s.

But for small details, samples b, c, d, it can lead to the structure being completely washed away, especially for sample c (with set sizes 4 μ m; 12 μ m; 2 μ m) with time. Rinsing time from 55s to 60s gives clear images, but samples c, d, e corrode quickly after 50s. Therefore, the smaller the structure, the more accurate the rinsing time is.

Moreover, the samples made in this photolithography system are verified through SEM imaging (at the Semiconductor Laboratory, Center for Research and Development - SHTP) achieving high definition when the smallest size of the nMOS part is 8 μ m. The research team succeeded in manufacturing a photolithography cabinet and conducted effective initial experiments on photolithography and corrosion parameters for our UVLED project (Fig. 3 and Fig.4) and sensor structures.

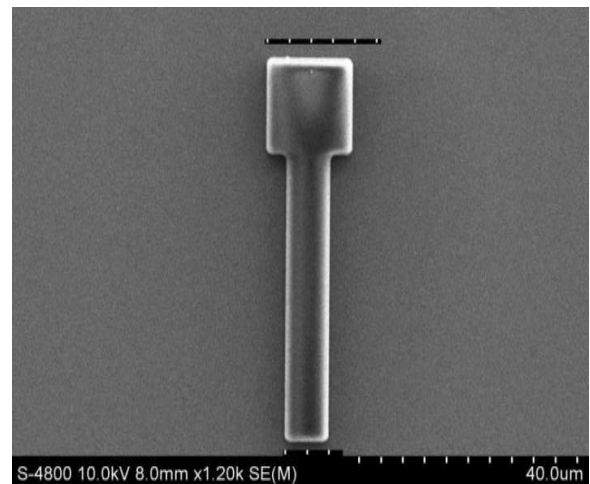


Fig. 8. The SEM of nMOS electrodes by photolithography UVLED for 45 seconds irradiation time (mask#2).

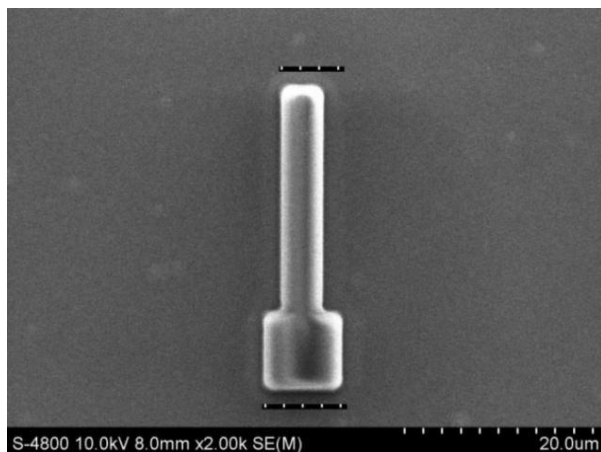


Fig. 9. The SEM of nMOS electrodes by photolithography UVLED for 55 seconds irradiation time (mask#2).

For the fabrication of UVLED electrodes like the mask of Figure 3 above, using similar experiments with UVLED source irradiation parameters of 365nm for photolithography time of 45s and sample washing time of 55s, the electrode images in sapphire substrate wafer, the result is very clear and the smallest size is from 150 μ m (see Fig.10 below). These below UVLED electrodes were fabricated in 2inch wafer with UVLED chip inside.

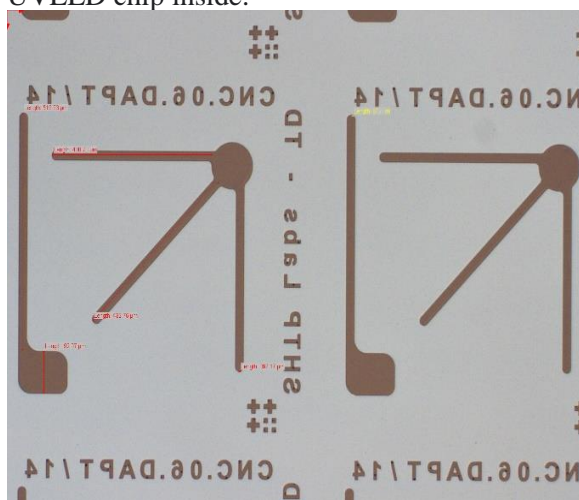


Fig. 10. The fabricated 365 nm UVLED electrodes.

UVLED electrodes were successfully fabricated on a 2-inch wafer and die and packaged to test some luminescence parameters and IV characteristics (as Fig.11). These results will be presented in another study.

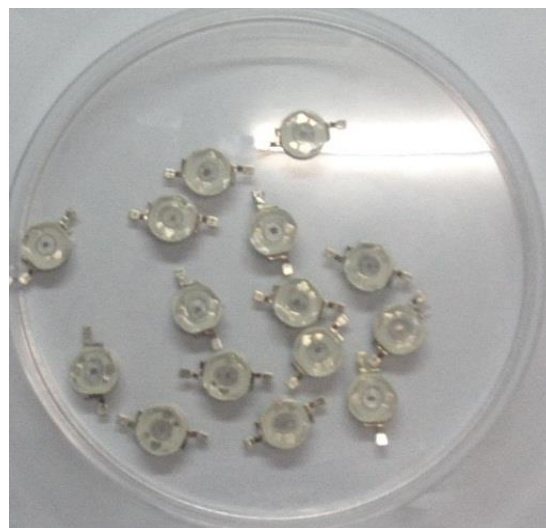


Fig. 11. The packaged 365 nm UVLED devices for PL measuring and testing applications.

CONCLUSION

Base on the above information, there are some conclusions for this work:

(1) The optimal parameter for fabricating process of these nMOS electrodes were clarified and determined as well as: irradiation time (tex) 45 seconds, rinsing time (tdev) 55 seconds, distance between emission source and mask (h) 10 cm, intensity for UV LED emission (I) 50 mA and irradiation angle (θ) 0 degree. The shapes of electrodes are verified through SEM imaging indicated that the achieving high definition with the smallest size of 8 μ m for the structure of nMOS.

(2) We also succeeded in designing and fabricating UVLED electrodes with the smallest dimensional material size reaching 120 μ m by SEM measurement [4]. Moreover, the fabricating TEGs was carried out as well as their testing of portable electronic devices 's application [5].

(3) This UVLED photolithography technology will be used for the fabrication of electrodes in future biosensors and MEMS collaborative projects.

The successful trial and manufacture of nMOS and UVLED electrodes using 365nm UVLED photolithography technology is an important technical step in the process of manufacturing biological sensors, MEMS, and other electronic components in our next works and others.

Acknowledgments

The research team would like to thank the funding from the University of Natural Sciences,

Vietnam National University-HCM (Code T2019-10) for this work.

We would like to thank the enthusiastic support of the professors of Ono and Toda lab (Tohoku University, Japan) for their comments and sharing many experiences about MEMS technology.

Acknowledging the contributions of members at BiSAE lab who supported the fabrication of photolithography equipment used for this work, and scientists from SHTP labs who supported SEM measurements. The author would like to respectfully acknowledge the opinions of scientists who have discussed and commented to help improve the quality of this report. We would like to thank the authors whom this article has referenced and cited.

References

- [1] Daniel R. Hines, Nathan P. Siwak, Lance A. Mosher and Reza Ghodssi: Book: *Lithography and Micromachining Techniques*, Part of the MEMS Reference Shelf book series MEMSRS, volume 1) (online, Jan 2011).
- [2] Yo-Sheng Lin, Guo-Hao Li, Nguyen Van Hieu, *A 75–85GHz Down-conversion mixer with integrated marchand baluns in 90 nm CMOS with excellent matching and port-to-port isolation for automotive radars*, Microwave and Optical Technology Letters, **57**(1) (2015) 73-80, <https://doi.org/10.1002/mop.28774>
- [3] Jaeger, Richard C., *Introduction to Microelectronic Fabrication (2nd ed.)*. New Jersey: Upper Saddle River: Prentice Hall, 2002.
- [4] Nguyen Van Hieu, Ho Thanh Huy, Nguyen Hoang Quan,... ,Nguyen Ngoc Dao: *Fabricating technology process of UVLED chips and devices project in SHTP*, MOST (2014-2017).
- [5] Nguyen Van Toan, Truong Thi Kim Tuoi, Nguyen Van Hieu and Takahito Ono. (Apr. 2021), *ThermoElectric Generator with a high integration density for portable and wearable self-powered electronic devices*, Energy Conversion and Management **245** 114575, <https://doi.org/10.1016/j.enconman.2021.114571>.

ADVANTAGES OF MICROWAVE RADIATION IN SYNTHESIS OF SUBMICRON ZEOLITE Y

Tam Minh Le, Nhung Thi Tran

Ho Chi Minh City University of Technology and Education, Linh Chieu Ward, Thu Duc City, Ho Chi Minh City, Vietnam;

Email: tamlm@hcmute.edu.vn

ABSTRACT

Zeolites have a wide range of applications that promotes innovative development of more efficient synthesis methods. Besides the conventional hydrothermal synthesis, utilizing microwave radiation is a promising alternative. Our recent research has demonstrated the progress in zeolite synthesis under microwave radiation, with zeolite 4A serving as a case study. In comparison to the conventional hydrothermal method, the novel approach required an extremely short time. The same technique was applied in this work for synthesis zeolite Y. To verify the formation of this zeolite type, various analyses including XRD, FTIR, and SEM were examined that showed a good agreement between the two approaches in production of zeolite type Y. Furthermore, beyond the time efficiency, the quality of the product in the case of microwave-assisted synthesis was found to be significantly superior to the conventional method. Lastly, we compared both materials in terms of their ability to adsorb methylene blue, a model compound representative of dye-polluted wastewater. The results obtained were impressive for the microwave-assisted synthesis, which consistent with porosity analysis via and BET measurement. The achievement suggested high potential for industrial-scale applications of zeolite Y synthesized under microwave radiation.

Keywords: zeolite Y, microwave-assisted synthesis, adsorption, methylene blue, submicron particles

INTRODUCTION

Accompanying the development of current industries, environmental impacts have become increasingly pronounced, in particular matters of pollution in wastewater sources caused by organic colorants. These contaminants were resulted from a variety of sources, including plating facilities, inorganic dye production, as well as textile and dyeing factories. To address the aforementioned challenges associated with wastewater, numerous techniques for removing these pollutants have been thoroughly investigated. These methods encompass reduction and precipitation, coagulation, lime softening, adsorption, ion exchange, reverse osmosis, and other methods [1-3]. Notably, adsorption onto solid substrates is the favored approach due to its notable efficiency, ease of management, and cost-effectiveness [4]. Within the realm of industrial adsorbents, substances such as activated carbon, activated alumina, clay, and zeolite are commonly employed. Synthetic zeolites, in particular, find wide utility in sectors such as detergent production and water softening, thanks to their substantial ion exchange capacity, mechanical robustness, and distinctive crystal structure.

Furthermore, zeolite stands out for its environmental friendliness and minimal ecological impact [5]. Among these options, zeolites are widely preferred, primarily because the raw materials required for their synthesis are cost-effective, including substances like kaolin and rice husk ash, which yield significant economic advantages. In contrast to activated carbon, silica gel, and other inorganic adsorbents, zeolite a crystalline structure with a precisely uniform molecular-sized pore system, endowing it with the unique ability to selectively adsorb substances with a high adsorption capacity – a major characteristic of zeolites [6].

Zeolite Y belongs to the faujasite family of zeolitic materials. Each basic lattice cell of zeolite Y contains 192 SiO_4 and AlO_4^- tetrahedra, the total number of oxygen atoms is 384. Zeolite Y was first discovered by Breck (Carbide company) in 1964 [7]. The current work focused on the synthesis of zeolite Y from two different crystallization techniques, including the hydrothermal and microwave-assisted methods.

EXPERIMENTAL

Kaolin in Lam Dong province (Vietnam) was used as a raw material. Distilled water was prepared from a Milli-Q ultrapure water system. Other used chemicals originated from Sigma-Aldrich (Germany) such as NaOH, Na₂SiO₃·9H₂O, AlCl₃·6H₂O. Methyl blue (C₆H₁₈ClN₃S·3H₂O) was purchased from Merck (Germany). Kaolin was heated at 900 °C for 2 hours to break down the structure of kaolin, remove chemical water and convert kaolin to metakaolin (Al₂Si₂O₇).

Regarding to preparation procedure, gels were prepared according to the following ratio of 15Na₂O:Al₂O₃:15SiO₂:450H₂O. First, NaOH was dissolved in water with pre-calculated amounts. Then, metakaolin was added into the above solution and the suspension was stirred for 5 minutes without heating. Then, AlCl₃·6H₂O were added into the beaker containing the NaOH and metakaolin solution while remaining good stirring conditions to form a homogeneous gel. Aging the gel by continuous stirring at room temperature for time 48 hours. Then, these gels were used to synthesis zeolite Y utilizing the two methods, i.e. the conventional hydrothermal and the microwave assisted syntheses with two products abbreviated as Y-HT and Y-MW, respectively. The first crystallization method was carried out in an autoclave at 100 °C for 9 hours. In the second method with microwave assistance, the gel mixture after aging was put into a Teflon reactor with a screw cap. Carrying out crystallization in a microwave oven at a frequency 2.45Hz, a power 800W for 6 minutes. In both methods, after crystallization, the reactors were naturally cooled down to the room temperature. The products after syntheses were vacuum filtered and washed with abundant amounts of distilled water to neutral pH. After drying at 60°C for 10 hours, zeolite Y crystals were obtained for the next investigation.

Absorption of methylene blue: 0.2g of zeolite was add into 100 ml of methylene blue solution with a concentration of 5 mg/l. Magnetically stir without heating the above suspension solution was kept for various time intervals. Then, the zeolite suspension after adsorption was filtered with a 0.22 μm filter and placed into a UV-Vis absorption spectrophotometer to determine the residual MB concentration.

RESULTS AND DISCUSSION

Raw material composition

As seen in Table 1, XRF showed that to prepare a gel with the ratio of

15Na₂O:Al₂O₃:15SiO₂:450H₂O, the reactant composition required an compensation of aluminum. Thus, Al₂O₃ need to be added, herein, the supplement of aluminum was fed with a calculated amount of AlCl₃·6H₂O.

Table 1. Chemical composition of calcinated kaolin via XRF determination

oxide	Comp.,%	oxide	Comp.,%
SiO ₂	56.26	MgO	0.08
Al ₂ O ₃	42.55	Na ₂ O	0.09
TiO ₂	0.18	CaO	0.03
Fe ₂ O ₃	0.24	K ₂ O	0.56

Solid phase analysis

As seen in the Fig.1a, the XRD patterns of the two samples Y-MW and Y-HT have the same diffraction patterns and those were also coincide with the picks in the standard spectrum of zeolite Y. Specifically, the positions of the 2θ angles of the diffraction picks at 6.2, 10.1, 11.9, 15.6, and 23.6°, corresponding to the (111), (220), (311), (331), and (533) faces, respectively. Thus, with the above synthesis conditions, Y-type zeolites were successfully synthesized from two different crystallization methods. This conclusion gained a good agreement with FTIR analysis which was shown in Fig.1b. In the IR spectrum of the synthesized zeolite Y samples, there are spectral clusters in the ~ 560 cm⁻¹ region that are attributed to the TO4 tetrahedral outer bond vibrations of the 6-membered double ring, their intensity is very sensitive to the zeolite crystal phase Y. Specifically, the properties of zeolite Y are also shown in areas such as: 447, 564 and 682 cm⁻¹. According to Huo et. al [8], the oscillation at 447 cm⁻¹ is related to asymmetric bending and narrowing of the Si-O or Al-O bond, while the oscillation at 564 cm⁻¹ is attributed to the narrowing of the double ring inside the tetrahedral structure. The spectrum in the 682 cm⁻¹ region is due to the symmetric stretching of the bonds within the tetrahedron T-O-T. Thus, instead of consuming 9 hours in the hydrothermal synthesis pathway, microwave radiation can significantly reduce reaction time to 6 minutes to produce zeolite Y with the same initial conditions such as composition, aging, post-processing.

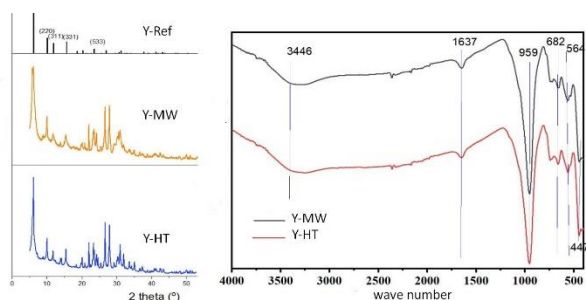


Figure 1. XRD and FT-IR spectra of Zeolite Y.

SEM analysis

Fig. 2 presents the SEM results of two zeolites Y-type with the same magnification for comparison purpose, both Y-MW and Y-HT samples have not only relatively uniform size but also high crystallinity. Furthermore, they tended to form larger agglomerates as secondary particles. Obviously, the obtained crystals in the case of microwave assisted synthesis (Fig. 2a) were much smaller than those resulted from the conventional hydrothermal method (Fig. 2b). Further primary particle size comparison was required that was conducted via dynamic laser scattering analysis (DLS). These two samples were treated under ultrasonic treatment at 60 °C for 60 mins before performing DLS analysis.

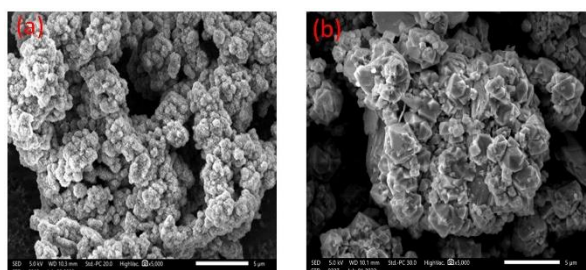


Figure 2. SEM images of Zeolite Y synthesized via (a) microwave assisted synthesis and (b) the conventional hydrothermal method.

The average size of the Y-MW sample was found at 0.642 μm, significantly smaller than the average size of the Y-HT sample, which was recorded at 2.641 μm. These evidences allow to draw a conclusion that microwave assisted synthesis formed homogeneous submicron particles of zeolite Y. Additionally, Si/Al ratios of these two samples were also measured via EDX analysis (as seen in Table 2) that showed the same Si/Al ratio at a nearly equal value of 1.6 for the two samples Y-HT and Y-MW. This ratio belonged to a suitable range of zeolite Y which was normally found from 1.6 to 3.0.

Table 2. DLS, EDX and BET determinations for the two zeolites Y-type.

Properties	Unit	Y-MW	Y-HT
Si composition	[%]	15.42	15.54
Al composition	[%]	9.26	9.17
Ratio of Si/Al	[-]	1.61	1.63
DLS average particle size	[μm]	0.64	2.64
Surface area	[m ² .g ⁻¹]	91.2	75.4
Pore volume	[cm ³ .g ⁻¹]	0.040	0.036
Pore size	[Å]	23.2	23.3

Comparison of Y-HT vs.-MW in MB removal

The zeolites produced through the two above methods were assessed for their ability to treat MB (methylene blue) solutions under the same conditions, including concentration (5 mg/L), temperature (30 °C), pH (7.5). After five-minute intervals, the remaining solutions were filtered and subjected to UV-VIS analysis at a wavelength of λ = 664nm.

As illustrated in Fig. 3, the adsorption kinetics of methylene blue (MB) showed a relatively quick establishment of equilibrium. The adsorption capacity exhibited a rapid increase from the initial stages up to 15 minutes. By the 20-minute, the adsorption capacity had reached a plateau, signifying the establishment of adsorption equilibrium. Notably, it is evident that Y-MW surpasses Y-HT in terms of adsorption capacity. This discrepancy can be attributed to the larger specific surface area achieved through microwave synthesis (91.5 m².g⁻¹), while the hydrothermal Y-HT method results in a smaller surface area (75.4 m².g⁻¹). It is worth noting that both materials share a nearly identical pore size of 23 nm, although the pore volume obtained from the microwave method is larger, with values of 0.0402 cm³.g⁻¹, in contrast to the hydrothermal method with a pore volume of 0.0359 cm³.g⁻¹.

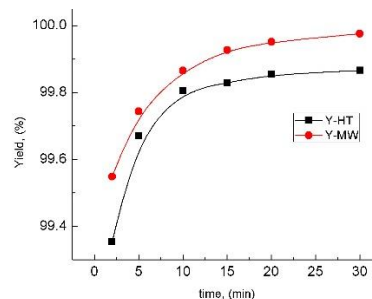


Figure 3: MB removal ability of Y-HT and -MW.

CONCLUSION

In this research, two variations of zeolite Y were synthesized using low-cost raw material, i.e.

kaolin, which provides the essential components of zeolite, namely SiO_2 and Al_2O_3 . The gel formulation was prepared based on XRF analysis to introduce a calculated amount of $\text{AlCl}_3 \cdot 6\text{H}_2\text{O}$ as a compensation aluminum source. To prove the formation and characteristics of zeolite Y-type, we conducted several solid phase analyses including SEM, EDS, DLS, XRD, FTIR, and SEM. Upon examination of the solid phase analysis via XRD, and in comparison to the standard spectrum, it was determined that both crystallization methods yielded the same type of zeolite structure, indicating a high level of crystallization in both cases. Additionally, FTIR analysis confirmed the formation of the Y zeolite samples formed through these two distinct crystallization methods. Furthermore, The SEM and DLS analyses revealed that the samples produced via the microwave method exhibited smaller and more uniform crystal sizes in contrast to the hydrothermal method. This observation serves as compelling evidence of the superior adsorption efficiency of the microwave-synthesized samples compared to those synthesized via the conventional hydrothermal method. Finally, the adsorption equilibrium was relatively quickly established due to kinetics interaction of this zeolite type and MB molecular. For future work, this achievement will support scaling up treatment processes capable for industrial application.

Acknowledgment

BIOGRAPHY



Dr. -Eng. Tam Minh Le. PhD at Max Planck Institute for Dynamics of Complex Technical Systems, Magdeburg, Germany. Postdoctoral research at Vietnam Academy of Science and Technology. Editorial Board Member of JCERU journal. Expertise in the fields of advanced materials, enantiomer separation, crystallization, chromatography, process analytical technology (PAT), chemical and bio-process engineering.



Dr. Nhung Thi Tran. has received a B.E. degree in chemical engineering from Ho Chi Minh city University of Technology, Vietnam, in 2010; a M.E. degree in chemical engineering in Gachon University, Korea, in 2012; and a Ph.D degree in materials science and engineering in Nanyang Technological University, Singapore, in 2017. She is currently a lecturer at Ho Chi Minh city University of Technology and Education, Vietnam.

The authors would like to thank HCMUTE for their supports to carry out this research.

References

- [1] P. Payra, P.K. Dutta, *Zeolites: a primer*, Handbook Zeolite Sci. Technol (2003) 1-19.
- [2] K.D. Mondale, R.M. Carland and F.F. Aplan, *the comparative ion exchange capacities of natural sedimentary and synthetic zeolites*, minerals engineering **8**(4/5) (1995) 535-548.
- [3] Chen N.Y., Garwood W. E., Dwyer F. G. , *Shape Selective Catalysis in Industrial Application*, Marcel Dekker, Inc. New York and Basel (1989).
- [4] L. Ayele, J. P. Pariente, Y. Chebude, I. Diaz, *Microporous Mesoporous Mater*, 215 (2015) 29.
- [5] P. Payra, P.K. Dutta, *Zeolites: a primer*, Handbook Zeolite Sci. Technol (2023) 1-19.
- [6] F. Roozeboom, H.E. Robson, S.S. Chan, *Study on the mechanism of crystallization of zeolites A, X and Y*, Zeolites: Science and Technology, Springer (1984) 127–147.
- [7] D. W. Breck, W. G. Eversole, R. M. Milton, T. B. Reed and T. L. Thom, Chapter 1. *The Properties of a New Synthetic Zeolite, Type A in Crystalline Zeolites* **78** (1956) 5963.
- [8] Huo, X. Xu, Z.Lv, J. Song, M. He, Z. Li, Q. Wang, L. Yan, Y. Li, *Thermal study of NaP zeolite with different morphologies*, J. Therm. Anal. Calorim, (2013) 365-369.

UNDERSTANDING THE PATHWAY OF FREE ELECTRONS AND REACTIVE SPECIES FROM PLASMA INTO THE LIQUID: APPLICATION FOR FABRICATION OF NOBLE METAL NANOPARTICLES AND GRAPHENE QUANTUM DOTS

Van-Phuoc Thai, Tran Ngoc Dam

Faculty of Mechanical Engineering, HCMC University of Technology and Education,
01 Vo Van Ngan, Thu Duc city, Ho Chi Minh City, Vietnam
Email: phuoctv@hcmute.edu.vn

ABSTRACT

Plasma contains a variety of free-charged and reactive radicals. These species are precious for fabricating noble metal nanoparticles and graphene quantum dots in an aqueous solution. However, the physicochemical processes are very complex when these species transfer from plasma into the liquid. They include the reactions between these species in the gas state and the bulk liquid, the diffusion, the shockwave, and more. Understanding the behavior of the processes is essential for broadening the application of plasma in nanofabrication and others. In this work, we presented a summary pathway of some typical species from plasma to bulk liquid, which can be used for the synthesis of noble metal nanoparticles (gold, silver, platinum) and graphene quantum dots.

Keywords: plasma-liquid interaction, reactive species, noble nanoparticles, graphene quantum dots

INTRODUCTION

Noble metal nanoparticles (NMNs) like gold nanoparticles (AuNPs), silver nanoparticles (AgNPs), and platinum nanoparticles (PtNPs) are important in nanotechnology. In a nanoscale, these metal particles present many unique features related to optical, electronic, thermal, and surface properties [1]. Due to these properties, noble metal nanoparticles have been utilized in many applications from catalysis and electrical conductors to biomedicine [2-4]. The common methods for generating NMNs are based on chemical synthesis, in which metal ions are reduced into neutral metal atoms by chemical reducing agents and then aggregated into nanoclusters. The reducing agents are commonly sodium borohydride (NaBH_4) and sodium citrate [4-7]. However, the aqueous NMNs synthesized via the chemical route often remains residual reducing agents (NaBH_4 , sodium citrate), which next interact and cover the surface of synthesized NMNs. This covering strongly affects and would change the properties of NMNs [8].

Plasma-liquid interaction (PLI) has been considered an efficient source for the NMNs synthesis. Plasma contains a variety of free electrons and reactive radicals such as H, O, OH and more [9]. Plasma in contact with liquids

provides these species into the liquid, could be used for NMNs synthesis [10]. For instance, free electrons and H radicals directly reduce metal ions into the metal atoms before growing into a nanoscale. H_2O_2 is also a reducing agent for AuNPs synthesis. The importance is that the synthesized NMNs solution contains no any surfactant that affects the surface properties of synthesized NMNs. It is a crucial advantage that improves and optimizes the ligand-coating process on the surface of NMNs.

Plasma in contact with liquid induces complex physicochemical processes in the plasma-liquid interface [9]. These include the reactions between the reactive species in the gas state and the bulk liquid, the diffusion and convection of species in the liquid, the shockwave from plasma into the liquid, the charge species moving under the electric field. Understanding these behavior is the key to optimize using the PLIs for the NMNs synthesis. This work presented the pathway of free electrons and some reactive species from plasma into the liquid, which can be used as agent for the synthesis of NMNs. Moreover, using PLIs with a possible mechanism for synthesis of graphene quantum dots (GQDs) was also introduced.

THE PATHWAY OF SPECIES FROM PLASMA INTO LIQUID

Free electrons induced in plasma are very active and take a part to interactions with other species in plasma. When plasma contacts with a water liquid, free electrons reacts with water molecules vaporizing from the liquid in forming H, OH, H₂O⁺, H₂O₂ and others (see in figure 1) [9]. All these species next transport into the bulk liquid and distribute to other regions via the diffusion and convection processes.

Solvated electrons

Free electrons, one of a fundamental species in plasma, absorb from the plasma into the liquid and become the solvated electrons (e_{aq}) or hydrated electrons. The solvated electrons are very precious for synthesis of NMNs that e_{aq} directly reduce almost metal ions into the neutral metal atoms. Reactions between e_{aq} with gold, silver, copper, and platinum ion forms with their redox potentials are shown in Table 1 [10]:

The redox potentials of reactions (1)÷(5) are all positive values, so the reduction of metal ions by e_{aq} proceeds spontaneously. The synthesis process of NMNs via e_{aq} from PLIs have well been studied in many works [8-11].

The attention for e_{aq} is the pathway of these species from plasma into the liquid. Firstly, the penetration of free electrons from plasma into the liquid is only in the nm range [12]. Secondly, the lifetime of e_{aq} is in a short period time < 300 μs [12]. In neutral water, e_{aq} can react themselves as reaction (6) with a fast rate constant of 6.0×10⁹ M⁻¹s⁻¹. e_{aq} is a charged species, so the drift distance of eaq in a solution is also affected by the applied electric field from plasma. Thus, the existence region of e_{aq} (figure 1) in liquid is only in the range < 1 μm [10] from the liquid-gas interface.

Table 1: Some important reactions for e_{aq} and their redox potential

Reaction	E ₀ (V)
1) 3e _{aq} + AuCl ₄ ⁻ → Au + 4Cl ⁻	1.0
2) e _{aq} + Ag ⁺ → Ag	0.8
3) 2e _{aq} + Cu ²⁺ → Cu	0.3
4) 2e _{aq} + PtCl ₆ ²⁻ → PtCl ₄ ²⁻ + 2Cl ⁻	0.8
5) 2e _{aq} + PtCl ₄ ²⁻ → Pt + 4Cl ⁻	0.7
6) 2e _{aq} + H ₂ O → H ₂ + 2OH ⁻	-
7) H ₂ O ₂ + e _{aq} + H ⁺ → OH + H ₂ O	1.0
8) H ₂ O ₂ + e _{aq} + H ⁺ → OH + H ₂ O	1.8
9) H ₂ O ₂ + 2OH ⁻ → O ₂ + H ₂ O + 2e _{aq}	0.2

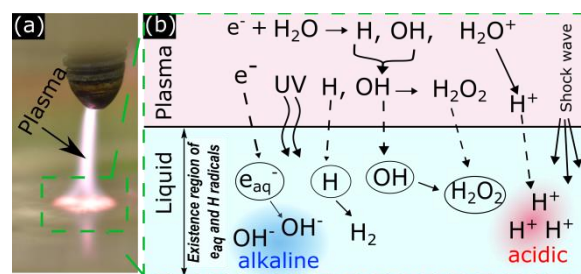


Figure 1. (a) Photo of a PLIs. (b) Transfer of free electrons and other reactive species from plasma into the liquid.

Hydrogen peroxide (H₂O₂)

The interaction of free electrons and vapor water molecules in the plasma-gas produces much OH radicals “e + H₂O → H + OH”. These OH radicals then combine into H₂O₂ as “OH + OH → H₂O₂” [13]. H₂O₂ features a high Henry constant of 9.1×10² mol m⁻³ Pa⁻¹ [13] so that easily absorb into the bulk liquid (figure 1). Unlike e_{aq}, H₂O₂ has a long lifetime and non-charged. Hence, H₂O₂ can stay everywhere in the liquid. H₂O₂ could be an oxidizing and also reducing agent, which dependent on the reaction and redox potential (Reactions 7-9 in Table 1). In most case, H₂O₂ is an oxidizing agent that oxidize silver, copper, and other into a higher oxidized state. In a basic solution, H₂O₂ plays a reducing agent that can reduce gold ions into gold neutral atoms in AuNPs synthesis [13].

Extremely acidic and alkaline region

The interaction between free electrons and water molecules in plasma is fast [9]. Consequently, the produced reactive species and ions (H⁺, OH⁻) in plasma are massively generated in a short time [9]. These species directly absorb into the bulk liquid and concentrate in a small region below the plasma-liquid interface. Meanwhile, the convection and diffusion of these species and other ions (H⁺, OH⁻) in a liquid are low speeds of ~ cm.s⁻¹ and ~ 10⁻⁵ cm².s⁻¹, respectively [9,13]. Therefore, the concentration of species and other ions in the region near the plasma-liquid interface is high. In addition, there is also the irradiation of UV lights and shockwave from plasma onto this region. This condition accelerates the dehydration process of carbohydrate molecules available in the region that form graphene quantum dots (GQDs). The synthesis of GQDs via the PLIs has increasingly been investigated [14-16].

CONCLUSION

Plasma-liquid interactions provide a variety of free electrons and reactive species in the liquid. These are precious materials for synthesizing many noble metal nanoparticles. However, solvated electrons (the main reducing species) are only available in a small region below the plasma-liquid interface when free electrons penetrate the bulk liquid. For successful synthesis of NMNs, metal ions should be carried to this residing region of solvated electrons with enough concentration. H₂O₂, an important product of PLIs, is also a reducing agent for AuNPs. However, this process should proceed in an alkaline condition.

Concentrating reactive species and ions with UV irradiation and shockwave from plasma in a small region induce an extreme region below the plasma-liquid interface. It accelerates the dehydration process of carbonate molecules and other that produce graphene quantum dots. It is crucial that GQDs can be synthesized in a condition at atmospheric pressure and ambient temperature. That is much advantageous compared with conventional methods, in which GQDs synthesized in a high temperature and high pressure condition.

Acknowledgment

Van-Phuoc Thai was funded by the Postdoctoral Scholarship Programme of Vingroup Innovation Foundation (VINIF), code VINIF.2023.STS.66.

References

- [1] Z. Zhang, P.C. Lin, *Noble metal nanoparticles: Synthesis, and biomedical implementations*. Elsevier, (2018) 177-233.
- [2] V. Amendola and et. al., *Surface plasmon resonance in gold nanoparticles: a review*, Journal of Physics: Condensed Matter 20 (2017) 203002.
- [3] J. Kim and et. al., *Effects of a potent antioxidant, platinum nanoparticle, on the lifespan of Caenorhabditis elegans*. Mechanisms of ageing and development, 129 (6) 322-331.
- [4] L. Xu and et. al., *Silver nanoparticles: Synthesis, medical applications and biosafety*. Theranostics 10.20 (2020) 8996.
- [5] M. Brust and et. al., *Synthesis of thiol-derivatised gold nanoparticles in a two-phase liquid-liquid system*, J. Chem. Soc., Chem. Commun, (7) 1994 801-802.
- [6] E. Ramirez and et. al., *Shape control of platinum nanoparticles*, Advanced Functional Materials 17.13 (2007) 2219-2228.
- [7] J. Turkevich and et. al., *A study of the nucleation and growth processes in the synthesis of colloidal gold*, Discussions of the Faraday Society 11 (1951) 55-75.
- [8] V.P. Thai and et. al., *Precise size-control and functionalization of gold nanoparticles synthesized by plasma-liquid interactions: using carboxylic, amino, and thiol ligands*, Nanoscale Advances 4.21 (2022) 4490-4501.
- [9] P.J. Bruggeman and et. al., *Plasma-liquid interactions: a review and roadmap*, Plasma sources science and technology 25.5 (2016) 053002.
- [10] V.P. Thai and et. al., *The essential role of redox potential/equilibrium constant in the ability of non-equilibrium plasma for nano-synthesis in liquids*, Journal of Applied Physics 128.4 (2020).
- [11] Q. Chen and et. al., *A review of plasma-liquid interactions for nanomaterial synthesis*, Journal of Physics D: Applied Physics 48.42 (2015) 424005.
- [12] J. Meesungnoen and et. al., *Low-energy electron penetration range in liquid water*, Radiation research 158.5 (2002) 657-660.
- [13] V.P. Thai and et. al., *Effect of voltage polarity and supply frequency on the properties of plasma contacting liquid electrodes and gold nanoparticle synthesis*, Plasma Sources Science and Technology 31.1 (2022) 015006.
- [14] D. Kurniawan and et. al., *Plasma-Enabled Graphene Quantum Dot Hydrogels as Smart Anticancer Drug Nanocarriers*, Small 19.20 (2023) 2206813.
- [15] D. Kurniawan and et. al., *Plasma-bioresource-derived multifunctional porous NGQD/AuNP nanocomposites for water monitoring and purification*, Chemical Engineering Journal 451 (2023) 139083.
- [16] Y. J. Yeh and et. al., *Plasma-enabled graphene quantum dot-based nanofiltration membranes for water purification and dye monitoring*, Journal of Membrane Science 670 (2023) 121334.

THE ANTIFUNGAL EFFICIENCY AGAINST *Rhizoctonia solani* CAUSING THE COLLAR ROOT ROT DISEASE ON *Brassica integrifolia* OF AgNPs@DA PREPARED BY γ -IRRADIATION

Le Quang Luan, Tran Duc Trong, Nguyen Thi Ngoc Anh, Ngo Tran Vu, Phan Le Tram Anh, Nguyen Trong Nghia, Nguyen Thanh Vu

Biotechnology Center of Ho Chi Minh City, 374, Highway 1, Trung My Tay Ward, District 12, Ho Chi Minh City, Vietnam.

Email: lequangluan@gmail.com

ABSTRACT

In this study, the silver nanoparticles (AgNPs) doped on diatomite (AgNPs@DA) were prepared by γ -irradiation technique and evaluated *in vitro* antifungal efficiency against *Rhizoctonia solani* causing the collar root rot disease on *Brassica integrifolia*. The results indicated that the increase of supplementation of product concentration into PGA medium increased the fungicidal efficiency of AgNPs against *R. solani*. Particularly, at the treatment of 10 ppm, its fungicidal efficiency was found about 57.0%, and the growth of *R. solani* was completely inhibited by the addition of 30 ppm AgNPs after cultivation for 40 hrs. In addition, the *in vivo* effectiveness of this product for preventing and treating the collar root rot disease (Rhizoctonia disease) caused by *R. solani* fungus on *B. integrifolia* was also investigated. The results showed that the treatment of 2 ppm of AgNPs reduced the disease incidence to about 15.56% compared to 84.44% in the untreated control. At the treatment of 10 ppm AgNPs, all plants were not infested after 12 days of infection. The *in vivo* elimination test after 6 treatment days also revealed that the treatment of 30 ppm AgNPs significantly reduced the disease incidence (to about 4.44%) compared to that of the untreated one (about 82.22%). While after 12 days treating with 10 ppm AgNPs, almost the infested plants were completely recovered. Thus, the AgNPs@DA has a potential to produce natural biological fungicides with safety for farmers and high efficiency in preventing as well as eliminating fungal diseases for vegetables production.

Keywords: *Brassica integrifolia*, *Rhizoctonia solani*, Rhizoctonia disease, Silver nanoparticle, Diatomite

INTRODUCTION

According to statistical data for the Ho Chi Minh City Department of Agriculture and Rural Development, in the first 6 months of 2023, the area planted with vegetables plantation in Ho Chi Minh City is about 10,622 hectares, accounting for 16.4% of the total agricultural production area of the entire city. Although only occupying a small space, the output reached 265,760 tons, increasing 4.1% over the same period and serving 33.3% of vegetable demand across the city [1]. However, vegetable growers are now facing many difficulties due to the spread of many diseases by microorganisms. Among them, the collar root rot disease caused by *R. solani* is now seriously affecting vegetable growth and yield. The disease usually occurs in monoculture with high humidity, causing a “damping off” symptom [2]. Moreover, a key survival structure for *R. solani* is sclerotia, compact masses of hardened fungal mycelia with

1-3 mm in diameter containing food reserves that are formed in response to stress, unfavorable growth conditions [2]. The broad host range and the ability to form sclerotia of *R. solani* make this pathogen very difficult to control. Nowadays, growers often use many chemical fungicides that cause environmental pollution and have a negative impact on vegetable quality.

As one kind of non-antibiotic, AgNPs could provide a novel solution for the above problems. AgNPs are widely proven to exhibit excellent antimicrobial activity against various pathogens, including bacteria, fungi, and viruses [3]. Behara et al. (2022) [4] and Nejad et al. (2017) [5] reported that AgNPs had a strong inhibition effect on the growth of *R. solani* causing the maize to sharp eyespot and the rice sheath blight diseases. Additionally, the study of Xiao et al. (2023) [6] demonstrated that AgNPs were safety for human use and had potential applications in various fields. Silver nanoparticle products are primarily

available in solution form, which is may unsuitable for prolonged use in farming and aquaculture disease prevention and treatment. These solutions are susceptible to being washed away and have limited stability under light and temperature, reducing retention time and easy degradation. However, recent advances in radiation technology can produce AgNPs in a solid form. The solid-state nanoparticles can have a silver content of up to 10,000 ppm, offering extended preservation compared to liquid solutions. This ensures prolonged efficacy and helps reduce the transportation and storage costs associated with AgNPs products. Therefore, this research aims to use AgNPs@DA prepared by γ -irradiation for preventing and treating the collar root rot (Rhizoctonia disease) caused by *R. solani* fungus on *B. integrifolia* as the natural fungicide.

EXPERIMENTAL

Materials

AgNPs@DA containing 4.000 ppm AgNPs synthesized by γ -irradiation method with particle size about 6.2 nm was prepared at Biotechnology Center of Ho Chi Minh city. The plant pathogenic fungi used in this study were *R. solani* (caused collar root rot disease) isolated from infected *Brassica integrifolia* in the Ho Chi Minh City. The PGA (potato glucose agar) media was used for *in vitro* test, and the swallow mustard variety namely *Brassica integrifolia* NV1 provided by Nam Viet Seed Co. was used for *in vivo* test.

In vitro antifungal activity of AgNPs@DA

The antifungal activity of AgNPs@DA was assessed using a PGA medium treated with various product concentrations (up to 30 ppm AgNPs). *R. solani* samples with diameter about 6 mm were placed at the center of petri dishes containing the medium have been supplemented with inoculants. These dishes were then incubated at room temperature. After 60 hours of incubation, the diameter of the fungal colony growth was measured. The antifungal efficacy was determined once the mycelial growth in the control plate reached the edge of the petri dish. The antifungal efficiency was quantified using the equation [3]: $D(\%) = (R_0 - R) \times 100/R_0$, where R_0 and R represent the mycelial diameters of the control and treated samples, respectively.

In vivo fungicidal effect of AgNPs@DA on *B. integrifolia*

In the prevention test, the nine-day-old and free disease *B. integrifolia* was sprayed 3 times every 2

days with 100 mL of AgNPs solution containing 2 - 10 ppm (the negative control was foliar sprayed with the same volume of distilled water, and the positive control was treated with AgNPs/chitosan at a concentration of 10 ppm). After that, these lower stems (15 plants/treatment) were wounded before inoculating with 100 mL of *R. solani* solution. The control plants were similarly treated with distilled water without inoculating with *R. solani*.

For the elimination test, the nine-day-old and free disease *B. integrifolia* (disease-free) (15 plants for each treatment) were wounded and inoculated with 100 mL of *R. solani* solution. After 8 days of inoculating and 50% of the tested plants were infected in all treatments; the tested plants were foliar sprayed with 100 mL AgNPs@DA solution with concentrations of 0, 10, 15, 20, 25 and 30 ppm every 2 days up to 3 times (the negative control was foliar sprayed with the same volume of distilled water and the positive control was treated with 30 ppm of the AgNPs/chitosan). The control plants were similarly treated with distilled water and the disease-free 15 plants were used.

The disease severity and disease incidence of each treatment were determined every 3 days until the negative control (inoculated by pathogens fungus and sprayed with only distilled water), which was dead or completely recovered and calculated based on QCVN 01-169: 2014 [7]. Each experiment was carried out in triplicate and data were statistically analyzed using the analysis of variance (ANOVA) test. The mean values were compared using Duncan's multiple range test at a probability level below 5%.

RESULTS AND DISCUSSION

In vitro antifungal activity of AgNPs@DA

The results in Figures 1 indicated that the fungal colonies on the control developed full of the petri dish after only 48 hours of incubation. In contrast, AgNPs@DA inhibited the growth of *R. solani* and the fungicidal efficiency was inversely proportional to the concentration of AgNPs. At a low AgNP concentration (<5 ppm), the fungicidal efficiency was low, with an achievement of about 37.50%. While the AgNP concentrations increased to 10 and 20 ppm, the fungicidal efficiency increased speedily, the antifungal efficiency was 57.00 and 76.1%, respectively, and the addition of 30 ppm completely inhibited the pathogenesis fungus. These results confirmed the antifungal efficacy of AgNPs synthesized by γ -irradiation. Min *et al.* (2009) [8] observed inhibition of the

hyphal growth of *R. solani* causing deformities of the hyphal walls which were then prone to collapse at very low concentrations (7 ppm) of AgNPs. The study of Ashraf et al. (2020) [9] has pointed out that AgNPs could impair the chitin biosynthesis of fungi. When chitin production was disrupted, fungal cells became deformed and osmotically unstable, disintegrating their cell walls. Otkarina et

al. (2021) [10] reported morphological changes of *R. solani* colonies when treated with AgNPs. These results indicated that the AgNPs@DA prepared through γ -irradiation possesses a robust antifungal capability. Moreover, it demonstrated long-term stability, effectively resisting the detrimental impacts of various environmental conditions.

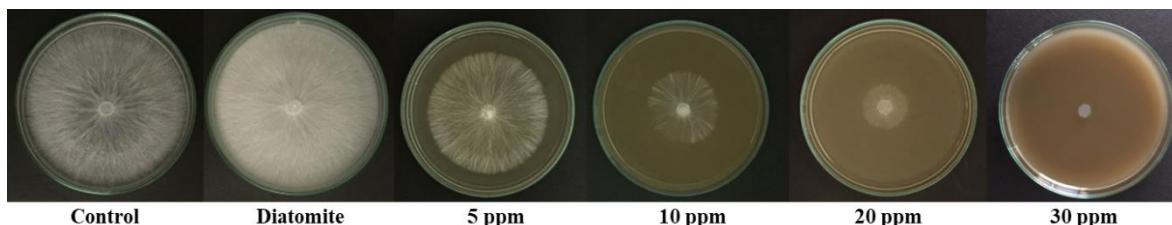


Figure 1. The growth of *R. solani* after 40 hours incubated on PGA media supplemented with various AgNPs@DA concentrations

In vivo fungicidal effect of AgNPS@DA on *B. integrifolia*

The prevention efficiency of AgNPS@DA against *R. solani*

Table 1. The effect of AgNPs@DA concentration on pathogen defense response of *B. integrifolia*

AgNPs concentration, mg/mL	Disease incidence, %				Disease severity, %			
	3 days	6 days	9 days	12 days	3 days	6 days	9 days	12 days
Control	0 ^a	0 ^a	0 ^a	0 ^a	11.11 ^a ± 0.00	11.11 ^a ± 0.00	11.11 ^a ± 0.00	11.11 ^a ± 0.00
Negative control	84.44 ^g ± 3.85	84.44 ^f ± 3.85	82.22 ^f ± 3.85	71.11 ^c ± 3.85	60.99 ^g ± 2.26	72.35 ^g ± 0.86	73.09 ^g ± 2.60	74.81 ^c ± 1.48
Positive control	28.89 ^b ± 3.85	15.56 ^b ± 3.85	0 ^a	0 ^a	17.53 ^b ± 0.86	14.57 ^b ± 0.86	11.11 ^a ± 0.00	11.11 ^a ± 0.00
2	68.89 ^f ± 3.85	57.78 ^e ± 3.85	48.89 ^e ± 3.85	15.56 ^b ± 3.85	43.70 ^f ± 1.48	46.67 ^f ± 1.48	39.75 ^d ± 1.71	24.94 ^b ± 3.42
4	62.22 ^e ± 3.85	53.33 ^{de} ± 0.00	37.78 ^d ± 3.85	4.44 ^a ± 3.85	37.28 ^e ± 0.86	36.79 ^e ± 1.71	26.91 ^c ± 2.26	15.06 ^a ± 3.42
6	60.00 ^e ± 0.00	51.11 ^d ± 3.85	22.22 ^c ± 3.85	2.22 ^a ± 3.85	34.82 ^d ± 1.48	30.37 ^d ± 1.48	18.52 ^b ± 1.48	13.08 ^a ± 3.42
8	48.89 ^d ± 3.85	37.78 ^c ± 3.85	8.89 ^b ± 3.85	0 ^a	24.44 ^c ± 1.48	19.50 ^c ± 0.86	13.09 ± 0.86	11.11 ^a ± 0.00
10	35.56 ^c ± 3.85	17.78 ^b ± 3.85	0 ^a	0 ^a	19.01 ^b ± 0.86	15.06 ^b ± 0.86	11.11 ^a ± 0.00	11.11 ^a ± 0.00

The data were converted using the formula $\text{Arcsine}(x)$ before undergoing statistical processing. The statistical ranking was then based on these converted numbers. In a column, means followed the same letter are not significantly different with $p < 0.05$. The duration was observed after *B. integrifolia* was infected with *R. solani*. Control: none-inoculated, negative control: inoculated and untreated, and positive control: inoculated and treated with 10 ppm AgNPs/chitosan

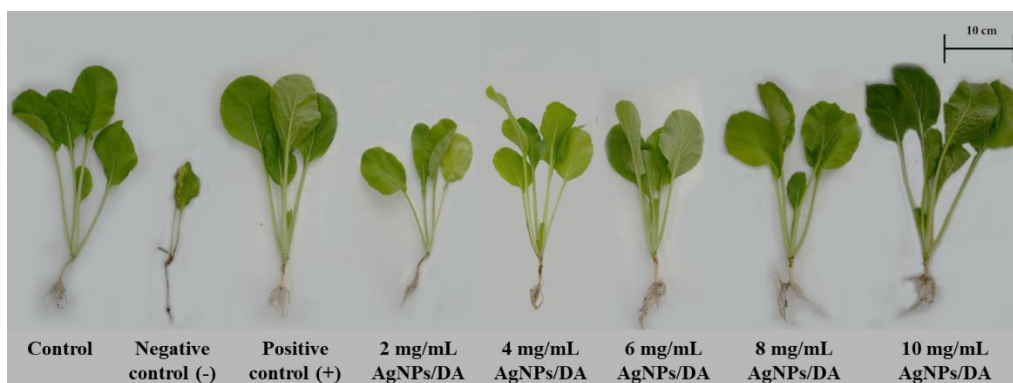


Figure 2. The growth of *B. integrifolia* after 12 days of infection in prevention test. Control; none-inoculated, negative control: inoculated and untreated, and positive control: inoculated and treated with 10 ppm AgNPs/chitosan

Several research reported the *in vitro* antifungal effect of AgNPs, but the result for *in vivo* studies on plants is still limited. In addition, *R. solani* is the causative fungus of collar root rot disease and all the diseases on the vegetable plant may suffer from, that caused by the *R. solani* is the most devastating. This study investigated the role of AgNPs@DA on the antifungal effect against *R. solani*. The results in Table 1 and Figure 2 showed that the disease incidence in negative control was 84.11% and disease severity was 60.99%. The lower stems of these *B. integrifolia* were rotten and appeared white mycelia in the wound, the rotten area was more than 50% of the lower stem area. After 12 days of infection, the disease severity increased to 74.81%, almost all infected plants

have died. Meanwhile, in the treated plants, the disease incidence and disease severity significantly decreased by increasing its concentration. While, in the treatment with 2, 4, and 6 ppm AgNPs, the disease incidence decreased from 71.11% to 15.56, 4.44 and 2.22%, respectively. The disease severity in these treatments also decreased from about 74.81% to 24.94, 15.06 and 13.08%, respectively. Among the treatments, the plants treated with 10 ppm were completely recovered, the disease incidence was 0% and the disease severity was 11.1% after 12 days of infection.

The elimination efficiency of AgNPs@DA on Rhizoctonia disease

Table 2. The eliminate efficacy of AgNPs@DA concentration on infected *B. integrifolia*

AgNPs concentration, mg/mL	Disease incidence, %				Disease severity, %			
	3 days	6 days	9 days	12 days	3 days	6 days	9 days	12 days
Control	0 ^a	0 ^a	0 ^a	0 ^a	11.11 ^a ± 0.0	11.11 ^a ± 0.0	11.11 ^a ± 0.0	11.11 ^a ± 0.0
Negative control	33.21 ^b ± 3.85	82.22 ^f ± 3.85	82.22 ^e ± 3.85	80.00 ^b ± 0.00	43.3 ^a ± 6.7	61.48 ^e ± 1.48	73.33 ^c ± 1.48	75.80 ^b ± 1.71
Positive control	31.36 ^b ± 3.85	28.89 ^b ± 3.85	4.44 ^a ± 3.85	0 ^a	41.1 ^a ± 3.9	17.53 ^b ± 0.86	12.10 ^{ab} ± 0.86	11.11 ^a ± 0.0
10	33.12 ^b ± 3.85	68.89 ^e ± 3.85	46.67 ^d ± 0.00	0 ^a	41.1 ^a ± 3.9	36.79 ^f ± 0.86	24.94 ^d ± 1.48	11.11 ^a ± 0.0
15	32.1 ^b ± 3.85	64.44 ^e ± 3.85	35.56 ^c ± 3.85	0 ^a	38.9 ^a ± 3.9	35.80 ^{ef} ± 0.86	21.48 ^c ± 1.48	11.11 ^a ± 0.0
20	30.89 ^b ± 3.85	55.56 ^d ± 3.85	33.33 ^c ± 0.00	0 ^a	42.2 ^a ± 3.9	33.83 ^e ± 0.86	20.00 ^c ± 1.48	11.11 ^a ± 0.0
25	32.65 ^b ± 3.85	37.78 ^c ± 3.85	11.11 ^b ± 3.85	0 ^a	41.1 ^a ± 3.9	26.42 ^d ± 2.26	15.06 ^b ± 3.08	11.11 ^a ± 0.0
30	31.46 ^b ± 3.85	35.56 ^c ± 3.85	4.44 ^a ± 3.85	0 ^a	41.1 ^a ± 3.9	21.98 ^c ± 1.71	13.09 ^{ab} ± 3.42	11.11 ^a ± 0.0

The data were converted using the formula before undergoing statistical processing. The statistical ranking was then based on these converted numbers. In a column, means followed by the same letter are not significantly different with $p < 0.05$. The duration was observed after *B. integrifolia* was treated with AgNPs@DA. Control: none-inoculated, negative control: inoculated and untreated, and positive control: inoculated and treated with 30 ppm AgNPs/chitosan.

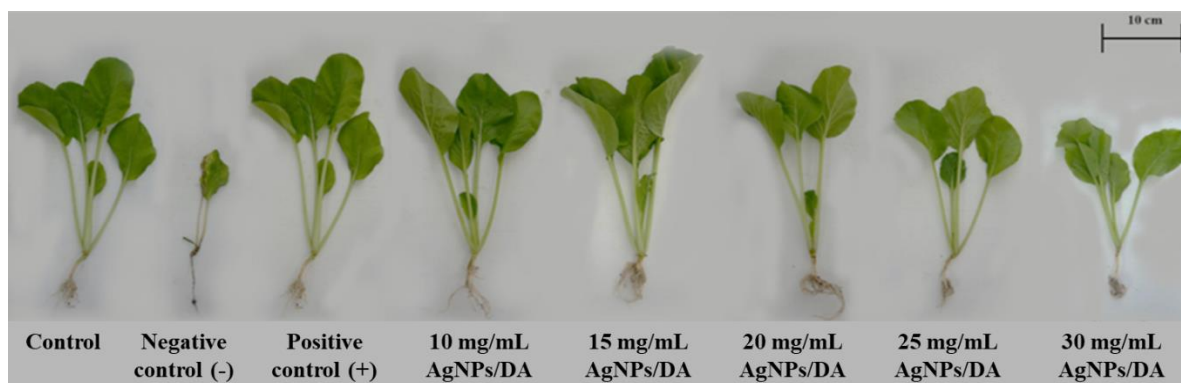


Figure 3. The growth of *B. integrifolia* after 12 days of infection in treatment test. Control: none-inoculated, negative control: inoculated and untreated, and positive control: inoculated and treated with 30 ppm AgNPs/chitosan

The results in Table 2 and Figure 3 showed that disease incidence and disease severity decreased by the increased AgNPs@DA concentration. After 12 days since the fungal

infection, the disease incidence was found at 6.7, 4.4 and 2.2%, the disease severities were determined about 12.6, 12.1 and 11.11%, respectively and these values were almost the

same as that of the control without inoculation of pathogenesis fungus. Meanwhile, in positive control (treated with 30 ppm AgNPs/chitosan) the disease incidence was about 42% and the disease severity was 3 folds higher than the same treated concentration of AgNPs@DA. In addition, in the control without inoculation of pathogenesis fungus, the infected plants appeared to have toxic symptoms such as curly leaves. It can be hypothesized that, after spraying, plant cells could retain AgNPs, which may kill the infecting pathogen fungus [11, 12].

CONCLUSION

The AgNPs@DA product prepared by γ -irradiation method showed a strong inhibition effect against *R. solani* on PDA media with the antifungal efficiency reaching ~100% by the treatment of 30 ppm AgNPs. The foliar treatment with 8 - 30 ppm AgNPs strongly reduced the disease incidence of the *B. integrifolia* infected by *R. solani* fungus. AgNPs@DA is a natural and high-tech product with great potential to be use as a bio-fungicide for preventing and eliminating fungal diseases in the vegetable. This is suitable for producing safe cargo-products with a low cost and sustainability.

References

- [1] Sở Nông nghiệp và PTNT thành phố Hồ Chí Minh, *Kết quả sản xuất nông nghiệp và phát triển nông thôn 6 tháng đầu năm 2023*, Hồ Chí Minh, 2023.
- [2] Dung, D.T. *Studies on Damping-off Diseases Caused by Rhizoctonia solani Kühn of Some Crops in Hanoi*, Journal of Scientific and Development **11**(4) (2013) 459-465.
- [3] Luan, L.Q., Xo, D.H. *In vitro and in vivo fungicidal effects of γ -irradiation synthesized silver nanoparticles against Phytophthora capsici causing the foot rot disease on pepper plant*, Journal Plant Pathology, **100**(2) (2018) 241-248.
- [4] Behara, L., Chandra, r. Lenka, S., Mahanty, A., Kumar, S., Rath, P.H., *Bacterial synthesized silver nanoparticle inhibits Rhizoctonia solani Kuhn, the causal organism for sheath blight disease of rice*, Oryza an International Journal on Rice, **60**(1) (2023) 166-174.
- [5] Nejad, M.S., Bonjar, G.H.S., Khatami, M., Amini, A., Aghighi, S. *In vitro and in vivo antifungal properties of silver nanoparticles against Rhizoctonia solani, a common agent of rice sheath blight disease*, IET Nanobiotechnology, **11**(3) (2017) 236-240.
- [6] Xiao, X., Zheng, Z., Yu, H., Huang, W., Ji, W., *Microwave-assisted synthesis of silver nanoparticles and their inhibitory activity against Rhizoctonia solani on maize*, Biomaterial and Bio-Inspired Materials. **10**, (2023) 1192609.
- [7] Bộ Nông Nghiệp và Phát Triển Nông Thôn, *Quy Chuẩn Kỹ Thuật Quốc Gia Về Phương Pháp Điều Tra Phát Hiện Dịch Hại Cây Rau Họ Hoa Thập Tự*, Hà Nội, 2014.
- [8] Min, J.S.K.S., Kim, S.W., Kim, J.H., Jung, K., Lamsal, S., Bin, Kim, M., Jung, Lee, Y.S. *Effects of colloidal silver nanoparticles on sclerotium-forming phytopathogenic fungi*. Plant Pathology Journal, **25**(4) (2009) 376–380.
- [9] Ashraf, H., Anjum, T., Riaz, S., Naseem, S. *Microwave Assisted Green Synthesis and Characterization of Silver Nanoparticles Using Melia azedarach for the Management of Fusarium Wilt in Tomato*. Frontiers in Microbiology, **11**:238 (2020).
- [10] Oktarina, H., Woodhall, J., Singleton, I., *The potential of silver nanoparticles to control Rhizoctonia solani (AG3-PT) growth in vitro*. Journal Natural, **21**(1), (2021).
- [11] Shrivastava, S., Bera, T., Roy, A., Singh. G., Ramachandrarao. P., Dash. D. *Characterization of enhanced antibacterial effects of novel silver nanoparticles*. Nanotechnology, **18** (2007) 103–112.
- [12] Panacek, A., Kvítek, L., Pucek, R., Kolar, M., Vecerova, R., Pizúrova, N., Sharma, V.K., Nevecna, T., Zboril, R., *Silver colloid nanoparticles: synthesis, characterization, and their antibacterial activity*. Journal of Physics Chemistry, **110** (2006) 16248–16253.

ORAL SESSIONS

NANOMATERIALS AND NANODEVICES
(NMD)

DEVELOPMENT OF NOVEL ANODE WITH NI-LOADED FLOWERLIKE CERIA FOR SOLID OXIDE FUEL CELL OPERATED WITH LIQUOR

Duc Minh Trinh Dinh, Phuc Hoan Tu and Yusuke Shiratori

Department of Mechanical Science and Engineering, School of Advanced Engineering, Kogakuin University, 2665-1 Nakano-machi, Hachioji, Tokyo 192-0015, Japan
Email: re23001@g.kogakuin.jp

ABSTRACT

Fermentation liquor or liquors (ethanol containing water) hold a potential as an emergency fuel, if they can be directly converted to electricity with the highly efficient solid oxide fuel cell (SOFC). Challenges in the internal reforming operation of SOFC with the ethanol containing water are sintering of Ni used in the anode under the high steam content in the fuel flow, and coking caused by the ethanol decomposition. To overcome these issues, a novel anode, composed of Ni-loaded flowerlike-CeO₂ (Ceria), abbreviated as Ni/C(F), and scandia-stabilized zirconia (ScSZ) was prepared, and its electrochemical performance in the feed of 25wt% ethanol-water at 750°C was evaluated and compared with that of the standard cermet anode (Ni-ScSZ). The Ni/C(F)-ScSZ anode exhibited higher open circuit voltage (OCV) and lower charge transfer resistance, although its larger surface diffusion resistance has to be reduced for performance improvement. Keywords: solid oxide fuel cell, direct internal reforming, flowerlike ceria, ethanol

INTRODUCTION

In Japan, frequently hit by large scale disasters such as typhoon and earthquake, there is a great desire for portable power generator. Solid oxide fuel cell (SOFC), all ceramic fuel cell operated at high temperature in the range of 600-900°C, is an electrochemical device which can directly convert chemical energy of a fuel into electrical energy with significantly higher power generation efficiency than that of heat engine [1]. Most of households in Japan stock liquors for drinking and cooking, that have calories, in other words, chemical energy. Therefore, in terms of creating portable power generator for emergency, it is quite attractive if SOFC can be operated by liquors.

SOFC anode is the porous composite of Ni and scandia stabilized zirconia (ScSZ), called cermet anode, which has large area of triple phase boundary (contact area of electronic conductor (Ni), ionic conductor (ScSZ) and gas phase (fuel)) called TPB, where electrochemical oxidation of H₂ ($H_2 + O^{2-} \rightarrow H_2O + 2e^-$) takes place for power generation.

For downsizing SOFC system, direct internal reforming (DIR) concept is promising, in which fuel reforming (hydrogen production from a fuel) takes place within the porous anode, thereby eliminating an external reformer [2]. In principle, DIR operation is possible, however, practically,

agglomeration of Ni and carbon deposition (coking) on Ni particles [3] during the direct feed of a hydrocarbon fuel are the bottlenecks for stable operation. To realize DIR-SOFC, novel anode material which can function not only as electrochemically active site but also as reforming catalyst has to be developed. This study focused on a unique catalyst support, flowerlike CeO₂ (ceria) abbreviated by Ce(F) [4-5]. Ce(F) loaded by Ni was mixed with ScSZ to form Ni/Ce(F)-ScSZ anode for the application to DIR-SOFC. Performance of SOFC single cell with this anode directly fueled by the aqueous solution of 25-30vol% ethanol, simulating spirits such as Shochu, popular in Japan, was evaluated.

EXPERIMENTAL

Preparation of Ce(F): Designated amount of Ce(NO₃)₃·6H₂O and polyvinylpyrrolidone (PVP) were dissolved in ethylene glycol, followed by the addition of ammonia solution. The resulting mixture was heat-treated at 180°C for 24 h (solvothermal process), followed by calcination at 600°C for 2 h in air to obtain Ce(F) powder.

Preparation of Ni/Ce(F)-ScSZ anode paste: The resulting powder was immersed in Ni(NO₃)₂·6H₂O solution to obtain 5wt% Ni-loaded Ce(F) (Ni/Ce(F)). Powder mixture of Ni/Ce(F) and ScSZ with 56wt% and 44wt%, respectively, was put into the organic binder composed of α -

terpineol and ethylene glycol, followed by pasting with a three-roller mill.

Preparation of SOFC single cell: The Ni/Ce(F)-ScSZ paste was screen-printed on the surface of a ScSZ electrolyte plate (200 μm in thickness) with the area of 1.4 x 1.4 cm^2 . After drying, the paste of NiO:ScSZ = 80wt%:20wt% was screen-printed on the first layer with the same area. Pt mesh with the area of 1.4 x 1.4 cm^2 was put onto the wet-state NiO-ScSZ as a current collector, followed by heat-treatment at 1200°C for 5 h to obtain porous anode layers.

Electrochemical test: Electrochemical tests of SOFC were conducted at 750°C with the feed of 80 ml min^{-1} H_2 with 4vol% H_2O and 1.6 ml min^{-1} of 30vol% ethanol- H_2O (simulating Shochu) to the anode side.

RESULTS AND DISCUSSION

As shown in Fig. 1, cell voltage of the SOFC with Ni/Ce(F)-ScSZ was lower than that with standard anode for both fuels., especially noticeable for the humidified H_2 . It is attributed to the lack of Ni continuity (electron conduction pass), as the fine Ni particles were dispersed on the petals of Ce(F), resulting in larger ohmic resistance. Nevertheless, even in the case of Ni/Ce(F)-ScSZ, power generation was possible, indicating that CeO_2 having electronic conductivity contributed to the establishment of electronic conduction paths.

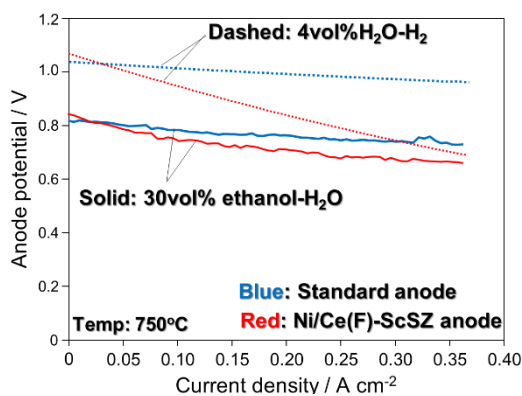


Figure 1. I-V curves of SOFC single cells with standard anode (Ni-ScSZ) and novel anode (Ni/Ce(F)-ScSZ) measured at 750°C in feeding 4vol% $\text{H}_2\text{O}-\text{H}_2$ and 30vol% ethanol- H_2O .

On the other hand, in the feed of 30vol% ethanol- H_2O , SOFC with Ni/Ce(F)-ScSZ exhibited the performance comparable to that of the standard anode. The open circuit voltage

(OCV) in the feed of 30vol% ethanol- H_2O reflects the reforming activity of an anode material, and it was enhanced by adopting Ni/Ce(F)-ScSZ instead of the standard anode material. Mechanism of the promotion of steam reforming of ethanol on the Ni/Ce(F) particles will be investigated soon.

CONCLUSION

Ni-loaded ceria with flowerlike morphology was studied for the application to SOFC anode. It was suggested that Ni/Ce(F)-ScSZ anode has a potential to enhance the performance of DIR-SOFC fueled by low-concentration ethanol aqueous solution such as liquor, although improvements of both electrochemical and reforming performances are indispensable.

Acknowledgment

This work was supported by JSPS KAKENHI, Fostering Joint International Research (B), Grant Number 20KK0248.

References

- [1] A.B. Stambouli, E. Traversa, *Solid oxide fuel cells (SOFCs): a review of an environmentally clean and efficient source of energy*, Renewable and sustainable energy reviews **6** (2002) 433-455.
- [2] Y. Shiratori, M. Sakamoto, *Performance improvement of direct internal reforming solid oxide fuel cell fuelled by H_2S -contaminated biogas with paper-structured catalyst technology*, J. Power Sources **322** (2016) 170-179.
- [3] Y. Liu, Z. Shao, T. Mori, *Development of nickel based cermet anode materials in solid oxide fuel cells—Now and future*, Materials Reports: Energy **1** (2021) 100003-1000028.
- [4] P. H. Tu, D. N. Le, T. D. Dao, Q. T. Tran, T. C. D. Doan, Y. Shiratori, C. M. Dang, *Paper-structured catalyst containing CeO_2 -Ni flowers for dry reforming of methane*, Int. J. Hydrogen Energy **45** (2020) 18363-18375.
- [5] P. H. Tu, T. G. H. Nguyen, M. Sakamoto, T. Uchida, T. C. D. Doan, M. C. Dang, Y. Shiratori, *Performance enhancement of Ni-loaded paper-structured catalyst for dry reforming of methane by the dispersion of ceria-based oxides*, ECS Transactions **91** (2019) 1661-1670.

CYTOTOXICITY OF NANOPLASTICS TO FISH GILL CELLS - ESTABLISHING WATERBOURNE NANOPARTICLES RISK ASSESSMENT

Quang Minh Luu¹, Casey Doolette¹, Enzo Lombi¹, Suresh Valiyaveetil², Ivan Kempson¹

¹Future Industries Institute, University of South Australia;

²National University of Singapore

Email: quang_minh.luu@mymail.unisa.edu.au

ABSTRACT

The widespread use of plastics in modern society has resulted in increased plastic pollution in natural environments [1]. These plastics eventually break down into nanoparticles, posing a serious threat to aquatic ecosystems [2]. Other studies focused on high concentrations of nanoplastics, leaving a gap in understanding their impact at environmentally relevant levels [3]. To address this, this research examined the toxicity of nanoparticles from common polymers (polystyrene, polyvinyl chloride, and poly (methyl methacrylate)) in a systematic manner, following ISO 21115:2019 guidelines [4]. The fish gill cell line (RTgill-W1) was exposed to nanoplastics at concentrations ranging from 3.125 µg/L to 3.125 mg/L for 2 to 72 hours and monitored changes in metabolic activity, cell membrane integrity, and lysosomal membrane integrity. These nanoparticles had a subtle effect on cell behaviour and structural integrity, which was dose- and time-dependent. Confocal Microscopy confirmed that plastic nanoparticles were internalised by the cells, suggesting that their presence could disrupt cellular function and increase vulnerability to other stressors.

Keywords: Nanoplastics, Cytotoxicity, Acute toxicity, Environmentally relevant concentration.

INTRODUCTION

From 1950 to 2018, worldwide plastic output climbed from 1.7 million to 359 million tonnes, with Europe accounting for 17%, the North American Free Trade Agreement (the United States, Canada, and Mexico) for 18%, and Asia for 51% of the growth [5]. Because of its low cost of manufacturing and excellent chemical features, such as being lightweight and sturdy in structure, plastic packaging has become a great benefit to our “throw-away civilisation” [6]. Just about half of used plastic packaging is actually retrieved for recycling, energy recovery, or disposal (56.8%); the rest ends up dumped illegally or littered (43.2%) [7]. Most plastics are resilient to biodegradation and can persist in the environment for more than a century [6, 8]. Furthermore, plastics fragment into smaller particles such as micro- and nano-plastics (MNPs) via abiotic and biotic degradation by environmental factors including UV light, thermodynamic changes, and exposure to seawater [8, 9].

Nanoplastics are primarily derived from two sources: primary plastic waste and secondary derivatives [10]. Primary nanoplastic wastes,

such as nanomedicine, nanoimaging, nanosensors, and personal care goods, are disposed of to the environment in nanoscale form [11-13]. Secondary derivatives are nanoplastics formed as a result of plastic disintegration caused by physical, chemical, or biological factors [10, 14]. The degradation routes can be classified as biotic and abiotic [15]. When particles are small enough to pass through microbial membranes, biotic biodegradation often occurs, and it can be further classified into aerobic and anaerobic degradation [16]. Photodegradation and hydrolysis are the most typical kinds of abiotic degradation [17].

The study by Lenz et al in 2016, based on the data of the concentrations of microplastics found in the environment from other studies, suggested the environmentally relevant concentration of nanoplastics should range between 1 pg/L and 1 µg/L, indicating the concentration of nanoplastics being studied recently is many times higher than in reality. In addition, due to the inconsistency in the toxicity assessment method of nanoplastics, the evaluation results are relatively unstable. Besides, many studies use the MTT method to determine cell survival, which has recently been controversial for its accuracy [18]. Nevertheless,

the number of studies on nanoplastics toxicity as well as their possible alterations to cells at the cellular level of marine organisms in a comprehensive manner is very limited. Therefore, this study used ISO 21115:2019 - an internationally recognized method for assessing the water quality to determine nanoplastics toxicity to fish at concentrations ranging from 3.125 µg/L to 3.125 mg/L and evaluated the association of nanoplastics with cells by staining them with fluorescent dyes and using confocal imaging techniques.

EXPERIMENTAL

Cell line

The epithelial cell line of rainbow trout gill (RTgill-W1) derived from histopathologically normal gill lamella of a rainbow trout *Oncorhynchus mykiss* was purchased from the American Type Culture Collection as required by ISO 21115:2019 protocol. The cell was cultured in an L15 media with 10% Fetal Bovine Serum (FBS) and 1% Penicillin/Streptomycin (P/S) in the dark at room temperature and the culture media was replaced every 2-3 days.

Nanoplastics sources

Polystyrene: A fluorescent yellow-green labelled polystyrene made up of monodisperse polystyrene microspheres (30 nm in nominal diameter) nanoplastic product was purchased from Sigma Aldrich, Australia.

Polyvinyl Chloride and Poly(Methyl Methacrylate): Fluorescein-5-isothiocyanate (FITC) labelled polyvinyl chloride and poly(methyl methacrylate) made up of monodisperse microspheres (125 nm and 178 nm in nominal diameter, respectively) nanoplastics were synthesised as described in previous work.

Nanoplastic characterisation

The particle diameter of nanoplastics was measured using Transmission Electron Microscopy (TEM) and Scanning Electron Microscopy (SEM). The size distribution and zeta potential were determined using Dynamic Light Scattering (DLS) and Zeta Potential Analyser on a Zetasizer Nano-ZS device. To confirm the fluorescence characteristic of the nanoplastic, the fluorescence and UV-Vis measurements were carried out using a Fluorescence Spectrophotometer and a UV-visible spectrophotometer.

Visualising nanoplastics uptake in cells

After 24 hours of 3.125 mg/L nanoplastic exposure, the exposed media was discarded, and each well was washed with DPBS 1X 2 times. Next, Hoechst 0.05% and CellBrite Red 0.5% in DPBS 1X solution were added to each well to stain the cells' nucleus and membrane, respectively, followed by 20 minutes of incubation at 19°C. Then, cells were washed twice with DPBS 1X before the new media was added. Finally, the sample was kept in the dark to bring to the Confocal Microscope for imaging to monitor the relative position of the nanoplastic and the cells.

Acute toxicity tests

The determination of toxicity that nanoplastics exert on fish gill cells was carried out generally in accordance with ISO 21115:2019 utilising AlamarBlue, 5-CFDA-AM and NeutralRed, which measures the metabolic activity, the integrity of cells' membrane and integrity of the lysosomal membrane, respectively using the Plate Reader with nanoplastics concentrations of: 3.125 µg/L, 15.625 µg/L, 31.25 µg/L, 312.5 µg/L, 1.5625 mg/L and 3.125 mg/L. However, beyond the ISO 21115:2019 protocol, which only assesses the acute toxicity at a single time point of 24 hours, this research investigated time points ranging from 2 to 72 hours to monitor the time-temporal kinetic effects that nanoplastics caused to cells.

Data analysis

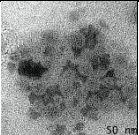
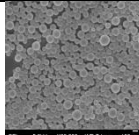
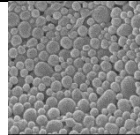
The variation between the two cell-free wells was examined to ensure there was no interference of the nanoplastic fluorescence on the measurement, and then the corresponding average of the two cell-free wells was subtracted to eliminate autofluorescence. Next, the mean value of fluorescence intensity of control and each nanoplastic concentration of each test plate was calculated. Then, the proportion of viability cells corresponding to the respective concentrations and exposure durations were determined using the following equation (The fluorescence intensity of the control wells represents 100% cell viability):

$$\text{Percentage compared to the respective control} = \frac{\text{Fluorescence unit of the test item} \times 100\%}{\text{Average fluorescence unit of the respective controls}}$$

RESULTS AND DISCUSSION

Nanoplastics characteristics

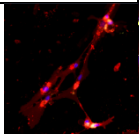
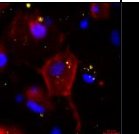
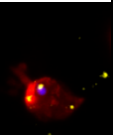
Table 1. Nanoplastics characteristics (Results and images prepared by QM Luu and NUS)

	PS	PVC	PMMA
Sizes (nm)	32.7 ±	125.4 ±	177.6 ±
	21.86 (STD)	39.15 (STD)	45.5 (STD)
Zeta Potential (mV)	-14.9 ±	-30.2 ±	-30.2 ± 7
	8.58 (STD)	7.57 (STD)	(STD)
Shape			

In general, results from Dynamic Light Scattering (DLS) identified the mean diameter of the PS, PVC and PMMA nanoplastic particles are about 30 nm, 125 nm and 177 nm, respectively. Additionally, they also confirmed that most of the nanoplastic particles used in this research have relatively homogenous sizes; Results from the Zeta potential measurement indicated that the zeta potential of nano PS, PVC and PMMA are -14.9 mV, -15.2 mV and -30.2 mV, respectively, showing their greater cells internalisation ability compared no neutral and positively charged nanoplastics.

Cells and nanoplastics interactions

Table 2. Accumulation of nanoplastics in cells' cytoplasm (Images prepared by QM Luu)

Nanoplastic & Magnification	PS (20X)	PVC (100X)	PMMA (100X)
Confocal images			

Confocal microscopy images show the intracellular capacity of all 3 nanoplastics with sizes ranging from 30 nm to 177 nm. In addition, it can be seen that the amount of nano-PS, which has the smallest size among the three research subjects, internalised the most. In addition, nanoplastics tend to accumulate near the cell nucleus, which can disrupt or hinder the cell's replication process, thereby increasing the possibility of cell death or mutation.

Acute toxicity assessment

Metabolic activity

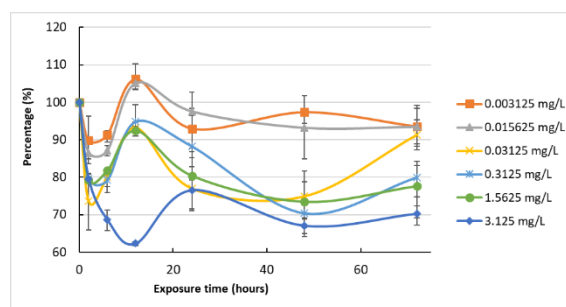


Figure 1. Metabolic activity of cells exposed to nano-PS (30 nm) compared to control samples (Mean ± SEM)

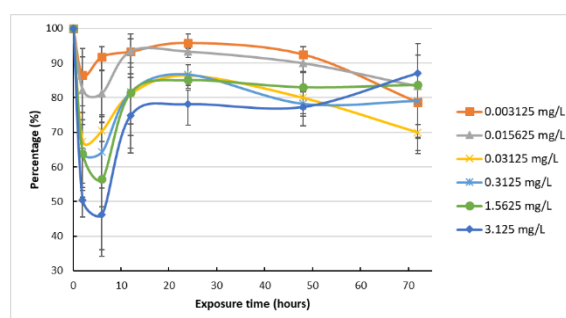


Figure 2. Metabolic activity of cells exposed to nano-PVC (125 nm) compared to control samples (Mean ± SEM)

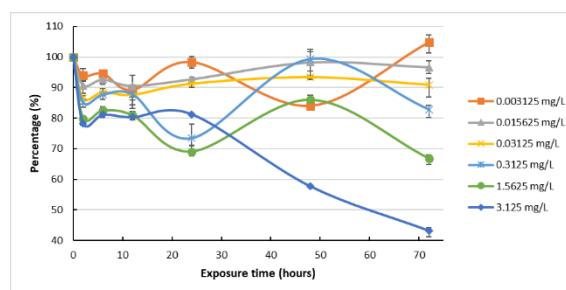


Figure 3. Metabolic activity of cells exposed to nano-PMMA (178 nm) compared to control samples (Mean ± SEM)

Integrity of cell membrane

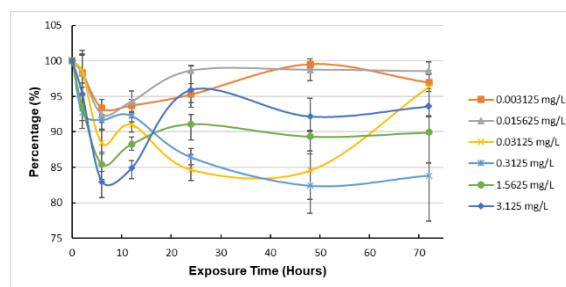


Figure 4. Integrity of cells membrane of cells exposed to nano-PS (30 nm) compared to control samples (Mean ± SEM)

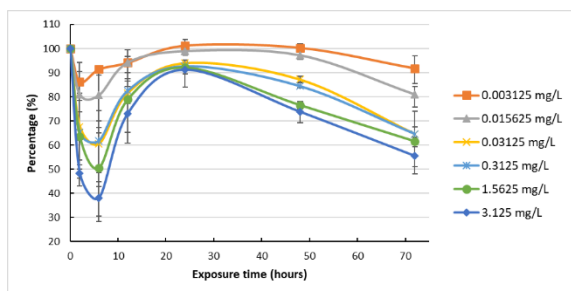


Figure 5. Integrity of cells membrane of cells exposed to nano-PVC (125 nm) compared to control samples (Mean \pm SEM)

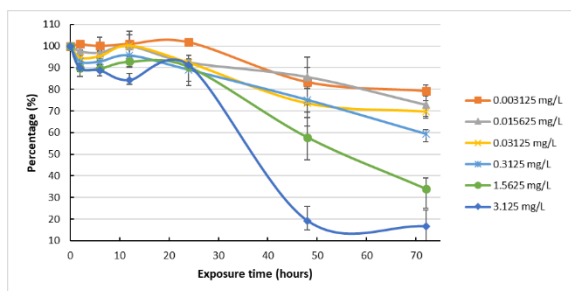


Figure 6. Integrity of cells membrane of cells exposed to nano-PMMA (178 nm) compared to control samples (Mean \pm SEM)

Integrity of lysosomal membrane

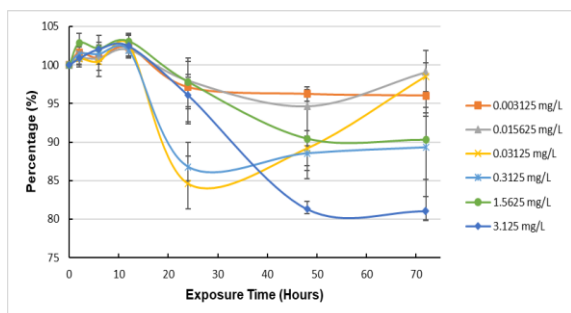


Figure 7. Integrity of lysosomal membranes of cells exposed to nano-PS compared to control samples (MEAN \pm SEM)

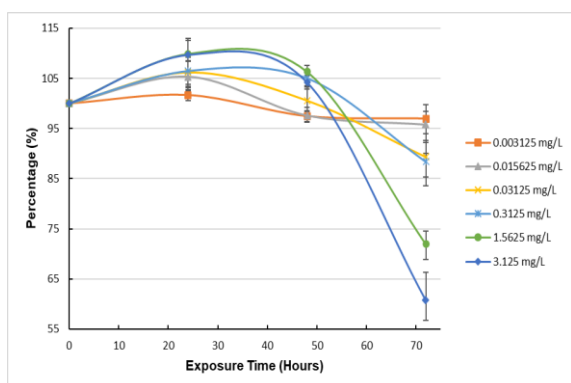


Figure 8. Integrity of lysosomal membranes of cells exposed to nano-PVC compared to control samples (MEAN \pm SEM)

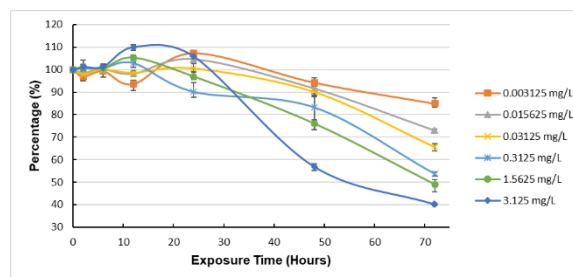


Figure 9. Integrity of lysosomal membranes of cells exposed to nano-PMMA compared to control samples (MEAN \pm SEM)

CONCLUSION

It appears reasonable to conclude that the nanoplastics at these low, but environmentally relevant concentrations, are having a slight effect on cell behaviour and structural integrity. It also appears that these effects are kinetic and therefore changes in the degree of stress imparted by nanoplastics are highly time dependent. This study can be considered as a reference method to contribute to the establishment of a robust and comprehensive analytical modality for the identification of the risks that nanomaterials in general and nanoplastics, in particular, can cause to the environment.

Acknowledgement

I would like to express my heartfelt gratitude to my supervisor, Associate Professor Ivan Kempson, for his unwavering support and guidance throughout my research. His expertise and mentorship have been invaluable.

I am also deeply thankful to my co-supervisors, Professor Enzo Lombi and Dr Casey Doolette. Their collaborative efforts and insights have greatly enriched my research. I would also like to extend my appreciation to the Future Industries Institute staff for providing remarkable facilities and their dedicated support. Their assistance has been crucial to the success of my work.

Furthermore, I would like to acknowledge and thank Associate Professor Suresh Valiyaveetil from the National University of Singapore for his invaluable collaboration, which has contributed significantly to the success of my research. His support and contributions have been instrumental in this endeavour.

References

- [1] Geyer, R., J.R. Jambeck, and K.L. Law, *Production, use, and fate of all plastics ever*

- made. *Science Advances*, 2017. **3**(7): p. e1700782.
- [2] Patil, S.S., et al., *Megaplastics to Nanoplastics: Emerging Environmental Pollutants and Their Environmental Impacts*, in *Microorganisms for Sustainability*. 2019, Springer Singapore. p. 205-235.
- [3] Lenz, R., K. Enders, and T.G. Nielsen, *Microplastic exposure studies should be environmentally realistic*. *Proceedings of the National Academy of Sciences*, 2016. **113**(29): p. E4121-E4122.
- [4] ISO_21115:2019, *Water quality – determination of acute toxicity of water samples and chemicals to a fish gill cell line (RTgill-W1)*. International Organization for Standardisation: Geneva.
- [5] PlasticsEurope, E., *Plastics—The Facts 2019. An Analysis of European Plastics Production, Demand and Waste Data*. PlasticEurope <https://www.plasticseurope.org/en/resources/publications/1804-plastics-facts-2019>, 2019.
- [6] Barnes, D.K., et al., *Accumulation and fragmentation of plastic debris in global environments*. *Philosophical transactions of the royal society B: biological sciences*, 2009. **364**(1526): p. 1985-1998.
- [7] Filiciotto, L. and G. Rothenberg, *Biodegradable Plastics: Standards, Policies, and Impacts*. *ChemSusChem*, 2020. **14**: p. 1-18.
- [8] Kik, K., B. Bukowska, and P. Sicińska, *Polystyrene nanoparticles: Sources, occurrence in the environment, distribution in tissues, accumulation and toxicity to various organisms*. *Environmental Pollution*, 2020. **262**: p. 114297.
- [9] Moore, C.J., *Synthetic polymers in the marine environment: a rapidly increasing, long-term threat*. *Environmental research*, 2008. **108**(2): p. 131-139.
- [10] Peng, L., et al., *Micro- and nano-plastics in marine environment: Source, distribution and threats — A review*. *Science of The Total Environment*, 2020. **698**: p. 134254.
- [11] Dalela, M., et al., *pH-sensitive biocompatible nanoparticles of paclitaxel-conjugated poly (styrene-co-maleic acid) for anticancer drug delivery in solid tumors of syngeneic mice*. *ACS applied materials & interfaces*, 2015. **7**(48): p. 26530-26548.
- [12] Hernandez, L.M., N. Yousefi, and N. Tufenkji, *Are there nanoplastics in your personal care products?* *Environmental Science & Technology Letters*, 2017. **4**(7): p. 280-285.
- [13] Wang, F., A. Salvati, and P. Boya, *Lysosome-dependent cell death and deregulated autophagy induced by amine-modified polystyrene nanoparticles*. *Open biology*, 2018. **8**(4): p. 170271.
- [14] Zhang, Z., et al., *The contamination of microplastics in China's aquatic environment: occurrence, detection and implications for ecological risk*. *Environmental Pollution*, 2022. **296**: p. 118737.
- [15] Huang, D., et al., *Recent advances on the transport of microplastics/nanoplastics in abiotic and biotic compartments*. *J Hazard Mater*, 2022. **438**: p. 129515.
- [16] Silva, R.R.A., et al., *Biodegradation of Polymers: Stages, Measurement, Standards and Prospects*. *Macromol*, 2023. **3**(2): p. 371-399.
- [17] Bher, A., et al., *Biodegradation of Biodegradable Polymers in Mesophilic Aerobic Environments*. *Int J Mol Sci*, 2022. **23**(20).
- [18] Ghasemi, M., et al., *The MTT Assay: Utility, Limitations, Pitfalls, and Interpretation in Bulk and Single-Cell Analysis*. *Int J Mol Sci*, 2021. **22**(23).

RESEARCH IN MANUFACTURING LYOPHILIZED BIO-PRODUCTS USED FOR THE EXTERNAL QUALITY ASSESSMENT PROGRAM IN HPV PCR TEST

Ngoc Nguyen Vo¹, Dinh Dung Vu¹, Thi Hong Phuong Nguyen¹, My Tran Thai¹ and Truc-Anh Thi Nguyen²

¹ Center for Standardization and Quality Control in Medical Laboratory of HCMC, 75A Cao Thang Street, District 3, Ho Chi Minh City 700000, Vietnam;

² HANHPHUCLAB Medical Testing & Diagnostic Center, 1032 3 Thang 2 Street, Ward 12, District 11, Ho Chi Minh City 700000, Vietnam.
Email: vnnguyen.sdh20@hcmut.edu.vn

ABSTRACT

HPV (Human papillomavirus) is the most common viral infection of the reproductive tract. WHO encourages countries to use HPV tests for cervical screening [1]. Screening can also detect cancer at an early stage where treatment has a high potential for cure. Therefore, it is essential to have methods to monitor test quality to ensure reliable test results. External quality assessment (EQA) and internal quality control (IQC) are mandatory tools for laboratory quality assurance (QA). Cervical cell samples with positive test results for HPV DNA Type 16 and HPV DNA Type 18 were collected from laboratories in Ho Chi Minh City. The samples were mixed into stock with excipients, then divided into 80 tubes (1.5ml volume), and lyophilized on an automatic lyophilizer system. Monitor the homogeneity and stability of the sample by visualizing the lyophilized product, the solution after reconstitution, and the DNA genotype present in the sample for a period of 6 months (analysis frequency once a month). This study seeks for the procedure of making lyophilized HPV samples and the standards of the samples. Research results create products that meet the requirements of the sample applied for the PCR HPV EQA program and the ISO 13485 standard.

Keywords: HPV (Human papillomavirus), PCR (Polymerase Chain Reaction), bio-product, EQA

INTRODUCTION

Cervical cancer is one of the most common diseases in women, with an estimated 528,000 new cases recorded in 2012. Nearly all cases of cervical cancer (95%) can be attributed to HPV infection [2]. HPV types 16 and HPV DNA Type 18 account for 63% of the types causing cervical cancer in the US, followed by types 31, 33, 45, 52, and 58 accounts for 10%. WHO encourages countries to use HPV tests for cervical screening. The typical pap smear test for cervical cancer screening can be inaccurate due to a variety of variables such as a thick smear, many inflammatory cells, a lot of mucus, blood, and so on. Therefore, the PCR HPV test is now increasingly popular for clinical indications due to its high sensitivity, specificity, and ability to determine the virus genotype. HPV genotype testing is performed by examining a sample of cervical cells to determine whether or not an HPV gene is present based on polymerase chain reaction. Ensuring reliable HPV test results are

used for prevention, screening, early diagnosis, and treatment, as well as for scientific research.

EQA is a critical approach for confirming test reliability [3]. EQA samples are unknown-value samples that the laboratories have to analyze when participating in the EQA program [4]. Presently, the EQA samples available in Vietnam are primarily supplied by foreign suppliers, making the EQA activities dependent and lacking initiative. At the same time, the high cost of providing samples leads to an increase in the EQA expenses for laboratories.

The objective of this study is the procedure of making lyophilized HPV samples and determining the standards of the samples to apply for the PCR HPV EQA program. As a result, research and production of HPV EQA samples are critical to proactively source samples, reduce costs, and assist laboratories in meeting test quality requirements.

The sample being used by laboratories for PCR HPV testing is currently a liquid smear

sample. Using liquid samples for EQA programs will have some limitations as follows: (1) Samples are difficult to transport and require careful and tight packaging; (2) Samples must be stored at cold temperatures; (3) Samples are easily affected by external influences such as temperature, light, humidity; (4) Sample production requires the use of stabilizers to ensure sample stability. Therefore the research use the freeze-dried method due to numerous advantages, including: (1) Long storage time; (2) Maintaining perishable substances such as vitamins, proteins, enzymes, and pigments, ...; (3) Convenient during sample transportation; (4) Might generate a variety of clinical scenarios; (5) Increased sample homogeneity and stability that are important standards in creating EQA samples. The expense of the freeze-drying system makes lyophilized sample production more expensive than liquid sample production. However, the freeze-drying technology can be utilized concurrently to create further EQA samples in the long run, thereby fulfilling the Prime Minister's Decision 316/QĐ-TTg.

EXPERIMENTAL

Objectives: Determine the procedure for making lyophilized HPV samples and the standards of the samples. The sample ensures homogeneity and stability in HPV DNA qualitative parameters and HPV genotyping over a period of 6 months.

Sample acceptance standards:

- The sample was positive for the HPV DNA Type 16 or HPV DNA Type.
- The sample has consent from the person giving the sample or the sample collection support unit (according to the Research information and informed consent form).
- Collected samples are stored at room temperature for no more than 28 days.

Sample size: Estimated 80 samples (40 samples for HPV DNA Type 18 and 40 samples for HPV DNA Type 16) built according to the following contents:

- Evaluate sample stability over time (6 months): 60 samples (30 samples/batch).
- Evaluate sample homogeneity after mixing and freeze-drying: 20 samples (10 samples/batch).

Research design:

- Develop a procedure for manufacturing freeze-dried HPV samples and sample standards for raw materials and finished products.

- Produce freeze-dried samples and evaluate the stability and homogeneity of EQA samples.
- Test for HPV genotyping results and check physical appearance of freeze-dried samples to assess the homogeneity.
- Test for HPV genotyping results and check physical appearance of freeze-dried samples at a frequency of 1 month/time with a quantity of 5 samples/time to assess the stability.
- Synthesize results and analyze data.
- Report research results.

Research implemented time and location:

February - September, 2023. Performed at the Biosafety Level II laboratory, CSQL of HCMC.

Method for manufacturing samples at pilot experiments:

Step 1: Prepare production materials

- Collect cervical smear samples once a week and store them at a temperature of 2-8°C.

Step 2: Determine the dilution factor for the threshold of positive values

- Mix samples with the same type of HPV DNA Type 16 and HPV DNA Type 18 based on the results of the collected samples.
- Define the dilution ratio for the experimental sample batch by diluting the stock solution from 10 to 150.

Step 3: Produce samples

- The experimental batch is produced using the dilution ratio defined in Step 2.

Sample freeze-drying method:

- Add excipients to the sample.
- Distribute into vials used in the freeze-drying process (1.5ml volume).
- Pre-freeze samples at -30°C for 24 hours.
- Freeze-dry samples on an Alpha 2-4 LD plus lyophilizer (Christ-Germany) at -40°C, pressure 0.025 mBar, time 24 hours.

Method for evaluating sample properties, homogeneity, and stability:

Follow the guidance of CLSI C53-A (2010) "Characterization and standardization of natural reference chemicals for the laboratory" to evaluate:

- Homogeneity: measurement method applied to determine the variation between samples of the same production batch.
- Stability: determine parameter values through different storage conditions, under transportation conditions, changes in temperature and fluctuations during transportation, and effects of light, humidity, and air in the short and long term.

Within the scope of this study, criteria for evaluating stability and homogeneity by visualizing the lyophilized product, the solution after reconstitution according to the physical standards of the samples, and the DNA genotype present in the sample after reconstituted. Stability is evaluated over time at storage conditions from 2-8°C.

RESULTS AND DISCUSSION

The manufacturing procedure

After grouping according to results from the sample collection support unit, positive cervical cell samples are mixed to create two stock sample batches of HPV DNA Type 16 and HPV DNA Type 18. Dilute by 10, 20, 50, 100 and 150 times to determine the dilution ratio for negative results. Table 1 shows the results of checking the sample batch results before freeze-drying.

Table 1. Results before lyophilization

Genotype of stock	Dilution ratio	Lot code	Results
HPV DNA Type 16	Stock	16(1)	HPV DNA Type 16 positive
	1:10	16(2)	HPV DNA Type 16 positive
	1:20	16(3)	HPV DNA Type 16 positive
	1:50	16(4)	HPV DNA Type 16 positive
	1:100	16(5)	HPV DNA Type 16 positive
	1:150	16(6)	Not detected
HPV DNA Type 18	Stock	18(1)	HPV DNA Type 18 positive
	1:10	18(2)	HPV DNA Type 18 positive
	1:20	18(3)	HPV DNA Type 18 positive
	1:50	18(4)	HPV DNA Type 18 positive
	1:100	18(5)	HPV DNA Type 18 positive
	1:150	18(6)	Not detected

From the results obtained before freeze-drying, the research team elected a dilution ratio of 1:50 for the experimental sample batches after considering two reasons: the optimal saving of collected sample sources and the stability of experimental sample batches. Add 10% D-mannitol and 1% sucrose as the excipients to each batch. Distribute samples into freeze-dried vials in 1.5 mL volume. The freeze-dried sample is evaluated and the description of the shape and color of the freeze-dried cake. The sample was reconstituted with sterile distilled water. The physical standards for a freeze-dried sample are

milky white, cakey, has a smooth surface, and has no water in the sample vial (Figure 1).



Figure 1. Freeze-dried samples passed the checklist for evaluating physical criteria

The homogeneity and stability

Perform PCR HPV test with a quantity of 10 tubes per batch to evaluate homogeneity. The results are shown in Table 2.

Table 2. Results for monitor homogeneity

Lot code	No. of samples	Physical standards	PCR HPV results
16(4)	10	Passed	HPV DNA Type 16 positive
18(4)	10	Passed	HPV DNA Type 18 positive

For stability, Table 3 displays the results of physical standards checking and genotyping results of HPV DNA for six months in both batches of experimental samples.

Table 3. Results in 6 months for monitor stability

Lot code	Month					
	1	2	3	4	5	6
16(4)	HPV DNA Type 16 (+), physical standards passed (5 samples per time)					
18(4)	HPV DNA Type 18 (+), physical standards passed (5 samples per time)					

The results above show that samples from both batches have a stable term of at least six months. Combining the evaluation criteria of morphology, color, cake formation of the sample after freeze-drying, and the results of HPV genotyping after 6 months, the research chose to develop a freeze-drying process using excipients comprised a mixture of D-mannitol 10% and sucrose 1%, sample volume 1.5ml, reconstituted with sterile distilled water. A sample dilution ratio

of 1:50 was found to be stable for at least six months. Through the results obtained, the PCR HPV freeze-drying production procedure is suitable for creating products that meet technical requirements for use in EQA programs. Samples with homogeneity and stability are appropriate for the required longevity of an EQA sample. In comparison with previous research on manufacturing PCR HBV and PCR HCV EQA samples of CSQL of HCMC, samples are stable for 3 months at 4°C [5]. This study reveals that longevity was enhanced longer, helping to minimize the frequency of delivery samples throughout the year and optimizing expenses for the laboratory. WHO guidelines recommend that international standards should be stable for many years. In 2008 at the WHO 57th Expert Committee on Biological Standardization meeting, standard samples from NIBSC were established as the 1st WHO international standards for HPV DNA Type 16 and HPV DNA Type 18. By recombinant plasmids containing HPV DNA, each standard has an assigned potency of 5.10^6 IU/ampoule when reconstituted as directed in H₂O. Accelerated thermal degradation studies carried out indicate that they are remarkably stable demonstrating no drop in activity after storage for 1 year at temperatures up to 45°C [6]. This stability study supports the long-term use and also indicates that the lyophilized material may be shipped at ambient temperature without resulting in unacceptable loss of potency.

CONCLUSION

The research came up with results and products that met the initial objectives:

- Determine the method and procedure for producing samples positive for HPV DNA type 16 and HPV DNA Type 18 through the process of determining the dilution ratio and sample freeze-drying process. Post-production samples achieve homogeneity and stability for at least 6 months under storage conditions of 2-8°C.
- Develop a production procedure that meets ISO 13485 standards and determine criteria for raw materials and finished product standards to apply to the implementation of the HPV EQA program.

The project was conducted in a limited time, so monitoring the stability of the sample was limited. The research has not yet monitored the sample's maximum stability time and stability under transport conditions. Besides, the team has not yet made a matrix of different types of HPV. Therefore, the authors have the following

recommendations: (1) Research to monitor stability under transport conditions and the maximum stability time of the sample; (2) Expand the scope of research into more different types of HPV to meet the needs of clinical diagnosis.

Acknowledgment

We acknowledge the materials and facilities from Center for Standardization and Quality Control in Medical Lab of Ho Chi Minh City as the research administration unit. This research also credits HANHPHUCLAB Medical Testing & Diagnostic Center contributed as the unit supporting research sample collection.

Author Contributions:

Project administration: N.N.Vo ;
Conceptualization: N.N.Vo, T.H.P.Nguyen;
Methodology: D.D.Vu, M.T.Thai; Validation: N.N.Vo, T.H.P.Nguyen, D.D.Vu; Writing-original draft preparation. M.T. Thai; Writing-review: N.N. Vo, N.T.H. Nguyen, M.T. Thai; Editing: T.T.A. Nguyen; Investigation. N.N. Vo.

References

- [1] World Health Organization. *WHO guideline for screening and treatment of cervical pre-cancer lesions for cervical cancer prevention: use of mRNA tests for human papillomavirus (HPV)*, 2021.
- [2] Okunade, K.S., *Human papillomavirus and cervical cancer. Journal of Obstetrics and Gynaecology*. 2020. **40**(5): p.602-608.
- [3] Tam, T. H. et al, *Những vấn đề cơ bản trong đảm bảo chất lượng xét nghiệm y khoa*, 1st ed, NXB Y học, TP. Hồ Chí Minh, 2015.
- [4] Tam, T. H. et al, *Ngoại kiểm tra chất lượng xét nghiệm*, 4th ed. NXB Y học, TP. Hồ Chí Minh, 2020.
- [5] Tam, T. H. et al, *Setting up the process in manufacturing External Quality Assessment Scheme Samples for PCR-HBV, PCR-HCV External Quality Assessment Schemes*, 2013.
- [6] Wilkinson DE et al. *Establishment of the 1st World Health Organization international standards for human papillomavirus type 16 DNA and type 18 DNA*. International journal of cancer. 2010;**126**(12):2969-83.

HETEROGENEOUS DISTRIBUTION OF TiO₂ NANOTUBES IN MONTMORILLONITE SHEETS FOR THE PHOTODEGRADED ENHANCEMENT OF RHODAMINE B

Tam Thi Bang Dao¹, Loan Thi Thu Ha¹, Truong Huu Nguyen², Do Trung Nguyen¹, Nhien Hon Le¹,
Chi-Nhan Ha– Thuc¹

¹ Faculty of Materials Science and Technology, University of Science, VNU-HCM, 227 Nguyen Van Cu Street, Ward 4, District 5, Ho Chi Minh City, 700000, Viet Nam.

² Laboratory of Advanced Materials, University of Science, VNU-HCM, 227 Nguyen Van Cu Street, Ward 4, District 5, Ho Chi Minh City, 700000, Viet Nam.

Email: htcnhan@hcmus.edu.vn

ABSTRACT

MMT/TiO_{2-NTs} nanocomposite materials were prepared by a simple wet agitation method at room temperature from TiO₂ nanotubes (TiO_{2-NTs}) and Montmorillonite (MMT). The synthesized MMT/TiO_{2-NTs} samples were applied as catalysts for photocatalytic degradation of Rhodamine B (RhB) under UVC light (15W, 254 nm). MMT was purified from Bentonite clay (Lam Dong, Vietnam). After purification, MMT has a characteristic lattice surface (001) at an angle of $2\theta = 6.1^\circ$. MMT's adsorption capacity and basal spacing were 70mg/g and 14.48 Å, respectively. TiO_{2-NTs} were synthesized by the hydrothermal method. TiO_{2-NTs} have a polycrystalline structure consisting of anatase and rutile phases. The average diameter and length of the TiO_{2-NTs} are 5 nm and 110 nm, respectively. The composition, surface morphology, crystal structure, bonding vibration, and photocatalytic efficiency characteristics were analyzed by measurements such as energy dispersive X-ray (EDX), scanning electron microscopy (SEM), transmission electron microscopy (TEM), X-ray diffraction (XRD), Fourier transforms infrared (FTIR) and ultraviolet-visible spectroscopy (UV-vis). The results showed that after modification into MMT, TiO_{2-NTs} were immobilized and randomly distributed on the surface or intercalated in the clay sheets of MMT. The photocatalytic efficiency of 10 ppm RhB degradation of MMT/TiO_{2-NTs} was 82% when excited by a UVC source for 210 min.

Keywords: photocatalyst, rhodamine B, degradation, montmorillonite

INTRODUCTION

In recent years, the use of photocatalytic semiconductor materials for application in the treatment of organic compounds has achieved remarkable achievements and attracted much attention from basic research to application due to the material's ability to generate strong oxidizing free radicals. In particular, TiO₂ is known as a potential photocatalyst in the field of environmental cleaning because of its chemical inertness, biocompatibility, ease of production, non-toxicity, and relatively low cost [6, 7]. Compared with the TiO₂ nanoparticle structure, tubular TiO₂ nanotubes (TiO₂ nanotubes – TiO_{2-NTs}) have superior properties in the field of photocatalysis [8-10]. However, TiO_{2-NTs} also have limitations in photocatalytic applications such as the easy recombination between photogenerated electron and hole pairs (10⁻⁹–10⁻¹²s) which reduces the degradation efficiency,

only photocatalytic activity under a near-ultraviolet light source, difficult to separate and recycle after water treatment process... Montmorillonite (MMT) is available from natural mineral sources such as bentonite, low cost, especially with the layered structure of medium capillary material, large surface area, thermal stability, good adsorption, and cation exchange capacity [14-16]. The use of MMT as a base phase for nanocomposites can take advantage of the good retention of pollutant agents as well as the catalytic activity center, thereby helping to improve the catalytic efficiency [17-20].

EXPERIMENTAL

Materials

Titanium dioxide (TiO₂) (Merck); bentonite, ethanol (Vietnam); nitric acid, sodium hydroxide, sodium chloride, rhodamine B (China).

Refining MMT from bentonite

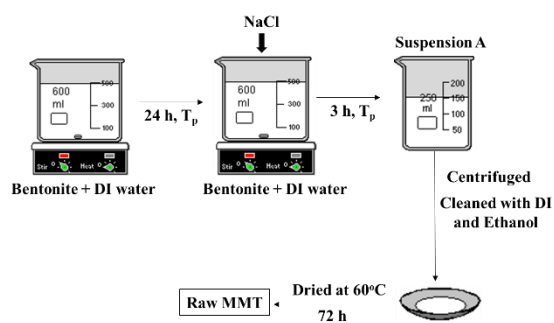


Figure 1. Steps for refining MMT from bentonite

Synthesis of TiO₂ nanotubes

TiO₂ powder was dispersed in a 10M NaOH solution. The suspension was then hydrothermally heated in a Teflon-lined autoclave at 130 °C for 24 h. The product after the hydrothermal process was filtered and washed with DI water to pH9, and soaked in 2M HNO₃ solution to pH7. The solid powder was recovered by centrifugation and dispersed in DI water (80°C) for 4 h. Then centrifuge to recover the solid powder and dry at 60°C until dry. The final product is calcined in air at 400°C for 2 hours. The end product is TiO₂-NTs.

Preparation procedure MMT/TiO₂-NTs

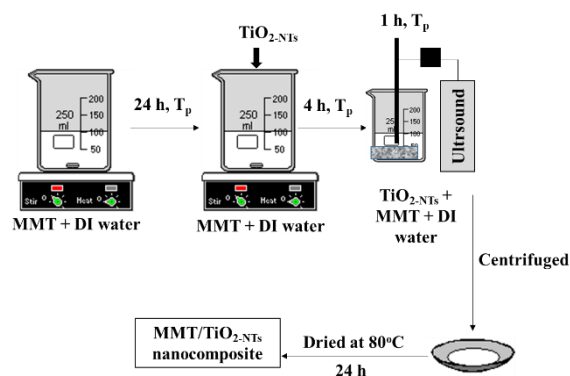


Figure 2. Steps for preparation of MMT/TiO₂-NTs

RESULTS AND DISCUSSION

Figure 3a shows that the MMT surface has a sheet shape with different sizes and shapes arranged randomly. The TEM image of TiO₂-NTs is presented in Figure 3b. The TiO₂-NTs are formed from different directions with relatively uniform sizes as an average tube diameter of about 5 nm and tube length of at least about 110 nm. The morphology of the MMT/TiO₂-NTs photocatalyst is described through the TEM analysis in Figure 3c. TiO₂-NTs are intercalated and dispersed randomly between MMT sheets to produce a heterogeneous structure [5-8].

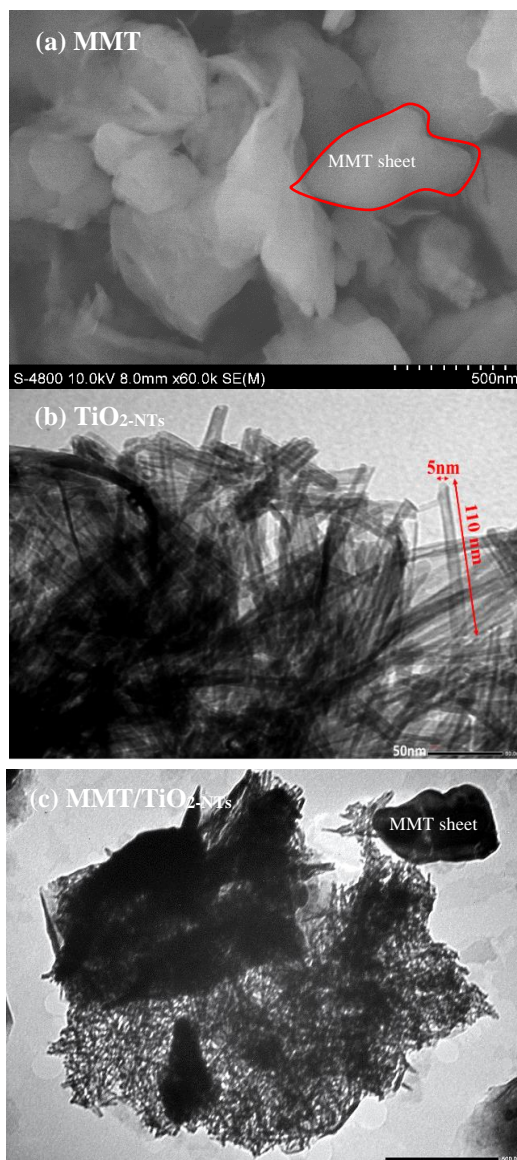


Figure 3. SEM image of MMT (a); TEM image of TiO₂-NTs (b); TEM image of MMT/TiO₂-NTs (c).

The structure of MMT, TiO₂, TiO₂-NTs, and MMT/TiO₂-NTs was also studied by X-ray diffraction as shown in Figure 4. The TiO₂ nanoparticles show the planes of anatase crystallization consisting of the diffraction peaks at (2θ) 25.3°; 37.9°; 47.8°; 54.3°; 55° and 62.7° corresponding to the network surfaces (101), (004), (200), (105), (211) and (204), respectively, with a strongest peak A(101). This structure corresponds to the highest photocatalytic activity of TiO₂. For the MMT sample, it has the d₀₀₁ spacing about 14.5 Å at (2θ) 6.1° and other diffraction peaks are observed at (2θ) 9.1°; 12.7°; 19.6°; 21.9°; 26.6°; and 35.0°. The two peaks at (2θ) 20.5° and 27.6° characterize the quartz structure in MMT. The XRD pattern of MMT/TiO₂-NTs nanocomposite shows the

existence of mainly three phases: MMT at (2θ) 5-20°, SiO₂ at (2θ) 26.6° and anatase at (2θ) 25.3°, in which, the phases MMT and SiO₂ are typical for MMT, and anatase represents for TiO₂. The peak A (101) has a low intensity compared to that of the TiO₂ sample, corresponding to a lower crystallization. This shows that during the hydrothermal process at 130°C, the crystal structure of TiO_{2-NTs} has been changed to reduce the anatase phase in TiO₂. Moreover, the d₀₀₁ spacing of MMT was reduced to 9.06 Å corresponding to a larger angle (2θ) 9.2° compared to pure MMT and MMT/TiO₂ nanocomposite. This could be explained by the TiO_{2-TNs} having entered the layer structure of MMT, leading to a decrease in the d₀₀₁ spacing of MMT [6-10].

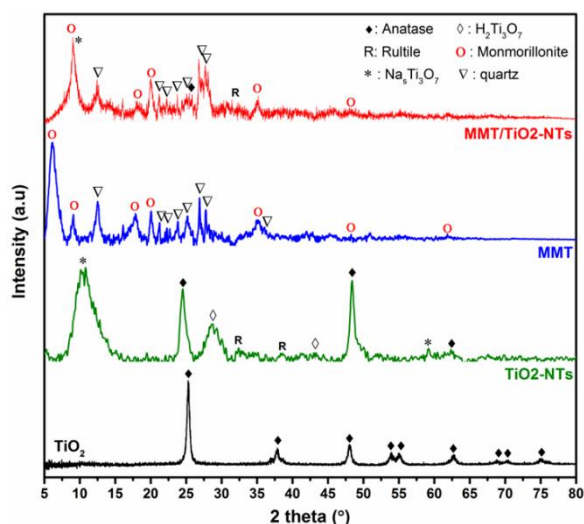


Figure 4. XRD patterns of TiO₂, TiO_{2-NTs}, MMT, and MMT/TiO_{2-NTs}

Characterization of variations on functional groups and chemical bonds of TiO₂, TiO_{2-NTs}, pure MMT, and MMT/TiO_{2-NTs} were evaluated through the FTIR spectrum as shown in Figure 5. TiO₂ nanoparticles have only one peak at wavenumbers of 430 cm⁻¹, corresponding to the stretching vibration of Ti-O, meanwhile, TiO_{2-NTs} have an adsorption band at 460-908 cm⁻¹ corresponding to the stretching vibration of the Ti-O band. TiO_{2-NTs} has also a peak at a wavenumber of 1641 cm⁻¹ could be attributed to interlayer H-O-H molecules. A wide-bulb peak at a wavenumber of 3390 cm⁻¹ characterizes the stretching vibration of the -OH group on the surface of TiO_{2-TNs}. The pure MMT has absorbance peaks at wavenumbers 3388 cm⁻¹ and 3621 cm⁻¹ that characterize the symmetrical stretching vibration of the -OH group of H₂O molecules absorbed in MMT. A vibration

at a wavenumber of 1639 cm⁻¹ characterizes for deformation of interlayer H-O-H molecules. A strong peak at a wavenumber of 987 cm⁻¹ characterizes asymmetrical stretching vibration of the -Si-O group. A peak at a wavenumber of 789 cm⁻¹ characteristics of Al-O stretching vibration, a peak at a wavenumber of 524 cm⁻¹ represents the Al-O-Si deformation vibration, and a peak at a wavenumber of 462 cm⁻¹ characteristics of Si-O-Si deformation. In comparison to FTIR spectra of pure TiO₂, TiO_{2-NTs}, MMT, and MMT/TiO_{2-NTs}, it seems that component peaks are present in the FTIR spectra of nanocomposites. It is also confirmed that the wide absorbance band of 462 – 789 cm⁻¹ corresponds to the adsorption of Ti-O. However, they did not show the stretching vibration of Si-O-Ti at wavenumber around 935 cm⁻¹ as expected or this peak overlapped with the strong peak of MMT or this might be due to the small proportion of TiO₂ in MMT [11-15].

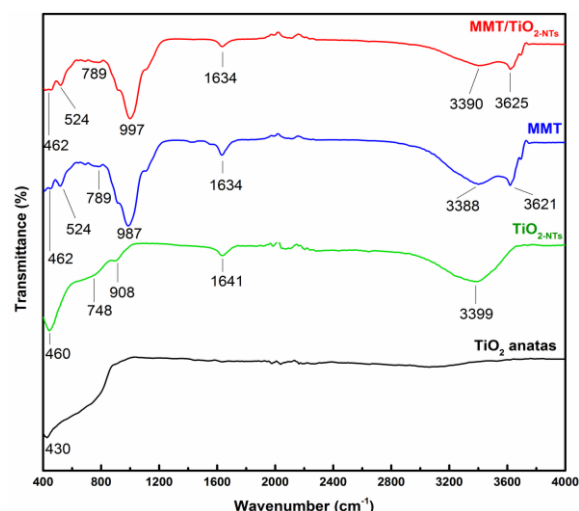


Figure 5. FTIR image of TiO₂, TiO_{2-NTs}, MMT, and MMT/TiO_{2-NTs}

The influence of UVC irradiation to trigger a photocatalytic effect likely to degrade rhodamine B of MMT, TiO₂, TiO_{2-TNs}, and MMT/TiO_{2-NTs} is shown in Figure 6a. Firstly, it could be seen that the energy of UVC irradiation alone is not enough to degrade rhodamine B. The rhodamine B degradation efficiency of MMT is the same without and within UVC irradiation because MMT has only adsorption properties without photocatalytic properties. TiO_{2-NTs} have higher photocatalytic efficiency to degrade rhodamine B than TiO₂ nanoparticles. In particular, the degradation efficiency of TiO₂ nanoparticles increased slightly to ca. 20%, corresponding to C/C₀ = 0.8 compared to less than 10% (C/C₀ = 0.9)

without irradiation. Meanwhile, the efficiency of $\text{TiO}_2\text{-NTs}$ increased significantly to 65% ($C/C_0 = 0.35$) compared to less than 10% ($0.9 C/C_0$) of a sample without UVC irradiation. Thus, under UVC irradiation, TiO_2 and $\text{TiO}_2\text{-NTs}$ are able to absorb photon energy to form hydroxyl free radicals ($\cdot\text{OH}$) free radicals, which are the main factors to degrade rhodamine B. The efficiency of $\text{MMT}/\text{TiO}_2\text{-NTs}$ is also significantly increased under UVC irradiation. it is recorded about 85% ($C/C_0 = 0.15$) compared to 73% ($C/C_0 = 0.27$) in dark condition for $\text{MMT}/\text{TiO}_2\text{-NTs}$. Thus, the results showed that under UVC irradiation, the photocatalytic effect of $\text{TiO}_2\text{-NTs}$ is increased through more production of free radicals ($\cdot\text{OH}$), leading to the capturing and degrading of rhodamine B molecules. The decoloration of the RhB after photocatalytic degradation is shown in Figure 6b. Initially, the 10 ppm RhB solution has a dark pink color, over time, the color gradually fades and is almost very pale at the end of the decomposition cycle [21].

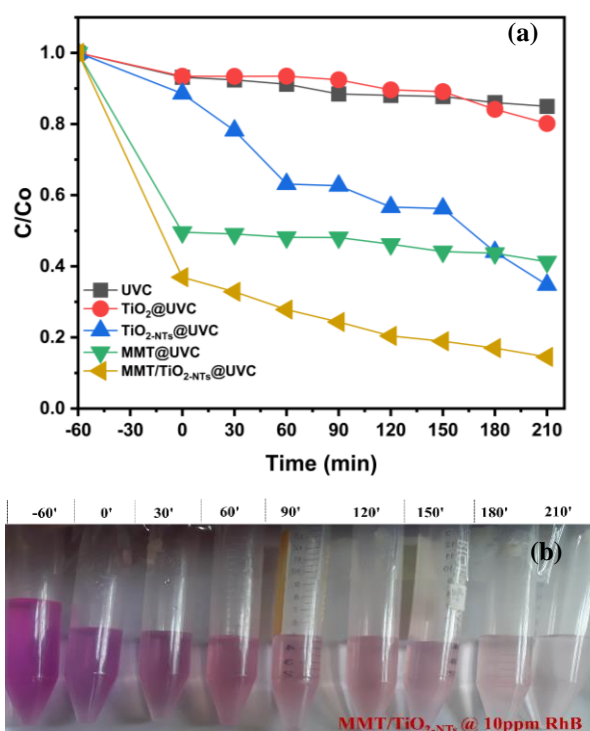


Figure 6. Photocatalytic degradation of rhodamine B with 10 ppm using different photocatalysts in the UVC irradiation condition (a); image of the decolorization of dyes in the experiment

CONCLUSION

The purified MMT from bentonite mineral is about 14.5 Å. $\text{TiO}_2\text{-NTs}$ were synthesized by

hydrothermal method with an average tube diameter of 5 nm, a tube length of 110 nm, and randomly oriented. Nanocomposite $\text{MMT}/\text{TiO}_2\text{-NTs}$ were synthesized by a simple wet stirring method with $\text{TiO}_2\text{-NTs}$ on the surface and interwoven into the flake-like structure of MMT to form a pillar-clay structure. MMT acts as an electron carrier, limiting the recombination of photogenerated e^- - h^+ pairs. The results also show that modifying MMT can not only enhance the adsorption capacity of MMT but also enhance the photocatalytic efficiency of $\text{TiO}_2\text{-NTs}$ ($[\text{RhB}] = 10$ ppm, $\text{H}\%_{\text{MMT}/\text{TiO}_2\text{-NTs}} = 82\%$).

References

- [1] Hannatu Abubakar Sani, Mansor B. Ahmad, Mohd Zobir Hussein, Nor Azowa Ibrahim, Aminu Musa, Tawfik A. Saleh. *Nanocomposite of ZnO with montmorillonite for removal of lead and copper ions from aqueous solutions*. Process Safety and Environment Protection. **109** (2017) 97–105.
- [2] A. Khataee, R. Darvishi Cheshmeh Soltani, Y. Hanifehpour, M. Safarpour, H. Gholipour Ranjbar, S. W. Joo. *Synthesis and characterization of dDysprosium-dDoped ZnO nNanoparticles for photocatalysis of a textile dye under visible light irradiation*. Industrial & Engineering Chemistry Research. **53** (2014) 1924–1932.
- [3] P. Pannak, A. Songsasen, W. Foytong, P. Kidkhunthod, W. Sirisaksoontorn. *Homogeneous distribution of nanosized ZnO in montmorillonite clay sheets for the photocatalytic enhancement in degradation of rhodamine B*. Research on Chemical Intermediates. **44** (2018) 6861–6875.
- [4] Amit Mishra, Manisha Sharma, Akansha Mehta, and Soumen Basu. *Microwave treated bentonite clay based TiO_2 composites: An efficient photocatalyst for rapid degradation of methylene blue*. Journal of Nanoscience and Nanotechnology. **17** (2017) 1149–1155.
- [5] Xu L., Tang C. Q., Qian J., Huang Z. B.; *Theoretical and experimental study on the electronic structure and optical absorption properties of P-doped TiO_2* . Applied Surface Science. **256**(9) (2010) 2668–2671.
- [6] Jiao Jin, Ting Xiao, Yanqing Tan, Jianlong Zheng, Ruohua Liu, Guoping Qian, Hui Wei, Junhui Zhang. *Effects of TiO_2 pillared montmorillonite nanocomposites on the properties of asphalt with exhaust catalytic*

- capacity. *Journal of Cleaner Production*. **205** (2018) 339–349.
- [7] Aydin Hassani, Alireza Khataee, Semra Karaca, Canan Karaca, Peyman, Gholami, *Sonocatalytic degradation of ciprofloxacin using synthesized TiO₂ nanoparticles on montmorillonite*. *Ultrasonics Sonochemistry*. **S1350–4177(16)** (2016) 30339–X.
- [8] Aydin Hassani et al. *Heterogeneous photocatalytic ozonation of Ciprofloxacin using TiO₂/MMT nanocomposite: Artificial neural network approach*. *RSC Adv*. **6** (2016) 87569–87583.
- [9] Jinhua Yin, Hai Guo, Yuanyuan Liu, Yunan Kong. *Effect of MMT Content on Structure of Polyimide/(TiO₂+MMT) Nanocomposite Films*. The 9th International Forum on Strategic Technology (IFOST), October 21-23, Cox's Bazar, Bangladesh. Corpus ID: (2014) 24094785.
- [10] Amit Mishra, Manisha Sharma, Akansha Mehta, and Soumen Basu. *Microwave Treated Bentonite Clay Based TiO₂ Composites: An efficient photocatalyst for rapid degradation of methylene blue*. *Journal of Nanoscience and Nanotechnology*. **17** (2017) 1149–1155.
- [11] Xufeng Niu et.al, *Fabrication and antibacterial properties of cefuroxime-loaded TiO₂ nanotubes*. *Applied Microbiology and Biotechnology*. **107(7)** (2020) 2947–2955.
- [12] Casu, Alberto; Lamberti, Andrea; Stassi, Stefano; Falqui, Andrea. *Crystallization of TiO₂ Nanotubes by In Situ Heating TEM*. *Nanomaterials*. **8(1)** (2018) 40.
- [13] H. Wang, H. L. Wang, W. F. Jiang, Z. Q. J. Li. *Photocatalytic degradation of 2, 4-dinitrophenol (DNP) by multi-walled carbon nanotubes (MWCNTs)/TiO₂ composite in aqueous solution under solar irradiation*. *Water Research*. **43** (2009) 204–210.
- [14] B. Ayoubi-Feiz, S. Aber, A. Khataee, E. J. Alipour. *Electrosorption and photocatalytic one-stage combined process using a new type of nanosized TiO₂/activated charcoal plate electrode*. *Environmental Science Pollution Research*. **21** (2014) 8555–8564.
- [15] Lê Thị Ngọc Tú, Vũ Thị Hạnh Thu. *Nghiên cứu quy trình và đánh giá tính năng quang xúc tác của vật liệu nano TiO₂ bằng axit terephthalic và methylene blue*. *Tạp chí Khoa học và Công nghệ*. **52(5)** (2014) 599–608.
- [16] B. Szczepanik. *Photocatalytic degradation of organic contaminants over clay-TiO₂ nanocomposites: A review*. *Applied Clay Science*. **141** (2017) 227–239.
- [17] Shiding Miao, Zhimin Liu, Buxing Han, Jianling Zhang, Xin Yu, Jimin Du and Zhenyu Sun. *Synthesis and characterization of TiO₂-montmorillonite nanocomposites and their application for removal of methylene blue*. *Journal of Materials Chemistry*. **16** (2006) 579–584.
- [18] Chung Leng Wong, Yong Nian Tan, Abdul Rahman Mohamed. *A review on the formation of titania nanotube photocatalysts by hydrothermal treatment*. *Journal of Environmental Management*. **92** (2011) 1669–1680.
- [19] Ch.Weber, S.Kaufhold. *Hamaker functions for kaolinite and montmorillonite*. *Colloid and Interface Science Communications*. **43** (2021) 100442.
- [20] M.Cox, J.R.Rus-Romero, T.S.Sheriff. *The application of montmorillonite clays impregnated with organic extractants for the removal of metals from aqueous solution: Part I. The preparation of clays impregnated with di-(2-ethylhexyl) phosphoric acid and their use for the removal of copper(II)*. *Chemical Engineering Journal*. **84(2)** (2001) 107–113.
- [21] A.A. Farghali, A.H. Zaki, M.H. Khedr. *Hydrothermally synthesized TiO₂ nanotubes and nanosheets for photocatalytic degradation of color yellow sunset*. *International Journal of Advanced Research*. **2(7)** (2014) 285-29.

REVISITING OXIDATION AND REDUCTION REACTIONS FOR SYNTHESIZING WATER INTERCALATED HYDROGEL OF REDUCED GRAPHENE OXIDE

Hon Nhien Le, Thi Quyen Dang, My Thoa Le, Thi Binh Yen Nguyen, Bich Ngoc Nguyen, Thi Cam Thuy Phan, Thi Thao Le, Huynh Anh Thai Nguyen, Thi Bang Tam Dao, Trung Do Nguyen and Chi Nhan Ha Thuc

Faculty of Materials Science and Technology, University of Science, VNU-HCM, 227 Nguyen Van Cu Street, Ward 4, District 5, Ho Chi Minh City, 700000, Viet Nam;

Vietnam National University, Area 6, Linh Trung, Thu Duc City, Ho Chi Minh City, 700000, Viet Nam

Email: lhnhien89@gmail.com

ABSTRACT

Natural graphite undergoes the chemical route of oxidation and reduction reactions to obtain graphene oxide (GO) and reduced graphene oxide (RGO) respectively. In graphite oxidation reaction, cascade design is recently reported to improve safety and efficiency in the synthesis of GO nanosheets. This study investigates influential factors of exothermic reaction temperatures to prevent thermal runaway in the oxidation reaction. In the next stage, chemical reduction reaction of GO nanosheets is developed using ammonium hydroxide solution, leading to the formation of water intercalated hydrogel of RGO nanosheets. Thanks to the hydrogel structure and three-dimensional assembly, ultrasound waves are transmitted through aqueous spaces to exfoliate the macroscopic RGO hydrogel into micro/nano RGO structures in water. Analytical results reveal homogeneous dispersions of RGO nanosheets derived from the ultrasonic exfoliation of RGO hydrogel in water medium. Consequently, the synthetic pathway of oxidation – reduction reactions is a promising technology for manufacturing GO and RGO nanomaterials.

Keywords: graphene oxide, reduced graphene oxide, graphene hydrogel, water intercalation, ultrasound

INTRODUCTION

A great deal of research and development has been given on the synthesis of graphite oxide (GrO) and graphene oxide (GO). Main challenges in scale-up reaction of graphite oxidation using Hummers reagents (KMnO_4 and concentrated H_2SO_4) are the costs and risks of explosive thermal runaway of manganese heptoxide (Mn_2O_7) or Mn(VII) compound [1,2]. To improve the safety and efficiency in the production technology, cascade design of graphite oxidation reaction has been proven to maintain exothermic reaction temperatures below the safety limit of 55°C and also harness exothermic energy for self-heating reactions. Chemical ratios are optimized to use less amount of KMnO_4 reagent and more amount of water reagent (graphite : KMnO_4 ratio of 1 : 2 w/w, graphite : H_2SO_4 of 1 : 30 w/v and water : H_2SO_4 of 2.4 : 1 v/v) [1].

A variety of chemical reducing agents were experimented for converting GO nanosheets into reduced graphene oxide (RGO), including hydrazine hydrate (N_2H_4), sodium borohydride

(NaBH_4), ascorbic acid ($\text{C}_6\text{H}_8\text{O}_6$), hydroiodic acid (HI), metals (Al, Fe, Zn and TiO_2) and biochemicals [3,4]. However, agglomeration of RGO nanosheets occurred because of hydrophobic force, π - π interaction force and van der Waals stacking potential [5]. Approaches to preventing irreversible restacking of RGO nanosheets are electrostatic stabilization, nanoparticle decoration, bio-inspired hydration and three-dimensional assembly [6-8]. Noticeably, it was demonstrated that three-dimensional hydrogel of SnO_2 -nanoparticle-decorated RGO nanosheets contained surface hydration and interlayer spacing for reversible assembly of RGO nanosheets [9].

Herein, we revisit the oxidation and reduction reactions with novel features for synthesizing hydrogel structure of non-stacking RGO nanosheets. Temperature trajectory in the process of graphite oxidation reaction was investigated to control thermal runaway. In next stage of chemical reduction reaction, it is found that ammonium hydroxide solution with high pH ~ 14 is a good reducing agent for the formation of

RGO hydrogel. Surface hydration is retained on RGO nanosheets after the reduction reaction. Water intercalation in the three-dimensional structure of RGO hydrogel not only preserves graphene nanosheets from irreversible van der Waals restacking but also provides solution-processable property.

EXPERIMENTAL

Synthesis of graphite oxide and graphene oxide. Natural graphite was converted into graphite oxide (GrO) using Hummers reagents, including KMnO_4 , H_2SO_4 96° and water. Cascade design was applied with optimized chemical amounts (graphite : KMnO_4 ratio is 1 : 2 w/w, graphite : H_2SO_4 ratio is 1 : 30 w/v and and water : H_2SO_4 ratio is 2.4 : 1 v/v) [1]. The first cascade step is the gradual pouring of graphite/ H_2SO_4 suspension into Mn(VII)/ H_2SO_4 solution. The second cascade step is the gentle pouring of graphite/Mn(VII)/ H_2SO_4 suspension (Mn(VII)- H_2SO_4 -intercalated graphite) into water under stirring. Both crucial cascade steps generated exothermic energy for self-heating reactions. After the main oxidation reaction, H_2O_2 solution 5% was added to the reaction suspension, followed by agitation, sedimentation and washing with HCl solution 5% and water. After washing with water and ethanol until pH ~ 6, the brown solid was dried and ground to obtain GrO product. Sonication of GrO powder in water was conducted to exfoliate the multilayer structure into GO nanosheets. After sedimentation and decantation, the aqueous dispersion of GO nanosheets was produced.

Synthesis of reduced graphene oxide hydrogel. Aqueous dispersion of GO nanosheets with certain solid concentration was mixed with ammonia solution 30% to obtain the highly alkaline pH of 14. The reduction reaction was conducted at the average temperature of 90°C without stirring. After certain periods of time, partially reduced graphene oxide (pGO) and reduced graphene oxide (RGO) were produced respectively. After the reduction reaction, black slurry was collected and washed with water. The black slurry was dried at 80°C to produce a macroscopic hydrogel of RGO nanosheets.

The investigation of reaction temperatures was performed using an infrared thermometer (Benetech GM-320). X-ray diffraction (XRD) was provided by the instrumentation of a Bruker D2 Phaser X-ray diffractometer. Scanning electron

microscopy (SEM) was analyzed with a Hitachi S-4800 system. Ultrasound was conducted using a Hielscher UP100H machine.

RESULTS AND DISCUSSION

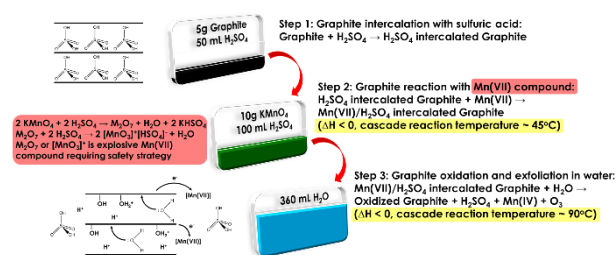


Figure 1. Cascade design mechanism of graphite oxidation reaction.

In the previous paper, the cascade design of graphite oxidation reaction was described and evidenced, including two main cascade steps [1]. As depicted in Figure 1, in the first cascade, the suspension of H_2SO_4 -intercalated graphite (graphite/ H_2SO_4 mixture) was slowly poured into the solution of Mn(VII)/ H_2SO_4 ($\text{KMnO}_4/\text{H}_2\text{SO}_4$ mixture). The first cascade facilitated graphite dispersion and graphite – Mn(VII) interaction, generating considerable exothermic energy. In the second cascade, the suspension of Mn(VII)/ H_2SO_4 -intercalated graphite (graphite/Mn(VII)/ H_2SO_4 mixture) was gently poured into water. The second cascade is highly exothermic due to the intense reaction between concentrated H_2SO_4 and water. The cascade steps and self-heating reactions save much amounts of time and energy for large-scale production.

Figure 2 presented the trajectory of reaction temperatures recorded in the cascade synthesis. When the graphite/ H_2SO_4 mixture was poured into the Mn(VII)/ H_2SO_4 mixture (the glass reactor was jacketed with ambient water (~ 29°C) in Figure 2B), the reaction temperature gradually increased to the peak at 52°C (below the thermal-runaway limit of 55°C). The exothermic energy was harnessed to facilitate graphite dispersion and intercalation with Mn(VII) compound, resulting in Mn(VII)/ H_2SO_4 -intercalated graphite. In the second cascade, the gentle pouring of graphite/Mn(VII)/ H_2SO_4 mixture into water under stirring generated intense exothermic energy to raise the reaction temperature to ~ 95°C in 2 minutes. Regarding reaction mechanism, highly positive Mn(VII) agents withdraw electrons from graphite, leaving electrophilic positions for oxidation reaction by water molecules. The

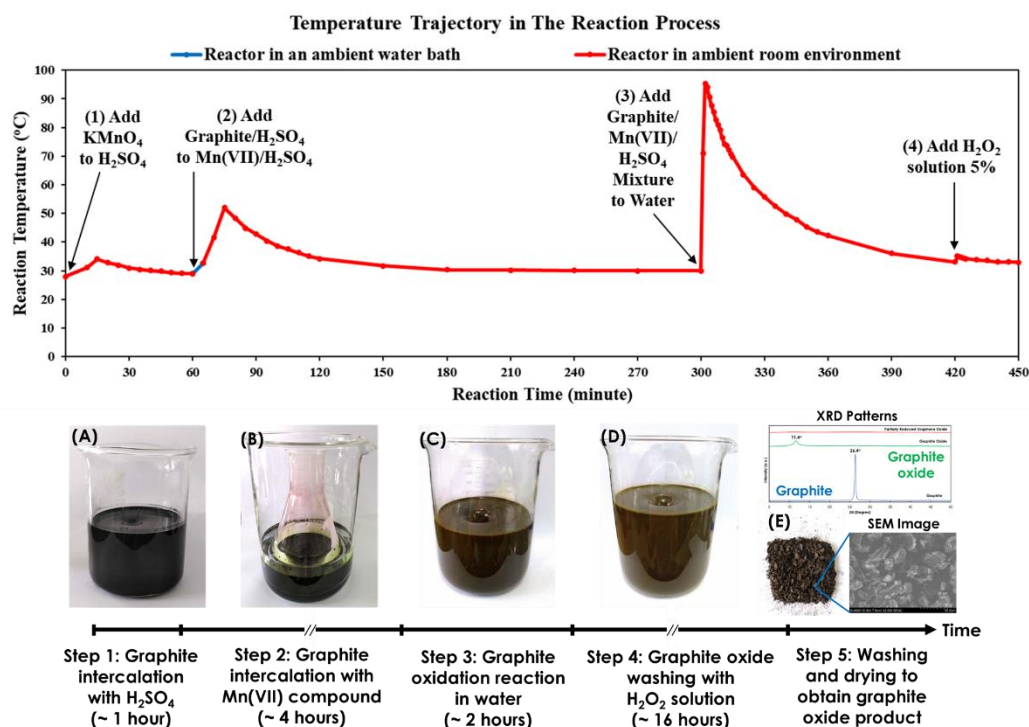


Figure 2. Trajectory of reaction temperatures in the graphite oxidation process, including (1) dissolution of KMnO_4 in H_2SO_4 solution, (2) addition of graphite/ H_2SO_4 mixture to $\text{Mn(VII)/H}_2\text{SO}_4$ solution, (3) addition of graphite/ $\text{Mn(VII)/H}_2\text{SO}_4$ to water and (4) addition of H_2O_2 solution 5% to the reaction. (A) Graphite/ H_2SO_4 mixture. (B) Addition of graphite/ H_2SO_4 mixture to $\text{Mn(VII)/H}_2\text{SO}_4$ mixture. (C) Addition of graphite/ $\text{Mn(VII)/H}_2\text{SO}_4$ mixture to water. (D) Addition of H_2O_2 solution 5% to the reaction. (E) Obtained GrO product with XRD pattern and SEM image.

oxidation reaction formed hydroxyl groups on graphite basal planes. Appropriate acidity in graphite galleries is beneficial to maintain hydroxyl groups and oxidation reaction by water. The accurate trajectory of reaction temperatures is important to control thermal runaway process in the reaction, especially the first cascade step.

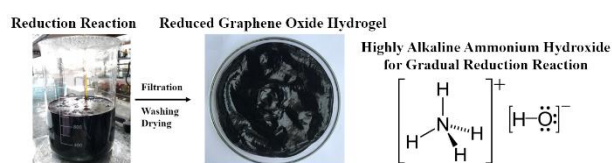


Figure 3. Chemical reduction reaction using ammonia solution to produce RGO hydrogel.

In the procedure of chemical reduction reaction, GO nanosheets were reduced by highly alkaline ammonia solution (ammonia hydroxide solution pH 14). Figure 3 exhibited the pictures of reduction reaction (at $\sim 90^\circ\text{C}$ and without stirring) and obtained product of RGO hydrogel. Strong alkali solutions (NaOH and KOH) were effective to produce stable RGO suspension [10,11]. Highly alkaline ammonia solution is a novel approach to mildly and gradually converting GO nanosheets into RGO nanosheets. Electrostatic repulsion and

surface hydration of remaining oxygen-containing functional groups prevent the restacking of RGO nanosheets. As a result, obtained RGO hydrogel is the three-dimensional structure of self-assembled RGO nanosheets intercalated with water molecules.

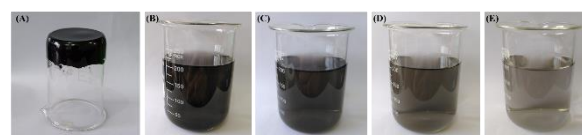


Figure 4. The RGO hydrogel (A) and homogeneous dispersions of RGO in water at different concentrations of 9 ppm (B), 7 ppm (C), 5 ppm (D) and 3 ppm (E).

Macroscopic RGO hydrogel has the properties of high water content and high viscosity (Figure 4A). Especially, ultrasonic process can exfoliate the macroscopic hydrogel in water medium. Thanks to the water intercalated structure, ultrasound waves are transmitted through aqueous spaces in RGO hydrogel, resulting in the ultrasonic exfoliation. Figures 4B - 4E presented homogeneous dispersions of RGO nanostructures in water at the concentrations of 9

ppm, 7 ppm, 5 ppm and 3 ppm. Surface hydration and water spacing are an bio-inspired approach to preventing irreversible stacking of graphene nanosheets. Non-stacking RGO nanosheets are simply separated and dispersed in water by ultrasound process. Solution-processable RGO nanomaterial is useful for many nanotechnologies and applications. In general, the concept of water intercalated structure of RGO hydrogel includes three-dimensional assembly of RGO nanosheets, surface hydration and water intercalation in the hydrogel network (Figure 5).

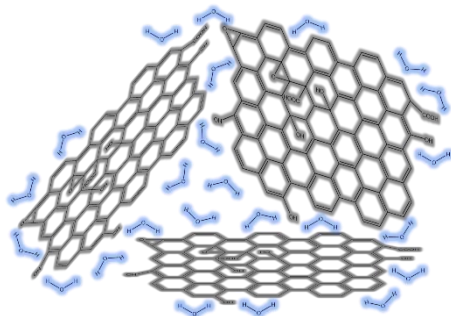


Figure 5. Drawing of water intercalated hydrogel structure of RGO nanosheets.

CONCLUSION

Cascade design of graphite oxidation reaction using Mn(VII) compound is an industrially scalable approach to harnessing exothermic energy and optimizing chemical ratios. The investigation of reaction temperatures demonstrated the safety of thermal runaway control and the efficiency of self-heating reactions. In the stage of reduction reaction using highly alkaline ammonia solution, GO nanosheets were reduced and self-assembled into the three-dimensional structure of RGO hydrogel. Water intercalation in the hydrogel structure prevents the irreversible restacking of RGO nanosheets. Water molecules in interlayer spaces are also aqueous medium for ultrasound transmission and hydrogel exfoliation. With the property of aqueous dispersibility, water intercalated structure of RGO hydrogel is a promising concept for graphene nanotechnology.

Acknowledgment

The authors would like to acknowledge the basic support of Fundamental Materials Science Laboratory, Faculty of Materials Science and Technology, University of Science, Vietnam National University, Ho Chi Minh City.

References

- [1] H. N. Le, D. Thai, T. T. Nguyen, T. B. T. Dao, T. D. Nguyen, D. T. Tieu, C. N. Ha Thuc, *Improving Safety and Efficiency in Graphene Oxide Production Technology*, J. Mater. Res. Technol. **24** (2023) 4440-4453.
- [2] P. Lakhe, D. L. Kulhanek, X. Zhao, M. I. Papadaki, M. Majumder, M. J. Green, *Graphene oxide synthesis: reaction calorimetry and safety*, Ind. Eng. Chem. Res. **59** (2020) 9004–9014.
- [3] R. Tarcan, O. Todor-Boer, I. Petrovai, C. Leordean, S. Astilean, I. Botiz, *Reduced graphene oxide today*, J. Mater. Chem. C **8** (2020) 1198.
- [4] V. Agarwal, P. B. Zetterlund, *Strategies for reduction of graphene oxide – A comprehensive review*, Chem. Eng. J. **405** (2021) 127018.
- [5] J. Luo, J. Kim, J. Huang, *Material Processing of Chemically Modified Graphene: Some Challenges and Solutions*, Acc. Chem. Res. **46** (2013) 2225–2234.
- [6] D. Li, M. B. Muller, S. Gilje, R. B. Kaner, G. G. Wallace, *Processable aqueous dispersions of graphene nanosheets*, Nature Nanotechnology **3** (2008) 101.
- [7] X. Yang, J. Zhu, L. Qiu, D. Li, *Bioinspired Effective Prevention of Restacking in Multilayered Graphene Films: Towards the Next Generation of High-Performance Supercapacitors*, Adv. Mater. **23** (2011) 2833.
- [8] J. Li, M. Östling, *Prevention of Graphene Restacking for Performance Boost of Supercapacitors – A Review*, Crystals **3** (2013) 163-190.
- [9] N. H. Le, H. Seema, K. C. Kemp, N. Ahmed, J. N. Tiwari, S. Park, K. S. Kim, *Solution-processable conductive micro-hydrogels of nanoparticle/graphene platelets produced by reversible self-assembly and aqueous exfoliation*, J. Mater. Chem. A **1** (2013) 12900.
- [10] X. Fan, W. Peng, Y. Li, X. Li, S. Wang, G. Zhang, F. Zhang, *Deoxygenation of Exfoliated Graphite Oxide under Alkaline Conditions: A Green Route to Graphene Preparation*, Adv. Mater. **20** (2008) 4490.
- [11] J. I. Paredes, S. Villar-Rodil, M. J. Fernández-Merino, L. Guardia, A. Martínez-Alonso, J. M. D. Tascón, *Environmentally friendly approaches toward the mass production of processable graphene from graphite oxide*, J. Mater. Chem. **21** (2011) 298.

OPTICAL PROPERTIES OF CORE /SHELL NANOPHOSPHORS DOPED WITH RARE EARTH IONS Er (III), Yb(III) and APPLICATION POTENTIAL

Tran Kim Anh^{1*}, Phan Lan², Wieslaw Streck³ and Le Quoc Minh⁴

¹ Institute of Materials Science, Vietnam Academy of Science and Technology (VAST) 18 Hoang Quoc Viet, Cau Giay, Hanoi, Vietnam.

²Advanced Materials and Devices Vietnam-Korea Institute of Science and Technonogy, Hoa Lac High-Tech Park, km 29 Thang Long Boulevard, Hanoi, Vietnam.

³Institute of Low Temperature and Structure Research, Polish Academy of Science, 2 Okolna Wroclaw, Poland.

⁴Graduate University of Science and Technology, VAST, 18 Hoang Quoc Viet, Hanoi, Vietnam.

*Email: kimanh101949@gmail.com

ABSTRACT

Optical properties of nanophosphors Gd_2O_3 doped Er^{3+} or codoped $Yb^{3+} - Er^{3+}$ were detail studied. Structure and morphology of the samples were measured by XRD, TEM, and FESEM. Nanophosphores with size 20-30 nm and monodisperse nanospheres 100-200 nm were synthesised by chemical many steps methods. The strong red emission and green, red or infrared were observed. The core shell structure such as $Gd_2O_3:Er^{3+}$, $Gd_2O_3: Yb^{3+}$, $Er^{3+}@ Silica$. Optical properties, photoluminescence and upconversion luminescence were studied in detail. Material with the impressive achievement in synthesis and application potential in biomedicine will be discussed ...

Keywords: $Gd_2O_3: Er(III)$ $Yb(III)@ Silica$, Upconversion luminescence , Photoluminescence spectra

INTRODUCTION

Upconversion and downconversion nanoparticles for biophotonics and nanomedicine [1, 2] have received attentions. Rare Earth (RE) nanophosphors have many applications due to advantages such as the significant physico-chemistry properties as well as owing to the unique 4f electronic orbitals structure and abundant electronic energy levels. The well-known upconversion was studied by F. Augel [3]. Applications presented in [4-8]. Our group in the long times studied nanophosphors doped rare earth ions such as Eu, Tb, Er, Yb..in some hot materials Y_2O_3 , Gd_2O_3 , NaYF such as synthesis of mesoporous-silica-coated $Gd_2O_3: Eu@silica$ particles as cell imaging and drug delivery agents, great monodispersity of $Gd_2O_3: Eu^{3+}$ and $Gd_2O_3: Eu^{3+}@Silica$ nanospheres in size around 200 nm with the low standard deviation were reported recently [9, 10, 11]. Recently, the nanospheres doped RE with the appropriate size and the required shape incorporated with strong

luminescence intensity is intensively undertaken. The chemical method enable control of the size and shape includes manipulation of optical properties toward to biomedicine application with more functions and higher performance. Specially study emission of Yb^{3+} , Er^{3+} co-doped- Gd_2O_3 nanoparticles. The high temperature annealed $Gd_2O_3: Yb^{3+}$, Er^{3+} nanospheres are 1100 °C higher than the combustion method. The upconversion luminescence intensity versus excited power of 975 nm diode laser were detail studied.

EXPERIMENTAL

Materials $Y_2O_3: Er$ $Gd_2O_3:Er$, Yb were studied.

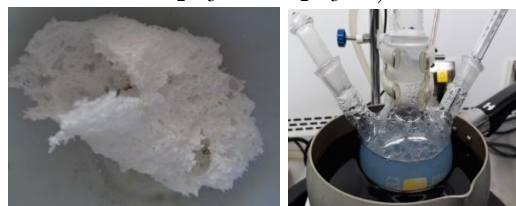


Fig 1. $Y_2O_3: Er(III)$ by combustion method.

Fig 2. The experimental synthesis nanospheres.

Materials $Y_2O_3:Er$ and $Y_2O_3:Eu$ were prepared by combustion method were presented in some our paper[9,10,11] with small amount of deionized water and EDTA- Na_2 vigorously stirred for 1h00 to form clear solution. The combustion was completed about 5 min. need without further of any external heating. The synthesized samples were carried out by using powder XRD system Model Bruker D8 – Advance using Cu $K\alpha$, 40kV, 20mA. D 5500 (VNU), JSM 7600F JEOL (AIST) HUS Spectro. The results of the XRD diffraction patterns confirm the formation of pure cubic phase. JCPDS 41-1015 $Y_2O_3:Er$

Nanomaterial Gd_2O_3 doped RE. Gd_2O_3 (99.95%), Er_2O_3 (99.99%), Yb_2O_3 (99.99%), Urea- HNO_3 . 65% (Merck). Gadolinium(III) nitrate hexahydrate ($Gd(NO_3)_3 \cdot 6H_2O$, fine powder, 99.99%, erbium(III)nitrate pentahydrate ($Er(NO_3)_3 \cdot 5H_2O$, powder, 99.99%) and ytterbium (III) nitrate pentahydrate ($Yb(NO_3)_3 \cdot 5H_2O$, powder, 99.99%), from Sigma-Aldrich; Urea ($CO(NH_2)_2$ powder, 98%, from Alomar Nomapur, Polyethylene glycol (PEG), and nitric acid (HNO_3 , solution, 65%) from Merck were purchased and used without further purification. The DI water was used for all the experimental processes. Synthesis of $Gd_2O_3:Yb^{3+}$, Er^{3+} nanospheres with cubic structure [12] Temperature at $90 \pm 1^\circ C$, reaction time from 120 to 150 min and the adding PEG implemented during the reaction proceeded at room temperature. Subsequently step by step thermal treatment at high temperature up to $1100^\circ C$ The drying and calcination process were subsequently the step by step procedure. Step by step heating at $200^\circ C$ for 2h; $400^\circ C$ for 2h and $650^\circ C$ for 3h to obtain $Gd_2O_3:Yb$ (III), Er (III) nanospheres. The calcination at higher temperature of nanosphor $Gd_2O_3:Yb$ (III), Er (III) was also accomplished step by step up to $1100^\circ C$ by Carbolite furnace Serial No: 12/00/3200

Measurement and Characterization: The morphology, size and shape of synthesized and the fabricated $Gd_2O_3:Yb$ (III), Er (III) were carried out with FESEM (Hitachi S-4800). X-ray diffraction (XRD) measurements were performed to determine the phase of the as-prepared samples at room temperature and of the calcined samples

with a Bruker D8-Advance diffractometer, using Cu $K\alpha$ radiation ($\lambda=1.5405\text{\AA}$), in the 2θ range from 10 to 70° with a scanning step of $0.02^\circ C/min$. The energy dispersion spectroscopy (EDS) was measured with a F6400 JEOL.

RESULTS AND DISCUSSION

Fig. 3a shows the XRD spectra of Gd_2O_3 nanostructures. Fig. 3(b) shows the FE-SEM image of Gd_2O_3 with 1.5% Er concentration. Fig.3(c) shows the FE-SEM image of Gd_2O_3 with 1.5% Er and 7.5% Yb concentration. Upconversion luminescent spectra also detail study for air temperature annealing

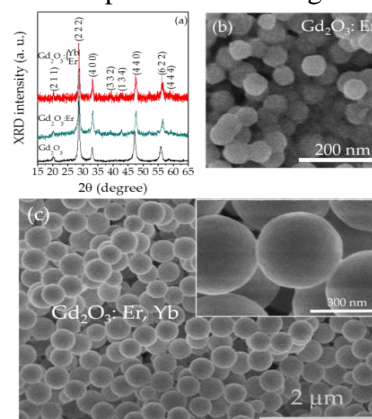


Fig 3 (a). The XRD spectra of Gd_2O_3 nanostructures. Fig 3(b). The FE-SEM image of Gd_2O_3 with 1.5% Er concentration. Fig 3(c). The FE-SEM image of Gd_2O_3 with 1.5% Er and 7.5% Yb concentration.

The luminescence properties Luminescent properties of $Gd_2O_3:1.5\%Er, 7.5\%Yb$. Optical properties of $Gd_2O_3:1.5\%Er, 7.5\%Yb$ were investigated. Luminescent Intensity depend excited power. Figure 4 shows The Upconversion luminescent spectra of ($Gd_2O_3:1.5\%Er, 7.5\%Yb$) $900^\circ C - 1100^\circ C$ annealing with different excited power 377, 503, 675, 750 mW and 1 W. Slope $n=1.92-1.94$ annealing $900^\circ C$, for Gd_2O_3 1.5% Er, 7.5% Yb for samples with PEG $n=1.97$ for samples annealing $1000^\circ C$ and $n=1.94$ for sample annealing $1100^\circ C$. Our calculate for all samples result n about 2. We can found that the final products obtained by the step by step calcination have beautiful nanospheres with size about 200 nm. Important is used this mechanism tailoring the color of upconverting emission. The red or the green will able the important role for

different cases application. Some our paper in past years concentrated to use upconversion for application in biomedicine.

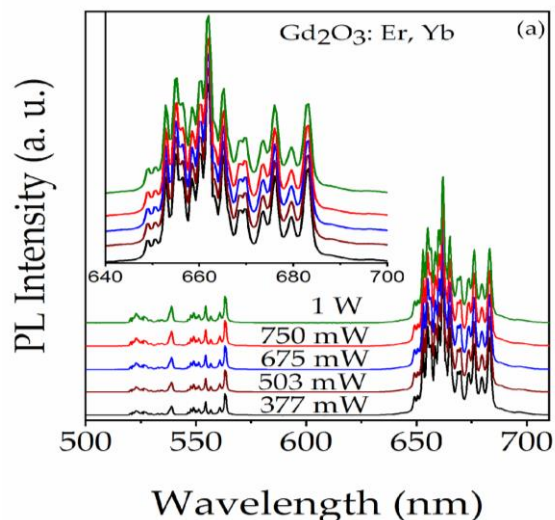


Fig 4. The Upconversion luminescent spectra of (Gd_2O_3 1.5% Er, 7.5% Yb 900 °C annealing with different excited power 377, 503, 675, 750 mW and 1 W.

We examined attack of the wet synthesis conditions and the step by step calcination procedure on UCL spectra and mechanism. To look more closely at the upconversion emission processes in the Gd_2O_3 : Yb, Er nanophosphors, the UC spectra in function of the pumping power of 975 nm laser has been measured. Fig.4 present the UC spectra of Gd_2O_3 :7.5% Yb (III) 1.5% Er (III) and Gd_2O_3 :7.5% Yb (III) 1.5% Er (III) with 0.5% PEG depends on the pumping power of 975 nm laser. The slops n were close to 2. Currently, research synthesis focused on the precise controlling morphology, desired nano-size range, enhancing UCL intensity and tuning color of RE based nanoparticles. Furthermore, studies of luminescence mechanism and understanding of luminescence processes are required to provide design and synthesis of more effective UC nanosphere. Indeed, the nanospheres doped with rare earth, especial Gd_2O_3 : Yb^{3+} , Er^{3+} monodisperse nanophosphors will be a most promising nanostructure to developing single particle image nanosensor for applied in versatile branches of modern technology, breakthrough engineering, biology and medicine. Develop from our paper for another rare earth ions [13].

CONCLUSION

In this paper we concentrated on demonstrated prepared nanospheres cover by polyethylene glycol and followed by a subsequently step by step calcination from 600°C to 1100°C for achievement of the monodisperse nanospheres Gd_2O_3 : Yb (III), Er (III). Gd_2O_3 : Yb, Er perfect nanospheres by subsequently step by step calcining procedure were 200 nm. The resultant morphology was remained spherical uniform without crack and unstacking. After high temperature treatment above 1000°C the Gd_2O_3 : Yb (III), Er (III) nanophosphors could be prepared a good re-dispersed suspension in water. The monospheres Gd_2O_3 : Yb (III), Er (III) showed the advanced performance capacity such as intense red color upconverting emission easy able redispersity and stable suspension in water. Upon 975 nm laser excitation nanophosphor Gd_2O_3 :7.5Yb (III) 1.5% Er (III) shined super bright red color. The upconversion process with the high emission intensity in red color and the transitions mechanism between the energy levels $^2H_{11/2}$ to $^4I_{15/2}$, $^4S_{3/2}$ to $^4I_{15/2}$ and $^4F_{9/2}$ to $^4I_{15/2}$ of Er^{3+} ions in Gd_2O_3 : Yb (III), Er (III) nanospheres were strongly depend on the synthesis conditions

Acknowledgment

This paper is funded by Vietnam National Foundation for Science and Technology Development (NAFOSTED) under grant number 103.03-2020.08. The authors grateful to Institute of Materials Science, VN Academy of Science and Technology.

References

- [1] Chuen Loo JF, Chien Y-H, Yin F, Kong SK, Ho H-P, Yong K-T, *Upconversion and downconversion nanoparticles for biophotonics and nanomedicine* Coordination Chemistry Reviews, **400** (2019).
- [2] Escudero A, Becerro AI, Carrillo-Carrión C, Núñez NO, Zyuzin MV, Laguna M, González-Mancebo D, Ocana M, Parak WJ, *Rare earth based nanostructured materials: synthesis, functionalization, properties and bioimaging and biosensing applications*, Nanophotonics, **6**(5) (2017) 881–921.

- [3] Auzel F, *Upconversion and Anti-Stokes Processes with f and d Ions in Solids* Chemical Reviews, Chem. Rev. **104**(1) (2004) 139-174.
- [4] Liu H, Liu J, *Hollow mesoporous Gd₂O₃:Eu³⁺ spheres with enhanced luminescence and their drug releasing behavior*, RSC Adv. **6** (2016) 99158–99164.
- [5] Zhang G, Zhang L, Si Y, Li Q, Xiao J, Wang B, Liang C, Wu Z, Zhang GTG, *Oxygen-enriched Fe₃O₄/Gd₂O₃ nanopeanuts for tumor-targeting MRI and ROS-triggered dual-modal cancer therapy through platinum (IV) prodrugs delivery*, Chem. Eng. J., **388** (2020) 124269.
- [6] Liu S-L, Wang Z-G, Xie H-Y, Liu A-A, Lamb DC, and Pang D-W, *Single-Virus Tracking: From Imaging Methodologies to Virological Applications*, Chem. Review, (2020).
- [7] Jason RC, Claire AM, Chris S, and Jennifer AD, *Refining Nanoparticle Responsiveness for Single Particle Imaging of Stimuli* ACS Photonics, (2021).
- [8] Zheng W, Sun B, Li Y, Wang R, Lei T, and Xu Y, *Near-infrared Laser Triggered Full-Color Tuning Photon Upconversion and Intense White Emission in Single Gd₂O₃ Microparticle*, ACS Sustainable Chem. Eng. (2020) 9b07464.
- [9] Tran Kim Anh, Pham Thi Minh Chau, Nguyen Thi Quy Hai, Vu Thi Thai Ha, Ho Van Tuyen, Sengthong Bounyavong, Nguyen Trong Thanh and Le Quoc Minh, *Journal of Electronic Materials* **47**(N1) (2018) 585-593.
- [10] T. Kim Anh, L.Quoc Minh, N.Vu, T.Thu Huong, N.Thanh Huong. C.Barthou and W.Strek, *Nanomaterials containing rare earth ions Tb, Eu, Er and Yb: preparation, optical properties and application potential*, *Journal of Luminescence* **102-103** (2003) 301-394.
- [11] Tran Kim Anh, Nguyen Thanh Huong, Do Thi Thao, Pham Thi Lien, Nguyen Van Nghia, Ha Thi Phuong, Robert Tomala and Le Quoc Minh, *High monodisperse nanospheres Gd₂O₃:Yb³⁺, Er³⁺ with strong upconversion emission fabricated by synergistic chemical method*. *Journal Nanopart.* **23** (2021) 264.
- [12] Le Q M, Tran T H, Nguyen T H, Hoang T K, Nguyen T B, Do K T, Tran K A, Nguyen D H, Le T L, Nguyen T Q, Dang M D, Nguyen N A T, and Nguyen V M, *Development of a fluorescent label tool based on lanthanide nanophosphors for viral biomedical application*. *Nanosci. Nanotechnol.* **3** (2012) 035003.
- [13] Tran Kim Anh, Paul Benalloul, Charles Barthou, Nguyen Vu, Lam Thi Kieu Giang and Le Quoc Minh, *Luminescence, Energy transfer and upconversion Mechanism of Y₂O₃ nanomaterials doped with Eu³⁺, Tb³⁺, Tm³⁺, Er³⁺ and Yb³⁺ ions*, *Journal of Nanomaterials*. Volume, ID 49247 *Luminescent Nanomaterials, Spe, Iss,* (2007).

PREPARATION AND *IN VITRO* ANTIBACTERIAL ACTIVITY AGAINST *PANTOEA STEWARTII* CAUSING JACKFRUIT BRONZING DISEASE OF NANO ZnO/OLIGOCHITOSAN

Nguyen Trong Hoanh Phong^{1*}, Bui Duy Du^{1,2,*}, Le Nghiem Anh Tuan², Tran Phuoc Tho², Nguyen Quoc Hien²

¹ Graduate University of Science and Technology, Vietnam Academy of Science and Technology, 18 Hoang Quoc Viet Street, Cau Giay District, Ha Noi City, Viet Nam;

² Institute of Applied Materials Science, Vietnam Academy of Science and Technology, 1B TL29 Street, Thanh Loc Ward, District 12, Ho Chi Minh City, Viet Nam

*Corresponding: Email: vina9802@gmail.com, sharahio@yahoo.com

ABSTRACT

Nano ZnO/oligochitosan (nano ZnO/OC) prepared in this study was nanomaterial consisting of nano ZnO with average size of $\sim 15.1 \pm 5.8$ nm dispersed in OC solution. Nano ZnO/OC exhibited the ability to resist *Pantoea stewartii* causing jackfruit bronzing disease. The OC with a low molecular weight (Mw) of about 3,300 g/mol had the main advantage that was completely soluble in both acidic and alkaline mediums up to pH 9. The studied material was characterized by gel permeation chromatography, proton nuclear magnetic resonance, transmission electron microscopy and X-ray diffraction. The results of the *in vitro* test against *P. stewartii* of nano ZnO/OC showed that the antibacterial efficacy attained to $\sim 85\%$ at a concentration of 500 mg/L. Therefore, the nano ZnO/OC had a great potential to use as an effective agent to control the jackfruit bronzing disease.

Keywords: Oligochitosan, nano ZnO/OC, antibacterial, *Pantoea stewartii*, jackfruit

INTRODUCTION

The use of nanomaterials to efficiently manage harmful plant pathogens is currently receiving significant attention and development. Nano ZnO is synthesized from low-cost raw materials through rational methods and processes, creating products that can be mass-produced [1]. Nano ZnO is biologically safer than Ag and CuO nanoparticles since it has low toxicity to humans and the environment [2]. Furthermore, the use of nano ZnO in plants also improves the creation of antioxidants and defense enzymes and promotes plant growth [3].

Chitosan (CS) is a β -1,4 linked polymer of glucosamine and lesser amounts of *N*-acetylglucosamine [4]. CS has biological properties such as antibacterial, antifungal, anticancer, biodegradation, biocompatibility, stimulating plant disease resistance and wound healing [5]. Modification of the Mw of CS to prepare water-soluble oligochitosan (OC) using chemical, biological, or ionizing radiation methods has broadened its applicability. The OC with low Mw, and water solubility has high antioxidant capacity, and can induce defensive

responses in plant tissues to resist pathogens [6,7]. The synthesis of ZnO nanoparticles by Zn^{2+} precipitation method was completed at alkaline pH. So in this study, OC with low Mw was used as a stabilizer due to CS with high Mw was precipitated at alkaline pH [8].

Currently, the jackfruit bronzing disease caused by gram-negative bacteria *Pantoea stewartii* is a serious disease wreaking havoc on super early jackfruit in Vietnam, especially in the rainy season. *P. stewartii* can host many plants, such as corn, rice, wheat, oats, and jackfruit [9]. It is facultative anaerobes, rod-shaped, non-flagellum, 1 - 2 μ m long, catalase-positive, whose colonies are yellow, slightly convex, and round with a size of 1 - 4 mm [10]. In Vietnam, the jackfruit growing area, mainly Thai jackfruit, was about 50,000 ha [11]. Over the years, super early Thai jackfruit has been infected by bronzing disease, which thrives during the rainy season. The bronzing disease causes the phenomenon of black rags on jackfruit [12].

To minimize the damage of this disease, integrated control measures such as field sanitation, proper fertilization, disease-resistant varieties, rain cover for fruit to prevent rainwater

from carrying bacteria into jackfruit, and pesticides use have been applied. However, the above measures have proven ineffective in controlling this disease.

In this report, we studied the preparation of nano ZnO/OC and tested *in vitro* the inhibitory effect against *P. stewartii* causing the jackfruit bronzing disease with the goal of using it as a disease-control agent in plants, particularly during the rainy season.

EXPERIMENTAL

ZnO 99%, NaOH 96% (Xilong - China). KI, Luria Bertani Broth (LB) and lactic acid (Merck - Germany). OC with Mw ~3,300 g/mol and degree of deacetylation (DD) of 91.36% determined by GPC chromatography and ¹H-NMR spectrum, respectively (Institute of Applied Materials Science - Vietnam). *P. stewartii* bacteria was supplied by the Institute of Agriculture Science for Southern Vietnam.

Preparation of nano ZnO/OC colloidal solution

Dissolve 1.3 g ZnO and 3.6 g lactic acid in 50 mL distilled water to obtain a zinc lactate solution. The zinc lactate solution was mixed into 100 mL OC solution (120 g/L OC). Solution of 9.5 g NaOH in 30 mL distilled water was added dropwise into the Zn²⁺/OC solution that was placed on a magnetic stirrer, stirring constantly until the NaOH solution was completely added, then distilled water was added to make 200 mL. This solution was treated in an ultrasonic bath for 5 min at a frequency of 14 kHz and a power of 500W to obtain nano ZnO/OC solution.

Characterization of materials

The powder of nano ZnO/OC was prepared by vacuum drying at 60°C. The TEM images were captured using a TEM S4800-NIHE - Japan. The XRD patterns were measured on an XRD D8 Advance-Bruker - Germany.

In vitro assay of antibacterial activity

The antibacterial activity of the nano ZnO/OC against *P. stewartii* was investigated using the agar diffusion method as proposed by El-Masry et al. [13] and Wiegand et al. [14] with a slight modification. Sterile filter papers with a diameter of 6 mm were impregnated with 20 µL of tested substances at concentrations of 425, 450, 475 and 500 mg/L. Distilled water was used at the control sample. Both test and control sterile filter papers were placed in petri dishes (diameter 90 mm)

containing LB agar. Petri dishes were incubated at 37°C for 24 hours. The diameter of the inhibition zone was measured on the Interscience Scan 500 - France.

All data were presented as mean ± standard deviation (SD). One Way ANOVA was performed for each treatment with five replicates. The means were compared using the least significant difference (LSD) at 0.05 probability level ($P \leq 0.05$).

RESULTS AND DISCUSSION

The average size of nano ZnO determined by TEM images (Figure 1) showed that the size of nano ZnO stabilized in OC was $\sim 15.1 \pm 5.8$ nm.

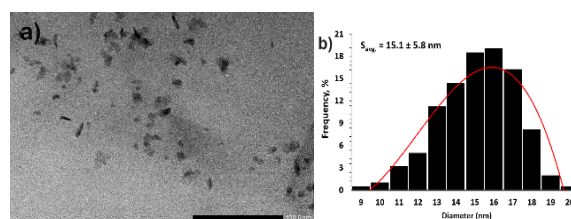


Figure 1. TEM images (a) and particle size distributions (b) of nano ZnO/COS.

The XRD patterns of OC and nano ZnO/COS are presented in Figure 2.

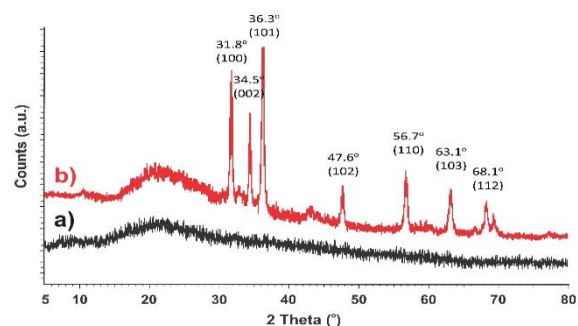


Figure 2. XRD patterns of OC (a) and nano ZnO/OC (b).

The XRD pattern in Figure 2a showed that there was only a diffraction peak at $2\theta \sim 19.3^\circ$, while according to Podgorbunskikh et al. [15], CS with high Mw had two diffraction peaks at $2\theta \sim 10^\circ$ and 20° . The reason for this phenomenon is that when CS reduces Mw, the intramolecular hydrogen bonds decrease, reducing the crystalline properties of CS. The XRD pattern in Figure 2b showed that zinc exists as ZnO with a wurtzite crystal structure with characteristic diffraction peaks at $2\theta \sim 31.8^\circ$, 34.5° , 36.3° , 47.6° , 56.7° , 63.1° , and 68.1° corresponding to reflection planes (100), (002), (101), (102), (110), (103) and (112), respectively [16].

The diameters of the inhibition zone against *P. stewartii* of the studied samples are presented in Table 1.

Table 1. The diameter of the inhibition zone against *P. stewartii* of nano ZnO/OC after 24 hours.

Material	Conc. (mg/L)	Diameter of the inhibition zone (mm)
Nano ZnO/OC	425	10.2 ± 0.7 ^a
	450	16.7 ± 1.2 ^b
	475	17.9 ± 0.7 ^{bc}
	500	18.9 ± 1.0 ^c
LSD _{0.05}		1.3

Results in Table 1 and Figure 3 showed that the diameter of the inhibition zone for *P. stewartii* of nano ZnO/OC at concentrations of 425, 450, 475 and 500 mg/L was 10.2, 16.7, 17.9 and 18.9 mm, respectively. This result demonstrated that ZnO nanoparticles exhibited antibacterial activity at a low concentration of 49 mg/L (eqv. to 500 mg/L nano ZnO/COS) and the antibacterial effect increased proportionally with ZnO nano concentration. This finding was also consistent with Gudkov et al. [17], who reported that ZnO nanoparticles had antibacterial properties at low concentrations ranging from 0.16 to 5.0 mM (eqv. 12.96 - 405 mg/L) had high antibacterial activity.

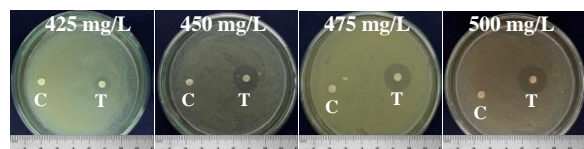


Figure 3. The diameter of the inhibition zone against *P. stewartii* of nano ZnO/OC after 24 hours. (Note: C is control and T is treatment).

Recently, the studies on ZnO nanoparticles' antibacterial activity in plants were also published. For example, Nandhini et al. [18] discovered that ZnO nanoparticles at a concentration of 500 mg/L were effective against *Sclerospora graminicola*, which causes downy mildew disease on pearl millet. Vera-Reyes et al. [19] reported that ZnO nanoparticles at a concentration of 700 mg/L inhibited 90% of *Clavibacter michiganensis*, and at a concentration of 1000 mg/L inhibited 67% of *Pseudomonas syringae in vitro* tests. As far as we know, no previous research on the use of nano ZnO to inhibit *P. stewartii* has been published.

CONCLUSION

In this work, the nano ZnO/OC was successfully prepared using the sol-gel method. The *in vitro* test of nano ZnO/COS against *P. stewartii* showed that its effectiveness within a concentration range of 425 mg/L to 500 mg/L. Therefore, the synthesized nano ZnO/OC product has the potential to be used as an effective plant disease control agent, particularly for the jackfruit bronzing disease in Vietnam.

Acknowledgment

This research was funded by the priority scientific directions of the Vietnam Academy of Science and Technology (grant No: VAST03.05/22-23).

References

- [1] A. Kalia, K.A. Abd-Elsalam, K. Kuca, *Zinc-based nanomaterials for diagnosis and management of plant diseases: Ecological safety and future prospects*, Journal of Fungi **6** (2020) 222.
- [2] W. Zhang, X. Liu, S. Bao, B. Xiao, T. Fang, *Evaluation of nano-specific toxicity of zinc oxide, copper oxide, and silver nanoparticles through toxic ratio*, Journal of Nanoparticle Research **18** (2016) 372.
- [3] M. Elsharkawy, A. Derbalah, A. Hamza, A. El-Shaer, *Zinc oxide nanostructures as a control strategy of bacterial speck of tomato caused by Pseudomonas syringae in Egypt*, Environmental Science and Pollution Research **27** (2020) 19049-19057.
- [4] D.X. Du, B.X. Vuong, *Study on preparation of water-soluble chitosan with varying molecular weights and its antioxidant activity*, Advances in Materials Science and Engineering **2019** (2019) 8781013.
- [5] T. Dai, M. Tanaka, Y.Y. Huang, M.R. Hamblin, *Chitosan preparations for wounds and burns: Antimicrobial and wound-healing effects*, Expert Review of Anti-infective Therapy **9** (2011) 857-879.
- [6] P. Li, Z. Cao, Z. Wu, X. Wang, X. Li, *The effect and action mechanisms of oligochitosan on control of stem dry rot of Zanthoxylum bungeanum*, International Journal of Molecular Sciences **17** (2016) 1044.
- [7] N.N. Thuy, H.D. Quy, N.N. Duy, N.Q. Hien, N.D. Hai, *Preparation, characterization, and antioxidant activity of water-soluble*

- oligochitosan*, Green Processing and Synthesis **6** (2017) 461-468,.
- [8] Q.Z. Wang, X.G. Chen, N. Liu, S.X. Wang, C.S. Liu, X.H. Meng, C.G. Liu, *Protonation constants of chitosan with different molecular weight and degree of deacetylation*, Carbohydrate Polymers **65** (2006) 194-201.
- [9] M. Jeger, C. Bragard, T. Candresse, E. Chatzivassiliou, K. Dehnen-Schmutz, G. Gilioli, D. Caffier, *Pest categorisation of *Pantoea stewartii* subs *stewartii**, EFSA Journal **16** (2018) e05356,.
- [10] R. Ibrahim, S.I. Ismail, M.Y. Ina-Salwany, D. Zulperi, *Biology, diagnostics, pathogenomics and mitigation strategies of jackfruit-bronzing bacterium *Pantoea stewartii* subspecies *stewartii*: What do we know so far about this culprit?*, Horticulture **8** (2022) 702.
- [11] M.V. Tri, N.V. Hoa, N.M. Chau, A. Pane, R. Faedda, A. De Patrizio, L. Schena, C.H.B. Olsson, S.A.I. Wright, M. Ramstedt, S.O. Cacciola, *Decline of jackfruit (*Artocarpus heterophyllus*) incited by *Phytophthora palmivora* in Vietnam*, Phytopathologia Mediterranea **54** (2015) 275-280.
- [12] R.M. Gapasin, R.P. Garcia, C.T. Advincula, C.S. De la Cruz, L.M. Borines, *Fruit bronzing: A new disease affecting jackfruit caused by (smith) mergaert *Pantoea stewartii* et al.*, Annals of Tropical Research **36** (2014) 17-31.
- [13] R.M. El-Masry, D. Talat, S.A. Hassoubah, N.M. Zabermaawi, N.Z. Eleiwa, R.M. Sherif, M.A.S. Abourehab, R.M. Abdel-Sattar, M. Gamal, M.S. Ibrahim, A. Elbestawy, *Evaluation of the antimicrobial activity of ZnO nanoparticles against enterotoxigenic *Staphylococcus aureus**, Life **12** (2022) 1662.
- [14] I. Wiegand, K. Hilpert, R.E. Hancock, *Agar and broth dilution methods to determine the minimal inhibitory concentration (MIC) of antimicrobial substances*, Nature Protocols **3** (2008) 163-175.
- [15] E. Podgorbunskikh, T. Kuskov, D. Rychkov, O. Lomovskii, A. Bychkov, *Mechanical amorphization of chitosan with different molecular weights*, Polymers **14** (2022) 4438.
- [16] N.N. Thanh, N.N. Thinh, N.V. Anh, *In situ synthesis and characterization of ZnO/chitosan nanocomposite as an adsorbent for removal of congo red from aqueous solution*, Advances in Polymer Technology **2020** (2020) 3892694.
- [17] S.V. Gudkov, D.E. Burmistrov., D.A. Serov, M.B. Rebezov, A.A. Semenova, A.B. Lisitsyn, *A mini review of antibacterial properties of ZnO nanoparticles*, Frontiers in Physics **9** (2021) 641481.
- [18] M. Nandhini, S.B. Rajini, A.C. Udayashankar, S.R. Niranjana, O.S. Lund, H.S. Shetty, H.S. Prakash, *Biofabricated zinc oxide nanoparticles as an eco-friendly alternative for growth promotion and management of downy mildew of pearl millet*, Crop Protection **121** (2019) 103-112.
- [19] I. Vera-Reyes, I.J.E. Esparza-Arredondo, R.H. Lira-Saldivar, C.A. Granados-Echegoyen, R. Alvarez-Roman, A. Vásquez-López, G. Santos-Villarreal, E.C. Díaz-Barriga, *In vitro antimicrobial effect of metallic nanoparticles on phytopathogenic strains of crop plants*, Journal of Phytopathology **167** (2019) 461-469.

NITROGEN-DOPED BIOCHAR FOR EFFICIENT REMOVAL OF H₂S FROM BIOGAS

Phuc Hoan Tu¹, **Yuma Horii**¹, **Youji Honda**², **Yuki Hamasaki**² and **Yusuke Shiratori**¹

¹ Department of Mechanical Science and Engineering, School of Advanced Engineering, Kogakuin University, 2665-1 Nakano-machi, Hachioji, Tokyo 192-0015, Japan.

² Low-Carbon Technology Group, Research Institute, Kyushu Electric Power Co., Inc., 2-1-47, Shiobaru, Minami-ku, Fukuoka, 815-8520, Japan.

Email: tuhoanphuc@cc.kogakuin.ac.jp

ABSTRACT

The rice husk biochar (RHBC), sewage sludge biochar (SSBC) and their nitrogen-doped biochar samples (RHBC-N and SSBC-N, respectively) were prepared, and tested as H₂S absorbents in the flow of simulated biogas (60% CH₄ and 40% CO₂). RHBC-N exhibited the highest breakthrough capacity of 16.3 mg H₂S-g BC⁻¹ compared with those of RHBC, SSBC and SSBC-N, 0.3, 0.25 and 0.08 mg H₂S-g BC⁻¹, respectively. Because the breakthrough capacity depends on the level of nitrogen doping, microstructure and the organic content, these were investigated by X-ray Photoelectron Spectroscopy (XPS), field emission scanning electron microscope (FE-SEM) and thermogravimetric analyzer (TG-DTA), respectively. The nitrogen-doped biochar is expected to contribute to the stable operation of SOFC running on biogas containing H₂S. Keywords: nitrogen-doped biochar, biogas, hydrogen sulfide, adsorption, desulfurization

INTRODUCTION

Efficient utilization of renewable energies and their spread has to be accelerated to stop global warming. Solid oxide fuel cell (SOFC), high temperature fuel cell operated in the range of 600-900°C, can be operated by biogas supply to generate electricity with electrical efficiency twice as high as that of conventional engine generators [1,2]. Regional bio-wastes are digested under anaerobic condition to produce biogas (45-75 vol% CH₄ and 25-55 vol% CO₂) containing hydrogen sulfide (H₂S) with 500–3000 ppm [3], which is well known as impurity strongly deactivates reforming catalyst and SOFC anode [4]. Therefore, the removal of H₂S from biogas (desulfurization) is an indispensable process for the operation of SOFC, and its concentration should be lowered to sub-ppm level to ensure the commercial durability of SOFC operation [5].

Here, biochars derived from rice husk and sewage sludge and them doped with nitrogen by an ammonia treatment were studied as a desulfurizer for contributing to the stable operation of biogas-fueled SOFC.

EXPERIMENTAL

Preparation of biochar: Rice husk (RH) or sewage sludge (SS) was put in an alumina tube and heated to 500°C at a rate of 10°C min⁻¹ in 50 mL min⁻¹ N₂ flow, then kept at this temperature for 120 min for pyrolysis, followed by natural cooling to room temperature to obtain biochar (BC). The produced BC was then powdered and stored in a glass flask. RH- and SS-derived BCs were labeled as RHBC and SSBC, respectively.

Preparation of N-doped biochar: 10 wt% NH₄⁺ solution (Fujifilm Wako Pure Chemical Corporation, Japan) simulating the concentrated digestate liquid was used as a nitrogen source. Carrier gas (N₂) was bubbled through this solution with 100 mL min⁻¹ at 30°C, corresponding to the gas phase composition of 15.7 vol% NH₃ and 3.8 vol% steam. 2 g of RHBC (or SSBC) was exposed to the ammonia-containing gas flow at 850°C for 270 min. The resulting sample was labelled as RHBC-N (or SSBC-N).

H₂S adsorption test: The 50 mL min⁻¹ gaseous mixture containing 20 ppm H₂S (N₂ with 40 ppm H₂S: 25 mL min⁻¹, CH₄: 15 mL min⁻¹, CO₂: 10 mL min⁻¹) was flowed through the glass tube (inner diameter of 0.75 cm) packed with 1.0 g of a biochar sample at 25°C. After starting the gas supply, outlet gas was collected every 30 min in a 5.0 L gas bag (F2S sampling bag, Asone Co.),

and the H₂S concentration was measured using a gas analyzer (Biogas 5000, Geotechnical Instrument Ltd., UK).

Breakthrough time (t_0) is the time when the adsorbate (here, H₂S) starts to penetrate the packed biochar. In this study, t_0 was defined as the time when 1 ppm of H₂S (the lower detection limit of Biogas 5000) is detected in the column outlet. After the breakthrough was reached, the outlet gas was collected twice a day (at 10 AM and 5 PM) in a 2.0 L plastic gas bag to measure the H₂S concentration using a detector tube 4LK (hydrogen sulfide detector tube, Gastec Corporation, Japan). The breakthrough capacity (q_0) was calculated using the following equation;

$$q_0 = (\rho v/m)C_0 t_0 \quad (1)$$

where ρ (g L⁻¹) is the density of H₂S gas, v (L h⁻¹) is the volumetric flow rate, m (g) is the adsorbent (biochar) mass and C_0 (ppm) is the H₂S concentration at the inlet.

Microstructure of biochars was investigated by field emission scanning electron microscope (FESEM-SU8010, Hitachi, Japan). For near-surface analysis, X-ray photoelectron spectroscopy (XPS) was conducted at room temperature using a monochromated Al K α ($h\nu = 1,486.7$ eV) X-ray source operated at 5 mA and 15 kV (JPS-9030, JEOL, Japan). All binding energies (BEs) were referred to the C1s line at 284.6 eV.

The contents of volatile solids (VS) and non-volatile solids (ash) corresponding to organic and inorganic substances, respectively, were analyzed by thermogravimetry and differential thermal analysis (TG-DTA) (Thermoplus EVO2, Rigaku Co., Ltd., Japan). 10 mg of a sample was heated to 800°C at a rate of 10°C min⁻¹ in 20 mL min⁻¹ air flow, and kept for 120 min at this temperature.

RESULTS AND DISCUSSION

Fig. 1 shows the H₂S adsorption curves of BC and ammonia-treated BC samples in the H₂S adsorption test. As summarized in **Table 1**, the t_0 of RHBC and SSBC were 4 h and 3 h, respectively. The ammonia-treated one (RHBC-N) exhibited a considerably longer t_0 of 200 h, corresponding to q_0 of 16.3 mg H₂S g-BC⁻¹, more than 50 times higher than that of RHBC. However, ammonia treatment was not effective for SSBC. Its t_0 was decreased from 3 h to 1 h.

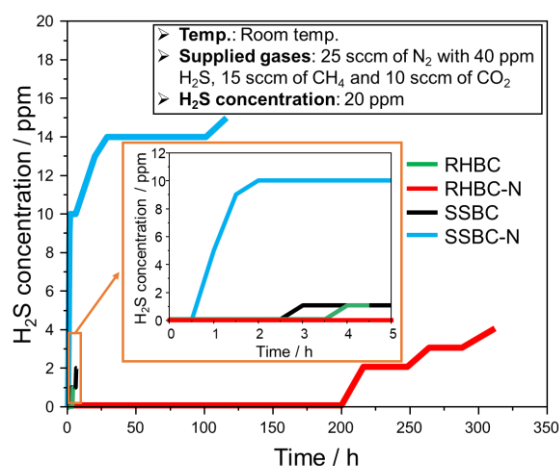


Figure 1. H₂S adsorption curves of biochar samples.

Table 1. Breakthrough time and breakthrough capacity of biochar samples for H₂S adsorption.

Sample	Adsorbate	t_0 / h	q_0 / mg H ₂ S g-BC ⁻¹	VS* / %
RHBC	20 ppm	4	0.3	55.6
RHBC-N	H ₂ S in	200	16.3	51.3
SSBC	simulated	3	0.25	9.1
SSBC-N	biogas	1	0.08	1.0

*Measured by TG-DTA.

The contents of organic components (VS: volatile solid) were 55.6, 51.3, 9.1 and 1.0 % for RHBC, RHBC-N, SSBC and SSBC-N, respectively. The low breakthrough capacity of SSBC and SSBC-N are caused by the extremely low organic content, as shown in **Table 1**.

Figs. 2a and **b** show the morphology of RHBC before and after ammonia treatment, respectively. The carbon surface of RHBC was doped with nitrogen by the ammonia treatment at 850°C through partial NH₃ gasification to deposit nitrogen functional groups on the carbon surface [6], followed by the gasification of carbon surface with 3.8 vol% steam to slightly reduce the organic content from 55.6 % to 51.3%. In the case of SSBC, ammonia vapor also modified the carbon surface to form the nitrogen functional groups. However, only 9.1 % of organic component in SSBC caused the lack of carbon surface after ammonia treatment (1.0 % of organic component in SSBC-N). Almost carbon was removed from the SSBC by the ammonia treatment (see **Figs. 2c** and **d**).

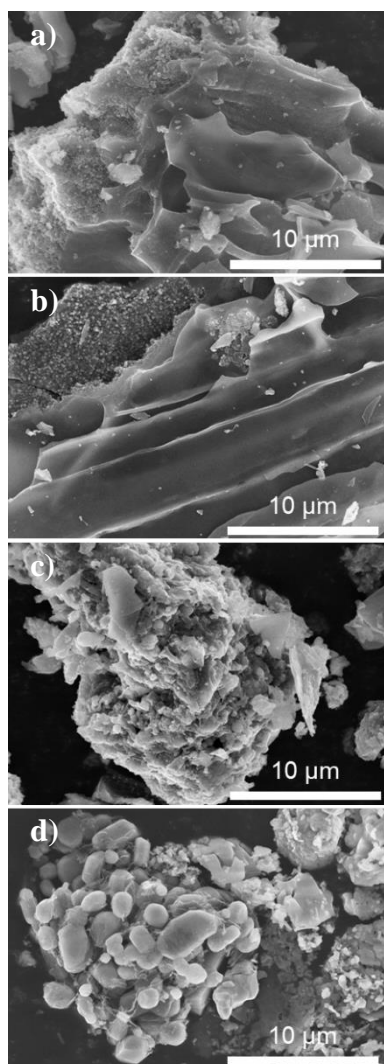


Figure 2: FESEM images of a) RHBC, b) RHBC-N, c) SSBC and d) SSBC-N.

Fig. 3 shows the XPS profiles of RHBC and RHBC-N before and after H₂S adsorption (denoted as RHBC-H₂S and RHBC-N-H₂S, respectively). All binding energies were calibrated based on the C 1s peak at 284.6 eV. The peaks of N 1s in the RHBC-N and RHBC-N-H₂S were found at 398.5 eV (see **Figs. 3a** and **b**). By the ammonia treatment, pyridinic- (dominant), pyrrolic-, and graphitic-N were formed. Especially, the pyridinic-N can act as the main absorption site of H₂S [7]. After the H₂S adsorption, in the S 2p profile of the ammonia-treated RHBC, which has the q_0 of 16.3 mg H₂S g-BC⁻¹, the peaks of SO₄²⁻ and C-S appeared (see **Fig. 3c**).

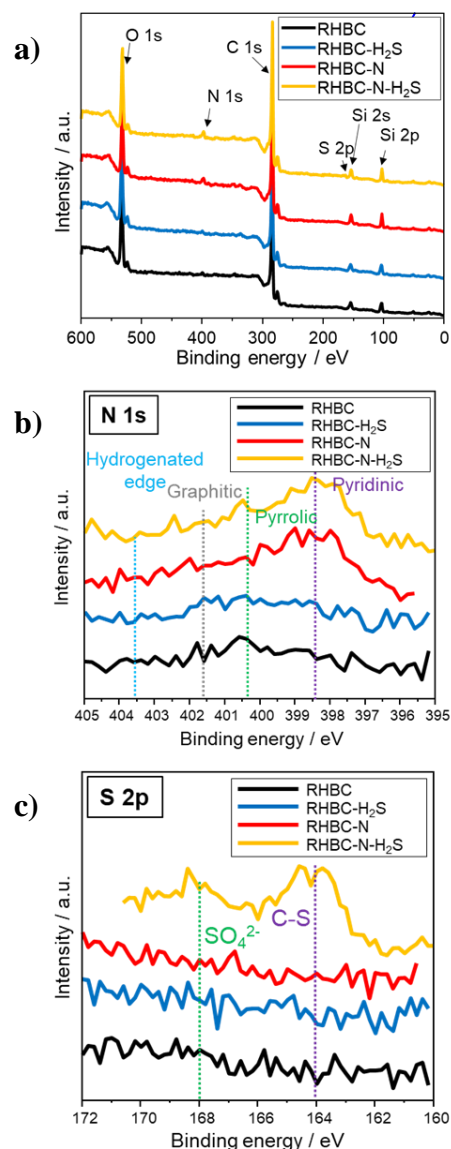


Figure 3: XPS survey profiles (8 scans) for RHBC, RHBC-H₂S, RHBC-N and RHBC-N-H₂S. a) wide scans, and focused ones on b) N 1s and c) S 2p.

The XPS profiles of SSBC and SSBC-N before and after H₂S adsorption (denoted as SSBC-H₂S and SSBC-N-H₂S, respectively) are shown in **Fig. 4**. For the SSBC, the peaks of C 1s at 284.6 eV were considerably reduced by the ammonia treatment (**Fig. 4a**), indicating the strong gasification of carbon surface as discussed in **Fig. 2**. For the pristine SSBC, peaks can be seen in the N 1s profile, however those were disappeared by the ammonia treatment as shown in **Fig. 4b**. Due to the very low q_0 of SSBC and SSBC-N, any peaks were not detected in the S 2p profiles (**Fig. 4c**).

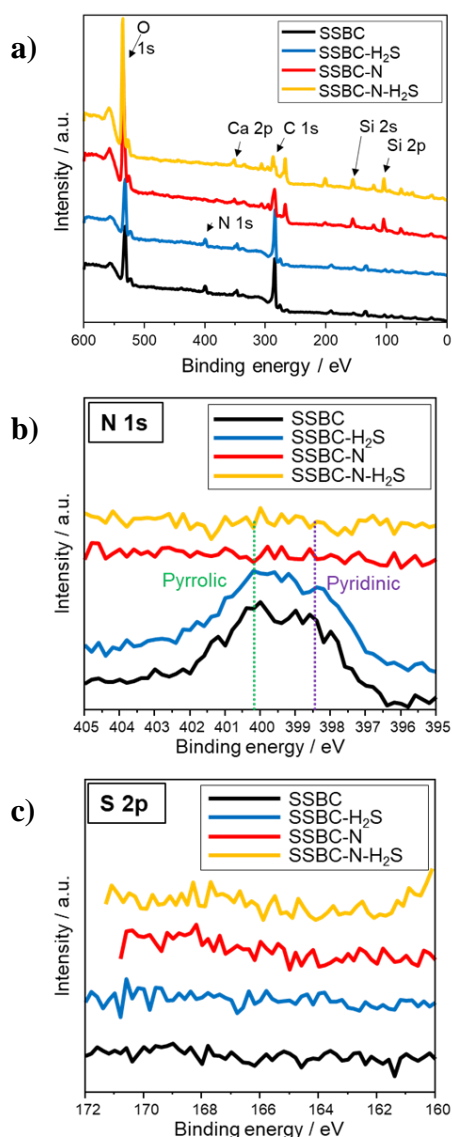


Figure 4: XPS survey profiles (8 scans) for SSBC, SSBC-H₂S, SSBC-N and SSBC-N-H₂S. a) wide scans, and focused ones on b) N 1s, and c) S 2p.

CONCLUSION

Rice husk biochar (RHBC) and sewage sludge biochar (SSBC) were prepared by carbonization, and doped with nitrogen by ammonia treatment named as RHBC-N and SSBC-N, respectively. The prepared biochar samples were tested as a desulfurizer for the removal of H₂S from the flow of simulated biogas containing 20 ppm H₂S. RHBC-N showed the highest breakthrough capacity (q_0) of 16.3 mg H₂S g-BC⁻¹, extremely higher than those of RHBC, SSBC and SSBC-N, thanks to the nitrogen-doped carbon groups at the surface of RHBC. For SSBC with low VS, nitrogen doping was not effective. RHBC-N developed in this study will be applied as the

desulfurizer for a simulated and a real biogases in the demonstration test of SOFC fueled by biogas.

Acknowledgment

This work was supported by JSPS KAKENHI, Fostering Joint International Research (B), Grant Number 20KK0248.

References

- [1] I. Aznam, A. Muchtar, MR. Somalu, NA. Baharuddin, NAH. Rosli, *Advanced materials for heterogeneous catalysis: A comprehensive review of spinel materials for direct internal reforming of methane in solid oxide fuel cell*, Chemical Engineering Journal **471** (2023) 144751-144769.
- [2] Y. Shiratori, T. Quang-Tuyen, K.Sasaki, *Performance enhancement of biodiesel fueled SOFC using paper-structured catalyst*, International journal of hydrogen energy **38** (2013) 9856-9866.
- [3] Y. Gao, J. Jiang, Y. Meng, F. Yan, A. Aihemaiti, *A review of recent developments in hydrogen production via biogas dry reforming*, Energy Conversion and Management **171** (2018) 133-155.
- [4] K. Haga, S. Adachi, Y. Shiratori, K. Itoh, K. Sasaki, *Poisoning of SOFC anodes by various fuel impurities*, Solid State Ionics **179**(2008) 1427-1431.
- [5] E. Brightman, DG. Ivey, DJL. Brett, NP. Brandon, *The effect of current density on H₂S-poisoning of nickel-based solid oxide fuel cell anodes*, Journal of Power Sources **196**(2011) 7182-7187.
- [6] H. Setiawan, M. Sakamoto, Y. Shiratori, *Study on biochar as desulfurizer for SOFC application*, Fuel Cells **21** (2021) 430-439
- [7] L. Leng, S. Xu, R. Liu, T. Yu, X. Zhuo, S. Leng, Q. Xiong, H. Huang, *Nitrogen containing functional groups of biochar: An overview*, Bioresource technology **298** (2020) 122286-122299.

APPLICATION OF DES IN FABRICATING SILVER NANOPARTICLES FOR TRICLOSAN DETECTION

Le Hong Tho^{1,2,3}, Nguyen Tran Truc Phuong^{1,2,3}, Nguyen La Ngoc Tran^{1,2,3}, Do Thao Anh^{1,2,3}, Le Thanh Tam^{1,2,3}, Hanh Kieu Thi Ta^{1,2,3}, Phan Huy Thong⁴, Truong Anh Phuc⁴, Pham Minh Chau⁴, Bach Thang Phan^{2,3}, Nhu Hoa Thi Tran^{1,2,*}

¹ Faculty of Materials Science and Technology, University of Science, Vietnam National University, Ho Chi Minh City, Viet Nam

² Vietnam National University, Ho Chi Minh City, Viet Nam

³ Center for Innovative Materials and Architectures (INOMAR), Vietnam National University, Ho Chi Minh City, Viet Nam

⁴ High School for the Gifted, Vietnam National University, Ho Chi Minh City, Viet Nam

Email: * tnhoa@hcmus.edu.vn

ABSTRACT

The specialty surface-enhanced Raman spectroscopy (SERS) of plasmonic materials offers better profiles for biosensors. However, an ideal plasmonic materials synthesis strategy has not yet been well developed. Here, we propose an effective procedure for synthesizing silver nanoparticles (Ag NPs) supported by deep eutectic solvents (DES). D-glucose, glycerol and urea are chosen to form DES, which directly acts as either a green solvent or a surfactant. Accordingly, our strategy helps to solve the time-consuming and toxicity issues. Further, the Ag NPs as-synthesized are coated on glass, and under excitation of laser 532 nm, SERS signals are collected to detect triclosan (TCS). Herein, the limit of detection (LOD) is comparatively low 10^{-8} M. Other experimental results also show the uniformity and consistency in SERS signals. This study furnishes evidence of the capability of DES to synthesize Ag NPs and also offers a novel pathway to fabricate nanomaterials in biosensors and biomedical applications.

Keywords: silver nanoparticles, DES, SERS, TCS, biosensors

INTRODUCTION

Silver nanoparticles (Ag NPs) are ubiquitous in materials science. The localized surface plasmon resonance (LSPR) responses for numerous applications of Ag NPs, especially in surface-enhanced Raman spectroscopy (SERS). SERS demonstrates its undoubting sensitivity, powerfulness, and multifunction in analytical probes of biosensors [1]. However, the limits of SERS's technical parameters contribute to restricting its clinical trials [2]. Besides, the optical properties of Ag NPs primarily depend on their size, shape, and morphology, which are adjustable within synthesis. Time-consuming procedures and toxic chemical compound usage downgrade the value of Ag NPs for biosensor applications [3]. Hence, more investigations for simple, effective, and eco-friendly Ag NPs synthesis are required.

Deep eutectic solvent (DES) belongs to a distinctive phenomenon of nature. Mixing two or more compounds typically in the solid phase makes a homogenous liquid at a specific temperature and molar ratio called DES [4,5].

DES shows superior environmentally friendly properties that are suitable for biomedical applications [5]. Besides, previous reports showed the developmental potential of DES in fabricating noble metal nanoparticles [6,7]. Herein, DES plays a crucial role in shape-controlling and acts as either a solvent or a surfactant [7]. With those decisive advantages, DES can replace conventional toxic solvents and reagents. In our study, we propose a procedure for Ag NPs synthesis using DES. It is novel to fabricate and apply these Ag NPs in SERS-based biosensors.

Triclosan (TCS) is chosen to be the analyte in SERS analysis. TCS was reported to be hazardous leading to hormonal havoc and cancers [8] although it has been still used as illegal antimicrobials since 1970s [9]. The wide usage of TCS has led to extreme exposure through merchandise such as foods, cosmetics, and cleansers [8]. Therefore, detecting TCS remains meaningful in real life. Ag NPs is applied in the SERS substrates ensuring the lowering limit of detection (LOD) of TCS.

EXPERIMENTAL

Materials synthesis: D-glucose, glycerol, and urea (molar ratio 1:2:1 [10]) are mixed and mechanically stirred until a homogenous liquid form. Adding L-ascorbic acid and AgNO₃ orderly helps the reaction occur and stir vigorously for 30 minutes. The obtained products are washed with DI water, centrifuged, and redispersed in DI water to form Ag NPs solutions. The SERS substrates are prepared by oxygen plasma, treated with 3-aminopropyltriethoxysilane (APTES), and coated by as-synthesized Ag NPs. These substrates are for further material characterization and analysis.

Characterization techniques: The UV-vis spectroscopy (HP 8453, Agilent Technologies, Santa Clara, CA, USA), X-ray diffraction (XRD, Bruker D8 Advance diffractometer, Cu-K α , λ = 1.54178 Å), and field-emission scanning electron microscopes (FESEM, Hitachi S4800, USA) are used to investigate the nanostructure and basic properties of Ag NPs samples.

Detection of TCS: 20 μ L of TCS (various concentrations from 10⁻⁸ to 10⁻³ M) is dropped on Ag NPs substrates. As soon as the samples are dry, Raman measurement is carried out under excitation of laser 532 nm. Different positions on the SERS substrate are chosen to test the consistency of the signals of the samples. Later, data analysis offers limit of detection (LOD), enhancement factor (EF), and other experimental properties.

RESULTS AND DISCUSSION

Figure 1 shows the UV-vis spectrum of Ag NPs solution. The maximum adsorption band of the colloid is 406 nm, similar to other reports [3,11]. A broad absorbance band and symmetrical peak shape response for the high exciton of even shape of Ag NPs [11]. XRD pattern (**Figure 2**) also proves the existence of Ag NPs thin film with the appearance of four specific peaks corresponding to the (111), (200), (220), and (311) planes. Attentionally, the intense peak at 38.2° stands for the (111) lattice plane of face-centered cubic (FCC) silver element [11]. Further investigation of FESEM images (**Figure 3**) shows the spherical shape and uniform size of Ag NPs. Besides, the agglomeration of colloids can be explained by a new peak appearing at 500 - 700 nm in the UV-vis spectrum (**Figure 1**). Without any strange peak presence in UV-vis and XRD results, DES shows the primary role in surfactant

through making dense hydrogen linkage around Ag NPs.

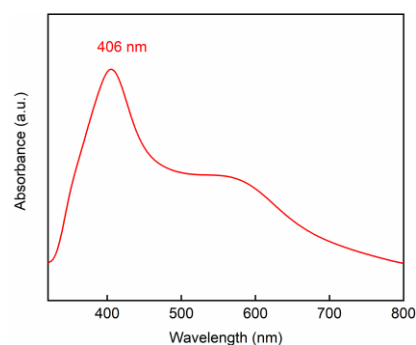


Figure 1. UV-vis spectrum of Ag NPs solution.

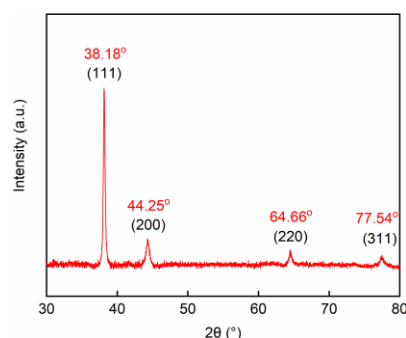


Figure 2. XRD pattern of Ag NPs thin film.

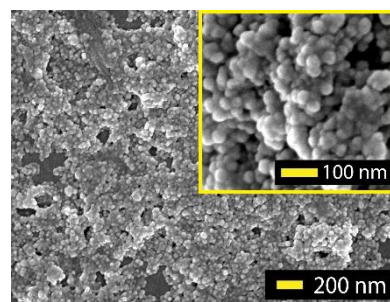


Figure 3. FESEM images of Ag NPs.

SERS analysis of TCS is carried out with the concentration range from 10⁻³ M down to 10⁻⁸ M. **Figure 4** represents the Raman spectra of TCS with peaks at different wavenumbers. The peaks at 700 cm⁻¹, 792 cm⁻¹, 1080 cm⁻¹, and 1266 cm⁻¹ are the most intense and enhanced ones attributed to the stretching vibrations of C-Cl, C-O-C, and alicyclic C-C [8]. Additionally, the LOD value is 10⁻⁸ M indicating favorable sensitivity. Meanwhile, **Figure 5** is the standard logarithmic curve with the strong linearity relationship between -Log C (C stands for TCS concentration) and Raman intensity of the peak at 700 cm⁻¹ wavenumber as follows the equation $y = -1019x + 9043$. The quantitative determination TCS exhibits superior reliability that the linear relationship coefficient value R² equals 0.9958

whereas the highest EF value reaches 1.91×10^7 . Hence, the Ag NPs synthesized in DES are suitable for TCS residue detection.

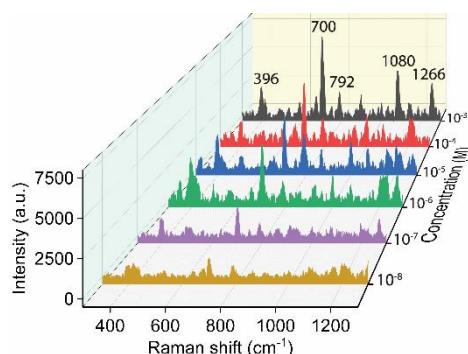


Figure 4. SERS spectra of TCS at different concentrations.

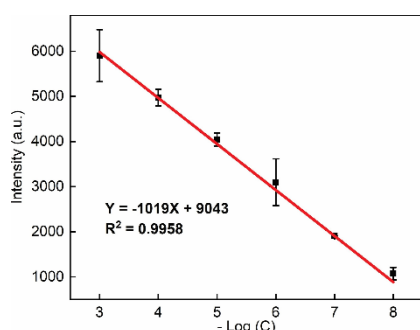


Figure 5. Calibration curve for linear relationship between $-\text{Log}(C)$ and Raman intensity at 700 cm^{-1} .

The consistency of Ag NPs thin film is further examined by collecting Ag Raman spectra from six different positions. The most intense peak at 700 cm^{-1} from SERS data is chosen to calculate the RSD value. As observed from Figure 6, the Raman intensities of peaks demonstrate relatively low variance that RSD equals 8.84%. This indicates the comparative predominance of Ag NPs in Raman signals enhancement while consistency is ensured.

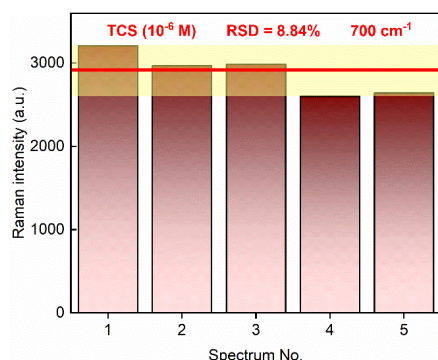


Figure 6. Raman intensity of enhanced peak at 700 cm^{-1} collecting from six different positions.

CONCLUSION

In this study, we successfully fabricated a novel material Ag NPs formed by DES within a rapid and nontoxic procedure, which strongly indicates the potential of DES in nanomaterials synthesis. Moreover, we offer a specific application of this Ag NPs in TCS detection. Experimental results prove the high sensitivity, comparable LOD (10^{-8} M), EF value (1.91×10^7), notable uniformity, and consistency in SERS signals. To sum up, our strategy for fabricating Ag NPs in DES could be applied in SERS-based biosensors to detect TCS in consumer goods at low concentrations.

Acknowledgment

This research is funded by University of Science, VNU-HCM under grant number T2023-149.

References

- [1] M. Arabi, A. Ostovan, Y. Wang, R. Mei, L. Fu, J. Li, X. Wang, and L. Chen, *Chiral Molecular Imprinting-Based SERS Detection Strategy for Absolute Enantiomeric Discrimination*, *Nat Commun* **13**, (2022).
- [2] X. Xi and C. Liang, *Perspective of Future SERS Clinical Application Based on Current Status of Raman Spectroscopy Clinical Trials*, *Frontiers in Chemistry*.
- [3] S. Irvani, H. Korbekandi, S. V. Mirmohammadi, and B. Zolfaghari, *Synthesis of Silver Nanoparticles: Chemical, Physical and Biological Methods*, 2014.
- [4] B. B. Hansen et al., *Deep Eutectic Solvents: A Review of Fundamentals and Applications*, *Chemical Reviews*.
- [5] E. L. Smith, A. P. Abbott, and K. S. Ryder, *Deep Eutectic Solvents (DESs) and Their Applications*, *Chemical Reviews*.
- [6] J. S. Lee, *Deep Eutectic Solvents as Versatile Media for the Synthesis of Noble Metal Nanomaterials*, *Nanotechnol Rev* **6**, 271 (2017).
- [7] F. A. Mahyari, M. Tohidi, and A. Safavi, *Synthesis of Gold Nanoflowers Using Deep Eutectic Solvent with High Surface Enhanced Raman Scattering Properties*, *Mater Res Express* **3**, (2016).
- [8] B. Zhao, T. Yang, Y. Qu, A. J. Mills, G. Zhang, and L. He, *Rapid Capture and SERS Detection of Triclosan Using a Silver Nanoparticle Core – Protein Satellite*

Substrate, Science of the Total Environment
716, (2020).

- [9] D. W. Larson, U. Matthes, J. A. Gerrath, J. M. Gerrath, J. C. Nekola, G. L. Walker, S. Porembski, A. Charlton, and N. W. K Larson, 5. Conover, W. J. *Practical Non-Parametric Statistics* 2nd Edn, Cambridge Univ. Press, 1991.
- [10] M. Zdanowicz, *Deep Eutectic Solvents Based on Urea, Polyols and Sugars for Starch Treatment*, *Int J Biol Macromol* **176**, 387 (2021).
- [11] S. Mukherji, S. Bharti, G. Shukla, and S. Mukherji, *Synthesis and Characterization of Size- And Shape-Controlled Silver Nanoparticles*, *Physical Sciences Reviews*.

SYNTHESIS, CHARACTERIZATION AND ANTIBACTERIAL ACTIVITY OF Fe₃O₄@Ag NANOCOMPOSITE

Khang Viet Mai, Tam Thanh Thi Nguyen, Anh Van Thi Le*, Diep Ngoc Le, Dung My Thi Dang, Hoa Mai Thi Le, Chien Mau Dang

Institute for Nanotechnology, Community 6, Linh Trung Ward, Thu Duc City, Ho Chi Minh City, Vietnam;

Vietnam National University Ho Chi Minh City, Ho Chi Minh City, Vietnam

Email: ltvanh@vnuhcm.edu.vn

ABSTRACT

This report presents an investigation into the synthesis, characterization, and antibacterial activity of the Fe₃O₄@Ag nanocomposite (Fe₃O₄@Ag). Magnetic nanoparticle Fe₃O₄, around of 20nm, was synthesis by co-precipitation method. After that, silver nanoparticles were introduced by drop AgNO₃ solution to make Fe₃O₄@Ag material. The material's morphology was determined by FESEM. The presence and ratio of metal component elements is determined by FTIR, AAS, XRD and RAMAN. Antibacterial activity of Fe₃O₄@Ag is tested on four trains *Escherichia coli*, *Staphylococcus aureus*, *Bacillus subtilis* and *Pseudomonas aeruginosa* in normal and magnetic environment and analysis FESEM image of cell's surface is recorded. The result show that the combination of iron oxide (Fe₃O₄) and silver (Ag) in the Fe₃O₄@Ag nanocomposite offers synergistic effects that could enhance antibacterial properties.

Keywords: Fe₃O₄@Ag, nanocomposite, antibacterial activity.

INTRODUCTION

Over the past twenty years, magnetic nanoparticles (MNPs) have been extensively employed in various applications due to their distinct magnetic properties, high surface area, and individual dimensions. Amongst them, magnetite nanoparticles (Fe₃O₄ NPs) has garnered significant attention due to its fascinating properties and diverse range of applications. The high saturation magnetization of Fe₃O₄ MNPs enables effortless magnetic separation of these nanoparticles under an external magnetic field, which plays a vital role in biomedical applications of Fe₃O₄ thanks to the manipulation of these particles to the intended location of use [1]. Fe₃O₄ has been studied in the field of biomedicine, including magnetic resonance imaging (MRI), cell separation, hyperthermia as a heat mediator, biosensing, and drug delivery for cancer treatment [2]. In the biomedical field, the magnetic nanoparticles (MNPs) typically utilized are typically below 20 nm in size, which results in the manifestation of superparamagnetic properties [3].

Silver nanoparticles (AgNPs) have garnered attention in multiple fields, including catalysis, electronics, biomedicine, and environmental applications [4]. The unique characteristics of Ag

NPs are attributed to their inherent properties, such as localized surface plasmon resonance, high surface area-to-volume ratio, excellent conductivity, and tunable optical properties [5]. Consequently, the synthesis of hybrid nanostructures combining Fe₃O₄ NPs and Ag NPs, known as Fe₃O₄@Ag NPs, serves as a strategy to harness and enhance the individual properties of each nanoparticle component.

In this study, we report that the synthesis of Fe₃O₄@Ag nanoparticles involves a two-step process. The first step involves the synthesis of magnetite nanoparticles via the co-precipitation method, followed by the deposition of silver nanoparticles onto their surface. The Fe₃O₄@Ag nanocomposite was characterized via different techniques in order to determine the material's morphology, size, presence, and ratio of metal component elements. *Escherichia coli*, *Staphylococcus aureus*, *Bacillus subtilis*, and *Pseudomonas aeruginosa* were used to evaluate the antibacterial activity of Fe₃O₄@Ag.

EXPERIMENTAL

1. Materials

The iron chloride II tetrahydrate (FeCl₂.4H₂O), iron chloride III hexahydrate (FeCl₃.6H₂O), NaOH (Sodium hydroxide),

AgNO₃, were provided by Merk. All solutions were prepared using ultrapure water with a resistivity of 18.2 MΩ cm.

Four bacterial strains were used in this study, including two models for Gram-positive bacteria (*Staphylococcus aureus* ATCC 6539 and *Bacillus subtilis*, isolated) and two Gram-negative bacteria (*Pseudomonas aeruginosa* ATCC 9027 and *Escherichia coli* ATCC 8739). These bacterial strains were cultured and preserved on Tryptone Soya Agar (TSA) medium. Tryptone soya broth (TSB), glutaraldehyde, ethanol from Merck. Phosphate-Buffered Saline (PBS), pH 7.4, NaCl 0.9% solution.

2. Synthesis of Fe₃O₄

The Fe₃O₄ NPs were synthesized by chemical co-precipitation method. Solid FeCl₃.6H₂O and FeCl₂.4H₂O (molar ratio 2:1) was dissolved in 100 ml DI water under N₂ medium with mechanical stirring (600 rpm) at 80°C for 30 minutes. The NaOH aqueous solution (2M) was gradually dropped into the mixture, the color of the solution changed from yellow/brown to dark brown/black as the precipitate forms, the pH of the solution is about 9-11. The obtained precipitate was then separated with magnet and were washed several times with DI water. After that, the precipitate was dried in vacuum oven at 50°C for 24h. The obtained Fe₃O₄ (black powder) was stored for later use.

3. Synthesis of Fe₃O₄@Ag

Previously prepared Fe₃O₄ NPs were dispersed in water under ultrasound for 1 h. AgNO₃ solution (1g/100ml) were slowly added drop by drop to the Fe₃O₄ solution, the molar ratio of Fe₃O₄ to AgNO₃ were 1:1. NaOH solution was dropped to adjust the mixture solution pH to 10. Then, the mixture was stirred for 1h at room temperature. The obtained Fe₃O₄@Ag NPs were separated with magnet and were washed several times with DI water. As the Fe₃O₄ were coated with Ag, the black Fe₃O₄ particles turned brownish. The particles were dried in vacuum oven at 50°C for 24h and Fe₃O₄@AgNPs were obtained later.

Fe₃O₄@Ag is characterized by X-Ray Diffraction (XRD), Fourier-transform infrared spectroscopy (FTIR), X-ray diffraction (XRD), and field emission scanning electron microscope (FESEM), and atomic absorption spectrophotometric (AAS).

4. Preparation of bacterial sample

Microorganisms were pre-cultured in TSA for 24h at 37°C to have separated colonies. The bacteria trains were transferred from mass to 10ml NaCl 0.9% solution and comparison with McFarland corresponds to a concentration of approx. 10⁸ cells/mL. For experiments, the bacterial suspension was diluted in NaCl 0.9% to obtain a microorganism suspension of about 10⁶ cells/mL. Transfer bacteria suspension into 9 ml TSB culture with 1mL solution of Fe₃O₄@Ag 10μM/mL. Microorganisms were culture in 24 hours, 37°C. Using a magnet to draw the material to the bottom of the test tube and collect the bacterial suspension. In addition, the bacterial strain samples without nanoparticles were used as negative control. All of the suspensions were transferred to Eppendorf, then centrifuged at 10,000rpm for 2 minutes to collect bacterial cells. Briefly, samples were washed with PBS solution and fixed with 2.5% glutaraldehyde for 30 minutes and dehydrated with a graded series of ethanol solutions (30%, 50%, 70%, 80%, 90%, and anhydrous ethanol) for 15 min each. Specimens were coated with silicon wafer and finally viewed under a Field emission scanning electron microscopy (FESEM) operating at 5.00 kV.

RESULTS AND DISCUSSION

XRD analysis

X-ray powder diffraction was used to analyze and determine the phase identification and crystalline structures of the Fe₃O₄@Ag nanoparticles. The X-ray diffraction pattern of the magnetite prepared exhibited distinct reflection planes (220), (311), (400), (511), and (440) with 2θ values of 30°, 35.5°, 43°, 57° and 63° respectively that corresponds Fe₃O₄-MNPs. Upon depositing silver onto the magnetite surface, the X-ray diffraction pattern reveals the presence of four additional diffraction peaks at 38.1°, 44.3°, 64.4°, and 77.4° degrees. These peaks correspond to the (111), (200), (220), and (311) planes of silver, respectively.

FTIR

Figure 2 shows the FT-IR spectrum for the formed Fe₃O₄@Ag. Peaks at 802.13 cm⁻¹, 772.36 cm⁻¹, 631.38 cm⁻¹ are contributing to Fe–O bond. The region surrounding the peaks at 3375, 1636, and 1370 cm⁻¹ corresponds to the stretching vibration of O-H bonds, the bending vibration of H-O-H bonds, and the bending vibration of O-H bonds caused by water absorption in the material

[6]. Due to silver being a metal element, no specific signals are found in the Fourier transform infrared spectroscopy spectrum.

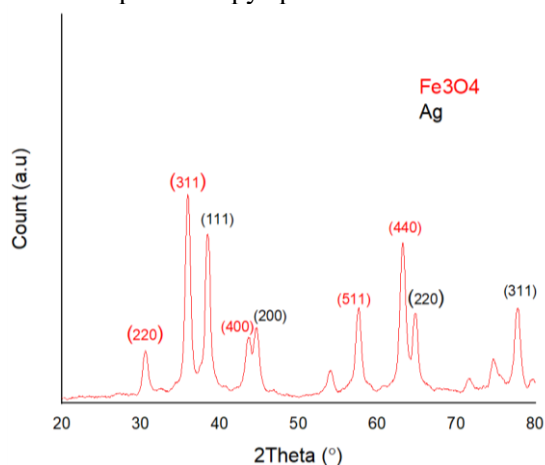


Figure 1. XRD spectrum of Fe₃O₄@Ag

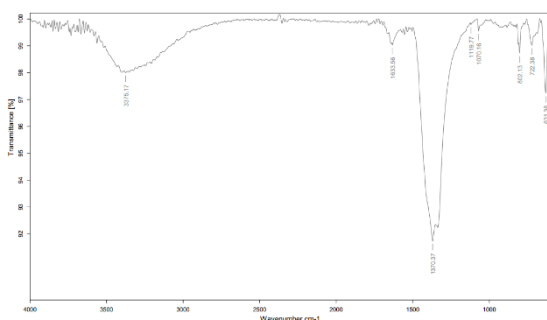


Figure 2. FTIR spectrum of Fe₃O₄@Ag

FESEM

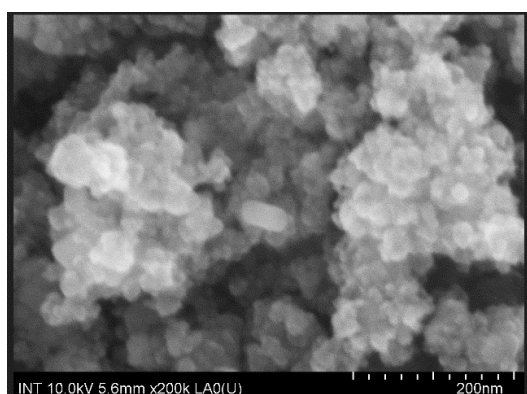


Figure 3. FESEM of Fe₃O₄@Ag

To examine the surface topography of the formed particles that were prepared, a field emission scanning electron microscope (FESEM) image was utilized. Based on the observations made from the image (Figure 3.), the MNPs exhibit a spherical shape and display uniformity in size within the nanometer range, specifically about 20-30 nm. Additionally, the nanoparticles in

certain areas are aggregated, forming larger aggregates.

RAMAN

Raman spectroscopy was utilized to investigate the composition of the Fe₃O₄@Ag, specifically magnetite. However, it is important to note that magnetite exhibits weak Raman scattering, particularly at lower laser powers. Based on Li S research an analysis of the Raman spectrum peaks of magnetite was conducted [7]. Among the various vibrational modes, it was determined that the peak at 670 cm⁻¹ is a distinctive characteristic band associated with magnetite.

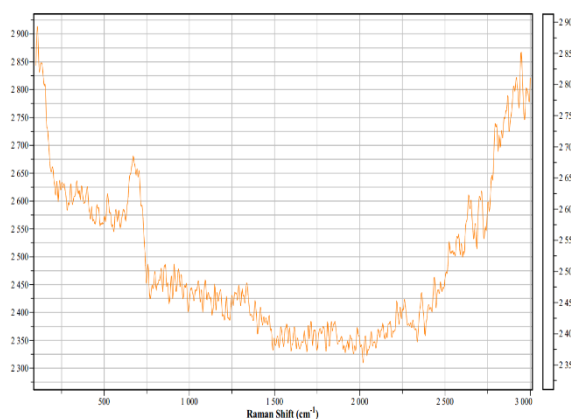


Fig 4. RAMAN spectrum of Fe₃O₄@Ag

AAS

The Ag and Fe₃O₄ content were measured by atomic absorption spectroscopy (AAS). To synthesis the Fe₃O₄@Ag, the molar ratio of Fe₃O₄ to AgNO₃ were 1:1. By utilizing AAS, the concentration (mg/L) of Fe and Ag in Fe₃O₄@Ag nanocomposite are 22.23 and 26.12, respectively.

Bacterial inhibition

The FESEM images showed that Fe₃O₄@Ag binds to the cellular surface of the bacterial membrane after 24 hours of treatment (Figure 5). Despite multiple washing steps to separate the nanomaterial from the bacterial biomass, the presence of nanoparticle clusters was observed on the bacterial wall.

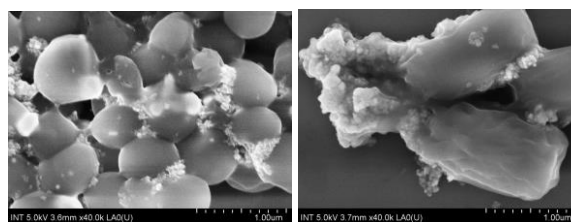


Figure 5. Binding of Fe₃O₄@Ag on cellular surface structures

The nanocomposite has harmful effects for cell of bacteria in the concentration 1 μ g/mL. Cell membranes were exhibited significant morphological changes. Meanwhile, there were not morphological changes in the untreated bacterial cultures. The difference in cell membrane morphology between control and treatment is shown in Figure 6. All four bacterial strains treated with the material showed adverse changes on the cell surface including: wrinkled, dented, deformed. This change in cell surface morphology has also been recorded on other Fe₃O₄ nanocomposite materials [8].

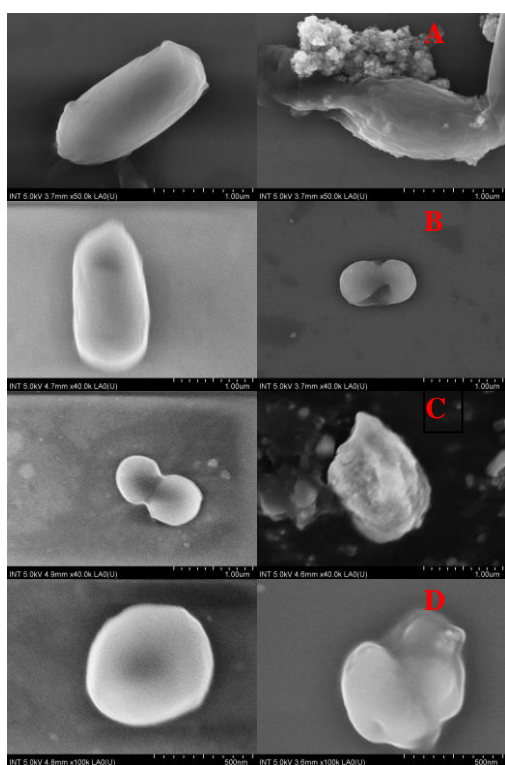


Figure 6. FESEM view of Fe₃O₄@Ag nanocomposites treated and control bacteria of *Bacillus subtilis* (A), *Escherichia coli* (B), *Pseudomonas aeruginosa* (C), *Staphylococcus aureus* (D).

CONCLUSION

In conclusion, the results show that Fe₃O₄@Ag nanocomposite is performed in circle shape, about 20-30nm size with specific characteristic. The nanoparticles have harmful effect to membrane of bacteria. This nanocomposite which combining Fe₃O₄ and Ag nanomaterial is expected to have outstanding antibacterial activity. This material is continued study about improve the material and investigate anti microorganism in magnetic environment.

Acknowledgment

The authors highly appreciate the financial support of Vietnam National University Ho Chi Minh City for this research under the grant number TX2023-32-01

References

- [1] Mohamed S. A., Al-Harbi M. H., Almulaiky Y. Q., Ibrahim I. H. and El-Shishtawy R. M., *Immobilization of horseradish peroxidase on Fe₃O₄ magnetic nanoparticles*, Electron. J. Biotechnol. **27** (2017) 84–90.
- [2] Winarti L., *Sistem penghantaran obat tertarget, macam, jenis-jenis system penghantaran, dan aplikasinya*, Stomatognatic **10** (2013) 75-81.
- [3] R. A. Revia and M. Zhang, *Magnetite nanoparticles for cancer diagnosis, treatment, and treatment monitoring: recent advances*, Biochem. Pharmacol. **10** (2015) 157–168.
- [4] K. S. Siddiqi, A. Husen, and R. A. K. Rao, *A review on biosynthesis of silver nanoparticles and their biocidal properties*, J.Nanobiotechnol. **16** (2018) 14.
- [5] C. Li, Z. Guan, C. Ma, N. Fang, H. Liu, and M. Li, *Bi-phase dispersible Fe₃O₄/Ag core-shell nanoparticles: Synthesis, characterization and properties*, Inorg. Chem. Commun, **84** (2017) 246–250.
- [6] Paul, R. C., Narula, R. C., & Vasisht, S. K., *Some compounds of iron (III) with bidentate bases*, Transition Metal Chemistry, **2**(1) (1977) 152-154.
- [7] Si H, Zhou C, Wang H, Lou S, Li S, et al. *Controlled synthesis of different types iron oxides nanocrystals in paraffin oil*. Journal of Colloid and Interface Science, **327** (2008) 466-471.
- [8] Senthilkumar P, Babu S, Jaishree V, Joshua Stephen K, Yaswant G, Ranjith Santhosh Kumar DS, Nair NS. *Solvothermal-assisted green synthesis of hybrid Chi-Fe₃O₄ nanocomposites: a potential antibacterial and antibiofilm material*. IET Nanobiotechnol;**14**(8) (2020) 714-721.

CHARACTERIZING JOULE HEATING EFFECTS ON CARBON NANOFIBERS: CALCULATING THE TEMPERATURE COEFFICIENT OF RESISTANCE FOR PRECISE NANOSTRUCTURE GROWTH CONTROL

Sura Nguyen¹, Arnoldo Salazar¹, Claudia B. Flores¹, Marc J. Madou¹, Nancy E. Ornelas¹, Alejandro Montesinos-Castellanos¹, and Sergio O. Martínez^{1,*}

¹School of Engineering and Sciences, Tecnológico de Monterrey, Ave. Eugenio Garza Sada 2501, Monterrey 64849, Mexico;
Email: smart@tec.mx

ABSTRACT

Joule heating (JH) plays a pivotal role in nanotechnology, allowing precise control over nanoscale material properties and growth processes. This study explores the application of JH on carbon nanofibers (CNFs), investigating their role in facilitating the localized growth of carbon nanotubes (CNTs) on suspended CNFs. The electrical behavior of CNFs during JH is systematically analyzed, considering factors like lattice vibration, electron liberation, and lattice structure distortion. Through a thorough analysis of experimental data and establishing temperature thresholds for these phenomena, we calculate the temperature coefficient of resistance (α), enabling accurate real-time temperature control. Precision in temperature measurement on CNFs is crucial for reproducible JH experiments and growing specific nanostructures. This research also establishes a correlation between structural changes in CNFs and their electrical and physical characteristics during JH. The observation of stable resistance above 1800°C is connected to constraints in the transition from sp^3 to sp^2 hybridizations. Furthermore, thermal expansion, driven by the creation of porous and graphitic structures at 2300°C, is investigated, with expansion parallel to the electrospun wire axis attributed to graphitic layer alignment. The study extends to localized chemical vapor deposition (CVD) of CNTs on CNFs, monitored by temperature, with Raman analysis confirming improved structural quality post-CVD. The resulting hybrid CNTs/CNFs exhibit impressive electrical conductivity (476 S.cm⁻¹), showcasing promising applications in high-performance carbon devices.

Keywords: Nanoreactor, Carbon nanofiber, Joule heating, Carbon nanotube, Chemical vapor deposition

INTRODUCTION

Carbon is gaining prominence in technological progress, following the historical path of silicon. This shift is primarily guided by continuous investigations into carbon nanotubes (CNTs), graphene, and carbon-based micro/nanoelectromechanical systems (C-MEMS and C-NEMS) [1-3]. Joule heating (JH), also known as resistive heating, plays a crucial role in processes such as chemical vapor deposition and annealing [4-7]. While prior research has applied JH to improve the electrical conductivity of carbon nanofibers (CNFs) [8], there remains a shortage of experimental investigations into the temperature generated by JH on individual CNFs [9-12]. This study aims to comprehensively analyze the electrical behavior of CNFs during JH experiments, aiming to determine the temperature coefficient of

resistance (α). Key observations encompass resistance saturation, fiber elongation, and the melting of the SiO₂ layer. Growing CNTs on CNFs enhances electrical conductivity, and the controlled JH process proves valuable in applications such as precise material deposition and fabrication processes. The study significantly contributes to understanding and applying JH for enhancing the properties of carbon-based materials across various technological applications.

EXPERIMENTAL

Fabrication of Carbon-Based Electrical Devices initiates with the electrospinning of a suspended fiber polymer precursor structure between two rectangular polymer precursor support structures on a silicon wafer with a 500 nm SiO₂ layer, using photolithography. Employing SU-8 resin as the polymer precursor,

we adhere to the detailed procedure outlined in Salazar et al.'s work [13], involving spin coating, photolithography, and NFES. Following this, the entire polymer structure undergoes pyrolysis in an OTF-1200X tube furnace (MIT) at 900°C, resulting in a monolithic glassy carbon device featuring suspended CNFs on two rectangular carbon electrodes (Figure 1.a).

In the Joule Heating Experiment, the carbon device is connected to an electrical circuit measuring system and placed inside a 3L stainless steel vacuum chamber. Before the experiment, the chamber is purged with nitrogen to prevent oxidation. Throughout the JH experiment, the pressure is maintained at 1 atm. Using an electric source meter (Keithley 2636B), we control and record electrical signals. The applied voltage gradually increases from 0.2V at a rate of 0.01 V.s⁻¹ until JH initiation. To promote CNT growth on CNFs, a precursor solution containing 0.04 g.mL⁻¹ ferrocene in ethanol is housed in a small stainless tube equipped with a tape heater. This tube is isolated from the main chamber by a fine needle valve, maintaining its temperature at 180°C to ensure proper vaporization of the precursor solution. Once CNFs reach the reaction temperature, the needle valve is slowly opened, allowing the vapor to come into contact with the fiber surface.

RESULTS AND DISCUSSION

The computation of α is rooted in the fundamental understanding that the temperature, structure, and resistance of CNFs are intricately linked. Within Sample Group 1, changes in surface sharpness arising from the vaporization of heteroatoms and void propagation at 1800°C significantly impact electrical conductivity. Sample Group 2 displays notable fiber elongation at 2300°C, attributed to the formation of porous structures and graphitic layers. Mechanical forces during fabrication likely influence the CNF structure, contributing to elongation. Sample Group 3 indicates heat dissipation, leading to substrate cracking at 1710°C. We derived an α value of -0.00043 K^{-1} for the CNFs. Having developed a technique for estimating temperatures on CNFs, our focus shifted to the targeted growth of CNTs on the suspended CNFs. The predicted temperatures offered a reliable means to consistently and precisely cultivate nanostructures, alleviating concerns about sample loss due to wire breakage. In Figure 1.b, we showcase the growth of CNTs on a single

CNF at 732°C using a vapor mixture of ferrocene and ethanol. The resulting hybrid carbon fibers exhibit superior electrical conductivity (476 S.cm⁻¹) compared to any glassy carbon fibers reported in the literature using JH [14].

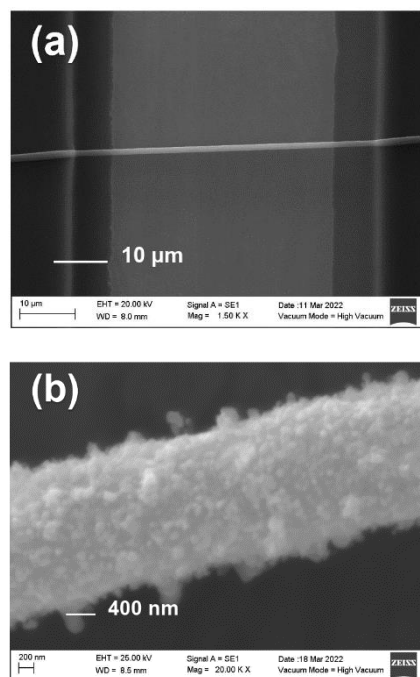


Figure 1: (a) SEM images depicting a pristine CNF on two rectangular carbon electrodes. (b) SEM image showcasing the surface of a hybrid of CNTs on carbon fibers fabricated by JH.

CONCLUSION

In summary, our investigation into the temperature-resistance dynamics of CNFs, conducted through the calculation of the temperature coefficient of resistance (α), has yielded valuable insights. The intricate interplay among temperature, CNF structure, and resistance has enabled the derivation of an α value of -0.00043 K^{-1} . This determination equips us with a potent tool for precisely controlling the JH effect on individually suspended CNFs. This understanding is pivotal for the regulated growth of CNTs through the precise timing of precursor injection. Moreover, the α value simplifies the JH experiment by consolidating the management of two parameters, voltage and resistance, into a singular parameter: temperature. This streamlined approach is particularly advantageous when dealing with glassy carbon fibers, where variations in the fabrication process lead to considerable variability in electrical resistance among fibers. The unique α value of glassy carbon, determined by its specific

structure, holds significant implications. Grasping the intricate relationship between resistance and temperature in CNFs is crucial for the effective utilization of glassy carbon in diverse applications, especially those reliant on temperature-dependent electrical properties. Individually suspended CNFs, amenable to controlled heating, open up possibilities for designing a nanofurnace capable of achieving extremely high temperatures at an ultrafast heating rate—a feat that is either impractical or prohibitively expensive with large furnaces.

Acknowledgment

The authors express gratitude for the financial assistance provided by CONACYT (grant no. PROALMEX 2015-267726) and the support received from the NANO – Sensors & Devices Research Group at Tecnológico de Monterrey (0020209I06) and the Federico Baur Endowed Chair in Nanotechnology (ILST002-21ID14002). Heartfelt thanks are extended to Regina Vargas, Iris Aguilar, M.F. Jimenez, and B. Jind for their invaluable contributions.

References

- [1] Madou, M.J., V.H. Perez-Gonzalez, and B. Pramanick, *Carbon: The Next Silicon?: Book 1-Fundamentals*, Momentum Press, 2016.
- [2] Madou, M.J., V.H. Perez-Gonzalez, and B. Pramanick, *Carbon: The Next Silicon?: Book 2-Applications*, Momentum Press, 2016.
- [3] De Volder, M.F.L., et al., *Hierarchical Carbon Nanowire Microarchitectures Made by Plasma-Assisted Pyrolysis of Photoresist*, ACS Nano **5**(8) (2011) 6593-6600.
- [4] Chiamori, H., et al. *Annealing nano-to-micro contacts for improved contact resistance*, Proc. The 5th International Conference on Nano/Micro Engineered and Molecular Systems, 2010, IEEE.
- [5] Ro, J.-S. and W.-E. Hong, *Joule-heating-induced annealing by applying electric field directly to intrinsic silicon film*, Japanese journal of applied physics **45**(11L) (2006) L1142.
- [6] Advincula, P.A., et al., *Tunable Hybridized Morphologies Obtained through Flash Joule Heating of Carbon Nanotubes*, ACS Nano, **17**(3) (2023) 2506-2516.
- [7] Guo, M., et al., *Challenges and Opportunities of Chemiresistors Based on Microelectromechanical Systems for Chemical Olfaction*, ACS Nano, **16**(11) (2022) 17778-17801.
- [8] Maitra, T., et al., *Improved graphitization and electrical conductivity of suspended carbon nanofibers derived from carbon nanotube/polyacrylonitrile composites by directed electrospinning*, Carbon **50**(5) (2012) 1753-1761.
- [9] Athanasopoulos, N., et al., *Numerical investigation and experimental verification of the Joule heating effect of polyacrylonitrile-based carbon fiber tows under high vacuum conditions*, Journal of composite materials, **46**(18) (2012) 2153-2165.
- [10] Caglar, H., et al., *Debonding of carbon fiber veil interleaved adhesively bonded GFRP joints via Joule heating*, Composites Part B: Engineering **230** (2022) 109544.
- [11] Ferrer-Argemi, L., et al. *Temperature-Dependent Electrical and Thermal Conductivity of Glassy Carbon Wires*. Proc. The 17th IEEE Intersociety Conference on Thermal and Thermomechanical Phenomena in Electronic Systems (ITherm), 2018, IEEE.
- [12] Salazar, A. and V.H. Perez-Gonzalez, *Reduction of electrical resistance on suspended glassy carbon nanofibers by localized thermal annealing*, Materials Today: Proceedings **48** (2022) 25-29.
- [13] Salazar, A., et al., *Nanogap fabrication by Joule heating of electromechanically spun suspended carbon nanofibers*, Carbon **115** (2017) 811-818.
- [14] Yao, Y., et al., *Carbon Welding by Ultrafast Joule Heating*, Nano Letters **16**(11) (2016) 7282-7289.

ANALYSIS OF INTERFACE AND BORDER TRAPS IN HfO₂/InGaAs DEVICES

Huy-Binh Do^{1*}, Maria Merlyne De Souza²

¹ Department of Materials Technology, Faculty of Applied Sciences, Ho Chi Minh City University of Technology and Education, Vietnam

² EEE Department, University of Sheffield, Sheffield, United Kingdom.
Email: binhdh@hcmute.edu.vn

ABSTRACT

The investigation of interface traps and border traps was conducted through a combination of experimental measurements and TCAD simulation. It was discovered that the oxidation occurring at the metals/HfO₂ interface has a significant impact on the values of both interface traps and border traps. This study thoroughly examines the effects of gate metals on acceptor-like traps and donor-like traps. Notably, the extracted values for interface traps, specifically $1.3 \times 10^{11} \text{ eV}^{-1}\text{cm}^{-2}$ and $3.8 \times 10^{11} \text{ eV}^{-1}\text{cm}^{-2}$ for acceptor-like traps, and donor-like traps, respectively. The Heiman method was employed to extract the lifetime of border traps. These findings serve as a guide for optimizing InGaAs devices and achieving low power consumption in these devices.

Keywords: InGaAs, capacitance-voltage measurement, border-like traps, interface traps, TCAD.

INTRODUCTION

Hf-based high-k oxides (Hf-based ferroelectrics) have been identified as one of the most promising candidates in future microelectronic applications due to their excellent compatibility with existing Complementary Metal Oxide Semiconductor (CMOS) processes [1-6]. Among III-V Materials, InGaAs is a promising epitaxial layer due to its high electron mobility and small band-gap of 0.74 eV [7] in high-speed and low-power logic technologies. Unlike a favorable Si/SiO₂ interface in silicon, there is a lack of native oxide in InGaAs, leading to techniques in plasma treatment of the surface [8], passivation using sub-nanometer AlN [9], and chemical treatment [10] to achieve interface engineering. This approach is based on the effect of InGaAs epitaxial layer on the properties of HfO₂ layers. However, gate metals may also induce trap states at the metal/HfO₂ interface [11], facilitating the diffusion of the oxygen vacancy in HfO₂ films. The passivation of the metal/HfO₂ interface was conducted using AlN layer [12], resulting in an increase of permittivity of HfO₂ of 47%. Although there are many studies of interface traps at HfO₂/InGaAs, arising from the interaction between HfO₂ and the InGaAs layer, the behavior of interface traps and border traps due to the

effects of gate metals have not been systematically examined.

To answer the questions raised by a metal-induced interface and border traps in HfO₂ and at the HfO₂/InGaAs interfaces, electrical properties of HfO₂ in metal/HfO₂/InGaAs structure is investigated in this study, using metal oxide semiconductor capacitors (MOSCAPs). TCAD simulation is adapted to simulate electrical characteristics and the band structure of devices. The properties of interface traps and border traps are extracted from a comparison of the theoretical capacitance-voltage (CV) characteristics and experiment. We explain systematically the role of gate metals on the formation of acceptor-like and donor-like traps at HfO₂/InGaAs interface as well as the border traps within HfO₂.

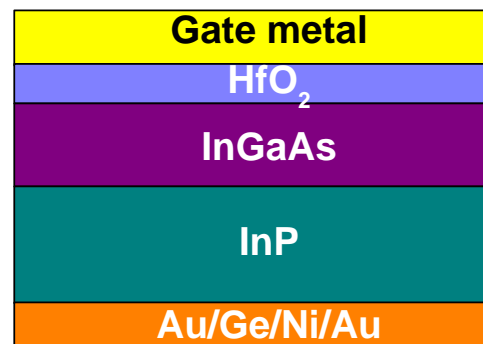


Figure 1. The schematic cross section of the metal/HfO₂/In_{0.53}Ga_{0.47}As structure.

EXPERIMENTAL

$\text{In}_{0.53}\text{Ga}_{0.47}\text{As}$ (IGA) MOSCAPs were fabricated following the process described below. The channel layer is a commercial 100-nm n-doped $\text{In}_{0.53}\text{Ga}_{0.47}\text{As}$ ($5.0 \times 10^{17} \text{ cm}^{-3}$ Si-doped) layer grown on n+-InP substrate by solid source molecular beam epitaxy. Acetone (ACE) and isopropanol (IPA) were used to clean the IGA surface before the native oxide was etched in dilute HCl. The samples were subsequently loaded into an ALD chamber for deposition of high-k with a growth temperature of 250°C. The deposition process includes 2 steps, (i) 5 cycles AlN layer with a thickness of ~ 0.7 nm, and (ii) HfO_2 layers which the thicknesses were varied from 50 cycles to 150 cycles. The growth rate of HfO_2 was determined to be ~ 0.73 Å/cycle. All of the thicknesses of HfO_2 were measured and fitted using SOPRA GES5 Ellipsometer because of a large number of samples. Thicknesses of 50 cycles of HfO_2 samples are doubly checked using the HRTEM (data not shown). Post deposition anneal (PDA) was conducted at 450°C for 2 minutes in forming gas (FG) after the high-k deposition. Finally, a contact was defined on HfO_2 via lithography/lift-off processes, followed by a post metallization anneal at 250°C for 30 seconds in FG.

HfO_2/IGA MOSCAPs were simulated using Silvaco TCAD 2-D device simulation tool. The structure of the MOSCAPs is illustrated in Figure. 1. To consider the effects of the high field on mobility and carrier concentration on carrier lifetime, a high field model and a concentration-dependent lifetime model were adapted, respectively. The Auger recombination model was utilized to account for the effect of high electron concentration (N_e). Shockley-Read-Hall model was used to simulate the trap-assisted recombination. The band-gap narrowing effect was included in the simulation to consider a shrinkage of the bandgap occurring when the impurity concentration is particularly high. To make sure that the models being used represent and replicate a real-world device accurately, TCAD parameters were calibrated against device structure in Figure. 1 through capacitance-voltage (CV) characteristics. Parameters of IGA are default values from Silvaco TCAD.

RESULTS AND DISCUSSION

It is seen in Figures. 2(a) - (d) that the simulation results fit well with experiment. The

process to calibrate the simulation curves consists of two steps: (i) adding interface traps to the AlON/IGA interface to fit C-V curves in the forward bias, and (ii) simulating C-V curves in reverse bias to obtain hysteresis by adding border traps in the bandgap of HfO_2 . One of the well-known methods to extract densities of interface traps (D_{it}) is the conductance method. This method is based on estimating the peak of equivalent parallel conductances calculated from measured impedance [13]. The advantage of this method is that the D_{it} can be extracted directly from experimental data. However, the extracted D_{it} is reported to be not correct in the case of large D_{it} , especially when $C_{ox} < qD_{it}$ [13]. Another popular method is the Terman method. To extract D_{it} , the ideal C-V curve is plotted. The stretch-out of the experimental curve as compared to ideal one provides the value of D_{it} . The D_{it} extracted by Terman method is typically larger (~ 10 times) than that extracted by conductance method [12].

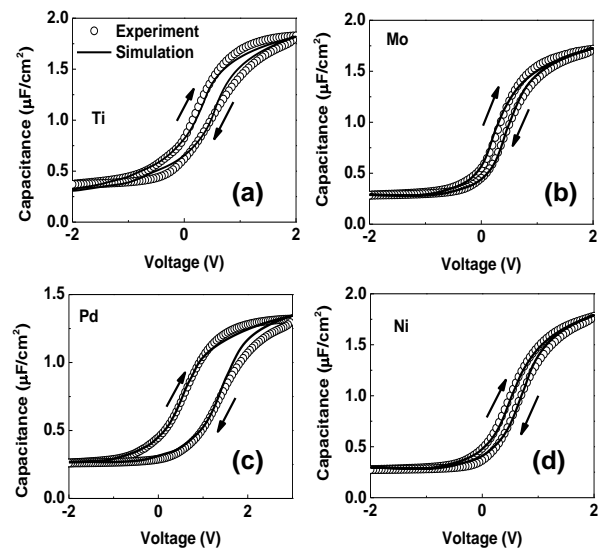


Figure 2. Results of C-V characteristics at 1 MHz from TCAD simulations and experiment of (a) Ti, (b) Mo (c) Pd and (d) Ni samples.

Figure 3(a) shows the D_{it} of all samples extracted from TCAD simulations. It is seen that D_{it} is minimum at mid-gap, and acceptor-like densities are smaller as compared to donor-like densities for all samples. The lifetime of interface traps is extracted to be 2.9×10^{-9} s that is the same as the previous study [14]. The smallest D_{it} ($1.39 \times 10^{11} \text{ eV}^{-1}\text{cm}^{-2}$ acceptor-like traps, and $3.81 \times 10^{11} \text{ eV}^{-1}\text{cm}^{-2}$ donor-like traps) is in the sample with a Mo gate. In our previous report, a combination of Mo/Ti gate metal and the passivation layer AlN between Ti and HfO_2 leads

to small D_{it} [12]. In that study, a thin AlN layer was believed to prevent the reaction between Ti and HfO_2 , diminishing the formation of oxygen vacancies in HfO_2 .

The extracted density of border traps (N_{BT}) are shown In Figure. 3(b). It is seen that the largest border traps of $2.2 \times 10^{20} \text{ eV}^{-1} \text{ cm}^{-3}$ occur in the Pd sample, explaining the largest hysteresis of 0.76 V of CV curves in Figure. 2(c). The extracted lifetime of border traps at the interface is $2.5 \times 10^{-5} \text{ s}$, which is larger than that of interface traps. The value of lifetime is the same as that in the study of Zhang et al. [15]. Similar to the extracted D_{it} , the smallest value of border traps, N_{BT} of $4.46 \times 10^{19} \text{ eV}^{-1} \text{ cm}^{-3}$ also occurs in the Mo sample, confirmed by the smallest hysteresis in its C-V hysteresis of 0.11 V shown in Figure. 2(b). Although the work-function of Ni and Pd is nearly the same, however, the quality of Ni sample is much better than that of Pd. The reasons of the degradation have been discussed in our previous report, where the formation energy of the metal-oxygen defect has a critical role that stabilises the metal/high-k interface [11].

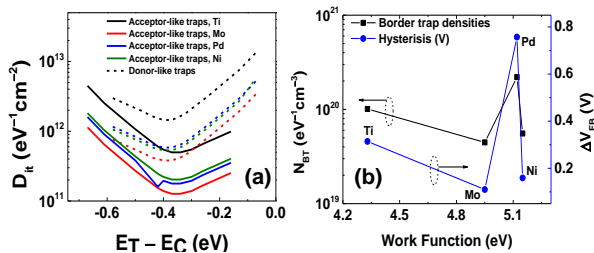


Figure 3. (a) Densities of interface traps extracted from TCAD simulations of the C-V curves. (b) Densities of border traps and the difference of flat band voltage of samples with different gate metals.

CONCLUSION

In summary, the impact of gate metals on interface traps and border traps in metal/ HfO_2 /AlN/InGaAs structure were systematically studied. Due to oxidation at the metal/ HfO_2 interface, low work function metal Ti creates the highest N_{BT} in HfO_2 , while the middle work function metal Mo induces the lowest D_{it} and N_{BT} . The extracted lifetime of interface and border traps in this study are $2.9 \times 10^{-9} \text{ s}$ and $2.9 \times 10^{-5} \text{ s}$, respectively. The Heiman method was utilized to investigate the border traps in HfO_2 . The lowest D_{it} and N_{BT} were found to be $1.39 \times 10^{11} \text{ eV}^{-1} \text{ cm}^{-2}$ and $4.46 \times 10^{19} \text{ eV}^{-1} \text{ cm}^{-3}$, respectively, for middle work function metal Mo. The results of this study provide guidance in

choice of gate metal for microelectronic devices and random-access memory.

Acknowledgment

This work was supported by the Ho Chi Minh City University of Technology and Education.

References

- [1] H. Wang, J. Liu, J. Wei, K. Xiao, Y. Chen, Y. L. Jiang, and J. Wan, *Au Nanoparticles/ HfO_2 /Fully Depleted Silicon-on-Insulator MOSFET Enabled Rapid Detection of Zeptomole COVID-19 Gene With Electrostatic Enrichment Process*, IEEE Transactions on Electron Devices **70** (2023) 1236-1242.
- [2] S. K. Das, B. Chettri, P. Karki, P. Chettri, U. Deka, and B. Sharma, *Analysis of certain electrical properties in Silicon nanowire field-effect transistors with high- κ HfO_2 as gate dielectrics*, Proc. The IEEE International Conference of Electron Devices Society Kolkata Chapter (EDKCON), 2022, 124-127.
- [3] M. S. Ram, J. Svensson, S. Skog, S. Johannesson, and L. E. Wernersson, *Low-Frequency Noise in Vertical InAs/InGaAs Gate-All-Around MOSFETs at 15 K for Cryogenic Applications*, Proc. IEEE Electron Device Letters **43** (2022) 2033-2036.
- [4] C. Liu, Z. Wang, Y. Zhang, H. Lü, and Y.-M. Zhang, *Nanolaminated HfO_2/Al_2O_3 Dielectrics for High-Performance Silicon Nanomembrane Based Field-Effect Transistors on Biodegradable Substrates*, Advanced Materials Interfaces **9** (2022) 2201477.
- [5] P. Kumar, K. Koley, R. Goswami, A. Maurya, and S. Kumar, *Electrical Noise Behaviour of High- κ Gate-All-Around MOSFET Based on Two-Port Device Network Analysis*, Proc. The 14th International Conference on Information Technology and Electrical Engineering (ICITEE), 2022, 68-72.
- [6] P. Kumar, M. Vashishath, N. Gupta, and R. Gupta, *High- κ Dielectric Double Gate Junctionless (DG-JL) MOSFET for Ultra Low Power Applications- Analytical Model*, Silicon **14** (2022) 7725-7734.
- [7] A. Vais, A. Alian, L. Nyns, J. Franco, S. Sioncke, V. Putcha, H. Yu, Y. Mols, R. Rooyackers, D. Lin, J. W. Maes, Q. Xie, M. Givens, F. Tang, X. Jiang, A. Mocuta, N. Collaert, K. D. Meyer, and A. Thean, *Record*

- mobility ($\mu_{eff} \sim 3100 \text{ cm}^2/\text{V}\cdot\text{s}$) and reliability performance ($V_{ov} \sim 0.5\text{V}$ for 10yr operation) of $\text{In}_{0.53}\text{Ga}_{0.47}\text{As}$ MOS devices using improved surface preparation and a novel interfacial layer, Proc. The IEEE Symposium on VLSI Technology, 2016, 1-2.
- [8] Q. H. Luc, S. P. Cheng, P. C. Chang, H. B. Do, J. H. Chen, M. T. H. Ha, S. H. Huynh, C. C. Hu, Y. C. Lin, and E. Y. Chang, *Effects of In-Situ Plasma-Enhanced Atomic Layer Deposition Treatment on the Performance of $\text{HfO}_2/\text{In}_{0.53}\text{Ga}_{0.47}\text{As}$ Metal-Oxide-Semiconductor Field-Effect Transistors*," IEEE Electron Device Letters **37** (2016) 974-977.
- [9] I. Pallecchi, G. Grassano, D. Marré, L. Pellegrino, M. Putti, and A. S. Siri, *SrTiO_3 -based metal-insulator-semiconductor heterostructures*, Applied Physics Letters **78** (2001) 2244-2246.
- [10] Y. Xuan, Y. Q. Wu, T. Shen, T. Yang, and P. D. Ye, *High performance submicron inversion-type enhancement-mode InGaAs MOSFETs with ALD Al_2O_3 , HfO_2 and HfAlO as gate dielectrics*, Proc. The IEEE International Electron Devices Meeting, 2007, 637-640.
- [11] H. B. Do, Q. H. Luc, M. T. H. Ha, S. H. Huynh, T. A. Nguyen, Y. C. Lin, and E. Y. Chang, *Study of the interface stability of the metal (Mo, Ni, Pd)/ $\text{HfO}_2/\text{AlN}/\text{InGaAs}$ MOS devices*, AIP Advances **7** (2017) 085208.
- [12] H. B. Do, Q. H. Luc, M. T. H. Ha, S. H. Huynh, T. A. Nguyen, C. Hu, Y. C. Lin, and E. Y. Chang, *Investigation of Mo/Ti/AlN/ HfO_2 High-k Metal Gate Stack for Low Power Consumption InGaAs NMOS Device Application*, IEEE Electron Device Letters **38** (2017) 552-555.
- [13] R. Engel-Herbert, Y. Hwang, and S. Stemmer, *Comparison of methods to quantify interface trap densities at dielectric/III-V semiconductor interfaces*, Journal of Applied Physics **108** (2010) 124101.
- [14] R. K. Ahrenkiel, R. Ellingson, S. Johnston, and M. Wanlass, *Recombination lifetime of $\text{In}_{0.53}\text{Ga}_{0.47}\text{As}$ as a function of doping density*, Applied Physics Letters **72** (1998) 3470-3472.
- [15] X.-Y. Zhang, C.-H. Hsu, Y.-S. Cho, S.-Y. Lien, W.-Z. Zhu, S.-Y. Chen, W. Huang, L.-G. Xie, L.-D. Chen, X.-Y. Zou, and S.-X. Huang, *Simulation and Fabrication of HfO_2 Thin Films Passivating Si from a Numerical* Computer and Remote Plasma ALD, Applied Sciences **7** (2017) 1244.

FABRICATION OF CALCIUM SILICATE HYDRATE (CSH) MINERAL FROM WASTED PV GLASS (WPVG) AND WASTED CALCIUM CARBIDE (WCC)

Pham Trung Kien^{1,2,3*}, Tran Ngo Quan^{1,2}, Nguyen Don Tin^{1,2}, Le Huynh Tuyet Anh^{1,2}

¹ Faculty of Materials Technology, Ho Chi Minh City University of Technology (HCMUT), 268 Ly Thuong Kiet Street, District 10, Ho Chi Minh City, Vietnam;

² Vietnam National University Ho Chi Minh City, Linh Trung Ward, Thu Duc District, Ho Chi Minh City, Vietnam

³ Polymer Research Center, Ho Chi Minh City University of Technology (HCMUT), 268 Ly Thuong Kiet Street, District 10, Ho Chi Minh City, Vietnam

Email: phamtrungkien@hcmut.edu.vn

ABSTRACT

In this study, the effect of different batch mixing of Wasted photovoltaic glass (WPVG) and Wasted calcium carbide (WCC) with CaO/SiO₂ molar ratio of 0.8; 1.0 and 1.2 followed by hydrothermal treatment at 180°C for 96h in NaOH8M was studied. The data indicate that the xonotlite is favorable form upon the CaO/SiO₂ starting materials of 1.0 to 1.2, and the needle-like crystallize forming with the size of less than 1µm.

Keywords: PV glass, calcium carbide, hydrothermal treatment, Calcium silicate hydrate (CSH).

INTRODUCTION

Nowadays, Calcium Silicate Hydrate (CSH) is an important material widely used in the fields of construction, interior and exterior decoration, high-tech materials,... thanks to its special mechanical and physical properties. Recent studies have shown that CSH minerals have outstanding potential for new applications in environmental protection, such as the removal of heavy metals from wastewater such as Cr(III) from plating factories.

Yearly, Vietnam use photovoltaic (PV) glass as solar panel to supply the renewable energy. Theoretically, the solar panel can be used up to 30 years life time. When damages or reduce the energy conversion, the PV glass will become the heavy waste. The recycle process of waste PV glass would be a sustainable development goal for Vietnam as well as ASEAN country.

In addition, the waste calcium carbide (WCC) from acetylene production also supplied the rich portlandite mineral [Ca(OH)₂]. The reuse of WCC can help to reduce the CO₂ footage during the production of Ca(OH)₂ from lime by thermal decomposition reaction. Thus, we have proposed the new idea to use WPVG and WCC as raw materials to supplied Calcium and Silica simultaneously to fabrication the CSH mineral

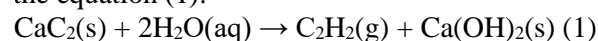
using hydrothermal treatment techniques [1-2]. Aiming to convert the calcium and silica content to Xonotlite [X, Ca₆(Si₆O₁₇)(OH)₂], our research group propose to use WPVG and WCC as raw materials with the Ca/Si molar ratio of 0.8; 1.0 and 1.2, follow by hydrothermal treatment at 180°C for 96 hour. The Xonotlite mineral is classified as Calcium Silicate Hydrate mineral materials (CSH) [3-6] owing the environmental friendly property since it can be used as heavy metal adsorbent materials.

EXPERIMENTAL

Raw materials study:

The wasted photovoltaic glass (WPVG) was collected at solar panel glass company. The WPVG was grounded by fast-grinding machine with the power of 3kW (3A model, Tuan Tu Agriculture manufacturer, Vietnam), then passed through the 0.45-mm sieve to collect the fined wasted glass powder (FWG). The chemical of FWG was analysis using Xray Fluorescing (XRF) characterization.

The Wasted calcium carbide (WCC) of which Ca(OH)₂ is the main phase identified by Xray Diffraction (XRD). In brief, WCC is the by product of acetylene gas production according to the equation (1):



Synthesize Calcium Silicate Hydrate (CSH) by hydrothermal reaction:

The WPVG and WCC were mixed with different CaO/SiO₂ molar ratio of 0.8; 1.0 and 1.2 to form the 6-mm diameter disk, follow by hydrothermal reaction at 180°C for 96 hours in the present of distilled water to study the effect of Calcium to Si molar ratio to the formation of CSH mineral materials. During the hydrothermal reaction, the 6-mm disk were contacted only with the steam water to prevent the washout phenomena as reported preivous [7] and the layout was shown in Figure 1. The flow chart of synthesized CSH mineral was shown in Figure 2

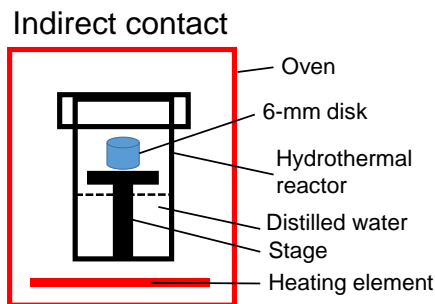


Figure 1. The schematic layout of hydrothermal reactor used. The 6-mm disk were contacted only with the steam water to prevent the washout phenomena. The hydrothermal set was placed inside the oven to supply the heat.

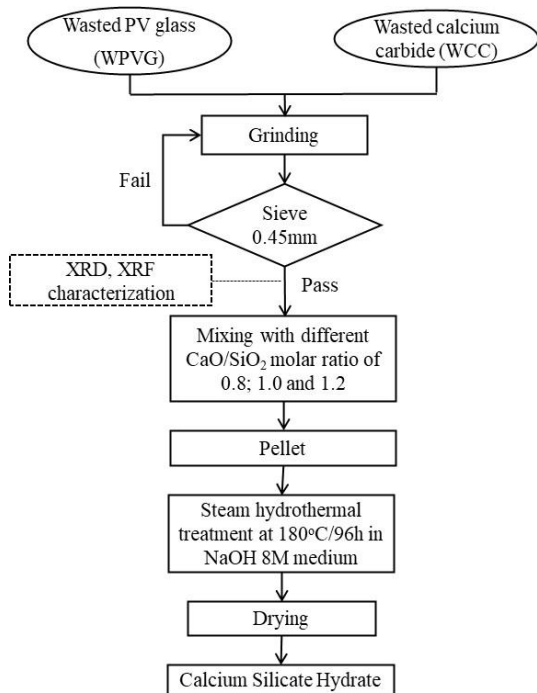


Figure 2. Flow chart of fabrication of CSH mineral from WPVG and WCC using steam hydrothermal method in the present of NaOH8M.

Materials characterizations method:

The chemical composition analysis of sample using Xray Fluorescing (XRF): the sample was characterized by Xray at 40kV (ARL Advant, Thermo Scientific).

The phase analysis using powder-type XRD: the sample was ground and put in XRD machine (Bruker D8 Advance, Germany) with the 2theta scanning from 5 to 60°, operation at 40kV and 40mA.

The chemical composition analysis using Xray Fluorescing (XRF): the sample was characterized by Xray at 40kV (ARL Advant, Thermo Scientific).

The morphology analysis using SEM: the sample was scattered on Carbon tape stick to Copper substrate, and carried the SEM analysis (Hitachi S-4800) at 10kV.

RESULTS AND DISCUSSION

Raw materials study:

Figure 3a shown the XRD patterns of WPVG as amorphous phase of quartz (SiO₂) with PDF#46-1045. It need to emphasized that SiO₂ is also the main component of PV glass. In addition, the XRD pattern of WCC also shown on Figure 3b, with the high crystallinity of portlandite (PDF#44-1481) at 2theta of 18 and 34 degree due to the chemical reaction of acetylene gas production according to the equation [1]:

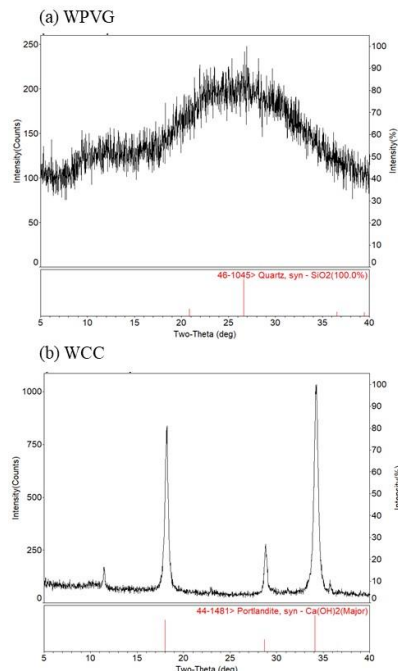
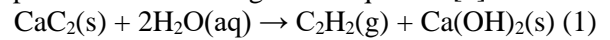


Figure 3. XRD patterns of raw materials: (a) WPVG and (b) WCC.

The chemical composition of WPVG and WCC were given in table 1 by XRF analysis. Based on these results, our research rroup can batch-mixed the WPVG and WCC with the CaO/SiO₂ molar ratio of 0.8; 1.0 and 1.2

Table 1: Chemical analysis of the WPVG and WCC

Oxide (wt.%)	SiO ₂	CaO	*LOI
WPVG	69.3	12.7	-
WCC	5.33	70.48	22.4

*LOI: loss on ignition

Figure 4 shown the SEM images of raw materials WPVG and WCC at different magnifications of 2,000X and 5,000X. In brief, the WPVG own its smooth surface due to its amouphous phase while the WCC has the plate-like shape crystallize with the average size of 20µm

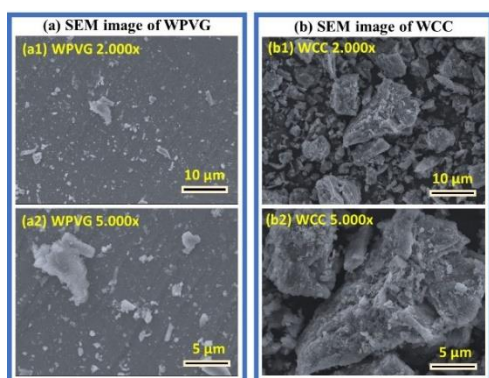


Figure 4. SEM image of raw materials: (a) WPVG at magnification of (a1) 2,000X and (a2) 5,000X; and (b) WCC at magnification of (b1) 2,000X and (b2) 5,000X.

Study the sample before and after steam hydrothermal treatment in the present of NaOH8M

Figure 5 shown the effect of different CaO/SiO₂ batch mixing molar ratio of 0.8; 1.0 and 1.2 then follow by hydrothermal reaction temperature at 180°C for 96 hour on the synthesized of CSH mineral by using XRD analysis. The peak of Xonotlite (PDF#23-0125) at 30 degree increase upon increase the CaO/SiO₂ molar ratio, indicating that CaO/SiO₂ of 1.0 to 1.2 is the good hydrothermal treatment condition to form xonotlite. In other word the forming of xonotlite mineral is more favour upon the CaO/SiO₂ between 1.0 and 1.2

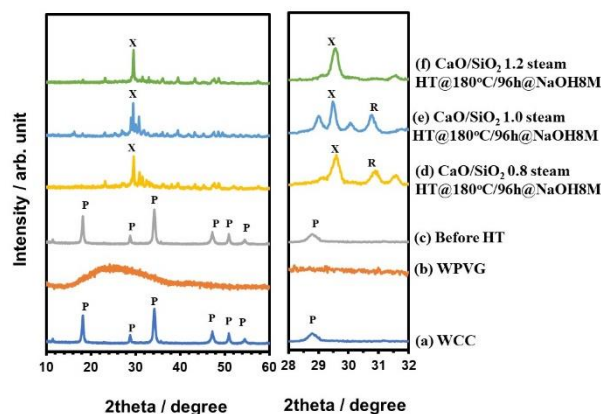


Figure 5. XRD patterns of the sample before and after steam hydrothermal treatment (HT) at 180°C for 96 hours (Figure 5c, 5d, 5e and 5f). In addition Figure 5a and b show XRD patterns of raw materials. The left XRD patterns shown the 2theta degree vary from 10 to 40, while the right XRD pattern zoom the 2theta degree vary from 28 to 32. Code: P-Portlandite Ca(OH)₂ (PDF#44-1481); X-Xonotlite Ca₆Si₆O₁₇(OH)₂ (PDF# 23-0125); R-Riversideite-9A Ca₅Si₆O₁₆(OH)₂ (PDF# 29-0329)

Figure 6 shown the SEM images of sample before and after steam hydrothermal treatment (HT) at 180°C for 96 hours (Figure 6a, b, c and d). Before steam HT, the sample have plate-like crystal morphology indicating by black arrow (Figure 6a). In contrast, the new small needle-like crystals were form on the surface of sample after hydrothermal treatment as shown on Figure 6b, c and d (the white arrow). These new small needle-like crystals were interlock together and enhance the mechanical property of sample due to the forming of new CSH minerals such as Xonotlite and/or Riversideite-9A.

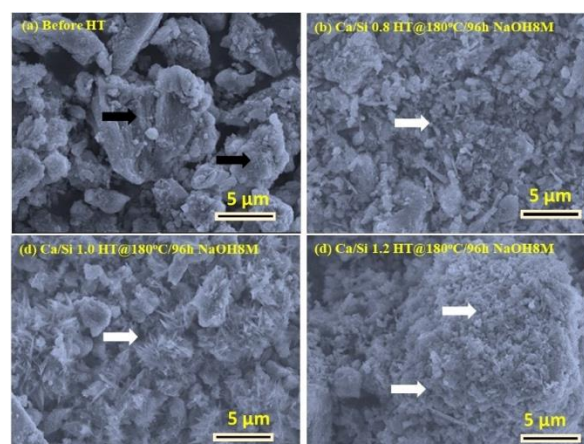


Figure 6. SEM images of the sample before and after steam hydrothermal treatment (HT) at 180°C for 96 hours (Figure 6a, b, c and d).

This research needs to put into the context of experiment conditions. To form the proper CSH mineral, the CaO/SiO₂ molar ratio of batch mixing is significant viral. In this research, we focus on study the effect of batch mixing of CaO/SiO₂ of 0.8; 1.0 and 1.2 then followed by steam hydrothermal treatment at 180°C for 96h in NaOH 8M on the formation of xonotlite. The finding from XRD, SEM data shown that the CaO/SiO₂ molar ratio between 1.0 and 1.2 give better forming of CSH as well as the sharpness of crystal on the surface. Thus, the next research on study the effect of hydrothermal treatment temprature, and hydrothermal duration time at will be carried out. The use of synthesized xonotlite may offer several benefits for heavy metal removal or thermal insulator in heat industry.

CONCLUSION

This study shown the ability to use WPVG and WCC as the source to supply Ca and Si. The 2 kinds of wasted materials were batch mixed with different CaO/SiO₂ molar ratio of 0.8; 1.0 and 1.2 followed by steam hydrothermal reaction at 180°C/96 in the present of NaOH8M. Results reveal that the forming of CSH favourble as the mixture CaO/SiO₂ increasa between 1.0 and 1.2. This research suggests the new cluster on synthesize CSH using hydrothermal treatment.

Acknowledgment

"This research is funded by Vietnam National University Ho Chi Minh City (VNU-HCM) under grant number B2023-20-19"

References

- [1] D. Minh, N. Thang, P. Kien. *Research on manufacturing decorative tiles from cullet and red mud*, The 11th international conference on ecomaterials (ICEM11) – Green Materials and Green Technology for Green Monozukuri (Fabrication with heart), Hanoi, Vietnam, (2013) 75-80.
- [2] K. Pham. *Ability to use wasted cullet in glass industry as environmental-friendly materials for sustainable development*, RCME 29-30 Oct 2015, Bangkok, section 1C-3, 1.
- [3] E. E. Lachowski, L.W. Murray, H.F.W. Taylor, *Truscottite: composition and ionic substitutions*, Mineralogical Magazine **43**(327) (1979) 333–336.
- [4] S. Merlino, E. Bonaccorsi, T. Armbruster, *Tobermorites; their real structure and order-disorder (OD) character*, American Mineralogist, **84**(10) (1999) 1613-1621.
- [5] O.A. Alawad, A. Alhozaimy, M.S. Jaafar, F.N.A. Aziz, A. Al-Negheimish, *Effect of autoclave curing on the microstructure of blended cement mixture incorporating ground dune sand and ground granulated blast furnace slag*, Int J Concr Structures Mater, **9**(3) (2015) 381-390.
- [6] Y.J. Zhu, X.X. Guo, T.K. Sham. *Calcium silicate-based drug delivery systems*, Expet Opin Drug Deliv, **14**(2) (2017) 215-228.
- [7] P.T. Kien, T.N. Quan, D. Q. Minh, *The effect of hydrothermal treatment time on the synthesized of Xonotlite using fined flint glass cullet (FFGC) and Calcium hydroxide*, Vietnam Journal of Catalysis and Adsorption **11**(2) 2022 62-66.

ANALYSIS OF THE EFFECT OF ENVIRONMENTAL TEMPERATURE ON THE MECHANICAL PROPERTIES OF ABS PLASTIC PRINTED MODELS UTILIZING FDM TECHNOLOGY

Nguyen Thi Hoa Cuc ¹, Nguyen Dang Nam ¹, Nguyen Hong Son ¹, Le Anh Gin ¹,
Nguyen Mai Tran Phong ¹, Truong Hoang Phuc ¹, Huynh Nguyen Vinh Phuc ¹,
Le Nguyen Trung Nam ¹, Pham Thi Hong Nga ¹, Nguyen Vinh Tien ² and Nguyen Thanh Tan ¹

¹ Faculty of Mechanical Engineering, Ho Chi Minh City University of Technology and Education,
01 Vo Van Ngan Street, Linh Chieu Ward, Thu Duc City, Ho Chi Minh City, Vietnam

² Faculty of Chemical and Food Technology, Ho Chi Minh City University of Technology and Education,
01 Vo Van Ngan Street, Linh Chieu Ward, Thu Duc City, Ho Chi Minh City, Vietnam

Email: tannt@hcmute.edu.vn

ABSTRACT

The article emphasizes and evaluates research on 3D printing in various environmental temperatures using FDM (Fused Deposition Modeling). FDM is a dominant technology with high performance used in 3D printing (especially plastic) in Viet Nam. 3D printed products depend on printing materials, printing design, layer height, infill speed, material shrinkage, flow, adhesion, support, cooling, heat dissipation, and temperature. In this article, we will conduct an in-depth study of the printing environment temperature for ABS material (Acrylonitrile Butadiene Styrene) to test the influence of the printing environment temperature on the material's mechanical properties. The printing environmental temperature is distributed from 30, 45, 60, and 75 °C, respectively. The study results show that for the printed sample to have the best mechanical properties, the printing environment temperature should be between 30 °C and 45 °C. with the recommended parameters: printing temperature 240 °C, printing angle 45 °C /-45°C, filling density 100% and thickness 0.2 mm.

Keywords: Fused Deposition Modeling (FDM); Heating chamber; Tension test; ABS 3D printing.

INTRODUCTION

Scott Crump developed FDM 3D printing technology in the late 1980s. FDM technology printers are based on the principle of additive material, a fibrous material that is melted at the appropriate temperature and extruded to flow at the spray head. The computer-controlled nozzle will move on a 2D profile, and the material being sprayed will solidify to create a printed layer. Then, gradually stack the next printing layer to create a 3D model. Today, research on 3D printing technology is increasingly being developed. As researched by Weng [1], Wojtyla [2], Rocha [3], Zur [4], and Hanemann [5] about the safety of FDM printing technology and some practical applications of FDM 3D printed models with ABS material. From there, one can see that 3D printing technology is increasingly being applied in life.

With the diversity of material technology, more and more materials can be printed with FDM technology. Common 3D printing materials on the market, such as PLA, ABS, PET, PETG,

PEEK, PVA, research on suitable materials for 3D printing and their applications are increasingly developing. We have some research on materials developed from 3D printing technology, such as Sihiprumnea [6] on ABS nanocomposites. However, to be able to print these materials well, it is necessary to do some research on printing parameters for each material, such as the research of Umesh [7], Ramesh [8], Khairul [9], and Łukasz [10]. Each type of material will have a different printing parameter. In particular, the printing environment's temperature dramatically influences the printed sample's surface quality and mechanical properties. However, studies on the effects of environmental temperature are pretty limited.

As research by S. Ding [11] on the mechanical properties of PEEK material has shown, the best printing temperature is 410 °C, and the printed sample has the best mechanical properties when heated after printing at 90 °C. ABS is another more common printing material; however, ABS plastic is very susceptible to errors

during printing. Since then, research to optimize the printing parameters of ABS material has also been developed. Research by Choi [12] on errors that occur when changing the print bed temperature for 3D printing with ABS has shown that the optimal print bed temperature is. In addition, research by Dhakal [13] on the mechanical properties of samples printed with ABS material shows that the pieces have the best quality when printed with an infill angle of $-45/45^\circ$ and a printing speed of 20 mm/s. Another study by Kousiatza [14] on the effects of printing temperature and printing environment temperature on the mechanical properties of samples printed with ABS resulted in the best mechanical properties of printed pieces when published at 285 °C in an environment at 70 °C.

EXPERIMENT

Acrylonitrile butadiene styrene (ABS) with the chemical formula $(C_8H_8 \cdot C_4H_6 \cdot C_3H_3N)_n$ is a common thermoplastic for making light, stiff, flexible products such as pipes and music tools (mainly records and clarinets), golf club heads (because of their excellent impact resistance), automatic parts, gear covers, gearbox head protection, toys.

The printed sample for the tensile and compression test was designed using 3D design software with dimensions as shown in Figure 1.

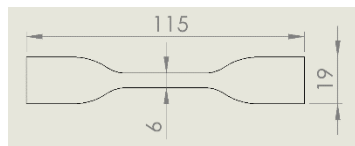


Figure 1. Dimensions of 3D printed sample

The research team processed the printed sample using an FDM X500 printer, as shown in Figure 2, with ABS material. Printing parameters are shown in Table 1.



Figure 2. FDM X500 3D printing

Printed samples are synthesized according to the printing environment temperatures, as shown in Figure 3.

Table 1. 3D printing parameters

Layer heigh	Nozzle	Heat Bed	Heating chamber	Speed	Infill
0.2	240	110	30	50	100
0.2	240	110	45	50	100
0.2	240	110	60	50	100
0.2	240	110	75	50	100



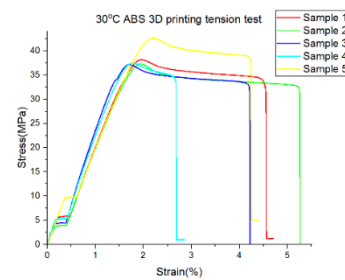
Figure 3. Completed 3D printed models

Each environmental temperature level will be tested five times using the M350-10CT machine in this tensile test. The result obtained is the stress-strain curve of each printed sample. From there, the durability of each printed sample can be determined with different printing environment temperatures.

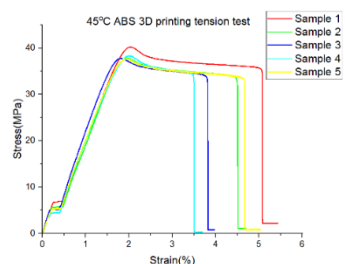
RESULTS AND DISCUSSION

Looking at the graph more closely, one can see that printed samples were destroyed near the clamping position. The stress-strain curves of the printed models are shown in Figure 4.

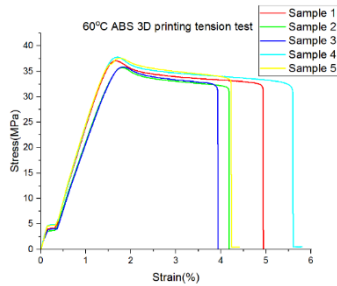
For easy comparison, the average lasting stress values and standard deviations are shown in Figure 5.



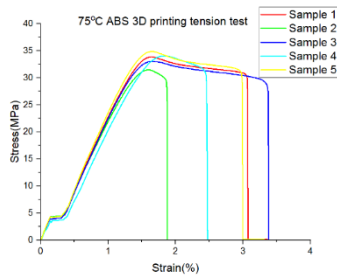
a) Samples at 30 °C



b) Samples at 45 °C



c) Samples at 60 °C



d) Samples at 75 °C

Figure 4. Stress-strain curves of the printed samples at different temperatures

From the stress and deformation results of the above tensile and compression samples, we can see that 3D printed samples have significant errors in their ability to withstand deformation, even though they are processed with the same parameters and environment printing parameters.

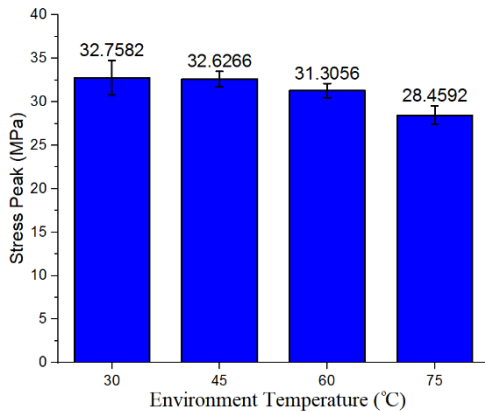


Figure 5. Average lasting stress of printed samples at different temperatures.

From the above results, one can see that the printing environment's temperature affects the printed sample's mechanical properties. However, the difference is not too significant. As the temperature increases, the maximum stress tends to decrease. However, when considering the Young's Module and maximum displacement of the printed samples as shown in Figure 6 and Figure 7. We see that the Young modulus of the two samples printed at ambient temperatures of

60°C and 75°C is higher than the other two samples. However, the deformation tolerance of printed samples at 45°C is the best.

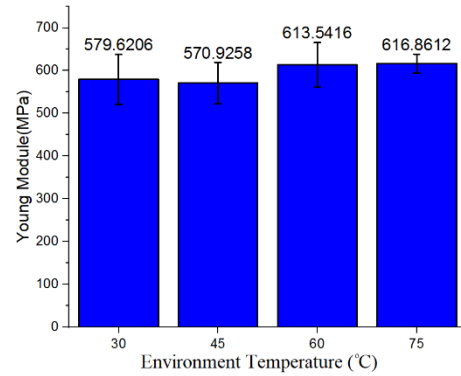


Figure 6. Average Young's modulus of printed samples at different temperatures

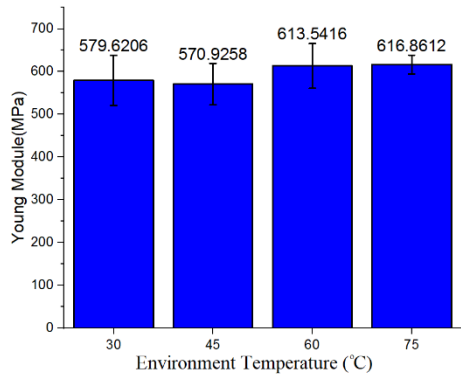


Figure 7. Average maximum displacement of printed samples at different temperatures

CONCLUSION

If we only consider the ability to withstand stress, one can see that the best temperature to print samples with ABS material is room temperature. However, when considering the ability to resist deformation, printed pieces published in an environment at a temperature of 45 °C give the best results.

When considering hardness, Young's Module of the two samples printed at printing environment temperatures of 60 °C and 75 °C has the highest hardness. Research has shown that the influence of printing environment temperature on the mechanical properties of 3D printed samples using FDM technology is quite significant. The results show that the best environmental temperature for 3D printing of ABS models is between 30 °C and 45 °C.

ABS 3D printed models have less bearing capacity than regular ABS materials. This result is due to the limitations of FDM 3D printing

technology. However, we can increase the mechanical properties of 3D printed samples by post-processing heat treatments. However, the difference in the results is not too significant considering that the error of FDM 3D printing technology is quite large and the number of test samples is low. This result is a limitation of the research; many models are needed for the higher test to give more accurate results.

Acknowledgments

We acknowledge HCMC University of Technology and Education, Dong Nhan Phat Co., Ltd, and Material Testing Laboratory (HCMUTE). They allowed me to join their team and access the laboratory and research machines. With their appreciated support, it is possible to conduct this research.

References

- [1] Z. X. Weng, J. L. Wang, T. Senthil, L. X. Wu, *Mechanical and thermal properties of ABS/montmorillonite nanocomposites for fused deposition modeling 3D printing*, *Materials & Design* **102** (2016) 276-283.
- [2] S. Wojtyła, P. Klama, T. Baran, *Is 3D printing safe? Analysis of the thermal treatment of thermoplastics: ABS, PLA, PET, and nylon*, *Journal of occupational and environmental hygiene* **14** (2017) D80-D85.
- [3] C. R. Rocha, A. I. R. Torrado Perez, D. A. Roberson, C. M. Shemelya, E. MacDonald, R. B. Wicker, *Novel ABS-based binary and ternary polymer blends for material extrusion 3D printing*, *Journal of materials research* **29** (2014) 1859-1866.
- [4] P. Żur, A. Kołodziej, A. Baier, G. Kokot, *Optimization of Abs 3D-printing method and parameters*, *European Journal of Engineering Science and Technology* **3** (2020) 44-51.
- [5] T. Hanemann, D. Syperek, D. Nötze, *3D printing of ABS barium ferrite composites*, *Materials* **13** (2020) 1481.
- [6] S. Dul, B. J. A. Gutierrez, A. Pegoretti, J. Alvarez-Quintana, L. Fambri, *3D printing of ABS Nanocomposites. Comparison of processing and effects of multi-wall and single-wall carbon nanotubes on thermal, mechanical and electrical properties*, *Journal of Materials Science & Technology* **121** (2022) 52-66.
- [7] U. K. Vates, N. J. Kanu, E. Gupta, G. K. Singh, N. A. Daniel, B. P. Sharma, *Optimization of FDM 3D printing process parameters on ABS based bone hammer using RSM technique*, *Materials Science and Engineering* **1206** (2021) 012001.
- [8] R. Raju, T. A. Selvakumar, P. M. Rizwan Ali, P. S. Kumar, D. Giridhar, *Experimentation and process parametric optimization of 3D printing of ABS-based polymer parts*, *Advances in Industrial Automation and Smart Manufacturing* (2021) 487-496.
- [9] K. A. Hamzah, C. K. Yeoh, M. M. Noor, P. L. Teh, Y. Y. Aw, S. A. Sazali, W. M. A. W. Ibrahim, *Mechanical properties and thermal and electrical conductivity of 3D printed ABS-copper ferrite composites via 3D printing technique*, *Journal of Thermoplastic Composite Materials* **35** (2022) 3-16.
- [10] Z. Lukasz, A. Raczyńska, M. Pańnikowska-Lukaszuk, *Thermovisual measurements of 3D printing of ABS and PLA filaments*, *Advances in Science and Technology* **12** (2018) 266-271.
- [11] S. L. Ding, B. Zou, P. Wang, H. J. Ding, *Effects of nozzle temperature and building orientation on mechanical properties and microstructure of PEEK and PEI printed by 3D-FDM*, *Polymer Testing* **78** (2019) 105948.
- [12] Y. H. Choi, C. M. Kim, H. S. Jeong, J. H. Youn, *Influence of bed temperature on heat shrinkage shape error in FDM additive manufacturing of the ABS-engineering plastic*, *World Journal of Engineering and Technology* **4** (2016) 186-192.
- [13] N. Dhakal, X. L. Wang, C. Espejo, A. Morina, N. Emami, *Impact of processing defects on microstructure, surface quality, and tribological performance in 3D printed polymers*, *Journal of materials research and technology* **23** (2023) 1252-1272.
- [14] Ch. Kousiatza, N. Chatzidai, D. Karalekas, *Temperature Mapping of 3D Printed Polymer Plates: Experimental and Numerical Study*, *Sensors* **17** (2017) 456.

ADSORPTION CHARACTERISTICS OF TRIAMINE-BEARING ACTIVATED RICE HUSK ASH FOR REMOVAL OF PHOSPHATE ANIONS FROM AQUEOUS SOLUTIONS

Phuoc Toan Phan^{1,2,3}, Quynh Anh Nguyen Thi^{1,2}, Tri Thich Le^{1,2}, Nhat Huy Nguyen^{2,4}, Trung Thanh Nguyen^{1,2}

¹Nanomaterial Laboratory, An Giang University, 18 Ung Van Khiem, Dong Xuyen district, Long Xuyen city, An Giang prov., Vietnam

²Vietnam National University Ho Chi Minh City, Linh Trung ward, Thu Duc city, Ho Chi Minh city, Vietnam

³Faculty of Engineering Technology Environment, An Giang University, 18 Ung Van Khiem, Dong Xuyen district, Long Xuyen city, An Giang prov., Vietnam

⁴Faculty of Environment and Natural Resources, Ho Chi Minh City University of Technology (HCMUT), 268 Ly Thuong Kiet, ward 14, District 10, Ho Chi Minh city, Vietnam

Email: ntthanh@agu.edu.vn

ABSTRACT

Among the material surface modification techniques to adsorb anions such as phosphate, the method of grafting organic functional groups such as amines is often used and shows very good efficiencies. This research grafted amine groups on the activated rice husk ash support to create a novel material for adsorbing phosphate ions in water. Experimental results clearly showed that contact time, initial pH, adsorbent dosage, anion concentration, and adsorption temperature were important factors affecting the phosphate adsorption capacity of the synthesized material. The kinetics, isotherms, and thermodynamics of the phosphate adsorption were also studied. The phosphate adsorption data was highly compatible with the pseudo-second-order kinetic model ($r^2 > 0.99$). Furthermore, this adsorption process was well described by the Freundlich isotherm model ($r^2 > 0.97$). The synthesized material has a maximum phosphate adsorption capacity of 78.1 mg/g at 25 °C and better durability than commercial anion exchange resin (Aqualite A420) after 10 regeneration cycles. Overall, there is a great potential to apply this novel material for the removal of phosphate anions in water and advanced wastewater treatment processes.

Keywords: amine grafting, phosphate adsorption, rice husk ash, TRI-ARHA.

1. INTRODUCTION

Phosphorus is an essential nutrient for energy transport, metabolism and development of organisms. In the aquatic environment, phosphorus exists in many forms including ortho phosphate, poly phosphate and organically bound phosphate. After natural transformation processes or wastewater treatment processes, phosphorus often exists in ionic forms such as H_2PO_4^- , HPO_4^{2-} and PO_4^{3-} , which are soluble forms of phosphate that aquatic plants can easily absorb [1]. The cause of phosphate pollution in water sources may be due to excessive use of phosphate fertilizers in agricultural production or ineffective treatment processes for phosphorus-containing wastewater. Excess phosphate content is one of the main factors causing eutrophication of water sources, leading to excessive growth of phytoplankton, causing severe oxygen

deficiency, reducing water quality and threatens the lives of aquatic species [2]. Therefore, research on removing excess phosphate in natural water or wastewater after primary and secondary treatment processes by advanced treatment works such as adsorption is very necessary.

In the field of adsorption, surface modification using chemical techniques has been and is being used very commonly in the process of synthesizing materials used to treat environmental pollution. The purpose of this modification is to (i) increase the positive charge on the surface of the material and (ii) create new functional groups on the surface with higher affinity for anions that need to be treated such as phosphate. One of the surface modification methods that has been used a lot in research on synthesizing phosphate adsorbent materials in recent years is to graft organic functional groups

such as amines onto the surface of carriers, popularly are mesoporous silica materials including MCM-41, MCM-48, SBA-15,... [3-5] or carbon materials derived from agricultural wastes such as rice husks, sugar cane bagasse, coconut shells, pine bark, sawdust, etc. [6]. The amine groups used for grafting can be mono-, di- and tri-amine through the reaction of organic silane compounds with the components in the carrier [3]. In general, the amine functional groups are immobilized to the carrier (composed mainly of silicon and carbon), which is then combined with metal cations or protons to provide active sites that allow effective adsorption for anions such as phosphates.

In Vietnam, rice husk ash is a large-volume waste generated from the process of using rice husks as fuel to provide heat for various types of production such as brick kilns, agricultural product dryers, winemaking furnaces, etc. Most of the current amount of rice husk ash has to be disposed of directly into the environment because there are not many effective solutions for reuse or recycling. According to recent research results of our group [7, 8], rice husk ash is known as a natural composite composed mainly of SiO₂ and carbon, and has very suitable properties as a carrier for grafting amino functional groups on the surface. The triamine-bearing activated rice husk ash material (TRI-ARHA) was successfully synthesized and demonstrated very good adsorption capacity for nitrate anion in aqueous solutions [7, 9]. In this study, TRI-ARHA material was used to remove phosphate anions in water. Factors affecting the adsorption efficiency and the phosphate adsorption nature of the material will be focused on clarifying through experiments, analysis, calculation of kinetic models, isothermal adsorption models and thermodynamics parameters of phosphate adsorption. Results from this study will contribute to completing a series of research projects on recycling waste rice husk ash into new adsorbents to treat multi-pollutants in wastewater.

2. MATERIALS AND METHODS

2.1 Raw rice husk ash and chemicals

Raw rice husk ash samples as input materials for the synthesis of adsorbent in this study were taken from brick kilns in Cho Moi district, An Giang province. The main chemicals included hydrofluoric acid (HF) used in the process of activating rice husk ash to create a carrier; N-[3-

(trimethoxysilyl)-propyl] diethylene triamine (TMPDT) along with toluene and pentane solvents are chemicals used for the process of grafting amines onto rice husk ash; HCl is used to activate/regenerate the material before and after adsorption; activated carbon (CAS[64365-11-3]) and commercial anion exchange resin (Akualite A420, made in China) were used as comparison materials; KH₂PO₄ is used to prepare synthetic wastewater solutions containing phosphate for adsorption experiments. All chemicals used in the research are sourced mainly from major brands in the world such as Merck, Andrich Sigma, Xilong... supplied through reputable chemical agents in Vietnam.

2.2 Preparation of adsorbent materials

The process of synthesizing TRI-ARHA material includes 3 stages: (1) creating a carrier by activating rice husk ash with HF acid, (2) grafting amino functional groups onto the surface of the activated rice husk ash carrier, and (3) activating amine sites on the material with HCl acid.

First, rice husk ash is activated with HF according to the following process: 20 g of dry rice husk ash into 800 mL of HF solution with a concentration of ~ 5% by volume and stir at a speed of ~ 100 rpm at room temperature. After 30 minutes of stirring, the remaining rice husk ash (insoluble solid part in HF solution) was separated from the solution by filtering and washing several times with distilled water to neutral pH. Continue, drying this rice husk ash overnight (~ 12 hours) at 110 °C, then cooled to obtain activated rice husk ash (ARHA).

The second stage is to graft amino groups onto the ARHA carrier to create TRI-ARHA material according to the following process: 1 g of ARHA into a double-necked glass flask containing 150 mL of toluene, stir well to obtain a homogeneous mixture. Continue, adding 0.3 mL of deionized water and stir well for 30 minutes. Then, place the flask submerged in a silicone oil bath on a magnetic stirrer-heater and control the temperature at a stable level of 85 °C. Next, add 5 mL of triamine silane solution to the mixture and continue to stir for 16 hours. The solid was obtained by filtering and washing with an equal amount of toluene and then pentane. Finally, dry the product at 100 °C for 1 hour.

Finally, before each adsorption experiment, the TRI-ARHA materials were activated by soaking with 0.1 M HCl acid solution for 3 hours

at a ratio of 1 g/L, then the materials were separated by filtering and drying naturally overnight. The regeneration process of used materials is carried out similarly to this activation process [7].

2.3 Adsorption experiments and calculation formulas

Experiments investigating the adsorption capacity of the material were performed in batches under laboratory conditions. Each experiment was repeated at least 3 times. The basic procedure for performing an adsorption experiment is as follows: accurately weigh the mass of adsorbent according to the solid/liquid ratio determined in each experiment and put it into a erlen (100 mL capacity) containing 50 mL of phosphate solution with a concentration of 5 - 160 mgPO₄³⁻-P/L was pH adjusted (with 0.1 M NaOH and 0.1 M HCl solutions) according to each experiment and stir well at 120 rpm. The experiments were performed at room temperature (~ 30 °C) and atmospheric pressure (~ 1 atm). After the appropriate adsorption time, the adsorbent was separated by centrifuging at 10,000 rpm for 10 minutes. The remaining phosphate concentration in the solution after adsorption was analyzed using the ammonium molybdate method according to TCVN 6202:2008 (Vietnam standards: Water quality - Determination of phosphorus - Spectrometric method using ammonium molybdate) on the UV-Vis spectroscopy (model SPECORD 210, Analytik Jena, Germany).

The adsorption capacity (mg/g) was evaluated through formula (1):

$$Q_e = \frac{C_0 - C_e}{m} \times V \quad (1)$$

where C_0 and C_e (mg/L) is the initial concentration and equilibrium concentration of phosphate in the solution. V (mL) is the solution volume. m (mg) is the amount of adsorbent.

Calculation of adsorption kinetic models:

The four adsorption kinetic models are pseudo-first-order, modified-pseudo-first-order, pseudo-second-order and intra-particle diffusion model, expressed by equations (2), (3), (4) and (5) respectively, were used to describe the kinetic experimental data [10].

$$\ln(Q_e - Q_t) = \ln Q_e - k_1 t \quad (2)$$

$$\frac{Q_t}{Q_e} + \ln(Q_e - Q_t) = \ln Q_e - K_1 t \quad (3)$$

$$\frac{t}{Q_t} = \frac{1}{k_2 Q_e^2} + \frac{t}{Q_e} \quad (4)$$

$$Q_t = k_{id} t^{0.5} + C \quad (5)$$

where Q_t and Q_e (mg/g) are the adsorption capacity of the material at time t (min) and equilibrium time. k_1 (min⁻¹) is the rate constant of the pseudo-first-order model. K_1 (min⁻¹) is the rate constant of the modified-pseudo-first-order model. k_2 (g/mg.min) is the rate constant of the pseudo-second-order model. k_{id} (mg/g.min) is the rate constant of the intra-particle diffusion model. C is the intercept point, related to the thickness of the adsorption boundary layer.

Calculation of isothermal adsorption equilibrium models:

The Langmuir, Freundlich, Tempkin and Redlich-Peterson isotherm models are presented in equations (6), (7), (8), (9), respectively. The Dubinin-Radushkevich model and the average adsorption energy E are defined by equations (10) and (11). These are the adsorption isotherm models used in this study. In particular, the Langmuir model assumes that a monomolecular layer is formed when the adsorption process takes place without any interactions between the adsorbed molecules [10]. The Freundlich isotherm can be applied to adsorption processes occurring on heterogeneous surfaces or multilayer adsorption. This isotherm gives an expression that defines the surface heterogeneity and the exponential distribution of active sites and their energies [11]. The Redlich-Peterson isotherm is a mixture of the Langmuir and Freundlich isotherms. This isotherm model is an empirical isotherm incorporating three parameters. It combines elements from both the Langmuir and Freundlich equations; therefore the adsorption mechanism is a mixture and does not follow ideal monolayer adsorption. Meanwhile, the Tempkin isotherm model takes into account the impact of adsorption or indirect adsorption interactions during the adsorption process; it also assumes that the heat of adsorption (ΔH) of all molecules in the layer decreases linearly as a result of increasing surface coverage. Finally, the Dubinin-Radushkevich isotherm model is often applied to distinguish physical and chemical adsorption based on the average adsorption energy E [11].

$$Q_e = \frac{K_L Q_{max} C_e}{1 + K_L C_e} \quad (6)$$

$$Q_e = K_F C_e^{1/n} \quad (7)$$

$$Q_e = \frac{RT}{bT} \ln(a_T C_e) \quad (8)$$

$$Q_e = \frac{a C_e}{1 + K_{RP} C_e^n} \quad (9)$$

$$Q_e = Q_{max} \exp \left(-\beta \left(RT \ln \left(1 + \frac{1}{C_e} \right) \right)^2 \right) \quad (10)$$

$$E = \frac{1}{\sqrt{2\beta}} \quad (11)$$

where C_0 and C_e (mg/L) are the concentration of pollutants in the solution at the initial time and the equilibrium time. V (mL) is the solution volume. m (mg) is the amount of adsorbent. Q_e (mg/g) is the amount of pollutant adsorbed. Q_{max} (mg/g) is the maximum adsorption capacity of the adsorbent. K_L (L/mg) is the equilibrium constant related to the adsorption energy. K_F (mg^{1-(1/n)}L^{1/n}/g) is the Freundlich constant. n is the adsorption intensity indicating the relative distribution of energy and heterogeneity of adsorption sites. b_T (J/mol) is the Tempkin constant related to the heat of adsorption. a_T (L/g) is the Tempkin isothermal constant. R is the gas constant (8.314 J/mol.K). T is absolute temperature (K). a (L/g) is the Redlich-Peterson isotherm constant. K_{RP} (L/mg) is constant. β (mol²/kJ²) is the Dubinin-Radushkevich constant. E (kJ/mol) is the average adsorption energy.

To calculate the total deviation of different isothermal models, chi-square analyzes will be performed and the mathematical expression is expressed by equation (12) [10]. The purpose of the chi-square test is to compare model results with experiments. The value of χ^2 becomes smaller when the values of $Q_{max, cal}$ obtained from the models are as close as possible to the experimental values. On the contrary, $Q_{max, cal}$ and $Q_{max, exp}$ are more different, the value of χ^2 will be even bigger.

$$\chi^2 = \sum \frac{(Q_{max,exp} - Q_{max,cal})^2}{Q_{max,cal}} \quad (12)$$



Figure 1. Raw rice husk ash (RHA), activated rice husk ash (ARHA) and activated rice husk ash after amine grafting (TRI-ARHA)

The results of analyzing the physicochemical characteristics of TRI-ARHA material including FTIR, XRD, BET, TGA, EDX, SEM-mapping,... have been published in a series of recent separate

where $Q_{max, cal}$ (mg/g) is the maximum adsorption capacity obtained from isothermal models. $Q_{max, exp}$ (mg/g) is the experimental maximum adsorption capacity of the adsorbent.

Calculation of thermodynamic parameters:

Adsorption equilibrium experiments were performed at different temperatures (288, 298, 308, 318 K) to evaluate thermodynamic parameters by calculating the Gibbs free energy change (ΔG) according to the equation (13). The variation values of enthalpy (ΔH°) and entropy (ΔS°) are calculated from the slope and intersection with the vertical axis in the linear plot of $\ln K_c$ with $1/T$ as equation (14) [12].

$$\Delta G = -RT \ln K_c \quad (13)$$

$$\ln K_c = \frac{\Delta S}{R} - \frac{\Delta H}{RT} \quad (14)$$

where ΔG (kJ/mol) is the change in free energy. T (K) is absolute temperature. R is the gas constant (8.314 × 10⁻³ kJ/K.mol). $K_c = C_A/C_e$ is the adsorption equilibrium constant with C_A (mg/L) being the concentration of adsorbed pollutant and C_e (mg/L) is the concentration of pollutant in the solution at the equilibrium time [13].

3. RESULTS AND DISCUSSION

3.1 Characteristics of synthetic materials

Images of the TRI-ARHA material compared to the ARHA carrier and raw rice husk ash - RHA are shown in Figure 1. The actual raw rice husk ash has an uneven color (with white, gray and black ash), mainly due to difference in combustion temperature and retention time of rice husks in the furnace. However, the ARHA carrier and TRI-ARHA material obtained after synthesis have a uniform black color and are in very fine powder form.

research works [7, 8, 14]. The results showed that TRI-ARHA has a specific surface area of ~ 402 m²/g and an amine content of ~ 23% [7]. The surface chemical composition of TRI-ARHA is

shown in characteristic bonds such as Si-O-Si (1030-1130 cm^{-1}), Si-H (650-840 cm^{-1}), C=C (1650 cm^{-1}), C-H (2930 cm^{-1}), -OH (3420 cm^{-1}) and -NH₂ (1480 cm^{-1}) are evidence for the presence of amine groups on the porous surface of the ARHA carrier [7]. EDX and SEM-mapping results determined that TRI-ARHA contains elements including O (36.4%), C (33.6%), Si (22.6%), N (7.4%) and these elements are very well dispersed on the surface of the material [7]. pH of the point of zero charge (pH_{pzc}) of TRI-ARHA material was determined to be ~ 5.9 [8].

3.2 Influencing factors and phosphate adsorption properties of TRI-ARHA material

Phosphates in solution can exist mainly in the non-ionic form H_3PO_4 when $\text{pH} < 2$ and in ionic forms such as H_2PO_4^- , HPO_4^{2-} and PO_4^{3-} in the corresponding pH ranges 2 – 7; 7 – 12.5 and > 12.5 [15]. In fact, research shows that the existing forms of phosphate ions (H_2PO_4^- , HPO_4^{2-} and PO_4^{3-}) depending on the pH of the solution can all be adsorbed - ion exchanged on the amine sites of the material [16]. In the adsorption experiments for phosphate ions in this study, the phosphate adsorption capacity of the materials was calculated for all forms of phosphate ions present in solution adsorbed by the material and expressed in form $\text{mgPO}_4^{3-}\text{-P/g}$ (amount of phosphate calculated as phosphorus per gram of material).

3.2.1 Effect of pH and TRI-ARHA dosage on phosphate adsorption capacity

The initial pH of the solution is a factor that greatly affects the surface charge of the adsorbent

and determines the state of existence of pollutants such as phosphates. Experimental results (Figure 2) show that pH is a factor that greatly affects the phosphate adsorption capacity of TRI-ARHA material. Specifically, the phosphate adsorption capacity of TRI-ARHA material reaches $> 10 \text{ mgPO}_4^{3-}\text{-P/g}$ in the pH range from 3 to 7, reaching the highest capacity of $\sim 13.8 \text{ mgPO}_4^{3-}\text{-P/g}$ at pH 5, when increasing $\text{pH} > 7$, the phosphate adsorption capacity rapidly decreases to $3.84 \text{ mgPO}_4^{3-}\text{-P/g}$ at pH 10.

In an environment of $\text{pH} > 7$, phosphate anions exist mainly in the form of HPO_4^{2-} and PO_4^{3-} which is considered more difficult to adsorb than the H_2PO_4^- form ($\text{pH} < 7$) [15]. In addition, TRI-ARHA material has $\text{pH}_{\text{pzc}} \sim 5.9$ [8], so in a pH environment > 5.9 , especially an alkaline environment ($\text{pH} > 7$), the material surface is mainly negatively charged, which can greatly hinder the electrostatic interaction process of phosphate anions on the surface of the material. Furthermore, at this time, phosphate also competes for adsorption with OH^- anions, which exist more in solution, causing the adsorption capacity of the material in this pH range to decrease rapidly. Meanwhile, in the $\text{pH} < 5$ environment, the phosphate adsorption capacity decreased slightly to $11.8 \text{ mgPO}_4^{3-}\text{-P/g}$ at pH 3, possibly due to the tendency to form more H_3PO_4 form which is not favorable for the adsorption process. In summary, experimental results show that the phosphate adsorption process on TRI-ARHA material can take place smoothly in a fairly wide pH range (pH 3-7), in which $\text{pH} \sim 5$ is the most suitable.

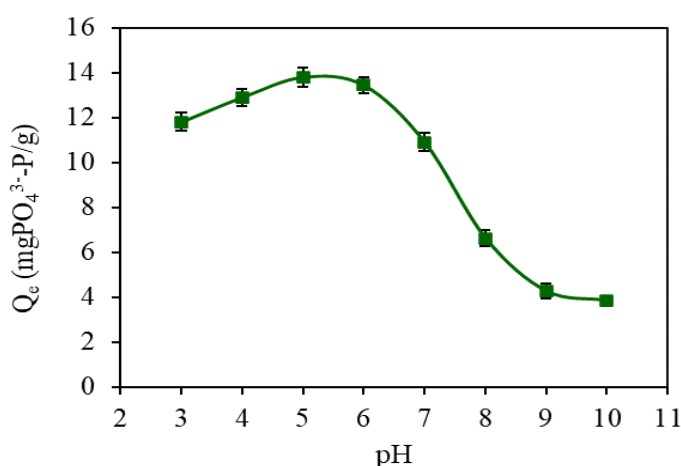


Figure 2. Effect of initial solution pH on the phosphate adsorption capacity of TRI-ARHA material (Experimental conditions: TRI-ARHA 0.6 g/L, $C_{\text{phosphate}} \sim 10 \text{ mgPO}_4^{3-}\text{-P/L}$, pH 3-10, adsorption time ~ 20 minutes, room temperature $\sim 30^\circ\text{C}$)

In the experiment to evaluate the effect of adsorbent dosage, experimental results within the survey range (Figure 3) recorded the highest adsorption capacity of $\sim 36.7 \text{ mgPO}_4^{3-}\text{-P/g}$ at the highest dosage of 0.1 g/L and reach the lowest value of $4.98 \text{ mgPO}_4^{3-}\text{-P/g}$ at a dose of 2 g/L. Phosphate removal efficiency increased from 36.7% to 99.5% when increasing the dosage from

0.1 g/L to 2 g/L. This result shows that under the same experimental conditions of phosphate concentration, pH, adsorption time and environmental temperature, the efficiency of phosphate treatment increases - proportional to the dose of adsorbent. On the contrary, the amount of adsorbed phosphate per unit mass of adsorbent decreases - inversely proportional to the dose of adsorbent.

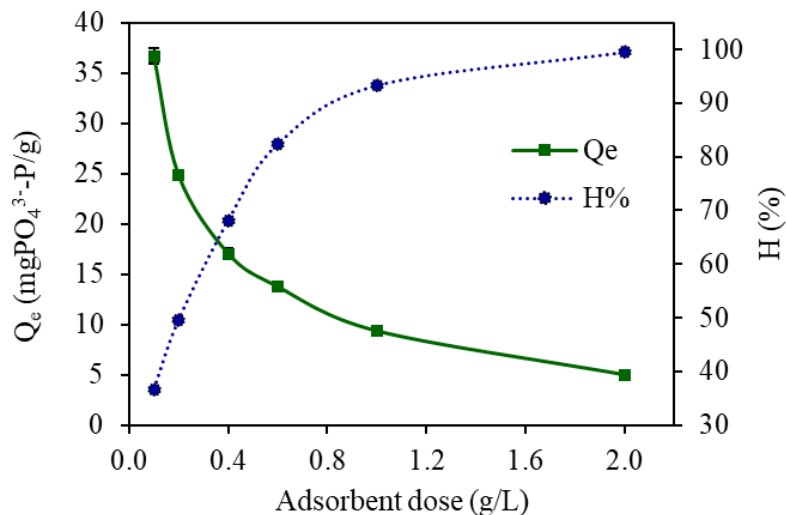


Figure 3. Effect of adsorbent dosage on phosphate removal ability of TRI-ARHA material (Experimental conditions: TRI-ARHA 0.1-2 g/L, $C_{\text{phosphate}} \sim 10 \text{ mgPO}_4^{3-}\text{-P/L}$, $\text{pH} \sim 5$, adsorption time ~ 20 minutes, room temperature $\sim 30^\circ\text{C}$)

3.2.2 Phosphate adsorption kinetics of TRI-ARHA material

Contact time is a factor that significantly affects the phosphate adsorption capacity of TRI-ARHA material as shown in Figure 4 (a). Experimental results show that the phosphate adsorption process takes place quite quickly with more than 80% of the adsorption capacity achieved in the first 10 minutes and adsorption equilibrium achieved after 20 minutes at all investigated concentrations. This time is significantly shorter than many other reports (30 minutes [15], 40 minutes [17], 120 minutes [18]) and is nearly similar to the grafted amine material on MCM-48 carrier in the study by Saad, et al. [19].

First-order, second-order and intra-particle diffusion kinetic models were used to calculate

the relevant kinetic parameters of the phosphate adsorption process on TRI-ARHA material. Table 1 presents the results obtained for the kinetic models. The results show that the pseudo-second-order model (Figure 4 (b)) has r^2 coefficients > 0.99 and much higher than the remaining models, which is determined to be the most suitable model to describe the phosphate adsorption kinetics on TRI-ARHA material. Furthermore, the $Q_{e,\text{cal}}$ values of the pseudo-second-order model are also closer to the experimental Q_e values than the remaining models. Therefore, the chemical adsorption process by ion exchange mechanism can be assumed to be the process that controls the adsorption rate of phosphate ions on TRI-ARHA material, which is consistent with theory as well as previous researches [10, 20].

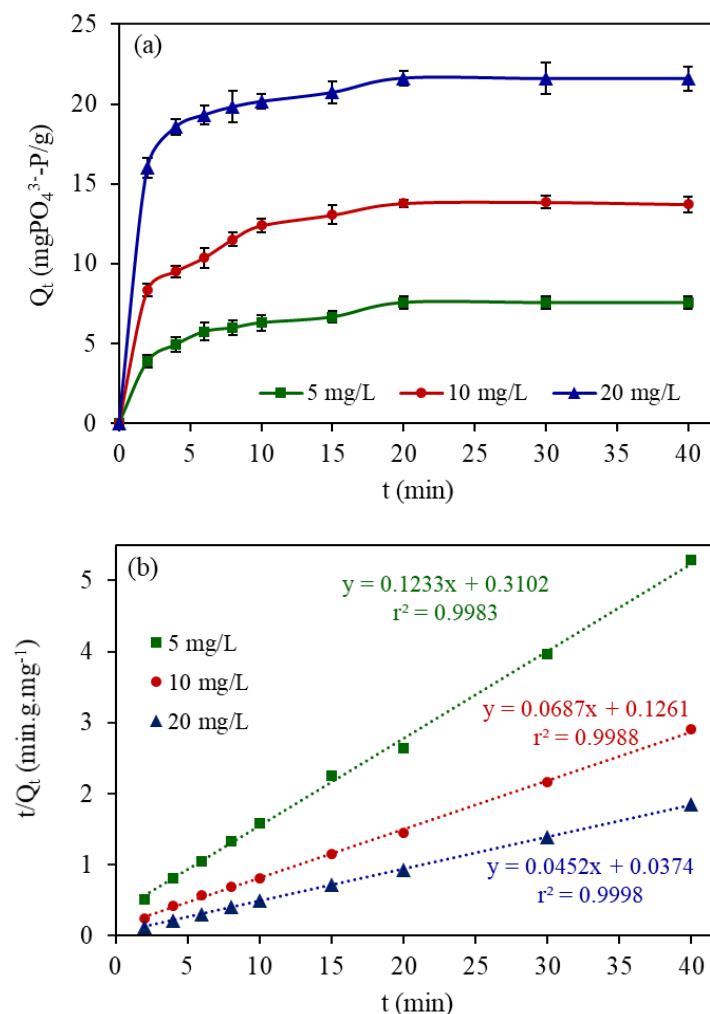


Figure 4. (a) Effect of contact time on phosphate adsorption capacity at different initial concentrations and (b) pseudo-second-order plot of TRI-ARHA material
(Experimental conditions: TRI-ARHA 0.6 g/L, $C_{phosphate} \sim 5, 10, 20 \text{ mgPO}_4^{3-}$ -P/L, pH ~ 5 , adsorption time: 0-60 minutes, room temperature $\sim 30^\circ\text{C}$)

Table 1. Kinetic parameters of phosphate adsorption models on TRI-ARHA material

Models	Parameters	Initial phosphate concentration		
		5 ppm	10 ppm	20 ppm
Pseudo-first-order	$Q_{e,cal}$ (mg/g)	3.5050	5.2530	4.6842
	k_1 (min^{-1})	0.0482	0.1251	0.0401
	r^2	0.8260	0.7578	0.7719
Modified-pseudo-first-order	$Q_{e,cal}$ (mg/g)	6.3975	10.718	10.396
	K_1 (min^{-1})	0.0382	0.1158	0.0353
	r^2	0.8395	0.7481	0.7892
Pseudo-second-order	$Q_{e,cal}$ (mg/g)	8.1103	14.556	22.124
	k_2 ($\text{g.mg}^{-1}.\text{min}^{-1}$)	0.0490	0.0374	0.0546
	r^2	0.9983	0.9988	0.9998
Intra-particle diffusion	k_{id} ($\text{mg.g}^{-1}.\text{min}^{-1/2}$)	0.7213	1.1313	0.9783
	C	3.6865	7.8293	16.466
	r^2	0.8507	0.8211	0.7636

3.2.3 Phosphate adsorption equilibrium of TRI-ARHA material

Adsorption isotherms can be constructed based on the results obtained at different isothermal conditions and equilibrium concentrations of the adsorbent and analyzed using isotherm models such as Langmuir, Freundlich, Tempkin, Redlich-Peterson and Dubinin-Radushkevich. Experimental results in Figure 5 show that the phosphate adsorption capacity on TRI-ARHA material gradually increases with increasing initial phosphate concentration. Meanwhile, increasing the adsorption temperature leads to a decrease in the phosphate adsorption capacity of the TRI-ARHA material. Table 2 presents a summary of the phosphate adsorption isotherm parameters of TRI-ARHA material at different temperatures calculated from commonly used isotherm models. The maximum phosphate adsorption capacity of TRI-ARHA material was experimentally recorded to be about 58.0 - 74.7 mgPO₄³⁻-P/g in the investigated concentration and temperature range. Calculation results of isothermal models (Table 2) show that the

correlation coefficients r^2 of the Langmuir, Freundlich and Redlich-Peterson models are all higher than 0.9, meaning these models are compatible with adsorption data. However, the experimental results show a better fit with the Freundlich isotherm model because of the highest r^2 values (0.9702 – 0.9847) and the lowest χ^2 values (10.596 – 15.326) among the survey models. This shows that phosphate ions can be adsorbed into multiple layers on the surface of the TRI-ARHA material. Furthermore, the n value of the Freundlich model (2.3796 – 2.7294) is in the range of $2 \leq n \leq 10$, proving that the phosphate adsorption process on TRI-ARHA is very favorable [15].

When considering the Dubinin-Radushkevich isotherm model, the E value - average adsorption energy calculated from the model can show the nature of the adsorption process. The calculation results obtained E values ranging from 113.17 - 188.54 kJ/mol (higher than 16 kJ/mol), indicating that the phosphate adsorption process on TRI-ARHA material is more chemical in nature [21, 22].

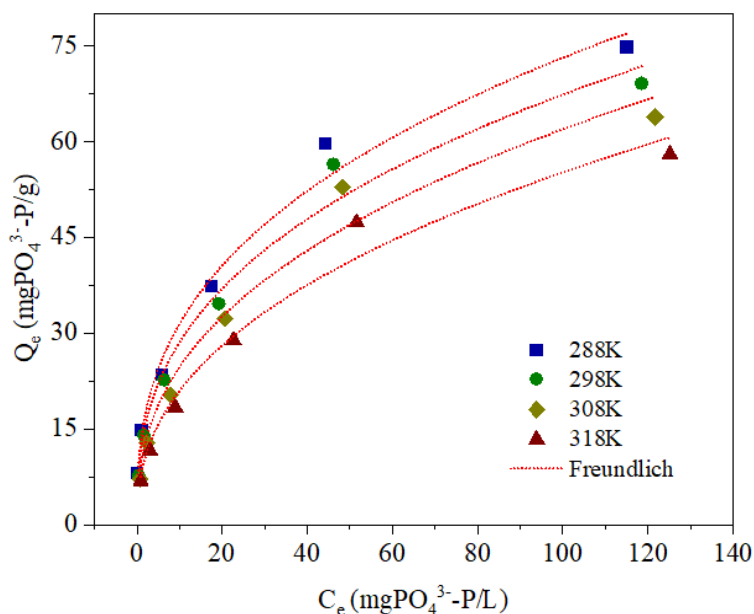


Figure 5. Phosphate adsorption isotherm of TRI-ARHA at different temperatures (Experimental conditions: TRI-ARHA 0.6 g/L, $C_{phosphate}$ 5-160 mgPO₄³⁻-P/L, pH ~ 5, adsorption time ~ 20 minutes, room temperature ~ 30 °C)

Table 2. Phosphate adsorption isotherm parameters of TRI-ARHA material at different temperatures

Isotherm models	Adsorption parameters	Adsorption temperature (K)			
		288	298	308	318
Langmuir	Q_{max} (mg/g)	84.443	78.056	74.549	69.511
	K_L (L/mg)	0.0558	0.0552	0.0466	0.0387

Freundlich	r^2	0.9392	0.9434	0.9650	0.9685
	χ^2	42.006	33.440	17.974	13.133
	K_F ($\text{mg}^{1-(1/n)}\text{L}^{1/n}/\text{g}$)	13.515	12.088	9.8222	7.9633
	n	2.7284	2.6816	2.5013	2.3796
	r^2	0.9847	0.9794	0.9702	0.9741
Tempkin	χ^2	10.596	12.187	15.326	10.777
	a_T (L/g)	4.0725	2.6737	1.4480	1.1608
	b_T (J/mol)	223.48	228.14	223.52	247.13
Redlich-Peterson	r^2	0.8695	0.8937	0.9128	0.9012
	χ^2	90.192	62.860	44.829	41.185
	a (L/g)	364.03	51.761	10.579	7.9273
	K_{RP} (L/mg)	26.240	3.6823	0.6084	0.5468
	n	0.6390	0.6580	0.7127	0.6950
	r^2	0.9797	0.9748	0.9714	0.9737
Dubinin-Radushkevich	χ^2	14.042	14.900	14.680	10.968
	Q_{max} (mg/g)	70.646	66.650	55.189	50.357
	β (mol^2/kJ^2)	$3.384 \cdot 10^{-5}$	$3.904 \cdot 10^{-5}$	$1.406 \cdot 10^{-5}$	$1.789 \cdot 10^{-5}$
	E (kJ/mol)	121.55	113.17	188.54	167.16
	r^2	0.6927	0.6723	0.7628	0.8081

3.2.4 Thermodynamic parameters of phosphate adsorption on TRI-ARHA material

Thermodynamic parameters of phosphate adsorption using TRI-ARHA material were studied by conducting adsorption experiments at temperatures ranging from 15 - 45 °C (288 - 318 K). The results in Table 3 recorded a negative value of ΔH (-30.721 kJ/mol) proving that the phosphate adsorption process on TRI-ARHA material is an exothermic process, so it has the

ability to adsorption increases as temperature decreases [15]. Negative values of ΔG indicate that phosphate adsorption occurs spontaneously. Furthermore, the negative values of ΔG increased as the temperature decreased, showing that the nature of the adsorption process is inversely proportional to temperature. Finally, the negative value of ΔS (-0.0897 kJ/mol) implies a decrease in randomness at the solid-liquid interface during the phosphate adsorption process on TRI-ARHA material.

Table 3. Thermodynamic parameters of phosphate adsorption using TRI-ARHA material at different temperatures

ΔH (kJ/mol)	ΔS (kJ/mol.K)	ΔG (kJ/mol)				r^2
		288 K	298 K	308 K	318 K	
-30.721	-0.0897	-4.8851	-3.9881	-3.0910	-2.1939	0.9958

3.3 Phosphate adsorption durability of TRI-ARHA material and comparison with other materials

For practical water and wastewater treatment applications, an excellent adsorbent must have both high adsorption capacity and good reusability to reduce overall costs. Test results (Figure 6) show that TRI-ARHA material maintains a fairly stable phosphate adsorption

efficiency after 10 regenerations compared to Akualite A420 resin. Specifically, after 10 regenerations, the adsorption capacity of TRI-ARHA still maintains ~ 93.1% compared to the efficiency of first use, while Akualite A420 only maintains ~ 85.5%. This result shows that TRI-ARHA is a very potential material that can be applied in phosphate treatment processes in water.

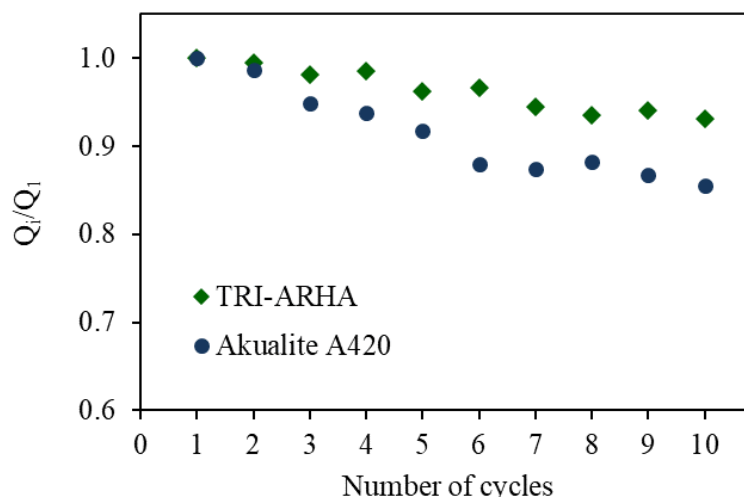


Figure 6. Phosphate adsorption durability of TRI-ARHA and Akualite A420 resin after 10 regenerations (Q_i with $i = 1, 2, 3, \dots, 10$ is the adsorption capacity of the material after 10 regenerations; Akualite A420 is a commercial anion exchange resin)

(Experimental conditions: material amount 0.6 g/L, $C_{phosphate} \sim 10 \text{ mgPO}_4^{3-}\text{-P/L}$, $\text{pH} \sim 5$, adsorption time ~ 20 minutes, room temperature $\sim 30^\circ\text{C}$)

Comparing the phosphate adsorption capacity of TRI-ARHA with some recently published adsorbents listed in Table 4. The results show that TRI-ARHA has very good adsorption capacity compared to other materials. This result shows that the effectiveness of the amine grafting

process on the ARHA carrier has increased the outstanding phosphate adsorption capacity of the TRI-ARHA material. This is due to the interaction of amino groups with ARHA, resulting in high amine content and good dispersion on the surface of the material [8].

Table 4. The phosphate adsorption capacity of TRI-ARHA compared to some previously researched and published adsorbents

Adsorbent	Q_{\max} (mg/g)	Experimental conditions	Reference
TRI-ARHA	78.1	5-160 mg/L, 25 °C, 20 minutes, pH ~ 5	This study
Mono-ammonium functionalized mesoporous MCM-41 silicas	20.0	5-100 mg/L, 25 °C, 180 minutes, pH ~ 5	[5]
Mono-ammonium functionalized mesoporous MCM-48 silicas	27.1	5-100 mg/L, 25 °C, 180 minutes, pH ~ 5	[5]
Mono-ammonium functionalized mesoporous SBA-15 silicas	55.9	5-100 mg/L, 25 °C, 180 minutes, pH ~ 5	[5]
Mono-ammonium functionalized mesoporous MCM-48 silica	46.0	100-700 mg/L, 25 °C, 60 minutes, pH ~ 5	[19]
Tri-ammonium functionalized SBA-15 silica	117.4	156-939 mg/L, 25 °C, 60 minutes, pH ~ 5	[3]
Amine-functionalized magnetic chitosan composite beads	41.5	20-140 mg/L, 30 °C, 40 minutes, pH ~ 7	[17]
Chitosan/multi-walled carbon nanotubes composite	36.1	25-200 mg/L, 20 °C, 30 minutes, pH ~ 3	[15]

4. CONCLUSION

This study has shown that TRI-ARHA material has many outstanding advantages in adsorbing phosphate such as high adsorption capacity, fast adsorption equilibrium time, wide effective pH range and good durability. The adsorption experimental data followed the pseudo-second-order kinetic model, showing that chemical adsorption is the main mechanism controlling the adsorption rate of the material. The phosphate adsorption equilibrium is best fit by the Freundlich isotherm model. Thermodynamic parameters show that the phosphate adsorption process on TRI-ARHA is feasible and spontaneous with the adsorption - ion exchange mechanism mainly thanks to the strong activity of the grafted triamine groups on the surface of the material. The research results have clarified the adsorption capacity and nature of TRI-ARHA material for phosphate anions in aqueous solution.

Acknowledgments

We acknowledge the support of time and facilities from An Giang University (AGU) and Ho Chi Minh City University of Technology (HCMUT), VNU-HCM for this study.

References

- [1] Trần Văn Nhân và Ngô Thị Nga, *Giáo trình công nghệ xử lý nước thải*. Hà Nội: Nhà xuất bản Khoa học và Kỹ thuật, 2002.
- [2] S. E. Jørgensen, W. D. Williams, U. I. E. T. Centre, and I. L. E. Committee, *Lakes and reservoirs: water quality: the impact of eutrophication*. UNEP-International Environment Technology Centre, 2001.
- [3] S. Hamoudi, A. El-Nemr, M. Bouguerra, and K. Belkacemi, *Adsorptive removal of nitrate and phosphate anions from aqueous solutions using functionalised SBA-15: Effects of the organic functional group*, The Canadian Journal of Chemical Engineering **90** (2011) 34-40.
- [4] M. Ebrahimi-Gatkash, H. Younesi, A. Shahbazi, and A. Heidari, *Amino-functionalized mesoporous MCM-41 silica as an efficient adsorbent for water treatment: batch and fixed-bed column adsorption of the nitrate anion*, Applied Water Science **7** (2017) 1887-1901.
- [5] R. Saad, S. Hamoudi, and K. Belkacemi, *Adsorption of phosphate and nitrate anions on ammonium-functionnalized mesoporous silicas*, Journal of Porous Materials **15** (2008) 315-323.
- [6] P. Loganathan, S. Vigneswaran, and J. Kandasamy, *Enhanced removal of nitrate from water using surface modification of adsorbents—A review*, Journal of environmental management **131** (2013) 363-374.
- [7] P. T. Phan, T. T. Nguyen, N. H. Nguyen, and S. Padungthon, *Triamine-bearing activated rice husk ash as an advanced functional material for nitrate removal from aqueous solution*, Water Science and Technology **79** (2018) 850-856.
- [8] P. T. Phan, T. T. Nguyen, S. Padungthon, T. Nguyen Thi, and N. N. Huy, *A novel conjugate mechanism for enhancing the adsorption capacity of amine-functionalized activated rice husk ash for simultaneous removal of organics and anions in wastewater: Experimental and theoretical explanations*, ACS Omega **7** (2022) 28866-28874.
- [9] Phan Phuoc Toan, Nguyen Thai Anh, Nguyen Nhat Huy, and Nguyen Trung Thanh, *Modelling approach to nitrate adsorption on triamine-bearing activated rice husk ash*, Engineering and Applied Science Research **47** (2020) 190-197.
- [10] W. Song et al., *Adsorption of nitrate from aqueous solution by magnetic amine-crosslinked biopolymer based corn stalk and its chemical regeneration property*, Journal of hazardous materials **304** (2016) 280-290.
- [11] N. Ayawei, A. N. Ebelegi, and D. Wankasi, *Modelling and Interpretation of Adsorption Isotherms*, Journal of Chemistry **2017** (2017) 3039817.
- [12] T. A. Nguyen, C.-C. Fu, and R.-S. J. C. E. J. Juang, *Effective removal of sulfur dyes from water by biosorption and subsequent immobilized laccase degradation on crosslinked chitosan beads*, Chemical Engineering Journal **304** (2016) 313-324.
- [13] M. Z. U. Rehman, Z. Aslam, R. A. Shawabkeh, I. A. Hussein, and N. Mahmood, *Concurrent adsorption of cationic and anionic dyes from environmental water on amine functionalized carbon*, Water Science and Technology **81** (2020) 466-478.
- [14] Phan Phuoc Toan, Nguyen Trung Thanh, and Ngo Thuy Diem Trang, *Characterizations and methyl orange*

- adsorption capacity of activated rice husk ash*, Journal of Science, Can Tho University **42** (2016) 50-57.
- [15] Y. Huang, X. Lee, M. Grattieri, F. C. Macazo, R. Cai, and S. D. Minteer, *A sustainable adsorbent for phosphate removal: modifying multi-walled carbon nanotubes with chitosan*, Journal of Materials Science **53** (2018) 12641-12649.
- [16] Y. Huang *et al.*, *Modified biochar for phosphate adsorption in environmentally relevant conditions*, Chemical Engineering Journal **380** (2020) 122375.
- [17] I. Aswin Kumar and N. Viswanathan, *Development and reuse of amine-grafted chitosan hybrid beads in the retention of nitrate and phosphate*, Journal of Chemical & Engineering Data **63** (2018) 147-158.
- [18] S. Mor, K. Chhoden, and K. Ravindra, *Application of agro-waste rice husk ash for the removal of phosphate from the wastewater*, Journal of Cleaner Production **129** (2016) 673-680.
- [19] R. Saad, K. Belkacemi, and S. Hamoudi, *Adsorption of phosphate and nitrate anions on ammonium-functionalized MCM-48: Effects of experimental conditions*, Journal of Colloid and Interface Science **311** (2007) 375-381.
- [20] R. Katal, M. S. Baei, H. T. Rahmati, and H. Esfandian, *Kinetic, isotherm and thermodynamic study of nitrate adsorption from aqueous solution using modified rice husk*, Journal of Industrial and Engineering Chemistry **18** (2012) 295-302.
- [21] P. S. Kumar, S. Ramalingam, S. D. Kirupha, A. Murugesan, T. Vidhyadevi, and S. Sivanesan, *Adsorption behavior of nickel (II) onto cashew nut shell: Equilibrium, thermodynamics, kinetics, mechanism and process design*, Chemical Engineering Journal **167** (2011) 122-131.
- [22] İ. Tosun, *Ammonium removal from aqueous solutions by clinoptilolite: Determination of isotherm and thermodynamic parameters and comparison of kinetics by the double exponential model and conventional kinetic models*, International Journal of Environmental Research and Public Health **9** (2012) 970-984.

INVESTIGATING FOR PHOTOCATALYTIC ACTIVITY OF HYBRID TiO₂/REDUCED GRAPHENE OXIDE AND APPLICATION IN REDUCING VOCs

Nguyen Thanh Danh^{1,4}, Nguyen Thi Phuong Thanh^{2,4}, Tran Quang Nguyen^{3,4}, Huynh Van Giang^{1,4}, Tran Kim Chi^{1,4}, Le Thuy Thanh Giang^{1,4}, Tran Quang Trung^{1,4*}.

¹ Faculty of Physics and Engineering Physics, University of Science, Ho Chi Minh City 700000, Vietnam;

² Laboratory of Advanced Materials, University of Science, Ho Chi Minh City 700000, Vietnam;

³ Department of IC Design and Hardware, University of Information Technology 700000, Vietnam;

⁴ Vietnam National University, Ho Chi Minh City 700000, Vietnam

Email: tqtrung@hcmus.edu.vn

ABSTRACT

In this study, rGO/TiO₂ hybrid nanostructures (rGO: reduced Graphene Oxide) have been successfully fabricated for potential application in treating volatile organic compounds (VOCs) that are harmful to the environment through the method of directly measuring the change in concentration of decomposed VOCs in real time under UV-excited conditions using a home-made measuring system. The results showed that hybrids TiO₂:rGONFs (reduced Graphene Oxide nano flake) samples with the weight ratio between two kinds of material are 99%: 1% and 98%: 2% which reduced VOCs faster than 2 times intrinsic TiO₂. The phenomenon of 2D materials involved in the hybrids lead to the fact that the photocatalytic activity of TiO₂ had been significantly improved, this can be explained as follows: When a heterogeneous hybrid was formed, because of the difference in energy levels of the conduction band between two materials was negligible, heterojunction barrier is not too high this made the photogenerated electrons from TiO₂ easily traverse through rGONFs under UV stimulation. This thing has significantly reduced the recombination of the generated carrier in TiO₂ during irradiation, which leads to an increase within the lifetime of the carrier and makes the photocatalytic reaction of the assembly become more effective.

Key words: rGO, TiO₂, photocatalysis, VOCs.

INTRODUCTION

Along with the development of industry and urban modernization, environmental pollution issues are increasing critically with many different types of pollutants in which volatile organic compounds (VOCs) being a direct cause of harm to human health, especially cancer. Photocatalytic oxidation (PCO) reaction is considered one of the most effective methods toward decomposing organic wastes under appropriate lighting conditions [1].

In recent years, nanostructured metal oxide semiconductors such as TiO₂, SnO₂, ZnO, WO₃, CuO... have been receiving considerable attention from researchers in applications of habitat improvement [2]. In particular, TiO₂ was specific interested by scientists because of its advantages for a photocatalyst. However, the intrinsic TiO₂ itself still has certain limitations like large band gap (3.2 eV in Anatase phase) and

high photo-induced charge recombination rate. Thus, methods of modifying surface and constructing nano material heterostructure (hybridization) have been developed and researched as an effective solution to improve the photocatalytic activity of TiO₂ [3–5].

After Novoselov and Geim discovered the monolayer structure of Carbon atoms by exfoliating Graphite flake in 2004 [6], Graphene materials quickly is attracted the attention of researchers due to its many outstanding advantages. However, the band gap of Graphene ~ 0 eV [6] that makes the applicability to optical processes of this material become limited. Instead of that, making a hybrid of Graphene with other semiconductors is seen to be a better way to increase the efficiency of the optical activities for host materials.

Graphene oxide (GO) is an oxidized derivative of Graphene with functional groups that make many specific physical and chemical

properties for this material. Many studies have shown that these defects play a role as electron traps [7–9], this fact increases the life time of photo-generated charge carriers, which is essential for applications like photocatalysis.

EXPERIMENTAL

1. Synthesis of Aqueous GO Dispersion

We prepared graphene oxide (GO) solution from the modified Hummers' method. 0.2g of Graphite flake were mixed with 46 ml of H₂SO₄ (98%) at 0°C, 0.6 g of KMnO₄ were added in small amounts. After 2 hours of mixing, the solution is stirred at room temperature for 30 minutes. The mixture was diluted with 92 ml of deionized (DI) water and incubated at 90°C for half an hour. Finally, 5 ml H₂O₂ (30%) was added to this suspension. This solution was continued to be centrifuged at 5,000 rpm for 5 minutes to separate the solid material at the bottom. Finally, the residual acid in GO was washed by DI water until pH ~ 7. GO product would be dispersed into solvent (Aceton/Ethanol) to form GO solution with concentration ~ 2 mg/ml.

2. Synthesis of hybrids TiO₂/rGO

To synthesis the TiO₂/rGO hybrid, we do follow steps: The GO (2.0 mg/ml) and TiO₂ (4.0 mg/ml) solutions were mixed under ultrasonic pulverized condition for half an hour, the mixture was continuously added 0.15 ml Hydrazine Monohydrate and stirred in 10 minutes. After the above stage, the solvent is

removed by heat, leaving a gray-white powder. Finally, the powder was subjected to a thermal shock at 350°C for 5 minutes, the result was a solid powdered TiO₂/rGO hybrid. For the purpose of investigating the enhanced activity of host materials which hybride with nano sheet rGO, the mass ratio of TiO₂:rGO samples were changed to 99:01 and 98:02, respectively. To simplify, the hybrid samples are abbreviated to TiO₂-rGO(99:1), TiO₂-rGO (98:2) with rGO content of 1% and 2%.

RESULTS AND DISCUSSION

1. Morphology and structure of nano materials

The characteristic structures of pure TiO₂ and TiO₂/rGO hybrid materials were analyzed through XRD patterns. The results shown in Figure a determining the existence of characteristic diffraction peaks of TiO₂ (anatase phase) at angles 2θ = 25.3, 37.80, 48.1; 53.9, 55.1 corresponding to the lattice families (101), (004), (200), (105) and (211). Specifically, the SEM image shows the formation of small rGO pieces with sizes from 20 nm to 30 nm scattered on the surface of TiO₂ nanoparticles as shown in Figure b. In addition, from the infrared spectrum (Figure c), the appearance of another peak found at position 745 cm⁻¹ representing the Ti-O-C bond, indicates the formation of a stable binding state between TiO₂ and rGO. This result has also been reported in similar studies in which Chen Ying's group is typical [10].

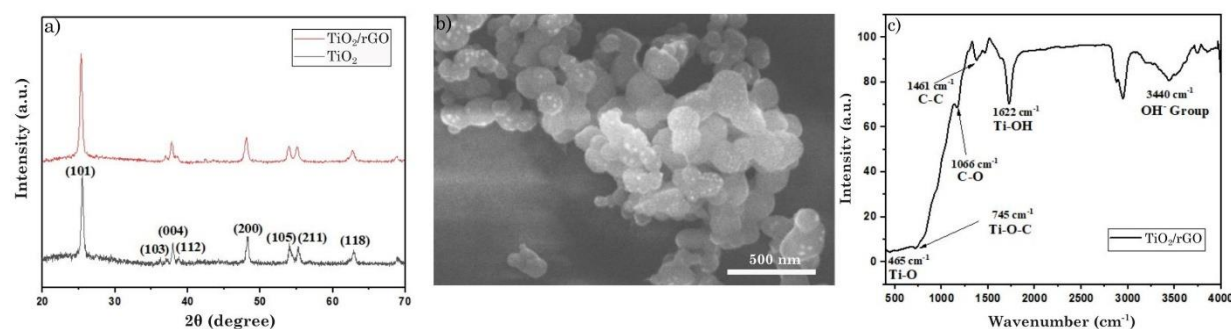


Figure 1. Structural and morphological analysis of TiO₂/rGO: a) XRD pattern; b) SEM image; c) FT-IR spectra

2. The ability to decompose VOCs of TiO₂/rGO hybrids

In this study, the photocatalytic activity of TiO₂ nanoparticles and TiO₂/rGO hybrid material with Toluene test gas acting as VOCs was determined through real-time direct measurement. The change in the concentration

of VOCs (Δ PCO) was recorded and calculated according to the following formula:

$$\Delta_{\text{PCO}} (\%) = \frac{C_0 - C_t}{C_0} \times 100\% \quad (1)$$

In which: C₀ (ppm) and C_t (ppm) are the concentrations of Toluene gas at the start and end time, respectively.

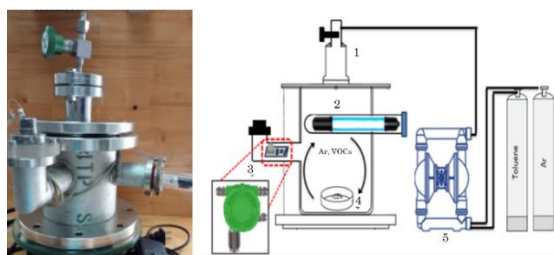


Figure 2. VOCs measurement system: (1) Gas supply valve to the system, (2) UV source, (3) VOCs gas sensor PQN-3835, (4) Sample, (5) Diaphragm pump

The main purpose of this study is to investigate the enhancement of photocatalytic capabilities of 2D materials rGO on TiO_2 host material. A constant amount of Toluene vapor (40 μl) is injected into the system and continuously circulated in the reaction chamber by a diaphragm pump. Changes in test gas concentration were continuously recorded through the PQN-3835 sensor during the reaction.

Figure a shows performance of Toluene gas decomposition catalyzed by pure TiO_2 samples with 4 curves corresponding to the test samples with mass of 300 mg, 400 mg, 500 mg, and 600 mg. First, it can be seen that the concentration of Toluene decreases by half in less than the first hour. Actual data also shows that after 4 hours of reaction, the amount of VOCs decomposed Δ_{PCO} in TiO_2 (300 mg), TiO_2 (400 mg), TiO_2 (500mg), and TiO_2 (600 mg) samples were: 84%, 86%, 91%, 97% respectively. Thus, the efficiency of the photocatalysis process increases gradually with the increase of the amount of TiO_2 material.

To investigate the effect of rGO on the photocatalysis of the TiO_2 host material, we selected a 300 mg TiO_2 sample to compare the catalytic efficiency between pure and hybrid materials. In which, the hybrids samples were prepared according to the mass ratio between TiO_2 and rGO respectively 99%:1%, 98%:2%. The results shown in Figure b indicate that although the mass of TiO_2 has decreased, with the participation of rGO, the two hybrids' samples show a superiority in Toluene decomposition compared to the pure TiO_2 sample. Specifically, similar to the pure TiO_2 sample (300 mg), the TiO_2/rGO hybrid samples all degraded $\sim 85\%$ of the original VOCs, however, the organic matter decomposition rate in the hybrid sample was ~ 4 times faster when after only 1 hour the Toluene concentration

decreased to a minimum constant value (the 300 mg pure TiO_2 sample needed 4 hours to reach this value).

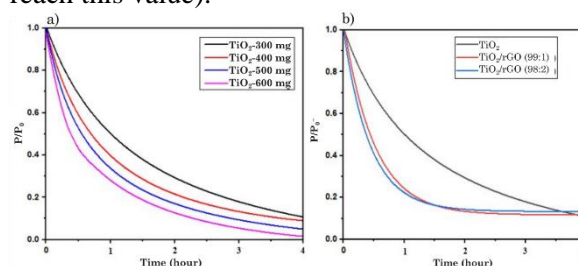


Figure 3. Photocatalytic of: a) pure TiO_2 , b) TiO_2/rGO

CONCLUSION

In summary, we demonstrated that rGO materials and TiO_2/rGO hybrid materials has been successfully synthesized with the desired morphology and material properties. The TiO_2/rGO composite material exhibits a good combination in which TiO_2 nanoparticles is well decorated on the surface of rGO. The excellent dispersion and attachment of TiO_2 is originated from Ti-O-C bonding interaction between TiO_2 and rGO which can be confirmed by FTIR spectra. The efficiency of photocatalytic reaction of TiO_2/rGO hybrid materials (with mass ratio 99%:1% and 98%:2%) showed photocatalytic performance of degradation toward toluene gas in comparison with pure sample in which toluene gas decomposition occurs at the rate more than twice as fast. This result leads to, in presence of rGO material that reduced the recombination rate of photogenerated electrons and holes and enhances the charge separation in TiO_2 materials under irradiation; thus leading to photocatalytic performance under UV irradiation was significantly improved.

Acknowledgment

This study was supported by University of Science, Ho Chi Minh City 700000, Vietnam (Number: T2022-82).

References

- [1] S. Weon, F. He, W. Choi, *Status and challenges in photocatalytic nanotechnology for cleaning air polluted with volatile organic compounds: Visible light utilization and catalyst deactivation*, *Environ Sci Nano*. **6** (2019) 3185–3214.
- [2] M.S.S. Danish, L.L. Estrella, I.M.A. Alemaida, A. Lisin, N. Moiseev, M. Ahmadi, M. Nazari, M. Wali, H. Zaheb, T.

- Senjyu, *Photocatalytic applications of metal oxides for sustainable environmental remediation*, Metals (Basel). **11** (2021) 1–25.
- [3] P.H. Ho, M.K. Li, R. Sankar, F.Y. Shih, S.S. Li, Y.R. Chang, W.H. Wang, F.C. Chou, C.W. Chen, *Tunable Photoinduced Carrier Transport of a Black Phosphorus Transistor with Extended Stability Using a Light-Sensitized Encapsulated Layer*, ACS Photonics. **3** (2016) 1102–1108.
- [4] Y. Lin, P. Ren, C. Wei, *Fabrication of MoS₂/TiO₂ heterostructures with enhanced photocatalytic activity*, CrystEngComm. **21** (2019) 3439–3450.
- [5] Y. Chen, X. Dong, Y. Cao, J. Xiang, H. Gao, *Enhanced photocatalytic activities of low-bandgap TiO₂-reduced graphene oxide nanocomposites*, Journal of Nanoparticle Research. **19** (2017) 1–13.
- [6] K.S. Novoselov, A.K. Geim, S. V. Morozov, D. Jiang, Y. Zhang, S. V. Dubonos, I. V. Grigorieva, A.A. Firsov, *Electric field in atomically thin carbon films*, Science (1979). **306** (2004) 666–669.
- [7] R.K. Paul, S. Badhulika, N.M. Saucedo, A. Mulchandani, *Graphene nanomesh as highly sensitive chemiresistor gas sensor*, Anal Chem. **84** (2012) 8171–8178.
- [8] Abid, P. Sehwat, S.S. Islam, P. Mishra, S. Ahmad, *Reduced graphene oxide (rGO) based wideband optical sensor and the role of Temperature, Defect States and Quantum Efficiency*, Sci Rep. **8** (2018) 1–13.
- [9] J.A. Quezada Renteria, C. Ruiz-Garcia, T. Sauvage, L.F. Chazaro-Ruiz, J.R. Rangel-Mendez, C.O. Ania, *Photochemical and electrochemical reduction of graphene oxide thin films: Tuning the nature of surface defects*, Physical Chemistry Chemical Physics. **22** (2020) 20732–20743.
- [10] M.J. Borah, A. Devi, R.A. Saikia, D. Deka, *Biodiesel production from waste cooking oil catalyzed by in-situ decorated TiO₂ on reduced graphene oxide nanocomposite*, Energy. **158** (2018) 881–889.

ASSESSING THE PH DETECTION CAPABILITIES OF POLYANILINE AND COMPOSITE MATERIALS INVOLVING REDUCED GRAPHENE OXIDE FOR SALIVARY BIOSENSING

Arveenamathii Veeriah¹, Aung Thiha², Fatimah Ibrahim^{1,2}, Karunan Joseph², Bojan Petrović³, Sanja Kojić⁴, Nurul Fauzani Jamaluddin², Goran M Stojanović⁴

¹ Department of Biomedical Engineering, Faculty of Engineering, Universiti Malaya, Kuala Lumpur,

² Centre for Innovation in Medical Engineering (CIME), Universiti Malaya, Kuala Lumpur, Malaysia

³ Department of Dental Medicine, Faculty of Medicine, University of Novi Sad, Novi Sad, Serbia

⁴ Faculty of Technical Science, University of Novi Sad, Novi Sad, Serbia

Email: fatimah@um.edu.my

ABSTRACT

Monitoring the pH levels in saliva within the oral cavity holds significant importance, serving as a valuable biomarker for prognosis and diagnosis, reflecting not only oral health but also various metabolic conditions. The lack of easily wearable intraoral pH sensors poses a significant challenge. This paper introduces a study involving the synthesis and assessment of conductive polymer polyaniline compounds for pH biosensing, with the aim of potentially developing intraoral biosensors for saliva analysis. Both reduced graphene oxide-polyaniline (rGO-PANI) and polyaniline (PANI) were employed as sensing materials to determine which material exhibited superior performance in pH biosensors. The study comprehensively evaluated these sensors, taking into account their sensitivity, repeatability, response time, stability, and pH range. Electrodeposition was employed to fabricate the sensors for both sensing materials. A comparative analysis of the performance of the two sensing materials was conducted using zero current potentiometry electrochemical analysis for the pH sensors. The analysis revealed that the rGO-PANI-based pH sensor performed better than the PANI-based pH sensor. These findings suggest that the rGO-PANI-based sensor could serve as a dependable tool for detecting pH variations in salivary analytes.

Keywords: pH sensor; rGO-PANI; PANI; electrodeposition; zero current potentiometry.

INTRODUCTION

The National Institute of Dental and Craniofacial Research (NIDCR) has developed a strategic approach to utilize saliva for clinical diagnostics, as it contains various analytes that can be utilized to assess health and disease status [1]. Saliva-based diagnostics offer a noninvasive method to evaluate the condition of individuals, providing information on their overall physiological state and oral as well as systemic health [2].

Salivary biomarkers have proven valuable in disease diagnosis and monitoring, offering early assessment of malignancy risk, disease progression, and therapy response. This noninvasive and cost-effective diagnostic method allows for accessible collection and storage of saliva, reducing patient discomfort and ensuring the safety of healthcare professionals. Salivary diagnostics exhibit accuracy, with

specific biomarkers linked to health and disease [3]. The pH value of saliva can impact biological, physiological, and medical conditions, with fluctuations serving as indicators of various processes [4]. Further investigation is required to understand the clinical significance of pH disparities fully. Electrochemical pH sensors, particularly metal oxide ones, are employed for monitoring pH changes and are well-suited for wearable applications in chronic diseases due to their unique properties [5].

Potentiometric sensors, an electrochemical sensor, are used to determine the concentration of a specific component in a solution by measuring the potential difference between two electrodes [6]. In this study, a potentiometric biosensor was used to detect bioanalytes in saliva at low concentrations and assess the pH of the solution.

Researchers have developed a wearable device with integrated sensors that can quickly

measure and monitor various levels in the body, including pH, glucose, urea, salinity, and dopamine, allowing for early-stage disease detection. Similarly, an intra-oral pH sensor has been created to diagnose and track common diseases by monitoring salivary pH through an electrochemical method [6]. Electrochemical biosensors, crucial for biomarker analysis, require biocompatible materials like nanoporous gold, graphene, carbon nanotubes, and mesoporous carbon [7]. However, there is currently a lack of easily accessible intra-oral pH sensors, vital for identifying and treating health conditions. This study aims to develop pH sensors using different sensing materials and evaluate their performance in terms of sensing capabilities.

EXPERIMENTAL

The electrodeposition method was used for carbon electrodes coated with polyaniline membranes based on Thu et al. [8]. Firstly, 0.2869g of graphene oxide pellets were dissolved in distilled water to obtain 1mg ml⁻¹ of graphene oxide solution. An electrode was dipped in the graphene oxide solution. The film was then electrochemically reduced for ten cycles using the cyclic voltammetry technique with potentials varying from 0 V to 1.2 V. After electrodeposition, the reduced graphene oxide modified screen-printed electrode was rinsed with distilled water and air-dried using nitrogen. After that, 0.5M sulphuric acid solution was prepared by diluting the concentrated acid with distilled water. The 0.5M sulphuric acid was then mixed with 0.1M aniline. The screen-printed electrode was then dipped into the sulphuric acid and aniline solution. The film was then electrodeposited using a cyclic voltammetry technique with potential varying from -2 V to 9 V. After that, the screen-printed electrode was rinsed with distilled water and air-dried using nitrogen. The rGO-PANI modified screen-printed electrode was prepared.

The PANI-based electrode was fabricated using an electrodeposition method similar to the previous section. A 0.5M sulphuric acid solution was prepared by diluting concentrated acid with distilled water and then mixed with 0.1M aniline. The electrode was dipped into the sulphuric acid and aniline solution, and the film was electrodeposited using cyclic voltammetry with a

potential range of -2 V to 9 V. After rinsing and air-drying, the PANI-modified electrode was prepared.

The evaluation of the rGO-PANI and PANIbased pH sensors involved designing pH solutions ranging from pH 5 to 9 and dropping them onto the electrodes. The potential was obtained using the zero current potentiometry method, and the assessment was repeated for each pH solution. The sensitivity, pH range, and sensor response time were evaluated by plotting the results into a sensor response graph and analyzing the data.

In order to assess the repeatability of the sensors, the zero current potentiometry technique was employed to measure the pH range from 5 to 8. This measurement was performed three times for each pH sensor. The acquired data was then utilized to determine the standard deviation for each pH value. By analyzing the standard deviation, the repeatability of both rGO-PANI and PANI-based pH sensors was determined. To evaluate the stability of the sensors, the zero current potentiometry method was applied to the sensors on three separate occasions over a period of three weeks. The obtained results were subsequently presented in a graphical format to illustrate the stability of the pH sensors throughout the three-week duration.

RESULTS AND DISCUSSION

The rGO-PANI electrode was fabricated by electrodeposition of aniline and sulphuric acid onto the surface of the rGO-modified screenprinted electrode, as shown in Fig.1.

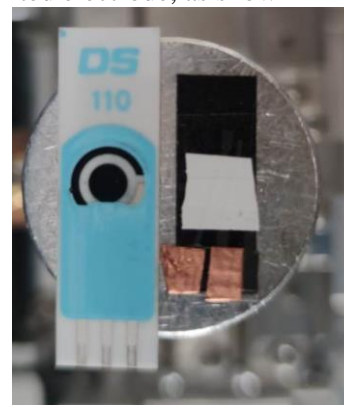


Figure 1. rGO-PANI modified screen-printed and PANI-based fabricated electrodes

The reduction peak of graphene oxide falls considerably in the successive cycles, indicating an irreversible process. The constant increase in

current density during the electro-deposition of polyaniline onto rGO suggests PANI spreading throughout the rGO surface, and the transition between distinct oxidation states of polyaniline can be observed as in Figure 2 (a) and (b).

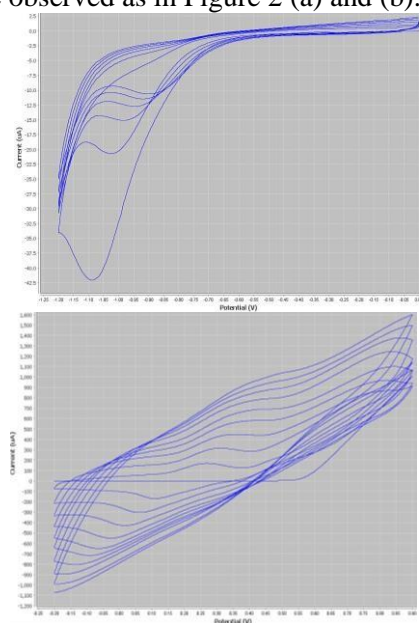


Figure 2. (a) Electro-reduction of graphene oxide coated screenprinted electrode. (b) Electro-deposition of polyaniline onto rGO coated screen-printed electrode.

The PANI electrode was prepared through the electrodeposition of 0.1M aniline and 0.5M sulfuric acid onto the electrode surface. The electrodeposition graph in Figure 3 illustrates the process of polyaniline deposition. The leucoemeraldine form of polyaniline transitions to the emeraldine salt, as indicated by the first anodic wave at +300 mV. The second anodic wave at +750 mV signifies the formation of the completely doped pernigraniline salt. The scan is terminated at 0V to obtain emeraldine.

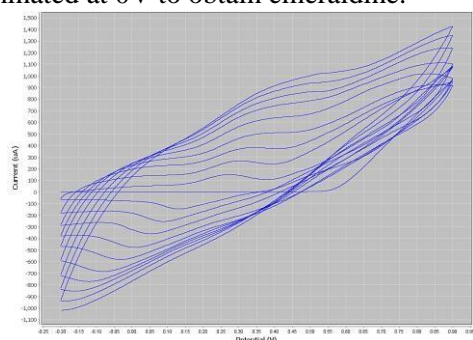


Figure 3. Electro-deposition of polyaniline (PANI) onto electrode.

The sensor response graphs of rGO-PANI and PANI are displayed in Figure 4 and Figure 5, respectively. Based on the sensitivity analysis, rGO-PANI electrode is 78.2 mV/pH, surpassing the ideal Nernstian response value of 59.14 mV/pH. Excluding pH 9.18, the sensitivity obtained is 48.1 mV/pH. The final sensitivity of the rGO-PANI electrode is 48.1 mV/pH for the pH range of pH 5 to pH 8. In addition, the sensitivity of the PANI electrode is 71.4 mV/pH, excluding pH 9.18, the sensitivity obtained is 45 mV/pH. The final sensitivity of the PANI electrode is 45 mV/pH for the pH range of pH 5 to pH 8.

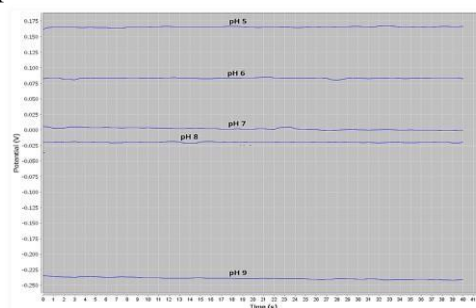


Figure 5. Zero current potentiometry of rGO-PANI

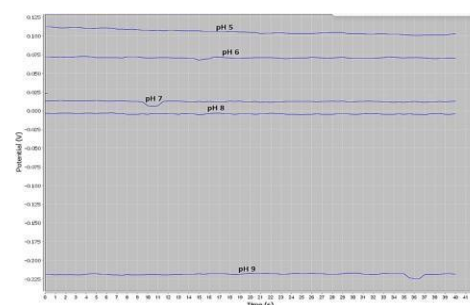


Figure 5. Zero current potentiometry of PANI

The stability of the rGO-PANI electrode was examined weekly for three weeks. The potential exhibited a slight drift at pH 5, pH 6, and pH 7.64, while pH 8 experienced a slightly higher drift potentially due to contamination during storage. The stability of the PANI electrode is characterised with pH 6 showing a higher drift compared to pH 5, pH 7.64, and pH 8 over the three-week period.

An additional evaluation was conducted after testing the electrode for sensitivity. Solutions of pH 7 and pH 8.5 were prepared to compare the sensor response graph of rGO-PANI and PANI electrode. The outcomes of this study were determined based on several factors

including sensitivity, response time, pH range, repeatability, and stability of pH sensors. The use of reduced graphene oxide-polyaniline (rGOPANI) and polyaniline (PANI) in the sensors was compared. The rGO-PANI sensor showed higher sensitivity compared to the PANI-based sensor. Both sensors had a pH range of 5 to 8, which is suitable for intraoral pH sensing. The response time for both sensors was 1 second, indicating rapid detection of analyte concentration changes. The PANI-based sensor had better repeatability compared to the rGO-PANI-based sensor, with lower standard deviation. The rGO-PANI sensor displayed more stable potential readings throughout the testing period. The research focused on the fabrication and characterization of electrodes, specifically rGO-PANI and PANI electrodes for salivary pH sensing. The cyclic voltammetry analysis confirmed the reduction of graphene oxide, and the electro-deposition process showed consistent growth of PANI on the rGO surface. The electrode fabrication results laid the foundation for evaluating pH sensing performance. Previous research has also been conducted on rGO-PANI and PANI electrodes, with a focus on their electrical conductivity [9].

CONCLUSION

In summary, the composite material of reduced graphene oxide-polyaniline exhibits the capability to discern alterations in the concentration of analytes, thereby providing insights into the pH levels of said analytes. Consequently, this pH sensor represents a userfriendly tool that may be effectively employed for the purpose of monitoring the salivary pH within the oral cavity, thereby allowing for the assessment of oral well-being and the detection of diverse metabolic states.

Acknowledgment

This project has received funding from Universiti Malaya Partnership Grant RK0062021, the European Union's Horizon 2020 research and innovation programme under the Marie Skłodowska-Curie grant agreement No. 872370 and 854194, and Universiti Malaya Impact Oriented Interdisciplinary Research Grant IIRG002A-2022HWB.

References

- [1] Schafer, C.A., Schafer, J.J., Yakob, M., Lima, P., Camargo, P. and Wong, D.T. *Saliva diagnostics: utilizing oral fluids to determine health status. Saliva: Secretion and Functions*, **24** (2014) 88-98.
- [2] Yoshizawa, J.M., Schafer, C.A., Schafer, J., Farrell, J.J., Paster, B.J. and Wong, D.T. Salivary biomarkers: toward future clinical and diagnostic utilities. *Clinical microbiology reviews*, **26**(4) (2013) 781-791.
- [3] Melguizo-Rodríguez, L., Costela-Ruiz, V.J., Manzano-Moreno, F.J., Ruiz, C. and Illescas-Montes, R. *Salivary biomarkers and their application in the diagnosis and monitoring of the most common oral pathologies*. *International Journal of Molecular Sciences*, **21**(14) (2020) 5173.
- [4] Baliga, S., Muglikar, S. and Kale, R., Salivary pH: A diagnostic biomarker. *Journal of Indian Society of Periodontology*, **17**(4) (2013) 461.
- [5] Yosipovitch, G., Kaplan, I., Calderon, S., David, M., Chan, Y.H. and Weinberger, A., *Distribution of mucosal pH on the bucca, tongue, lips and palate. A study in healthy volunteers and patients with lichen planus, Behçet's disease and burning mouth syndrome*. *Acta dermato-venereologica*, **81**(3) (2001) 178-180.
- [6] Manjakkal, L., Dervin, S. and Dahiya, R., *Flexible potentiometric pH sensors for wearable systems*. *RSC advances*, **10**(15) (2020) 8594-8617.
- [7] Otero, F. and Magner, E., *Biosensors recent advances and future challenges in electrode materials*. *Sensors*, **20**(12) (2020.) 3561.
- [8] Van Chuc, N., Binh, N.H., Thanh, C.T., Van Tu, N., Le Huy, N., Dzung, N.T., Minh, P.N., Thu, V.T. and Dai Lam, T., *Electrochemical immunosensor for detection of atrazine based on polyaniline/graphene*. *Journal of Materials Science & Technology*, **32**(6) (2016) 539-544.
- [9] J. Khaw, L.F., Koh, W.S., Yeap, S.P., Lim, K., Ahmad, A.L., Toh, P.Y. and Khosravi, *Shape-controlled synthesis of polyaniline and its synergistic effect with reduced graphene oxide for the fabrication of flexible electrode*. *Polymer Engineering & Science*, **63**(7) (2023) 2295-2308.

BIOGRAPHY



Professor Fatimah Ibrahim, a distinguished Professor at the Biomedical Engineering Department of Universiti Malaya. Her received PhD from Universiti Malaya, an MScEE in Medical Systems from the University of Hertfordshire, and a BScEE (Hons) from Marquette, Wisconsin. Her area of expertise are physiological measurement and modeling, Health informatics, BIOMEMS, Biosensors and bioinstrumentation.

CURRENT DRIVEN AND LASER INDUCED GENERATION OF HYDROGEN FROM WATER AND ALCOHOLS

W. Strek, P. Wiewiorski, W. Mista, R. Tomala, M. Stefanski
Institute for Low Temperature and Structure Research,
Polish Academy of Sciences, Wroclaw, Poland

ABSTRACT

The generation of hydrogen from water is conventionally performed by electrolysis methods. Recently we have reported the laser induced (LI) process of hydrogen generation from water and alcohols as solvent and vapor using graphene foam as photocatalyst. In this lecture we present the LI processes occurring by the interaction of focused laser beam by use of graphene aerogel both as electrode and optical target. Interaction of laser beam with a surface of graphene leads to the multiphoton ionization assisted by the broadband white light emission and ejection of hot electrons responsible for dissociation of water and alcohol molecules. Efficiency of the process was significantly enhanced by simultaneous application of lighting and electric field. It occurred with no CO₂ and a limited amount of CH₄ emissions.

BIOGRAPHY



Prof. Dr hab. Wieslaw Strek (1948) is employed at the Institute of Low Temperature and Structure Research of Polish Academy of Sciences in Wroclaw, Poland since 1971.

His research activity includes optical studies of rare earth and transition metal ions in crystal, glasses and nanostructures, laser spectroscopy, optical sensors, laser materials and graphene applications. He has participated in many national and international research projects. Author and co-author of more than 800 scientific publications (13.500 citations, Hirsch index - 57). Member of editorial boards of Journal of Alloys and Compounds, (Elsevier), Rare Earth Journal (Elsevier), Results in Physics (Elsevier), Polish Materials Science, Materials (MDPI). He is a member of European Society of Art, Literature and Science.

He has completed scientific internships in Denmark many times, multiple research stays in Brazil, Belarus, France, Finland, Israel, Germany, China, Japan, Italy, Russia, Vietnam, USA,

He was a member of organizing committees of International Conference of f-elements, International Conference on Luminescence (ICL), Rare Earth Spectroscopy (RES), Excited States of Transition Elements (ESTE), International Conference on Sol-Gel Materials and a supervisor of 15 doctoral thesis. He was co-creator more than 30 patents and patent applications in counterfeiting materials, nanotechnology, sol-gel technology, thermal insulation porous materials, graphene technologies, luminescent materials, lighting, hydrogen generation, cryo-medicine and laser therapy.

ORAL SESSIONS
***APPLICATIONS OF MICRO-
NANOTECHNOLOGY***
(AMN)

UTILISING GRAPHENE NANORIBBONS AS CONDUCTIVE MATERIAL ENABLES FOR THE STABLE AND HIGH-RATE OPERATION OF LiFePO₄ OLEVINE CATHODES IN Li-ION BATTERIES

Trung Thien Nguyen¹, Liem Thanh Pham², Quynh Nhu Nguyen², Man Van Tran²

¹Central Laboratory for Analysis, University of Science, Vietnam National University Ho Chi Minh City.

²Applied Physical Chemistry Laboratory, University of Science, Vietnam National University Ho Chi Minh City

E-mail: ngttrung@hcmus.edu.vn

ABSTRACT

The work employed graphene nanoribbons (GNBs) as a conductive agent in the cathode material LiFePO₄. This utilization aimed to enhance the redox reaction rate and permit a high-rate battery performance. Consequently, the cathodes consisted of 5 wt.% graphene nanoribbons and 10 wt.% conductive carbon nanoparticles demonstrated the highest capacity, measuring 163.25 mAh g⁻¹ at 0.1C and 130.60 mAh g⁻¹ at 2C, while maintaining excellent capacity retention after 100 cycles. Furthermore, it has been observed that graphene nanoribbons exhibit favorable effects on the charge transfer process. However, the presence of a large number of GNBs in the cathode attributed to a decrease in adhesion qualities, necessitating additional refinement in the slurry mixing procedure.

Key words: Li-ion batteries, LiFePO₄ cathode, high-rate performance, graphene nanoribbons, conductive agent.

INTRODUCTION

Rechargeable lithium-ion batteries (LIBs) are widely adopted for energy storage in portable electronics, electric tools, and household appliances due to their high energy density, eco-friendliness, and durability. They have also become the preferred technology for electric vehicles (EVs) because of their exceptional electrochemical performance, portability, and lightweight design [1-6]. In recent times, EV manufacturers have sought cost-effective materials. Lithium iron phosphate (LiFePO₄ – LFP) has gained attention as a promising cathode material [7-9] due to its excellent cycle stability, affordability, thermal and chemical stability, abundance, and environmental friendliness. However, LFP faces challenges including poor electronic conductivity (10⁻⁹ S.cm⁻¹) and limited ionic diffusion (10⁻¹³ – 10⁻¹⁶ cm².s⁻¹), mainly due to strong covalent oxygen linkages (P-O bonds) [8,10]. Researchers have explored solutions, including coating with conductive materials, nano structuring, and foreign ion doping. Notably, using conductive carbon agents is a common technique to improve high-rate performance [11,12]. Graphene, a single layer of carbon atoms arranged in a two-dimensional honeycomb nanostructure, exhibits remarkable

electrical conductivity, chemical tolerance, unique mechanical properties, and a large surface area. These attributes make graphene a promising material for enhancing high-speed electron transport in cathode materials [13-15].

In this research, we utilized graphene nanoribbons, which possess intrinsic qualities including exceptional purity (>99.9%), high crystalline structure, cost-effectiveness, uniform length up to 200 nm [16], and the ability to be customized. These nanoribbons were incorporated as conductive materials with varying compositions to enhance the high-rate capabilities of LFP cathodes. Furthermore, the investigation involved characterizing the morphology and electrochemical characteristics of graphene nanoribbon-modified LFP cathodes to illustrate the superior performance of graphene nanoribbons as a conductive additive.

EXPERIMENTAL

Chemicals: The active cathode material, LFP, was supplied by MTI Corp, USA. IMERYS supplied C-ENERGY™, super C65 carbon black. Solef™ 5130/1001 Polyvinylidene fluoride (PVDF) was purchased from Solvay, and N-methylpyrrolidone (NMP) from Sigma Aldrich, USA. Graphene nanoribbons supplied by

Ntherma Corp, USA were dispersed in NMP from Sigma Aldrich, USA with a ratio of 1:50 (w/w). A solution consists of 1.0 M lithium hexafluorophosphate (LiPF_6 , 151.905 $\text{g}\cdot\text{mol}^{-1}$, Sigma Aldrich, USA) in ethyl carbonate (EC, 99%, Sigma Aldrich, USA), dimethyl carbonate (DMC, 98%, Sigma Aldrich, USA), diethyl carbonate (DEC, 99%, Sigma Aldrich, USA) was used as an electrolyte (Table 1).

Electrode fabrication: The positive electrode contains LFP as the active material, conductive agent, and polyvinylidene fluoride with the corresponding mass fraction of 80:15:5 to be evaluated. Four distinct samples were investigated: G0C15, G5C10, G10C5, and G15C0, where "G" represented the wt.% of graphene nanoribbons and "C" denoted the wt.% of C65 (Table 1). The cathode materials were mixed by the Thinky machine (Japan) to make a homogenous one. Then, the resulting slurry was cast onto an aluminum foil, vacuum-dried, and roll-pressed. Subsequently, the cathodes were stored in an Argon-filled glovebox (with H_2O and O_2 content of less than 0.5 ppm) (Mbraum, Germany). The mass loading of the electrode was controlled around $4 \text{ mg}\cdot\text{cm}^{-2}$.

Table 1. Detailed conductive agents and electrolyte system

Sample code	Conductive materials (wt.%)		Electrolyte system
	Graphene nanoribbons	Conductive carbon (C65)	
G0C15	-	15	1.0 M LiPF_6 in EC: DMC: DEC (1:1:1 – v/v)
G5C10	5	10	
G10C5	10	5	
G15C0	15	-	

Material and electrochemical measurements: All electrode morphology was evaluated by Scanning electron microscopy (SEM, S-4800, Hitachi, Japan) from R&D center, Saigon high tech park, Ho Chi Minh City, Vietnam. The 2032-type coin cell was assembled in an Ar-filled glovebox with lithium metal as the counter and reference electrode, and the electrolyte system mentioned previously.

The half-cells were cycled at a constant current density of 0.5C in charge state and at a constant current density of 2C in discharge state ($1\text{C} = 150 \text{ mA}\cdot\text{g}^{-1}$) for 100 cycles, in which they were performed at 0.1, 0.2, 0.5, and 1C formation cycles, repeated one time each step. The rate capability was tested at 0.1, 0.2, 0.5, 1, and 2C in the discharge rate, repeated three times each step

at a constant current density of 0.5C in the charge rate. Additionally, the cells were tested at 30 °C with a voltage range of 2.5 – 4.0 V versus Li^+/Li using a battery testing system (Lanhe, CT2001A, China). The electrochemical impedance spectroscopy (EIS) was carried out by VSP3 (Biologic, France) apparatus using a signal amplitude of 8.0 mV and a frequency from 1 MHz down to 10 mHz.

RESULTS AND DISCUSSION

In Figure 1, electrodes with graphene nanoribbons are visibly more porous than the baseline sample (G0C15), which has densely packed LFP particles. The increased graphene nanoribbon content enhances surface porosity, potentially weakening adhesion to the current collector and causing electrode peeling during extended cycling tests. Consequently, replacing conductive carbon nanoparticles with graphene nanoribbons reduces electrode adhesion and mechanical stability.

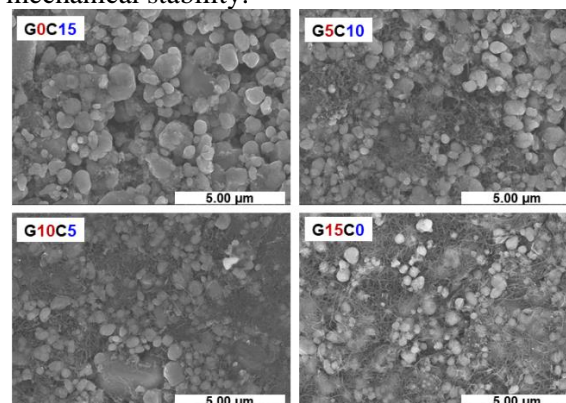


Figure 1. SEM of all samples

In Figure 2a, different ratios of graphene added to LFP cathode materials for rate capability were investigated. Among them, G5C10, G10C5, and G15C0 showed significantly higher discharge capacities at 0.1C: 163.25, 164.89, and 157.27 $\text{mAh}\cdot\text{g}^{-1}$ compared to the baseline (G0C15) with 146.77 $\text{mAh}\cdot\text{g}^{-1}$. At 2C, these samples also demonstrated superior capacitance, around 30% higher than G0C15 (130.60, 135.64, and 124.45 compared to 101.61 $\text{mAh}\cdot\text{g}^{-1}$, respectively). However, when returning to 0.1C, the graphene-based cathodes did not fully retain their initial capacity, unlike G0C15, which reached nearly 100%. In brief, G10C5 performed the best due to its optimal graphene content, improving electrochemical properties without affecting the electrode's mechanical integrity.

The long-term cycling stability of all samples under a high current density of 2C were shown in

Figure 2b. Notably, as we increased the quantity of graphene nanoribbons in the cathodes, a pattern emerged: higher graphene content corresponded to lower capacity retention. Specifically, the initial capacities for the G0C15, G5C10, G10C5, and G15C0 cathodes were recorded as 106.45, 130.60, 135.64, and 130.21 mAh.g⁻¹, respectively. Remarkably, it was observed that the G15C0 cell could operate efficiently for approximately 30 cycles before experiencing a rapid capacity decline. In contrast, G5C10 performed well at the 100th cycle, retaining a high capacity of 128.26 mAh.g⁻¹ with a retention rate of 98.21%. Conversely, the pristine G0C15 sample exhibited 77.42 mAh.g⁻¹ with a retention rate of 72.7%. The outstanding cycling performance of G5C10 is attributed to graphene nanoribbons acting as effective connectors that facilitate electron transport between LFP particles. Moreover, C65, as a stabilizer, supports addressing structural irregularities within the LFP, promoting efficient electron flow through the electrode. Consequently, all samples, including those with graphene nanoribbons, significantly enhance cycling stability while boosting initial discharge capacity.

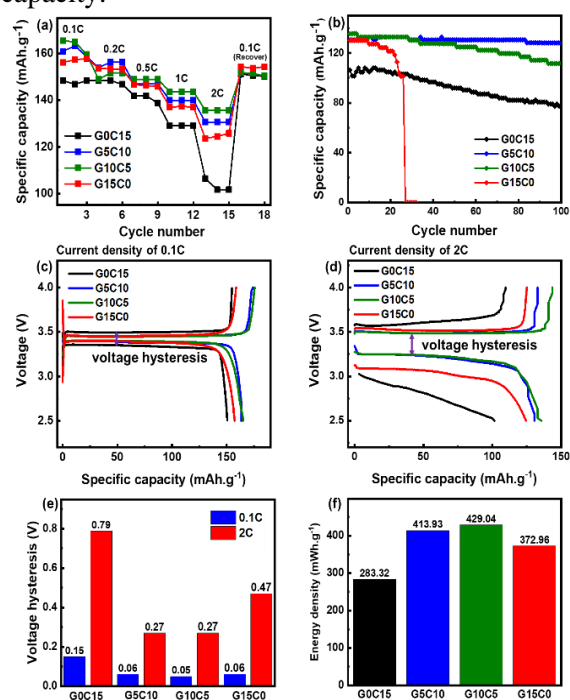


Figure 2. (a) Rate capability performance, (b) Cycling performance at current density of 2C, Voltage profile at current density of (c) 0.1 C and (d) 2C, (e) Voltage hysteresis at current density of 0.1C and 2C, (f) Energy density at current density of 2C.

Figure 2c illustrates the characteristic voltage plateaus, around 3.5 V (versus Li⁺/Li), resulting from the Fe³⁺/Fe²⁺ redox reaction and lithiation/delithiation at a 0.1C current density in the electrodes. At this current density, the charge-discharge profiles of all cathodes were identical. However, both the G5C10 and G10C5 cathodes exhibited an initial discharge capacity approximately 10% higher than that of the G0C15 cathodes. Furthermore, at a higher current density of 2C (**Figure 2d**), the G5C10 and G10C5 samples demonstrated superior initial discharge capacity. In contrast, the baseline sample exhibited a sharp decline in discharge rate at 2C, resulting in the poorest capacity and the highest voltage hysteresis (**Figure 2e**).

Regarding the polarization, determined by the voltage difference between charge and discharge plateaus, generally increases with higher current densities (**Figure 2e**). In contrast, the G5C10 and G10C5 samples displayed the lowest voltage hysteresis at 2C, measuring 0.27 V, while the cathodes G0C15 and G15C0 recorded values of 0.79 V and 0.47 V, respectively. Consequently, the G5C10 and G10C5 samples demonstrated superior performance at both low and high current rates. Furthermore, these samples exhibited the highest energy density (**Figure 2f**), with values of 413.93 and 429.04 mWh.g⁻¹, representing a remarkable 46.1% and 51.4% increase compared to the G15C0 sample, which recorded 283.31 mWh.g⁻¹. Intriguingly, despite the G15C0 sample containing a full load of graphene nanoribbons, its energy density was only 372.96 mWh.g⁻¹.

CONCLUSION

In summary, the right amount of graphene nanoribbons greatly boosts the high-rate performance of LFP cathodes. However, excessive graphene nanoribbons can weaken the adhesion to aluminum foil. The cathode with 5 wt.% graphene nanoribbons and 10 wt.% conductive carbon nanoparticles showed the highest capacity, reaching 163.25 mAh.g⁻¹ at 0.1 C and 130.60 mAh.g⁻¹ at 2C. Moreover, G5C10 electrodes had excellent cycling performance, retaining 98.21% capacity after 100 cycles at a 2C current density. This improvement is attributed to the effective electron conductivity of the network formed by graphene nanoribbons and carbon nanoparticles. While C65 fills electrode imperfections, graphene nanoribbons act as bridges, enhancing electron transport. In

conclusion, graphene nanoribbons hold promise as cathode additives in high-power LIB applications.

Acknowledgement

This research was funded by Vingroup and supported by VINIF (project code VINIF.2020.NCUD.DA039). We appreciate the technical and material support from Ntherma Corporation (USA) and the R&D center at Saigon High Tech Park.

References

- [1] Broussely, Michel, and Gianfranco Pistoia, *Industrial applications of batteries: from cars to aerospace and energy storage*, (2007).
- [2] Scrosati, Bruno, Josef Hassoun, and Yang-Kook Sun. *Lithium-ion batteries. A look into the future*. Energy & Environmental Science. **4**(9) (2011) 3287-3295.
- [3] Scrosati, Bruno. *History of lithium batteries*. Journal of solid-state electrochemistry. **15**(7) (2011) 1623-1630.
- [4] Ding, Yuanli, Zachary P. Cano, Aiping Yu, Jun Lu, and Zhongwei Chen. *Automotive Li-ion batteries: current status and future perspectives*. Electrochemical Energy Reviews. **2**(1) (2019) 1-28.
- [5] Liang, Yeru, Chen-Zi Zhao, Hong Yuan, Yuan Chen, Weicai Zhang, Jia-Qi Huang, Dingshan Yu et al. *A review of rechargeable batteries for portable electronic devices*. InfoMat. **1**(1) (2019) 6-32.
- [6] Masias, Alvaro, James Marcicki, and William A. Paxton. *Opportunities and challenges of lithium-ion batteries in automotive applications*. ACS energy letters. **6**(2) (2021) 621-630.
- [7] Yuan, Li-Xia, Zhao-Hui Wang, Wu-Xing Zhang, Xian-Luo Hu, Ji-Tao Chen, Yun-Hui Huang, and John B. Goodenough. *Development and challenges of LiFePO₄ cathode material for lithium-ion batteries*. Energy & Environmental Science. **4**(2) (2011) 269-284.
- [8] Zhang, Wei-Jun. *Structure and performance of LiFePO₄ cathode materials: A review*. Journal of Power Sources. **196**(6) (2011) 2962-2970.
- [9] Fergus, Jeffrey W. *Recent developments in cathode materials for lithium-ion batteries*. Journal of power sources. **195**(4) 2010 939-954.
- [10] Padhi, Akshaya K., Kirakodu S. Nanjundaswamy, and John B. Goodenough. *Phospho-olivines as positive-electrode materials for rechargeable lithium batteries*. Journal of the electrochemical society **144**(4) (1997) 1188.
- [11] Miranda, D.; Gören, A.; Costa, C.M.; Silva, M.M.; Almeida, A.M.; Lanceros-Méndez, S. *Theoretical simulation of the optimal relation between active material, binder and conductive additive for lithium-ion battery cathodes*. Energy. **172** (2019) 68–78.
- [12] Le Thanh Nguyen Huynh, Thi Thuy Dung Tran, Hoang Hai Au Nguyen, Thi Thu Trang Nguyen, Van Man Tran, Akhil Grag, and My Loan Phung Le. *Carbon-coated LiFePO₄-carbon nanotube electrodes for high-rate Li-ion battery*. Journal of Solid-State Electrochemistry. **22**(7) (2018) 2247-2254.
- [13] Brownson, Dale AC, Dimitrios K. Kampouris, and Craig E. Banks. *An overview of graphene in energy production and storage applications*. Journal of Power Sources. **196** (2011) 4873-4885.
- [14] Ni, Wei, and Lingying Shi. *Layer-structured carbonaceous materials for advanced Li-ion and Na-ion batteries: Beyond graphene*. Journal of Vacuum Science & Technology A: Vacuum, Surfaces, and Films. **4** (2019).
- [15] Zhang, Huang, Dong Liu, Xiuzhen Qian, Chongjun Zhao, and Yunlong Xu. *A novel nano structured LiFePO₄/C composite as cathode for Li-ion batteries*. Journal of Power Sources. **249** (2014) 431-434.
- [16] Ntherma Corporation. *Graphene*. October, (2023).
- [17] Guan, Yibiao, Jinran Shen, Xufang Wei, Qizhen Zhu, Xiaohui Zheng, Shuqin Zhou, and Bin Xu. *High-rate performance of a three-dimensional LiFePO₄/graphene composite as cathode material for Li-ion batteries*. Applied Surface Science. **481** (2019) 1459-1465.

DEVELOPMENT OF POLYETHERSULFONE MEMBRANES INCORPORATED WITH TiO₂ AND CU NANOPARTICLES

Huong Thi Giang Duong¹, Hieu Trung Nguyen² and Ha Manh Bui¹

¹ Faculty of Environment, Saigon University, 273 An Duong Vuong Street, Ward 3, District 5, Ho Chi Minh City, Vietnam;

² Institute of Applied Technology, Thu Dau Mot University, 06 Tran Van On Street, Phu Hoa Ward, Thu Dau Mot City, Binh Duong Province, Vietnam;
Email: huongduong@sgu.edu.vn

ABSTRACT

This study chemically reduced Cu²⁺ ions using ascorbic acid to form Cu NPs that were then precipitated onto TiO₂ through the sol-gel method at various molar ratios. Characterization techniques such as FTIR, SEM, TEM-EDS, UV-Vis DRS, XRD, XPS, and ESR were used to show that the synthesized Cu-TiO₂ photocatalysts had reduced bandgap, particle sizes between 50 nm and 150 nm, and generated reactive free radicals under light irradiation. The 25% Cu-TiO₂ photocatalyst exhibited the highest catalytic efficiencies for the degradation of dye with and without H₂O₂, achieving 68% and 92%, respectively. Photocatalytic membranes made with this catalyst demonstrated a degradation efficiency of 86% and remained stable after five continuous cycles. The photocatalytic degradation of foulants enabled the sodium alginate-fouled photocatalytic membranes to recover their water permeability. While the modified membranes had slightly lower pure water flux than pristine PES membranes, their water permeability was still high and acceptable. These results suggest that Cu-TiO₂/PAA/PES photocatalytic membranes have potential for use in mitigating membrane fouling in practical applications.

Keywords: Antifouling photocatalytic membranes, Cu@TiO₂ composite photocatalyst, Dip-coating modified membranes, PES filtration membranes.

INTRODUCTION

Membrane filtration has a long history in water and wastewater treatment [1] and it's a crucial component in the water treatment process due to its economic and environmental benefits [2]. However, membrane fouling is a persistent issue during prolonged operation, requiring frequent cleaning or even replacement of fouled membranes [3]. Common strategies to mitigate fouling, such as changing membrane operation modes or implementing pretreatment methods, are often inefficient and costly [4]. An alternative approach gaining traction is modifying membrane surfaces to enhance their hydrophilicity. This study introduces covalent chemical bonding between polyacrylic acid (PAA) and the PES membrane using oxygen plasma, marking a unique approach in the development of photocatalytic antifouling Cu@TiO₂/PAA/PES membranes.

EXPERIMENTAL

Cu@TiO₂/PES membrane fabrication

The fabrication process for Cu@TiO₂/PES comprises three key stages, as illustrated in Figure 1:

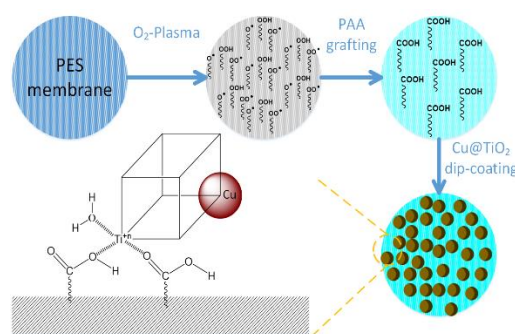


Figure 1. Schematic illustrating the fabrication process of Cu@TiO₂/PES membrane

Membrane Permeability and Antifouling

The water permeabilities of both pristine PES membranes and the modified membranes were assessed using a vacuum filtration system with a membrane active area of 9.08 cm². This vacuum filtration setup featured a pressure gauge and allowed precise control over the vacuum pump's

speed. The fouled membrane represents as The Flux Recovery Ratio (FRR).

RESULTS AND DISCUSSION

Fourier transform infrared spectroscopy (FTIR) and EDS

The functional groups and specific bonds present in the Cu@TiO₂ photocatalysts were examined through FTIR spectroscopy, as depicted in Figure 2. Since this photocatalyst exhibits hydrophilic properties, water vapor adsorption on its surface is an inevitable occurrence. Notably, the characteristic wave number at 3440 cm⁻¹ corresponds to the stretching vibration of the -OH functional group, with the wave numbers at 1635 cm⁻¹ and 1380 cm⁻¹ signifying the distinct bending vibrations of this hydroxyl functional group [5]. The presence of these Cu nanoparticles is more explicitly demonstrated through EDS analysis, as depicted in Figure 4d. This analysis reveals the presence of elements such as oxygen, titanium and copper within the composite photocatalyst. It is worth noting that the signal intensity of the Cu element is relatively low, reflecting its minimal incorporation into the TiO₂ photocatalyst.

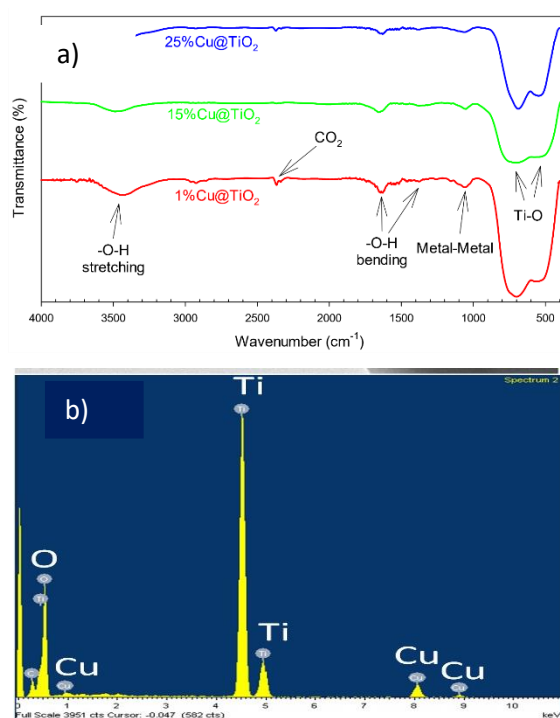


Figure 2. FTIR and EDS spectra of Cu@TiO₂ composite photocatalysts

Membrane's permeability and antifouling activity

One of the pivotal parameters for membranes employed in wastewater filtration is their water permeability. Consequently, it is imperative to assess the impact of the modification process on the water permeability of the photocatalytic membrane. The PES membrane used in this study inherently exhibits hydrophilic characteristics, boasting a Water Contact Angle (WCA) of 0°, which resulted in a notably high water permeability of approximately 2013 L·m⁻²·h⁻¹. Furthermore, the pure water flux of the pristine PES membrane remained remarkably stable over a 300-minute period of water filtration.

However, the incorporation of a photocatalytic coating and an intermediate PAA layer on the membrane surface did exert an influence on the pure water flux of the photocatalytic membrane, diminishing it in comparison to the pristine PES membrane (1868 L·m⁻²·h⁻¹). Nevertheless, when juxtaposed with other hydrophobic membranes sharing similar parameters, such as PVDF, PTFE, or PSf, the water permeability of this photocatalytic membrane remains quite high and within acceptable bounds. More precisely, after 300 minutes of water filtration, the permeability of the photocatalytic membrane experienced only a marginal reduction of about 10% in comparison to the pristine PES membrane, and it also exhibited relative stability.

Figure 3 highlights that when the photocatalytic membrane was fouled by sodium alginate, the water permeability of the fouled membrane witnessed a substantial decline to approximately 220 L·m⁻²·h⁻¹, marking a reduction of roughly 90% when contrasted with the original membrane. However, after undergoing photocatalysis treatment, the water permeability of the fouled photocatalytic membrane rebounded to the level of 1832 L·m⁻²·h⁻¹. Consequently, the Flux Recovery Ratio (FRR) of the photocatalytic membrane, in this scenario, stood at approximately 98%. This robustly demonstrates that the modified membrane in this study exhibits a notable antifouling capability under the specified experimental conditions.

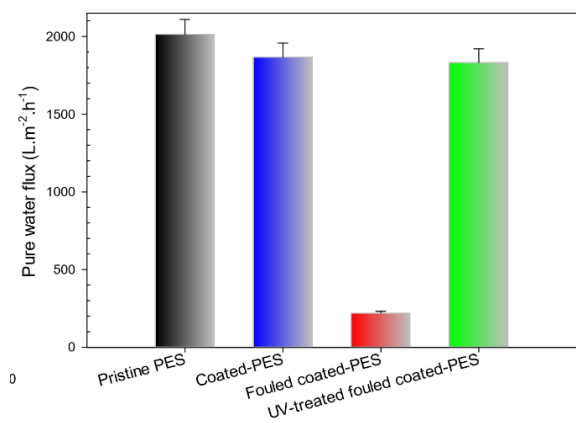


Figure 3. The antifouling performance of photocatalytic membrane

Conclusion

Through a suite of characterizations encompassing FTIR and EDS, the successful synthesis of the composite photocatalyst was convincingly demonstrated. The resultant photocatalyst exhibits a reduced bandgap of 3.32 eV and boasts a small, uniform particle size ranging from 50 to 150 nm, which effectively triggers the generation of reactive free radicals under light irradiation. The powder photocatalyst yielded the highest catalytic efficiency at 73%, corresponding to a molar ratio of 25% Cu@TiO₂. Notably, the Flux Recovery Ratio (FRR) of the coated photocatalytic membrane after undergoing photocatalytic treatment was remarkably high, reaching approximately 98%. It's important to note that, despite the higher surface roughness of coated photocatalytic membranes when compared to pristine PES membranes, the antifouling ability may not be significantly compromised due to the high photocatalytic activity of the modified membranes. This study underscores the potential of the Cu@TiO₂/PAA/PES photocatalytic membrane for further research and practical application in wastewater treatment.

References

- [1] J. Sójka-Ledakowicz, T. K., Wademar Machnowski and H. H. Knudsen. *Membrane filtration of textile dyehouse wastewater for technological water reuse*. *Desalination* **119** (1998) 1-9.
- [2] K., Mohammadreza, D. P. Suhas, M. E., Capela and T. M. Aminabhavi. *Sustainability considerations in membrane-based technologies for*

- industrial effluents treatment*. *Chemical Engineering Journal* **368** (2019) 474-494.
- [3] S., Xiafu, G., Nicholas, P. Hankins and V. Gitis. *Fouling and cleaning of ultrafiltration membranes: A review*. *Journal of Water Process Engineering* **1** (2014) 121-138.
- [4] L., Pierre, V. Chen and T. A. Fane. *Fouling in membrane bioreactors used in wastewater treatment*. *Journal of membrane science* **284** (2006) 17-53.
- [5] S., Érika Nascimbén, Z. L., Cecilia, and G., Veréb. *Photocatalytic membrane filtration and its advantages over conventional approaches in the treatment of oily wastewater: a review*. *methods* **13** (2020) 14-22.

DETECTION AND QUANTIFICATION OF BOVINE SERUM ALBUMIN USING SCREEN-PRINTED GOLD ELECTRODES AND ELECTROCHEMICAL MEASUREMENTS

Chi Tran Nhu¹, **Linh Huynh Thi Thuy**², **Viet Nguyen Canh**³, **Loc Do Quang**³, **Chieu Le Van**⁴, **Trung Vu Ngoc**⁵, **Chun-Ping Jen**⁶, **Trinh Chu Duc**¹ and **Tung Bui Thanh**^{1*}

¹ Faculty of Electronics and Telecommunications, University of Engineering and Technology, Vietnam National University, Hanoi, Vietnam;

² Faculty of Engineering and Technology, Hue University, Hue, Vietnam;

³ Faculty of Physics, VNU University of Science, Hanoi, Vietnam;

⁴ Faculty of Environmental Science, VNU University of Science, Hanoi, Vietnam;

⁵ Hanoi University of Public Health, Hanoi, Vietnam;

⁶ Department of Mechanical Engineering and Advanced Institute of Manufacturing for High-Tech Innovations, National Chung Cheng University, Chia-Yi, Taiwan, ROC.

*Email: tungbt@vnu.edu.vn

ABSTRACT

In this study, a gold surface-modified process has been proposed and developed to immobilize anti-bovine serum albumin (anti-BSA) and detect bovine serum albumin (BSA) through specific bonds between antigen and antibody. Experiments were performed on the screen-printed gold electrode surface, an electrochemical electrode with a three-electrode configuration, including working, counter, and reference electrodes. Both fluorescence and electrochemical measurements were used to detect and quantify BSA protein concentrations. The results demonstrate that BSA-fluorescein isothiocyanate conjugate was kept on the gold electrode surface through the fluorescent signal observed under the microscope and the change of cyclic voltammetry (CV) signal after each surface modification process step. In contrast, the control electrode was implemented without the step of self-assembled monolayer incubation, the fluorescent signal did not appear on the electrode surface, and CV signals were almost unchanged after each step. Furthermore, different BSA concentrations ranging from 0.1 µg/ml to 5 µg/ml were also investigated using the CV measurement. The results demonstrated the proposed immunosensor's performance for BSA detection and laid a good foundation for protein detection and biosensor development research.

Keywords: Protein detection, bovine serum albumin, screen-printed gold electrode, cyclic voltammetry

INTRODUCTION

Immunosensor is a type of biosensor widely used in many fields, such as biomedical diagnosis, food safety, and environmental monitoring [1,2]. Immunosensors are used to detect an antigen through its specific binding to antibodies immobilized on the sensor's surface [3]. The immunosensor demonstrates numerous advantages, including good stability and sensitivity, low cost, fewer reagents and samples, and simple operation [4,5]. Through the specific recognition between antigen and antibody, the immunosensor can detect bacteria, viruses, protein biomarkers, and nucleic acids [6].

Bovine Serum Albumin (BSA) is a popular protein derived from bovine blood plasma. BSA has a similar structure to human serum albumin (HAS), so it has been widely used as a model

protein in different fields [7]. Besides, BSA is an essential protein in cow-derived products, including milk and meat. Therefore, the detection and quantification of BSA concentration is important to evaluate cow health and the quality of products from cows [8]. Various methods were used to detect and quantify BSA concentrations. Nonetheless, there is a critical need for the development of new, rapid, and straightforward methods for BSA detection.

In this study, an immunosensor was developed to detect and quantify BSA protein using electrochemical measurements. The immunosensor was constructed by functionalizing the surface of a gold electrode on a screen-printed electrode to immobilize anti-albumin antibody. The results were verified by both the fluorescence and electrical

measurements. In addition, the relationship between BSA concentration and the electrical signal was also determined.

EXPERIMENTAL

The screen-printed gold electrode surface functionality process was divided into five main steps, as shown in Figure 1. 11-Mercaptoundecanoic acid (11-MUA), N-(3-Dimethylaminopropyl)-N'-ethyl carbodiimide hydrochloride (EDC) and N-Hydroxysuccinimide (NHS) were purchased from Sigma-Aldrich Chemical Co (St. Louis, Missouri, USA). Bovine serum albumin-fluorescein isothiocyanate conjugate (BSA-FITC) and anti-albumin antibody (anti-BSA) were used as an antigen-antibody pair, purchased from Sigma-Aldrich Chemical. Experiments were performed on the screen-printed gold electrodes purchased from Biodevice Technology, Ltd (Japan). An inverted microscope system (CKX41, Olympus, Melville, NY, USA) and a wireless potentiostat device (ECWP100plus, Zensor R&D, Taichung City, Taiwan) were utilized to detect and quantify the protein concentration.

The screen-printed gold electrode included working, counter, and reference of gold material, carbon, and Ag/AgCl, respectively. At first, the electrode was immersed in 5 mM 11-MUA solution for 24 hours at room temperature to form a self-assembled monolayer on the gold electrode surface, as shown in the first step in Figure 1. Then, the solution mixture of 0.4 M EDC and 0.2 M NHS was dripped onto the working electrode surface to activate the carboxyl group of 11-MUA and form NHS ester groups. The activation process took 30 minutes in a chamber with high

humidity. In the third step, the working electrode was incubated in 5 μ M anti-BSA solution for 2 hours at 4°C. During the incubation of anti-BSA, the ester groups covalently coupled with the amine group of anti-BSA to form stable amide bonds. In order to prevent the nonspecific bonds between antigens and residual ester groups, 1 μ M biotin solution was used to block the electrode surface. Finally, 5 μ l of BSA-FITC 5 μ M protein solution was dripped onto the gold electrode surface to specifically bind to anti-BSA. The incubation process of BSA-FITC was carried out for 2 hours at 4°C and under low light conditions. After each step in the process, the electrode was gently washed with PBS 1X solution to remove unbound biomolecules.

RESULTS AND DISCUSSION

After functionalization, the electrode was examined under a microscope and immersed in a 5 mM potassium ferro/ferricyanide solution for cyclic voltammetry (CV) measurements. The CV measurement parameters were configured with a starting voltage of 600 mV, an ending voltage of -200 mV, and a scan rate of 50 mV/s. The results indicate the appearance of fluorescent green BSA-FITC signal on the working electrode, and significant changes in the cyclic voltammetry (CV) signal were observed after each step of the process, as illustrated in Figure 2.

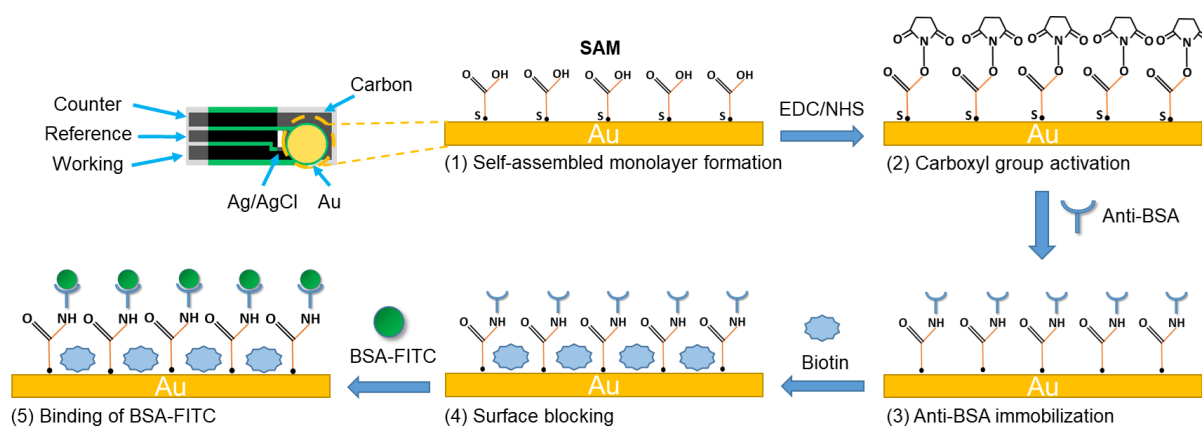


Figure 1. The screen-printed gold electrode surface functionality process for immobilizing anti-BSA and detection BSA.

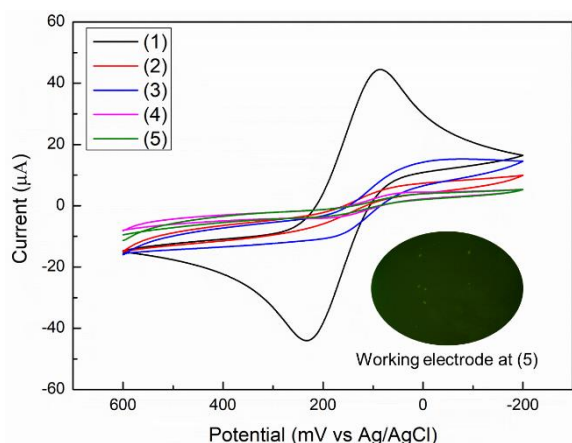


Figure 2. The change of CV signal after each step of gold electrode surface functionalization process; (1) Bare (Au); (2) 11-MUA/Au; (3) EDC/NHS/11-MUA/Au; (4) Anti-BSA/EDC/NHS/11-MUA/Au; (5) BSA/Anti-BSA/EDC/NHS/11-MUA/Au

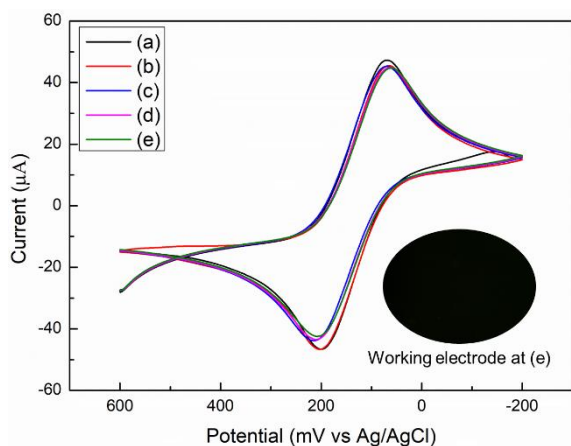
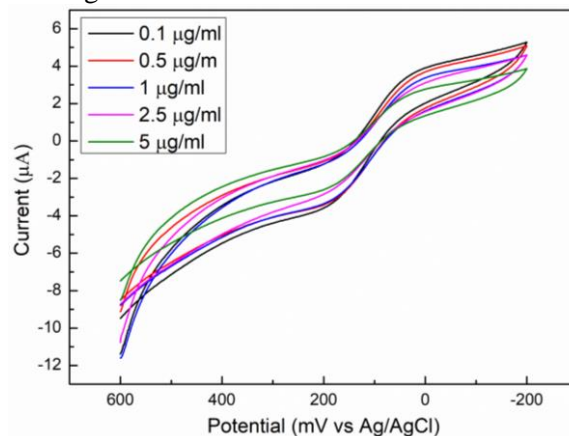


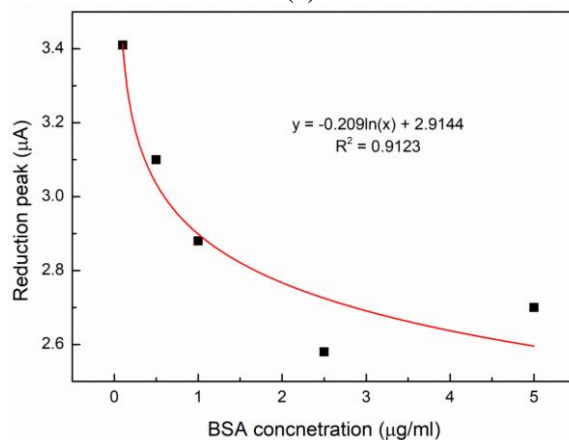
Figure 3. The change of CV signal on the control electrode skipped the step of 11-MUA incubation; (a) Bare (Au); (b) EDC/NHS/Au; (c) Anti-BSA/EDC/NHS/Au; (d) Biotin/Anti-BSA/EDC/NHS/Au; (e) BSA/Biotin/Anti-BSA/EDC/NHS/Au.

Specifically, the amplitude of the reduction peak decreased strongly from 50.4 μA to 6.89 μA after the step of 11-MUA incubation. This result shows that a self-assembled monolayer was formed on the electrode surface, prohibiting the generation of electrons to reduce Fe^{3+} to Fe^{2+} . Subsequently, the amplitude of the reduction peak further decreased to 3.17 μA , confirming the presence of BSA-FITC protein on the electrode surface. As a consequence, both fluorescence and CV measurements demonstrated the success of the proposed process. BSA proteins are specifically bound to anti-BSA and kept on the gold electrode surface.

By contrast, BSA-FITC proteins were not kept on the control electrode surface and skipped the step of 11-MUA incubation. Only a dark color was observed on the working electrode, and CV signals were almost unchanged after each process step, as shown in Figure 3. The absence of signal change indicates that no layer was formed on the gold electrode surface. These results follow the theoretical predictions that a self-assembled monolayer was not formed, resulting in the absence of active carboxyl groups capable of binding with Anti-BSA.



(a)



(b)

Figure 4. (a) The change of CV signals at the different BSA concentrations; (b) The relationship between the amplitude of reduction peak and BSA concentration.

Five different BSA protein concentrations were investigated to determine the relationship between the BSA concentration and the amplitude of the reduction peak. The experimental results show that the amplitude of the reduction peak decreased gradually when the BSA concentration increased, as shown in Figure 4 (a). The amplitude of the reduction peak decreased from 3.41 μA to 2.7 μA as the BSA concentration increased from 0.1 $\mu\text{g/ml}$ to 5

µg/ml. The result can be explained that higher protein concentrations lead to the formation of a thicker protein layer, which hinders the exchange of electrons between the electrode and the redox solution. This results in a decrease in the redox current.

The formula expressed the relationship between the amplitude of the reduction peak and BSA concentration: $reduction\ peak = -0.209\ln[BSA] + 2.9144$ ($R^2 = 0.9123$), as shown in Figure 4 (b). As can be seen, the BSA concentration can be quantified based on the amplitude value of the reduction peak from CV signals.

CONCLUSION

The paper proposed an immunosensor to detect and quantify BSA concentration by electrochemical measurements. The sensor was developed by functionalizing the screen-printed gold electrode surface. The functionalization process included five main steps to attach anti-BSA on the gold electrode and specifically bind to BSA. The experimental results confirm that BSA-FITC proteins have been successfully immobilized on the gold electrode surface, as indicated by fluorescence and cyclic voltammetry (CV) measurements. Furthermore, the control electrode results further confirmed the proposed process's success. The results also show the relationship between the BSA concentration and CV signals. The BSA concentration was inversely proportional to the reduction peak of the CV signal according to the formula $reduction\ peak = -0.209\ln[BSA] + 2.9144$ ($R^2 = 0.9123$). In the future, the research can be expanded to recognize and distinguish many different types of proteins in the sample solution.

Acknowledgment

This work was funded by the Vietnam Ministry of Science and Technology under Grant NĐT.101.TW/21. Chi Tran Nhu was funded by the Master, PhD Scholarship Programme of Vingroup Innovation Foundation (VINIF), code VINIF.2022.TS015.

References

[1] Y. Zha, S. Lu, P. Hu, H. Ren, Z. Liu, W. Gao, C. Zhao, Y. Li, Y. Zhou, *Dual-Modal Immunosensor with Functionalized Gold Nanoparticles for Ultrasensitive Detection of Chloroacetamide Herbicides*, ACS Applied

Materials and Interfaces. **13** (2021) 6091–6098.

- [2] J. Huang, F. Wei, Y. Cui, L. Hou, T. Lin, *Fluorescence immunosensor based on functional nanomaterials and its application in tumor biomarker detection*, RSC Advances. **12** (2022) 31369.
- [3] E. Gizeli, C.R. Lowe, *Immunosensors*, Current Opinion in Biotechnology. **7** (1996) 66–71.
- [4] L. Fang, X. Liao, B. Jia, L. Shi, L. Kang, L. Zhou, W. Kong, *Recent progress in immunosensors for pesticides*, Biosensors and Bioelectronics. **164** (2020) 112255.
- [5] S. Gao, J.M. Guisán, J. Rocha-Martin, *Oriented immobilization of antibodies onto sensing platforms - A critical review*, Analytica Chimica Acta. **1189** (2022) 338907.
- [6] B. Gil Rosa, O.E. Akingbade, X. Guo, L. Gonzalez-Macia, M.A. Crone, L.P. Cameron, P. Freemont, K.L. Choy, F. Güder, E. Yeatman, D.J. Sharp, B. Li, *Multiplexed immunosensors for point-of-care diagnostic applications*, Biosensors and Bioelectronics. **203** (2022) 114050.
- [7] L. Roufegarinejad, R. Amarowicz, A. Jahanban-Esfahlan, *Characterizing the interaction between pyrogallol and human serum albumin by spectroscopic and molecular docking methods*, Journal of Biomolecular Structure & Dynamics. **37** (2019) 2766–2775.
- [8] A. Jahanban-Esfahlan, A. Ostadrahimi, R. Jahanban-Esfahlan, L. Roufegarinejad, M. Tabibiazar, R. Amarowicz, *Recent developments in the detection of bovine serum albumin*, International Journal of Biological Macromolecules. **138** (2019) 602–617.

A NOVEL SURFACE FUNCTIONALIZATION PROCESS FOR CARBON ELECTRODES BASED ON THE COMBINATION OF CONDUCTING POLYMER AND GOLD NANOPARTICLES FOR PROTEIN DETECTION

**Chi Tran Nhu¹, Loc Do Quang², Phu Nguyen Dang¹, Huu Nguyen Cong³, Thuy Nguyen Tran³
Trinh Chu Duc¹ and Tung Bui Thanh^{1*}**

¹ Faculty of Electronics and Telecommunications, University of Engineering and Technology, Vietnam National University, Hanoi, Vietnam;

² Faculty of Physics, VNU University of Science, Hanoi, Vietnam;

³ Cardiovascular Centre, E Hospital, Hanoi, Vietnam.

*Email: tungbt@vnu.edu.vn

ABSTRACT

In this work, a screen-printed carbon electrode surface functionalization process was proposed to immobilize antibodies or antigens on the electrode. The highlight of the proposed process is the combination of conducting polymer and gold nanoparticles to enhance the electrical signal of the immunosensor. The process was divided into five main steps, including the formation of a conducting polymer layer on the carbon electrode using aniline, gold nanoparticle coating, and the formation of a self-assembled monolayer using 11-Mercaptoundecanoic acid, the carboxyl group activation, and protein immobilization. In the experiments, bovine serum albumin–fluorescein isothiocyanate conjugate (BSA-FITC) was utilized to evaluate the performance of the proposed process. After being coated with gold nanoparticles, the electrode surface morphology was evaluated through the scanning electron microscope (SEM) technique. Besides, fluorescence and cyclic voltammetry (CV) measurements were also used to recognize the presence of BSA-FITC on the electrode surface. The results show that a nanocomposite layer of polyaniline (PANI) and gold nanoparticles has been successfully formed on the electrode surface. The gold nanoparticles were evenly distributed on the carbon electrode surface thanks to the PANI membrane. CV signal of the modified electrode was significantly higher than that on bare carbon and gold particle-coated electrodes. The fluorescence signal on the modified electrode surface under the microscope demonstrates the immobilization of BSA-FITC on the electrode. In contrast, the BSA-FITC protein was not kept on the control electrode, which was implemented without the step of gold nanoparticle coating. Furthermore, the change of CV signal after each step also verified the formation of a new layer on the electrode surface. The achieved results demonstrated the proposed process's good performance and can potentially develop a high-sensitivity immunosensor in the future.

Keywords: Protein detection, screen-printed carbon electrode, electrode surface functionality, polyaniline, gold nanoparticles.

INTRODUCTION

Conducting polymers are known as polymeric materials with intrinsic conductivity, requiring no additional conductive fillers [1]. Conducting polymers are promising materials frequently employed in biomedical applications because of their benefits, including conductivity, biocompatibility, and cost-effective processability [2]. Besides, conducting polymers are more biocompatible than traditional metal or semiconductor materials. Conducting polymers, like polypyrrole, polyaniline (PANI), and polythiophene (PT), are commonly utilized as surface modifiers for electrodes [3]. Among

them, Polyaniline (PANI) has garnered extensive attention in research due to its favorable redox activity, high thermal stability, and relatively straightforward synthesis methods [4]. The electrical conductivity of polyaniline can be readily adjusted by employing dopants or through oxidation-reduction reactions [5].

One of the drawbacks of polyaniline is its limited functionality in neutral pH conditions (typically below pH 4). This limitation restricts its use in various bioelectrochemical applications. This problem can be addressed by incorporating gold nanoparticles (AuNPs). AuNPs induce structural changes in the polymer,

while the polymer stabilizes the metal catalyst against fouling effects and acts as a scaffold to facilitate the even dispersion of the gold nanoparticles [6]. The electronic interactions between the AuNPs and the polymer matrix significantly enhance the nanocomposite's conductivity and electrocatalytic activity, which plays an important role in developing the immunosensor.

In this study, an immunosensor was developed on the carbon electrode for protein detection based on the combination of PANI and AuNPs. The electrode surface morphology was evaluated by the scanning electron microscope measurement. The performance of the carbon electrode surface functionalization process was evaluated by both fluorescence and electrical measurements.

EXPERIMENTAL

Chemicals used to modify the carbon electrode surface include aniline, chloroauric acid (HAuCl_4), 11-Mercaptoundecanoic acid (11-MUA), N-(3-Dimethylaminopropyl)-N'-ethyl carbodiimide hydrochloride (EDC) and N-Hydroxysuccinimide (NHS). These chemicals were purchased from Sigma-Aldrich Chemical Co (St. Louis, Missouri, USA). Bovine serum albumin-fluorescein isothiocyanate conjugate (BSA-FITC) was utilized as the analyte, purchased from Sigma-Aldrich Chemical. The screen-printed carbon electrodes were employed in the experiment, provided by Biodevice

Technology, Ltd (Japan). The performance of the proposed process was evaluated through fluorescence measurements conducted with an inverted fluorescence microscope IX 71 (Olympus, Melville, NY, USA) equipped with a Phantom VEO 710L high-speed camera (Ametek, USA) as well as electrical measurements using μStat 200 Bipotentiostat (Metrohm DropSens, Oviedo, Spain).

The process was divided into five main steps, including the formation of a conducting polymer layer on the carbon electrode using aniline, gold nanoparticle coating, and the formation of a self-assembled monolayer using 11-Mercaptoundecanoic acid, the carboxyl group activation, and protein immobilization, as shown in Figure 1. Experiments were carried out on the electrochemical screen-printed carbon electrode. The working and counter electrodes were carbon, while the reference electrode was Ag/AgCl. The process was carried out on the working electrode surface. At first, the electrode was subjected to electrolysis using the CV scanning method in a solution mixture containing Aniline 0.1 M and H_2SO_4 0.5 M to form a polyaniline layer on the electrode surface. The applied voltage ranged from -0.2 V to 1.0 V, with a scan rate of 50 mV/s for 10 cycles. Then, the electrode was electrolyzed in a solution mixture of HAuCl_4 0.2 mM and H_2SO_4 0.5 M to deposit gold nanoparticles on the electrode surface. The applied voltage ranged from -0.4 V to 1.2 V, with a scan rate of 50 mV/s for 20 cycles. The

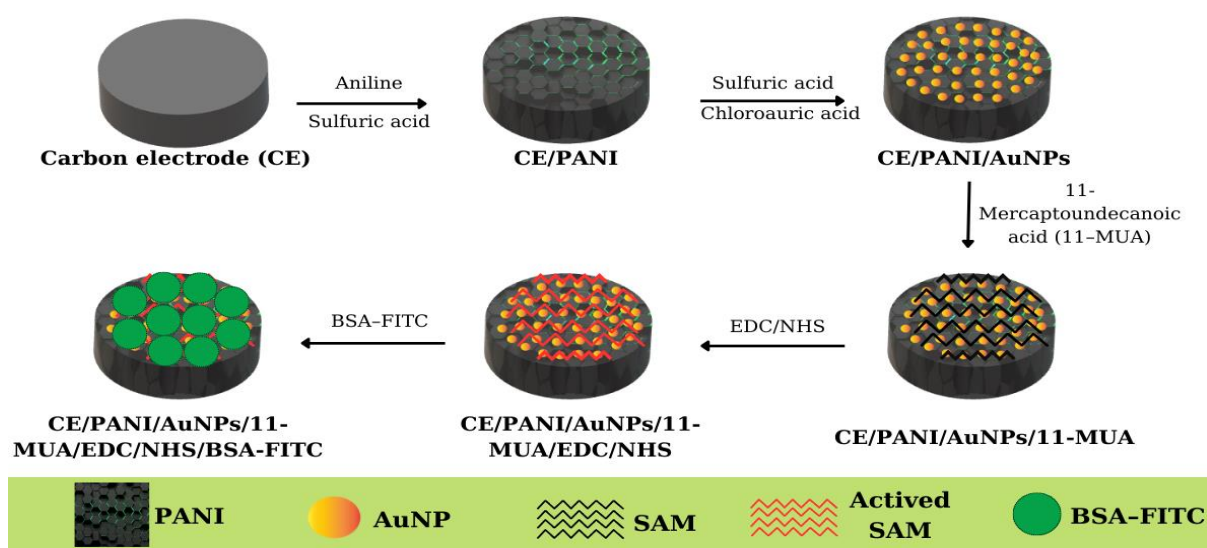


Figure 1. The carbon electrode surface functionalization process using conducting polymer and gold nanoparticles.

following steps involved the functionalization of gold nanoparticles to enable protein capture. The electrode was incubated in 5 mM 11-MUA solution to form a self-assembled monolayer (SAM) on the surface of gold nanoparticles. The carboxyl group of 11-MUA was then activated by the solution mixture of EDC 0.4 M and NHS 0.2 M. Finally, the electrode was incubated with 5 μ M BSA-FITC solution for 2 hours in the temperature condition of 4 °C. During the BSA incubation process, the amine group (NH₂) of BSA-FITC binds to ester groups on the electrode surface. After each process step, the electrode was gently washed with PBS 1X solution. The electrodes were then placed on the microscope to observe the change of the electrode surface. Besides, CV measurements were carried out to assess the efficacy of each step.

RESULTS AND DISCUSSION

After the step of gold nanoparticle coating, the scanning electron microscope measurement was used to examine the surface morphology and the distribution of gold nanoparticles on the electrode surface. The result shows that the gold nanoparticles were combined with the PANI layer to create a composite material on the electrode surface, as shown in Figure 2. The PANI layer played a crucial role in ensuring the uniform distribution of gold nanoparticles on the electrode surface.

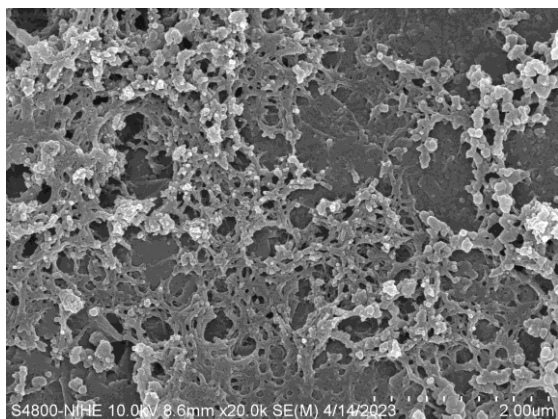


Figure 2. SEM image of AuNP/PANI/AuNP electrode.

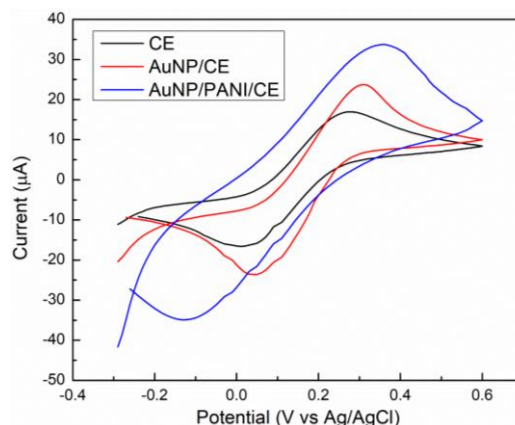


Figure 3. The change comparison of CV signals between two electrodes: AuNP/CE and AuNP/PANI/CE.

CV measurements were conducted to compare the amplitude of electrical signals between the AuNP/CE and AuNP/PANI/CE electrodes. The results show that the amplitude of CV signals on both electrodes increased significantly compared to the bare electrode, as shown in Figure 3. The amplitude of the oxidation peak increased from 16.94 μ A to 23.74 μ A for the AuNP/CE electrode and to 33.76 for the AuNP/PANI/CE electrode. As can be seen, the oxidation peak amplitude of the AuNP/PANI/CE electrode was double that of the bare electrode and substantially higher than that of the AuNP/CE electrode. The results also demonstrate that the combination of the PANI layer and the gold nanoparticles enhanced the electrode's contact area and current transmission capacity.

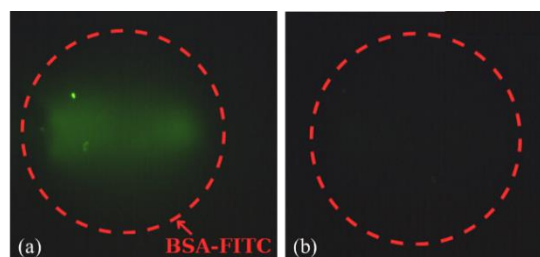


Figure 4. The electrode surface under the microscope; (a) The modified electrode with the full process; (b) The control electrode skipped the step of gold nanoparticle coating.

For the fluorescence measurement, the result shows that BSA protein was kept on the electrode surface through the green color observed under the microscope, as shown in Figure 4 (a). A clear and uniform fluorescent signal over the entire electrode area indicates the efficiency of protein immobilization. By contrast, no fluorescent

signal appeared on the control electrode skipped the step of gold nanoparticle coating, as shown in Figure 4 (b). This result demonstrates the absence of BSA proteins immobilized on the control electrode surface.

For the electrical measurement, CV signals changed significantly after each step of the process, as shown in Figure 5. At first, the amplitude of the oxidation peak increased after the composite material layer of PANI and gold nanoparticles were formed on the electrode surface. Then, the amplitude of the oxidation peak was decreased in the next steps. Especially, the amplitude of the CV signal was very small in the step of BSA-FITC incubation. This result can be explained by the fact that a large amount of protein was retained and covered the electrode surface, preventing the oxidation-reduction process on the electrode surface. Therefore, the reduction and oxidation peaks dropped sharply. Besides, the CV signal changes also demonstrated each step's success in the proposed functionalization process.

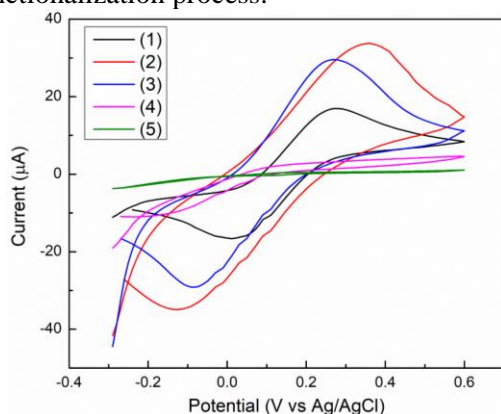


Figure 5. The change of CV signals after each step of carbon electrode surface functionalization process; (1) Bare (CE); (2) AuNP/PANI/CE; (3) 11-MUA/AuNP/PANI/CE; (4) EDC/NHS/11-MUA/AuNP/PANI/CE; (5) BSA/NHS/11-MUA/AuNP/PANI/CE.

CONCLUSION

This report introduced a novel carbon electrode surface functionalization process for protein detection. The process utilized a combination of conducting polymer and gold nanoparticles to enhance the electrode's contact area and current transmission capacity. The SEM results show that gold nanoparticles were distributed uniformly on the electrode through the PANI layer. The amplitude of the CV signal was notably increased when PANI was employed. The experimental results also show BSA protein

was immobilized on the electrode surface. The presence of BSA protein was verified by both fluorescence and CV measurements. This work provides a high-sensitivity immunosensing platform that can be developed to detect and quantify the protein for disease diagnosis in the future.

Acknowledgment

This work was funded by the Vietnam Ministry of Science and Technology under Grant NĐT.101.TW/21. Chi Tran Nhu was funded by the Master, PhD Scholarship Programme of Vingroup Innovation Foundation (VINIF), code VINIF.2022.TS015.

References

- [1] S.A. Umoren, M.M. Solomon, V.S. Saji, *Polymeric Materials in Corrosion Inhibition: Fundamentals and Applications*, Polymeric Materials in Corrosion Inhibition: Fundamentals and Applications, 2022, 1-612.
- [2] L. Poole-Warren, P.J. Martens, R.A. Green, *Biosynthetic polymers for medical applications*, Elsevier, 2016.
- [3] J.R. Crespo-Rosa, A. Sierra-Padilla, J.J. García-Guzmán, D. López-Iglesias, D. Bellido-Milla, J.M. Palacios-Santander, L. Cubillana-Aguilera, *Polyaniline Nanofibers-Embedded Gold Nanoparticles Obtained by Template-Free Procedure with Immobilization Prospects*, *Sensors* **21** (2021) 8470.
- [4] S. Mahalakshmi, V. Sridevi, *In Situ Electrodeposited Gold Nanoparticles on Polyaniline-Modified Electrode Surface for the Detection of Dopamine in Presence of Ascorbic Acid and Uric Acid*, *Electrocatalysis* **12** (2021) 415-435.
- [5] S. Bhadra, S. Chattopadhyay, N.K. Singha, D. Khastgir, *Improvement of conductivity of electrochemically synthesized polyaniline*, *Journal of Applied Polymer Science* **108** (2008) 57-64.
- [6] S.A. Ansari, A. Ahmed, F.K. Ferdousi, M.A. Salam, A.A. Shaikh, H.R. Barai, N.S. Lopa, M.M. Rahman, *Conducting poly(aniline blue)-gold nanoparticles composite modified fluorine-doped tin oxide electrode for sensitive and non-enzymatic electrochemical detection of glucose*, *Journal of Electroanalytical Chemistry* **850** (2019) 113394.

DETECTION OF A549 LUNG CANCER CELLS BASED ON COMPLEX APTAMER - INCORPORATING GOLD NANOPARTICLES SCREEN-PRINTED GOLD ELECTRODE

Phu Nguyen Van¹, Chi Tran Nhu², Hoang-Anh Phan², Hien Vu-Dinh³, Chun-Ping Jen^{3,4}, Tung Bui Thanh², Trinh Chu Duc², and Loc Do Quang^{1*}

¹Faculty of Physics, VNU University of Science, Hanoi, Vietnam

²Faculty of Electronics and Telecommunications, VNU University of Engineering and Technology, Hanoi, Vietnam

³Department of Mechanical Engineering and Advanced Institute of Manufacturing for High-Tech Innovations, National Chung Cheng University, Chia-Yi, Taiwan, ROC

⁴School of Dentistry, College of Dental Medicine, Kaohsiung Medical University, Kaohsiung, Taiwan, ROC

*Email: locdq@hus.edu.vn

ABSTRACT

In this study, a procedure of surface functionality was proposed and performed on the screen-printed gold electrode to detect A549 lung cancer cells. The surface functionalization process was divided into four main steps, including the formation of self-assembled monolayer (SAM) using 3-Aminopropyltriethoxysilane (APTES), coating of gold nanoparticles (AuNPs), aptamer incubation and binding of A549 lung cancer cells. Gold nanoparticles with a diameter of 13 nm were utilized to achieve uniform distribution and high density in the working electrode area. AuNPs were immobilized on the gold electrode area via APTES bridges. The experimental results show that the fluorescence signal was observed on the working electrode representing the immobilization of fluorescently labeled cells. In contrast, the fluorescence signal was not observed on the control electrode which was implemented without the APTES coating step. For the electrochemical impedance spectroscopy (EIS) method, the electrode surface impedance increased significantly after each step of the proposed process. Especially, the charge transfer resistance increased strongly according to the immobilization of A549 lung cancer cells on the electrode surface. This work demonstrates an impressive arrest potential of the proposed method for the detection of A549 lung cancer cells. In addition, this study lays a good foundation for expanding future research in the field of cancer diagnosis.

Keywords: Screen-printed gold electrode, surface functionalization, biosensor, lung cancer cell detection.

INTRODUCTION

In recent years, lung cancer has remained one of the leading causes of cancer-related deaths worldwide, with its early detection and diagnosis playing a pivotal role in improving patient outcomes. For successful treatment, it is important to monitor A549 lung cancer cells quickly, accurately, and sensitively. Currently, a lung cancer diagnosis in general often includes a combination of clinical, imaging, and laboratory methods [1]. These methods aim to identify and characterize the presence of cancer cells or tumors in the lungs. They can help determine if a lung nodule is cancerous or benign. Although they provide valuable diagnostic information, it is essential to be aware of their potential impact and not to overuse them. Moreover, these devices

are highly specialized and serve as a standard for other methods. Therefore, the initial cost to purchase and install this equipment can be huge. One of the commonly used methods today to identify A549 lung cancer cells is based on identification through biopsy, in which a lung tissue sample is taken for examination. It provides a definitive confirmation of the presence of cancer cells and allows for detailed analysis of the tumor. However, most biopsy procedures involve inserting a needle, endoscope, or surgical instrument into the body, which can be invasive and pose some risk of complications, such as bleeding or infection. Recent advances in the field of biosensors and electrochemical technology have opened up promising avenues for the rapid and sensitive detection of cancer

cells, including A549 lung cancer cells [2]. One of them is the cellular impedance sensor which is based on electrochemical biosensing technology. This method relies on the fundamental principle that as cells adhere and grow on the surface of a microelectrode, they can influence the impedance at the interface of these electrodes. This modulation in impedance serves as a window into the biological information about the physiological functions of these cells. Building upon these foundational principles, scientists have developed a range of electrochemical impedance sensors. These sensors feature adapted working electrodes, harnessing an innovative technique for capturing tumor cells. Remarkably, these sensors have successfully detected various human tumor cell types, including but not limited to HeLa, MCF-7 (breast cancer), HL-60 (human promyelocytic leukemia cell line), and HepG2 (hepatocellular carcinomas), as previously demonstrated [3].

In this study, a surface functionalization procedure was developed for the detection of A549 lung cancer cells using a screen-printed gold electrode. The process involved four key steps, starting with the formation of a Self-Assembled Monolayer (SAM) using 3-Aminopropyltriethoxysilane (APTES). Gold nanoparticles (13 nm in diameter) were then applied to ensure even distribution and high-density coverage on the electrode. An aptamer incubation process increased the surface's specificity for A549 cells. This was followed by binding A549 cells to the modified electrode, enabling their selective detection. The approach involved DNA molecule adsorption and the creation of spatial site resistance due to methyl groups on the APTES-coated surface. The results demonstrated effective capture of A549 cells, even at low concentrations (2×10^4 cells/mL). Moreover, the experimental findings substantiate that the fluorescence signal detected on the working electrode corresponds to the successful immobilization of fluorescently labeled cells. Additionally, to corroborate these results, we employed the electrochemical impedance spectroscopy (EIS) technique. This method holds promise for A549 lung cancer cell detection and paves the way for further cancer diagnosis research.

MATERIALS AND METHODS

Chemicals and Solutions

In this work, gold nanoparticles with a size of 13 nm and a concentration of 179 ppm were procured from TANBead, a reputable supplier based in Taoyuan City, Taiwan. 3-Aminopropyltriethoxysilane (APTES), utilized for gold electrode silanization, was acquired from Sigma-Aldrich, headquartered in St. Louis, MO, USA. For cell staining purposes, this study used calcein green AM, in addition to various other chemicals such as phosphate-buffered saline (PBS, 10X), bovine serum albumin (BSA), and yeast tRNA, all of which were sourced from Thermo Fisher Scientific (Eugene, OR, USA). The complete DNA aptamer sequence, 5'-ACGC TCGG ATGC CACT ACAG GGTT GCAT GCCG TGGG GAGG GGGG TGGG TTTT ATAG CGTA CTCA GCTC ATGG ACGT GCTG GTGA C-3', modified with 5'-thiol (5'-C6SH), was provided by MdBio, Inc. (Taiwan). Two crucial solutions utilized in this study include a binding buffer for facilitating aptamer treatment. It consisted of 15 mg of BSA, 0.72 mg of $MgCl_2$, and 150 μL of Yeast tRNA (with a concentration of 10 mg/mL). These components were diligently diluted in 15 mL of PBS (1X, pH 7.4). All aqueous solutions were meticulously prepared using ultrapure water with a conductivity of $18.2 M\Omega \times cm$ at $25^\circ C$, obtained via a Direct-Q system (Milli-Q, Millipore Simplicity, Billerica, MA, USA). In addition, sucrose solution with a concentration of 8.62 wt% was used in the process of removing the cell culture solution to obtain purified cells.

Apparatus

In this study, a PalmSens 4 potentiostat (PalmSens, Houten, Netherlands) was used to conduct the electrochemical impedance measurements of this proposed study.

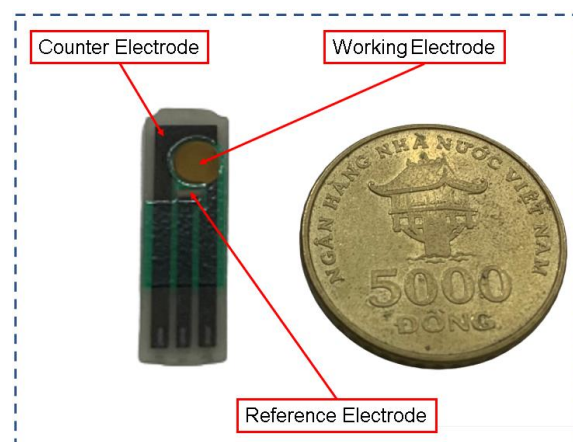


Figure 1. Screen-printed gold electrode.

Impedance values and data acquisition were performed using PStTrace software (PalmSens, Utrecht, Netherlands). Besides, electrochemical measurements were conducted with a three-electrode configuration (BioDevice Technology, Ltd. Japan). The working electrode was made of gold material, while the counter and reference electrodes were made of carbon and Ag/AgCl, respectively (Fig.1).

EXPERIMENTAL

In this study, the proposed idea of this electrochemical biosensor is shown in Fig. 2. The self-assembly process of gold nanoparticles on the screen-printed gold electrode. AuNPs have been modified in the SAM area through APTES bridges. Such bridges were covalently bonded to the hydroxyl groups (-OH) from the NaOH solution. The amino groups of APTES were lightly protons attached in a slightly acid solution, which became positively charged (NH_3^+), while AuNPs were surrounded by the negative charges of the citrate groups, which facilitated electrostatic interactions between amino groups and AuNPs.

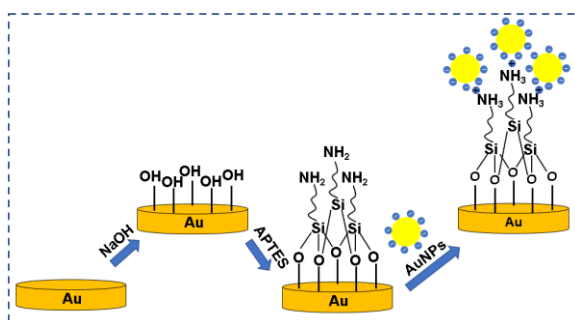


Figure 2. Gold nanoparticle self-assembly on the screen-printed gold electrode.

Subsequently, SH-aptamer was meticulously diluted within the binding buffer, attaining a concentration of 10 μ M. This aptamer solution was then thoughtfully incubated for 30 minutes at a temperature of 4°C. Crucial gold-sulfur (Au-S) bonds were established during this incubation period. These bonds played a pivotal role in the effective immobilization of the SH-aptamer on the gold surface, making it readily accessible for the subsequent capture of A549 target cells.

RESULTS AND DISCUSSION

In this work, a comparative analysis was performed to detect A549 cells using fluorescence-based methods following the execution of the proposed electrode

functionalization steps. Additionally, the research utilizes impedance spectroscopy (EIS) as a complementary technique to draw comparisons with the fluorescence measurement results previously mentioned.

Fluorescence signal detecting A549 cells

In this work, after being incubated in aptamer solution for 30 minutes at a temperature of 4°C, the gold electrode was washed again with PBS 1X solution.

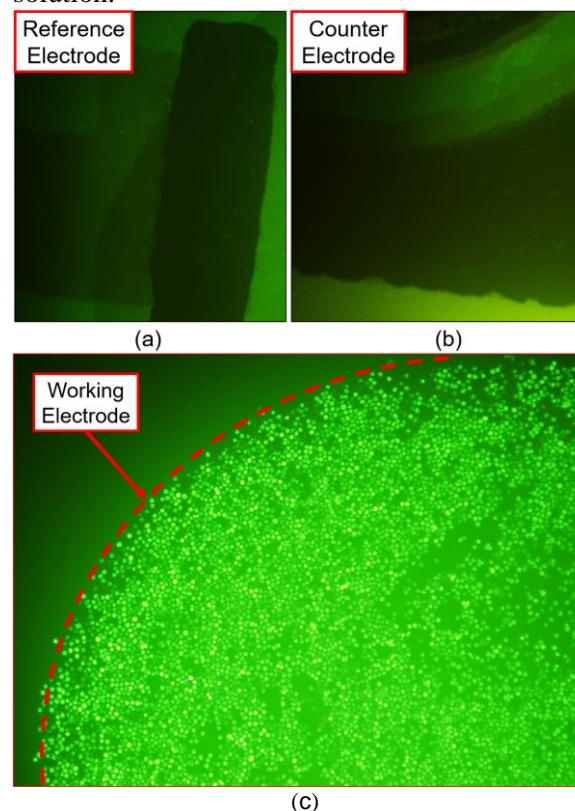


Figure 3. Fluorescence image of the electrodes with total surface modification: (a) reference electrode; (b) counter electrode; (c) and working electrode.

Next, the fluorescence measurement was used to demonstrate the performance of the proposed method. An electrode is placed on the working area of the microscope and observed through the camera. Fluorescence images show that the fluorescence signal is absent from the reference and counter electrodes, as shown in Fig. 3 (a) and (b). Besides, fluorescence-dyed A549 cell images appeared on the working electrode where the functionalization steps were performed, as shown in Fig. 3 (c). Moreover, fluorescence imaging demonstrated the effective immobilization of SH-Aptamer on the gold surface, ensuring specific binding of A549 cells and their readiness to capture target cells.

Electrochemical impedance spectroscopy (EIS) analysis

Electrochemical Impedance Spectroscopy (EIS) is a widely utilized method for characterizing electrochemical systems, including biosensors. This non-destructive measurement technique offers the capability to monitor sensor development progress over time. EIS was employed to study charge transfer kinetics at electrode interfaces and processes related to mass transport. These attributes of EIS make it a valuable tool for diagnosing and predicting the behavior of electrochemical systems.

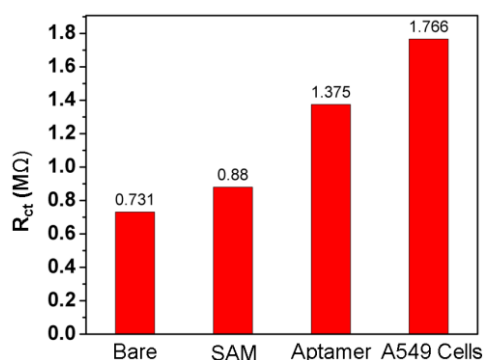


Figure 4. The graph of the impedance at the survey voltage value is 10mV.

In this work, the study analyzed the change in electrostatic impedance in the frequency range 100 Hz to 1 MHz with an applied voltage of 10 mV with PBS 1X solution. The impedance response was quantified using the previously studied simplified Randles circuit [4]. The results show that the electrode surface impedance (R_{ct}) increases significantly after each step of the proposed process, as shown in Fig. 4. Specifically, the surface impedance (R_{ct}) value corresponding to the bare electrode is 0.731 MΩ. This figure increases to 0.88 MΩ after the formation of a self-assembled monolayer (SAM). In addition, the R_{ct} value is 1.375 MΩ according to the appearance of the SH-aptamer bond on the gold surface, and the R_{ct} value is 1.766 MΩ after capturing A549 target cells. The specific binding between the aptamer and the A549 cells increases the charge transfer resistance of the electrode surface. It can be seen that the amount of A549 cells captured on the electrode is proportional to the charge transfer resistance. This outcome serves as additional confirmation of the successful functionalization process of the gold electrode surface. In the future, biosensors and biochips can be developed to detect different types of cancer cells and diagnose diseases in biomedical.

CONCLUSION

This study proposed a surface functionalization process on screen-printed gold electrodes to detect A549 lung cancer cells. The process includes steps such as creating a self-assembled monolayer using 3-Aminopropyltriethoxysilane (APTES), coating with 13 nm gold nanoparticles (AuNPs) for uniform distribution, annealing with aptamers, and binding specific for A549 lung cancer cells. Fluorescence signals were observed on the working electrode, indicating successful cell immobilization, while the control electrode lacked this signal. Electrochemical impedance spectroscopy (EIS) showed a significant increase in electrode surface impedance after each modification step, with notable resistance changes upon A549 cell immobilization. Additionally, charge transfer resistance correlated with A549 cell concentration. This method shows promise for A549 lung cancer cell detection and provides a foundation for future cancer diagnosis research.

Acknowledgment

Phu Nguyen Van was funded by the Master, Ph.D. Scholarship Programme of Vingroup Innovation Foundation (VINIF), code VINIF.2023.ThS.105. This research is funded by University of Science, Vietnam National University, Hanoi under project number TN.23.07.

References

- [1] R. Nooreldeen, H. Bach, *Current and Future Development in Lung Cancer Diagnosis*, International Journal of Molecular Sciences. **22** (2021) 8661.
- [2] M.S. Sumitha, T.S. Xavier, *Recent advances in electrochemical biosensors – A brief review*, Hybrid Advances. **2** (2023) 100023.
- [3] Z.W. Lee, J. Zhou, C.-S. Chen, Y. Zhao, C.-H. Tan, L. Li, P.K. Moore, L.-W. Deng, *The Slow-Releasing Hydrogen Sulfide Donor, GYY4137, Exhibits Novel Anti-Cancer Effects In Vitro and In Vivo*, PLoS ONE. **6** (2011) e21077.
- [4] A.R. Harris, P.J. Molino, R.M.I. Kapsa, G.M. Clark, A.G. Paolini, G.G. Wallace, *Correlation of the impedance and effective electrode area of doped PEDOT modified electrodes for brain-machine interfaces*, The Analyst. **140** (2015) 3164–3174.

REMOVAL OF IRON IN NATURAL IRON-ALUM WATER USING CATION EXCHANGE METHOD: AN OPTIMIZATION STUDY

**Le Ba Tran^{1,2,3,4}, Tri Thich Le^{1,2}, Nhat Huy Nguyen^{2,4}, Surapol Padungthon⁵,
Trung Thanh Nguyen^{1,2,*}**

¹Nanomaterial Laboratory, An Giang University, An Giang Province, Vietnam

²Vietnam National University Ho Chi Minh City, Ho Chi Minh City, Vietnam

³Faculty of Engineering - Technology - Environment, An Giang University, An Giang Province, Vietnam

⁴Faculty of Environment and Natural Resources, Ho Chi Minh City University of Technology (HCMUT),
Ho Chi Minh City, Vietnam

⁵Department of Environmental Engineering, Khon Kaen University, Khon Kaen, Thailand

E-mail: ntthanh@agu.edu.vn

ABSTRACT

In this study, the cation exchange method was used to treat iron ions and other metal ions in natural iron-alum water to ensure the iron content in surface water is below the level affecting human health according to QCVN 08:2023/BTNMT. Meanwhile, this method can recover metal ions (e.g., Fe, Al, Ca, and Mg) that are considered toxic in water to synthesize materials capable of treating other environmental pollutants. In particular, the research was conducted with the goal of finding suitable parameters (material packing height, pH, and flow rate through the material) for the cation exchange process to treat iron in water on site. First, the study conducted individual surveys of parameters and found suitable parameters such as height of 80 cm, pH 6.5, and flow rate of 30 L/h. An experimental design includes 20 surveys was then conducted to find the optimal parameters affecting the remaining iron content in natural iron-alum water. When the input iron content was 8.25 mg/L, the optimal conditions found at material layer height of 76.47 cm, pH 6.6, and column flow of 28.66 L/h. The remaining iron content was found to be less than 0.5 mg/L, with a treatment efficiency of about 95%. This result has shown the effectiveness of iron treatment in natural iron-alum water by cation exchange method with different iron contents, as well as the relevance of the model in practice.

Keywords: natural iron-alum water, cation exchange method, recovery of metal ions, iron treatment, ion exchange column

INTRODUCTION

The iron-alum water is natural water with high levels of metals such as iron, aluminum and other metals (Ca, Mg, and Si) released from acid sulfate soil [1, 2]. Iron plays an important role in humans in hemoglobin, myoglobin and some enzymes. Iron deficiency in the body will cause anemia and affect health. However, when the iron content exceeds the body's ability to absorb it, it will cause serious problems for the human body. Besides, high iron content will also change color and taste, cause yellowing on clothes and cause water pipe corrosion problems [3]. Plant absorbs too much iron, it will lead to poisoning [4].

The common methods of treating iron in water include: oxidation and precipitation process [5], zeolite softening/ion exchange [6, 7], calcium carbonate materials [8], filter media separation[9], removal through supercritical fluid, removal

through supercritical fluid,... However, the ion exchange method is an effective method in removing iron at concentrations less than 5 mg/L [10], selectivity of metals, wide applicable pH range and high regeneration capacity [11]. Research on the treatment of metals in water using the ion exchange method has been carried out previously. However, for iron in natural iron-alum water, treatment studies using ion exchange resins have not been conducted. In this study, the method of treating natural iron-alum water with ion exchange resins was implemented to treat water sources with high iron content exceeding the iron content standard in surface water according to QCVN 08:2023/BTNMT, this is National technical regulation on Surface water quality of Vietnam, which stipulates that the iron content in surface water must not exceed 0.5 mg/L. This study focuses on simultaneously evaluating three

factors (pH, flow, ion exchange layer height) that affect the remaining iron content under different experimental conditions using a continuous flow experimental model. (Fixed – bed). At the same time, we also calculated the optimal parameters of the iron treatment process in natural iron alum water using Design expert 12 software.

EXPERIMENTAL

Chemicals: used in the study include: HCl (36%), H₂SO₄ (98%), HNO₃, NaOH, NH₄Cl, CaCl₂, MgCl₂, Ion exchange resin 225H was manufactured by Ion Exchange (India) Ltd.

The experiments conducted included: 1 round cylindrical plastic pipe (diameter is 4.2 cm, height 1.5 m), the pump can adjust the flow (10 L/h to 50 L/h) from bottom to top. The natural iron-alum water is taken directly from the surface water source and passed through a coarse filter screen to remove suspended sediments before being passed directly through the column. The solution pH is adjusted with HCl and NaOH. After running through the column, the natural iron-alum water sample was analyzed for iron content and other ion content. Iron content was analyzed according to TCVN 6177:1996 (ISO 6332: 1988 (E)) and aluminum content were analyzed by AAS atomic absorption machine, Calcium and Magnesium were analyzed by Ca and Mg analysis method according to TCVN 6224 – 1996 (Standard Method 2320B:2005).

Develop optimization experiments

This study was conducted in 2 parts. In the first part, the study investigated individual factors, namely ion exchange layer height, pH, and flow rate that affect the remaining iron ion content in natural iron-alum water. Then, use the values of these factors as an information basis to build optimization experiments. These factors are the independent variables while the remaining iron content is the response variable.

In optimization experiments, 20 experiments will be performed. All experiments were performed at 5 levels (- α , -1, 0, +1, + α), 14 experiments were outside the center range and 6 experiments were repeated at the center to evaluate errors.

RESULTS AND DISCUSSION

Survey of background factors

In this experiment, the effect of flow rate (L/h) on the removal of iron ions in natural iron-alum water by ion exchange resin 225H was

investigated, with the iron ion content in the input water being 8.25 mg/L, the height of the resin layer was 100 cm (diameter was 4.2 cm) and the pH was 6.5. The remaining iron content in natural iron-alum water was shown in Figure 1. The results show that it was when the flow rate was less than or equal to 30 L/h the remaining iron content in natural iron-alum water was less than 0.5 mg/L, ensuring the quality of surface water (QCVN 08-2023/BTNMT). When the flow rate was higher, there may not be enough contact time between iron ions and resin particles, leading to reduced ion exchange efficiency. From there, it can be seen that the smaller the flow rate (the longer the contact time), the greater the ion exchange efficiency.

When the flow rate was 30 L/h, conduct a survey of pH values ranging from 3.5 - 8 to investigate the efficiency of iron ion exchange in natural iron-alum water of this research model. The ability to remove iron through the remaining iron ion content in water was described in Figure 2.

Experiment on the relationship between pH and ion exchange efficiency. In particular, when the pH value is greater than 6.5, the efficiency gradually decreases and the exchange efficiency decreases clearly when pH 8. This shows that the reduced treatment efficiency is because the iron ions in natural iron-alum water may have changed from a dissolved state to a precipitated state, so the ion exchange process cannot be carried out and These precipitates stick to the surface of the ion exchange resin, causing interference (expanding the phase diagram of iron ions in the solution [12]), This is most clearly seen in practice when pH=8.5, iron precipitates are formed in natural iron-alum water and create iron flocs.

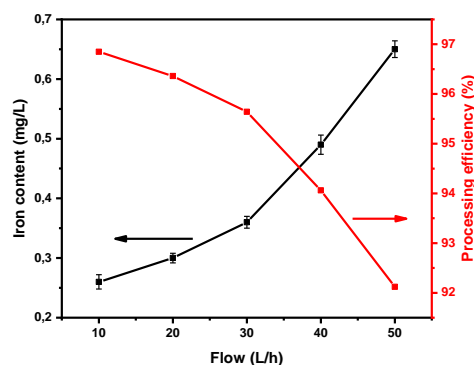


Figure 1. Effect of flow rate on ion exchange capacity

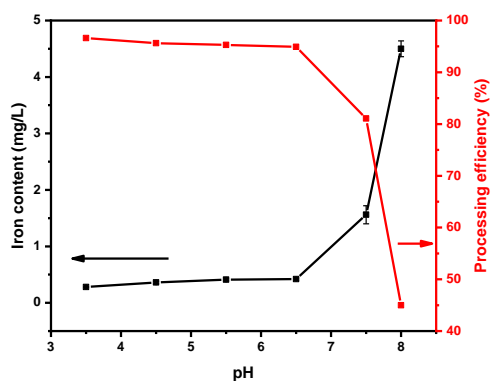


Figure 2. Effect of pH on iron treatment ability of ion exchange resin

In the experiment, we investigated the influence of ion exchange layer height at pH 6.5 and flow rate of 30 L/h, within the investigation range from height 20 cm to 120 cm. When the ion exchange resin layer was larger than 80 cm, the efficiency of the ion exchange process reaches over 90%, the remaining iron content in natural iron-alum water was less than 0.5 mg/L, this is also very close to the manufacturer's recommended conditions (0,75 m with Co-Flow Regeneration and 1m with Counter Current regeneration). From there, it can be seen that the appropriate material layer height is 80 cm (0.8 m) when applied to the iron treatment process in natural iron-alum water (Figure 3).

After the survey, the corresponding results found included: pH 6.5; The flow rate is 30 L/h and the material layer height is 80 cm, which is suitable for the iron treatment process in natural iron-alum water. A survey to evaluate the effectiveness of iron treatment in natural iron-alum water using the parameters just found showed that the remaining iron content after treatment was 0.42 mg/L, with a treatment efficiency of 94.91 %. Besides, the aluminum treatment efficiency reached 87.9%, Calcium and magnesium were not found after the treatment process (Table 1).

Table 1. The ion exchange column processing capabilities

Parameters	Ion metal			
	Fe	Al	Ca	Mg
Input water (mg/L)	8.25	1.24	0.68	0.52
After processing (mg/L)	0.42	0.15	-	-

Processing efficiency	94.91 %	87.9 %	100 %	100 %
QCVN 08:2023/BTN MT (mg/L)	0.5	-	-	-

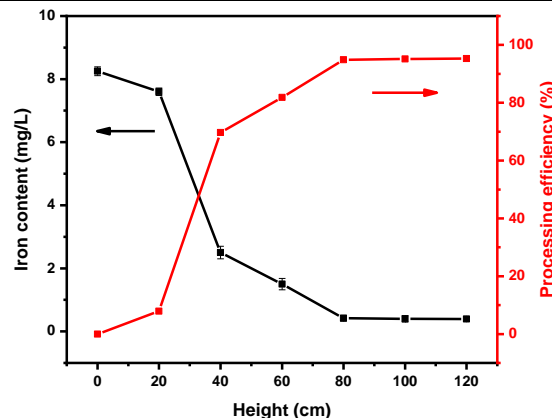


Figure 3. Effect of layer height on iron treatment ability of ion exchange resin

Statistical analysis and assessment of model suitability

The multivariate quadratic equation calculated from the optimized software includes the following variables: ion exchange resin layer height (x_1); pH (x_2); Flow rate (x_3) after removing unimportant variables is expressed according to the second-order multivariate regression equation is then rewritten as follows:

$$Y = 0.402 - 0.548x_1 + 0.092x_3 + 0.292x_1^2$$

Optimal parameters found from the model: pH 6.6, the flow was 28.66 L/h and height was 76.47. After 6 times of conducting repeated experiments based on the optimal parameters for the model. The output iron content was equal to or less than 0.5 mg/L. The test at 3 locations showed that the output iron content was all below 0.5 mg/L, processing ability also reached over 93%. For other metals such as aluminum, calcium and magnesium, the results also show that the processing ability was always above 85%.

CONCLUSION

In this study, the results show that the optimal values of the parameters are as follows: pH 6.6, flow rate of 28.66 L/h and height of 76.47 cm. The efficiency is about 95% and the remaining iron content in natural iron alum water is less than 0.5 mg/L. In addition, the processing efficiency of metals such as aluminum, calcium, and magnesium also reached over 85%. This method also shows that it can be applied in practice.

Through the analysis results of 3 samples, the iron content in the output water is all below 0.5 mg/L.

Acknowledgment

The authors would like to thank the support of the Faculty of Engineering - Technology - Environment, An Giang University, Vietnam and the Faculty of Environment and Natural Resources, Ho Chi Minh City University of Technology, Vietnam.

References

- [1] T. T. Nguyen, K. A. Huynh, S. Padungthon, A. Pranudta, P. Amonpattaratkit, L. B. Tran, *et al.*, *Synthesis of natural flowerlike iron-alum oxide with special interaction of Fe-Si-Al oxides as an effective catalyst for heterogeneous Fenton process*, *Journal of Environmental Chemical Engineering* **9** (2021) 105732.
- [2] L. B. Tran, T. T. Nguyen, S. Padungthon, T. T. Le, Q. A. Nguyen Thi, and N. H. Nguyen, *Advanced natural hydrated iron-alum oxides cation exchange resin for simultaneous phosphate and hardness removal*, *npj Clean Water*, **5** (2022) 43.
- [3] V. Kumar, P. K. Bharti, M. Talwar, A. K. Tyagi, and P. Kumar, *Studies on high iron content in water resources of Moradabad district (UP), India* *Water Science* **31** (2017) 44-51.
- [4] A. Asati, M. Pichhode, and K. Nikhil, *Effect of heavy metals on plants: an overview*, *International Journal of Application or Innovation in Engineering & Management* **5** (2016) 56-66.
- [5] E. A. Boyle, J. M. Edmond, and E. R. Sholkovitz, *The mechanism of iron removal in estuaries*, *Geochimica et Cosmochimica Acta* **41** (1977) 1313-1324.
- [6] A. Dąbrowski, Z. Hubicki, P. Podkościelny, and E. Robens, *Selective removal of the heavy metal ions from waters and industrial wastewaters by ion-exchange method*, *Chemosphere* **56** (2004) 91-106.
- [7] M. Al-Anber and Z. A. Al-Anber, *Utilization of natural zeolite as ion-exchange and sorbent material in the removal of iron*, *Desalination* **225** (2008) 70-81.
- [8] H. A. Aziz, M. S. Yusoff, M. N. Adlan, N. H. Adnan, and S. Alias, *Physico-chemical removal of iron from semi-aerobic landfill leachate by limestone filter*, *Waste Management* **24** (2004) 353-358.
- [9] B.-Y. Cho, *Iron removal using an aerated granular filter*, *Process Biochemistry*, **40** (2005) 3314-3320.
- [10] A. Colter and R. L. Mahler, *Iron in drinking water*: University of Idaho Moscow, 2006.
- [11] D. W. O'Connell, C. Birkinshaw, and T. F. O'Dwyer, *Heavy metal adsorbents prepared from the modification of cellulose: A review*, *Bioresource technology* **99** (2008) 6709-6724.
- [12] W. Stumm and G. F. Lee, *The chemistry of aqueous iron*, *Schweizerische Zeitschrift für Hydrologie* **22** (1960) 295-319.

OPTIMIZING E-TEXTILE PH SENSORS: A COMPARATIVE EVALUATION OF RGO-PANI AND RuO₂ MATERIALS

Nurul Fauzani Jamaluddin², Fatimah Ibrahim^{1,2}, Aisyah Hani Zulkiflee¹, Aung Thiha², Bojan Petrović³, Sanja Kojić⁴, Goran M Stojanović⁴

¹ Department of Biomedical Engineering, Faculty of Engineering, Universiti Malaya, Kuala Lumpur,

² Centre for Innovation in Medical Engineering (CIME), Universiti Malaya, Kuala Lumpur, Malaysia

³ Department of Dental Medicine, Faculty of Medicine, University of Novi Sad, Novi Sad, Serbia

⁴ Faculty of Technical Science, University of Novi Sad, Novi Sad, Serbia

Email: fatimah@um.edu.my

ABSTRACT

Wearable devices have emerged as a promising solution in the medical field, offering early diagnosis and effective monitoring. E-textile is a type of biosensor that can potentially be used in wearable devices for pH monitoring purposes. The purpose of this research paper is to compare the effectiveness of two different pH sensing materials: reduced graphene oxide-polyaniline (rGO-PANI) modified screen electrode and Ruthenium (IV) Oxide (RuO₂) coated thread for creating e-textiles. The study evaluated the sensitivity of both sensing materials for pH detection and found that both are suitable for this purpose. However, the results show that the rGO-PANI-modified electrode is more sensitive (with a sensitivity of -54.2 mV/pH) compared to the RuO₂-coated thread (with a sensitivity of -47.7 mV/pH). The findings of this study suggest that e-textile biosensors have great potential in the medical field and that their sensitivity can be further improved through material modification and optimization.

Keywords: E-textile, reduced graphene oxide-polyaniline, Ruthenium (IV) Oxide, thread sensor

INTRODUCTION

Chronic diseases are responsible for a significant proportion of global deaths, accounting for approximately 75%, and have a considerable economic impact [1]. However, wearable devices have emerged as a promising solution in the medical field, offering early diagnosis and effective monitoring. Utilising non-invasive and dynamic measurements of biomarkers found in biological fluids can provide continuous and real-time physiological insights, making it possible to track and manage chronic diseases more efficiently [2].

A wearable device is a portable device that consists of biosensors attached to a person's body in various ways, such as through clothing, bandages, watches, glasses, contact lenses, and rings [1], [3]. These devices are designed to offer unique features that set them apart from conventional devices, including ease of use, portability, and adaptability to various environments. E-textile is one of the innovative biosensors that is designed to accurately measure various biological parameters by analyzing sweat. These textile-based bio-sensors are precisely engineered to be in close contact with the skin and

provide conformable, non-invasive monitoring of vital signs and other physiological data [4]. E-textiles can monitor important biological parameters such as ECG, EMG, EEG, and sweat analysis. Sweat analysis has become increasingly important in health and performance monitoring due to its composition. One example of its significance is pH sensing through sweat, which has the potential to provide valuable insights into an individual's health and well-being.

pH is a measure of acidity or alkalinity in a solution. The pH level of sweat is closely linked to an individual's hydration status. When a person's body becomes dehydrated, the concentration of electrolytes in their sweat increases, resulting in more acidic pH levels. Monitoring sweat pH can be helpful for individuals, athletes, and healthcare professionals to determine hydration levels and take the necessary steps to maintain proper fluid balance [5]. Athletes and fitness enthusiasts can especially benefit from tracking sweat pH to optimize their training and performance. It is essential to maintain the correct pH balance in sweat to prevent issues such as muscle cramps and fatigue during physical activity.

However, there are several challenges associated with using e-textiles for pH sensing. These challenges include ensuring that the e-textile sensors remain durable and stable over time while achieving high accuracy and sensitivity in pH measurements [2], [4]. This paper aims to evaluate the performance of two different pH sensing materials: reduced graphene oxide-polyaniline (rGO-PANI) modified screen electrode and Ruthenium (IV) Oxide (RuO₂) coated thread for e-textile fabrication in the future.

EXPERIMENTAL

Fabrication of rGO-PANI biosensor

The synthesis of rGO-PANI followed the method employed by Thu et al. (2018). Initially, a graphene oxide solution with a concentration of 1 mg/ml was prepared by mixing 1 ml of a 4 mg/ml graphene oxide aqueous dispersion with 3 ml of deionized water. Subsequently, the graphene oxide solution underwent sonication to achieve a homogeneous mixture. To eliminate dissolved oxygen and other impurities in the GO solution, a nitrogen purging method was implemented, utilizing nitrogen gas. The carbon-coated electrode was then immersed in this solution. Next, the GO-modified electrode underwent reduction via the cyclic voltammetry (CV) technique. The potential range applied for the reduction of the thread was between 0.2 V and -1.2 V. Following reduction, the thread was thoroughly rinsed, dried, and thereby prepared as the conductive modified electrode with rGO.

Subsequently, a solution was prepared by combining 0.1M aniline with 30 ml of 0.5M sulfuric acid. To obtain the desired 30 ml of 0.5M sulfuric acid, 15 ml of 1M sulfuric acid was mixed with 15 ml of deionised water. Next, 0.2621 ml of the 0.1M aniline solution was added to the 30 ml of 0.5M sulfuric acid. The resulting mixture was then placed on a magnetic hotplate stirrer, and a stir bar was immersed to provide simultaneous stirring and heating.

Fabrication Process of RuO₂ Biosensor

The fabrication process of the RuO₂-coated thread followed the methodology described by [6]. Initially, 0.0104g of ruthenium trichloride hydrate (RuCl₃ · nH₂O) was dissolved in deionized water, resulting in a 10 ml solution with a concentration of 5 ml RuCl₃. Subsequently, the dropwise addition of a 5 ml NaOH solution was carried out until the precipitation of solid RuOH₃ precursor occurred. The obtained precursor was

isolated through centrifugation and then suspended in deionized water. The resulting suspension was evenly spread onto the thread, allowed to dry at room temperature, and subsequently subjected to an oven temperature of 350 °C for a duration of 3 hours. As a result, the RuO₂-coated thread was successfully formed.

Consequently, 1 ml of 25% glutaraldehyde solution and 4 ml of DI water were mixed and placed in microcentrifuge tubes. The RuO₂ deposited threads were dipped in the diluted glutaraldehyde solution and then heated to 50 °C in the oven for 30 minutes.

Evaluation Method

The evaluation of the rGO-PANI and RuO₂-based pH sensors involved designing pH solutions ranging from pH 5 to 9 and dropping them onto the electrodes. The potential was obtained using the zero current potentiometry method, and the assessment was repeated for each pH solution. The sensitivity and pH range were evaluated in this study.

RESULTS AND DISCUSSION

Figure 1 shows the conductive modified rGO-PANI electrode and RuO₂ thread sensor fabricated in this study.

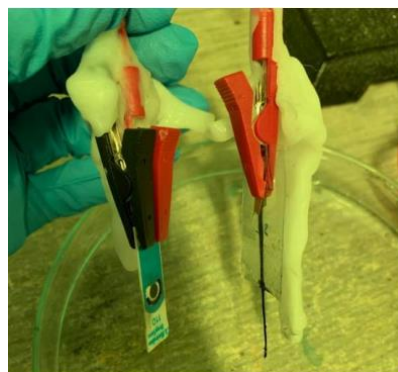


Figure 1. The fabricated conductive modified rGO-PANI electrode and RuO₂ thread sensor

Vollamogram of rGO-PANI Modified Electrode

The voltammogram of rGO electrode fabrication using the cyclic voltammetry (CV) technique is shown in Figure 2. The synthesis of the rGO-PANI composite involved chemically polymerising aniline monomers onto the surface of rGO sheets. The fabrication process of rGO comprised cyclically varying the potential between -0.2 and 1.2 V, with a scan rate of 50 mV/s, in a solution containing 1 mg/ml of graphene oxide solution for a total of 20 cycles.

Analysis of the CV data obtained during the fabrication process revealed distinct redox peaks, signifying the successful reduction of graphene oxide to rGO. The voltammogram of rGO displayed a clearly defined redox peak at a reduction potential of -0.5 V, aligning with the expected behaviour of rGO. This result shows that the CV method employed on a carbon thread proved effective in the fabrication of rGO from graphene oxide.

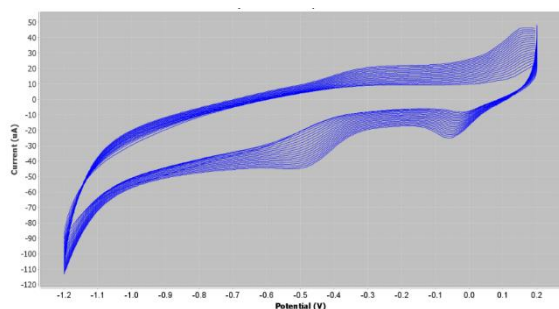


Figure 2. Voltammogram of rGO electrode fabrication using the cyclic voltammetry (CV) technique

While, Figure 3. presents the cyclic voltammogram achieved through the systematic variation of the potential applied to the working electrode, ranging from -0.2 V to 0.9 V, with a scan rate of 50 mV/s.

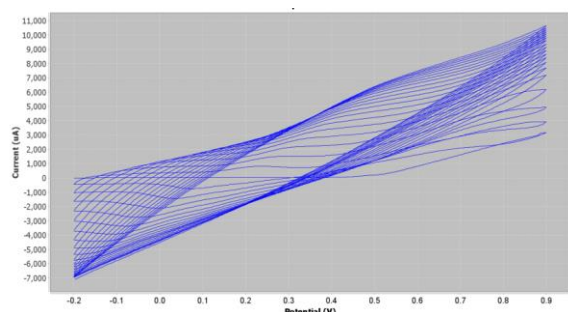


Figure 3. Voltammogram of electrodeposition of aniline on rGO-coated screen printed electrode

The experiment was conducted in a solution comprising 0.1 M aniline and 0.5 M sulfuric acid. The obtained voltammogram exhibited distinctive peaks, appearing at approximately 0.1 V and 0.8 V, representing the reduction and oxidation processes of polyaniline (PANI) respectively. The peak at 0.1 V corresponds to the reduction of PANI, transforming it from its emeraldine salt state to leucoemeraldine form. Conversely, the peak at 0.8 V corresponds to the oxidation of leucoemeraldine form back to the emeraldine salt state. Additionally, the voltammogram depicted a minor peak around 0.6 V, indicating the

occurrence of PANI doping.

The fabricated voltammogram of PANI on rGO carbon thread using cyclic voltammetry method provides important information on the electrochemical behavior of PANI. The rGO carbon thread provides a stable platform for the deposition of PANI, and the cyclic voltammetry method allows for precise control of the electrochemical polymerization process.

rGO-PANI and RuO₂-Based Sensors Assessment

Figure 4 and Figure 5 illustrate the response characteristics of these materials in relation to pH variations, specifically concerning the rGO-PANI modified electrode and the RuO₂-coated carbon thread. Open circuit potentiometry is a measurement technique determining the potential difference between two electrodes without any current flow. In this technique, when the sensor contacts a pH solution, a potential difference arises at the pH-sensitive electrode due to the hydrogen ion concentration difference with the reference electrode. This potential difference is measured without current flowing through the sensor.

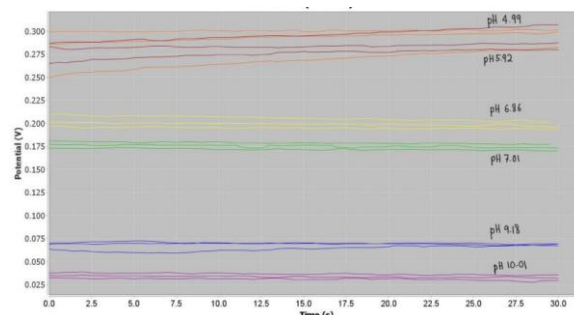


Figure 4. Open circuit potentiometry of rGO-PANI modified screen-printed electrode

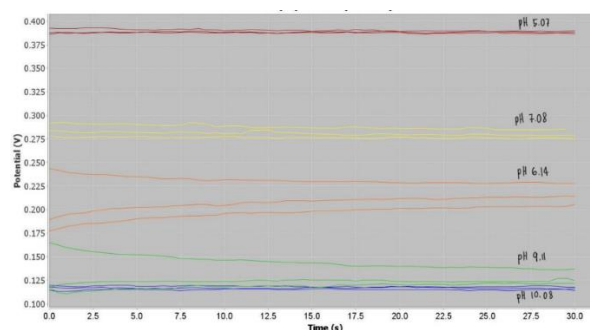


Figure 5. Open circuit potentiometry of RuO₂-coated carbon thread.

All sensors have a positive potential at low pH levels, which denotes their tendency to attract electrons. The potential of the sensors decreases

as the pH rises. At acidic pH levels, PANI commonly exists in its protonated state called emeraldine salt. During this state, the PANI demonstrates a positive electrical potential due to the existence of positively charged protons linked to the nitrogen atoms within the polymer chain. As the pH rises, the proton concentration diminishes, causing PANI to undergo deprotonation and convert into its emeraldine base form. In this form, PANI loses its positive charge, leading to a reduction in its electrical potential.

At high pH levels, the PANI is expected to be fully deprotonated, and the potential of the rGO-PANI sensor should turn negative. However, the potential of rGO-PANI sensor did not turn negative, and there can be certain factors that may influence or limit the extent of the potential shift. One of the contributing elements could be partial deprotonation, which might occur when the pH of the PANI is high and prevent it from totally deprotonating, resulting in a partial rather than full change in the negative potential. The PANI molecule's equilibrium or deprotonation kinetics may be constrained in this way. In addition, the potential response may be influenced by how the rGO-PANI surface interacts with the buffer solution or other species found in the solution. These surface interactions may hinder fully realising the negative potential shift at high pH levels. As a result, the sensitivity of the rGO-PANI sensor is -54.2 mV/pH in this study.

While for RuO₂-coated thread, at low pH values, the potential was positive, similar to the rGO-PANI coated carbon electrode, indicating an electron-attracting behavior. However, as the pH increases, the potential becomes more positive, demonstrating an enhanced affinity for electrons with increasing pH. The result also shows that the final sensitivity RuO₂ sensor obtained from the graph trendline is -47.7 mV/pH, which is lower than the rGO-PANI sensor.

CONCLUSION

This paper demonstrates that both rGO-PANI-modified electrodes and RuO₂ thread sensing can be used to detect pH. Although the RuO₂ sensor demonstrated a lower sensitivity compared to the rGO-PANI sensor, further evaluation needs to be conducted such as stability and response time to ensure the suitability of RuO₂ coated thread suitable for wearable e-textile pH sensing.

Acknowledgement

This project has received funding from Universiti Malaya Partnership Grant RK006- 2021, the European Union's Horizon 2020 research and innovation programme under the Marie Skłodowska-Curie grant agreement No. 872370 and 854194, and Universiti Malaya Impact Oriented Interdisciplinary Research Grant IIRG002A-2022HWB.

References

- [1] S. M. A. Iqbal, I. Mahgoub, E. Du, M. A. Leavitt, and W. Asghar, *Advances in healthcare wearable devices*, npj Flexible Electronics, **5**(1) (2021).
- [2] Y. Shi, Z. Zhang, Q. Huang, Y. Lin, and Z. Zheng, *Wearable sweat biosensors on textiles for health monitoring*, Journal of Semiconductors, **44**(2) (2023).
- [3] K. Du, R. Lin, L. Yin, J. S. Ho, J. Wang, and C. T. Lim, *iScience Electronic textiles for energy, sensing, and communication*.
- [4] M. Hirman, J. Navratil, M. Radouchova, J. Stulik, and R. Soukup, *Influence of Sweat on Joint and Sensor Reliability of E-Textiles*, Energies (Basel), **15**(2) (2022).
- [5] D. Liu et al., *Wearable Microfluidic Sweat Chip for Detection of Sweat Glucose and pH in Long-Distance Running Exercise*, Biosensors (Basel), **13**(2) (2023).
- [6] E. Tanumihardja, W. Olthuis, and A. van den Berg, Ruthenium oxide nanorods as potentiometric pH sensor for organs-on-chip purposes, *Sensors (Switzerland)*, **18**(9) (2018).

ANTIVIRAL ACTIVITY AGAINST NEWCASTLE DISEASE VIRUS OF RADIATION SYNTHESIS SILVER NANOPARTICLES CAPPED WITH LOW MOLECULAR WEIGHT CHITOSAN

Nguyen Trong Nghia, Nguyen Van Linh, Le Thanh Giau, Huynh Cong Duy, Nguyen Thi Le Thuy, **Le Quang Luan***

Biotechnology Center of Ho Chi Minh City, 374, Highway 1, Trung My Tay Ward, District 12, Ho Chi Minh City, Vietnam.

Email: lequangluan@gmail.com

ABSTRACT

Colloidal silver nanoparticles (AgNPs) with particle sizes about 5.2, 10.2 and 15.9 nm stabilized in low molecular weight chitosan (LMwC) were synthesized by γ -irradiation. The antiviral activity of AgNPs/LMwC samples was evaluated on Newcastle disease virus (NDV) via hemagglutination inhibition test using chicken red blood cell (RBCs) and the quantity of virus plaque assay by Real-time PCR using chicken embryo fibroblasts cells (CEF) as an infection model. After treating with AgNPs for 120 minutes, the results indicated that the agglutination activity of NDV with chicken RBC depended on the particle size of AgNPs/LMwC sample. The quantitative results analyzed by Real-time PCR revealed that the inhibition effect of AgNPs products on NDV was increased with a reduction of the particle size and an increase in silver content. Particularly, the virus's inhibition efficiency was about 63.5% at the treatment of 5 ppm AgNPs with particle size about 5.2 nm. At the same time, these efficiencies were determined about 76.2% and 67.1% in the treatment of 15 ppm AgNPs with particle size about 10.2 nm and 20 ppm AgNPs with particle size about 15.9 nm, respectively. This study demonstrates that AgNPs/LMwC and synthesized by γ -irradiation have strong antiviral activity against NDV. This product may potentially be used in poultry as a virucide for treating or preventing disease caused by NDV in particular and other viruses in general.

Keywords. Antiviral activity, Newcastle disease virus, silver nanoparticles, γ -irradiation.

INTRODUCTION

Newcastle disease (ND) is caused by an avian paramyxovirus belonging to the genus Avulavirus in the Paramyxoviridae family, a highly infectious and dangerous disease because it significantly affects poultry with a fast and widespread transmission, high morbidity, and mortality rate that can reach up to 100% if not treated promptly [1]. Newcastle disease is recognized as one of the major contributors to significant economic losses in the poultry industry worldwide [2].

Silver nanoparticles are already in high demand in various fields, including health care, medical, and industrial purposes, due to their unique physical and chemical properties. They have also been widely recognized as effective antimicrobial agents against various bacteria and fungi, including antibiotic-resistant strains, even at low concentrations [3]. In addition to their antibacterial and antifungal properties, AgNPs have recently been studied for their antiviral activities against several kinds of viruses such as

hepatitis B, herpes simplex, respiratory syncytial, H5N1 influenza A virus, human immunodeficiency virus (HIV1) and coronavirus (SARS-CoV-2) [4-5]. The primary antiviral mechanism of AgNPs is physical inhibition of the binding between the virus and host cell. Numerous research studies have explored the antiviral properties of AgNPs against animal viral diseases and have demonstrated that AgNPs can inhibit the Tacaribe virus in bats, infectious bursal disease virus, which causes Gumbo disease in chickens, and transmissible gastroenteritis virus (TGEV), a virus that can result in severe diarrhea in pigs. The antiviral activity of AgNPs can also be affected by the type of stabilizer used during their synthesis. For instance, a study showed that AgNPs stabilized by curcumin exhibit more excellent antiviral activity against RSV than those stabilized by citric acid [6].

Considering all of the above, a sound effect can be suggested if a new biological virucide is prepared using the combination of chitosan and

AgNPs. The objective of the present study was to synthesize AgNPs stabilized in LMwC by γ -irradiation method and evaluate their antiviral effectiveness against the Newcastle disease virus.

EXPERIMENTAL

Materials: Low molecular weight (Mw) chitosan with Mw ~130 kDa, chicken embryo fibroblasts (CEF) cell line and NDV solution were provided by the Biotechnology Center of Ho Chi Minh City (Vietnam). Other pure-grade chemicals were used without purification, and distilled water was used throughout the experiments.

Preparation of silver nanoparticles by γ -irradiation: Colloidal AgNPs/LMwC were prepared by the γ Co60 irradiation method with a dose rate of 10 kGy/h by a Gamma cell (GC 5000, BRIT, India) at the Biotechnology Center of Ho Chi Minh City at Ag⁺ concentrations of 1.0, 5.0 and 10 mM with radiation doses from 12, 24 and 36 kGy, respectively [7].

Identify sizes of AgNPs/LmWC: The synthesized AgNPs size and morphological characteristics were identified by TEM (model JEM 1400, JEOL, Japan) and statistically calculated from about 300 particles following the method described by Luan *et al.*, [7].

Prepare Newcastle disease virus: The virus was cultured and activated using chicken embryo fibroblast (CEF) primary cells in RPMI (Roswell Park Memorial Institute) medium culture containing 5% FBS (Fetal bovine serum) and 1% streptomycin/penicillin at a temperature of 38.5°C and 5% CO₂. When the cells reached 90% confluence, NDV stock solution was added to the cell culture dish and incubated for 5 minutes. Then, RPMI medium culture containing 0.5% FBS and 1% streptomycin/penicillin was added, and the cells were further incubated under the same conditions. After 24 hours, the virus was harvested by centrifugation, and the cells were removed. The harvested virus was used to infect the next round of cells for virus propagation and activation. After three passages of cell culture and virus infection, the virus was collected and concentrated using a super centrifugation method with a sucrose density gradient.

Prepare a 1% chicken red blood cell solution: 1 mL of the chicken blood was centrifuged at 800 rpm for 5 minutes to collect the RBCs residue while removing leukocytes and serum. The RBCs were washed thrice by mixing the residue with 1X PBS (Phosphate-buffered

saline) and centrifuging at 800 rpm for 5 minutes each time. The washed RBCs were diluted with 1X PBS to obtain a 1% RBCs solution. These RBCs suspensions were used in spot and plate hemagglutination tests.

The hemagglutination (HA) inhibition test:

The virus was treated with AgNPs/LMwC of different particle sizes (5.2, 10.2 and 15.9 nm) at a concentration of 20 ppm for various time intervals (30, 60, 90, 120 and 150 minutes). After treatment with AgNPs, the virus solution was collected by super-centrifugation with a sucrose density gradient. The HA test was conducted using a U-bottom 96-well plate. Initially, 50 μ L of 1X PBS was dispensed into all wells except for the first series. Next, 100 μ L of viral fluid treated with AgNPs was added to the first well, and a secondary dilution of the treated virus samples was performed. Subsequently, 50 μ L of 1% chicken RBCs solution was added to all wells. The ability of the virus to agglutinate chicken erythrocytes was used to determine its virulence [8]. The agglutination titres of the untreated virus group were compared with those of the treated virus group with AgNPs/LMwC.

The quantity of virus plaque assay by real-time PCR: CEF cells were cultured in a 24-well plate with an initial cell density of 2×10^5 cells/well, and incubated at 38.5°C and 5% CO₂ in RPMI medium supplemented with 10% FBS and 1% Streptomycin/Penicillin for 24 hours until the monolayer of cells covered 90% of the culture surface. Afterward, the AgNPs/LMwC-treated virus solution was added to each well at various concentrations, and the cells were incubated for 1 hour at 38.5°C and 5% CO₂. Then, 0.5 mL of fresh culture medium was added to each well, and the cells were further incubated at 38.5°C and 5% CO₂ for 48 hours [8]. After removing the culture medium, the cells were washed with PBS and collected for RNA extraction using Trizol. The extracted RNA was dissolved in 20 μ L of DEPC-treated water (diethylpyrocarbonate), stored at -80°C, and quantified using real-time-PCR with the Maximo One Step RT-qPCR kit Green (Gene One), using specific primers NVD-F: TAGGTGTAG GGAACAATCAACTCAGC and NDV-R: CCCTGGTTGTGCTTACGGAT for NDV.

RESULTS AND DISCUSSION

In this study, solutions containing different concentrations of silver ions (1, 5, and 10 mM) stabilized in 3% chitosan with a low molecular

weight of around 130 kDa were irradiated at 8, 16 and 28 kGy, respectively. As shown in Figure 1, the peak intensity values of the irradiated samples in UV-Vis spectra decreased from 1.05 to 0.75 as the silver concentration in the irradiated sample increased from 1 to 10 mM. At the same time, the λ_{\max} values of these samples shifted from 400 to 412 nm. TEM images and corresponding histograms of particle size distributions of AgNPs in Figure 1 also showed that the AgNPs were almost spherical. The average particle size in AgNPs product was increased by the increase of Ag^+ concentration in the solution. Additionally, the average size of AgNPs is about 5.2 nm at Ag^+ concentration of 1.0 mM, and it was increased to

10.2 and 15.9 nm when the Ag^+ concentration increased to 5.0 and 10 mM, respectively. The stabilizing effect of silver nanoparticles and the ability to capture OH^\bullet radicals of chitosan are because in an aqueous solution, Ag^+ forms a complex with chitosan by electrostatic bonding with the amine group (NH_2Ag^+). When exposed to irradiation with solvated electrons (e_{aq}^-) and H^+ , Ag^+ is reduced to Ag^0 . This creates stable silver nanoparticles on the lattice structure of chitosan. Moreover, the chitosan-coated silver nanoparticles have a high positive charge on their surface (due to the protonation of the $-\text{NH}_2$ group), enhancing the antibacterial activity of the AgNPs.

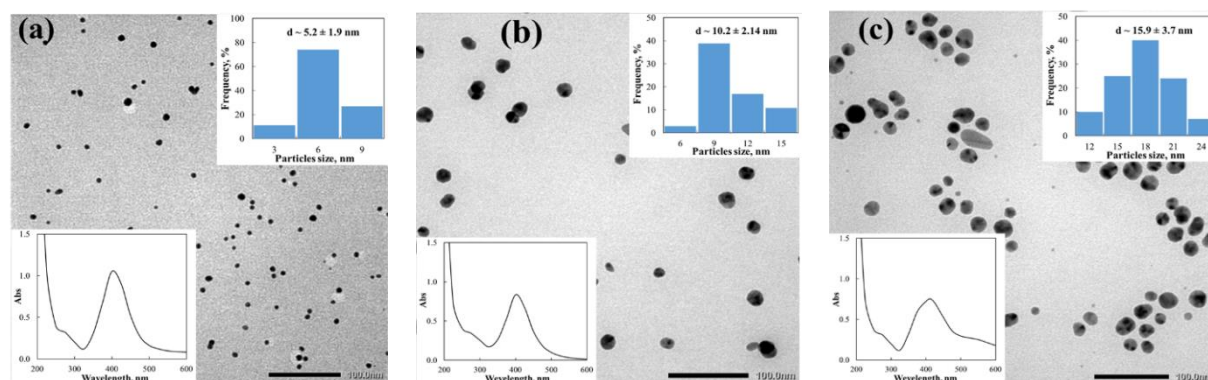


Figure 1. UV-Vis spectra, TEM images and particle size distributions of AgNPs/LMwC samples (a: 5.2, b: 10.2 and c: 15.9 nm)

The antiviral effect of AgNPs/LMwC by RBCs agglutination: The viral, which is collected through sucrose density ultracentrifugation accumulated fluid, was tested for its activity by measuring its ability to agglutinate chicken erythrocytes. The results of the test indicated that the highest virus dilution at which the virus was capable of causing erythrocyte agglutination was 1/32 (Figure 2). The strength of the viral activity increased as the dilution increased. The titer of the NDV samples, which were collected and used to evaluate the inhibitory efficacy of AgNPs, was determined at a viral dilution of 1/32. The NDV sample was treated with AgNPs of different sizes (5, 10, and 15 nm) at a concentration of 20 ppm for various processing times (30, 60, 90, 120 and 150 min). The efficacy of AgNPs treatment on viral activity was evaluated by assessing chicken erythrocyte agglutination. The results showed that AgNPs of different sizes did not cause erythrocyte agglutination and did not affect the viral activity at 30, 60 and 90 min treatment times. However, after 120 and 150 min treatment times, the viral

activity decreased, resulting in erythrocyte agglutination titers at 1/16 dilution for all three AgNPs sizes. Thus, the study recorded a reduction in the activity of the NDV after treatment with AgNPs for 120 minutes.

The antiviral effect of AgNPs/LMwC by Realtime-PCR: The antiviral effects of silver nanoparticle-based substances were validated by treating the NDV with AgNPs for 120 minutes and then infecting CEF cells. Two days post-infection, viral RNA was extracted from the infected cell medium and analyzed using quantitative realtime-PCR to detect NDV genes. The results in Figure 5 show that the virus inhibition efficiency of AgNPs/LMwC with a particle size of about 5.2 nm was found to be around 63.5% at a treatment concentration of 5 ppm. The antiviral effect increased by 76.7% when the concentration of AgNPs was increased to 10 ppm. Furthermore, when the size of AgNPs was increased to approximately 10.2 nm, the inhibitory effect increased to 76.2% at a treatment concentration of 15 ppm compared to the control sample (Figure 3). Additionally, the results

depicted in Figure 5 demonstrate that a virus inhibitory efficiency of 67.1% was achieved when treated with 20 ppm AgNPs of approximately 15.9 nm in size.

Yin et al. (2013) [9] conducted a study on the *in vitro* inhibition of NDV by silver nanoparticles and found that AgNPs have an inhibitory effect on NDV. They suggested that this effect may be

due to the binding of AgNPs to the cell surface receptors, changing their conformation and thereby reducing the number of virus particles binding to the cell surface. Additionally, they proposed that AgNPs may interact with the virus attached to the cell surface, damaging its capsid and preventing the adsorption and entry of the virus into the cell.

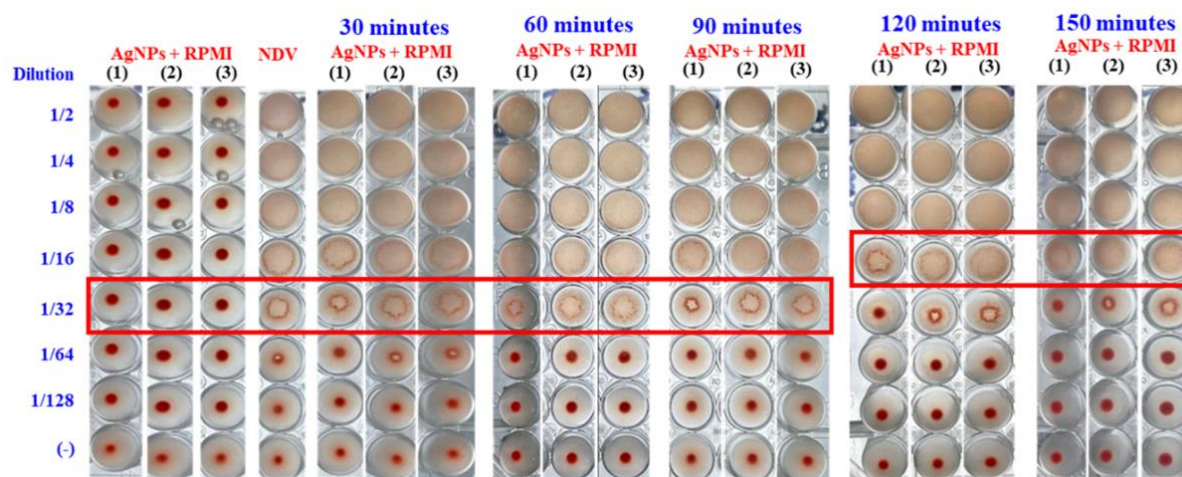


Figure 2. The erythrocyte agglutination rates were determined after treating with NDV and AgNPs/LMwC with different particle sizes at various time intervals: (1) 5.2 nm, (2) 10.2 nm, and (3) 15.9 nm. AgNPs + RPMI: only AgNPs in culture medium, none NDV; NDV stock: NDV untreated.

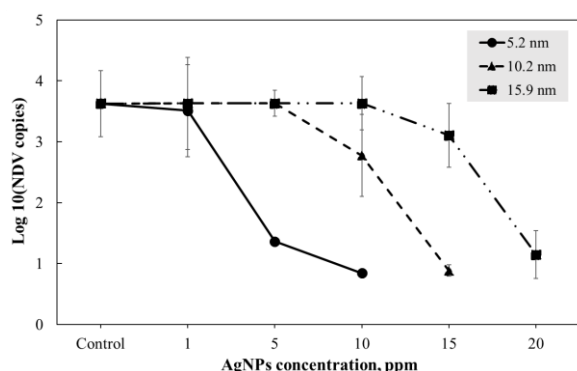


Figure 3. Virucidal activity of AgNPs/LMwC against NDV identified in Realtime-PCR

CONCLUSION

AgNPs/LMwC products with particle sizes of about 5.2, 10.2, and 15.9 nm were successfully synthesized by γ -irradiation. These products show inhibitory activity on the NDV in the process of infecting cells, with an inhibitory effect of 63.5 - 76.2% under *in vitro* conditions. Thus, AgNPs/LMwC synthesized by the γ -irradiation method could be potentially and effectively used as a virucidal product to control NDV, a serious pathogenic virus in poultry.

References

- [1] B.T.L. Minh, N. M. Thuong, *Effect of garlic on immune response of pheasants to Newcastle disease virus vaccine*, J. Sci. Can Tho Uni., **58**(1) (2022) 143-147.
- [2] R. Ananth, J.J. Kirubaharam, M.L.M. Priyadarshini, A. Albert, *Isolation of NDV of high virulence in unvaccinated healthy village chickens in south India*. Int. J. Poul. Sci., **7**(4) (2008) 368-373.
- [3] H.S. Shin, *Mechanism of growth of colloidal silver nanoparticles stabilized by polovinyl pyrrolidone in γ -irradiated silver nitrate solution*, J. Colloid. Interface. Sci., **274**(1) (2004) 89-94.
- [4] M.J. Saadh, S.M. Aldalaen, *Inhibitory effects of epigallocatechin gallate (EGCG) combined with zinc sulfate and silver nanoparticles on avian influenza A virus subtype H5N1*. Eur. Rev. Med. Pharmacol. Sci., **25**(6) (2021) 2630-2636.
- [5] S.S. Jeremiah, K. Miyakawa, T. Morita, Y. Yamaoka, A. Ryo, *Potent antiviral effect of AgNPs on SARS-CoV-2*, Biochem. Biophys. Res. Commun., **533** (2020) 195-200.
- [6] R. Pangestika, R. Ernawati, *Antiviral activity effect of silver nanoparticles solution against the growth of infectious bursal disease virus*

- on embryonated chicken eggs with elisa test*, The Veterinary Medicine International Conference, (2017) 536–548.
- [7] L.Q. Luan, D.H. Xo, *In vitro and in vivo fungicidal effects of γ -irradiation synthesized silver nanoparticles against Phytophthora capsici causing the foot rot disease on pepper plant*, J. Plant. Pathol., **100** (2018) 241–248.
- [8] OIE. *Newcastle disease terrestrial manual 2012. Version adopted by the world assembly of delegates of the OIE.*, Paris, France, (2012).
- [9] J. Yin, X. Li, C. Zheng, *Mechanisms and inhibitory effects of silver nanoparticles against Newcastle Disease Virus in vitro*. China Poult., (2013) 15:006.

POSTER SESSIONS

*FUNDAMENTALS OF
NANOTECHNOLOGY*
(FON)

NANOMATERIALS AND NANOTECHNOLOGY IN CONSTRUCTION INDUSTRY – NANO CEMENTS AND NANO CONCRETES

Tran Cong Phong^{1,2}, Nguyen Thi Le Thuy³, Tran Cong Quang Anh⁴, Nguyen Thanh Nhon^{1,5}

¹Institute for Advanced Study in Technology, Ton Duc Thang University, Ho Chi Minh City, Vietnam;

²Faculty of Electrical and Electronics Engineering, Ton Duc Thang University, Ho Chi Minh City, Vietnam

³R&D Department, BSB Nanotechnology Joint Stock Company, Ho Chi Minh City, Vietnam

⁴School of Architecture and Urban Planning, Nanjing University, Nanjing, Jiangsu, China

⁵Faculty of Civil Engineering, Ton Duc Thang University, Ho Chi Minh City, Viet Nam

Email: tranconghong@tdtu.edu.vn

ABSTRACT

Nanotechnology has evolved over the past two decades, bringing about significant innovations and achievements across all industries. In the construction industry, new-generation materials like nano-cement and nano-concrete demonstrate how nanotechnology and nanomaterials can impart extraordinary properties to materials. These properties include enhancing physical and mechanical attributes, prolonging material durability, and increasing tolerance to harsh climatic conditions, salinity, alum, or corrosive substances like caustic soda and acids. With their small size and large surface area, nanomaterials are used in small quantities but offer high efficiency, contribute to economic growth, reduce material usage, and are environmentally friendly. In this paper, we introduce nanomaterials, nanotechnology and their roles in the construction industry.

Keywords: Nanocement, nanoconcretes, nanotechnology, nanomaterial, construction industry.

INTRODUCTION

Nanotechnology involves the manipulation of matter at the atomic and molecular scale. Nanomaterials are materials with at least one dimension in the nanometer range, which typically spans from 1 to 100 nanometers. At this scale, materials exhibit unique properties that differ from those of their bulk counterparts.

Nanomaterials and nanotechnology have the potential to revolutionize the construction industry. These materials can be used to develop new building materials with enhanced properties, such as strength, durability, ductility, and fire resistance. Nanotechnology can also be used in the development of more efficient and sustainable construction methods and techniques.

Some of the potential applications of nanomaterials and nanotechnology in the construction industry can be listed as Self-healing concrete, Lighter and stronger building materials, Smart coatings, Nanoparticle sensors,...

Besides, construction materials such as Cement and Concrete with particles in nano scale will enable extraordinary properties in each application. We will discuss these materials and their benefits in detail in the following sections.

NANOMATERIALS IN CONSTRUCTION INDUSTRY

Traditional materials constituting construction mixtures normally cause serious shortcomings that not only impose constraints in structural design, but also affect the long-term durability of structures [1]. This is because of the inner structure, arrangement and bonding of different components of cementitious composites.

Types of nano materials

a. Nano Titanium dioxide (TiO₂)

b. Carbon nanotubes (CNT's)

c. Nano silica (NS)

d. Nano-clay

e. Nano Polycarboxilates

f. Nano Cr₂O₃, Nano Fe₂O₃, etc.

In the following sections, we introduce in detail the roles of each nano materials in construction products, through analyzing the principles and mechanisms of connection of materials in the matrix of products.

NANOTECHNOLOGY IN CONSTRUCTION INDUSTRY

There are some definitions of Nanotechnology. In general, Nanotechnology,

defined by the National Nanotechnology Initiative, is the manipulation of nanomaterials. It is inclusive of all types of research and technologies that deal with these special properties. This field is related to the creation and production of these materials, as well as their toxicity and environmental impact.

Discovering the roles of nanotechnology in construction industry is also to find the reason to develop these new technologies.

Nanotechnology has the potential to revolutionize the construction industry in a number of ways. For example, nanomaterials can be used to develop new building materials with enhanced properties, such as strength, durability, ductility, and fire resistance. Nanotechnology can also be used to develop new construction methods and techniques that are more efficient and sustainable.

Here are some specific examples of the roles of nanotechnologies in the construction industry:

Self-healing concrete – Nanomaterials can be used to develop concrete that can repair itself when cracks occur. This reduces the need for maintenance, lowers costs, and extends the lifespan of concrete structures by improving their durability and self-healing properties. By incorporating nanoparticles into the concrete mixture, the material can repair itself over time by self-healing cracks and weak spots.

Lighter and stronger building materials: Nanomaterials can serve as building materials due to their lightweight and enhanced strength compared to traditional materials. This reduction in weight leads to cost savings in construction, increases earthquake resistance, and simplifies transportation. Furthermore, these materials enable faster construction timelines, and improved energy efficiency, help minimize waste and reduce the environmental impact of building projects. Some common examples of lightweight and strong building materials include insulated concrete forms, structural insulated panels, and engineered wood products. By utilizing these materials, architects and builders can create durable and sustainable structures that meet the demands of modern construction.

Smart coatings: Nanomaterials can be used to develop coatings that can change color, temperature, or other properties in response to environmental stimuli. This innovation holds the potential to make buildings more energy-efficient and comfortable for their occupants. Nanomaterials in smart coatings offer numerous

benefits, including improved durability, enhanced optical properties, and reduced weight. These tiny particles can be tailored to provide specific properties, such as self-healing, anti-corrosion, and UV protection. With their unique surface properties, nanomaterials can also improve the overall performance of the coating, leading to a more efficient and sustainable application.

Nanoparticle sensors: Nanoparticle sensors are also achievements of nanotechnology. They can be used to monitor the condition of buildings and infrastructure in real time. This could help to identify potential problems early on and prevent catastrophic failures.

In addition to these specific examples, nanotechnology can also be used to improve the efficiency and sustainability of the construction industry in a number of other ways. For instance, nanotechnology can introduce new approaches for recycling construction materials and reducing the energy consumption of construction processes.

Along with the strong development of nanotechnology, there is an expansion of applications into multi-industry and multi-function applications. Indeed, we can list some additional potential applications of nanomaterials:

Fire-resistant materials: Nanomaterials can be used to develop fire-resistant materials that can protect buildings and infrastructure from fires.

Antibacterial and self-cleaning materials: Nanomaterials can be utilized to create antibacterial and self-cleaning materials. These materials are designed to reduce the spread of diseases within buildings while also protecting their surfaces, people, and the environment.

Energy-efficient materials: Nanomaterials can also improve the thermal and chemical properties of concrete, making it more sustainable and energy-efficient. This can help to reduce the energy consumption of buildings.

Environmental remediation materials: Nanomaterials can be used to develop environmental remediation materials that can help to clean up contaminated soil and water.

Overall, nanotechnology has the potential to make a significant impact on the construction industry. As nanotechnology continues to develop, we can expect to see even more innovative and groundbreaking applications in the years to come.

NANOCEMENTS

Nanomaterials applied in Cements made important developments as mentioned ultrahigh strength, photo catalytic, self-heating, bendable.

Starting from the constituent of cements, namely calcium carbonate, silica, aluminium, and iron ore, improvements have been achieved by the addition of Nanoparticles in the cement namely Nano silica and Silica Fume, Titanium Dioxide, Iron oxide, Chromium oxide and nano clay [2].

Nanosilica takes important role in hydration of cement relating to C-S-H gel, calcium silicate hydrate, or calcium hydroxide monohydrates etc. Some studies predicted and verified that partial replacement of cement with nanosilica increases durability, high performance of material, besides reduce the cost and efforts thank for the low amount used.

The capillary pores of concrete decrease significantly by addition nanosilica, and the inner structure thus compressive strength enhances. P.Di Mida et al. observed the increasing of 8 to 18 % enhancement in the compressive strength if using nanosilica instead of silica powder [3].

Some benefits of nanosilica presented in the research of Ref. 4, such as improving strength, workability and setting time, heat of hydration, fire and abrasion resistance or leaching. These results were also highlighted by Meral et al. [5] and V. Ershadi et al. [6] while founding the improve impermeability and physical properties as compressive strength of the hardened material with addition of Nanosilica.

Nano Titanium Dioxide used for anticorrosion, self-cleaning concrete or photocatalytic concrete, or smog eating concrete or green concrete, besides environmental pollution cleaning and self-disinfecting.

Sorathiya [1] proved that nano-TiO₂ in concrete that had appreciably higher compressive strength, with optimum concentration of 1 %, comparable to that of the normal concrete, by increase in strength as the pores has been filled with this nanomaterial. This emphasized one more time the high economy and performance of nanomaterials with very low percentage used.

Nano Iron III oxide (Fe₂O₃) at 1.0 % in cement and concrete also improved their strength, in an observation of Nazari. According to the research, nano- Fe₂O₃ increase High Performance

Concrete (HPC) or high strength concrete (HSC) with slight increase in cost.

Nano Chromium III Oxides (Cr₂O₃) used less in this industry, but still there are some benefits from this material. Nano Cr₂O₃ improves both

flexural strength and splitting tensile strength. A reduction of water absorption was also observed in the samples with those NPs. The pore structures of self-compacting concrete containing Nano Cr₂O₃ is improved also increasing the content of all meso pores and macro pores [7].

Nanoclay is a wider group of nano minerals and described as hydrous silicates. The large surface area of these NPs and their abundance because of their small size can facilitate the chemical reaction to produce a dense cement matrix with more calcium silicate hydrate (C-S-H) and less calcium hydroxide [2].

Carbon Nano Tube (CNT) and carbon nanofiber can increase the resistance of the cement-based materials (CBMS) to rebar corrosion. Furthermore, the incorporation of CNT and carbon nanofiber in the reinforced cement composite delays the onset of active corrosion of rebar and reduces the corrosion rate of rebar, which results from the reduced porosity of the matrix and the controlled coalescing process of cracking [8].

Nano polycarboxylates are increasingly being used in the construction industry due to their unique properties, such as high strength, durability, and sustainability. These nanomaterials can improve the mechanical performance of construction materials, including concrete, mortar, and grout. They can also enhance the environmental resistance of building materials and reduce the need for chemical additives. In summary, nano polycarboxylates are a promising innovation in the construction industry, offering improved performance and sustainability.

Polycarboxylate ether plasticizer (PCE) and NanoSilica in admixtures of cements pastes enhanced mechanical strengths, produced high packing density and accelerated the pozzolanic activity to produce more C-S-H gel by consuming calcium hydroxide Ca(OH)₂ in order to improve the mechanical properties of cement pastes [9].

Some nanomaterials extracted from agriculture or upcycled from by-products of other industries, such as nanocellulose, have the capability to increase the durability of buildings by improving their mechanical and thermal properties [10]

NANOCONCRETES

Concrete is a composite material of nano to micro components, which means it can be enhanced at both microscopic and nanoscopic levels in its development.

Nanotechnology has the potential to revolutionize the concrete industry by helping us to develop new and improved concrete materials. It can help us gain a deeper understanding of how concrete behaves at the nanoscale, potentially leading to innovative methods for enhancing its strength, durability, and sustainability. Furthermore, nanotechnology can contribute to reducing the environmental impact of concrete production and construction.

As cement is a major constituent in the concrete, all properties and benefits of nanotechnology applicable to cement will also enhance Nano concrete. We discussed benefits of nano materials in previous section.

CONCLUSION

Nanotechnology is still a relatively new technology, but it has the potential to have a major impact on the construction industry. As research in this area progresses, we can expect to see more and more innovative and groundbreaking applications of nanomaterials and nanotechnology in the years ahead.

The researchers and producers continuously work to improve the durability and sustainability of concrete. They have achieved a significant increase in material strength by incorporating nanoparticles.

These materials are expected to be green, high efficiency for sustainable future.

References

- [1] J. Sorathiya, *Effect on Addition of Nano "Titanium Dioxide" (TiO₂) on Compressive Strength of Cementitious Concrete*, Kalpa Publications in Civil Engineering **1** (2017) 219-225.
- [2] More Hitesh, *A Review on Nano Materials in Cement*, International Journal for Research in Applied Science and Engineering Technology **8** (2020) 362-366.
- [3] P. Di. Maida, et al., *Pullout behaviour of polypropylene macro-synthetic fibers treated with nanosilica* Elsevier-Material and Design **82** (2015) 39-44.
- [4] A.M. Rashad, *A comprehensive overview about the effect of nano-SiO₂ on some properties of traditional cementitious materials and alkali-activated fly ash*, Construction and building materials **52** (2014) 437-464.
- [5] Meral Oltulu, S. Remzi, Ahin, *Single and combined effects of nano-SiO₂, nano-Al₂O₃, and nano-Fe₂O₃ powders on compressive strength and capillary permeability of cement mortar containing silica fume*, Elsevier-Material Science and Engineering A **528** (2011) 7012-7019.
- [6] V. Ershadi, T. Ebadi, A.R. Rabani, L. Ershadi, H., *The Effect of Nanosilica on Cement Matrix Permeability in Oil Well to Decrease the Pollution of Receptive Environment.*, Soltanian Int. Jour. of Environmental Science and Development **2** (2011) 2.
- [7] A. Nazari, S. Riahi, *Abrasion resistance of concrete containing SiO₂ and Al₂O₃ nano particles in different curing media*, Energy building **43** (2011) 2939-2946.
- [8] S. Du, J. Wu, et al, *Nanotechnology in Cement-Based Materials: A Review of Durability, Modeling, and Advanced Characterization*, Nanomaterials (Basel) **9** (2019) 1213.
- [9] S amar Madjid, et al., *Influence of nanosilica and a polycarboxylate superplasticizer on the rheological and electrokinetical properties of cement pastes*, Scientific Research and Essays **9** (2014) 1003-1118.
- [10] H. Saleem, et al., *Recent Advancements in the Nanomaterial Application in Concrete and Its Ecological Impact*, Materials (Basel) **14** (2021) 6387.

AB INITIO STUDY OF HYDROGENATED TWO-DIMENSIONAL SILICON CARBIDE

Phi Minh Nguyen and Tran Thi Thu Hanh

Laboratory of Computational Physics, Faculty of Applied Science, Ho Chi Minh City University of Technology (HCMUT), Vietnam National University Ho Chi Minh City, Ho Chi Minh City, Vietnam.

Email: nguyenminhphi228@gmail.com

ABSTRACT

For a better understanding of two-dimensional silicon carbide (2D-SiC) characteristics in fuel cell applications and semiconductor devices, the interaction between 2D-SiC and hydrogen was simulated using the ab initio method. Hexagonal prisms 2D-SiC have been created using the bond length obtained from molecular dynamics simulation. The converged cut-off energy is 200 Ry, and a suitable number of k-points, (3×3×1) MP, were used for the 98-atom 2D-SiC model. Out of the four tested adsorption sites, only two were found to be stable: on top of Si and on top of C. Other adsorption sites were determined to be unstable, with the adsorbed hydrogen atoms relaxing back to the more stable configuration on top of the Si atom.

Keywords: 2D material, density functional theory, fuel cell.

INTRODUCTION

To replace fossil fuels, one of the valuable and promising candidates is fuel cells. Hydrogen fuel cells, with outstanding characteristics such as environmental friendliness, renewability, and applicability in the transportation, and energy industry [1-3], are the answer to fuel shortages and environmental pollution caused by fossil fuels. To produce materials suitable for various fuel cell applications, computational simulations are essential.

The existence of 2D-SiC was first predicted through first-principles calculations combined with statistical physics at high temperatures by the research group of Yakobson and Shi in 2015 [4]. In the same year, Shisheng Lin and colleagues synthesized the first thin SiC sheets with thicknesses ranging from 0.3–5 μm through high-temperature chemical reactions between graphene and Si [5]. By 2021, 2D-SiC was finally realized when Sakineh Chabi's research group successfully exfoliated wet 2D-SiC layers from the hexagonal 6H-SiC, yielding ultra-thin 2D-SiC sheets with a thickness of only 0.25 nm. This result was surprising because the sp^3 bonds in 6H-SiC are much stronger than the van der Waals bonds in graphene, making it challenging to exfoliate the layers. Their findings showed that 2D-SiC can exist stably under standard conditions without structural changes over time [6]. Research also revealed that the structure of 2D-SiC is entirely flat, with both Si and C atoms lying in the same

plane, devoid of any corrugation seen in materials like silicene and germanene [7, 8]. This indicates a complete sp^2 hybridization between Si and C, similar to that in graphene. However, the Si-C bond length fluctuates between 1.77 and 1.85 \AA [9], larger than the carbon-carbon bond length in graphene (1.42 \AA), making the hexagonal lattice of 2D-SiC about 20 – 30% larger. The larger surface area of 2D-SiC could enhance its hydrogen adsorption capacity compared to graphene. In graphene, the short C-C bonds do not provide enough sites for hydrogen adsorption, resulting in a low hydrogen adsorption density of less than 1 wt% under standard conditions [10, 11]. With longer bonds, there is reason to believe that SiC can easily adsorb hydrogen with a 1:1 adsorption ratio, one hydrogen per Si or C surface atom.

CALCULATION

To obtain a stable 2D SiC model, we employed molecular dynamics simulations using the LAMMPS (Large-scale Atomic/Molecular Massively Parallel Simulator) package. The objective of this classical simulation was to determine the Si-C bond length at 300K using the Vashista potential [12]. After multiple heating and cooling steps, the final Si-C bond length was established at 1.787 \AA . Subsequently, this bond length was employed in the initial setup for ab initio calculations.

The first principle calculation was carried out using the SIESTA (Spanish Initiative for Electronic Simulations with Thousands of Atoms), based on the DFT method to calculate the ground-state energies. The calculation was carried out by norm-conserving pseudopotential, Perdew–Burke–Ernzerhof approximation for the exchange and correlation energy, double-zeta polarized basis set, force tolerance of 0.02 eV/Å and convergence energy test for both k-point set and cutoff energy.

After obtaining a fully relaxed 2D SiC model, we proceeded with a hydrogen adsorption simulation. We place a hydrogen atom on top of a potential adsorption site. The structural optimization, facilitated by conjugate gradients in SIESTA, helped us identify the most stable adsorption site for hydrogen. All ground state energies were recorded and analyzed to determine the most stable hydrogen adsorption configuration.

RESULT AND DISCUSSION

The initial 2D SiC model was cut from the previous MD simulation and consisted of 98 Si and C atoms. The coordinates of these atoms were brought into the SIESTA simulation (See Figure 1). A larger unit cell was chosen to minimize boundary interactions. Periodic conditions were applied in two dimensions. For the third dimension, a vacuum space of 40 Å was created to eliminate interactions in the repeated layer. Different models require different suitable numbers of k-points and cutoff energy, so we conducted converged energy tests for k-point and cutoff energy.

The number of k-points was gradually increased from (1×1×1) to (13×13×1) using Monkhorst Pack (MP) (See Figure 2). Energy convergence was achieved with a small number of k-points, specifically (3×3×1) MP, due to the large number of atoms already present in the 2D SiC unit cell. Because a large number of k-points can slow down the simulation, we determined that (3×3×1) was sufficient for energy calculations.

The cutoff kinetic energy was also tested, ranging from 50 Ry to 300 Ry (as shown in Figure 3 and Table 1). After 100 Ry, the total energy began to stabilize, and we chose 200 Ry for the stable cutoff energy. The combination of (3×3×1) MP k-points and 200 Ry for cutoff energy produced the 2D SiC model with a 1.85 Å for Si-C bond length and a honeycomb structure with 120° angle (See Figure 4). These results for bond

length, k-points, and cutoff energy will be used in subsequent calculations.

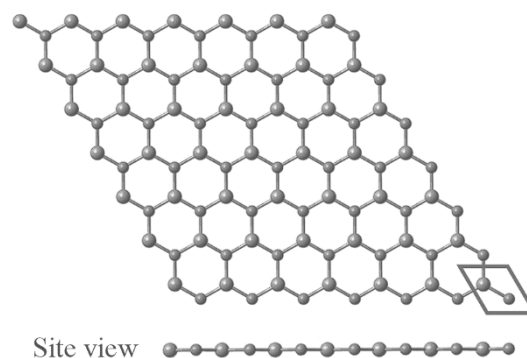


Figure 1. The 2D-SiC prism model was extracted from the MD simulation, displaying a) the top view and b) the side view.

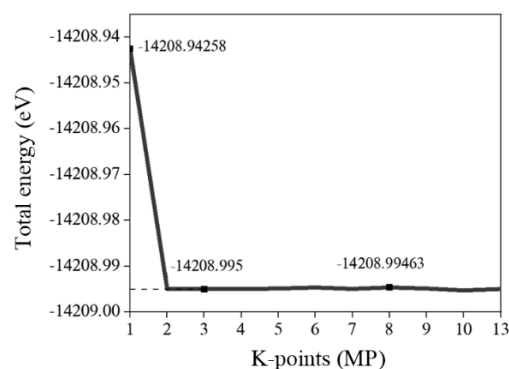


Figure 2. Total energy converged through different k-point results.

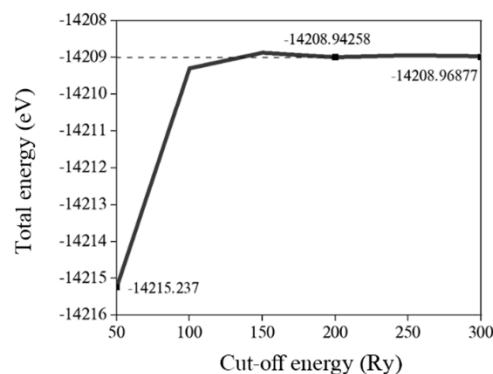


Figure 3. Total energy converged through different cut-off energy results.

Table 1. The total energy of 2D-SiC with different cut-off values.

Cut-off energy (Ry)	Total energy (eV)
50	-14215.23772
100	-14209.29754
150	-14208.87478
200	-14208.94258
250	-14208.94226
300	-14208.96877

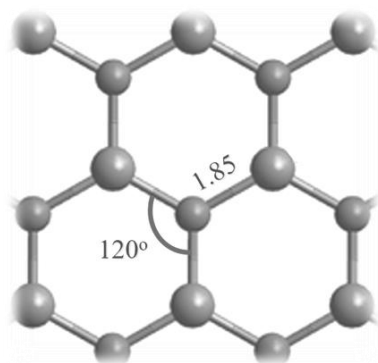


Figure 4. The relaxed structure of 2D-SiC.

For the hydrogen adsorption simulation, a hydrogen atom was placed on top of the adsorption site, maintaining a distance of 1.5 Å from the 2D-SiC surface. This distance was chosen based on our experience with hydrogen models [13-15], as hydrogen bond lengths are typically around 1.75 Å in molecular form [16]. This distance strikes a balance between proximity to the relaxed results, ensuring the adsorption reaction occurs, and minimizing calculation time.

Four adsorption sites for hydrogen were tested, including on top of the C atom (T_C), on top of the Si atom (T_{Si}), at the honeycomb center (C), and in the middle of the Si-C bond (Bridge site) (as shown in Figure 5). All adsorption sites were symmetrically chosen across a 2D-SiC unit cell surface to identify all locally favorable adsorption sites. The simulation was initially run with $(3 \times 3 \times 1)$ k-points and a 200 Ry mesh cutoff, which was determined from previous convergence tests to provide quick results.

The coordinate optimization by conjugate gradients minimizes the forces on the model and automatically moves the hydrogen atom to the local minimum positions. Out of four adsorption site, only two adsorption site are stable, which is T_C and T_{Si} . After the optimization, hydrogen on both center and bridge sites are unstable and move to the more stable T_{Si} site. With these results only T_C , and T_{Si} will be considered in further calculation. These results predict the change of Si-C bonding from sp^2 to sp^3 , similar in graphene [1].

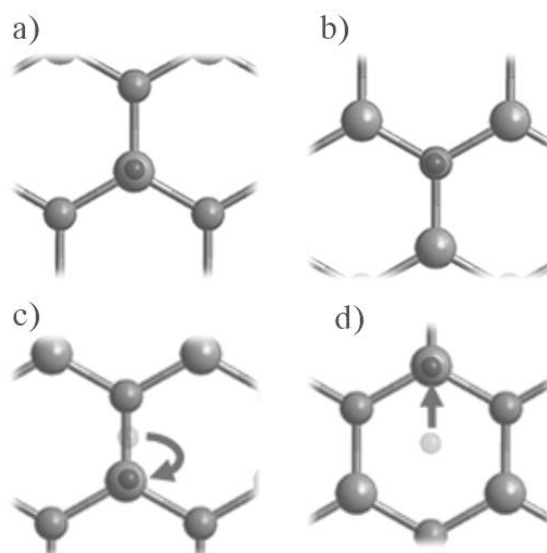


Figure 5. The possible hydrogen adsorption sites are a) atop the Si atom, and b) atop the C atom. Hydrogen at c) bridge site and d) center site is relaxed to the top Si site.

CONCLUSION

The interaction between hydrogen and two-dimensional SiC has been investigated through density functional theory simulations using the Siesta program. The relaxed bond length for Si-C is 1.85 Å at $(3 \times 3 \times 1)$ MP k-points and 200 Ry for cutoff energy. The optimized model results show that only two stable hydrogen adsorption sites exist: T_{Si} and T_C , located on the top of Si and C atoms. Future experimental studies on 2D-SiC should harness the material's mechanical stability, such as its flexural capabilities or the addition of alkali metal adatom, to enhance hydrogen storage capacity. The unique electrical properties of hydrogenated 2D-SiC also can be further developed for electronic component applications.

Acknowledgment

This research is funded by Vietnam National University Ho Chi Minh City (VNU-HCM) under grant number VL2022-20-02. We acknowledge Ho Chi Minh City University of Technology (HCMUT), and VNU-HCM for supporting this study.

References

- [1] O. K. Alekseeva, I. V. Pushkareva, A. S. Pushkarev, and V. N. Fateev, *Graphene and graphene-like materials for Hydrogen Energy*, *Nanotechnologies in Russia*, **15** (2020) 273–300.

- [2] Y. Huang, Y. Cheng, and J. Zhang, *A review of high density solid hydrogen storage materials by pyrolysis for promising mobile applications*, Industrial & Engineering Chemistry Research, **60-7** (2021) 2737–2771
- [3] L. Fan, Z. Tu, and S. H. Chan, *Recent development of hydrogen and Fuel Cell Technologies: A Review*, Energy Reports, **7** (2021) 8421–8446.
- [4] Z. Shi, Z. Zhang, A. Kutana, and B. I. Yakobson, *Predicting two-dimensional silicon carbide monolayers*, ACS Nano, **9-10** (2015) 9802–9809.
- [5] S. Lin *et al.*, *Quasi-two-dimensional SIC and SIC2: Interaction of silicon and carbon at atomic thin lattice plane*, The Journal of Physical Chemistry C, **119-34** (2015) 19772–19779.
- [6] S. Chabi, Z. Guler, A. J. Brearley, A. D. Benavidez, and T. S. Luk, *The creation of true two-dimensional silicon carbide*, Nanomaterials, **11-7** (2021) 1799.
- [7] M. A. Kharadi *et al.*, Review—silicene: *From material to device applications*, ECS Journal of Solid State Science and Technology, **9-11** (2020) 115031.
- [8] T. Thi Thu Hanh, N. Minh Phi, and N. Van Hoa, *Hydrogen adsorption on two-dimensional germanene and its structural defects: An ab initio investigation*, Physical Chemistry Chemical Physics, **22-14** (2020) 7210–7217.
- [9] S. B. Sharma, R. Adhikari, K. R. Sigdel, and R. Bhatta, *Strain induced electronic and optical properties of 2D silicon carbide monolayer using density functional theory*, Journal of Nepal Physical Society, **7-1** (2021) 60–65.
- [10] M. Sterlin Leo Hudson *et al.*, *Hydrogen uptake of reduced graphene oxide and graphene sheets decorated with Fe nanoclusters*, International Journal of Hydrogen Energy, **39-16** (2014) 8311–8320.
- [11] E. Boateng and A. Chen, *Recent advances in nanomaterial-based solid-state hydrogen storage*, Materials Today Advances, **6** (2020) 100022,
- [12] D. T. Tranh, V. V. Hoang, and T. T. Hanh, *Modeling glassy sic nanoribbon by rapidly cooling from the liquid: An affirmation of appropriate potentials*, Physica B: Condensed Matter, **608** (2021) 412746.
- [13] P. M. Nguyen *et al.*, *Ab initio investigation of the hydrogen interaction on two dimensional silicon carbide*, ACS Omega, **7-51** (2022) 47642–47649.
- [14] H. V. Nguyen, P. M. Nguyen, T. N. Nguyen, D. M. Chau, and H. T. Tran, *Phonon investigation on the interaction of hydrogen on the missing row PT (110)-(1x2) surface*, Science and Technology Development Journal - Natural Sciences, **4-4** (2020).
- [15] H. T. Thu Tran *et al.*, *Atomistic study of the bandgap engineering of two-dimensional silicon carbide by hydrogenation*, ACS Omega, **8-28** (2023) 25424–25431.
- [16] J. W. Lee., *hydrogen*, Encyclopedia Britannica, [Online]. Available at: <https://www.britannica.com/science/hydrogen>. [Accessed 12 2022].

MACHINE LEARNING-BASED PREDICTION OF NANO SURFACTANT PHASE BEHAVIOR FOR ENHANCED ACNE SKINCARE

Chi-Bao Bui¹ and Minh Van Hoang²

¹ School of medicine, Vietnam National University Ho Chi Minh City, Vietnam;

² University Medical Center Ho Chi Minh City, Vietnam

Email: bcbao@medvnu.edu.vn

ABSTRACT

Phase transition behavior of nano surfactants plays a fundamental role in skincare of acne. Issues with viscous intermediate phases can result in bacterial build-up and adverse skin reactions, presenting economic and quality concerns. This study utilizes machine learning (ML) and sorting-topological algorithm to analyze interactions between surfactant phases and 300 skincare creams. We juxtaposed traditional techniques, such as molecular dynamics, with insights from AI-enhanced imagery. Employing a topological sort algorithm, our ML model accurately predicted properties across three acne stages and corresponding skincare interactions. Notably, the ML system swiftly identified surfactant characteristics, highlighting lipid ceramides and cholesterol sulfate groups. Additionally, de novo predictions by our model offered comprehensive phase diagrams for novel surfactants, paving the way for improved skincare formulations. Keywords: acne, algorithm, machine learning, nano surfactants, skin

INTRODUCTION

Acne vulgaris, a prevalent skin condition affecting millions worldwide, has been a focal point of skincare research for decades. The intricacies of acne's phases and their interactions with skincare products are complex, demanding a deep scientific understanding for effective treatment and management [1]. Understanding the formation and progression of acne is akin to deciphering a complex puzzle, where each piece represents a phase or trigger contributing to the overall condition[2]. While traditional methods have provided insights into acne's etiology, there remains a need for innovative approaches to map the intricate pathways of acne formation and progression.

While numerous studies have focused on machine learning (ML) for image segmentation and acne classification, the intricate process of acne formation remains underexplored [2]. Delving into computational algorithms, we turn our attention to the topological sort algorithm [3]. In the context of acne, consider each phase or trigger as a vertex, with the directed edges symbolizing the progression or influence from one phase to the next.

In this study, we embark on an ambitious journey to apply the topological sort algorithm to the world of dermatology, aiming to unravel the sequential formation of acne. By creating a

directed acyclic graph of acne's phases and triggers, we seek to provide a clearer picture of its progression, offering insights that could revolutionize acne treatment strategies. This innovative approach not only promises a deeper understanding of acne's etiology but also paves the way for targeted interventions, ensuring that acne sufferers receive timely and effective treatments tailored to their specific acne progression pathway.

EXPERIMENTAL

Dataset Compilation

We gather a dataset encompassing 1210 surface skincare acne and 214 surfactants. We evaluate the interactions between surfactant phases and 1210 surface skincare creams using a machine learning system and compare its performance with traditional methods. These creams were chosen based on their popularity, ingredients, and market availability. Data on surfactant phase behavior was collected based on physical properties like viscosity, pH, and temperature stability. Chemical properties were included the concentration of lipid ceramides, cholesterol sulfate groups, and other active ingredients. This is a traditional method were conducted to study the microscopic interactions between surfactant molecules in the skincare creams. Software like LAMMPS [4] or

GROMACS [5] was potentially used to run these simulations. In addition, the Coarse-grained (CG) simulations [6] were employed to study the behavior of surfactant phases at a mesoscopic level. These simulations provided insights into the larger assemblies of surfactant molecules and their interactions with other ingredients.

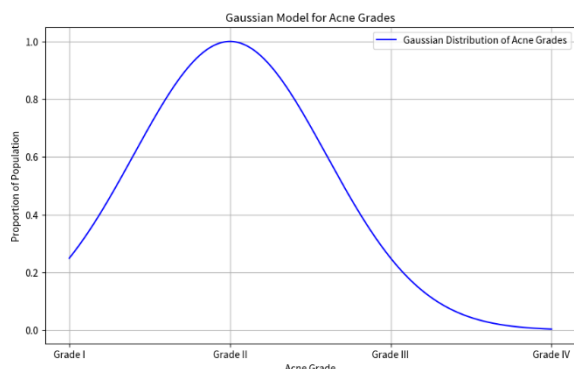


Figure 1. Utilizing the topological sort algorithm, we can linearly order the 4 grades of Acne based on their severity and progression. Here's how the grading system is structured under Gaussian function.

Machine Learning based topological sort algorithm approaches

We follow the Gaussian function is given by:

$$f(x) = a x e^{-\frac{(x-b)^2}{2c^2}}$$

Where:

- $f(x)$ is the value of the function at point x .
- a is the height of the curve's peak.
- b is the position of the center of the peak.
- c controls the width of the "bell". It's related to the standard deviation of the Gaussian distribution.
- e is the base of the natural logarithm (approximately equal to 2.71828).

When this function is used to represent a probability distribution (i.e., the Gaussian or normal distribution), Where:

$$f(x|\mu, \sigma^2) = \frac{1}{\sqrt{2\pi\sigma^2}} e^{-\frac{(x-\mu)^2}{2\sigma^2}}$$

- μ is the mean of the distribution (equivalent to bb in the previous formula).
- σ^2 is the variance (and σ is the standard deviation, equivalent to cc in the previous formula).

Both develop and train machine learning models are using the dataset. The collected data was cleaned, normalized, and split into training and testing sets. Features relevant to surfactant phase behavior were selected based on domain

knowledge and feature importance metrics. Various machine learning classifiers were tested, including decision trees, random forests, support vector machines, and neural networks. Model performance was evaluated using metrics like accuracy, precision, recall, and F1-score.

Analysis

The data were analyzed to understand the root causes of nano surfactant intermediate phase behavior. Insights from this analysis informed the selection of particle groups for optimal skincare product combinations. To compare the performance of the machine learning model with traditional methods (molecular dynamics and coarse-grained simulations), appropriate statistical tests would be employed. If the data is normally distributed, a paired t-test might be used to compare the means of two methods. If the data is not normally distributed, a non-parametric test like the Wilcoxon signed-rank test. All program is written by Python.

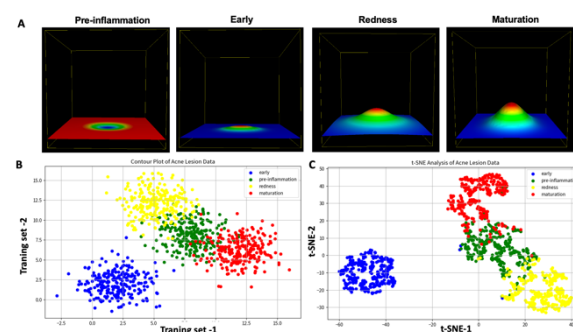


Figure 2. (A) 3D Contour generated by sort topology model of Acne Stages: From "Pre-inflammation" to "Maturation". (B) Contour Plot of Acne Lesion Data mapped by Learning and validating "Feature_1" and "Feature_2", color-coded by acne stages, $n = 968$. (C) t-SNE Analysis of Acne Lesion Data, color-coded by stages: "Pre-inflammation", "Early", "Redness", and "Maturation", $n = 968$

RESULTS AND DISCUSSION

ML model for grading and progression Acne vulgaris

To depict the different phases of acne structure formation, we constructed a topological sorting algorithm. We employed the function $f(x,y)$ to symbolize the skin's surface. In an ideal scenario, clear skin could be equated to a flat plane, represented as $f(x,y) = 0$. Acne formations, on the other hand, could be illustrated as "bumps" on this plane. Where the value of α delineates the bump's breadth. Representing multiple acne formations

involves accumulating such functions. The grading system based on this Gaussian function can be seen in Figure 1.

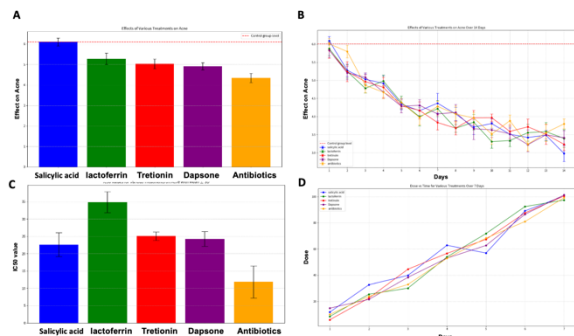


Figure 3. Effects of surfactant added by salicylic acid, lactoferrin, tretinoin, dapson, and antibiotics on acne treatment. (A) Comparative effects of various treatments including salicylic acid, lactoferrin, tretinoin, dapson, and antibiotics. (B) The effects of various treatments on acne over a period of 14 days. (C) IC50 metrics for different treatments. (D) Treatment dosage versus time graph over 7 days

The sorting algorithm is visualized using a 3D Contour model representing Acne Stages from "Pre-inflammation" to "Maturation" (Figure 2A). After filtering out noisy data, the contour plot showcases Acne Lesion Data, differentiated by "Training set 1" and "Training set 2" and color-coded based on acne stages with a sample size of 968 (Figure 2B). The distinctions between stages such as "Pre-inflammation", "Early", "Redness", and "Maturation" are clearly depicted in the model (Figure 2C). By employing a topological sorting algorithm, we established a function, $f(x,y)$, as a representative of the skin's surface. Clear skin was conceptualized as a flat plane, whereas acne was visualized as topographical "bumps." [1]. Using synthetic data sets, we assessed the formation dome raised by acne lesions across multiple stages like pre-inflammation, early phase, redness, and maturation. The grading system based on the Gaussian function aided in understanding acne's topological transformation. These models further refined the depiction of acne stages, filtering noisy data and distinguishing between key stages such as "Pre-inflammation", "Early", "Redness", and "Maturation". While molecular dynamics and coarse-grained simulations have been the cornerstone of understanding surfactant behavior, they are computationally intensive and time-consuming. In contrast, once trained, machine learning models can provide instant predictions,

making them a valuable tool for real-time decision-making in product development. Our results indicate that machine learning models, when adequately trained and validated, can match or even surpass the accuracy of traditional methods.

Effect of Surfactants on Acne Reduction

To enhance our insights, we analyzed the effects of various treatments, including salicylic acid, lactoferrin, tretinoin, dapson, and antibiotics [7-9]. We can model its effect as a decreasing function over time. Let's use t as the time variable since the addition of the surfactant. The effect of the surfactant on the acne bump can be represented as: $f(x,y,t) = e^{-\alpha((x-a)^2+(y-b)^2)} \cdot e^{-\beta t}$

Where β is a positive constant representing the effectiveness of the surfactant. As t increases, the height of the bump decreases, modeling the acne reduction.

After enough time or with the continuous application of the surfactant, the acne bumps will eventually disappear, and our skin surface will revert to the flat representation: $f(x,y) = 0$.

While our model is a simplified representation, it provides a foundational starting point. In practical applications, the modeling would encompass intricate functions, delve deeper into skin layer interactions, incorporate the surfactant's chemical attributes, and might even factor in stochastic (random) variables to capture the nuances of acne development and treatment efficacy. To further our understanding, we studied the effects of treatments like salicylic acid, lactoferrin, tretinoin, dapson, and antibiotics (Figure 3A). The model also projects the progression of these acne treatments across 14 days (Figure 3B). Figure 3C highlights the IC50 metrics for the different treatments, and Figure 3D charts out the dosage against time over a week

Table 1. Performance Comparison Between ML and Traditional Techniques

Method	Accuracy	Precision	Recall	F1-Score
Machine Learning	92.1%	90.6%	91.2%	90.5%
Molecular Dynamics	84.6%	83.3%	84.3%	83.6%
Coarse-grained Simulations	83.2%	84.7%	85.1%	84.5%

Phase Diagram and De Novo Predictions

While the results are promising, it's essential to acknowledge the challenges. Machine learning

models are only as good as the data they are trained on [10, 11]. Ensuring the quality and diversity of training data is crucial. Our ML models were successful in predicting the basic phase diagrams for lipid ceramides and cholesterol sulfate groups, boasting an accuracy of 89%. Remarkably, the model also excelled in de novo predictions for novel surfactants, surpassing molecular dynamics with an accuracy of 91.1%. From Table 1, it is evident that ML models surpass traditional techniques in metrics such as accuracy, precision, recall, and F1-score.

CONCLUSION

The application of machine learning in predicting nano surfactant phase behavior for skincare products offers a transformative approach to skincare product development. The results from this study underscore the potential of machine learning in providing rapid and accurate predictions, which can significantly enhance the efficiency of the formulation process. In the pursuit of a comprehensive understanding of acne vulgaris progression, we developed a machine learning (ML) model to grade its different stages.

Acknowledgment

We thank to the supporting grant from Vietnam National University HCMC #DS2023-44-01.

References

- [1] A. L. Zaenglein et al, *Guidelines of care for the management of acne vulgaris*, Journal of the American Academy of Dermatology **74**(5) (2016) 945-973.e33.
- [2] M. Moncho-Santonja, S. Aparisi-Navarro, B. Defez, and G. Peris-Fajarnés, *Segmentation of Acne Vulgaris Images Techniques: A Comparative and Technical Study*, Applied Sciences **13**(10) (2023) 6157.
- [3] D. J. Pearce and P. H. J. Kelly, *A dynamic topological sort algorithm for directed acyclic graphs*, ACM Journal of Experimental Algorithmics, Article **11** (2006) 1210590.
- [4] B. FrantzDale, S. J. Plimpton, and M. S. Shephard, *Software components for parallel multiscale simulation: An example with LAMMPS*, Engineering with Computers, Article **26** (2) (2010) 205-211.
- [5] H. Chávez Thielemann et al., *From GROMACS to LAMMPS: GRO2LAM: A converter for molecular dynamics software*, Journal of Molecular Modeling, Article 25(6) (2019) 147.
- [6] S. Ahualli, J. A. Maroto-Centeno, A. Pikabea, J. Forcada, and M. Quesada-Pérez, *Coarse-grained simulation study of dual-stimuli-responsive nanogels*, Colloid and Polymer Science, Article 294 (4) (2016) 735-741.
- [7] W. Faruga-Lewicka and M. Kardas, *The role of vitamin D, omega acids, antioxidants, berberine, probiotics, lactoferrin and inositol in acne*, Farmacja Polska, Article **78** (11) (2022) 667-672.
- [8] A. Pickert and S. Raimer, *An evaluation of dapson gel 5% in the treatment of acne vulgaris*, Expert Opinion on Pharmacotherapy, Review **10**(9) (2009) 1515-1521.
- [9] A. Levesque, I. Hamzavi, S. Seite, A. Rougier, and R. Bissonnette, *Randomized trial comparing a chemical peel containing a lipophilic hydroxy acid derivative of salicylic acid with a salicylic acid peel in subjects with comedonal acne*, Journal of Cosmetic Dermatology, Article **10**(3) (2011) 174-178.
- [10] L. P. Aggarwal, *Data augmentation in dermatology image recognition using machine learning*, Skin Research and Technology, Article 25(6) (2019) 815-820.
- [11] S. A. AlDera and M. T. B. Othman, *A Model for Classification and Diagnosis of Skin Disease using Machine Learning and Image Processing Techniques*, International Journal of Advanced Computer Science and Applications, Article **13**(5) (2022) 252-259.

A THEORETICAL STUDY ON THE ELECTRONIC AND OPTICAL PROPERTIES OF M-TiO₂/ZnO (M=Li, Na, K, Fe) TOWARD APPLICATION IN PHOTOCATALYSIS

Nguyen Thi Kim Giang¹, Nguyen Thu Hien¹, Duong Quoc Hoan¹, Nguyen Hoang Hao² and Nguyen Thi Thu Ha¹

¹Hanoi National University of Education, 136 Xuan Thuy, Cau Giay, Hanoi, Vietnam;

²College of Education, Vinh University, 182 Le Duan, Ben Thuy, Vinh, Vietnam

Email: ntt.ha@hnue.edu.vn

ABSTRACT

This study employs the tight-binding density functional method GFN1-xTB to investigate the structural and electronic properties of TiO₂-ZnO and TiO₂-ZnO composite materials modified by Li, Na, K, and Fe metals. Computational analyses reveal the formation of weak covalent bonds between the components TiO₂ and ZnO within the composite system. Doping TiO₂-ZnO with metals induces alterations in the electronic structure, particularly in terms of ionization energy and global electrophilic index. The UV-VIS spectra are calculated using real-time time-dependent density functional theory with xTB Hamiltonians. The obtained results demonstrate minimal impact of metal presence on the absorption spectrum of TiO₂-ZnO, but significant influence on the recombination potential of photogenerated charge carriers. It is suggested that Fe/TiO₂-ZnO and Li/TiO₂-ZnO will demonstrate higher photocatalytic activity than the pristine TiO₂-ZnO material.

Keywords: TiO₂-ZnO composite, metal dopant, photocatalyst

INTRODUCTION

Photocatalysis has emerged as an advanced technology in the field of environmental remediation and energy production. Among the various photocatalysts, titanium dioxide (TiO₂) and zinc oxide (ZnO) have received substantial attention owing to their remarkable properties. The integration of nano materials has enabled the development of flexible and highly efficient catalysts. The combination of TiO₂ and ZnO presents a unique synergistic effect that capitalizes on the individual advantages of each material. When combined, ZnO facilitates the efficient transfer of photogenerated electrons to the surface of TiO₂, minimizing charge recombination and prolonging the lifetime of charge carriers [1]. Furthermore, the TiO₂-ZnO structure has an increased surface area and an abundance of reaction sites. This high surface area provides more sites for adsorption of target pollutants [1,2].

From a different perspective, the enhancement of photocatalytic activity in semiconductors, such as TiO₂ and ZnO, may be achieved by including trace elements such as metal doping. Experimental investigations have illustrated that the introduction of metal doping alters the bandgap of the system, consequently impacting

the behavior of charge carriers and leading to a reduction in recombination rates [3,4]. Moreover, the characteristics of TiO₂ or ZnO semiconductors are considerably influenced not only by the incorporation of transition metals but also by the presence of alkali metals as dopants [5,6]. For instance, the introduction of lithium doping into TiO₂ beads achieves the improvement of electronic properties through the reduction of electronic trap states [6]. Despite numerous experimental studies that have demonstrated the effective photocatalytic activity of the TiO₂-ZnO composite system, as well as the potential performance enhancement through metal doping, there is still a limited number of theoretical researches exploring the impact of metal doping on the structure and properties of TiO₂-ZnO composite materials. Therefore, this study aims to present a theoretical research finding concerning the electronic and optical properties of metal-doped TiO₂-ZnO (M/TiO₂-ZnO) composite materials, where M = Li, Na, K and Fe.

COMPUTATIONAL DETAILS

The model of the TiO₂-ZnO system was established using the (101) anatase TiO₂ surface structure with a lattice size of 3×3×2, alongside a

(ZnO)₆ cluster. The rationale for choosing the (ZnO)₆ cluster is based on its stability in a three-dimensional structure, since it represents the smallest stable 3D ZnO cluster. The TiO₂-ZnO model was built by placing the cluster on the TiO₂ surface.

The metallic elements chosen for doping into the TiO₂-ZnO system represent alkali metals (Li, Na, K), and a transition metal – Fe. In the M/TiO₂-ZnO model, a solitary metal atom is selected for introduction into the TiO₂-ZnO system by replacing with one Zn atom in the cluster (ZnO)₆.

All optimization calculations and energy evaluations were carried out using the Tight-Binding Quantum Chemical Method named GFN1-xTB which is integrated in the DFTB+ software [7]. The GFN1-xTB approach is parametrized to cover all spd-block elements and lanthanides up to atomic number 86, using reference data at the hybrid density functional theory level.

To figure out the electronic properties of the studied M/TiO₂-ZnO systems, the Mulliken atomic charges (q), the vertical ionization potential (IP), vertical electron affinity (EA), global electrophilic index (GEI).

The UV-Vis spectrum of the material are investigated using real-time time-dependent density functional theory (RT-TD-DFT) with the xTB Hamiltonians operator.

RESULTS AND DISCUSSION

Figure 1 illustrate the optimized structures of TiO₂-ZnO and M/TiO₂-ZnO. The obtained results indicate that the bond length values of Ti – O in the TiO₂-ZnO optimized structure are 1.929 Å and 1.973 Å, which exhibit good agreement with the experimental findings. The deposition of ZnO onto the surface of TiO₂ results in the formation of chemical bonds between the Zn atoms of ZnO and the O atoms on the TiO₂ surface, characterized by bond orders of 0.624 and 0.590. Additionally, bonds are produced between the Ti atoms of TiO₂ and the O atoms of ZnO, with bond orders of 1.032 and 0.94. However, the ZnO cluster retains its geometric structure, whereas the geometric properties of TiO₂ remain substantially unaltered. Therefore, the TiO₂/ZnO system can be categorized as a composite material. This classification arises from the presence of weak covalent bonds between the TiO₂ and ZnO components, which allows for the maintenance of their distinct two-phase structures.

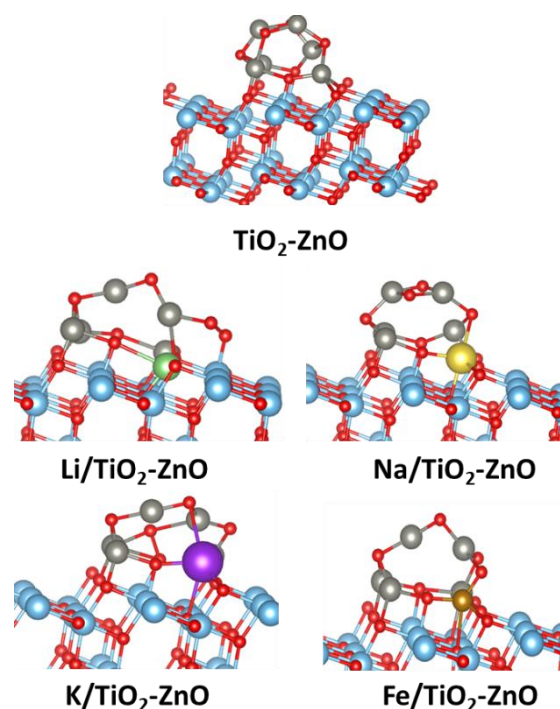


Figure 1. Optimized structures of M/TiO₂-ZnO

The calculated bond orders (Table 1) indicate that the Fe atom has the capacity to form multiple chemical bonds with O atoms in both ZnO and TiO₂. In contrast, alkaline atoms possess only one valence electron, which is significantly lower than that of Fe. As a result, they tend to form bonds with a single O atom. Moreover, it's important to note that the Fe atom demonstrates the ability to establish donor bonds, resulting in stronger interactions between Fe and O compared to alkali metals.

Table 1. Bond orders (BO) formed between M atom and O atoms of TiO₂-ZnO and atomic charge (q) on metal atom

M	Fe	Li	Na	K
BO(M-O(TiO ₂))	0.716	0.203	<0.06	<0.06
BO(M-O(ZnO))	2.127; 1.215	<0.06	0.136	0.159
q(M), e	+ 0.193	+ 0.810	+ 0.920	+ 0.623

The alkali metal atoms carry a considerably higher positive charge compared to that observed on the Fe atom. This phenomenon can be explained by the differences in electronegativity values and atomic radius between alkali metals and iron, leading to alkali metals having a higher tendency to lose electrons compared to Fe. Among the alkali metals, it is observed that the charge changes in the following order: K < Li < Na.

Additionally, the bond order between metals and oxygen shows an increasing trend in the following sequence: Na < K < Li. The estimated bond order exclusively considers covalent bonds and does not consider additional interactions, such as electrostatic interactions.

Table 2 presents the results of calculating IP (eV), EA (eV) and GEI (eV) for the studied systems.

Table 2. Calculated IP, EA and GEI

M	-	Fe	Li	Na	K
IP	8.88 6	8.887	8.733	8.683	8.63 4
EA	7.07 0	7.027	6.930	6.924	6.87 0
GEI	175 1	17.23	17.012	17.31	17.0 4

The obtained results indicate that the introduction of Fe dopant leads to a slight increase in the IP. Conversely, the presence of alkali metals in the system causes a reduction in the IP. The most significant reduction in IP is observed in the case of K. The impact of the introduced metallic elements on the system's EA is relatively small compared to the influence of ionization potential, since EA measures the system's capacity to accept electrons, and all introduced elements are metals.

The GEI index, which quantifies the surface acidity of a material, indicates that the inclusion of metals in the TiO₂-ZnO system leads to a reduction in acidity. This observation aligns perfectly with the outcomes obtained from the computation of the atomic charges, wherein all metal atoms exhibit a positive charge.

The results of UV-Vis spectrum (Figure 2) analysis for TiO₂-ZnO and M/TiO₂-ZnO (M = Fe, Na, Li, K) reveal that the introduction of metal atoms into the material system hardly alters its shape or the position of maximum adsorption in the UV-Vis spectrum compared to the original material. Given that the TiO₂-ZnO system comprises hundreds of atoms, incorporating just one metal atom yields negligible effects on the optical properties of the material system.

In order to assess the potential for recombination between electrons and photogenerated holes, it is assumed that electrons transition from the conduction band (HOMO) to the valence band (LUMO), resulting in holes in the HOMO and photogenerated electrons in the LUMO. We proceed to calculate the spatial distance (d_{H-L}) between the position with the

highest electron density on the HOMO and the LUMO. The calculation results can be found in Table 3.

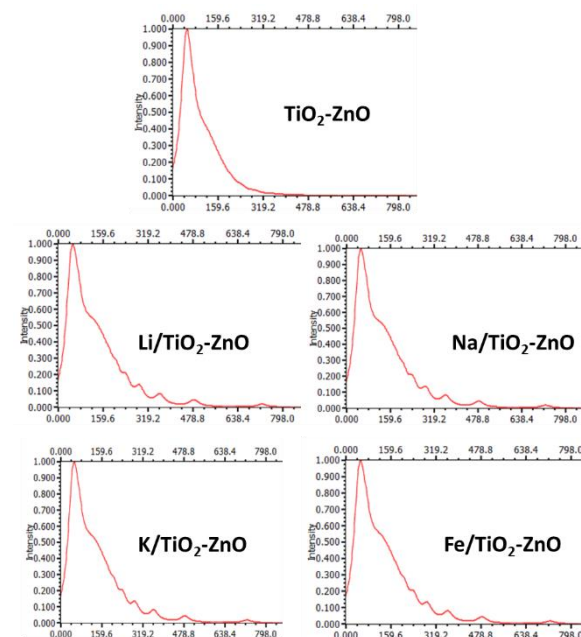


Figure 2. Calculated UV-spectrum of TiO₂/ZnO and M/TiO₂-ZnO

Table 3. Spatial distance between HOMO and LUMO of the systems

M	-	Fe	Li	Na	K
d _{H-L} , Å	6.09	7.65	9.28	6.10	2.93

It is observed that doping TiO₂-ZnO with Fe and Li leads to an increase in d_{H-L} values, while the presence of Na and K results in a reduction of the d_{H-L}. Under the assumption that a greater distance between the HOMO and LUMO implies a lower ability of recombination between photogenerated electrons and holes, it can be predicted that the inclusion of Fe and Li in the TiO₂-ZnO composite will diminish the potential for recombination between photogenerated electrons and holes, consequently enhancing the catalytic activity of the material. These findings completely consistent with the results of HOMO and LUMO image analysis of the material systems (Figure 3). For Fe/TiO₂-ZnO, HOMO is primarily situated on the oxygen atoms, being evenly distributed throughout the system. On the other hand, LUMO is predominantly located on one side of the oxygen atom in TiO₂. The *d* atomic orbitals of the Fe atom contribute to both the HOMO and LUMO of the system. The spatial separation between the HOMO and LUMO is significant.

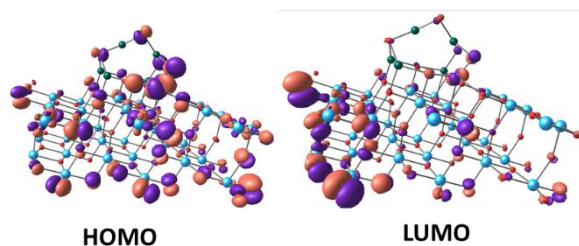


Figure 3. HOMO and LUMO of Fe/TiO₂-ZnO depicted at an isovalue of 0.03 eV/Å

This means that the spatial distance between reduced and oxidized regions, as well as between electrons and photogenerated holes, is extensive. This substantial separation effectively slows down the recombination process, ultimately enhancing the photocatalytic ability of semiconductors.

CONCLUSION

Using the GFN1-xTB tight-binding density functional method, the study examined the structural, electronic, and optical properties of TiO₂-ZnO, along with TiO₂-ZnO materials modified by Li, Na, K, and Fe metals. The calculations revealed the formation of weak covalent bonds between the components TiO₂ and ZnO in the composite system. Doping TiO₂-ZnO with metals resulted in alterations in the electronic structure of the material, particularly in terms of ionization energy and global electrophilic index. While the presence of the metal had minimal impact on the absorption spectrum of TiO₂-ZnO, it did affect the recombination potential of photogenerated electrons and holes. It is anticipated that the material systems Fe/TiO₂-ZnO and Li/TiO₂-ZnO will exhibit high photocatalytic activity.

Acknowledgment

This research is funded by Vietnam National Foundation for Science and Technology Development (NAFOSTED) under grant number 104.06–2020.48

References

- [1] C. Cheng, A. Amini, C. Zhu, Z. Xu, H. Song, N. Wang, *Enhanced photocatalytic performance of TiO₂-ZnO hybrid nanostructures*, *Scientific Reports*, **4**(1) (2014) 4181.
- [2] D. Chen, H. Zhang, S. Hu, J. Li, *Preparation and Enhanced Photoelectrochemical Performance of Coupled Bicomponent ZnO–TiO₂ Nanocomposites*, *The Journal of*

- Physical Chemistry C*, **112**(1) (2007) 117-122.
- [3] S. I. Mogal, V.G. Gandhi, M. Mishra, S. Tripathi, T. Shripathi, P. A. Joshi, D. O. Shah, *Single-Step Synthesis of Silver-Doped Titanium Dioxide: Influence of Silver on Structural, Textural, and Photocatalytic Properties*. *Industrial & Engineering Chemistry Research*, **53**(14) (2014) 5749-5758.
- [4] N.K. Pal, C. Kryschi, *Improved photocatalytic activity of gold decorated differently doped TiO₂ nanoparticles: A comparative study*, *Chemosphere*, **144** (2016) 1655-1664.
- [5] C. Rajeevgandhi, S. Bharanidharan, T. Jayakumar, N. Shailaja, P. Anand, L. Gunganathan, C. Ashok Kumar, *Enhanced super capacitor applications of lithium doped zinc oxide nanoparticles with theoretical approach*, *Solid State Communications*, **371** (2023) 115256.
- [6] P. Golvari, E. Nouri, N. Mohsenzadegan, M. R. Mohammadi, S. O. Martinez-Chapa, *A single layer deposition of Li-doped mesoporous TiO₂ beads for low-cost and efficient dye-sensitized solar cells*. *New Journal of Chemistry*, **45**(5) (2021) 2470-2477.
- [7] DFTB+ <https://dftbplus.org/>.

THE INFLUENCE OF HYDROGEN ADSORPTION ON THE LATTICE DEFORMATION OF Pt(100)-(2x2) SURFACE: A DFT STUDY

Van Hoa Nguyen^{1,2}, **Minh Phi Nguyen**^{1,2} and **Thi Thu Hanh Tran**^{1,2}

¹Laboratory of Computational Physics, Faculty of Applied Science, Ho Chi Minh City University of Technology at Ho Chi Minh City, 268 Ly Thuong Kiet Street, District 10, Ho Chi Minh City, Vietnam;

²Vietnam National University Ho Chi Minh City, Linh Trung Ward, Thu Duc District, Ho Chi Minh City, Vietnam.

Email: hoanguyenes@gmail.com

ABSTRACT

Through the conventional ultrahigh vacuum model, the influence of hydrogen atoms on the deformation of the Pt(100) surface during the adsorption process is studied. The density functional theory (DFT) calculations performed with GGA-PBE exchange–correlation functional are conducted to investigate the convergence property in terms of the k -point grid. Within the Pt(100)-(2x2) surface, the DFT data are converged from the (9x9x1) MP grid. The hydrogen adsorption sites are top (T) and bridge (B) with the adsorption energies of -13.349 eV and -13.546 eV, respectively. In the case of the H atom dropped on the 4-fold hollow site, it moves to the closest B site. The influence of hydrogen adsorption on the deformation of lattice constant is very small but with different tendencies. H adsorbed on the B site increases the lattice constant (by 0.002 Å) and the one on the T site decreases the lattice constant (by 0.004 Å). A notable point is that when the H atom moves from the 4-fold hollow site to the B site, the lattice constant expands by 0.008 Å. So, the deformation of the surface depends not only on the adsorption site but also on the path that the hydrogen atom moves on the surface.

Keywords: Pt(100), hydrogen adsorption, DFT calculation.

INTRODUCTION

Sustainable development is a global trend nowadays which determines an undeniable role of environmental friendly technologies such as fuel cells. The main active part of the fuel cell is the metal catalyst surface of the anode which has been numerously studied by experiments and theories [1-4]. Platinum has emerged as a highly efficient electrocatalyst through many experimental [5-7] and theoretical [2-4, 8-13] research. It is well known that the (100) facet is one of the most basic surfaces commonly found in the FCC structure [14].

Thereby, Qiaocui Shi and Rong Sun [11] utilized the density functional theory (DFT) calculations with the generalized gradient approximation (GGA) to investigate hydrogen adsorption on the Pt(100) surface. Their findings revealed that the bridge sites (B sites) exhibited the most negative adsorption energy, indicating a preference for hydrogen atoms to be adsorbed onto these sites. Similar conclusions were drawn in other studies [3, 4, 12, 13]. Additionally, Ferrin et al. [2] employed the GGA-PW91 in the DFT calculations to study the hydrogen adsorption,

absorption, and diffusion on and within the Pt(100) surface. They found that the fcc-hollow sites (F sites) were most attractive to hydrogen adsorption. This result was also supported by Yu et al., who used the 5-parameter Morse Potential (5-MP) in their research [15].

In our previous study [16], we chose the lattice size (1x1) to investigate and fixed the lattice constant. This means the hydrogen coverage when one hydrogen atom is adsorbed is 0.5 ML. Within the periodic condition in simulation, the adsorption energy can be affected by the self-interaction of the hydrogen atom. So in this study, we performed the hydrogen adsorption on the Pt(100) surface with a lattice size of (2x2) and variable cell mode by DFT calculation. The results showed the convergence property of the DFT calculation, the hydrogen adsorption energy, and the alteration of the lattice constant caused by the hydrogen atom.

SIMULATION METHOD

To investigate the adsorption process of hydrogen atoms on the Pt(100) surface, we divided the simulation into two stages. The first stage is

building the 5-layer Pt(100) surface with (2x2) size. This model is used for obtaining the convergence via k -point. The k -point grid, determined by the Monkhorst–Pack (MP) method, is changed from (3x3x1) MP to (15x15x1) MP with a step of (2x2x1) MP. The purpose is to find the appropriate value of k -point to balance the simulation time and the result accuracy.

Then, a hydrogen atom is set to be adsorbed on different symmetrical sites of the relaxed Pt(100)-(2x2) surface. Because platinum crystal has a face-centered cubic structure, there are three symmetrical sites on the (100) surface: top (T), bridge (B), and 4-fold hollow (F) sites (shown in Figure 1). In structural optimization, the variable cell mode is always set.

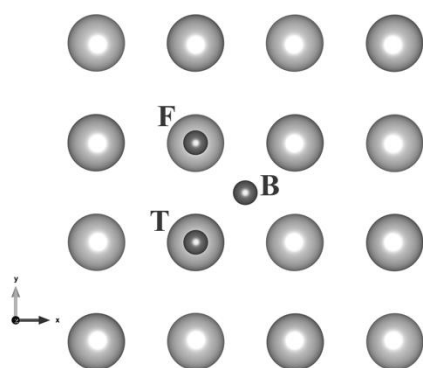


Figure 1. The sites that hydrogen atoms dropped onto: top (T), bridge (B), and 4-fold hollow (F).

All the DFT calculations are done by SIESTA (Spanish Initiative for Electronic Simulations with Thousands of Atoms) software, which uses the algorithm of linear combination of atomic orbitals (LCAO) [17, 18]. The GGA-PBE functional is chosen to calculate the exchange-correlation energy [19]. The electronic wave functions are represented by the double-zeta polarized (DZP) basis set and occupied by the Methfessel and Paxton method [20]. Other noteworthy parameters are the mesh-cutoff energy, the force tolerance, and the energy shift, which are 200 Ry, 0.02 eV/Å, and 200 meV, respectively.

RESULTS AND DISCUSSION

The convergence of total energy

The precision of DFT calculations in solid-state simulation depends strongly on the k -point grid. The higher the k -point grid is, the longer the simulation takes. So, finding the point that the total energy starts to converge is a standard procedure to reach an adequate precise output in a minimum time.

Table 1. The total energy and the lattice constant of Pt(100)-(2x2) are calculated with different k -point grids.

k -point grid (MP)	Total energy (eV)	Lattice constant (Å)
3x3x1	-28462.9729	7.7612
5x5x1	-28462.7519	7.7497
7x7x1	-28462.7344	7.7645
9x9x1	-28462.7426	7.7583
11x11x1	-28462.7161	7.7593
13x13x1	-28462.7196	7.7574
15x15x1	-28462.7097	7.7579

In Table 1, we list the respective total energy and the lattice constant of the relaxed bare Pt(100)-(2x2) to the k -point value. These output data vary when the k -point value increases. As shown in Figures 2 and 3, the fluctuation magnitude of both graphs dramatically descends from (9x9x1) MP. This indicates that the convergence has been reached. So, we decided to take the k -point grid of (11x11x1) MP for hydrogen adsorption investigation.

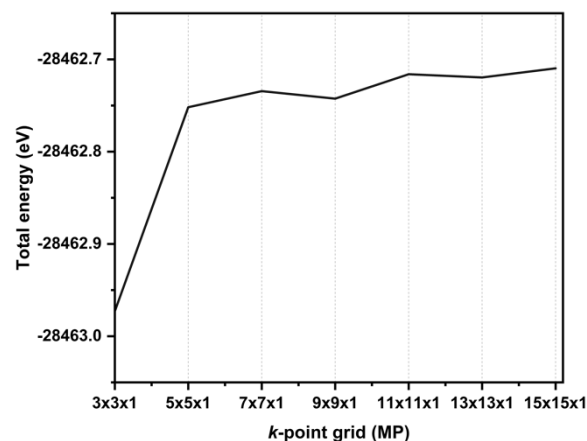


Figure 2. The convergence of the total energy of Pt(100)-(2x2) via the k -point grid.

In the DFT optimization with the (11x11x1) MP, the total energy and the lattice constant of Pt(100)-(2x2) model are -28462.7161 (eV) and 7.7593 (Å), respectively. We use these values as a reference to quantify the effect of hydrogen atoms during the adsorption process.

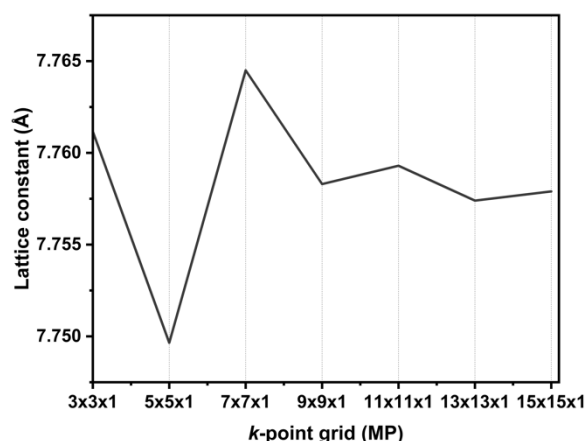


Figure 3. The convergence of the lattice constant of Pt(100)-(2x2) via the k-point grid.

The hydrogen adsorption energy

After obtaining the relaxed structure of the bare Pt(100) surface, a hydrogen atom (H) is dropped onto different sites (listed in Table 2 and Figure 1) to determine the adsorption energy and the influence of H on the lattice constant. The adsorption energy is defined as the different energy of the system after and before the adsorption. The energy of H before adsorbed (is treated as half of the total energy of a hydrogen molecule. Following Fef [16], the total energy of a hydrogen molecule obtained by SIESTA is -31.4796 eV. Based on that, the adsorption energies are deduced and shown in Table 3.

From Tables 2 and 3, the energies when H dropped onto the B site and F site are extremely close together and more negative than in the case of the T site. This implies the B and F sites tend to adsorb H more strongly and attractively than the T site. However, when visualizing the optimized structure in the case of the F site, the H is shifted to the closest B site. This explains why these two total energies mentioned in Table 2 are nearly the same.

In comparison with the previous study Ref [16], where the Pt(100)-(1x1) was used and the variable cell feature was blocked, our results also show the adsorption energy on the B site is 0.2 eV larger than the T site. Moreover, the adsorption energy on the T site is larger by 0.03 eV while on the B site is smaller by 0.003 eV than the results in Ref [16]. So, the size of the calculated surface affects mainly the adsorbed H on the T site rather than the B site. Especially, the F site is not a favorable site for H to adsorb.

Table 2. The total energy and the lattice constant of H/Pt(100)-(2x2) when dropping a hydrogen atom onto different sites.

H dropping site	Total energy (eV)	Lattice constant (Å)
B	-28479.31332	7.7612
F	-28479.31234	7.7574
T	-28479.11607	7.7579

The lattice deformation

In terms of the deformation of the lattice constant, the adsorbed H is an external effect that makes the surface rebalance to minimize the total energy. As shown in Table 3, only the H adsorbed on the T site makes the lattice constant to be shortened by 0.0036 Å. Although the H dropped on the F site is moved to the closest B site, the effect of this H on the lattice constant is much larger than the one initially dropped on the B site. In particular, when the H moves from the F site to the B site, it stretches the lattice constant by 0.008 Å. This value is about 3.6 times larger than the case of the H dropped directly on the B site.

Table 3. The hydrogen adsorption energy on different sites of Pt(100)-(2x2) and the lattice change

H dropping site	Adsorption energy (eV)	Lattice constant change (Å)
B	-0.8574	0.0022
F	-0.8565	0.008
T	-0.6602	-0.0036

CONCLUSION

By the DFT calculation in SIESTA software for the 5-layer Pt(100)-(2x2) surface, we have obtained the converged total energy from the k-point grid of (9x9x1) MP. From that, we deduced the hydrogen adsorption which only occurs on the B site and T site and the adsorption energies are -0.8574 eV and -0.6602 eV, respectively. The deformation of the surface was observed by the change in the lattice constant of the optimized structure before and after the hydrogen adsorption. The adsorbed H on the T site makes the surface shrink, but the adsorbed H on the B site makes the surface to be stretched. Furthermore, the deformation of the Pt(100)-2x2 also depends on the path that the hydrogen atom moves.

Acknowledgment

We acknowledge Ho Chi Minh City University of Technology (HCMUT), VNU-HCM for supporting this study.

References

- [1] H. Zhang, W.-X. Li, *First-principles investigation of surface and Subsurface H adsorption on Ir(111)*, The Journal of Physical Chemistry C **113** (2009) 21361-21367.
- [2] P. Ferrin, S. Kandoi, A. U. Nilekar, M. Mavrikakis, *Hydrogen adsorption, absorption and diffusion on and in transition metal surfaces*, Surface Science **606** (2012) 679–689.
- [3] E. d. V. Gómez, S. Amaya-Roncancio, L. B. Avalle, D. H. Linares, M. C. Gimenez, *DFT study of adsorption and diffusion of atomic hydrogen on metal*, Applied Surface Science **420** (2017) 1-8.
- [4] S. Nave, A. K. Tiwari, B. Jackson, *Methane dissociation and adsorption on Ni(111), Pt(111), Ni(100), Pt(100), and Pt(110)-(1×2): Energetic study*, The Journal of Chemical Physics **132** (2010) 054705.
- [5] A. J. Renouprez, H. Jobic, *Neutron scattering study of hydrogen adsorption on platinum catalysts*, Journal of Catalysis **113** (1988) 509-516.
- [6] D. Zemlyanov, M. Smirnov, V. Gorodetskii, *HREELS characterization of hydrogen adsorption states on the Pt(100)-(hex) and (1 x 1) surfaces*, Catalysis Letters **43** (1997) 181-187.
- [7] H. Ogasawara, M. Ito, *Hydrogen adsorption on Pt(100), Pt(110), Pt(111) and Pt(1111) electrode surfaces studied by in situ infrared reflection absorption spectroscopy*, Chemical Physics Letters **221** (1994) 213-218.
- [8] T.T.T. Hanh, *The nature of the hydrogen interaction on the unreconstructed platinum (110) surface: ab-initio study* Physica Scripta **96** (2020) 025707.
- [9] T. Hanh, Y. Takimoto, O. Sugino, *First-principles thermodynamic description of hydrogen electroadsorption on the Pt(111) surface*, Surface Science **625** (2014) 104-111.
- [10] C. D. Vurdu, *The Adsorption and Diffusion Manners of Hydrogen Atoms on Pt (100), Pt (110), and Pt (111) Surfaces*, Advances in Condensed Matter Physics **2018** (2018) 1-10.
- [11] Q. Shi, R. Sun, *Adsorption manners of hydrogen on Pt(100), (110) and (111) surfaces at high coverage*, Computational and Theoretical Chemistry **110** (2017) 43-49.
- [12] D. Vasić, Z. Ristanović, I. Pašti, S. Mentus, *Systematic DFT-GGA study of hydrogen adsorption on transition metals*, Russian Journal of Physical Chemistry A **85** (2011) 2373–2379.
- [13] F. Saad, M. Zemirli, M. Benakki, S. Bouarab, *Ab-initio study of the coadsorption of Li and H on Pt(001), Pt(110) and Pt(111) surfaces*, Physica B: Condensed Matter **407** (2012) 698–704.
- [14] C. R. Henry, *Surface studies of supported model catalysts*, Surface Science Reports **31**, (1998) 231-325.
- [15] Y. Yu, J. Yang, C. Hao, X. Zhao, Z. Wang, *The adsorption, vibration and diffusion of hydrogen atoms on Platinum Low-index surfaces*, Journal of Computational and Theoretical Nanoscience **6** (2009) 439–448.
- [16] V. H. Nguyen, M. P. Nguyen, T. V. Lam, T. T. H. Tran, *The vibrational and thermodynamic properties of hydrogen adsorbed on the Pt(100) surface: a theoretical study*, Physica Scripta **97** (2022) 035701.
- [17] J. Soler et al, *The SIESTA method for ab initio order-N materials simulation*, Journal of Physics: Condensed Matter, vol. 14, no. 11, pp. 2745-2779, 2002.
- [18] P. Ordejón, E. Artacho, J. Soler, *Self-consistent order-N density-functional calculations for very large systems*, Physical Review B **53** (1996) R10441-R10444.
- [19] J. Perdew, K. Burke, M. Ernzerhof, *Generalized Gradient Approximation Made Simple*, Physical Review Letters **77** (1996) 3865-3868.
- [20] M. Methfessel, A. T. Paxton, *High-precision sampling for Brillouin-zone integration in metals*, Physical Review B **40** (1989) 3616.

POSTER SESSIONS
NANOFABRICATION TECHNIQUES
(NFT)

FACILE FABRICATION OF SILVER NANOWIRES AND POLYHEDRAL SILVER NANOPARTICLES AS PROMISING SERS SUBSTRATES

†Tuan-Kiet Duong^{1,2}, †Thu Anh Nguyen^{1,2}, Tuyen Thi Thanh Huynh^{1,2}, Tuan-Vu Pham^{1,2}, Minh-Vu Dinh Pham^{1,2}, Phuong-Phong Thi Nguyen^{1,2}, Khuong Quoc Vo^{1,2*}.

¹ Department of Physical Chemistry, Faculty of Chemistry, Ho Chi Minh City University of Science, Vietnam National University, Ho Chi Minh City, 227 Nguyen Van Cu Street, Ward 4, District 5, Ho Chi Minh City 70000, Vietnam.

² Vietnam National University, Ho Chi Minh City, Vietnam.

*Corresponding author

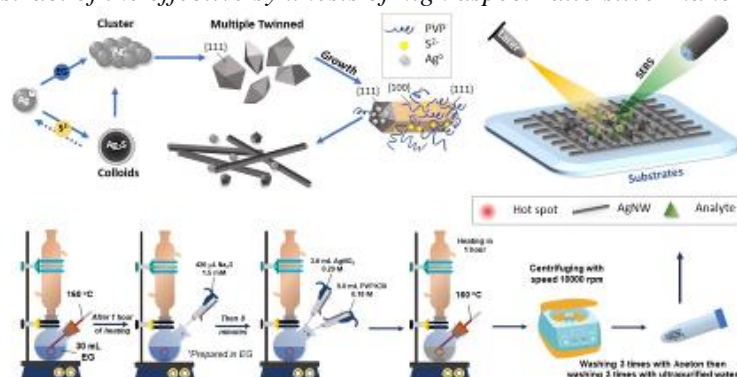
†These authors contributed equally to this work.

Email: vqkhuong@hcmus.edu.vn

ABSTRACT

One-dimensional silver nanowires have gained considerable attention in various applications involving sensing, agriculture, antibacterial, and electric because of their distinctive electromagnetic and optical properties. Therefore, in this study, we focus on developing a rapid and facile controlled synthesis of silver nanowires (AgNWs) by the modified polyol method. Tailoring the parameters such as time reaction, Na₂S, and PVP concentration, silver nanoparticles were transformed from polygonal to wires nanostructures with a relatively high aspect ratio. The role of these factors that influenced AgNW formation was also clarified. AgNWs with an average length of approximately 6.5 μm and aspect ratio (length/width, R) of more than 600 were obtained with high yield. The properties of the as-prepared AgNWs were characterized via UV-Vis spectroscopy, field emission scanning electron microscopy (FE-SEM), X-ray diffraction (XRD), X-ray photoelectron spectroscopy (XPS), transmission electron microscopy (TEM), and high-resolution transmission microscopy (HR-TEM). Specifically, the high aspect ratio nanowire and polygonal structures can intertwine to form the matrix, which enhances numerous electromagnetic enhancement sites ("hot spots") at the close contact point of silver nanoparticles. we initially investigated the SERS activity of PAgNPs/AgNWs-substrates in detecting methylene blue with a concentration ranging from 10⁻⁵ to 10⁻⁹ M.

Figure: Graphical abstract of the effective synthesis of high aspect ratio silver nanowires.



Keywords: Silver nanowires, Silver polygonal nanoparticles, SERS, methylene blue, polyol.

INTRODUCTION

Nanotechnology still achieves considerable attention from many scientists due to its wide applicability [1, 2]. In the past few years, noble metal nanomaterials with distinct properties, such as surface plasmon resonance, and enhanced electromagnetic fields compared to bulk

materials, are an integral part of nanotechnology [3, 4]. Among them, silver nanomaterials have attracted great interest because of their ability to synthesize in many shapes like nanocubes [5], nanorods [6], nanoplates, and, notably, silver nanowires (AgNWs) [7].

In this study, AgNWs and polyhedral silver nanoparticles PAgNPs were rapidly synthesized by the modification of a less time-consuming polyol method, using ethylene glycol as the reducing agent, introducing Na₂S as an additive agent that could govern the direction growth of AgNWs as well as increasing the ability to synthesize large quantities. Reaction parameters such as concentration of PVP and Na₂S are investigated for their influence on the formation of AgNWs. Moreover, the SERS activities of the mixture of AgNWs and polyhedral are thus studied with methylene blue (MB) at trace concentration, showing the remarkable possibility for application in amplifying the Raman signal.

EXPERIMENTAL

Chemicals

Silver nitrate (AgNO₃, 99.8%) was bought from Sinopharm, China. Sodium sulfide nonahydrate (Na₂S.9H₂O, 98.0%) and polyvinylpyrrolidone K30 (PVP K30) were purchased from Shanghai, China. Ethylene glycol (EG, 95.0%) and methylene blue (MB) were obtained from GHTech, China. Acetone (95.0%) was sourced from Chemsol, Vietnam. Chemicals and additive reagents were in high purity grade and used as obtained. EG was used for all reagent preparation and product formulation processes. All glassware and magnetic stirring bars were treated with aqua regia (HNO₃/HCl, volume ratio 1:3), and then they were rinsed again with distilled water before conducting the synthetic experiment.

Synthesis of Silver nanowires (AgNWs)

The synthesis process was modified based on Guo's procedure [18]. In a typical process, 30 mL of ethylene glycol (EG) was added into a 250 mL three-necked flask and heated at 150 °C for 1 hour under magnetic stirring at 300 rpm. Then, 420 μL Na₂S (1.5 mM) was quickly added. After 8 minutes, the mixture of 9 mL of PVP K30 (0.18 M) in EG and 3 mL of AgNO₃ (0.29 M) in EG was injected. After boiling for 1 hour, the solution changed from deep yellow to milky brown.. The obtained nanomaterials were replicately washed with DI water three times before obtaining the AgNWs/AgNPs product.

Characterization

The optical properties of AgNWs were analyzed via UV-Vis NIR-V670 spectrophotometer (JASCO, Japan) using a

couple of Quartz cuvettes (1 cm path length). Measurements were performed in the wavelength range from 300 to 800 nm at a 400 nm/min scanning speed. SEM evaluated the morphology of AgNWs/AgNPs conducted on a JEOL JSM-7600F scanning electron microscope (USA). TEM images were constructed using a JEM-1400 transmission electron microscope (JEOL Ltd., Tokyo, Japan).

SERS measurements

Methylene Blue (MB) was used as the probe molecules to determine the SERS performance of PAgNPs/AgNWs substrates. The PAgNPs/AgNWcolloid substrate was prepared by centrifuging the as-synthesized AgNPs/AgNWs colloidal solution at 10000 rpm for 10 mins and then redispersed in 1.0 mL of ethanol.

RESULTS AND DISCUSSION

Effect of time reaction

The synthesis process of AgNWs and PAgNPs was affected by various factors, and the synthesis time is one of the critical parameters that effected to the length of silver nanowires. Therefore, different reaction times of 2, 4, 6, and 8 hours were respectively investigated to determine the effects of reaction time on the morphology of AgNWs and PAgNPs.

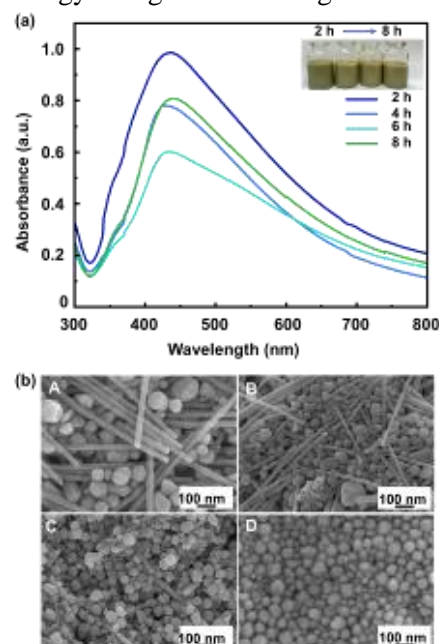


Figure 1. (a) UV-Vis spectra of silver nanoparticle colloids synthesis with different time reactions, and (b) corresponding SEM images of silver nanoparticles synthesized at 2h, 4h, 6h, 8h, respectively.

The crystal structures of AgNPs at different reaction times were examined with X-ray diffraction (XRD) patterns. The results, as presented in **Fig. 2(a)**, clearly showed distinct diffraction peaks at 38.3, 44.4, 64.2, 77.2, and 82.3 corresponding to the (111), (200), (220), and (311) planes of the face-centered cubic (FCC) crystal structure of silver (Ag Fcc JPCDS No. 03-0921) [8, 14]. The HRTEM image provided further insights into the crystal structure, revealing a lattice spacing of 0.204 nm, corresponding to the (100) plane of the FCC crystal structure of silver. This confirmed the highly crystalline nature of the silver nanoparticles, with the (100) plane enclosing the surrounding facets of the AgNWs. Based on these observations, a reaction time of 2 hours was chosen for studying other factors.

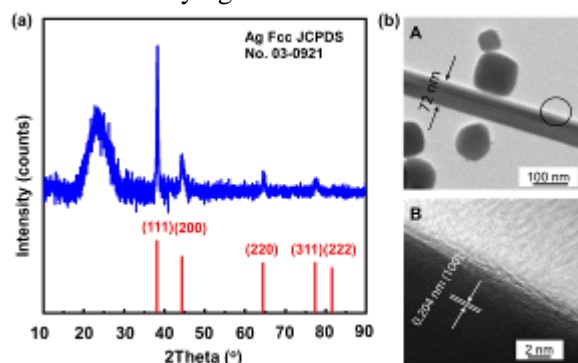


Figure 2. (a) XRD patterns of silver nanoparticles were synthesized at 2h, 4h, 6h, and 8h, respectively (b) (A) TEM and (B) HRTEM image of silver nanoparticles synthesis at 2h reaction.

Effects of Na₂S concentration

The previous studies supposed that the presence of Na₂S facilitates the formation of AgNWs, and the length and diameter of AgNWs can be controlled by adjusting the concentration of Na₂S [19-21]. In this study, the investigation of the effect of Na₂S concentration was studied by changing the Na₂S concentration conditions from 1; 1.5; 2; 2.5, to 3 mM, sequentially. The UV-Vis results and SEM images are shown in **Fig. 3(a)**. Besides, SEM images (**Fig. 3(b)-A,C**) corresponding to the sample synthesized at 1.5 mM Na₂S showed that the density of polyhedral particles (82.33 ± 3.27 nm) could be more dominant than the wire form. In the polyol method, the reduction of AgNO₃ by EG occurs for a long time, but adding a small amount of Na₂S could significantly reduce the reaction time [21, 22]. In this synthesis, the amount of Ag₂S

colloidal particles was formed would reduce the concentration of free Ag⁺ ions in the early stages of the reaction.

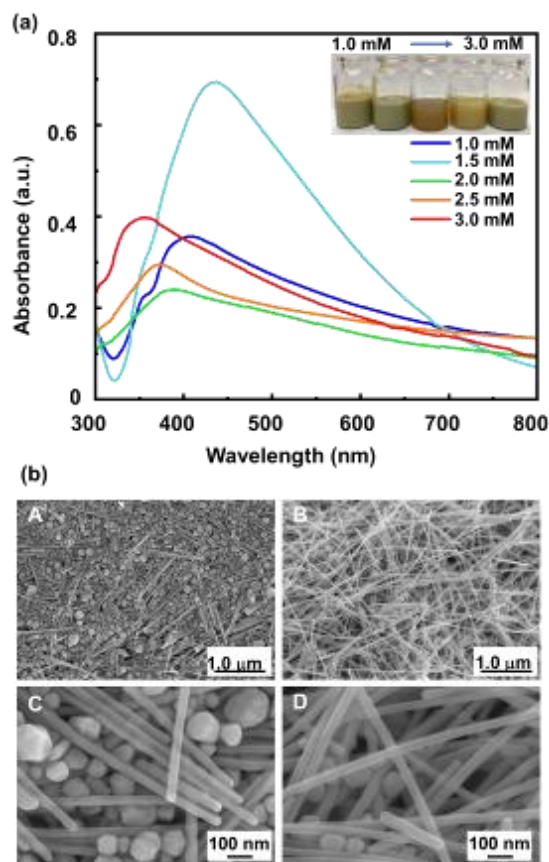


Figure 3. (a) UV-vis spectra and images (right inset) of AgNWs colloidal solutions synthesized with various Na₂S concentrations ranging from 1 to 3 mM (b) SEM images of the synthesized AgNWs with concentrations of Na₂S ((A) scale bar 1.0 μm, and (C) 100 nm); 1.5 mM, (B scale bar 1.0 μm, and (C) 100 nm, D) 3 mM, respectively.

Effects of PVP concentration

To comprehend the role of PVP in this process, AgNWs are prepared with the different concentrations of PVP while keeping the time of reaction at 2h, 30 mL of EG, 420 μL Na₂S in EG (1.5 mM); 3 mL of AgNO₃ in EG (0.29M). The color of the colloidal solutions changes from yellow, brown-orange, khaki, and beige (**Fig. 4(a)**). The sample synthesized with 0.12 M of PVP did not present any characteristic SPR peak in the 300-800 nm wavelength region. When the concentration of PVP is increased to 0.14 M, it can be clearly observed that the appearance of the SPR peak at 410 nm and the shoulder at 360 nm mainly contributed to polyhedral. (**Fig.4(b)-A, B**).

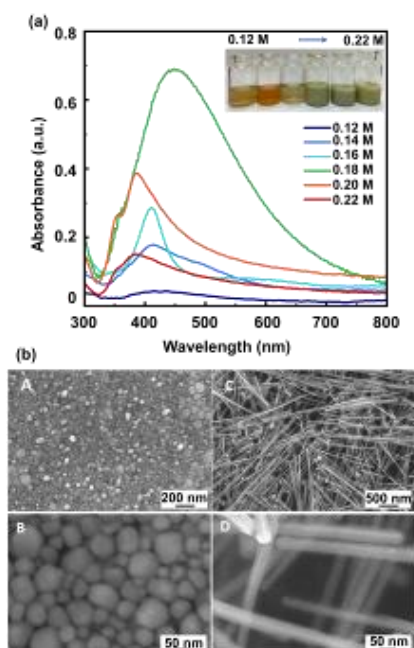


Figure 4. (a) UV-vis spectra and images of AgNWs colloidal solutions synthesized with various PVP concentrations ranging from 0.12 to 0.22 M (b) SEM images of the synthesized AgNWs with concentrations of PVP (A, B) 0.14 M, (C, D) 0.20 M, respectively.

SERS activity of AgNWs substrates in trace methylene blue detection

To investigate the effectiveness of different substrate types in enhancing Raman scattering, three substrates were synthesized: PAgNPs/AgNWs, PAgNPs, and AgNWs. In **Fig. 5 (a-b)**, the SERS spectrum obtained for methylene blue (MB) at a concentration of 10^{-5} M clearly demonstrates that the PAgNPs/AgNWs substrate has been shown to provide better performance than solely using each kind of nanomaterial. Moreover, PAgNPs/AgNWs substrates were initially used to detect various concentrations of MB ranging from 10^{-5} to 10^{-9} M. The results (**Fig 5(c)**) indicated that the PAgNPs/AgNWs have the capacity to detect trace MB of about 10^{-9} M. This finding highlights the potential of these substrates for molecular trace detection and analysis, particularly in the field of dye molecules such as MB.

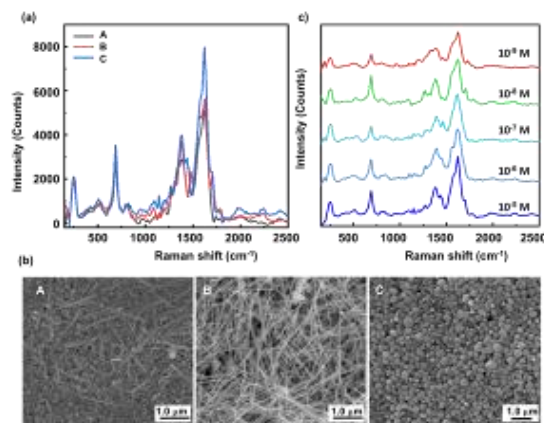


Figure 5. (a) SERS spectra of 10^{-5} M Methylene blue (MB) on PAgNPs/AgNWs (A), AgNWs (B), AgNPs substrates (C) (b) SEM image of PAgNPs/AgNWs (A), AgNWs (B), AgNPs substrates (C), respectively (c) SERS spectra of various concentrations of MB ranging from 10^{-5} to 10^{-9} M on PAgNPs/AgNWs substrates.

CONCLUSION

In conclusion, this study has successfully synthesized one-dimensional silver nanostructures (AgNWs) and polyhedral AgNPs (PAgNPs), through the polyol method. By carefully controlling key parameters such as reaction time, Na_2S concentration, and PVP concentration, an average size of 72 nm polyhedral NPs and silver nanowires with aspect ratios of more than 600 were obtained.

Acknowledgment

This research is funded by the University of Science VNU-HCM under grant number T2023-38

References

- [1] Lan, J., *Overview of Application of Nanomaterials in Medical Domain*. Contrast Media Mol Imaging, **2022** (2022) 3507383.
- [2] Verma, A. and M. Yadav, *Application of nanomaterials in architecture – An overview*. Materials Today: Proceedings, **43** (2021) 2921-2925.
- [3] Sui, M., et al., *Strongly confined localized surface plasmon resonance (LSPR) bands of Pt, AgPt, AgAuPt nanoparticles*. Scientific Reports, **9**(1) (2019) 16582.
- [4] Borah, R., et al., *Plasmon resonance of gold and silver nanoparticle arrays in the Kretschmann (attenuated total reflectance) vs. direct incidence configuration*. Scientific Reports, **12**(1) (2022) 15738.

SYNTHESIS OF NANO SULFUR IN CHITOSAN COPPER COMPLEX

Nguyen Hong Nhung^{1*}, Le Nghiem Anh Tuan², Tran Phuoc Tho², Nguyen Quoc Hien²,
Bui Duy Du^{1,2,*}

¹ Graduate University of Science and Technology, Vietnam Academy of Science and Technology, 18 Hoang Quoc Viet Street, Cau Giay District, Ha Noi City, Viet Nam;

² Institute of Applied Materials Science, Vietnam Academy of Science and Technology, 1B TL29 Street, Thanh Loc Ward, District 12, Ho Chi Minh City, Viet Nam

*Corresponding: Email: vina9802@gmail.com, nhung_ziz@yahoo.com

ABSTRACT

Sulfur (S) was one of the inorganic elements used by plants to develop and produce phytoalexin to resist certain diseases. This study reported a method for preparing nano S stabilized in the chitosan-Cu²⁺ complex by hydrolysis of Na₂S₂O₃ in an acidic medium. The obtained nano S/chitosan-Cu²⁺ (SNPs/CS-Cu²⁺) complex consisting of 0.32% S, 4% CS and 0.7% Cu (w/v), contained SNPs with size from 28.1 to 40.5 nm depending on molecular weight (Mw) of CS. The X-ray diffraction pattern of SNPs/CS-Cu²⁺ complex showed that SNPs had orthorhombic crystal structures. The FT-IR spectra of CS and the CS-Cu²⁺ complex were also measured. The product of SNPs stabilized in CS-Cu²⁺ complex has potential for use as plant-disease control agents.

Keywords: Nano sulfur, chitosan, hydrolysis, nano S/chitosan-copper complex

INTRODUCTION

Today, nanotechnology has been applied in many fields including medicine, energy, electronics, and agriculture [1]. Nanomaterials, particularly nanocomposites have been used in agriculture as a plant protection agent because of their antibacterial, antifungal, and antiviral activities [2-4] and/or nano-nutrient fertilizer properties [5]. Nanoparticles capable of inhibiting plant diseases are metal, metal oxide, metalloid and carbon nanoparticles [6].

The SNPs/CS-Cu²⁺ material was made up of single materials including SNPs, CS and Cu²⁺. S is an element with a high fungicidal activity that has been used in the treatment of cancer cells and plant diseases from ancient times [7]. CS prepared from shrimp shells is a non-toxic biopolymer with anticancer [8], antibacterial [9], antifungal [10], and nematocidal properties [11]. Therefore, CS has the potential to be used as a plant-disease control agent. CS contains functional groups -OH and -NH₂ that can form complexing with Zn²⁺, Cu²⁺ and Fe²⁺ ions [12,13]. The CS-Cu²⁺ complex releases Cu²⁺ ions in a controlled manner, thus reducing the ion's toxicity [14].

Currently, the methods to synthesize SNPs include acidification of sodium thiosulphate [15,16] or polysulfide [17] in the presence of stabilizer, ultrasonic treatment [18], mechanical

dispersion [15] and sublimation [19] of S powder. In this report, SNPs were synthesized by hydrolysis of sodium thiosulfate in lactic acid, stabilized in the CS-Cu²⁺ complex solution, and studied the size of SNPs depending on Mw of CS was also investigated. The obtained product is orientated to use as a plant-disease control agent.

EXPERIMENTAL

Na₂S₂O₃·5H₂O 99%, Cu(NO₃)₂·3H₂O 99%, C₂H₅OH 99.7% (Xilong, China), CS has different average molecular weight (Mw) of 45.000 g/mol, 60.000 g/mol, 90,000 g/mol and deacetylation degrees (DD) were 92.6, 92.1 and 91.5, respectively (Institute of Applied Material Science, Vietnam), lactic acid 99% (Aldrich Sigma, Germany) and deionized water.

Preparation of SNPs/CS-Cu²⁺ complex solutions

4 g CS with different Mw of 45.000 g/mol, 60.000 g/mol and 90.000 g/mol) was dissolved in 80 ml of lactic acid 4% to obtain CS solutions. The CS-Cu²⁺ complex solution was prepared with the -NH₂/Cu²⁺ molar ratio of 2/1. The number of moles of the -NH₂ group in CS was calculated by formula (1): $N_{-NH_2} = \frac{m}{MM}$, where m (g) is the amount of CS, \overline{MM} (g/mol) is the average molecular weight of the monomer in CS, which was calculated by the formula (2): $\overline{MM} = DD \cdot M_{glu}$.

+ (1 - DD).M_{N-acetylglu}. [20]. Based on the above calculation, the number of moles of -NH₂ and Cu²⁺ was 0.022 and 0.011 mol, respectively. Thus, CS-Cu²⁺ complex was prepared by dissolving 2.66 g Cu(NO₃).3H₂O in a 80 ml CS solution. Then the solution of 2.48 g Na₂S₂O₃.5H₂O in 20 ml deionized water was added drop by drop into the CS-Cu²⁺ complex solution, stirring with a magnetic stirrer until the Na₂S₂O₃ solution was completely added to obtain solution containing 0.32% S, 4% CS and 0.7% Cu (w/v).

Characterization of materials

Diameters of SNPs were measured by transmission electron microscope (TEM) on a TEM S4800-NIHE - Japan and the particle size distribution was determined by DLS spectrum on a HORRIBA SZ-100Z2 - Japan. Crystal structure of materials was determined by X-ray diffraction (XRD) pattern on a XRD D8 Advance-Bruker - Germany. FT-IR spectra were taken on a spectrophotometer FT-IR 840S-Shimadzu - Japan.

RESULTS AND DISCUSSION

The TEM images in Figure 1 showed that the SNPs stabilized in the CS-Cu²⁺ complex had an angular shape.

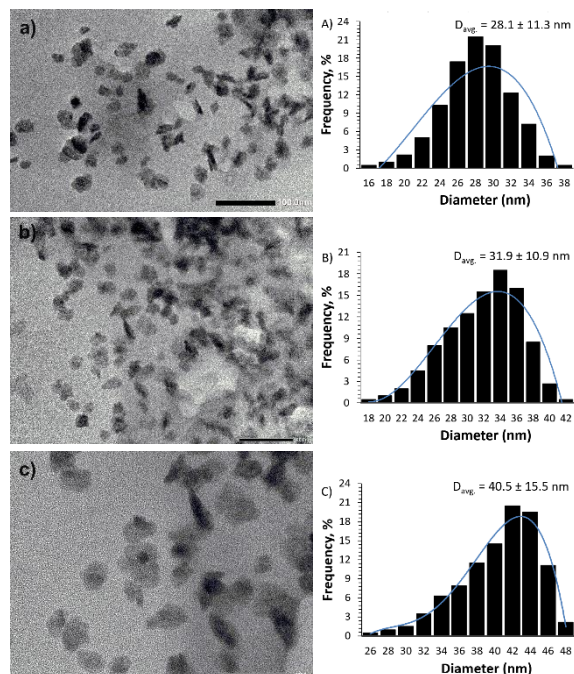


Figure 1. TEM images and distribution of SNPs/CS-Cu²⁺ complex with CS Mw 90,000 g/mol (a, A), 60,000 g/mol (b, B) and 45,000 g/mol (c, C)

The average size of SNPs measured through the TEM images of the SNPs/CS-Cu²⁺ complex

samples using CS Mw of 90,000, 60,000 and 45,000 g/mol was 28.1, 31.9 and 40.5 nm, respectively. The particle size distributions in Figure 1 also showed that the particle size of SNPs/CS-Cu²⁺ complex samples in the range of 16-38, 18-42 and 26-48 nm for CS Mw of 90,000; 60,000 and 45,000 g/mol, respectively. The above results demonstrated that the Mw of CS in the CS-Cu²⁺ complex affected the size of the SNPs.

This result is also consistent with the study of Aranaz et al. (2018) when stabilizing Ag nanoparticles in CS solution with different Mw. CS with Mw > 30 g/mol has the effect of creating smaller and more stable Ag nanoparticles than CS with Mw from 5-30 g/mol [21]. Similarly, Phu et al. (2010) also demonstrated that CS with higher Mw has a better protective effect on Ag nanoparticles than CS with smaller one due to steric effects. Long-chain polymers with more functional groups create an effect that prevents nanoparticles from coming close to each other and agglomeration [22].

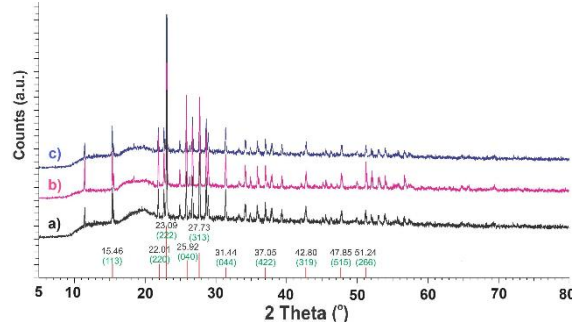


Figure 2. XRD patterns of SNPs/CS-Cu²⁺ complex samples with CS Mw of 90,000 (a), 60,000 (b) and 45,000 g/mol (c)

The XRD patterns of all powder samples of SNPs/CS-Cu²⁺ complex that are presented in Figure 2 showed the highly crystalline state of S particles. Specifically, the peaks at 2θ ~22.01°, 23.09°, 27.73°, 31.44°, 42.80° and 47.85° corresponded to crystal planes (220), (222), (313), (044), (319) and (515), respectively, which were consistent with JCPDS No. 08247. This result was also consistent with other authors' findings when studying the XRD patterns of SNPs prepared by hydrolysis of Na₂S₂O₃ in an acidic medium [17,23]. Furthermore, the XRD patterns in Figure 2 also indicated diffraction peaks characteristic for crystal structure of CS at 2θ ~10° and 20° with low intensity, proving the complex formation of CS and metal ions has reduced the crystallinity of CS [14].

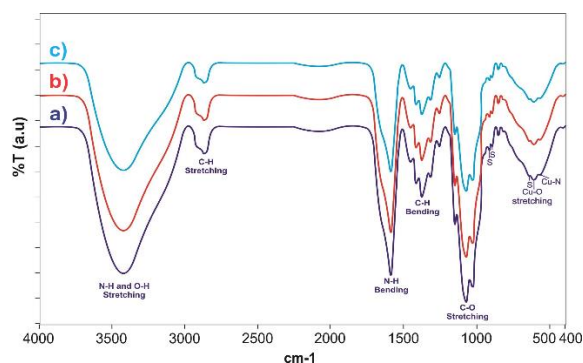


Figure 3. FT-IR spectrum of samples nano S/CS-Cu²⁺ complex with CS Mw 90,000 (a); 60,000 (b) and 45,000 g/mol (c)

The FT-IR spectra of SNPs/CS-Cu²⁺ complex samples in Figure 3 appeared characteristic peaks of CS. The peak at 3450 cm⁻¹ was assigned to the N-H and O-H stretch vibrational. Two peaks at 2880 cm⁻¹ and 2920 cm⁻¹ were assigned to the symmetric and asymmetric vibrations of the -CH₂ group, while the peak at 1420 cm⁻¹ was typical for the stretching vibration of -CH₂ group. Two peaks at 1650 cm⁻¹ and 1590 cm⁻¹ were assigned to the N-H bending vibration of the secondary amide.

Three new peaks at 1150 cm⁻¹, 1075 cm⁻¹ and 1025 cm⁻¹ correspond to the asymmetric stretching of the C-O-C bond, the stretching of C-O bond of C3 (secondary OH) and the C-O stretching vibration of C6 (primary OH) [24]. In addition, the FT-IR spectra also appeared characteristic peaks for the orthorhombic element S (α -sulfur) at 463 cm⁻¹, 644 cm⁻¹, 894 cm⁻¹ and 916 cm⁻¹ when compared with the FT-IR spectrum of standard α -sulfur [25].

CONCLUSION

SNPs/CS-Cu²⁺ complex containing 0.32% S, 4% CS and 0.7% Cu (w/v) was successfully prepared and characterized in this study. In addition, the size of SNPs depending on the Mw of the CS was demonstrated. The SNPs/CS-Cu²⁺ complex has potential applications as plant-disease control agents in agriculture.

Acknowledgment

This research was funded by the program selected basis topic of the Vietnam Academy of Science and Technology (grant No: CSCL19.02/23-24).

References

[1] M. Wypij, J. Trzcińska-Wencel, Golińska, G.D. Avila-Quezada, A. Ingle, M. Rai, *The strategic applications of natural polymer nanocomposites in food packaging and agriculture: Chances, challenges, and*

consumers' perception, *Frontiers in Chemistry* **10** (2023) 1106230.

- [2] C. Krishnaraj, R. Ramachandran, K. Mohan, T. Kalaichelvan, *Optimization for rapid synthesis of silver nanoparticles and its effect on phytopathogenic fungi*, *Spectrochimica Acta Part A, Molecular and Biomolecular Spectroscopy* **93** (2012) 95-99.
- [3] E.K. Elbeshehy, A.M. Elazzazy, G. Aggelis, *Silver nanoparticles synthesis mediated by new isolates of Bacillus spp., nanoparticle characterization and their activity against Bean Yellow Mosaic Virus and human pathogens*, *Frontiers in Microbiology* **6** (2015) 453.
- [4] A. Pasha, D.V. Kumbhakar, S.S. Sana, D. Ravinder, B.V. Lakshmi, S.K. Kalangi, S.C. Pawar, *Role of biosynthesized Ag-NPs using aspergillus niger (MK503444.1) in antimicrobial, anti-cancer and anti-angiogenic activities*, *Frontiers in Pharmacology* **12** (2022) 812474.
- [5] B.D. Du, D.T.B. Ngoc, N.D. Thang, L.N.A. Tuan, B.D. Thach, N.Q. Hien, *Synthesis and in vitro antifungal efficiency of alginate-stabilized Cu₂O-Cu nanoparticles against Neoscytalidium dimidiatum causing brown spot disease on dragon fruit plants (Hylocereus undatus)*, *Vietnam Journal of Chemistry* **57** (2019) 318-323.
- [6] W. Elmer, C. Ma, J. White, *Nanoparticles for plant disease management*, *Current Opinion in Environmental Science & Health* **6** (2018) 66-70.
- [7] S. Shankar, R. Pangeni, J.W. Park, J.-W. Rhim, *Preparation of sulfur nanoparticles and their antibacterial activity and cytotoxic effect*, *Materials Science and Engineering: C* **92** (2018) 508-517.
- [8] S. Kuppasamy, J. Karuppaiah, *Antioxidant and cytotoxic efficacy of chitosan on bladder cancer*, *Asian Pacific Journal of Tropical Disease* **2** (2012) S769-S773.
- [9] J. Li, S. Zhuang, *Antibacterial activity of chitosan and its derivatives and their interaction mechanism with bacteria: Current state and perspectives*, *European Polymer Journal*, **138** (2020) 109984.
- [10] D. Meng, B. Garba, Y. Ren, M. Yao, X. Xia, M. Li, Y. Wang, *Antifungal activity of chitosan against Aspergillus ochraceus and its possible mechanisms of action*, *International Journal of Biological Macromolecules* **158** (2020) 1063-1070.

- [11] M.S. Khalil, M.E.I. Badawy, *Nematicidal activity of a biopolymer chitosan at different molecular weights against root-knot nematode, Meloidogyne incognita*, Plant Protection Science **48** (2012) 170-178.
- [12] X. Wang, Y. Du, L. Fan, H. Liu, Y. Hu, *Chitosan-metal complexes as antimicrobial agent: Synthesis, characterization and structure-activity study*, Polymer Bulletin, **55** (2005) 105-113.
- [13] R.C. Choudhary, R.V. Kumaraswamy, S. Kumari, S.S. Sharma, A. Pal, R. Raliya, P. Biswas, V. Saharan, *Cu-chitosan nanoparticle boost defense responses and plant growth in maize (Zea mays L.)*, Scientific Reports **7** (2017) 1, 9754.
- [14] M.A. Akhtar, K. Ilyas, I. Dlouhy, F. Siska, A. Boccaccini, *Electrophoretic Deposition of Copper(II)-Chitosan Complexes for Antibacterial Coatings*, International Journal of Molecular Sciences **21** (2020) 2637.
- [15] K.J. Rao, S. Paria, *Use of Sulfur Nanoparticles as Green Pesticide on Fusarium solani and Venturia inaequalis Phytopathogens*, RSC Advances **3** (2013) 10471-10478.
- [16] K. Khairan,, Z. Jalil, *Green synthesis of sulphur nanoparticles using aqueous garlic extract (Allium sativum)*, Rasayan Journal of Chemistry **12** (2019) 50-57.
- [17] P. Paralikar, M. Rai, *Bio-inspired synthesis of sulfur nanoparticles using leaf extract of four medicinal plants with special reference to their antibacterial activity*, IET Nanobiotechnology **12** (2018) 25-31.
- [18] T. Seitzhan, S. Aidarova, N. Bekturganova, G. Alimbekova, K. Musabekov, S. Kumargalieva, *Surface-modification of sulfur nanoparticles with surfactants and application in agriculture*, Advanced Materials Research **785** (2013) 475-479.
- [19] X. Xie, L. Li, P. Zheng, W. Zheng, Y. Bai, T. Cheng, J. Liu, *Facile synthesis, spectral properties and formation mechanism of sulfur nanorods in PEG-200*, Materials Research Bulletin **47** (2012) 3665-3669.
- [20] L. Gritsch, C. Lovell, W.H. Goldmann, A.R. Boccaccini, *Fabrication and characterization of copper(II)-chitosan complexes as antibiotic-free antibacterial biomaterial - ScienceDirect*, Carbohydrate Polymers **179** (2018) 370-378.
- [21] I. Aranaz, C. Castro, A. Heras, N. Acosta, *On the ability of low molecular weight chitosan enzymatically depolymerized to produce and stabilize silver nanoparticles*, Biomimetics **3** (2018) 21.
- [22] D.V. Phu, V.T.K. Lang, N.T.K. Lan, N.N. Duy, N.D. Chau, B.D. Du, B.D. Cam, N.Q. Hien, *Synthesis and antimicrobial effects of colloidal silver nanoparticles in chitosan by γ -irradiation*, Journal of Experimental Nanoscience **5** (2010) 169-179.
- [23] R.M. Tripathi, R.P. Rao, T. Tsuzuki, *Green synthesis of sulfur nanoparticles and evaluation of their catalytic detoxification of hexavalent chromium in water*, RSC Advances **8** (2018) 36345-36352.
- [24] F. Brunel, N.E. El Gueddari, B.M. Moerschbacher, *Complexation of copper (II) with chitosan nanogels: toward control of microbial growth*, Carbohydrate Polymers **92** (2013) 1348-1356.
- [25] A.M. Awwad, N.M. Salem, A.O. Abdeen, *Noval approach for synthesis sulfur (S-NPs) nanoparticles using Albizia julibrissin fruits extract*, Advanced Materials Letters **6** (2015) 432-435.

FABRICATION OF LOW-COST MICROFLUIDIC DEVICE BASED ON DRY-FILM PHOTORESIST USING LASER DIRECT WRITING

Van Nhat Pham¹, Trong Nghia Nguyen², Van Toan Nguyen³, and Tien-Anh Nguyen^{3,*}

¹Department of Advanced Materials Science and Nanotechnology, University of Science and Technology of Hanoi, VAST, 18 Hoang Quoc Viet, Hanoi, Vietnam

²Center for Environmental Physics and Technology, Institute of Physics, VAST, 18 Hoang Quoc Viet, Hanoi, Vietnam

³Department of Physics, Le Quy Don Technical University, 236 Hoang Quoc Viet, Hanoi, Vietnam
Email: anhnt@lqdtu.edu.vn

ABSTRACT

Microfluidic devices have potential applications in biological cell manipulation, especially in single-cell capture, because of their unique features, including high throughput, good stability, and easy integration. The soft-lithography method is commonly used to fabricate those chips. However, it requires complicated processes and clean-room facilities. Therefore, this traditional technique has several disadvantages, including time consumption, high-cost materials, and being hard to procedure, especially in limited resources areas. In contrast, laser direct writing (LDW) applied on dry film photoresists, enables to manufacture of microfluidic chips in normal room conditions. In this paper, we demonstrated an efficient procedure to fabricate a high-resolution micro-structure from dry film photoresist using the LDW technique without the requirement of clean room facilities. The finest dimension of the micro-structure gap was 13 μm to form trap-cell structures. The prototype microfluidic system was tested in capturing single cells to validate the application. The combination of dry film photoresist and the LDW proves effectiveness in the microfabrication of high-resolution microstructures in the conventional laboratory, which is very important in limited-resource countries.

Keywords: Dry film photoresist, hydrodynamic trapping structure, microfluidics, laser direct writing.

INTRODUCTION

In recent years, microfluidic devices have emerged as potential tools for single-cell analysis because of their unique features, such as high throughput, good stability, and easy integration [1, 2]. Those devices integrate microstructures similar to the cell size inside microchannels like blood vessels to capture single cells from the cell suspension flow. Several approaches have been developed for trapping an individual cell based on different physical phenomena, including hydrodynamic-based [3], dielectrophoretic-based [4], and magnetic-based [5]. The hydrodynamic-based method utilizes fluidic resistance created by individual microstructures inside a microchannel to collect single cells without any other supporting apparatus. The main challenge in the hydrodynamic trapping is the requirement for precise fabrication of microstructures and further investigation of trapped cell affection. In the dielectrophoresis-based technique, a uniform

electric field is applied to control the motion of a single cell. However, the electric signal may damage to the trapped cells and affect their proliferation. In the magnetic-based platform, magnetic force captures magnetic particles that labelled cells with magnetic beads. This method brings precise and high trapping efficiency. However, it requires preparing steps to bond cells with magnetic beads, which are time-consuming and affect cell behaviour.

Microfluidic devices are commonly manufactured by the soft-lithography technique using SU-8 photoresist moulding and Polydimethylsiloxane (PDMS) replication [6]. The SU-8 mould is usually designed by using special CAD software and manufacturing the corresponding photomask with designed micropatterns. Then, the photomask is used in different photolithography procedures in the cleanroom to fabricate the mould. This fabrication process sometimes requires multiple repetitions to obtain successfully fabricated

mould. As a result, this process is complicated, time-consuming, and costly. Therefore, it is necessary to devise a new fabrication method to overcome the challenges of conventional fabrication methods. Recently, dry film photoresists have been widely used in fabricating microfluidic channels, providing many advantages, including no edge bead, thickness uniformity over the whole wafer, fast processing, straight sidewalls, requiring fewer sophisticated tools, and overall lower fabrication cost [7,8]. Thus, using a dry film photoresist is a convenient solution for cleanroom facilities with limited budget constraints [8]. Although utilizing dry film photoresists helps avoid all complicated photolithography processes in the clean room, it still requires the use of photomasks.

Recently, laser direct writing lithography (LDWL) has emerged as a powerful tool replacing the soft lithography technique in fabricating microfluidic devices [9, 10]. In LDWL, the designed micropatterns from a computer-aided design (CAD) file are precisely exposed onto the photoresist-covered substrate by a highly focused laser beam which is directed by a spatial light modulator (SLM). The SLM performs essentially as a programmable mask. This technique completely not only precludes the use of photomasks but also resolves the resolution issues encountered in the proximity exposure [11] Moreover, this method brings several advantages including non-contact, high-speed and flexible patterning technology, exhibiting great potential for the fabrication on non-planar surfaces. Besides, the development of new polymer materials has advanced microfabrication techniques by either simplifying the existing procedures or enabling out-of-cleanroom processing. In recent times, customized microchannels can be generated with complex features such as junctions, bifurcations, hierarchies, and gradually changed geometry by using the state-of-the-art versatile grayscale LDWL technology [12]. Therefore, LDWL has been demonstrated as a promising modern technique for microfluidic applications.

In this paper, we demonstrated a novel way to fabricate a high-resolution micro-structure from dry film photoresist using laser direct laser writing technique. The finest dimension of the micro-structure was 5 μm which was based on to form a trap in the microfluidic channel. The PDMS microfluidic was experienced for trapping single cells to ensure the application of this

technique for lab-on-chip. The combination of dry film photoresist and laser direct writing brings high-resolution microstructures of dry film moulds which were fabricated in the conventional laboratory rather than the clean room.

EXPERIMENTAL

2.1 Materials

In this work, the mixture 10:1 of Sylgard 184 (Dow, USA) was used as material for microfluidic channel. The Riston (Dupont, USA) negative dry film photoresist with 38 μm thick was used to fabricate a rigid mold. The common glass slide for microscopy with 25 \times 75 \times 1 mm as the substrate for dry film mould. The laser writing system was built on the inverted microscope Ti2-E of Nikon. The original manual stage of the microscope was replaced by a motorized stage PZ 2150 of ASI (Applied Scientific Instrumentation). A 405 nm semiconductor laser from Roithner Lasertechnik was used to write. The intensity can change by applying a pulse width modulation technique with the 256 discrete level. The use of a pinhole of 50 micrometers improved the beam profile of the laser. An objective 10x/0.45 focused the laser light on the dry film with the diameter at FWHM was about 5 μm . The speed of 250 $\mu\text{m/s}$ and laser intensity of 4.7 μm at the output of the objective remained unchanged for all samples. During the writing, the laminated dry films were placed on the XY Piezo Motor stage (PI, USA) with the piezo smallest move by 2 nm. The chemicals as anhydrous sodium carbonate (Sigma, USA), distilled water and drying air was used at standard conditions. The bonding of PDMS and glass slide was performed by a plasma cleaner (Harrick Plasma, USA).

2.2 Design of microstructures

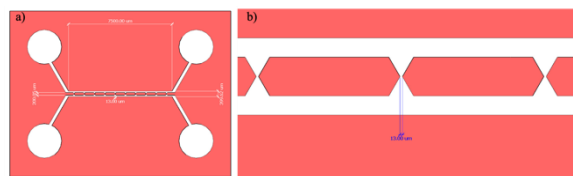


Figure 1. The design of microchannel (a) and the zoomed in trapping microstructures (b).

Figure 1 illustrates the 2D design of the microfluidic devices and trap-cell structures inside the microchannels. The design included four inlets/outlets for two main channels. There are ten trap-cell structures between the main channels with the smallest gap of approximately

13 μm for trapping cells. In working conditions, the cells in suspended flow will be injected in one of four inlets and flow out by the others. The cells with their size bigger than the trap space will be trapped. The Sketchup software was used and exported as a 3D file format (.stl). Then the code file was obtained by Cura software, which was used for 3D printing. A text file of coordinates was created using a lab-made, written in LabVIEW after adding speed of movement and laser intensity information. The final text file was loaded to the control software of the laser writing system to transfer designed patterns onto dry film.

2.3 Fabrication process

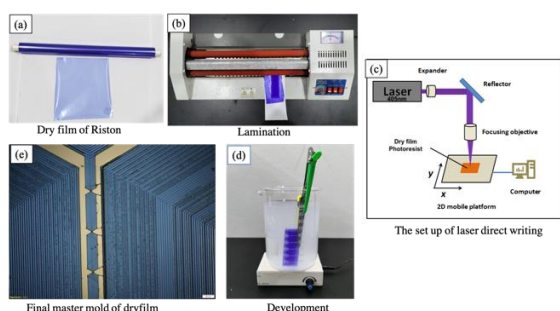


Figure 2: The entire fabrication process of LDW on the dry film photoresist. (a) The negative photoresist of Riston was used. (b) The lamination of dry film on a clean glass substrate. (c) Laser direct writing lithography process. (d) Development to remove undesired regions. (e) The final microstructures.

Figure 2 depicts the fabrication process of the microfluidic device using the LDW technique on the dry film photoresist, which was a part of the soft lithography technique [6]. The only difference compared to the typical procedure here is that instead of using a photomask with a UV 365 nm wavelength source, the laser 450 nm was used. Via a focused lens system, the size of the laser beam could be decreased down to 5 μm which enables it to work with cells (with approximately 10-15 μm diameter). Moreover, without using a photomask at high resolution, mostly using a chrome mask, the total time for the entire process will be decreased significantly.

The dry film of Riston was laminated onto a glass slide as a substrate with a designed thickness corresponding to the number of laminated layers using a conventional office laminator. The temperature of the roller was set at 100 $^{\circ}\text{C}$ which was optimized for the good adhesion of dry film on glass substrate. The

lamination will be repeated until the desired thickness is reached. In this work, only one layer of photoresist will be laminated, corresponding to the 40 μm height of the channel. After that, the laminated dry film photoresist sample was written using laser focused system as illustrated in Fig. 2(c). The duration of writing depended on some factors as the width of the laser beam, the area of micro-structures, the speed of laser movement, and the repeats of exposure. Hence, the design required 35 minutes to complete the writing with 5 μm of laser beam width at 250 $\mu\text{m}/\text{s}$ and 1 time of exposure. The exposed dry film was post-exposure baked at 100 $^{\circ}\text{C}$ for 01 minute in a hot plate before development (Fig. 2d) in Na_2CO_3 1% w/w solution for 01 minute to obtain the expected pattern (Fig. 2e).

A common PDMS casting procedure was applied to obtain the microstructures. The inlets/outlets were created using a punch with outer diameter by 1.5 mm. The package microfluidic chip on the glass substrate was completed by oxygen plasma treatment. The alcohol sterilization was performed right before working with cells. The alcohol sterilization was performed right before working with cells.

The mouse macrophage cells in DMEM (Thermo Fisher, USA) were used to test the working of the microchannel. The number of cells in the solution was controlled at 10^2 - 10^3 cell/ml.

RESULTS AND DISCUSSION

3.1. Characterization of microstructures

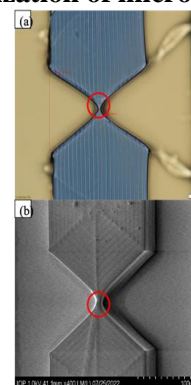


Figure 3: The optical image (a) and SEM (b) image of fabricated dry film microstructure

The dry-film microstructures were characterized by an optical microscope as well as the SEM (as illustrated in Fig. 3). It was clear to see the difference between the design and the final structure is that they still had remained dry film at the middle position. It can be explained at

this position the photoresist was overexposed. However, the energy of UV was not enough to cure all the parts that led to form a small channel. This hypothesis was validated by cell trapping experiments below.

3.2. Cells trapping experiment

The cells and DMEM solution were injected into a microchannel through a glass syringe (Hamilton 1 ml, USA). The passing of cells through of microchannel is shown in Fig.4. Due to the bigger dimension of the trapping structure, the cell can easily pass through. This was not the expected result. The reason could be given that related to dry film thickness. Because the dry film was used for industry with fixed 40 μm thickness and the aspect ratio was only 1.5, this means that if thinner dry film can be used, a smaller structure can be obtained. The recommended thickness was 10-20 μm . To do that, the other way to reform the photoresist layer will be to apply spin coating.

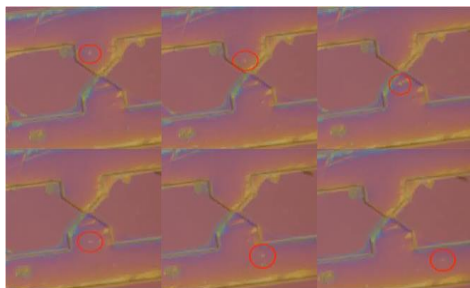


Figure 4: Tracking of cells moving through the microstructure.

Although, the final structure was not succeeded to trap the cells however, the smallest configuration by 13 μm much best

CONCLUSION

In conclusion, the use of the LDW photolithography technique for Riston dry film photoresist was successfully performed in fabricating microstructures inside microchannels. Without using a photomask and the size of the laser beam was only 5 μm , the LDWP is the most potential method to generate the finest structure at low-cost which is more suitable for Vietnam conditions. Although in this work, the single-cell trapping was not successful, however, the device could be applied for other applications such as microparticle separation in future work.

Acknowledgment

This research is funded by University of Science and Technology of Hanoi under grant number USTH.AMSN.01/21-22

References

- [1] TA. Nguyen, et al., *Microfluidic Impedance Biosensors For Monitoring A Single And Multiple Cancer Cells In Anticancer Drug Treatments*, Proc.BME6, 2018, 681-685.
- [2] B. Xiong, et al., *Recent developments in microfluidics for cell studies*, Advanced materials, **26** (2014), 5525-32.
- [3] TA. Nguyen, et al., *Microfluidic chip with integrated electrical cell-impedance sensing for monitoring single cancer cell migration in three-dimensional matrixes*, Analytical chemistry **85** (2013), 11068-76.
- [4] D. Das, et al., *A microfluidic device for continuous manipulation of biological cells using dielectrophoresis*, Medical engineering & physics **36** (2014), 726-731.
- [5] H. Xu, et al., *Magnetic-Based Microfluidic Device for On-Chip Isolation and Detection of Tumor-Derived Exosomes*, Analytical Chemistry **90** (2018), 13451-13458.
- [6] Qin, D, et al., *Soft lithography for micro- and nanoscale patterning*, Nature Protocols **5** (2010), 491.
- [7] Y.C. Tsai, et al., *Fabrication of microfluidic devices using dry film photoresist for microchip capillary electrophoresis*, Journal of Chromatography A **1111** (2006), 1111 267-271.
- [8] P. Mukherjee, et al., *Rapid Prototyping of Soft Lithography Masters for Microfluidic Devices Using Dry Film Photoresist in a Non-Cleanroom Setting*, Micromachines **10** (2019), 192
- [9] Y. Liao, et al., *Rapid prototyping of three-dimensional microfluidic mixers in glass by femtosecond laser direct writing*, Lab on a Chip **12** (2012), 746-749.
- [10] D.H. Kam and J. Mazumder, *Three-dimensional biomimetic microchannel network by laser direct writing*, Journal of Laser Applications **20** (2008), 185-191.
- [11] J. Liu, et al., *Intensity modulation based optical proximity optimization for the maskless lithography*, Optics Express **28** (2020), 548-557.
- [12] N. Xiang N, et al., *Investigation of the maskless lithography technique for the rapid and cost-effective prototyping of microfluidic devices in laboratories*, Journal of Micromechanics and Microengineering **23** (2013), 025016.

FABRICATION OF 3D MICRO-SCALE POROUS PCL SCAFFOLDS BY USING A FOOD ENHANCER AS PARTICLE-LEACHING POROGEN FOR BONE TISSUE ENGINEERING

Thanh H. Thai*, Thy Minh Nguyen*, Phan Thi Thanh Tam, Thi-Hiep Nguyen

School of Biomedical Engineering, International University, Vietnam National University- HCMC

Email: thanhthai.thd@gmail.com

**Authors contributed equally*

ABSTRACT

Three-dimensional (3D) scaffolds have been a prominent substitute for repairing and regenerating bone tissue defects caused by trauma or illness. The particle-leaching method has shown its advantages in fabricating bone scaffolds through its porogen particle characteristics. In this article, monosodium glutamate (M), salt (N), sugar (S), and food enhancer products that are harmless to the whole population were used as the porogen material for bone scaffolds. Their morphological particles fabricated micro-scale and interconnective pores and improved the hydrophilicity of Polycaprolactone (PCL) scaffolds. Furthermore, these scaffolds showed proper porous that facilitated cell living in vitro environments.

INTRODUCTION

Bone tissue engineering (BTE) is a field of study that aims to develop biological substitutes for bone tissue repair and regeneration. It combines the principles of engineering and life sciences to create scaffolds that provide appropriate cell adhesion, proliferation, and function, as well as tissue restoration and vascularization. The scaffold-based tissue engineering approach involves the use of biodegradable and porous scaffolds with signaling factors to guide the spatially and temporally complex process of bone fracture repair. [1] Polycaprolactone (PCL) is a biodegradable polymer that has been widely used in the field of bone tissue engineering due to its biocompatibility and load-bearing applications. The biocompatibility and hydrophilicity of PCL with other biomaterials allow it to form composite scaffolds for bone regeneration. [2]

The particle-leaching method is one of the most popular approaches to fabricating porous scaffolds. This approach can control the macro- and micro-scale pore size and porosity of the scaffolds very well.

In this article, food enhancer products such as monosodium glutamate (M), salt (N), and sugar (S) were used as the porogen material for polycaprolactone (PCL) scaffolds. They would facilitate hydrophilicity and cell viability in vitro environments.

EXPERIMENTAL

Preparation of PCL solution

The PCL concentration was initially investigated at different percentages to determine the most suitable value for the procedure. After SEM observation, the highest concentration of PCL in acetone was fixed at 33%, allowing the appropriate mixing of porogen and solvent with relatively defined pore formation.

Preparation of porogen

Three kinds of porogen agents, such as sodium chloride (N), sucrose (S), and monosodium glutamate (M), with various shapes and sizes, were used to inspect the changes in the scaffold morphology. The particulates were first sieved based on the pre-selected particulate diameter, <200 μm for N and <500 μm for S and M. The weight of the porogen mixture was fixed at 2.5 times the weight of the PCL solution for optimal porosity. Each separate mixture was added to the PCL solution while being continuously stirred by a glass rod until a slurry texture appeared.

Particulate leaching method

This fabrication technique was adapted from Tripathi et al. with modifications. [3] The slurry was poured into a cylindrical mold of 10 mm diameter and 2.5 mm height. A hand pressure of 1N was applied to the mold to shape the scaffold and eliminate unexpected bubbles. The molds

were kept at room temperature for two days to evaporate the solvent completely. The samples were stirred in distilled water for 48 hours for the leaching process to form the porous structure. Finally, the scaffolds were air-dried and stored at room temperature. The process is illustrated in Figure 1.

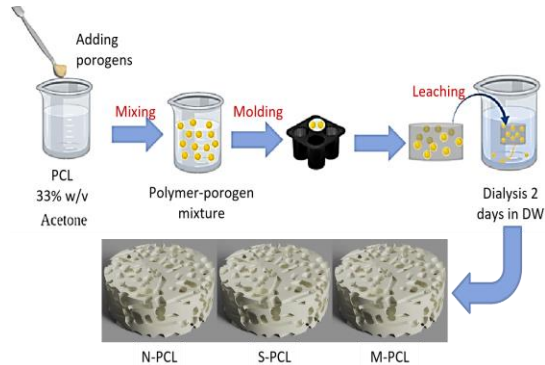


Figure 1. Schematic of the particulate leaching procedure

Surface wettability

Contact angle measurements were carried out manually according to ASTM D5725 with modifications. [4] A water droplet of 0.2 mL was dispensed onto the scaffolds, which were mounted onto a glass slide. After different time points of 0s, 10s, and 1min of dropping, the evolution of the droplet shape was recorded using a DSLR camera (Canon). Recorded images were analyzed using ImageJ software (NIH, USA) to determine the contact angle. The experiment was repeated 3 times.

Cell viability over time

After scaffolds sterilization, the set of samples was prepared to fit the bottom surface area of the 96-well plates and preconditioned with DMEM media prior to cell seeding. After removing the medium, the cells were seeded at 5×10^4 cells per mL on top of each scaffold and cultured for a period of 1–4 days at 37°C, 5% CO₂. The culture medium was replaced on day 2. At specific time points, 100 μ L resazurin solution (0.02 mg/mL) per well was supplied and incubated for 4 hours for measurement. The fluorescence of the solutions was excited at 530 nm wavelength, and the emitted signal was 590 nm using a microplate reader (VarioskanTM, ThermoScientific, USA). Each sample was replicated 3 times.

RESULTS AND DISCUSSION

Microstructure observation

The pore geometries were examined by microscopic view, demonstrating a uniform pore network with distinct pores from the three porogens. Compared to the interior, the surface represented fewer pores, but rather the pore shapes only; however, a well-interconnected pore-channel system was more observable in the sliced images. The pores of N-PCL were small quadrilaterals, whereas S-PCL produced a large square shape. Two rod and oval-shaped pores are formed for the M-PCL scaffold. The pore wall's texture also differed between the groups, showing a smoother wall obtained for the ones with N. Meanwhile, rougher edges were found in scaffolds of the S and M. (Figure 2)

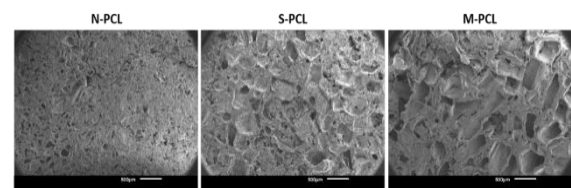


Figure 2. SEM images of the 3D PCL scaffolds at 50x magnification (scale bar: 500 μ m)

The pore sizes ranged following the pre-determined sieved measures of the particles as expected. N-PCL had pores sizes of less than 200 μ m, whereas sizes of less than 500 μ m were observed for S-PCL and M-PCL, respectively. In addition, only the M-PCL scaffold passed the normal distribution test based on the curve in, resulting in an even arrangement of pore size compared to the others. Overall, the controllable effect of pore size arrangement was obtained in the PCL scaffolds. (Figure 3)

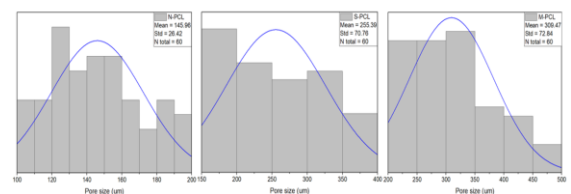


Figure 3. The average pore diameter (μ m) and pore size distribution graph of the 3D PCL scaffolds ($n = 60$).

Wettability assay

The wettability of the scaffold's surface is an important parameter for bone tissue engineering studies, which was assessed by contact angle measurement of the water droplets in Figure 4. It is understood that a low contact angle leads to better water infiltration in the scaffolds.

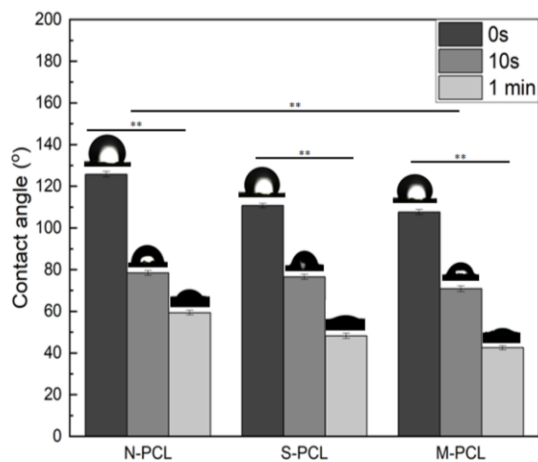


Figure 4. Contact angle measurement of the 3D PCL scaffolds at different time points. ($n=3$, **: $p < 0.01$).

After 1 min count, all the droplets were no longer visible. The values decreased in the order of N, S, and M, which is true due to the increase of pore size from 200 μm to 500 μm . The trend was consistent for each given time point, and the results were significantly different. The M-PCL scaffold had the lowest contact angle over time, referring to the highest water permeation. The data illustrated the increase of surface wettability associated with larger pores in the scaffolds.

Cell viability

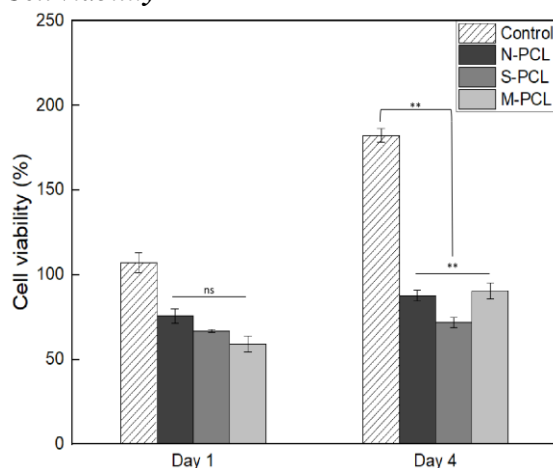


Figure 5. Cell viability of the 3D PCL scaffolds over 1 and 4 days. ($n=3$, ns: $p > 0.05$ and **: $p < 0.05$).

Before proceeding with cell proliferation, the cells were seeded directly on top of the scaffolds for up to four days. Despite the lower viability percentage than the control group, the cells could survive and multiply normally on the samples. Interestingly, on day 1, the percentage of viable cells on the N-PCL scaffold was much higher

than expected but showed no significant difference from the other ones. However, the growth rate of the S-PCL and M-PCL scaffolds significantly increased after four days of culturing, resulting in the M-PCL having the highest rate of living cells. It appeared that larger pore sizes accounted for greater cell survival over time. (Figure 5)

CONCLUSIONS

The results showed that the fabrication of the 3D micro-scale scaffolds was not complicated by using the particle-leaching approach. This approach, combined with the new progen materials, such as monosodium glutamate, improved the hydrophobicity of PCL scaffolds as well as enhanced cell living on the scaffolds in an in vitro study.

Acknowledgement

The research was funded by VinIF, Vingroup JSC, and supported by the Master, PhD Scholarship Program of Vingroup Innovation Foundation (VINIF), Vingroup Big Data Institute (VinBigdata), code VINIF.2021.TS.097.

References

- [1] Manzini, B.M., Machado, L.M.R., Noritomi, P.Y. et al., *Advances in Bone tissue engineering: A fundamental review*, Journal of Biosciences **46** (2021) 17.
- [2] Bagheri, L., Valizadeh, H., Dindar-safa, K. et al., *Fabricating a robust POSS-PCL nanofiber scaffold for nesting of mesenchymal stem cells: potential application in bone tissue regeneration*, Journal of Biological Engineering **16** (2022) 35.
- [3] A. Tripathi, S. Saravanan, S. Pattnaik, A. Moorthi, N.C. Partridge, N. Selvamurugan., *Bio-composite scaffolds containing chitosan/nano-hydroxyapatite/nano-copper-zinc for bone tissue engineering*, International Journal of Biological Macromolecules **50** (2012) 294-299.
- [4] J.-P. Chen, M.-J. Tsai, H.-T. Liao, *Incorporation of biphasic calcium phosphate microparticles in injectable thermoresponsive hydrogel modulates bone cell proliferation and differentiation*, Colloids and Surfaces B: Biointerfaces **110** (2013) 120-129.

FINE-TUNING THE HIGH ASPECT RATIO BRANCHES AND SMALL CORES OF GOLD NANOSTAR WITH NONIONIC-SURFACTANT FOR STUDYING THEIR SERS IMPROVEMENT ACTIVITY

† **Huong-Vy Thuy Ngo**^{1,2}, † **Sy Van Vu**^{1,2}, **Thao Phuong Do**^{1,2}, **Quang Duy Nguyen**^{1,2},
Vi Phuong Dang^{1,2}, **Phuong-Phong Thi Nguyen**^{1,2}, **Khuong Quoc Vo**^{*1,2}.

¹ Faculty of Chemistry, University of Science, Vietnam National University - Ho Chi Minh City, 227 Nguyen Van Cu Street, Ward 4, District 5, Ho Chi Minh City 70000, Vietnam.

² Vietnam National University, Ho Chi Minh City, Vietnam.

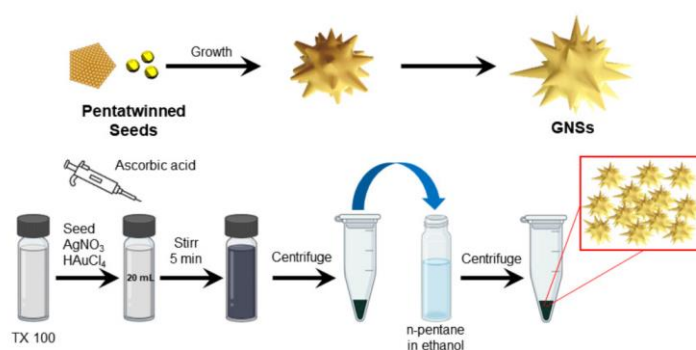
† These authors contributed equally to this work.

*Corresponding author

Email: vqkhuong@hcmus.edu.vn

ABSTRACT

A new type of gold nanostars with unique structures like high aspect ratio branches and small cores is extremely intriguing among many plasmonic metallic nanomaterials due to their specific intrinsic features. That declared excellent potential for advanced optical sensing techniques, such as Surface-Enhanced Raman scattering. Thus, we have proposed a novel modification synthesis method for gold nanostars (GNSs) with the support of the non-ionic surfactant Triton-X, which helps to tune the high aspect ratios and the core of GNSs. The influences of many important factors, such as seed concentration and acid ascorbic concentration, on the formation of GNSs, were carefully studied. Importantly, this study also demonstrated the ability to significantly modify the morphology in the gold nano-star colloidal solution compared with previous studies. To determine the morphology and crystalline structure of the nanomaterials, several methods were employed. These include (SEM), (TEM), (HRTEM), and (SAED). The optical properties of the GNSs were also observed using UV-Vis absorbance spectroscopy. Because of the above advantages, the as-developed GNSs were feasible for developing SERS substrates due to the ability to form many “hotspots” for SERS enhancement.



Keywords: Star-shaped, gold nanoparticles, Triton X, high aspect ratio branches.

INTRODUCTION

Nanotechnology unveils distinct material properties, sparking interest in noble metal nanoparticles like gold nanostars (GNSs) due to their unique structural and optical traits. They excel in constructing surface-enhanced Raman spectroscopy (SERS) substrates for hazardous chemical detection. To harness these properties

effectively, controlling the morphology during synthesis is crucial. This study's objective is to develop a novel synthesis method for GNSs, incorporating unique features like high aspect ratio branches and small cores using non-ionic surfactants, particularly Triton X. Optimizing acid ascorbic concentration, Triton X concentration, and seed concentrations to control the size and aspect ratio of GNSs.

EXPERIMENTAL

Materials.

Gold (III) chloride trihydrate ($\text{HAuCl}_4 \cdot 3\text{H}_2\text{O}$), silver nitrate (AgNO_3 , 99.9%), L(+)-ascorbic acid ($\text{C}_6\text{H}_8\text{O}_6$, 99.7%), sodium borohydride (NaBH_4 , 96%), and Triton X were purchased from Sigma-Aldrich (Germany).

Synthesis of gold nanostars by seed-mediated method.

Adding a 0.6 mL NaBH_4 of 0.01 M into a 10 mL prepared solution from 25 mL mixture including Triton X (0.61 mL, 2.15M), HAuCl_4 (0.625 mL, 10 mM) and DI water.

Seed colloid, AgNO_3 (200 μL , 10 mM), and HAuCl_4 (0.4 mL, 25 mM) were mixed in the 2.15 M Triton X dissolved in DI water. Then, quickly adding 0.1 M ascorbic acid to the as-prepared mixture, an intense greenish-blue color appeared, indicating the formation of GNSs. The gold solution was stirred for 5 minutes, then centrifuged and dispersed with 5 mL of MilliQ water. Afterwards, the above-dispersed solution was added to 5 ml of 8.4 mM n-pentane in ethanol and centrifuged due to the trapping reaction intermediates of n-pentanethiol.

Characterization.

The UV-Vis absorption spectra were collected on a UV-Vis-NIR-V670 spectrometer (Jasco, Japan). SEM images of GNSs were observed by using JEOL JSM-7600F (USA). The particle sizes were analyzed using ImageJ. The morphology of GNSs was evaluated by Transmission Electron Microscope (TEM) using a JEM-2100 (JEOL Ltd, Japan), equipped with selected area electron diffraction (SAED). High-resolution transmission electron microscopy (HRTEM) was performed on a JEOL ARM 200F (Jeol Ltd, Japan) at an acceleration voltage of 120 kV. The X-ray diffraction (XRD) pattern was obtained on a D8 Advance-Bruker (Germany).

RESULTS AND DISCUSSION

The influences of seed concentrations.

Observing the UV-Vis spectrum (Fig. 2A), when using a seed amount of 0.02, 0.06 and 0.14 nM, the first LSPR band on the left corresponds to the core of GNSs [1]. The remaining LSPR band on the right (main LSPR band) corresponds to the longitudinal resonance of the GNSs branch [2]. When increasing the seed concentration from 0.02, 0.06 to 0.14 nM there is a redshift, broad spectrum and lower intensity predicting a shape

change from star nanoparticles with few branches to more branches and smaller-sized particles.

Observing Fig 2B, it was found that when using seed with a concentration of 0.02 nM, the nanostructure formed was star-shaped with branches but in small quantity, the shape of each branch on the nanoparticle was relatively small and short. Continue to conduct experiments to increase the seed concentration to 0.06 and 0.14 nM Fig 2C,D, with a well-developed star shape with an increase in the number of long branches, growing evenly in many directions, branch length and tips with uniform sharpness.

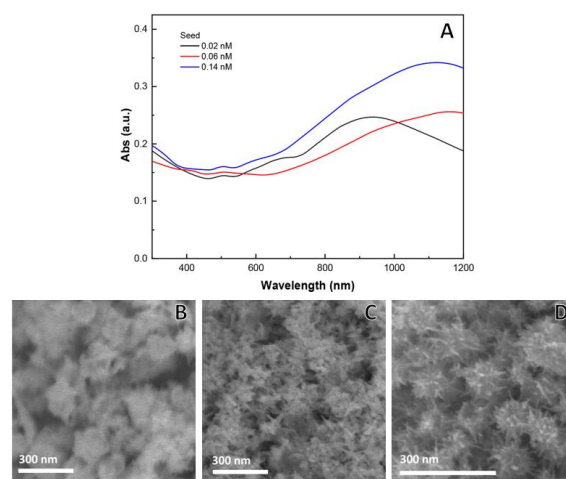


Figure 2. (A) UV-vis spectroscopy. SEM images of GNSs synthesized with (B) 0.02, (C) 0.06, and (D) 0.14 nM concentrations of seed colloidal.

Observing the TEM image (Fig. 3) shows the change in multi-branched morphology more clearly. The length from the core center to the peak averages from 90-160 nm when increasing the seed concentration from 0.02 to 0.14 nM.

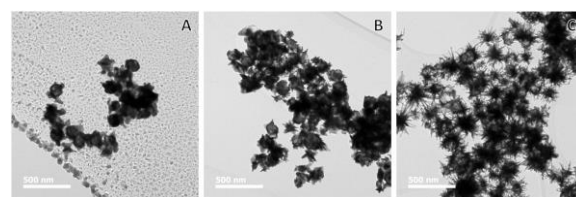


Figure 3. TEM images of GNSs synthesized with (A) 0.02, (B) 0.06, and (C) 0.14 nM concentrations of seed colloidal

The structure of the material was also verified again through HR-TEM images (Figure 4A). When selecting the area at the top of the star nanobranch, the distance between the crystals at the tips was similar to the previous 0.242nm analysis results, corresponding to the plane (111) of Au (Figure 4B, small image at 2nm scale) [3].

The SAED comprising bright spots on planes confirmed the polycrystalline structure of GNSs. The rings were indexed according to (111), (200), and (220) planes of fcc gold [4]. The crystal structure of GNSs was further characterized by the XRD method (Fig 5). There are high-intensity peaks at 38.18°, 44.42°, 63.00° and 77.49° respectively assigned to the (111), (200), (220) and (311) planes of the crystal structure fcc facets of gold [5,6].

Controlling synthesis of GNSs tips and core by modifying the acid ascorbic concentration.

Fig. 8 shows the absorption spectra of the colloidal gold nanostars with different volumes of acid ascorbic in the growth solution.

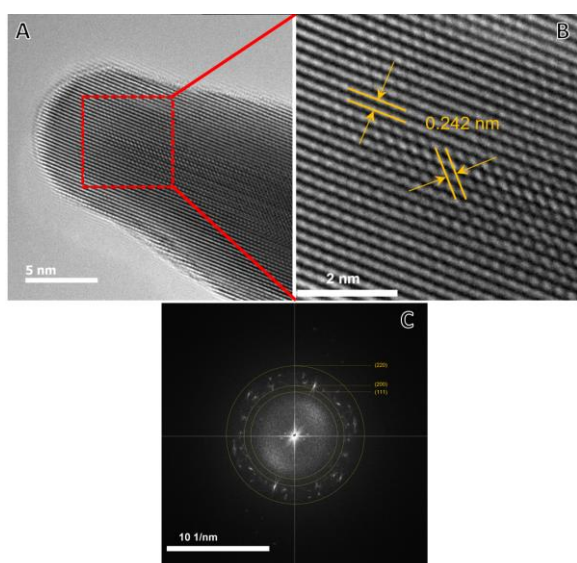


Figure 4. (A) HRTEM image and zoomed-in (B) of SGNPs and corresponding (C) SAED.

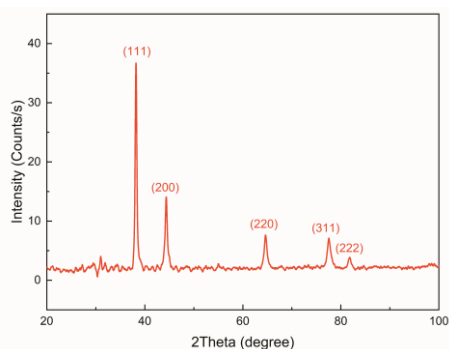


Figure 5. XRD spectrum of GNSs .

In Fig 6A, the synthesized GNS has low monodispersity, developing with a large core with an uneven number of branches among particles. When increasing acid ascorbic concentration to 3.9 mM (Fig 6B), the final GNSs formed with more monodispersed cores and branches. In the TEM image, with the synthesis conditions using a

1.0 mM concentration of ascorbic acid (Fig 7A), it can be seen that the core of the particle accounts for the major morphology, and the surrounding protrusion branches could not be created with a high-proportion pointed branch. That caused no difference between the overall size and the size of the branches part.

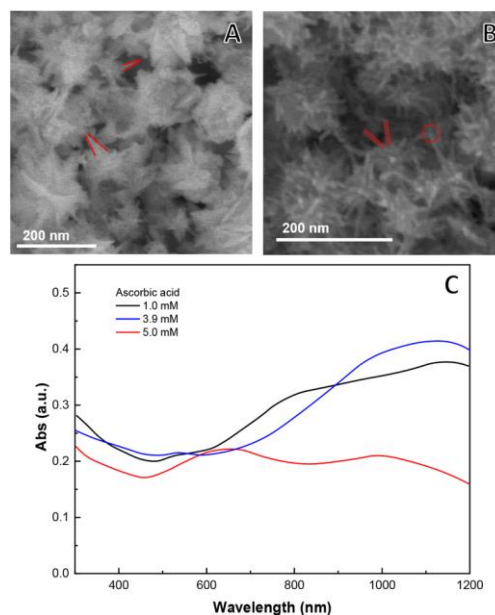


Figure 6. SEM of GNSs synthesized with (A) 1.0 mM, (B) 3.9 mM concentration of AA and (C) UV-vis spectroscopy of as-prepared GNSs.

On the contrary, after increasing the ascorbic acid concentration to 3.9 mM (Fig 7B), the large numbers and the lengths of these branches are equivalent to the diameter of the GNS core. The average size of GNS from one branch tip to another is estimated at 170 ± 15 nm.

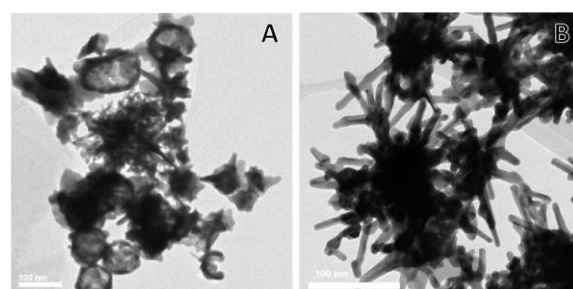


Figure 7. TEM images of gold nanoparticles with (A) 1.0 mM and (B) 3.9 mM of AA.

Effect of Triton X.

In Figure 8A, we have investigated the role of Triton X by modifying their concentrations. UV-Vis spectra examining three concentrations show that two distinct peaks are observed: 1000 - 1200 nm and 500 - 550 nm. With the increasing surfactant concentration, the absorption intensity

continues to rise, and the wavelength shift becomes more pronounced, moving towards around 1200 nm. However, the peak at the wavelength range of 1000 - 1200 nm for Triton-X at a concentration of 0.05 M is the sharpest in the three UV spectra, proving that the nanoparticles grow relatively uniformly and monodisperse. When significantly reducing the Triton X concentration, particularly to 0.05 M, we observe notable differences in their SEM image compared to Triton 0.15 M. After examining nanoparticle growth through three different Triton concentrations, we conclude that Triton can help adjust the morphology of nanoparticles and prevent interactions between nanostars. For the growth of 6-branched nanostars, it is evident that a low Triton concentration yields the most favourable results.

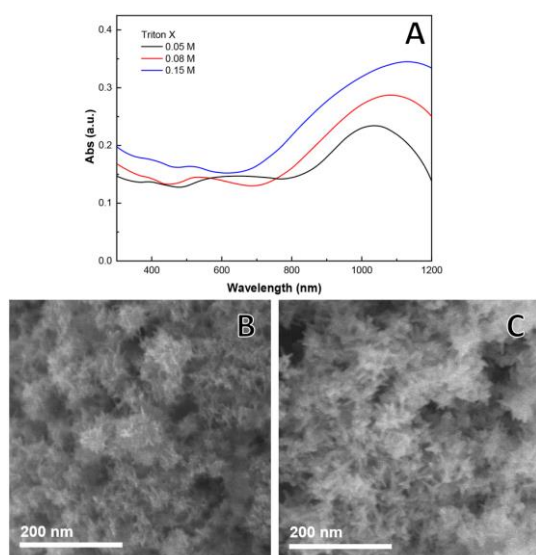


Figure 8. (A) UV-Vis spectra of GNSs and SEM images (B) 0.05 M, (C) 0.15 M concentration of Triton X.

CONCLUSION

Gold nanostars with high aspect ratio branches and small cores were successfully synthesized by a seed-mediated method using nonionic-surfactant by modifying parameters for seed, ascorbic acid, and Triton X concentrations. The results show that the GNSs were synthesized under appropriate conditions including seed solution concentration of 0.14 nM, ascorbic acid 3.9 mM and Triton-X 0.05 M. Average particle size of GNSs at these conditions is 170 nm, the optical properties and particle morphology of GNS were determined through UV Vis, SEM, TEM, and HR-TEM analysis methods. In addition, the results of XRD and SAED diagrams confirm that the GNS particles are formed with a pure nanocrystalline

structure and have a face-centred cubic crystalline structure. With the results achieved through this research, GNS will be a potential material in manufacturing surface-enhanced Raman scattering (SERS) substrates.

Acknowledgement

We appreciate the invaluable analysis method supported by the Research Institute of Clean Manufacturing System, Korea Institute of Industrial Technology (KITECH), and KITECH school, University of Science and Technology (UST).

Author conceptualization: Huong-Vy Thuy Ngo, Sy Van Vu, Phuong-Thao Do, Quang Duy Nguyen, Vi Phuong Dang, Khuong Quoc Vo
Methodology and analysis: Quang Duy Nguyen, Phuong-Phong Thi Nguyen, Phuong-Thao Do, Khuong Quoc Vo

Writing and editing: Huong-Vy Thuy Ngo, Sy Van Vu, Phuong-Thao Do, Quang Duy Nguyen, Vi Phuong Dang, Khuong Quoc Vo.

Supervision and editing: Khuong Quoc Vo

References

- [1] Kong, X.-T.; Wang, Z.; Govorov, A. O., Plasmonic Nanostars with Hot Spots for Efficient Generation of Hot Electrons under Solar Illumination. **2017**, *5* (15).
- [2] Yuan, H.; Fales, A. M.; Khoury, C. G.; Liu, J.; Vo-Dinh, T., Spectral characterization and intracellular detection of Surface-Enhanced Raman Scattering (SERS)-encoded plasmonic gold nanostars. **2013**, *44* (2), 234-239.
- [3] Quang, A. T. N.; Nguyen, T. A.; Vu, S. V.; Lo, T. N. H.; Park, I.; Vo, K. Q., Facile tuning of tip sharpness on gold nanostars by the controlled seed-growth method and coating with a silver shell for detection of thiram using surface enhanced Raman spectroscopy (SERS). *RSC Advances* **2022**, *12* (35), 22815-22825.
- [4] Mao, W.; Son, Y. J.; Yoo, H. S., Gold nanospheres and nanorods for anti-cancer therapy: comparative studies of fabrication, surface-decoration, and anti-cancer treatments. *Nanoscale* **2020**, *12* (28), 14996-15020.
- [5] Nehl, C. L.; Liao, H.; Hafner, J. H., Optical Properties of Star-Shaped Gold Nanoparticles. *Nano Letters* **2006**, *6* (4), 683-688.
- [6] Van Vu, S.; Nguyen, A.-T.; Cao Tran, A.-T.; Thi Le, V.-H.; Lo, T. N. H.; Ho, T. H.; Pham, N. N. T.; Park, I.; Vo, K. Q., Differences between surfactant-free Au@Ag and CTAB-stabilized Au@Ag star-like nanoparticles in the preparation of nanoarrays to improve their surface-enhanced Raman scattering (SERS) performance. *Nanoscale Advances* **2023**, *5* (20), 5543-5561.

GREEN-SYNTHESIS OF MULTIFUNCTIONAL SILVER NANOCOMPOSITE HYDROGELS FROM THE EXTRACTS OF *SYZYGIUM RESINOSUM* (GAGNEP) IN THERMOSENSITIVE POLYMER SOLUTIONS

Anh-Quan Hoang^{1,2}, Le-Hang Dang¹, Thi-Phuong Le¹, Ngoc-Quyen Tran¹, Phuong-Tung Nguyen^{1,3*}

¹Institute of Applied Materials Science, VAST, Ho Chi Minh City, Vietnam

²Graduate University of Science and Technology, VAST, Ha Noi, Viet Nam

³CIRTEch Institute, HUTECH University, Ho Chi Minh City, Viet Nam

Email: phuongtungng@iams.vast.vn; phuongtungng@gmail.com

ABSTRACT

Trauma wound is an inevitable health issue in life. Many researchers have endeavored to develop multifunctional materials to enhance wound healing after injury. *Syzygium resinosum* (Gagnep) Merr. et Perry, the leaves have been used as a traditional medicine for their notable biomedical activities in bacteria inhibition and cell proliferation. Silver nanoparticles (AgNPs) were synthesized using the *Syzygium resinosum* (SR) extract, which was added as a reducing and capping agent due to its rich phenol and polyphenol composition. SR extraction process was evaluated to obtain the highest total bioactive content. Silver nanoparticles (AgNPs), synthesized in the herbal extract solution, and Pluronic polymer were used to create a thermosensitive polymeric nanocomposite solution that can form a multifunctional hydrogel film on the wound surface at body temperature. Phytochemical analysis was performed to determine the total phenolic contents by using the Folin–Ciocalteu method. Antimicrobial and antioxidant activities of the SR extract and SR-AgNPs were tested using the Kirby-Bauer and DPPH methods. The synthesized products were characterized using different techniques, such as UV–visible spectroscopy, dynamic light scattering (DLS), Fourier transform infrared (FTIR) spectroscopy, X-ray diffraction (XRD), and transmission electron microscopy (TEM). The results proved that SR extract, SR-AgNPs, and the multifunctional hydrogel system have high efficiency in antimicrobial and antioxidant activities. This is the basis for further trials on applying these multifunctional hydrogel materials to treat open wounds.

Keywords: Silver nanoparticles, *Syzygium resinosum*, thermosensitive hydrogel, herbal extract, multifunctional hydrogel.

INTRODUCTION

Recently, the use of extracts from medicinal herbs containing phenolic compounds as reducing agents for the synthesis of silver nanoparticles has attracted substantial attention due to its friendly environment, high safety, and low cost. The mixture of many components in the extract acts as both reducing and stabilizing agents for the synthesized nanoparticles. Many researchers have successfully synthesized silver nanoparticles by using extracts from medicinal herbs.

The development of multifunctional hydrogels or heat-sensitive hydrogels containing biologically active agents to enhance wound healing is an attractive approach in the world as well as in Vietnam. The thermosensitive polymer solution (at a temperature of 25–32 °C) contains

active agents that can adhere to the wound surface (35–37 °C) to create a swellable hydrogel film to absorb exudates or create a moisture environment to release bioactive agents for cell growth. In addition, these materials are kept in a cool environment before use, therefore reducing the pain to patients as applied to the wounds.

However, there are few studies on synthesizing silver nanoparticles from herbal extracts combined with hydrogels for wound healing effects in the world (only a few publications from 2019 up to now) and Vietnam. Until now, the source of Vietnamese medicinal herbs with healing effects is very rich but still used for traditional and heirloom remedies.

In this research, we study the combination of 3 active agents for wound healing, such as nanosilver with strong antibacterial activity synthesized in the herbal extract solution (from

the grass plant and manioc cassava with healing effect without scar formation), pluronic polymer to create a thermosensitive polymeric nanocomposite solution that can form a multifunctional hydrogel film on the wound surface. This material could contribute to the effectiveness of wound treatment and have much scientific and practical significance.

EXPERIMENTAL

Materials: *Syzygium resinosum* (Gagnep) leaves were collected on January 22, 2022 from Thai Binh province, and were processed by Dr. Luu Hong Truong and his colleagues at the Institute of Applied Materials and Science. The leaves specimen was sorted, then completely cleaned and dried.

The chemicals used were Ethyl acetate (EA), n-Butanol (Bu), Chloroform (Chlo), absolute Methanol, Gallic acid, Sodium hydrogen carbonate (NaHCO₃), Folin-Ciocalteu reagent, distilled water (DW), silver nitrate (AgNO₃)

Methods:

Preparation of the extraction: The amount of SR leaves was weighted and filled with alcohol: water solvent with the chosen ratio for primary extraction. The mixture was then incubated for seven days. After the period ended, the dissolved solution was collected and then the solvent was removed to make the total extract (TE). Similar to the total extraction process, the TE continued to be extracted with other solvents to make the Fractional extraction (FE).

Preparation of multifunctional hydrogel

Silver nanoparticles (AgNPs) were synthesized using the *Syzygium resinosum* (SR) extract. Silver nanoparticles (AgNPs), synthesized in the herbal extract solution, and Pluronic polymer were used to create a thermosensitive polymeric nanocomposite solution that can form a multifunctional hydrogel film on the wound surface at body temperature.

Characteristics and evaluation of the material: Phytochemical analysis was performed to determine the total phenolic contents by using the Folin–Ciocalteu method. Antimicrobial and antioxidant activities of the SR extract and SR-AgNPs were tested using the Kirby-Bauer and DPPH methods. The synthesized products were characterized using different techniques, such as UV–visible spectroscopy, dynamic light scattering (DLS), Fourier transform infrared

(FTIR) spectroscopy, X-ray diffraction (XRD), and transmission electron microscopy (TEM)

RESULTS AND DISCUSSION

Table 1. TPC results for FE using different solvent systems of Ethyl acetate (EA), Chloroform (Chlo), and n-Butanol (Bu) chosen from a typical trial

	Sample	C (mg Gallic acid / g extract)
Ethyl Acetate	EA1	189.96
	EA2	184.78
	EAc	207.00
Chloroform	Chl1	128.48
	Chl2	138.11
	Chl2	134.81
n-Butanol	Bu1	173.36
	Bu2	162.51
	Bu2	156.18

From the experimental results, it was clear that Ethyl acetate as a solvent had a greater ability to separate unnecessary organic substances than both Chloroform and n-Butanol, leading to a larger total phenolic content in the sample.

Table 2. Radical scavenging activity of FE using different solvent systems of Ethyl acetate (EA), Chloroform (Chlo), and n-Butanol (Bu) chosen from a typical trial

	Sample	Absorbance at 515nm	% Inhibition
Positive control	(+)	0.4244	
Ethyl Acetate	EA1	0.2101	50.49
	EA2	0.1748	58.82
	EA3	0.2094	50.66
Chloroform	Chl1	0.2070	51.23
	Chl2	0.1888	55.51
	Chl3	0.2283	46.21
n-Butanol	Bu1	0.1805	57.47
	Bu2	0.2392	43.64
	Bu3	0.2025	52.29

For DPPH radical scavenging assay (RSA), the trend observed was relative to that of TPC. The result showed that three Ethyl acetate FEs had the highest, but unstable % inhibition (50.49%, 58.81%, and 50.66%) despite having the highest TPC result from the previous assessment. As far as everything was concerned, Ethyl acetate FEs remained the most reliable specimens among

other FEs, having much higher antioxidant activity and simultaneously, much higher TPC.

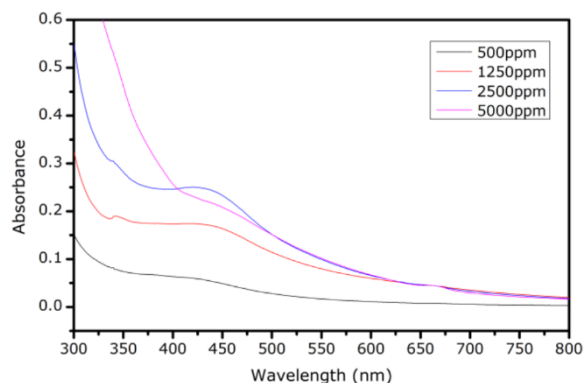


Figure 1. UV-VIS spectra reflecting the effect of different fraction extract concentrations on AgNPs synthesis in 5% polymer system

Table 3. DLS results for AgNPs synthesis in 5% polymer system with different sample concentrations at 37 °C

Sample concentration (ppm)	Diameter (nm)	PI
500	96.8	1.236
1250	66.4	0.736
2500	60.7	0.978
5000	109.3	0.675

According to Figure 1, 2500ppm was claimed as the best option for AgNPs synthesis as it showed the highest absorbance in the wavelength that identified AgNPs, and also, it had the smallest size of AgNPs relied on DLS result. Specifically, it achieved absorbance of 0.2505 at 421nm wavelength and average nanoparticle size of 60.7 nm. Therefore, 2500ppm was chosen to perform the next investigation.

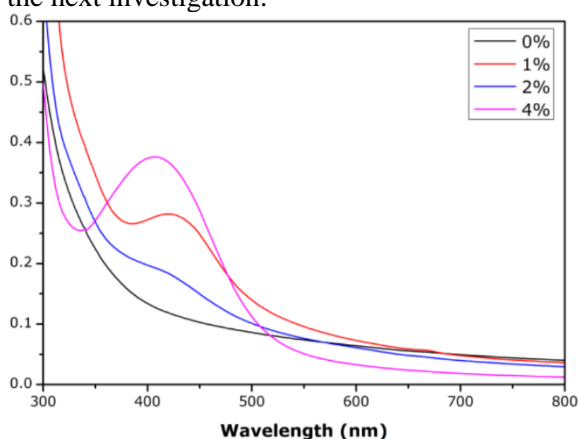


Figure 3a. UV-VIS spectra reflecting the effect of different F127 concentrations on AgNPs synthesis with 2500 ppm of FE

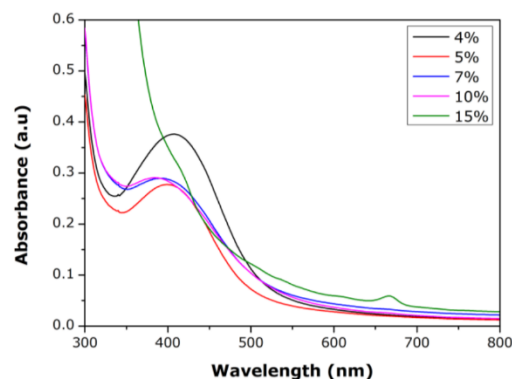


Figure 3b. UV-VIS spectra reflecting the effect of different F127 concentrations on AgNPs synthesis with 2500 ppm of FE

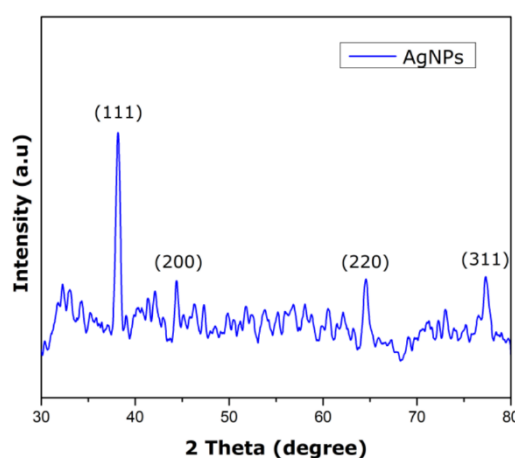


Figure 4. XRD spectra of synthesized AgNPs

According to UV-VIS from Figure 1 and 3, there was a signal at 420 nm, which was belonged to the signal range of AgNPs (400–500 nm) [1]. In addition, the XRD pattern has four peaks at 2θ values of 38.26° , 44.38° , 64.56° , 77.38° corresponding to the (111), (200), (220), (311) planes were detected and assigned to crystallized AgNPs, similar to another study [2].

Table 4. The gelation and melting points of 10%, 12%, 15%, 18%, and 20% polymer solution

F127 polymer solution (%)	Gel-setting point (°C)	Gel-melting point (°C)
10	-	-
12	-	-
15	33	60
18	25	75
20	20	83

(* The symbol “-” means no gel-sol transition)

According to the gelation test, ideal concentration of F127 to make the hydrogel at

body temperature was 15%. Thus, this concentration was chosen to investigate the AgNPs released from the hydrogel.

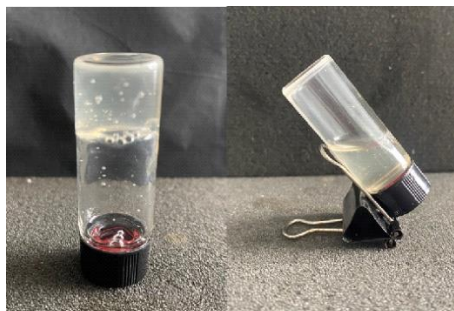


Figure 3. The gelation of material at body temperature (37 °C)

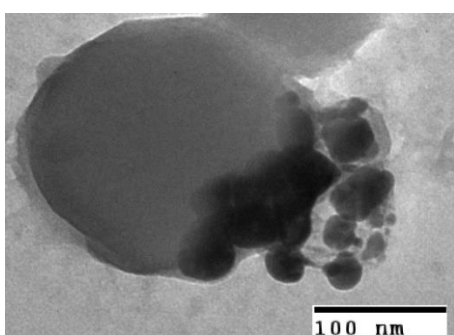
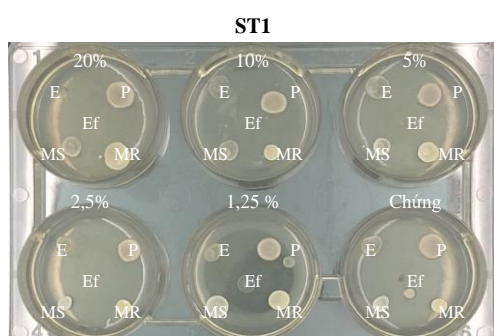


Figure 4. TEM image of AgNPs synthesized in 4 % polymeric solution with 2500ppm fractional extract

The result of the TEM image (Figure 4) displayed that most of AgNPs had spherical shapes, which corresponded to the signal of UV-VIS spectra at 420 nm wavelength [15], [16]. The size of AgNPs was approximately 20 to 25 nm, affirming the success of AgNPs fabrication.



(*E: *Escherichia coli* ATCC 25922; P: *Pseudomonas aeruginosa* ATCC 27853; Ef: *Enterococcus faecalis* ATCC 29212; MS: *Staphylococcus aureus* ATCC 29213; MR: Methicilin-resistant *Staphylococcus aureus*)

Figure 5. Antibacterial activities of AgNPs synthesized in 4 % polymeric solution with 2500ppm fractional extract

Figure 5 showed the significant antibacterial activity of the material against the *E. Coli* and *E. faecalis*.

CONCLUSION

The success in green synthesis of AgNPs was proven by UV-VIS spectrophotometry, DLS, XRD, and TEM imaging. 2500ppm of fractional extract and 7.5% polymeric system were the most suitable conditions for AgNPs synthesis.

In further study, the polymer could be changed to copolymer (such as F127-chitosan, F127-Alginate, etc.) or evaluated by pH to enhance the property of polymeric system approaching the success in synthesizing the hydrogel toward wound healing application.

References

- [1] Sastry, M., Mayya, K. S., & Bandyopadhyay, K, *pH Dependent changes in the optical properties of carboxylic acid derivatized silver colloidal particles*, Colloids and Surfaces A: Physicochemical and Engineering Aspects, **127**(1-3) (1997) 221-228.
- [2] Mollick, M. M. R., Bhowmick, B., Maity, D., Mondal, D., Bain, M. K., Bankura, K., ... & Chattopadhyay, D, *Green synthesis of silver nanoparticles using Paederia foetida L. leaf extract and assessment of their antimicrobial activities*, International Journal of Green Nanotechnology, **4**(3) (2012) 230-239.
- [3] Kim, J. S., Kuk, E., Yu, K. N., Kim, J. H., Park, S. J., Lee, H. J., ... & Cho, M. H, *Antimicrobial effects of silver nanoparticles*, Nanomedicine: Nanotechnology, biology and medicine, **3**(1) (2007) 95-101.
- [4] Creighton, J. A., Blatchford, C. G., & Albrecht, M. G, *Plasma resonance enhancement of Raman scattering by pyridine adsorbed on silver or gold sol particles of size comparable to the excitation wavelength*, Journal of the Chemical Society, Faraday Transactions 2: Molecular and Chemical Physics, **75** (1979) 790-798.

FABRICATION AND CHARACTERIZATION OF PLATINUM CONDUCTIVITY ELECTRODE BY LIFT-OFF PROCESS

Ha Van Nguyen, Vi Nhat Hoang Ngo, Thang Minh Bui, Diep Ngoc Le, Dung My Thi Dang, Tin Chanh Duc Doan, Chien Mau Dang, Ngan Nguyen Le

Institute for Nanotechnology, Community 6, Linh Trung Ward, Thu Duc City, Ho Chi Minh City, Vietnam;

Vietnam National University Ho Chi Minh City, Ho Chi Minh City, Vietnam

Email: lnngan@vnuhcm.edu.vn

ABSTRACT

Photolithography, a technique recognized as the application of optical agents on the surface of a photoresist, has facilitated the generation of pre-designed microstructures in microfabrication processes. This method finds significant application in the manufacturing of micro-electromechanical systems (MEMS), particularly in the realm of high-precision thin film electrode manufacturing. In this study, a platinum thin film electrode was produced using the lift-off technique for the purpose of assessing liquid conductivity. The fabricated electrode was evaluated through various microscopic and electrochemical techniques, including Atomic Force Microscopy (AFM), Field Emission Scanning Electron Microscopy (FE-SEM), and Cyclic Voltammetry (CV). The CV method serves as an accessible means of electrochemical assessment, also providing a relatively accurate determination of the electrode's surface area. The obtained FE-SEM and AFM images revealed a notably smooth electrode surface with surface roughness on the order of a few nanometers. These results underscore the high-quality fabrication of platinum thin film electrodes through the lift-off technique, yielding components of small dimensional discrepancies. The calculated electrode surface area using the CV method exhibited high precision, deviating from the design parameters by only approximately 1.89%. Thus, the manufactured platinum thin film electrode holds promise for future applications in precise determination of solution conductivity.

Keywords: photolithography, lift-off, platinum electrode, conductivity electrode

INTRODUCTION

Photolithography is a technique employed for transferring sample images or patterns onto a layer of photoresist. This method finds widespread application in the manufacturing of micro-electromechanical systems (MEMS). Fundamentally, there are two processes utilizing the photolithography technique to create intricate details: photolithography – etching, in which a metal thin film is deposited beneath the photoresist layer [1, 2] and photolithography – lift-off, in which a metal thin film is deposited on top of the exposed photoresist layer [3, 4]. Despite having been developed for quite some time, the photolithography – lift-off process continues to be researched and applied in the fabrication of microcomponents up to the present day [5-7].

In this research paper, the research team conducted the fabrication of Platinum electrodes using the sputtering – lift-off process. The fabricated Platinum electrodes were evaluated

through various microscopic and electrochemical techniques, including Atomic Force Microscopy (AFM), Field Emission Scanning Electron Microscopy (FE-SEM), and Cyclic Voltammetry (CV). These electrodes were designed for applications related to measuring the conductivity of solutions, aiming to assist in monitoring water quality under various conditions.

EXPERIMENTAL

1. Materials

Sulfuric acid (98%), hydrogen peroxide (30%), ethanol (99.5%), iso-propanol (99.5%), and acetone (99.5%) were provided by Sigma-Aldrich. Negative photoresist N1410, adhesion promoter Hexamethyl Disilazane (HMDS), and developer ma-D533S were supplied by Micro Resist Technology (Germany). All solutions were prepared using ultrapure water with a resistivity of 18.2 MOhm.cm.

2. The fabrication of Platinum electrodes utilizing the sputtering-lift-off process

The Platinum electrodes were fabricated following the process outlined in **Figure 1** below. Initially, the Si wafer was cleaned and thermally oxidized to create a layer of SiO₂ on top. Subsequently, a layer of negative photoresist was spin coated onto the wafer surface. UV light was exposed through a mask onto the photoresist layer. The development step was carried out immediately afterward using developer ma-D533S. Ti/Pt was deposited onto the sample using the sputtering method. In the final step of the lift-off process, the photoresist layer was completely removed together with the metal layer deposited on top, leaving the platinum layer serving as the conductive electrode.

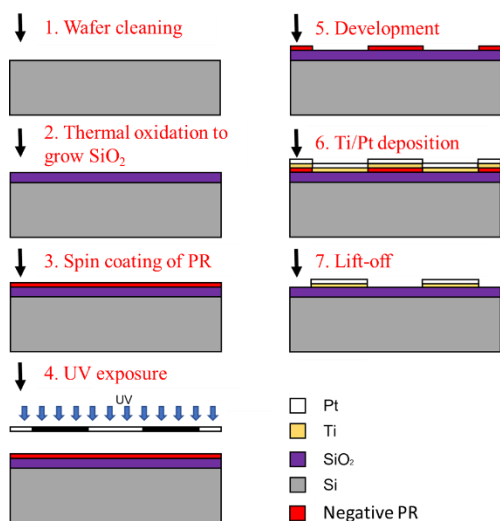


Figure 1. The photolithography-lift-off process employed for fabricating Platinum conductivity electrodes

3. The assessment of the fabricated electrode

The surface of the Platinum electrode was evaluated using Atomic Force Microscopy (AFM) and Field Emission Scanning Electron Microscopy (FE-SEM). Cyclic Voltammetry (CV) techniques was used to evaluate work capability of Platinum electrodes.

The ion exchange process $[\text{Fe}(\text{CN})_6]^{-3/-4}$ on the Pt electrode was conducted in an electrolyte solution containing 1.0 mM K₃[Fe(CN)₆] and 0.1 M KCl through CV scanning at gradually increasing scan rates (5–175 mV.s⁻¹). A three-electrode classical cell setup was employed, with a Platinum electrode serving as the working electrode (WE), a Pt wire acting as the counter electrode (CE), and an Ag/AgCl electrode (3 M

NaCl) functioning as the reference electrode (RE). The experimental configuration was arranged as depicted in **Figure 2**.

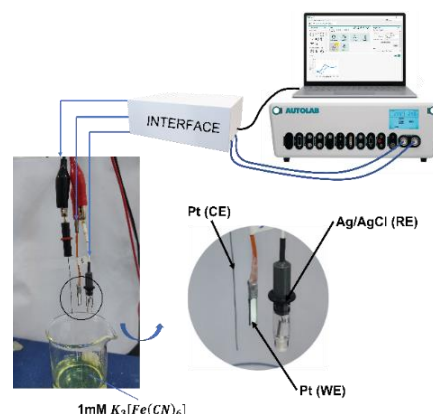
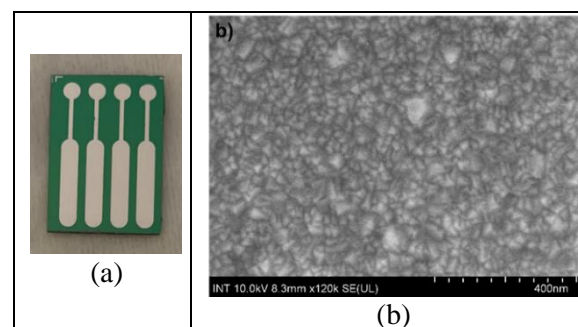


Figure 2. The CV system of the Pt electrode with a scan rate ranging from 5 to 175 mV.s⁻¹ 5 in a solution containing 1.0 mM K₃[Fe(CN)₆] and 0.1 M KCl.

RESULTS AND DISCUSSION

1. The results of the electrode surface evaluation

Following the aforementioned fabrication process, we obtained Platinum electrodes in a flat stick shape as depicted in **Figure 3a**. FE-SEM and AFM images of the Platinum surface revealed a fairly uniform and relatively flat surface, with a few elevated regions measuring approximately 10 nm higher than the surrounding surface (**Figure 3b** and **Figure 3c**). The average surface roughness (R_{ms}) of the sample was approximately 1.69 nm. Consequently, the electrode surface area could be considered equivalent to the geometric area in the design, specifically 20.14 mm².



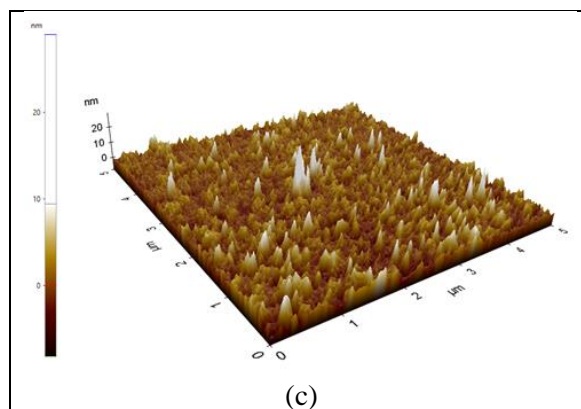


Figure 3. The fabricated Platinum electrode (a); FE-SEM image (b) and AFM image (c) of the Platinum surface

2. Results of cyclic voltammetry scanning

The results of cyclic voltammetry scans (CV) corresponding to different scan rates are presented in **Figure 4a**. In the first CV curve (**Figure 5**), characteristic oxidation-reduction peaks appear at +0.15/+0.24V, indicating the electrochemical activity of Pt. The electron transfer process is nearly reversible in the oxidation-reduction reaction of the $[\text{Fe}(\text{CN})_6]^{-3/-4}$ ion pair on the Pt electrode surface. Although there is a potential difference compared to other studies, this can be attributed to the polycrystalline nature of the Pt electrode. Depending on the different crystal planes of Pt during fabrication, different oxidation-reduction peak potentials will be observed.

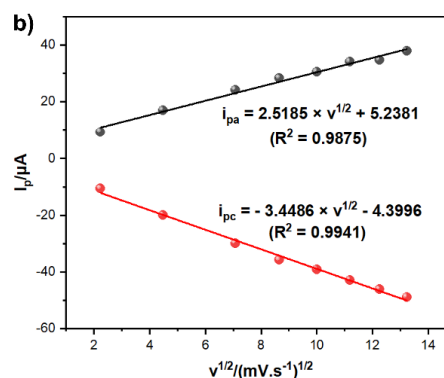
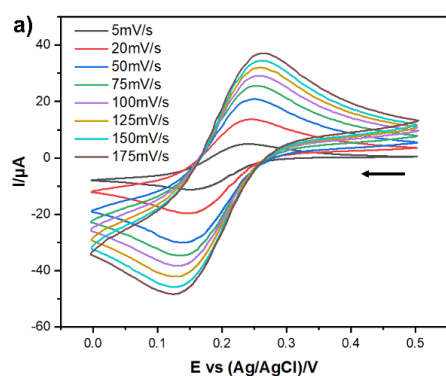


Figure 4. (a) The CV curves of Pt in a solution containing 1.0 mM $\text{K}_3[\text{Fe}(\text{CN})_6]$ and 0.1 M KCl at scan rates of: 5, 20, 50, 75, 100, 125, 150, and 175 $\text{mV}\cdot\text{s}^{-1}$; (b) The dependence of peak current (i_{pa} , i_{pc}) on the square root of the scan rate ($v^{1/2}$)

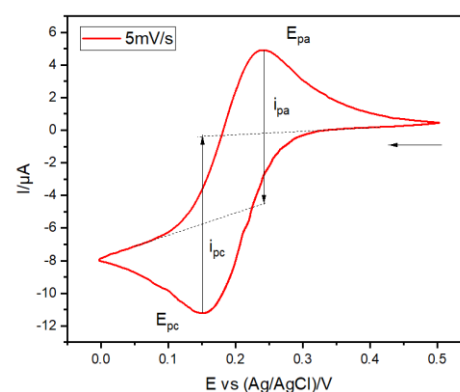


Figure 5. The CV curve of the Pt electrode at a scan rate of 5 $\text{mV}\cdot\text{s}^{-1}$ in a solution containing 1.0 mM $\text{K}_3[\text{Fe}(\text{CN})_6]$ and 0.1 M KCl

The difference between the anodic and cathodic peak potentials $\Delta E_p = E_{pa} - E_{pc} \approx 0,091\text{V}$, and the relative ratio between the two peak currents $i_{pa}/i_{pc} \approx 0,9$ indicate that the electron transfer process is nearly reversible in the oxidation-reduction reaction of the $[\text{Fe}(\text{CN})_6]^{-3/-4}$ pair on the Pt electrode. At scan rates higher than 5 $\text{mV}\cdot\text{s}^{-1}$, irreversible reactions occurred. The linear correlation between the peak current and the square root of the scan rate ($v^{1/2}$) indicates that the kinetics of the process are primarily governed by diffusion (**Figure 4b**). The regression equations for the anodic and cathodic peak currents are as follows:

$$i_{pa} (\mu\text{A}) = 2.5185 \times v^{1/2} + 5.2381 \quad (\text{with } R^2 = 0.9875)$$

$$i_{pc} (\mu\text{A}) = -3.4486 \times v^{1/2} - 4.3996 \quad (\text{with } R^2 = 0.9941).$$

The electroactive surface area of Pt was calculated using the Randles-Sevcik equation:

$$I_p = 2.69 \times 10^5 (n^{3/2} A C_0 D_0^{1/2} \nu^{1/2})$$

where I_p represents the peak current, n is the number of electrons transferred, A is the electroactive surface area, D_0 is the diffusion coefficient, C_0 is the concentration of $K_3[Fe(CN)_6]$, and ν is the scan rate. With parameters $n = 1$, $\nu = 0,005 \text{ V.s}^{-1}$, $C = 1 \text{ mM} = 1 \times 10^{-6} \text{ mol.cm}^{-3}$, and the diffusion coefficient of $[Fe(CN)_6]^{3-/4-}$ as $D = 8,76 \times 10^{-6} \text{ cm}^2.\text{s}^{-1}$ at 25°C , the electroactive surface area of the electrode was calculated as $A \approx 19,76 \text{ mm}^2$. This result deviates by 1.89% from the geometric area as designed.

CONCLUSION

In this study, we have successfully fabricated Platinum electrodes using the photolithography-lift-off process. The evaluation results also demonstrate the electrodes possess relatively good quality, with low surface roughness, measuring approximately 1.69 nm. The electroactive surface area of the electrodes is also quite satisfactory, being only 1.89% lower than the designed area. This indicates that this fabrication process can be effectively employed not only for Platinum electrodes intended for conductivity measurement but also for a variety of electrodes in diverse applications.

Acknowledgment

The research was sponsored by the Ministry of Science and Technology under Research Project Contract Number: 122/2021/HĐ-ĐTĐL.CN-ĐP.

References

- [1] Y. Al-Hadeethi, A. Al-Mujtabi, F.M. Al-Marzouki, A.Y. Mahmoud, A. Umar, A.M. Abdel-Daiem, M.S. Ansari, *Investigating the optimum parameters of a negative photoresist to prepare a V-grooved diffraction grating on Si using photolithography and reactive ion etching techniques*, *Ceramics International* **47**(8) (2021) 10705-10715.
- [2] C. Zamponi, H. Rumpf, C. Schmutz, E. Quandt, *Structuring of sputtered superelastic NiTi thin films by photolithography and etching*, *Materials Science and Engineering: A* **481-482** (2008) 623-625.
- [3] Y. Xie, S. Ouyang, D. Wang, W.-Y. Lee, Z. Bao, J.R. Matthews, W. Niu, R.A. Bellman, M. He, H.H. Fong, *High performance top contact fused thiophene-diketopyrrolopyrrole copolymer transistors using a photolithographic metal lift-off process*, *Organic Electronics* **20** (2015) 55-62.
- [4] S. Watanabe, J. Sakurai, S. Hata, *Fabrication of Cu-Zr-Ti thick film metallic glass structure by double metal mask lift-off process*, *Microelectronic Engineering* **135** (2015) 45-51.
- [5] L. Kelly, H. Northfield, S. Rashid, X. Bao, P. Berini, *Fabrication of high frequency SAW devices using tri-layer lift-off photolithography*, *Microelectronic Engineering* **253** (2022) 111671.
- [6] S. Takase, K. Yamada, Y. Nakagawa, C. Oka, J. Sakurai, S. Hata, *Thick film MEMS process using reverse lift-off*, *Microelectronic Engineering* **281** (2023) 112081.
- [7] D. Yang, A.G. Ramu, Y. Lee, S. Kim, H. Jeon, S. V E, A.M. Al-Mohaimed, W.A. Al-onazi, T.s. Algarni, D. Choi, *Fabrication of ZnO nanorods based gas sensor pattern by photolithography and lift off techniques*, *Journal of King Saud University - Science* **33**(3) (2021) 101397.

A GREEN SYNTHESIS OF CuO/ZnO NANOCOMPOSITES FROM *Boehmeria nivea* LEAF EXTRACT FOR ANTIBACTERIAL ACTIVITIES

Vien Ky Le¹, Truong Phi Le¹, Quy Ngoc Nguyen Le², Quan Phu Pham², Ngoc Hong Nguyen², Lien Hong Huynh², Ngoc Xuan Dat Mai³, Linh Ho Thuy Nguyen³, Lan Thi My Nguyen¹, Thanh Van Tran Thi², Kim Ngoc Pham^{2,*}

¹ Faculty of Biology and Biotechnology, University of Science at Ho Chi Minh City, 227 Nguyen Van Cu, Ward 4, District 5, Ho Chi Minh City, Vietnam;

² Faculty of Materials Science and Technology, University of Science at Ho Chi Minh City, 227 Nguyen Van Cu, Ward 4, District 5, Ho Chi Minh City, Vietnam;

³ Center for Innovative Materials and Architectures (INOMAR), Vietnam National University, Linh Trung Ward, Thu Duc, Ho Chi Minh City, Vietnam

Email: kyvienle2001@gmail.com, phamkngoc@hcmus.edu.vn

ABSTRACT

This work endeavors to synthesize copper oxide (CuO), zinc oxide (ZnO) nanoparticles (NPs), and CuO/ZnO nanocomposites using a green synthesis approach from *Boehmeria nivea* leave extracts. The active constituents within the extracts, namely alkaloids, flavonoids, and phenolics, serve a dual role as reducing agents and surface stabilizers during the nanoparticle synthesis process. The structural and surface morphology of the nanomaterials are examined using scanning electron microscopy (SEM) and X-ray diffraction (XRD). Fourier transform infrared (FTIR) spectroscopy is employed to elucidate the materials' functional groups and unique bonding characteristics. CuO NPs exhibit a monoclinic crystal structure and adopt a nanorod morphology, while the ZnO NPs display hexagonal shapes at the nanoscale and tend to aggregate into larger spherical particles. The microstructure and morphology of CuO/ZnO nanocomposites are notably influenced by varying the mass ratios of the metal salts. Furthermore, the antibacterial properties of these nanocomposites are assessed against two bacterial strains, *Escherichia coli*, and *Staphylococcus aureus*. The minimum bactericidal concentrations (MIC) for CuO/ZnO nanocomposites are determined to be 500 ppm and 1000 ppm for *Escherichia coli* and 2000 ppm and 8000 ppm for *Staphylococcus aureus*, respectively. This work highlights the potential utility of CuO/ZnO in antibacterial applications.

Keywords: *Boehmeria nivea*, Antibacterial activities, CuO/ZnO, Green synthesis

INTRODUCTION

Nanomaterials encompass a wide range of materials with structures in the form of particles, rods, fibers, tubes, sheets, and more, meticulously organized at the super microscale level, typically within the size range of 1 to 100 nanometers. These nanomaterials exhibit distinctive physical, chemical, and electronic properties compared to their conventional counterparts of the same category [1]. The synthesis process of nanomaterials commonly follows two principal approaches: "bottom-up" involves the assembly of atoms, molecules, or ions to create nanostructures, whereas "top-down" focuses on breaking down larger systems to produce nano-sized units [2]. Within the "bottom-up" approach, the "green synthesis" method has garnered significant attention, aiming to generate environmentally friendly products. This method is more

straightforward than traditional chemical processes, supercritical fluid, or sol-gel techniques. Green synthesis employs natural compounds from plant extracts as both reducing agents and stabilizers in the synthesis of nanostructures, presenting several advantages, including ease of scalability, cost-effectiveness, avoidance of toxic chemicals, and reduced energy requirements. Based on these principles, this research introduces a green synthesis method for copper oxide, zinc oxide, and CuO/ZnO nanocomposites using extracts from *Boehmeria nivea* leaves, focusing on their potential applications in antibacterial product development.

EXPERIMENTAL PROCEDURE

Extraction of Boehmeria nivea

Fresh leaves were grown and collected in District 6, Ho Chi Minh City. After harvesting, the leaves were washed and dried at 45 °C for three

days, then ground into powder. 5 g leaf powder added into 100 mL of DI water, stirring magnetically at 80 °C for 1 hour. The mixture is filtered to collect the extract solution and then preserved at 4 °C.

Synthesis of nanomaterials

For each experiment, 10 mL extract solution was added to 40 mL copper salt, zinc salt, and mixtures of copper and zinc salt solution with different ratios, respectively.

The mixtures were magnetically stirred at room temperature for one hour. Subsequently, the samples were dried and treated at 650 °C for 2 hours. The nano particles obtained are depicted in Figure 1.



Figure 1: The color of CuO, ZnO NPs, and CuO/ZnO nanocomposites after heat treatment.

Antibacterial test

The *Escherichia coli* (ATCC 25922) and *Staphylococcus aureus* (ATCC BAA-1708) strains were activated overnight in an MHB medium and adjusted to a 10^6 CFU/mL bacterial density. The bacterial suspension added ZnO nanoparticles at various concentrations in 10% DMSO. Positive controls used 3% streptomycin instead of nanoparticles, while the negative control contained only 10% DMSO without nanoparticles. After a 24-hour incubation at 37°C, 0.1% resazurin reagent was added to each sample to determine Minimum Inhibitory Concentration (MIC) and Minimum Bactericidal Concentration (MBC). In the MBC experiment, 50 µL of each sample was diluted and plated on MHA if no color change occurred within the material concentration range. The bactericidal rate was calculated as follows:

Bactericidal rate (%) = $(1 - T/C) \times 100\%$, where C is the bacterial density in the negative control after 24 hours (CFU/mL), and T is the bacterial density after 24 hours with the antibacterial agent (CFU/mL).

RESULTS AND DISCUSSION

Composition and structure

Figure 2 displays the FTIR spectrum of the extract from *Boehmeria nivea* leaves. In the wavenumber range of $3690 - 2900 \text{ cm}^{-1}$, a distinct peak indicates the stretching vibration of the -OH group, commonly found in compounds such as phenols, alcohol, and water. A signal at 1596 cm^{-1} represents the stretching vibration of the C=O group, and peaks at 1423 and 1087 cm^{-1} correspond to stretching vibrations related to the C-O groups. These characteristic groups, including -OH, C=O, and C-O, suggest the presence of compounds like phenols, ketones, esters, aldehydes, alkaloids, and flavonoids, known for their ability to reduce copper and zinc salts. Even after heating, the FTIR spectrum continues to reveal stretching vibrations of the -OH signals and C-O bonds in the particles. Furthermore, the results confirm specific signals for ZnO at 456 cm^{-1} and CuO at 486 cm^{-1} , supporting the formation of CuO NPs and ZnO NPs, as described by Widiarti et al. (2017) [3]. CuO/ZnO nanocomposites display combined signals from CuO and ZnO, with peak intensities depending on the ratio and composition of CuO NPs and ZnO NPs in the material.

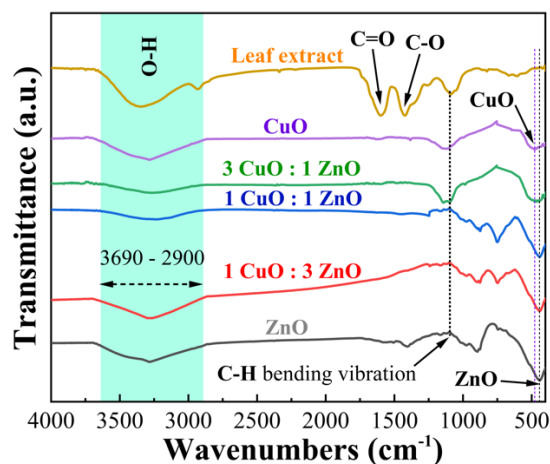


Figure 2: FTIR spectra of leaf extract, CuO, ZnO NPs, and CuO/ZnO nanocomposites.

From the XRD pattern (Figure 3), characteristic peaks of CuO NPs are observed at two theta angles of 32.60 ($\bar{1}10$), 35.62 (002), 38.81 (111), and other prominent peaks. These characteristic peaks closely match the JCPDS standard card: 05-0667. The CuO NPs exhibit a monoclinic crystal structure.

For the ZnO NPs material, the preferred peaks appear at two theta angles such as 31.87 (100), 34.53 (002), 36.36 (101), and other corresponding peaks, which match the parameters from the JCPDS standard card: 36-1451. These results

confirm that the ZnO NPs exhibit a hexagonal wurtzite crystal structure. Nevertheless, the characteristic peaks of CuO at 35.62 (002) and 38.81 (111) are present in the composite materials without any significant shifts. The same holds for ZnO, with its peaks at 31.87 (100), 34.53 (002), and 36.36 (101), exhibiting congruence with the findings reported by Govindasamy in 2021 [4]. The intensity of the diffraction peaks of CuO and ZnO in the CuO/ZnO composites varies depending on the initial concentration of the reaction salt solution.

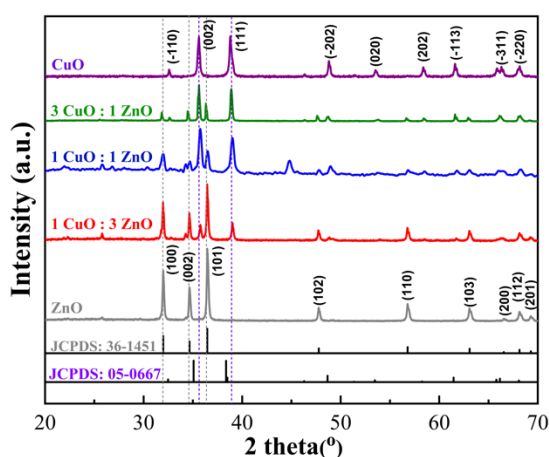


Figure 3: XRD pattern of the nanomaterials.

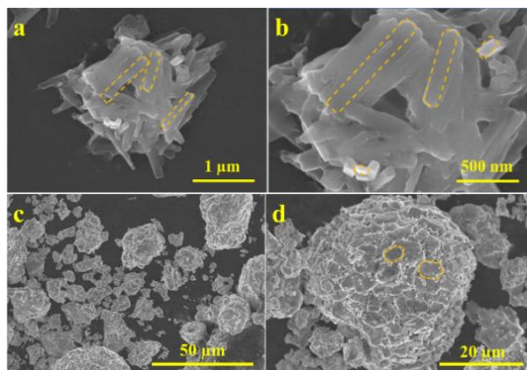


Figure 4: SEM images of a,b) CuO; c,d) ZnO NPs.

In the SEM image (Figure 4), CuO NPs exhibit a nano-rod-like structure with an average diameter of approximately 70 nm, which is relatively uniform and smaller than the dimensions reported by Shrestha et al. in 2010 when synthesized using the hydrothermal method, where the rod diameter could reach up to 150 nm [5]. The synthesized nano-rods are pretty long, with a length of approximately 650 nm. The morphology image of ZnO reveals the presence of large spherical aggregates with an average diameter of about 15 µm, composed of hexagonal-shaped ZnO NPs.

The size of the ZnO NPs can reach a diameter of 4 µm. These spherical aggregates can be considered as the 3D structure of ZnO, which forms a complex microstructural framework [6]. The spherical structure closely resembles the findings reported by Yin et al. in 2014 when synthesized using a chemical method [7]. The formation of these spherical aggregates can be attributed to the process where, upon nucleation in a zinc salt solution, the initial nano-sized particles are formed and subsequently act as nuclei for the gradual growth of other nanomaterials, giving rise to a snowball effect.

Antibacterial results

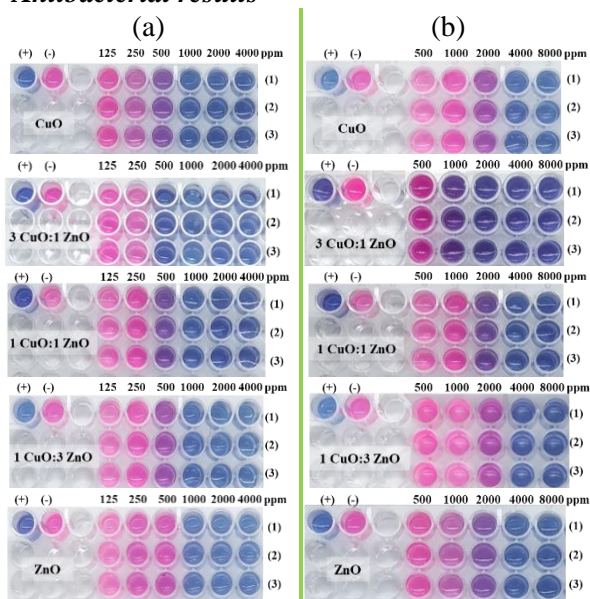


Figure 5: The MIC results of nanomaterials against a) *E. coli* and b) *S. aureus*.

In Figure 5, the Minimum Inhibitory Concentration (MIC) for CuO NPs and CuO/ZnO nanocomposite materials against *E. coli* is 500 ppm, showing improvement over Ambarasan et al. findings of 625 ppm for CuO NPs and ZnO NPs. In contrast, the MIC for ZnO NPs is higher at 1000 ppm, twice that of CuO NPs and CuO/ZnO nanocomposites. This higher MIC is due to the larger size of ZnO NPs, limiting their antibacterial efficacy. The MIC values for *S. aureus* are significantly higher, requiring a concentration of 2000 ppm for inhibition, which is considerably more significant than the MIC for *E. coli*. This difference is attributed to the antibiotic resistance genes the *S. aureus* strain carries, enabling it to survive in environments with potent inhibitory agents more effectively than strains lacking such resistance genes. Notably, the 3 CuO : 1 ZnO exhibits superior inhibitory effects at a

concentration of 1000 ppm compared to other materials.

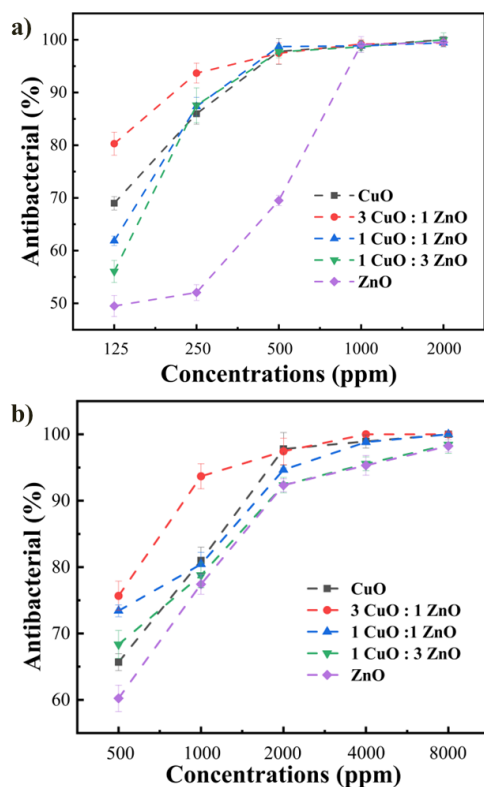


Figure 6: Bactericidal rate of the materials against a) *E. coli* and b) *S. aureus*.

Figure 6a shows that the antibacterial efficacy increases proportionally with the concentration of the materials, ranging from 125 ppm to 2000 ppm. Among these materials, the 3 CuO : 1 ZnO nanocomposite exhibited the best antibacterial performance against *E. coli*, achieving an 80% bacterial reduction at 125 ppm. At the same time, ZnO NPs showed the lowest efficacy, with only a 51% bacterial reduction. This suggests that ZnO NPs in aggregated spheres decrease the effective surface area and demonstrate inefficient antibacterial properties. In Figure 6b, the superior antibacterial activity against *S. aureus* is observed with the 3 CuO : 1 ZnO nanocomposite at a concentration of 500 ppm, which resulted in a 76% reduction in *S. aureus* compared to the other materials. The pure CuO NPs showed more potential antibacterial properties than ZnO NPs.

CONCLUSION

This research study reports the synthesis process of CuO NPs, ZnO NPs, and CuO/ZnO nanocomposite from organic extracts of *Boehmeria nivea* leaves. Based on SEM images, CuO NPs were observed to form rod-like

structures with a thickness of 70 nm, while ZnO NPs exhibited the formation of large spherical clusters with an average diameter of 15 μm . All the synthesized materials demonstrated inhibitory and bactericidal capabilities, with 3 CuO : 1 ZnO nanocomposite displaying a notable 80% bacterial reduction at 125 ppm against *E. coli* and a 76% reduction at 500 ppm against *S. aureus*. The research results provided an effective approach for synthesizing antibacterial materials based on CuO NPs, ZnO NPs, and their composites.

Acknowledgment

The authors acknowledge the support of XRD and FTIR measurements from the INOMAR Center, VNU-HCM.

References

- [1] A. Gopinadh, J.R. Dev, *The changing phase of prosthodontics: Nanotechnology*, Journal of Dental and Allied Sciences **4** (2015) 78.
- [2] D.G. Ullman, D. Craig, *The importance of drawing in the mechanical design process*, Computers & Graphics **14** (1990) 263–274.
- [3] N. Widiarti, S. Wahyuni, *Synthesis CuO-ZnO nanocomposite and its application as an antibacterial agent*, IOP Conference Series: Materials Science and Engineering **172** (2017) 012036.
- [4] G.A. Govindasamy, N.H. Harun, *Compositions and antimicrobial properties of binary ZnO–CuO nanocomposites encapsulated calcium and carbon from Calotropis gigantea targeted for skin pathogens*, Scientific Reports **11** (2021) 99.
- [5] K.M. Shrestha, K.J. Klabunde, *Synthesis of CuO Nanorods, Reduction of CuO into Cu Nanorods, and Diffuse Reflectance Measurements of CuO and Cu Nanomaterials in the Near Infrared Region*, The Journal of Physical Chemistry C **114** (2010) 14368–14376.
- [6] L. Wang, L. Shao, *The antimicrobial activity of nanoparticles: present situation and prospects for the future*, International Journal of Nanomedicine **12** (2017) 1227–1249.
- [7] J. Yin, Q. Lu, *Water Amount Dependence on Morphologies and Properties of ZnO nanostructures in Double-solvent System*, Scientific Reports **4** (2014) 3736.

APPLICATION OF PHOTSENSITIVE INK IN CHIP FABRICATION TECHNOLOGY

Thang Minh Bui, Hoa Hong Chung, Ngan Huu Dinh, Linh Duy Nguyen, Vi Nhat Hoang Ngo, Dung Dang Thi My, Ngan Nguyen Le, Tin Chanh Duc Doan and Chien Mau Dang

Institute for Nanotechnology, Community 6, Linh Trung Ward, Thu Duc City, Ho Chi Minh City, Vietnam;

Vietnam National University Ho Chi Minh City, Ho Chi Minh City, Vietnam

Email: bmthang.int@vnuhcm.edu.vn

ABSTRACT

The applications of microelectromechanical Systems (MEMS) in the fabrication of sensors have become diverse thanks to low power consumption and the ability to provide highly accurate and sensitive measurements. This paper studies the use of photosensitive ink in the photolithography step of the microfabrication technology for fabricating electrodes. The electrode dimensions analyzed by an optical microscope GX 51 (Olympus) showed an error margin of 7.7 %, as compared to the drawing design. The results show a promising application of the proposed photosensitive ink to the semiconductor industry at a low cost.

Keywords: Photolithography, Electrodes, MEMS, Photosensitive, Electrode fabrication

INTRODUCTION

The photolithography technique has been developed since the early 20th century and is widely used in the semiconductor industry to fabricate electronic circuits on silicon wafers. Additionally, photolithography is employed in materials science and technology to manufacture small material components and microelectromechanical systems (MEMS) devices. Photolithography is an essential step in the fabrication of microelectronic components. However, one limitation of photolithography is that light is subject to scattering, making it impossible to focus the light beam to a size smaller than a specific limit. Therefore, it is not feasible to fabricate nanoscale components using photolithography (the best resolution of photolithography equipment is 50 nm) [1].

Consequently, electron beam lithography is an alternative technology when fabricating nanoscale components. In photolithography, external factors such as humidity, room temperature, and environment cleanliness, as well as process parameters like exposure time, spin coating speed, and sample heating temperature, all significantly affect the quality of the photoresist layer [2,3]. Each laboratory optimizes these parameters to achieve the best quality components.

In this study, we present a detailed overview of the printing technology in the PCB industry

based on microfabrication techniques. We then apply photosensitive ink in microfabrication technology with details at the micrometer scale to reduce costs and enable widespread application in normal environmental conditions.

EXPERIMENTAL

Materials

The chemicals used for the experiments included FX-500 photopolymer ink, with a viscosity of 150 dps at 25 °C solution with blue color. The transparent XSJ-001 photopolymer ink solution was also used. The developer solution, Na₂CO₃, was purchased from China. These solutions were prepared at various concentrations depending on the experimental objectives. The solvents from China, such as 99% ethanol, 98% isopropanol, and acetone, were obtained from Merck, Germany. All aqueous solutions were prepared using ultrapure water with a resistivity of 18.2 MΩ.cm.

Manufacturing process.

The manufacturing process involved the fabrication of electrodes on a (100) silicon wafer, specifically a mono-crystalline silicon wafer with a 4-inch diameter, a thickness of 380 μm, and a surface resistance of 5-10 Ω.cm. The silicon wafer used in this process was obtained from Okmetic in Finland. Before electrode fabrication, the wafers underwent a series of cleaning steps using piranha

solution, acetone, isopropanol, and DI water. Following cleaning, a SiO₂ layer was deposited on the wafer surface using the oxidation furnace PEO 601 from ATV in Germany. The wafer was cleaned using piranha solution, acetone, isopropanol, and DI water. The next step involved the photolithography process.

RESULTS AND DISCUSSION

Microscopic optics

Figure 3 Illustration of the actual dimensions of the electrode, measured using the GX 51 microscope, on the electrode's surface area of 9.5 mm × 17.6 mm. It can be observed that there is a discrepancy in the electrode's dimensions during the design process, measuring 350 μm, and after fabrication, measuring 377 μm, with an approximate error of 7.7 % compared to the initial

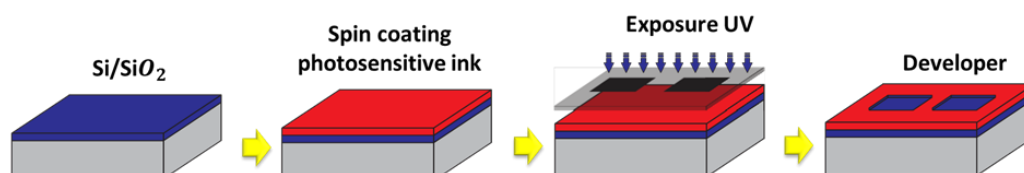


Figure 1. The image shows the process of lithography using photosensitive ink.

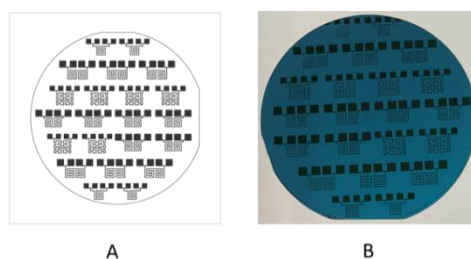


Figure 2. Electrochemical A) Design mask image B) Experimental fabrication image.

Figure 1 describes a wafer spun on a Suss MicroTec spin coater at 800 revolutions per minute for 10 seconds. After coating the wafer, it was pre-baked on a hotplate at 90°C for 15 seconds. The sample was then transferred to the stage of the MJB4 lithography system. The mask was placed between the lens system and the piece, and adjustments were made to ensure the sample surface was in close contact with the mask. The MJB4 lithography system was set with an exposure time of 5 seconds and a light intensity of 15.8 mW/m². After UV exposure, the sample was immersed in a NaCl developer solution for rinsing [4]. The piece was agitated until all the photoresist exposed to UV light was washed away. Next, the sample was rinsed in DI water to remove any remaining developer on the sample surface. To fully cure and firmly adhere the photoresist layer to the substrate and evaporate all the solvents from the photoresist, the sample was dried at 120°C for 90 seconds. A Ti/Pt layer was then deposited using a Leybold Univex 350 sputtering system. Finally, the lift-off step was performed using acetone [5].

measurements. This discrepancy is acceptable and does not significantly affect the quality of the electrode.

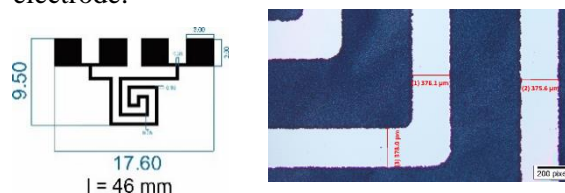


Figure 3. Electrochemical A) Design mask image B) Experimental fabrication image.

The result measures the thickness of the coating layer.

The thickness of the coating layer is measured using the Dektak 6M Stylus Profiler device at different positions on the wafer, and the deviation from the wafer surface is calculated. After measuring the thickness of the coating layer at other places, the obtained results in Table 1 show that the thickness of the optical ink coating layer is relatively uniform, approximately 419.91 nm.

Table 1. The electrode thickness was measured using the Dektak 6M Stylus Profiler.

Position	Thickness of photosensitive ink (nm)
1	411.25
2	423.31
3	425.18
Thickness average	419.91

photosensitive glass for the gravure printing process (2008) 1635–1639.

CONCLUSION

In this study, I investigated fabricating electronic components using the photolithography method with photoresist used in electronic circuit fabrication. Through this, the process and suitable parameters for the photolithography process were optimized, allowing for the experimental fabrication of the sensor mask for the sensor. This aims to save costs while maintaining accuracy.

The observation of the sample under photosensitive reveals well-defined grooves and precise details. The adhesion of the optical adhesive layer was tested using long-term ultrasonic vibration, and the results showed excellent adhesion. This demonstrates that the identified parameters are entirely suitable. Additionally, the size of the produced mask and the deviation after fabrication are approximately 7% compared to the design.

Acknowledgment

This work was supported by the Ministry of Science and Technology under grant number ĐTĐL.CN-122/21.

References

- [1] F. Mcgrath et al., *Applied Surface Science Structural, optical, and electrical properties of silver gratings prepared by nanoimprint lithography of nanoparticle ink*, *Appl. Surf. Sci.*, **537**(2020) (2021) 147892.
- [2] M. G. Mohammed and R. Kramer, *All-Printed Flexible and Stretchable Electronics*, (2017).
- [3] P. Jiang, Z. Ji, X. Zhang, Z. Liu, and X. Wang, *Recent advances in direct ink writing of electronic components and functional devices*, *Prog. Addit. Manuf.*, (2017).
- [4] W. Whyte, *Cleanroom Technology: Fundamentals of Design, Testing and Operation*, (2001).
- [5] Æ. D. Hu, *Application of micro structured*

A REVIEW ON BIOSYNTHESIS OF SILVER AND ZINC OXIDE NANOPARTICLES USING PLANT EXTRACTS IN VIETNAM (2020 - NOW)

An Thu Thi Truong, Dung My Thi Dang, Tin Chanh Duc Doan, Chien Mau Dang

Institute for Nanotechnology, Community 6, Linh Trung Ward, Thu Duc City, Ho Chi Minh City, Vietnam;
Vietnam National University Ho Chi Minh City, Ho Chi Minh City, Vietnam

Email: tttan@vnuhcm.edu.vn

ABSTRACT

This review delves into using indigenous plants in Vietnam as reducing agents for synthesizing silver (AgNPs) and zinc oxide nanoparticles (ZnO NPs). The biosynthesis method explored herein emerges as a time-effective, economical, non-toxic, and environmentally friendly alternative, proving more effective than other techniques. Numerous studies have documented the successful production of AgNPs and ZnO NPs utilizing diverse native plant species, yielding particles with an average size ranging from 5 to 80 nm and 5 to 112 nm, respectively. These nanoparticles exhibit predominantly spherical morphologies and find versatile applications in antibacterial, antifungal, and anti-cancer activities, as well as in the photocatalytic removal of toxic dyes, among other uses. The findings underscore the need for extensive research on indigenous plants to enhance further the synthesis of AgNPs and ZnO NPs in future endeavors.

Keywords: AgNPs, ZnO NPs, biosynthesis, indigenous plants

INTRODUCTION

Nanomaterials, typically ranging from 1 to 100 nm, have found widespread applications across various sectors, including food, healthcare, biotechnology, textiles, renewable energy, environmental solutions, and electronics. This technology sector is pivotal and holds exceptional promise for the future.

The synthesis of nanomaterials generally falls into two categories: the "top-down" approach employing physical methods and the "bottom-up" approach involving chemical or biological methods. While physical methods suffer from limitations such as high energy demands, large operational spaces, and imperfections on nanoparticle surfaces, chemical methods present drawbacks such as the use of toxic chemicals, aggregation, and the generation of harmful by-products. To overcome these challenges, the exploration of plants, bacteria, fungi, actinomycetes, and algae for nanomaterial biosynthesis has gained momentum. These biological sources are preferred due to their eco-friendly, cost-effective, and biocompatible attributes. Among these, plants have emerged as a focus of extensive research due to their rich repository of natural compounds, abundant species, simple processes, and faster synthesis capabilities than bacteria or fungi. These natural

compounds, encompassing terpenoids, flavonoids, phenolics, saponins, alkaloids, tannins, carbohydrates, and among others, served as both reducing and stabilizing agents in biosynthesis [1].

In the realm of metal and metal oxide nanoparticles, significant attention has been directed towards the biosynthesis of silver nanoparticles (AgNPs) and zinc oxide nanoparticles (ZnO NPs) using plant extracts. This focus is underpinned by their distinct characteristics, including shape, size, and orientation, making them invaluable for applications such as antibacterial, anticancer, antifungal, and antioxidant activities, drug delivery, diagnostics, and medicinal uses. [1, 2].

Vietnam, endowed with a diverse flora comprising more than 13,000 plant species, has long harnessed these resources for various purposes, including food, medicine, biotechnology, textiles, and environmental solutions. Consequently, this review article aims to encapsulate the current landscape of utilizing indigenous plants in Vietnam for synthesizing AgNPs and ZnO NPs and their recent applications.

BIOSYNTHESIS OF SILVER AND ZINC OXIDE NANOPARTICLES USING PLANT

EXTRACTS IN VIETNAM AND THEIR APPLICATIONS

Biosynthesis of silver nanoparticles (AgNPs)

Vietnam has witnessed numerous successful endeavors in synthesizing silver nanoparticles (AgNPs) using plant extracts. Various plant parts, including leaves, roots, flowers, seeds, and other components, have been utilized for extracting biological compounds. For example, plant species used in this biosynthesis process *Curcuma longa*, *Callisia fragrans*, *Camellia sinensis*, *Piper betle*, *Phyllanthus urinaria*, *Pouzolzia zeylanica*, *Paramignya trimera*, *Muntingia calabura*, and *Quisqualis indica*. The synthesis process typically involves collecting, washing, drying, and grinding the plant material into powder, which is then extracted using distilled or deionized water to obtain biomass containing bio-compounds. This biomass is subsequently mixed with an Ag salt precursor and heated to form AgNPs. The color change of the solution serves as a confirmation of the synthesized nanoparticles. Key influencing factors such as temperature, pH, retention time, and mixing ratio influence the synthesis of AgNPs. Characterization techniques like ultraviolet spectroscopy (UV-Vis), Fourier-transform infrared spectroscopy (FT-IR), X-ray diffraction (XRD), scanning electron microscopy (SEM), transmission electron microscopy (TEM), dynamic light scattering (DLS), and energy dispersive spectroscopy (EDS) are employed to analyze the properties of AgNPs.

Many studies have shown that native plant extracts can act as both reducing and stabilization agents for synthesizing AgNPs. The morphology, size, and efficiency of AgNPs depend on the plant species and other influencing factors. These nanoparticles are predominantly spherical, although some studies have reported hexagonal or triangular morphologies. AgNPs exhibit an average size ranging from 3 to 80 nm, with a majority of publications demonstrating sizes less than 30 nm. Smaller-sized AgNPs exhibit enhanced antibacterial capabilities due to their increased ability to penetrate cell membranes. Studies have shown high antibacterial activity of AgNPs against a variety of bacteria, including *E. coli*, *L. fermentum*, *P. aeruginosa*, *B. subtilis*, *B. cereus*, *S. aureus*, *S. typhi*, *S. pyogenes*, and *S. enteritidis* [3-10]. Furthermore, Dai Hai Nguyen *et al.* (2020) successfully synthesized biogenic silver nanoparticles using leaf extracts from plants like *Phyllanthus urinaria*, *Pouzolzia zeylanica*,

Scoparia dulcis, *Momordica charantia*, and *Psidium guajava* for antifungal evaluations against *A. niger*, *A. flavus*, and *F. oxysporum* [11].

In addition, the use of plant extracts synthesized AgNPs was studied for the reduction of nitrophenols (o-, m-, and p-nitrophenols) and toxic dyes (methylene blue, methyl orange, rhodamine 6G, and rhodamine B) [12-14]. Among them, Minh-Trong Tran *et al.* (2021) introduced a new approach utilizing plant embryos cultured from *Panax vietnamensis* roots. This method ensures the stable composition and content of biological compounds, enhancing the efficiency of AgNP synthesis.

Noteworthy contributions have been made by Lan Anh Thi Nguyen *et al.* (2023), who synthesized AgNPs using *Callisia fragrans* leaf extract, exhibiting anticancer activity against various cell lines, including MCF-7, HepG2, KB, LU-1, and MKN-7. These nanoparticles displayed inhibitory concentrations at 50% (IC50 values) of 2.41, 2.31, 2.65, 3.26, and 2.40 $\mu\text{g}\cdot\text{mL}^{-1}$, respectively, and had a spherical shape with an average size of 48 nm [15]. Another author also successfully synthesized AgNPs for anticancer activity against for the AGS gastric cancer cell line [8]. Additionally, Tam KT *et al.* (2023) explored the green synthesis of AgNPs for applications in colorimetric detection of Hg^{2+} and antibacterial activity [16].

Biosynthesis of Zinc oxide nanoparticles (ZnO NPs)

Similar to the synthesis of silver nanoparticles (AgNPs), the biosynthesis of zinc oxide nanoparticles (ZnO NPs) involves replacing the silver salt precursor with a zinc salt precursor. Despite being less explored compared to AgNPs, significant strides have been made in this field.

Tu Uyen Doan Thi *et al.* (2020) successfully synthesized ZnO NPs using orange fruit peel for antibacterial activities against *E. coli* and *S. aureus*. Deionized water was employed to extract compounds from orange peels, and a zinc nitrate precursor ($\text{Zn}(\text{NO}_3)_2\cdot 6\text{H}_2\text{O}$) was mixed with the extract. The research highlighted the significant impact of temperature and pH on the size, morphologies, properties, and bactericidal activity of ZnO NPs [17]. Similarly, Quynh Mai Thi Tran *et al.* (2021) investigated the biosynthesis of ZnO NPs utilizing aqueous *Piper betle* leaf extracts to assess their antibacterial activity. The study meticulously examined factors like zinc salt concentration, extract volume, and pH. The

resulting ZnO NPs, with an average particle size of approximately 112 nm, exhibited hexagonal and spherical shapes. Notably, ZnO NPs and those coated on medical sutures displayed robust antibacterial activity against *E. coli* and *S. aureus* [18].

In 2022, Nhu Thu Thi Vo *et al.* synthesized ZnO NPs using rosin obtained from *Pinus latteri* trees and a zinc chloride precursor. The resulting ZnO NP samples exhibited crystallinity with a grain size ranging from 30 to 100 nm. These nanoparticles demonstrated photocatalytic capabilities for decomposing methylene blue and methyl orange and antibacterial effects against *E. coli* [19].

Another notable research conducted by Thao Thi Truong *et al.* (2022) explored the sol-gel method for synthesizing ZnO NPs using *Piper chaudiocanum* L. leaf extracts. Distilled water and a zinc acetate dihydrate precursor ($Zn(CH_3COO)_2 \cdot 2H_2O$) were utilized for biosynthesis, resulting in ZnO NPs with high purity, a wurtzite hexagonal structure, and a size range of 28-37 nm. Their Pb(II) adsorption ability is more effective than the traditional sol-gel method (using oxalic acid) [20]. Interestingly, their subsequent study in 2023 optimized the synthesis process using the co-precipitation method with *P. chaudiocanum* L. extract. The resulting ZnO NPs exhibited varying crystallite sizes (22, 27, 30, 33, 32, 35, and 40 nm) and showcased enhanced antibacterial activity against *P. aeruginosa* and *S. aureus*. Moreover, these NPs demonstrated cytotoxic effects against the KB human cancer cell line, suggesting their potential in developing drugs for treating human carcinoma cells and infectious diseases [21].

CONCLUSION

Indigenous plants in Vietnam have emerged as valuable resources for nanoparticle synthesis, demonstrating superior biological activity compared to conventional methods. While silver nanoparticles (AgNPs) and zinc oxide nanoparticles (ZnO NPs) are primarily utilized for antibacterial purposes, their potential extends to anticancer and antifungal applications, as well as photocatalytic degradation of toxic dyes and the development of colorimetric sensors. Using native plant extracts in synthesizing AgNPs and ZnO NPs has revealed their multifaceted activity mechanisms.

Despite these promising developments, the full potential of native plants remains untapped,

and their applications have not reached optimal effectiveness. Further exploration is essential, particularly in medicine, where these nanoparticles hold immense promise. By delving deeper into the unique properties of indigenous plant extracts, researchers can unlock innovative pathways, leading to enhanced and targeted applications in the synthesis of AgNPs and ZnO NPs. Continued research and exploration are imperative to harness these natural sources' full benefits in nanotechnology, paving the way for transformative advancements in medical science and beyond.

Acknowledgment

The authors would like to thank Vietnam National University Ho Chi Minh City (VNUHCM) for the financial support of this research (Grant No. TX2023-32-01).

References

- [1] Xu J, Huang Y, Zhu S, Abbas N, Jing X, Zhang L, *A review of the green synthesis of ZnO nanoparticles using plant extracts and their prospects for application in antibacterial textiles*, Journal of Engineered Fibers and Fabrics, 16 (2021) 1-14.
- [2] Vijayaram S, Razafindralambo H, Sun YZ, Vasantharaj S, Ghafarifarsani H, Hoseinifar SH, Raeeszadeh M, *Applications of Green Synthesized Metal Nanoparticles-A Review*, Biological Trace Element Research, (2023) 1-27.
- [3] Trung ND, Nhuan NT, Van LT, Minh NV, Anh NP, Tri N, *Biofabrication of silver nanoparticles using Curcuma longa extract: Effects of extraction and synthesis conditions, characteristics, and its antibacterial activity*, J. Biochem. Technol, 11 (2020) 57-66.
- [4] Doan VD, Huynh BA, Nguyen TD, Cao XT, Nguyen VC, Nguyen TL, Nguyen HT, Le VT, *Biosynthesis of silver and gold nanoparticles using aqueous extract of Codonopsis pilosula roots for antibacterial and catalytic applications*, Journal of Nanomaterials, (2020) 1-8.
- [5] T. My-Thao Nguyen, T. Thanh-Tam Huynh, Chi-Hien Dang, Dinh-Tri Mai, T. Thuy-Nhung Nguyen, Dinh-Truong Nguyen, Van-Su Dang, Trinh-Duy Nguyen & Thanh-Danh Nguyen, *Novel biogenic silver nanoparticles used for antibacterial effect and catalytic degradation of contaminants*, Research on

- Chemical Intermediates, 46 (2020) 1975-1990.
- [6] Nguyen VT, *Sunlight-driven synthesis of silver nanoparticles using pomelo peel extract and antibacterial testing*, Journal of Chemistry, (2020) 1-9.
- [7] Nguyen NH, Nhi TT, Van Nhi NT, Cuc TT, Tuan PM, Nguyen DH, *Comparative Study of the Silver Nanoparticle Synthesis Ability and Antibacterial Activity of the Piper Betle L. and Piper Sarmentosum Roxb. Extracts*, Journal of Nanomaterials, (2021) 1-9.
- [8] Van Hao N, Hung NP, Hoa VX, Ha NT, Van NT, Van Trinh P, *Green, facile and fast synthesis of silver nanoparticles by using solution plasma techniques and their antibacterial and anticancer activities*, RSC advances, **13** (32) (2023) 21838-21849.
- [9] Tran KK, Hoang PH, Tran HT, Dinh VT, Do HT, *Biosynthesis of Silver Nanoparticles Using Tea Leaf Extract (Camellia Sinensis) for Photocatalyst and Antibacterial Effect*, Heliyon, 9 (2023) 1-10.
- [10] Dien TN, Thi HN, *Antibacterial activity of silver nanoparticle LED-synthesized using Citrus maxima peels*, International Journal of Plant Based Pharmaceuticals, **3**(2) (2023) 141-147.
- [11] Nguyen DH, Lee JS, Park KD, Ching YC, Nguyen XT, Phan VH, Hoang Thi TT, *Green Silver Nanoparticles Formed by Phyllanthus urinaria, Pouzolzia zeylanica, and Scoparia dulcis Leaf Extracts and the Antifungal Activity*, Nanomaterials (Basel), **10** (3) (2020) 542.
- [12] Trieu QA, Le CT, Pham CM, Bui TH, *Photocatalytic degradation of methylene blue and antibacterial activity of silver nanoparticles synthesized from Camellia sinensis leaf extract*, Journal of Experimental Nanoscience, **18** (1) (2023) 2225759.
- [13] Tran MT, Nguyen LP, Nguyen DT, Le Cam-Huong T, Dang CH, Chi TT, Nguyen TD, *A novel approach using plant embryos for green synthesis of silver nanoparticles as antibacterial and catalytic agent*, Research on Chemical Intermediates, 47 (2021) 4613-4633.
- [14] Le HT, Nguyen LA, *Biosynthesis, characterization and photocatalytic activity of silver nanoparticles produced from AgNO₃ solution using aqueous extract of Ocimum bacilicum L. leaf as the reducing agent*, GSC Advanced Research and Reviews, **14**(1) (2023) 151-158.
- [15] Nguyen LA, Van Mai B, Van Nguyen D, Nguyen NQ, Van Pham V, Pham TL, Le HT, *Green synthesis of silver nanoparticles using Callisia fragrans leaf extract and its anticancer activity against MCF-7, HepG2, KB, LU-1, and MKN-7 cell lines*, Green Processing and Synthesis, **12**, (1) (2023) 20230024.
- [16] Tam KT, Thuy NT, Ngan NT, Khai NM, Van Thanh D, *Green synthesis of Piper chaudiocanum stem extract mediated silver nanoparticles for colorimetric detection of Hg²⁺ ions and antibacterial activity*, Royal Society Open Science, **10**, (2) (2023) 220819.
- [17] Thi TU, Nguyen TT, Thi YD, Thi KH, Phan BT, Pham KN, *Green synthesis of ZnO nanoparticles using orange fruit peel extract for antibacterial activities*, RSC advances, **10**(40) (2020) 23899-23907.
- [18] Thi Tran QM, Thi Nguyen HA, Doan VD, Tran QH, Nguyen VC, *Biosynthesis of zinc oxide nanoparticles using aqueous piper betle leaf extract and its application in surgical sutures*, Journal of Nanomaterials, (2021) 1-15.
- [19] Nhu VT, Dat ND, Tam LM, Phuong NH, *Green synthesis of zinc oxide nanoparticles toward highly efficient photocatalysis and antibacterial application*, Beilstein Journal of Nanotechnology, **13**(1) (2022) 1108-1119.
- [20] Truong TT, Khieu TT, Nguyen TH, Nguyen TT, *Green Synthesis of ZnO Nanoparticles using Piper chaudiocanum L. Leaf Extract: Characterization and its Application in Pb (II) Adsorption*, VNU Journal of Science: Natural Sciences and Technology **38**(3) (2022) 1-13.
- [21] Truong TT, Khieu TT, Luu HN, Truong HB, Nguyen VK, Vuong TX, Tran TK, *Characterization and Bioactivity of Piper chaudiocanum L. Extract-Doped ZnO Nanoparticles Biosynthesized by Co-Precipitation Method*, Materials, **16**(15) (2023) 5457.

POSTER SESSIONS

NANOMATERIALS AND NANODEVICES
(NMD)

IZOD IMPACT STRENGTH OF ABS, PETG, ASA, AND PLA PLASTIC MATERIALS USING FDM 3D PRINTING METHOD

**Nguyen Pham Ngoc Tuyen¹, Le Vu Phong¹, Lam Huy Nhuc¹, Nguyen Van Hieu¹, Vu Dinh Canh¹,
Pham Thi Hong Nga¹, Nguyen Vinh Tien², Dang Minh Phung¹,
Vo Xuan Tien¹ and Dang Quang Khoa¹**

¹ Faculty of Mechanical Engineering, Ho Chi Minh City University of Technology and Education,
01 Vo Van Ngan Street, Linh Chieu Ward, Thu Duc City, Ho Chi Minh City, Vietnam

² Faculty of Chemical and Food Technology, Ho Chi Minh City University of Technology and Education,
01 Vo Van Ngan Street, Linh Chieu Ward, Thu Duc City, Ho Chi Minh City, Vietnam

Email: hongnga@hcmute.edu.vn

ABSTRACT

This research paper examines the impact resistance of four different plastic materials using the Izod impact test method according to ASTM D256-10. The four materials tested were ABS, PETG, ASA, and PLA, popular and low-cost materials used in a wide range of applications. They are widely utilized in 3D printing and injection molding applications because they produce high-quality parts. By conducting Izod impact testing and scanning the microstructure of specimens made using the FDM method from four materials, we can better understand their impact resistance and how they compare to each other. The research highlights the significance of the Izod impact test as a valuable method for characterizing the behavior of polymers when they withstand sudden impacts and absorb energy. This information can be helpful for junior designers and engineers who need to select plastic materials for applications where impact resistance is critical.

Keywords: impact resistance, ASA, PETG, ABS, PLA.

INTRODUCTION

The 3D printing technology gained attention in the late 1990s and is used widely in many industries [1,2]. Among the various 3D printing methods available, FDM (Fused Deposition Modeling) is one of the most commonly adopted techniques. FDM offers numerous advantages and has found widespread application in various industries.

The fundamental principle behind the FDM manufacturing process involves melting the raw material and shaping it to create desired structures. The material, a filament, is housed on a roll and pulled by a drive wheel. The filament from the feeder is put into the extruder (extrusion heater). It passes through the extrusion nozzle head (liquefier head), where it reaches the melting point (semi-liquid). According to the setup in the CAD data, the extrusion nozzle precisely deposits the liquid plastic layer by layer onto the platform [3,4]. There are a variety of materials that can be applied with this technique, and they have good impact resistance properties.

The Izod impact test is a popular method to define the impact resistance of plastic materials

[5] by assessing their toughness and capacity to resist sudden impact. Many previous studies have verified that the Izod impact test is an efficient method to evaluate the impact resistance of plastics. Nevertheless, there is much to learn in comparing the differences between these materials' resistance under this test. The research paper aims to fill this gap by investigating different polymers' impact resistance, employing the Izod impact test method following the ASTM D256-10 [6]. The four materials tested were chosen as PLA [7], PETG [8], ABS [9], and ASA because they are commonly used in various applications where impact resistance is critical and prevalent materials used in the 3D printing process of the FDM method.

This study involved conducting Izod tests using a pendulum impact tester on specimens of each of the four materials printed with 100% infill density. The quality of the layers and morphology were also evaluated using Scanning Electron Microscopy (SEM) [10].

EXPERIMENTAL

In this research, the following four plastic materials were used in manufacturing:

- ABS (Acrylonitrile Butadiene Styrene)
- PETG (Polyethylene Terephthalate Glycol)
- ASA (Acrylonitrile Styrene Acrylate)
- PLA (Polylactic Acid)

For each type of material, seven specimens specify the dimensions and notch geometry for the Izod impact testing of plastics. The specimens had a length of 63.5 mm and a width of 12.5 mm, the standard outer dimensions for this test method. A notch with a radius of 0.25 mm and an angle of 45° was milled into each specimen using a notching machine [11], leaving a height of 10.5 mm at the base of the notch as Fig. 1. The notch radius was chosen to comply with method A of ASTM D256-10.

The 3D printing technique was Fused Deposition Modeling (FDM) [12], and all specimens were products of CoreXY. The manufacturing parameters of four different plastic materials are shown in Table 1, which were set based on the manufacturer's recommendations.

Table 1. The manufacturing parameters for PLA, PETG, ABS, and ASA materials.

Parameters	PLA	PETG	ABS	ASA
Nozzle Temp. (°C)	200	230	240	200
Bed Temp. (°C)	60	80	120	60
Printing Speed (mm/s)	60			
Innitial layer heigh (mm)	0.15			
Layer thickness (mm)	0.1			
Line width (mm)	0.6			
Wall Thickness (mm)	1.2			
Infill density (%)	100			

The Izod impact tests were performed using the Tinius Olsen machine as Fig. 2, model IT504, at the Ho Chi Minh City Center of Supporting and Enterprise Development.

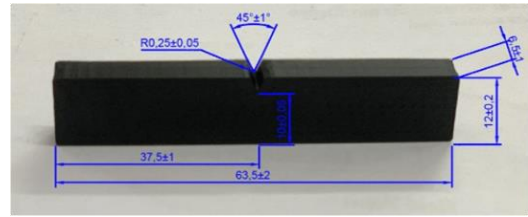
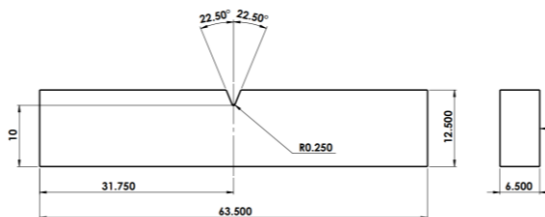


Figure 1. Dimensions of Izod-Type Test Specimen on CAD and after 3D printing.

Imaging was also conducted at Ho Chi Minh City University of Technology and Education using a Hitachi Scanning Electron Microscope (SEM), model TM4000, to study the bond quality between the layers of each material.

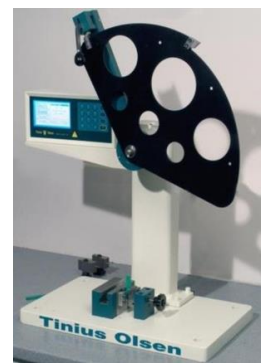


Figure 2. The Tinius Olsen Izod impact tester

RESULTS AND DISCUSSION

The average results of the Izod impact test for four plastic materials are presented in Fig. 3.

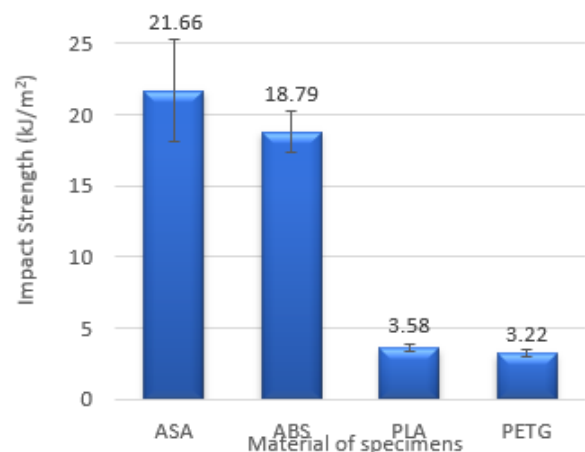


Figure 3. The average Izod impact strength for four different plastic materials.

According to the plot of Fig. 3, the highest impact strength is ASA at 21.66 kJ/m², followed by ABS at 18.79 kJ/m², PLA at 3.58 kJ/m², and PETG at 3.22 kJ/m². The results demonstrate that ASA exhibits significantly superior impact

resistance compared to PLA when subjected to the same temperature and printing parameters in Table 1. The experimental analysis conducted in

this study consistently showed that ASA can withstand impacts up to six times better than PLA.

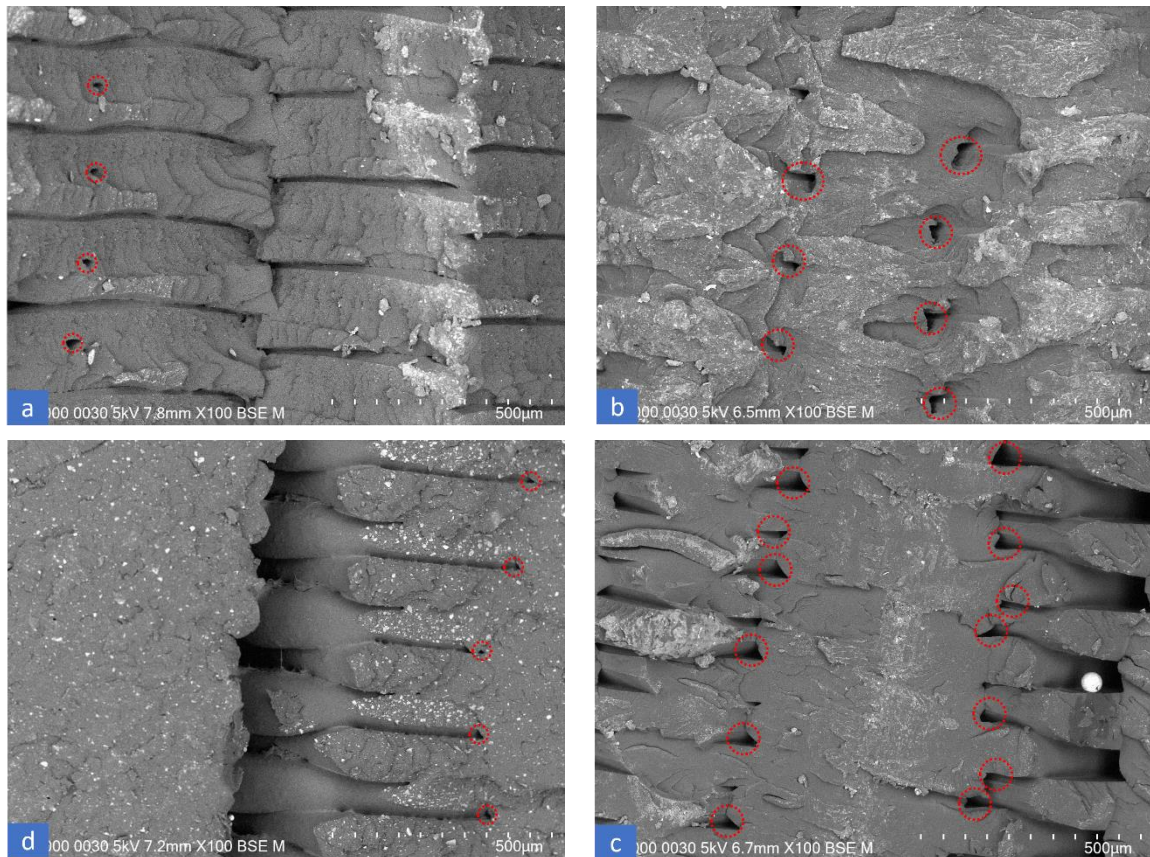


Figure 4. SEM images of 3D printed specimens: (a) ASA; (b) ABS; (c) PLA; and (d) PETG.

The SEM images of 3D printed and Izod impact-tested specimens are presented in Fig. 4(a-d) for ASA, ABS, PLA, and PETG, respectively. ASA exhibits exceptional interlayer adhesion, enhancing impact resistance, strength, durability, and overall printing process quality [13]. By comparing filament and printed microstructure, it can be observed that ASA exhibits an excellent filling ratio and the highest impact strength compared to other materials such as ABS, PLA, and PETG.

Both ABS and ASA specimens demonstrate a strong bonding microstructure, high filling ratio, and good interlayer adhesion in Fig. 4(a-b). In contrast, despite possessing a favorable bonding microstructure, PLA and PETG exhibit inadequate adhesion, low filling ratio, and distinct separation lines between layers in Fig. 4(c-d).

Also, in Fig. 4, certain micro-holes and voids resulting from the printing process are highlighted using red circles, serving as indicators of the interlayer and intralayer bonding

quality and the printability of different materials. These voids play a significant role in reducing strength due to localized strains and porosity [14]. It leads to a low-impact resistance capability of PLA and PETG materials.

CONCLUSION

This paper aimed to investigate the Izod impact test for ASA, ABS, PLA, and PETG materials. The study involved experimental analysis to determine the impact resistance properties of these materials. The following conclusions were drawn from the study:

- The Izod impact test proved to be an effective method for evaluating the impact strength of ASA, ABS, PLA, and PETG materials. It provided valuable insights into the materials' ability to withstand sudden impacts and absorb energy.

- The experimental results indicated that the impact resistance varied among the materials. ABS and ASA demonstrate superior impact resistance compared to the other plastic materials. Nevertheless, designers and engineers should

consider other factors, such as flexural and tensile strength, depending on the specific application to ensure an informed and suitable material selection.

Acknowledgments

We acknowledge HCMC University of Technology and Education, Dong Nhan Phat Co., Ltd, and Material Testing Laboratory (HCMUTE). They allowed me to join their team and access the laboratory and research machines. With their appreciated support, it is possible to conduct this research.

References

- [1] Moayyad Alssabbagh, *et al.*, *Evaluation of 3D printing materials for fabrication of a novel multi-functional 3D thyroid phantom for medical dosimetry and image quality*, *Radiation Physics and Chemistry* **135** (2017) 106-112.
- [2] Ammar Alzarrad, *et al.*, *3D Printing Applications in Construction from The Past and into The Future*, in *Conference: Creative Construction Conference* (2019) 754-760.
- [3] John Ryan C. Dizon, *et al.*, *Mechanical characterization of 3D-printed polymers*, *Additive Manufacturing* **20** (2018) 44-67.
- [4] A. Mitchell, *et al.*, *Additive manufacturing — A review of 4D printing and future applications*, *Additive Manufacturing* **24** (2018) 606-626.
- [5] Nikhil P Raut, A.B. Kolekar, *Experimental analysis of 3D printed specimens with different printing parameters for Izod impact strength*, *Materialstoday: Proceedings* **80** (2023) 156-162.
- [6] ASTM International. (2018). *Standard Test Methods for Determining the Izod Pendulum Impact Resistance of Plastics* (ASTM D256-10).
- [7] Hadi Noori, *Interlayer fracture energy of 3D-printed PLA material*, *Int J Adv Manuf Technol* **101** (2019), 1959-1965.
- [8] Cosmin-Florin Popa, *et al.*, *Influence of thickness on the IZOD impact strength of FDM printed specimens from PLA and PETG*, *Procedia Structural Integrity* **41** (2022) 557-563.
- [9] Ruben Bayu Kristiawan, *et al.*, *A review on the fused deposition modeling (FDM) 3D printing: Filament processing, materials, and printing parameters*, *Open Engineering* **11** (2021) 639-649.
- [10] Avin Abdullah, *et al.*, *Scanning Electron Microscopy (SEM): A Review*, *Proceedings of 2018 International Conference on Hydraulics and Pneumatics – HERVEX* (2018).
- [11] Anne Schmitz, *Effect of notch geometry on Izod impact bar results*, *White Paper University of Wisconsin-Stout Menomonie, WI, USA* (2019).
- [12] Rahmatabadi D, Aminzadeh A, Aberoumand M, Moradi M. *Mechanical characterization of fused deposition modeling (FDM) 3D printed parts*, *Fused depos. Model. Based 3D print* (2021) 131-150.
- [13] S. Raam Kumar, *et al.*, *Polymer additive manufacturing of ASA structure: Influence of printing parameters on mechanical properties*, *Materialstoday: Proceedings* **39** (2021) 1316-1319.
- [14] Tao Y, Kong F, Li Z, Zhang J, Zhao X, Yin Q, *et al.*, *A review on voids of 3D printed parts by fused filament fabrication*, *J Mater Res Technol* **15** (2021) 4860-4879.

MANUFACTURING INVESTIGATION OF FILM CS/PVA/CUR – ORIENTATION FOR WOUND DRESSING APPLICATION

Do Trung Nguyen, Tam Thi Bang Dao, Nhien Hon Le, Chi-Nhan Ha-Thuc

Faculty of Materials Science and Technology, University of Science, VNU-HCM, 227 Nguyen Van Cu Street, Ward 4, District 5, Ho Chi Minh City, 700000, Viet Nam.

Email: htcnhan@hcmus.edu.vn

ABSTRACT

This research presents the preparation of polymeric thin films from chitosan (CS) and polyvinyl alcohol (PVA) for application in healing wounds and burns. Synthetically, chitosan solution containing 2% chitosan and 2% acetic acid solution is mixed with polyvinyl alcohol solution 2%. The casting of CS/PVA mixtures at 60°C produces homogeneous CS/PVA thin films. In addition, to improve the stability of CS/PVA films in aqueous environments, citric acid is added to make CS/PVA films crosslinked and durable, especially when in contact with wounds and secretions in a long time. Particularly, to attain effective antibacterial activity, natural curcumin is extracted from yellow turmeric in order to modify CS/PVA films. Morphology, structure and antimicrobial properties of as-prepared CS/PVA/curcumin films are investigated using UV-VIS, FTIR, SEM and mechanical tensile measurement methods. On the basis of analytical results, the blend films are evaluated and improved for potential application of wound dressing. Keywords: Wound dressing, crosslinking, chitosan, polyvinyl alcohol, curcumin

INTRODUCTION

Currently, wound dressings using derivatives from nature are popular biomedical materials, because they provide many properties for each stage in wound healing process. The dressing has been designed to eliminate harmful bacteria that cause infection, with the combination of antibacterial agents. Chitosan (CS) is a biomaterial with abundant supply and suitable properties such as environmentally friendly, antibacterial and biocompatible, but CS has poor mechanical and physical properties. Therefore, scientists usually combine CS with polyvinyl alcohol (PVA) to produce polymer blend films with better mechanical characteristics [1-4]. In addition, curcumin (Cur), a natural extract derived from turmeric plant, is used in the formulation of polymer blend films for enhanced antibacterial activity and better wound healing.

Aiming to improve the antimicrobial property, curcumin (CUR) is a natural compound extracted from yellow turmeric with antimicrobial activity, eco-friendliness and low cost. CUR is also an active agent with antifungal, bactericidal, anti-inflammatory and skin protection effects. Moreover, CUR is also a good antioxidant agent, capable of inhibiting free radicals that damage skin wounds [2]. For the purposes mentioned above, the research topic is

to prepare and investigate blend films of CS/PVA/CUR for application in wound dressings. The research uses environmentally friendly materials and methods for making blend films, followed by analytical characterizations for evaluating mechanical and physical properties and antimicrobial activity.

EXPERIMENTAL

Preparation of CS/PVA films

The synthesis of CS/PVA was prepared in accordance with the procedure as described. At first, CS powder was dissolved in acetic acid solution 2% and stirred magnetically at 55°C-60°C for 5 hours to make a complete homogeneous CS solution 2%. Besides, PVA solution 2% was prepared by dissolving PVA in water at 75°C - 80°C for 8 hours. Next, the PVA solution and the CS solution were mixed together in a ratio of 2:8, followed by stirring without heating for 8 hours. The homogeneous mixture was filtered through a cellulose paper to obtain a transparent and homogeneous solution 2% (w/v). CS/PVA films were formed by solution casting method. The solution was placed in a petri dish, degassed and dried in an oven at 60°C for 24 hours. The dry film was separated from the petri dish and stored in a bag containing hydroscopic silica beads at room temperature.

CS/PVA film crosslinked with citric acid (CA)

After preparing CS/PVA solution 2%, CA was added to the solution, which was magnetically stirred and heated at 50 °C for 2 hours (CA is 1% of PVA/CS total weight). The mixture was poured into a petri dish, degassed and dried in an oven at 60 °C for 24 hours. Finally, a dry film is obtained and cured at 100 °C for 20 minutes to finish the curing process. The films were stored in a bag containing silica beads at room temperature.

Synthesis of CS/PVA film with CA and Cur

Curcumin powder was dissolved in ethanol at a ratio of 0.1 g Curcumin in 20 ml of ethanol. The process of synthesizing CS/PVA/CA/Curcumin is similar to the synthesis of CS/PVA/CA film. After obtaining the CS/PVA/CA blend, Curcumin was added at the proportions of 1%, 2% and 3% of the total weight of CS/PVA, followed by sonication for 10 minutes.

Denotations of as-prepared materials include CS/PVA film, CS/PVA/CA film, M1 film (CS/PVA/CA film with 1% Cur), M2 film (CS/PVA/CA film with 2% Cur), and M3 film (CS/PVA/CA film with 3% Cur).

RESULTS AND DISCUSSION

The incorporation of curcumin in CS/PVA film is prepared and presented in Figure 1. Visually, the film is smooth and uniform. The color of the films changed from light yellow to dark orange (M1 to M3) when increasing the amount of curcumin in the film (from 1% to 3%). The thickness of the CS/PVA/Curcumin films stitched with CA is shown in Table 1. With the solution volume of 30 ml in a petri dish, it was observed that when the films were collected, the thickness was quite similar.

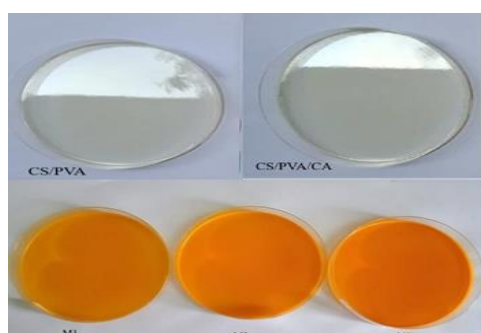


Figure 1. Color of the film

Mechanical properties of CS/PVA, CS/PVA/CA and CS/PVA/CA/Curcumin films

Membrane samples are mechanically tested to measure physical properties, including tensile strength and elongation at rupture. The results are shown in Figure 2 and Figure 3. The tensile strength and elongation at rupture of CS/PVA films are ~ 29.51 MPa and ~ 139.97 % respectively, while those of CS/PVA/CA films are ~ 60.33 MPa and ~ 64.06 % respectively. This result showed that the film with the CS : PVA ratio of 2 : 8 and 1% CA (dried at 100 °C for 20 minutes) was cross-linked in the structure. When more crosslinks between CA and polymer molecules were formed, mobility and movement of polymer chains in the film were reduced. As a result, the film is more rigid and brittle, the tensile strength increased and the elongation at the break decreased.

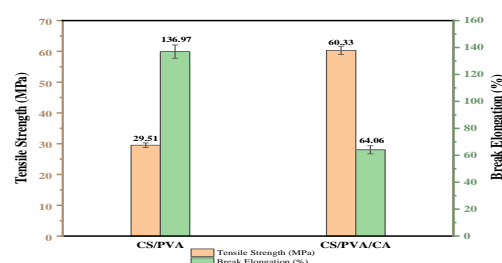


Figure 2. Tensile Testing of films

Figure 3 shows the tensile strength and elongation at rupture of CS/PVA/CA films with 1%, 2% and 3% curcumin. The tensile strengths of CS/PVA/CA film, film with 1% curcumin and film with 2 % curcumin decreased gradually from ~ 60.33 MPa to ~ 55.77 Mpa, but the film with 3% curcumin increased to ~ 74.39 Mpa.

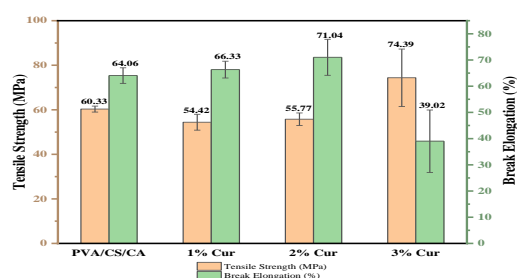


Figure 3. Tensile Testing of films

The elongation at rupture tended to increase by ~ 64.06% to 71.04% and decreased to ~ 39.02 % for the film with 3 % curcumin. This deviation may be due to the excessive curcumin content on the membrane, causing the accumulation and aggregation. Thus, the film ratio of 2% curcumin gives the best mechanical and physical tensile properties among the films with curcumin coating

on the surface. Therefore, CS/PVA/CA film with 2 % curcumin film was chosen to carry out further survey.

Fourier Transform Infrared spectroscopy

From Figure 4, it can be seen that the FT-IR spectrum of the CS/PVA/CA film shows that PVA occurs at 3400 and 2947 cm^{-1} , corresponding to the stretching oscillation of the -OH group. The wide signal range at about 3210 cm^{-1} - 3450 cm^{-1} is the stretching vibration of the overlapping -OH and N-H groups, the C=O group of CA and the N-H group of CS have the same cis structure coincide, so the stretching oscillation of N-H at 3245 cm^{-1} . Also due to its cis structure, there is no signal of the coplanar bending oscillation of N-H at 1540 cm^{-1} . The absorption peak at the wavenumber of at 2921 cm^{-1} characterizes the stretching vibration of the C-H group on the alkyl group. Moreover, CS showed the absorption band in the range of 1630 cm^{-1} , 1547 cm^{-1} và 1329 cm^{-1} corresponding to the characteristic for prolonged vibration of amide I, II, III. The absorption peak at the wavenumber of 1401 cm^{-1} is the scissor vibration of -CH₂ group, at 1261 cm^{-1} and 1020 cm^{-1} is the asymmetric stretching vibration of C-O-C. At the peak of 1071 cm^{-1} is the asymmetric stretching oscillation of C-C-O. Absorption peaks at 645 cm^{-1} and 589 cm^{-1} oscillate due to C on the ring [8-9].

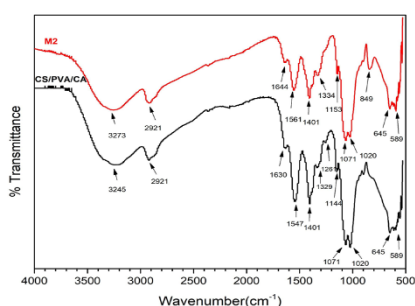


Figure 4. FTIR results of CS/PVA/CA and M2 films

In the M2 film, when Curcumin was added on the CS/PVA film with the addition of CA crosslinking agent, the FTIR results showed that in addition to the typical stitches on the CS/PVA/CA film, the FTIR results also showed absorption spectral peaks characteristic of Curcumin as shown in figure 4. For Cur, the characteristic FTIR pattern showed at the wavenumber of 1280 cm^{-1} due to the C-O stretching vibration of the benzene ring. The absorption peak at wave number 3273 cm^{-1} is the oscillation of the -OH group on the benzene ring

and the hydroxyl group near the C=O group. Besides, the interaction of C-O group in Curcumin and NH in CS causes the number of N-H group waves to shift from 1547 cm^{-1} to 1561 cm^{-1} . We see that the oscillation at wavenumber 1329 cm^{-1} shifts to 1334 cm^{-1} and the stronger signal is the oscillation of the stretched C-N group of amide III and the symmetric bending deformation of the CH₃ group in the superimposed Curcumin on top of other. The C-O group of Curcumin interacts with the O-H group of CS, so the oscillation of the C-O group shifts from 1144 cm^{-1} to 1153 cm^{-1} . There is also an additional oscillation at 849 cm^{-1} which is the shaking oscillation of CH₃. The absorption peak at 1401 cm^{-1} is the scissor oscillation of the CH₂ group superimposed with the asymmetric bending vibration of the CH₃ group, so the signal tip is more bulbous. At 1644 cm^{-1} is the stretching vibration of the C=O bond. In addition, there are points of Curcumin whose signal sequence coincides with the films, so they overlap. It was found that the oscillation tips in the M2 film did not differ much from that of the CS/PVA/CA film, possibly due to the insufficient amount of Curcumin added to the membrane and because during the crosslinking process to form a complete film, for the network circuit of the film to be more tightly arranged, leading to the displacement of the oscillating tips on the film shown in Figure 4.

Ultraviolet-visible spectroscopy

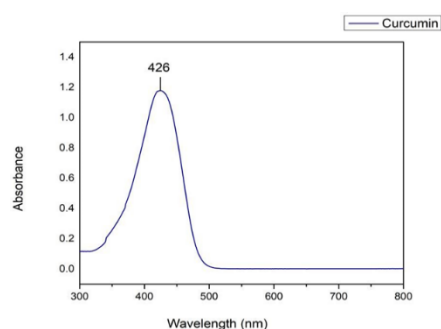


Figure 5. UV-Vis spectrum of Curcumin in M2 film structure

To determine the maximum absorption wavelength, UV-Vis spectroscopy of curcumin solution was analyzed in the range from 300 nm to 800 nm. In Figure 5, the results show the absorbance of curcumin at $\lambda_{\text{max}} = 425 \text{ nm}$ [1] [5]. Different maximum absorption wavelengths have been observed in different solvents (408 nm in carbon tetrachloride and 430 nm in DMSO). On average, the maximum wavelength was found at

418 nm. The maximum absorbance of curcumin in methanol and ethanol is about 420 nm [6]. In recent studies, it has been found that changing the solvent has only a small effect on the absorption spectrum of curcumin. UV-Vis spectra of curcumin in toluene were observed with only a small shift in comparison with the solvents of acetonitrile and ethanol [2]. The UV-Vis spectrum of curcumin in Figure 5 has $\lambda_{\max} = 426$ nm, which proves that M2 film sample contains curcumin.

Scanning Electron Microscope

In order to evaluate the morphology and surface structure of CS/PVA/CA and M2 films, SEM analysis was conducted. SEM images in Figures 6A and 6B show that the surface of CS/PVA/CA and M2 films is quite uniform, the particles are arranged on the surface with a certain order. It is inferred that curcumin molecules are dispersed uniformly in the matrix structure of the film. Curcumin molecules are evenly dispersed on the CS/PVA matrix. While relatively uniform morphologies are observed on the surfaces of CS/PVA/CA film and M2 film (Figures 6A and 6B), SEM image at high magnification of M2 film (Figure 6C) shows some molecular clusters on the film structure.

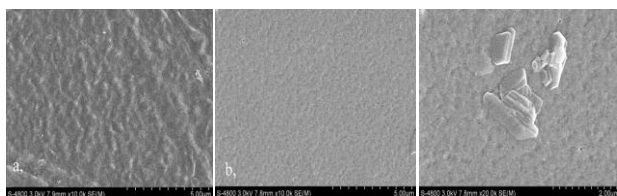


Figure 6. SEM image of CS/PVA/CA (a) and M2 (b) films at 10000x magnification. (c) SEM image of the M2 film at 20000x magnification

Antibacterial testing results

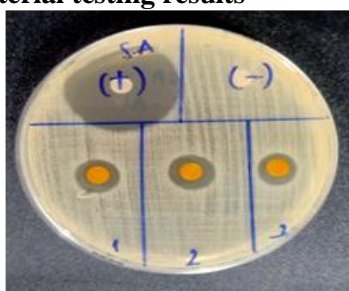


Figure 7. Antibacterial results of CS/PVA/CA (1), M2 (2), CS/PVA/CA/Curcumin films prepared by dip coating method

The antibacterial ability of the films was evaluated by diffusion method through agar spread with bacteria. For Figure 7, it was observed that all film samples showed

antibacterial rings, indicating that the film is resistant to S.A. bacteria. This demonstrates that the Curcumin on the membrane surface is capable of protecting wounds from bacterial attack, which is one of the positive conditions for wound healing.

CONCLUSION

From the analytical results (photography, FTIR, UV-Vis and tensile testing), the CS/PVA blend films incorporated with crosslinking agent (CA) and natural curcumin were successfully prepared using the solution casting procedure. With the addition of crosslinking CA, mechanical properties of the film are greatly improved in comparison with original CS/PVA film. In addition, the CS/PVA/CA film containing curcumin has tensile properties that are comparable with those of CS/PVA/CA films. Regarding analysis of SEM imaging, the surface morphology of the film is quite uniform, suggesting the compatibility of chemical components in the blend films. Antimicrobial activity of CS/PVA/CA films with the presence of 2 % curcumin is effective against the gram-negative bacteria of Escherichia Coli. The properties of CS/PVA/CA/curcumin blend films have been investigated and evaluated for wound dressing application.

Acknowledgment

The authors would like to express gratitude to University of Science – VNUHCM for the funding of grant number T2023-63.

References

- [1] G. M. P. D. S. Tripathi, *Physicochemical and bioactivity of cross-linked chitosan–PVA film for food*, International Journal of Biological Macromolecules **45** (2009) 372-376.
- [2] A. K. a. A. Karimi, *Mechanical properties of PVA material for tissue engineering applications*, Advanced Performance Materials (2013) 90-100.
- [3] P. S. S. M. K. Soni Himesh, *Quantitative and quantitative profile of Curcumin from ethanolic extract of Curcumin longa*, International Research Journal of Pharmacy **2** (2011) 180-184.
- [4] V. V. P. and E. S. Selvaraj Dhivya, *Wound dressings - a review*, BioMedicine **5** (2015) 24-28.

- [5] M. I. H. U. a. M. A. S.A. Mirmohammadi, *Hybrid organic-inorganic nanocomposites based on poly(epsilon-caprolactone)/polyhedral oligomeric silsesquioxane: Synthesis and in vitro evaluations*, International Journal of Polymeric Materials and Polymeric Biomaterials **63** (2014) 6.
- [6] H. M. S. A. N. Badreldin H. Alia, *Some Biological Properties of Curcumin: A Review*, Natural Product Communications 1 (2006) 509-521.
- [7] R. Ciriminna, F. Meneguzzo, R. Delisi & M. Pagliaro, *Citric acid: emerging applications of key biotechnology industrial product*, BMC chemistry **11** (2017) 22.
- [8] Mohan, P.R.K., et al., *Water soluble complexes of Curcumin with cyclodextrins: Characterization by FT-Raman spectroscopy*, Vibrational Spectroscopy **62** (2012) 77-84.
- [9] P. R. Krishna Mohan, G. S., C. V. Muraleedharan, Roy Joseph, *Water soluble complexes of curcumin with cyclodextrins: Characterization by FT-Raman spectroscopy*, Vibrational Spectroscopy **62** (2012) 77-84.
- [10] H. Wu, Y. Lei J. Lu , R. Zhu , D. Xiao, C. Jiao & M. Li, *Effect of citric acid induced crosslinking on the structure and properties of potato starch/chitosan composite films*, Food Hydrocolloids **97** (2019) 105-208.

POROUS SILICA-COATED GOLD NANOPARTICLES CONJUGATE-BASED LATERAL FLOW IMMUNOASSAY (LFIA) FOR RAPID DETECTION OF *E. COLI*

Nguyen T.T Huyen^{1,2}, Thu Thao Pham¹ and Truong TN Lien^{1*}

¹Convergence Technology Division, Vietnam-Korea Institute of Science and Technology
Hoa Lac High-tech Park, Km29 Thang Long Boulevard, Hanoi 100000, Vietnam

²Hanoi University of Science and Technology, Dai Co Viet Street, Hanoi, Vietnam

*Email: ttlien@most.gov.vn

ABSTRACT

E. coli (*Escherichia coli*) is a common type of bacteria found in the gut of humans and animals. However, some strains of *E. coli* can cause serious infectious diseases, especially when they are present in food and water. The causing illness strains of *E. coli* usually produce symptoms such as diarrhea, nausea, abdominal pain, and fever. In more severe cases, they can cause kidney inflammation, sepsis, and other health problems. Foodborne illness has emphasized developing a rapid diagnostic device for effective treatment and mitigation. Lateral flow immunoassay (LFIA) is a class of diagnostic devices that provides quick results, easy to handle, low cost, and is on-site applicable. Here, we describe an antibody (Ab)-labeled porous silica-coated gold nanoparticles (Au@p-SiO₂)-based LFIA for detecting *E. coli*. The intrinsic properties of silica, such as optical transparency, high biocompatibility, colloidal stability, controllable porosity, and accessible surface modification, provide silica materials with numerous potentials in biomedicine. Therefore, coating Au nanoparticles with silica typically enhances the crucial applications of metal nanoparticles in biomedicine. *E. coli* Ab was conjugated with the AuNPs, which served as a detecting probe. The fabricated LFIA strip was optimized for parameters such as membrane pore size, blocking conditions, Ab coating concentration, and conjugate incubation. The optimized LFIA strips were validated in spiked buffer samples, and the optimal detection limit was 10² CFU/ml. The fabricated LFIAs are reported to have storage stability at 4°C and room temperature (RT). Hence, the developed LFIA can be used as a portable, cost-effective diagnostic device to detect *E. coli* rapidly.

Keywords: Au@pSiO₂, lateral flow immunochromatographic, *E. coli*

INTRODUCTION

Escherichia coli, one of the acute foodborne pathogens, can contaminate multiple foods and may cause intussusception [1] or diarrhea-related hemolytic uremic syndromes imbalances [2]. Infection with *E. coli* has caused many outbreaks and foodborne accidents worldwide, especially in developing countries with limited food monitoring and control systems. Therefore, controlling and ensuring food safety is crucial in preventing the spread of *E. coli* and other infectious diseases. Quick and reliable testing methods are immediately needed to mitigate foodborne pathogens [3]. The conventional phenotype-based technique regarded as the gold standard for detecting bacteria detection is culturing [4,5]. In addition, other genotype-based methods have been developed recently, including PCR amplified, which are rapid and highly sensitive [6]. However, these methods are time-

consuming, require skilled labor, and are not feasible for on-site detection to rapidly screen bacterial-infected patients [7,8]. Lateral Flow Immunoassay (LFIA) tests have been considered biosensors used for rapid, on-site, and cost-effective detection [9,10]. LFIA devices are more convenient for deployment outside healthcare facilities, particularly in developing countries, for mass screening programs [11,12]. LFIA is particularly attractive in countries with limited laboratory infrastructure and trained personnel. It has advantages over conventional gold-standard techniques as they can be portable, easy to fabricate, and do not require any skilled labor [13].

In recent years, the development of nanomaterials synthesis protocols and characterization has revolutionized the generation of beneficially functional metal nanoparticles, contributing to the variety of

applications in biomedical fields. Among the nanomaterials of interest, porous silica-coated gold nanoparticles (Au@pSiO₂) have been characterized as one of the most favorable candidates for biomedicine, providing an ideal platform to invest more research efforts for delivering different strategies for accurate signal detection [14-16]. The highly developed synthetic methods for silica can ensure the preparation of the Au@pSiO₂ with precise adjustable size, morphology, pore structure, and surface modifications. From the perspective of applications, the high porosity of the Au@pSiO₂ enables a much higher loading capacity for molecules such as small drugs, nucleic acids, and proteins. These molecules can be released in appropriate environments [17].

Therefore, we reported an Au@pSiO₂-based (LFIA) to detect *E.coli*. Antibodies (Ab)-labeled Au@pSiO₂ were immobilized on the conjugate pad for colorimetric detection. Further, anti-*E.coli* Ab and anti-IgG secondary Ab were fixed on the nitrocellulose (NC) membrane as test and control lines, respectively, to determine the presence of *E.coli* in the sample. The optimized LFIA strips were validated in spiked buffer samples, and the optimal detection limit was 10² CFU/ml.

EXPERIMENTAL

Materials

Chloroauric acid tetrahydrate (HAuCl₄.4H₂O), trisodium citrate dehydrate, cetyltrimethylammonium bromide (CTAB), tetra-ethyl orthosilicate (TEOS), sodium hydroxide (NaOH), tri-sodium citrate (Na₃C₆H₅O₇), ammonium hydroxide (NH₄OH.H₂O), hydrochloric acid (HCl), (3-Aminopropyl) triethoxysilan (APTEST), fomaldehit, TRIS Hydrochloride (Tris HCl), HEPES, MES, 4-Mercaptosuccinic acid, ethanol, distilled water was used in experiment.

Synthesis of Au@pSiO₂

A triple-neck round bottom flask was filled with 24 mL de-ion (DI) water, 0.6 mL NaOH 0.5 M, and 0.05g CTAB. The solution was stirred and heated 80°C for 15 minutes. Then, 1 mL of 3.7 wt% formaldehyde solution and HAuCl₄ 0.05 M was added. The mixture was stirred for another 10 min. After that, TEOS was added. The solution was stirred for 1 hour. The precipitation was collected by centrifugation and scattered in 80 mL ethanol. Then, hydrochloric acid was added to regulate the pH value of the solution to

less than 1. The solution was sonicated for 30 min and stirred overnight. The final product of Au@pSiO₂ was collected after washing with distilled water.

Synthesis of Au@p-SiO₂-NH₂

To achieve amino-functionalization of silica-coated gold nanoparticles (i.e., Au@pSiO₂-NH₂), 3.4 mg of 3-aminopropyl trimethoxysilane (APTES) were added to the 10 mL ethanol solution. Then, the obtained dispersion was stirred for 4 h. The resultant nanoparticles were washed three times with DI water. Finally, the obtained material was designated as nanoparticles Au@pSiO₂-NH₂.

Characterization of nanoparticles

Transmission electron microscopy (TEM) images were recorded using a JEM-2011F microscope (JEOL, Japan) operated at 200 kV. The samples for TEM measurements were dispersed in DI water and then dipped and dried on holey carbon films supported on a Cu grid. The UV-vis spectra were collected using a V-770 spectrophotometer (Jaco, Japan). The materials' point of zero charge (PZC) was determined with a Zetasizer Nanoseries ZS instrument (Anton Paar).

Antibody conjugation with Au@pSiO₂-NH₂

In brief, 100 µL anti-*E.coli* antibodies were activated using a 50 µL EDC/sulfo-NHS mixture (4 mg EDC and 4 mg sulfo-NHS) for 15 mins in PBS buffer pH 7.4. Then, 1 ml of Au@pSiO₂-NH₂ was added. After reacting for 1 hour at room temperature, 10% BSA was added to the solution and incubated for 30 min to block nonspecific sites on the nanoparticles.

Fabrication of lateral flow test strips

Anti-*E.coli* Ab and anti-IgG secondary Ab were diluted with PBS buffer to a concentration of 1 mg/mL, which was then dispensed on NC membrane as the control line and test line and incubated at 37°C for 2 h to immobilize the antibodies. The Au@pSiO₂-NH₂-anti-*E.coli* Ab conjugates were sprayed on the conjugate pad, and the sample pad was soaked in the treating buffer for half an hour and dried in an oven for 2h. Then, these elements were consecutively mounted on a PVC adhesive backing pad with a 2 mm overlap between each adjacent pad. The assembled pads were cut into strips (3 mm) by a Rapid Test Cutter.

RESULT AND DISCUSSION

The principle of the improved LFIA is based on an on-strip sandwich Ag–Ab reaction and the protocol is illustrated in Figure 1. In the presence of target *E.coli*, the target would bind to the Au@pSiO₂-NH₂-Ab, forming Au@SiO₂-NH₂-Ab - target complexes, which would, in turn, interact with the immobilized Ab at the test line to produce a color signal detectable by the naked eye. The excess Au@pSiO₂-NH₂-Ab complexes would bind to the immobilized anti-IgG secondary Ab at the control line. The developed test line intensity was further analyzed by the Color Grab application.

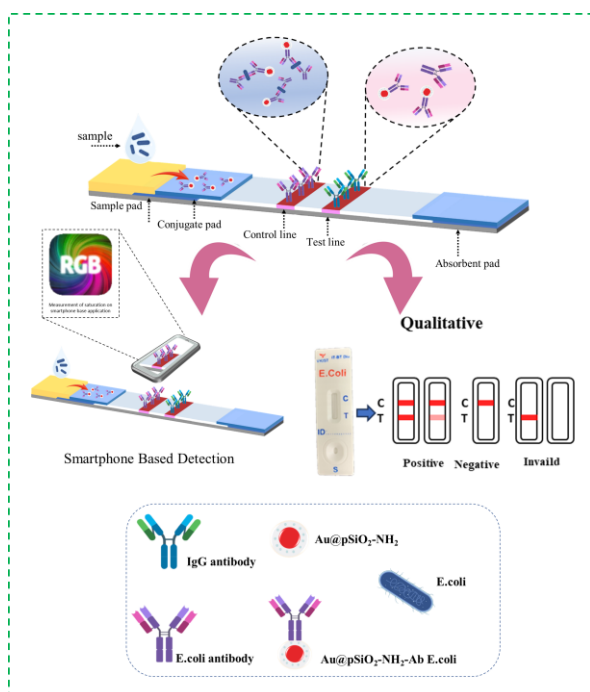


Figure 1. Fabricated Lateral flow immunoassay device for *E.coli* detection and a method for quantifying *E.coli* concentration.

Characterization of Au@pSiO₂, antibody conjugation

Au@pSiO₂, Au@pSiO₂-NH₂, and Au@pSiO₂-NH₂-Ab *E.coli* were characterized by dynamic light scattering (DLS), zeta potential, ultraviolet-visible (UV-Vis) spectrophotometry, transmission electron microscopy (TEM), scanning electron microscopy (SEM). The SEM images could confirm the monodisperse spherical morphology of the Au@pSiO₂ and Au@pSiO₂-NH₂. SEM images showed that there was a single gold nanoparticle as a core with a uniform size of ~25 nm and radial silica as a shell. The gold core was obtained by reducing chloroauric acid with sodium citrate [18]. CTAB was used as a

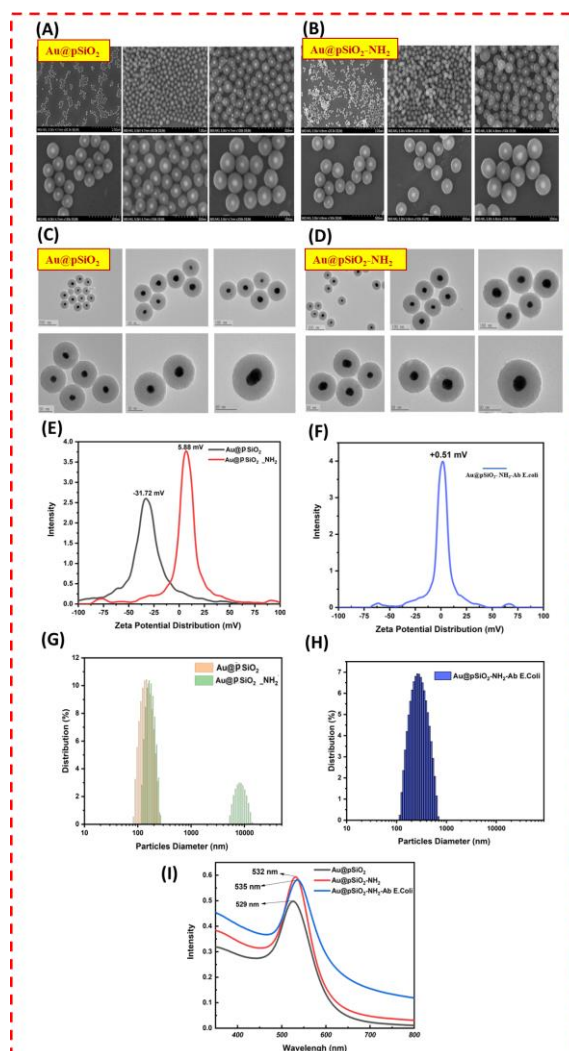


Figure 2. SEM image (A, B), TEM image (C, D), Zeta potential (E), DLS (G) of Au@pSiO₂ and Au@pSiO₂-NH₂, respectively. Zeta potential (F), DLS (H) of Au@pSiO₂-NH₂-Ab, and UV-vis spectra of Au@pSiO₂, Au@pSiO₂-NH₂ and Au@pSiO₂-NH₂-Ab.

templating agent, and TEOS was hydrolyzed under alkaline conditions to obtain monodisperse Au@pSiO₂ with controllable particle size [19]. The average sizes determined from SEM analysis of Au@pSiO₂ and Au@pSiO₂-NH₂ were 80 ± 20 nm and 90 ± 20 nm, respectively (Figure 2A, B). TEM image showed the surface of Au@SiO₂ and Au@pSiO₂-NH₂ was relatively clean, indicating the existence of porous in the silica shells after the removal of CTAB templates (Figure 2C), and a thin proteinaceous layer was observed around the Au@pSiO₂, confirming the layering of NH₂ group around Au@SiO₂ (Figure 2D). Further, zeta potential and DLS were performed to study the surface charge and hydrodynamic diameter of the synthesized Au@pSiO₂ and Au@pSiO₂-NH₂

before and after conjugation with Ab. Surface functionalization of Au@pSiO₂ particles by amine group, zeta potential gave positive value, zeta potential shifted from -31.72 to +6.88 mV (Figure 2E). After binding the antibody, the zeta potential changed to +0.5 mV (Figure 2F), indicating the overall reduction in the negative charge of the AuNPs due to the deposition of positively charged Ab. Furthermore, Au@pSiO₂-NH₂-Ab was uncharged at that potential, and no false positive occurred. The DLS analysis data revealed that the Au@pSiO₂, Au@pSiO₂NH₂, and Au@pSiO₂-NH₂-Ab average sizes were 267 nm, 277 nm, and 279 nm, respectively (Figure 2G, H). UV-Vis spectra of both Au@pSiO₂, Au@pSiO₂-NH₂, and Au@pSiO₂-NH₂-Ab were determined in the 400–800 nm range. The redshift of 6 nm was observed in the spectra of Au@pSiO₂ conjugated with Ab (Au@pSiO₂-NH₂-Ab) for Au@pSiO₂ (532 nm to 539 nm, as shown in Figure 2I).

Optimization of LFIA

LFIA strips are an assembly of different components with different characteristic properties. These components and parameters vary according to the object and method of detection. The pore size of the nitrocellulose membranes, blocking of a sample pad, antibody conjugation, and running buffer were optimized. The pore size of the nitrocellulose membrane is an essential factor for the attachment of antibodies and is directly responsible for signal generation via capillary action. Nitrocellulose membranes of different pore sizes (5, 8, 10, 12, and 15 μm) were utilized to prepare the LFIA, and 15 μm showed an intense signal when compared (Figure 3A). To obtain stable running buffers, different buffer types (borate pH 8.0, borate pH 9.0, PBS pH 7.4, PBS pH 6.0, and HBS pH 7.4) were validated for the survey (Figure 3B). It was observed that the HBS running buffer was selected as the optimal buffer running on the nitrocellulose membrane. Determination of an efficient blocking agent for the NC membrane is crucial to minimize the negative interaction that may result from the variations such as pH and composition of antibodies. Therefore, different blocking agents, such as 1% ethanolamine (A), 1% BSA (B), 2% BSA (C), 3% BSA (D), and 4% BSA (E), were used to determine the best-blocking agent. When using blocking buffers from A to C, testing with a negative sample caused the test strip signal to appear on both the control and test lines. This results in false positive

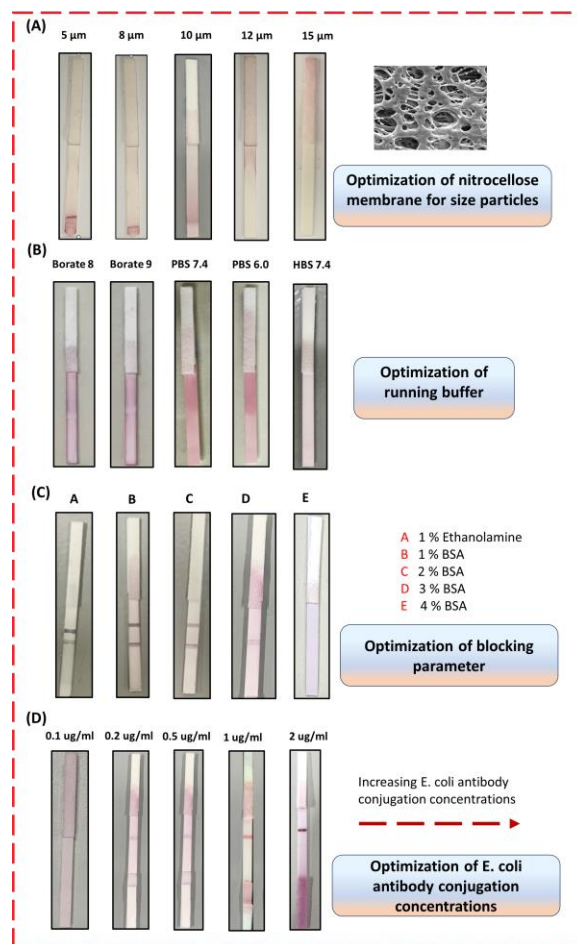


Figure 3. Optimization of different parameters for developing LFIA strips for E.coli detection. (A) Optimization of pore size of nitrocellulose membrane. (B) Optimization of running buffers (C) Optimization of blocking parameters (D) Optimization of capture antibody concentration at the test line of the LFIA strip.

signals that compromise the accuracy and sensitivity of the analysis process. A high BSA concentration (4%) causes signal loss on the nitrocellulose membrane. However, when using a blocking buffer with 3% BSA, it is observed that it did not result in false positive phenomena and yielded high signal detection. Finally, different concentrations of E.coli antibody (0.10, 0.20, 0.50, 1.00, and 2.00 mg/ml) were used to coat the test line on the NC membrane. It was observed that as the concentration of E.coli Ab increased, the intensity of the test line band also increased. Therefore, 1 mg/ml Ab was standardized as the ideal coating concentration for LFIA development with maximum binding efficiency (Figure 3D).

Testing of LFIA strips

Various steps involved in the sample acquisition and testing are depicted in Figure 4A.

The clinical samples were diluted in a Tris pH 10.8 buffer before addition to the strip for testing to ensure the easy and even flow of the sample. The LFIA test was interpreted by observing the formation of red color dot/s on the NC membrane. The test strip activity was evaluated on negative control samples and clinical samples. Observation of the negative control samples (where only the running buffer was dropped on the membrane) showed that all the test strips displayed a single dot on the control line (Figure 4B). This indicates that the test strips functioned normally and no-false positive resulted. For the detection of *E. coli*, the lowest detectable LFIA strip was 10^2 CFU/mL (Figure 4C). The visual LOD or sensitivity of the LFIA strip to *E. coli* was comparable with the previous studies [20,21].

Further, as the concentration of *E. coli* bacteria increased, the red dot signal on the test strip became stronger. This can be explained by the fact that as more *E. coli* bacteria were transported to the test strip, more specific binding occurred through the sandwich immunoassay. The developed lateral flow assay (LFA) strip showed specificity for *E. coli*. The assay's specificity was investigated concerning other bacteria such as gram's negative (*Pseudomonas*, *Klebsiella*), the most common bacterial contamination in food samples. Cross-reactivity studies using a developed LFA strip showed an obvious ruby red line on C and T lines for the *E. coli* sample tested and no band appeared on the T line for negative control (lysis buffer). No dot appeared on the T line for *Pseudomonas* and *Klebsiella* samples tested. These showed no cross-reactivity in the developed LFA strip when tested with *Enterobacteriae sp.* and *Pseudomonadaceae sp.* (Figure 4D). Besides, all test strips could produce results within 15-20 min, which can be considered rapid tests comparable to the previous studies [22].

Testing and analysis of the color intensity of the developed LFIA

To evaluate the performance of the manufactured LFIA (Lateral Flow Immunoassay) strips, a series of dilutions ranging from 10^2 CFU/ml to 10^6 CFU/ml of *E. coli* were tested. It was observed that the visual strength of the test line decreased as the concentration of *E. coli* decreased. Compared to the negative control, a visible test line was observed at 10^2 CFU/ml and higher (Figure 4C), which was considered the visual Limit of Detection (LOD). Furthermore,

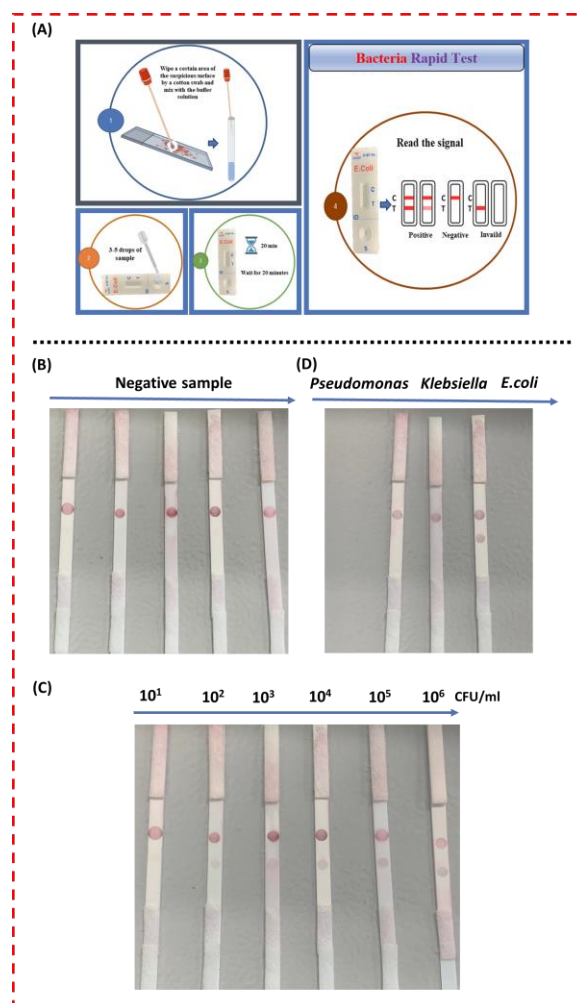


Figure 4. Analytical test of LFIA strips. (A) The steps in using a rapid test strip. (B) Image negative sample test. (C) Images of LFIA strips for *E. coli* dilutions (10^2 CFU/ml - 10^6 CFU/ml). (D) Specificity of test strips.

the color saturation at the test line was analyzed using a smartphone-based application. Color saturation refers to the intensity of color in an image, where higher saturation indicates purer and more vivid colors, while lower saturation indicates washed-out or pale colors. Smartphone-based detection offers several advantages, such as portability, applicability in the field, and cost-effective diagnosis. These characteristics make it an ideal approach for point-of-care applications. The relationship between color saturation and the concentration of *E. coli* was found to be linear, as depicted in Figure 5A. This phenomenon can be explained as follows: When the concentration of *E. coli* is high, there is a more significant interaction between *E. coli* and the anti-*E. coli* antibodies on the test strip. The test strip is designed to capture and form complexes between the antibodies and *E. coli* bacteria. As the

concentration of *E. coli* increases, more antigen-antibody complexes are formed on the test strip, resulting in a more pronounced display of the red color. This is because the quantity of these complexes is directly proportional to the concentration of *E. coli*.

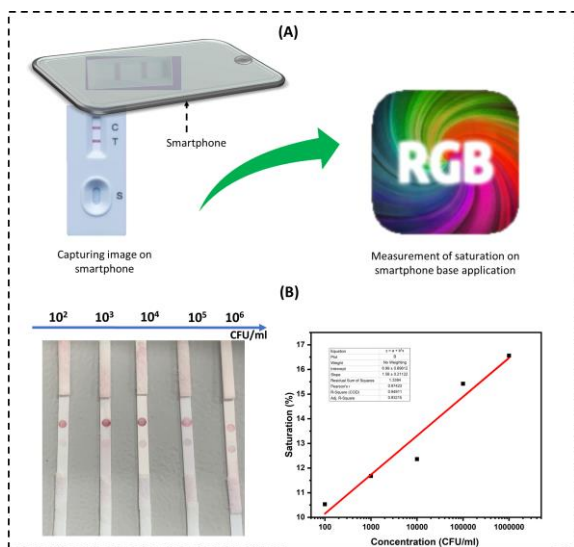


Figure 5. Analytical test of LFIA strips. (A) Illustration of smartphone-based analysis using colorimeter application to measure color saturation values. (B) Color saturation graph obtained by the scanner of the smartphone-based application.

Therefore, comparing the intensity of color at the specific location on the test strip provides a simple and rapid method for quantifying *E. coli* bacteria. By measuring the color intensity, we can estimate the concentration of *E. coli* straightforwardly and efficiently.

CONCLUSIONS

This study reported the development of LFIA based on porous silica-coated gold nanoparticles conjugate to detect *E. coli* quickly. We successfully synthesized uniform porous silica-coated gold nanoparticles. With several analytical tools, we have obtained the monodispersed Au@pSiO₂ with a size of about 80 nm, with high porosity and colloidal stability in aqueous solutions. Anti-*E. coli* antibody was also successfully conjugated with Au@pSiO₂ at pH 9.2. LFIA strip has high specificity, which only detected *E. coli* but not other cross-related bacteria. The visual LOD of this disposable LFIA strip was obtained to be 10² CFU/ml. The method is rapid, on-site, simple, user-friendly, and specific without special equipment. The

technique potentially has many practical applications, especially for screening purposes.

Acknowledgment

All authors are grateful for the financial support from Vingroup Innovation Foundation (granted No.VINIF.2022.DA00032).

References

- [1] P. I. Cha, B. Gurland, and J. D. Forrester, "First reported case of intussusception caused by Escherichia coli O157: H7 in an adult: literature review and case report," *Surg Infect (Larchmt)*, vol. 20, no. 1, pp. 95–99, 2019.
- [2] E. Kintz, L. Byrne, C. Jenkins, N. McCarthy, R. Vivancos, and P. Hunter, "Outbreaks of Shiga toxin-producing Escherichia coli linked to sprouted seeds, salad, and leafy greens: a systematic review," *J Food Prot*, vol. 82, no. 11, pp. 1950–1958, 2019.
- [3] D. Shahdeo, N. Chauhan, A. Majumdar, A. Ghosh, and S. Gandhi, "Graphene-based field-effect transistor for ultrasensitive immunosensing of SARS-CoV-2 spike S1 antigen," *ACS Appl Bio Mater*, vol. 5, no. 7, pp. 3563–3572, 2022.
- [4] M. H. Legese, G. M. Weldearegay, and D. Asrat, "Extended-spectrum beta-lactamase- and carbapenemase-producing Enterobacteriaceae among Ethiopian children," *Infect Drug Resist*, pp. 27–34, 2017.
- [5] S. Singh, P. Mishra, I. Banga, A. S. Parmar, P. P. Tripathi, and S. Gandhi, "Chemiluminescence based immunoassay for the detection of heroin and its metabolites," *Bioimpacts*, vol. 8, no. 1, p. 53, 2018.
- [6] J. Pu *et al.*, "Vanadium metal-organic framework-derived multifunctional fibers for asymmetric supercapacitor, piezoresistive sensor, and electrochemical water splitting," *SmartMat*, vol. 3, no. 4, pp. 608–618, 2022.
- [7] A. Roberts, S. Mahari, and S. Gandhi, "Biological/synthetic receptors (antibody, enzyme, and aptamer) used for biosensors development for virus detection," in *Advanced Biosensors for Virus Detection*, Elsevier, 2022, pp. 113–131.
- [8] A. Kaushik, R. Khan, P. Solanki, S. Gandhi, H. Gohel, and Y. K. Mishra, "From nanosystems to a biosensing prototype for an efficient diagnostic: A special issue in honor of professor Banshi D. Malhotra," *Biosensors*, vol. 11, no. 10. MDPI, p. 359, 2021.

- [9] R. Charlermroj, M. Makornwattana, S. Phuengwas, and N. Karoonuthaisiri, "A rapid colorimetric lateral flow test strip for detection of live Salmonella Enteritidis using whole phage as a specific binder," *Front Microbiol*, vol. 13, p. 1008817, 2022.
- [10] D. Yu *et al.*, "Rapid and visual detection of specific bacteria for saliva and vaginal fluid identification with the lateral flow dipstick strategy," *Int J Legal Med*, pp. 1–11, 2023.
- [11] P. Mishra *et al.*, "An immunochromatographic dipstick as an alternate for monitoring of heroin metabolites in urine samples," *RSC Adv*, vol. 8, no. 41, pp. 23163–23170, 2018.
- [12] W.-Y. Hsieh *et al.*, "Development and efficacy of lateral flow point-of-care testing devices for rapid and mass COVID-19 diagnosis by the detections of SARS-CoV-2 antigen and anti-SARS-CoV-2 antibodies," *Diagnostics*, vol. 11, no. 10, p. 1760, 2021.
- [13] A. V Orlov, J. A. Malkerov, D. O. Novichikhin, S. L. Znoyko, and P. I. Nikitin, "Express high-sensitive detection of ochratoxin A in food by a lateral flow immunoassay based on magnetic biolabels," *Food Chem*, vol. 383, p. 132427, 2022.
- [14] F. da S. Bruckmann, F. B. Nunes, T. da R. Salles, C. Franco, F. C. Cadoná, and C. R. Bohn Rhoden, "Biological applications of silica-based nanoparticles," *Magnetochemistry*, vol. 8, no. 10, p. 131, 2022.
- [15] H. Yu *et al.*, "Antibody-conjugated silica-coated gold nanoparticles in targeted therapy of cervical cancer," *Am J Transl Res*, vol. 14, no. 3, p. 1518, 2022.
- [16] C. Trayford *et al.*, "Mesoporous Silica-Coated Gold Nanoparticles for Multimodal Imaging and Reactive Oxygen Species Sensing of Stem Cells," *ACS Appl Nano Mater*, vol. 5, no. 3, pp. 3237–3251, 2022.
- [17] K.-C. Kao and C.-Y. Mou, "Pore-expanded mesoporous silica nanoparticles with alkanes/ethanol as pore expanding agent," *Microporous and mesoporous materials*, vol. 169, pp. 7–15, 2013.
- [18] D.-B. Grys *et al.*, "Citrate coordination and bridging of gold nanoparticles: The role of gold adatoms in AuNP aging," *ACS Nano*, vol. 14, no. 7, pp. 8689–8696, 2020.
- [19] M. Lv *et al.*, "One-pot synthesis of stable Pd@ mSiO₂ core-shell nanospheres with controlled pore structure and their application to the hydrogenation reaction," *Dalton Transactions*, vol. 48, no. 20, pp. 7015–7024, 2019.
- [20] Y. M. Lukman, Z. N. Dyana, N. Rahmah, and A. R. Khairunisak, "Development and evaluation of colloidal gold lateral flow immunoassays for detection of Escherichia coli O157 and Salmonella typhi," in *Journal of Physics: Conference Series*, IOP Publishing, 2018, p. 012049.
- [21] M. S. Suria, A. T. Mohd Afendy, M. Noor Azlina, and I. Zamri, "Lateral flow assay strip for detection of Escherichia coli O157: H7.," *Int Food Res J*, vol. 22, no. 6, 2015.
- [22] Y. Ren *et al.*, "An aptamer-exonuclease III (Exo III)-assisted amplification-based lateral flow assay for sensitive detection of Escherichia coli O157: H7 in milk," *J Dairy Sci*, vol. 104, no. 8, pp. 8517–8529, 2021.

MICROWAVE ABSORPTION PROPERTIES OF NiFe₂O₄ POWDER SYNTHESIZED BY OXALATE-ASSISTED HYDROTHERMAL METHOD

Tran Quang Dat¹, Tran Tuan Vu¹, Pham Xuan Quang¹, Nguyen Nguyen Long¹, Ngo Ngoc Huynh¹, Vu Tuan Anh¹, Nguyen Thi Thanh¹, Le Dinh Vi¹, Nguyen Van Tuan¹ and Pham Van Thin¹

¹ Faculty of Physical and Chemical Engineering, Le Quy Don Technical University

Email: dattq@lqdtu.edu.vn

ABSTRACT

Nickel ferrite was synthesised using hydrothermal methods that utilised oxalic acid as a precipitant. The structural, microstructural, magnetic, and microwave absorption properties were examined using a number of different characterisation methods. The structure of NiFe₂O₄ was a wood-like morphology with spherical nanoparticles (40 nm). At 10 kOe, the NiFe₂O₄ powder exhibited ferromagnetic behaviour with a magnetization of 32 emu/g. The NiFe₂O₄ material provides a synergistic effect between magnetic and dielectric loss for the efficient dissipation of wave energy across a broad frequency range. Maximum reflection loss was -58.2 dB at 14.7 GHz for a 30% of weight, 2.0 mm thick sample. With only 2.5 mm of thickness, an effective absorption bandwidth of up to 14.1 GHz was achieved. The prepared NiFe₂O₄ ferrite can serve as an electromagnetic wave-absorbing material with high absorption, a broad frequency range, low cost, and simple fabrication.

Keywords: Oxalate, NiFe₂O₄, ferrite, hydrothermal, microwave absorption.

INTRODUCTION

The recent development of modern communication has led to the widespread utilization of electromagnetic (EM) wave technologies in various sectors, both civilian and military. These technologies encompass personal mobile phones, radio and television, wireless telecommunications equipment, and radar [1]. The detrimental effects of electromagnetic pollution have resulted in the impairment of electrical devices and posed a threat to human well-being. In order to surmount these challenges, significant endeavors are currently underway to develop materials that possess the ability to absorb microwaves [2]. The ferrite materials, specifically MFe₂O₄ where M represents Ni, Zn, Mn, and Co, possess a spinel cubic structure that has achieved significant interest as a potential microwave absorber. This is primarily due to their notable characteristics such as high saturation magnetization, environmentally friendly nature, exceptional chemical stability, and affordability [1]. Various essential strategies, such as the regulation of morphology and the combination with other microwave absorbers, have been extensively employed to enhance the microwave absorption performance of MFe₂O₄. The MFe₂O₄ has the ability to adopt various morphologies such as

flower-like structures, nanoribbons, nanosheets, and column-like structures with a wood-like texture [3-5]. This is primarily attributed to the characteristics of nickel ion precursors. The absorption performance can be influenced by the morphology, as it has the ability to adjust the path of electromagnetic wave propagation and induce multiple scattering within the absorbers.

The wood-like NiFe₂O₄ powders were prepared in this study through the utilization of the oxalate-assisted hydrothermal method. Extensive investigations were carried out to examine the absorption properties of the composite material across the frequency range spanning from 2 to 18 GHz. The distinctive characteristics of the composite material result in a significant enhancement of its microwave absorption capabilities.

EXPERIMENTAL

First, 2 mmol Ni(NO₃)₂·6H₂O and 4 mmol Fe(NO₃)₃·9H₂O were dissolved in an 80 mL solution of ethylene glycol and deionized water (1:3 vol ratio) under magnetic stirring (solution A). Additionally, 40 mmol of H₂C₂O₄·2H₂O was dissolved in 20 mL of water (solution B). Solution B was added slowly to solution A. The oxalate precipitates were heated at 140 °C for 12 h in a Teflon-lined autoclave. After the reaction, the autoclave was cooled to room

temperature. The light green precipitates were collected by centrifugation and washed with water and ethanol. The products were dried at 70 °C for 24 h. The dried precipitates were heated at 600 °C for 3 h in air.

Scanning electron microscopy (SEM, S4800) and X-ray diffraction (XRD, Bruker D5, CuK₁ radiation = 1.54056 Å) and energy-dispersive X-ray spectroscopy (EDX) were used to analyze the NiFe₂O₄ material's morphologies and crystal structures. A vibrating sample magnetometer (VSM), specifically a Lakeshore 7400, was used to take the magnetic readings.

The experiment involved combining NiFe₂O₄ material and paraffin wax to create a homogeneous mixture. The mixture consisted of 30% absorber mass material. The compacted mixtures exhibited a toroidal shape, characterized by an inner diameter of 3.04 mm and an outer diameter of 7.0 mm. The microwave absorption capabilities of the Keysight PNA-X N5242A vector network analyzers were assessed. Transmission line calculations were conducted to analyze the microwave absorption characteristics. The reflection loss (RL) was determined through the utilization of the following equations, which offer a comprehensive analysis **Error! Reference source not found.**

$$RL(dB) = 20 \cdot \log \left| \frac{Z_{in} - 1}{Z_{in} + 1} \right| \quad (1)$$

$$Z_{in} = \sqrt{\frac{\mu_r}{\epsilon_r}} \tanh \left(j \frac{2\pi f d}{c} \sqrt{\mu_r \epsilon_r} \right) \quad (2)$$

The input impedance (Z_{in}) of the absorber, as well as the complex relative permittivity (ϵ_r) and permeability (μ_r), were taken into account. The speed of light in vacuum (c), frequency of light (f), and thickness of the samples (d) were also included.

RESULTS AND DISCUSSION

Fig. 1 displays the XRD structure of NiFe₂O₄ material. Diffraction peaks are observed at 18.3°, 30.3°, 35.7°, 37.4°, 43.4°, 53.8°, 57.4°, and 63.0°. These peaks correspond to the crystal planes (111), (220), (311), (222), (400), (422), (511), and (440) of the face-centered cubic trevorite structure [3]. The Scherrer formula calculates nanoparticle crystallite sizes. The NiFe₂O₄ crystallite size is 40 nm, determined from the (311) peak.

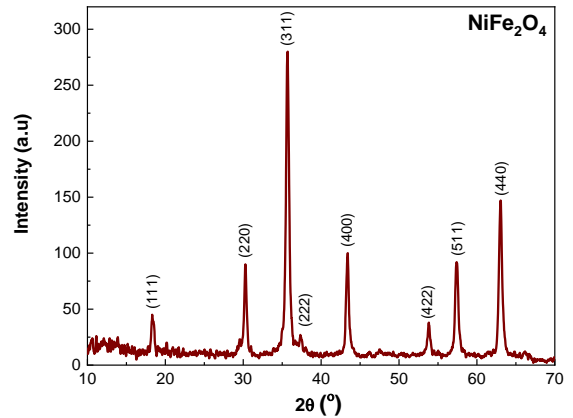


Fig. 1. XRD patterns of NiFe₂O₄.

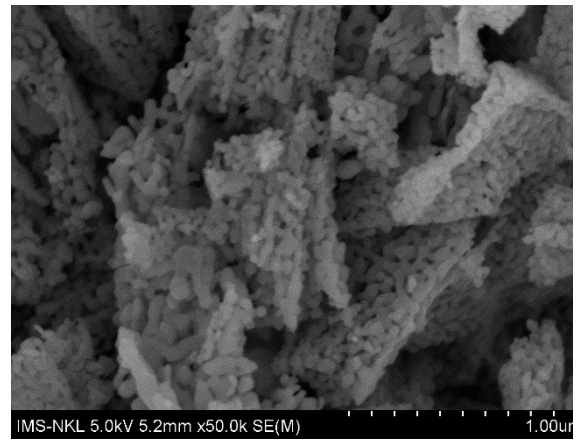


Fig. 2. SEM image of NiFe₂O₄.

A unique wood-texture-column-like structure is seen in the SEM image of the NiFe₂O₄ - based material (Fig. 2). The NiFe₂O₄ powders consist of highly compacted nanoparticles resembling wood. There are gaps between the particles. The NiFe₂O₄ particles are 30-50 nm in size. This result is consistent with the X-ray diffraction analysis.

NiFe₂O₄ material EDX spectrum in Fig. 3. This image shows Fe, Ni and O in the sample, confirming the synthesis of NiFe₂O₄ material. Moreover, the ratio of Fe to Ni in the sample material has attained the designated value of 2:1.

Fig. 4 displays the magnetic hysteresis loop of the NiFe₂O₄ powder. The curve shows that both remanence and coercive force are near zero. This study suggests that the material has superparamagnetic properties [5]. The maximum magnetization of the NiFe₂O₄ powder is 32 emu/g.

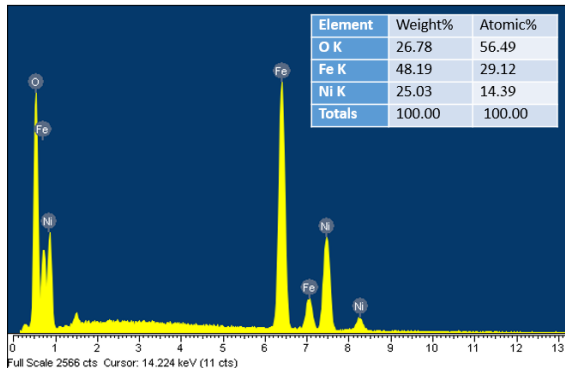


Fig. 3. EDX spectrum of NiFe_2O_4 .

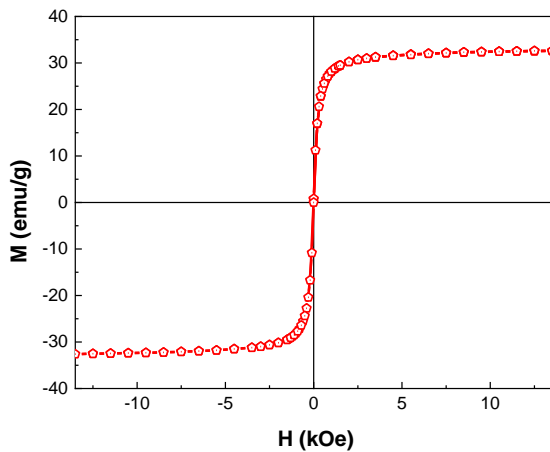


Fig. 4. Magnetic hysteresis loop of NiFe_2O_4 .

Fig. 5 shows the frequency dependency curves of the complex permittivity and permeability of the NiFe_2O_4 sample with a 2 mm thickness. In this figure, both the real and imaginary parts of the complex permittivity decrease regularly with frequency. The real part ranges from 4.9 to 8.9. The imaginary part of the complex permittivity ranges from 0.8 to 2.8. The permeability's real part slightly varies in amplitude from 2 to 18 GHz. In contrast, the imaginary part of permeability shows minor changes.

RL readings can be performed between 1.5 and 3.5 mm and 2 to 18 GHz. Cover plots in Fig. 6 show the range of RL values for NiFe_2O_4 samples. RLmin falls down as thickness increases up. NiFe_2O_4 has the best reflection loss of -58.2 dB at 14.7 GHz, and it is only 2.0 mm thick. At this thickness, the effective bandwidth for absorption is found to be 13.8 GHz. At a thickness of 2.5 mm, the NiFe_2O_4 material has the widest range of frequencies it can absorb, at 14.1 GHz.

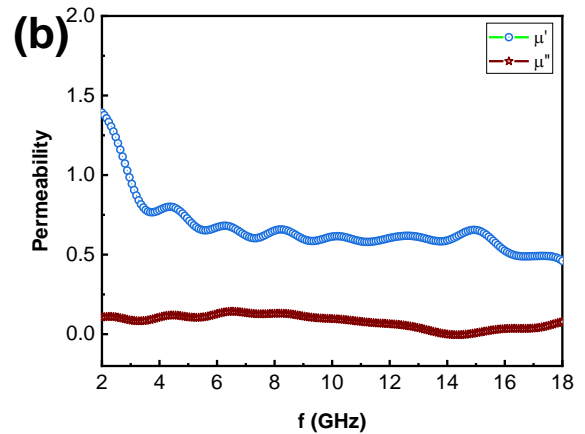
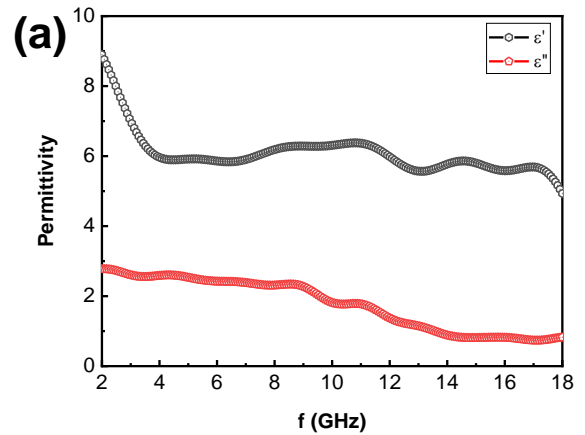


Fig. 5. The complex permittivity (a) and complex permeability (b) of NiFe_2O_4 .

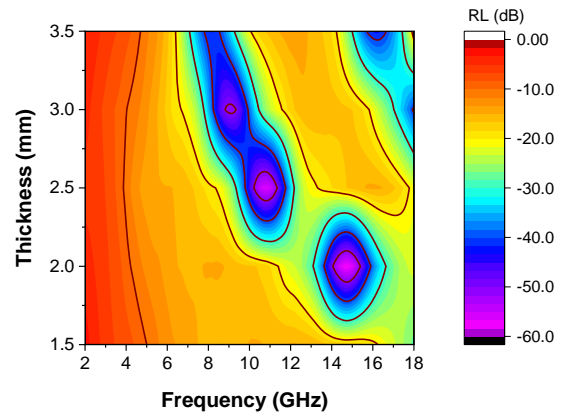


Fig. 6 The reflection loss of NiFe_2O_4 .

The NiFe_2O_4 material's structure and composition contribute to its strong microwave absorption ability. The magnetic dissipation in NiFe_2O_4 powder is due to its strong magnetic properties, including ferromagnetic natural resonance and exchange resonance [2]. Additionally, the numerous oxygen vacancies and lattice defects in the porous structure would

function as dipoles in the electromagnetic field, resulting in a significant dipole polarisation effect [6]. This is attributed to the high specific surface area of the NiFe₂O₄ wood-like texture [7]. A wood-texture column structure can promote reflection and scattering within its interior space, preventing sections from stacking together [8]. The good impedance matching of NiFe₂O₄ material is due to its lower real permittivity and higher permeability, which are caused by its physicochemical properties like higher crystallinity, oxygen vacancies, and wood-like morphology [9-10].

CONCLUSION

In summary, the synthesis of NiFe₂O₄ with a wood-like morphology was achieved using a two-step technique. The material NiFe₂O₄ shown a noteworthy capability for absorbing microwaves. At a filler loading level of 30%, the composite material achieves a minimum reflection loss of -58.2 dB at its thickness is 2 mm. Additionally, the composite material exhibits an effective absorption bandwidth of 14.1 GHz when its thickness is only 2.5 mm. Consequently, the NiFe₂O₄ material synthesised in this study exhibits promising potential for efficient broad band absorption.

Acknowledgment

Le Quy Don Technical University in Vietnam provided funding for this work.

References

[1] A. Houbi, Z.A. Aldashevich, Y. Atassi, Z. B. Telmanovna, M. Saule and K. Kubanych, *Microwave absorbing properties of ferrites and their composites: A review*, J. Magn. Mater. **529** (2021) 167839.

[2] T.Q. Dat, N.T. Ha and D.Q. Hung, *Reduced graphene oxide-Cu_{0.5}Ni_{0.5}Fe₂O₄-Polyaniline nanocomposite: Preparation, characterization and microwave absorption properties*, J. Electron. Mater. **46** (6) (2017) 3707-3713.

[3] S. Hoghoghifard and M. Moradi, *Influence of annealing temperature on structural, magnetic, and dielectric properties of NiFe₂O₄ nanorods synthesized by simple hydrothermal method*, Ceram. Int. **48** (2022) 17768-17775.

[4] N.V. Tung, T.Q. Dat, N.T. Ha, N.T. Nam and D.Q. Hung, *Synthesis of reduced graphene oxide - Mn_{0.8}Zn_{0.2}Fe₂O₄ - porous polyaniline*

nanocomposite materials for effective microwave absorption in X-band, LQDTU Journal of Science and Technology **15** (2020) 13-23.

[5] T.Q. Dat, N.T. Ha, N.V. Tung and P.V. Thin, *Microwave absorption performances of copper/nickel ferrite@fiber polyaniline*, LQDTU Journal of Science and Technology **16**, (2021) 5-13.

[6] T.Q. Dat, N.V. Tuan, N.V. Tung and P.V. Thin, *Facile synthesis of MoS₂ nanomaterial as a promising microwave absorber*, LQDTU Journal of Science and Technology **17** (2022) 5-16.

[7] Q. Chang, H. Liang, B. Shi and H. Wu, *Sodium oxalate-induced hydrothermal synthesis of wood-texture column-like NiCo₂O₄ with broad bandwidth electromagnetic wave absorption performance*, J. Colloid Interface Sci. **600** (2021) 49-57.

[8] T.Q. Dat, P.X. Quang, N.V. Hoang, N.V. Tuan, N.T. Ha, N.V. Tung and P.V. Thin, *Synthesis of Mxene-MoS₂ composite with effective microwave absorption performance*, Proc. The 5th International conference on Advance materials and nanotechnology (2022) 121-127.

[9] P.T. Tho, C.T.A. Xuan, N. Tran, N.Q. Tuan, W.H. Jeong, S.W. Kim, T.Q. Dat, V.D. Nguyen, T.N. Bach, T.D. Thanh, D.T. Khan and B.W. Lee, *Ultra-wide effective absorption bandwidth of Cu, Co, and Ti co-doped SrFe₁₂O₁₉ hexaferrite*, Ceram. Int. **48** (19) (2022) 27409-27419.

[10] C.T.A. Xuan, P.T. Tho, T.Q. Dat, N.V. Khien, T.N. Bach, N.T.M. Hong, T.A. Ho, D.T. Khan, H.N. Toan and N. Tran, *Development of high-efficiency microwave absorption properties of La_{1.5}Sr_{0.5}NiO₄ and SrFe₁₂O₁₉-based materials composites*, Surf. Interfaces. **39** (2023) 102890.

HIGHLY TOUGH AND ANTIBACTERIAL NANOCOMPOSITE FILM OF POLY(VINYL ALCOHOL)/GRAPHENE-OXIDE-ZnO FOR BIOMEDICAL APPLICATION

Hon Nhien Le, Le Nguyen Nhut Linh, Thi Bang Tam Dao, Trung Do Nguyen and Chi Nhan Ha Thuc

Faculty of Materials Science and Technology, University of Science, VNU-HCM, 227 Nguyen Van Cu Street, Ward 4, District 5, Ho Chi Minh City, 700000, Viet Nam;
Vietnam National University, Area 6, Linh Trung, Thu Duc City, Ho Chi Minh City, 700000, Viet Nam
Email: lhnhien89@gmail.com

ABSTRACT

In this study, cascade design of graphite oxidation reaction is applied for producing graphene oxide nanosheets (GO). The nano-hybrid of graphene oxide nanosheet – zinc oxide nanoparticle (GO-ZnO) is synthesized using sonochemical method. Obtained GO-ZnO nanomaterial is characterized and used for preparing polymeric films based on polyvinyl alcohol (PVA) by means of solution casting method. Nanocomposite thin films of PVA/GO-ZnO were investigated using moisture analysis, immersion in ethanol solution and mechanical tensile measurement. It is found that appropriate formulation of PVA/0.5%GO-ZnO film gave the improved tensile strength of 39.99 MPa, elastic modulus of 97.06 MPa and especially the elongation of 670.32 %. After immersion in ethanol solution 75 % for 1 hour, tensile elongation and energy to break of PVA/0.5%GO-ZnO/ethanol films increased significantly to 897.29 % and 708.95 kgf/mm respectively. The antiseptic ethanol immersion made the nanocomposite film extraordinarily tough and effectively antimicrobial for wound dressing application. In general, the nanocomposite film of PVA/0.5%GO-ZnO/ethanol is a novel formulation for biomedical purposes.

Keywords: polyvinyl alcohol nanocomposite, graphene oxide – zinc oxide, highly tough, antibacterial film, wound dressing, biomedical application

INTRODUCTION

Biomedical research is presently focusing on advanced nanomaterials, especially graphene based nanosheets, for biosensing, bioimaging, nanomedicine, drug delivery and wound healing [1-4]. Graphene oxide (GO) is a two-dimensional nanosheet with strong mechanical strength, large surface area, oxygen-containing functional groups and antibacterial activity. The combination of GO and zinc oxide nanoparticle (ZnO) produces GO-ZnO nano-hybrid with effective antibacterial property and low toxicity [5]. Besides, polyvinyl alcohol (PVA) is a biocompatible polymer for biomedical materials, including wound dressing, contact lense, artificial cartilage and drug delivery vehicle. Many of scientific papers have reported PVA based membranes and hydrogels for biomedical applications [6].

In this study, multi-layered graphite oxide (GrO) and exfoliated GO nanosheets were synthesized using the cascade design of graphite oxidation reaction. Nano-hybrid of GO-ZnO was

prepared via a sonochemical method and mixed with PVA solution for casting and drying at 60 °C, producing nanocomposite film of PVA/GO-ZnO with good tensile properties, particularly high elongation. It is found that the immersion of PVA/GO-ZnO film in antiseptic ethanol 75% resulted in significant enhancement of tensile toughness and antibacterial activity. Therefore, the formulation of PVA/GO-ZnO/ethanol nanocomposite film provides the advantages of extraordinary toughness and antimicrobial activity for biomedical applications, particularly wound dressing.

EXPERIMENTAL

Synthesis of graphite oxide and graphene oxide. Our previous paper presented the cascade design of graphite oxidation reaction [7]. Briefly, 5 g natural graphite and 50 mL concentrated H₂SO₄ 96% were mixed for 1 hour and then poured slowly into the solution of 10 g KMnO₄ and 100 mL H₂SO₄ 96%. After agitation for 4 hours at room condition, the suspension of

graphite/Mn(VII)/H₂SO₄ was poured slowly into 360 mL water under stirring. After additional reaction with 150 mL H₂O₂ solution 5%, obtained graphite oxide was washed with HCl solution 5% and excessive water. Sonication of suspension of graphite oxide in water produce GO nanosheets. Supernatant solution of GO nanosheets in water was used for next synthesis.

Synthesis of graphene oxide – zinc oxide. 250 mL Zn²⁺ solution 500 ppm was dropped slowly into 250 mL GO solution 400 ppm under stirring. After the adsorption of Zn²⁺ on GO nanosheets, the suspension was sonicated for 15 minutes, adjusted to pH 10 using ammonia solution, and sonicated for 15 minutes [5]. After sedimentation, filtration and washing with water, GO-ZnO nanocomposite was obtained via the sonochemical procedure.

Synthesis of poly(vinyl alcohol)/graphene-oxide-ZnO nanocomposite films. Commercial polyvinyl alcohol (PVA, n = 1750 ± 50) was dissolved in water at 80 °C to obtain a PVA solution 10%. GO-ZnO dispersion was dropped into the PVA solution 10% and sonicated for 15 minutes. In the next stage, PVA/GO-ZnO suspensions were used in the method of solution casting at 60 °C for producing PVA/GO-ZnO thin films. The casting of PVA solution 10% at 60 °C gave blank PVA films as control samples.

RESULTS AND DISCUSSION

In Figure 1A, the SEM image showed the GO-ZnO nano-hybrid structure containing ZnO nanoparticles and GO nanosheets. Figure 1B presented EDS spectrum and elemental compositions of GO-ZnO nanomaterial. Atomic proportions of carbon, oxygen and zinc are 58.52 %, 34.89 % and 6.58 % respectively. ZnO nanoparticle has theoretical Zn : O ratio of 1 : 1. Therefore, theoretical atomic proportion of ZnO nanoparticles is 13.16 %. Accordingly, ZnO nanoparticles occupied 31.7 % in the total weight of GO-ZnO nanomaterial. Figures 1C and 1D revealed the elemental mapping of zinc atoms (blue dots) and oxygen atoms (red dots) on GO-ZnO. Zinc atoms were derived ZnO nanoparticles. Oxygen atoms were originated from ZnO nanoparticles and functional groups on GO nanosheets. As a result, ZnO nanoparticles and oxygen-containing functional groups were well-distributed on the carbon network of GO platform. The nanostructures are hydrophilic to retain hydration layers on the surface, which is

beneficial to prevent $\pi - \pi$ restacking of graphene based nanosheets [3]. The GO-ZnO nanomaterial was prepared and preserved for next synthesis of PVA/GO-ZnO nanocomposite.

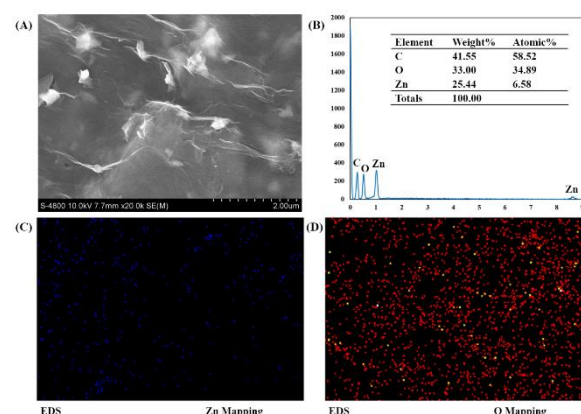


Figure 1. (A) SEM image of GO-ZnO hydrogel. (B) EDS spectrum with elemental proportions of GO-ZnO. (C, D) Elemental zinc mapping and elemental oxygen mapping on GO-ZnO structure.

Figure 2 presents X-ray diffraction analysis (XRD) of GrO and GO materials. In XRD pattern of GrO, there are a main peak at $2\theta = 12^\circ$ (001 lattice) and another peak at $2\theta = 42^\circ$ (100 lattice), indicating the multi-layered structure with interlayer distance of 0.74 nm. Therefore, ultrasonic treatment of GrO in water makes the hydrophilic multi-layered structure exfoliated into GO nanosheets. XRD pattern of GO-ZnO showed no peaks of layered structure of GrO and the presence of characteristic peaks of ZnO nanocrystals at 31.9° (100 lattice), 34.6° (002 lattice), 36.4° (101 lattice), 47.7° (102 lattice), 56.7° (110 lattice) and 63° (103 lattice). The XRD of GO-ZnO nanocomposite presented the random assembly of graphene based nanosheets and the formation of ZnO nanocrystals.

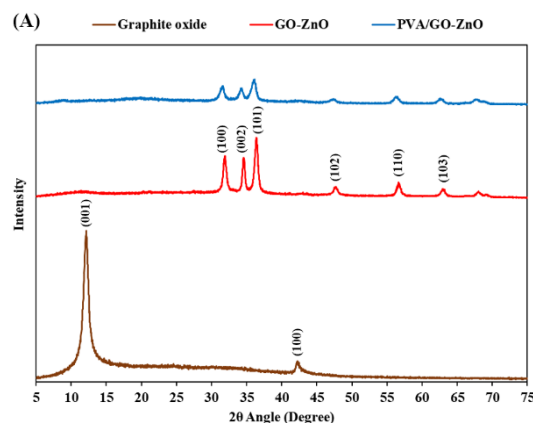


Figure 2. XRD patterns of GrO powder, GO-ZnO nanomaterial and PVA/GO-ZnO film.

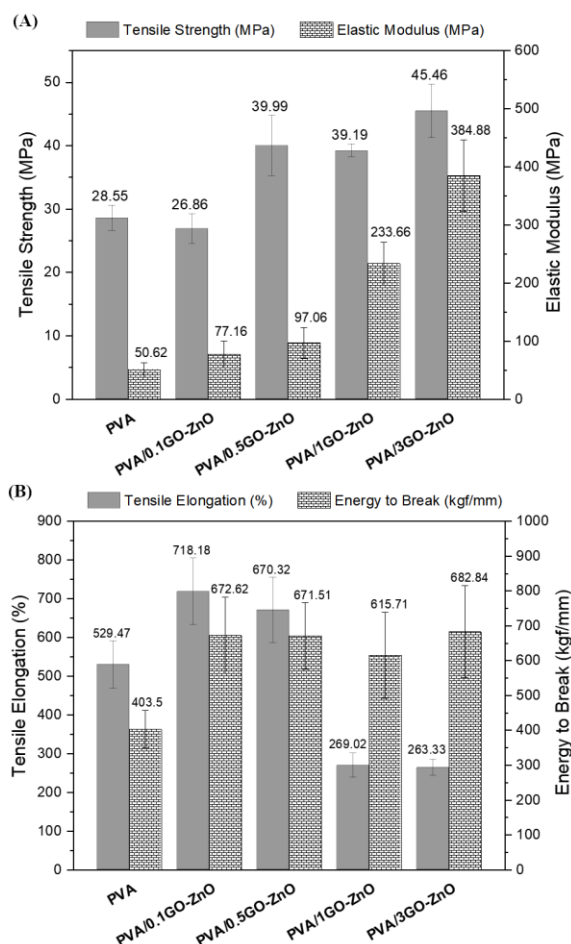


Figure 3. Tensile properties of thin films of PVA and PVA/GO-ZnO nanocomposites.

As-prepared PVA films have tensile strength of 28.55 MPa, elastic modulus of 50.62 MPa, elongation at break of 529.47 % and break energy of 403.5 kgf/mm (Figure 3). Although the tensile strength of 28.55 MPa is moderate compared to those of PVA films reported in previous literature (25 – 57 MPa), the elongation of 529.47 % is excellently higher than the typical value of 220.7 % [6]. The improvement of tensile elongation as well as break energy of PVA is assigned to the moisture content (~ 12 %) in the film. Water molecules function as plasticizers in the polymer structure, facilitating better movement of PVA chains during the tensile test. As a result, the PVA film with good toughness and biocompatibility is a potential material for biomedical applications. In Figures 3A and 3B, mechanical tensile properties of PVA/GO-ZnO nanocomposites were described. The nanocomposite film of PVA/0.5GO-ZnO showed the best properties, specifically tensile strength of 39.99 MPa, elastic modulus of 97.06 MPa, elongation of 670.32 % and break energy of 671.51 kgf/mm. Although

PVA/3GO-ZnO film had the highest tensile strength and elastic modulus, elongation property was considerably reduced to 263.33 %. Appropriate GO-ZnO amount in PVA matrix resulted in better nanocomposite morphology and reinforcement effect. The tensile strength, elastic modulus, elongation and break energy of PVA/0.5GO-ZnO film are 40.07 %, 91.74 %, 26.6 % and 66.42 % respectively higher than those of PVA film. Therefore, the PVA/0.5GO-ZnO nanocomposite film was further investigated in next experiments of immersion in antiseptic ethanol solution 75 %.

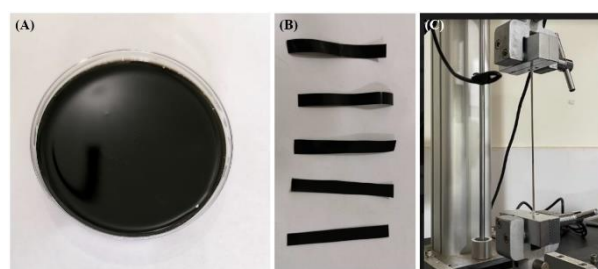


Figure 4. (A) As-synthesized PVA/0.5GO-ZnO film. (B) Thin ribbons of PVA/0.5GO-ZnO E75%-1h film (after 1-hour ethanol immersion process). (C) Tensile testing of a PVA/0.5GO-ZnO E75%-1h film sample.

The picture of a PVA/0.5GO-ZnO film (moisture ~ 12 %) is exhibited in Figure 4A. Thin films of PVA/0.5GO-ZnO E75%-1h (after immersion in ethanol solution 75 % for 1 hour) are showed in Figure 4B. Tensile testing of PVA/0.5GO-ZnO E75%-1h films were conducted to investigate effect of swelling in ethanol solution on mechanical properties. In Figure 4C, a PVA/0.5GO-ZnO E75%-1h film was stretched in the tensile testing. Figure 5 presents tensile properties of PVA/0.5GO-ZnO films before and after ethanol immersion process. The tensile strength of PVA/0.5GO-ZnO E75%-1h film slightly decreased to 36.37 MPa compared with PVA/0.5GO-ZnO film, while the elastic modulus dropped to 41.74 MPa. The interconnected network of PVA chains and GO-ZnO nanosheets was swelled and loosened, declining the tensile strength and elastic modulus. However, PVA/0.5GO-ZnO E75%-1h film showed the excellent elongation of 897.29 % that was 33.86 % higher than PVA/0.5GO-ZnO film and 69.47 % higher than PVA film. The result confirmed that solvent molecules (ethanol and water) plasticized the films to enhance the elongation value. The entanglement of PVA chains is reduced in the

swollen membranes for tensile elongation as well as more flexible movements in biomedical dressings. Energy to break is calculated by integral about the stress – strain curve of PVA/0.5GO-ZnO E75%-1h film, giving the break energy of 708.95 kgf/mm. The result showed the increase of 75.7 % in break energy compared to PVA film. It is proved that the novel formulation of PVA/0.5GO-ZnO/ethanol thin film provides the significant enhancement of tensile toughness.

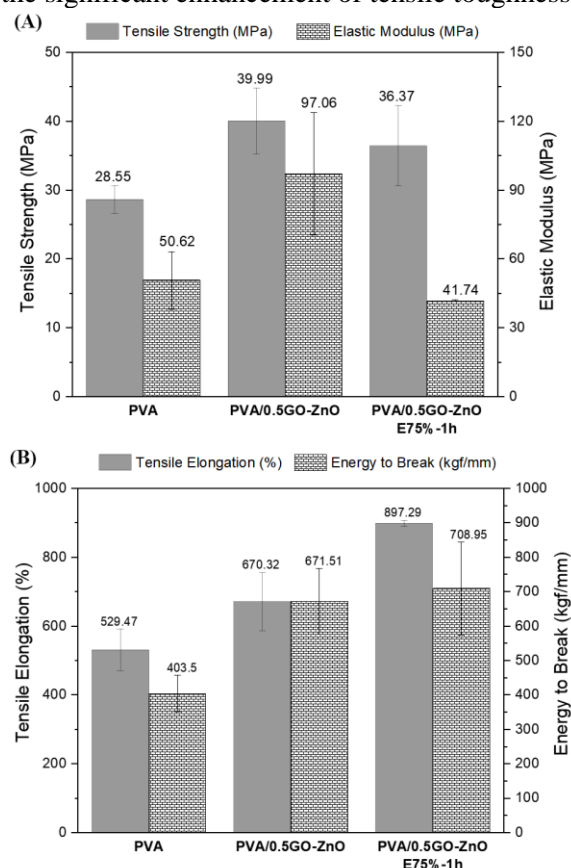


Figure 5. Tensile properties of PVA thin film and PVA/0.5GO-ZnO membrane.

CONCLUSION

The synthesis, analysis and investigation of nanocomposite formulations presented novel improvements of PVA/GO-ZnO materials. XRD, SEM and EDS of GO-ZnO nano-hybrid indicated ZnO crystal, GO assembly, functional groups, nanostructures, elemental composition and mapping. The reinforcement of 0.5 % GO-ZnO in PVA film resulted in the best enhancement, especially the tensile strength of 39.99 MPa, elongation value of 670.32 % and break energy of 671.51 kgf/mm. After immersion in ethanol 75 % for 1 hour, PVA/0.5GO-ZnO E75%-1h film showed significantly better tensile elongation (897.29 %) and break energy (708.95 kgf/mm),

which were respectively 69.47 % and 75.7 % higher than those of blank PVA film. Highly tough and antibacterial PVA/GO-ZnO/ethanol films are promising to biomedical applications.

Acknowledgment

The research and development is conducted at Fundamental Materials Science Laboratory, Faculty of Materials Science and Technology, University of Science, Vietnam National University, Ho Chi Minh City.

References

- [1] Y. Qu, F. He, C. Yu, X. Liang, D. Liang, L. Ma, Q. Zhang, J. Lv, J. Wu, *Advances on graphene-based nanomaterials for biomedical applications*, Mater. Sci. Eng. C **90** (2018) 764–780.
- [2] F. Wahid, X.-J. Zhao, S.-R. Jia, H. Bai, C. Zhong, *Nanocomposite hydrogels as multifunctional systems for biomedical applications: Current state and perspectives*, Compos. B: Eng. **200** (2020) 108208.
- [3] N. H. Le, H. Seema, K. C. Kemp, N. Ahmed, J. N. Tiwari, S. Park, K. S. Kim, *Solution-processable conductive micro-hydrogels of nanoparticle/graphene platelets produced by reversible self-assembly and aqueous exfoliation*, J. Mater. Chem. A **1** (2013) 12900.
- [4] H. N. Le, T. P. Huynh, T. T. N. Bui, M. H. Do, K. Q. Luu, C. N. Ha Thuc, *Synthesis Of Graphene Oxide – Gold Nanobipyramids For Antibacterial Coating On Water Filtration Membrane*, Vietnam J. Sci. Technol. **60** (6A) (2022) 1-14.
- [5] H. N. Le, T. B. T. Dao, M. H. Do, T. T. N. Bui, T. D. Nguyen, C. N. Ha Thuc, *Upgrading Water Purification Membrane With Photocatalytic And Antibacterial Coating Of Graphene Oxide – Zinc Oxide Nanocomposite*, Vietnam J. Sci. Technol. **60** (6A) (2022) 114-130.
- [6] N. Jain, V. K. Singh, S. Chauhan, *A review on mechanical and water absorption properties of polyvinyl alcohol based composites/films*, J. Mech. Behav. Mater. **26** (2018) 213-222.
- [7] H. N. Le, D. Thai, T. T. Nguyen, T. B. T. Dao, T. D. Nguyen, D. T. Tieu, C. N. Ha Thuc, *Improving Safety and Efficiency in Graphene Oxide Production Technology*, J. Mater. Res. Technol. **24** (2023) 4440-4453.

ZnO THIN FILM LAYER - AN IMPORTANT ROLE FOR ENHANCING THE PHOTOLUMINESCENCE OF CdSe QUANTUM DOTS

Phan Van Cuong^{1,2}

¹Department of Physics, Nha Trang University, 02 Nguyen Dinh Chieu Street. Nha Trang, Vietnam

²Physical Society of Khanh Hoa, Vietnam

Email: cuongpv@ntu.edu.vn

ABSTRACT

CdSe quantum dots (QDs) were successfully prepared and used for spin coating on glass substrate (CdSe). Then ZnO thin film was deposited on the CdSe quantum dot coated glass substrate (ZnO/CdSe). Notably, with the ZnO thin film deposited on CdSe QDs, the PL intensity was enhanced over two times compared to the CdSe QD layer only.

Keywords: Nanocomposite, nanomaterial, quantum dot, luminescence, nanoparticle

INTRODUCTION

Colloidal semiconductor nanocrystals, so-called quantum dots (QDs), have generated tremendous interest both for fundamental research and technical applications such as light emitting diodes (LEDs) [1], bioimaging [2], and solar cells [3]. Because of their size-dependent photoluminescence (PL) related to quantum-size effect tunable across the wide visible spectrum, CdSe QDs have become the most extensively investigated QDs [4]. Since core CdSe QDs usually have low luminescence efficiency, much experimental work has been devoted to surface passivation to improve the luminescence efficiency of QDs. Several methods of organic and inorganic surface modification have been developed to mediate the problems by passivation of the surface defects of QDs. The organic passivation methods such as polymer encapsulation, surface grafting, and ligand exchange [5–7] have usually accompanied a decrease in quantum yield (QY) and an undesirable size increase relative to the original QDs and more QDs being included in the polymer encapsulation. In this report, CdSe quantum dots (QDs) were successfully prepared by TOPO-TOP based organometallic synthesis method. The products were used for spin coating on glass substrate. Then ZnO thin film was deposited on the CdSe quantum dot coated glass substrate. Room temperature photoluminescence (PL) and its enhancement of CdSe QDs with and without ZnO thin film were studied. In detail, CdSe QDs was characterized by field-emission transmission electron microscope (FE-TEM – Titan G2

ChemiSTEM Cs Probe from FEI Co.). The photoluminescence of the samples is measured under excitation by an iHR320 imaging spectrometer (Horiba Jobin Yvon). The results show that ZnO thin film plays an important role for enhancing the PL of CdSe QDs.

EXPERIMENTAL

Synthesis of CdSe quantum dots

The CdSe QDs were prepared by TOPO-TOP based organometallic synthesis. A 2 M stock solution of trioctylphosphine selenide (TOP : Se) was prepared by dissolving 15.8 g of Se into 100 mL of TOP. The stock solution was filled in 100 mL three-neck round-bottomed flask and fitted with a thermocouple temperature sensor and condenser, with TOPO (10g), HDA (10g) and TOP (2.5 mL), and heat to 170°C under vacuum for 1-2h and raise the temperature to 340–350°C. In a separate vial, mix Cd(acac)₂ (620 mg), HDDO (1 g), and TOP (5 mL) and heat under vacuum to 100°C; the solution should become homogeneous. Cool the mixture to approximately 80°C and add 5 mL of a 2 M TOP : Se. The solution mixture of cadmium and selenium precursors was rapidly injected into the hot flask containing the coordinating solvent, and then cooled using each solvent. The QDs extracted from same hot batch were divided into different cooling solvents. The synthesized CdSe QDs were spin-coated on glass substrate at a speed of 3000 rpm.

ZnO thin film deposition

RF sputtering method was used to deposit ZnO thin film layer on CdSe QDs coated on glass substrate which was mentioned above. The ZnO

target (99.99%) is used and the pressure is at 7.10^{-3} torr inside chamber, 20W sputter power, Ar gas is flowed at 15sccm and the sputtering time is 15 minutes at room temperature.

Sample characterization

CdSe QDs was characterized by field-emission transmission electron microscope (FE-TEM – Titan G2 ChemiSTEM Cs Probe from FEI Co.). The photoluminescence of the samples is measured under excitation by an iHR320 imaging spectrometer (Horiba Jobin Yvon).

RESULTS AND DISCUSSION

TEM image of the CdSe QDs are shown in figure 1a. The black scale bar in the images indicate the lengths of 20 nm. The images display the shape and size distribution of the synthesized QDs. Spherical nanostructures are observed, which have an average diameter of about 5 nm.

Figure 1b indicates the clearly changes in the PL intensity, peak position, and FWHM. Notably, with the ZnO thin film deposited on CdSe QDs, the PL intensity was enhanced over two times compared to the CdSe QD layer only. The increase of PL is also affected by the direction of the excitation beam to the CdSe QDs side or to the thin ZnO thin film layer.

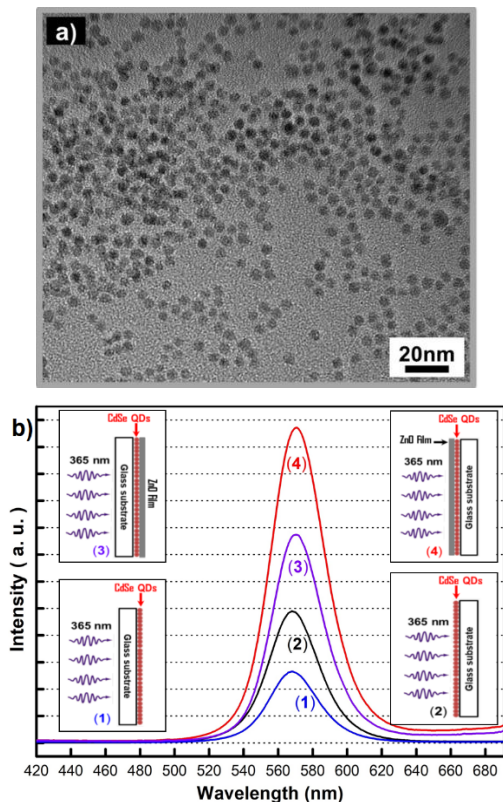


Figure 1. TEM images of CdSe quantum dots (a). The PL intensity of ZnO thin film deposited on

CdSe QDs was enhanced compared to the CdSe QD layer only (b).

CONCLUSION

CdSe QDs were successfully synthesized. ZnO thin film was deposited on the CdSe QDs. With the ZnO thin film deposited on CdSe QDs, the PL intensity was enhanced over two times compared to the CdSe QD layer only. The direction of the excitation beam to the CdSe QDs side or to the thin ZnO thin film layer also affected to the PL increase of nanocomposite.

Acknowledgment

The results was supported by the Nano Applied Physics Laboratory (NAPL), Department of Physics, Kyungpook National University, Daegu, 41566, Republic of Korea

References

- [1] P. O. Anikeeva, et al. Nano Letters, **7**(8) (2007) 2196-2200.
- [2] H. Tada, et al. Cancer Research, **67**(3) (2007) 1138-1144.
- [3] B. Farrow and P. V. Kamat, Journal of the American Chemical Society, **131**(31) (2009) 11124-11131.
- [4] M. G. Bawendi, et al. The Journal of Chemical Physics, vol. **96**(2) (1992) 946-954.
- [5] W. T. Al-Jamal, et al. Small, **4**(9) (2008) 1406-1415.
- [6] J. K. Kim, S. H. Lim, Y. Lee et al., Proceedings of the NSTI Nanotechnology Conference and Trade Show, **3** (March 2004) 379-382.
- [7] X. Ji, J. Zheng, J. Xu et al., Journal of Physical Chemistry B, **109**(9) (2005) 3793-3799.

GRAFT-POLYMERIZATION OF ACRYLAMIDE ONTO PRE-IRRADIATED POLYVINYL PYRROLIDONE MATRIX AND EVALUATION OF COMBINED COPOLYMER PRODUCT AND GRAPHENE OXIDE NANOFUIDS ON THE EOR POTENTIAL IN HIGH-TEMPERATURE OFFSHORE OILFIELDS

**Anh-Quan Hoang¹, Lieu Nguyen Thi^{1,2}, Anh-Tuyen Luu³, Van-Toan Le⁴, Duy-Khanh Pham¹,
Phuong-Tung Nguyen^{1*}**

¹Institute of Applied Materials Science, VAST, Ho Chi Minh City, 700000, Vietnam

²Industrial University of Ho Chi Minh City, Ho Chi Minh City, 700000, Vietnam

³Center for Nuclear Technologies, Ho Chi Minh City, 700000, Vietnam

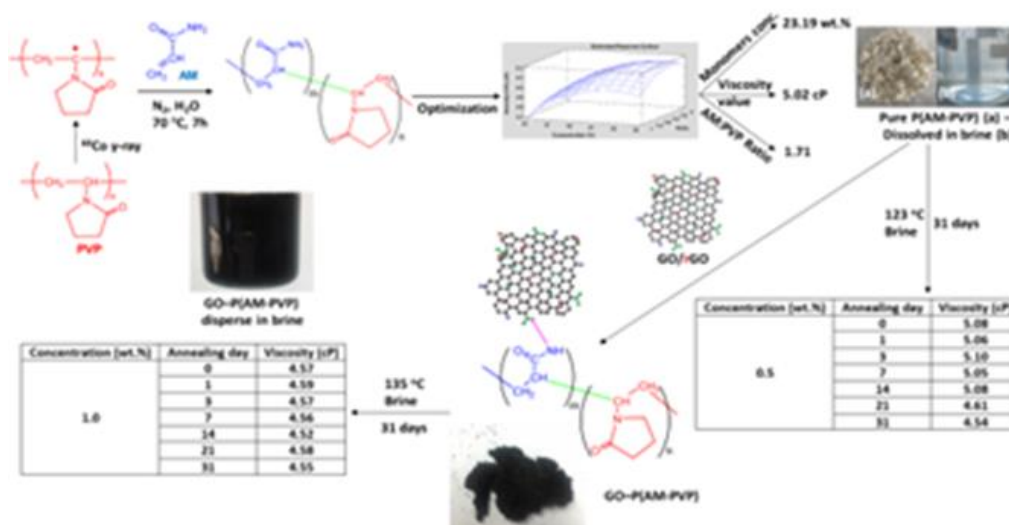
⁴Dalat Nuclear Research Institute, Dalat City, 670000, Vietnam

Email: phuongtungng@iams.vast.vn

ABSTRACT

Polymer solutions are widely used in oil and gas exploration and production. To meet the requirements of working effectively in the harsh conditions in offshore oilfields, thermal resistance and salt-stable in seawater with high hardness polymer solutions are required. In the present research, the irradiation-induced grafting of acrylamide (AM) onto polyvinylpyrrolidone (PVP) matrix with a number-average molecular weight (Mn) of 30000 by gamma pre-irradiation technique was reported. Effects of the total dose, monomer concentration, reaction time, and temperature on the grafting percentage are studied in detail. Then the conjugation of synthesized P(AM–PVP) copolymers on the thermostable GO nanosheets was performed to get GO-P(AM-PVP) nanocomposite. The structure of graft-polymers and GO–P(AM-PVP) nanocomposite was analyzed using FTIR, and Raman spectroscopies. SEM analyses and elemental mapping were performed to observe the composites morphology and atoms distribution of copolymers on the GO surface, respectively. Besides that, the surface chemistry of materials was investigated with XPS techniques. The molecular weight of the polymers was determined by GPC. The advantages of P(AM-PVP) copolymer and GO-copolymer nanofluids in high viscosity, solubility in seawater, and stability at high White-Tiger Oligocene reservoir temperatures (> 128 °C and 135 °C) were confirmed by bottle tests at 128 °C and 135 °C in 31 days. These features render them suitable for EOR and other applications in HT offshore reservoirs.

Graphical Abstract



Keywords: Pre-irradiation-induced grafting polymerization, GO-polymer nanocomposite nanofluid, EOR, high-temperature offshore reservoirs.

INTRODUCTION

With economic development and world population growth, energy demand is increasing enormously and is forecast to increase by up to 30% in 2050 [1]. In the next few decades, oil and gas will still be the primary source of energy, which cannot yet be replaced by renewable energy. Besides, oil and gas are the primary, irreplaceable source of input materials for the chemical industry of essential compounds. To be able to satisfy the oil and gas demand of the world market while large, easy-to-exploit oil fields are exhausted, petroleum operators must step up to enhance oil recovery (EOR) to get a part of the oil amount trapped in the reservoirs after the primary and secondary exploitation stages (about 70% of the original oil in place). Until now, the polymer injection is a chemical EOR method that is widely used and more effective due to the availability and low cost of polymers, especially partially hydrolyzed acrylamide (AM) polymers (HPAM) [2]. However, along with the decline in easy-to-exploit oil fields, oil exploitation conditions are becoming increasingly tricky, moving farther out to sea and with higher reservoir temperatures. Therefore, the polymer injection agent is required to be more thermally and chemically stable at high temperatures, and injection seawater has a high content of multivalent ions, which are significant limitations of HPAM [3]. Petroleum chemistry experts have long been trying to create and test polymers for injection to EOR in HT offshore fields. Among the many copolymers between acrylamide-viscosity agents and monomers that improve thermal stability, AMPS, NVP, and later ATBS are most interesting [4,5]. Besides the advantages, the component monomers of these copolymers also have limitations, such as consuming a lot of AMPS monomer to limit the degree of hydrolysis of the AM radical while only being stable up to 120 °C; NPV is expensive and has low viscosity, etc. These heat-stable copolymers are usually synthesized by free radical polymerization with chemical initiators.

For overcoming some of the mentioned limitations, we have used Gamma irradiation to activate the free radical polymerization of AM and NPV. The copolymer product P(AM-NPV) continues to be grafted with graphene oxide to blend the nanofluid system for thermal durability and chemical stability at 134 °C [6].

To limit the difficulty of transporting a large amount of irradiated liquid product from the irradiation site to the offshore oil and gas exploitation platform, in this report, we study pre-irradiation of PVP and then perform the graft polymerization of AM onto PVP frame.

EXPERIMENTAL

Materials

Graphite powder, AM, NVP, potassium permanganate (KMnO₄; 99%), hydrogen peroxide (H₂O₂; 36%), sodium nitrate (NaNO₃), and sulfuric acid (H₂SO₄; 95%) were supplied by Across Organic, Fisher Chemical and used without pre-purification. The brine used in study was prepared in laboratory. Its properties were similar to those of real White Tiger (WT) oilfield (located at Cuu Long Basin of Vietnam).

Methods

Graft polymerization of AM onto pre-irradiated PVP sheets

Graft polymerization of monomers onto pre-irradiated PVP sheets performed in two steps:

- Polymer pre-irradiation: PVP K30 is packed in PE bags and irradiated at 5, 10, 15, 20, and 30 kGy.
- Mixtures of AM in DI water at different concentrations and N-methyl pyrrolidone were placed in reaction containers aerated with nitrogen. The solution was stirred at 200 rpm and slowly added irradiated PVP at 20% w/v, then heated to 70 °C and kept at different time intervals. The product was washed and purified to remove all unreacted monomers and PAM. The P(AM-PVP) copolymers product was collected and oven-dried at 50 °C.

Synthesis of GO-P(AM-PVP) nanocomposite

0.03 g of GO was dispersed in 30 mL of DI water, added 15.1 mg of L-ascorbic acid into the solution and stirred at 60 °C for 60 min. Cooled down solution was used immediately in the next stage. Stirred a solution of 0.03 g of optimized P(AM-PVP) copolymers in 50 mL of water for 5 min. The rGO dispersion was slowly added to the P(AM-PVP) solution, kept stirring for 30 min. Sonicated the mixture of rGO and P(AM-NVP) for 30 min, kept stirring overnight at 60 °C, and reduced in vacuo. Then, added acetone into the solution and centrifuged at 5000 rpm for 15 min. The product was freeze-dried to obtain solid rGO-P(AM-PVP) nanocomposites.

Thermal and chemical stabilities of copolymers and GO-copolymer dispersion screening

Dispersed amounts of copolymers and GO copolymers in brine to obtain 1.0 wt.% of dispersion concentration. Then diluted them with brine to the designed concentrations. Measured the dispersions viscosity and placed in heat-resistant ampules. Ampules were bowered nitrogen and place the ampules in an oven, heated to 128 °C (the Miocene reservoir's temperature, WT Oilfield). Then, in the same way, placed ampules with GO-copolymer dispersion in an oven and heated to 135 °C (the Oligocene reservoir's temperature, WT Oilfield). The transparency was observed, and the viscosity of mixtures was measured after 1, 3, 7, 14, 21, and 31 days.

Product characterization

The structure of graft-polymers and GO-P(AM-PVP) nanocomposite was analysed using FTIR, and Raman spectroscopies. SEM analyses and elemental mapping were performed to observe the composites morphology and atoms distribution of copolymers on the GO surface, respectively. Besides that, the surface chemistry of materials was investigated with surface analysis system spectroscopy (XPS) techniques. The molecular weight of the polymers was determined by GPC.

RESULTS AND DISCUSSION

Tab. 1. Copolymer product yield vs. PVP irradiation dose, 20% AM monomer, T_{rea} 70°C

No	Reaction time, h	Product yield, %				
		5kGy	10kGy	15kGy	20kGy	30kGy
1	0	0	0	0	0	0
2	3	2.50	4.7	13.80	21.67	27.87
3	5	6.45	13.25	34.40	45.52	58.50
4	7	12.70	24.42	54.50	85.00	88.12
5	8	12.72	24.38	55.10	85.15	88.78

Tab. 2. Copolymer product yield vs. AM concentration, PVP irra. at 20kGy, T_{rea} 70°C

No	Reaction time, h	Product yield, %			
		10%A M	20%A M	30%A M	40%A M
1	0	0	0	0	0
2	3	15,50	21,67	27,60	32,50
3	5	34,70	45,52	45,80	52,80
4	7	73,60	85,00	72,80	72,50
5	8	73,70	85,15	73,00	72,70

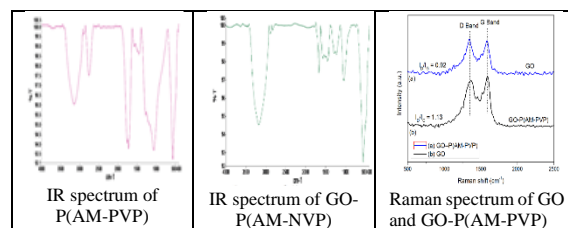


Fig. 1. P(AM-PVP) copolymer and GO-P(AM-PVP) copolymer characterization.

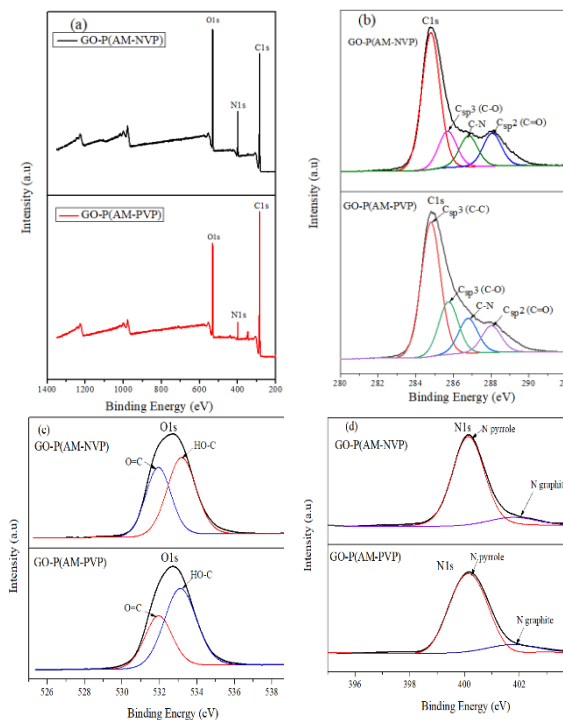


Fig. 2. Images XPS spectrum of GO-P(AM-NVP)/GO-P(AM-PVP) (a), and XPS spectrum of C1s(b), O1s(c), N1s(d) of these materials

The chemical composition and elemental state of GO-P(AM-NVP) and GO-P(AM-PVP) materials were characterized by X-ray photoelectron spectroscopy (XPS). The spectrum results in Figure 2a shows that in both spectra, in addition to the appearance of the C1s peak at 285 eV and O1s peak at 532 eV typical of GO, a new peak in the 400eV binding energy region was detected. in GO-P(AM-NVP) and GO-P(AM-PVP) attributed to N1s [9]. This proves that in the materials GO-P(AM-NVP) and GO-P(AM-PVP) there are three elements C, O, N, and also proves that (AM-NVP), and (AM-PVP) copolymers have been successfully attached onto GO sheets. Figure 2a also shows that the characteristic peak for N1s in the GO-P(AM-PVP) spectrum has lower intensity than the N1s peak in the GO-P(AM-NVP) spectrum, which can be explained by the Pre-irradiation of PVP material causes N-binding to be reduced.

The N1s spectral band (Figure 2d) includes two peaks distributed in the energy region of 400.3eV and 401.9eV assigned to pyrrole nitrogen and graphite nitrogen related to N3- in NVP and AM, respectively. Pyrrole nitrogen refers to sp² hybridized N bonded to two Csp² atoms and one H atom forming a 5-membered heterojunction of NVP. Graphite nitrogen refers to an sp²-hybridized N atom bonded to three adjacent sp²-hybridized C atoms forming an unconjugated six-membered heterojunction. Figure d also shows that the N1s peak intensity of the GO-P(AM-PVP) material is lower than that of the GO-P(AM-NVP) material, similar to the general spectrum results of the two materials in figure 2a. This result is also consistent with a previous report. [7].

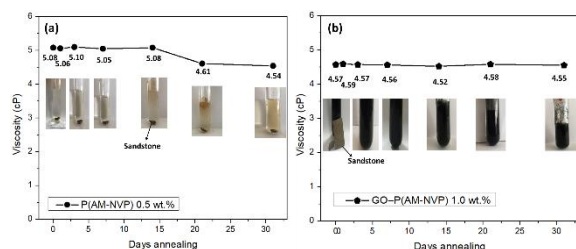


Fig. 3. Evaluation of chemical and thermal stability of copolymer and GO-copolymer solutions.

Figure 3a,b show the viscosity and appearance of 0.5 w% P(AM-PVP) dispersed in seawater incubated at 128 °C and 1 w% GO-P(AM-PVP) dispersed in seawater set at 135 °C for 31 days. Figure 3a shows that the 0.5 w% P(AM-PVP) solution, when incubated at 128 °C for 14 days, has almost no change in viscosity and appearance. Nevertheless, after 21 days and 31 days, the viscosity of the solution decreased by 8.81% and 13.66%, respectively. This demonstrates that increasing the viscosity of the injection fluid by using properly designed GO-copolymer composite, will improve the mobility ratio of the injection fluid accordingly in more favorable direction. Therefore, the efficiency of vertical and horizontal sweeping increases compared to the simple water injection method.

CONCLUSION

The graft copolymerization of the AM and pre-irradiated PVP was successfully carried out with high efficiency and allowed to obtain thermostable P(AM-PVP) copolymers with easy-to-design properties, simplicity, low cost and green for the environment. These properties are suited to the required reservoir conditions and

safely scale up for producing the stable copolymers, which can be applied for EOR at HT (up to 128 °C) and high-salinity brine. Moreover, it was found that 1.0 wt.% in brine dispersion of P(AM-PVP) covalently attached to partial rGO exhibited high stability in both viscosity and appearance during the annealing at 135 °C in 31 days. As a result, the produced GO-P(AM-NVP) nanocomposite had excellent dispersion stability in high-salinity and HT conditions.

Acknowledgment

This research is funded by Vietnam National Foundation for Science and Technology Development (NAFOSTED) under grant number 103.02-2018.333. We also thank VAST for providing the necessary help.

References

- [1] Energy Information Administration, International Energy Outlook, vol. **0484**, pp. 70–99, Jul. 2019
- [2] D. W. Green and G. Paul Willhite, *Enhanced Oil Recovery*, Society of Petroleum Engineers, USA, 2018.
- [3] Editor: D.O. Shah and Schechter, *Improved Oil Recovery by Surfactant and Polymer Flooding*, 1st Edition - January 28, 1977
- [4] M. Lin, et al., *Temperature resistance of AM/AMPS/NVP copolymer microspheres*, Iranian Polymer Journal **29** (2020) 445-453.
- [5] S. JOUENNE, *Polymer flooding in high temperature, high salinity conditions: Selection of polymer type and polymer chemistry, thermal stability*, Journal of Petroleum Science and Engineering **195** (2020) 107545.
- [6] T.L. Nguyen et al., *Stable dispersion of graphene oxide-copolymer nanocomposite for enhanced oil recovery application in high-temperature offshore reservoirs*, Colloids and Surf A: Physicochemical and Eng. Aspects. **628** (2021) 127343.
- [7] Sandeep Yadav et al., *An Update on Graphene Oxide: Applications and Toxicity*. ACS Omega **7**(40) (2022) 35387-35445.

EFFECTS OF IRRADIATION ON NAFION UNDER DRY AND HYDRATED CONDITIONS

Dinh Tran Trong Hieu^{1,2} and **Tran Duy Tap**^{1,2*}

¹ Faculty of Materials Science and Technology, University of Science, 227 Nguyen Van Cu, District 5, Ho Chi Minh City, Vietnam.

² Vietnam National University, Ho Chi Minh City, Vietnam
Email: tdtap@hcmus.edu.vn

ABSTRACT

Although Nafion membranes have been increased in applications for transportation, utilization of these membranes in the case of high energy radiation environments have not investigated sufficiently. This study presents the effects of gamma irradiation on Nafion membranes at dose of 200 kGy upon air, water, and hydrogen peroxide (6% concentration) environments. The crystallinity of irradiated Nafion increases at an irradiation dose of 200 kGy in air, resulting from the re-crystallization of the amorphous phase of the polymer backbones. However, the crystallinity decreases upon irradiation in water, especially in hydrogen peroxide environments. This result associates with the degradation of the inherent crystalline phase of the polymer main chains. Thermogravimetric analysis (TGA) results confirmed these findings, showing an increase in the dissociation temperature of SO₃⁻ groups and the decomposition temperature of the polymer main chains. These results suggest that gamma irradiation affects both the polymer main chains and the side-chains containing SO₃⁻ groups, which play a role in proton transport. Note that an irradiation dose of 200 kGy in air enhances thermal stability and crystallinity of polymer main chains in Nafion membrane.

Keywords: Gamma irradiation, chemical degradation, Nafion, fuel cell, crystallinity.

INTRODUCTION

The transition to renewable energy sources has prompted the search for clean and sustainable energy solutions. Proton exchange membrane fuel cells (PEMFCs), particularly hydrogen fuel cells, offer a high-efficiency and eco-friendly option for reducing fossil fuel consumption and CO₂ emissions in various applications.

Polymer electrolyte membranes (PEMs) play a crucial role in PEMFCs by facilitating proton conduction and preventing gas permeation. Perfluorosulfonic acid (PFSA), particularly commercially available Nafion, Dow, Aciplex, and Fumapem membranes, are commonly used in hydrogen fuel cells [1]. Nafion, the most widely used commercial material, consists of a hydrophobic backbone (polytetrafluoroethylene or PTFE) and a hydrophilic perfluorosulfonic ionomer side chain with sulfonic acid groups [2]. Figure 1 depicts the chemical structure of Nafion. Although Nafion membranes possess desirable characteristics such as high proton conductivity, mechanical strength, thermal stability, electrochemical and chemical resistance, their performance can be affected by factors such as humidity, temperature, and gas diffusion during

fuel cell operation [2]. Water absorption by the membrane influences its microstructure, proton conduction, and ion exchange with the electrode. Additionally, cost remains a concern [2].

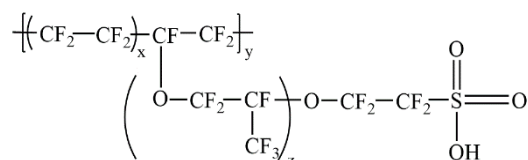


Figure 1. Chemical structure of Nafion membrane.

To address these challenges, researchers have explored methods to enhance the durability and performance of Nafion membranes in hydrogen fuel cells. While blending methods increase complexity, time, and cost of synthesis, radiation modification of Nafion offers advantages such as impurity-free products, room temperature processing, and scalability for industrial use. This study examines the effects of gamma radiation (1.17 and 1.33 MeV from a Co-60 isotope source) on Nafion membranes irradiated at a dose of 200 kGy, with a dose rate of 10 kGy/hour in air, water, and hydrogen peroxide environments. The structures and thermal properties of irradiated

membranes are investigated using Fourier transform infrared (FT-IR) spectroscopy, thermogravimetric analysis (TGA), and X-ray diffraction (XRD).

EXPERIMENTAL

E. I. du Pont de Nemours & Co. Inc. supplies Nafion membranes with an approximate thickness of 50 μm . The initial surface contaminants are removed using an acetone solution. Nafion membranes are irradiated with gamma radiation from a Co-60 source (14000 Ci, Gamma Chamber 5000-BRIT, India) at a dose and a dose rate of 200 kGy and 10 kGy/hour, respectively in air, water, and hydrogen peroxide environments. The irradiated membranes are characterized using FT-IR, TGA, and XRD. These measurements were described elsewhere [3].

RESULTS AND DISCUSSION

Figure 2 illustrates the FT-IR spectra of Nafion membranes before and after exposure to gamma radiation upon various conditions: a) un-irradiation, b) dry environment, c) water environment, and d) 6% H_2O_2 solution. The bending vibrations of water molecules are identified in the range of 2100-500 cm^{-1} , while the stretching vibrations of water molecules are associated with the range of 3800-2500 cm^{-1} [4]. A new peak at 1770 cm^{-1} is believed to be caused by the oscillation of the $-\text{COOH}$ group at the polymer backbone and the side chains. Furthermore, the spectral curves of the dry condition exhibit different shapes compared to those upon the water and 6% H_2O_2 conditions due to strong irradiation influence, resulting in changes in the chemical structure.

Figure 3 depicts the TGA profiles of Nafion membranes before and after being exposed to gamma radiation under different conditions: a) un-irradiation, b) dry environment, c) water environment, and d) 6% H_2O_2 solution. Nafion exhibited degradation by at least three stages [5].

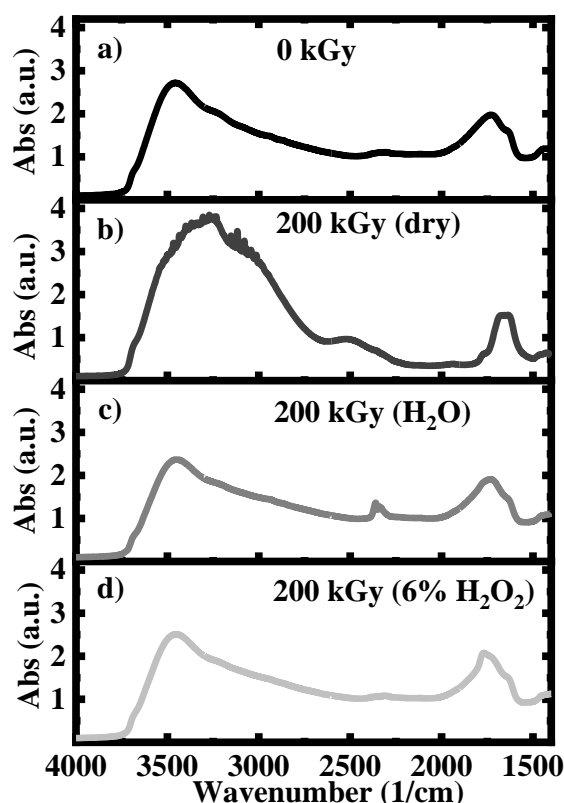


Figure 2. FT-IR spectra of Nafion membranes before and after irradiation upon different environments.

Water bonded to the sulfonic groups of Nafion desorbs and leads to weight loss at around 100 $^{\circ}\text{C}$ (T_1) [6]. The second weight loss stage occurs between 330 $^{\circ}\text{C}$ and 365 $^{\circ}\text{C}$ (T_2) and is caused by the decomposition of sulfonic acid groups, side chains, and the release of gases like H_2O and CO_2 [13]. Weight loss in the third stage, around 500 $^{\circ}\text{C}$ (T_3), is due to the thermal decomposition of the Nafion backbone. This decomposition releases gases such as HF and COF_2 , which are typical of the decomposition of fluorinated compounds [7]. The detailed values of decomposition temperature are presented in Figure 4.

Figure 4 presents the decomposition temperatures of irradiated Nafion membranes. At T_1 stage, the irradiated membranes upon dry and water environments show higher temperatures than the original membrane. This can be attributed to the presence of crosslinks, which hinder water release. At T_2 stage, the side chains are more strongly cleaved in water and H_2O_2 environments.

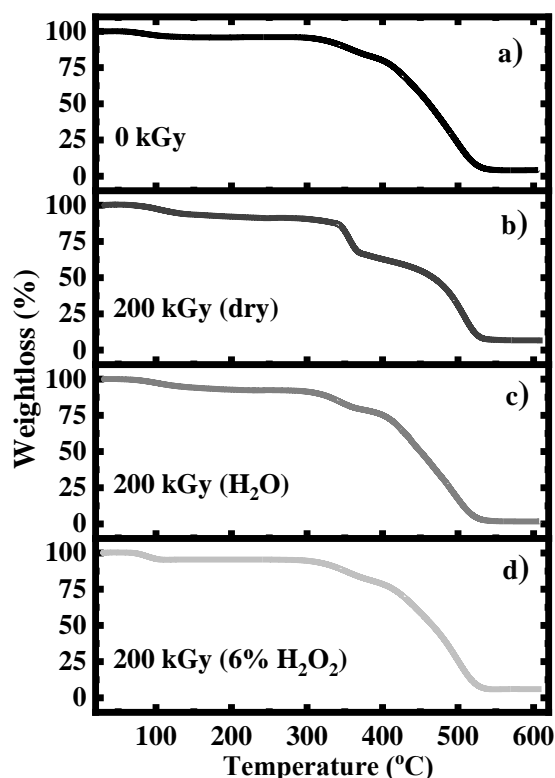


Figure 3. TGA profiles of Nafion irradiated at different environments.

This could be due to the cleavage of side chains into shorter chains and subsequent rearrangement. At T3 temperature, the irradiated membranes in a water environment exhibit significantly reduced temperatures compared to the original sample. This is due to the presence of $\bullet\text{OH}$ free radicals that have a significant impact on the polymer backbone.

Figure 5 shows the XRD profiles of the Nafion membranes before and after exposure to gamma radiation. The non-irradiated membrane shows a crystal peak (100) at 17.94° [8]. A low intensity scattering peak at 15.32° is assigned to the amorphous phase of the perfluoroether side chain terminating with sulfonic acid groups and the main PTFE chains [8]. The XRD profiles of irradiated membranes show significant changes in the intensity and shape of the scattering peaks upon water and H_2O_2 environments.

Figure 6 illustrates the change of crystal size L (a) and crystallinity (b) at an irradiation dose of 200 kGy [9].

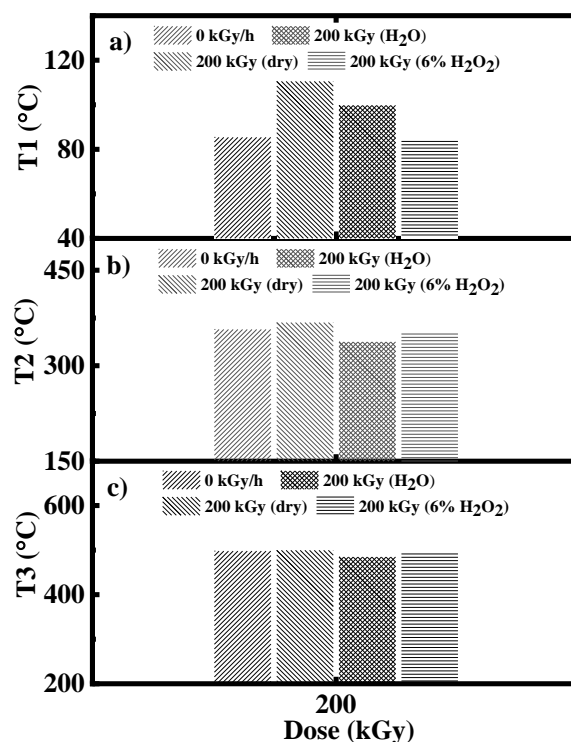


Figure 4. The values of decomposition temperature of irradiated Nafion membranes.

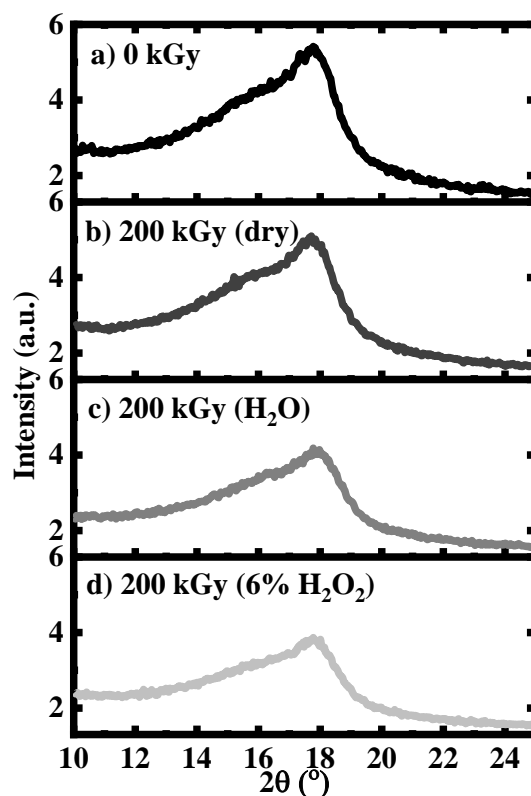


Figure 5. XRD profiles of Nafion membranes irradiated at different environments.

The crystallite size increases upon dry condition and then gradually decreases under

water, and 6% H₂O₂. The increase in crystallinity (upon dry condition) can be attributed to the recrystallizing within the amorphous phase of the main polymer chains. The drop of crystallite size and crystallinity under water, and 6% H₂O₂ should be associated to the combinative effects of water and hydrogen peroxide radiolysis.

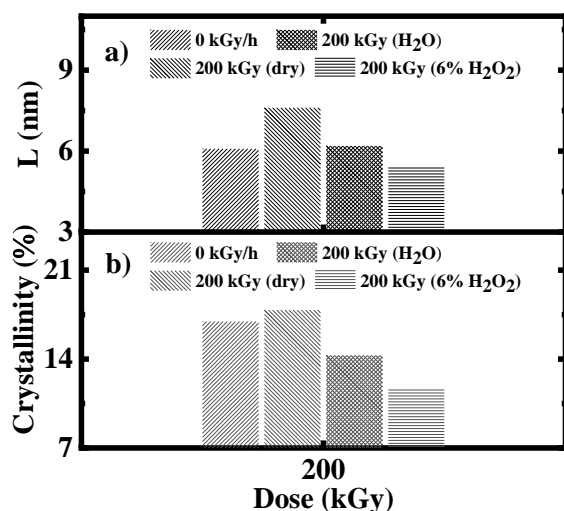


Figure 6. The change of crystal size *L* and crystallinity upon irradiation at different environments.

CONCLUSION

The effects of gamma irradiation at 200 kGy on Nafion membranes upon various environments of dry, water, and 6% H₂O₂ were investigated. The crystallinity of irradiated membrane upon air condition increases due to re-crystallization of polymer chains in the amorphous phase of the backbone. However, crystallinity decreases in water, specifically in hydrogen peroxide environments, due to degradation of inherent crystalline phase of the polymer main chains. The TGA results suggest the formation of cross-linking phase in the amorphous main and side chains, which hinder the water release. Notably, irradiation at 200 kGy in air improves thermal stability and crystallinity of Nafion membrane.

Acknowledgment

This work was funded by Vingroup Big Data Institute (VINBIGDATA), Vingroup and supported by Vingroup Innovation Foundation (VINIF) under project code VINIF.2020.DA08.

References

[1] Garland NL, Benjamin TG, Kopasz JP, *Materials issues in polymer electrolyte*

membrane fuel cells, Mater. Matters **3** (2008) 62452.

- [2] Zatoń M, Rozière J, Jones DJ, *Current understanding of chemical degradation mechanisms of perfluorosulfonic acid membranes and their mitigation strategies: a review*, Sustainable Energy & Fuels **3** (2017) 409-438.
- [3] Hao LH, Hieu DT, Luan LQ, Phuong HT, Dinh VP, Tuyen LA, Hong PT, Van Man T, Tap TD, *Electron and gamma irradiation-induced effects in poly (ethylene-co-tetrafluoroethylene) films*, Journal of Applied Polymer Science **29** (2022) 52620.
- [4] Nishiyama H, Takamuku S, Oshikawa K, Lacher S, Iiyama A, Inukai J, *Chemical states of water molecules distributed inside a proton exchange membrane of a running fuel cell studied by operando coherent anti-Stokes Raman scattering spectroscopy*, The Journal of Physical Chemistry C **18** (2020) 9703-9711.
- [5] Zhang S, Yuan X, Wang H, Mérida W, Zhu H, Shen J, Wu S, Zhang J, *A review of accelerated stress tests of MEA durability in PEM fuel cells*, International journal of hydrogen energy **1** (2009) 388-404.
- [6] Gong C, Pinatti L, Lavigne G, Shaw MT, Scola DA, Montgomery T. Shaw, and Daniel A. Scola, *Thermal stability of end-capped and linear sulfonated polyimides, sulfonated polystyrene, and Nafion 117*, Journal of Applied Polymer Science **3** (2018) 45694.
- [7] De Almeida S, Kawano Y, *Thermal behavior of Nafion membranes*, Journal of Thermal Analysis and Calorimetry **3** (1999) 569-577.
- [8] Schulze M, Lorenz M, Wagner N, Gülzow E, *XPS analysis of the degradation of Nafion*, Fresenius' journal of analytical chemistry **365** (1999) 106-113.
- [9] Pajuste E, Reinholds I, Vaivars G, Antuzevičs A, Avotiņa L, Sprūģis E, Mikko R, Heikki K, Meri RM, Kaparkalējs R, *Evaluation of radiation stability of electron beam irradiated Nafion® and sulfonated poly (ether ether ketone) membranes*, Polymer Degradation and Stability **200** (2022) 109970.

SYNTHESIS AND CHARACTERIZATION OF PIPERINE AND ZnO NANOPARTICLES FOR PIPERINE-LOADED ZnO NANOPARTICLES

Nguyen Phuc Nguyen^{1,2}, Huy Duc Huynh Do³, Linh Thi Thuy Vo^{1,2}, Chien Mau Dang^{1,2}, Duy Ba Ngo³, Ngan Nguyen Le^{1,2}

¹ Institute for Nanotechnology, Community 6, Linh Trung Ward, Thu Duc City, Ho Chi Minh City, Vietnam;

² Vietnam National University Ho Chi Minh City, Ho Chi Minh City, Vietnam

³ Nong Lam University, Linh Trung Ward, Thu Duc City, Ho Chi Minh City, Vietnam
Email: lnngan@vnuhcm.edu.vn

ABSTRACT

Presently, a myriad of alkaloids, such as piperine, find extensive applications in the field of medicine. Piperine, a notable alkaloid derived from *Piper nigrum L.*, has garnered significant attention in recent years in biology and medicine due to its remarkable properties. Consequently, our objective was to extract piperine for the purpose of studying its distinctive characteristics. Concurrently, nanotechnology has emerged as a focal point in the realm of biomedical science, owing to its transformative contributions. Notably, nanoparticle-based materials have gained prominence due to their exceptional functionalities, closely tied to their minute size. These properties can be fine-tuned by modifying the surface ligand, primarily through controlling the nanoparticle size. Leveraging the exceptional attributes of both zinc oxide and piperine nanoparticles, our endeavor entailed synthesizing zinc oxide nanoparticles functionalized with piperine ligands, thereby resulting in piperine-incorporated zinc oxide nanoparticles ($ZnOs^{piperine}$). This deliberate approach aimed to augment the unique properties of the nanoparticles. The synthesis procedure encompassed a series of sequential steps. Initially, piperine was extracted from black pepper using a maceration technique combined with a rotary evaporator, yielding a solid matrix rich in piperine. Subsequently, nanometer-sized zinc oxide nanoparticles were created through a simple chemical method employing Zn^{2+} zinc salt and KOH solution. To validate and characterize the synthetic route, a comprehensive array of qualitative and quantitative assessments, including field emission scanning electron microscopy (FE-SEM) and optical Fourier transform infrared spectroscopy (FTIR), were conducted. Experimental investigations were then undertaken to evaluate the properties of the aforementioned entities. The results of these experiments will serve as a reference and guide for our future endeavors, specifically in combining zinc oxide nanoparticles with piperine ligands ($ZnOs^{piperine}$).

Keywords: zinc oxide nanoparticles, piperine, piperine-loaded zinc oxide nanoparticles.

INTRODUCTION

In the natural world, various derivatives possessing enhanced anti-inflammatory and antibacterial properties have been identified, such as chitosan extracted from crustacean shells, curcumin extracted from turmeric, or piperine extracted from pepper. Within Vietnam's abundant black pepper production, researchers consistently prioritize the utilization of piperine for investigating and evaluating its antibacterial potential.

Piperine has long been recognized for its anti-inflammatory and antimicrobial effects in animal models of arthritis and wound healing in mice. Classified as an alkaloid, piperine exhibits anti-inflammatory and antioxidant properties,

effectively reducing levels of free radicals [1]. Notably, piperine has been reported to elevate TGF- β levels, facilitating collagen repair, and inhibiting NF- κ B activation in rodent periodontal tissues [2]. Furthermore, piperine demonstrates the ability to suppress nitric oxide production and the expression of certain proinflammatory cytokines [3].

Previous studies have indicated that piperine, when combined with metal alloys, can enhance its medicinal effectiveness [4-6]. Metal-piperine complexes, such as the ZnO-Pip-NC complex (zinc oxide nanocomposite containing piperine) or $AuNPs^{piperine}$ (gold nanoparticle-coated piperine), have exhibited remarkable physicochemical properties. However, the anti-

inflammatory properties of piperine-metal complexes remain relatively unexplored and require further investigation.

In this study, piperine was extracted by soaking in ethanol, followed by evaporation and drying to obtain a concentrated form. Subsequently, zinc oxide nanoparticles were synthesized using a simple chemical method. The resulting materials would be utilized for further synthesis of ZnO-Pip-NC. Piperine and zinc oxide nanomaterials were assessed and characterized by field emission scanning electron microscopy (FE-SEM) and optical Fourier transform infrared spectroscopy (FTIR).

EXPERIMENTAL

1. Materials

Ethanol (98%), zinc nitrate hexahydrate ($\text{Zn}(\text{NO}_3)_2 \cdot 6\text{H}_2\text{O}$) and potassium hydroxide (KOH) were provided by Sigma-Aldrich. All solutions were prepared using ultrapure water with a resistivity of 18.2 M Ω ·cm.

2. Extraction of piperine

To obtain piperine, we employ the eco-friendly green extraction method. The process involves maceration and rotary evaporation. Initially, black pepper is pulverized into a fine powder and immersed in absolute alcohol (98% ethanol) for a duration of one day. Subsequently, the extract is filtered to separate the residual black pepper. The same volume of ethanol is utilized for a second maceration, followed by filtration to obtain the extract and separate the black pepper residue. This process is repeated for a third maceration. Consequently, three bottles of black pepper extract are obtained, which are combined for the subsequent evaporation step.

The evaporation of the extract is carried out using a rotary evaporator, ensuring that the temperature does not exceed 50 degrees Celsius to prevent ingredient damage and denaturation. After the evaporation process, a concentrated, liquid form of medicinal herbs is obtained.

To obtain a solid extract, the medicinal herbs obtained post-evaporation are subjected to drying at a temperature of 50 degrees Celsius until a constant mass is achieved. This yields flexible solid medicinal herbs containing piperine.

3. Synthesis of zinc oxide nanoparticles

Initially, we prepare a 25 ml solution of zinc salt Zn^{2+} by dissolving it in deionized (DI) water, resulting in a concentration of 0.4 M. Subsequently, the solution is subjected to stirring

with heating at a speed of 400 rpm for a duration of 3 hours. Following this, a 25 ml solution of potassium hydroxide (KOH) with a concentration of 0.8 M is gradually added to the zinc salt solution while continuing the stirring process for an additional hour. As a result, the solution undergoes a gradual transformation, transitioning into a milky white appearance. At this time, $\text{Zn}(\text{OH})_2$ precipitate is formed.

To separate the precipitate or suspension from the reaction solution, centrifugation is employed. The centrifugation is carried out at 8000 rpm and a temperature of 4 degrees Celsius for a period of 15 minutes. Subsequently, the resulting substance is subjected to heating at 400 degrees Celsius for 2 hours, resulting in the production of fine, white powder consisting of zinc oxide nanoparticles (ZnO NPs).

RESULTS AND DISCUSSION

1. Results of extracted piperine

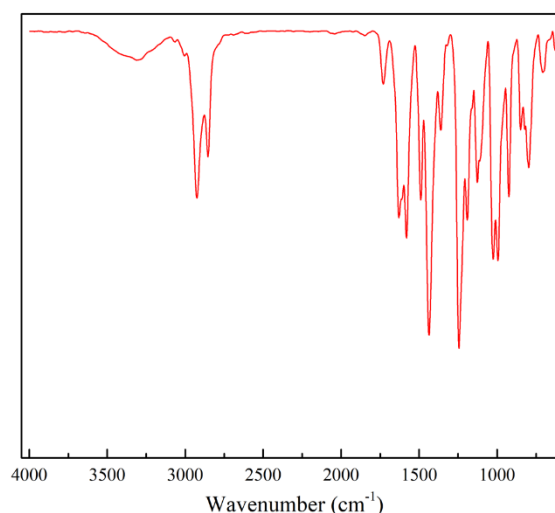


Figure 1. FTIR spectrum of extracted piperine

By utilizing FTIR (Fourier Transform Infrared) spectroscopy for the identification of piperine in samples, distinct peaks within the wavelength range of 2940 to 1026 reveal the presence of piperine (Figure 1). Notably, N-H peaks at 1580.99 and 1632.58 indicate the presence of amide groups. Peaks at 2937.3 and 2854.0 signify the existence of aromatic and aliphatic C-H bonds, respectively. Other characteristic peaks include 2935.6 (C-H) and 2843.9 (NCH₂). Furthermore, the (C=O) bond exhibits intense vibration at 1632.53 and medium absorption at 1583.38. Peaks at 1442.83, 1490.7, and 1538.38 correspond to the (C=C aromatic) bond. Additionally, there are distinctive peaks

associated with phenolic C-O stretching vibrations at 1027.31, 1131.31, 1131.07, 1195.45, and 1250.89. Upon observing the figure, it becomes apparent that the peak overlap ratio indicates the presence of piperine at a level of 83.6%.

2. Results of zinc oxide nanoparticles synthesis



Figure 2. FE-SEM image of synthesized zinc oxide nanoparticles

Based on the procedure employed for synthesizing zinc oxide nanoparticles (ZnO NPs), the resulting particles predominantly exhibit a spherical morphology, with a minor proportion of rod-shaped particles present at a low frequency (Figure 2). The particle size distribution ranges from a few hundred nanometers to less than 100 nanometers, characterized by distinct boundaries between the different size ranges.

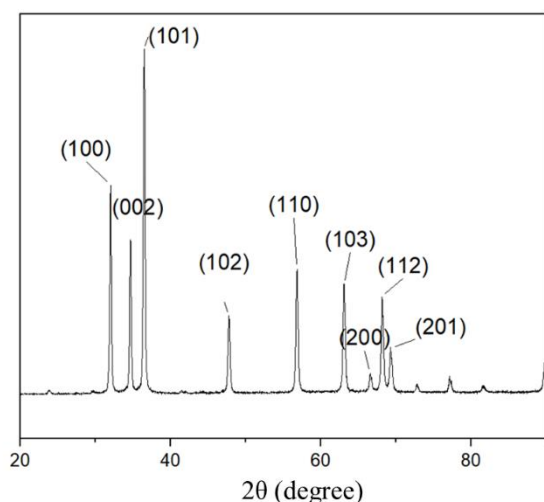


Figure 3. XRD patterns of ZnO nanoparticles

XRD patterns of ZnO nanoparticles, as shown in Figure 3, indicated that the zinc oxide nanoparticles had crystal structures completely similar to the standard spectrum of ZnO.

3. The proposed process aims to synthesize zinc oxide nanoparticles ($ZnOs^{piperine}$) in conjunction with piperine

Regarding the creation of ZnO nanoparticles, two methods for producing ZnO/piperine will be considered. The first method involves generating piperine ligands immediately after the formation of ZnO nanoparticles. The second method entails creating piperine ligands simultaneously with the synthesis of ZnO nanoparticles.

In the first method, following the precipitation of $Zn(OH)_2$, the piperine extract is promptly added to the solution and stirred for a duration of 2 hours. Subsequently, the suspension is separated from the reaction solution through centrifugation at 8000 rpm and a temperature of 4 degrees Celsius for 15 minutes. The resulting solid particles are then dried for 5 hours and stored in a sealed container for further analysis.

In the second method, after the dissolution and stirring of zinc salt Zn^{2+} for 3 hours, the piperine extract is added and the mixture is stirred for an additional 2 hours. Next, KOH solution is slowly introduced into the combined solution, and stirring is continued for 1 hour. The subsequent steps for suspension and processing are identical to those described in the first method.

Both methods offer distinct approaches to incorporating piperine ligands into the synthesis of ZnO nanoparticles, providing alternative paths for further investigation and analysis.

For the future evaluation of the product, several analytical methods will be employed, including HPLC-MS (High-Performance Liquid Chromatography-Mass Spectrometry), TLC (Thin-Layer Chromatography), and XRD (X-Ray Diffraction) spectroscopy. These techniques will enable comprehensive analysis and characterization of the synthesized $ZnOs^{piperine}$ nanoparticles, allowing for the determination of their chemical composition, purity, and crystal structure. HPLC-MS will provide precise identification and quantification of piperine and other compounds present in the sample. TLC will be utilized for qualitative analysis, aiding in the separation and identification of different components. XRD spectroscopy will provide valuable information about the crystalline nature and crystallographic structure of the synthesized nanoparticles. Together, these analytical methods will contribute to a thorough evaluation of the final product's properties and composition.

In addition, the antibacterial properties will be tested on eight strains of bacteria, including

Pseudomonas, *S. Aureus*, *E. coli*, and *Salmonella*. These bacteria strains will consist of four ATCC strains and four field strains. The synthesized ZnO_s^{piperine} nanoparticles will be exposed to these bacterial strains to assess their potential antibacterial efficacy against a variety of microorganisms. This evaluation aims to investigate the antimicrobial activity of the nanoparticles and their potential applications in combating bacterial infections.

CONCLUSION

In this study, we have successfully synthesized ZnO nanoparticles and extracted piperine from *Piper nigrum L.*. These are two main ingredients for synthesis of ZnO_s^{piperine}. This nanocomposite is expected to have many outstanding advantages such as good antibacterial, anti-inflammatory and can heal wounds faster.

Acknowledgment

This research is funded by Vietnam National University HoChiMinh City (VNU-HCM) under grant number VL2023-32-01.

References

- [1] R.S. Vijayakumar, D. Surya, N. Nalini, *Antioxidant efficacy of black pepper (Piper nigrum L.) and piperine in rats with high fat diet induced oxidative stress*, Redox report: communications in free radical research **9**(2) (2004) 105-110.
- [2] L. Marques da Fonseca, L.R. Jacques da Silva, J. Santos Dos Reis, M.A. Rodrigues da Costa Santos, V. de Sousa Chaves, K. Monteiro da Costa, J.N. Sa-Diniz, C.G. Freire de Lima, A. Morrot, T. Nunes Franklim, D.C. de Alcântara-Pinto, M.E. Freire de Lima, J.O. Previato, L. Mendonça-Previato, L. Freire-de-Lima, *Piperine Inhibits TGF- β Signaling Pathways and Disrupts EMT-Related Events in Human Lung Adenocarcinoma Cells*, Medicines (Basel, Switzerland) **7**(4) (2020) 19.
- [3] S. Umar, A.H.M. Golam Sarwar, K. Umar, N. Ahmad, M. Sajad, S. Ahmad, C.K. Katiyar, H.A. Khan, *Piperine ameliorates oxidative stress, inflammation and histological outcome in collagen induced arthritis*, Cellular Immunology **284**(1) (2013) 51-59.
- [4] S. Bawazeer, I. Khan, A. Rauf, A.S.M. Aljohani, F.A. Alhumaydhi, A.A. Khalil, M.N. Qureshi, L. Ahmad, S.A. Khan, *Black pepper (Piper nigrum) fruit-based gold nanoparticles (BP-AuNPs): Synthesis, characterization, biological activities, and catalytic applications – A green approach*, Green Processing and Synthesis **11**(1) (2022) 11-28.
- [5] Z. Yang, M. Pu, X. Dong, F. Ji, V. Priya Veeraraghavan, H. Yang, *Piperine loaded zinc oxide nanocomposite inhibits the PI3K/AKT/mTOR signaling pathway via attenuating the development of gastric carcinoma: In vitro and in vivo studies*, Arabian Journal of Chemistry **13**(5) (2020) 5501-5516.
- [6] S. Kancharana, R.V. Chengalva, S.R. Kothapalli, M. Yegireddy, S. Bollini, P. Tollamadugu Naga Venkata Krishna Vara, *Assessment of acaricidal activity of nanoscale ZnO encapsulated piperine formulation against Rhipicephalus microplus*, IET nanobiotechnology **14**(8) (2020) 722-731.

BIO-DEGRADABLE FILAMENT BASED ON PLA/THERMOPLASTIC CASSAVA STARCH BLENDS WITH POLY(ETHYLENE GLYCOL): A STUDY OF PHYSICAL, MECHANICAL CHARACTERIZATION, AND PRINTABILITY ASSESSMENT

Tien Trung Vu¹, Huy Lam Pham¹, Duc Bau Nguyen¹, Chi Thien Pham¹, Thien Dinh Le¹, Chi Nhan Ha Thuc^{1*}

¹ Faculty of Materials Science and Technology, University of Science, Vietnam National University-Ho Chi Minh City, 227 Nguyen Van Cu, Ward 4, District 5, Ho Chi Minh City, Vietnam.

Email: htcnhan@hcmus.edu.vn

ABSTRACT

This study prepared a Biodegradable composite based on Polylactide Acid/ Thermoplastic Starch and the plasticizing effect by PEG with different molecular weights (MW) = 1000, 6000 were studied. The effect of MW of PEG on PLA was characterized in terms of mechanical properties, melting flow index (MFI), thermal, and morphology was investigated. The results presented structure and properties of PLA/PEG blends were different from virgin PLA and the MW of PEG is 6000 g/mol increasing the Flexural strength, Impact strength, and increased toughness of PLA virgin. By DSC analysis, it was found that the glass transition temperature (T_g) and cold crystallization temperature decreased in the case of the PLA/PEG blend, with 7% PEG6000 loading with PLA virgin, the blend PLA/PEG6-7 showed optimum structural and mechanical properties to develop the bio-degradable blended with cassava thermoplastic starch (TPS). Besides, the bio-degradable composite from PLA/PEG6-7 with Cassava thermoplastic starch (TPS) was studied, with increasing the content of TPS in the blend. The result indicates that the blend PLA/PEG6-7 with 10wt.% TPS shows a high melt flow index (MFI) higher than PLA virgin, and the mechanic properties of this blend are enough to produce the 3D filament.

Keywords: Fused filament fabrication (FFF), 3D printing, cassava thermoplastic starch, polylactide, biodegradability.

INTRODUCTION

Due to its superior biodegradability, biocompatibility, mechanical strength, and availability of renewable resources, poly(lactic acid) (PLA) has attracted greater attention. ability to process thermoplastics, among other things [1, 2]. As a result, its uses in the fields of medicine, pharmaceuticals, packing, clothes, and the environment have generated considerable interest. However, PLA's intrinsic brittleness, increased cost, and relatively slow rate of deterioration restrict its potential uses. The polymer PLA is relatively rigid and brittle and plasticizers are widely used in the plastics industry to improve the processability, flexibility, and ductility of PLA. One of the most popular methods to reduce the brittle of PLA and increase its toughness is by blending with other polymers, PLA has been plasticized with a number of polymers, including polycaprolactone [3], polyamide 11 [4], poly(propylene glycol),

polystyrene [5], poly(ethylene glycol) (PEG)[8], etc.

Polyethylene glycol (PEG) is one of the most effective plasticizers for PLA, due to its great biocompatibility, dispersibility, high mobility, non-toxicity, and hydrophilicity. According to several studies adding PEG can considerably increase the mobility of the PLA molecular chain while still maintaining biodegradability and biocompatibility. There have been a number of research recently on PLA/PEG blends that analyze the impact of PEG on the structural, thermal, and mechanical properties of PLA fabricated polylactic acid-polyethylene glycol-hydroxyapatite composite for interference screws used for the treatment of ruptured ligaments.

In previous research, we produced a biodegradable and compostable polymer composition based on materials from a natural and renewable source PLA and thermoplastic potato starch (TPS) that has been modified with epoxidized soybean oil (ESO) [6]. As a result, we

increased the ductility of PLA and decreased the price of the granulation without compromising the capacity to decompose and biodegrade. The next step was to conduct a study on the composition's potential as a sustainable component for 3D printing.

This article studies the effect of molecular weight (MW) of PEG (1000, 6000 g/mol) on the properties of virgin PLA. Besides, blends of PLA/TPS were prepared to combine the good mechanical properties of PLA with the low cost of thermoplastic starch. PEG as a compatible additive was used in order to achieve strong interfacial adhesion improving the thermal and mechanical properties. The filament based on the PLA/PEG/TPS blend is also investigated.

EXPERIMENTAL

Materials

PLA (LX175, MFR = 7 g 10 min⁻¹ at 190°C and 2.16 kg) was purchased from Total Corbion (USA), Poly Ethylene Glycol (PEG1000) with a weight-average molecular weight of 1000 g/mol obtained from Shanghai Zhanyun Chemical (China). Poly Polyethylene glycol (PEG6000) with a weight-average molecular weight of 6000 g/mol obtained from Himedia (China). Cassava Starch (5% moisture) was obtained from Vietnam and Glycerol (purified 99% from Malaysia).

Preparation of the PLA/PEG Blends

The PLA/PEG blends were prepared by melt blend by a laboratory mixer (Internal mixer: MX300-Thailand) at 190°C with a capacity of 200g. Blending was carried out with the speed of the rotor of 40rpm and the total time for blending was 10 minutes. PLA was initially melted for 8 minutes and then continue to add PEG1000, or PEG6000 into the internal mixer for another 2 minutes. The blend was compression-molded at 190°C and then cooled through a cold compression process at 20°C (COMPRESSION MACHINE: PR2D-W300L350-PM-WCL-HMI) with a flat and rectangular mold into the sheet with 1 and 4mm for subsequent test.

Preparation of the PLA/PEG/TPS Blends

The starch was dried at 80°C for 3 hours to remove moisture. Thermoplastic starch (TPS) is obtained by melt blend with Glycerin, used as a plasticizer. The ratio of TPS component was followed with 2, 10, 15, and 20 wt% mixed with PLA/PEG blend.

Filament (PLA/PEG/TPS) Formation

The filament extruder system used to obtain the PLA/PEG/TPS filament ($\varnothing = 1.75$ mm), a single-screw extruder (L/D = 32, with three heating barrel zones and one die head zones), Cooling batch filled with water (20°C) and chiller to control the temperature and equipped a laser diameter measurement system (laser sensor accuracy 0.01 mm), and a winding system. The extrusion temperature of each heating zone was installed at 140 °C, 150 °C, 170 °C and for die head zones at 170 °C. The extrusion speed was set at 15 rpm.

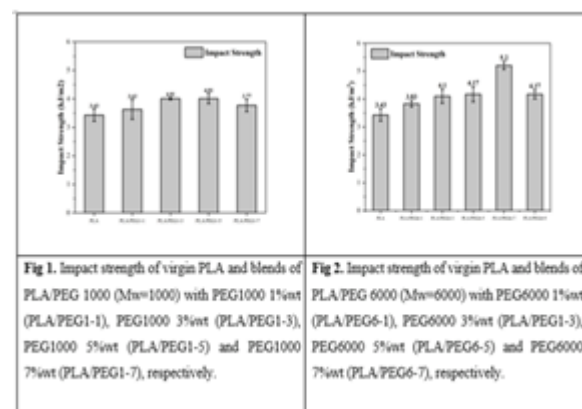
Testing and analysis

Fourier transform infrared (FTIR) spectrometer, Mechanical properties, Melt flow index (MFI), Differential scanning calorimetry (DSC), Scanning electron microscopy (SEM).

RESULTS AND DISCUSSION

Mechanical property of PLA/PEG

The effect of molecular weight or PEG on mechanical properties of PLA was studied. Fig 1 and 2 represent the impact strength of sample virgin PLA and blends of PLA with different molecular weight of PEG. It can be seen that increasing the PEG content, both different molecular weights, PEG1000 and PEG6000, the impact strength of the blends all increase when adding the PEG. Which indicated that the plasticizer effect of PEG and enhances the mobility of PLA chains, thereby improving the crystallization and impact strength of PLA.[7]



Melt Flow Index (MFI) of PLA/PEG

Effect of the content and MW of PEG on melt flow index (MFI) of PLA/PEG blends is shown in Fig 3 and Fig 4. Although just a small quantity of PEG of both molecular weights is added, it can be seen that the MFI of the blends for PEG1000 and PEG6000 is significantly increased, indicating that the added PEG1000 or PEG6000

effectively improves the plasticization of the blends, reduce the intermolecular force and enhance the mobility of the macromolecular chain, decrease the melt viscosity, as discussed previously.

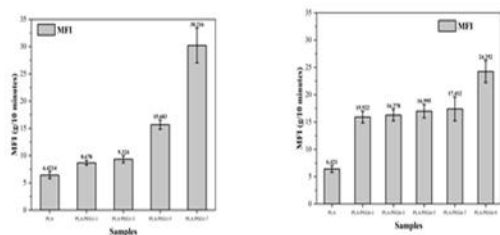


Fig 3. MFI of virgin PLA and blends of PLA/PEG 1000 ($M_n=1000$) with PEG1000 1%wt (PLA/PEG1-1), PEG1000 3%wt (PLA/PEG1-3), PEG1000 5%wt (PLA/PEG1-5) and PEG1000 7%wt (PLA/PEG1-7), respectively. Fig 4. MFI of virgin PLA and blends of PLA/PEG 6000 ($M_n=6000$) with PEG6000 1%wt (PLA/PEG6-1), PEG6000 3%wt (PLA/PEG6-3), PEG6000 5%wt (PLA/PEG6-5) and PEG6000 7%wt (PLA/PEG6-7), respectively.

FTIR of PLA/PEG blends

Figure 5 shows FTIR spectra of virgin PLA, PEG6000 and PLA/PEG blends with 7wt% PEG6000. PLA shows characteristic stretching vibrations of the C=O, Symmetric and asymmetric stretching vibrations of $-CH_3$ group, C-O stretching vibrations at wavenumbers 1714, 2996, 2945, and 1080cm^{-1} . Bending vibrations for $-CH_3$ asymmetric and $-CH_3$ symmetric have been identified at 1466 and 1339cm^{-1} , respectively [8]. Meanwhile, IR spectra of PEG show the broad peak was observed at 3399cm^{-1} , which corresponds to terminal hydroxyl group of chain of polymer. For the spectrum of the PLA/PEG6-7 blend, the characteristic vibrational shows almost same typical absorption peaks of the function group as virgin PLA and PEG, besides, the vibrational peaks of the functional group $-OH$ in the PEG spectra shifts from 3399cm^{-1} to 3400cm^{-1} , which indicates that an interaction is formed between the PLA and PEG segments. In addition, the characteristic C-H stretching vibration peak shifts from 2945cm^{-1} in the PLA spectrum to 2943cm^{-1} in the PLA/PEG6-7 blend spectrum, the C=O stretching vibration peak of the blend move to lower position. These shifts of absorption peaks indicate that there is intermolecular interaction (hydrogen bond) between PEG6000 and PLA in the matrix polymer.

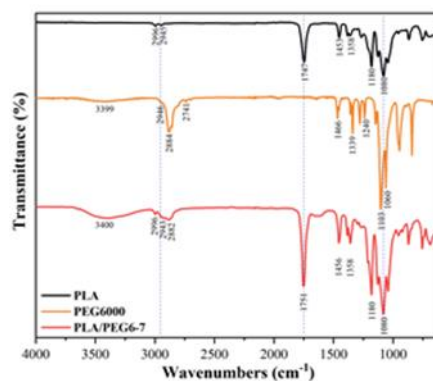


Fig 5. FTIR spectra of virgin PLA, PEG6000 and PLA/PEG6000 blend with 7wt% PEG6000 (PLA/PEG6-7), respectively

Differential Scanning Calorimetry of PLA/TPS/PEG

The glass transition, melting point, cold crystallization enthalpy and degree of crystallinity for the plasticized PLA with TPS were found to be 43°C , 154°C , 79.58J/g and 28.57%, respectively. The reducing of degree of crystallinity (χ_c) due to the appear of TPS was reduced mobility of PLA chains and reduced the crystallinity of PLA matrix, this result have shown in the cold crystallization enthalpy (a slight reducing from 81.3J/g (PLA/PEG6-7) to 79.58J/g (PLA/PEG6-7/TPS10)). In addition, the melting peak of virgin PLA is observed the presence of double peaks. However, the melting peak of plasticized PLA (PLA/PEG6-7) becomes narrow and appear a shoulder peak and same results with PLA/PEG6-7/TPS10 blend. That proves that the plasticizer PEG is also effective on the crystalline of PLA and enhance the interfacial interaction of plasticized PLA with TPS.

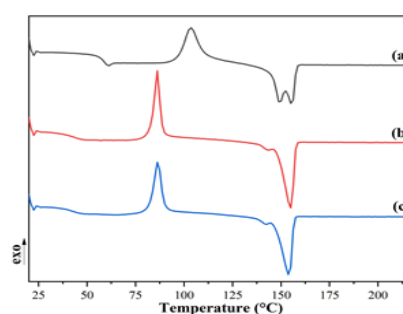


Fig 6. DSC thermograms of (a) virgin PLA, (b) PLA/PEG6-7 and (c) PLA/PEG6-7/TPS10, respectively. Results for the second heating stage (25°C - 220°C , $10^\circ\text{C}/\text{minutes}$)

Morphological Analysis

Figure 7 are the results of SEM micrographs of the fracture surfaces of PLA/PEG6-7 and PLA/PEG6-7/TPS10 samples after the samples were tested by impact method. It can be shown that the compositions with PEG shows the

smooth surface and without any defects or agglomerate areas can be observed, which indicated plasticizer PEG make a good compatible and uniformity with PLA matrix.

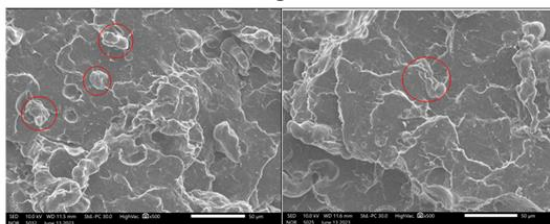


Fig 7. SEM micrographs of fracture morphology of the plasticized PLA with 10wt% TPS (PLA/PEG6-7/TPS10) blend after impact testing

CONCLUSION

In this work, we presented the effect of PEG with different molecular weight (MW=1000, 6000) on the mechanical properties, MFI of the PLA/PEG blend. In addition, It showed that PEG, as plasticizer for PLA, had more effective compatible additive for PLA and TPS. Mixing PLA, PEG and TPS has improved the flowability of the blend. Furthermore, we shown the blend of PLA/PEG6-7/TPS10 with 10wt% TPS was stable to make the filament which shows a comparable quality to commercial filament

Acknowledgment

This research was funding supported by Vietnam National University Ho Chi Minh City (VNU-HCM) under grant number T2023-65.

References

- [1] A. Kumar, K. Mohanta, D. Kumar, O. Parkash, *Properties and industrial applications of rice husk: a review*, Emerging technology and advanced engineering **2** (2012) 2250-2459.
- [2] S. Inkinen, M. Hakkarainen, A. Albertsson, A. Sodergard, *From lactic acid to poly(lactic acid) (pla): characterization and analysis of pla and its precursors*, Biomacromolecules **12** (2011) 523-532.
- [3] K. M. Nampoothiri, R. P. John, N. R. Nair, *An overview of the recent developments in polylactide (pla) research*, Bioresource Technology **101** (2010) 8493-8501.
- [4] I. E. Yuzay, R. Auras, H. Soto Valdez, S. Selke, *Effects of synthetic and natural zeolites on morphology and thermal degradation of poly(lactic acid) composites*, Polymer Degradation and Stability **95** (2010) 1769-1777.

- [5] M. Murariu, P. Dubois, *Pla composites: from production to properties*, Advanced Drug Delivery Reviews **107** (2016)17-46.
- [6] Przybytek, A.; Sienkiewicz, M.; Kucinska-Lipka, J.; Janik, H.; *Preparation and Characterization of Biodegradable and Compostable PLA/TPS/ESO Compositions*. Ind. Crops Prod. **122** (2018) 375.
- [7] B. Wang, K. Hina, H. Zou, D. Zuo, *Thermal, Crystallization, Mechanical and decomposition properties of poly(lactic acid) plasticized with poly(ethylene glycol)*, Vinyl and Additive Technology, **24** (2018) 154-163.
- [8] B. W. Chieng, N. A. Ibrahim, W. M. Z. W. Yunus & M. Z. Hussein, *Poly(lactic acid)/poly(ethylene glycol) polymer nanocomposites: effects of graphene nanoplatelets*, Polymers **6** (2014) 93-104.

SYNTHESIS OF REDUCED GRAPHENE OXIDE/V₂O₅ MICROFLOWERS COMPOSITES FOR REMOVAL OF HYDROGEN SULFIDE GAS

Nhu Quynh Thi Nguyen, Diep Ngoc Le, Thang Minh Bui, Chien Mau Dang, Tin Chanh Duc Doan

Institute for Nanotechnology, Community 6, Linh Trung Ward, Thu Duc City, Ho Chi Minh City, Vietnam;

Vietnam National University Ho Chi Minh City, Ho Chi Minh City, Vietnam

Email: Indiep@vnuhcm.edu.vn

ABSTRACT

Studies show that chemically modified graphene and graphene can be applied to air and water purification. Besides, V₂O₅ is known as a candidate for gas sensors. Therefore, this article presents the fabrication process and evaluates the H₂S adsorption capacity of composite materials made of like-flower V₂O₅ (V₂O₅(F)) and reduced graphene oxide. Graphite oxide was prepared by Hummer's improved method and then reduced to reduced graphene oxide (rGO). V₂O₅(F)-rGO composite materials were synthesized by the hydrothermal method, and the change in V₂O₅:GO ratio and hydrothermal time were investigated to evaluate their influence on the structure of composite materials. V₂O₅(F)-rGO materials were analyzed using FESEM, RAMAN, TGA, etc. The resulting V₂O₅(F)-rGO material has a structure of 1-2 nm sized V₂O₅ flowers covering reduced layers of graphene oxide. Composite V₂O₅(F)-rGO is capable of adsorbing H₂S gas, with the largest total adsorption capacity reaching 2.64 mg/g after 50 minutes of adsorption. V₂O₅ composite material has the potential to remove H₂S gas from biogas with a simple, economical synthesis process.

Keywords: reduced graphene oxide, modified reduced graphene oxide, flower-like structure, V₂O₅, H₂S adsorption.

INTRODUCTION

Hydrogen sulfide (H₂S) is a gas that occurs naturally in crude oil, natural gas, hot springs, and some foods and is also produced through bacterial decomposition in human and animal waste. However, high concentrations of H₂S can affect the environment [1]. Therefore, the issue of H₂S treatment needs attention. Adsorption is a common method to remove H₂S. There are two types of adsorption: physical adsorption and chemisorption. In chemisorption, the H₂S is adsorbed much more strongly. This is because the sulfur end of the H₂S molecules is more negative than the hydrogen [2,3].

V₂O₅, also known as vanadium pentoxide, is a transition metal oxide that possesses advantageous properties for gas sensing applications [4]. These properties include its widespread availability, excellent catalytic activity, distinctive electrical characteristics, and high conductivity. Reduced graphene oxide (rGO) is an rGO graphite-based material with high surface area and unique electrical properties that can be beneficial for gas sensors [5,6].

This study presents the process of synthesizing composite materials from like-flower rGO and V₂O₅ that have many advantages in gas adsorption [7]. Since then, H₂S adsorption has been applied to biogas filtration. The advantage of this process is that the synthesis process from graphite material is cheap, abundant, economical, has high economic efficiency, etc., with potential for mass production at low cost.

EXPERIMENTAL

Graphite oxide synthesis

Graphite oxide was prepared by the Hummers method [8]. Natural graphite (5 g) and sulfuric acid (200 mL) were first mixed in a beaker cooled by an ice bath. Then, potassium permanganate (20 g) and sodium nitrate (5 g) were slowly added to the mixture. The mixture was kept at 40 °C and stirred for 3 hours. After 3 hours, 200 ml of DI water was slowly added to dilute the mixture. The mixture was stirred for 15 minutes, and then it was oxidized with 1.2 liters of a 2% hydrogen peroxide solution. Graphite oxide subsequently settled as sediment after sitting for 16 hours. The

Graphite oxide layer was washed and decanted with 1.2 liters of a 3% hydrochloric acid solution three times. Finally, the dried graphite oxide powder was obtained by drying the sediment at 60 °C.

Reduced graphene oxide synthesis (rGO)

0.1 g of graphite oxide was dispersed in 100 mL of DI water by sonication for 1 hour into a graphene oxide solution. Then, 1 g of sodium borohydride (NaBH₄) was added to reduce graphene oxide to reduced graphene oxide (rGO). The mixture was stirred and heated at 100°C for 2 hours with a circulation system. Subsequently, the reaction mixture was filtered, washed with DI water, and dried at 40°C for 12 h to obtain reduced graphene oxide.

Preparation of V₂O₅ flower-like (V₂O₅(F))

7mL of hydroperoxide (H₂O₂) was dripped slowly in 30 mL of VOC₂O₄ solution 0.083 M (2.5 mmol) under magnetic stirring. Subsequent to 30 minutes of stirring, 90 mL of ethanol (C₂H₅OH) was added to the solution and continued stirring for 30 minutes. Then, the resulting solution was transferred into a Teflon-lined autoclave (150 mL) and hydrothermal treatment at 180°C for 24 hours. Following this, the results were collected by centrifugation, washed three times with ethanol, and dried. After that, the powder was calcined at 350 °C for 4 hours to obtain V₂O₅ flower-like.

Preparation of V₂O₅(F)-rGO

Graphite oxide was exfoliated via ultrasonication with 30mL of of VOC₂O₄ solution 0.083 M (2.5 mmol). 7mL of hydroperoxide (H₂O₂) was dripped slowly in solution under magnetic stirring. Subsequent to 30 minutes of stirring, 90mL of ethanol (C₂H₅OH) was added to the solution and continued stirring for 30 minutes. Then, the resulting solution was transferred into a Teflon-lined autoclave (150mL) and hydrothermal treatment at 180°C for 24 hours. Following this, the results were collected by centrifugation, washed three times with ethanol, and dried. The experiment was conducted with weight-different GO, specifically 0.0045g (V₂O₅(F)-rGO-1) and 0.045 g (V₂O₅(F)-rGO-2).

Adsorption experiment

Weigh 0.025 g of material sample into the middle of a horizontal test tube, 10 cm long, 0.7 cm inner diameter. The H₂S+N₂ gas mixture passes through the tube at a flow rate of 100 ml/min, the initial concentration of the H₂S gas

mixture is about 50 ppm. The adsorption time was investigated for 50 minutes. The H₂S gas sensor is used to measure the change in gas concentration at the outlet over time.

The total adsorption capacity (q) is determined according to the formula:

$$q = \frac{\rho v}{m} \int_0^t (C_0 - C) dt \quad (1)$$

where ρ is the density of H₂S gas, v is the volumetric flow rate, m is the adsorbent mass C_0 is the H₂S concentration at the inlet, and C is the H₂S concentration at the outlet at time t [9]

Material evaluation

The synthesized material was surface evaluated using field emission scanning electron microscopy (FE-SEM). The material structure of material was evaluated by the following methods: Raman spectroscopy.

RESULTS AND DISCUSSION

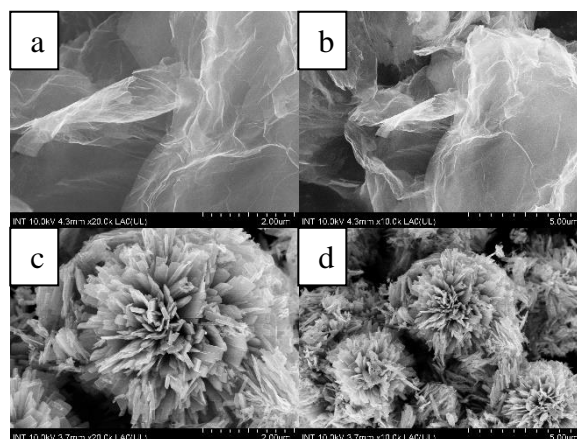


Figure 1. Fesem images of rGO (a, b) and V₂O₅(F) (c, d)

Figure 1 is a fesem photo of rGO and flower-like V₂O₅. From image 1 a,b) the layered structure of rGO can be observed. Graphene layers of rGO are several micrometers in size, about 10 nanometers thick. The separated and non-overlapping layers indicate a good reduction of graphite oxide to reduced graphene oxide. Fesem images of V₂O₅ show that V₂O₅ flowers are about 5 micrometers in diameter. The rod-like petals are about 2-3 micrometers long, 100 nanometers wide, and about 30-50 nm thick.

Figure 2 is a fesem images of V₂O₅(F)-rGO-1 and V₂O₅(F)-rGO-2. The results show the layered structure of rGO and flower-like V₂O₅ attached between the graphene layers. However, the size of the V₂O₅ flower is only about 1-2 um, the size and number of petals are smaller than the V₂O₅(F) sample. The V₂O₅(F)-rGO-1 sample has a larger

V_2O_5 :rGO ratio, so the number of V_2O_5 flowers attached to the graphene layers is also larger.

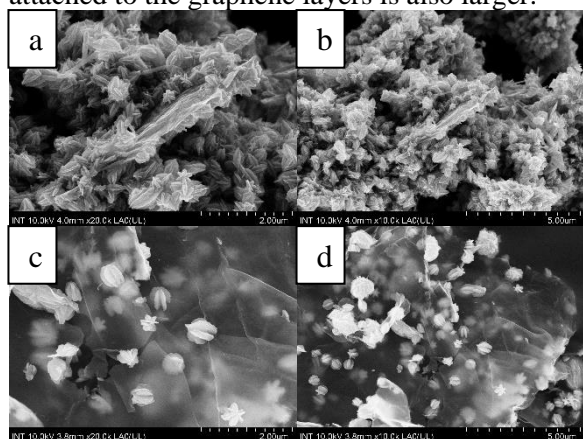


Figure 2. Fesem images of $V_2O_5(F)$ -rGO-1 (a, b) and $V_2O_5(F)$ -rGO-2 (c, d)

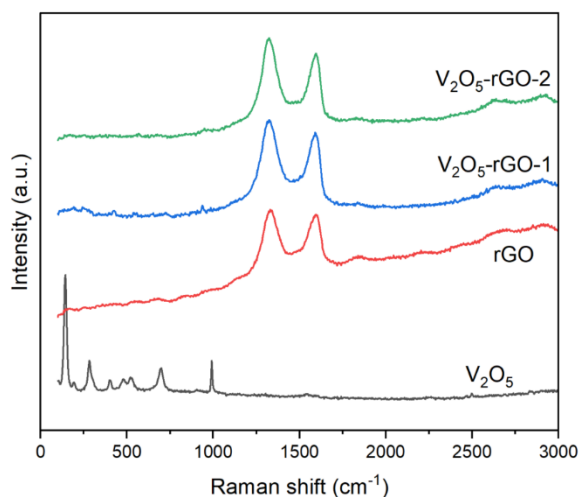


Figure 3. Raman spectra of $V_2O_5(F)$ -rGO-1 and $V_2O_5(F)$ -rGO-2

Raman spectrum analysis results show the existence of reduced graphene oxide layers in the structure of V_2O_5 -rGO samples. The Raman spectrum of V_2O_5 -rGO samples shows characteristic D and G peaks at 1330 and 1602 cm^{-1} , respectively, similar to the Raman spectrum of reduced graphene oxide [10,11]. Peak G represents the vibration of carbon atoms linked together by sp^2 hybridization, while peak D represents the vibration of carbon atoms with sp^3 hybridization.

H_2S adsorption results for material samples measured with an H_2S - N_2 gas mixture with an initial concentration of 50 ppm and an approximate flow rate of 100 ml/min are shown in Figure 4. The total adsorption capacity (q) calculated using Equation (1) is summarized in Table 1. Sample V_2O_5 has the lowest adsorption

capacity, which is the sample without rGO. Sample $V_2O_5(F)$ -rGO-2 is the sample with the best adsorption capacity and is also the sample with more rGO. This result shows that the adsorption potential is improved when adding rGO to the $V_2O_5(F)$ -rGO composite.

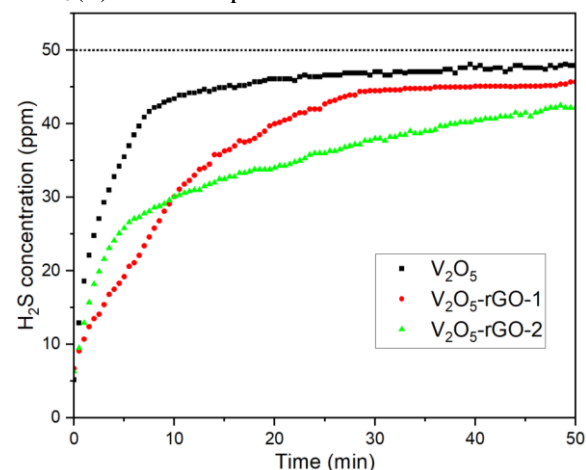


Figure 4. Results of H_2S adsorption tests for $V_2O_5(F)$ -rGO composite

Table 1. Total H_2S adsorption capacity (q) of the $V_2O_5(F)$ -rGO composite

Sample	V_2O_5	$V_2O_5(F)$ -rGO-1	$V_2O_5(F)$ -rGO-2
q (mg/g)	1.413	2.267	2.641

CONCLUSION

The $V_2O_5(F)$ -rGO material can be synthesized by the hydrothermal method to be used as an H_2S adsorbent. The H_2S adsorption capacity of the material increases when increasing the amount of rGO in the $V_2O_5(F)$ -rGO mixture. The total adsorption capacity after 50 minutes of $V_2O_5(F)$ -rGO-2 material is 2.64 mg/g , nearly two times higher than that of the V_2O_5 sample. However, because the adsorption time of the material is still short, it is necessary to investigate further adsorption conditions such as adsorbent content, flow rate, initial concentration, etc. to increase the adsorption efficiency of the V_2O_5 material.

Acknowledgment

The authors highly appreciate the financial support of Vietnam National University Ho Chi Minh City for this research under the grant number C2023-32-01.

References

- [1] F.I.M. Ali, F. Awwad, Y.E. Greish, S.T. Mahmoud, *Hydrogen sulfide (H₂S) gas sensor: A review*, IEEE Sens J. **19** (2018) 2394-2407.
- [2] G. LIST, *Bleaching and Purifying Fats and Oils. 2*, (2009).
- [3] M. Khabazipour, M. Anbia, *Removal of hydrogen sulfide from gas streams using porous materials: A review*, Ind Eng Chem Res. **58** (2019) 22133-22164.
- [4] V. Amiri, H. Roshan, A. Mirzaei, M.H. Sheikhi, *A review of nanostructured resistive-based vanadium oxide gas sensors*, Chemosensors. **8** (2020) 105.
- [5] D.G. Papageorgiou, I.A. Kinloch, R.J. Young, *Graphene/elastomer nanocomposites*, Carbon N Y. **95** (2015) 460-484.
- [6] P. Avouris, C. Dimitrakopoulos, *Graphene: synthesis and applications*, Materials Today. **15** (2012) 86-97.
- [7] K. Karthik, K. Pradeeswari, R.M. Kumar, R. Murugesan, *Microwave-assisted V₂O₅ nanoflowers for efficient lithium-ion battery*, Materials Research Innovations. (2019).
- [8] C. Botas, P. Álvarez, P. Blanco, M. Granda, C. Blanco, R. Santamaría, L.J. Romasanta, R. Verdejo, M.A. López-Manchado, R. Menéndez, *Graphene materials with different structures prepared from the same graphite by the Hummers and Brodie methods*, Carbon N Y. **65** (2013) 156-164.
- [9] H. Setiawan, M. Sakamoto, T. Fujisaki, S.M. Lyth, Y. Shiratori, *Development of a sustainable nitrogen-doped biochar desulfurizer for solid oxide fuel cell systems*, Biomass Bioenergy. **167** (2022) 106631.
- [10] J. Ribeiro-Soares, M.E. Oliveros, C. Garin, M. V David, L.G.P. Martins, C.A. Almeida, E.H. Martins-Ferreira, K. Takai, T. Enoki, R. Magalhães-Paniago, A. Malachias, A. Jorio, B.S. Archanjo, C.A. Achete, L.G. Cançado, *Structural analysis of polycrystalline graphene systems by Raman spectroscopy*, Carbon N Y. **95** (2015) 646-652.
- [11] G. Surekha, K.V. Krishnaiah, N. Ravi, R. Padma Suvarna, *FTIR, Raman and XRD analysis of graphene oxide films prepared by modified Hummers method*, J Phys Conf Ser. **1495** (2020) 12012.

INTERLAYER COUPLING AND GIANT MAGNETORESISTANCE IN A SYMMETRIC SPIN-VALVE STRUCTURE BASED ON PERPENDICULARLY ANISOTROPIC [Co/Pd] MULTILAYERS

Thi Ngoc Anh Nguyen^{1,2}, Julia Kasiuk³, Wen-Bin Wu⁴, Janusz Przewoźnik⁵, Czesław Kapusta⁵, Ivan Svito³, Khanh Tung Do¹, Thanh Huong Nguyen¹, Quang Ngan Pham¹, Hong Ky Vu¹, Johan Åkerman⁶

¹Institute of Materials Science, Vietnam Academy of Science and Technology, Hanoi, Vietnam;

²Graduate University of Science and Technology, Vietnam Academy of Science and Technology, Hanoi, Vietnam;

³Faculty of Physics, Belarusian State University, Minsk, Belarus

⁴College of Physical Science and Technology, Dalian University, Dalian, China

⁵AGH University of Krakow, Faculty of Physics and Applied Computer Science, Department of Solid State Physics, Krakow 30-059, Poland

⁶Department of Physics, University of Gothenburg, Göteborg, Sweden

Email: ngocanhnt.vn@gmail.com

ABSTRACT

In the present study, interlayer coupling and magnetoresistance were analyzed in an FM/NM/FM spin-valve (SV) structure with two symmetric [Co/Pd]_{x2} ferromagnetic (FM) layers with strong perpendicular magnetic anisotropy separated by a nonmagnetic (NM) Pd_{8 nm} spacer. The ferromagnetic interlayer coupling revealed between the two FM layers enhances with decreasing temperature due to the extensive Pd polarization. The giant magnetoresistance is also shown to demonstrate strong temperature dependence, while the corresponding field region with the opposite orientation of the FM magnetic moments can be tuned by changing the thickness of the Pd spacer or by pinning the FM moments through interfacial exchange coupling with an antiferromagnetic (AFM) IrMn layer.

Keywords: multilayered films, perpendicular magnetic anisotropy, giant magnetoresistance, interlayer coupling, spin valves

INTRODUCTION

Spin valves (SVs), consisting of two FM layers separated by an NM spacer, are a core part of magnetic memory, logic and sensor devices exploiting an effect of giant magnetoresistance (GMR) for switching between high and low resistance states [1]. Thin films with perpendicular magnetic anisotropy (PMA) are promising candidates for magnetic memory and spintronics applications as functional elements of SVs, magnetic tunnel junctions, synthetic antiferromagnets [2]. They demonstrate high thermal and magnetic stability, sharp and adjustable magnetization switching parameters, strong and tunable magnetic interaction between the FM layers [3]. The present study is focused on the analysis of interlayer coupling and magnetoresistance (MR) in an FM/NM/FM spin-valve (SV) structure, which contains two symmetric [Co/Pd]_{x2} FM layers with strong PMA separated by the Pd NM spacer as well as the

possibility of tuning switching fields of the FM layers.

EXPERIMENTAL

The thin FM/NM/FM films of the Ta₅/Pd₅/[Co_{0.5}/Pd_{1.2}]_{x2}/Co_{0.5}/Pd₈/[Co_{0.5}/Pd_{1.2}]_{x2}/Co_{0.5}/Pd₃/Ta₅ composition (thickness is specified in nm), denoted as [Co/Pd]/Pd/[Co/Pd], were deposited on flat wafers of thermally oxidized silicon Si/SiO₂ using ultra-high vacuum magnetron sputtering (*AJA International, Inc.*) at room temperature (RT). The IrMn_{6 nm} AFM layer was also deposited on top or under the FM/NM/FM structure in some of the films studied for pinning the FM magnetic moments. The top Pd_{3 nm}/Ta_{5 nm} bilayer was used to prevent oxidation of the MLs, while the bottom Ta_{5 nm}/Pd_{5 nm} bilayer serves to promote *fcc* (111) texture and to improve the PMA of the following [Co/Pd] multilayers (MLs) [3]. The magnetic and magnetoresistive properties of the films were characterized using

the vibrating sample magnetometry (VSM) and electric resistivity options of the Quantum Design PPMS in the temperature range $T = 2\text{-}300\text{ K}$ and a magnetic field range $H = 0\text{-}90\text{ kOe}$.

RESULTS AND DISCUSSION

The magnetization reversal of the [Co/Pd]/Pd/[Co/Pd] film was analyzed by measuring their anomalous Hall effect (AHE) voltage as a function of a perpendicular external field H . The corresponding $U_{\text{AHE}}(H)$ curves are shown in Fig. 1(a) for different temperatures. As can be seen from the figure, each of the FM layers, bottom and top, switches its magnetization M separately that yields the field regions with the opposite orientation of magnetization of the layers (plateau in the $U_{\text{AHE}}(H)$ curves). A significant increase in the film resistance due to the GMR effect is characteristic of these field regions (Fig. 1(b)).

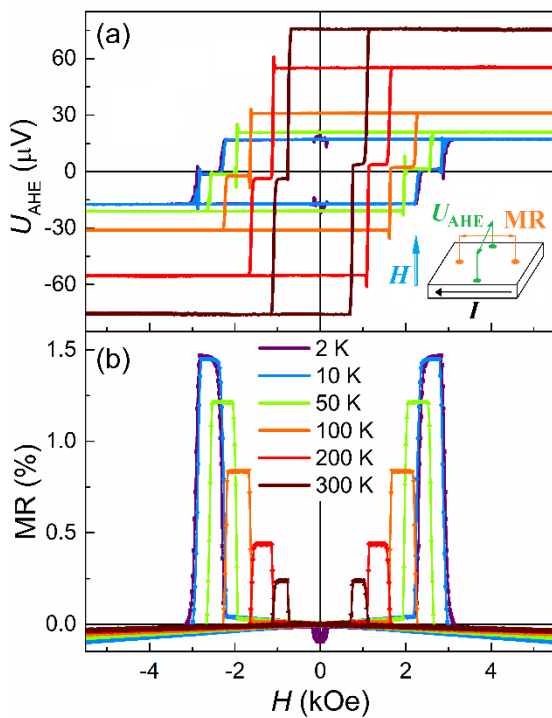


Figure 1. Field dependences of the AHE voltage (a) and MR (b) of the [Co/Pd]/Pd/[Co/Pd] film measured at different temperatures in a perpendicular field H ; sketch in inset to (a) shows configuration of probes for U_{AHE} and MR measurements

The MR(H) curves show sharp peaks with a plateau at the top, which arise as the result of an abrupt magnetization reversal and a stable difference in the coercive field H_C of the FM

layers with temperature. The latter is ensured by different thicknesses of the Pd sublayers. A thinner Pd spacer ($t_{\text{Pd}} \leq 5\text{ nm}$) (not shown here) provides joint switching of the FM layers due to their rigid coupling, with no steps being observed in the magnetization reversal curves. A significant increase in the GMR effect with decreasing temperature is mainly associated with the low-temperature alignment of the magnetic moments in two FM layers along the film normal due to a decrease in their temperature-induced fluctuations [1], since their collinear orientation being crucial for the GMR effect.

Despite separate switching, the FM layers in the film studied show ferromagnetic interaction, as evidenced by the negative shift of minor hysteresis loops [4] corresponding to the magnetization reversal of the bottom FM layer with a stable orientation of magnetization of the top FM layer (Fig. 2). This shift is -24 Oe at RT and increases up to -53 Oe at $T = 2\text{ K}$. Intensifying the low-temperature interlayer coupling relates to the FM-proximity induced Pd polarization, which expands with decreasing temperature and provides more strong indirect FM interaction between the [Co/Pd] layers through the magnetically polarized Pd atoms [5]. Simultaneously, Pd polarization is responsible for the interlayer coupling between the FM layers arising through a quite thick Pd NM spacer of 8 nm , whereas for such a thick spacer made of a non-polarizable metal, attenuation of the interaction would be expected [6].

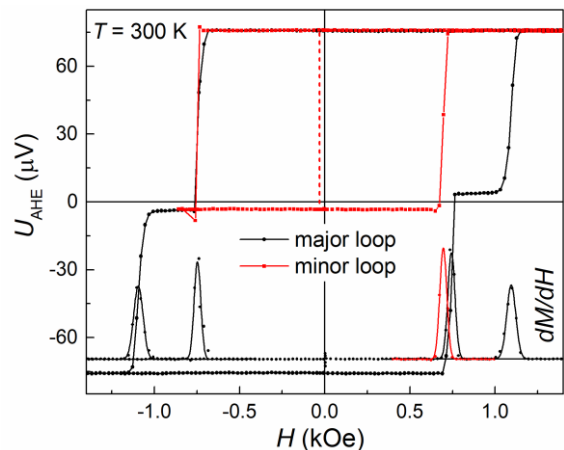


Figure 2. Room temperature $U_{\text{AHE}}(H)$ curve of the [Co/Pd]/Pd/[Co/Pd] film accompanied by its minor hysteresis loop (dashed red line indicates its shift) and their first derivatives

The possibility to manipulate switching parameters between parallel and antiparallel orientation of FM layers in SVs expands their applicability in MR devices. The fields corresponding to switching between high and low resistance can be tuned by varying the thickness of the Pd spacer and/or Pd sublayer, while their correlated change allows expanding the field range of the AFM ordering between the FM layers. In addition, pinning the magnetic moments of FM layers (top or bottom, Fig. 3) by an exchange-coupled AFM layer is shown to shift effectively their switching fields and diverse the configuration of magnetic moments in the film in the high-resistance state.

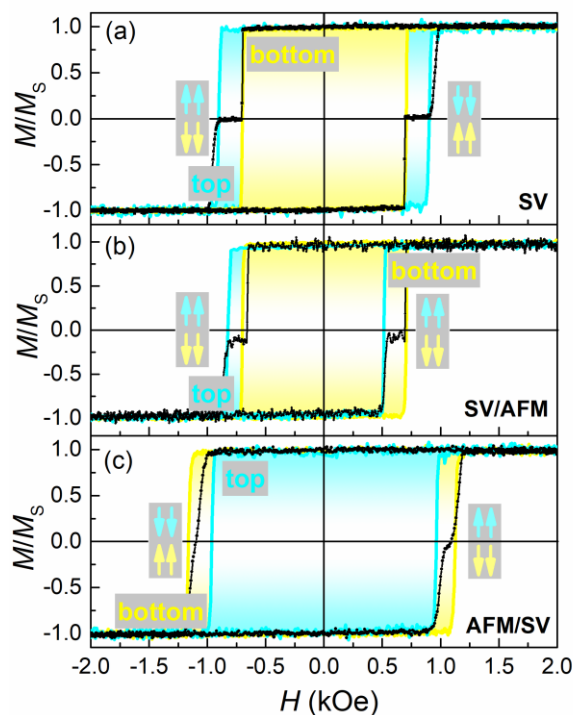


Figure 3. (a) RT magnetization curves (black lines) of the [Co/Pd]/Pd/[Co/Pd] (SV) (a), [Co/Pd]/Pd/[Co/Pd]/IrMn (SV/AFM) (b) and IrMn/[Co/Pd]/Pd/[Co/Pd] (AFM/SV) (c) films; color curves in (a) show the $M(H)$ dependences of $Pd_{iPd}/[Co/Pd]$ films ($t_{Pd} = 5$ and 8 nm), corresponding to the bottom FM (yellow) and top FM (blue) layers of SV structure; similarly, in (b) and (c), blue and yellow curves correspond to magnetization reversal of top and bottom FM layers, respectively. The sketches show the magnetic ordering in the FM layers in the field ranges corresponding to the plateaus on the $M(H)$ curves

Namely, depositing the IrMn AFM layer above the top [Co/Pd] FM layer leads to the exchange bias shift of the hysteresis loop of the top FM layer without any significant changes of the loop corresponding to the bottom FM layer. In doing so, both plateaus of the $M(H)$ curve are characterized by up/down antiparallel alignment of magnetic moments of the top/bottom FM layers (Fig. 3(b)), in contrast to the [Co/Pd]/Pd/[Co/Pd] film without AFM layer, where up/down spin configuration in the negative fields changes to the down/up configuration in the positive fields (Fig. 3(a)). In contrast, depositing the IrMn AFM layer under the bottom [Co/Pd] FM layer of the SV structure leads to a significant increase in the H_C field of the bottom FM layer due to the pinning of its magnetic moments by the AFM layer. Because of the ferromagnetic coupling between the FM layers, the H_C parameter of the top FM layer is also increased, but it is now less than that of the bottom layer, in contrast to the unpinned film. Therefore, the magnetic moments orientation in the top/bottom FM layers of this film in the AFM state changes between the down/up configuration in the negative fields to the up/down one in the positive fields (Fig. 3(c)).

CONCLUSION

The GMR effect arising in the perpendicularly anisotropic FM/NM/FM films with antiparallel orientation of the FM magnetic moments was studied in the [Co/Pd]/Pd/[Co/Pd] film with ferromagnetic coupling between the FM layers. It is shown that the field range of the GMR manifestation, corresponding to the difference in switching fields of FM layers, can be tuned by varying the thickness of the Pd spacer and/or Pd sublayer. Simultaneously, pinning of the FM moments by the exchange-coupled AFM layer is shown to shift effectively their switching fields and diverse the configuration of magnetic moments in the film in the high-resistance state. The tunable and expandable field range of the GMR effect in such a symmetric SV structure makes it a candidate for use as a magnetoresistive sensor.

Acknowledgment

This work was financially supported by Vietnam Academy of Science and Technology under Project QTBY01.02/23-24 and Belarusian Republican Foundation for Fundamental Research under Project F23V-003.

References

- [1] H. Hasegawa, *Theory of the temperature-dependent giant magnetoresistance in magnetic multilayers*, Phys. Rev. B **47** (1993) 15080-15085.
- [2] R.A. Duine, K.-J. Lee, S.S.P. Parkin, M.D. Stiles, *Synthetic antiferromagnetic spintronics*, Nature Phys. **14** (2018) 217-219.
- [3] T.N. Anh Nguyen, et al., *Effect of flattened surface morphology of anodized aluminum oxide templates on the magnetic properties of nanoporous Co/Pt and Co/Pd thin multilayered films*, Appl. Surf. Science **427** (2018) 649-655.
- [4] L. Li, Y. Lu, Z. Liu, Y. Lv, Y. Zhang, S. Liu, C. Hao, W. Lv, *Interlayer exchange coupling and magnetic reversal in Co/Pt multilayers*, J. Magn. Magn. Mater. **325** (2013) 117-121.
- [5] J.W. Knepper, F.Y. Yang, *Oscillatory interlayer coupling in Co/Pt multilayers with perpendicular anisotropy*, Phys. Rev. B **71** (2005) 224403.
- [6] S.S.P. Parkin, *Systematic Variation of the Strength and Oscillation Period of Indirect Magnetic Exchange Coupling through the 3d, 4d, and 5d Transition Metals*, Phys. Rev. Letters **67** (1991) 3598-3601.

A STUDY ON MECHANICAL AND ELECTRICAL PROPERTIES OF SOME SYSTEMS OF NANO ENERGY CONVERSION DEVICES (TENG, THEG).

Nguyen Thi Thuy Duong¹, Doan Thanh Tung^{1*}, Duong Van Thiet², Nguyen Tuan Dung¹, Hoang Tran Dung¹, Nguyen Thi Ngoc Linh³, Le Trong Lu¹, Phan Ngoc Minh^{4*}

¹ Institute for Tropical Technology-Vietnam Academy of Science and Technology (VAST),
18 Hoang Quoc Viet, Hanoi 100000, Vietnam

² School of Mechanical and Automotive Engineering, Hanoi University of Industry,
Hanoi 100000, Vietnam

³ Thai Nguyen University of Sciences, Tan Thinh Ward,
Thai Nguyen City 250000, Thai Nguyen, Vietnam

⁴ Graduate University of Science and Technology-VAST,
18 Hoang Quoc Viet, Hanoi 100000, Vietnam

Email: dtungtnt167@gmail.com, pnminh@vast.vn

ABSTRACT

Nanoenergy conversion materials have been studied by many scientists because of their applicability in self-powered devices. The materials with potential applications at present are triboelectric materials and thermoelectric materials. Many different types of polymeric materials have been studied and applied for triboelectric nanogenerator (TENG) such as polymethyl methacrylate (PMMA), cellulose, polyvinyl chloride (PVC), teflon, kapton, etc., which have shown good triboelectric performance. Thermoelectric generator (ThEG) have the effect of converting heat energy into electricity and vice versa based on the Seebeck and Peltier effect. In which thermoelectric materials are studied on different types of materials with the aim of improving the thermoelectric coefficient ZT for application from room temperature to high temperature range. In this report, we work on two types of materials: *i*) polymer blend materials between PMMA and cellulose were fabricated by solvent casting method. PMMA film is brittle, not meeting the requirements of TENG for continuous impact and friction. Cellulose combined with PMMA is selected an optimal ratio for good mechanical properties and still maintains the ability of electric friction. Example the polymer blend nitrocellulose (NC)/PMMA film with the NC:PMMA weight ratio of 80:20 has a durability after 1000 impacts and still provide peak-to-peak voltages up to several hundred volts; *ii*) Bi₂Te₃ two-dimensional layer structure thermoelectric materials were prepared by wet chemical method.

Keywords: Triboelectric nanogenerator (TENG), Thermoelectric generator (ThEG), energy conversion, polymethyl methacrylate (PMMA), 2D material

INTRODUCTION

Energy conversion devices play an important role in developing self-power independent electronics such as wearables, implantable, detection sensor devices, IoT devices, and robotics [1-4]. The various energy sources can be changed into electrical energy with specific generators, such as a piezoelectric nanogenerator (PENG) that uses polarization under pressure [5], an electromagnetic generator (EMG) that uses electro-magnetic induction [6], a triboelectric nanogenerator (TENG) that uses triboelectrification and electrostatic induction [7], or a thermoelectric generator (ThEG) that use heat energy [8].

As a new mechanical energy extraction system, TENG has proved its high vitality and great advantage, promising many applications in different fields [9]. Many different types of polymeric materials have been studied and applied for TENG such as polymethyl methacrylate (PMMA), cellulose, polyvinyl chloride (PVC), teflon, kapton, etc., which have shown good triboelectric performance [10]. In addition, wearables can also make direct use of heat energy from the wearer's body or generate heat from motion friction to recover and convert energy through thermoelectric nanogenerators (TEG or PyENG). Recently, layer structure semiconductor materials for TEG have attracted

great scientific interest due to their anisotropic properties and ease of control of carrier concentration, while the material also exhibits quantum confinement effects with state densities at the Fermi level and scattering phonon increases so gives a high ZT value [11]. However, the voltage achieved by thermoelectric devices is usually quite low, so some scientists have combined it with TENG for better application.

In this report, we fabricate two separate materials including TENG composite material of PMMA combined with nitrocellulose (NC) and Bi₂Te₃ two-dimensional layer structure thermoelectric materials. These materials have quite good properties that can guide future hybrid nano-generators combining triboelectricity and thermoelectricity.

EXPERIMENTAL

Chemical

Polymethyl methacrylate resin, nitrocellulose, N,N-Dimethylformamide (DMF), Bismuth (III) nitrate pentahydrate (Bi(NO₃)₃ · 0.5H₂O, 98%), sodium tellurite (Na₂TeO₃, 98 %), ascorbic acid (C₆H₈O₆, Sigma-Aldrich, reagent grade), Sodium hydroxide (NaOH) ethylene glycol (C₂H₆O₂, 99%), absolute ethanol, distilled water.

Fabrication of NC/PMMA polymer blend membrane

The NC/PMMA polymer blend is fabricated by solvent casting method with 10 cm x 10 cm silicon mold. NC and PMMA were dissolved in DMF solvent at a concentration of 0.3% separately using a magnetic stirrer at a temperature of 60 degrees Celsius. Then they were mixed in different ratios (NC/PMMA: 100/0, 80/20, 50/50, 20/80, 0/100) and continued to stir vigorously for one hour. The silicone mold is dried in a vacuum oven at a temperature of 60°C for 24 hours.

Synthesis of 2D Bi₂Te₃ nanomaterials

2D nanostructured Bi₂Te₃ material was synthesized using solvothermal as following process: Firstly, 12 mmol of Na₂TeO₃ and 2.4 g of NaOH were added into 60 mL of ethylene glycol solution in a three-neck flask. The mixture was stirred until completely dissolved. Next, 3 mmol of Bi(NO₃)₃ and 0.5 g of ascorbic acid were added into the above solution to form a transparent solution. The three-neck flask was then heated to 180°C under nitrogen for 2h. Finally, the obtained Bi₂Te₃ nanomaterial was purified by centrifugation and washed with distilled water and

ethanol several times and then dried at 80 °C for 12h.

RESULTS AND DISCUSSION

NC/PMMA TENG

Figure 1 shows the TENG electrode fabricated from NC/PMMA polymer blend material using the solvent casting method. This TENG membrane has transparent characteristics.

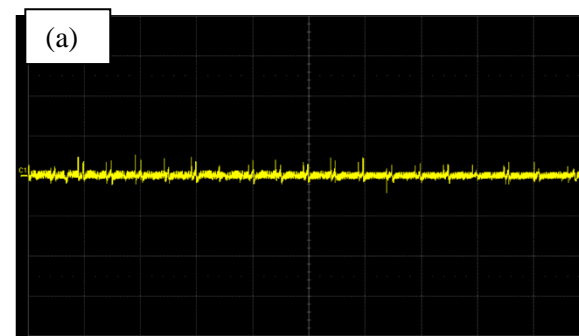


Fig.1. NC/PMMA blend polymer membrane

According to table 1, the tensile strength of pure NC membrane (44.52 MPa) is much higher than that of pure PMMA membrane (22.36 MPa). When mixed with PMMA, the tensile strength of this composite polymer changes non-linearly. This value is small with low NC ratio (3.77 MPa and 7.03 MPa) and reaches good value with NC:PMMA ratio of 80:20 (43.09 MPa). The same thing happens with the elastic modulus and elongation at break.

Table 1. Mechanical parameters of NC:PMMA membrane

NC:PMMA	Tensile strength (MPa)	Elastic modulus (MPa)	Elongation at break (%)
100:0	44.52	2129.78	16.37
80:20	43.09	1862.14	15.28
50:50	3.77	1025.83	0.38
20:80	7.03	1465.25	1.57
0:100	26.36	1481.89	10.63



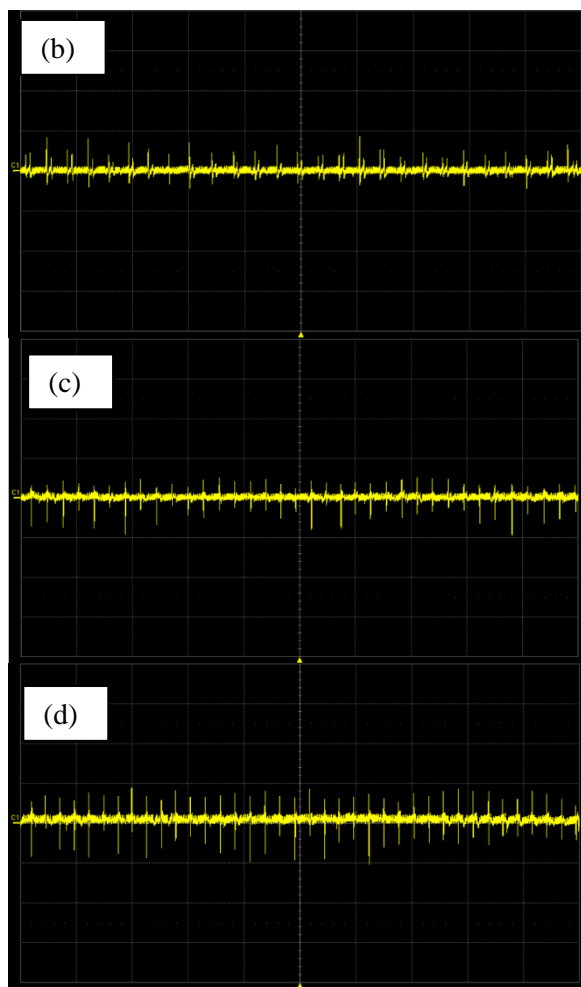


Fig. 2. Electro-tribological characteristics of NC/PMMA with ratios: a) 100:0, b) 80:20, c) 20:80, d) 0:100

PMMA has a large electrofriction contribution (table 2), while NC has a lower electrofriction output. However, the mechanical properties of PMMA are low, so the durability of the electrode will not be good. Therefore, the NC:PMMA ratio of 80:20 has both good mechanical properties and appropriate frictional electricity generation of TENG membrane ($V_{p-p} = 127.8$ V). TENG NC/PMMA film still maintains its durability and ability to generate electric friction after 1000 contact-separate cycles.

Table 2. Friction generation voltage of NC/PMMA polymer blend membrane

NC:PMMA	V max	V min	V peak to peak
100:0	53.4	-42.2	95.6
80:20	84.4	-43.4	127.8
50:50	58.6	-86.9	145.5
20:80	51.5	-95.1	146.6

0:100	88.8	-103.0	191.8
-------	------	--------	-------

2D Bi₂Te₃ nanomaterials

SEM image of Bi₂Te₃ nanoparticles shows a nanosheet shape with a thickness of only a few tens of nanometers (Figure 3). This 2D shape will help the material improve its thermoelectric properties when made into a complete device. Besides, the size of the nanosheets is uneven, increasing the ability to scatter phonons effectively but not scattering many carriers [12].

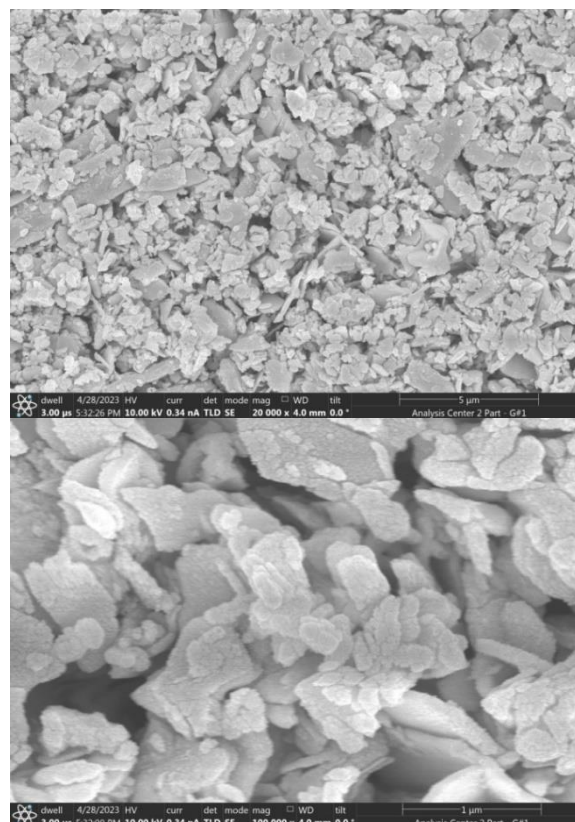
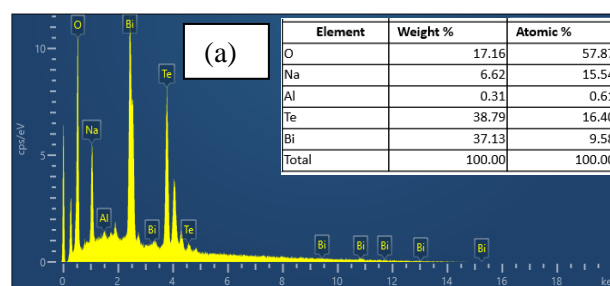


Fig. 3. SEM image of Bi₂Te₃ nanosheets



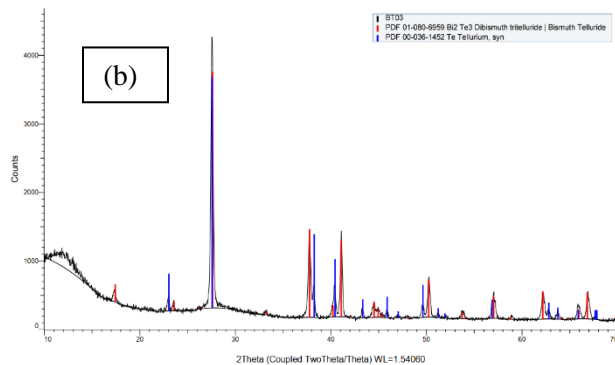


Fig. 4. EDS and XRD of Bi_2Te_3 nanosheets

EDS analysis in Fig. 4a shows the appearance of elemental compositions Bi and Te. Besides, there is the appearance of Na and O due to the synthesis process using NaOH. To confirm the phase structure of the material more accurately, the XRD spectrum (Figure 4b) shows that most of the peaks that appear coincide with the standard spectrum of Bi_2Te_3 .

CONCLUSION

Two materials for TENG and ThEG have been successfully fabricated in research. With the ability to create electro-friction of PMMA combined with NC, it has increased mechanical properties while still ensuring electro-friction performance. The 2D material Bi_2Te_3 has a synthesized 2D structure with a size small enough to enhance the thermoelectric effect. NC/PMMA and Bi_2Te_3 demonstrate the possibility of combining the two effects and their potential for use in hybrid nanogenerators.

Acknowledgment

This work was funded by Vietnam Academy of Science and Technology (ĐL0000.08/22-24).

References

- [1] C. Xu, Y. Yang, and W. Gao, *Skin-interfaced sensors in digital medicine: from materials to applications*, *Matter* **2** (2020) 1414-1445.
- [2] S.M. Won, E. Song, J.T. Reeder, and J.A. Rogers, *Emerging modalities and implantable technologies for neuromodulation*, *Cell* **181** (2020) 115-135.
- [3] X. Liu, Y. Zhao, D. Geng, S. Chen, X. Tan, and C. Cao, *Soft humanoid hands with large grasping force enabled by flexible hybrid pneumatic actuators*, *Soft Robot* **8:2** (2021) 175-185.

- [4] S. Chen, S. Brahma, J. Mackay, C. Cao and B. Aliakbarian, *The role of smart packaging system in food supply chain*, *J. Food Sci.* **85** (2020) 517-525.
- [5] Z. L. Wang, J. Song, *Piezoelectric nanogenerators based on zinc oxide nanowire arrays*, *Science*, **312** (2006) 242.
- [6] P. Glynn-Jones, M. J. Tudor, S. P. Beeby, N. M. White, *An Electromagnetic, Vibration-Powered Generator for Intelligent Sensor Systems*, *Sensors and Actuators A Physical*, **110** (2004) 344.
- [7] D. Kim, Y. Oh, B. W. Hwang, S. B. Jeon, S. J. Park, Y. K. Choi, *Triboelectric Nanogenerator Based on the Internal Motion of Powder with a Package Structure Design*, *ACS Nano*, **10** (2016) 1017.
- [8] H. You, Z. Li, Y. Shao, X. Yuan, W. Liu, H. Tang, Q. Zhang, Y. Yan, X. Tang, *Flexible Bi_2Te_3 -based thermoelectric generator with an ultra-high power density*, *Applied Thermal Engineering*, **202** (2022) 117818.
- [9] S. Wang, L. Lin, and Z. L. Wang, *Triboelectric nanogenerators as self-powered active sensors*, *Nano Energy*, **11** (2015) 436.
- [10] T. Ghomian and S. Mehraeen, *Survey of energy scavenging for wearable and implantable devices*, *Energy*, **178** (2019) 33.
- [11] X. Gong, R. Qian, H. Xue, W. Lu and Z. An, *Progress of microscopic thermoelectric effects studied by micro- and nano-thermometric techniques*, *Front. Phys.*, **17** (2022) 23201.
- [12] F. Wu, H. Song, J. Jia, X. Hu, *Effects of Ce, Y, and Sm doping on the thermoelectric properties of Bi_2Te_3 alloy*, *Progress in Natural Science: Materials International*, **23** (2013) 408-412.

PAPER-STRUCTURED CATALYST FOR ETHANOL STEAM REFORMING

Manaya Baba¹, Dinh Trinh Minh Duc¹, Ryota Hino², Takeshi Goto², Yusuke Shiratori¹

¹ Department of Mechanical Science and Engineering, School of Advanced Engineering, Kogakuin University, 2665-1 Nakano-machi, Hachioji, Tokyo 192-0015, Japan

² 7000-36 Nakagawa, Hosoe-cho, Kita-ku, Hamamatsu, Shizuoka 431-1394, F.C.C. Co., Ltd.

Email: s520048@g.kogakuin.jp

ABSTRACT

Solid oxide fuel cell (SOFC), which is considered to be the most efficient way to generate electricity from hydrogen, has gained attention as a promising technology for suppressing CO₂ emission. There is also particular interest in hydrogen production from ethanol, liquid fuel for potable use, using catalysts. Paper-structured catalyst (PSC), which can be applied on the anode of SOFC, is able to realize the reforming-integrated SOFC to enable us to directly feed ethanol to SOFC for power generation. To improve the performance of Ni-loaded hydrotalcite (HT) dispersed-PSC (Ni/HT-PSC) for ethanol steam reforming, polyvinylpyrrolidone (PVP), which is expected to suppress the agglomeration of Ni, has been introduced. However, ethanol steam reforming tests revealed that the introduction of PVP had negative effect. It is considered that the presence of PVP strengthened the interaction between ceramic fibers and Ni to promote coking.

Keywords: Fibers, carbon nanotubes, nanocomposite.

INTRODUCTION

A solid oxide fuel cell (SOFC) operated at high temperature (600-900°C), which has highest power generation efficiency among several types of fuel cell, is one of the most promising power generators contributing to the reduction of CO₂ emission. Paper-structured catalyst (PSC) [1], composed of an inorganic fibre network in which metal-loaded catalyst particles are dispersed, allows us to easily endow catalytic function to a cell stack to create reforming-integrated SOFC. In this study, steam reforming of ethanol (SRE) was evaluated using the PSC to be applied to the reforming-integrated SOFC fuelled by aqueous solution of ethanol (20-30vol% ethanol in water).

EXPERIMENTAL

Preparation of PSC: 5 g of ceramic fibre (SiO₂-Al₂O₃: Cf) and 2 g of hydrotalcite ([Mg₆Al₂(OH)₁₆CO₃]4H₂O: HT) were dispersed in 1.0 L distilled water. Designated amounts of cationic polyelectrolyte, PDADMA, stabilized zirconia sol (Zs), which serves as an inorganic binder through a high-temperature heat treatment and anionic polyelectrolyte, A-PAM, were added to the slurry. Then, an organic pulp fibre suspension was poured into the mixture and solidified by dewatering using 200 mesh. The

wet-state paper sheet with a diameter of 16 cm was pressed at 350 kPa and dried to form raw paper followed by heat treatment at 800°C. Pieces of the paper were immersed in a Ni(NO₃)₂·6H₂O aqueous solution for Ni loading. After the impregnation process, the samples were heat treated at 800°C to have Ni-loaded HT-dispersed PSC (Ni/HT-PSC).

On the other hand, aiming at the prevention of Ni agglomeration, polyvinylpyrrolidone (PVP), which is considered to have electrostatic interaction with Ni surface [2], was added to the impregnation solution by 2wt% to have Ni(PVP)/HT-PSC.

SRE test: Four donut-shaped Ni/HT-PSCs (outer diameter: 20 mm, inner diameter: 6.0 mm, thickness: 1.0 mm) were stacked and placed in an alumina cylinder. At a prescribed temperature (500-730°C), using a liquid pump, the aqueous solution of ethanol was supplied to the fixed bed reactor at LHSV of 27.2 h⁻¹. Composition of the outlet gas (reformat) was analysed by an automatic gas chromatograph (GC-20B, Shimadzu, Japan).

RESULTS AND DISCUSSION

Ethanol consumption rates were measured in the SRE tests. Under the assumption of

competitive adsorption of ethanol and steam, based on the Langmuir-Hinshelwood mechanism considering their partial pressures, rate constants of the ethanol consumption, k_0 , were estimated and plotted in Fig. 1. When PVP was added in the impregnation solution for Ni loading, contrary to expectation, reforming reaction was depressed. Activation energies, E_a , estimated from the gradients of the Arrhenius plots were 96.4 and 126.4 kJ mol⁻¹ for the PSCs without and with the addition of PVP, respectively.

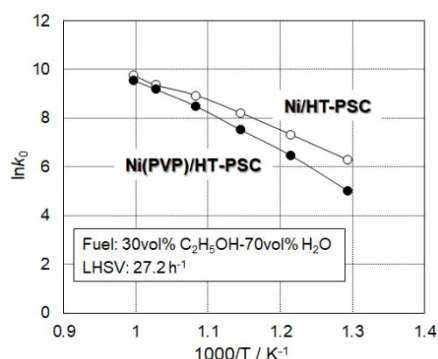


Figure 1. Arrhenius plots for the rate constants of ethanol consumption estimated by the SRE tests.

As summarized in Table 1, SRE (R1) is considered to be composed of DOE (R2), SRM (R3), WGS (R4) and DOM (R5).

Table 1. Reactions included in SRE.

SRE	$C_2H_5OH + 3H_2O \rightleftharpoons 2CO_2 + 6H_2$	(R1)
DOE	$C_2H_5OH \rightleftharpoons CO + CH_4 + H_2$	(R2)
SRM	$CH_4 + H_2O \rightleftharpoons 3H_2 + CO$	(R3)
WGS	$CO + H_2O \rightleftharpoons H_2 + CO_2$	(R4)
DOM	$CH_4 \rightleftharpoons 2H_2 + C$	(R5)

Reported values of E_a are 77.5, 162.2, 90.9 and 65.4 kJ mol⁻¹ for DOE, SRM, WGS and DOM, respectively [3,4]. When PVP was not added, the E_a estimated in this study was close to the reported value for WGS. On the other hand, in the case with PVP, that was in between the reported values for WGS and SRM, suggesting that SRE was affected by the retardation of SRM.

Considering the reformat compositions, separation analyses of SRE were performed for both Ni/HT-PSC and Ni(PVP)/HT-PSC, and summarized in Figs. 2a and 2b, respectively. These results indicate that by the addition of PVP especially decrease in the rate of SRM became noticeable. PVP addition may strengthen the interaction between the surface of Cf, having poor

function as catalyst support, and Ni, resulting in the performance drop of the PSC.

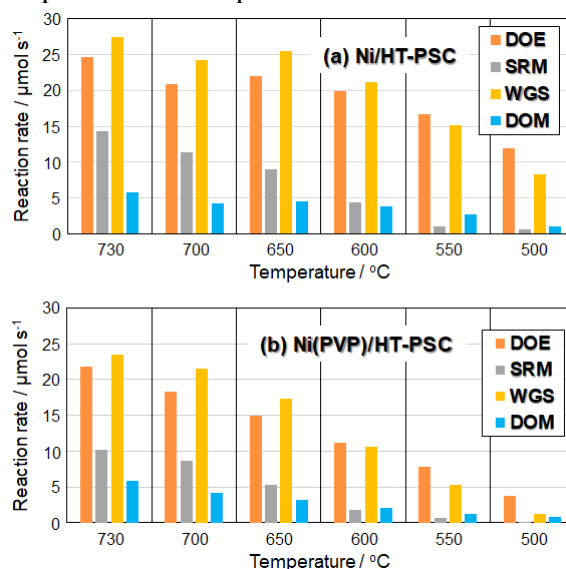


Figure 2. Results of separation analyses of SRE in the feed of 30vol% ethanol aqueous solution for (a) Ni/HT-PSC and (b) Ni(PVP)/HT-PSC.

CONCLUSION

For enhancing the catalytic performance of Ni/HT-PSC for the steam reforming of ethanol (SRE), PVP, which is expected to act as an aggregation inhibitor of Ni, was added in the impregnation solution for Ni loading. However, by this addition, SRM, one of the component reactions of SRE, was retarded.

References

- [1] Y. Shiratori, M. Sakamoto, *Performance improvement of direct internal reforming solid oxide fuel cell fuelled by H₂S-contaminated biogas with paper-structured catalyst technology*, J. Power Sources **332** (2016) 170-179.
- [2] M. Okumura *et al.*, *Theoretical investigation of the hetero-junction effect in PVP-stabilized Au₁₃ clusters. The role of PVP in their catalytic activities*, Chem Phys Lett. **459** (2008) 133-136.
- [3] N.R. Peela, D. Kunzru, *Steam Reforming of Ethanol in a Microchannel Reactor: Kinetic Study and Reactor Simulation*, Ind. Eng. Chem. Res. (2011) **50**(23) 12881–12894.
- [4] H.Y. Wang, A.C. Lua, *Deactivation and kinetic studies of unsupported Ni and Ni–Co–Cu alloy catalysts used for hydrogen production by methane decomposition*, Chem Eng J. **243** (2014) 79-91.

GREEN SYNTHESIS AND CHARACTERIZATION OF TiO₂ NANOPARTICLES VIA ALOE VERA EXTRACT APPLICATION IN SUNSCREEN CREAM COSMETIC

Vu Nang An^{1,2}, Nguyen Thi Kim Ngan^{1,2}, Nguyen Thai Ngoc Uyen^{1,2}, Tran Mai Anh^{1,2}

¹ Faculty of Materials Science and Technology, University of Science, VNU–HCM, 700000, Viet Nam;

² Vietnam National University Ho Chi Minh City, 700000, Viet Nam.

Email: tmanh@hcmus.edu.vn

ABSTRACT

In this study, Titanium dioxide nanoparticles (nano TiO₂) has been synthesized using the green method from Aloe vera extract. The advantages of biosynthesis are friendly, less energy, pressure and cost-effective nature. Nanoparticles were characterized by SEM, TEM, XRD and UV-VIS. The SEM and TEM analysis show images of the surface of the TiO₂ nanocluster, the nanoparticle size in the range from 11,5 – 20,9 nm, average particle size approximately 16,6 nm. The sharp peaks XRD pattern shows purity and tetragonal structure with anatase phase. This application of green TiO₂ nanoparticles is being explored in facial cream. The results showed that the 20% concentration of nanopowder gave higher UV absorption than the commercial nanopowder. At higher concentrations, the UV absorption efficiency is reduced because the ingredients mixed in the facial cream reduce the photocatalytic ability.

Keywords: Titanium dioxide nanoparticles; Aloe vera extract; biosynthesis; facial cream

INTRODUCTION

Sunlight's ultraviolet (UV) radiation, which can lead to skin cancer, is among the most significant causes of skin diseases. Sunscreen creams have been devised to protect skin from the damaging effects of sunlight [1-3]. Titanium dioxide (TiO₂) nanoparticles (NPs) are the most desirable mineral nanostructures for sunscreen formulations due to their distinctive optical and antibacterial properties [4, 5]. TiO₂ nanoparticles are extensively used as a whitener, abrasive, pearlescent colorant, and opacifier in various soaps, hair dyes, and skin care products [6]. Due to its light-scattering properties and high refractive index, it appears dazzling white [7]. TiO₂ nanoparticles have been used in sunscreens for several years because, at diameters below 100nm, their whiteness is replaced by transparency, resulting in a pleasing appearance when applied to the skin [8]. Currently, TiO₂ concentrations between 2% and 15% are permitted in sunscreen formulations, while its dosage can reach up to 25% [9-11]. The physical method necessitates expensive apparatus, high temperature and pressure, and sufficient space to initiate the reaction. For a chemical route synthesis, toxic chemicals considered hazardous to the environment are frequently used, and their management requires a person. In contrast, green

synthesis technology is regarded as the most environmentally friendly method because it does not require high-end apparatus, hazardous chemicals, or high temperatures [12-15]. Green synthesis can be broken down into three categories: a) Utilizing microorganisms such as fungi, yeast, and bacteria b) Employing plant parts and their extracts or powder, and c) Employing templates such as DNA and viruses [16]. Plants and plant extracts have grown in popularity over time. Most studies have focused on plant elements such as leaves, seeds, and flowers. They are favored mainly due to their capacity to reduce titanium ions. In addition, plants are readily available and secure to handle. Bioactive substances derived from plants include alkaloids, diterpenoids, lactones, glycosides, steroids, polysaccharides, terpenoids, flavonoids, phenolic acids, vitamins, enzymes, minerals, sugars, salicylic acids, saponins, amino acids, tannins, and sterols, which function as reducing and stabilizing agents.

This study seeks to develop a novel method for synthesizing TiO₂ nanoparticles using Aloe Vera extract. TiO₂ NPs are then utilized as a UV filter in sunscreen cream formulations. The other objective of this study was to assess their contribution to the efficacy of sunscreens.

EXPERIMENTAL

Preparation of Aloe vera plant extract

A fresh and healthy Aloe vera plant was taken from the National University - Linh Trung - Thu Duc metropolitan region campus in Ho Chi Minh City. Using an electronic weighing balance, 50g of the leaves were weighed and transferred to a 500 ml receptacle containing 250 ml of distilled water. The contents were simmered at 90°C for two hours. The Whatman filter paper was used to filter the extract. The filtrate was stored for nanoparticle synthesis.

Preparation of titanium dioxide nanoparticles

Titanium isopropoxide ($C_{12}H_{28}O_4Ti$) was prepared using double-distilled water at a concentration of 0.1 M. Under constant agitation, aloe vera leaf extract was added drop by drop to create a solution with a pH of 7. The mixture was continually stirred for 4 hours. This procedure involved the formation and separation of nanoparticles using Whatman filter paper. The particulates were repeatedly washed with double-distilled water to eliminate any by-products. The nanoparticles were desiccated overnight at 100°C and calcined for four hours at 500 °C.

Fabrication of sunscreen lotion with nanoparticles of TiO₂

In this study, two sunscreen cream samples were formulated using TiO₂ nanoparticles synthesized from aloe vera extract and commercial TiO₂ powder, with constituents enumerated in Tables 1 and 2, respectively. First, the mixture of isopropyl myristate and TiO₂ was agitated and heated at 60 to 70 °C until it was homogenous (mixture A). Slowly adding mixture A to the oil phase until the mixture was homogenous. Next, the water phase (consisting of aloe vera gel and RO water) was added slowly to the oil phase while agitating continuously at 50 to 60 °C until homogeneous. The mixture was mixed with phenoxyethanol until a delicate, creamy consistency was achieved. This cream mixture was kept at ambient temperature for two hours in order to stabilize it and conduct additional experiments. Table 3 lists all sunscreen samples with their label.

Table 1. The ratio of ingredients mixed with TiO₂ nanoparticles synthesized from experiments

No.	Ingredients	Ratio (%)			
		TN1	TN2	TN3	DC
1	Isopropyl myristate	10	40	48	10
2	TiO ₂	5	20	25	-
3	Beeswax	0.5	0.5	0.5	0.5
4	Propane-1,2,3-triol (Glycerin)	5	5	5	5
5	Cetearyl Alcohol	3	3	3	3
6	Aloe vera gel	1	1	1	1
7	2-Phenoxyethan-1-ol(Phenoxyethanol)	0.5	0.5	0.5	0.5
8	RO water	75	30	15	80

Table 2. The ratio of ingredients mixed with commercial TiO₂

No.	Ingredients	Ratio (%)		
		TM1	TM2	TM3
1	Commercial TiO ₂	5	20	25
2	Beeswax	0.5	0.5	0.5
3	Propane-1,2,3-triol (Glycerin)	5	5	5
4	Cetearyl alcohol	3	3	3
5	Aloe vera gel	1	1	1
6	2-Phenoxyethan-1-ol (Phenoxyethanol)	0.5	0.5	0.5
7	RO water	85	70	65

Table 3. Information on sunscreen cream samples used in the experiment

Classification	Label	Meaning
TiO ₂ nanoparticles synthesized from experiments	TN1	Sample of TiO ₂ nanoparticles mixed cream with 5% concentration
	TN2	Sample of TiO ₂ nanoparticles mixed cream with 20% concentration
	TN3	Sample of TiO ₂ nanoparticles mixed cream with 25% concentration
	TN DC1	The solution sample contains 5% TiO ₂ nanoparticles
	TN DC2	The solution sample contains 20% TiO ₂ nanoparticles
	TN DC3	The solution sample contains 25% TiO ₂ nanoparticles
Commercial TiO ₂	TM1	Sample of TiO ₂ nanoparticles mixed cream with 5% concentration
	TM2	Sample of TiO ₂ nanoparticles mixed cream with 25% concentration
	TM3	Sample of TiO ₂ nanoparticles mixed cream with 25% concentration

Pure cream sample	DC	The cream sample does not contain TiO ₂ nanoparticles
Commercial sunscreen	TN	Commercial sunscreens on the market

RESULTS AND DISCUSSION

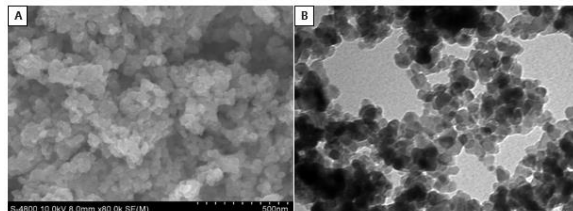


Figure 1. SEM (a) and TEM (b) of TiO₂ nanoparticles

SEM images (Figure 1a) show that TiO₂ particles exhibit agglomeration to form TiO₂ nanoclusters. According to TEM (Figure 1b) results, TiO₂ has an uneven shape and size. Combining SEM and TEM images of TiO₂ nanomaterials shows that TiO₂ nanoparticles have a spherical shape, with size distribution from 11.5 - 20.9 nm, with an average diameter of about 16.6 nm. Meanwhile, a few previous publications by K. Ganapathi Rao and Abdul Khadar in 2015 successfully manufactured nano TiO₂ using aloe vera extract, with average particle sizes of 32 nm and 30 nm [17, 18].

Experimental sunscreen products TN1, TN2, and TN3 were made according to the ingredients listed in Table 1. The results of evaluating the visual properties of these samples are presented in Table 4. All three cream samples are milky white, creating a smooth, silky, and light cream texture, uniformly dispersed, without air bubbles. After the centrifugation test at 5000 rpm, no layer separation phenomenon was observed for 30 minutes. Therefore, Cetearyl alcohol is used as a stable emulsifier. Experimental TiO₂ nano cream samples are homogeneous in the mixture. There is no phenomenon of white streaks on the skin. It does not cause skin irritation due to too much oil, creating a comfortable feeling, and it absorbs quickly for the user.

SPF value represents the rated value measuring the skin's ability to protect against solar energy (UV radiation) when using sunscreen. The in vitro SPF values of the survey samples were calculated and shown in Table 5. The results show that sample TN1 and sample TN2 have SPF indexes of 31.29 and 45.88, respectively, showing that when the concentration of TiO₂ nanomaterials is from 5% to 20%, the surface area is large,

improving efficiency. Photocatalytic, high light absorption and scattering reduce the light transmission ratio to the ability to absorb UV rays. When the concentration of nanomaterials increased to 25% (sample TN3), the SPF value was 34.41, a decrease compared to samples TN1 and TN2. This result shows that as the TiO₂ nanomaterial increases, the nanoparticles tend to agglomerate, and the distribution area is uneven, leading to a decrease in the ability to reflect UV rays. For samples of nanomaterials dissolved in the solvent, the SPF value is correspondingly lower than that of nano TiO₂ cream samples, which shows that SPF also depends on the ingredients in the mixture. Commercial TiO₂ nano cream samples in samples (TM1), (TM2), and (TM3) and TiO₂ cream samples on the market combining ZnO and TiO₂ (TN) have lower SPF values than the corresponding manufactured samples. Compared to cream samples without nano (DC), samples containing nano TiO₂ recorded higher SPF values. That shows the effectiveness of applying nano TiO₂ in sunscreen against radiation. SPF value is calculated according to the formula:

$$SPF = \frac{\sum_{290}^{400} E(\lambda) \times R(\lambda)}{\sum_{290}^{400} E(\lambda) \times R(\lambda) \times T(\lambda)}$$

where E (λ): Radiation intensity of sunlight (AS/NZA 4399:1996); R (λ): CIE reference erythema activity spectrum (CIE J.6: 17-22,1987); T (%): Transmittance

Sunlight consists mainly of 90-95% UVA and 5-10% UVB rays. The ozone layer absorbs most UVC rays. The molecular mechanisms by which UV radiation causes skin cancer involve direct or indirect DNA damage, formation of pyrimidine dimers, immunosuppression, ROS response, or alterations in transcription. UVB radiation is the main cause of immediate skin damage, leading to sunburn and erythema, and can directly attack cell DNA, leading to changes associated with skin cancer. Research increasingly proves that UVA radiation as a carcinogen penetrates deep into the dermis has a higher oxidative impact than UVB, and can shorten telomeres [30]. Therefore, in addition to evaluating the SPF (UVB) protection value, the protection value (PA) for UVA rays is based on the in vitro evaluation method recorded in Table 6. The results show that three nano TiO₂ ratios correspond to PA values greater than 16. According to the FDA, PA values are divided into groups: PA corresponds to values lower than 2; PA+ corresponds to values from 2 to 4; PA++

corresponds to values from 4 to 8; PA +++ corresponds to values from 8 to 16; PA ++++ corresponds to a value greater than 16. Therefore, the tested sunscreen samples can protect against UVA rays. Intending to apply nano TiO₂ at the appropriate ratio, the SPF and PA results are consistent with FDA standards, limiting the ability to combine materials, as shown in the 20% nano TiO₂ experimental ratio in the anti-bacterial cream sample. Suitable sunlight does not leave white streaks on the skin when used. PA value is calculated according to the formula:

$$PA = \frac{\sum_{290}^{400} E(\lambda) \times M(\lambda)}{\sum_{290}^{400} E(\lambda) \times M(\lambda) \times T(\lambda)}$$

where E (λ): Radiation intensity of sunlight (AS/NZA 4399:1996); M (λ): Minimum blackness that immediately maintains the operating spectrum (1.0); T (%): Transmittance

Table 4. Evaluation of some properties of sunscreen mixed with experimental TiO₂ nanomaterials

Evaluation	TN 1	TN 2	TN 3
Color	White milk	White milk	White
Form	Creamy, smooth, light	Creamy, smooth, light	Creamy, smooth, light
Air bubbles	No	No	No
Level when applied to the skin surface	Absorbs quickly, leaving no white streaks	Absorbs quickly, leaving no white streaks	Absorbs quickly, leaving no white streaks
Physical stability	No layer separation	No layer separation	No layer separation
Odor	Odourless	Odourless	Odourless

Table 5. SPF value recorded from experimental samples

Samples	The SPF value corresponds to each ratio of TiO ₂ nanoparticle usage		
	5%	20%	25%
Sample of TiO ₂ nanoparticles cream	31.29 (TN1)	45.88 (TN2)	34.41 (TN3)
Commercial TiO ₂ cream sample	26.3 (TM1)	31.71 (TM2)	25.36 (TM3)
TiO ₂ in dissolved solvent	26.89 (TN DC1)	32.16 (TN DC2)	38.14 (TN DC3)
Commercial sunscreen sample	24.8 (TN)		
The cream sample does not contain TiO ₂ nanoparticles	24.63 (DC)		

Table 6. PA values recorded from sunscreen samples

Samples	PA value corresponds to each concentration using TiO ₂ nanomaterials		
	5%	20%	25%
Sample of TiO ₂ nanoparticles cream	31.29 (TN1)	45.88 (TN2)	34.41 (TN3)
Commercial TiO ₂ cream sample	26.3 (TM1)	31.71 (TM2)	25.36 (TM3)
Commercial sunscreen sample	24.8 (TN)		

CONCLUSION

TiO₂ nanoparticles were successfully manufactured through the green synthesis method from aloe vera leaf extract and after calcination at 500 °C for 4 hours. SEM and TEM image analysis results show that the obtained TiO₂ has a spherical shape, distributed into clusters with an average particle size of about 16 nm. The sunscreen formula containing nano TiO₂ material is milky white and does not leave white streaks on the skin; it absorbs quickly. The SPF value recorded is 45.88, and PA⁺⁺⁺ of the sunscreen sample contains 20% TiO₂ concentration under FDA standards and can protect against UV rays.

Acknowledgment

This research is funded by the University of Science, Vietnam National University Ho Chi Minh City (US, VNU-HCM) under grant number C2023-18-31. The authors are grateful for this financial support.

References

- [1] Proksch, E., J.M. Brandner, and J.-M. Jensen, *The skin: an indispensable barrier*, *Experimental Dermatology*, **17**(12) (2008) 1063-1072.
- [2] Ahmadi, F. and M. Jorjani, *Sunblock comparison SPF= 30 and SPF= 100 in advance of sunburn*, *Pajoohandeh*, **7** (2002) 217.
- [3] Patil, S., et al., *Determination of active phytochemicals from formulated sunscreen cream containing Pongamia pinnata leaves and Punica granatum peel extract by high performance thin layer chromatography*, *World J Pharm Res*, **4** (2015) 802-12.
- [4] Zhang, F., et al., *Controllable synthesis of Ag@ TiO₂ heterostructures with enhanced photocatalytic activities under UV and visible excitation*, *RSC advances*, **6**(3) (2016) 1844-1850.

- [5] Zhu, H.-Y., et al., *Novel multifunctional NiFe₂O₄/ZnO hybrids for dye removal by adsorption, photocatalysis and magnetic separation*, Applied surface science **369** (2016) 1-10.
- [6] Berardinelli, A. and F. Parisi, *11 - TiO₂ in the food industry and cosmetics*, in *Titanium Dioxide (TiO₂) and Its Applications*, F. Parrino and L. Palmisano, Editors. 2021, Elsevier, 353-371.
- [7] Bodurov, I., T. Yovcheva, and S. Sainov, *Refractive index investigations of nanoparticles dispersed in water*, Journal of Physics: Conference Series, **558**(1) (2014) 012062.
- [8] Pulvin, S., S. Tanvir, and W.A. Anderson, *Toxicity associated with the photo catalytic and photo stable forms of titanium dioxide nanoparticles used in sunscreen*, 2015.
- [9] Morsella, M., et al., *Improving the Sunscreen Properties of TiO₂ through an Understanding of Its Catalytic Properties*, ACS Omega, **1**(3) (2016) 464-469.
- [10] Taheriniya, S. and Z. Behboodi, *Comparing green chemical methods and chemical methods for the synthesis of titanium dioxide nanoparticles*, International Journal of Pharmaceutical Sciences and Research, **7**(12) (2016) 4927.
- [11] Sundrarajan, M. and S. Gowri, *Green synthesis of titanium dioxide nanoparticles by Nyctanthes arbor-tristis leaves extract*, Chalcogenide Lett. **8**(8) (2011) 447-451.
- [12] Rao, K.G., et al., *Green synthesis of TiO₂ nanoparticles using Aloe vera extract*, Int. J. Adv. Res. Phys. Sci, **2**(1A) (2015) 28-34.
- [13] Rao, A., D. Kelleher, and C. Miller, *No Shortcuts to Shifting Deep Structures in Organisations*, IDS Bulletin **46**(4) (2015) 82-91.
- [14] Patidar, V. and P. Jain, *Green synthesis of TiO₂ nanoparticle using Moringa oleifera leaf extract*, Int. Res. J. Eng. Technol., **4**(3) (2017) 1-4.
- [15] Yedurkar, S.M., C.B. Maurya, and P.A. Mahanwar, *Synthesis of nanoparticles by green chemistry process and their application in surface coatings: A review*, Archives of Applied Science Research, **8**(5) (2016) 55-69.
- [16] Răileanu, M., et al., *The Influence of Ni Dopant on the Structure and Photocatalytic Properties of Sol-Gel TiO₂ Nanopowders*. Water, Air, & Soil Pollution, **224**(11) (2013) 1773.
- [17] Abdul, K., *PENGARUH OTORITAS PENGAMBILAN KEPUTUSAN TERHADAP EFEKTIVITAS PENGELOLAAN SEKOLAH DI KOTA MATARAM*, Jurnal Pendidikan Ekonomi Dan Bisnis (JPEB), **4**(2) (2016).
- [18] Rajakumar, A.A.R., B. Priyamvada, V. G. Khanna, D. K. Kumar, and P. J. Sujin, *Eclipta prostrata leaf aqueous extract mediated synthesis of titanium dioxide nanoparticles*. **68** (2012) 115-117.
- [19] Amaro-Ortiz, B.Y., and J. A. D’Orazio, *Ultraviolet Radiation, Aging and the Skin: Prevention of Damage by Topical cAMP Manipulation*, Molecules **19** (2014) 6202-6219.

EFFECTS OF GAMMA IRRADIATION UPON VARIOUS DOSE RATES ON NAFION MEMBRANES

Tran Duy Tap^{1,2*} and Dinh Tran Trong Hieu^{1,2}

¹ Faculty of Materials Science and Technology, University of Science, 227 Nguyen Van Cu, District 5, Ho Chi Minh City, Vietnam.

² Vietnam National University, Ho Chi Minh City, Vietnam
Email: tdtap@hcmus.edu.vn

ABSTRACT

The effects of gamma irradiation with various dose rates of 0, 2.5, 5, and 10 kGy/h at a dose of 300 kGy on Nafion membranes are investigated using X-ray diffraction (XRD), thermogravimetric analysis (TGA), and Fourier-transform infrared spectroscopy (FT-IR). The cross-linking formation in the irradiated membranes was observed as qualitatively determined by the increase in the decomposition temperatures of water and the main chains. This cross-linking is formed in both the side chains and the amorphous domains of the backbones. Decrease in crystallinity is observed for all irradiation dose rates, reflecting the degradation of the inherent crystalline phase of the polymer main chains. At 300 kGy, the effects by the irradiation at 2.5 kGy/h show more pronounced than those at the higher dose rates of 5 and 10 kGy/h. The obtained results in this study provide a further understanding in membrane degradation for modifying improved membrane fuel cell.

Keywords: Gamma irradiation, chemical degradation, Nafion, fuel cell, crystallinity.

INTRODUCTION

Nafion membranes are now widely used in direct methanol fuel cells (DMFC), polymer exchange membrane fuel cells (PEMFC), and electrolyte membrane water electrolysis [1]. The advantages of the membranes include high proton conductivity, chemical stability, and mechanical strength. However, the stability of Nafion membrane under DMFC conditions is not sufficient to meet the expected lifetime requirement for commercial DMFC [2]. Moreover, the membrane exhibits a few additional disadvantages such as low conductivity at low water content, low mechanical strength at higher temperatures, methanol crossover, and moderate glass transition temperatures [2]. To overcome these disadvantages, it is possible to modify Nafion membranes by using radiation such as UV rays, X-rays, electron beams, and gamma rays [3]. Among these radiations gamma radiation from radioactive isotope sources shows high energy, depth penetration, which allows to conduct the irradiation with large-scale processing. This work reports a study of gamma irradiation on Nafion membranes with an irradiation dose of 300 upon dose rates of 0, 2.5, 5, and 10 kGy/h. The irradiated Nafion membranes are characterized

using Fourier transform infrared (FTIR) spectroscopy, X-ray diffraction (XRD), and thermogravimetric analysis (TGA).

EXPERIMENTAL

The commercial Nafion membranes (Dupont Corporation) are approximately 50 μm thick. All samples were cleaned on the surface with an acetone solution. The samples were exposed to gamma radiation with a Cobalt-60 source (14000 Ci, Gamma Chamber GC-5000-BRIT, India) at dose rates of 0, 2.5, 5, and 10 kGy/h with a dose of 300 kGy under dry condition. Detailed measurements of FT-IR, XRD, and TGA for the irradiated membranes are represented in the previous report [4].

RESULTS AND DISCUSSION

In Figure 1, the absorbance of 1020-1080 cm^{-1} decreases as the dose rate increases (0-5 kGy/h). This absorption feature indicates the degradation of $-\text{SO}_3\text{H}$ and $\text{C}-\text{O}-\text{C}$ groups nearest to the sulfonic acid end group due to irradiation [5]. Especially, for a dose rate of 10 kGy/h, the absorption intensity drops dramatically. The absorption peak at 1730 cm^{-1} and the shoulder at 1630 cm^{-1} are associated with the bending vibrations of water molecules. Moreover, the

peaks around 3236 and 3465 cm^{-1} are attributed to symmetric and asymmetric O–H stretching vibrations, respectively. The trend of this O–H stretching region (the absorbance increases with dose rate) is quite dis-similar to the bending O–H region. However, for the dose rate of 10 kGy/h, the absorbance decreases dramatically. It is possible that the membrane has been degraded upon high irradiation dose of 300 kGy [5].

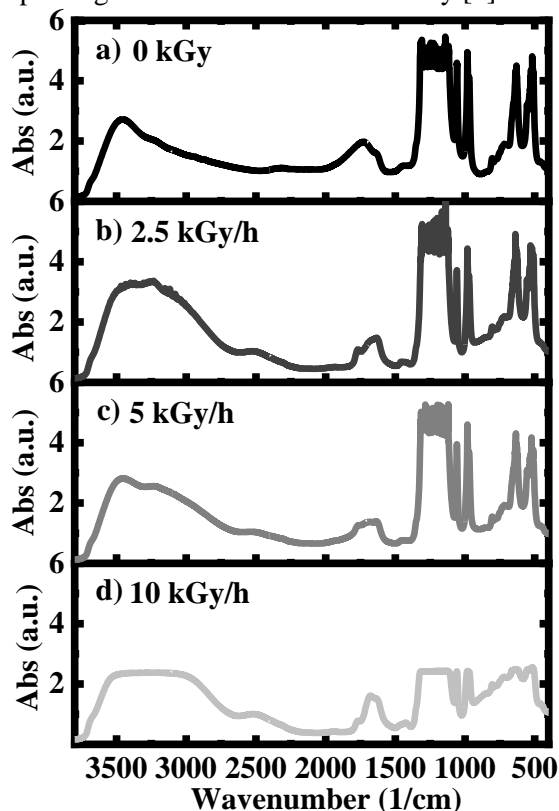


Figure 1. FT-IR spectra of irradiated Nafion at a dose of 300 kGy.

Figure 2 depicts the TGA profiles of Nafion membranes before and after being exposed to gamma radiation under different rate doses: a) un-irradiation, b) 2.5 kGy/h, c) 5 kGy/h, and d) 10 kGy/h. The weight loss observed at approximately 100 °C (T1) can be attributed to the release of water molecules that are bounded to the sulfonic groups of Nafion [6]. The second weight loss occurs between 330 °C and 365 °C. This is a result of the decomposition of the sulfonic acid groups and the side chains containing the $-\text{OCF}_2\text{CF}_2-\text{SO}_3\text{H}$ moiety [6]. In the third stage, the weight loss is caused by thermal degradation of the Nafion backbone, occurring at around 500 °C (T3) [6]. The detailed values of decomposition temperature are presented in Figure 3.

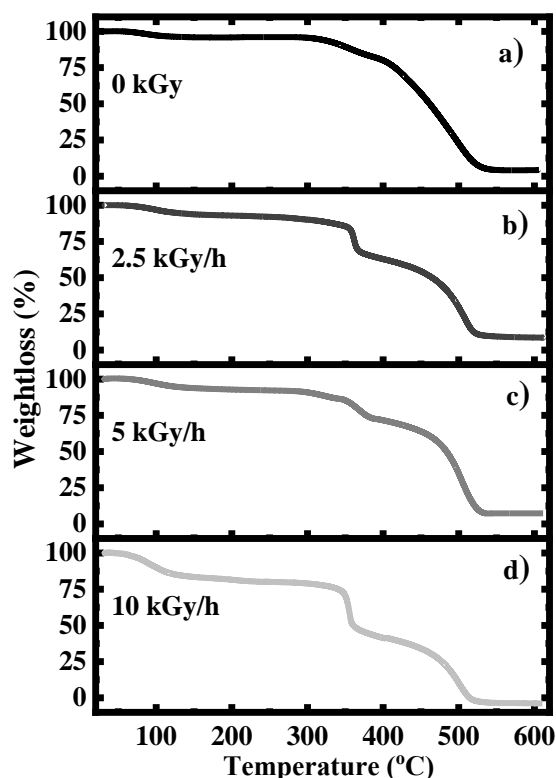


Figure 2. TGA profiles of Nafion irradiated by gamma irradiation at the dose of 300 kGy.

Figure 3a and 3b illustrates the thermal decomposition stages, denoted as T1 and T3 [7]. In the T1 stage, it is observed that the irradiated membranes exhibit higher temperatures compared to the original membrane [7]. A similar result is also observed for the case of T3. This result is indicative for the cross-linking formation in the irradiated membranes. The residual mass values obtained from the TGA profiles are presented in Figure 3c. During the decomposition of the sulfonic group, one or both of the ether bonds may decompose, leading to the formation of small fluorocarbon molecules. Consequently, the weight reduction of the Nafion membrane does not reach 0%. It could be the result of incomplete decomposition of the ether bonds or the presence of residual small fluorocarbon molecules components in the membrane.

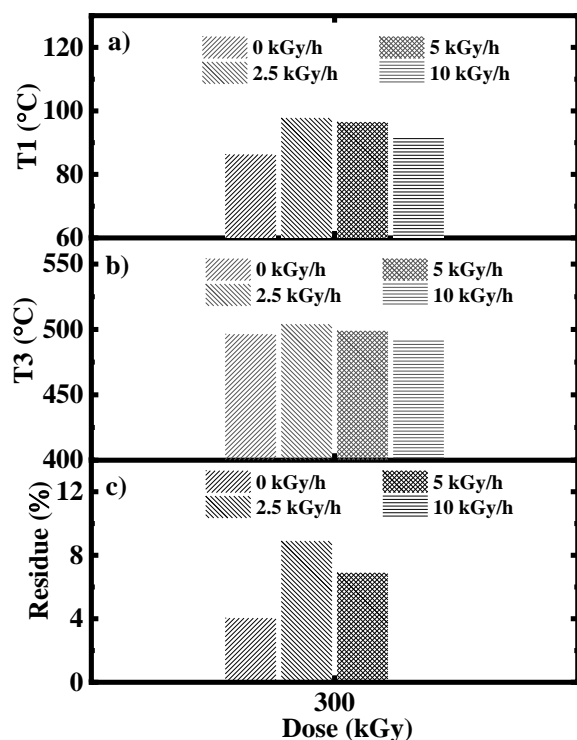


Figure 3. The values of decomposition temperature and residue of irradiated Nafion membranes at a dose of 300 kGy.

Figure 4 depicts the XRD profiles of irradiated Nafion membranes upon irradiation at 300 kGy. The unirradiated membrane exhibits a crystal peak (100) at 17.94° [8]. Additionally, a weak scattering peak at 15.32° is attributed to the amorphous phase of the perfluoroether side chain that terminates with sulfonic acid groups and the main PTFE chains. The peak shape and peak intensity of the irradiated samples exhibit a significant change as compared to those of the pristine membranes. The lower peak intensity at 17.94° should relate to the decrease in crystallinity [8].

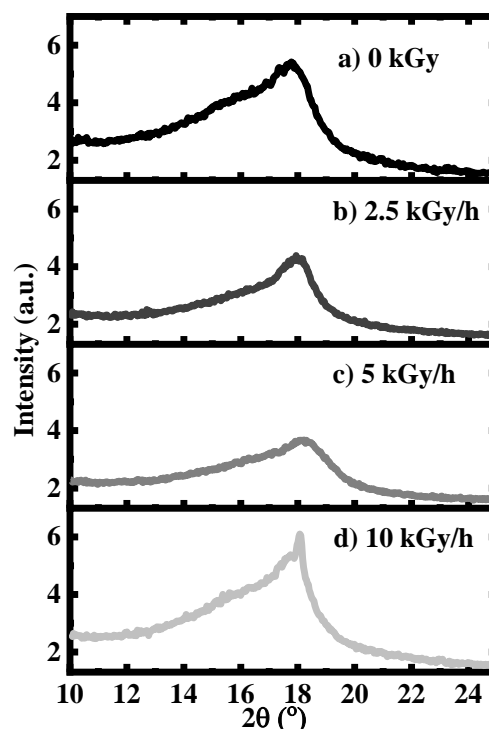


Figure 4. XRD patterns of the unirradiated and irradiated Nafion membranes by gamma irradiation at a dose of 300 kGy.

Figure 5 illustrates the change in calculated crystallinity values in the Nafion membranes. Clearly, all irradiated membranes show lower crystallinity than the pristine membrane. This decrease in crystallinity should associate to the degradation of the inherent crystalline phase of the polymer main chains due to the irradiation. Nafion membrane at a dose rate of 2.5 kGy/h results in the strongest reduction in crystallinity compared to doses of 5 and 10 kGy/h at the same total dose of 300 kGy is likely due to the cumulative effect of prolonged exposure at the lower dose rate [9].

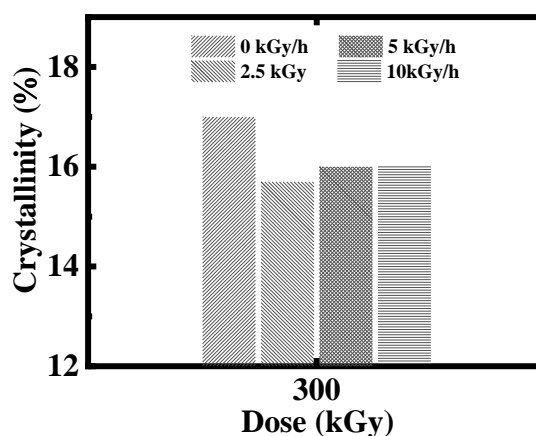


Figure 5. The change of crystallinity upon irradiation.

CONCLUSION

This work reports the effects of gamma irradiation on Nafion membranes at a dose of 300 kGy with different dose rates of 0, 2.5, 5, and 10 kGy/h. All irradiated membranes show lower crystallinity than the original membrane, reflecting the degradation of the inherent crystalline phase of the polymer main chains. At an irradiation dose of 300 kGy, the effects by the irradiation at 2.5 kGy/h show more pronounced than those at the higher dose rates of 5 and 10 kGy/h. The cross-linking was found to be generated in the irradiated membranes, leading to the higher temperature for the de-absorption of water molecules that are bounded to the sulfonic groups.

Acknowledgment

This work was funded by Vingroup Big Data Institute (VINBIGDATA), Vingroup and supported by Vingroup Innovation Foundation (VINIF) under project code VINIF.2020.DA08.

References

- [1] Karimi MB, Mohammadi F, Hooshyari K, *Recent approaches to improve Nafion performance for fuel cell applications, A review*, International Journal of Hydrogen Energy **54** (2019) 28919-28938.
- [2] Ma J, Ni HJ, Su DY, Huang MY, Wang XX, *The research status of Nafion ternary composite membrane*, International journal of hydrogen energy **17** (2012) 13185-13190.
- [3] Almeida SH, Kawano Y, *Effects of X-ray radiation on Nafion membrane*, Polymer degradation and stability, **2** (1998) 291-297.
- [4] Hao LH, Hieu DT, Luan LQ, Phuong HT, Dinh VP, Tuyen LA, Hong PT, Van Man T, Tap TD, *Electron and gamma irradiation-induced effects in poly (ethylene-co-tetrafluoroethylene) films*, Journal of Applied Polymer Science **29** (2022) 52620.
- [5] Nishiyama H, Takamuku S, Oshikawa K, Lacher S, Iiyama A, Inukai J, *Chemical states of water molecules distributed inside a proton exchange membrane of a running fuel cell studied by operando coherent anti-Stokes Raman scattering spectroscopy*, The Journal of Physical Chemistry C **18** (2020) 9703-9711.
- [6] Gong C, Pinatti L, Lavigne G, Shaw MT, Scola DA, *Montgomery T. Shaw, and Daniel A. Scola, Thermal stability of end-capped and linear sulfonated polyimides, sulfonated polystyrene, and Nafion 117*, Journal of Applied Polymer Science **3** (2018) 45694.
- [7] De Almeida S, Kawano Y, *Thermal behavior of Nafion membranes*, Journal of Thermal Analysis and Calorimetry **3** (1999) 569-577.
- [8] Schulze M, Lorenz M, Wagner N, Gülzow E, *XPS analysis of the degradation of Nafion*, Fresenius' journal of analytical chemistry **365** (1999) 106-113.
- [9] Naikwadi AT, Sharma BK, Bhatt KD, Mahanwar PA, *Gamma radiation processed polymeric materials for high performance applications: A review*, Frontiers in Chemistry **10** (2022) 837111.

SYNTHESIS OF RASPBERRY-LIKE NANOGAPPED IRON OXIDE GOLD (Fe₃O₄-Au) FOR PHOTOTHERMAL EFFECT-BASED LATERAL FLOW SENSING APPLICATION

Nam Luyen Van^{1,2}, Thu Thao Pham¹, Truong TN Lien^{1*}

¹Convergence Technology Division, Vietnam-Korea Institute of Science and Technology Hoa Lac High-tech Park, Km 29 Thang Long Boulevard, Hanoi 100000, Vietnam

²Hanoi University of Science and Technology, Dai Co Viet street, Hanoi 100000, Vietnam

*Email: ttnlien@most.gov.vn

ABSTRACT

The photothermal effect of nanoparticles has recently attracted a lot of interest from scientists due to the benefits in the biomedical field. The gold decorated-magnetic nanoparticles applied for lateral flow immunoassay (LFIA) test strips allow reading of both optical and magnetic signals. In this study, we investigated the photothermal properties of raspberry-like nanogapped iron oxide gold to improve the performance of the test strip. We successfully synthesized Fe₃O₄-PEI composites with high magnetism, approximately 70 emu/g by solvothermal method, and an average diameter from 100 to 120 nm. Iron oxide is surrounded by polyethyleneimine (PEI) to have a positive charge in the outer layer. This has been proven by the Zeta potential value, +41.1mV. In order to attach gold nanoparticles onto the surface of Fe₃O₄-PEI, we synthesized gold nanoparticles with size 20 nm and then dispersed in HEPES buffer 10 mM and pH 7.4. The Zeta potential of the gold nanoparticles solution is +22.9 mV. Fe₃O₄-PEI composite was then modified with 20 nm gold nanoparticles to have a raspberry nanostructure by electrostatic force. We discovered that the concentration of nanoparticles and the wavelength of laser irradiation are the two most important factors influencing the yield of the photothermal effect. The photothermal effect of nanoparticles increased proportionally to nanoparticle concentration. The critical point is that the Fe₃O₄-Au demonstrated better photothermal properties than individual Fe₃O₄ nanoparticles and gold nanoparticles under 808 nm laser irradiation. After 5 minutes of stable laser irradiation, the temperature difference of magnetic nanoparticles compared with gold decorated-magnetic nanoparticles increased by 16%. In summary, we successfully develop and optimize the photothermal effect measurement system to detect optical signals of nanoparticles.

Keywords: Photothermal effect, Fe₃O₄@Au nanocomposites, raspberry nanostructure, lateral flow sensor.

INTRODUCTION

In recent years, nanomaterials such as metal oxides, metal sulfides, carbon nanomaterials, gold nanomaterials, especially magnetic nanoparticles, have had many applications in cancer diagnosis and treatment. in tumor phototherapy and in biology [1-3]. Gold nanomaterials are widely used in tumor therapy based on their unique physicochemical properties along with high biocompatibility and surface plasmon resonance effect [4]. For example, stellate gold nanoparticles are surface functionalized by a layer of TAT peptide. After 4 hours of incubation of the TAT layer on BT54 breast cancer cells, photothermal effect analysis was performed using a laser source with wavelength of 850 nm, an emission density of 0.2W/cm². The results showed that the

photothermal effect was enhanced after coating TAT layer on gold nanoparticles, opening up many applications for cancer therapy [5]. Similarly, iron oxide nanoparticles also have many applications in cancer diagnosis and treatment, being used as a contrast enhancer for MIR nuclear magnetic resonance imaging and tumor therapy [6]. However, Fe₃O₄ magnetic iron oxide particles have poor stability and are easily oxidized to form a mixture of iron (II) oxide FeO and iron (III) oxide Fe₂O₃. Magnetic iron oxides are also limited by their weak absorption. in the near infrared region. To solve this problem, surface functionalization of magnetic iron oxide nanoparticles has become a trend in recent years. Gold-coated magnetic nanoparticles have the superparamagnetic properties of magnetic nanoparticles and the surface plasmon resonance

effect of the gold shell opens up many promising applications in tumor detection through analysis of photothermal effects [7,8].

For immunochromatography test strips, there are many different methods to read test strip results, such as based on color lines, optical reading method, or magnetic reading method. Reading test strip results using the photothermal method can take advantage of the surface plasmon resonance effect of gold nanoparticles, besides the measuring equipment system is simple and compact. In this work, we employed gold-coated magnetic nanoparticles to replace AuNPs as a labeling agent of LFIA [9,10]. The most distinctive property of these nanoparticles is the photothermal effect produced after excited by a laser light source. Based on the temperature variation emitted by these particles on the test line, we can calculate the concentration of the analytes to be detected.

EXPERIMENTAL

Reagents

Iron (III) chloride hexahydrate ($\text{FeCl}_3 \cdot 6\text{H}_2\text{O}$, 99%, Merck); ethylene glycol (EG); polyethyleneimine (PEI); sodium acetate anhydrous (NaAc); gold (III) chloride trihydrate (HAuCl_4); ethanol, deionized water

Synthesis of Fe_3O_4 -PEI composites

We have synthesized the magnetic nanoparticles functionalized with PEI by solvothermal method. Typically, 0.68 g $\text{FeCl}_3 \cdot 6\text{H}_2\text{O}$ was first dissolved in 20 mL ethylene glycol by ultrasonic treatment, then add 1 g PEI and 0.6 g NaAc to the solution mixture. The mixture was stirred vigorously and heat to 60 °C for 20 minutes, which was transferred to an autoclave and reacted at 220 °C for 2 h.

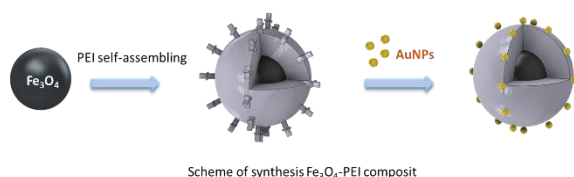


Figure 1. Scheme of synthesis raspberry-like nanogapped iron oxide gold Fe_3O_4 @Au

After the reaction, the black products obtained were rinsed three times with ethanol and deionized water. Finally, the obtained nanoparticles were dried at 60 °C and stored in a vacuum.

Synthesis the gold nanoparticles by chemical reduction method

Firstly, add 3.5 mL of 30 mM HAuCl_4 into a three-neck flask containing 150 mL of deionized water. Then, add 5 mL of 38.8 mM sodium citrate to the solution and stir for 1 min and obtain a clear solution. Add 1 ml of NaBH_4 solution and stir. Then let the solution stand for 6 hours. After 6h, add 40 ml PVP solution 5 mM and stir for 24 h. The resulting wine-red products was centrifuged at 13000 rpm for 15 minutes and then stored at room temperature.

Synthesis of raspberry-like nanogapped iron oxide gold Fe_3O_4 @Au

Magnetic nanoparticles after demagnetization were dispersed at 10 mg in 1.5 ml of water by ultrasonic vibration. Then, drop 1.5 ml magnetic nanoparticles solution into 30 ml HEPES containing gold nanoparticles under ultrasonic for 30 minutes. Thereafter, shake the solution 15 minutes, rinse several times with deionized water and store in a vacuum.

Characterization measurement

The nanostructure and morphologies of the synthesized Fe_3O_4 -PEI composites and raspberry-like nanogapped iron oxide gold Fe_3O_4 @Au were characterized by X-ray diffraction (XRD), field emission scanning electron microscopy (FE-SEM). Magnetic properties were also investigated through the vibrating sample magnetometer method (VSM).

Conduct a photothermal effect survey through a device containing a laser source with different excitation wavelengths of 780 nm, 808 nm and 980 nm, a thermal imaging camera and a smartphone with integrated FLIR One software. FLIR One Pro thermal camera is the latest generation thermal camera line for phones from FLIR with a thermal resolution of 160x120 pixels, an image resolution of 1440 x 1080, and can measure temperatures up to 400 °C. Temperature accuracy is ± 3 °C with ambient temperature from 15 to 35 °C. The camera's connector can connect to both phones using Android and IOS operating systems. The software used integrated on smart phones is FLIR One software that comes with the thermal camera. Sample excitation laser exposure time is 3 minutes. Photothermal measurement results were calculated and analyzed based on the temperature difference between the original nitrocellulose membrane and the membranes coated with solutions containing gold-coated

magnetic nanoparticles with different concentrations.

To investigate the photothermal effect of nanoparticles, it is necessary to prepare samples of gold-coated magnetic nanoparticles with different concentrations: 1000 $\mu\text{g/mL}$; 100 $\mu\text{g/mL}$; 10 $\mu\text{g/mL}$; 1 $\mu\text{g/mL}$. After being prepared, nanoparticle samples were dripped onto nitrocellulose membranes that were cut to a size of 1.3*1.3 cm. The volume applied to the nitrocellulose membrane is 10 μL . Then, dry the nitrocellulose membranes by vacuum for 30 minutes.

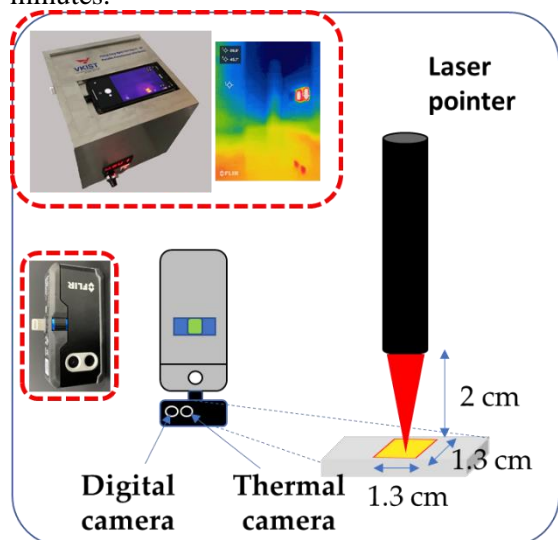


Figure 2. Schematic diagrams of the sample on nitrocellulose substrate upon laser irradiation

RESULTS AND DISCUSSION

Characterization of morphology and crystal structure

The magnetic nanoparticles after synthesized were investigated by field emission scanning electron microscopy (FE-SEM) with a magnification of 50k and transmission electron microscopy TEM. Figure 1a show the FE-SEM images of Fe_3O_4 -PEI with spherical shape and uniform size from 100 to 120 nm. Figure 1b illustrates the TEM images of Fe_3O_4 -PEI, the surface layer-polyethyleneimine PEI was lighter than the core. Besides, the PEI polymer layer also plays a role in stabilizing the nanoparticles and helping to disperse the nanoparticles in the solvent.

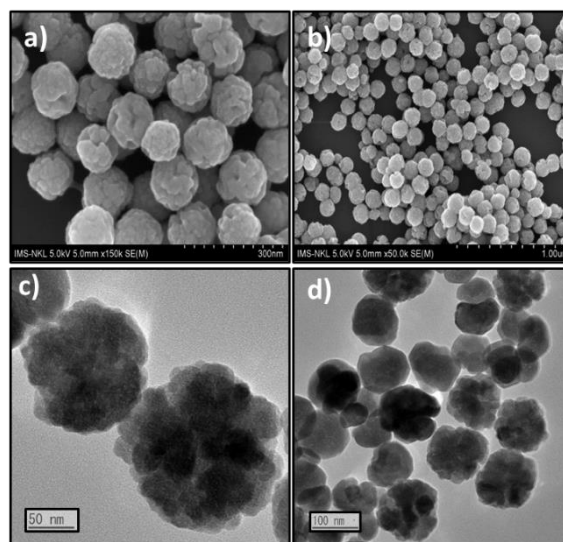


Figure 3. FE-SEM images (a,b) and TEM images (c,d) of Fe_3O_4 -PEI composite

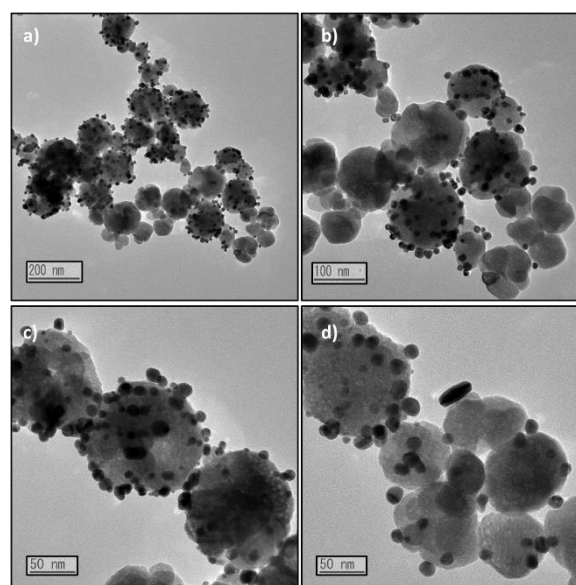


Figure 4. TEM images of raspberry-like nanogapped iron oxide gold $\text{Fe}_3\text{O}_4@Au$

After synthesis magnetic nanoparticles, to increase the stability and biological, we were function surface with the polyethyleneimine PEI. Besides, positively charged PEI easily binds to negatively charged gold nanoparticles based on electrostatic interactions. Figure 4a,b,c,d show TEM images with different magnifications of raspberry-like nanogapped iron oxide gold $\text{Fe}_3\text{O}_4@Au$. Gold nanoparticles with diameter 15-20 nm surround the surface of magnetic nanoparticles.

The successful synthesis of raspberry-like nanogapped iron oxide gold $\text{Fe}_3\text{O}_4@Au$ was confirmed by the X-ray diffraction pattern shown in Figure 5. The characteristic diffraction peaks of Fe_3O_4 -PEI and $\text{Fe}_3\text{O}_4@Au$ were located at $2\theta =$

30,211°; 35,513°; 43,138°; 53,553°; 57,064°; 62,689°, which corresponded to (220), (311), (400), (511), (440), respectively. The 2θ diffraction peak has the greatest intensity at the position corresponding to the (311) crystal face. Moreover, the results show the appearance of characteristic diffraction peaks of Au which indicates that gold nanoparticles were successfully formed on the surface of Fe₃O₄ nanoparticles.

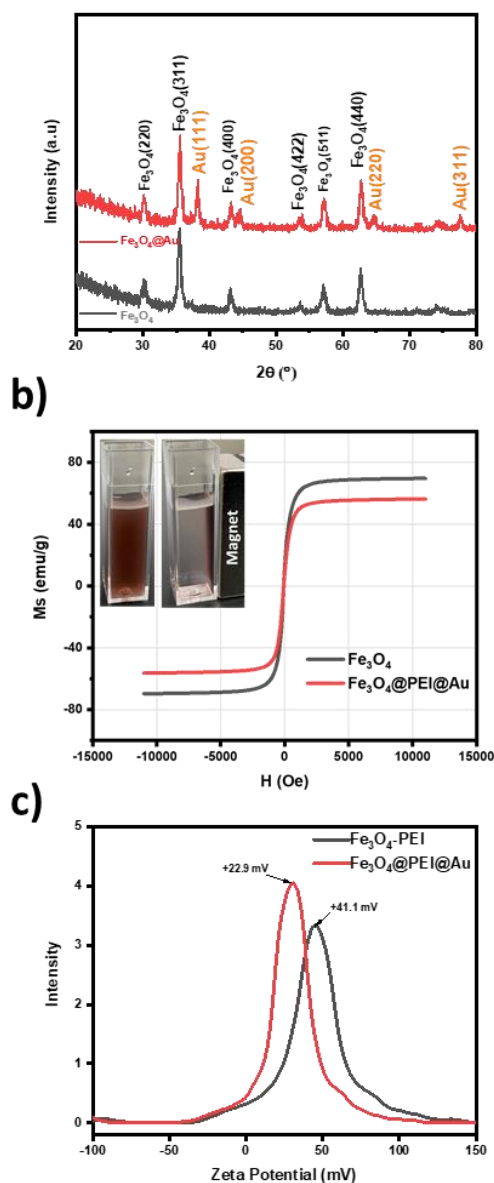


Figure 5. XRD patterns of the Fe₃O₄-PEI composite and raspberry-like nanogapped iron oxide gold Fe₃O₄@Au (a), magnetic hysteresis curve of Fe₃O₄-PEI and Fe₃O₄@PEI@Au (b) and Zeta potential of Fe₃O₄-PEI and Fe₃O₄@PEI@Au (c)

The magnetic properties of Fe₃O₄-PEI and Fe₃O₄@PEI@Au were characterized by VSM and Figure 5b shows the typical room temperature magnetization curve of the samples. As the result, magnetism of Fe₃O₄ NPs was reduced compare with Fe₃O₄@Au, specifically from 70 emu/g to 56 emu/g.

The zeta potential was performed to study the surface charge of magnetic nanoparticles before and after binding AuNPs. The zeta potential of magnetic nanoparticles Fe₃O₄-PEI is +41.1 mV and shifted to +22.9 mV after binding AuNPs. The potential charge indicates that Au layer was attached successfully on the surface of magnetic nanoparticles.

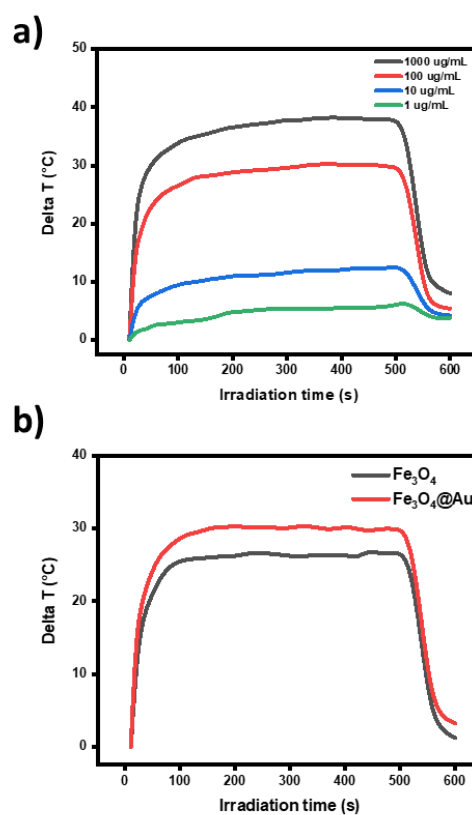


Figure 6. Temperature difference of Fe₃O₄@PEI@Au particles at different concentrations (a) and comparison temperature difference between Fe₃O₄-PEI and Fe₃O₄@PEI@Au (b)

The photothermal effect has been studied for raspberry-like nanogapped iron oxide gold Fe₃O₄@Au with varying concentrations suitable for quantitative detection on immunochromatographic test strips. The concentrations investigated were 1000 μg/mL and 100 μg/mL, 10 μg/mL, 1 μg/mL, respectively. The

results shown in Figure 6a indicates that the temperature difference changes when changing the particle concentration. At the highest concentration 1000 $\mu\text{g/mL}$, the generated temperature reached approximately 40 $^{\circ}\text{C}$. Furthermore, under 808 nm laser irradiation, $\text{Fe}_3\text{O}_4@Au$ NPs has better photothermal properties than Fe_3O_4 NPs in the same concentration.

CONCLUSION

In this study, we successfully synthesized Fe_3O_4 -PEI composites and raspberry-like nanogapped iron oxide gold $\text{Fe}_3\text{O}_4@Au$ with spherical shape and uniform size from 100 nm to 120 nm. The analysis results of structural morphology, magnetic properties and surface potential have shown the successful synthesis of a raspberry-shaped gold-attached magnetic particle structure. We discovered that the concentration of nanoparticles and the wavelength of laser irradiation are the two most important factors influencing the yield of the photothermal effect. Especially, $\text{Fe}_3\text{O}_4@Au$ nanoparticle has better photothermal properties than Fe_3O_4 NPs under 808 nm laser irradiation.

Acknowledgment

All authors are grateful for the financial support from ministry-project level 05.2021M001

References

- [1] J. Baranwal, B. Barse, A. Di Petrillo, G. Gatto, L. Pilia, and A. Kumar, *Nanoparticles in Cancer Diagnosis and Treatment*, Materials (Basel) **16**(15) (2023), doi: 10.3390/ma16155354.
- [2] H. Huang and J. F. Lovell, *Advanced Functional Nanomaterials for Theranostics*, (2017), doi: 10.1002/adfm.201603524.
- [3] T. I. Shabatina, O. I. Vernaya, N. L. Shimanovskiy, and M. Y. Melnikov, *Metal and Metal Oxides Nanoparticles and Nanosystems in Anticancer and Antiviral Theragnostic Agents*, Pharmaceutics **15**(4) (2023), doi: 10.3390/pharmaceutics15041181.
- [4] P. Huang et al., *Biodegradable Gold Nanovesicles with an Ultrastrong Plasmonic Coupling Effect for Photoacoustic Imaging and Photothermal Therapy* **, (2013) 14208–14214, doi: 10.1002/ange.201308986.
- [5] H. Yuan, A. M. Fales, and T. Vo-dinh, *TAT Peptide-Functionalized Gold Nanostars:*

Enhanced Intracellular Delivery and Efficient NIR Photothermal Therapy Using Ultralow Irradiance, (2012).

- [6] G. Thomas et al., *Innovative Magnetic Nanoparticles for PET/MRI Bimodal Imaging*, ACS Omega **4**(2) (2019) 2637-2648, doi: 10.1021/acsomega.8b03283.
- [7] Y. Hu et al., *Multifunctional $\text{Fe}_3\text{O}_4@Au$ core/shell nanostars: A unique platform for multimode imaging and photothermal therapy of tumors,* Sci. Rep. **6** (2016) 1-12, doi: 10.1038/srep28325.
- [8] Q. Tian et al., *Multifunctional polypyrrole@ Fe_3O_4 nanoparticles for dual-modal imaging and in vivo photothermal cancer therapy*, Small **10**(6) (2014) 1063-1068, doi: 10.1002/smll.201302042.
- [9] F. Liu et al., *Highly sensitive and selective lateral flow immunoassay based on magnetic nanoparticles for quantitative detection of carcinoembryonic antigen*, Talanta (2016), doi: 10.1016/j.talanta.2016.08.048.
- [10] W. Ren and J. Irudayaraj, *Magnetic Control-Enhanced Lateral Flow Technique for Ultrasensitive Nucleic Acid Target Detection*, ACS Omega **7** (33) (2022) 29204-29210, doi: 10.1021/acsomega.2c03276.

RESEARCH AND FACILE SYNTHESIS Fe-Co/CF-700 HYBRID COMPOSITE AS AN ANODE ELECTRODE FOR LITHIUM-ION BATTERIES

Do Thao Anh^{1,2}, **Nguyen La Ngoc Tran**^{1,2}, **Nguyen Tran Truc Phuong**^{1,2}, **Doan Le Hoang Tan**^{2,3}, **Le Hong Tho**^{1,2}, **Le Thanh Tam**^{1,2}, **Bach Thang Phan**^{2,3}, **Nguyen Tuan Loi**⁴, **Pham Dang Hung**⁵, **Truong Quang Kha**⁵, **Nhu Hoa Thi Tran**^{1,2*}

¹Faculty of Materials Science and Technology, VNUHCM-University of Science, 227 Nguyễn Văn Cừ Street, Ward 4, District 5, Ho Chi Minh City, Viet Nam

²Vietnam National University Ho Chi Minh City, Community 6, Linh Trung Ward, Thu Duc City, Ho Chi Minh City, Vietnam;

³Center for Innovative Materials and Architectures (INOMAR), Community 6, Linh Trung Ward, Thu Duc City, Ho Chi Minh City, Vietnam;

⁴Institute of Fundamental and Applied Sciences, Duy Tan University, Ho Chi Minh City, 700000, Viet Nam

⁵High School for the Gifted, Vietnam National University, Ho Chi Minh City, Viet Nam

Email: ttnhoa@hcmus.edu.vn

ABSTRACT

Lithium-ion batteries (LIBs) have established themselves as indispensable power sources in modern electronic devices and components, largely attributed to their exceptional attributes, including high energy density, substantial capacity, extended usage duration. In a recent investigation, we have successfully synthesized a novel hybrid nanostructured material, Fe-Co/CF, employing a straightforward and expeditious chemical method that combines a ZIF-67 precursor with Fe₃O₄ nanoparticles (Fe₃O₄ NPs). This innovative hybrid material effectively amalgamates the advantageous characteristics of its foundational components, augmented specific capacity, and reduced volume expansion during operational cycles. Electrochemical tests such as Galvanostatic charge/discharge (GCD) profiles and Coulombic efficiency (CE) were conducted to thoroughly examine the performance of the Fe-Co/CF-700 electrode. The convincing results demonstrate the high electrochemical performance of the Fe-Co/CF-700 hybrid, achieving an impressive capacity of about 523 mAh/g while still maintaining a Coulombic efficiency (CE) of 98% after 20 cycles at a constant current density of 0.1 A/g. These findings clearly emphasize the great promise of Fe-Co/CF-700 hybrids composite as a transformative candidate to boost anode electrode technology in LIB applications in the future.

Keywords: Lithium-ion batteries, hybrid nanostructure, high electrochemical performance

INTRODUCTION

The pursuit of high energy density lithium-ion batteries (LIBs) has driven investigations into electroactive materials offering high theoretical specific capacity at low cost. In this vein, Fe₃O₄ nanoparticles (NPs) has emerged as a promising LIB anode material owing to its exceptionally high capacity on the order of 926 mAh/g [1]. Moreover, iron is inexpensive and Fe₃O₄ NPs possesses a sufficiently high redox potential to prevent Li dendrite formation during cycling. Capitalizing on inexpensive Fe₃O₄ anodes material with high Li⁺ ion storage capacity could enable dramatic improvements in LIB energy

density without prohibitive cost increases. However, Fe₃O₄ NPs is prone to aggregation and volume expansion during cycling, rapidly decreasing its capacity [2]. Overcoming these limitations is critical to fully harness Fe₃O₄'s promise for superior Li⁺ ion storage.

Metal-organic frameworks (MOFs) have become attractive precursors for engineering magnetic iron oxide nanocomposites like Fe₃O₄. Pyrolysis ZIF-67 belonging to the MOF family, which converts organic ligands into a carbon framework (CF), yielding porous nanostructured carbon with retained crystallinity and large pore volumes. The carbon nanopores promote rapid mass transfer and metal ion adsorption.

Additionally, the porous carbon support prevents aggregation of embedded Fe_3O_4 nanoparticles, conferring enhanced stability compared to bare nanoparticles by isolating the magnetic domains. Overall, pyrolyzed MOFs enable tailored synthesis of iron oxide/carbon nanocomposites with controlled nanostructure and porosity for applications in energy storage [3]. In recent years, research on Cobalt zeolitic imidazolate framework (ZIF-67) materials in the field of energy storage has received a lot of attention. Mingxuan Guo *et al.* [4] showed hybrid porous carbons delivered an initial capacity of 677 mAh/g at 50 mA/g, which was maintained at 312 mAh/g after 100 cycles. As nearly reported by Wang *et al.* [5] the Si@NC-ZIF composite exhibited excellent capacity retention of 1623.05 mAh/g after 100 cycles at 200 mA/g, with the retention rate reaching 86.29 %.

In this study, the carbon framework based on ZIF-67 has demonstrated the ability to alleviate the volume change of Fe_3O_4 and improve the Li^+ transport kinetics. The Fe-Co/CF-700 hybrid nanostructure as an anode material showed high electrochemical performance.

EXPERIMENTAL

Materials synthesis. Fe_3O_4 -Co carbon framework (Fe-Co/CF) hybrid composites are synthesized by dispersing Fe_3O_4 NPs, $\text{Co}(\text{NO}_3)_2 \cdot 6\text{H}_2\text{O}$, 2-methylimidazole and PVP in 80 mL of methanol. The mixture is ultrasonicated for 10 minutes before being stirred for 24 hours. The precipitate is then washed repeatedly with methanol using centrifugation at 4500 rpm for 5 minutes, followed by vacuum drying. The dried sample is directly carbonized under N_2

atmosphere in a tube furnace at 700°C for 2.5 hours, with a heating rate of 5°C per minute, the sample is denoted as Fe-Co/CF-700. For comparison, Fe_3O_4 and Co/CF are also synthesized separately and used as anode electrode materials.

Preparation of anode electrodes. A slurry active anode material is prepared by dissolving active material, Super P (carbon black), and polyvinylidene fluoride 10% (PVDF 10%) binder in N-methylpyrrolidone (NMP) solvent. After covering the Cu foil with mud and drying it in a vacuum oven, cut it into a round electrode with a diameter of 15 mm. The prepared electrodes are used as anodes, with Li metal foil as counter electrodes in coin-type half cells assembled in an Ar-filled glove box. The separator is a polypropylene (Celgard 2400) membrane, and the electrolyte is 1.0 M LiPF₆ in a 1:1 volume ratio of ethylene carbonate (EC)/diethylene carbonate (DEC). CR 2032 coin-type half cells are assembled for electrochemical performance measurements of the electrode samples.

Characterization techniques. Powder X-ray diffraction (PXRD, Bruker D8 Advance diffractometer, λ is 1.54178 Å) and Fourier-transform infrared spectroscopy (FTIR, Bruker Vertex 70), nitrogen adsorption isotherms at 77 K using N_2 atmosphere is collected on NOVA 3200e and field emission scanning electron microscope (FESEM, Hitachi S4800, USA) operated at an accelerating voltage of 5 kV are used to evaluate the properties and morphology of materials. Meanwhile, the Galvanostatic charge/discharge (GCD) profiles and coulombic efficiency (CE) at

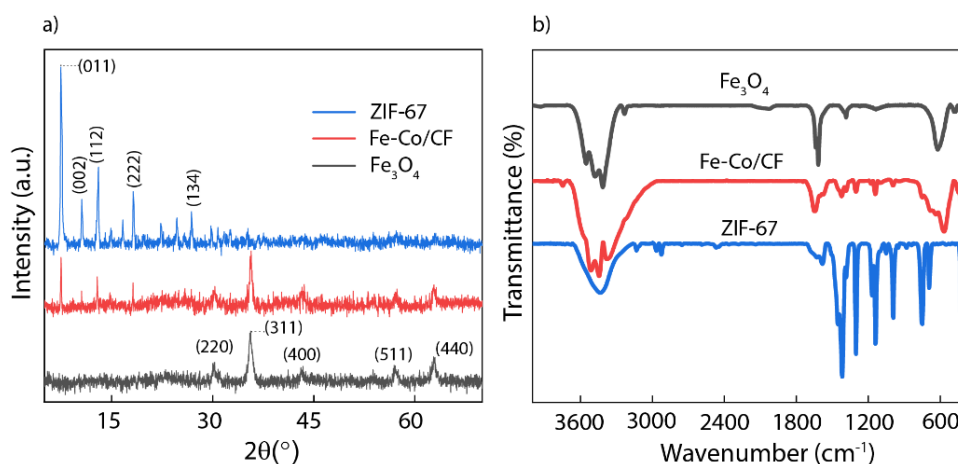


Figure 1. Characterization of Fe_3O_4 , ZIF-67 and Fe-Co/CF (a) XRD patterns; (b) FTIR spectrum.

a fixed current density were used for electrochemical testing in LIB.

RESULTS AND DISCUSSION

XRD patterns shown in **Figure 1a** of ZIF-67, Fe₃O₄ NPs, and Fe-Co/CF hybrid composite. Fe-Co/CF showed crystal facets (220), (311), (400), (511), and (440) corresponding to lattice planes of Fe₃O₄ NPs, respectively. [1,2]. At the same time, it also showed the crystal faces (011), (002), (112), (222) which were consistent with the XRD pattern of ZIF-67 [5,6]. The FTIR spectrum shown in **Figure 1b**, Fe-Co/CF exhibits a peak at 424 corresponding to Co-N bonding in ZIF-67 [7,8] while a peak at 565 cm⁻¹ of Fe-O bonding indicates the presence of Fe₃O₄ [7]. According to Chen *et al.* [7] reported, the incorporation of Fe₃O₄ into ZIF-67 shifted the N-H peak from 1577 cm⁻¹ to 1570 cm⁻¹, indicating that Fe₃O₄ bonded to ZIF-67 through Fe-N bonding. The peaks at 1618 cm⁻¹ and around 3400 cm⁻¹ were corresponding to the vibrations of O-H, N-H groups on the surface of Fe-Co/CF [9].

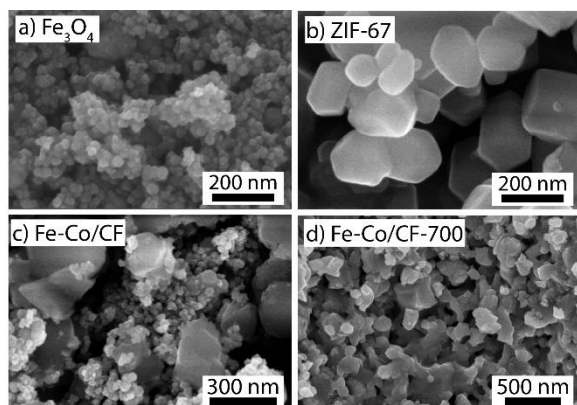


Figure 2. FESEM images of (a) Fe₃O₄ NPs, (b) ZIF-67, (c) Fe-Co/CF and Fe-Co/CF-700.

The FESEM images of materials were shown in **Figure 2**. Fe₃O₄ NPs (**Figure 2a**) have a spherical shape particle size of about 30 nm while ZIF-67 (**Figure 2b**) forms characteristic rhombic dodecahedral shape [4,6], nanosize about 200 nm. Fe-Co/CF in **Figure 2c** showed that Fe₃O₄ NPs were embedded into the ZIF-67 particles to form a hybrid composite structure while still maintaining the nano size. After that, the Fe-Co/CF-700 undergoes sintering at the high temperature, they were tightly linked together, Fe₃O₄ NPs were embedded deeper inside the carbon framework, which formed from organic ligands of ZIF-67.

Figure 3a showed the cycling performance of the three samples at a current density of 0.1 A/g for 20 cycles. In comparison, Fe-Co/CF-700 exhibited superior cycling performance in terms of specific capacity and stability. After 20 cycles, Fe-Co/CF-700 delivered a specific discharge capacity of 531 mAh/g with CE 98%, considerably higher than the corresponding values for Co/CF (316 mAh/g with CE 98%) and Fe₃O₄ (88 mAh/g with CE 92%). **Figure 3b** presented the discharge-charge voltage profiles of Fe-Co/CF-700 for the first, tenth and twentieth cycles. In the first cycle, a reduction peak appeared at 0.64 V and then shifted to 0.80 V in cycle 10 and 0.85 V in cycle 20, showing a change in the structure of the Fe-Co/CF-700 electrode [5]. Similarly, the oxidation peak at 2.1 V in the first cycle also shifted to 2.2 V in the 10th and 20th cycles. The initial discharge and charge capacities of Fe-Co/CF-700 were 969 mAh/g and 688 mAh/g, respectively, with a CE of 71%. This indicated formation of a solid electrolyte interphase (SEI) film on the anode electrode [5,10]. In the 10th cycle, the discharge/charge

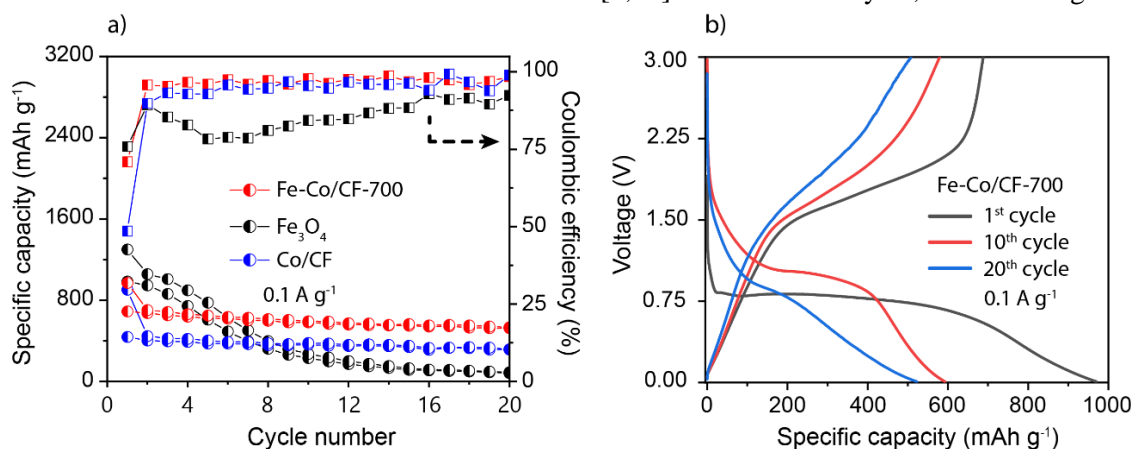


Figure 3. (a) Cycling performance of Fe₃O₄, Co/CF and Fe-Co/CF-700, (b) Galvanostatic charge-discharge profiles of Fe-Co/CF-700 at a current density of 0.1 A/g.

capacity was 592/579 mAh/g and in the 20th cycle it was 523/531 mAh/g with a CE of 97% and 98%, respectively. This minimal capacity loss demonstrated that utilizing a carbon graphite framework from pyrolysis of ZIF-67 to mitigate volume expansion of Fe₃O₄ had beneficial effects.

CONCLUSION

In summary, Fe-Co/CF-700 was prepared a facile and broadly applicable way for LIBs efficiently. The ZIF-67- derived graphite carbon framework not only provides carbon to improve electrical conductivity, increasing Li⁺ ion exchange sites and electron mobility, but also helps mitigate the volume expansion of Fe₃O₄ nanoparticles during cycling. Therefore, the Fe-Co/CF-700 composite exhibits remarkable Li⁺ ion storage capability, showing high capacity of 523 mAh/g after 20 cycles and a CE up to 98%. Therefore, this hybrid nanostructure Fe-Co/CF-700 can be an advanced electrode for high-performance LIBs, establishes a novel methodology for designing active materials for next-generation energy storage systems.

Acknowledgment

The research is funded by the University of Sciences, Vietnam National University-HCM (U2022-22).

References

- [1] F. Shi, Q. Liu, Z. Jin, G. Huang, B. Xing, J. Jia, C. Zhang, *A facile method to prepare Fe₃O₄@CTP QDs composite as advanced anode material for lithium ion batteries*, J Alloys Compd. **890** (2022) 161911.
- [2] Z. Liu, Z. Zhao, S. Wang, C. Xiong, *Solvent-induced synthesis of hollow structured Fe₃O₄-based anode materials for high-performance Li-ion batteries*, Journal of Materiomics. **6** (2020) 485–493.
- [3] X.N. Lv, P.F. Wang, Y.H. Zhang, Q. Shi, F.N. Shi, *MOF-derived CoFe₂O₄/FeO/Fe nanocomposites as anode materials for high-performance lithium-ion batteries*, J Alloys Compd. **923** (2022) 166316.
- [4] M. Guo, T. Gao, H. Ma, H. Li, *Weaving ZIF-67 by employing carbon nanotubes to constitute hybrid anode for lithium ions battery*, Mater Lett. **212** (2018) 143–146.
- [5] M. Wang, F. Xi, S. Li, W. Ma, X. Wan, Z. Tong, B. Luo, *ZIF-67-derived porous nitrogen-doped carbon shell encapsulates photovoltaic silicon cutting waste as anode in high-performance lithium-ion batteries*, Journal of Electroanalytical Chemistry. **931** (2023) 117210.
- [6] M. Shahsavari, M. Mortazavi, S. Tajik, I. Sheikhshoae, H. Beitollahi, *Synthesis and Characterization of GO/ZIF-67 Nanocomposite: Investigation of Catalytic Activity for the Determination of Epinine in the Presence of Dobutamine*, Micromachines. **13** (2022) 88.
- [7] M. Chen, N. Wang, X. Wang, Y. Zhou, L. Zhu, *Enhanced degradation of tetrabromobisphenol A by magnetic Fe₃O₄@ZIF-67 composites as a heterogeneous Fenton-like catalyst*, Chemical Engineering Journal. **413** (2021) 127539.
- [8] R. Ediati, P. Elfianuar, E. Santoso, D.O. Sulistiono, M. Nadjib, R. Ediati, P. Elfianuar, E. Santoso, D.O. Sulistiono, M. Nadjib, *Synthesis of MCM-41/ZIF-67 Composite for Enhanced Adsorptive Removal of Methyl Orange in Aqueous Solution*, Mesoporous Materials - Properties and Applications. (2019).
- [9] S.W. Huang, Y.F. Lin, Y.X. Li, C.C. Hu, T.C. Chiu, *Synthesis of Fluorescent Carbon Dots as Selective and Sensitive Probes for Cupric Ions and Cell Imaging*, Molecules. **24** (2019) 1785.
- [10] X. He, Y. He, C. Wang, B. Zhu, A. Liu, H. Tang, *Oxygen vacancy-rich Fe₃O₄ nanoparticle synthesized via facile electrochemical method as anode material for high-performance lithium-ion batteries*, Journal of Physics and Chemistry of Solids. **171** (2022).

IMPACT STRENGTH CHARACTERISTIC ANALYSIS OF 3D PRINTED ASA MATERIAL BY FUSED DEPOSITION MODELING METHOD

**Do Thanh Trung¹, Ho Van Nghia¹, Nguyen Mai Tran Phong¹, Pham Thi Hong Nga¹,
Nguyen Thanh Tan¹, Truong Nguyen Luan Vu¹, Hoang Van Huong¹, and Nguyen Vinh Tien²**

¹Faculty of Mechanical Engineering, Ho Chi Minh City University of Technology and Education,
01 Vo Van Ngan Street, Linh Chieu Ward, Thu Duc City, Ho Chi Minh City, Vietnam

²Faculty of Chemical and Food Technology, Ho Chi Minh City University of Technology and Education,
01 Vo Van Ngan Street, Linh Chieu Ward, Thu Duc City, Ho Chi Minh City, Vietnam

Email: hongnga@hcmute.edu.vn

ABSTRACT

This article explores the characteristics of a 3D ASA (Acrylonitrile Styrene Acrylate) model through the Fused Deposition Modeling (FDM) method, the results of a model evaluation and optimization process. In this study, we focused on adjusting the infill percentage (IP) at 30%, 50% with Tri-hexagon Infills or Grids. The collected results show total impact force (J), distribution of impact force per sample area (KJ/m²), distribution of impact force per sample thickness (J/m) as experimental responses. To determine the optimal parameters, regression equation analysis was performed to identify the most important parameters. Furthermore, they indicated that both input parameters significantly influence the output responses, and the interaction between the two input parameters reveals a fact: increasing the IP leads to heavier sample masses, while the infills affect the mechanical characteristic of the samples.

Keywords: Acrylonitrile styrene acrylate, Polymer, Impact Strength, Fused Deposition

INTRODUCTION

ASA, short for Acrylonitrile Styrene Acrylate, is favored for its durability and resistance to UV radiation, high temperatures, and certain chemicals. Its UV resistance makes it ideal for outdoor use, preventing degradation, while its heat and oil resistance maintain color integrity [1-5]. This versatility allows ASA to be used in outdoor designs. However, ASA's specific properties in 3D FDM printing remain unclear [6-10].

At present, many researches about the impact testing data for 3D FDM printed materials remains are published but yet in few numbers. Ziemian [11] scrutinized the influence of infill orientation on ABS 3D models using the Izod impact test, with vertically oriented specimens displaying the highest average impact energy among the various orientations. Zhang [12] delved into the impact of ASA and PVC ratios on material strength through Izod impact testing. Rahman [13] conducted an investigation into the impact strength properties of Polyether Ether Ketone (PEEK) utilizing Charpy impact testing, revealing that samples positioned at a 0° angle absorbed the most average impact energy, looking closely by those at a 90° angle [14].

In our research, we employed FDM for 3D printing using SolidWorks to design components, saved in STL format. Within slicing software [14], we carefully adjusted critical parameters like nozzle size, filament diameter, layer height, infill density, and printing temperature. With these parameters set, the slicing software generated G-code tailored to the 3D printer. In the FDM process, the printer's extrusion head systematically deposits ASA material layer by layer, mirroring the object's design contours. No reinforcement was used in this ASA printing method.

EXPERIMENTAL

The study employs a statistical experimental design technique known as Response Surface Methodology (RSM) to model and analyze one response variable alongside multiple predictor variables. RSM is strategically utilized to identify the optimal set of predictor variables that yield the highest or lowest response value. By fitting a polynomial equation to the data, a mathematical representation of the response surface is constructed.

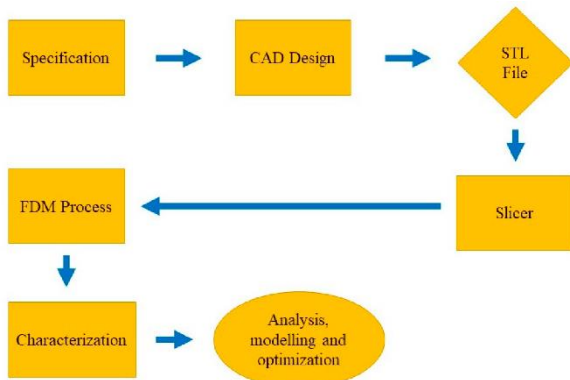


Figure 3. Experimental Implementation Flowchart

Enhancing the ability to make informed decisions in product design, process optimization, and quality control greatly relies on comprehending the relationships between response variables and predictor factors, as revealed by RSM data. Table 1 provides a comprehensive overview of the independent process parameters, accompanied by their corresponding designated levels. These designated levels encompass an array of testing targets allocated to determined factors within the experimental design.

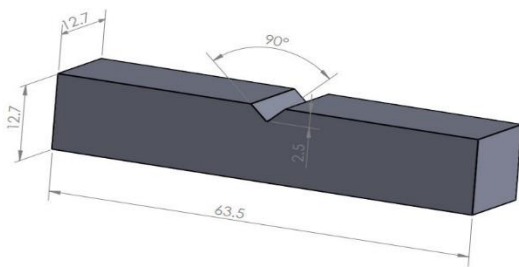


Figure 2. Mechanical design of ASTM D256

Table 1. The Testing parameters along with their corresponding design levels

Parameter	Infill Percentage	Pattern
Acronym	IP	W
Unit	%	-
-2	30	Cubic
-1	50	Cubic
0	30	Tri- Hexagonal
1	50	Tri-Hexagonal
2	30	Grid
3	50	Grid

3D Printer Machine Data (Core XY):

- Top/Bottom and Wall speed: 60 mm/s
- Infill speed: 80 mm/s

- Travel (non-printing) speed: 200 mm/s
- Printing Area: x-y-z=360-390-350 mm
- MCU: LPC1768 (100 MHz)
- CPU: H3 (1.2 GHz)
- Bed temperature: 130 °C
- Fan speed: 30%
- Nozzle temperature: 240 °C
- Build surface: PEI.

The machine used for Izod Impact Testing is a Low Energy Plastic Impact Tester Tinius Olsen MODEL IT503/504, hammer weight is first identified as 0.9 kg. Fracture types were observed and appeared in 1 class according to the ASTM D256 standard: partial break. The ensuing equations elucidate the computation process utilized to determine the impact energy of each individual sample [14]:

$$Impact\ Energy(Joule) = WgL\cos(\theta_f) \frac{\pi}{180} - \cos(\theta_i) \frac{\pi}{180} - f_L \quad (1)$$

$$Impact\ Energy \left(\frac{Joule}{meter} \right) = \frac{Impact\ Energy(Joule)}{Sample\ Thickness(meter)} \quad (2)$$

- W = pendulum hammer weight used (kg)
- g = acceleration due to gravity (9.81 m/s²)
- L= length of hammer arm (m)
- θ_f = Impact angle (°)
- f_L = friction impact (J)
- θ_i = Release angle (°)



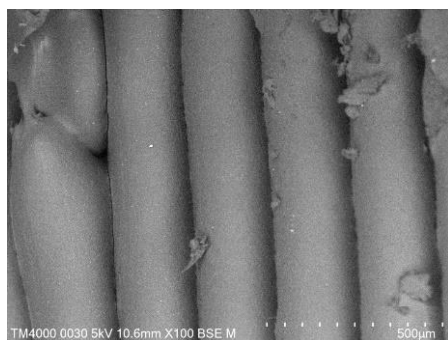
Figure 3. Model is clamped before testing.

To analyze post-test pattern structures, Scanning Electron Microscopy (SEM) was employed. SEM provides insights into microstructure, texture, and surface features, aiding our comprehension of model properties and behavior. The SEM machine used in this study is the Tabletop Microscopes TM4000, operating at 100x magnification and a length scale of 500 μm.

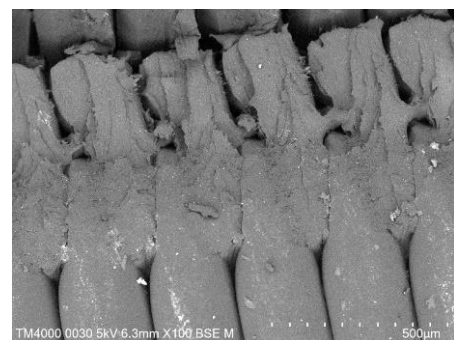
RESULTS AND DISCUSSION

Table 1. Measurement results from 6 models after Izod Impact Testing

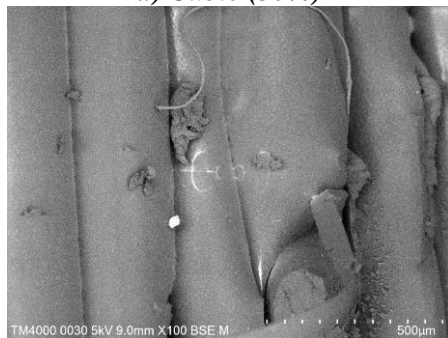
No.	Pattern	Infill Percentage	3D Printer Requirement			Izod Impact Strength		
			Layer Height (mm)	Wall thickness (mm)	Top/Bottom Thickness (mm)	J	kJ/m ²	J/m
1	Cubic	30%	0.15	1.20	0.80	3.35	25.18	261.91
2	Cubic	50%	0.15	1.20	0.80	3.27	24.55	255.36
3	Grid	30%	0.15	1.20	0.80	2.58	19.35	201.28
4	Grid	50%	0.15	1.20	0.80	2.78	20.85	216.83
5	Tri-Hexagon	30%	0.15	1.20	0.80	3.30	24.79	257.77
6	Tri-Hexagon	50%	0.15	1.20	0.80	3.58	26.89	279.67



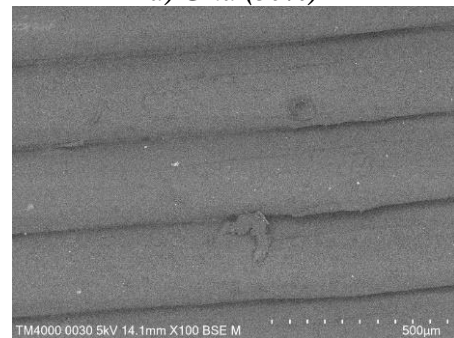
a) Cubic (30%)



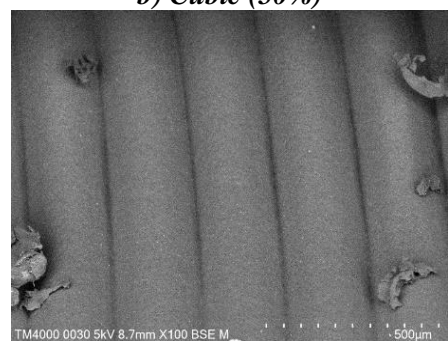
d) Grid (50%)



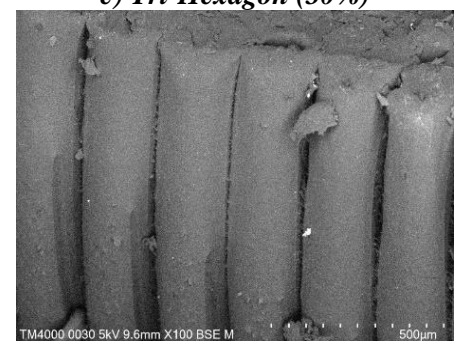
b) Cubic (50%)



e) Tri-Hexagon (30%)



c) Grid (30%)



f) Tri-Hexagon (50%)

Figure 4. SEM results

The data in Figure 4 reveals how Infill Percentage and Pattern affect texture and composition. For instance, a Tri-Hexagon pattern

at 50% Infill causes surface tearing, linked to material density impacting endurance and deformation. Structural failure occurs with a 30%

Grid pattern but changes at 50% Infill, causing more pull-back micro strings. Pull-back strings vary with Pattern; Cubic patterns resemble sandy textures. In Table 2 data, Infill Percentage significantly influences ASA plastic sample durability and properties. For instance, Tri-Hexagonal 50% withstands 3.58 J impact force, 0.28 J more than 30%. Infill pattern matters too; Cubic 30% withstands 3.35 J versus 3.30 J for Tri-Hexagonal 30%. Thus, consider force distribution based on infill pattern in ASA material applications for arrangement and construction. Measured results provide three impact resistance parameters: total impact force J, impact force per area kJ/m^2 , and impact force per thickness J/m. Infill Percentage isn't the sole determinant. Grid 50% and Cubic 30% samples illustrate this. Grid 50% withstands 216.828 J/m per thickness, while Cubic 30% reaches 261.909 J/m. This highlights infill patterns' advantages, enhancing cost-efficiency while maintaining mechanical quality.

CONCLUSION

In summary, our analysis shows that ASA material in the Tri-Hexagonal configuration offers the highest Impact Strength, while the Grid pattern is the weakest choice. For unexpected impacts, the Cubic pattern at 30% Infill Percentage excels in resilience. However, at higher Infill Percentages, the Tri-Hexagonal pattern proves to be the optimal choice.

Acknowledgments

We acknowledge HCMC University of Technology and Education, Dong Nhan Phat Co., Ltd, and Material Testing Laboratory (HCMUTE). They allowed me to join their team and access the laboratory and research machines. With their appreciated support, it is possible to conduct this research.

References

[1] J. K. Fink, *Polyolefins and Styrenics, Handbook of Engineering and Specialty Thermoplastics* **1** (2010) 331.
[2] U. L. Prospector, *Acrylonitrile Styrene, Acrylate (ASA) Plastic* (2018).
[3] B. A.S.F. BASF Corporation, Lurence W. Mckeen, *The effect of UV light and weather on plastics and elastomers* (2013) 104-107.
[4] T. Letcher, M. Waytashek, *Material Property Testing of 3D-Printed Specimen in PLA on an*

Entry-Level 3D Printer, Advanced Manufacturing **2A** (2014).
[5] J. M. Chacon, M. A. Caminero, E. Garcia-Plaza, P. J. Nunez, *Additive Manufacturing of PLA structures using fused deposition modeling: Effect of process of parameters on mechanical properties and their optimal selection*, *Materials and Design* **124** (2017) 143-157.
[6] D. Croccolo, M.D. Agostinis, and G. Olmi, *Experimental characterization and analytical modelling of the mechanical behaviour of fused deposition processed parts made of ABS-M30*, *Computational Materials Science*, **79** (2013) 506-518.
[7] C. Ziemian, M. Sharma, S. Ziemian, *Anisotropic Mechanical Properties of ABS Parts Fabricated by Fused Deposition Modelling*, *Intechopen* (2012) 321-326.
[8] Y. L. Liang, H. J. Sue, R. Minkwitz, *Rubber content effect on scratch behavior in acrylonitrile-styrene-acrylate copolymers*, *Journal of Applied Polymer Science* **126** (2012) 1088-1096.
[9] F. Senatov, K. Niaza, M. Zadorozhnyy, A. Maksimkin, S. Kaloshkin, Y. Estrin, *Mechanical properties and shape memory effect of 3D-printed PLA-based porous Scaffolds* (2016).
[10] M. F. Afrose, S. H. Masood, P. Iovenitti, M. Nikzad, I. Sbarski, *Effects of part build orientations on fatigue behaviour of FDM-processed PLA material*, *Progress in Additive Manufacturing* **1** (2015) 21-28.
[11] S. Ziemian, M. Okwara, C. W. Ziemian, *Tensile and fatigue behavior of layered acrylonitrile butadiene styrene*. *Rapid Prototyping Journal* **21** (2015) 270-278.
[12] Zhang Y, *Study of Poly (vinyl chloride)/Acrylonitrile–Styrene–Acrylate Blends for Compatibility, Toughness, Thermal Stability and UV Irradiation Resistance*, *Applied Polymer Science* **130** (2013).
[13] K. M. Rahman, T. Letcher, R. Reese, *Mechanical Properties of Additively Manufactured PEEK Components Using Fused Filament Fabrication* *Advanced Manufacturing* **2A** (2015) 97-100.
[14] Cahyadi William, *Mechanical Properties of 3D Printed Acrylonitrile Styrene Acrylate* (2019) 132.

THE FLEXURAL STRENGTH OF 3D PRINTING ABS, PETG, ASA AND PLA PLASTICS

**Phan Huu Phuc¹, Le Mai Hieu¹, Huynh Nham Than¹, Nguyen Xuan Tung¹, Nguyen Hoai Linh¹,
Tran Van Dung¹, Pham Thi Hong Nga¹, Hadi Sutanto², Hoang Van Huong¹
and Nguyen Van Thuc¹**

¹ Faculty of Mechanical Engineering, Ho Chi Minh City University of Technology and Education,
01 Vo Van Ngan, Linh Chieu Ward, Thu Duc City, Ho Chi Minh City, Vietnam

² Faculty of Engineering, Atma Jaya Catholic University,

Jl. Jenderal Sudirman 51, Jakarta 12930, Indonesia

Email: hongnga@hcmute.edu.vn

ABSTRACT

This paper investigates the flexural strength of 3D printing samples from ABS, PETG, ASA, and PLA plastics. These materials are widely used in research and practical applications. The flexural strength is measured by the 3-point method, according to ASTM D790. The results show that the flexure strength values are 72.26 MPa, 68.23 MPa, 61.63 MPa, and 56.50 MPa corresponding to PETG, ABS, ASA, and PLA. PETG plastic has the highest flexural strength of 72.26 MPa, while the commonly used PLA plastic has the lowest flexure strength of 56.50 MPa. The difference between these materials is sufficient, it is a necessary document to apply for research and development purposes. Based on the results of these studies, we can have a deeper knowledge of the mechanical and material properties of 3D printing samples from ABS, PETG, ASA, and PLA plastics. These discoveries could possibly be applied to plastic product research and development.

Keywords: FDM, flexural strength, mechanical properties, plastic materials.

INTRODUCTION

3D printing technology is becoming one of the most common additive manufacturing processes, with numerous advantages over traditional machining methods. 3D printing allows for the creation of models with complex geometries while also saving money on materials. There are various additive manufacturing technologies; the most prevalent 3D printing technology with a basic operating principle is fused deposition modeling (FDM).

The ASTM D790 flexural test is a typical method for assessing the flexural strengths of plastic materials [1-3]. Knowing the flexural properties of plastics and how to utilize their mechanical qualities is useful in industry and in everyday life. Hernandez et al [4] investigated the tensile, compressive, and flexural properties of Acrylonitrile butadiene styrene (ABS) plastic materials in prior investigations on the flexural strength of plastic materials. Günay *et al.* [5] used the FDM approach to model the tensile and flexural strength of Polylactic acid (PLA) polymers. According to research, the greatest flexural strength is around 65.06 MPa when

printing circumstances such as printing speed, raster angle, and fill rate are used. In fact, the flexural stress that a material experiences depends on where along the force's axis the force is applied. In fact, the flexural stress that a material experiences can be defined as the sum of its tensile and compressive stresses, depending upon where the force is delivered along the force's axis [6].

Gupta *et al.* [7] indicated that PLA's biocompatibility and biodegradability make it one of the most promising plastic polymers. ABS has good mechanical qualities, including strength, toughness, and impact strength [8]. Acrylonitrile styrene acrylate (ASA) material has some similar mechanical properties to ABS. According to Yong *et al.* [9], some industrial companies developed ASA polymer to advance the toughness [9]. However, Srinivasan *et al.* [10] showed that Polyethylene terephthalate glycol (PETG) has some features that are better than PLA. The flexure strength comparison between these mentioned plastics in 3D printing technology is rarely discussed and needs more investigation.

This paper aims to provide more data on the flexural properties of four different plastics, including PLA, PETG, ABS, and ASA. The results from the paper help researchers evaluate the properties of plastic materials manufactured by FDM 3D printing or for research purposes.

EXPERIMENTAL

Four sample groups of the material were 3D printed using FDM, then they were tested for flexural properties on a universal testing machine. The printing samples were manufactured by a core XY printer with an X-Y-Z printing area size of 380 mm x 380 mm x 380 mm, and printed according to FDM technology [11]. The printing parameters of each type of plastic are shown in Table 1.

Table 1. The manufacturing parameters for PLA, PETG, ABS, TPU and ASA materials.

Parameters	PLA	PETG	ABS	ASA
Print Temperature (°C)	200	230	240	200
Bed Temperature (°C)	60	80	120	60
Speed (mm/s)	60			
Initial layer height (mm)	0.2			
Layer thickness (mm)	0.1			
Line width (mm)	0.6			
Wall Thickness (mm)	1.2			
Infill density (%)	100			



Figure 1. Testing machine AG-X plus Shimadzu.

The testing sample has dimensions of 127 mm x 12.7 mm x 3.2 mm according to ASTM D790 standard [12]. ASTM D790 flexural strength test in this paper is performed with the bending test method at 3 points as shown in

Figure 2, the direction of force application will be vertical from top to bottom. The flexural strength experiment was carried out by Universal Testing Machine 20kN, model AG-X plus Shimadzu - Japan at Ho Chi Minh City Center of Supporting and Enterprise Development as shown in Figure 1. For each material, three parameters are given for the 3-point flexural test. The direction of force application will be vertical from top to bottom [13].

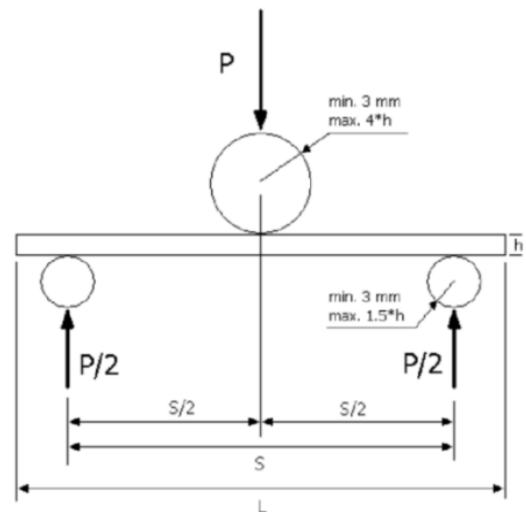
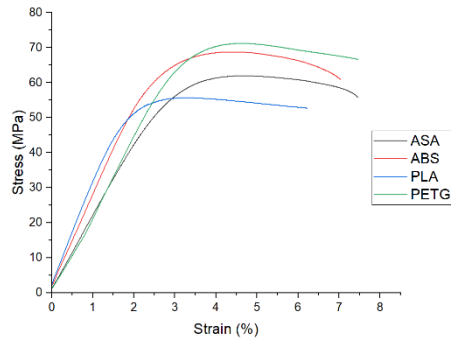


Figure 2. Diagram of the support and tip of 3-point test according to ASTM D790 standard.

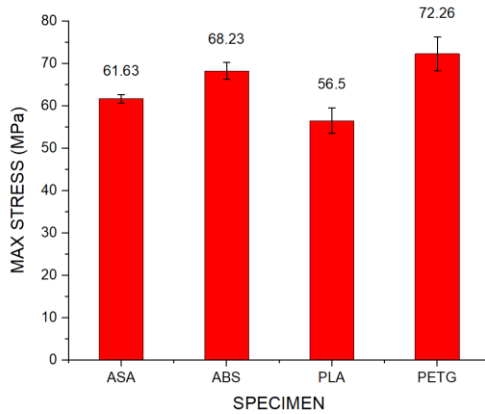
Specimen inspection process begins with measuring and checking samples must have the same dimensions in width, length, and thickness, the tolerance should not exceed ± 0.03 mm at the center of the testing sample. Then, mount the specimen by placing the sample horizontally on two supports. Align the sample so that it is perpendicular to the tip of the load and the midpoint of the specimen coincides with the top of the tip. We set the input parameters for the machine as follows: distance of 2 supports: 48 mm, and pressing speed of the loading tip: 1.22 mm/min. The pace of each tension test was maintained constant at 5 mm/min, while the speed of each compression and flexure test remained constant at 1.3 mm/min.

RESULTS AND DISCUSSION

Figure 3 reveals that the flexure strength values for PETG, ABS, ASA, and PLA are 72.26 MPa, 68.23 MPa, 61.63 MPa, and 56.50 MPa, respectively. PETG plastic has the maximum flexural strength of 72.26 MPa, while PLA plastic, which is routinely used, has the lowest flexural strength of 56.50 MPa. The distinction between these items is adequate.

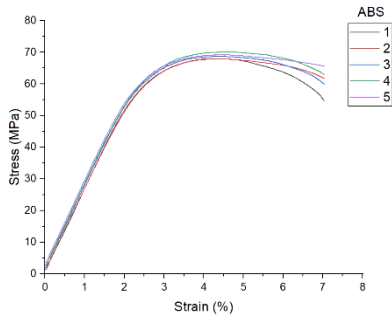


a) Stress-Strain curves

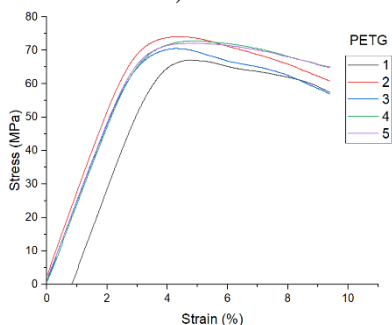


b) Comparison of flexure strengths

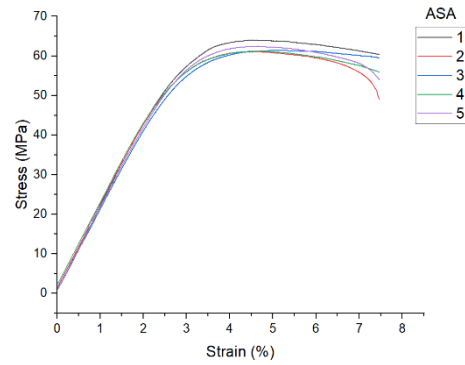
Figure 3. The average flexure strength results



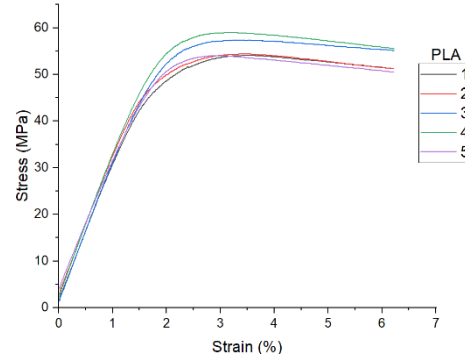
a) ABS



b) PETG



c) ASA



d) PLA

Figure 4. Stress-Strain curves of 3D printing samples from ABS, PETG, ASA, and PLA plastic

Figure 4 shows the Stress-Strain curve diagrams for each material, which show the results in greater detail for each material. We can better grasp the link between stress and strain in each type of plastic material based on Figure 4. Each chart contains a minor variance, which could be due to the specimen being produced unevenly in material layers during the 3D printing process, although this has no significant impact on the mechanical properties of the samples. It is an essential record when applying for research and development. We may gain a better understanding of the mechanical and material properties of 3D printing samples made of ABS, PETG, ASA, and PLA plastics based on the findings of these investigations.

CONCLUSION

This study examines the flexural strength of PLA, PETG, ASA, and ABS 3D printed materials. The flexure strength values for PETG, ABS, ASA, and PLA are 72.26, 68.23, 61.63, and 56.50 MPa. PETG plastic exhibits the maximum flexural strength of 72.26 MPa, whereas PLA plastic, which is widely used, has the lowest flexural strength of 56.50 MPa. The distinction between these items is adequate; it is an essential record when applying for research and

development funding. We may gain a better understanding of the mechanical and material properties of 3D printing samples made of ABS, PETG, ASA, and PLA plastics based on the findings of these investigations. These findings could be applied to plastic product research and development.

Acknowledgments

We acknowledge HCMC University of Technology and Education, Dong Nhan Phat Co., Ltd, and Material Testing Laboratory (HCMUTE). They allowed me to join their team and access the laboratory and research machines. With their appreciated support, it is possible to conduct this research.

References

- [1] A.J. Qureshi, S. Mahmood, W.L.E. Wong, D. Talamona, *Design for Scalability and Strength Optimisation for components created through FDM process*, Conference: 20th International Conference on Engineering Design **6** (2015), 255-266.
- [2] M. Jaroslav, E. Hnátková, M. Žaludek, P. Krátký, *Effect of Processing Parameters on Mechanical Properties of 3D Printed Samples*, Materials Science Forum **919** (2018) 230–235.
- [3] ASTM D790-03, *Standard Test Methods for Flexural Properties of Unreinforced and Reinforced Plastics and Electrical Insulating Materials* (2017).
- [4] R. Hernandez, D. Slaughter, D. Whaley, J. Tate, B. Asiabanpour, *Analyzing the tensile, compressive, and flexural properties of 3D printed Abs P430 Plastic based on printing orientation using fused deposition modeling*, Solid Freeform Fabrication 2016: Proceedings of the 26th Annual International (2016).
- [5] M. Günay, *Modeling of tensile and bending strength for PLA parts produced by FDM*, *International Journal of 3D Printing Technologies and Digital Industry*, International journal of 3D printing technologies and digital industry **3** (2019) 204-211.
- [6] ME Vallejos, RJ Aguado, R Morcillo-Martín, JA Méndez, F Vilaseca, Q Tarrés, P Mutjé, *Behavior of the Flexural Strength of Hemp/Polypropylene Composites: Evaluation of the Intrinsic Flexural Strength of Untreated Hemp Strands*, Polymers **15** (2023) 371.
- [7] B. Gupta, N. Revagade, J. Hilborn, *Poly(lactic acid) fiber: An overview*, Progress in Polymer Science **32** (2007) 455-482.
- [8] Mohammad Ra, Mohsen. Es, M. Moradi, *Effect of reprocessing on shrinkage and mechanical properties of ABS and investigating the proper blend of virgin and recycled ABS in injection molding*, Mater. Sci. Forum **214** (2014) 2359-2365.
- [9] Yong. D, Jun Gao, Y. Jian-bo, L. Xiao, *Dynamic rheological behavior and mechanical properties and of PVC/ASA blends*, Journal of Polymer Research **19** (2012).
- [10] S. Prathap, R. Asrith, A. Kannan, Deepak, *Influence of fused deposition modeling process parameters on the mechanical properties of PETG parts*, Mater. Sci. Forum **27** (2020) 1877-1883.
- [11] B. K. Ruben, I. Fitriani, A. Dody, Z. Arifin, Ubaidillah, *A review on the fused deposition modeling (FDM) 3D printing: Filament processing, materials, and printing parameters*, Open Engineering **11** (2021) 639-649.
- [12] Chander Go, V. Jayaraman, V. Sriram, *Comparision of ISO and ASTM standards in determining the flexural strength of denture base resin*, Eur Oral Res (2019) 137-140.
- [13] Z. Sharma, *Anisotropic Mechanical Properties of ABS Parts Fabricated by Fused Deposition Modelling*, Mechanical Engineering, InTech (2012) 159-180.

FORMATION AND CHARACTERIZATION OF LIME ESSENTIAL OIL-ENCAPSULATED NANOEMULSION

Nguyen Thi Lan Phi^{1,2}, **Tran Ngoc Thanh Mai**^{1,2}, **Do Thanh Nhan**^{1,2} and **Pham Van Hung**^{2,3}

¹ Ho Chi Minh City University of Technology, 268 Ly Thuong Kiet, Ward 15, District 10, Ho Chi Minh City, Vietnam;

² Vietnam National University Ho Chi Minh City, Community 6, Linh Trung Ward, Thu Duc City, Ho Chi Minh City, Vietnam;

³ International University, VNU-HCM, Community 6, Linh Trung Ward, Thu Duc City, Ho Chi Minh City, Vietnam

Email: lanphi@hcmut.edu.vn

ABSTRACT

In this study, lime essential oil (EO) nanoemulsions from Persian lime (*Citrus latifolia*) were prepared using the ultrasonic emulsification technique and stabilized by a combination of whey protein and Tween-80. The results indicated that the emulsion carriers and ultrasonic conditions significantly influence in the average size, size distribution (PDI), zeta potential and encapsulation efficiency (EE) of EO-encapsulated nanoemulsion. The nanoemulsion containing 5 wt% oil phase (50% Lime EO + 50% Coconut oil), 2.5 wt% Tween-80, 5 wt% WPI in the aqueous phase was found to have an average droplet size of 124.3 ± 0.3 nm, PDI value of 0.31 ± 0.06 and zeta potential of -30.8 ± 4.2 mV when the ultrasonic parameters was set at 750 W and 40% amplitude in 5 min. The EE of the prepared nanoemulsions was higher than 80%, demonstrating that the encapsulation systems used in the present work were effective for entrapping lime EO. As a result, lime EO-encapsulated nanoemulsions indicate great potential to be applied for develop water-based food products and beverages as a flavoring and antimicrobial agents.

Keywords: Lime essential oil, nanoemulsion, antioxidant, antimicrobials

INTRODUCTION

Lime essential oils (Eos) are defined as aromatic oily liquids that exhibit excellent antimicrobial, antioxidant and medicinal properties. The lime EOs have been used in beverages, confectionaries, pharmaceuticals, cosmetics and perfumes as natural flavoring materials [1]. Therefore, the increasing demand of lime EO's consumption also strengthens the importance of researching this field. Although lime EOs had high functionality and application, practical applicability is still challenging as the EOs are highly volatile and get easily degraded upon oxidation through direct exposure to light, heat, oxygen and humidity [1, 2]. Besides that, the poor water solubility of EO limits its incorporation into food and beverage products. In these respects, the nanoencapsulation of essential oils seems to be a new approach to overcome these impediments. Among different methods of encapsulation, nanoemulsion consists of a biphasic liquid system of one liquid solution dispersed in a continuous medium and no polymer shells are used.

By reducing the emulsions to nano size, several advantages over conventional emulsions can be obtained. The physical stability of the encapsulated active substances against gravitational separation, flocculation, and coalescence is greatly improved which can be explained by the Stokes law that a droplet move is proportional to the square of its radius. Moreover, an increase in surface area may lead to the improvement in the bioavailability of flavors and food ingredients to increase the flavor or odor thresholds [3]. The small particle size also gives them an optically transparent when the size of droplets is often much smaller than the wavelength of light and improves the solubility of poorly water-soluble ingredients like EOs, which makes them suitable to be incorporated into food and beverages systems. In addition, the nanoemulsions form has higher activity levels of encapsulated ingredients, thus increasing the distribution in food matrices so that the antimicrobial activity of EOs can be effectively improved [4, 5].

Even though many studies on the preparation of EO nanoemulsions have been reported, studies involving EOs of Persian lime are still limited. Therefore, The objective of this study is to prepare nanoemulsion of essential oil of *C. latifolia* Tanaka using the ultrasonic emulsification technique and determine characterization of the system including average size, size distribution (PDI), zeta potential and encapsulation efficiency (EE).

EXPERIMENTAL

Materials

Persian lime (*Citrus latifolia*) was purchased from an organic farm located in Thanh Loi Commune, Ben Luc District, Long An Province - 10°44'24.3"N 106°21'51.9"E. After that, the stem and unqualified ones were removed; only fresh green fruits with a diameter ranging from 3.5-6 cm were collected and washed through with water to remove dirt and impurities. Lime fruits were kept in a refrigerator at 4-5°C until use.

Extraction of lime EO

Hydro-distillation method was used to extract EO from lime peel. Generally, weighed lime flavedo was ground with distilled water by the blender to reduce its size and added along with water into the distillation chamber. After extraction, the lime EO was collected by a separating funnel, the water phase was dried over anhydrous Na₂SO₄. EO vials were stored in the freezer for further processes and analyses.

Nanoemulsion formation

Lime EO nanoemulsion was prepared in two main stages. Pre-emulsion system was prepared first by mixing the organic phase, containing oil (lime EO + coconut oil) and Tween-80 with the aqueous phase, containing WPI and citrate buffer using a magnetic stirrer. The lime EO concentrations of 25, 50, 75, 100 wt% were used in the oil. Then, nanoemulsion was prepared by sonifying the pre-emulsion by using an ultrasonicator. Droplet size, PDI and zeta potential were measured using a DLS while creaming index was measured based on the height of the cream layer.

Similar procedure was conducted as mentioned in the 2.2.3 section at different the Tween-80 concentrations (0, 2.5, 5, 7.5, and 10 wt%), different WPI concentrations (0, 1, 5, 10, 15, 20, 30 wt%) in the emulsion, different ultrasonic amplitude (20% and 40%) or different

time periods (1, 5, 10, 15, 20, 25 min) the emulsion.

Determination of encapsulation efficiency (EE)

Determination of EE using an UV-vis spectrophotometry by establishing the calibration curve of EO and calculating the amount of surface EO. The EE was estimated by the ratio of the total amount of loaded EO to the initial amount of EO.

Data analysis

Each experiment was repeated three times and the results are presented as mean \pm standard deviation. One-way analysis of variance (ANOVA) was used to test the level of confidence at the 5% of significance to assess whether the difference between the analyzed samples was statistically significant (p -value < 0.05).

RESULTS AND DISCUSSION

Effect of lime EO concentrations

Initially, the influence of the oil phase compositions on the initial size of the oil droplets formed in nanoemulsions were examined with different mass ratios of lime EO and carrier oil (coconut oil) along with standardized formulation: 5% (w/w) oil phase (lime EO + coconut oil), 20% (w/w) WPI, 2.5% (w/w) Tween-80, and 72.5% (w/w) aqueous phase with ultrasonic process (40% amplitude, 15 minutes). As the lime EO concentration increased, the mean droplet size decreased until it reached a minimum value ($d = 116.8 \pm 1.4$ nm) when the lipid phase contained 75% (w/w) lime EO (Fig. 1). When there was only lime EO in the oil phase, the mean droplets size increased significantly ($p < 0.05$). System containing 50% EO had the mean droplet size ($d = 119.9 \pm 10.5$ nm) not significantly different from that of the 75% EO sample ($p > 0.05$). Low PDI values (under 0.5) and a monodisperse distribution (data not shown) were observed with different lipid phase compositions, indicated that those systems were relatively homogenous. An increase in lime EO to 100% resulted in a broader size distribution ($PDI = 0.46 \pm 0.06$). As a result, the oil phase properties (e.g., viscosity, interfacial tension and polarity) and surfactant properties (e.g., solubility, partitioning and optimum curvature) had an important impact on the formation of small oil droplets.

The zeta potential measured in those systems with different lime EO ratios were not significant differences ($p > 0.05$) with the results ranging from -29.4 to -32.1 mV.

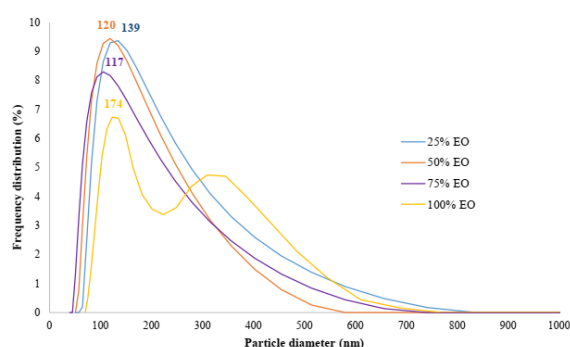


Fig. 1. Average particle size and particle size distributions of lime EO nanoemulsion with different EO concentrations

Effect of Tween-80 concentrations

The effect of Tween-80 was investigated in nanoemulsions containing 5% lipid phase (50% lime EO + 50% coconut oil), 20% WPI with different Tween-80 concentrations (0, 2.5, 5, 7.5 and 10%). Emulsions without Tween-80 resulted in larger mean size ($d = 274.1 \pm 2.3$ nm) compared with the systems that had both Tween-80 and WPI ($d \approx 119.9 - 125.6$ nm with no significant difference $p > 0.05$) (Fig. 2). The reduction in size may be due to the presence of the unsaturated nonpolar chains of Tween-80 that affect the packing parameter. Broader size distribution obtained when increasing the Tween-80 concentrations (with PDI values of 0.35, 0.41, 0.56, 0.95 and 1.18 for 0, 2.5, 5, 7.5 and 10% Tween-80 samples, respectively) ($p < 0.05$).

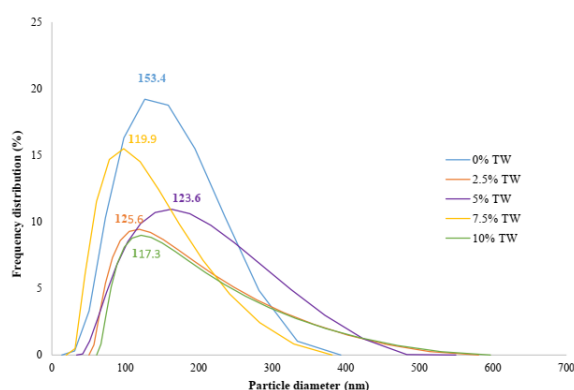


Fig. 2. Average particle size and particle size distributions of lime EO nanoemulsion with different Tween-80 concentrations

A significant increase of zeta potential ($p < 0.05$) was observed markedly when increasing Tween-80 concentration (Data not shown). Emulsions are stabilized by two main processes: steric stability by the adherence of the surfactant to the droplet surface and electrostatic stability by

the differences between surface charges. In this case, Tween-80 exhibited less surface charge compared with WPI due to the steric repulsion is predominant. A concentration of 2.5% Tween-80 was used in the following experiments.

Effect of WPI Concentration

The influence of different WPI concentrations (1-30%) on the particle size distribution of the lime nanoemulsions was evaluated. Smaller sizes of nanoemulsions were observed upon either increasing the amount of WPI to a certain percentage ($p < 0.05$) (Fig. 3). Typically, the average droplet size of the 20% WPI sample was considerably small ($d = 119.9 \pm 0.11$ nm) in comparison with that of the 1% WPI sample ($d = 130.9 \pm 2.2$ nm). The main reason came from the amphiphilic property of the globular milk proteins (mainly β -Lactoglobulin and α -Lactalbumin) in WPI that can absorb each other at the oil-water interface of the droplet size, thus, increasing WPI concentration means having sufficient emulsifier to reduce the interfacial tension to form colloidal aggregates. Sufficient amount of surfactant allows the diffusion from the organic phase into the aqueous phase happen completely when they come into contact as well as favor different structural organizations of the surfactant. However, the difference in size from 5% to 20% WPI samples were not significant ($p > 0.05$). Narrower size distribution when increasing the amount of WPI was observed, with PDI values ranging from 0.396 (1% WPI) to 0.226 (20% WPI). It is noticeable that increasing the WPI concentration to 30% resulted in larger droplet size ($d = 132.6 \pm 3.7$ nm) and broader size distribution ($PI = 0.76 \pm 0.02$) (Data not shown). The increase in size may be attributed to a high degree of flocculation or coalescence. Instead of monomodal distribution like other samples with lower WPI content, a bimodal distribution in the 30% WPI emulsion (data not shown) may be due to an over-processing phenomena that affecting the flocculation of the newly-created fine droplets during cavitation release by the sonication treatment. Therefore, intermediate level of WPI (around 5% w/w) may be more suitable for preparation of physically stable nanoemulsions. The highest value of zeta potential (-40.2 ± 1.8 mV) was obtained in the system containing 30% WPI. As mentioned, the surface charge is contributed by WPI and the stability of emulsions mainly due to the electrostatic repulsion. For the

5, 10, 15 and 20% WPI systems, the values of zeta potential were not significantly different ($P>0.05$).

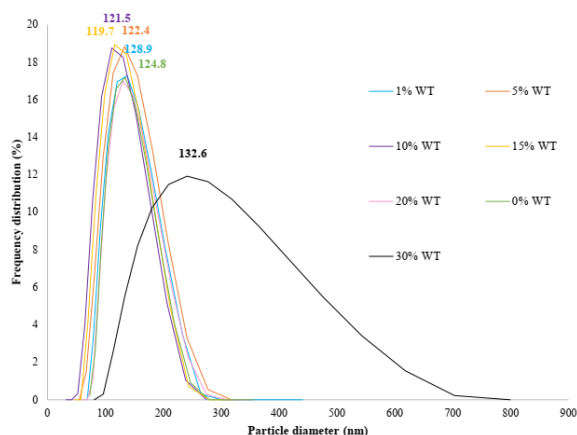


Fig. 3. Average particle size and particle size distributions of lime EO nanoemulsion with different WPI concentrations.

Encapsulation efficiency (EE) of nanoemulsion

The EE of lime EO in nanoparticles ranged from $86.69 \pm 0.94\%$ to $94.53 \pm 0.95\%$. They were found to be higher than 80%, demonstrating that the encapsulation systems used in the present work were effective for entrapping lime EO. The sample with the highest EO content (75 wt% in the oil phase) had the highest EE of 94.53%.

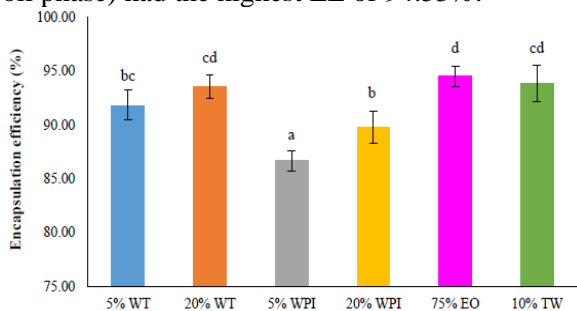


Fig. 4. Encapsulation efficiency of lime EO in nanoparticles

CONCLUSION

In this study, the nanoemulsion of lime EO was successfully prepared using ultrasonication method. From the results, the emulsion composition (oil phase and surfactants) as well as ultrasonic parameters (time and amplitude) had an influence on the average size, size distribution and zeta potential. The nanoemulsion containing 5% oil phase (50% Lime EO + 50% Coconut oil), 2.5% Tween-80, 5% WPI and 87.5% aqueous phase was found to have an average droplet size ($d = 124.30 \pm 0.35$ nm), PDI value (0.314 ± 0.06), zeta potential (-30.8 ± 4.2 mV) and encapsulation efficiency ($EE = 91.84\%$) when the ultrasonic

parameters was set at 750W, 40% amplitude in 5 min.

Acknowledgment

This research is funded by Vietnam National University in Ho Chi Minh City (VNU-HCM) under grant number B2023-20-11.

References

- [1] B. Ali, N.A. Al-Wabel, S. Shams, A. Ahamad, S.A. Khan, F. Anwar, *Essential oils used in aromatherapy: A systemic review*. Asian Pacific Journal of Tropical Biomedicine **5** (2015) 601-611.
- [2] R. Amorati, M.C. Foti, L. Valgimigli, *Antioxidant activity of essential oils*. Journal of Agriculture and Food Chemistry **61** (2013), 10835-10847.
- [3] S. Tiwari, B.K. Singh, N.K. Dubey, *Encapsulation of essential oils - A booster to enhance their bio-efficacy as botanical preservatives*. Journal of Scientific Research **64** (2020) 175-178.
- [4] S.N. Liew, U. Utra, A.K. Alias, T.B. Tan, C.P. Tan, N.S. Yussof, *Physical, morphological and antibacterial properties of lime essential oil nanoemulsions prepared via spontaneous emulsification method*. LWT **128** (2020) 109388.
- [5] F. Salaun, *Microencapsulation – Processes, technologies and industrial applications*, IntechOpen, London, 2019, 45-60.

FORMULATION OF NANOPARTICLES LOADED WITH CASHEW NUT TESTA EXTRACT USING LECITHIN AS A LIPOPHILIC EMULSIFIER BY W/O/W DOUBLE METHOD

Hoang Van Thanh¹, Nguyen Xuan Hoan¹, Nguyen Ngoc Quynh Ngan^{2,3}, Pham Van Hung^{2,3},
Nguyen Thi Lan Phi^{3,4}

¹Ho Chi Minh City University of Industry and Trade (HUIT), 140 Le Trong Tan Street, Tay Thanh Ward, Tan Phu District, Ho Chi Minh City, Vietnam;

²International University, VNU-HCM, Quarter 6, Linh Trung Ward, Thu Duc City, Ho Chi Minh City, Vietnam;

³Vietnam National University in Ho Chi Minh City, Quarter 6, Linh Trung Ward, Thu Duc City, Ho Chi Minh City, Vietnam;

⁴Ho Chi Minh City University of Technology, VNU-HCM, 268 Ly Thuong Kiet Street, District 10, Ho Chi Minh City, Vietnam.

Email: lanphi@hcmut.edu.vn

ABSTRACT

Cashew nut testa (CSNT), which contains high amounts of bioactive compounds, could be of interest to food development as a source of natural antioxidants. In this study, the W/O/W double nanoemulsion method was applied and successfully created nanoemulsion using lipophilic emulsifier and hydrophilic emulsifier, namely Lecithin, and the mixture of Whey protein isolate (WPI) and Tween 80 to develop biocompatible carriers to improve the bioavailability of CSNT extract. This research aimed to assess the influence of WPI:Tween 80 (5:0 - 1:4 v/v) and O:W₁ (90:10 - 50:50 v/v) ratios on physical properties of nanoemulsion. The optimal conditions for formulating the nanoemulsion with the greatest zeta potential include a ratio of O:W₁ of 80:20 (v/v) and a ratio of WPI:Tween 80 of 3:2 (v/v). The optimum nanoemulsion had droplet size, polydispersity index and zeta potential were 152.1 ± 4.4 nm, 0.384 ± 0.021 and -57.9 ± 0.7 mV, respectively. Moreover, the results showed that the CSNT extract was successfully encapsulated in nanoemulsion with encapsulation efficiencies of phenolic, flavonoid, and catechin compounds of $80.8 \pm 1.0\%$, $74.8 \pm 1.0\%$ and $76.9 \pm 1.4\%$, respectively. This research provides useful information to develop a novel encapsulation formulation of W/O/W nanoemulsions for cashew nut testa extract.

Keywords: Cashew nut testa extract, w/o/w double nanoemulsions, total phenolic content, encapsulation efficiency

INTRODUCTION

Testa is a thin antioxidant-rich covering of reddish-brown color that covers the cashew nut. Due to its bitter and astringent flavor, the testa is removed and thrown during processing [1]. The testa accounts for roughly 1–3% weight of cashew nuts. It has been discovered to be a rich source of hydrolyzable tannins such as catechin, epicatechin, and epi-gallocatechin, with polymeric proanthocyanidins being the predominant polyphenols [2] and possessed significant antioxidant and free radical scavenging activities. Nanoemulsions help load hydrophobic active substances and improve their bioavailability in the pharmaceutical, food, and cosmetics sectors [3]. Encapsulation and/or conjugation may be utilized to efficiently deliver active cargo through nanoemulsions [4]. The

purpose of this project was to create to formulate the nanoparticles of the extract from cashew nut testa using the W/O/W double nanoemulsion methods with Lecithin as lipophilic emulsifier, WPI and Tween 80 as hydrophilic emulsifier and determine characteristics of the nanoparticles. Bioactive compounds activities, including total phenolic compounds (TPC), total flavonoid compounds (TFC), total catechin content (TCC), and antioxidant capacity utilized to determine encapsulation efficiencies of nanoemulsion; physical properties including nano-droplet size, distribution and zeta potential were determined.

EXPERIMENTAL

Prepare W/O/W double nanoemulsions with WPI: Tween 80 ratios

First, the oil phase containing Lecithin and soybean oil was dissolved using a magnetic stirrer at 40°C for 10 minutes. At the same time, the internal water phase comprising of cashew testa extract and distilled water was also mixed well and poured into the oil phase. In which, the O:W₁ ratios fixed at 80:20 (w/w), the emulsifier (Lecithin) concentrations was constant with 5%. Water-in-oil (W₁/O) primary nanoemulsions were created by mixing the internal water phase and the oil phase at a speed of 20 000 rpm for 5 minutes using an Ultra-Turrax dispersion instrument (T10, IKA, Germany). The emulsification was accomplished using an ultrasonic homogenizer with a 3 mm titanium alloy microtip probe (Sonics VCX 500, 500 W, 20 kHz, USA). The Vibra-Cell™ VCX 500 was set to approximately 500 W and 20 kHz with 40% amplitude for 6 minutes of effective time in 5 s pulses (5s off and 5s on). After that, the external water phase, which containing WPI solution, Tween 80, and double distilled water, was dissolved using a magnetic stirrer at 40°C for 10 minutes. The ratios between WPI and Tween 80 were varied from 5:0 to 1:4 (v/v). Then, adding 20ml of the W₁/O emulsions to the external water phase, the ratio of W₂: W/O at a constant 80:20 (v/v) and stirring at 10 000 rpm for 2 minutes. The high intensity ultrasonic homogenizer (Sonics VCX 500, 500 W, 20 kHz, USA) with a titanium alloy microtip probe of 3 mm diameter was utilized once more with its specifications adjusted to approximately 500 W and 20 kHz with 40% amplitude but for 4 minutes effective time, in 5 s pulses (5 s off and 5 s on).

Prepare W/O/W double nanoemulsions with different O:W₁ ratios

The same procedure as in Experiment 1 was used to create W/O/W nanoemulsions. Whereas the W₂:W/O ratios fixed at 80:20 (w/w), the emulsifier (Lecithin) concentrations 5% and ratio of WPI and Tween 80 was 3:2(v/v). The O:W₁ ratio varied from 90:10 to 50:50, w/w.

RESULTS AND DISCUSSION

The appropriate conditions to formulate nanoemulsion

Effect of WPI: Tween 80 ratios on the formulation of nanoemulsion

Z - Average, the polydispersity index (PI) and Zeta potential of the W/O/W nanoemulsions, which prepared using different WPI:Tween 80

ratios, varied from 5:0 to 1:4 (v/v), were measured and presented in Table 1.

Table 1. Effects of WPI: Tween 80 ratios on EE, Z - Average, PI and Zeta *

WPI: Tween 80 ratios	Z - Average (nm)	PI	Zeta potential
5:0	165.1 ± 7.200 ^a	0.620 ± 0.050 ^b	-56.5 ± 1.5 ^a
4:1	144.5 ± 5.444 ^a	0.346 ± 0.026 ^a	-55.3 ± 3.1 ^{ab}
3:2	146.9 ± 3.970 ^a	0.384 ± 0.021 ^a	-58.1 ± 1.3 ^a
2:3	136.1 ± 7.518 ^a	1.452 ± 0.112 ^c	-55.8 ± 1.8 ^{ab}
1:4	132.6 ± 5.650 ^b	0.510 ± 0.030 ^{ab}	-51.6 ± 1.7 ^b

* Values of Z - Average, PDI and Zeta potential.

The values of were means ± standard deviations (n = 3). Means sharing the different letters were significantly different (p ≤ 0.05), according to Turkey's test. Data measured at room temperature.

Table 1 shows the droplet size distribution of double emulsions with different WPI:Tween 80 ratios. Double emulsions coded as "1:4" had the narrowest size distribution with 132.6 ± 5.650 nm, and it is the only sample had the droplet size significantly different compared to the remained emulsions. Double emulsions coded as "3:2", "2:3" and "4:1", had similar size distribution with the value of 146.9 ± 3.970, 136.1 ± 7.518, and 144.5 ± 5.444 nm, respectively (p < 0.05). Therefore, the ratio of WPI:Tween 80 is not of paramount importance for the droplet size of this experiment. The largest size recognized was of "5:0" emulsion with a figure of 165.1 ± 7.2 nm. Only two samples had good PI in this experiment, namely "4:1" and "3:2" with 0.346 ± 0.026 and 0.384 ± 0.021, respectively, representing that they belonged to a moderate polydisperse group of distribution type. A small value of PDI indicates a monodispersed population, while a large PDI indicates a broader droplet size distribution. Table 1 also shows that the 3:2 emulsion has the best zeta potential with 58.1 ± 1.3 mV.

Effect of O:W ratios on the formulation of nanoemulsion

Z - Average, the polydispersity index (PI) and Zeta potential of the nanoemulsions, which prepared using different O:W₁ ratios, varied from

90:10 to 50:50 (v/v), were measured and presented in Table 2.

Table 2. Effects of O/W1 ratios on Z – Average, PI and Zeta potential *

O/W1 ratios	Z - Average (nm)	PI	Zeta potential
90:10	132.600 ± 10.025 ^{ab}	2.314 ± 0.138 ^d	-51.3 ± 1.2 ^{bc}
80:20	152.133 ± 4.419 ^a	0.384 ± 0.021 ^a	-57.9 ± 0.7 ^a
70:30	138.533 ± 6.918 ^{ab}	0.844 ± 0.070 ^b	-56.3 ± 0.9 ^a
60:40	140.700 ± 5.966 ^{ab}	1.836 ± 0.006 ^c	-55.2 ± 2 ^{ab}
50:50	128.433 ± 8.690 ^b	1.790 ± 0.011 ^c	-50.9 ± 2.5 ^c

* Values of the Z - Average, PDI, and zeta potential. The values were means ± standard deviations (n = 3). Means sharing the different letters were significantly different (p ≤ 0.05) according to Tukey's test. Data measured at room temperature.

Comparing these data to the outcome of the "3:2" emulsion in experiment 1, we can observe that, except for the "80:20" emulsion, the rest of the samples exhibited a decrease in size. As the internal water phase rises, the oil droplets absorb larger water droplets, causing the droplet sizes of W/O/W emulsions to expand.

According to Table 2., except "80:20" emulsion, all the values of PDI were greater than 0.7, which suggests that all of the nanoemulsion systems that were created during experiment 2 had inadequate stability for a nano delivery / colloidal system. Kết quả cho thấy các nhũ trong ổn định với tỷ lệ O/W1 80:20 có độ ổn định cao hơn các nhũ tương khác với $-57,9 \pm 0,7$ mV, tiếp theo là kích thước tương tự được quan sát từ nhũ tương "70:30" là $56,3 \pm 0,9$ mV.

Encapsulation efficiency of nanoemulsions

Determination of total bioactive compounds activities of the extract

The results of bioactive compounds activities including total phenolic content, total flavonoid content, total catechin content and antioxidant capacity of cashew nut testa extract is shown in Table 3.

Table 3. Total phenolic content, total flavonoid content, total catechin content, and antioxidant capacity of cashew nut testa extract

Parameters	Cashew nut testa extract
Total phenolic content (mg GAE/g dry basis)	20.673 ± 0.368
Total flavonoid content (mg RE/g dry basis)	11.553 ± 0.551
DPPH radical scavenging (%)	28.000 ± 1.214
Total catechin content (mg CE/ g dry basis)	10.459 ± 0.321

* The values are means ± standard deviations (n = 3).

Table 3 shown that the total phenolic content, total flavonoid content, total catechin content, and DPPH radical scavenging of cashew nut testa extract were 20.673 ± 0.368 (mg GAE/g dry basis), 11.553 ± 0.551 (mg RE/ g dry basis), 10.301 ± 0.212 (mg CE/g dry basis) and $28.000 \pm 1.214\%$, respectively.

Total bioactive compounds activities of the nanoemulsion

In the formulation of nanoemulsion, cashew nut testa extract included 2% and was diluted with double-distilled water at a ratio of 1:1 (double-distilled water also comprised 2% of the nanoemulsion). Therefore, in 2 mL of manufactured nanoemulsion, there was 0.04 mL of cashew nut testa extract that had been diluted by a factor of 2 if the encapsulation effectiveness was 100%. The bioactive compounds activities of a 2 mL nanoemulsion preparation, including total phenolic content, total flavonoid content, and total catechin content, were determined and given in Table 4.

Table 4. Total phenolic content, total flavonoid content, and total catechin content of the emulsion

Parameters	Nanoemulsion
Total phenolic content (mg GAE/g sample)	0.004 ± 0.000
Total flavonoid content (mg RE/g sample)	0.003 ± 0.000
Total catechin content (mg CE/g sample)	0.002 ± 0.000

Encapsulation efficiency

The encapsulation efficiencies of prepared nanoemulsion for phenolic content, flavonoid content, and catechin content was measured and presented in Table 5.

Table 5. Encapsulation efficiency of prepared nanoemulsion for total phenolic content, total flavonoid content and total catechin content

Parameters	Encapsulation efficiency of nanoemulsion (%)
Total phenolic content	80.861 ± 1.040
Total flavonoid content	74.810 ± 1.081
Total catechin content	76.935 ± 1.463

From Table 5, it is obvious that the prepared nanoemulsion revealed best encapsulation efficiency for phenolic content, with 80.861 ± 1.040%. Meanwhile, the flavonoid and catechin content were encapsulated at 74.810 ± 1.081% and 76.935 ± 1.463 %, respectively. Tyagi et al (2021), who conducted the research in question, were able to effectively encapsulate 87% of the TCC in green tea extract in their nanoemulsion. According to a study that was published by Macedo et al. (2013), the EE of TFC of their nanoemulsion was around 82%. According to Niknam et al. (2020), the TPC of W/O/W nanoemulsion was found to be 68.6%. When compared to the findings presented in these other articles, the encapsulation efficiencies of prepared nanoemulsions in this study, which were all in the range of approximately 70% to approximately 80%, can be considered to be at a level that satisfies the criteria for the level of satisfaction desired.

CONCLUSION

This work demonstrates that cashew nut testa extract can be encapsulated in nanoemulsion using a two-step emulsification procedure with high-energy emulsification techniques employing Lecithin as a lipophilic emulsifier and Tween 80 and WPI as hydrophilic emulsifiers. The optimal process conditions for preparing nanoemulsions by examining the droplet sizes, zeta potentials, and polydispersity of the nanoemulsion were: ratio of O:W₁ was 80:20 (v/v); the ratio of WPI:Tween 80 was 3:2 (v/v). T nanoemulsion with the lowest zeta potential of approximately -58.1 ± 1.3 mV, a size measurement of 146.9 ± 3.970 nm, and a PDI of 0.384 ± 0.012 was obtained. The final EE of ideal nanoemulsions produced by the optimal procedure which can be considered that reach satisfy level were 80.861 ± 1.040%, 74.810 ± 1.081%, and 76.935% ± 1.463% for TFC, TPC, and TCC, respectively.

Acknowledgment

This research is funded by Vietnam National Foundation for Science and Technology Development (NAFOSTED) under grant number 10/2020/TN.

References

- [1] J. Trox, V. Vadivel, W. Vetter, W. Stuetz, D.R. Kammerer, R. Carle, et al., *Catechin and epicatechin in testa and their association with bioactive compounds in kernels of cashew nut (Anacardium occidentale L.)*. Food chemistry **128** (2011) 1094-1099.
- [2] V. Viswanath, V.V. Leo, S. Sabna Prabha, C. Prabhakumari, V.P. Potty, M.S. Jisha, *Thermal properties of tannin extracted from Anacardium occidentale L. using TGA and FT-IR spectroscopy*. Natural Product Research, **30** (2016) 223-227.
- [3] L.H. Chen, L.C. Cheng, P.S. Doyle, *Nanoemulsion-loaded capsules for controlled delivery of lipophilic active ingredients*. Advanced Science **7** (2020) 2001677.
- [4] R.J. Wilson, Y. Li, G. Yang, C.X. Zhao, *Nanoemulsions for drug delivery*. Particuology **64** (2021) 85-97.

FORMATION AND CHARACTERIZATION OF NANO STARCH PARTICLES ENCAPSULATED BOTH CURCUMIN AND CATECHIN.

Bui Thanh Vy^{1,2}, Chau Minh Thuan^{1,2}, Mai Nguyen Tram Anh^{1,2,3} and Pham Van Hung^{1,2,3}

¹Department of Food Technology, International University, VNU-HCM

²Vietnam National University in Ho Chi Minh City, Quarter 6, Linh Trung Ward, Thu Duc City, Ho Chi Minh City, Vietnam.

³Laboratory of Interdisciplinary Researches and Analysis in Chemistry, Food and Environment, IU, VNU-HCM.

Email: pvhung@hcmiu.edu.vn

ABSTRACT

The adaptability of debranched starch nanoparticles has drawn the interest of scientists in many fields. In addition, the evidence on the synergistic impact of catechin and curcumin indicates that they might be potential antiviral agents against SARS-CoV2. This study aimed to investigate morphology and characteristics of curcumin-catechin co-loaded starch nanoparticles (cur-cate-SNPs) formulated from debranched medium chain-length cassava starch using the nanoprecipitation technique. The average particle size of cur-cate-SNPs was between 234 and 275 nm, and the polydispersity index was less than 0.5. Curcumin-catechin was encapsulated and sustained in debranched starch nanoparticles with high curcumin and catechin loading efficiencies of 88.38% and 73.68%, respectively.

Keywords: *nanostarch, nanoencapsulation, curcumin, catechin, SARS-CoV2.*

INTRODUCTION

Nanoencapsulation is a process of entrapping and preserving bioactive compounds within a matrix of coating materials at a nanoscale, usually 1 to 100 nm; some nanomaterials may have sizes up to 600 nm [1]. Nanoencapsulation of food elements employs various nanotechnologies to transport nutrients, nutraceuticals, and other bioactive compounds into body cells while remaining protected from the rigors of food production and harmful environmental influences.

Nanoprecipitation is one of the most common techniques to fabricate starch nanoparticles with sufficiently small size, using less toxic solvents and saving energy [2, 3]. Nanoprecipitation occurs due to the displacement of organic solvent by diffusion with an anti-solvent, usually by dropping technique under continuous stirring. Furthermore, Hung et al. [3] successfully loaded curcumin into debranched starch nanoparticles using the nanoprecipitation method.

Starch, due to the demand for a natural, biodegradable, and renewable carbohydrate, has been found as a source of nano-carrier material. It has been proven that carbohydrate-based nano-delivery systems have promising applications for encapsulating food ingredients and bioactive

compounds [1, 4, 5]. SNPs were successfully produced from native starch but had low yields and large average sizes [3]. Those shortcomings of native starch can be resolved with debranched starch, a short linear glucan isolated from amylopectin hydrolyzed by debranching enzymes [6]. Hung et al. [3] were successfully fabricated SNPs from the DBS using nanoprecipitation with relatively high loading efficiency and smaller particle size than those from the native starch.

Catechin and curcumin are two naturally occurring plant chemicals whose potential health benefits have been intensively explored. It has been shown that both substances possess antioxidant, anti-inflammatory, and anticancer effects. Studies suggest that the co-delivery of catechin and curcumin enhances antioxidant activity and anti-inflammatory effects, potentially acting as potential antiviral drugs, especially against SARS-CoV2 [7]. Regardless of their benefits to human health, curcumin is highly hydrophobic, and they both have poor bioavailability, which puts barriers to the food and pharmaceutical industries to incorporate them into food and drug systems. Overall, the project aims to investigate the fabrication of curcumin and catechin in nano starch particles by

nanoprecipitation using absolute ethanol. The morphology, particle sizes, size distribution, and solubility of the cur-cate-SNPs were studied.

EXPERIMENTAL

Materials

The native cassava starch was purchased from Nam Bao Tin Import-Export Co., Ltd. Curcumin and catechin in food-grade quality were supplied from Merck Co. (Germany). Absolute ethanol was purchased from Fisher Company (USA). Other compounds were analytical quality.

Debranching of native cassava starch

Native cassava starch was debranched into medium chain-length starch ($15 < DP < 30$) using the pullulanase as Hung et al. [3] previously published with slight modification. The process started with 5% (w/v) starch suspension preparation by dissolving 5.0 g of native cassava starch into 100 ml of acetate buffer 0.1 M (pH 5.2). The mixture was cooked in a boiling water bath with continuous stirring for 30 minutes. Then it was cooled to 50°C and mixed with 1 ml of pullulanase solution comprising 16 NPUN/g starch. The debranching occurred in a shaking water bath at 50°C for 3 hours. The enzyme was inactivated in a 90°C water bath for 30 minutes. The debranched starch solution was then freeze-dried overnight to obtain the powder for further investigation and formation of starch nanoparticles.

Formation of curcumin-catechin starch nanoparticles

Starch nanoparticles were formulated from the debranched cassava starch using the nanoprecipitation method according to Hung et al. [3] with minor modifications. Curcumin and catechin were dissolved in absolute ethanol to create a curcumin-catechin solution. DBS powder was blended with distilled water to create a 1% debranched starch solution. The curcumin-catechin solution was added to the debranched starch solution, stirred, and homogenized. The mixture was left at room temperature for 24 hours for equilibration. The nanoparticles were fabricated by adding dropwise absolute ethanol to the mixture, stirring under magnetic stirring. The precipitation was collected and freeze-dried to obtain curcumin-catechin-loaded starch nanoparticles (cur-cate-SNPs) for future examination. The control nanoencapsulation samples with only catechin (6.0 mg/mL) and

curcumin (6.0 mg/mL) solution were prepared with similar procedures described above.

Observation of the morphology of nanoparticles

The morphology of cur-cate-SNPs was examined using scanning electron microscopy (SEM) (JOEL JSM-IT200). After coating dry samples with gold/palladium (60:40 w/w), micrographs were collected at an accelerating potential of 10 KV. The SEM images were obtained at a magnification of 10,000 times for further analysis.

Evaluation of the particle size and polydispersity index of nanoparticles

The size distribution, average size, and polydispersity index of cur-cate-SNPs were estimated using dynamic light scattering (DLS) (Malvern Zetasizer Nano-ZS, Malvern, Worcestershire, UK). Cur-cate-SNPs powders were resuspended in distilled water and measured at 25°C.

Determination of loading efficiency and loading ability of nanoparticles

Loading efficiency (LE) (%) and loading ability (LA) (mg/g) of starch nanoparticles with curcumin and catechin are calculated separately.

Determination of Curcumin Content in the Starch Nanoparticles

Total curcumin content in cur-cate-SNPs was determined according to Li et al. [8] with modifications. The cur-cate-SNPs were washed with ethanol, centrifuged, and resuspended in distilled water. While the supernatant was used to determine the free curcumin content, the residue was sonicated to extract the entrapped curcumin. The curcumin concentration was determined on a UV-vis spectrophotometer at 419 nm.

Calibration curve equation: $Y = 0.1361X + 0.0078$ with $R^2 = 0.999$.

Where: X is the curcumin concentration in $\mu\text{g/mL}$ and Y is the absorbance at 419 nm.

Determination of Catechin Content in the Starch Nanoparticles

Cur-cate-SNPs (2 mg) were washed with distilled water to remove surface catechin, then a suspension was obtained and centrifuged at 4500 rpm for 5 minutes. The supernatant was used to determine the free catechin content, and the residue was resuspended in distilled water to extract the entrapped catechin from nano-starch capsules. The suspension was centrifuged again and collected. The free and entrapped catechin

concentrations were determined using a UV-vis spectrophotometer at 500 nm using the Vanillin-HCl assay. The working vanillin reagent was prepared daily by mixing a 1% vanillin solution in methanol with an 8% HCl solution in a 1:1 ratio. Culture tubes were dispensed with 1.0 mL aliquots of each extract, and the absorbance was determined after 20.0 minutes in the water bath at 30°C.

Calibration curve equation:

$$Y = 0.4144X - 0.0018 \text{ with } R^2 = 0.995$$

Where: X is the catechin concentration in mg/mL and Y is the absorbance at 500 nm.

Data analysis

All experiments were conducted in duplicate and triplicate. Minitab software version 18.1 (Minitab, Inc., USA) was used for statistical analysis of variances (ANOVA) with a 95% confidence level.

RESULTS AND DISCUSSION

Morphology of curcumin-catechin-loaded starch nanoparticles

The morphology of the starch nanoparticles loaded with both curcumin and catechin using the nanoprecipitation technique is presented in Figure 1.

SEM images reveal irregular shapes and high agglomeration in loaded starch nanoparticles. Curcumin-catechin-loaded samples showed spherical and ellipsoidal nanoscale structures, while control samples had spherical and plate-like shapes. These observations align with previous studies on debranched starch nanoparticles entrapped in curcumin using nanoprecipitation. Ethanol functioned as an anti-solvent in nanoprecipitation, producing well-dispersed but irregular granules.

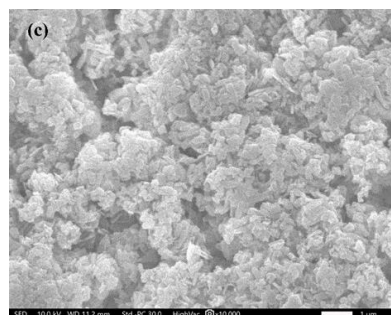
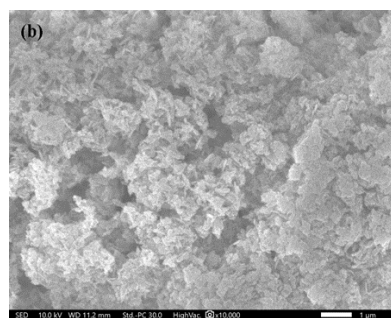
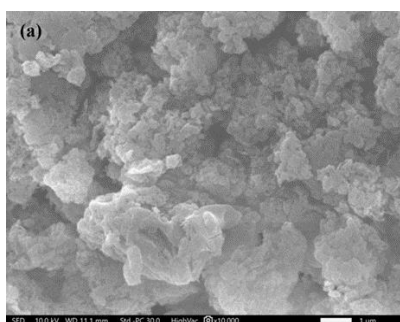


Figure 1. SEM images of loaded starch nanoparticles. (a, curcumin-catechin-loaded starch nanoparticles; b, control curcumin-loaded starch nanoparticles; c, control catechin-loaded starch nanoparticles).

Average particles size, size distribution, and polydispersity index of curcumin-catechin-loaded starch nanoparticles

Table 1 indicates the average size in diameter (nm) and the polydispersity index (PDI). The control catechin nano samples had the smallest size (252.5 nm), followed by the curcumin-catechin-loaded starch nanoparticles and the control curcumin ones, which are 255.1 nm and 273.5 nm, respectively. However, there was no significant difference between the cur-cate-SNPs and the control samples. As polydispersity indexes revealed, only the cur-cate-SNPs had a PDI value of less than 0.5 (PDI~0.260) while the control SNPs with whether loaded curcumin or catechin showed significantly higher levels of PDI values which were 0.628 and 0.832, respectively. Specifically, PDI less than 0.5 demonstrates that the starch nanoparticles had good uniformity and stability in a food system. Overall, this thesis confirmed that the curcumin-catechin-loaded starch nanoparticles with sufficient small size (Z-average<300 nm) and good homogeneity (PDI <0.5) were successfully fabricated from medium-chain length debranched cassava starch.

Table 1. Size characteristic of curcumin-catechin loaded starch nanoparticles (*)(**).

Sample	Z-average (nm)	PDI
Cur-cate-SNPs	255.1 ± 20.4 ^{ab}	0.260 ± 0.232 ^b
Control cur-SNPs	273.5 ± 41.3 ^a	0.628 ± 0.149 ^{ab}
Control cate-SNPs	252.5 ± 75.2 ^{ab}	0.832 ± 0.290 ^a

(*) All data are the means of triplicate experiments ± standard deviations.

(**) Data followed by the same letter in the same column are not significantly different ($P < 0.05$).

Loading efficiency (%) and loading ability (mg/g) of curcumin-catechin-loaded starch nanoparticles

The cur-cate-SNPs exhibited the most excellent loading efficiency (88.38%-curcumin, 73.62%-catechin), followed by the control cur-SNPs (77.81%) and control cate-SNPs (24.07%). Similarly, the loading ability of the cur-cate-SNPs (4.56 mg curcumin/g nano starch, 82.00 mg catechin/g nano starch) was higher than those of the control cur-SNPs (4.00 mg curcumin/g nano starch) and the control cate-SNPs (49.50 mg catechin/g nano starch). However, statistically, there was no significant difference between the cur-cate-SNPs and control cur-SNPs in loading efficacy and loading ability. Likewise, there was no significant difference in the loading ability between the cur-cate-SNPs and control cate-SNPs.

CONCLUSION

This project successfully fabricated curcumin-catechin-loaded starch nanoparticles (cur-cate-SNPs) from pure curcumin-catechin and medium chain-length debranched cassava starch using nanoprecipitation. The nanoparticles had an average particle size of 234-275 nm and a polydispersity index of less than 0.5. The nanoencapsulation of curcumin and catechin in debranch cassava starch showed potential applications in functional foods and pharmaceuticals.

Acknowledgment

This research is funded by Vietnam National University in Ho Chi Minh City (VNU-HCM) under grant number B2022-28-02.

References

- [1] M. Pateiro, B. Gomez, P.E.S. Munekata, et al., *Nanoencapsulation of promising bioactive compounds to improve their absorption, stability, functionality and the appearance of the final food products*. *Molecules* **26** (2021) 1547.
- [2] T.T.M. Duyen, P.V. Hung, *Morphology, crystalline structure and digestibility of debranched starch nanoparticles varying in average degree of polymerization and fabrication methods*. *Carbohydrate Polymers* **256** (2021) 117424.
- [3] P.V. Hung, T.T.M. Duyen, N.T.L.Phi, T.N. Quynh, *Fabrication and functional properties of curcuma starch nanoparticles as affected by different degree of polymerization of debranched curcuma starch*. *Starch - Starke* **74** (2021) 2100163.
- [4] C.G. Awuchi, S. Morya, T.A. Dendegh, et al., *Nanoencapsulation of food bioactive constituents and its associated processes: A revisit*. *Bioresource Technology Reports* **19** (2022) 101088.
- [5] M. Fathi, A. Martín, D.J. McClements, *Nanoencapsulation of food ingredients using carbohydrate based delivery systems*. *Trends in Food Science and Technology* **39** (2014) 18-39.
- [6] Y. Qin, J. Wang, C. Qiu, et al., *Effects of degree of polymerization on size, crystal structure, and digestibility of debranched starch nanoparticles and their enhanced antioxidant and antibacterial activities of curcumin*. *ACS Sustainable Chemistry and Engineering* **7** (2019) 8499-8511.
- [7] A.B. Jena, N. Kanungo, V. Nayak, et al., *Catechin and curcumin interact with S protein of SARS-CoV2 and ACE2 of human cell membrane: insights from computational studies*. *Scientific Reports* **11** (2021) 2043.
- [8] J. Li, G.H. Shin, I. W. Lee, et al., *Soluble starch formulated nanocomposite increases water solubility and stability of curcumin* **56** (2016) 41-49.

LOW-FREQUENCY MAGNETOELECTRIC EFFECT IN COMPOSITES BASED ON MODIFIED BARIUM TITANATE

Vladimir Laletin¹, Natallia Poddubnaya^{1,*}, Mikhail Kudybin¹, Tran Dang Thanh^{2,**}, Pham Hong Nam², and Nguyen Thi Ngoc Anh²

¹Institute of Technical Acoustics, National Academy of Sciences of Belarus, Vitebsk, 210009, Belarus

²Institute of Materials Science, Vietnam Academy of Science and Technology, 18-Hoang Quoc Viet, Hanoi, Vietnam

Email: *poddubnaya.n@rambler.ru; **thanhtd@ims.vast.ac.vn

ABSTRACT

The results of studies of the influence of the sintering temperature of bulk composite ferrite-piezoelectric ceramics on the magnetoelectric and dielectric characteristics of the resulting materials with a mass ratio of ferrite to piezoelectric equal to 1:1 are presented. For the first time in lead-free bulk composites based on barium titanate ($\text{Ba}_{0.9}\text{Ca}_{0.1}\text{TiO}_3 - \text{NiFe}_{1.9}\text{Co}_{0.02}\text{O}_{4-\delta}$), a magnetoelectric coefficient exceeding 100 mV/(cm Oe) was obtained.

Keywords: magnetoelectric effect, magnetoelectric coefficient, bulk composite, lead-free ceramics

INTRODUCTION

Piezoceramics based on the lead zirconate titanate (PZT) system is the basis of most piezoelectric transducers used in various electronic devices. This choice is objectively determined by its piezoelectric properties. Recently, the search for new, more environmentally friendly materials has become relevant, which has served to intensify research into ceramics based on barium titanate (BTO). In the past, the piezoelectric properties of BTO ceramics were inferior to those of lead-based PZT materials, and barium titanate was mainly used as a dielectric material in capacitors. Unmodified barium titanate ceramics, obtained using the conventional solid-phase reaction method, have a piezoelectric modulus d_{33} of not more than 190 pC/N. Since 2009, researchers have focused on manipulating the BTO phase boundary through ionic substitution. The highest piezoelectric modulus $d_{33} \sim 620$ pC/N was realized in the composition $(1-x)\text{BaTi}_{0.8}\text{Zr}_{0.2}\text{O}_3 - x\text{Ba}_{0.7}\text{Ca}_{0.3}\text{TiO}_3$ near the interface between the rhombohedral R and tetragonal T phases [1, 2]. Subsequently, similar BTO systems modified with calcium and antimony were studied to achieve high piezoelectric characteristics. Thanks to the wide region of phase coexistence, it was possible to achieve $700 \text{ pC/N} > d_{33} > 600 \text{ pC/N}$ in a wide range of compositions $(1-x)\text{BaTi}_{0.89}\text{Sn}_{0.11}\text{O}_3 - x\text{Ba}_{0.7}\text{Ca}_{0.3}\text{TiO}_3$ [3].

Research in 2020 showed similar properties for BTO ceramics modified with calcium and zirconium (20 - 40%) [4, 5]. For this reason, to obtain high magnetoelectric (ME) characteristics, we used calcium-modified BTO ceramics. The composition of nickel ferrite $\text{NiFe}_{1.9}\text{Co}_{0.02}\text{O}_{4-\delta}$, modified with cobalt, was chosen as the magnetostrictive component. Its choice was due to its high resistivity, which at room temperature is about $108 \Omega\text{m}$ [6].

EXPERIMENTAL

Nickel ferrite $\text{NiFe}_{1.9}\text{Co}_{0.02}\text{O}_4$ was obtained by double high-temperature synthesis of dehydrated powders NiO, Fe_2O_3 , Co_2O_3 of analytical grade. The composition of the charge was calculated taking into account the content of the main substance. The mixture of powders was mixed in a jasper mortar in the presence of ethyl alcohol for 30 minutes. The dried mixture was mixed with a solution of a plasticizer - polyvinyl alcohol (PVA) and pressed under a pressure of $5 \cdot 10^7$ Pa. The synthesis was carried out in air at a temperature of 1050°C for two hours. The synthesized ferrite was crushed and ground in a jasper mortar, briquetted again with the addition of PVA and synthesized at a temperature of 1050°C for two hours. The synthesized and ground ferrite powder was sifted. The technology for producing BTO is similar to the technology for producing nickel ferrite.

To prepare a bulk composite, the initial components with a weight ratio of piezoelectric to ferrite equal to 1:1 were mixed with the addition of ethyl alcohol for an hour. The resulting mixture was dried, mixed with PVA plasticizer and pressed into briquettes under a pressure of $2 \cdot 10^8$ Pa. The compositions were sintered in air at temperatures of $T = 1240, 1260$ and 1280 °C for two hours. The furnace was cooled at a rate of 50 °C/h. The sintered composite ceramics were ground, and electrodes were applied to its surface by burning silver paste. The resulting samples were polarized in silicone oil at temperatures up to 75 °C in an electric field of 1000 V/mm for an hour.

The linear ME effect was studied by measuring the voltage that appears on the sample when an alternating and slowly varying magnetic field is applied to it. The biasing field was created using an electromagnet, and the alternating magnetic field was created using Helmholtz coils. The amplitude of the alternating field was 80 A/m, the frequency was 1 kHz. The magnitude of the slowly varying magnetic field varied from -200 kA/m to 200 kA/m. The studies were carried out with longitudinal orientation of the samples. In this case, the electric polarization vector, perpendicular to the sample plane, is directed parallel to the constant and alternating magnetic fields - the longitudinal effect.

The ME voltage coefficient (α_E) was determined based on the sample thickness (h), voltage value (dU) and alternating magnetic field strength (dH):

$$\alpha_E = dU/(h \cdot dH) \quad (1)$$

RESULTS AND DISCUSSION

The physical properties of the composites are given in the Table 1. The density of composite ceramics (ρ) increases linearly with increasing sintering temperature. Also, with increasing sintering temperature, the dielectric constant (ϵ) naturally increases. In this case, the dielectric loss tangent ($\text{tg}\delta$) increases. On the contrary, with increasing sintering temperature the resistivity (ρ) decreases. The addition of calcium to the composite made it possible to reduce the sintering temperature of ceramics by ~ 50 °C. The introduction of cobalt, in turn, increased the resistance, which made it possible to select an effective polarization mode for the material and improve the ME properties.

Table 1. The physical properties of the composites $\text{Ba}_{0.9}\text{Ca}_{0.1}\text{TiO}_3 - \text{NiFe}_{1.9}\text{Co}_{0.02}\text{O}_{4-\delta}$.

T (°C)	1240	1260	1280
ρ (g/cm ³)	4.77	5.01	5.22
ρ ($\times 10^8$ Ωm)	3.2	2.2	0.57
ϵ	145	183	244
$\text{tg}\delta$	0.088	0.18	0.31
α_E , mV/(cm Oe)	108	99	79

The Figure 1 shows the results of studying the linear ME stress coefficient for longitudinal orientation of samples obtained at different sintering temperatures.

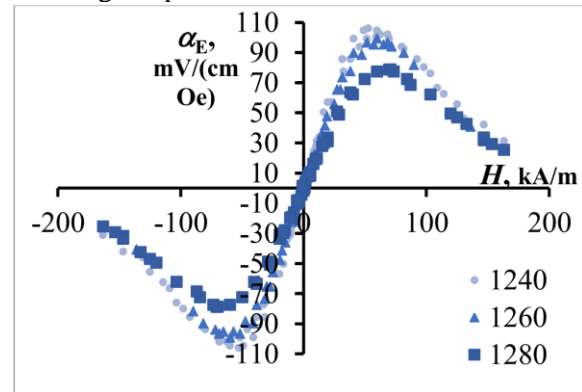


Figure 1. ME longitudinal coefficient in $\text{Ba}_{0.9}\text{Ca}_{0.1}\text{TiO}_3 - \text{NiFe}_{1.9}\text{Co}_{0.02}\text{O}_{4-\delta}$ composites.

CONCLUSION

The field dependence of the ME coefficient has a typical form characteristic of ferrite-piezoelectric composite materials and its maximum value decreases with increasing sintering temperature of ceramics. The value of the low-frequency ME coefficient obtained in $\text{Ba}_{0.9}\text{Ca}_{0.1}\text{TiO}_3 - \text{NiFe}_{1.9}\text{Co}_{0.02}\text{O}_{4-\delta}$ ceramics exceeded 100 mV/(cm Oe) and amounted to 108 mV/(cm Oe), which is an excellent indicator for lead-free materials.

Acknowledgment

The work was carried out with the support of the budget funding program within the framework of research work 1.14 “Synthesis, structure and properties of ferroelectric, magnetic and composite materials with high magnetoelectric and dielectric characteristics” and the task to support senior researchers in 2023 “Code NVCC04.01/23-23”.

References

- K. Xu, J. Li, X. Lv, J. G. Wu, X. X. Zhang, D. Q. Xiao, and J. G. Zhu, *Adv. Mater.* **28** (2016) 8519.
- B. Wu, H. J. Wu, J. G. Wu, D. Q. Xiao, J. G. Zhu, and S. J. Pennycook, *J. Am. Chem. Soc.* **138** (2016) 15459.
- H. Tao, H. J. Wu, Y. Liu, Y. Zhang, J. G. Wu, F. Li, X. Lyu, C. L. Zhao, D. Q. Xiao, J. G. Zhu, and S. J. Pennycook, *J. Am. Chem. Soc.* **141** (2019) 13987.
- J. Wu, *J. Appl. Phys.* 127 (2020) 190901.
- M. Acosta, N. Novak, W. Jo, J. Rodel, *Acta Materialia* **80** (2014) 48-55.
- J. Smith and H. Wayne, *Ferrites*, Moscow: Foreign Liter 1962.

ENVIRONMENTALLY FRIENDLY SYNTHESIS AND CHARACTERIZATION OF STAR-SHAPED GOLD NANOPARTICLES AND ASSESSMENT OF THEIR ANTIBACTERIAL PROPERTIES

Tien Huu Nguyen, Anh Van Thi Le*, Diep Ngoc Le, Dung My Thi Dang, Hoa Mai Thi Le, Chien Mau Dang

Institute for Nanotechnology, Community 6, Linh Trung Ward, Thu Duc City, Ho Chi Minh City, Vietnam;

Vietnam National University Ho Chi Minh City, Ho Chi Minh City, Vietnam

Email: ltvanh@vnuhcm.edu.vn

ABSTRACT

This study focuses on a sustainable approach to produce star-shaped gold nanoparticles (SGN). The study highlights the importance of reducing the environmental impact of nanoparticle synthesis. SGN is synthesis by a green synthesis method using collagen as stabilizers, ensuring minimal waste generation and hazardous chemical usage. The synthesized AuNPs are thoroughly characterized using advanced techniques including UV-Vis, DLS, FESEM, XRD, and spectroscopy to determine their size, shape, and crystal structure. Furthermore, the antibacterial properties of these SGN is evaluated in *Escherichia coli*, *Staphylococcus aureus*, *Bacillus subtilis* and *Pseudomonas aeruginosa* which microorganisms with the ability to thrive and survive on the human body. The FESEM image of the bacteria's cell surface illustrates the observed effect of SGN on bacterial cells. The results demonstrate that star-shaped gold nanoparticles exhibit an approximate size of 70 nm, as confirmed by UV-VIS analysis indicating the correct peak, and their star shape has been examined through FESEM analysis. The observed detrimental effects of these nanoparticles further highlight their potential as an alternative antibacterial agent in biomedical applications. This research contributes to the expanding synthesis of eco-friendly nanomaterials and their application in resistant to pathogenic microorganisms.

Keywords: star-shaped gold nanoparticles, anti-bacteria, environmentally friendly synthesis.

INTRODUCTION

Star-shaped gold nanoparticles (SGN) have attracted significant attention due to their unique multidimensional branched structure and enhanced plasmon resonance in the near infrared (NIR) region. These properties make them highly suitable for a range of medical applications. Compared to other gold nanoparticles, SGN exhibit superior capability in generating hot spots at the tips of their branches, making them a promising tool for various applications.

The scientists have successfully synthesized SGN using different methods. One group, led by H. Yuan, synthesized SGN by seed-mediated method and modify with PEGylated for cancer cell detection [1]. Another research team, led by C. Song, developed a seed-mediated method for synthesizing uniformly shaped and sized SGN. Surface modifications using 4MBA and RGD were also performed to create SGN with specific properties and the ability to interact with cancer cells [2].

It is worth mentioning that SGN have shown antibacterial properties as well. H. Wang synthesized SGN and modified their surface with vancomycin (Van). They tested the interaction of the SGN@Van with NIR 808nm in MRSA cells. The result showed that SGN particles interacted with bacterial cell surfaces and, caused red fluorescence in MRSA cells, disrupting the cell membrane and releasing cellular components [3].

Collagen, a vital protein in the human body, has also been explored for its role in shaping SGN and improving drug delivery of antibacterial agents. Collagen's structure and properties contribute to firm and smooth skin, making it an intriguing candidate for biomedical applications [4].

In this scientific article, we aim to synthesize SGN using a green synthesis method by utilizing collagen as a reducing and stabilizing agent. Various analytical techniques, including UV-Vis spectroscopy, DLS, and FESEM, will be employed to characterize the shape, size, and

crystal structure of the synthesized SGN. In addition, we conducted an assessment of the antibacterial activity of SGN by examining the surface morphology of the bacterial membrane.

EXPERIMENTAL

1. Materials

Tetrachloroauric (III) acid trihydrate ($\text{HAuCl}_4 \cdot 3\text{H}_2\text{O}$, 99.5%), L (+)-ascorbic acid ($\text{C}_6\text{H}_8\text{O}_6$, 99.0%), were purchased from Sigma Aldrich, silver nitrate (AgNO_3 , 99.0%) obtained from Merck. Collagen, MW 4000Da, from fish skin (Weishardt, Naticol®, powder). Deionized (DI) water (resistivity of $18.2 \text{ M}\Omega \text{ cm}$) was used in the preparation of the star-shaped gold nanoparticles.

In this study, four different bacterial strains were utilized: two Gram-positive models are *Bacillus subtilis* (isolated) and *Staphylococcus aureus* (ATCC 6539), and two Gram-negative models, *Pseudomonas aeruginosa* (ATCC 9027) and *Escherichia coli* (ATCC 8739). The bacterial strains were cultivated and preserved using Tryptone Soya Agar (TSA) medium. Tryptone soya broth (TSB), glutaraldehyde, ethanol from Merck. Phosphate-Buffered Saline (PBS), pH7.4, NaCl 0.9% solution.

2. Method

Synthesis star-shaped gold nanoparticles (GNS)

GNS was synthesized follow Vo et al [3]. Collagen powder is dissolved in DI water and stirring at room temperature for 90 minutes to make up the collagen concentration at 0.05mM. A synthesis process involved stirring 160 μL of 25 mM HAuCl_4 solution, 40 μL of 10 mM AgNO_3 solution, and 4.0mL of 0.05mM collagen for 15 minutes at room temperature. After 30 minutes of magnetic stirring, 2.0 mL of freshly made ascorbic acid solution (5.0 mM) was gradually added to the previous solution, the color of the colloidal solution changed from light yellow to dark blue in ascorbic acid solution dropping process. Stirring continuous in 15 minutes. Final, the volume was adjusted to 40 mL using DI water.

This solution was kept at 25°C for 3 hours before analyzed performance by DLS, UV-Vis, FESEM analysis and bacterial treatments.

Antibacterial activity of GNS

Microorganisms were pre-cultured in TSA at 37°C for 24 hours to obtain separated colonies. The bacterial strains were then transferred to 10ml of 0.9% NaCl solution, resulting in a concentration of approximately 10^8 cells/mL as compared to the

McFarland standard. For the experiments, the bacterial suspension was diluted in 0.9% NaCl to a concentration of approximately 10^6 cells/mL. Subsequently, the bacteria suspension was transferred to TSB culture supplemented with SGN at a final concentration of 100 $\mu\text{g/mL}$.

After 24 hours of incubation at 37°C, collect the bacterial suspension to treat, control samples were without nanoparticles. The collected suspensions were then transferred to Eppendorf tubes and centrifuged at 10,000 rpm for 2 minutes to collect the bacterial cells. The samples were washed with PBS, fixed with 2.5% glutaraldehyde, dehydrated with a graded series of ethanol solutions, coated onto a silicon wafer, and finally observed under a FESEM operating at 5.00 kV.

RESULTS AND DISCUSSION

UV-VIS analysis

The UV-VIS analysis of the SGN synthesized with collagen at a concentration of 0.05mM revealed an absorbance intensity of 0.2 and an SPR (Surface Plasmon Resonance) resonance wavelength at 570nm. Furthermore, the analysis illustrated the anisotropic characteristics of the star-shaped gold nanoparticles.

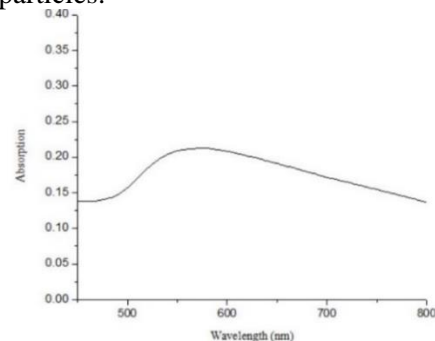


Figure 1. UV-VIS spectra of gold nanostructure obtained with collagen concentration 0.05mM

Dynamic Light Scattering (DLS)

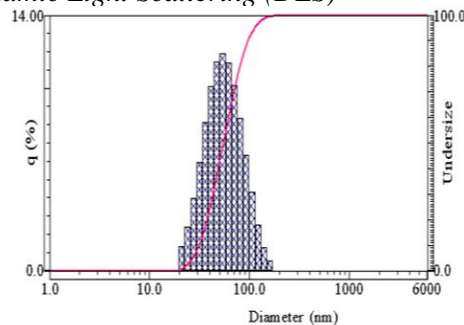


Figure 2: Size distribution analysis of gold nanoparticles by DLS

The average particle diameter of GNS in the colloid solution as 68.2 ± 23 nm was provided by the DLS analysis (Figure 2.). Under certain storage conditions and durations, gold nanoparticles (GNS) can undergo agglomeration. However, in this particular experiment, the GNS remained stable for approximately 48 hours.

FESEM

The nanoparticles were purified by three times centrifugation (10.000rpm, 5 minutes) to remove the free collagen and finally redispersed in DI water. In Fig. 3 representative FESEM images of SGN that obtained mostly have a star shape nanostructure of size less than 100nm. SGN with single crystalline tips can be synthesized in Chitosan stabilization.

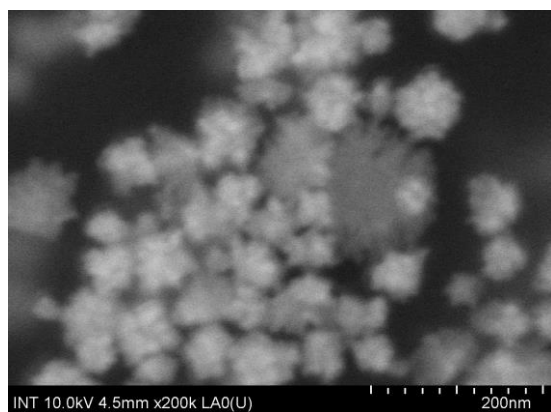


Figure 3. FESEM image of SGN

Bacterial inhibition of SGN

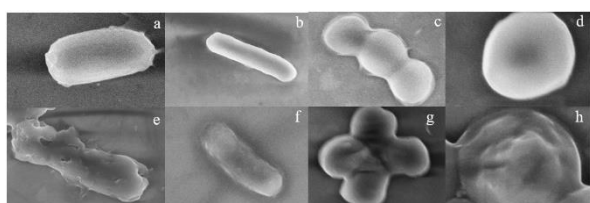


Figure 4. FE-SEM image of bacteria before and after exposure. *B. subtilis*, *E. coli*, *P. aeruginosa*, and *S. aureus* (a-d, respectively) and SGN treatment showing the disruption of the cell membrane (e-h, respectively).

The morphological changes in the SGN treated bacteria were extensively studied by FESEM. The control bacterial strains of *B. subtilis*, *E. coli*, *P. aeruginosa* and *S. aureus* showed smooth membranes and competent cells (Figure 4 a–d). After 24 hours of exposure to the SGN, almost all the cells showed membrane disruption or loss in their original morphological structure (Figure 4 e–h). Some holes and wrinkle in the cells can be seen. This indicates

that the SGN exhibit antibacterial activity by disrupting the cell integrity.

CONCLUSION

In conclusion, the mechanism of creating star-shaped gold nano materials from chitosan involves the formation of a chitosan solution, a dispersed gold solution, the combination of these two solutions, the mineralization and reduction of gold ions, and the star-shaping process to create the final star-shaped gold nano material. This method offers several advantages, including its simplicity, speed, cost-effectiveness, environmental friendliness, and antibacterial properties. However, one notable drawback is its low stability, with a current storage time limitation of approximately 44 hours. Future research efforts will be dedicated to enhancing the stability of the method and further exploring the antibacterial activity of star-shaped gold nanoparticles.

Acknowledgment

The authors highly appreciate the financial support of Vietnam National University Ho Chi Minh City for this research under the grant number TX2023-32-01.

References

- [1] H. Yuan, C. Khoury, H. Hwang, C. Wilson, G. Grant and Tuan Vo-Dinh, *Gold nanostars: surfactant-free synthesis, 3D modelling, and two-photon photoluminescence imaging*, *Nanotechnology* **23** (2012) 075102.
- [2] C. Song, F. Li, W. Chen, X. Guo, D. Chen, J. Zhang, J. Zhang and L. Wang, *Gold nanostars for Cancer Cells-Targeted SERS-Imaging and NIR Light-Triggered Plasmonic Photothermal Therapy (PPTT) in the First and Second Biological Window*, *J. Mater. Chem. B* (2019).
- [3] H. Wang, Z. Song, S. Li, Y. Wu and H. Han, *One Stone with Two Birds: Functional Gold nanostar for Targeted Combination Therapy of Drug-Resistant Staphylococcus aureus Infection*, *ACS Appl. Mater. Interfaces* **11** (2019) 32659-32669.
- [4] V. Khuong, N. Thu, H. Tien, H. Nguyen, N. Phong, and N. Hong-Tham, *Environmentally Friendly Controlled Synthesis of Gold Nanostars with Collagen by One-Step Reduction Method*, *Journal of Nanomaterials* **22** (2022).

NICKEL/CERIA NANOROD FOR CO₂ METHANATION: EFFECT OF THE ACTIVE PHASE LOADING

Nguyen Tri^{1,4}, Do Ba Long^{1,2,3}, Ho Thi Yen Bang^{2,3}, Thanh Gia-Thien Ho¹, Nguyen Phung Anh¹
Nguyen Thi Thuy Van^{1,4}, Cam Anh Ha^{2,3}, Hoang Tien Cuong^{1,4}, Luu Cam Loc^{1,2,3,4*}

¹Institute of Chemical Technology – Vietnam Academy of Science and Technology, 01A TL29 Street, Thanh Loc Ward, District 12, Ho Chi Minh City, Vietnam

²Department of Chemical Engineering, Ho Chi Minh City University of Technology (HCMUT), 268 Ly Thuong Kiet Street, District 10, Ho Chi Minh City, Vietnam.

³Vietnam National University Ho Chi Minh City, Linh Trung Ward, Ho Chi Minh City, Vietnam

⁴Graduate University of Science and Technology – Vietnam Academy of Science and Technology, 18 Hoang Quoc Viet Street, Hanoi, Vietnam

*Corresponding author: lcloc@ict.vast.vn

ABSTRACT

Carbon dioxide (CO₂) methanation is an advantageous process to circulate the carbon on the Earth, mitigating the release and loss of CO₂ into the atmosphere. Herein, the Ni/CeO₂ catalyst is fabricated by a facile impregnation method and investigated on the influence of Ni active phase content on the characterization and catalytic activity in the CO₂ methanation. The physicochemical properties of the as-synthesis catalyst were studied by several techniques: XRD, EDS, SEM, H₂-TPR, CO₂-TPD, and Raman. The catalytic survey and the analysis show the excellent performance of Ni/CeO₂ with a Ni loading of 15 wt.% (15NiCe). It was found that a coordination of highly Ni dispersion with small Ni crystal size (~23 nm) and a suitable basicity can be achieved by changing the active site loading on ceria, leading to an enhancing catalytic activity.

Keywords: nickel catalyst, ceria nanorod, CO₂ methanation, active phase loading.

INTRODUCTION

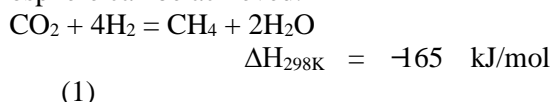
The increase share of renewable energy (RE) in the power grid is an orientation for the future to meet the requirement of global energy demand. Though the challenge in the past is reducing the cost of renewable energy, now the innovation of technology has allowed the usage of this green energy at a lower cost. Over a decade, from 2009 to 2019, the price of solar energy has deeply fallen from \$359 to \$40 per each MWh, declined by 89%, the decrease in other RE's global average cost is also observed [1]. The policies all over the world have stimulated the R&D activities to develop the technology related to the RE to tackle the complex climate change, a great challenge of our time. Those renewable energy introduce a greener power source to meet the goal of Net Zero by 2050, migrating from the domination of fossil fuel in our economy to a world predominated by RE like wind and solar [2].

Towards the popularity of RE in the future, a lot of hardships need to be overcome, and one of those is the fluctuation or instability of RE

sources. The problem can be solved by the method of storing the power obtained from the RE sectors. With that orientation, the storage of RE by transforming the obtained power into the chemical form under the formation of H₂ is more appealing than the application of batteries due to the lower cost [3]. Nevertheless, the low density of H₂ molecules results in another issue to store and transform the chemical to consume in the modern cities and factories. The Power-to-Gas (PtG) technology, especially the transformation of CO₂ into CH₄, introduces an avenue to put the RE into the modern power grid. The technology uses the H₂ collected from the electrolysis of water, using the power from RE sources, to thermally hydrogenate the greenhouse gas, CO₂, into Substitute Natural Gas (SNG). The improvement of studying the water electrolysis for producing H₂ nowadays also paves the way for the development of the CO₂ methanation reaction [4].

The increase in the number of CO₂ methanation publishes and patents shows the important role of this process in the future [3]. The

motivation to study on this C1 reaction comes from not only the energy aspect but also from the ability to recycle used carbon. This reaction allows the used carbon (CO₂) to be recycled again into CH₄ so that a circulation of carbon is formed and a mitigation of releasing CO₂ into the atmosphere can be achieved.



The thermal CO₂ methanation (Eq. 1) is exothermic and thermodynamically favorable at low temperature and high pressure. However, a catalyst system, with a common active site of Ni metal, is required to overcome the kinetic limitation of the reaction. The Ni-based catalyst has been a well-known object to investigate in the CO₂ methanation reaction beside the noble catalyst due to its reasonable cost and abundance. On the other hand, the rare earth oxide CeO₂,... have been recently studied as a promoter or a support for the Ni-based catalyst due to the fact that they can generate oxygen vacancies, enhancing the activity of the catalyst in the reaction [5]. The interesting redox property of CeO₂ can be altered by its morphology, several studies have been done to elucidate the correlation between the morphology of CeO₂ and its catalytic performance [6]. Our previous paper has found the CeO₂ nanorod (r-CeO₂) can generate more oxygen vacancies as well as enhance the catalytic behavior of the Ni/CeO₂ catalyst in the combined CO₂ and steam reforming of methane [7]. Hence, the rod structure of CeO₂ continues to be utilized in this work to support the Ni-based catalyst. For further comprehend compared to other published literature on Ni/CeO₂ in hydrogenation of CO₂ to methane, this research illuminates the influence of reduction condition on the characteristics and the catalytic activity of the Ni/CeO₂ catalyst system.

EXPERIMENTAL

r-CeO₂ was tailored based on the procedure in our previous paper [7]. Nickel supported on CeO₂ was prepared by the simple impregnation method. The designated amount of Ni(NO₃)₂·6H₂O was diluted in DI water and impregnated on the r-CeO₂ powder. The mixture was aging for 12 h and then dried in hot air at 80, 100, and 120 °C for 2 h at each temperature level. The dried sample was calcined at 600 °C for 4 h to achieve the precursor NiO/CeO₂. Before testing the activity, the sample was pre-treated in H₂ flow at 450 °C for 2h. The surveyed contents of Ni in this work were 5, 10,

15, and 20 wt.%. The abbreviation of the studied catalyst is xNiCe, with x is wt.% of Ni, and xNiCe(C) is designated as the calcined samples.

The prepared catalysts were determined physico-chemical characteristics by several methods such as isotherm nitrogen adsorption, XRD, Raman, SEM, H₂-TPR, and CO₂-TPD detailed in our previous work [8].

The catalytic activity investigation was conducted in a catalyst bed reactor placed in a furnace with a 6 L/h feed flowrate, and a CO₂:H₂:N₂ mole ratio of 3:12:85. The catalyst bed consists of 0.5 g catalyst particles and 0.5 g quartz, both of which are in the same size range of 0.25–0.50 mm. The studied temperature range for catalytic activity is from 250 °C to 400 °C, and the heating rate of the furnace is 10 °C/min. The composition of the feed stock and product gas is determined by Plus 6890 Gas Chromatograph (GC) using a TCD detector (capillary column HP–PLOT Molesieve 5A) and a FID detector (capillary column DB624).

RESULTS AND DISCUSSION

The SEM images of xNiCe samples are given in the Fig.1. When the Ni content is low (10 wt.%), the catalyst particles is obviously observed. The accumulation is more intensive as the weight percentage of Ni is increase, which makes the surface morphology hardly observe. Several 2D rod individuals can be observed in the SEM image of 10NiCe which can be the presence of CeO₂ nano rod. As for the other two images, the Ni nanoparticles are suggested to be in form of aggregated particles surrounding the CeO₂ material.

The XRD patterns (Fig.2a) show the diffraction peaks at 2θ = 28.6, 33.1, 47.6, and 56.4° corresponding to the (111), (200), (220), and (311) crystal plane of fluorite type crystal structure of CeO₂ (JCPDS 81-0792). The presence of Ni metal site correlates with the characteristic peaks at 2θ = 44.5° (111) and 51.8° (200) (JCPDS 04-850). It can be seen that the intensity of Ni characteristic peak at 2θ = 44.5° increases as the Ni content rises, corresponding to the Ni crystal sizes calculated from the Debye-Scherrer formula (Fig.2b). The fact that the NiO peak intensity increases proportionally to the NiO loading proves that NiO exists in the form of independent particles interacting with the support surface. The growth in Ni crystal sizes indicates the aggregation of Ni sites on the surface of CeO₂ as the Ni loading increases, which is a common

phenomenon in the impregnation method for synthesis of catalysts.

The basic property of xNiCe (x = 10, 15, and 20) is studied by the CO₂-TPD analysis (not shown). The detected CO₂ desorption temperature is in range of 50–400 °C, associating to the weak and medium basic sites on the catalysts' surface. The hydroxyl groups (OH⁻) and oxygen vacancies belong to the CeO₂ structure can be in responsibility to adsorb CO₂ inducing these basic sites [9, 10]. The basic nature of the catalyst plays an important role in the CO₂ related reactions, the ability to adsorb CO₂ can either ameliorate the activity of the catalyst or deteriorate the

performance because the basic property is too strong and exert influence on the competitive adsorption between CO₂ and H₂ in CO₂ methanation reaction. The desorbed CO₂ amounts calculated from the CO₂-TPD profiles is showed in Fig.2b. In respect with the calculated area, the CO₂ adsorption capacity increases when the Ni loading increases. The reduction of NiO species on the CeO₂ surface have been investigated and known for the promotion effect of inducing more oxygen vacancies [1]. Hence, more oxygen vacancies could have been formed with more NiO in the catalyst structure, leading to an increase of CO₂ adsorption capacity as it can be seen.

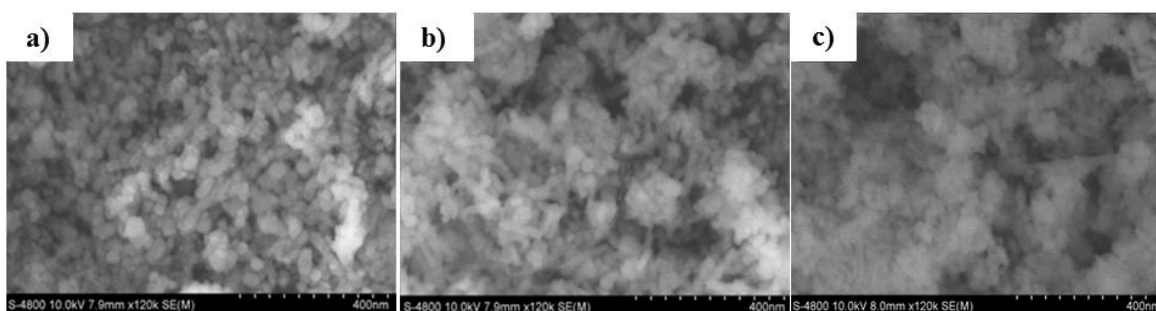


Figure 1. SEM images of NiCe catalysts reduced at 450 °C for 2 h; a) 10NiCe, b) 15NiCe, and c) 20NiCe

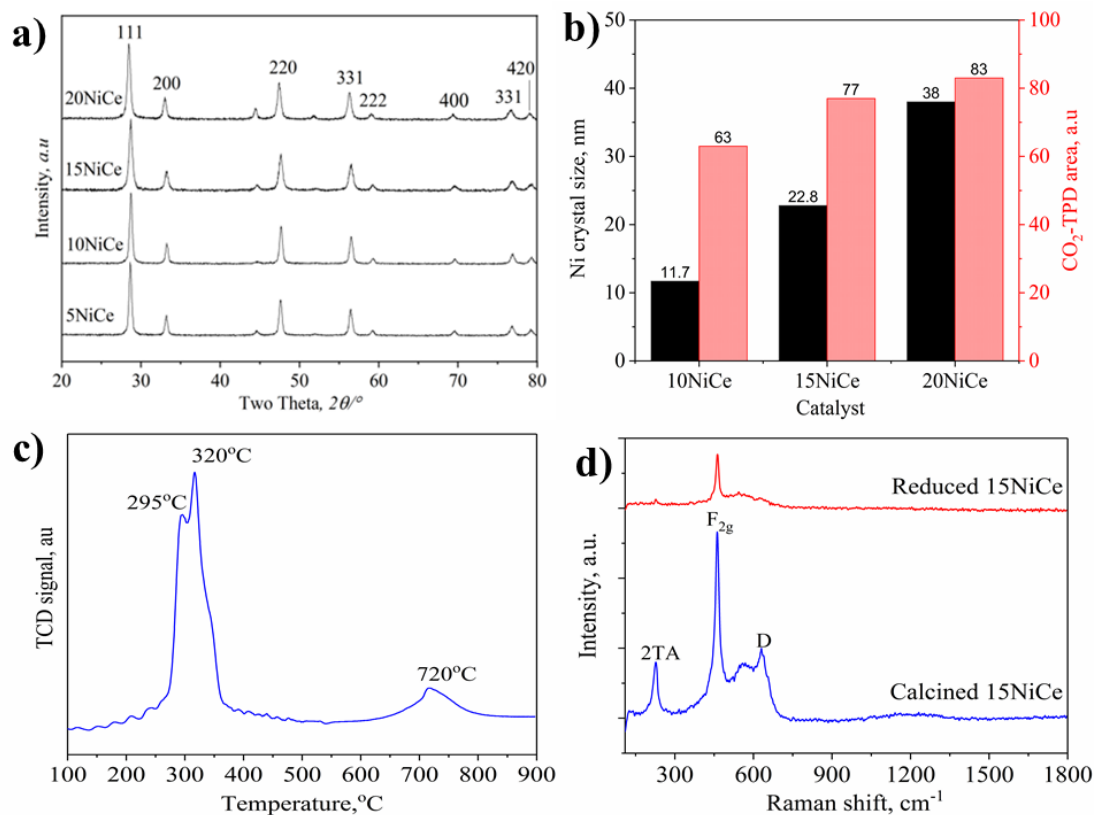


Figure 2: XRD patterns (a), Ni crystal size (calculated at 2θ = 44.5°) and the desorbed CO₂ amount (b) of reduced NiCe catalysts with different Ni loading; H₂-TPR profile of calcined 15NiCe catalyst (c) and Raman spectroscopy of calcined and reduced 15NiCe catalyst (d).

The reducibility of 15NiCe sample is studied by H₂-TPR analyse (Fig.2c). The TCD signal in the low temperature range of 100–200 °C is in respect with the reduction of adsorbed oxygen on the catalyst's surface. The reduction of NiO species in the catalyst is associated to the reduction peak from 250 °C to 350 °C, which is divided into two regions. The first reduction region is proposed to be ascribed to the NiO nanoparticles of small size and even dispersion on the CeO₂ surface. At slightly higher temperature, the reduction peak is associated with the reduction of bulk NiO species dispersed in the pore structure of CeO₂. The NiO's reduction peak at higher temperature has also been known for the stronger interaction of NiO-CeO₂, making it harder to reduce the metal oxide species [12]. The reduction peak at approximately 700–750 °C correlates with the reduction of CeO₂, forming oxygen vacancies in the support structure, in responsible for the enhancement of CO₂ adsorption as discussing above.

The material's oxygen vacancies are further studied by Raman spectroscopy (Fig.2d). The Raman bands at approximately at 220 cm⁻¹ (the second order transverse acoustic (2TA) mode) and 460 cm⁻¹ (the common Ce-O symmetrical stretch vibration (F_{2g}) mode) in CeO₂ fluorite structure can be seen at both calcined and reduced samples. The Raman band at around 600 cm⁻¹ correlate with the defect-induced mode (D) caused by oxygen vacancies in CeO₂. Both the bands are detected with lower intensity in the reduced sample, implying the oxygen vacancy density has been reduced after the reduction treatment.

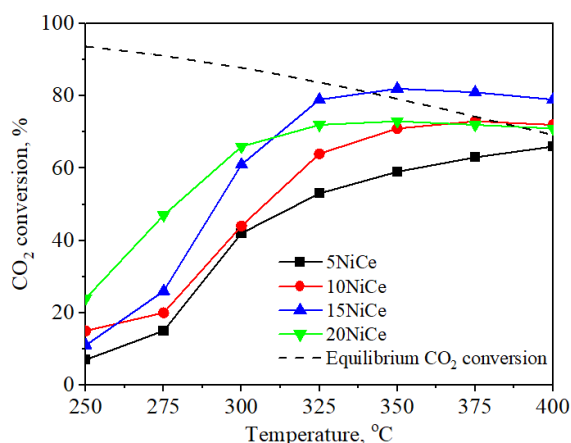


Figure 3. CO₂ conversion in methane production from carbon dioxide over NiCe catalysts

The catalytic activity of NiCe catalysts with different Ni contents is given in Figure 3, with the catalytic conversions quickly increase as the reaction temperature rises from 250 °C to 300 °C, above this mark, the conversions slowly increase or even slightly drop. As it is surveyed, the catalytic activity is improved as the Ni weight percentage is higher, giving more active sites for the activation of reactants. Nevertheless, the reasonable active sites are needed since too high Ni density on the catalyst surface can have a backward effect on the activity due to the agglomeration of active metal. In this work, 15 wt.% of Ni is chosen to be the suitable Ni content loading on the CeO₂ surface with the higher CO₂ conversion as a temperature profile, compared to other Ni content studied catalysts. The activity decrease in 20NiCe catalyst can result from the growth of particle size and the higher basic property as analyzed in XRD and CO₂-TPD.

CONCLUSION

To recap, a Ni-based catalyst supported on ceria nanorod has been synthesized and studied in the CO₂ methanation reaction. A reasonable Ni loading of 15 %.wt can avoid the declined activity caused by the agglomeration, resulting in the good performance in the thermal catalytic reaction of converting the greenhouse gas into the SNG, a substance containing the energy in the chemical form. This research's results show the correlation of the Ni loading on the ceria support, the catalysts' properties, and the catalytic performance in CO₂ methanation reaction.

Acknowledgement:

This research is funded by Vietnam National Foundation for Science and Technology Development (NAFOSTED) under grant number 104.05-2021.66

Reference

- [1] Roser, M. *Why did renewables become so cheap so fast?* Cheap-renewables-growth (2020), Available from: <https://ourworldindata.org/cheap-renewables-growth>.
- [2] Bouckaert, S., et al., *Net Zero by 2050: A Roadmap for the Global Energy Sector*. (2021) Special Report, International Energy Agency.
- [3] Lee, W.J., et al., *Recent trend in thermal catalytic low temperature CO₂ methanation:*

- A critical review. Catalysis Today*, **368** (2021) 2-19.
- [4] Götz, M., et al., *Renewable Power-to-Gas: A technological and economic review. Renewable energy*, **85** (2016) 1371-1390.
- [5] Li, L., et al., *Research progress and reaction mechanism of CO₂ methanation over Ni-based catalysts at low temperature: a review. Catalysis*, **12**(2) (2022) 244.
- [6] Tang, R., et al., *Enhanced CO₂ methanation activity over Ni/CeO₂ catalyst by one-pot method. Molecular Catalysis*, **508** (2021) 111602.
- [7] Loc, L.C., et al., *Effect of CeO₂ morphology on performance of NiO/CeO₂ catalyst in combined steam and CO₂ reforming of CH₄. International Journal of Nanotechnology*, **15**(11-12) (2018) 68-982.
- [8] Long, D.B., et al., *High active and coke-resistant CeNiO₃-based catalyst for methane bi-reforming. Journal of Science: Advanced Materials and Devices*, **8**(3) (2023) 100610.
- [9] Zhang, H., et al., *Structure and catalytic performance of Mg-SBA-15-supported nickel catalysts for CO₂ reforming of methane to syngas. Chemical Engineering & Technology*, **36**(10) (2013) 1701-1707.
- [10] Sagar, G.V., et al., *Dispersion and reactivity of copper catalysts supported on Al₂O₃-ZrO₂. The Journal of Physical Chemistry B*, **110**(28) (2006) 13881-13888.
- [11] Zhang, Q., et al., *Tuning particle sizes and active sites of Ni/CeO₂ catalysts and their influence on maleic anhydride hydrogenation. Nanomaterials*, **12**(13) (2022) 2156.
- [12] Du, X., et al., *Morphology dependence of catalytic properties of Ni/CeO₂ nanostructures for carbon dioxide reforming of methane. The Journal of Physical Chemistry C*, **116**(18) (2012) 10009-10016.

Ni/ KCC-1 CATALYST FOR CH₄ PRODUCTION FROM CO₂: IMPACT OF PRETREATMENT REGIMES AND ACTIVE PHASE LOADING

Do Ba Long^{1,2,3+}, Phan Hong Phuong^{1,2+}, Nguyen Tri^{3,4}, Nguyen Duong Thanh Phat^{1,2}, Cam Anh Ha^{1,2,4}, Trung Dang-Bao^{1,2}, Luu Cam Loc^{1,2,3,4*}

¹ Ho Chi Minh City University of Technology (HCMUT), 268 Ly Thuong Kiet Street, District 10, Ho Chi Minh City, Vietnam.

² Vietnam National University Ho Chi Minh City, Linh Trung Ward, Ho Chi Minh City, Vietnam

³ Institute of Chemical Technology – Vietnam Academy of Science and Technology, 01A TL29 Street, Thanh Loc Ward, District 12, Ho Chi Minh City, Vietnam

⁴ Graduate University of Science and Technology – Vietnam Academy of Science and Technology, 18 Hoang Quoc Viet Street, Hanoi, Vietnam

Email: lcloc@ict.vast.vn

+ participate equally.

ABSTRACT

This work has introduced a series of Ni based catalysts supported on fibrous silica micro-spheres (KCC-1). The KCC-1 material fabricated by a conventional hydrothermal method had a less concentric structure and appears in “tagetes erecta-like” shape rather than a dandelion-like morphology of the original KCC-1. The effects of Ni loading and the heat-treatment regime on the performance and physicochemical characterization of Ni based catalysts supported on KCC-1 were investigated. The activity in CO₂ methanation of the catalysts calcined and reduced at suitable regimes (450 °C-2h and 450 °C-1h, respectively) was evaluated. An amount of 25 wt% of Ni on KCC-1 support was chosen to be the reasonable Ni content for a harmonization of the amount of active sites and resistance to metallic sintering.

Keywords: Ni/ KCC-1 catalyst, CH₄ production, CO₂, pretreatment regimes, active phase loading

INTRODUCTION

The gradual increase of CO₂ concentration in the atmosphere, reaching approximately 400 ppm to date, has stimulated the worldwide investigation to reduce CO₂ emission [1, 2]. CCUS (Carbon Capture, Utilization, and Storage) has been regarded as a potential technology to mitigate this greenhouse gas [3-7]. Using the captured CO₂ from the CCUS technology, the Power-to-Gas process converts CO₂ into CH₄ via the Sabatier reaction (CO₂ methanation reaction), this pathway has caught the interest of researchers as a means of storing the unstable renewable energy [8]. Renewable energy (wind, solar, etc.) is utilized to produce green hydrogen through water electrolysis, and this hydrogen is used to hydrogenate CO₂ into CH₄ for storage purposes.

Since nickel is an inexpensive active component, the development of nickel-based catalysts for thermal CO₂ methanation is essential to achieve high CO₂ conversion and CH₄

selectivity [9]. Though the reaction is carried out at mild conditions, the exothermic nature of the reaction can cause the agglomeration of the active sites in the catalyst structure [10, 11]. This issue can be overcome by tailoring support with high surface area, thermal stability, and high porosity for anchoring the active sites. Recently, KCC-1 material has been seen as a potential support with several advantages compared to other mesoporous silica, e.g. SBA-15, and MCM-41. These fibrous silica micro-spheres can offer easy accessibility for both active sites and reactants, high specific surface area, and multi-dimensional structure, which can optimistically alter the catalytic activity [12].

In this study, the metallic nickel is supported on the KCC-1 for the catalytic investigation in the CO₂ methanation reaction. The support material, KCC-1, was prepared by a conventional hydrothermal method. The simple impregnation procedure was utilized to prepare the Ni/KCC-1 catalyst with various metallic loading. Then, a facile route for enhancing the characterization of

the Ni/KCC-1 catalysts was conducted by investigating the effect of heat treatment modes. The activity of the catalysts prepared with the suitable conditions would be assessed by evaluating their performance in CO₂ methanation.

EXPERIMENTAL

Fabrication of fibrous KCC-1 silica microsphere and Ni/KCC-1 catalysts

The fibrous silica material was synthesized by the hydrolysis method as reported in paper [13]. Ni/KCC-1 catalysts were denoted as xNi/KCC-1, in which x is the wt% of Ni (x = 15, 20, 25, 30). The simple impregnation method was utilized for the preparation of the catalysts. After the KCC-1 was impregnated with Ni(NO₃)₂ solution and kept aging for 12 h, the mixture was dried in hot air at 60 °C for 12 h and then calcined in hot oven. The NiO species in the catalyst were reduced into Ni metallic sites in H₂ flow. Effects of the conditions of calcination (m °C, n h) and reduction (z °C, t h) on catalyst' characteristics were investigated. The samples' abbreviation was noted as C.x-y (calcined at x °C for y h) and R.z-t (reduced at z °C for t h).

Characterization and catalytic activity

The characterization of the catalysts was performed using various techniques [14].

In a typical survey, 0.2 g fresh catalyst particles (0.25–0.5 mm) calcined at suitable m °C and n h was mixed with 0.8 g of the same size quartz particles. The mixture was prepared as the catalyst bed in a fixed bed catalytic reactor. The catalytic reaction was studied in a temperature range of 300–400 °C with a CO₂:H₂:N₂ = 3:12:85 volume ratio in the feed stock, and a total flow rate of 6 L/h. Prior to the catalytic examination, the catalysts were activated in a H₂ flow (3 L/h) at z °C for t h. The CO₂ conversion and CH₄ selectivity were determined by using 6890 Plus Gas Chromatograph with TCD and FID detectors (capillary column HP-PLOT Molesieve 5A and capillary column DB624, respectively).

RESULT AND DISCUSSION

Formation of KCC-1

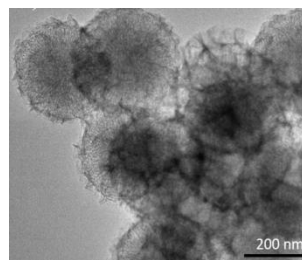


Figure 1. HR-TEM image of KCC-1 support

The formation of KCC-1 micro-particles are confirmed by the HR-TEM image (Fig.1). The material prepared by the same method of solvothermal treatment as in literature [13] also possesses the same bicontinuous structure and concentric pattern. The denser core structure is due to the easier silica condensation with more formed silica networking in the center of the water phase in the reverse micelle. Besides, the hydrophilic component in the surfactant CTAB could attract more water molecules, which slows the hydrolysis process and the silica condensation in the outer part of the micelle. The Raman spectrum of the KCC-1 hardly shows any corresponding Raman bands of typical silica material in the shift range of below 1000 cm⁻¹. Further increase of the investigated Raman shift range exhibits a Raman band at around 2300 cm⁻¹, which could be associated with the CO₂ adsorption on the surface of silica [15]. This work's KCC-1 induces a type IV nitrogen adsorption-desorption pattern and a H4 hysteresis loop (not presented).

Impact of calcination and reduction regimes

The XRD patterns of 25Ni/KCC-1 calcined at different temperatures and duration all exhibited characteristic diffraction peaks of NiO at 2θ = 37.2, 43.4, and 62.9°. All the NiO crystalline sizes calculated by the Debye Scherrer equation at 2θ = 44.3° fluctuate in the range of 13-15 nm. The smallest crystalline size was recorded at a condition of 450 °C - 2 h, and this was chosen as a suitable calcined mode for the preparation of NiO/KCC-1 precursor.

The XRD patterns of reduced samples exhibited the characteristic diffraction peaks at 2θ = 44.8, and 51.9° of Ni phase. It was noted that the sample reduced at 400 °C for 2 h still exhibited the diffraction peaks of NiO at 2θ = 37.1, and 44.3°, indicating a part of NiO still remained in the structure of the catalyst. Increasing to 450 °C completely transformed the NiO phase into metallic Ni, and the smallest Ni crystal size was achieved at a reduction temperature of 450 °C.

Following the examination, different reduction durations were surveyed, and the result showed that the sample reduced at 450 °C for 1 h had the smallest Ni crystalline size. After being surveyed, the catalysts have been treated at much milder conditions (calcined at 450 °C - 2 h and reduced at 450 °C - 1 h) compared to the initial.

Impact of Ni loading on KCC-1

The metal-support interaction and the reducibility of the NiO/KCC-1 precursors with different Ni loading are explored through H₂-TPR profiles (not presented). The reduction of NiO species in this work are taken place in the temperature range of 260–600 °C, including a high intense reduction peak at 260–400 °C characterized to the reduction of oxygen on the surface and dispersed NiO phase; and a broad peak at 400–600 °C ascribed to the reduction of NiO species strongly attaching to the support surface. After being reduced, the metallic Ni sites disperse on the KCC-1 surface with the morphology observed in Fig.2.

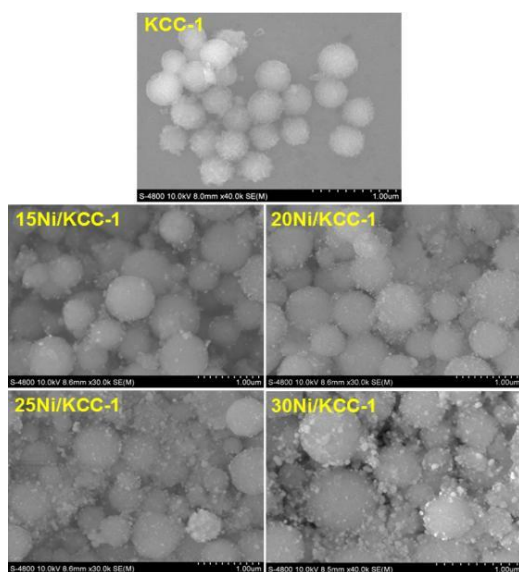


Figure 2. SEM images of *x*Ni/KCC-1 catalyst

The metal-support interaction and the reducibility of the NiO/KCC-1 precursors with different Ni loading are explored through H₂-TPR profiles (not presented). The reduction of NiO species in this work are taken place in the temperature range of 260–600 °C, including a high intense reduction peak at 260–400 °C characterized to the reduction of oxygen on the surface and dispersed NiO phase; and a broad peak at 400–600 °C ascribed to the reduction of NiO species strongly attaching to the support surface. After being reduced, the metallic Ni sites

disperse on the KCC-1 surface with the morphology observed in Fig.2.

The presence of Ni metallic phase in these SEM images are confirmed and studied through the XRD analysis. The calculated Ni crystalline size is all lower than 100 nm, indicating a good dispersion of Ni on KCC-1 and the increase of Ni crystalline size when Ni content in the catalyst is in good agreement with the morphology observed in SEM images.

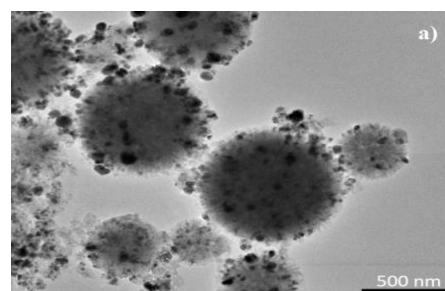


Figure 3: HR-TEM image of 25Ni/KCC-1

The morphology of 25Ni/KCC-1 sample observed on HR-TEM image (Fig. 3) shows the Ni particles are decorated on the surface of KCC-1. It could be seen that metallic Ni sites formed as pseudo spherical particles are located on the edge of the fibrous silica KCC-1. Hence, these particles could be agglomerated into large particles during the heat treatment. The analyzed mean diameter of Ni particles from the HR-TEM image (not shown) is 33.8 ± 11.7 nm.

The TPD profiles (not presented) of as-synthesized catalysts showed the presence of weak (below 200 °C) and medium (200–400 °C) basic sites. The capacity of weak basic sites gradually decreases as the Ni loading increases and these sites are proposed to be corresponding to the hydroxyl groups on the surface of silica-based material [16, 17]. Hence, a moderate number of basic sites of this study's *x*Ni/KCC-1 catalysts could favor the catalytic reaction of CO₂ methanation. The Ni component covers the fibrous structure of KCC-1, and in addition, the metallic Ni could be the bridge among KCC-1 microspheres as observed in the SEM images when the Ni loading increases. Hence, loading Ni particles on the surface of the support significantly decreases the specific surface area of the material. Nevertheless, 25Ni/KCC-1 still possessed a large specific surface area of 314.5 m²/g regarding the high weight percentage of Ni, implying the enhanced effect of KCC-1 support in the aspect of dispersing the active phase for catalytic reactions.

Catalytic activity

The xNi/KCC-1 catalysts with the suitable treatment conditions obtained via the XRD analysis survey were investigated in the CO₂ methanation. The catalytic activities were plotted against reaction temperature (not shown). When the reaction temperatures were raised gradually, the CO₂ conversion of all the catalysts increased as the kinetic of the reaction is favorable. The catalytic conversions reached the maximum values, approximately the equilibrium values, at 375 °C or 400 °C. When the Ni content was raised from 15% to 25%, catalytic activity increased due to more active sites for the reaction to take place. As a result, the activity of 25Ni/KCC-1 catalyst has the highest CO₂ conversion (76.9%) at 375 °C among tested materials. Increasing to 30 wt.%Ni might enhance the catalytic performance at lower temperatures. However, the severe sintering phenomenon could be the reason for the deterioration of catalytic CO₂ conversion at higher temperatures. Considering CH₄ yield functions, the 25Ni/KCC-1 catalyst still exhibited the highest performance. Hence, the suitable Ni loading on KCC-1 support was asserted to be 25 wt%.

The xNi/KCC-1 catalysts with the suitable treatment conditions obtained via the XRD analysis survey were investigated in the CO₂ methanation. The catalytic activities were plotted against reaction temperature. When the reaction temperatures were raised gradually, the CO₂ conversion of all the catalysts increased as the kinetic of the reaction is favorable. The catalytic conversions reached the maximum values, approximately the equilibrium values, at 375 °C or 400 °C. When the Ni content was raised from 15% to 25%, catalytic activity increased due to more active sites for the reaction to take place. As a result, the activity of 25Ni/KCC-1 catalyst has the highest CO₂ conversion (76.9%) at 375 °C among tested materials. Increasing to 30 wt.%Ni might enhance the catalytic performance at lower temperatures. However, the severe sintering phenomenon could be the reason for the deterioration of catalytic CO₂ conversion at higher temperatures. Considering CH₄ yield functions, the 25Ni/KCC-1 catalyst still exhibited the highest performance. Hence, the suitable Ni loading on KCC-1 support was asserted to be 25 wt%.

CONCLUSION

This work has utilized the conventional hydrothermal method for tailoring KCC-1

material, a support for the Ni based catalysts. Via a facile route of studying the effect of calcined and reduced regimes, Ni/KCC-1 catalysts have been prepared with lower temperatures and shorter time (calcined at 450°C for 2 h and reduced at 450°C for 1 h). The series of Ni/KCC-1 catalysts exhibited moderate basic sites and strong metal-support interaction, which could enhance the performance of catalysts. Though the as-synthesized KCC-1 was not able to uniformly disperse the Ni particles, leading to the agglomeration of active sites, the dominant role of active site content was considered. The optimal Ni content is 25 wt% on the as-synthesized KCC-1 support for the CO₂ methanation. This catalyst has the highest CO₂ conversion and CH₄ yield at 375°C.

References

- [1] Xu, L., et al., *Rare earths modified highly dispersed fibrous Ni/KCC-1 nanosphere catalysts with superb low-temperature CO₂ methanation performances*. Applied Surface Science, **608** (2023) 155258.
- [2] Li, L., et al., *Research progress and reaction mechanism of CO₂ methanation over Ni-based catalysts at low temperature: a review*. Catalysts, **12**(2) (2022) 244.
- [3] Hu, F., et al., *Enhancement of hollow Ni/CeO₂-Co₃O₄ for CO₂ methanation: From CO₂ adsorption and activation by synergistic effects*. Chemical Engineering Journal, **461** (2023) 142108.
- [4] Zhang, T., et al., *Enhancing the low-temperature CO₂ methanation over Ni/La-CeO₂ catalyst: The effects of surface oxygen vacancy and basic site on the catalytic performance*. Applied Catalysis B: Environmental, **312** (2022) 121385.
- [5] Sodeifian, G., S.A. Sajadian, and R. Derakhsheshpour, *CO₂ utilization as a supercritical solvent and supercritical antisolvent in production of sertraline hydrochloride nanoparticles*. Journal of CO₂ Utilization, **55** (2022) 101799.
- [6] Singh, T., et al., *Emerging technologies for the development of wood products towards extended carbon storage and CO₂ capture*. Carbon Capture Science Technology, (2022) 100057.
- [7] Navas-Angueta, Z., et al., *Revisiting the role of steam methane reforming with CO₂ capture and storage for long-term hydrogen*

- production*. Science of the total Environment, **771** (2021) 145432.
- [8] Götz, M., et al., *Renewable Power-to-Gas: A technological and economic review*. Renewable energy, **85** (2016) 1371-1390.
- [9] Le, T.A., et al., *CO and CO₂ methanation over supported Ni catalysts*. Catalysis Today, **293** (2017) 89-96.
- [10] Su, X., et al., *Catalytic carbon dioxide hydrogenation to methane: A review of recent studies*. Journal of energy chemistry, **25**(4) (2016) 553-565.
- [11] Ghaib, K. and F.-Z. Ben-Fares, *Power-to-Methane: A state-of-the-art review*. Renewable and Sustainable Energy Reviews, **81** (2018) 433-446.
- [12] Bahari, M., et al., *Development of fibrous mesoporous silica for catalytic reaction: a short review*. Materials Today: Proceedings, **42** (2021) 33-38.
- [13] Febriyanti, E., et al., *Further insight into the definite morphology and formation mechanism of mesoporous silica KCC-1*. Langmuir, **32**(23) (2016) 5802-5811.
- [14] Long, D.B., et al., *High active and coke-resistant CeNiO₃-based catalyst for methane bi-reforming*. Journal of Science: Advanced Materials and Devices, **8**(3) (2023) 100610.
- [15] Bayal, N., R. Singh, and V. Polshettiwar, *Nanostructured silica-titania hybrid using dendritic fibrous nanosilica as a photocatalyst*. ChemSusChem, **10**(10) (2017) 2182-2191.
- [16] Mihet, M., et al., *CO₂ methanation using multimodal Ni/SiO₂ catalysts: Effect of support modification by MgO, CeO₂, and La₂O₃*. Catalysts, **11**(4) (2021) 443.
- [17] Alreshaidan, S.B., et al., *Effect of Modified Alumina Support on the Performance of Ni-Based Catalysts for CO₂ Reforming of Methane*. Catalysts, **12**(9) (2022) 1066.

FABRICATION AND EVALUATION OF THE RESISTANCE TEMPERATURE DETECTOR USING PLATINUM MATERIALS DEPOSITED BY THE SPUTTERING METHOD.

Linh Duy Nguyen, Hoa Hong Chung, Ngan Huu Dinh, Thang Minh Bui, Vi Nhat Hoang Ngo, Dung Dang Thi My, Ngan Nguyen Le, Tin Chanh Duc Doan and Chien Mau Dang

Institute for Nanotechnology, Community 6, Linh Trung Ward, Thu Duc City, Ho Chi Minh City, Vietnam;

Vietnam National University Ho Chi Minh City, Ho Chi Minh City, Vietnam

Email: bmthang.int@vnuhcm.edu.vn

ABSTRACT

In this work, the chip of platinum electrodes was fabricated on the silicon platform. The fabrication technique combines photolithography, sputtering, and lift-off methods. Before the platinum layer was fabricated by lithography, sputtering, and lift-off techniques, the titanium layer had been deposited as an adhesion layer. The electrical-optic and physical properties of the fabricated electrodes were characterized by the surface resistance measurement (Keithley 2400), the optical microscope GX 51 (Olympus), the stylus profiler Dektak 6M (Veeco), and the Atomic Force Microscope (AFM). The thickness of the platinum electrodes was approximately 224 nm with a surface resistance value of 8.1 Ω . It can be seen that the platinum film fabricated by sputtering has a nanostructure with an average roughness Rms of 1.69 nm. It can be seen that the electrodes fabricated with a micromet thickness are very suitable when used as a base electrode applied to a temperature sensor system.

Keywords: Electrochemical sensor, electrodes, photolithography, sputtering, temperature sensor.

INTRODUCTION

Temperature measurement and surveying are essential in manufacturing and scientific research. With stable operation, high accuracy, and a wide measurement range, the Resistance Temperature Detector (RTD) is widely used in many production systems. Although it was invented quite a long time ago in 1860 by C. W. Siemens [1], to this day, there have been numerous studies on the fabrication and characterization of RTD sensors, such as investigating the phase variation of RTD sensors made from glass-metal alloys [1], designing and fabricating temperature sensors for weather monitoring system using microelectromechanical systems (MEMS) technology [2], manufacturing Nickel RTD sensors using surface printing methods [3], etc. In general, most of the studies focus on improving materials, developing new fabrication methods, and diversifying applications, with very few studies on optimizing the fabrication process and design for RTD temperature sensors.

In the study, the focus is primarily on the design and manufacturing process, followed by the evaluation of the electrode properties and the

investigation of the stability of the thermistor sensor. This allows for a comparative analysis to determine the design of a high-strength thermistor sensor for practical applications in temperature measurement and monitoring.

EXPERIMENTAL

Materials

All chemicals and additives used for investigation experiments have analytical purity and were purchased from Sigma-Aldrich without further purification. These include sulfuric acid (H_2SO_4), hydrogen peroxide (H_2O_2), ethanol (C_2H_5OH), isopropanol ($(CH_3)_2CHOH$), and acetone ($(CH_3)_2CO$). Additionally, some chemicals used in the lithography process, such as Photoresist Negative - N1410 Hexamethyl Disilazane (HMDS) Developer ma-D533S, are purchased from Germany. Distilled water (DI) with a resistivity of not less than 18.2 $M\Omega.cm$ is used in the research processes.

Fabrication of the thin film Pt electrodes.

The temperature electrodes are designed in various shapes with lengths $L = 45$ mm, $L = 55$ mm, $L = 65$ mm, $L = 85$ mm. We utilize

CorelDRAW software to design the Mask for the lithography process.

The electrode fabrication process uses the photolithography technique with the following basic steps: Firstly, the negative photoresist ma-N1410 is coated onto the wafer surface using the DELTA 6RC spin coater device from SUSS Microtec, Germany. Secondly, UV light with a wavelength of 365 nm and a power of 350 W is used for a 5-second exposure time. Finally, the image is developed. The entire experimental process of electrode fabrication is conducted in a cleanroom (class 1000).

The 200 nm thick platinum films was

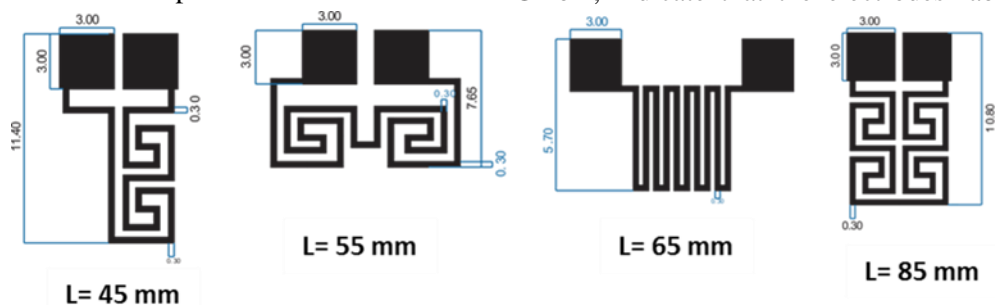


Figure 1. The image depicts the shape of the temperature electrode designs along the length.

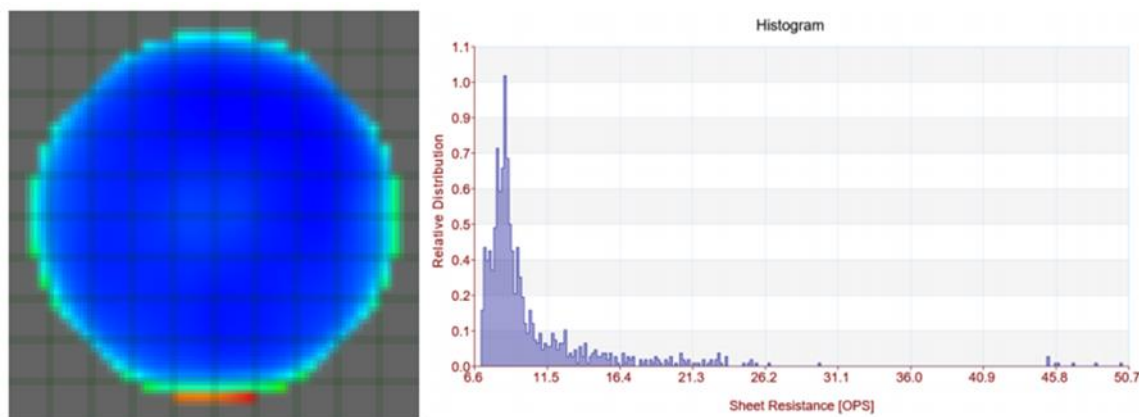


Figure 2. The image demonstrates the distribution of electrical resistance on the surface of a 4-inch wafer.

deposited using the DC sputtering technique at room temperature from target metallic Ti (99.95% in purity) and Pt (99.99% in purity) on SiO₂ commercial substrates. (The deposition process was executed under the total pressure P_{Ar} of 7×10⁻³ Torr, and the temperature electrode was fabricated using the magnetron DC sputtering method at a pressure of 6 x 10⁻³ (mbar) and a power of 50 (W) for the deposition time of Ti and Pt materials of 180 (s) and 600 (s), respectively.

In addition, various devices are used to investigate the properties of materials after fabrication. The physical properties of the

modified electrode were examined by using an Atomic Force Microscope AFM XE7, Park System, Korea, and the thickness of the Pt electrodes was measured by a stylus profiler Dektak 6M (Veeco US); the Keithley 2400 device was used to investigate the variation of resistance with temperature.

RESULTS AND DISCUSSION

The result of surface resistance.

The results of surface resistance measurements from the EddyCus® TF map 2525SR device, manufactured by SURAGUS GmbH, indicate that the electrodes fabricated

using the sputtering method exhibit relatively uniform resistance across the 4-inch wafer surface. **Figure 2** shows that the average surface impedance is 8.1 Ω, indicating a consistent relationship between the thickness and surface impedance of the electrodes.

The results of thickness.

The Ti/Pt layer thickness of the electrode was measured using the Dektak 6M Stylus Profiler (Veeco, USA) at different positions on the sensor. The measurements were conducted on two other electrodes. The results obtained are shown in Table 1. The average thickness of the

Ti/Pt coating layer was found to be approximately 224 nm.

Table 1. The result of measuring electrode thickness using the Dektak 6M Stylus Profiler device.

Position	Thickness Ti/Pt (nm)
1	220,52
2	228,14
3	217,87
4	232,34
Average	224,7

The surface topography of the electrode is characterized using Atomic Force Microscopy (AFM). In Figure 3, the AFM image of the Pt electrode reveals a relatively flat and uniform surface. The average surface roughness over a 2×2 μm area is measured to be Rms = 1.69 nm. This indicates suitable suitability for electrode fabrication applications.

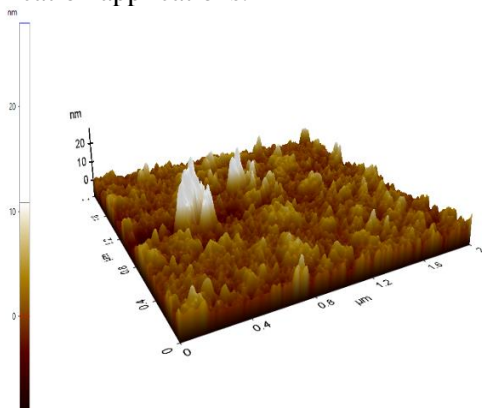


Figure 3. Atomic force microscopy (AFM) analysis of electrodes.

The results of the temperature-resistance measurements of the electrodes are indicated in figure 4. All electrodes exhibit a linear relationship between temperature and resistance, with the squared correlation coefficients (R²) of all electrodes greater than 0.99. This indicates a high degree of fit between the collected data and the regression model equation, allowing for accurate prediction of temperature values based on measured resistance values. Competition the reflectivity of temperature values through resistance, it can be seen that the sensor with a wire length L = 55 mm has the most accurate linear regression with an R² value of 0.9995, indicating that this sensor design has a stronger relationship between temperature and resistance.

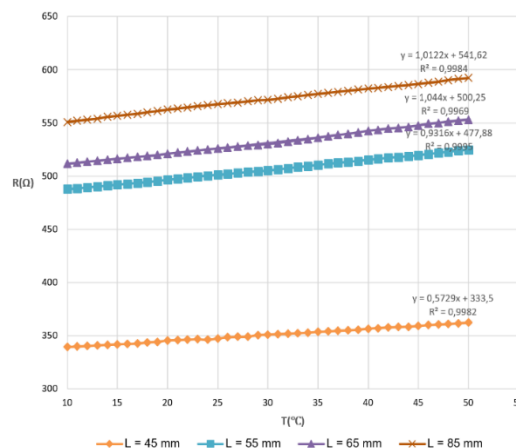


Figure 4. The temperature-resistance graph of platinum wire electrodes with lengths (L = 45 mm, 55 mm, 65 mm, 85 mm).

The Temperature - resistance graph of platinum wire electrodes with lengths (L = 45 mm, 55 mm, 65 mm, 85 mm). The resistance values R₀ (T₀ = 10 °C) of the electrodes also increase with the increasing length of the wire when the values of the sensor layer thickness T = 200 nm and the width dimension W = 377 mm are the same. This is consistent with the theoretical formula for the resistance value of a conductor wire [4-6].

$$R(T_0) = \rho(T_0) \cdot \frac{L}{D \cdot W}$$

CONCLUSION

The research focuses on designing and fabricating various types of temperature-sensing electrodes with different wire lengths. The studied material layer has a thickness of 224 nm and a smooth surface with a root mean square roughness (Rms) of 1.69. The electrode has a length of L= 55 mm and high precision (R² = 0.9995) and sensitivity. This noble metal electrode offers several benefits, including integration into conductivity measurement microchips, ease of use, and low production cost.

Acknowledgment

This work was supported by the Ministry of Science and Technology under grant number ĐTĐL.CN-122/21.

References

- [1] H. Zhang et al., *Graphic abstract SC*, Acta Mater., (2018)
- [2] J. Haitao Zhang, Dongwoo Lee, Ye Shen, Yucong Miao, Jinhye Bae, Yanhui Liu and J. J. V. Schroers, Yong Xiang, *Combinatorial*

temperature resistance sensors for the analysis of phase transformations demonstrated for metallic glasses.

- [3] V. S. Turkani et al., *Nickel based RTD fabricated via additive screen printing process for flexible electronics*, IEEE Access, **7** (2019) 37518–37527.
- [4] P. Lugoda et al., *Flexible temperature sensor integration into e-textiles using different industrial yarn fabrication processes*, Sensors (Switzerland), **20**(1) 2020.
- [5] A. Manuscript, *is important to measure temperature distribution without affecting the ultrasonic field and heat d M us pt*, (2017) 0–22.
- [6] J. Kim, J. Kim, Y. Shin, and Y. Yoon, *A Study on the Fabrication of an RTD (Resistance Temperature Detector) by Using Pt Thin Film*, Korean J. Chem. Eng., **18**(1) (2001) 61–66.

INVESTIGATION ON THE ELECTROCHEMICAL PROPERTIES OF A Pt ELECTRODE CHIP WITH THE CONDUCTIVITY SENSOR SYSTEM DESIGNED TO MEASURE SALINITY

Vi Nhat Hoang Ngo, Thang Minh Bui, Linh Duy Nguyen, Ngan Nguyen Le, Tin Chanh Duc Doan, Dung My Thi Dang and Chien Mau Dang

Institute for Nanotechnology, Community 6, Linh Trung Ward, Thu Duc City, Ho Chi Minh City, Vietnam;

Vietnam National University Ho Chi Minh City, Ho Chi Minh City, Vietnam

Email: nhnvi.int@vnuhcm.edu.vn

ABSTRACT

Determining water salinity through conductivity is a highly sensitive and quick response method recognized by many international organizations. Herein, we present a fundamental study investigating the electrochemical properties of a planar 2-platinum-electrode chip fabricated on the silicon platform by photolithography, sputtering, and lift-off methods. The electrode characteristics were studied by cyclic voltammetry (CV). Electrochemical impedance spectroscopy (EIS) was used to study the conductivity of the sensor in a frequency range from 0.10 Hz to 1.0 MHz. The electrodes on chip offered a conductivity range of 0.50 mS/cm to 12.90 mS/cm, which corresponds to a salinity range of 0.25 psu to 6.89 psu, respectively. The designed sensor possesses the characteristics of wide range which is of great significance for on-site observation of physical parameters of the river water environment.

Keywords: Conductivity electrodes, Salinity sensors, Platinum chip, 2-electrode system, Electrochemical impedance spectroscopy

INTRODUCTION

Salinity is a vital ecological factor that greatly impacts agricultural activities. In Vietnam, this indicator has a significant impact on productivity and quality in aquaculture, especially during times when the Mekong Delta region faces high risk of salinity. Therefore, measuring water salinity is essential to ensure sustainable and effective agricultural development.

Currently, the popular methods for salinity determination are based on: density [1,2], refractometer [3-6] and conductivity [7,8]. As the conductivity sensor is highly sensitive and easy to measure, the determination of salinity via conductivity is the most used and recognized by many international measurement organizations.

The conductivity is directly proportional to the conductance measured from the electrodes. The cell constant of a conductivity electrode depends primarily on the physical geometry and design. The Randles model, Fig 1 was used to model the system.

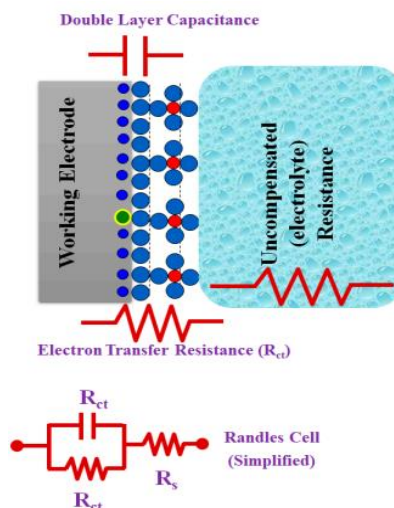


Figure 1. A simple scheme to describe the EIS circuit and the redox reaction takes place at the surface of working electrodes in a conventional electrochemical cell (i.e., three-electrode system).

The impedance of the measurement cell consists of the resistance of the liquid and the impedance of the electrode interface. As shown in Fig. 1, the impedance of electrode interface

consists of a parallel connection of double-layer capacitance and Faradaic impedance. The Faradaic impedance is further divided into charge transfer resistance and Warburg impedance. The frequency – domain impedance spectroscopy measurements can be separated into three frequency domain, the first one at a high – frequency range attributed to the charge transfer at the counter electrode; the second one in the intermediate and the solid-liquid interface; and the last one at a low – frequency region usually reflects surface due to the dynamics of the electrolyte particles where the diffusion processes and effects on the surface due to interaction electrode – electrolyte may play a relevant role [9].

After the conductivity measurement, salinity was determined from the Practical Salinity Scale 1978 [10]. According to this definition, salinity can be calculated from three parameters: conductivity, temperature, and pressure – this relationship is built on experimental data.

From surveys in the literature, we found that electrodes based on the platinum material possessed a great electrochemical stability in the positive potential window, increases mass transfer, has a fast electron transfer rate and has a large active area to volume ratio, high catalytic activity [11], integrated micro- and nano-electrodes based on noble metals in the field of electroanalysis have proven their ability to achieve high sensitivity with good selectivity.

Following this approach, we present a fundamental study investigating the electrochemical property of a planar 2-platinum-electrode chip that was fabricated on the silicon platform by photolithography, sputtering, and lift-off methods. The chemically stable structure of the platinum film formed from sputtering deposition is expected to enable the electrode to achieve a good sensitivity and improve reproducibility.

EXPERIMENTAL

Pt electrode systems

Thin - film Pt electrodes were fabricated by Institute for Nanotechnology (Ho Chi Minh City, Vietnam) using photolithography combined with sputtering and lift-off, as shown in **Figure 2**. The conductivity sensor includes 2 Pt electrodes with a geometric area (S) of 0.20 cm² each. These electrodes placed symmetrically with a distance of 0.19 cm (L).

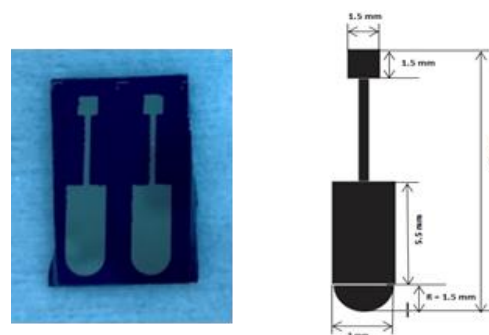


Figure 2. Pt electrodes on chip and its dimensions.

Reagents

Conductivity standard solutions (Hanna instruments): 500 $\mu\text{S}\cdot\text{cm}^{-1}$; 1000 $\mu\text{S}\cdot\text{cm}^{-1}$; 1413 $\mu\text{S}\cdot\text{cm}^{-1}$; 5000 $\mu\text{S}\cdot\text{cm}^{-1}$; 12900 $\mu\text{S}\cdot\text{cm}^{-1}$; KCl (ReagentPlus® 99%, Sigma-Aldrich), $\text{K}_3[\text{Fe}(\text{CN})_6]$ (ReagentPlus® 99%, Sigma-Aldrich). All experiments were studied at room temperature (28 °C). Deionized water (DI) with a resistivity of 18.2 $\text{M}\Omega\text{ cm}$ was utilized.

Electrochemical measurements

Electrochemical measurements were performed using Autolab PGSTAT302N (Eco Chemie, Utrecht, The Netherlands) driven via Nova software.

Electrode kinetics was studied by cyclic voltammetry at various scan rates (5–500 mV/s) in solution containing 1.0 mM $\text{K}_3\text{Fe}(\text{CN})_6$ and 0.1 M KCl. Three-electrode system includes a Pt electrode-on-chip serving as a working electrode, a wire Pt electrode (BASi, USA) serving as a counter electrode, a Ag/AgCl electrode in 3.0 M KCl solution serving as a reference electrode (**Figure 3**, left side).

Electrochemical Impedance Spectroscopy (EIS) was employed to investigate the conductivity behavior of the electrodes on chip. The EIS measurements were carried out using two-electrode system (**Figure 3**, right side) with a frequency range of 10 – 10⁶ Hz and an amplitude of 10 mV in KCl standard solutions from low to high concentrations.

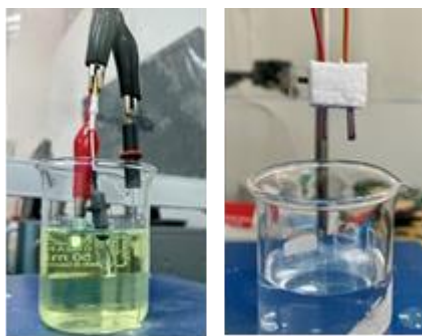


Figure 3. Three-electrode system (left side) for CV measurements and two-electrode system (right side) for EIS measurements

RESULTS AND DISCUSSION

Cyclic voltammetry

Both the anodic and cathodic current peaks increase with an increasing scan rate, as illustrated in **Figure 4**. The typical redox peak of the Fe^{3+}/Fe^{2+} at $\sim 0.2/0.3$ V, this value corresponds to the study of Shewakena et al (2020 [12]). Furthermore, there aren't any other peaks, proving that the electrode made by this method is not contaminated.

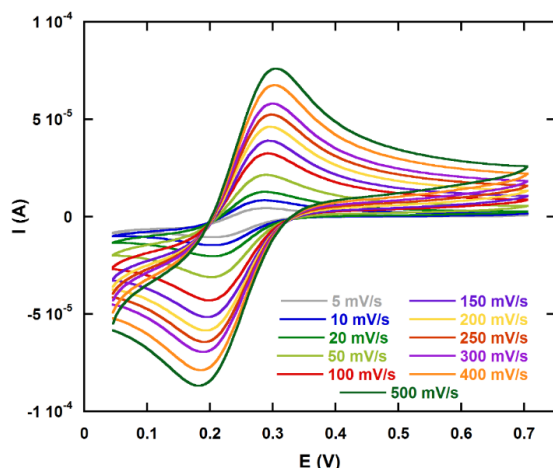


Figure 4. The CV voltammograms of the 1.0 mM Fe(III) in 0.1 M KCl at various scan rates of: 5-500 mV/s.

The determination of the oxidation current peak from the scan rate with its square root is detailed. The active surface area (A_{act}) of the electrode was calculated from cyclic voltammetric technique at various scan rates via RandlesSevick equation. The equation for a reversible process at $T = 298$ K is as follows:

$$i_p = (2.69 \times 10^5) n^{3/2} A C D^{1/2} v^{1/2}$$

where I_p is the peak current (A), n is the electron transfer number, D_0 is the diffusion coefficient which is equal to $7.6 \times 10^{-6} \text{ cm}^2 \text{ s}^{-1}$ [13] v is the scan rate ($\text{mV} \cdot \text{s}^{-1}$) and C_0 is the

concentration of $K_3Fe(CN)_6$ ($\text{mol} \cdot \text{cm}^{-3}$): $i = 1.047 \times 10^{-4} v^{1/2} - 1.924 \times 10^{-6}$. From the slope of the I_p versus $v^{1/2}$ the active surface area of the electrode is estimated to be 0.196 cm^2 . This value is not much different from the geometric area value (0.20 cm^2).

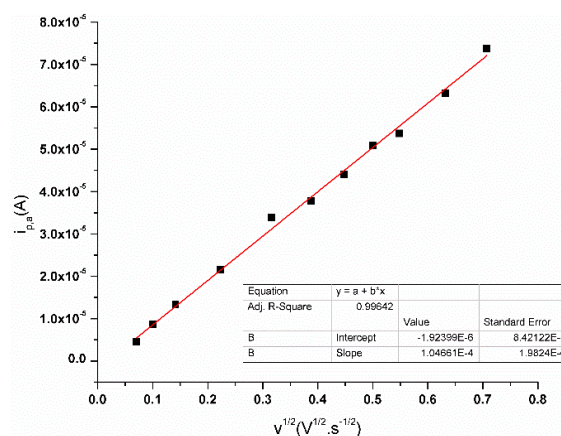


Figure 5. Dependence of the peak current i_{pa} on the square root of the scanning speed $v^{1/2}$.

The investigation of kinetics was carried out using Cyclic Voltammetry (CV) with the scan rate varying from 5 mV/s to 500 mV/s (**Fig. 5**). It can be observed that the plot of the peak current (I_p) against the square root of scan rate ($v^{1/2}$) gives a linear function with a correlation coefficient $R_2 = 0.9964$ (**Fig. 5**), indicating that the redox process is a reversible reaction at the Pt electrode.

Electrochemical impedance spectroscopy (EIS)

During the measurement, an AC voltage of 10 mV was applied to the electrode and the current was measured over a frequency range of 0.1 Hz to 1 MHz. The magnitude of the impedance for different concentration solutions is plotted as a function of frequency (**Fig. 6**). The spectra are characterized by a plateau with a certain bandwidth. In the frequency range in between these cut-off frequencies, the impedance is mostly governed by the resistance of the solution. In this frequency band, the sensors are sensitive to changes in conductivity. However, due to the shift of the resistive plateau towards higher frequencies for higher electrolyte conductivities, an adaptation of the measuring frequency is required, in order to get optimal accuracy, linearity, sensitivity, and dynamic range [14]. The impedance at the plateau level, shift in an upward or downward direction in response to change in conductivity.

In practical application, it is essential to select the operating frequency to obtain the resistance of the solution accurately and precisely. Furthermore,

full spectral data is not available when a sensor is operated at a single frequency [15]. Therefore, the conductivity was determined by dividing $K = 0.98 \text{ cm}^{-1}$ (actual value from CV measurement) with the impedance value at a fixed frequency of 10 kHz, which fell within the limits of the plateau for the bulk of the measurements. The conductivity values at room temperature (28 °C) are shown in **Table 1**.

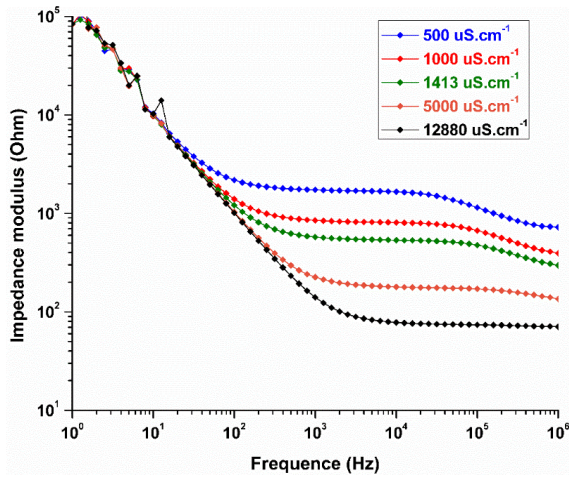


Figure 6. Bode plot of 2-electrode conductivity measurement system.

Salinity range

After the conductivity measurement, the salinity value is calculated based on the actual conductivity at room temperature according to The Practical Salinity Scale 1978.

Table 1. Salinity values is converted from the conductivity value at a frequency of 10 Hz at room temperature according to The Practical Salinity Scale 1978.

Conductivity		Salinity	
Standard solution at 25 °C	Experiment at 28 °C	Standard solution at 28 °C	Experiment at 28 °C
500	577.1396	0.228	0.254
1000	1203.577	0.465	0.542
1413	1832.059	0.666	0.840
5000	5607.998	2.521	2.738
12880	13279.25	6.948	6.899

Fig 7 compares the salinity obtained with the standard solutions to the salinity measured in practice at the room temperature 28 °C. Expect that these two values are similar to each other. Indeed, the graph below shows the linear dependence of these two values with correlation coefficient $R^2 = 0.998$ and slope $a = 1.044$.

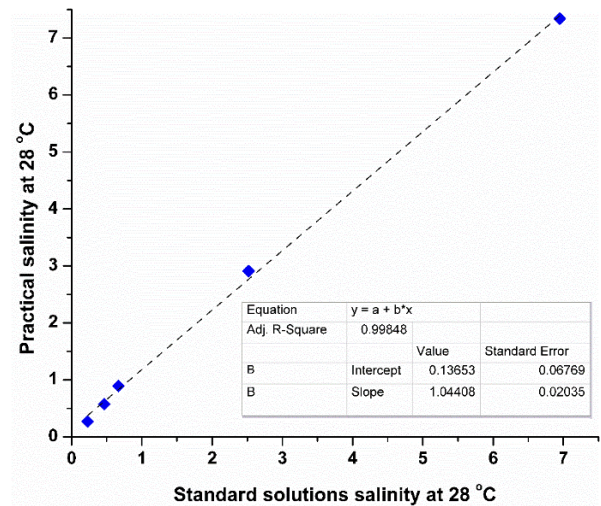


Figure 7. Correlation between theoretical salinity value and experimental salinity value.

CONCLUSION

A conductivity measurement system with nano Pt electrodes has been fabricated and evaluated for use as a miniature salinity sensor. The electrodes have a size of 0.196 mm and cell constant $K=0.98 \text{ cm}^{-1}$. The complex impedance of the system is measured in the frequency range from 0.1 Hz - 1.0 MHz in solutions with conductivity from 500 - 12880 uS.cm^{-1} . The salinity value is determined through the impedance value at a specified frequency of 10 kHz is very close to the theoretical value.

Acknowledgment

This work was supported by the Ministry of Science and Technology under grant number ĐTĐL.CN-122/21.

References

- [1] R. K. Bhattacharjya, B. Datta, and M. G. Satish, *Artificial Neural Networks Approximation of Density Dependent Saltwater Intrusion Process in Coastal Aquifers*, J. Hydrol. Eng., **12**(3) (2007) 273–282.
- [2] H. J. Diersch, *Finite element modelling of recirculating density-driven saltwater intrusion processes in groundwater*, Adv. Water Resour., **11**(1) (1988) 25–43.
- [3] D. Malardé, Z. Y. Wu, P. Grosso, J. L. De Bougrenet De La Tocnaye, and M. Le Menn, *High-resolution and compact refractometer for salinity measurements*, Meas. Sci. Technol., **20**(1) 2009.
- [4] S.-M. Tseng and C.-L. Chen, *Side-polished fibers*, Appl. Opt., **31**(18) (1992) 3438.

- [5] H. Minato, Y. Kakul, A. Nishimoto, and M. Nanjo, *Remote Refractive Index Difference Meter for Salinity Sensor*, IEEE Trans. Instrum. Meas., **38**(2) (1989) 608–612.
- [6] A. W. Domański, M. Roszko, and M. Swiło, *Compact optical fiber refractive index differential sensor for salinity measurements*, Conf. Rec. - IEEE Instrum. Meas. Technol. Conf., **2** (1997) 953–956.
- [7] X. Huang, M. C. Mowlem, R. Pascal, K. Chamberlain, C. Banks, and H. Morgan, *A miniature high precision conductivity and temperature sensor system for ocean monitoring*, 14th Int. Conf. Miniaturized Syst. Chem. Life Sci. 2010, MicroTAS 2010, **3**(12) (2010) 1715–1717.
- [8] C. Thirstrup and L. Deleebeeck, *Review on Electrolytic Conductivity Sensors*, IEEE Trans. Instrum. Meas., **70** (2021).
- [9] H. Kaden, F. Königer, M. Strømme, G. A. Niklasson, and K. Emmerich, *Low-frequency dielectric properties of three bentonites at different adsorbed water states*, J. Colloid Interface Sci., **411** (2013) 16–26.
- [10] E. Lewis, *The practical salinity scale 1978 and its antecedents*, IEEE J. Ocean. Eng., **5**(1) (1980) 3–8.
- [11] Q. Shen, L. Jiang, H. Zhang, Q. Min, W. Hou, and J. J. Zhu, *Three-dimensional dendritic Pt nanostructures: Sonoelectrochemical synthesis and electrochemical applications*, J. Phys. Chem. C, **112**(42) (2008) 16385–16392.
- [12] S. Shewakena Beshahwored, *Cyclic Voltammetric (Cv) Evaluation of Electrochemical Behaviors of K₃[Fe(CN)₆] and Uric Acid*, Int. Res. J. Nat. Sci., **8**(2) (2020) 52–59.
- [13] L. D. Nguyen, T. S. Vinh Nguyen, T. M. Huynh, R. Baptist, T. Chanh Duc Doan, and C. M. Dang, *Voltammetric determination of iron(III) using sputtered platinum thin film*, Electrochim. Acta, **320** (2019) 134607.
- [14] C. Huck et al., *Capacitively coupled electrolyte-conductivity sensor based on high-k material of barium strontium titanate*, Sensors Actuators, B Chem., **198** (2014) 102–109.
- [15] G. J. A. M. Brom-Verheijden, M. H. Goedbloed, and M. A. G. Zevenbergen, *A Microfabricated 4-Electrode Conductivity Sensor with Enhanced Range*, (11) (2018) 797.

ASSESSING THE ANESTHETIC EFFECTIVENESS OF CLOVE BASIL ESSENTIAL OIL MICROEMULSION IN *Hemibagrus wyckioides*

Phuong Hong Lam, Huyen Da Nguyen Vo, Mai Thi Le, Dung My Thi Dang, Chien Mau Dang

Institute for Nanotechnology, Community 6, Linh Trung Ward, Thu Duc City, Ho Chi Minh City, Vietnam;

Vietnam National University Ho Chi Minh City, Ho Chi Minh City, Vietnam

Email: dtmdung@vnuhcm.edu.vn

ABSTRACT

The anesthetic property of clove basil essential oil, attributed to its bioactive compounds, was employed in this experiment. Clove basil essential oil was synthesized into the oil-in-water microemulsion with 10% oil content, featuring particle size around 40 nm and a low polydispersity index (less than 0.5). Effective anesthesia in fish was achieved at concentrations of 100 ppm and higher. This suggests the promising potential of using clove basil essential oil formed in microemulsion as an anesthetic agent in aquaculture.

Keywords: microemulsion, clove basil, *H. wyckioides*, anesthetic, essential oil.

INTRODUCTION

Currently, herbal essential oils have garnered significant attention for their diverse biologically active compounds. In aquaculture, these natural extracts are also used as a safe and practical alternative to synthetic pharmaceuticals [1]. *Ocimum gratissimum* (clove basil) is one of the most popular herbs and thrives in tropical climates such as Brazil, India, Vietnam and so on [2]. The clove basil essential oil has a significant eugenol content [3], ranging from 40% to 70% [4], which has an anesthetic and stress-reducing effect [5]. Some previous research indicated that the essential oil of clove basil had an anesthetic ability on some fish species such as *Ictalurus punctatus* (silver catfish) [6] *Pseudoplatystoma reticulatum* (American catfish) [7]. Nevertheless, clove basil essential oil shares common drawbacks with other plant essential oils, including high volatility, hydrophobicity, susceptibility to oxidation, low stability, and an unclear mode of action, which have limited their broad practical application. To overcome these limitations, a suitable approach is to synthesize essential oil in microemulsion. Microemulsions are stable and transparent systems, which help to enhance water solubility and mask strong aromas of essential oil [8].

In this study, clove basil essential oil was synthesized into an oil-in-water microemulsion. Subsequently, this microemulsion underwent testing on *Hemibagrus wyckioides* (Asian red tail catfish), a highly prized and economically significant fish species, to assess its anesthetic

effect. It forms the foundation for the development of herbal-based anesthetics.

EXPERIMENTAL

Preparing clove basil essential oil microemulsion

In the experiment, clove basil essential oil underwent chemical composition analysis using the gas chromatography-mass spectrometer (GC-MS) method. Tween 20 and propylene glycol from Sigma-Aldrich were employed as the surfactant and co-surfactant for microemulsion preparation. Various surfactant-to-co-surfactant ratios (1:1, 2:1, and 3:1) and essential oil-to-surfactant ratios (1:9, 2:8, 3:7, 4:6, 5:5, 6:4, 7:3, 8:2, 9:1) were tested. The process involved magnetic stirring at 700 rpm for 30 minutes at room temperature, before gradual water addition. Microemulsion formation was confirmed if the solution appeared transparent. The formed microemulsions were evaluated in some characteristics, particularly: the droplet sizes and polydispersity index (PDI) were determined by the LB-550 Dynamic Light Scattering (DLS) system, the electrical conductivity was determined by the Hemera system, and zeta potential was analyzed with the ZetaPhoremeter-CAD. The turbidity was determined by UV-Vis at the wavelength of 502 nm. The stability of the microemulsion was assessed through a centrifugation test at 4000 rpm for 15 minutes, comparing turbidity before and after centrifugation.

Assessing the anesthetic effectiveness of clove basil essential oil microemulsion in fish

The test subjects were Asian red tail catfish (*Hemibagrus wyckioides*), weighing 3.40 ± 0.22 g and measuring 8.00 ± 1.00 cm in length. In 5 L water tanks, the clove basil essential oil microemulsion (10% essential oil, w/w) was added at concentrations of 0 (control), 50, 100, and 200 ppm. Fish stocking (10 fish/tank) occurred once the microemulsion dispersed uniformly in water. Observations were recorded during three stages: stage 1, from stocking fish until fish exhibited slowed and lethargic activity; stage 2, from when fish became lethargic until they partially or completely lost balance; stage 3, from complete loss of balance until fish regained normal activity, with a maximum observation time of 30 minutes. After 30 minutes of anesthesia, fish were placed in clean water tanks, and the time taken for complete recovery (normal swimming and responsiveness) was recorded. Each treatment was repeated three times. An additional treatment using tween 20 and propylene glycol mixture, equivalent to the highest microemulsion concentration testing, was included to assess the influence of surfactant on the anesthetic effect of the clove basil essential oil microemulsion.

RESULTS AND DISCUSSION

Preparation of clove basil essential oil microemulsion

The GC-MS analysis revealed that the clove basil essential oil utilized in this experiment primarily consisted of eugenol (46.8%), followed by β -caryophyllene (31.8%), α -caryophyllene (7.1%), methyl eugenol (5.1%), α -pinene (2.7%), and various minor components.

In this experiment, tween 20 and propylene glycol served as a surfactant and co-surfactant to create the microemulsion. Microemulsion formation was observed with essential oil-to-surfactant ratios of 1:9 and 2:8 at various water ratios. However, at a 3:7 ratio, no microemulsion formed when water exceeded 50% (w/w), and the formation of microemulsion became more limited in the subsequent oil-to-surfactant ratios. Furthermore, among various surfactant-to-co-surfactant ratios, the 1:1 ratio yielded the smallest microemulsion formation area, while the 2:1 and 3:1 ratios produced relatively larger microemulsions with similar formation areas. To synthesize an oil-in-water microemulsion, a formulation was selected based on tests involving

particle size, polydispersity index (PDI), electrical conductivity, zeta potential, and turbidity. This formulation consisted of a 10% essential oil ratio and a 40% mixture of 2:1 surfactant to co-surfactant ratio. The resulting microemulsion appeared pale yellow, transparent liquid, and exhibited uniform properties with a mean particle size of 40 nm and a PDI of 0.22. Detailed characteristics of this microemulsion can be found in Table 1 and Figure 1.

Table 1. The characteristics of the clove basil essential oil microemulsion

Characteristics	Value
Droplet size (nm)	40.78 ± 2.20
PDI	0.22 ± 0.04
Electrical conductivity ($\mu\text{S}/\text{cm}$)	111.07 ± 0.1
Zeta potential (mV)	13.19 ± 0.61

(Note: Mean \pm SD)

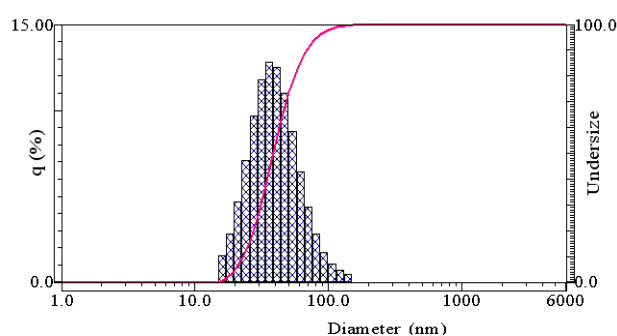


Figure 1. The particle size distribution of the clove basil essential oil microemulsion

The microemulsion in the selected formulation exhibited an electrical conductivity of approximately $111.07 \mu\text{S}/\text{cm}$, confirming its classification as an oil-in-water microemulsion. Conductivity is a key factor in distinguishing microemulsion types, with water-in-oil microemulsions typically having low conductivity due to the absence of water in the continuous phase, while oil-in-water microemulsions tend to show high conductivity [9]. Additionally, the microemulsion displayed a PDI value of 0.22. Furthermore, centrifugation at 4000 rpm for 15 minutes showed the microemulsion remaining transparent and no phase separation. The turbidity changed by 0.07% when comparing before and after centrifugation but remained below 1%, indicating its stability.

Assessing the anesthetic efficiency of the clove basil essential oil microemulsion in Asian red tail catfish

Table 2. The anesthetic and recovery time of fish when exposed to the clove basil essential oil microemulsion at different concentrations

The different stages of anesthetizing fish (minutes)	Experimental concentrations		
	50 ppm	100 ppm	200 ppm
Stage 1	4.67±1.16 ^a	3.67±1.16 ^a	1.00±0.00 ^b
Stage 2	15.00 ± 1.73 ^a	7.67±1.53 ^b	3.67±0.58 ^c
Stage 3		5.00 ±1.73 ^b	22.67±0.58 ^a
Recovery stage	3.67 ± 1.53 ^a	2.67±0.58 ^a	4.33±0.58 ^a

(Note: Mean ± SD, the superscript letters following the values in the same row are similar, indicating that the difference is not significant, $p > 0.05$).

The results of evaluating the anesthetic activity of clove basil essential oil microemulsion on Asian red tail catfish are shown in Table 2. The findings revealed that the tested clove basil essential oil microemulsions at concentrations of 100 ppm and higher effectively induced fish anesthesia. Nevertheless, the anesthetic effect varied at each concentration. At 50 ppm, the fish displayed initial signs of slow movement after 4.6 minutes. Over the following 15 minutes, their activity decreased without losing balance. Subsequently, the fish rapidly regained full activity and returned to their normal state within 3.6 minutes after being transferred to clean water. At 100 ppm, fish displayed initial sluggishness within 3-4 minutes of exposure to the microemulsion. Over the next seven minutes, they began to lose complete balance, which lasted and returned to more activity for approximately 5 minutes. Recovery in clean water took approximately 3 minutes.

At 200 ppm, fish became susceptible (swimming slowly and lethargic) within 1 minute of exposure to the microemulsion-mixed water. They started losing balance and became inactive after 3.67 minutes. Fish remained anesthetized (initially lying upside down and inactive, then gradually becoming active but still slow, lethargic, and slow to react to external stimulation) for approximately 22.67 minutes. Recovery time in clean water was about 4 minutes. Thus, the higher the concentration, the anesthetic effect was longer than at low concentrations.

In the control treatment and the treatment containing tween 20 and propylene glycol at a concentration equivalent to the concentration of

these two substances in the 200 ppm clove basil essential oil microemulsion, the fish still behaved normally during the testing progress. It was shown that tween 20 and propylene glycol at the tested concentrations did not affect the anesthetic performance of the clove basil essential oil microemulsion and were not harmful to the test subjects.

Clove basil essential oil, mainly eugenol, is recognized for its anesthetic effect. Previous studies have highlighted the anesthetic properties of eugenol and essential oils rich in eugenol [10]. Furthermore, linalool, α -pinene, and β -caryophyllene exhibit fish anesthetic properties. These compounds are responsible for the anesthetic effect of clove basil essential oil on various fish species. For example, they have proven effective on silver catfish (*Rhamdia quelen*) at concentrations of 30-300 mg/L [11] and tambaqui (*Colossoma macropomum*) at concentrations of 15-300 mg/L [12]. However, factors like species, fish age, weight, environmental conditions, and other variables can lead to variations in anesthetic concentration and induction times. Eugenol has a similar structure to isoeugenol, which has an anesthetic effect based on the mechanism of blocking Na^+ , K^+ and Ca^{2+} ion channels, inhibiting N-methyl D-aspartate (NMDA) receptors and enhancing GABA-A receptors. This affects the response of fish to external stimulation [13].

The findings revealed that the clove basil essential oil in microemulsion form exhibited anesthetic property in Asian red tail catfish. The anesthetic performance, including the level and duration of anesthesia, varied with different microemulsion concentrations. Generally, higher

concentrations resulted in longer times for both inducing and maintaining anesthesia.

CONCLUSION

In this experiment, clove basil essential oil microemulsion was synthesized as an oil-in-water type with a particle size of 40 nm and a PDI value of 0.22. The microemulsion exhibited anesthetic effect on Asian red tail catfish (weight of 3.40 ± 0.22 g and 8.00 ± 1.00 cm in length) at concentrations of 100 ppm and higher. Higher concentrations resulted in longer anesthetic duration, with recovery times in clear water ranging from 3 - 4 minutes. While further experiments are required for a more accurate assessment, the results indicate the potential use of clove basil essential oil, and plant essential oils in general, in aquaculture by addressing some of the limitations associated with essential oils through microemulsion synthesis.

Acknowledgment

This research is funded by Vietnam National University Ho Chi Minh City (VNU-HCM) under grant number 562-2022-32-01.

References

- [1] P. Bolouri *et al.*, *Applications of Essential Oils and Plant Extracts in Different Industries*, *Molecules*, **27**(24) (2022) 8999.
- [2] O. C. Ugbogu *et al.*, A review on the traditional uses, phytochemistry, and pharmacological activities of clove basil (*Ocimum gratissimum* L.), *Heliyon*, **7**(11) (2011) e08404.
- [3] S. M. Hoseini, A. Taheri Mirghaed, and M. Yousefi, *Application of herbal anaesthetics in aquaculture*, *Rev Aquac*, **11**(3) (2019) 550-564.
- [4] R. S. Melo *et al.*, *Chemical Composition and Antimicrobial Effectiveness of Ocimum gratissimum L. Essential Oil Against Multidrug-Resistant Isolates of Staphylococcus aureus and Escherichia coli*, *Molecules*, **24**(21) (2019) 3864.
- [5] R. Tarkhani, A. Imani, H. Jamali, and K. Sarvi Moghanlou, *Anaesthetic efficacy of eugenol on Flowerhorn (Amphilophus labiatus × Amphilophus trimaculatus)*, *Aquac Res*, **48**(6) (2017) 3207-3215.
- [6] I. W. R. Swastika Braja, I. D. G. Mayun Permana, and L. Suhendra, *Formulation and Stability of Clove Leaf (Syzygium aromaticum L.) Essential Oil Microemulsion*, *Int J Curr Microbiol Appl Sci*, **11**(9) (2022) 197-211.
- [7] Y. Li *et al.*, *Enhanced Antioxidant and Antiproliferative Activities of Cymbopogon citratus (DC.) Stapf Essential Oils in Microemulsion*, *ACS Sustain Chem Eng*, **7**(18) (2019) 15173-15181.
- [8] L. Pavoni, D. R. Perinelli, G. Bonacucina, M. Cespi, and G. F. Palmieri, *An Overview of Micro- and Nanoemulsions as Vehicles for Essential Oils: Formulation, Preparation and Stability*, *Nanomaterials*, **10**(1) (2020) 135.
- [9] S. Yotsawimonwat, S. Okonoki, K. Krauel, J. Sirithunyalug, B. Sirithunyalug, and T. Rades, *Characterisation of microemulsions containing orange oil with water and propylene glycol as hydrophilic components.*, *Pharmazie*, **61**(11) (2006) 920-6.
- [10] S. M. Hoseini, A. Taheri Mirghaed, and M. Yousefi, *Application of herbal anaesthetics in aquaculture*, *Rev Aquac*, **11**(3) (2019) 550-564.
- [11] L. de L. Silva *et al.*, *Essential oil of Ocimum gratissimum L.: Anesthetic effects, mechanism of action and tolerance in silver catfish, Rhamdia quelen*, *Aquaculture*, **350-353** (2012) 91-97.
- [12] C. de Lima Bojink, C. A. Queiroz, E. C. Chagas, F. C. M. Chaves, and L. A. K. A. Inoue, *Anesthetic and anthelmintic effects of clove basil (Ocimum gratissimum) essential oil for tambaqui (Colossoma macropomum)*, *Aquaculture*, **457**, (2016) 24-28.
- [13] S. H. Hoseinifar, Y.-Z. Sun, Z. Zhou, H. Van Doan, S. J. Davies, and R. Harikrishnan, *Boosting Immune Function and Disease Bio-Control Through Environment-Friendly and Sustainable Approaches in Finfish Aquaculture: Herbal Therapy Scenarios*, *Reviews in Fisheries Science & Aquaculture*, **28**(3) (2020) 303-321.

DYE-SENSITIZED SOLAR CELLS WITH Z907 DYE AND ECO-FRIENDLY EUTECTIC ELECTROLYTE BASED ON UREA-ACETAMIDE MIXTURE: PHOTOVOLTAIC PERFORMANCE AND STABILITY COMPARISON WITH POPULAR IONIC LIQUID ELECTROLYTE

Ha-Phuong Thi Ngo^{1,2#}, Anh-Tho Ngoc Vo^{1,2#}, De Nguyen^{1,2}, Hoang-Em Danh^{1,2}, My-Duyen Thi Duong^{1,2}, Thuy Thanh Doan Nguyen^{1,2}, Phuong Tuyet Nguyen^{1,2,3*}

¹Faculty of Chemistry, University of Science, Ho Chi Minh City, Vietnam

²Vietnam National University Ho Chi Minh City, Vietnam

³Faculty of Interdisciplinary Science, University of Science, Ho Chi Minh City, Vietnam

Same contribution as the first authors

Email: ntphuong@hcmus.edu.vn

ABSTRACT

Electrolyte plays a crucial role in dye-sensitized solar cells' performance and long-term stability. To minimize the use of hazardous and volatile chemicals but DSCs still remains good performance and stability, this study developed novel eco-friendly eutectic electrolytes using urea and acetamide as additives without adding any solvents. The DSC devices with new eutectic electrolytes achieved higher photovoltaic performance with the most popular commercial ionic liquid electrolytes, yet at a significantly low-cost. For more details, the influence of eutectic components on the DSC devices' performance was discussed by J-V and electrochemical impedance analysis. The results allow us to target such potential eutectic electrolytes for commercialization.

Keywords: Dye-sensitized solar cell; electrolyte; urea; acetamide; deep eutectic solvent

INTRODUCTION

Dye-sensitized solar cells (DSCs) were initiated by O'Regan and Grätzel in 1991, which are well-known for being more cost-effective than silicon solar cells and simple fabrication process [1]. Dye-sensitized solar cells included three essential components: a monolayer dye sensitizer anchoring on the mesoporous surface of TiO₂ photo-anode, a counter electrode with a platinum-coated conductive glass substrate, and an electrolyte between two electrodes containing a redox couple, typically I⁻/I₃⁻, additives and solvents [2].

Among three critical components, the electrolyte plays a vital role in conversation effectively from light to electricity and stability of DSCs devices. The electrolyte dramatically affects four parameters that determine effective DSCs, namely short circuit current density (J_{SC}), open circuit voltage (V_{OC}), fill factor (FF), and efficiency (η) [3]. Typically, the organic solvents e.g. acetonitrile (ACN), 3-methoxypropionitrile, valeronitrile, are used in the electrolytes for high solar cell performance and fundamental studies

because of their low viscosity, good solubility [3]. However, the significant drawbacks are that the nitrile solvents have low boiling points and easy evaporation by heat stress [4]. The electrolyte evaporation and seepage make DSCs unsuitable for long-term photostability [5]. Additionally, nitrile solvents were reported to intermediate thermal degradation of Ruthenium dyes through substituted reactions of thiocyanate groups [6], [7]. Hence many studies have not employed the liquid electrolytes using nitrile solvents but ionic liquid for long-term stability purposes.

Ionic liquid has been intensively investigated as an alternative electrolyte for DSCs with its quantities, namely good chemical and thermal stability, negligible vapor pressure, nonflammability, and high ionic conductivity [8]. However, ionic liquid electrolytes are still faced with challenges, including too much viscosity causing low ionic diffusion, which leads to the diminished conversion efficiency of the devices; high cost, and low purity; the electrolyte waste has demerits on the environment and human health [9]. To reduce these problems, in recent years, the

deep eutectic solvent (DES) was investigated as a new kind of ionic liquid because it witnessed many characteristics and properties as an ionic liquid [10]. The form of DES typically includes at least one hydrogen bond donor strongly associated with a hydrogen bond acceptor via hydrogen bond interactions, and hence the melting point of the DES compound is much lower than original components [11]. The deep eutectic solvent is a potential candidate for the electrolytes in DSCs with its own merits, such as green solvents, biodegradable, high thermal stability, low vapor pressure, and inexpensive and straightforward fabrication [12]. In the case of DSCs, DES has been applied as an additive or a solvent in the electrolyte [13]-[15]. Some DES have been used in DSCs such as choline chloride or choline iodide mixed with ethanol; phenol [13]; glycerol [16]; ethylene glycol [14]; or with urea [9],[14];... Among those, choline chloride with urea showed impressive results, which was very competitive to the commercial ionic liquid EMITCB, due to its shielding effects on TiO₂ surface, turning out that it could be utilized to DSCs electrolyte not only as a solvent but also as an effective additive. The additive is added to the electrolyte to enhance the DSCs performance by increasing the V_{OC} [14] and reducing the back electron loss in DSCs. [17] But the most popular additive – 4-*tert*-butylpyridine (4-TBP) is highly toxic, volatile and degrades Ruthenium dyes at elevated temperature, thus we targeted to replace 4-TBP by urea.

However, using urea could help to improve the V_{OC} but not the J_{SC} . To overcome this limit, our recent study showed that acetamide, also an eco-friendly additive could increase V_{OC} , and more apparently J_{SC} , thanks to its capacity to aid through the efficient diffusion of the redox couples in the electrolyte [15]. So, our hypothesis is that combination of urea and acetamide in the electrolyte can enhance the DSCs photovoltaic performance. On the other hand, we consider DSCs long term stability, so urea and acetamide should be mixed in ionic liquid electrolytes so-called “robust” electrolyte. To minimize the drawbacks of the popular ionic liquids *e.g.* high cost, low purity, difficult synthesize, *ect.*, we aim to produce the electrolyte mixture from the original components including iodine, iodide substance, urea, acetamide without any addition of liquid or ionic liquid solvents. The solid 1-ethyl-3-methylimidazolium iodide (EMII) is normally used as I⁻ resource in the electrolyte, together with

I₂ to form a redox couple. These solid compounds should be in liquid phase to have high ionic conductivity for electrolyte use.

Therefore, in this study, we developed an eutectic electrolyte based on EMII, iodine, urea, and acetamide as a novel eco-friendly electrolyte for DSCs device, in comparison with prevalent ionic liquid electrolyte using the additives 4-TBP, GuSCN, and 1-ethyl-3-methylimidazolium tetracyanoborate (EMITCB) solvent. By varying the ratio of urea and acetamide, we successfully synthesize the electrolyte in liquid phase at low temperature without any solvents. The electrolyte mixtures were implemented to DSCs devices which were characterized photovoltaic performance and long-term test by current density–voltage (J–V) curve measurement and electrochemical impedance spectroscopy (EIS).

EXPERIMENTAL

Preparation and characterization of eutectic electrolytes

All pure components, including EMII, I₂, urea, acetamide purchased from Sigma Aldrich, were vacuum-dried before use. The eutectic electrolyte mixtures comprising of EMII, iodine, urea, or/and acetamide, were prepared in vials with the appropriate molar ratio. The eutectic system was denoted by the molar ratio between EMII: Urea: I₂, which is 2:1:0.03, referred to as "E-U," and EMII: Acetamide: I₂, which is 2:1:0.03, referred to as "E-A." For electrolyte solutions containing both of urea and acetamide, they are designated based on the molar ratio between urea and acetamide in the mixture. For example, E-UA9:1 corresponds to an eutectic electrolyte solution with the EMII: Urea: Acetamide: I₂ ratio of 2: 0.9: 0.1: 0.03, and similarly for other ratios.

The ionic liquid electrolyte comprising 1 M EMII, 0.2 M I₂, 0.1 M GuSCN, and 0.5 M 4-TBP dissolved in EMITCB solvent, named iL-4-TBP, along with the electrolyte solution containing the same concentrations of EMII, I₂, EMITCB without any additives, named iL-No, were prepared as the control samples to be compared with the eutectic ones.

Characterization

The thermal properties of the electrolyte mixtures were investigated using a differential scanning calorimeter. The samples were measured over a temperature range of -30 °C to 100 °C at a rate of 10 K.min⁻¹ under a nitrogen atmosphere.

The samples were measured in the wavenumber range of 450 cm^{-1} to 4000 cm^{-1} using a Fourier FT/IR - 6600 instrument from JASCO, Japan.

DSC device fabrication and characterization

The cells were fabricated following the procedure reported elsewhere [14], [15]. Eutectic electrolytes were injected into the cells in comparison to the iL-No and iL-4-TBP ones.

DSC device characterization

The DSC devices were characterized by J – V curves measured under simulated sunlight with an irradiance of $1000\text{ W}\cdot\text{m}^{-2}$ - AM 1.5 using a Versa-STAT3 electrochemical workstation.

RESULTS AND DISCUSSION

Characterization of DES electrolytes

Melting temperature

After mixing the pure solid substances, a mixture of electrolyte solutions with much lower melting temperatures than the theoretical melting point of each constituent is obtained (Figure 1). These electrolyte solutions can exist in a liquid state within a low-temperature range of $24.7\text{ }^{\circ}\text{C}$ to $36.8\text{ }^{\circ}\text{C}$.

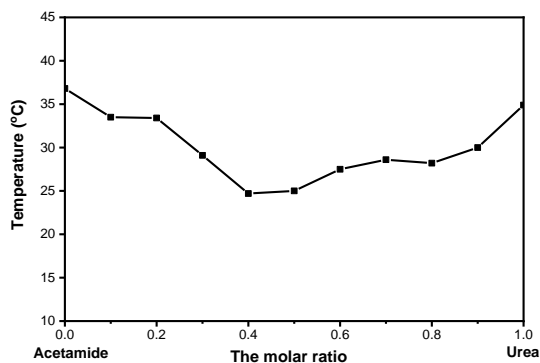


Figure 1. Melting temperature of electrolyte solutions as a function of urea and acetamide concentrations.

Figure 1 illustrates that when the ratio between urea and acetamide in the electrolyte solution is 0.4:0.6 or 0.5:0.5 (corresponding to the electrolyte solution E-UA4:6 or E-UA5:5), the mixture has the lowest melting temperature within the system of electrolyte solutions under investigation, suggesting a eutectic point for the mixture at about $24.7 - 25\text{ }^{\circ}\text{C}$. This ratio results in the lowest possible melting temperature, likely due to a stronger hydrogen bonding environment compared to the other ratios.

The IR spectra of pure EMII, urea, acetamide, and the mixed eutectic electrolytes are depicted in

Figure 2. The IR spectrum of pure EMII reveals characteristic vibrational signals at 1573 cm^{-1} corresponding to the C=N group, 2985 cm^{-1} for C-H (sp^3) stretching, and a range of vibrations between $3089 - 3143\text{ cm}^{-1}$ attributed to C-H (sp^2) bonds. The IR spectrum of pure urea exhibits two stretching vibrations at 3440 cm^{-1} and 3359 cm^{-1} corresponding to the primary amide group's N-H (NH_2) stretching, a deformation vibration at 1614 cm^{-1} of N-H; C=O stretching at 1624 cm^{-1} , and C-N group vibrations at 1461 cm^{-1} . The IR spectrum of pure acetamide shows N-H group stretching vibrations at 3405 cm^{-1} and 1614 cm^{-1} , C-N bond vibrations at 1392 cm^{-1} , C=O stretching at 1662 cm^{-1} , and CH (sp^3) vibrations in the 3000 cm^{-1} region.

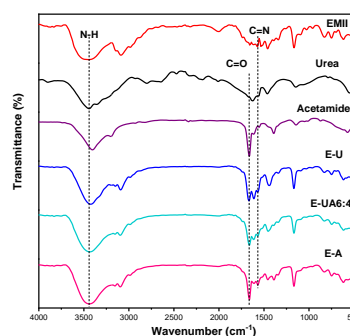


Figure 2. FT-IR spectra of pure EMII, urea, acetamide, and the mixed eutectic electrolyte solutions using only urea (E-U) or acetamide (E-A) and DES between urea and acetamide with the molar ratio of 6:4 (E-UA6:4).

After the formation of the eutectic electrolyte solution, the FTIR spectrum of the electrolyte solution replicates the characteristic signals of the pure EMII, urea, and/or acetamide molecules, indicating that the molecular structure of these constituents remains intact and unaltered, without any destruction. When comparing the spectra of the electrolyte solutions to the spectra of pure EMII, urea, and acetamide, a notable shift towards lower wavenumbers is observed, signifying the formation of intermolecular hydrogen bonds between the original components. Observation of FT-IR spectrum of the electrolyte solution containing both urea and acetamide represented by E-UA6:4 in Figure 2 illustrates N-H stretching at 3445 cm^{-1} of E-UA6:4 is shifted to higher wavenumbers compared to this signal of pure urea or electrolyte containing only urea (E-U). Moreover, the infrared region at around $1500\text{ cm}^{-1} - 1700\text{ cm}^{-1}$ of E-UA6:4 also exhibited three characteristic peaks corresponding to C=N group

of EMII, as well as with the C=O group of acetamide, but these are shifted absorption band positions and intensity peaks. Therefore, this could demonstrate that formation of chemical interaction or intermolecular hydrogen bonds formed between the H of the NH₂ group in urea and the C=N group of EMII, as well as with the C=O group of acetamide.

DSCs devices

All the electrolytes containing urea demonstrated higher open-circuit voltages (V_{oc}) compared to the cell using the standard 4-TBP and GuSCN electrolyte (Figure 3). The open-circuit voltage tended to decrease as the urea content in the system decreased (indicating an increase in acetamide content). The cell with the highest open-circuit voltage was E-U (707 ± 4 mV), while the cell with the lowest open-circuit voltage among the eutectic multi-component electrolyte solutions was E-A (665 ± 7 mV).

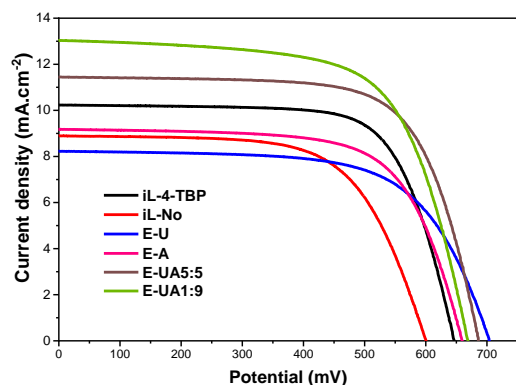


Figure 3. Characteristic J-V curves of different DES electrolytes.

From the J-V curves, it is evident that the short-circuit current (J_{sc}) of the electrolyte system under investigation increases as the acetamide content in the electrolyte solution rises (indicating a decrease in urea content). Specifically, cell E-UA1:9 (12.27 ± 0.37) exhibited a short-circuit current value that was 1.74 mA.cm^{-2} higher compared to the cell using the standard electrolyte solution (10.53 ± 0.10).

CONCLUSION

In the studied electrolyte solutions, the addition of urea to the electrolyte mixture increased V_{oc} and inhibited the recombination reaction between the electrons on TiO₂ and the electrolyte of the DSCs. However, when the urea content was high, J_{sc} decreased compared to the cell without additives in the electrolyte.

The addition of acetamide to the electrolyte mixture increased the current density and ion conductivity of the DSCs. Although its ability to limit recombination between electrons on the TiO₂ surface and the electrolyte was not as good as urea and the additive TBP + GuSCN, acetamide still helped to limit the electron recombination better than the DSCs without additives. However, a high acetamide content would lead to a decrease in the photoconversion efficiency.

Among all the eutectic electrolytes, E-UA5:5 yielded the best results. At a mole ratio of 5:5 between urea and acetamide in the mixture, it achieved the lowest melting temperature (25 °C), the highest ion conductivity, and the best photoelectrochemical parameters, comparable to the standard cell.

Acknowledgment

This research is funded by Vietnam National University, Ho Chi Minh City (VNUHCM) under grant number B2023-18-06

References

- [1] B. O'regan and M. Grätzel, *Nature*, vol. 353, no. 6346, pp. 737–740, 1991.
- [2] J. Gong, et.al, *Renew. Sustain. Energy Rev.*, vol. 68, pp. 234–246, Feb. 2017.
- [3] J. Wu et al., *Chem. Rev.*, vol. 115, no. 5, pp. 2136–2173, 2015.
- [4] R. A. A. Talip, et.al, *Sustain.*, vol. 12, no. 18, 2020.
- [5] R. Harikisun and H. Desilvestro, *Sol. Energy*, vol. 85, no. 6, pp. 1179–1188, 2011.
- [6] P. Tuyet Nguyen, et.al, *Sol. Energy Mater. Sol. Cells*, vol. 93, no. 11, pp. 1939–1945, 2009.
- [7] P. Tuyet Nguyen, et.al, *Sol. Energy Mater. Sol. Cells*, vol. 94, no. 10, pp. 1582–1590, 2010.
- [8] P. Wang, et.al, *J. Phys. Chem. B*, vol. 107, no. 48, pp. 13280–13285, 2003.
- [9] D. Nguyen et al., *RSC Adv.*, vol. 11, no. 35, pp. 21560–21566, 2021.
- [10] E. L. Smith, A. P. Abbott, and K. S. Ryder, *Chem. Rev.*, vol. 114, no. 21, pp. 11060–11082, 2014.
- [11] F. M. Perna, et.al, *Curr. Opin. Green Sustain. Chem.*, vol. 21, pp. 27–33, 2020.
- [12] M. Heydari Dokoohaki, et.al, *J. Phys. Chem. C*, vol. 125, no. 28, pp. 15155–15165, 2021.
- [13] P. T. Nguyen et al., *J. Mol. Liq.*, vol. 277, pp. 157–162, 2019.

- [14] D. Nguyen et al., RSC Adv., vol. 11, no. 35, pp. 21560–21566, 2021.
- [15] D. Nguyen, et.al, J. Aust. Ceram. Soc., 2023.
- [16] H.-R. Jhong, et.al, Electrochem. commun., vol. 11, no. 1, pp. 209–211, 2009.
- [17] D. Nguyen, et.al., J. Aust. Ceram. Soc., vol. 58, no. 3, pp. 913–921, 2022.

IMPACT OF ELECTROLYTES ON PROPERTIES OF GRAPHENE OXIDE EXFOLIATED BY ELECTROCHEMICAL METHOD

Huy-Binh Do^{1*}, Dong-Nghi Le¹, Tien-Luat Nguyen¹, Phuong V Pham², Tuan-Huu Nguyen¹, Thuy-Hong-Lam Ngo¹, Anh-Vu Phan-Gia¹

¹ Department of Materials Technology, Faculty of Applied Sciences, Ho Chi Minh City University of Technology and Education, Vietnam

² Department of Physics, National Sun Yat-sen University, Kaohsiung 80424, Taiwan

*Email: binhdh@hcmute.edu.vn

ABSTRACT

In this study, we utilized graphite extracted from discarded Zn-batteries to produce graphene oxide (GO) through electrochemical exfoliation. We examined the influence of different electrolytes on the exfoliation process. Our findings revealed that the optimal I_D/I_G value in Raman spectra was 5% for NaOH and 2.5% for KOH. Scanning electron microscopy (SEM) images confirmed the formation of multi-wall GO in the exfoliated samples. X-ray diffraction (XRD) spectra also supported our results, showing a broadening of the peak at $2\theta = 26.5^\circ$. This study provides a systematic investigation into the reutilization of graphite rods to fabricate GO, thereby contributing to environmental conservation by reducing industrial waste.

Keywords: graphene oxide, electrochemical exfoliation, electrolyte solution, battery recycling

INTRODUCTION

In recent years, there has been a notable increase in battery consumption due to the arrival of the technological age. As a consequence, used batteries have become a hazardous form of waste, directly impacting the environment. Proper disposal of these batteries has become an urgent matter due to the unique chemical components found in each type [1]. Notably, graphite rods within Zinc-carbon batteries can serve as potential sources for recycling graphite. Therefore, the recycling of graphite rods from disposed batteries is crucial, aiming to reuse graphite in batteries, reduce pollution, and enable the production of graphene oxide (GO). Graphene oxide was initially synthesized through the process of oxidizing and exfoliating naturally crystalline graphite [2]. GO has 2D structure as graphene, however, layers of carbon are covalently bonded to oxygen-containing groups such as hydroxyl, epoxide, carbonyl, etc [3]. These functional groups are present both on the basal plane and at the edges, and they are introduced during the chemical exfoliation process of graphite flakes. The presence of these functional groups in GO enables easy processing and provides it with high colloidal stability in water, giving rise to a distinctive range of mechanical, colloidal, and optical properties [4]. The properties of GO can be enhanced using

chemical engineering techniques, resulting in a wide range of applications such as solar cells [5], sensors [6], supercapacitors [7], cellular migration [8], drug delivery [9], membranes [10], multifunctional gels [11], water purification [12].

In this study, graphene oxide is fabricated using the electrochemical exfoliation of graphite rods obtained from disposed Zinc-batteries. The effects of electrolyte concentrations on properties of exfoliated GO are investigated. The GO fabricated was thoroughly analyzed in terms of its morphology, structure, and crystalline properties, using scanning electron microscopy (SEM), and X-Ray diffraction analysis (XRD).

EXPERIMENTAL

The electrolytic solution used in this study was created by dissolving KOH in 200 ml of water and $(\text{NH}_4)_2\text{SO}_4$ in 40 ml of water. The KOH and $(\text{NH}_4)_2\text{SO}_4$ solutions were prepared individually, then combined and stirred for 10 minutes. The anode and cathode were obtained from graphite rods with a diameter of 6 mm (Pinaco, the eagle brand). The tip of the cathode was ground to approximately 200 μm in diameter. Prior to the experiment, all electrodes underwent a cleaning process using acetone and isopropanol (IPA), followed by annealing at 130°C for 24 hours. The experimental setup involved an electrochemical chamber, as showed in Figure

1(a), where a specially designed cap allowed for unrestricted movement of the cathode. To begin the experiment, all electrodes were linked to a DC power supply, and the bias voltage was gradually raised up to 60 V. Hitachi FE-SEM S-4800 was utilized to obtain scanning electron microscope (SEM) images.

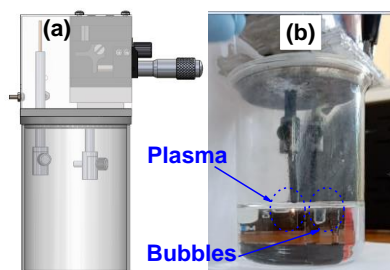


Figure 1. (a) The electrochemical cell was illustrated schematically. (b) Observations revealed that plasma generation occurred specifically at the cathode, while bubbles were observed exclusively at the anode within the electrolyte solution.

RESULTS AND DISCUSSION

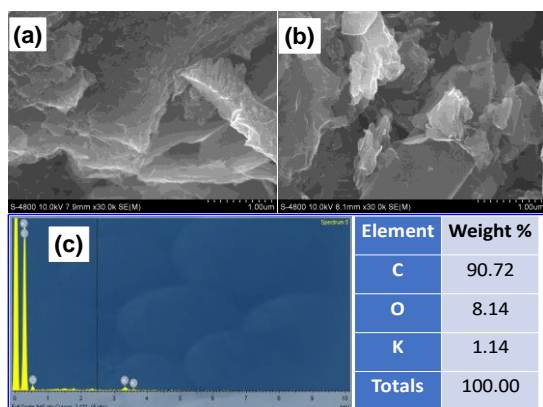


Figure 2. The scanning electron microscope (SEM) images depict (a) graphite and (b) graphene oxide (GO) obtained using the plasma-assisted exfoliation method with 2.5%. (c) The Energy-Dispersive X-ray Spectroscopy (EDS) spectrum of GO after the filtration process.

Fig. 2 displays electron microscope images obtained from a field emission scanning electron microscope (FESEM). The images compare graphite powder, which was directly obtained by grinding a graphite rod, with exfoliated graphene oxide collected after filtration. In Fig. 2(a), the graphite powder exhibits a stacked layer structure, indicating the presence of multiple layers. On the other hand, Fig. 2(b) shows the

result of plasma-assisted electrochemical exfoliation, where randomly crumpled nano-sheets are formed. Figure 2(c) presents an investigation of the purification of exfoliated graphene oxide (GO) through an Energy-Dispersive X-ray (EDX) spectrum analysis.

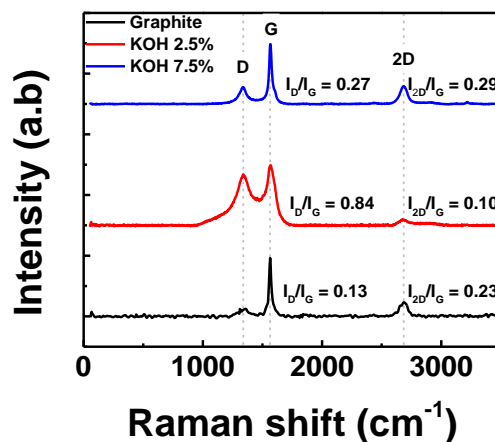


Figure 3. The Raman spectra of graphite powder (black line) and graphene oxide (red and blue lines).

Raman spectra of graphite and GO in Fig. 3 illustrates structural changes during the chemical conversion from graphite to graphene oxide. It is well-known that C=C bonds exhibit high Raman intensities [13]. In the case of graphite spectra (represented by the black line), the peak with the highest intensity occurs at 1568.8 cm^{-1} , corresponding to its G bands. This peak results from the first-order scattering of the E_{2g} phonon of sp^2 carbon atoms [14]. The G band is observed in all sp^2 carbon materials, including graphite, amorphous carbon, carbon nanotubes, and graphene. Additional weak bands are associated with the D band at 1342.3 cm^{-1} and the 2D band at 2682.3 cm^{-1} . The D band is known as a defect band and arises from edge effects, structural defects, and the breaking of symmetry in sp^2 bonds. The presence of the 2D peak in the Raman spectra of graphene oxide is attributed to the linear dispersion of its electronic bands, resulting in either triple resonance or double resonance. It is important to note that the Raman spectra of graphene oxide are influenced not only by the phonon properties but also by its electronic structures.

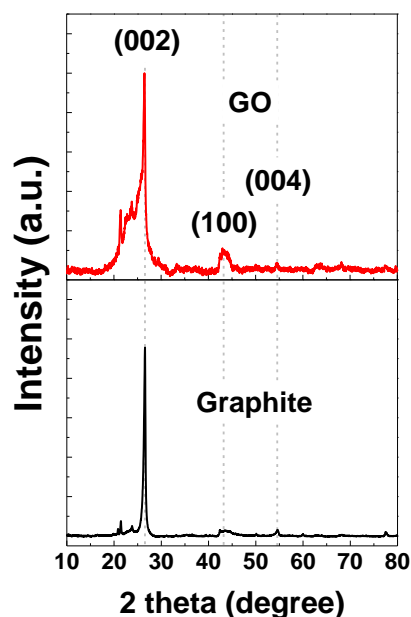


Figure 4. XRD patterns recorded for graphite and graphene oxide obtained from plasma-assisted exfoliation.

The graphite-based material (GF) was analyzed using X-ray diffraction (XRD) in Fig. 4 (black line). A distinct diffraction peak at $2\theta = 26.54^\circ$ was observed, exhibiting a narrow peak width and high intensity. This peak corresponds to the crystal plane (002) of graphite, which possesses a hexagonal structure and an interlayer distance of $d = 0.34$ nm [15]. Additionally, a peak with small intensity at $2\theta = 54.5^\circ$ was detected, corresponding to the crystal plane (004). The (004) peak is weaker as compared to the (002) peak because it is a result of a second-order diffraction [16]. The XRD pattern of the GO sample shows a significant shift and expansion towards lower angles. This broad peak locates from $2\theta = 20.53^\circ$ to approximately $2\theta = 26.65^\circ$, indicating an expanded interlayer distance ranging between 0.33 nm and 0.43 nm. These changes indicate that the graphite is exfoliated to GO during electrochemical exfoliation process. Additionally, a lower intensity peak at $2\theta = 42.60^\circ$ ($d = 0.21$ nm) is observed, corresponding to the (100) peak. This peak can be attributed to the presence of disorder in carbon materials [17, 18]. The appearance of (100) peak is a result of the oxidation of SO^{4-} ions during the exfoliation process at the anode.

CONCLUSION

In conclusion, graphene oxide (GO) was successfully synthesized from disposed zinc batteries. Raman spectra analysis revealed that the

presence of cation K^+ effectively reduced defects on the graphene surface and its edges. X-ray diffraction (XRD) spectra demonstrated a broadening of the (002) peak of carbon. The confirmation of obtained GO was further supported by scanning electron microscopy (SEM) and energy-dispersive X-ray spectroscopy (EDS) analysis. Importantly, no toxic elements were detected in the exfoliated GO, emphasizing the potential of this study in producing cost-effective GO while contributing to environmental protection through the repurposing of discarded batteries.

Acknowledgment

This work was funded by the Ho Chi Minh City University of Technology and Education, Vietnam.

References

- [1] D. Acuti, L. Lemarié, and G. Viglia, *How to enhance the sustainable disposal of harmful products*, *Technological Forecasting and Social Change* **186** (2023) 122151.
- [2] A. Hussain, Y. Weng, and Y. Huang, *Graphene and Graphene-Based Nanomaterials: Current Applications and Future Perspectives*, *Drug Delivery Using Nanomaterials* (2022) 209-228.
- [3] S. Lin, J. Tang, K. Zhang, Y. Chen, R. Gao, H. Yin, and L.-C. Qin, *Tuning oxygen-containing functional groups of graphene for supercapacitors with high stability*, *Nanoscale Advances* **5** (2023) 1163-1171.
- [4] R. Kumar and R. Thangappan, *Electrode material based on reduced graphene oxide (rGO)/transition metal oxide composites for supercapacitor applications: a review*, *Emergent Materials* **5** (2022) 1881-1897.
- [5] M. Kladkaew, J.-Y. Lin, N. Chanlek, V. Vailikhit, and P. Hasin, *Well-Dispersive Polypyrrole and MoSe_2 Embedded in Multiwalled Carbon Nanotube@Reduced Graphene Oxide Nanoribbon Electrocatalysts as the Efficient Counter Electrodes in Rigid and Plastic Dye-Sensitized Solar Cells*, *ACS Applied Energy Materials* **6** (2023) 397-415.
- [6] R. Arreguin-Campos, K. Eersels, R. Rogosic, T. J. Cleij, H. Diliën, and B. van Grinsven, *Imprinted Polydimethylsiloxane-Graphene Oxide Composite Receptor for the Biomimetic Thermal Sensing of *Escherichia coli**, *ACS Sensors* **7** (2022) 1467-1475.

- [7] B. Singh, R. Kaur, R. Kaur, K. Singh, and S. Rana, *A highly stable solid-state supercapacitor device based on robust layer-by-layer electrodeposited poly-(3, 4-ethylenedioxythiophene)-reduced graphene oxide-molybdenum disulfide nanocomposite electrode*, *Journal of Energy Storage* **56** (2022) 105926.
- [8] S. Sun, C. He, C. Li, D. Peng, W. Bai, Y. Zhang, M. He, L. Lv, Y. Dong, P. Ma, Q. Zhou, L. Zhan, and X. Wang, *Graphene oxide-based plasma membrane-philic delivery platform to generate tolerogenic dendritic cells in GVHD immunotherapy*, *Nano Today* **46** (2022) 101578.
- [9] A. Shafiee, S. Iravani, and R. S. Varma, *Graphene and graphene oxide with anticancer applications: Challenges and future perspectives*, *MedComm* **3** (2022) e118.
- [10] J. Ye, C. Zheng, J. Liu, T. Sun, S. Yu, and H. Li, *In Situ Grown Tungsten Trioxide Nanoparticles on Graphene Oxide Nanosheet to Regulate Ion Selectivity of Membrane for High Performance Vanadium Redox Flow Battery*, *Advanced Functional Materials* **32** (2022) 2109427.
- [11] Y. Yan, L. Lu, Y. Li, W. Han, A. Gao, S. Zhao, J. Cui, and G. Zhang, *Robust and Multifunctional 3D Graphene-Based Aerogels Reinforced by Hydroxyapatite Nanowires for Highly Efficient Organic Solvent Adsorption and Fluoride Removal*, *ACS Applied Materials & Interfaces* **14** (2022) 25385-25396.
- [12] H. Qu, X. Xiao, Z. Han, M. Hu, S. Shen, L. Yang, F. Jia, T. Wang, Z. Ye, W. Sun, Y. Wang, L. Huang, Z. Zhu, P. Servati, J. Tang, and J. Chen, *Graphene Oxide Nanofiltration Membrane Based on Three-Dimensional Size-Controllable Metal–Organic Frameworks for Water Treatment*, *ACS Applied Nano Materials* **5** (2022) 5196-5207.
- [13] B. Paulchamy, G. Arthi, and B. Lignesh, *A simple approach to stepwise synthesis of graphene oxide nanomaterial*, *J Nanomed Nanotechnol* **6** (2015) 1.
- [14] N. A. Kumar, H.-J. Choi, Y. R. Shin, D. W. Chang, L. Dai, and J.-B. Baek, *Polyaniline-grafted reduced graphene oxide for efficient electrochemical supercapacitors*, *ACS nano* **6** (2012) 1715-1723.
- [15] M. Salverda, A. R. Thirupathi, F. Pakravan, P. C. Wood, and A. Chen, *Electrochemical exfoliation of graphite to graphene-based nanomaterials*, *Molecules* **27** (2022) 8643.
- [16] N. Cao and Y. Zhang, *Study of reduced graphene oxide preparation by Hummers' method and related characterization*, *Journal of Nanomaterials* **2015** (2015).
- [17] N. Sazali, M. Deraman, R. Omar, M. Othman, M. Suleman, S. Shamsudin, N. Tajuddin, M. Hanappi, E. Hamdan, and N. Nor, *Preparation and structural characterization of turbostratic-carbon/graphene derived from amylose film*, *Proc. the AIP Conference*, 2016.
- [18] V. Thirumal, A. Pandurangan, R. Jayavel, and R. Ilangovan, *Synthesis and characterization of boron doped graphene nanosheets for supercapacitor applications*, *Synthetic Metals* **220** (2016) 524-532.

A TCAD STUDY OF ELECTRICAL PROPERTIES OF GaN/Ga₂O₃ P-N JUNCTION DIODES

Huy-Binh Do^{1*}, Duyen-Thi Nguyen¹, Khanh Nguyen¹, Duc-Minh Truong¹, Hoang-Minh Le², Thanh-Son Nguyen³, and Anh-Vu Phan-Gia¹

¹ Faculty of Applied Sciences, Ho Chi Minh City University of Technology and Education, Vietnam

² Faculty of electrical and electronics engineering, Ho Chi Minh City University of Technology and Education, Vietnam

³ Faculty of Fundamental Sciences, University of Architecture Ho Chi Minh City, Vietnam

*Email: binhdh@hcmute.edu.vn

ABSTRACT

Ga₂O₃ and GaN are promising candidates for the fabrication of high power semiconductor devices due to their wide band-gap range, determined from 3.0 eV to 4.9 eV. Among these materials, the GaN/Ga₂O₃ P-N junction diode has an excellent performance even at high temperatures, making it suitable for high-power applications. In this work, GaN/Ga₂O₃ P-N junction diodes are investigated using computer-aided design (TCAD) simulations. The properties of the diode were optimized in terms of the thickness of the p-type GaN layer and its doping concentration. It was found that the current-voltage (IV) characteristic of the diode decreases as the thickness of GaN layer increases. To achieve a high current output, the optimized thickness is determined to be 500 nm. Furthermore, the doping concentration within the diode strongly influences the output current. The highest current is obtained for an un-doped GaN sample, and the increase in the doping concentration leads to a decrease in the obtained current.

Keywords: GaN, Ga₂O₃, P-N junction diode, band structure of diodes

INTRODUCTION

Beta gallium oxide (β -Ga₂O₃) is a potential wide bandgap semiconductor usable in several applications, including power devices, UV photodetectors, photocatalysts, gas sensors, solar cells, and transparent conducting materials in optoelectronic devices [1, 2]. Ga₂O₃ has gained attention due to its ultra-wide band-gap (4.6 - 4.9 eV), high critical field of 8 MV/cm, high saturation electron velocity of 2×10^7 cm/s, and electron mobility of 200 cm²/Vs at room temperature [3]. Ga₂O₃ material illustrates an advantage as compared to other wide band-gap materials such as SiC and GaN when low-cost Ga₂O₃ wafer can be directly produced using Czochralski (CZ) [4], floating zone (FZ) or edge-defined film-fed (EFG) methods [5]. In order to utilize Ga₂O₃ in high power applications, it is important to improve the Baliga's Figure of Merit (BFOM) in metal-oxide semiconductor field-effect transistors (MOSFETs) [6]. This figure of merit is determined by two key factors: dielectric breakdown ($E_{ox,br}$) and maximum surface electric field ($E_{SURF\ max}$). Literature report the $E_{SURF\ max}$ values for SiO₂ and HfO₂ are 1.56 MV/cm and 2.60 MV/cm, respectively [7].

The full potential of Ga₂O₃ devices has not yet been realized due to the lack of suitable shallow acceptors for p-doping in β -Ga₂O₃, while p-type doping is available in GaN. GaN is emerging as a potential material for the next generation of power devices, because of its wide band-gap of 3.4 eV [8-10]. Many works have been done to realize GaN power devices [11-14]. Therefore, the integration of β -Ga₂O₃ and GaN in bipolar devices has the potential to mitigate the drawbacks of Ga₂O₃ while leveraging the properties of p-type GaN. Recently, Ga₂O₃/NiO_x PN junction diode was fabricated with extremely high breakdown voltage (8.32 kV) and power figure-of-merit (13.2 GW/cm²) [15]. The study facilitates the combination of n-type Ga₂O₃ with other p-type wide band-gap semiconductor materials.

This study aims to contribute to the development of a GaN/Ga₂O₃ diode that can be utilized in high-power device applications. The simulated device is calibrated against experimental GaN and Ga₂O₃ diodes, considering the effect of thickness of GaN layer and its doping concentration on the behaviors of GaN/Ga₂O₃ diodes. The band structures of

devices are investigated to understand factors that affect the properties of GaN/Ga₂O₃ diode.

METHODOLOGY AND SETTINGS

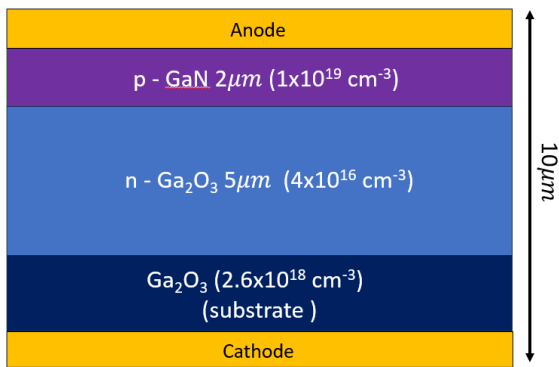


Figure 1. Schematic cross section of GaN/Ga₂O₃ p-n diode.

The GaN/Ga₂O₃ p-n diode was simulated using the 2-D device simulation tool. The device structure is illustrated in Fig. 1. All devices have the same n-type doping concentration of $2.6 \times 10^{18} \text{ cm}^{-3}$ in Ga₂O₃ substrate, and initial p-type doping concentration of $1 \times 10^{19} \text{ cm}^{-3}$ in GaN drift layer was used in the calibration process. To investigate the properties of the diodes, the thicknesses of the GaN layer were varied at 10 nm, 20 nm, 50 nm, 100 nm, 500 nm and 2 μm. In order to consider the impact of carrier concentration and high electrical field on the mobility, a concentration-dependent lifetime model and a high field model were used. The Auger recombination model was adapted to consider the influence of high electron concentration, and a thermal model was used to examine the self-heating effect.

RESULTS AND DISCUSSION

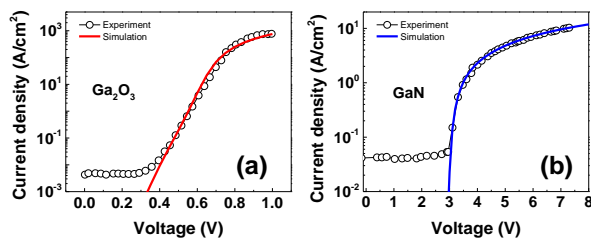


Figure 2. The simulated current-voltage (I-V) characteristics of both (a) the Ga₂O₃ diode and (b) the GaN diode as compared to the experimental results obtained from the same devices [16, 17].

TCAD parameters are calibrated against experimental Ga₂O₃ and GaN diodes. The current-voltage (I-V) results are shown in Fig. 2(a) for Ga₂O₃ diode and in Fig. 2(b) for GaN diode. Figure 2 illustrates that simulation I-V curves fit

well with the experiment [16, 17]. The calibrated parameters are used in simulation of all GaN/Ga₂O₃ p-n diodes, including the investigate of impacts of GaN drift layer thickness and the doping concentration of this layer on the behaviors of diodes. The electron mobility of Ga₂O₃ was extracted to be $115 \text{ cm}^2/\text{Vs}$, which is in an agreement with experimental report [18].

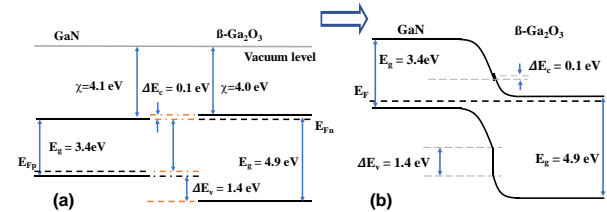


Figure 3. Band-diagram of GaN/Ga₂O₃ p-n junction diode (a) before and (b) after forming the p-n junction simulated by TCAD.

The band diagram of the GaN/Ga₂O₃ p-n junction diode, as depicted in Figure 1, is illustrated in Figure 3. Before the formation of the p-n junction, the energy levels of the conduction band (CB) minimum in both GaN and Ga₂O₃ are nearly identical. However, a depletion region is observed after the junction region is formed, having a CB offset of 0.1 eV and a valence band (VB) offset of 1.4 eV. The CB and VB offsets values are consistent with the findings of a previous report [19].

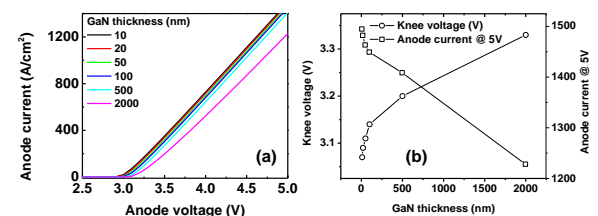


Figure 4. (a) I-V characteristics of GaN/Ga₂O₃ p-n junction diode as a function of GaN thickness, and (b) knee voltage and current density at $V_{anode} = 5 \text{ V}$ as a function of GaN thickness

Figure 4 (a) shows the I-V characteristics of the GaN/Ga₂O₃ p-n junction diode as a function of GaN thickness. As the thickness of GaN increases, it is observed that the current density decreases. However, the reduction in current density is not linear with respect to the GaN thickness shown in Figure 4(b). The threshold voltage of the diode, namely the knee voltage, is illustrated in Figure 4(b). It is observed that the knee voltage decreases significantly for small thicknesses (<100 nm) of GaN. However, as the

GaN thickness exceeds 100 nm, the reduction in knee voltage becomes less noticeable.

The impacts of doping concentration of GaN layer on GaN/Ga₂O₃ p-n junction diodes are investigated in Fig. 5. Figure 5(a) illustrates the ratio of I_{on}/I_{off} , which is greater than 1.0×10^{15} . This high ratio indicates that GaN/Ga₂O₃ is a highly promising candidate for high-power device applications. Figure 5(b) indicates that the current tends to decrease as the doping concentration in GaN increases. This reduction can be attributed to the changes occurring within the band structure of the diode. Figure 5(c) illustrates a slight change in the knee voltage, from 3.54 V to 3.73 V, when the doping concentration is increased from $1.0 \times 10^{16} \text{ cm}^{-3}$ to $1.0 \times 10^{18} \text{ cm}^{-3}$. The electrical properties of the diode can be explained by simulating their band diagram. Figure 5(d) shows a change in the shape of the GaN/Ga₂O₃ junction, varying from a linear-junction (represented by the black solid line) to an abrupt-junction (represented by the blue dashed line). This change results in an increase of Schottky barrier within the depletion region, which explains the decrease of the observed I-V characteristic.

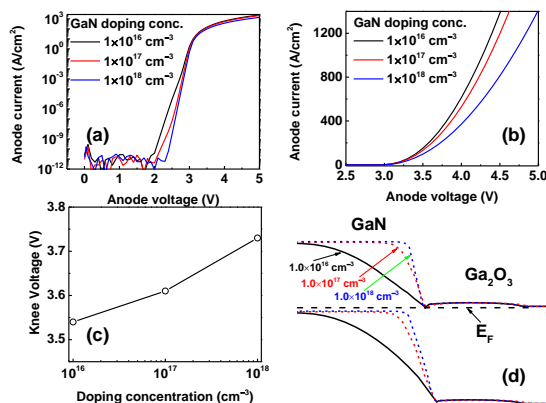


Figure 5. I-V characteristics of GaN/Ga₂O₃ p-n junction diode as a function of doping concentration in GaN, presenting in (a) log scale, and (b) linear scale. (c) Knee voltage as a function of doping concentration in GaN. (d) Band diagram at GaN/Ga₂O₃ junction when the doping concentration in GaN is changed from $1.0 \times 10^{16} \text{ cm}^{-3}$ to $1.0 \times 10^{18} \text{ cm}^{-3}$.

CONCLUSION

In conclusion, the GaN/Ga₂O₃ p-n junction diode was investigated using TCAD simulations. The impacts of GaN thickness and its doping concentration on I-V characteristics of GaN/Ga₂O₃ diodes was conducted. It is observed

that the knee voltage is strongly dependent on the thickness of GaN when its thickness is less than 100 nm. The dependence becomes little when the GaN thickness increases. It was observed a change in the shape of the GaN/Ga₂O₃ junction when the doping concentration is increased from $1.0 \times 10^{16} \text{ cm}^{-3}$ to $1.0 \times 10^{18} \text{ cm}^{-3}$, moving from a linear-junction to an abrupt-junction. This change leads to an increase in the Schottky barrier within the depletion region. The study provides thorough guidance for fabricating GaN/Ga₂O₃ p-n junction diodes, applicable in high power device applications.

Acknowledgment

This work was funded by the Ho Chi Minh City University of Technology and Education, Vietnam.

References

- [1] H. von Wenckstern, *Group-III Sesquioxides: Growth, Physical Properties and Devices*, *Advanced Electronic Materials* **3** (2017) 1600350.
- [2] S. J. Pearton, J. Yang, P. H. Cary, IV, F. Ren, J. Kim, M. J. Tadjer, and M. A. Mastro, *A review of Ga₂O₃ materials, processing, and devices*, *Applied Physics Reviews* **5** (2018).
- [3] J. Yang, M. Xian, P. Carey, C. Fares, J. Partain, F. Ren, M. Tadjer, E. Anber, D. Foley, A. Lang, J. Hart, J. Nathaniel, M. L. Taheri, S. J. Pearton, and A. Kuramata, *Vertical geometry 33.2 A, 4.8 MW cm² Ga₂O₃ field-plated Schottky rectifier arrays*, *Applied Physics Letters* **114** (2019).
- [4] Z. Galazka, R. Uecker, D. Klimm, K. Imscher, M. Naumann, M. Pietsch, A. Kwasniewski, R. Bertram, S. Ganschow, and M. Bickermann, *Scaling-Up of Bulk β -Ga₂O₃ Single Crystals by the Czochralski Method*, *ECS Journal of Solid State Science and Technology* **6** (2017) Q3007.
- [5] A. Kuramata, K. Koshi, S. Watanabe, Y. Yamaoka, T. Masui, and S. Yamakoshi, *High-quality β -Ga₂O₃ single crystals grown by edge-defined film-fed growth*, *Japanese Journal of Applied Physics* **55** (2016) 1202A2.
- [6] Z. Cheng, J. Shi, C. Yuan, S. Kim, and S. Graham, *Semiconductors and Semimetals*, edited by Y. Zhao and Z. Mi, Elsevier, 2021.
- [7] H.-B. Do, A.-V. Phan-Gia, V. Q. Nguyen, and M. M. De Souza, *Optimization of normally-off β -Ga₂O₃ MOSFET with high Ion and*

- BFOM: A TCAD study*, AIP Advances **12** (2022).
- [8] H.-B. Do, J. Zhou, and M. M. De Souza, *Origins of the Schottky Barrier to a 2DHG in a Au/Ni/GaN/AlGaN/GaN Heterostructure*, ACS Applied Electronic Materials **4** (2022) 4808-4813.
- [9] J. Zhou, H. B. Do, and M. M. D. Souza, *A new back-to-back graded AlGaN barrier for complementary integration technique based on GaN/AlGaN/GaN platform*, Proc. the 7th IEEE Electron Devices Technology & Manufacturing Conference (EDTM), 2023, 1-3.
- [10] J. Zhou, H.-B. Do, and M. M. De Souza, *Impact of an Underlying 2DEG on the Performance of a p-Channel MOSFET in GaN*, ACS Applied Electronic Materials **5** (2023) 3309-3315.
- [11] D. Kinzer, *GaN power IC technology: Past, present, and future*, Proc. the 29th International Symposium on Power Semiconductor Devices and IC's (ISPSD), 2017, 19-24.
- [12] L. Zhang, X. Wang, J. Zeng, L. Jia, Z. Cheng, Y. Ai, Z. Liu, W. Tan, and Y. Zhang, *AlGaN/GaN Heterojunction Bipolar Transistors With High Current Gain and Low Specific on-Resistance*, IEEE Transactions on Electron Devices **69** (2022) 6633-6636.
- [13] H. Ohta, N. Kaneda, F. Horikiri, Y. Narita, T. Yoshida, T. Mishima, and T. Nakamura, *Vertical GaN p-n Junction Diodes With High Breakdown Voltages Over 4 kV*, IEEE Electron Device Letters **36** (2015) 1180-1182.
- [14] A. Hickman, R. Chaudhuri, S. J. Bader, K. Nomoto, K. Lee, H. G. Xing, and D. Jena, *High Breakdown Voltage in RF AlN/GaN/AlN Quantum Well HEMTs*, IEEE Electron Device Letters **40** (2019) 1293-1296.
- [15] J. Zhang, P. Dong, K. Dang, Y. Zhang, Q. Yan, H. Xiang, J. Su, Z. Liu, M. Si, J. Gao, M. Kong, H. Zhou, and Y. Hao, *Ultra-wide bandgap semiconductor Ga₂O₃ power diodes*, Nature Communications **13** (2022) 3900.
- [16] I. C. Kizilyalli, A. P. Edwards, O. Aktas, T. Prunty, and D. Bour, *Vertical Power p-n Diodes Based on Bulk GaN*, IEEE Transactions on Electron Devices **62** (2015) 414-422.
- [17] J. Yang, S. Ahn, F. Ren, S. Pearton, S. Jang, J. Kim, and A. Kuramata, *High reverse breakdown voltage Schottky rectifiers without edge termination on Ga₂O₃*, Applied Physics Letters **110** (2017).
- [18] Y. Kang, K. Krishnaswamy, H. Peelaers, and C. G. Van de Walle, *Fundamental limits on the electron mobility of β -Ga₂O₃*, Journal of Physics: Condensed Matter **29** (2017) 234001.
- [19] P. Li, H. Shi, K. Chen, D. Guo, W. Cui, Y. Zhi, S. Wang, Z. Wu, Z. Chen, and W. Tang, *Construction of GaN/Ga₂O₃ p-n junction for an extremely high responsivity self-powered UV photodetector*, Journal of Materials Chemistry C **5** (2017) 10562-10570.

EFFECT OF CALCINATION TEMPERATURE OF NATURAL CLAY TOWARD FORMATION OF LIMESTONE CALCINED CLAY CEMENT

Pham Trung Kien^{1,2,3*}, Tran Ngo Quan^{1,2}, Nguyen Don Tin^{1,2}

¹ Faculty of Materials Technology, Ho Chi Minh City University of Technology (HCMUT), 268 Ly Thuong Kiet Street, District 10, Ho Chi Minh City, Vietnam;

² Vietnam National University Ho Chi Minh City, Linh Trung Ward, Thu Duc District, Ho Chi Minh City, Vietnam

³ Polymer Research Center, Ho Chi Minh City University of Technology (HCMUT), 268 Ly Thuong Kiet Street, District 10, Ho Chi Minh City, Vietnam
Email: phamtrungkien@hcmut.edu.vn

ABSTRACT

In this study, we form the activated clay was formed by calcined fresh clay at 600°C/2h. After calcination, the activated clay with needle-like shape crystals were form own the size of 1µm. In addition, the kaolinite 1A form fresh clay was thermally decompose, resulting to new activated clay. This research aim to find the technology to form the clinker-free mortar/plaster, thus can help to reduce the CO₂ footprint.

Keywords: clay, calcined clay, LC3, CO₂ footprint, kaolinite

INTRODUCTION

In recent years, there has been a significant amount of research worldwide on fired clay and its applications as a partial substitute for clinker in cement. This not only helps the cement industry reduce CO₂ emissions per ton of cement but also has the potential to reduce production costs. The fired clay used as a pozzolanic material in Limestone Calcined Clay Cement (LC3) typically contains an average of 40-60% kaolin. In cement production, CO₂ emissions result from the decomposition of limestone (approximately 0.53 tons of CO₂ per ton of clinker) [1] and the use of fossil fuels such as coal, oil, where coal combustion emits approximately 0.0946 kg of CO₂/MJ, and burning diesel fuel releases about 3 tons of CO₂ per ton of diesel. To reduce CO₂ emissions, attractive research on new technology on raw materials have been find out recently [2-5]. However, the new concept on reduces the kaolinite at low temperature, thus forming the kaolinite-free clay or activated-clay is not widely proposed. By this concept, our research group propose to calcined the fresh clay at low temperature, aiming to precalcine the clay, thus reduce the CO₂ release during the clinker process. In addition, the forming activated clays could be used in clinker-free mortar, and might be significantly contribute to the reduce of CO₂ footage in cement industry. This research aims

with eco-friendly materials carried out by our group in recently year [6-7].

EXPERIMENTAL

Raw materials study

The fresh clay was collected at clay mine in INSEE cement factory, Hon Chong, Kien Giang. Its characterized such as phase, chemical composition, chemical bonding and thermal stability was tested by Xray Diffraction, Xray Fluorescing (XRF), FTIR and thermal analysis. characterization.

Preliminary study on calcination effect

The fresh clay was calcined at 600°C for 2h, follow by normal cooling. The calcined clay were characterized by XRD, XRF, SEM and FTIR. The flow chart of fabrication calcined clay was shown in Figure 1.

Materials characterizations method

The chemical composition analysis of sample using Xray Fluorescing (XRF): the sample was characterized by Xray at 40kV (ARL Advant, Thermo Scientific).

The phase analysis using powder-type XRD: the sample was ground and put in XRD machine (Bruker D8 Advance, Germany) with the 2theta scanning from 5 to 60°, operation at 40kV and 40mA.

The chemical composition analysis using Xray Fluorescing (XRF): the sample was

characterized by Xray at 40kV (ARL Advant, Thermo Scientific).

The morphology analysis using SEM: the sample was scattered on Carbon tape stick to Cupper substrate, and carried the SEM analysis (Hitachi S-4800) at 10kV.

The chemical bonding of samples were analysis using FTIR: the sample(s) were mixed with KBr with the ratio of 1:200, press to make the transparent pellet, and carried out under infrared ray (Thermo Nicolet iS50, ATR).

The thermal analysis using DSC/TG: the sample was heated up to 1000°C using DSC/TGA technique (STA 449, Netzsch, Germany).

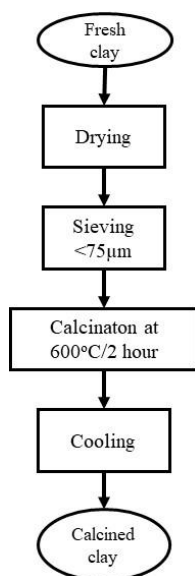


Figure 1. Flow chart of fabrication calcined clay

RESULTS AND DISCUSSION

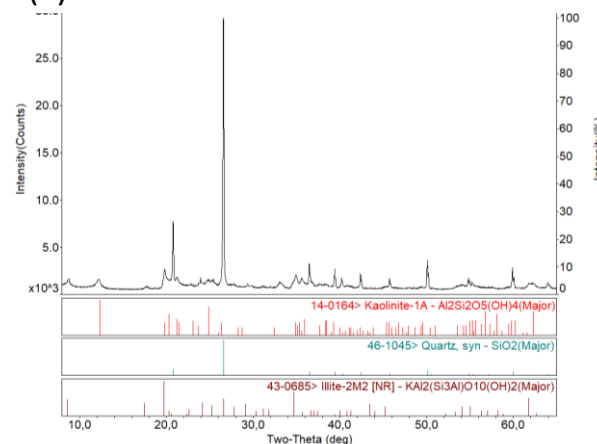
Raw materials study

Figure 2 shown the XRD patterns of fresh clay (before calcined) and calcined at 600°C/2h. In brief, the fresh clay was composed of kaolinite-1A with the chemical formular of $Al_2Si_2O_5(OH)_4$ (PDF# 14-0164); Quartz SiO_2 (PDF#46-1045) and illite $KAl_2(Si_3Al)O_{10}(OH)_2$ (PDF#43-0685) with the strongest 2theta of 28 degree as shown in Figure 2a. In contrast, upon calcined at 600°C/2h, the peak of kaolinite 1A is disappear, meanign that the kaolinite mineral was decomposed at 600°C/2h.

In order to understand the thermal decomposition of fresh clay, the thermal analysis of fresh clay were carried out. Figure 3 shown the DSC/TG of fresh clay. The endothermic peak was shown at 500°C, indicating the heat decompose of

kaolinite 1A, thus the starting temperature for decomposed was selected as 600°C in this study.

(a) Before calcined



(b) Calcined at 600°C/2h

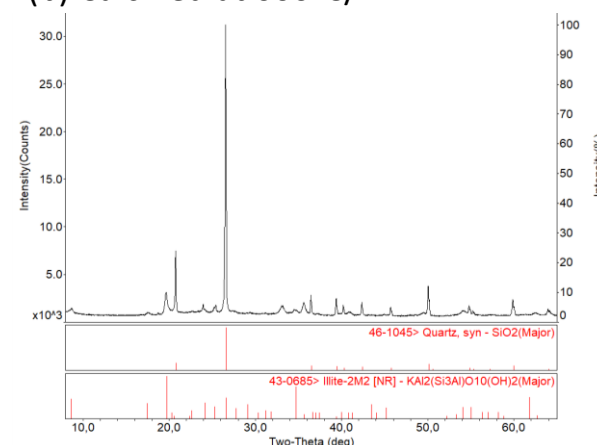


Figure 2. XRD patterns of raw materials: (a) fresh clay before calcined and (b) Calcined at 600°C/2h.

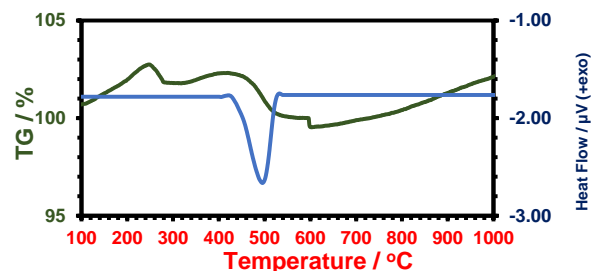


Figure 3. DSC/TG patterns of fresh clay. The endothermic peak was shown at nearly 500°C.

Table 1. Chemical analysis of the fresh clay and calcined clay

Oxide (wt.%)	SiO ₂	CaO	Al ₂ O ₃	Fe ₂ O ₃	*LOI
Before calcined	55.4	0.51	20.0	10.8	8.07
Calcined 600°C/2h	56.2	0.8	17.7	13.3	0.78

*LOI: loss on ignition

Figure 4 shown the SEM images of raw materials fresh clay and calcined clay at different magnifications of 500X and 5,000X. In brief, the fresh clay has the plate-like shape indicating by black arrow. Upon calcined at 600°C/2h, the new needle-like shape was form as indicating by white arrow.

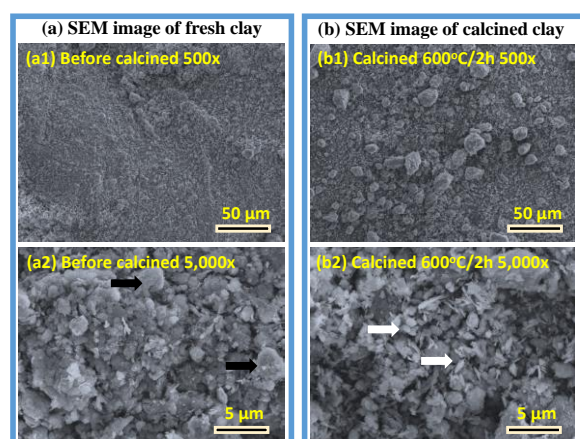


Figure 4: SEM image of raw materials: (a) fresh clay at magnification of (a1) 500X and (a2) 5,000X; and (b) calcined clay at magnification of (b1) 500X and (b2) 5,000X.

This research needs to put into the context of experiment conditions. Currently, the cement industry used clay, limestone as raw materials to supply the CaO, SiO₂ by mixing and calcined at 1450°C in rotation kiln follow by supper quenching to form clinker. This process will utilize the fuel to decompose Clay and limestone to obtain SiO₂ and CaO. However, if we can precalcined the clay at low temperaerature, we can decompose the kaolinite 1A, thus forming the new needle-like shape crystals. The new activated calcined clay can accelarte the settign property of clinker-free mortar, thus reduce the need of using clinker. Consequently, the CO₂ footage can be reduce during the cement process.

CONCLUSION

This research shown the ability to use calcined clay in mixture of clinker-free mortar, thus reduce the CO₂ footprint over the global. By calcined the fresh clay at 600°C/2h, the kaolite 1A was thermally decomposed, and forming the needle-like shape crystal, thus make the calcined clay become more active.

Acknowledgment

We acknowledge Ho Chi Minh city university of Technology (HCMUT) VNU-HCM for supporting this study.

References

- [1] R. Jaskulski, D.J Niedzwiedzka, Y. Yakymchko. "Calcined Clay as Supplementary Cementitious Material", *Materials*, **13**(21) (2020) 1-36.
- [2] J. Yu, H.L. Wu, D.K. Mishra, G. Li, C.K.Y. Leung. *Compressive strength and environmental impact of sustainable blended cement with high-dosage limestone and calcined clay (LC2)*. *J. Clean. Prod.*, 278 (2021).
- [3] D. Zhang, B. Jaworska, H. Zhu, K. Dahlquist, V.C. Li, F. Zunino, E. Boehm-Courjault, K. Scrivener. *The impact of calcite impurities in clays containing kaolinite on their reactivity in cement after calcination*. *Mater. Struct.*, **53**(2) (2020) 1-15.
- [4] M. Sharma, S. Bishnoi, F. Martrena, K. Scrivener. *Limestone calcined clay cement and concrete: a state-of-the-art review*. *Cement Concr. Res.*, 149 (2021).
- [5] A. Parashar, S. Bishnoi. *Hydration behaviour of limestone-calcined clay and limestone-slag blends in ternary cement*. *RILEM Tech. Lett.*, 6 (2021) 17-24.
- [6] P.T. Kien, T.N. Quan, D. Q. Minh. *The effect of hydrothermal treatment time on the synthesized of Xonotlite using fined flint glass cullet (FFGC) and Calcium hydroxide*. *Vietnam Journal of Catalysis and Adsorption* **11**(2) (2022) 62-66.
- [7] PT Kien, TN Quan. *Characteristic of xonotlite synthesized by hydrothermal reaction using rice hush ash and its application to absorb chrome (III) solution*. *Materials and technologies*, **55**(6) (2021) 833-838.

INFLUENCE OF GLASS FIBER ON THE MECHANICAL BEHAVIOR OF POLYBUTYLENE TEREPHTHALATE/ GLASS FIBER BLEND

Luong Quoc Khanh¹, **Tran Hoang Phuc**¹, **Nguyen Dinh Quang**¹, **Le Viet Thanh Nam**¹,
Nguyen Trong Thuc¹, **Nguyen Pham Ngoc Tuyen**¹, **Pham Thi Hong Nga**¹, **Pham Quan Anh**¹,
Ho Thi My Nu² and **Nguyen Chi Thanh**¹

¹ Ho Chi Minh City University of Technology and Education, No. 1 Vo Van Ngan Street, Thu Duc, Ho Chi Minh City, Vietnam

² Ho Chi Minh City University of Food Industry, Vietnam, 140 Le Trong Tan Street, Tay Thanh, Tan Phu, Ho Chi Minh City, Vietnam

Email: hongnga@hcmute.edu.vn

ABSTRACT

This study has analyzed and evaluated the mechanical properties of Polybutylene terephthalate (PBT)/glass fiber (GF) blend. A practical application of PBT's potential is to be recycled into a flame-retardant and durable material by adding an appropriate amount of glass fiber. PBT/GF mixtures are prepared by injection molding with 5, 10, 15, 20, and 25% GF in each PBT/GF blend. After injection molding, samples are tested for tensile strength according to ASTM D638. The average tensile strength of PBT/GF at ratios of 95/5, 90/10, 85/15, 80/20, and 75/25 are 41.30, 56.09, 59.96, and 64.41 MPa. It shows that the tensile strength of the PBT/GF mixture increases as glass fiber content increases. This research aims to serve as a reference for developing a method of mixing materials to produce the desired mechanical properties.

Keywords: Polybutylene terephthalate, Glass fiber, PBT/GF blend, Tensile strength, Polymer

INTRODUCTION

Polybutylene terephthalate (PBT) is an essential engineering polymer in many industrial applications because it has good tensile strength and bending modulus [1-3]. In addition to the amount of domestic solid waste released into the environment, many components, such as fabric, rubber, and plastic, are experiencing difficulties in disposal and recycling. The reuse and recycling of plastic materials is something that researchers are interested in. Because PBT still has some limitations in terms of mechanical properties, it has yet to receive much attention. Studies on PBT recycling are few, while recycling resources are enormous, such as toothbrush bristles [4]. Emel Kuram [5] studied the recyclability of a mixture of PBT/PC/ABS (acrylonitrile-butadiene-styrene) with glass fiber. The study results show that the mechanical properties, such as deformation at breakage and impact strength of recycled PBT/PC/ABS-GF blends are higher than those of neat PBT/PC/ABS-GF mixtures. However, research has also shown that recycled PBT/PC/ABS-GF blends have lower tensile and

yield strength than pure PBT/PC/ABS-GF blends.

Polybutylene terephthalate is a high-performance thermoplastic in the polyester terephthalate family. However, PBT is an engineering plastic with comprehensive mechanical properties such as high hardness, high tensile strength, good electrical insulation, and water resistance. Because of the above advantages, applying PBT in the electrical, electronic, and automotive components industries is quite prevalent [6]. However, with the above benefits, PBT has some disadvantages, such as the low thermal deformation temperature of PBT due to its low glass transition temperature, low solvent absorption, and low impact strength. Therefore, the application of PBT is limited by impact working conditions or some other conditions such as high-temperature environments [7]. There are many techniques to improve the mechanical properties of polymers, the most popular of which is the mixing method.

The mixing method is optimal and effective. Mix two or more plastics to offset each other's

¹ Corresponding author, Pham Thi Hong NGA, Ho Chi Minh City University of Technology and Education, No. 1 Vo Van Ngan Street, Thu Duc City, Ho Chi Minh City, 71307, Vietnam; E-mail: hongnga@hcmute.edu.vn.

weaknesses while retaining their advantages [8]. The use of this method to improve the mechanical properties of PBT materials has also been applied by researchers and has shown positive results [9]. The study by Dekkers et al. investigated the effects of styrene-ethylene/butadiene-styrene (SEBS) on a mixture of PBT, polycarbonate (PC), and poly(phenylene ether) (PPE). At a temperature of 25 °C, the results obtained showed that the impact intensity of the PBT/PC/PPE/SEBS ratio (46/10/30/14) reaching 600 J/m was 12 times higher than that of the PBT/PPE/SEBS (46/30/14) balance with an impact strength of 50 J/m [10]. Besides the significant variation in impact intensity, the SEM image shows the presence of PC wrapped around PPE/SEBS particles as a bridge to enhance surface adhesion in PBT/PC/PPE/SEBS mixtures. These results show that the mixture's tensile strength and thermal stability are increased.

Injection molding is a reasonably common processing technique for glass fiber-reinforced PBT. It makes the product stable and accurate in size, short injection molding cycles, and low cost [11]. Fiber-reinforced PBT is used in various insulating parts for electrical engineering, electronics, and automotive component manufacturing. Therefore, research on fiber-reinforced PBT processing became necessary [12]. In addition, glass fiber affects the ignition of PBT. Therefore, many researchers focus on manufacturing and improving fireproof glass fiber-reinforced PBT. Ramani [13] studied flame-resistant GF-reinforced PBT and found that glass fiber does not change the degradation behavior of PBT. Florian Kempel et al. [14] confirmed that the volume of GF-reinforced PBT was reduced by 2.5 times compared to pure PBT.

Glass fiber is formed from melting and is produced in various components by varying the number of raw materials, such as sand to make silicon, clay to produce alumina, calcite to produce calcium oxide, and colemanite to produce boron oxide. Moreover, shredded fibers, direct drawn coarse fibers, assembly coarse fibers, and carpets are the most important products used in injection molding, filament winding, extrusion, sheet casting, and manual stacking to form glass fiber-reinforced composites.

Studies of the failure mechanism revealed that PBT is a polymer sensitive to strain rates. It becomes stiffer at higher strain rates and creates

a high ductility limit on flexible PC domains. The mechanical test results of PBT/PC/elastomer blends reinforced with glass fiber show that blends have improved impact strength [15]. Therefore, we carry out this research to improve the tensile strength of PBT by mixing PBT-30GF, which is available in the market for more applications in daily life, such as automotive interior and exterior manufacturing, home electrical appliances, etc. To facilitate the study, this study incorporated PBT and glass fiber to improve mechanical properties.

MATERIALS AND METHODS

Table 1. Composition of the sample (wt.%).

Sample	PBT (wt.%)	GF (wt.%)
PBT-5GF	95	5
PBT-10GF	90	10
PBT-15GF	85	15
PBT-20GF	80	20
PBT-25GF	75	25

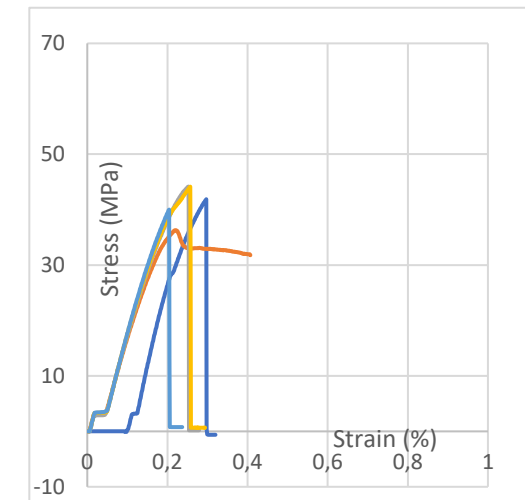
This research uses three plastic materials, PBT and PBT-30GF, which use PBT-30GF to supply glass fiber for the TA Co., Ltd mixture. COMA provides PBT plastic from Lanxess (Germany) from India/China. PBT and PBT-30GF were mixed in the proportions stated in Table 1 and dried at 110 °C for about 3 to 4 hours, with a moisture content of less than 0.03%. Using injection molding method with Toshiba 100-ton plastic injection machine.

After injection molding, samples obtained at each rate proceed to ASTM D638 tensile measurement on Shimadzu material testing machines. Before proceeding with the size, ensure the measuring medium is at a temperature of 23 ± 2 °C and a relative humidity of $50 \pm 5\%$ in the air. In addition, laboratory samples need to be stored for at least 40 hours. Conduct measurement: First, enter the measurement parameters into the machine at a speed of = 5 mm/min. Next, clamp the sample tightly to the handle of the device. Then, start measuring the tensile strength so that the support moves until the example is completely broken. Finally, record the test data of the sample and remove the piece from the grip. Proceed to repeat the sequence of steps for the following models.

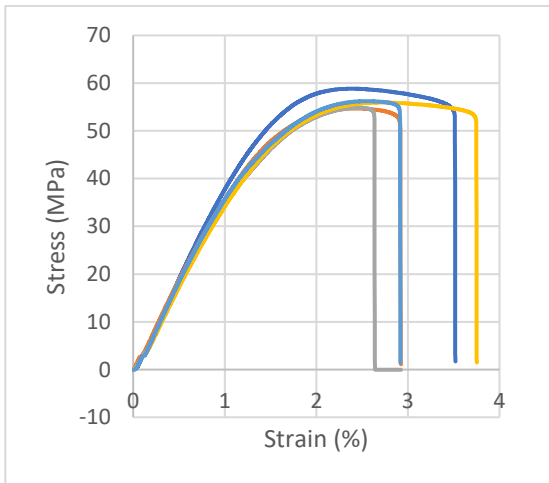
RESULTS AND DISCUSSION

Figure 1 shows tensile stress curves and scale deformation. There is a difference between the

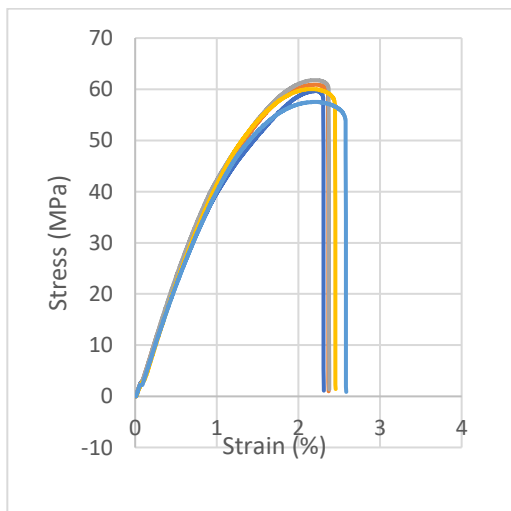
proportion of glass fiber added to the PBT mixture. When the stress peaks, all samples immediately break, indicating a brittleness similar to neat PBT.



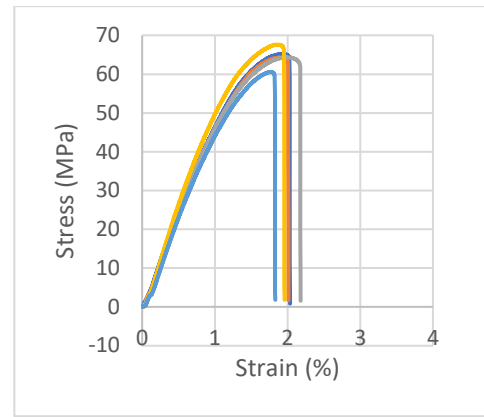
(a) PBT-5GF sample



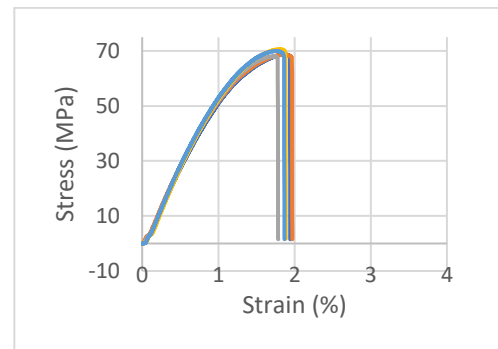
(b) PBT-10GF sample



(c) PBT-15GF sample



(d) PBT-20GF sample



(e) PBT-25GF sample

Figure 1. Tensile stress-strain curve of PBT/GF models

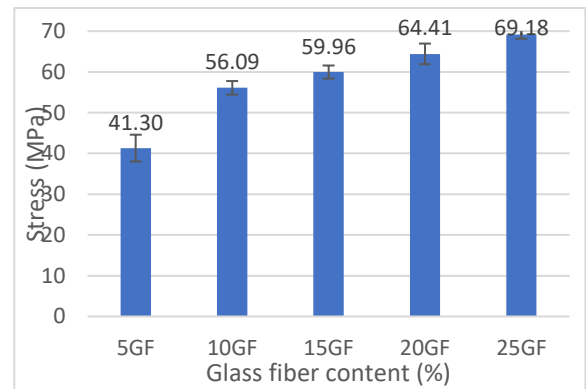


Figure 2. Average tensile strength of samples

Figure 2 shows that the mixture makes quite a difference when increasing the glass fiber content. The tensile strength of samples PBT with 5, 10, 15, 20, and 25% glass fiber gradually increased from 41.30, 56.09, 59.96, 64.41, to 69.18 MPa, respectively. The sample with the highest tensile strength of PBT/25%GF is 67.5 % higher than the lowest sample (PBT/5%GF). It was found that PBT reinforced with glass fiber yielded composites with significantly improved tensile strength [15].

CONCLUSIONS

The influence of glass fiber content in the PBT/ glass fiber blend on tensile strength has been investigated. The glass fiber content in the PBT/ glass fiber mixture is not only directly proportional to tensile strength but also increases the tension of the sample.

Acknowledgments

This work belongs to the project in 2023 funded by Ho Chi Minh City University of Technology and Education, Vietnam.

References

- [1] Rice F, General L, Fang Z., *Effect of a novel phosphorous-nitrogen containing intumescent flame retardant on the fire retardancy and the thermal behaviour of poly (butylene terephthalate)*, *Polymers. Degrad. Stab.* **91** (2006) 1295-1299.
- [2] Braun US, Bahr H, Sturm H, ScharTEL B., *Flame retardancy mechanisms of metal phosphinates and metal phosphinates in combination with melamine cyanurate in glass-fiber reinforced poly (1,4-butylene terephthalate): The influence of metal cation*, *Polym. Adv. Technol.* **19** (2008) 680-692.
- [3] Van TT, Nga THP, Hoang-Khang L, Ngoc TNN, Huy H-ND, Duy-Quang D, Tran MTU, Hoang VH, *A Study of Poly(butylene Terephthalate) and Thermoplastic Polyurethane*, *Polym. Sci. - A.* **63** (2022) S58-S63.
- [4] Nga THP, *A study of recycled Poly(butylene Terephthalate) and Low-density polyethylene (R-PBT/LDPE) blend*, *Polym. Sci. - A.* **63** (2021) 800-803.
- [5] Kuram E, Ozelik B, Yilmaz F, *The influence of recycling number on the mechanical, chemical, thermal and rheological properties of poly(butylene terephthalate)/ polycarbonate binary blend and glass-fibre-reinforced composite*, *J. Thermoplast. Compos. Mater.* **29** (2016) 1443-1457.
- [6] Wei Y, Lu H, Tai Q, et al., *The flame retardant mechanism of poly (1,4-butylene terephthalate) contains microscopic ammonium polyphosphate and melamine cyanurate*, *Polymers. Adv. Technol.* **22** (2011) 2136-2144.
- [7] Kumar R, Kar KK, Kumar V., *Studies of the effect of compatibility, on mechanical, thermal, and flow properties of polycarbonate/poly (butylene terephthalate) mixtures*, *Mater. Res. Express.* **5** (2018) 2053-1591.
- [8] Ngoc-Thien T, Nga THP, *Investigation of the effect of Polycarbonate rate on mechanical properties of Polybutylene terephthalate/Polycarbonate blends*, *Int. J. Polym. Sci.* **2021** (2021) 7635048.
- [9] Chiou KC, Chang FC, *Reaction compatibility of polyamide-6 (PA6)/polybutylene terephthalate (PBT) blended by multifunctional epoxy resins*, *J. Polym. Sci. B. Polym. Phys.* **38** (2000) 23-33.
- [10] Dekkers MEJ, Hobbs SY, Watkins VH, *Morphology and deformation behavior of hard mixtures of poly (butylene terephthalate)/polycarbonate and poly (phenylene ether)*, *Polymers* **32** (1991) 2150-2154.
- [11] Francesco A, Corrado B, Martino C, Maurizio F, Sreepadaraj K, *Study of glow wire ignition temperature (GWIT) and comparative tracking index (CTI) performance of engineering thermoplastics and correlation with material properties*, *Polym. Degrad. Stab.* **96** (2011) 566-573.
- [12] Shuidong Z, Lingcao T, Jizhao L, Hanxiong H, Guo J, *The relationship between the structure and properties of recycled fiberglass-reinforced flame retardant poly (butylene terephthalate)*, *Polymers. Degrad. Stab.* **105** (2014) 140-149.
- [13] Ramani A, Dahoe AE, *On the performance and mechanism of bromine and halogen-free flame retardants in formulations of fiberglass reinforced poly (butylene terephthalate)*, *Polymers. Degrad. Stab.* **104** (2014) 71-86.
- [14] Kempel F, ScharTEL B, Linteris GT, Stoliarov SI, Lyon RE, Walters RN, Hofmann A., *Prediction of mass loss rate of polymeric materials: Impact of upper formatium residues*, *Fire and Flame* **159** (2012) 2974-2984.
- [15] Wu JS, Yu DM, Mai YW, Yee AF, *Impact strength and fracture mechanism of PBT/PC/IM mixture, Part IV Impact strength and destructive mechanism of PBT/PC mixture without impact modifier*, *J. Mater. Sci.* **25** (2000) 1-9.

TENSILE STRENGTH OF POLYBUTYLENE TEREPHTHALATE/ POLYAMIDE 6/ GLASS FIBER BLENDS

**Nguyen Cong Dat, Nguyen Tran Dan Truong, Nguyen Quang Tuan, Ha Trong Kien,
Hua Phan Hieu, Ngo Quoc Bao, Pham Thi Hong Nga, Pham Quan Anh and Tran Ngoc Thien**
Ho Chi Minh City University of Technology and Education, No. 1 Vo Van Ngan, Thu Duc City,
Ho Chi Minh City, Vietnam
Email: hongnga@hcmute.edu.vn

ABSTRACT

This study analyzes and evaluates the mechanical and physical properties of Polybutylene terephthalate (PBT)/Polyamide 6 (PA6) mixture and the effect of glass fiber (GF) when mixed with PBT/PA6 mixture. One potential practical application area is recycling PBT and PA6 into insulation or fire retardant materials by mixing with an appropriate amount of fiberglass. The PBT/PA6/GF mixture is prepared by injection molding method with 0, 9, 12, 15 and 18% GF in the PBT/PA6 mixture at a ratio of 50/50. After injection molding, samples are tested for tensile strength according to ASTM D638. After pressing the injection into the product and putting it into the measurement process, the results corresponding to each ratio of 9, 12, 15, and 18% are 42.52 MPa, 46.59 MPa, 43.28 MPa, 45.39MPa and 40.07 MPa, thereby, we see that the PBT / PA6 model reinforced with GF gives better measurement results than the PBT/PA6 model without adding GF, the sample is supported with 9 to 15% GF relatively evenly but through the piece of 18% GF, the tensile surface tends to decrease. This research aims as a reference for the development of methods for mixing materials to produce desired physicomechanical properties.

Keywords: Poly(butylene terephthalate), Polyamide 6, Glass fiber, PBT/PA6/GF, tensile strength

INTRODUCTION

According to World Bank statistics, over 2 billion tons of solid waste per year are generated worldwide, with various components such as plastic, fabric, and rubber. However, plastic waste accounts for up to 10% of destruction and is extremely difficult to decompose or treat thoroughly. Therefore, reusing or recycling plastic materials is a significant concern to researchers [1-3]. While common plastics like Polypropylene (PP), Polyvinyl chloride (PVC),... There are still little-noticed plastics such as Polybutylene terephthalate (PBT) while the recycling source is vast, in fact, toothbrush bristles [4]. The reason is that PBT has mechanical limitations. Typical PBT studies, such as Emel Kuram's [5], still investigate the effectiveness of recycling PBT/PC/ABS mixtures with or without fiberglass. The results show that mechanical properties such as deformation at the fracture point and impact strength of recycled PBT/PC/ABS-fiberglass (GF) mixtures are higher than those of the original PBT/PC/ABS-GF mixtures. However, recycled PBT/PC/ABS-GF blends have lower tensile strength and yield limits than the original PBT/PC/ABS-GF blends.

So, we decided to do this research to improve the tensile strength of PBT by blending PBT with PA6 and fiberglass. From there, PBT can be more widely applied in automobile manufacturing and household electrical appliances,...

Polybutylene terephthalate is a semi-crystalline engineering plastic material belonging to the polyester polymer family. Based on mechanical properties advantages such as strength, high rigidity, good electrical insulation, and water resistance [6-7], PBT has a lot of potential for development when applied in automotive, electrical, and electronic [8-9]. However, disadvantages remain, such as high shrinkage, easy to deform, uneven shrinkage, poor notched impact strength, and low deformation temperature. Therefore, using PBT plastic is difficult under impact conditions or in high-temperature environments [10-12]. To improve the mechanical properties of polymers, the most popular is the blending method.

Polyamide 6 (PA6) is a high-tech polymer line, the consumption of which in the engineering and industrial fields is extensive. PA6 plastic resins have toughness, high tensile strength, significant impact, and abrasion resistance. You

can also add fiberglass, mineral fillers, and flame retardants to improve the necessary properties. PA6 plastic has good mechanical characteristics such as high hardness and impact resistance, thermal stability, wear resistance, chemical resistance, and electrical insulation. However, there are still drawbacks, such as poor acid resistance dimensional strength.

Injection molding is a standard manufacturing process for fiberglass-reinforced PBT because it results in stable and accurate dimensions, short pressing cycles, and low cost. After being strengthened, PBT is widely used in electrical engineering, electronics, and automobile component manufacturing. Therefore, the study of reinforcement for PBT became necessary [13]. In addition, fiberglass affects the combustion capacity of PBT. Therefore, many studies on fire protection for fiberglass PBT have been conducted. For example, A. Ramani [14] studied fiberglass-reinforced flame retardant PBT and found that this glass fiber did not change the degradability of PBT. Florian Kempel [15] confirmed the study's results that the mass of fiberglass-reinforced PBT was reduced by 2.5 times compared to the original PBT.

From the studies on PBT, PA6, and fiberglass mixtures mentioned above, especially Shuidong's research [13], this is the study of PBT's mechanical properties and properties using injection molding after fiberglass reinforcement. The study results show the ability to improve the mechanical properties of fiberglass for PBT/PA6/GF mixtures, especially tensile strength.

EXPERIMENTAL

This study used three types of plastic materials, PBT, PA6, and PBT-30GF, which used PBT-30GF to supply fiberglass to the TA Co., Ltd. mix. COMA supplied PBT plastic supplied PBT-30GF plastic from Lanxess (Germany) from India/China. PA6 resins are supplied by MoSuCo Co., Ltd. of LiBoLon plastic company originating from Hong Kong. PBT, PA6, and PBT-30GF are mixed in the proportions in Table 1 and dried at 110 °C for about 2 to 4 hours, with a moisture content of less than 0.03%, using an injection molding method with a Toshiba 100-ton plastic injection machine.

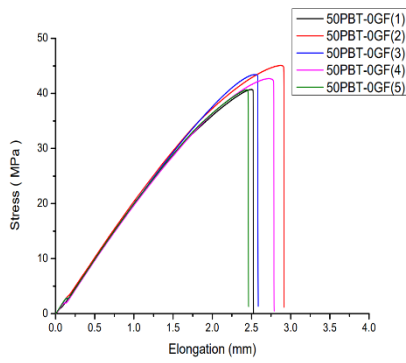
Table 1. PBT/PA6/GF mixture ratio

Sample	PBT (wt.%)	PA6 (wt.%)	GF (wt.%)
0GF	50	50	0
9GF	45.5	45.5	9
12GF	44	44	12
15GF	42.5	42.5	15
18GF	41.5	41.5	18

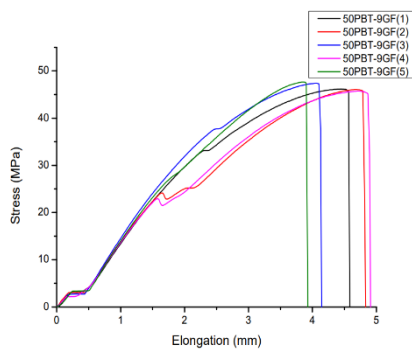
After injection molding, samples obtained at each rate proceed to ASTM D638 tensile strength measurement on Testometric materials testing machines. Randomly select five pieces for each scale, with 20 models to measure. Before proceeding with the size, ensure the measuring medium is at a temperature of 23 ± 2 °C and a relative humidity of $50 \pm 5\%$ in the air. In addition, laboratory samples need to be stored for at least 40 hours. Conduct measurement: First, enter the measurement parameters into the machine at a speed of = 5 mm/min. Next, clamp the sample tightly to the handle of the device. Next, measure tensile strength; the bracket moves until the model is completely damaged. Finally, record the test data of the sample and remove the piece from the grip. Proceed to repeat the sequence of steps for subsequent models.

RESULTS AND DISCUSSION

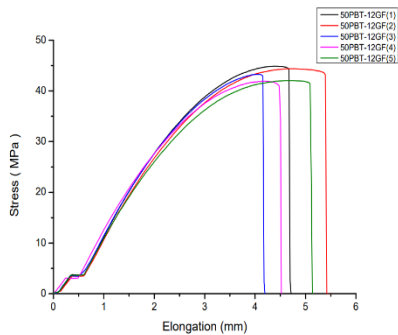
Figure 1 shows tensile stress and strain curve at scale. There is no difference between the fiberglass ratios added to the PBT/PA6 mixture. When the stress peak is reached, all samples immediately break, indicating that it has a brittleness similar to pure PBT. The PBT/PA6/0%GF chart shows that it is the fastest and most brittle compared to the rest of the samples, which indicates that adding fiberglass to the PBT/PA6 mixture results in a mixture with better mechanical properties.



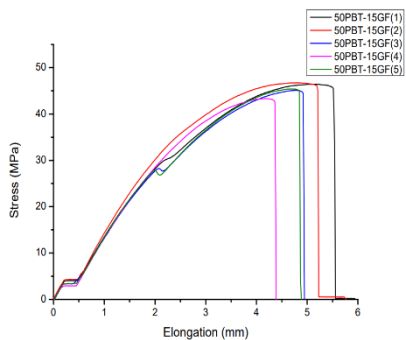
a) PBT/PA6/0%GF



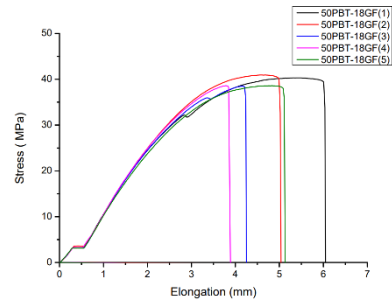
b) PBT/PA6/9%GF



c) PBT/PA6/15%GF



d) PBT/PA6/15%GF



(e) PBT/PA6/18%GF

Figure 1. Strain-stress curves of the samples

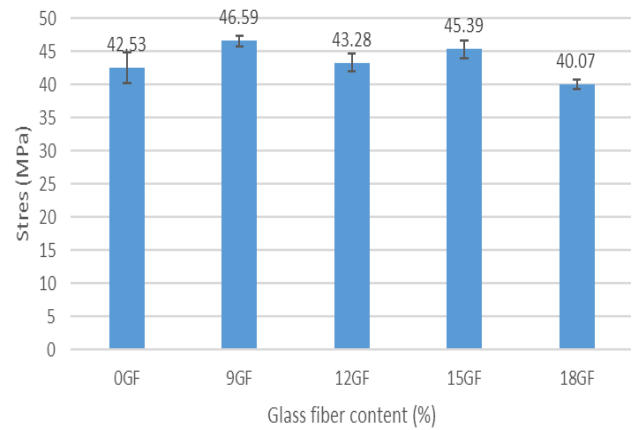


Figure 2. Average tensile strength of PBT/PA6/GF models.

Figure 2 shows that the mixture produces little difference. We see that three samples, PBT/PA6/9%GF, PBT/PA6/12%GF, and PBT/PA6/15%GF, give results ranging from 43 MPa to 47 MPa relatively evenly, but by the PBT/PA6/18%GF model, the tensile strength has shown signs of reduction but not significant. These results suggest that PBT composites are strongly affected by fiberglass added to the mixture.

CONCLUSION

The effect of fiberglass content in PBT/PA6/GF mixtures on tensile strength has been investigated, and the following conclusions have been drawn. Adding fiberglass to the PBT/PA6 mixture with a ratio of 50/50 gives relatively stable and effective results. However, the sample still inherits the disadvantages of PBT in that it is brittle like that of PBT when the stress peak is reached. There is no sign of stretching but breaking immediately; instead, adding fiberglass makes the mixture stable and inherits many good mechanical properties of fiberglass. The higher the fiberglass content mechanical properties, the

better. This result can make PBT and PA6 recycling more effortless.

Acknowledgment

This work belongs to the project in 2023, funded by Ho Chi Minh City University of Technology and Education (HCMUTE), Vietnam. We acknowledge HCMUTE and Material Testing Laboratory. They were permitted to join their group and use their equipment for study. We also acknowledge the assistance of the IWNA 2023 Committee in sharing our study. With their appreciated support, it is possible to conduct this research.

References

- [1] W. Baolong, W. Di, Z. Lien, J. Zheng, Z. Kai, *High-Density Polyethylene-Based Ternary Blends Toughened by PA6/PBT Core-Shell Particles*, *Polymer-Plastics Technology and Engineering*, **56** (2017) 1908-1915.
- [2] D. Bin, Lv Hanxiao, S. Shixin, S. Shulin, Zhang Huixuan, *Modification of the reactive core-shell particles properties to prepare PBT/PC blends with higher toughness and stiffness*, *J. Polym. Res.* **85** (2017).
- [3] T. Lei, W. Lulin, C. Pingxu, F. Jinfeng, Xiao Peng, Ye Nanbiao, Zhang Mingqiu, *Toughness of ABS/PBT blends: The relationship between composition, morphology, and fracture behaviour*, *Journal of Applied Polymer Science* **135** (2018) 46051.
- [4] N. T. H Pham, *Characterization of virgin Poly(butylene Terephthalate) and recycled Poly(butylene Terephthalate) from toothbrush bristles*, *IOSR-JMCE* **18** (2021) 50-56.
- [5] E. Kuram, B. Ozcelik, F. Yilmaz, G. Timur, Z. M. Sahin, *The Effect of Recycling Number on the Mechanical, Chemical, Thermal, and Rheological Properties of PBT/ PC/ABS Ternary Blends: With and Without Glass-Fiber*. **18** (2021) 50-56.
- [6] J. Xiao, H. Yuan, Y. Ling, et al., *Fire retardant synergism between melamine and triphenyl phosphate in poly (butylene terephthalate)*, *Polymer degradation and stability* **91** (2006) 2093-2100.
- [7] F. Hui, F. Wu, *Nonisothermal crystallization kinetics of poly(butylene terephthalate)/ multiwalled carbon nanotubes nanocomposites prepared by in situ polymerization*, *Journal of Applied Polymer Science* **131** (2014) 40849.
- [8] Y. Wei, H. Lu, Q. Tai, et al., *Flame retardancy mechanisms of poly(1,4-butylene terephthalate) containing microencapsulated ammonium polyphosphate and melamine cyanurate*, *Polymers for Advanced Technologies* **22** (2011) 2136-2144.
- [9] K. Banik, G. Mennig, *Effect of mold temperature on the long-term viscoelastic behavior of polybutylene terephthalate*, **48** (2008) 957-965.
- [10] Kumar R., Kar K. K., Kumar V., *Studies on the effect of compatibilizers on mechanical, thermal and flow properties of polycarbonate/poly (butylene terephthalate) blends*, *Mater. Res. Express* **5** (2018) 015306.
- [11] W. Liu, W. Kuo, C. Chiang, F. Chang, *In situ compatibilization of PBT/PPO blends*, *European Polymer Journal* **32** (1996) 91-99.
- [12] Hao Y., Bian J., Yang H. et al., *Effect of epoxy resin on the thermal, mechanical and rheological properties of polybutylene terephthalate/glycidyl methacrylate functionalized methyl methacrylate-butadiene blend*, *Chem. Res. Chin. Univ.* **32** (2016), 140-148.
- [13] Shuidong Z., Lingcao T., Jizhao L., Hanxiong H., Guo J., *Relationship between structure and properties of reprocessed glass fiber reinforced flame retardant poly(butylene terephthalate)*, *Polymer Degradation and Stability* **105** (2014) 140-149.
- [14] Ramani A., Dahoe A. E., *On the performance and mechanism of brominated and halogen free flame retardants in formulations of glass fibre reinforced poly(butylene terephthalate)*, *Polymer Degradation and Stability* **104** (2014) 71-86.
- [15] Kempel F., Scharrel B., Linteris G. T., Stoliarov S. I., Lyon R. E., Walters R. N., Hofmann A., *Prediction of the mass loss rate of polymer materials: Impact of residue formation*, *Combustion and Flame* **159** (2012) 2974-2984.

BACTERICIDAL ACTIVITY OF CLOVE BASIL ESSENTIAL OIL MICROEMULSION ON *Aeromonas hydrophila*

Phuong Hong Lam, Mai Thị Le, Huyen Da Nguyen Vo, Dung My Thi Dang, Chien Mau Dang

Institute for Nanotechnology, Community 6, Linh Trung Ward, Thu Duc City, Ho Chi Minh City, Vietnam;

Vietnam National University Ho Chi Minh City, Ho Chi Minh City, Vietnam

Email: dtmdung@vnuhcm.edu.vn

ABSTRACT

In this experiment, clove basil essential oil was prepared in microemulsion and its bactericidal activity was evaluated on *Aeromonas hydrophila*, a common bacterial species that causes hemorrhagic disease in catfish. The results demonstrated that the prepared microemulsion was an oil-in-water type, characterized by transparency, a particle size of 44 nm with a low PDI of 0.21. Furthermore, the clove basil essential oil microemulsion had bactericidal activity on *A. hydrophila* with a minimum inhibitory concentration (MIC) of 1.25 % (v/v). This showed the potential application of clove basil essential oil microemulsion to prevent bacterial diseases in catfish, especially the disease caused by *Aeromonas hydrophila*.

Keywords: clove basil, microemulsion, *Aeromonas hydrophila*, bactericidal activity, MIC.

INTRODUCTION

Aeromonas hydrophila a well-known opportunistic pathogenic bacterium commonly found in freshwater fish. It causes infection following injury to fish or when fish have to suffer environmental stressors or another major pathogen [1]. *A. hydrophila* is a gram-negative rod, with motility thanks to a single polar flagellum and the size of $0.3\text{-}1.0\ \mu\text{m} \times 1.0\text{-}3.5\ \mu\text{m}$, belonging to the genus *Aeromonas*, the family *Aeromonadaceae* [2]. The pathogenesis of *A. hydrophila* is related to multiple virulence factors including biological activities, adhesion to organs and extracellular factors such as enzymes and toxins [3]. Diseases caused by *Aeromonas* sp. in fish often manifest in different forms: skin and muscle necrosis, red hemorrhagic spots on skin and fin, fin rays truncated and destroyed, scales blistered and peeled off [1]. Abdominal sinuses are swollen and contain fluid, internal organs are hemorrhagic, and intestines are inflamed and filled with flatulence [1].

Currently, antibiotics or antiseptics have shown less effectiveness in preventing disease caused by *Aeromonas* in fish [1], another more promising alternative is enhancing the immunity of fish through dietary supplements [1, 4] or the use of probiotics [1, 5]. Furthermore, the substitution of antibiotics with herbal essential oils is also a notable trend. *Ocimum gratissimum* (clove basil) is a popular herb in some tropical

countries, including Vietnam. It has several bio-active compositions such as eugenol, β -caryophyllene, camphor, linalool, and α -humulene [6, 7], which have shown good bactericidal activity in some previous experiments [8, 9]. Some studies also indicated that the bactericidal ability of essential oils was enhanced when synthesized in microemulsion and nanoemulsion forms. For instance, *Ocimum* sp. essential oil was encapsulated in a nanoscale led to enhanced antibacterial activity against tested microorganisms, including *Escherichia coli*, *Staphylococcus aureus*, and *Bacillus subtilis* [10].

Hence, this experiment aimed to assess the antibacterial potential of clove basil essential oil in microemulsion form against *Aeromonas hydrophila*. The findings provided a basis for developing alternative strategies to pharmaceutical products to prevent hemorrhagic diseases caused by *A. hydrophila* in catfish.

EXPERIMENTAL

Preparing clove basil essential oil microemulsion

The chemical compositions of clove basil essential oil used in this experiment were analyzed by gas chromatography-mass spectrometry (GC-MS). Based on several results before, in this experiment, clove basil essential oil microemulsion was prepared with the surfactant and co-surfactant of tween 20 (Sigma-Aldrich)

and propylene glycol (Sigma-Aldrich) (the mixed rate of 2:1). Clove basil essential oil and surfactant were stirred with the ratio of 1:4 at 700 rpm (room temperature) for 30 min. Subsequently, water was gradually added and continued to be stirred until the solution became transparent. The formed microemulsion was allowed to stabilize for 24 hours before evaluating the characteristics of the microemulsion. Droplet sizes and polydispersity index (PDI) were analyzed with a Horiba LB550 particle size analyzer. Electrical conductivity was measured using the Hemera system, and zeta potential was determined by ZetaPhoremeter-CAD. Turbidity was measured using a UV-Vis spectrophotometer at 502 nm. Microemulsion stability was assessed via a centrifugation test at 4000 rpm for 15 minutes, comparing turbidity before and after centrifugation [11].

Evaluating the bactericidal activity of clove basil essential oil microemulsion on *A. hydrophila*

The bactericidal ability of clove basil essential oil microemulsion against *Aeromonas hydrophila* was evaluated through MIC (minimum inhibitory concentration) and MBC (minimum bactericidal concentration) test. The *A. hydrophila* strain in this experiment was identified based on its biochemical characteristics. The specific colonies of *A. hydrophila* recovered on tryptone soya agar (TSA) (incubation at 35°C overnight) were mixed in 10 mL of NaCl 0.9% solution to achieve the suspension turbidity to be equivalent to 10⁸ CFU/mL. The clove basil essential oil microemulsion was mixed into tryptone soya broth (TSB) tubes (10 mL/tube) with a concentration range of 0 (control), 0.156, 0.312, 0.625, 1.25, 2.5, and 5.0 % (v/v). Besides, a test tube with propylene glycol and tween 20 at a concentration equivalent to their highest concentration in the microemulsion to assess their impact on the antibacterial activity of the microemulsion. The bacterial suspension was added to each test tube to reach the concentration of 10⁶ CFU/mL. All of the test tubes were incubated at 35 °C for 18-24 hours. To verify bacterial growth in all test tubes, 1 mL of each test tube's bacterial broth was spread onto TSA plates and incubated at 35°C for 18-24 hours. Observed bacterial growth in a series of test tubes and on TSA plates after incubation to determine MIC and MBC values. Examined the effects of clove basil essential oil microemulsion on bacteria via FESEM imaging following fixation of bacterial samples in a 2.5% glutaraldehyde solution.

RESULTS AND DISCUSSION

Formulating clove basil essential oil microemulsion

The major chemical compositions of clove basil essential oil are shown in Table 1.

Table 1. The major chemical compositions of clove basil (*O. gratissimum*) essential oil

The major compositions	% area
Eugenol	46.8 %
Methyl eugenol	5.1%
α-Caryophyllene	7.1%
β-Caryophyllene	31.8%
α-Pinene	2.7%
Eucalyptol	1.9%

The resulting clove basil microemulsion was pale yellow, and transparent with a particle size of approximately 44.03 ± 6.49 nm and a low polydispersity index (around 0.21), indicating good uniformity. Its electrical conductivity was 104.5 ± 0.7 μS/cm, confirming it as an oil-in-water microemulsion. Furthermore, the zeta potential was 14.85 mV, the turbidity was very low, less than 1% and after centrifuging the prepared microemulsion at 4000 rpm for 15 minutes, the solution was still transparent and not separated, the turbidity changed but still below 1%, exhibiting good stability.

Results of bactericidal activity of clove basil essential oil microemulsion on *A. hydrophila*

After 24 hours of incubation, test tubes with concentrations ranging from 0.156% to 0.625% (v/v) exhibited turbidity, while those with concentrations of 1.25% and higher remained transparent (Figure 1).

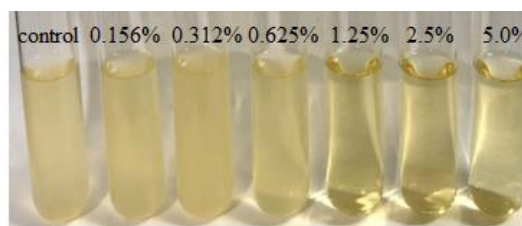


Figure 1. The MIC test tubes after incubating at 35°C for 24h

There was bacterial growth in the control tube and the test tube with tween 20 and propylene glycol. After spreading the suspension from each test tube on TSA and incubating for 24 hours, the growth of bacteria was observed in the disks corresponding to microemulsion concentrations of 0.625 % and lower (Figure 2). These results demonstrated that the clove basil essential oil

microemulsion effectively inhibits *A. hydrophila*, with a MIC and MBC of 1.25% (v/v).

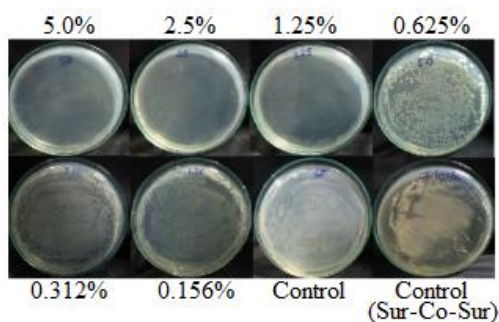


Figure 2. The plates were spread with the suspension from the MIC test tubes after incubating for 24 h.

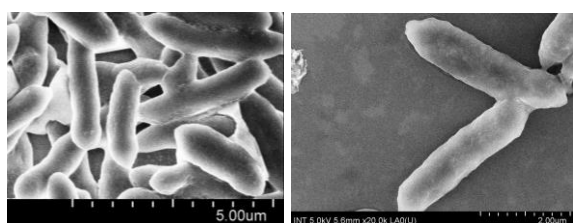


Figure 3. Normal *A. hydrophila* cells captured by FESEM

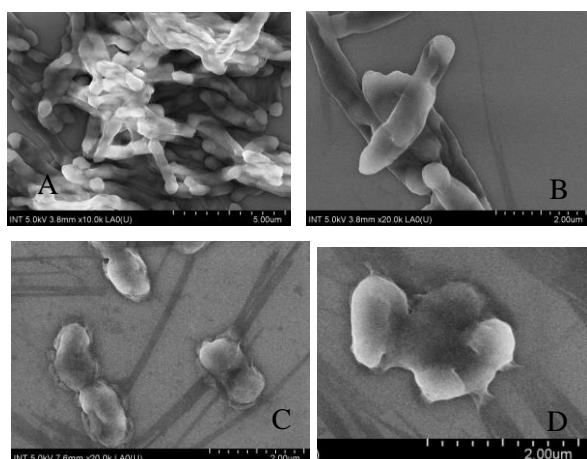


Figure 4. The *A. hydrophila* bacterial cells were treated by clove basil essential oil microemulsion at different concentrations (A, B: at 0.63%, C: at 1.25%, D: at 2.5 %).

FESEM images revealed morphological differences between normal bacterial cells and those treated with clove basil essential oil microemulsion at concentrations of 0.625%, 1.25% and 2.5%. Normal *A. hydrophila* cells appeared rod-shaped with smooth membrane surfaces and distinct edges (Figure 3). However, upon microemulsion treatment, most bacterial cells exhibited shrinkage, sunken surfaces, and a wrinkled appearance (Figure 4). In Figures 4A and

4B, bacterial cells treated with 0.625% clove basil essential oil microemulsion showed smaller cells with wrinkles and dents on the cell surface. Figure 4C illustrated that bacteria treated at a concentration of 1.25% exhibited cell deformation, and at 2.5%, cell structure was disrupted.

Ocimum gratissimum essential oil has antimicrobial effectiveness on both gram-negative and positive species thanks to the bio-active compounds. Eugenol and caryophyllene, which are the primary compositions of clove basil essential oil, could prevent adhesion, biofilm forms, and expression of virulent factors [12]. Eugenol disrupts the bacterial cell walls, increases membrane non-specific permeability, interferes with ions and ATP transport, and alters bacterial cell morphology. Furthermore, eugenol could inhibit enzymes of bacterial cells, which leads to disrupting bacterial metabolism and function [13]. Additionally, caryophyllene changes cell membrane permeability and integrity, resulting in membrane damage and intracellular component leakage, ultimately leading to cell death [14]. Other ingredients, like α -pinene and eucalyptol, have demonstrated antibacterial properties through similar mechanisms [15, 16]. Furthermore, synthesizing essential oils in microemulsion form with smaller sizes and a higher surface-to-volume ratio enhanced the efficient dispersion of the essential oil to target sites. These factors accounted for the antibacterial capability of the clove basil essential oil microemulsion and the morphological changes in bacteria upon exposure to it.

CONCLUSION

In this experiment, the clove basil essential oil microemulsion, an oil-in-water microemulsion containing 10% essential oil with a particle size of 44 nm (with PDI value of 0.21), demonstrated the ability to inhibit *A. hydrophila*, with MIC and MBC values of 1.25 % (v/v). Exposure to this microemulsion at the minimum inhibitory concentration and higher caused most bacterial cells to shrink and develop wrinkled surfaces with dents and lose their cell structure. These findings suggest the potential application of clove basil essential oil microemulsion in preventing hemorrhagic diseases caused by *A. hydrophila* in catfish.

Acknowledgment

This research is funded by Vietnam National University Ho Chi Minh City (VNU-HCM) under grant number 562-2022-32-01.

References

- [1] Semwal, A., A. Kumar, and N. Kumar, *A review on pathogenicity of Aeromonas hydrophila and their mitigation through medicinal herbs in aquaculture*. Heliyon, 9(3) (2023) e14088.
- [2] Percival, S.L. and D.W. Williams, *Chapter Three - Aeromonas, in Microbiology of Waterborne Diseases*, S.L. Percival, et al., (2014), Academic Press: London. 49-64.
- [3] Sun J, Zhang X, Gao X, Jiang Q, *Characterization of Virulence Properties of Aeromonas veronii Isolated from Diseased Gibel Carp (Carassius gibelio)*. International Journal of Molecular Sciences **17**(2016).
- [4] Hoseini, S., A. Mirghaed, and M. Ghelichpour, *Effects of dietary tryptophan levels and fish stocking density on immunological and antioxidant responses and bactericidal activity against Aeromonas hydrophila in rainbow trout (Oncorhynchus mykiss)*. Aquaculture Research **51**(2020).
- [5] Akbari H, Shekrabi SPH, *Effects of Potential Probiotic Enterococcus casseliflavus (EC-001) on Growth Performance, Immunity, and Resistance to Aeromonas hydrophila Infection in Common Carp (Cyprinus carpio)*. Probiotics and Antimicrobial Proteins **13**(5) (2021) 1316-1325.
- [6] N C Huong, T T K Ngan, *Physical and Chemical Profile of Essential oil of Vietnamese Ocimum gratissimum L*. IOP Conference Series: Materials Science and Engineering **736** (2020) 062010.
- [7] P N T Dung, T P Dao, *Extraction and analysis of chemical composition of Ocimum gratissimum L essential oil in the North of Vietnam*. IOP Conference Series: Materials Science and Engineering, **1092** (2021).
- [8] Mak, K.K, Kamal, M., *A comprehensive review on eugenol's antimicrobial properties and industry applications: A transformation from ethnomedicine to industry*. Pharmacognosy Reviews **13** (2019) 1.
- [9] Santos, E.L., *Enhanced antibacterial effect of antibiotics by the essential oil of Aloysia gratissima (Gillies & Hook.) Tronc. and its major constituent beta-caryophyllene*. Phytomedicine Plus **1**(4) (2021) 100100.
- [10] da Silva Gündel, S., *Basil oil-nanoemulsions: Development, cytotoxicity and evaluation of antioxidant and antimicrobial potential*. Journal of Drug Delivery Science and Technology **46**(2018) 378-383
- [11] Badawi, A.A., Nour, *Preparation and Evaluation of Microemulsion Systems Containing Salicylic Acid*. AAPS PharmSciTech **10** (2009) 1081–1084.
- [12] Hu Q, Zhou M, *Progress on the Antimicrobial Activity Research of Clove Oil and Eugenol in the Food Antisepsis Field*. J Food Sci **83**(6) (2018) 1476-1483.
- [13] A. Marchese, R. Barbieri, *Antimicrobial activity of eugenol and essential oils containing eugenol: A mechanistic viewpoint*. Crit Rev Microbiol. 2017 Nov; **43**(6) (2017) 668-689.
- [14] Moo CL, *Antimicrobial activity and mode of action of 1,8-cineol against carbapenemase-producing Klebsiella pneumoniae*. Sci Rep, (2021) 20824.
- [15] Borges MFdA, *Potential Antibacterial Action of α -Pinene*. Medical Sciences Forum **12** (1) (2022) 11.
- [16] Martínez-Pabón, *Thymol, menthol and eucalyptol as agents for microbiological control in the oral cavity: A scoping review*. Revista Colombiana de Ciencias Químico - Farmacéuticas **49**(1) (2020).

LOW-COST AND GOOD PERFORMANCE SERS SUBSTRATES BASED ON POLYDIMETHYLSILOXANE (PDMS) AND SILVER NANOPARTICLES

Nguyen Thuy Ngoc Thuy^{1*}, Tran T. T. Van^{2,3}, Tran Luu Minh Hieu¹, Tran Hoang Tan¹

¹Faculty of Applied Sciences, HCMC University of Technology and Education

²Faculty of Materials Science and Technology, University of Science

³Vietnam National University, Ho Chi Minh City, Vietnam

*Email: thuyntn@hcmute.edu.vn

ABSTRACT

Surface-enhanced Raman scattering (SERS) substrates have been widely investigated recently due to high potential application in many fields such as bio-chemical sensors, food-safety, environment, etc. The ability for enhancing Raman intensity of targeted-molecules makes SERS effectively detect molecule at very low concentration. The advantage of polymer SERS substrate is low-cost and flexible. In this study, polydimethylsiloxane (PDMS) SERS substrate have been developed successfully based on silver nanoparticles and high-roughness PDMS surface structure. For Raman intensity enhancement, PDMS surface need to have enough high-roughness to keep silver nanoparticles on its surface and reduce the light reflection. For this purpose, PDMS solution was poured onto high-roughness aluminum substrate which has modified-surface by electrochemical method. After baking, PDMS was detached to aluminum substrate. Then, the silver nanoparticles were prepared on the PDMS surface. Finally, the Raman measurement of Rhodamine B have been analysis. The results show that it is possible to detect Rhodamine B on this PDMS SERS substrate at low concentration of 0.1 ppm.

Keywords: surface-enhanced Raman scattering (SERS), polydimethylsiloxane (PDMS)

INTRODUCTION

Surface-enhanced Raman scattering (SERS) is an effective technique to detect substances at very low concentration [1,2]. The ability for enhancing Raman scattering is due to the plasmonic effect of metal nanoparticles [6] (silver, gold, etc) combined with micro/nano 3D-structure surface. The SERS substrate based on polymer material substrate, especially polydimethylsiloxane (PDMS), have many advantages that is the reason to get attention for research recently [3,4,5]. There are a lot of ways to make micro/nano 3D-structure on PDMS substrate such as using plasma treatment or based on other micro/nano 3D-structure surface.

In this work, Aluminum has surface-treatment by electrochemical method firstly. Then nano 3D-structure PDMS substrate was fabricated following treated Aluminum. Finally, the SERS substrate was developed by covering silver nanoparticle (Ag-NPs) on the nano 3D-structure surface of PDMS substrate. The Raman spectra of Rhodamine B at low concentration has been analysis for surface-enhanced Raman scattering purpose.

EXPERIMENTAL

The Ag-NPs were fabricated by chemical reduction method using reduction agent ethylene glycol (EG), Silver nitrate AgNO_3 , and polyvinylpyrrolidone (PVP). The results show the Ag-NPs spherical shape has diameter from 40-60 nm. The Aluminum has surface-treatment by electrochemical in two steps to make uniform nano 3D-structure on the surface. The first step in sulfuric acid and the second step in oxalic acid. After that, the PDMS was fabricated as shown in Figure 1. Firstly, the prepolymer and the curing agent (Sylgard 184, Dow Corning) was mixed at a 20:1 weight ratio, degassing for 1 h in vacuum, casting the mixture into an Aluminum surface-treatment substrate, then curing in a hot plate for 40 mins at 90 °C, and finally manually peeling off PDMS membranes. After that, Ag-NPs were deposited on the PDMS membranes by dropped-casting and then curing in a hot plate for 30 mins at 50 °C to make PDMS SERS substrate.

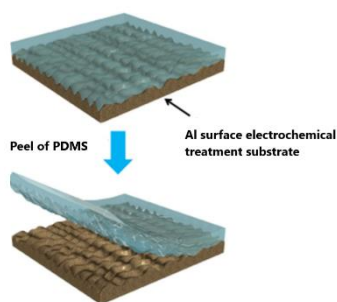


Figure 1. The fabrication of PDMS substrate with nano 3D-structure surface from Aluminum electrochemical surface-treatment substrate.

RESULTS AND DISCUSSION

Figures. 2 show the OM images of Aluminum surface before (a) and after (b) electrochemical treatment. It's clearly to see that on the Al surface, there is a uniform 3D-structure formation after electrochemical treatment.

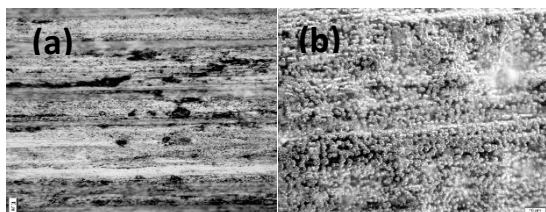


Figure 2. The OM images of aluminum surface before (a) and after (b) electrochemical treatment.

Figure 3(a) shows SEM image of PDMS surface. The PDMS surface have nano 3D-structure that have been useful to keep Ag-NPs from slipping and reduce the light reflection. Figure 3(b) shows SEM image of PDMS surface with covering Ag-NPs. To improve the adhesion and uniform dispersion of Ag-NPs on PDMS surface, the PDMS was treated by oxygen plasma.

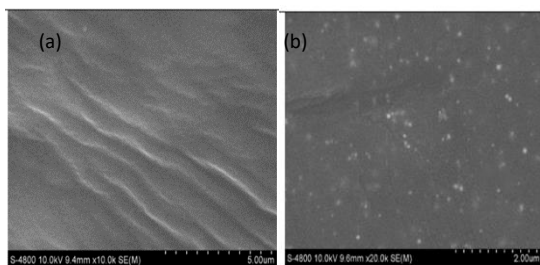


Figure 3. The SEM images of PDMS substrate (a) and with Ag-NPs coating (b)

Figures. 4 show the Raman spectra of Rhodamine B with various concentration 10 ppm, 1 ppm, and 0.1 ppm. According to this result, the

SERS has ability to detect Rhodamine B at low concentration of 0.1 ppm.

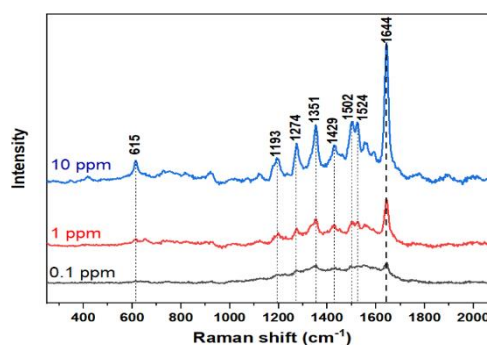


Figure 4. Raman spectra of Rhodamine B with different concentration.

CONCLUSION

In summary, the SERS substrate has been developed by depositing Ag-NPs on nano 3D-structure PDMS substrate that is fabricated from Aluminum electrochemical surface treatment. The surface-enhanced Raman scattering is observed by analysis Raman spectra of Rhodamine B at low concentration of 0.1 ppm.

Acknowledgment

This work was supported by the Ho Chi Minh City University of Technology and Education.

References

- [1] Nguyen Thuy Ngoc Thuy, Huynh Nguyen Thanh Luan, Van Vo Kim Hieu, Mai Thi Thanh Ngan, Nguyen Tri Trung, Le Vu Tuan Hung, and Tran T. T. Van, *Optimum fabrication parameters for preparing high performance SERS substrates based on Si pyramid structure and silver nanoparticles* RSC Adv., 11 (2021) 31189.
- [2] S. M. Kong, D. Shin, J. W. Oh, H. Park, J. S. Lee, N. I. Won, Y. H. Na, *One-pot platform for the collection and detection of nanoparticles: Flexible surface-enhanced Raman scattering (SERS) substrates with nano-pore structure*, Chemical Engineering Journal, **471**(1) September (2023) 144753.
- [3] Y. Zhang, Y. Wang, A. Liu, S. Liu, *Fabrication of flexible SERS substrate based on Au nanostars and PDMS for sensitive detection of Thiram residue in apple juice*, Spectrochimica Acta Part A: Molecular and Biomolecular Spectroscopy, **297**(5) (2023) 122721.
- [4] S. Lin, W. Hasi, S. Han, X. Lin and L. Wang, *A dual-functional PDMS-assisted paper-*

- based SERS platform for the reliable detection of thiram residue both on fruit surfaces and in juice*, *Anal. Methods*, **12** (2020) 2571-2579.
- [5] C. Novara, S. D. Marta, A. Virga, A. Lamberti, A. Angelini, A. Chiado, P. Rivolo, F. Geobaldo, V. Sergo, A. Bonifacio, and F. Giorgis, *SERS-Active Ag Nanoparticles on Porous Silicon and PDMS Substrates: A Comparative Study of Uniformity and Raman Efficiency*, *J. Phys. Chem. C* **120**(30) 16946–16953.
- [6] Y. Guo, J. Yu, C. Li, Z. Li, J. Pan, A. Liu, B. Man, T. Wu, X. Xiu, and C. Zhang, *SERS substrate based on the flexible hybrid of polydimethylsiloxane and silver colloid decorated with silver nanoparticles*, *OPTICS EXPRESS*, **26**(17) (2018) 21784.

TITANIUM DIOXIDE NANOPARTICLES IN ANTIBACTERIAL AND SELF-CLEANING EFFECTS APPLICATION

Dang Monica^{1,2,3}, Chinh Dung Trinh^{2,3}, Chien Mau Dang^{2,3}

¹ Gifted high school, Ho Chi Minh City, Vietnam

² Institute for Nanotechnology, Community 6, Linh Trung Ward, Thu Duc City, Ho Chi Minh City, Vietnam;

³ Vietnam National University Ho Chi Minh City, Ho Chi Minh City, Vietnam

Email: monica.d.int@gmail.com

ABSTRACT

The TiO₂ nanoparticles are obtained using wet chemical method at room temperature. The proportion of acetic acid affect the absorption and dispersion of the TiO₂ nanoparticles in the solution. The TiO₂ nanoparticles were in an anatase phase with the particle size of less than 10 nm. The absorption of TiO₂ solution was in a wavelength range 300 - 330 nm. The TiO₂ solution's antibacterial and self-cleaning effects are oriented towards manipulating practical coating on materials' surface (stainless steel medical instruments, office glass and more). In the study, TiO₂ coating film on stainless steel and glass substrate perform effective degradation of methylene blue 0.1 M within 30 minutes under direct day light exposure.

INTRODUCTION

The possible applications of TiO₂ nanoparticles on the subject of photocatalytic disinfection published in 1985 has increased the use of TiO₂ nanoparticles in photodynamic therapy studies. In recent years, researchers are focused on TiO₂ nanoparticles' applications as photosensitizing agents in photodynamic inactivation of antibiotic-resistant bacteria [1-5]. TiO₂ nanoparticles themselves, as well as their composites, combinations, or hybrids with other molecules, were successfully tested as photosensitizers in photodynamic therapy [6-8].

Titanium dioxide nanoparticles, also known as nanocrystalline titanium dioxide or ultrafine titanium dioxide, are particles of titanium dioxide with diameters less than 100 nm [9,10]. Titanium minerals are mainly rutile, anatase, and brookite with the titanium content of 94 - 99%, 90 - 95% and 90 - 100% respectively [11-20]. This present study is to investigate the antibacterial and self-cleaning effects of the TiO₂ nanoparticles.

EXPERIMENT

2.1 Synthesis of TiO₂ nanoparticles

All of the chemicals were analytical grade. 1mL of acetic acid CH₃COOH (99.5%, M = 60, d = 1.05 g/cm³, Merck) is added into 30 mL Ethanol

CH₃CH₂OH (99.5%, M = 46, d = 0.793 g/cm³, Merck) at room temperature. Then, 1 mL Tetraisopropylorthotitanate Ti(OC₃H₇)₄ (M = 284.25 g/mol, d = 0.96 g/ml, Merck) is slowly added dropwise into the solution.

2.2 Preparation of TiO₂ coating

A thin layer of photocatalytic TiO₂ nanoparticles was deposited on glass substrate. Before coating, glass slids (2.5 x 10 cm) were ultrasonically cleaned and washed thoroughly. The coated glass substrate is heated at 300°C for 2 hours.

2.3 Characterization

The asorbance of the TiO₂ nanoparticles was measured by Varian's Cary 100, UV-Visible spectrophotometer in the range from 200nm - 1100 nm. The TiO₂ nanoparticle's pore size is measured by Horiba's Laser Particle Size Analyzer LB 550, dynamic range varies from 1-6000 nm. The Raman spectrum is measured by JOBINYVON's LABRAM 300.

RESULTS AND DISCUSSION

The proportion of acetic acid on TiP (α = TiP/CH₃COOH) was modified in an increasing direction, the corresponding samples were collected with α = 0; 0.5; 1; 1.5; 2.0.

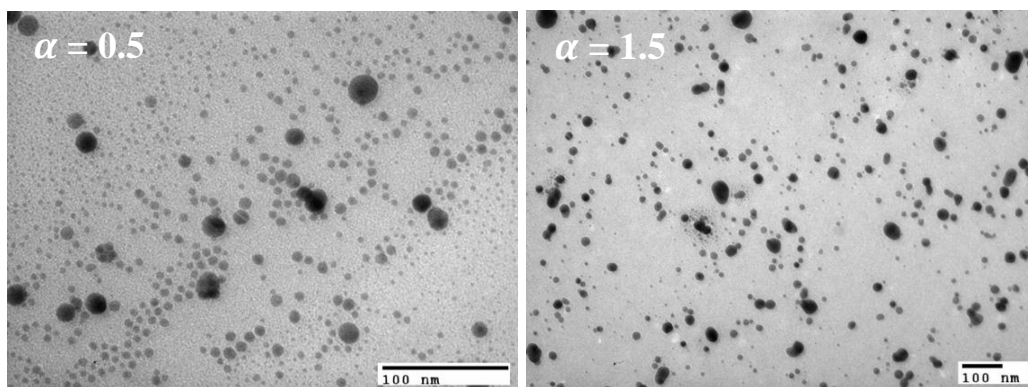


Figure 1. TEM micrographs of TiO_2 nanoparticles synthesized with $\alpha = 0.5, 1.5$.

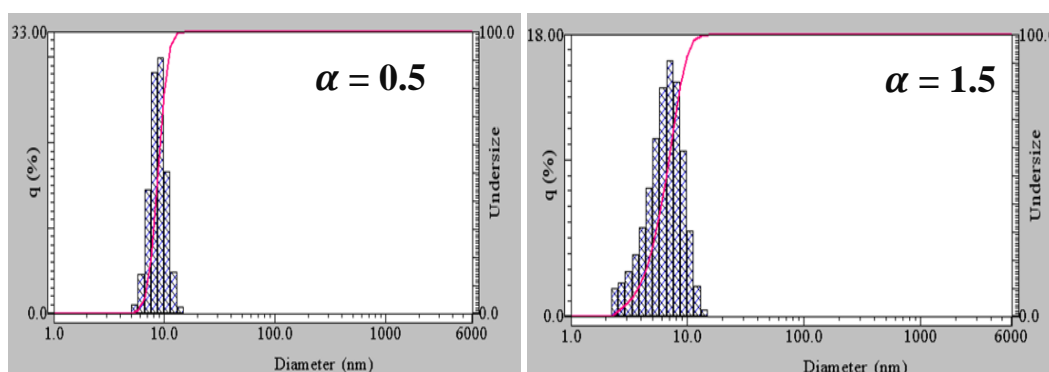


Figure 2. The size distribution diagram of TiO_2 nanoparticles synthesized with $\alpha = 0.5, 1.5$.

The TEM images (**Figure 1**) and particle size distribution chart (**Figure 2**) of two representative samples $\alpha = 0.5$ and $\alpha = 1.5$ show the particle size variation between 6 – 10 nm. Specifically, $\alpha = 1.5$'s size is distributed between 8 – 10 nm, and $\alpha = 2.0$'s is 6 – 8 nm.

The Raman spectrum results of sample $\alpha = 1.5$ and $\alpha = 2.0$ illustrate the existence of 4 raman modes' frequencies: 163 cm^{-1} , 408 cm^{-1} , 523 cm^{-1} , 651 cm^{-1} in respective of 4 oscillations: Eg, B1g, A1g and E1g of TiO_2 nanoparticles (**Figure 3**). However, there are minor errors in these peaks compared to the standard ones. This can be explained by the formation of the anatase phase of TiO_2 nanoparticles.

The UV-Vis results of 5 samples $\alpha = 0; 0.5; 1; 1.5; 2.0$ show the appearance of CH_3COOH helps establish the TiO_2 nanoparticles' UV

intensity wavelength between 280 – 340 nm (**Figure 4 (a)**). The sample $\alpha = 0$ (CH_3COOH excluded) has no UV absorbance region but has an intensity peak at ~ 410 nm. This may not be caused by the absence of TiO_2 nanoparticles, but rather by a formation of a chemical radical in the solution. The intensity at UV wavelength of $\alpha = 2.0$ sample being lower than the other peaks indicates the degradation of the TiO_2 nanoparticle's absorbing ability in the solution compared to other samples. An excessive amount of acid at $\alpha = 2.0$ had degraded the absorbing ability in the solution of the TiO_2 nanoparticle.

The results of Raman spectrum, UV-Vis and Tem have shown that $\alpha = 1.5$ is the most adequate sample for our method in collecting TiO_2 nanoparticles.

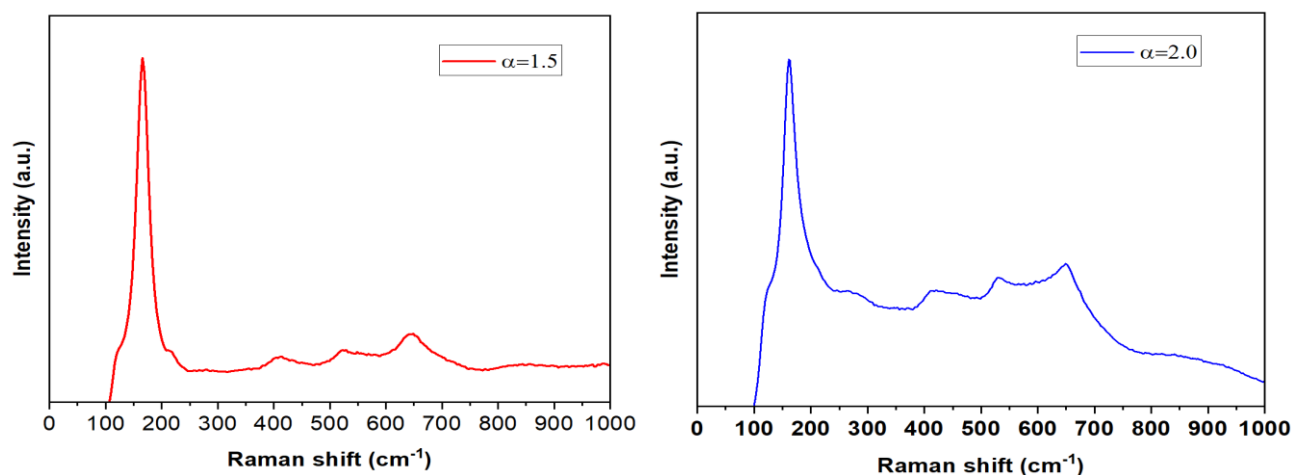


Figure 3. The Raman spectrum of TiO_2 nanoparticles synthesized with $\alpha = 1.5$ and 2.0 .

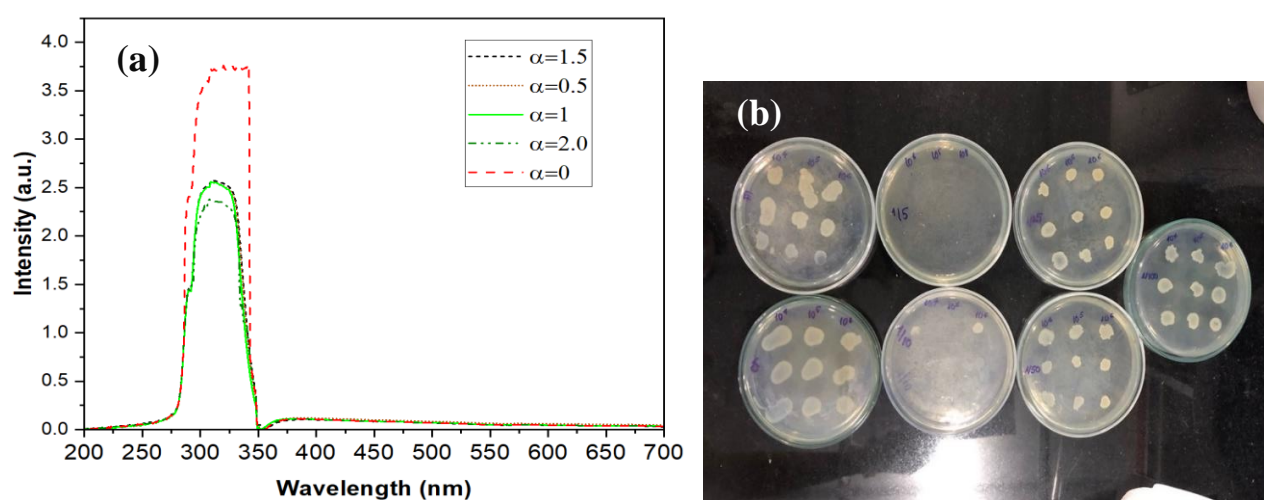


Figure 4. The UV-Vis spectra of TiO_2 nanoparticles synthesized with $\alpha = 0; 0.5; 1; 1.5$ and 2.0 (a). Photographs of antibacterial test against *Escherichia Coli* bacteria (agar-well diffusion method) for TiO_2 nanoparticles (b).

Figure 4 (b) is the result of TiO_2 nanoparticle's antibacterial effect. The experiment is based on the sample $\alpha = 1.5$ and *Escherichia Coli* bacteria (*E. coli*). The process includes preparing THA environment, petri plates, sterile steam them. The bacterial suspension is diluted – dilute bacteria into saline solution 0.9 % (the bacteria is cultured in THA environment for 24 hours). Then, the turbidity of the bacterial suspension is compared to Mc Farland 0.5 and is serially diluted into 10⁶, 10⁵, 10⁴ CFU/mL. The experiment begins with pouring into each plate the sample with respective concentrations of 0.3 M; 0.15 M; 0.006 M; 0.003 M; 0.0015 M and 10 mL THA (leave cool until 50 °C to reach the test concentrations). After the THA is cooled, at each concentration, drop 5 microlitres of bacteria at 10⁴, 10⁵, 10⁶ CFU/mL, each drop is added 3 times. The

experiment was repeated 3 times. Results have shown that the minimum Inhibitory Concentration (MIC) is 0.3 M.

CONCLUSION

TiO_2 nanoparticles are obtained using wet chemical method at room temperature. The proportion of acetic acid affect the absorption and dispersion of the TiO_2 nanoparticles in the solution. The TiO_2 nanoparticles were in an anatase phase with the particle size of less than 10 nm. The absorption of TiO_2 solution was in a wavelength range 300 - 330 nm. The TiO_2 solution's antibacterial and self-cleaning effects are oriented towards manipulating practical coating on materials' surface (stainless steel medical instruments, office glass and more). In the study, TiO_2 coating film on stainless steel and glass substrate perform effective degradation of

methylene blue 0.1 M within 30 minutes under direct day light exposure. TiO₂ solution with concentration at 0.3 M has the ability to inhibit E. coli bacteria.

Acknowledgment

The authors are very grateful to Vietnam National University Ho Chi Minh City (VNUHCM) for financial support this work under grant number TX2023-32-01.

References

- [1] Hark Karkee, Alexander Gundlach-Graham 2023 *Environmental Science & Technology* **57** 37.
- [2] Pamela Santos-Aguilar, Judith Bernal-Ramírez, Eduardo Vázquez-Garza, Lydia Yerid Vélez-Escamilla, Omar Lozano, Gerardo de Jesús García-Rivas, Flavio F. Contreras-Torres 2023 *ACS Omega* **8** 21.
- [3] Jing Li, Jiawei Dong, Yanshan Huang, Jiana Su, Yu Xie, Yundang Wu, Wei Tang, Yongtao Li, Weilin Huang, Chengyu Chen. 2022 *Environmental Science & Technology* **56** 23.
- [4] Ding, Yong, Bin Ding, Hiroyuki Kanda, Onovbaramwen Jennifer Usiobo, Thibaut Gallet, Zhenhai Yang, Yan Liu et al 2022 *Nature Nanotechnology* **17** 6.
- [5] Nabi, Iqra, Kejian Li, Hanyun Cheng, Tao Wang, Yangyang Liu, Saira Ajmal, Yang Yang, Yiqing Feng, and Liwu Zhang 2020 *Iscience* **23** 7.
- [6] Ajmal, N., Saraswat, K., Bakht, M. A., Riadi, Y., Ahsan, M. J., & Noushad, M. 2019 *Green Chemistry Letters and Reviews* **12** 3.
- [7] Kim, M. G., Kang, J. M., Lee, J. E., Kim, K. S., Kim, K. H., Cho, M., & Lee, S. G. 2021 *ACS omega*, **6** 16.
- [8] Maiti, M., Sarkar, M., Maiti, S., Malik, M. A., & Xu, S. 2020 *Journal of Cleaner Production* 255.
- [9] Khashan, K. S., Sulaiman, G. M., Abdulameer, F. A., Albukhaty, S., Ibrahim, M. A., Al-Muhimeed, T., & AlObaid, A. A. 2021 *Applied Sciences*, **11** 10.
- [10] Xing, Y., Li, X., Guo, X., Li, W., Chen, J., Liu, Q., ... & Bi, X. 2020 *Nanomaterials* **10** 7.
- [11] Akhtar, S., Shahzad, K., Mushtaq, S., Ali, I., Rafe, M. H., & Fazal-ul-Karim, S. M. 2019 *Materials Research Express*, **6** 10.
- [12] Tichapondwa, S. M., Newman, J., & Kubheka, O. 2020 *Physics and Chemistry of the Earth, Parts a/B/C* 118–119.
- [13] Ismael, M. 2020 *Journal of Environmental Chemical Engineering*, **8** 2.
- [14] Singh, J., Juneja, S., Soni, R. K., & Bhattacharya, J. 2021 *Journal of Colloid and Interface Science* **590** 60-71.
- [15] Nasikhudin, Diantoro, M., Kusumaatmaja, A., & Triyana, K. 2018 In *Journal of Physics: Conference Series* **10** 11.
- [16] Anandgaonker, P., Kulkarni, G., Gaikwad, S., & Rajbhoj, A. 2019 *Arabian Journal of Chemistry* **12** 8.
- [17] Sathiyar, K., Bar-Ziv, R., Mendelson, O., & Zidki, T. 2020 *Materials Research Bulletin* 126.
- [18] Seneviratne, K. L., Munaweera, I., Peiris, S. E., Peiris, C. N., & Kottegoda, N. 2021 *Iranian Journal of Catalysis*, **11** 3.
- [19] Malakootian, M., Nasiri, A., & Amiri Gharaghani, M. 2020 *Chemical Engineering Communications* **207** 1.
- [20] Hajizadeh, H., Peighambaroust, S. J., Peighambaroust, S. H., & Peressini, D. 2020 *Journal of food science*, **85** 4.

BIOMASS-BASED POLYURETHANE NANOCOMPOSITE MATERIALS: SYNTHESIS, PHYSICO-MECHANICAL PROPERTIES, AND FIRE-RESISTANCE

Thanh N. Phan-Huynh, Tuyet Minh Nguyen-Ha, Tuan An Nguyen, Lam H. Pham, Khoa T.D. Nguyen, Quoc Doan Tran, Nhat Thong Tran, Minh Tri Le-Phuoc, My Trinh Nguyen, and DongQuy Hoang

Faculty of Materials Science and Technology, University of Science, Vietnam National University, Ho Chi Minh City 700000, Viet Nam

Email: thanhphn.h.1720@gmail.com; hdtquy@hcmus.edu.vn

ABSTRACT

In this study, liquefied bio-polyol from bamboo powder was used in bio-based rigid polyurethane foams (B-PU) incorporating nano silica (3 – 7 php) and different environmentally halogen-free flame retardants (FRs) including aluminum diethyl phosphinate, diammonium phosphate, and aluminum trihydroxide. The purpose of this study was to investigate the influence of nano silica and flame retardants on cell structure, flammability, thermal properties as well as apparent density, and mechanical and others property of B-PU. B-PU with optimized nano silica and additives had an LOI value above 21% and passed the V-0 rating. The cone calorimeter test indicated that the peak heat release rate of the nanocomposite foams in the presence of FRs was reduced by 32.37–41.68% compared to that of neat B-PU nanocomposite. Moreover, thermal properties of flame-retardant nanocomposite foams, compared to neat B-PU, were significantly improved. Finally, the B-PU foam and its nanocomposites demonstrated effective thermal insulation with a low thermal conductivity range when compared with other current bio-based insulation panels. The findings of this research hold significant implications for the progress in fabricating polyurethane nanocomposites derived from biomass resources, which exhibit great flame retardancy and high insulation performance, possess heightened thermal stability, and align with the ongoing path of sustainable development investigations.

Keywords: Insulation performance, Flame retardancy, Functional bio-polyurethane nanocomposite, Sustainable PU nanocomposite foam, Bamboo-liquefied bio-polyol.

1. INTRODUCTION

Rigid polyurethane foams (PUFs) are of interest in the construction, buildings, and transportation sectors due to their effective thermal insulation performance [1]. However, one of their disadvantages is great dependence on fossil sources, which are increasingly depleted, polluting, and non-recyclable. Accordingly, numerous studies have been focused on the substitution of petro-based polyols by renewable resources such as bio-polyols from vegetable oil [2-4] and also from lignocellulosic biomass [5-8]. However, PUFs synthesized from bio-polyols often exhibit some disadvantages, which cause some limitations in their application. Researchers have recently developed nanosilica reinforcers from rice husk waste to improve the properties of PUFs matrix, including mechanical properties, thermal stability, and dimensional stability, even at low contents. [9,10]. Furthermore, the

flammable characteristic of polyurethane foams has limited their applicability. According to our statistics, until now, no publication investigating the flame retardancy of biobased PUFs from bamboo-based polyols has been reported. Therefore, this paper focuses on evaluating the physical-chemical properties, thermal stability, and fire-retardant performance of biobased PUFs from bamboo-based polyols reinforced with nanosilica and three friendly flame retardants additives (aluminum hydroxide (ATH), aluminum diethylphosphinate (OP), and diammonium hydrogen phosphate (DAP) using recent techniques including cone calorimetry, combustion test, morphology, and thermal analysis.

2. EXPERIMENTAL

2.1. Material

Methylene diphenyl diisocyanate (MDI) and polyol (C-polyol) (Dow Chemical, China). Silicone oil (BYK, Germany). Dibutyltin dilaurate (DBDL) and triethylamine (TEA) (Merck, Germany). Aluminum diethyl phosphinate (OP, Clariant, Germany), aluminum trihydroxide (ATH, Guangdong, China), and diammonium phosphate (DAP, Guangdong, China). Nano silica and bio-polyol were synthesized in the laboratory [6,11].

2.2. Preparation of flame-retardant B-PU nanocomposites

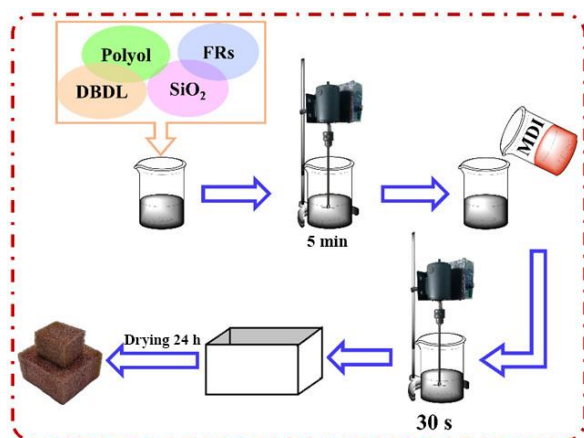


Fig. 1. Synthesis process of PU nanocomposite

The one-shot and free rise technique were used to prepare nanocomposite foams. First, polyol, bio-polyol, DBDL, nano SiO₂, and FR were stirred in a metal cup at 1000 rpm for 5 min. Next, MDI

was added by continuously stirring for 30 s, then quickly poured into a paper mold (70 × 70 × 140 mm) and let it expand freely. Finally, the nanocomposite foams were dried for 24 h. B-PU without nano SiO₂ / FR were prepared by the same procedure.

2.3. Characterization method

The morphology of nanocomposite foams was investigated using scanning electron microscopy (SEM, Hitachi S-4800, Tokyo, Japan). The apparent density of B-PU and B-PU nanocomposites was measured according to ASTM D1622. The compression properties of all foams were determined using a universal testing machine (Shimadzu – Autograph ASH-X, Japan) according to ASTM D1621. The evaluation was based on the ASTM D3801 standard for vertical burning (UL-94V) and ASTM D635 for horizontal burning (UL-94HB). The assessment of flammability performance was also conducted on block specimens with dimensions of 50 × 50 × 25 mm. Limited oxygen index (LOI, Qualitest, USA) testing following ASTM D2863. Thermogravimetric analysis (Q50 Universal V4.5A TA instrument, USA).

3. RESULTS AND DISCUSSION

3.1. Synthesis and physico-mechanical properties of B-PU and B-PU nanocomposite

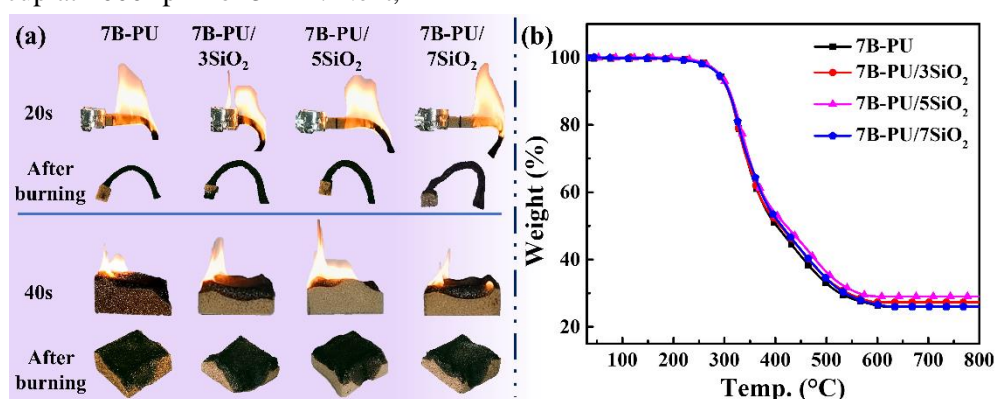


Fig. 2. Horizon burning and block combustion tests (a); TGA curves of 7B-PU, 7B-PU/SiO₂ samples (b)

Fig. 2a shows the horizon burning and combustion test of 7B-PU with and without nano silica. In general, the results from the tests indicated the presence of SiO₂ made the combustion rate decrease and lightly increased the thermal stability. In the horizon burning test, compared with 7B-PU, the foam with 3 php of nano SiO₂, there is no change in the burning rate

(409 mm/min). Samples with 5 and 7 php nano, despite decreasing the combustion rate (about 236 mm/min) and both 7B-PU/7SiO₂ and 7B-PU/5SiO₂ were self-extinguished. After the combustion test, however, 7B-PU/7SiO₂ foam was damaged in comparison with 7B-PU/5SiO₂ foam. The TGA graphs (Fig. 2b) also pointed out the thermal stability of 7B-PU/5SiO₂ is better

than the others. At 700 °C, the mass residues of 7B-PU and 7B-PU/7SiO₂ are 26 wt%, those of 7B-PU/3SiO₂ and 7B-PU/5SiO₂ are 27.4 and 29.1 wt%, respectively. Therefore 5 php nano SiO₂ was chosen for further study and discussion. The influence of components on the foam properties of nanocomposites was exhibited in Fig. 3. In fact, the components affected the pore size of the nanocomposites. Accordingly, the average pore size of the 7B-PU sample was measured at about 793 μm. However, the addition of nano SiO₂ to

this sample (7B-PU/5SiO₂) leads to reducing the average pore size by about 624 μm. Accordingly, the presence of ATH, OP, and DAP significantly reduced the pore size of nanocomposites. Specifically, the samples 7B-PU/5SiO₂/ATH250, 7B-PU/5SiO₂/OP100, and 7B-PU/5SiO₂/DAP80 have average pore sizes of 480, 616, and 601 μm, respectively. Moreover, the 7B-PU/5SiO₂/OP100 sample has a larger and uniform pore size compared to 7B-PU/5SiO₂/ATH250 and 7B-PU/5SiO₂/DAP80 samples.

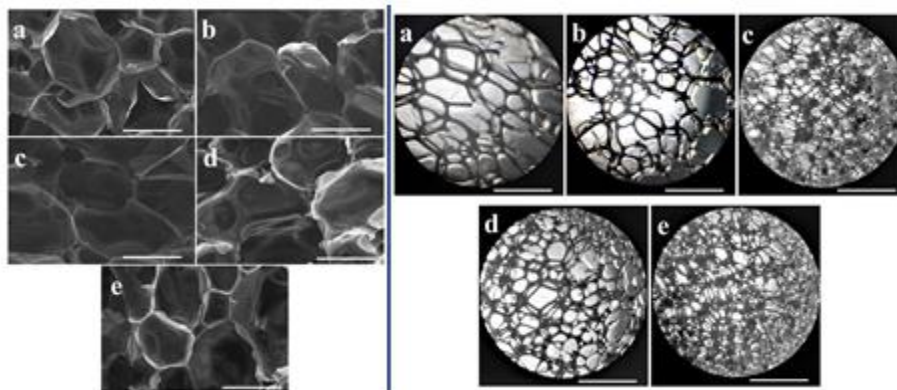


Fig. 3. SEM images with 500 μm-ruler (left) and optical micrographs (OM) with 1500 μm-ruler (right) of a) 7B-PU, b) 7B-PU/5SiO₂, c) 7B-PU/5SiO₂/ATH₂₅₀, d) 7B-PU/5SiO₂/OP₁₀₀ and e) 7B-PU/5SiO₂/DAP₈₀

3.2. Flame retardancy of B-PU and B-PU nanocomposite foams

The flame-retardant performance of 7B-PU and its nanocomposites is shown in Fig. 5. In the combustion block, the flames of 7B-PU and 7B-PU/5SiO₂ could extinguish after 65 and 57 s, respectively. Notwithstanding the shortened after flame time of 7B-PU/5SiO₂, it failed to meet the UL94 flammability rating test (both horizontal and vertical). Therefore, three different kinds of FRs were introduced to 7B-PU/5SiO₂ to boost the flame retardancy of the nanocomposites.

With the addition of FRs, once exposed to the flame after 10 s, the extinguishing time significantly reduced to 4s for 7B-PU/5SiO₂/ATH100 and 1s for 7B-PU/5SiO₂/OP30, compared to that of 7B-PU and 7B-PU/5SiO₂. Moreover, the flame of 7B-PU/5SiO₂/DAP20 could self-extinguish quickly. The 7B-PU/5SiO₂/FRs with the addition of 100 php ATH, 30 php OP, and 20 php DAP almost passed the block combustion test and horizontal burning test standard, however, UL94 V-0 rating in vertically exposed fire direction failed to achieve. Therefore, more fillers need to be added into foam formulations to boost the fire resistance until reaching V-0 standard, which is the most difficult one to achieve in the UL94 flammability

standard. Ultimately, V-0 standard could be achieved with the addition of 250 php ATH, 100 php OP, and 80 php DAP in the B-PU nanocomposite foam formulations.

The three representatives of 7B-PU/5SiO₂/FRs both passing the horizontal and vertical burning test were further accessed their flame-retardant properties by LOI and cone calorimeter. Compared to the low LOI value of 7B-PU/5SiO₂ (19 %), the LOI values of 7B-PU/5SiO₂/ATH250, 7B-PU/5SiO₂/OP100, and 7B-PU/5SiO₂/DAP80 are 24, 23, and 26%, respectively.

4. CONCLUSION

Sustainable polyurethane foams synthesized from bio-polyol derived from biomass incorporating 5php nano silica had improved the cellular structure, thermal property, and compressive strength compared to foam without nano silica. Bio-based polyurethane nanocomposite foams exhibited high thermal stability, considerable flame retardancy, and self-extinguishing behavior. Flame retardant nanocomposite foams containing ATH (41.29 wt%), DAP (18.37 wt%), and OP (21.95 wt%) were successfully prepared. The addition of FRs effectively increased LOI values to 23 – 26%,

lowered the parameters of the combustion process obtained from cone calorimetry, and passed the V-0 rating in the vertical burning test. The FR additives allowed to attain smaller cells. This study showcased a highly promising approach to developing environmentally friendly high-

performance fire-retardant and thermal insulating polyurethane nanocomposite materials using bio-polyol from biomass that could be utilized as a template for the future development of next-generation building bio-insulation materials.

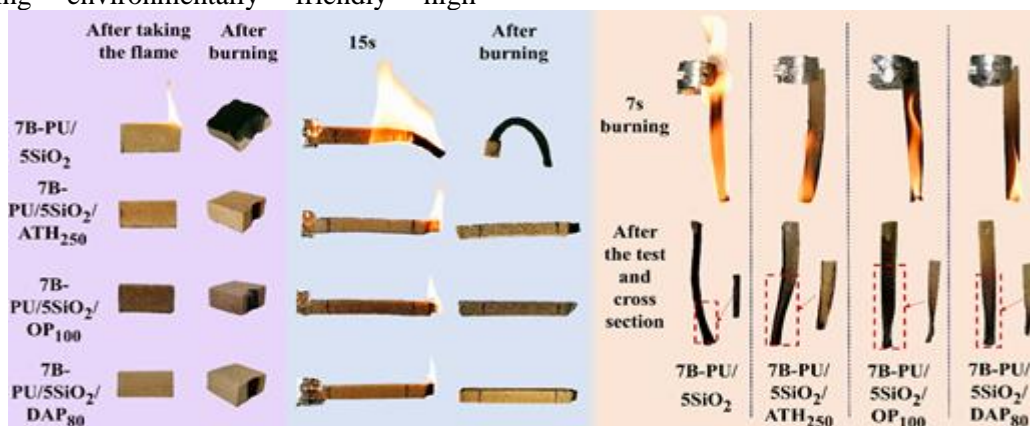


Fig. 4. Block combustion, horizon, and vertical burning test of 7B-PU/5SiO₂ without and with FRs

Acknowledgment

This research is funded by University of Science VNU-HCM under grant number T2023-60.

References

- [1] M.F Sonnenschein, Polyurethanes: science, technology, markets, and trends, second ed., John Wiley & Sons, Hoboken, 2021.
- [2] M. Kurańsk, A. Prociak, *The influence of rapeseed oil-based polyols on the foaming process of rigid polyurethane foams*, Ind. Crops. Prod. **89** (2016) 182-187.
- [3] I. Omrani, A. Farhadian, N. Babanejad, H.K. Shendi, A. Ahmadi, M.R. Nabid, *Synthesis of novel high primary hydroxyl functionality polyol from sunflower oil using thiol-yne reaction and their application in polyurethane coating*, Eur. Polym. J. **82** (2016) 220-231.
- [4] M. Evtiouguina, A.B. Timmons, J.J.C. Pinto, C.P. Neto, M.N. Belgacem, A. Gandini, *Oxypropylation of cork and the use of the ensuing polyols in polyurethane formulations*, Biomacromolecules. **3** (2002) 57-62.
- [5] T.A. Nguyen, T.M.N. Ha, B.T. Nguyen, D. Ha, T.V. Vo, D.M. Nguyen, D.K. Vo, N.T. Nguyen, T.V. Nguyen, D.Q. Hoang, *Microwave-assisted polyol liquefaction from bamboo for bio-polyurethane foams fabrication*, J. Enviro. Chem. Eng. **11** (2023), 109605.
- [6] S. Hu, X. Luo, Y. Li, *Polyols and polyurethanes from the liquefaction of lignocellulosic biomass*, ChemSusChem. **7** (2014) 66-72.
- [7] X. Huang, C.F.D Hoop, J. Xie, Q. Wu, D. Boldor, J. Qi, *High bio-content polyurethane (PU) foam made from bio-polyol and cellulose nanocrystals (CNCs) via microwave liquefaction*, Mater. Des. **138** (2018) 11-20.
- [8] T. Saffar, H. Bouafif, F.L. Braghiroli, S. Magdouli, A. Langlois, A. Koubaa, *Production of bio-based polyol from oxypropylated pyrolytic lignin for rigid polyurethane foam application*, Waste Biomass Valor. **11** (2020) 6411-6427.
- [9] J. Tao, F. Yang, T. Wu, J. Shi, H.B. Zhao, W. Rao, *Thermal insulation, flame retardancy, smoke suppression, and reinforcement of rigid polyurethane foam enabled by incorporating a P/ Cu-hybrid silica aerogel*, Chem. Eng. J. **461** (2023) 142061.
- [10] E. Burgaz, C. Kendirlioglu, *Thermomechanical behavior and thermal stability of polyurethane rigid nanocomposite foams containing binary nanoparticle mixtures*, Polym. Test. **77** (2019), 105930.
- [11] N.T. Nguyen, N.T. Tran, T.P. Phan, A.T. Nguyen, M.X.T. Nguyen, N.N. Nguyen, Y.H. Ko, D.H. Nguyen, T.T.T. Van, D.Q. Hoang, *The extraction of lignocelluloses and silica from rice husk using a single biorefinery process and their characteristics*, J. Ind. Eng. Chem. **108** (2022) 150-158.

A SIMPLE METHOD FOR THE SYNTHESIS OF CALCIUM OXIDE NANOPARTICLES FROM EGG SHELLS AND EVALUATION THEIR PROPERTIES

Le Thi Mai Hoa^{1,2}, Dung My Thi Dang^{1,2}, Hoang Tuan Minh^{2,3} and Tin Chanh Duc Doan^{1,2}

¹ Institute for Nanotechnology, Community 6, Linh Trung Ward, Thu Duc City, Ho Chi Minh City, Vietnam

² Vietnam National University Ho Chi Minh City, Ho Chi Minh City, Vietnam

³ The Faculty of Materials Technology, Ho Chi Minh City University of Technology

Email: ltmhoa@vnuhcm.edu.vn

ABSTRACT

Calcium oxide nanoparticles (CaO NPs) have excellent catalytic and biological properties. These properties are most needed for many applications in environmental and medicinal science. In this paper, calcium oxide nanoparticles (CaO NPs) are synthesized by the thermal annealing of egg shell at 600 °C for 2 h. The synthesized CaO nanoparticles are characterized by X-Ray diffraction (XRD), field emission scanning electron microscopy (FE-SEM). The FE-SEM images indicate that the CaO NPs are spherical in shape with an average particle size of 120 nm. The XRD patterns emphasized the crystalline structure of CaO. These results give a promising and economic strategy of synthesizing the CaO nanoparticles.

Keywords: Egg shell, nanoparticles, calcium oxide, X-Ray diffraction.

INTRODUCTION

Due to the industrialization and population growth, solid wastes are increased causing problems in the environment [1]. Eggs are broadly consumed nutritious food and their shells are discarded as waste after consumption [2]. Egg shell can be a potential candidate for CaO nanoparticle synthesis because CaCO₃ is the basic content of egg shell and can be converted to calcium oxide (CaO) by thermal treatment [3, 4]. CaO is useful in numerous fields such as production of bio-ceramics, chemisorbent for toxic gases, pollutant and removal of heavy metals and in many other clinical applications [3-5]. The CaO nanoparticles have been synthesized by several methods such as chemical precipitation, hydrothermal, sol-gel have been used for CaO nanoparticles synthesis [6]. In this study, CaO nanoparticles are prepared from egg shells. The property of CaO nanoparticles is confirmed by structure of crystal and morphology of surface.

EXPERIMENTAL

Materials

Sodium hydroxide (NaOH), nitric acid (HNO₃, 65 %) are purchased from Sigma-

Aldrich and used without further purification. Deionized (DI) water utilized in this study are prepared in the laboratory using a water purification system (Ultra RS-U20i) with a resistance of 18.2 MΩ. Waste eggshells are collected from University canteen.

Synthesis of Calcium oxide nanoparticles

Waste egg shells are collected from University canteen and washed with hot water. The cleaned eggshells are dried at 60 °C for 24 hours and crumpled to form its powder. 100 mg of powder is mixed with 10 % HNO₃ to obtain Ca(NO₃)₂. The next step is the formation of Ca(OH)₂, a total of 50 ml of 3 M sodium hydroxide is added slowly to Ca(NO₃)₂, after 2 h the precipitation of Ca(OH)₂ is obtained. The obtained Ca(OH)₂ precipitates are calcined at 600 °C for 2 h to achieve CaO nanoparticles.

Characterization

Size, shape and surface morphology of the CaO nanoparticles are examined by field emission scanning electron microscope (FE-SEM, Hitachi SU8010). The crystal structure is analyzed by X-ray diffraction (XRD, D8 Advance Eco, Bruker AXS, Germany) using Cu-Kα radiation ($\lambda = 0.1542$ nm, 40 kV and 10

mA) with a scan rate of 2° min^{-1} in the diffraction angular range of 10° - 90° .

RESULTS AND DISCUSSION

Surface morphology of egg shell powder, Ca(OH)_2 and synthesized CaO nanoparticles is investigated by FE-SEM as shown in Figure 1. The results reveal that the egg shell has a non-porous and irregular crystal structure, the Ca(OH)_2 has a hexagonal shape, the CaO nanoparticles are approximately spherical in morphology agglomerating to each other. Size of CaO nanoparticles is in the range 50-130 nm.

The phase structures of egg shell, Ca(OH)_2 , CaO are identified using a $\text{Cu K}\alpha$ X-Ray diffraction as presented in Figure 2 and Table 1. X-Ray diffraction patterns of CaO show the peaks at 32.4, 37.5, 54.1, 64.3 and 67.5 corresponding to (111), (002), (022), (113) and (222) planes of cubic system CaO , respectively, as shown in Table 1. The plane values of X-Ray patterns emphasize the crystalline structure of CaO [3-5]. The average particle size calculated using the full width at half maximum (FWHM) is found to be 137 nm.

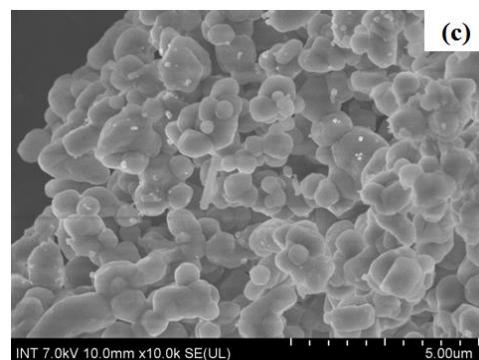
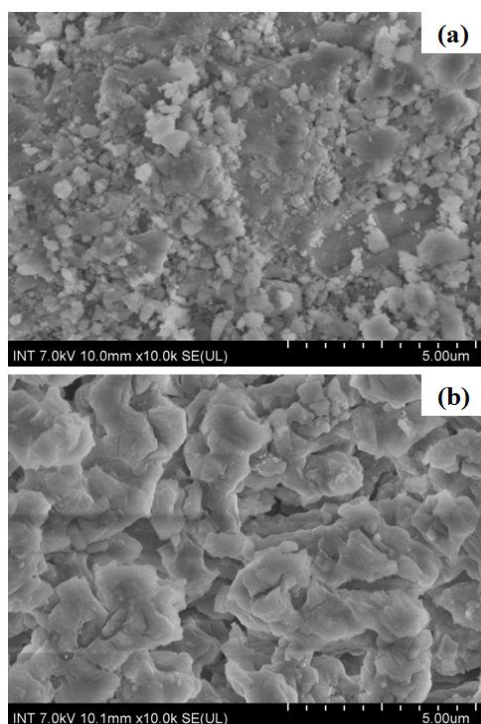


Figure 1. FE-SEM images of (a) egg shells powder, (b) Ca(OH)_2 powder, (c) CaO nanoparticles.

Table 1. X-Ray data of CaO nanoparticles

No	2θ ($^\circ$)	FWHM	Intensity (a.u)	(hkl)
1	32.4	0.1459	850	111
2	37.5	0.2038	2205	002
3	54.1	0.2446	1192	022
4	64.3	0.2039	369	113
5	67.5	0.2242	353	222

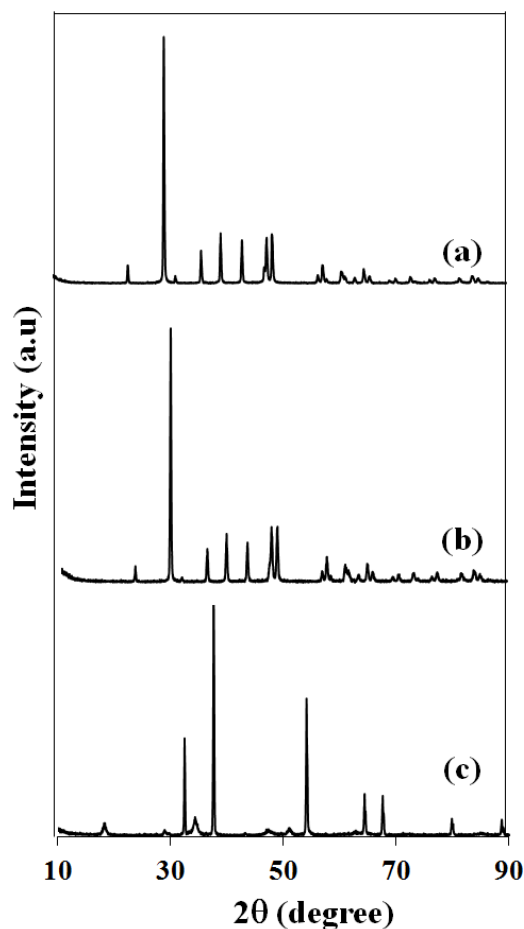


Figure 2. X-Ray pattern of (a) egg shells powder, (b) Ca(OH)_2 powder, (c) CaO nanoparticles.

CONCLUSION

In this work, the desired goals by the conversion of egg shell wastes to CaO nanoparticles is achieved. The FE-SEM image of CaO nanoparticles indicates that the particles are spherical in morphology and the particle size is in the range 50 nm - 130 nm. The X-Ray study reveals that the egg shell is changed to CaO. The utilizing waste materials as a precursor for CaO synthesis is a cheap, green and sustainable method.

Acknowledgment

The authors are very grateful to Vietnam National University Ho Chi Minh City (VNU-HCM) for financial support this work under grant number TX2023-32-01.

References

- [1] S. Thakur, S. Singh, B. Pal, *Superior adsorption removal of dye and high catalytic activity for transesterification reaction displayed by crystalline CaO nanocubes extracted from mollusc shells*, Fuel Process. Technol. **213** (2021) 106707.
- [2] A. V. Borhade, A. S. Kale, *Calcined eggshells as a new biosorbent to remove of dyes from aqueous solution*, Appl. Water Sci. **7** (2017) 4255-4268.
- [3] M. Elaheh, *Ultrasonic-assisted preparation of nano egg shell powder: a novel catalyst in green and high efficient synthesis of 2-aminochromenes*, Ultrason. Sonochem., **20** (2013) 1436-1441.
- [4] T. Witoon, *Characterization of calcium oxide derived from waste egg shell and its application as CO₂ sorbent*. Ceram. Int., **37** (2011) 3291-3298.
- [5] L. Habte, N. Shiferaw, D. Mulatu, T. Thenepalli, R. Chilakala, J. W. Ahn, *Synthesis of Nano-Calcium Oxide from Waste Egg shell by sol-gel method*, Sustainability, **11** (2019) 3196.
- [6] V. Jadhav, A. Bhagare, S. Wahab, et al., *Green synthesized Calcium oxide nanoparticles using leaves aqueous extract of moringa oleifera and evaluation of their antibacterial activities*, Journal of Nanomaterials, (2022) ID 9047507.

MAGNETITE NANOPARTICLES DECORATED ON CELLULOSE AEROGEL FOR *p*-NITROPHENOL FENTON DEGRADATION

Nguyen Thi Thuy Van¹, Nguyen Quang Khai², Thieu Ngoc Quan², Nguyen Hoang Diem Trinh², Ho Gia Thien Thanh¹, Do Ba Long¹, Anh Ngoc Phan³, Nguyen Tri¹, Huynh Ky Phuong Ha^{*2}

¹Institute of Chemical Technology – VAST, No.1A, TL29 Str., Dist. 12, Ho Chi Minh City, Vietnam

²University of Technology – VNU-HCM, 268 Ly Thuong Kiet Str., Dist. 10, Ho Chi Minh City, Vietnam

³School of Engineering, Newcastle University, Newcastle upon Tyne NE1 7RU, UK

*Corresponding author: hkpha@hcmut.edu.vn

ABSTRACT

In this study, well-dispersed Fe₃O₄ NPs were incorporated into the three-dimensional structures of cellulose aerogels (CAs) to enhance the degrading effectiveness of *p*-nitrophenol (PNP) treatment and improve the catalyst's recovery. As-synthesized samples were analyzed by powder X-ray diffraction, Fourier transform infrared spectroscopy, field emission scanning electron microscopy, energy dispersive X-ray analysis. Then, using ultraviolet–visible spectroscopy, the difference in the degradability of PNP of the obtained material samples was also investigated to determine their potential applications. Results highlighted that the Fe₃O₄-3@CA-K catalyst with an Fe₃O₄ loading of 0.40 g/g_{CA} demonstrated the highest PNP removal efficiency (92.5%) in all Fe₃O₄@CA samples with a H₂O₂ content of 5 g/L.

Keywords: cellulose aerogel, magnetite nanoparticle, *p*-nitrophenol, Fenton degradation, cross-linker

INTRODUCTION

Cellulose aerogel from water hyacinth has been fabricated and published in many previous works [1-3]. It has different applications and have many special properties, such as extremely low density (0.003–0.500 g/cm³), high porosity (80%–99.8%), high surface area (100–1600 m²/g) and high compressive strength (5.20 kPa–16.67 MPa), and has good surface activity. They have shown potential applications in the environment, life science and catalysis, making them the most promising hybrid materials. However, studies that have modified metallic NP catalysts on CA to create heterogeneous catalyst systems for environmental treatment applications are rare. Moreover, CA materials from water hyacinth have high potential as materials that enable catalysts to decompose difficult organic pollutants, such as *p*-nitrophenol (PNP) with high concentrations.

Herein, a straightforward and ecofriendly approach for decorating CAs with Fe₃O₄ with different synthesis methods was established, and PNP degradation performance was evaluated. Simultaneously, the findings demonstrated that CA is an exceptional matrix for supporting Fe₃O₄ NPs. Besides, Fe₃O₄ modified on a CA surface (Fe₃O₄@CA) was produced from water hyacinth. We examined the physicochemical features of the

catalyst system, and PNP degradation, recovery and reuse, to validate the product's prospective applicability.

METHODOLOGY

Preparation of Fe₃O₄@CA using kymene (CA-K) or using PVA and GA (CA-P) as the cross-linker

CA-K samples: 100 mL solution of 2% w/w cellulose fibers with water was mixed to generate a homogenous solution. Then, 0.5 mL of kymene was added and stirred for 2 h with a magnetic stirrer at 800 rpm. The mixture was refrigerated for 24 h before being sublimated at –70 °C to obtain an aerogel sample. Finally, the obtained materials were placed in an oven at 80 °C for 3 h to enhance the cross-linking of kymene in the aerogel cellulose product [2].

CA-P samples: A solution of PVA (5% w/w in water) was added to 100 mL of 2% (w/w in water) mixture of cellulose fibers at a PVA-to-cellulose ratio of 4:3. The mixture was stirred for 1 h before 0.1 mL of 1% H₂SO₄ and 0.25 mL of GA (25% w/w in water) was added and then stirred for 2 h with a magnetic stirrer at 800 rpm. The freeze-drying method was carried out for the cellulose hydrogel at –70 °C for 24 h to obtain CA-P. To improve the cross-linking of the PVA-GA, we

further cured the aerogel material at 80 °C for 3 h [2].

The samples of Fe₃O₄@CA-K and Fe₃O₄@CA-P were fabricated by the co-precipitation method: 1.6 g of CA-K (or CA-P) was immersed in 100 mL of a mixture of an aqueous solution of FeSO₄·7H₂O and FeCl₃·6H₂O (1:1 molar ratio). Then, 200 mL of distilled water was added to the mixture in a 500 mL beaker with a magnetic stirrer, keeping the inert medium for the reaction at 75 ± 5 °C throughout. During the process, the pH was then raised to 11.5 with a 1 M NaOH solution, and the reaction was conducted for 40 min. The obtained material was washed with ethanol and then with distilled water until pH 7 was reached. The sample was dried by freeze-dried for 24 h to obtain Fe₃O₄-X@CA-K with X was varied (1, 2, 3 and 4) corresponding to the content of Fe₃O₄ in samples (0.17, 0.25, 0.40 and 0.49 g/g_{CA}, respectively). The samples of Fe₃O₄@CA-P were selected according to the best ratio and molar number of Fe₃O₄-X@CA-K.

Fenton-like degradation experiments

In the experiment, a solution containing 1.00 g of PNP and 500 mL distilled water (2000 ppm) was utilized as the treated solution. PNP degradation reaction at room temperature was accelerated through magnetic stirring. The starting pH of the process was set at 3 with a 95% H₂SO₄ solution. Fe₃O₄@CA-K (or Fe₃O₄@CA-P) samples and H₂O₂ were added to the solutions. During the reaction, the samples were obtained every 20 min, and the elimination of PNP under ultraviolet–visible (UV–Vis) light was monitored. The total reaction time was increased to 180 min, and the wavelength range was 190–800 nm. The spectrum's highest absorption was observed at 317 nm wavelength.

RESULTS AND DISCUSSION

Catalytic activity

Effect of Fe₃O₄ loading: PNP was selected as the model organic pollutant for the evaluation of the catalytic activity of Fe₃O₄@CA-K in a Fenton-like system. The pH value plays a crucial role in the Fenton process because it governs the generation of hydroxyl radicals [4]. The literature reports that an acidic pH is useful in removing pollutants because H₂O₂ has high stability at low pH levels and does not dissociate into O₂ and H₂O [5]. Based on prior research, the investigation of the Fenton decomposition process has shown that a pH level of 3 is considered to be the most [6-8].

Therefore, for the purpose of this investigation, a fixed pH value of 3 was used in the examination of additional variables in the degrading response of PNP. Fe₃O₄@CA-K samples with various Fe₃O₄ content were subjected to the PNP degradation process, which was conducted at an initial pH of 3 and H₂O₂ concentration of 4.0 g/L at a stirring speed of 300 rpm. Figure 1 illustrates the removal of PNP with an initial concentration of 2000 ppm after 180 min of reaction. After 100 min of reaction, the PNP conversion efficiency were 57.6% for Fe₃O₄-1@CA-K, 79.1% for Fe₃O₄-2@CA-K, 85.5% for Fe₃O₄-3@CA-K and 86.2% for Fe₃O₄-4@CA-K. The conversion yields of Fe₃O₄-3@CA-K and Fe₃O₄-4@CA-K were practically stable. Thus, Fe₃O₄-3@CA-K was selected for all subsequent experiments.

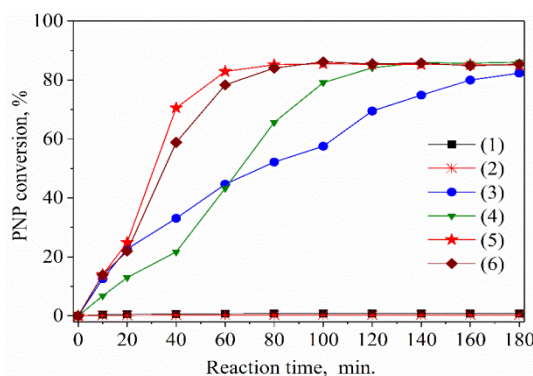


Figure 1. Activity of samples in the heterogeneous Fenton degradation of PNP; 1) PNP + H₂O₂; 2) PNP + Fe₃O₄-1@CA-K; 3) PNP + H₂O₂ + Fe₃O₄-1@CA-K; 4) PNP + H₂O₂ + Fe₃O₄-2@CA-K; 5) PNP + H₂O₂ + Fe₃O₄-3@CA-K; 6) PNP + H₂O₂ + Fe₃O₄-4@CA-K.

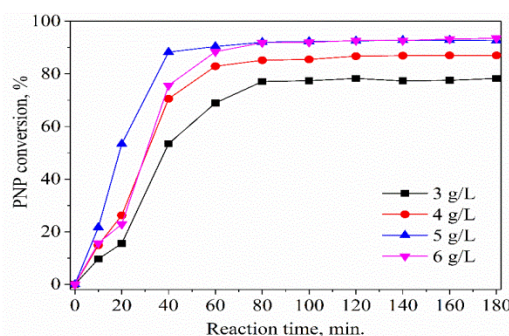


Figure 2. Effect of H₂O₂ dosage on the heterogeneous Fenton degradation of PNP over Fe₃O₄-3@CA-K catalyst.

Effect of H₂O₂ dosage: In the presence of iron, H₂O₂ plays a critical role as an oxidizing agent. The purpose of the experiment was to optimize Fenton degradation such that the optimum

performance can be obtained with the smallest quantity of H_2O_2 . The effects of H_2O_2 content on Fe_3O_4 -3@CA-K are shown in Figure 2. After 80 min, the elimination effectiveness of PNP with varying H_2O_2 dosages was almost stable. When the dosage of H_2O_2 was raised from 3 g/L to 5 g/L, the conversion efficiency of PNP significantly increased from 77.1% to 92.0%. The experimental results suggested that when the concentration of Fe_3O_4 had a specified value, raising the H_2O_2 dosage caused the production of $\cdot OH$ radicals, which considerably enhanced the oxidation rate and degree of mineralization [9]. The further enhancement from 5 g/L to 6 g/L initiated no notable change in PNP degradation. After 80 min of reaction, the PNP conversion efficiency reached 85.5% with 6 g/L of H_2O_2 and 92% with 5 g/L of H_2O_2 .

Effects of cross linkers: The effects of different cross-linkers on PNP conversion efficiency were investigated (Figure 4). The results showed that the degradation performance of PNP was reduced in the order Fe_3O_4 -3@CA-K > Fe_3O_4 -3@CA-P (Figure 4). CA samples using kymene as a cross-linker had significantly better PNP degradation efficiency.

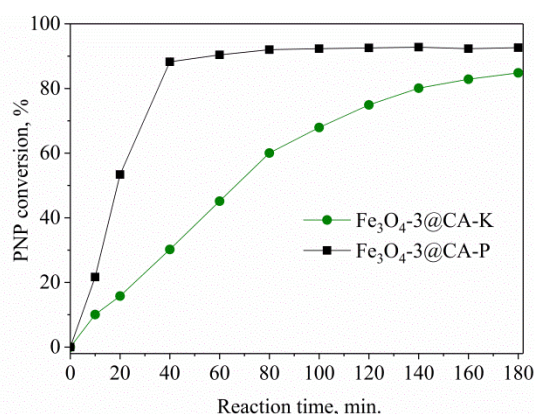


Figure 3. Effects of cross-linkers on the heterogeneous Fenton degradation of PNP

Material characterization

The XRD patterns of Fe_3O_4 @CA samples (Figure 4) show the typical peaks of Fe_3O_4 crystals at $2\theta = 30.88^\circ, 36.09^\circ, 43.86^\circ, 53.64^\circ, 57.79^\circ$ and 63.43° , which corresponded to the diffraction lattice surfaces (220), (311), (400), (422), (511) and (440) (JCPDS card 01-075-0449) and were similar to the results of the previous studies [10,11]. Besides, the peaks at $2\theta = 16.51^\circ$ and 23.14° , which are characteristic peaks for crystalline cellulose corresponding to diffraction lattice surfaces (110) and (200), respectively [12].

These results confirmed the presence of Fe_3O_4 crystal in the CA structure.

The surface morphology of CA using kymene and the mixture of PVA and GA as cross-linkers before and after being doped with Fe_3O_4 was observed using scanning electron micrographs (Figure 5). Figures 5a and b confirm that CA with kymene as cross-linker has a higher porosity than that of PVA-GA mixture. Figures 4c–d show small Fe_3O_4 NPs with reasonably uniform distribution on the surface of the material.

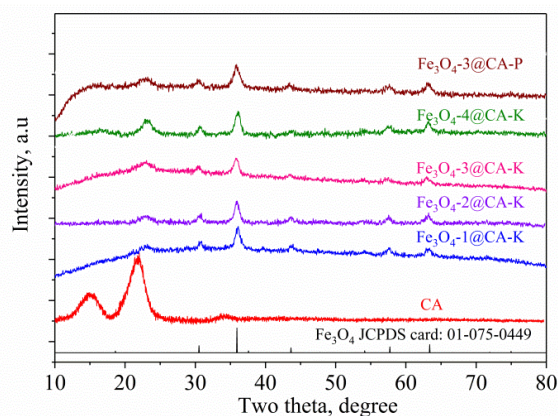


Figure 4. XRD patterns of samples

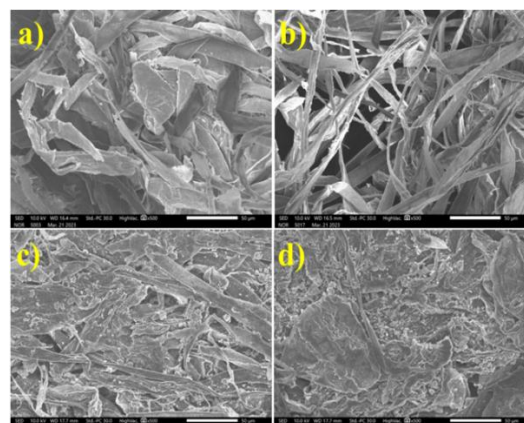


Figure 5. SEM images of samples; a) CA-P, b) CA-K, c) Fe_3O_4 -3@CA-K, d) Fe_3O_4 -3@CA-P

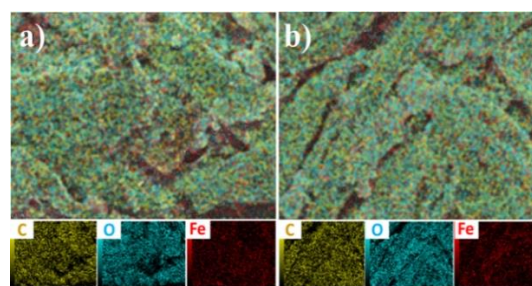


Figure 6. EDS mapping of elements of samples; a) Fe_3O_4 -3@CA-K, b) Fe_3O_4 @CA-P

The composition of the synthesized samples was determined by EDS and mapping (Figure 6). The Fe_3O_4 @CA catalyst involved Fe, O and C elements, and the EDS results of all samples indicated no statistically significant difference between the actual results and calculated values. This result can be explained by the high porosity of the aerogel samples, which easily loaded on Fe_3O_4 NPs on the surfaces [13]. The CA samples from WH in this study had a high porosity (98.2%), which is comparable to the results of aerogels in a previous study [3]. The distribution of Fe and O elements on the catalyst surface was rather uniform during synthesis. The Fe_3O_4 NPs were effectively produced and incorporated into the surfaces of cellulose fibers.

TEM analysis was used to investigate the microstructural characteristics of Fe_3O_4 -3@CA-K samples containing dark-field represented Fe_3O_4 NPs (Figure 7). Using ImageJ software, the size distribution of Fe_3O_4 NPs obtained from TEM images revealed that the spherical NPs were distributed in the range of 5–15 nm. This result was completely consistent with the sample's XRD analysis and SEM image.

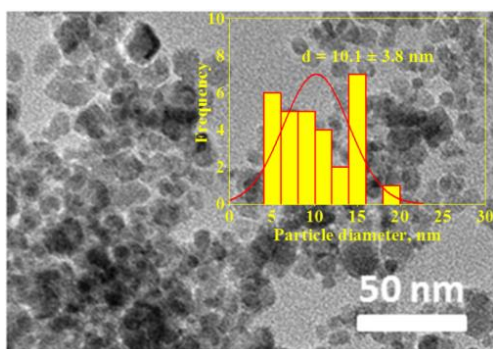


Figure 7. TEM image (a) and the size distribution histogram (b) of magnetite nanoparticles decorated of the Fe_3O_4 -3@CA-K sample.

CONCLUSION

The sample Fe_3O_4 -3@CA-K catalyst was confirmed as the best material under the optimal conditions (H_2O_2 concentration of 5.0 g/L, pH 3, and Fe_3O_4 catalyst dosage with a content of 0.4 g/g CA) after 100 min of reaction in the Fenton system. The degradation rate of PNP with a high concentration of up to 2000 ppm reached 92.5%. Consequently, this finding will renew interest in future dyestuff remediation strategies based on stable and robust catalytic activity in repetitive reaction cycles and straightforward, inexpensive

and environmentally friendly synthesis procedures.

Acknowledgement

This research is funded by The Royal Academy of Engineering (FF\1920\1\45), The Royal Society (ICA\R1\191220), U.K.

References

- [1] Nguyen, T.T.V., et al., *Synthesis, characteristics, oil adsorption, and thermal insulation performance of cellulosic aerogel derived from water hyacinth*. ACS Omega, **6**(40) (2021) 26130-26139.
- [2] Van Nguyen, T.T., et al., *Insights into the effects of synthesis techniques and crosslinking agents on the characteristics of cellulosic aerogels from Water Hyacinth*. RSC Adv., **12**(30) (2022) 19225-19231.
- [3] Phat, L.N., et al., *Fabrication and modification of cellulose aerogels from Vietnamese water hyacinth for oil adsorption application*. Korean J. Chem. Eng., **38**: (2021) 2247-2255.
- [4] Neppolian, B., J.-S. Park, and H. Choi, *Effect of Fenton-like oxidation on enhanced oxidative degradation of par-chlorobenzoic acid by ultrasonic irradiation*. Ultrason. Sonochem., **11**(5) (2004) 273-279.
- [5] Zaharia, C., et al., *Textile wastewater treatment by homogenous oxidation with hydrogen peroxide*. Environ. Eng. Manag. J., **8**(6) (2009) 1359-1369.
- [6] Gangwar, A., et al., *Magnetic nanocomposites of Fe_3C or Ni-substituted ($\text{Fe}_3\text{C}/\text{Fe}_3\text{O}_4$) with carbon for degradation of methylene orange and p-nitrophenol*. J. Clean. Prod., **309** (2021) 127372.
- [7] Ren, H., et al., *Synthesis and characterization of saponin-modified Fe_3O_4 nanoparticles as heterogeneous Fenton-catalyst with enhanced degradation of p-nitrophenol*. J. Chem. Technol. Biotechnol., **92**(6) (2017) 1421-1427.
- [8] Tang, X., et al., *Sulfidation modified Fe_3O_4 nanoparticles as an efficient Fenton-like catalyst for azo dyes degradation at wide pH range*. Powder Technol., **376** (2020) 42-51.

- [9] Segura, Y., et al., *Enhancement of the advanced Fenton process (Fe^0/H_2O_2) by ultrasound for the mineralization of phenol*. Appl. Catal. B: Environ., **113** (2012) 100-106.
- [10] Shaker, S., et al., *Preparation and characterization of magnetite nanoparticles by sol-gel method for water treatment*. Int. J. Innov. Res. Sci. Eng., **2**(7) (2013) 2969-2973.
- [11] Mohammed, A.A. and S.S. Isra'a, *Bentonite coated with magnetite Fe_3O_4 nanoparticles as a novel adsorbent for copper (II) ions removal from water/wastewater*. Environ. Technol. Innov., **10** (2018) 162-174.
- [12] Abdelghaffar, F., *Biosorption of anionic dye using nanocomposite derived from chitosan and silver Nanoparticles synthesized via cellulosic banana peel bio-waste*. Environ. Technol. Innov., **24** (2021) 101852.
- [13] Dasgupta, J., et al., *The effects of thermally stable titanium silicon oxide nanoparticles on structure and performance of cellulose acetate ultrafiltration membranes*. Sep. Purif. Technol., **133** (2014) 55-68.

POSTER SESSIONS
APPLICATIONS OF MICRO-
NANOTECHNOLOGY
(AMN)

UTILIZATION OF RESPONSE SURFACE METHODOLOGY IN THE OPTIMIZATION OF ELECTRODEPOSITION PREPARATION OF FTO/AUNPS ELECTRODES

Van Loc Thai^{1,2}, Van Vien Nguyen^{1,2}, Hoang Long Ngo³, Canh Minh Thang Nguyen^{1,2}, Hoa Thi Lai⁴, Thanh Tung Nguyen^{3,*}, Viet Hai Le^{1,2}, Thai Hoang Nguyen^{1,2,*}

¹University of Science, 227 Nguyen Van Cu Street, Ward 4, District 5, Ho Chi Minh City 700000, Vietnam

²Vietnam National University Ho Chi Minh City (VNUHCM), Quarter 6, Linh Trung Ward, Thu Duc City, Ho Chi Minh City 700000, Vietnam

³NTT Hi-Tech Institute, Nguyen Tat Thanh University, 298-300A Nguyen Tat Thanh Street, Ward 13, District 4, Ho Chi Minh City 700000, Vietnam

⁴Center for Innovative Materials & Architectures (INOMAR), Quarter 6, Linh Trung Ward, Thu Duc City, Ho Chi Minh City 700000, Vietnam

*Corresponding authors: tungnt@ntt.edu.vn, nthoang@hcmus.edu.vn

ABSTRACT

In this research, gold nanoparticles coated on fluorine-doped tin oxide glass (AuNPs/FTO) electrodes were synthesized via electrodeposition of HAuCl₄ in H₃PO₄ using cyclic voltammetry. For response surface methodology (RSM), a central composite design model consisting of 15 runs with three different electrodeposition parameters, such as potential window, scan rate and scan cycle was used to optimize the preparation parameters. Optimization and experimental data analysis using RSM were performed using Design Expert 11 statistical data analysis program. Data was fitted into a polynomial equation that shows all of the possible interactions of the parameters and their effects on the response (the electrocatalytic activity in the 5x10⁻³ M K₃[Fe(CN)₆] in 0.5 M KNO₃ solutions by cyclic voltammetry). The optimized preparation parameters consist of potential window ranging from -0.51V to 0.6V, scan rate of 81 mV.s⁻¹, and cycle number of 70, with the current density of 965.909 $\mu\text{A}\cdot\text{cm}^{-1}$. These factors have been compared with the experiment and the results show that there is no large error, which proves that the model can provide good repeatability and accurate optimization.

Keywords: Gold nanoparticles, electrodeposition, response surface methodology, cyclic voltammetry, Design Expert 11

1. INTRODUCTION

In the recent years, gold nanoparticles (AuNPs) are often used to increase the sensitivity in the electrochemical systems. AuNPs have a large surface area, high surface to volume ratio, and unique optical property, which play a crucial role by supporting the development of high sensitivity sensors to detect the aqueous contaminants [1]. To fabricate AuNPs, electrochemical deposition or electrodeposition has been considered one of the most an effective method due to its easy process, short time, low cost, as well as high surface coverage and high uniformity of nanoparticles [2-4]. Another noteworthy use of electrochemical deposition process is that by varying the potential, time, or solution concentration it is able to control the nanoparticle size and distribution [5], which

directly affects the catalytic activity of AuNPs [6, 7].

Conventionally, the one-factor-at-a-time approach has been widely used to optimize the effects of various factors in order to attain the best system performance. In this approach, different experimental factors are varied one at a time while keeping all other variables fixed. This approach is a traditional and time-consuming method, which also fails to consider any possible interaction between the factors [8, 9]. To overcome this issue, response surface methodology (RSM), a kind of mathematical and statistical method for designing experiments and building models, which is proposed to evaluate relative significance of several independent factors as well as to predict the optimum

operating conditions for desirable responses [10, 11].

In this regard, a 3-factor-5-level central composite design (CCD) was used to investigate the effect of potential window, scan rate and cycle number on the electrochemical properties of the FTO/AuNPs electrodes fabricated by electrodeposition using cyclic voltammetry method. Optimization and experimental data analysis using RSM were performed using Design Expert 11 statistical data analysis program. The optimized parameters were calculated and would be utilized to fabricate the optimal FTO/AuNPs electrodes.

2. EXPERIMENTAL SECTION

2.1. Materials and chemicals

FTO conductive glasses (thickness of 2.2 mm, 8 Ω) were acquired from Greatcell Solar Materials (Australia). Tetrachloroauric(III) acid tetrahydrate ($\text{HAuCl}_4 \cdot 4\text{H}_2\text{O}$, 99.5%) was obtained from Merck (Germany). Potassium hexacyanoferrate(III) trihydrate ($\text{K}_3[\text{Fe}(\text{CN})_6] \cdot 3\text{H}_2\text{O}$, 99.5%) and phosphoric acid (H_3PO_4 , 85%) were purchased from Fisher (USA). Potassium nitrate (KNO_3 , 99.5%) was from China. All chemicals and reagents were used as received without further purification.

2.2. Fabrication of the electrodes

Gold nanoparticles were deposited onto FTO electrodes via cyclic voltammetry (CV) method on a Autolab N302 potentiostat (Eco Chemie, Netherlands) with FTO working electrode (1.0 x 1.0 cm) as working electrode, a platinum counter electrode and an Ag/AgCl (3 M KCl) reference electrode. The distances from the working electrode to the counter and the reference electrodes were 1 cm, with the conductive surface of the FTO/AuNPs electrode facing towards the counter electrode. The solution consisted of 0.5 mM HAuCl_4 and 0.1 M H_3PO_4 in 20 mL deionized water. The electrodeposition process was conducted at different potential window, different scan rate and different cycle number. After the process, the fabricated FTO/AuNPs electrode was left still in air at room temperature for 30 min, then was washed with deionized water and left drying in air. The obtained electrodes were denoted as FTO/AuNPs-A-B-C, with A (V) being the potential window, B ($\text{mV} \cdot \text{s}^{-1}$) being the scan rate, and C (cycles) being the cycle number.

2.3. Characterization the electrodes

Electrochemical measurements were conducted on the same potentiostat with the three-electrode system, consisting of a platinum counter electrode, an Ag/AgCl (3 M KCl) reference electrode, and the FTO/AuNPs working electrode. The distances from the working electrode to the counter and the reference electrodes were 1.0 cm, with the conductive surface of the FTO/AuNPs electrode facing towards the counter electrode. Cyclic voltammetric (CV) measurements were carried out in an electrolyte solution containing 0.005M $\text{K}_3[\text{Fe}(\text{CN})_6]$ and 0.5 M KNO_3 with a scan rate of $100 \text{ mV} \cdot \text{s}^{-1}$ and potential range from -0.1 to 0.7 V.

2.4. Experimental design

A rotatable central composite design (CCD) with three independent factors and five levels (indicated as -1.68, -1, 0, +1, and +1.68) and quadratic programming methodologies were employed to determine the optimal parameters for the fabrication of FTO/AuNPs electrodes. The optimization process involved variation of three input variables of potential window (A) from 0.9 to 1.4 V, scan rate (B) from 66 to $134 \text{ mV} \cdot \text{s}^{-1}$, and cycle number (C) from 26 to 94 cycles (Table 1), which was conducted using Design Expert (11.0, Stat-Ease, USA) as statistical data analysis program. The factors were coded at. Baseline tests were carried out to ascertain the coded values of the parameters and for optimizing the fabrication process. The model's components, such as the independent factors and electrochemical catalytic properties, were fitted using a second-degree polynomial as defined by Equation 1.

$$Y_i = \beta_0 + \sum_{i=1}^3 \beta_i X_i + \sum_{i=1}^3 \sum_{j=1}^3 \beta_{ij} X_i X_j + \sum_{i=1}^3 \beta_{ii} X_i^2 \quad (\text{Eq. 1})$$

With Y_i being the response variable; β_0 representing the model constant; β_i , β_{ii} , and β_{ij} referring to the linear coefficient, the quadratic coefficient, and the cross product, respectively; and X_i and X_j denoting the variables under examination ($x_1 = \text{potential window}$, $x_2 = \text{scan rate}$, and $x_3 = \text{cycle number}$). The outcomes of the developed models, being the electrochemical catalytic properties (in this case, the anodic peak current density - J_{pa}), are listed in Table 1.

3. RESULTS AND DISCUSSIONS

First, 16 designed runs with the results of response as electrochemical catalytic properties

of FTO/AuNPs electrodes are presented in **Table 1**. An analysis of variance (ANOVA) was conducted to determine the impact of electrochemical catalytic properties of FTO/AuNPs electrodes, as shown in **Table 2**. The anodic peak current density J_{pa} of FTO/AuNPs electrodes (Y) was assessed as a function of potential window (A), scan rate (B) and cycle number (C) and calculated as the sum of a constant, three first-order effects (A, B and C), three interaction effects (AB, AC and BC) and three second-order effects (A^2 , B^2 and C^2). The model fitness was verified by the correlation coefficient R^2 of the model and p-value for lack of fit. The model probability value (P) of 0.0156, which is less than 0.05, indicate that the model terms are significant [12]. Moreover, the lack of fit is not statistically significant since the p-value (0.2074) were greater than 0.05. The relatively high sum of the squared ($R^2 = 0.9094$) value indicates that the quadratic equation for electrochemical catalytic properties of FTO/AuNPs electrodes is appropriately capable of representing the system under the experimental range. Additionally, the difference between R^2 (0.9094) and the adjusted R^2 (0.7735) is less than 0.2, indicating a good agreement between the two and thus signifying the strength of the model. Typically, regarding the electrochemical catalytic properties of FTO/AuNPs electrodes, variables with p-values higher than 0.05 are often regarded as statistically insignificant; in contrast, those with p values lower than or equal to 0.05 are regarded as significant [12]. According to the claim, in a statistically valid manner, the codes A, B, AB, A^2 , and C^2 are shown to significantly affect J_{pa} of FTO/AuNPs electrodes.

$$Y = -0.003813 + 0.006876A - 6.66671 \times 10^{-6}B + 0.000033C + 0.000021AB - 3.24042 \times 10^{-6}AC - 7.48719 \times 10^{-8}BC - 0.003630A^2 - 7.42429 \times 10^{-8}B^2 - 1.78974 \times 10^{-8}C^2 \text{ (Eq. 2)}$$

Quadratic **Equation 2** was constructed to simulate J_{pa} of FTO/AuNPs electrodes as the function of the independent variables. The largest coefficients were those of the factors A and A^2 , then C and AB in decreasing order, showing that the potential window makes the largest impact on the electrochemical properties of FTO/AuNPs electrodes, followed by cycle number. Additionally, the positive sign indicates synergetic effect of the respective term, while the negative term refers to antagonistic effect of the term [13]. Accordingly, the positive value of the coefficient of A (0.006876) and C (0.000033) implies that J_{pa} of FTO/AuNPs electrodes can be enhanced by increasing potential window and cycle number. However, as shown in the negative value of the coefficient of A^2 (-0.003630), if the potential window increased too much, it would have negative influence on the J_{pa} of the electrodes. On the other hand, the negative value of the coefficient of B (-6.66671×10^{-6}) suggests that the electrochemical properties of FTO/AuNPs electrodes can be diminished when increasing the scan rate. Moreover, J_{pa} of FTO/AuNPs electrodes increased with the increase of three factors, but then decreased when they exceeded certain values. Specifically, when the potential window increased from 0.9 to 1.15 V, J_{pa} increased from 676.35 to 964.88 μA ; then it decreased to 752.54 μA at the potential window of 1.4 V (Run #1, 11, and 14 in **Table 1**). Similarly, when the scan rate increased from 66 to 100 then 134 $mV \cdot s^{-1}$, J_{pa} increased from 924.65 μA to 964.88 μA , then decreased to 798.22 μA (Run #1, 3, and 8 in **Table 1**). Also, when the number of cycle number increases from 26 to 60 cycles, J_{pa} increased from 758.31 μA to 964.88 μA , but when the cycle number further increased to 94, the J_{pa} decreased to 727.58 μA (Run #1, 10, and 13 in **Table 1**).

Table 1. Experimental matrix based on CCD for electrochemical catalytic properties of FTO/AuNPs electrodes

Run	Potential range	Potential window	Scan rate ($mV \cdot s^{-1}$)	Cycle number (cycles)	J_{pa} ($\mu A \cdot cm^{-2}$)	E_{pa} (V)
1	-0.55–0.6	1.15	100	60	964.88	0.31296
2	-0.55–0.6	1.15	100	60	940.45	0.30289
3	-0.55–0.6	1.15	66	60	924.65	0.30289
4	-0.70–0.6	1.3	80	80	895.05	0.31296
5	-0.70–0.6	1.3	120	40	891.75	0.31296
6	-0.70–0.6	1.3	120	80	862.55	0.30289
7	-0.40–0.6	1.0	80	80	858.12	0.33310

8	-0.55–0.6	1.15	134	60	798.22	0.33310
9	-0.70–0.6	1.3	80	40	797.10	0.32303
10	-0.55–0.6	1.15	100	26	758.31	0.33310
11	-0.80–0.6	1.4	100	60	752.54	0.35324
12	-0.40–0.6	1.0	80	40	728.64	0.35324
13	-0.55–0.6	1.15	100	94	727.58	0.32303
14	-0.30–0.6	0.9	100	60	676.35	0.34317
15	-0.40–0.6	1.0	120	80	583.99	0.37338
16	-0.40–0.6	1.0	120	40	566.95	0.45395

Table 2. Analysis of variance (ANOVA) for electrochemical catalytic properties of FTO/AuNPs electrodes

Source	Sum of squares	Degrees of freedom	Mean square	F value	p value	
Model	1.987x10 ⁻⁷	9	2.197x10 ⁻⁸	6.69	0.0156	Significant
A (Potential window)	5.128x10 ⁻⁸	1	5.128x10 ⁻⁸	15.62	0.0075	
B (Scan rate)	2.517x10 ⁻⁸	1	2.517x10 ⁻⁸	7.67	0.0325	
C (Cycle number)	1.960x10 ⁻⁹	1	1.960x10 ⁻⁹	0.5968	0.4691	
AB	3.100x10 ⁻⁸	1	3.100x10 ⁻⁸	9.44	0.0219	
AC	7.560x10 ⁻¹⁰	1	7.560x10 ⁻¹⁰	0.2303	0.6483	
BC	7.175x10 ⁻⁹	1	7.175x10 ⁻⁹	2.19	0.1898	
A ²	6.179x10 ⁻⁸	1	6.179x10 ⁻⁸	18.82	0.0049	
B ²	8.170x10 ⁻⁹	1	8.170x10 ⁻⁹	2.49	0.1658	
C ²	4.748x10 ⁻⁸	1	4.748x10 ⁻⁸	14.46	0.0089	
Residual	1.970x10 ⁻⁸	6	3.283x10 ⁻⁹			
Lack of Fit	1.940x10 ⁻⁸	5	3.880x10 ⁻⁹	13.00	0.2074	Not significant
Pure Error	2.984x10 ⁻¹⁰	1	2.984x10 ⁻¹⁰			
Cor Total	2.175x10 ⁻⁷	15				

Impact of the interdependent fabrication parameters on the electrochemical catalytic properties of FTO/AuNPs electrodes was investigated by constructing three-dimensional (3D) surface response curves (**Figure 2**), which presents the interactions between each two of the three independent variables and J_{pa} as a single response, while the other factor was set constant at the central level. The steeper the 3D surface plot, the more obvious the interaction between the variables. Their corresponding contour plots are the bottom projections of the 3D response surfaces and represent the interaction between two factors. If the contour plot appears to be more elliptical, the interaction between the two factors is significant; in contrast, if it is more circular, the

interaction is not significant [9]. As observed in **Figure 2**, J_{pa} of FTO/AuNPs electrodes tended to increase with the increase of three factors, but when they exceeded certain values, their influence on the electrochemical catalytic properties of FTO/AuNPs electrodes showed a downward tendency. Specifically, potential window (A) has a greater influence on electrochemical catalytic properties of FTO/AuNPs electrodes compared to scan rate (B) and cycle number (C) (**Figure 2a** and **2b**), while there is no much difference in the effect of scan rate and cycle number (**Figure 2c**). Finally, all of the produced surfaces are smooth and both factors have a comparable influence on the electrochemical catalytic properties, and there is

no abnormal interaction between the variables. Moreover, data obtained by the 3D response surface plots are in accordance with those obtained from quadratic model equation.

Based on the predicted optimal conditions, three FTO/AuNPs electrodes were fabricated and their J_{pa} were measured to verify the accuracy of this prediction, which shows no significant difference (< 5%) between the predicted and the actual FTO/AuNPs electrodes (Table 3).

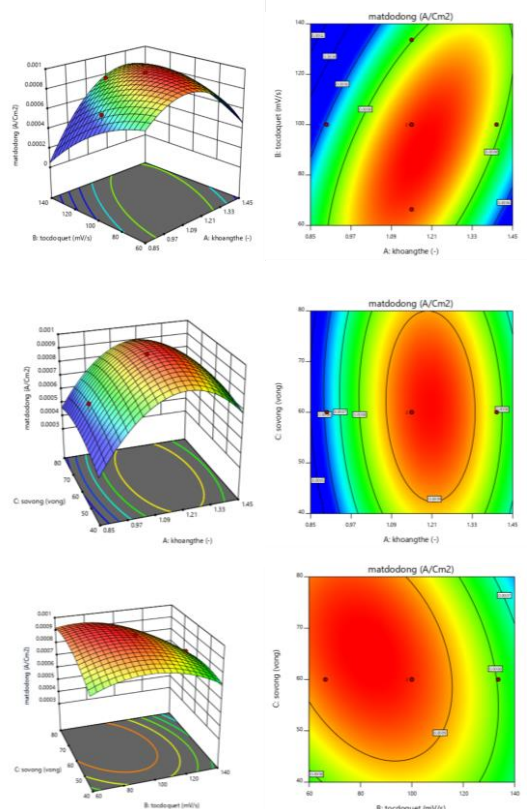


Figure 2. 3D and 2D response surfaces plots of (a) AB (potential window x scan rate), (b) AC (potential window x cycle number), and (c) BC (scan rate x cycle number)

Table 3. Electrochemical catalytic properties of the optimized FTO/AuNPs electrodes

Electrodes	Calculated J_{pa} ($\mu A.cm^{-2}$)	Measured J_{pa} ($\mu A.cm^{-2}$)	Difference (%)
FTO/AuNPs-1.19-98-60	965.091	932.20	3.49%
FTO/AuNPs-1.11-81-70	965.909	918.18	4.86%
FTO/AuNPs-1.15-86-66	970.272	927.99	4.36%

4. CONCLUSION

In this research, RSM involving experimental design and regression analysis was used to study the influence of potential window, scan rate and cycle number in the fabrication process of FTO/AuNPs electrodes on their electrochemical catalytic activity. It is revealed that potential window has a dominant influence on its electrochemical catalytic activity, while scan rate and cycle number only exert a minor effect. The ANOVA showed high coefficient of the determination values ($R^2 = 0.9094$ and adjusted $R^2 = 0.7735$), thereby indicating the precision and reliability of the model. It can be concluded that the central composite design of experiment and response surface methodology can be useful for the parameter optimization of FTO/AuNPs electrode fabrication.

References

- [1] C. Fang; R. Dharmarajan; M. Megharaj; R. Naidu: *Gold nanoparticle-based optical sensors for selected anionic contaminants*. TrAC Trends in Analytical Chemistry **86** (2017) 143-154.
- [2] M. Negahdary; A. Sharma; T. D. Anthopoulos; L. Angnes: *Recent advances in electrochemical nanobiosensors for cardiac biomarkers*. TrAC Trends in Analytical Chemistry **164** (2023).
- [3] H. C. Chiang; Y. Wang; Q. Zhang; K. Levon: *Optimization of the Electrodeposition of Gold Nanoparticles for the Application of Highly Sensitive, Label-Free Biosensor*. Biosensors (Basel) **9** (2019).
- [4] K. J. Stine: *Biosensor Applications of Electrodeposited Nanostructures*. Applied Sciences **9** (2019).
- [5] U. S. Mohanty: *Electrodeposition: a versatile and inexpensive tool for the synthesis of nanoparticles, nanorods, nanowires, and nanoclusters of metals*. Journal of Applied Electrochemistry **41** (2010) 257-270.
- [6] S. Panigrahi; S. Basu; S. Praharaj; S. Pande; S. Jana; A. Pal; S. K. Ghosh; T. Pal: *Synthesis and Size-Selective Catalysis by Supported Gold Nanoparticles: Study on Heterogeneous and Homogeneous Catalytic Process*. The Journal of Physical Chemistry C **111** (2007) 4596-4605.
- [7] P. Kalimuthu; S. A. John: *Size dependent electrocatalytic activity of gold nanoparticles immobilized onto three dimensional sol-gel*

- network. Journal of Electroanalytical Chemistry **617** (2008) 164-170.
- [8] V. Czitrom: *One-Factor-at-a-Time versus Designed Experiments*. The American Statistician **53** (1999).
- [9] M. A. Bezerra; R. E. Santelli; E. P. Oliveira; L. S. Villar; L. A. Escalera: *Response surface methodology (RSM) as a tool for optimization in analytical chemistry*. Talanta **76** (2008) 965-77.
- [10] A. Freeny; G. E. P. Box; N. R. Draper: *Empirical Model Building and Response Surfaces*. Technometrics **30** (1988).
- [11] N. R. Draper; J. A. John: *Response-Surface Designs for Quantitative and Qualitative Variables*. Technometrics **30** (1988).
- [12] D. C. Montgomery, *Design and analysis of experiments*. 5th ed.; John Wiley: New York, 2001.
- [13] Z. Lalegani; S. A. Seyyed Ebrahimi: *Optimization of synthesis for shape and size controlled silver nanoparticles using response surface methodology*. Colloids and Surfaces A: Physicochemical and Engineering Aspects **595** (2020).

SUSTAINABLE MATERIALS FOR GREEN ELECTRONICS: RRAM DEVICES EMPLOYING LOTUS PETIOLE CELLULOSE FIBERS

Hau Huu Ho Do^{1,2*}, Ngoc Hong Nguyen^{1,2}, Nam Hoang Vu^{1,2}, Hanh Kieu Ta Thi^{1,2}, Thang Bach Phan^{2,3}, Tu Uyen Doan Thi^{2,4}, Trang Thuy Phan Thi^{2,4}, Truong Nguyen Huu^{2,4}, Vinh Cao Tran^{2,4}, Ngoc Kim Pham^{1,2,*}

¹Faculty of Materials Science and Technology, University of Science, Ho Chi Minh City, Vietnam;

²Vietnam National University, Ho Chi Minh City, Vietnam;

³Center for Innovative Materials and Architectures (INOMAR), Ho Chi Minh City, Viet Nam;

⁴Laboratory of Advanced Materials, University of Science, Ho Chi Minh City, Vietnam

*Email: huu hau7399@gmail.com, phamkngoc@hcmus.edu.vn

ABSTRACT

The utilization of natural materials in contemporary electronics has garnered significant attention due to their distinct properties and environmental advantages. Cellulose, an abundant biopolymer, exhibits promising electrical and mechanical characteristics, rendering it suitable for integration into electronic systems. Its structural attributes and surface chemistry contribute to its favorable dielectric properties and low leakage current. The added advantages of biocompatibility and biodegradability enhance its appeal for sustainable electronics. This study investigates the feasibility of utilizing cellulose derived from lotus petioles as a dielectric material in resistive random-access memory (RRAM) devices. The Ag/cellulose/Pt device was fabricated via a solution-based method and demonstrated reliable resistive switching at low operating voltages without forming process. An endurance test involving 50 sweeping cycles revealed that the resistance window remained stable approximately tenfold. Given the increasing demand for innovative materials in electronics, this work of cellulose-based RRAM devices signifies a promising pathway toward advancing both technology and sustainability.

Keywords: Cellulose fiber, lotus petiole, memristor, RRAM, electrodes.

INTRODUCTION

Resistive random-access memory (RRAM or ReRAM) is a non-volatile (NV) random-access (RAM) computer memory that works by changing the resistance across a dielectric solid-state material, often referred to as a memristor [1]. RRAM has attracted considerable attention as a promising candidate for next-generation memory devices due to its high speed, low power consumption, high density, and scalability [2].

One of the critical factors that determines the performance and functionality of RRAM is the choice of electrode materials. The electrode is essential in providing electrical contacts, facilitating charge injection and transport, and influencing the dielectric layer's formation and rupture of conductive filaments [3]. Therefore, selecting suitable electrode materials is crucial for optimizing the RRAM characteristics and achieving desired memory functions. Among various electrode materials, platinum (Pt) is widely used as an inert electrode in RRAM devices. Pt is a noble metal with high electrical

conductivity, good chemical stability, high melting point, and low reactivity with most dielectrics [4]. Pt electrodes can provide stable and reproducible switching behavior, low operation voltage, high on/off ratio, and long retention time in RRAM devices [4]. On the other hand, silver (Ag) is a highly reactive metal that is responsible for the electrochemical mechanism. The redox reaction helps to form and rupture the conductive filaments connecting two electrodes [5].

Cellulose fiber from lotus petiole has emerged as a promising option for an eco-friendly and biodegradable insulator layer for RRAM devices [6]. Cellulose fiber is a natural polymer that is abundant, renewable, cheap, biocompatible, and biodegradable [7]. Lotus petiole fiber has many attractive properties and advantages, such as high mechanical strength, large surface area, high porosity, good thermal stability, low density, and excellent water absorption capacity [8]. Lotus petiole fiber has been widely used in various applications, such as

papermaking, textiles, packaging, biomedical devices, sensors, etc. [9].

This work studies the recent advances and applications of lotus petiole fiber as an eco-friendly and biodegradable insulator layer for RRAM devices. The Ag/nanocellulose/Pt structure has been completed with the deposition of silver film as a top electrode. The resistive switching performance was investigated under an external electric field. The threshold characteristic has been recorded in the ultra-low operation voltage and is stable for over 50 cycles. The valuation of the memory device provides a significant understanding of organic materials-based RRAM.

EXPERIMENTAL PROCEDURE

The cellulose fibers were initially extracted from the lotus petiole, purified by acid hydrolysis in NaOH, and bleached with NaClO. The obtained cellulose was then diffused in an ethanol solution before being deposited on the cleansed commercial Pt substrate and dried, which acted as the bottom electrode of a memory device. On the cellulose film, Ag top electrodes were subsequently deposited using a shadow mask and sputtering technique to fabricate the configuration of the Ag/cellulose/Pt device. The schematic of device fabrication is presented in **Figure 1**.

The morphology of isolated cellulose microfiber was observed using a scanning electron microscope (SEM S4800, Hitachi). In the meantime, the memory devices' current-voltage (I-V) characteristics were measured with a Keithley 2400 to investigate their RS behavior. The top Ag electrode was biased to apply the voltage while the bottom Pt electrode was grounded at room temperature. A DC survey was carried out utilizing the voltage sequence $0 \rightarrow 0.5 \text{ V} \rightarrow 0 \rightarrow -0.5 \text{ V} \rightarrow 0$. In addition, a compliance current of $I_{cc} = 10 \text{ mA}$ was applied to safeguard the devices against permanent failure.

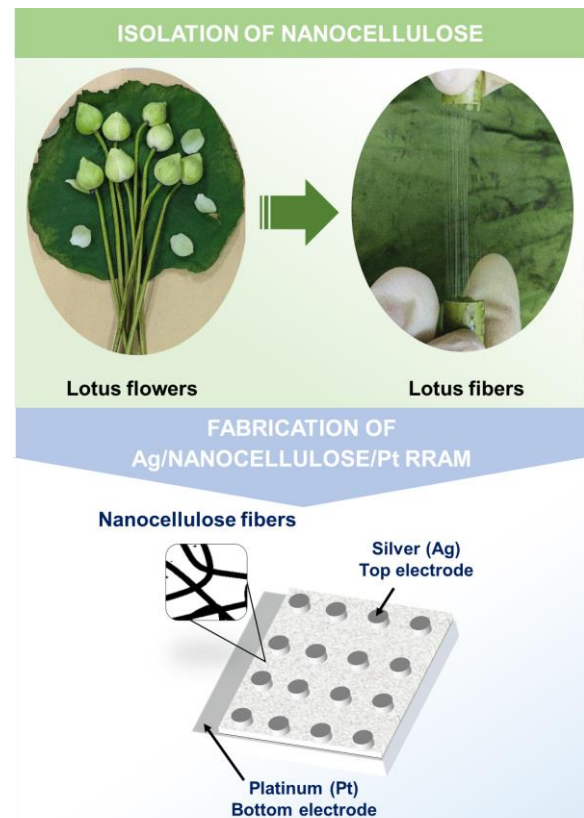


Figure 1. Schematic of device fabrication

RESULTS AND DISCUSSION

The fiber size of cellulose fiber and the image of Ag/nano cellulose/Pt device are shown in **Figure 2**. The size of nano cellulose fibers is depicted in **Fig. 2a**; the surface of the fiber is smooth, with fibers stacking, intertwining randomly, and nano-sized fibers around 50 nm. Nanocellulose films exhibit high uniformity, with closely packed fibers and lower porosity. In subsequent steps, nanocellulose is used as the RS material layer in Ag/nanocellulose/Pt devices (**Fig. 2b**). To record the current-voltage (I-V) characteristics of resistive memory devices, an external electric field is applied to the Ag top electrode while the Pt bottom electrode is grounded.

Fig. 3 depicts the voltage characteristics of the Ag/nanocellulose/Pt device in the range of -0.5 V to $+0.5 \text{ V}$. This structure demonstrated reversible analog resistive switching (RS) characteristics. **Fig. 3a** shows the structure's linear and logarithmic I-V characteristics (**Fig. 3b**). The initial state of the structure was in a high resistance state (HRS) with a current of approximately 10^{-4} A . When scanning the voltage from $0 \rightarrow +0.5 \text{ V}$, the current remained in the HRS

state until +0.48 V, which suddenly increased at the voltage $V_{SET} \sim +0.48$ V, reaching a conduction current of $\sim 10^{-5}$ A. This process corresponds to the transition from HRS \rightarrow low resistance state (LRS) or the "write" process. When the voltage decreased from +0.5 V to 0, the conduction current gradually reduced, returning to a present value of $\sim 10^{-8}$ A. This process corresponds to the transition from LRS to HRS, or the "erase" process. When sweeping the voltage from 0 V to -0.5 V and back to 0 V, the conduction current switching process was similar to the negative biasing. This I-V curve is characteristic of symmetric threshold switching (TS) behavior. The resistance ratio between HRS and LRS states is approximately ten times. Other devices, such as Ti/ZnO/Ti [10] and s-In/Nb: SrTiO₃/In [11], exhibited stable and repeatable threshold RS behavior similar to our research.

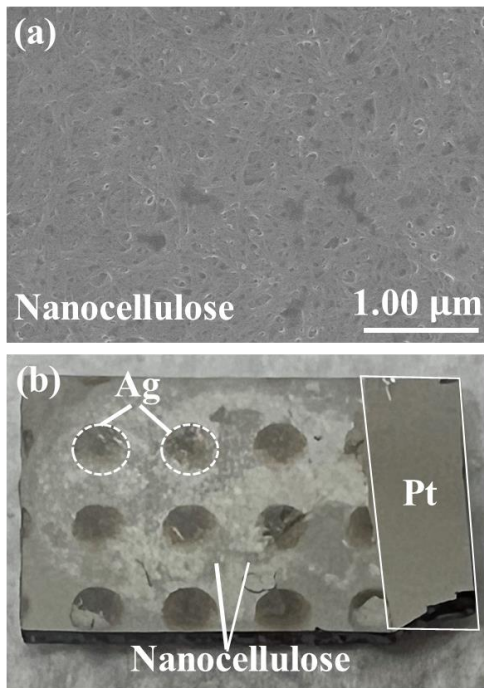


Figure 2. SEM images of nano cellulose (a) and image of Ag/nanocellulose/Pt RRAM device (b).

To explore the endurance characteristics, the current values of the two states of LRS and HRS for cycles of both devices were displayed in Fig. 4. This plot gives the good endurance characteristics of the device. The distinctive I-V curves may be reproduced after 50 consecutive read/write cycles with negligible degradation, which illustrates the robustness of nanocellulose (Fig. 4a-b). This demonstrates the robustness of cellulose, as the localized heating generated during continuous voltage application at the

surveyed location could potentially compromise materials with lower thermal stability.

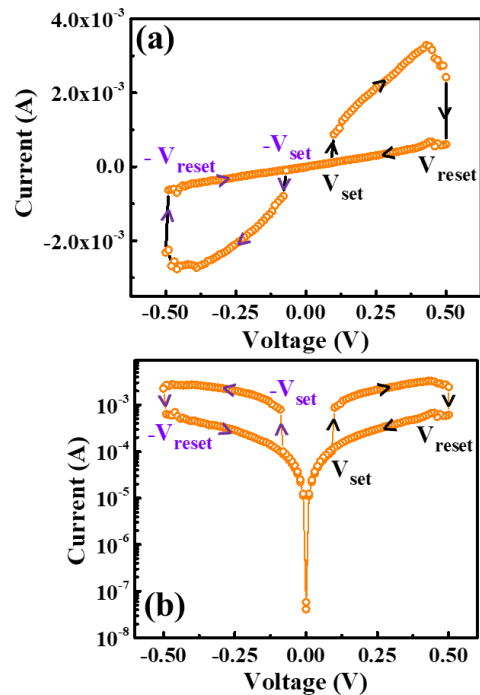


Figure 3. The linear (a) and logarithmic (b) I-V characteristics of the Ag/nanocellulose/Pt device.

According to the previous results, the Ag/nanocellulose/Pt device is stable in both states (10^{-4} and 10^{-3} , corresponding to HRS and LRS). Ag ions form and migrate through the nanocellulose layer to the Pt electrode when a positive voltage is given to the Ag electrode. This results in forming a conductive filament of Ag atoms, which reduces the device's resistance. This is known as the set process or transitioning from the HRS to the LRS. The reverse occurs when a negative voltage is applied to the Ag electrode. The Ag ions are removed from the filament and returned to the Ag electrode, breaking the filaments and raising the device's resistance during the reset process, also known as switching from LRS to HRS.

CONCLUSION

In summary, this study utilized nanocellulose material isolated from lotus stems, with fiber sizes of approximately 50 nm, exhibiting high uniformity and low porosity. This nanocellulose was employed as an RS layer in the RRAM device. Furthermore, the Ag/Nanocellulose/Pt device demonstrated robust RS performance, showcasing excellent efficiency at low operational states (-0.5 V to +0.5 V) and reasonably good repeatability. These results

highlight the potential of incorporating green materials into electronic devices, contributing to environmental preservation, and utilizing abundant plant-derived resources.

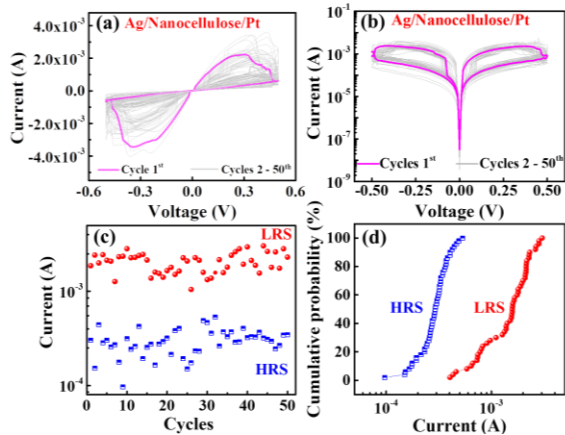


Figure 4. The semi-logarithmic plot of I - V characteristics (a, b), endurance characteristics at HRS and LRS, and cumulative distribution of current during 50 cycles of the Ag/nanocellulose/Pt device (c, d).

Acknowledgment

This research is funded by Vietnam National Foundation of Science and Technology Development (NAFOSTED), under grant number 103.02-2021.86.

References

[1] F. Zahoor, T. Z. Azni Zulkifli, and F. A. Khanday, *Resistive Random Access Memory (RRAM): An Overview of Materials, Switching Mechanism, Performance, Multilevel Cell (MLC) Storage, Modeling, and Applications*, *Nanoscale Res Lett* **15** (2020).

[2] Z. Shen, C. Zhao, Y. Qi, W. Xu, Y. Liu, I. Z. Mitrovic, L. Yang, and C. Zhao, *Advances of RRAM Devices: Resistive Switching Mechanisms, Materials and Bionic Synaptic Application*, *Nanomaterials* **10** (2020).

[3] T. T. Ngo, U. Tu Thi Doan, Q. T. T. Vo, T. L. Huynh, N. H. Vu, H. K. T. Ta, L. Thi Mai Hoa, Y. Kawazoe, P. T. Nguyen, and N. K. Pham, *Study of Digital and Analog Resistive Switching Memories Based on Methylammonium Lead Iodide (MAPbI₃) Perovskite by Experiments and DFT Calculations*, *J Phys D Appl Phys* **56** (2023).

[4] C. Sun, S. M. Lu, F. Jin, W. Q. Mo, J. L. Song, and K. F. Dong, *Control the Switching Mode*

of Pt/HfO₂/TiN RRAM Devices by Tuning the Crystalline State of TiN Electrode, *J Alloys Compd* **749** (2018).

[5] W. Wang, M. Wang, E. Ambrosi, A. Bricalli, M. Laudato, Z. Sun, X. Chen, and D. Ielmini, *Surface Diffusion-Limited Lifetime of Silver and Copper Nanofilaments in Resistive Switching Devices*, *Nat Commun* **10** (2019).

[6] P. T. Chandane, T. D. Dongale, P. B. Patil, and A. P. Tiwari, *Organic Resistive Switching Device Based on Cellulose-Gelatine Microcomposite Fibers*, *Journal of Materials Science: Materials in Electronics* **30** (2019) 21288.

[7] M. Ioelovich, *Cellulose: Nanostructured Natural Polymer* (LAP Lambert Academic Publishing Sunnyvale, CA, USA, 2014).

[8] Y. Pan, G. Han, Z. Mao, Y. Zhang, H. Duan, J. Huang, and L. Qu, *Structural Characteristics and Physical Properties of Lotus Fibers Obtained from Nelumbo Nucifera Petioles*, *Carbohydr Polym* **85** (2011) 188.

[9] C. Cheng, R. Guo, L. Tan, J. Lan, S. Jiang, Z. Du, and L. Zhao, *A Bio-Based Multi-Functional Composite Film Based on Graphene and Lotus Fiber*, *Cellulose* **26** (2019) 1811.

[10] A. Shih, W. Zhou, J. Qiu, H. J. Yang, S. Chen, Z. Mi, and I. Shih, *Highly Stable Resistive Switching on Monocrystalline ZnO*, *Nanotechnology* **21** (2010).

[11] J. Sun, C. H. Jia, G. Q. Li, and W. F. Zhang, *Control of Normal and Abnormal Bipolar Resistive Switching by Interface Junction on In/Nb: SrTiO₃ Interface*, *Appl Phys Lett* **101** (2012).

MAGNETORESISTANCE AND LOW-FREQUENCY NOISE STUDY IN NANO-SCALE ORTHOGONAL MAGNETIC TUNNEL JUNCTIONS

Thi Ngoc Anh Nguyen^{1,2}, **Pham Quang Ngan**¹, **Do Khanh Tung**¹, **Nguyen Thanh Huong**¹, **Vu Hong Ky**¹, **Pham Hong Nam**¹

¹Institute of Materials Science, Vietnam Academy of Science and Technology, Hanoi, Vietnam;

²Graduate University of Science and Technology, Vietnam Academy of Science and Technology, Hanoi, Vietnam;

Email: ngocanhnt.vn@gmail.com

ABSTRACT

Magnetic tunnel junctions (MTJs) with high magnetoresistance ratio (MR) can be used as effective magnetic field sensors. However, the high-noise level at low frequency in MTJ sensors is one of the most difficult issues in developing ultrasensitive magnetic field sensors and their application in point-of-care devices. The MTJs, which have a circular shape of various sizes (80–400 nm in diameter), were fabricated, the resistance-area (RA) products are of order 2,8-4,7 MΩ μm² and MR ratios are greater than 100% at room temperature (RT). In this study, low-frequency noise (LFN) of developed MTJs were investigated thoroughly. We found that the noise spectral power density in all junction sizes is 1/f-like in the investigated frequency range (5 Hz ÷ 20 kHz). The results indicated that 1/f noise in these nano MTJs is dominated by magnetic noise, originating from thermal magnetic fluctuations. A strong reduction of normalized 1/f noise was observed of all MTJ sizes by applying a strong vertical field with respect to the intrinsic thermal noise. The results may open a new approach for reducing this magnetic 1/f noise hence increasing the sensitivity in MTJ nanosensors.

Keywords: Magnetic tunnel junctions, magnetic sensors, low-frequency noise, 1/f magnetic noise, 1/f electric noise

INTRODUCTION

Magnetoresistance (MR) magnetometers based on anisotropic/giant/tunneling magnetoresistance (AMR/GMR/TMR) effects utilizing a change in resistance caused by an external magnetic field are successfully employed in many applications [1,2]. Among other emerging applications, the detection of magnetic fields in the picotesla range is a very promising candidate for biomedical applications [3-5]. Although the most studied MR based biosensors are based on the GMR effect, especially due to their high linear response to the applied field as well as the simplification of the technological process [3,5], TMR-based sensors offer better sensitivity and resolution thanks to their higher MR ratio, reveal their potential to detect weak magnetic fields at low frequencies, as required for magnetic sensors and especially biomedical applications where low frequency signals are of interest [4,6]. However, compared with other MR sensors, TMR sensors suffer from higher noise, specially the 1/f noise of both electric and magnetic origins which commonly

becomes dominant at low frequency, responsible for the limitation of the sensor field detectivity [7,8]. Compared to fully in-plane or perpendicular anisotropy MTJs, orthogonal MTJs can provide higher sensitivity and wider sensing ranges [9,10].

The development of magnetic field MTJ sensors for biomedical applications primarily focuses on high TMR ratio at low resistance-area product (RA), equivalent magnetic noise reduction and sinking their size while keeping the required values of a limit of detection. In this study, we present the correlation between noise performance of nano-sized orthogonal MTJs and three factors: bias voltage, a strong external hard axis field, and junction area in order to exploit the noise sources as well as find ways to reduce the noise in such MTJs.

EXPERIMENTAL

We investigated nano-sized MTJ devices consisting of buffer/PtMn(15 nm)/Co₇₀Fe₃₀(2.5 nm)/Ru(0.9 nm)/Co₇₀Fe₃₀(1.0 nm)/Ta (0.3 nm)/Co₄₀Fe₄₀B₂₀(2 nm)/MgO tunnel barrier(1.1 nm)/Fe₈₀B₂₀(2.1 nm)/capping multilayered film.

The MTJ stack has been deposited on thermally oxidized Si substrates using magnetron sputtering with base pressure of 7.5×10^{-10} Torr. The Ta and MgO/TaB/Ta/Ru served as the buffer layer and capping layer, respectively. The lower 2.0 nm thick CoFeB layer is a reference layer with in-plane magnetic anisotropy, and the upper 2.1 nm thick FeB layer is a free layer with a relatively weak perpendicular (canted) magnetic anisotropy [11]. Here a bottom-pinned exchange biased synthetic antiferromagnetic (SAF) PtMn/CoFe/Ru/CoFe structure was used to stabilize the pinned layer in the in-plane direction.

MTJs with a circular shape of various sizes (80 - 400 nm in diameter) were fabricated using optical and e-beam lithography (EBL) combined with an Ar ion-milling and a lift-off technique. After microfabrication, an annealing process was carried out at 350 °C for 1 h in a magnetic field of 7500 Oe applied along the easy axis of the reference layer to fix the magnetization direction of the reference layer as well as to achieve a high TMR ratio through the crystallized of CoFeB/MgO/FeB junction [10,11].

To characterize the performances of the TMR-based sensor, the MR curves were measured as a function of the external magnetic field up to 2000 Oe and 4000 Oe applied parallel and perpendicular to the sensor surface, respectively. To characterize the low-frequency noise (LFN) of the MTJs, noise spectra were measured in the low-frequency range of up to 20 kHz using the home-built measurement setup, including two independent amplifier channels, which has been described in the previous work [10]. Noise measurements at different bias voltages (V_{bias}) and hard-axis fields (H_{DC}) produced by a permanent magnet applied perpendicular to the sensor surface were performed. All measurements were done at RT.

RESULTS AND DISCUSSION

3.1. TMR ratio and RA characterization

MTJs with high TMR and low RA are required for magnetic sensors. Fig. 1(a) describes the variation of the TMR ratio and RA product for the MTJ devices with different sizes under an in-plane applied field. In our study, MTJs with junction areas ranged from 0.05 to 0.125 μm^2 , corresponding to MTJ diameters of 80-400 nm, all showed high TMR ratios ($> 100\%$) and relatively low in-plane RA products of about 2.86-4.71 $\Omega\mu\text{m}^2$ with relatively small variation ($3.785 \pm$

0.925 $\Omega\mu\text{m}^2$), confirming a high quality of all MTJs studied. The variation of TMR ratio as well as the RA product is not device size dependence which is in a good agreement with the previous calculated report [12]. The out-of-plane TMR (TMR_{oop}) ratios are somehow of the same order as the in-plane TMR (TMR_{ip}) ratios (Fig. 1(b)) confirmed the orthogonal magnetization configuration between the free and pinned layers in the MTJ structure. The higher $\text{TMR}_{\text{oop}}/\text{TMR}_{\text{ip}}$ relates to the stronger PMA of the FeB free layer in the smaller MTJs. When the size of MTJ is decreased the number of domain walls decreased, leading to the better uniform magnetization and the stronger PMA [10].

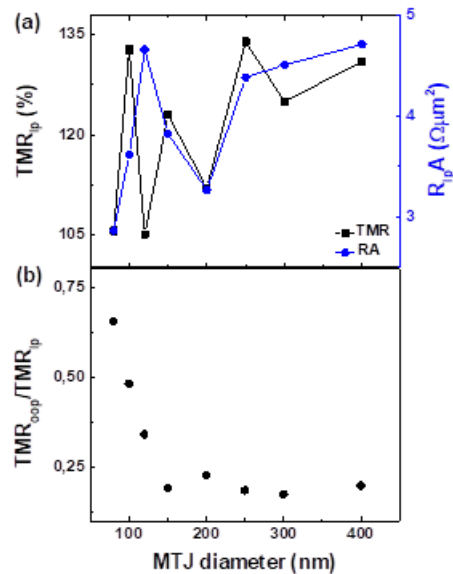


Figure 1. The variation of the TMR and RA product under an in-plane applied field (a) and the ratio between in-plane TMR and out-of-plane TMR (b) for the MTJ devices with different size

3.2. Low-frequency noise and its origins

In order to clarify the origin of the electric and magnetic noises, we measured noise as a function of bias voltage in the absence of a magnetic field (Fig. 2(a)) and as a function of hard-axis bias field (Fig. 2(b)) in all MTJ sizes at RT. Since the noise spectra of 300 nm and 400 nm MTJs were already reported [10,13], here the smaller MTJ device with diameter of 100 nm has been selected for analysis. Fig. 2(a) shows the noise spectra for 100 nm MTJ as a function of bias voltage in the range of 0-80 mV in which the background noise level ($V_{\text{bias}}=0$ mV) is around 10^{-15} V^2/Hz at 10 Hz, related to the external noise, thermal (Johnson) noise of the junction and amplifier noise [10,13], which is 10^3 - 10^5 times less than that of other

voltages, confirmed the electric origin of the noise. The noise spectra show a typical $1/f$ noise behavior which is dominant in the low frequency range for all voltages is very similar to our previous reports on 300 and 400 nm MTJs [10,14] as well as to others MTJ sizes (80-250 nm) (data is not shown here).

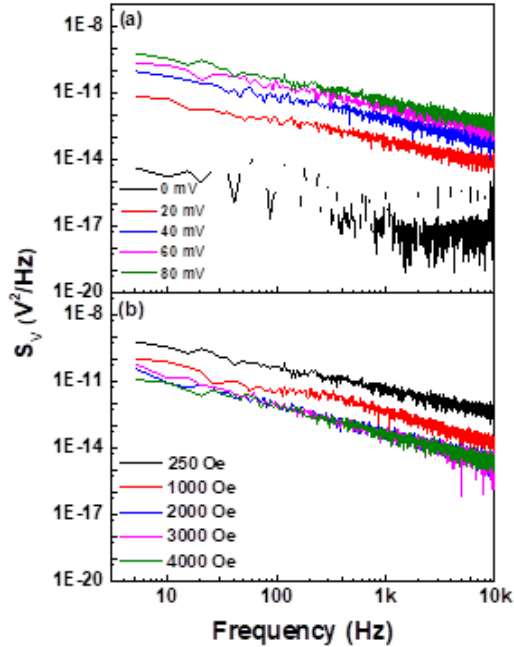


Figure 2. Noise spectra of the 100 nm MTJ sensor (a) at different bias voltages at the zero field and (b) under different hard-axis bias fields; the bias voltage is 80 mV

In order to evaluate the role of a strong hard-axis field, the noise spectral density of 100 nm MTJ was taken in the presence of a hard-axis field H_{DC} (250 Oe - 4000 Oe) shown in Fig. 2(b). It is clear that the observed noise spectrum of the device follows $1/f$ -like behavior for the all H_{DC} . The noise spectral density shows a strong field dependence, and decreases dramatically when the magnetic field increases from 250 Oe (unsaturated field) to 4000 Oe (saturated field) by a factor of 40. This indicates the noise in the 100 nm MTJ has a magnetic field dependent component and a strong external hard-axis field can significantly suppress the magnetization fluctuations of the free layer and lower the magnetic field noise. Such significant magnetic field dependence also observed in 300 nm and 400 nm MTJs [10,13] and all other MTJ sizes (data is not shown here) confirms magnetic origin (not electric) which plays an important role in the observed noise in the nano MTJs.

The LFN in MTJs is often associated with the noise in parallel (P) and antiparallel (AP) states [14] in which the noise in the P state mainly reflects the spin independent resistance fluctuations in the tunneling barrier while the noise in AP state mainly refers to domain wall hopping between pinning sites. In the other words, the barrier noise sets the minimum noise level in any type of MTJ device.

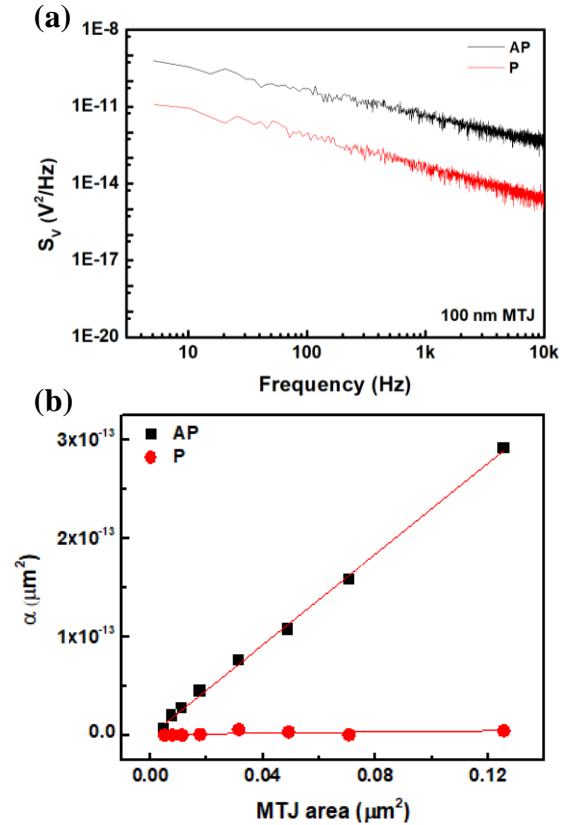


Figure 3. (a) Noise spectra of 100 nm MTJ in parallel (P) and antiparallel (AP) states; (b) Hooe parameter α in parallel (P) and antiparallel (AP) states with different MTJ size. The solid curve shows the linear fit to the data.

It is worth noting that the AP and P noise spectra of 100 nm MTJ both show $1/f$ behavior, the noise level in the AP state is higher than in P state due to the resistance increase as can be seen in Fig. 3(a). The $1/f$ noise of different MTJs can be compared/quantified using the Hooe parameter $\alpha = AfS_V(f)/V^2$ (units in μm^2), where A is the junction area, f is the frequency, S_V is the noise power spectral density, and V is the applied voltage. Low value of $\alpha_P=1.15e^{-15} \mu\text{m}^2$ confirmed the quality of MgO barrier and well as interfaces in MTJ stack. Fig. 3(b) presents Hooe parameter α in P and AP states with different MTJ sizes, the

value of α_P is quite stable with increasing junction area reflecting the nearly-perfect quality of the MgO barrier while the α_{AP} is increased dramatically/linearly with increasing junction area presenting the increasing of formation and manipulation of domain walls, the main source of $1/f$ magnetic noise in nano MTJs. In the other words, when the size/area of MTJ is decreased the number of domain walls decreased, and when the device size is closed to single domain there is just a few or even no domain wall exists, leading to the noise level is lower in the smaller MTJs which is in a good agreement with our previous report [10].

CONCLUSION

We have performed LFN studies on orthogonal MTJs as the function of hard axis field, bias and the junction size. The noise measurements at the low frequency in all MTJs show a pure $1/f$ spectrum. The $1/f$ noise dependence of V_{bias} and H_{DC} confirm the electric and magnetic origins in these nano-scale MTJ sensors in which magnetic noise is dominant and strongly correlated to device size. The $1/f$ noise becomes smaller when the size of MTJ sinks, or the strong H_{DC} is applied. The results open a new approach for reducing the $1/f$ noise level in nano-sized MTJ sensors towards the new generation of biosensor and memory technologies.

Acknowledgment

This work was financially supported by the Vietnamese Ministry of Science and Technology (MOST) with grant number NĐT.88.JP/20. We would like to thank our Japanese collaborators: Minori Goto, Miyoshi Fukumoto, Hiroyuki Tomita, Tatsuki Watanabe, and Yoshishige Suzuki in Osaka University and Hitoshi Kubota, Akio Fukushima, Kei Yakushiji in AIST, Japan.

References

- [1] H. Schewe, W. Schelter, *Industrial applications of magnetoresistive sensors*, Sens. Act. A: Phys. **59**(1-3) (1997) 165-167
- [2] S. Tumanski, *Thin Film Magnetoresistive Sensors*, 1st Edition, 2001 by CRC Press
- [3] A. Guedes et al., *Hybrid GMR Sensor Detecting 950 pT/sqrt(Hz) at 1 Hz and Room Temperature*, Sensors **18**(3) (2018) 790
- [4] S. Cardoso et al., *Magnetic tunnel junction sensors with pTesla sensitivity*, Microsyst. Tech. **20** (2014) 793–802
- [5] V.D. Krishna et al., *GMR-based Biosensor for Detection of Influenza a Virus*, Front. Microbiol. **7** (2016) 400
- [6] Z.Q. Lei et al., *Liver cancer immunoassay with magnetic nanoparticles and MgO-based magnetic tunnel junction sensors*, J. Appl. Phys. **111** (2012) 07E505
- [7] C. Fermon and M. Pannetier-Lecoecur, *Noise in GMR and TMR Sensors, Giant Magnetoresistance (GMR) Sensors: From Basics to State of the Art Applications*, Berlin, Germany: Springer (2013) 47–70
- [8] A. Gokce et al., *1/f noise in magnetic tunnel junctions with MgO tunnel barriers*, J. Appl. Phys. **99**(8) (2006) 08A906
- [9] P. Wisniowski et al., *Magnetic Tunnel Junctions Based on Out-of-Plane Anisotropy Free and In-Plane Pinned Layer Structures for Magnetic Field Sensors*, IEEE Trans. Magn. **48** (2012) 3840–3842
- [10] T.N. Anh Nguyen et al., *Low frequency 1/f noise in deep submicrometer-sized magnetic tunnel junctions*, J. Appl. Phys. **129** (2021) 024503
- [11] H. Kubota et al., *Enhancement of perpendicular magnetic anisotropy in FeB free layers using a thin MgO cap layer*, J. Appl. Phys. **111** (2012) 07C723
- [12] A. H. Lone, S. Shringi, K. Mishra, S. Srinivasan, *Cross-sectional Area Dependence of Tunnel Magnetoresistance, Thermal Stability and Critical Current Density in MTJ*, IEEE Trans. Magn. **57**(2) (2021) 20287906
- [13] T.N. Anh Nguyen et al., *Highly Sensitive Detection of Weak Low Frequency Magnetic Fields Using Single Nanoscale Orthogonal MgO Magnetic Tunnel Junctions under a Large Bias Field*, Mater. Trans. **64** (2023) 2128-2133
- [14] J. M. Almeida et al., *1/f noise in linearized low resistance MgO magnetic tunnel junctions*, J. Appl. Phys. **99** (2006) 08B314

ZERO-DISPERSION WAVELENGTH SHIFTING IN 1,2-DIBROMOETHANE-CORE PHOTONIC CRYSTAL FIBERS FOR GENERATING SUPERCONTINUUM LIGHT SOURCE

Bao Tran Le Tran ¹, Trong Dang Van ¹, Anh Ta Tram ², Nam Nguyen Trong ¹, Tuyet Dang Thi ¹,
Luu Mai Van ³, Vinh Nguyen Thanh ¹, Tan Tran Duy ⁴, Lanh Chu Van ^{1*}

¹ Department of Physics, Vinh University, 182 Le Duan, Truong Thi Ward, Vinh City, Vietnam;

² Vinh Medical University, 161 Nguyen Phong Sac, Hung Dung Ward, Vinh City, Vietnam;

³ Hanoi Open University, B101 Nguyen Hien, Bach Khoa Ward, Hai Ba Trung District, Ha Noi City, Vietnam;

⁴ Truong Xuan High School, Thap Muoi District, Dong Thap Province, Vietnam

Email: chuvanlanh@vinhuni.edu.vn

ABSTRACT

We report the numerical simulation of 1,2-dibromoethane photonic crystal fibers with zero-dispersion wavelength (ZDW) varying according to their structural parameters. These fibers are designed with a difference in the diameter of the air holes between the rings to control dispersion and nonlinearity. In case the hole pitch is small, dispersion properties are quite diverse including anomalous dispersion curves with one or two ZDWs. For the large ones, it is possible to achieve anomalous dispersion with one ZDW for all structures. On the ground of the good confinement of light in the core of PCFs, the ZDW value increases when the hole pitch is larger. ZDW shifts to shorter wavelengths when the filling factor increases to 0.55 or 0.6, after which it follows in the opposite direction. The nanometer-scale shift of the ZDWs will be applied to create supercontinuum light sources.

Keywords: Photonic crystal fiber design, nonlinear optics, zero-dispersion wavelength, 1,2-dibromoethane-core, nanometer-scale shift

INTRODUCTION

Generating supercontinuum in photonic crystal fibers (PCFs) is increasingly receiving attention from the scientific community around the world. PCF is a highly nonlinear medium formed by microscopic air holes in a periodic arrangement surrounding a central defect region. The contrast of refractive index in PCFs is much higher than in conventional optical fibers leading to high optical field confinement. Therefore, PCFs are particularly interesting for nonlinear applications, e.g., in optical parametric oscillators based on phase matching of nonlinearities near zero dispersion wavelength (ZDW). On the other hand, fiber structures with ZDW compatible with the wavelength of the pump light can generate supercontinuum sources with a broad spectrum [1-3]. It is not complicated to achieve this if the size and shape of the PCF microstructure are properly adjusted. For instance, the ZDW can be shifted to a wavelength region shorter than 1270 nm, which is superior to standard single-mode silica fibers, using PCFs with small cores. In hexagonal-shaped structures, the anomalous

dispersion region is expanded further and the ZDW is blue-shifted in the case of increasing the size of air holes in the cladding [3].

The presence of a liquid optical field has, in recent years, effectively controlled the optical properties of a fiber structure such as dispersion characteristics. It is the result of the integration of nanophotonics and microfluidic techniques. In this way, people have filled the central cavity with liquids with high nonlinear refractive index, even hundreds of times higher than fused silica. At this time, light is guided in the core as in the basic mode. The most significant concern is whether the use of liquid will cause disadvantages in experimental operations. The support of advanced techniques such as pressure infiltration or capillary forces has significantly reduced the leakage of liquid during its infiltration into the fiber core [4]. As evidenced by a series of theoretical and experimental works on liquid core PCFs have been reported [2, 5-7].

Our intention in this work is to use a 1,2-dibromoethane core fiber design for numerical studies of chromatic dispersion properties around wavelengths of 500–3500 nm, and then calculate

the ZDWs through continuously controlling geometrical parameters. Hieu et al. [8] have also taken full advantage of the above liquid type with a seven-ring air hole fiber model in the photonic cladding. It should be noted that increasing the number of layers leads to a decrease in confinement loss but causes an obstacle in the fiber production process. Therefore, we report the simulation of a five-ring air-hole PCF with dissimilar dimensions for the purpose of effectively controlling the ZDW of the fiber.

MODELING AND PROPERTIES OF PCFs

Figure 1 displays a cross-section of the proposed PCF made of fused silica glass using the stack and draw method. It includes five rings of air holes ordered in a hexagonal lattice with a 1,2-dibromoethane core. The diameter of two symmetrical air holes on the horizontal axis (d_1) is 1.8 times larger than that of the remaining air holes (d_2). Core diameter D_C as a function of hole pitch (A) and d_2 is calculated according to the formula: $D_C = 4A - 1.9d_2$. This design results in a change in the effective refractive index for dispersion control and reduced loss.

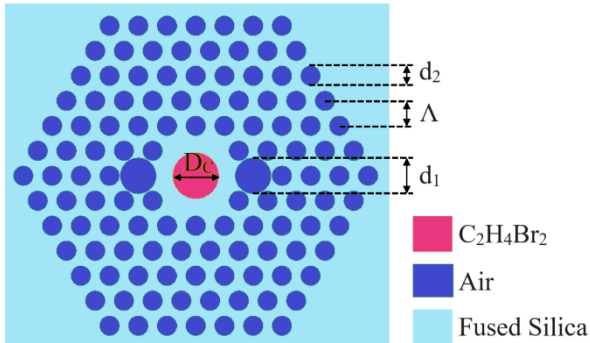


Figure 1. Cross section of the designed PCF with a 1,2-dibromoethane core.

The developed fiber is numerically investigated based on Lumerical Mode Solutions software. The refractive index of fused silica glass and 1,2-dibromoethane as a function of wavelength λ is described by the Sellmeier relation [8]:

$$n(\lambda) = \left(1 + \frac{A_1 \lambda^2}{\lambda^2 - B_1} + \frac{A_2 \lambda^2}{\lambda^2 - B_2} + \frac{A_3 \lambda^2}{\lambda^2 - B_3} \right)^{1/2} \quad (1)$$

where the coefficients A_x and B_y ($x, y = 1, 2, 3$) for fused silica are $A_1 = 0.6694226$, $A_2 = 0.434584$, $A_3 = 0.8716947$, $B_1 = 44801 \text{ nm}^2$, $B_2 = 132.85 \text{ nm}^2$, $B_3 = 95341482 \text{ nm}^2$. The figures for 1,2-dibromoethane are $A_1 = 1.3163728$, $A_2 = 0.4013224$, $B_1 = 16161.22 \text{ nm}^2$, $B_2 = 142229890.2$

nm^2 . Figure 2 shows that the real refractive index of 1,2-dibromoethane is larger than that of fused silica glass in the visible-to-near-infrared range. The fact that the core refractive index of hollow-core PCFs is smaller than its cladding refractive index leads to light transmission according to the photonic bandgap. Filling the core with a liquid with a refractive index higher than the cladding causes the refractive index difference to follow the opposite trend, that is, the 1,2-dibromoethane PCFs guide light like conventional solid core ones.

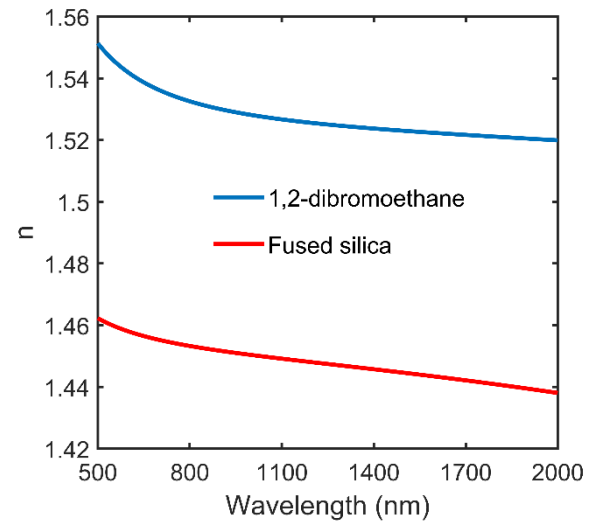


Figure 2. Refractive index characteristic of the materials.

DISCUSSION OF ZDW SHIFT IN PCFs

The propagation of ultrashort pulses in a zero-dispersion significantly decreases the dispersion expansion of optical signals in telecommunications systems. ZDW can be determined by the following formula [3]:

$$k'' = \frac{\partial^2 k}{\partial \omega^2} \quad (2)$$

Chromatic dispersion calculations are performed for wavelengths between 0.8 and 3.5 μm , for hole pitches between 1.0 and 2.0 μm , and for filling factors d_2/A between 0.3 and 0.7. Detailed information about the change in fundamental mode dispersion depending on A and d_2/A is shown in Figures 3–5. The results show that waveguide dispersion controls the dispersion variation strongly (Figure 3), i.e. anomalous dispersion with one or two ZDWs is achieved for each specific application. Furthermore, the strong configuration of waveguide dispersion can shift the ZDW to blueshift wavelengths by falling the

core size while keeping the hole pitch. This can be seen in the dispersion curves with one ZDW in Figures 4 and 5.

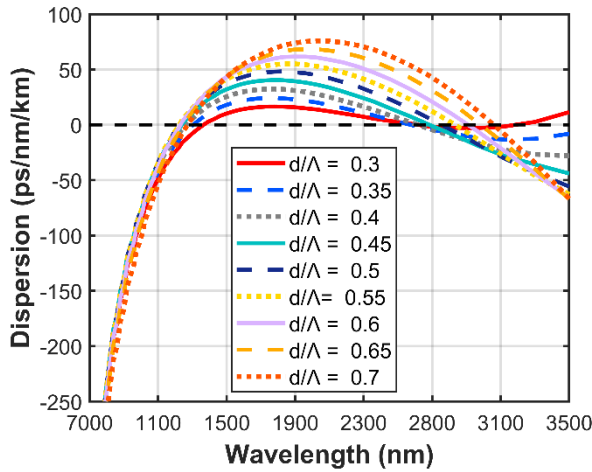


Figure 3. Dispersion characteristics of the fundamental mode for the lattice constant of 1.0 μm .

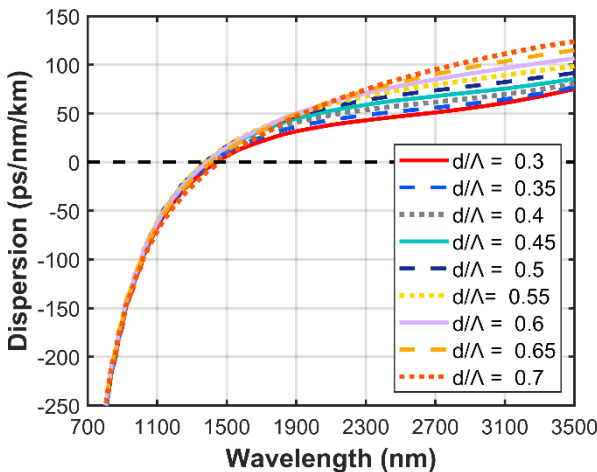


Figure 4. Dispersion characteristics of the fundamental mode for the lattice constant of 1.5 μm .

On the other hand, how to choose a pump source for supercontinuum generation to achieve high efficiency is also governed by the ZDW shift. A pump laser with a wavelength at the peak of the dispersion curve is recommended for supercontinuum generation in anomalous dispersion fibers with two ZDWs [9]. Whereas, those with one ZDW require an input wavelength close and larger than ZDW. The variation of ZDWs with Λ and d_2/Λ is illustrated in Figure 6 while their values are presented in Table 1. It is clear that ZDWs experience a downward trend as the filling factor increases. Up to a certain value of d_2/Λ , such as 0.55 or 0.6, these curves follow the opposite trend. The most pronounced increase is

observed in the case of ZDW_2 ($\Lambda = 1.0 \mu\text{m}$). Additionally, the ZDWs are shifted toward the red wavelength with increasing hole pitch since the light is tightly confined in the core.

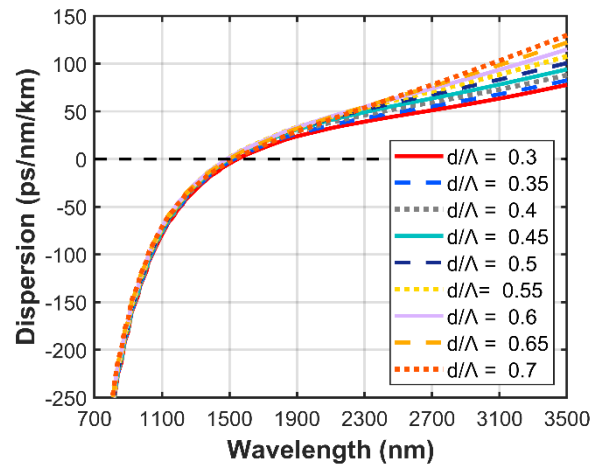


Figure 5. Dispersion characteristics of the fundamental mode for the lattice constant of 2.0 μm .

Table 1. The value of ZDWs of PCFs.

d_2/Λ	$\Lambda = 1.0 \mu\text{m}$		$\Lambda = 1.5 \mu\text{m}$	$\Lambda = 2.0 \mu\text{m}$
	ZDW ₁	ZDW ₂	ZDW ₁	ZDW ₁
0.3	1.365	2.616	1.443	1.548
0.35	1.306	2.574	1.416	1.528
0.4	1.263	2.614	1.393	1.512
0.45	1.237	2.683	1.381	1.499
0.5	1.227	2.755	1.375	1.49
0.55	1.225	2.833	1.376	1.485
0.6	1.23	2.909	1.386	1.485
0.65	1.245	2.981	1.413	1.497
0.7	1.272	3.058	1.456	1.528

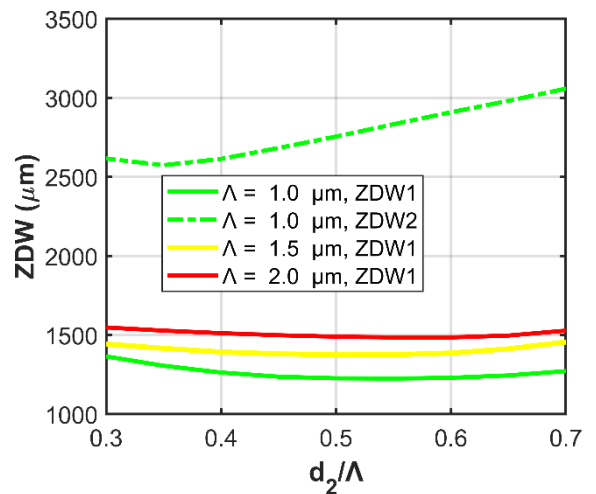


Figure 6. ZDW shift with filling factor and lattice constant.

After determining the shift of the ZDW in the near-infrared range (approximately 100 nm in this work) and choosing the appropriate pump wavelength, new frequency components are created on the ground of the appearance of nonlinear processes [1]. This means that input pulse broadening in the near-infrared region is observed when the peak power is large enough.

CONCLUSION

We have reported the simulation of ZDW shift in 1,2-dibromoethane PCFs. This important dispersion property allows fine-tuning of pump source specifications such as the input wavelength for supercontinuum generation. The results show a shift toward longer wavelengths of ZDW with filling factors and an increase in the hole pitch. Interestingly, it is possible to modify the ZDW in the 100 nm range by varying the air hole size in the cladding. The degree of such shift is superior to some previous works [3, 5, 9], which is very beneficial for near-infrared supercontinuum light sources.

Acknowledgment

This research is funded by Vietnam's Ministry of Education and Training (B2023-TDV-07).

Le Tran Bao Tran was funded by the Master, PhD Scholarship Programme of Vingroup Innovation Foundation (VINIF), code VINIF.2023.TS.133.

Dang Van Trong was funded by the Master, PhD Scholarship Programme of Vingroup Innovation Foundation (VINIF), code [VINIF.2022.TS136].

References

- [1] G. P. Agrawal, *Nonlinear Fiber Optics*, Academic Press, Oxford, 2013.
- [2] L. T. B. Tran, C. V. Lanh, *Broadband supercontinuum generation in a square lattice photonic crystal fiber with C₆H₆-core using low pump power*, The European Physical Journal D 77 (2023) 90 (11pp).
- [3] L. V. Hieu, R. Buczynski, C. L. Van, M. Trippenbach, K. Borzycki, N. M. An, R. Kasztelanic, *Measurement of temperature and concentration influence on the dispersion of fused silica glass photonic crystal fiber infiltrated with water-ethanol mixture*, Optics Communications 407 (2018) 417-422.
- [4] J. R. Bautista-Quijano, H. Brünig, P. Pötschke, *Improved sensitivity of liquid sensing melt-spun polymer fibers filled with carbon nanoparticles by considering solvent-polymer solubility parameters*, Materials Research Express 10 (2023) 055307 (26pp).
- [5] H. V. Thuy, R. Kasztelanic, A. Anuszkiewicz, G. Stepniewski, A. Filipkowski, S. Ertman, D. Pysz, T. Wolinski, D. X. Khoa, M. Klimczak, R. Buczynski, *All-normal dispersion supercontinuum generation in photonic crystal fibers with large hollow cores infiltrated with toluene*, Optical Materials Express 8 (2018) 3568-3582.
- [6] C. V. Lanh, L. T. B. Tran, N. T. Thuy, H. T. Duc, D. V. Trong, D. M. Trang, T. N. Hoang, T. D. Thanh, D. Q. Khoa, *Comparison of supercontinuum generation spectral intensity in benzene-core PCFs with different types of lattices in the claddings*, Optical and Quantum Electronics 54 (2022) 840 (16pp).
- [7] L. V. Hieu, H. V. Thuy, N. T. Hue, C. L. Van, R. Buczynski, R. Kasztelanic, *Supercontinuum generation in photonic crystal fibers infiltrated with tetrachloroethylene*, Optical and Quantum Electronics 53 (2021) 187 (18pp).
- [8] L. V. Hieu, H. V. Thuy, L. C. Trung, H. D. Quang, N. T. Hue, V. T. M. Ngoc, M. Klimczak, R. Buczynski, R. Kasztelanic, *Silica-based photonic crystal fiber infiltrated with 1,2-dibromoethane for supercontinuum generation*, Applied Optics 60 (2021) 7268-7278.
- [9] N. T. Thuy, *Dispersion Optimization in GeO₂-doped Silica Photonic Crystal Fibers with Circular Lattice*, Majlesi Journal of Electrical Engineering 17 (2023) 59-67.

DEVELOPMENT AND IMPLEMENTATION OF AN ELECTRONIC CIRCUIT BOARD FOR CONDUCTIVITY METER: DESIGN, SIMULATION, AND FABRICATION

Nhat Minh Nguyen, Danh Van Tran, Ngan Nguyen Le, Tin Chanh Duc Doan, Dung My Thi Dang, Chien Mau Dang

Institute for Nanotechnology, Community 6, Linh Trung Ward, Thu Duc City, Ho Chi Minh City, Vietnam;
Vietnam National University Ho Chi Minh City, Ho Chi Minh City, Vietnam
Email: ddctin@vnuhcm.edu.vn

ABSTRACT

In order to address the challenge of fabricating conductivity measurement circuit at a lower cost compared to the currently available conductivity sensing circuits in the world. Simultaneously, the manufacturing of the conductivity measurement circuitry must also attain high performance to meet the demands of mass production for integration into brine monitoring station systems. This paper described about design, simulation of conductivity measurement circuit using LTSpice and Altium, fabrication the printing circuit boards (PCB) of it. The main objective is to sense the conductivity of aquaculture water. The research objective will be geared towards the fabrication of conductivity measurement PCB through various approaches, including the utilization of modules, functional Integrated Circuit (IC), or a combination of both methodologies. Employing prototype boards, the construction of probes, encompassing both commercial and custom-made variants, will be conducted. Subsequent performance assessment will be carried out by comparing their efficiency against commercial circuit boards such as Atlas and Hemera. Programming software for relevant functions such as temperature compensation, calibration, conversion of conductivity to salinity values, and other auxiliary features will be developed.

Keyword: Printing circuit boards (PCB), Conductivity sensor, Integrated Circuit (IC), Operation amplifier (Opamp).

INTRODUCTION

The research on manufacturing conductance sensor circuit boards has been conducted based on numerous experiments that were previously conducted on conductance sensors and reading circuits. Understanding the structure, operating principles, and issues related to conductance sensors [1] helps grasp the fundamental principles to coordinate with electrical circuit principles, making the manufacturing of reading circuits easier.

Basic surveys on conductance sensors were conducted using Arduino Uno microcontroller [2] as the foundation for developing the conductance reading circuit in this paper. There are multiple methods for collecting and processing electrical signals from the conductance reading circuit, with the simplest being the use of a multimeter [3] to read voltage values.

Additionally, there are methods for manufacturing conductance sensors using printed circuit board (PCB) techniques and developing related formulas [4].

Experimentation was conducted with a conductance sensor reading circuit using a 4-bit ADC - low-resolution analog-to-digital converter, and a testing and evaluation procedure was established involving multiple stages and iterations [5].

Experiments were conducted on various commercial conductance reading modules under different conditions such as wire lengths, standard solution compositions, etc. [6] to obtain the most accurate assessment of the effectiveness of the sensor along with its corresponding reading circuit. This served as the groundwork for evaluating the manufactured reading circuits.

EXPERIMENTAL

When placing the probe into a solution with a certain salinity value, it creates resistance between the electrodes. To measure this resistance, a voltage (or current) needs to be applied to one electrode, which generates a current (or voltage) across the impedance formed by the other.

Figure 1 shows the block diagram of the conductivity meter. The oscillator generates a sine

wave applied to one of the electrodes after passing through Input Buffer Stage. The other electrode is coupled to the input of a Transimpedance Amplifier (Current-to-voltage converter). After RMS Circuit LTC1966, the output DC voltage be gain with Output gain Stage which is read out through ADC of Arduino.

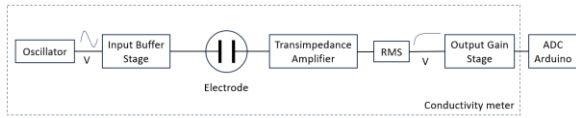


Figure 1. Block diagram of conductivity meter with sine wave of oscillator and dc voltage output.

Figure 2 shows the circuit simulate in LTSpice. Circuit based on Rail to Rail operation amplifier AD820 in order to use a single power supply allowing compatibility with the Arduino. Oscillator input use a fairly simple mini board for sinusoidal signal generation populate with the AD9833, in simulation simply use AC voltage to supply input. This case use sine voltage with 620mV amplitude and 10kHz frequency.

Input buffer Stage is primarily designed to increase the power supplied to the entire circuit. During the power supply process, the electricity passes through various load components, causing voltage drop if the power supply does not have sufficient capacity. This voltage will supply to one of the electrodes. The salinity sensor simulation block has been modeled based on extensive research and experiments conducted by researchers. The other electrode is coupled to the input of a Transimpedance Amplifier, transfer current of electrode to voltage.

In order to micro controller process sine signal, use RMS circuit LTC1966. Sine voltage will be transfer to DC voltage. The value of DC voltage is small, when read by ADC will less exactly. Output Gain Stage response multiple this DC voltage to ADC can read with high accurate.

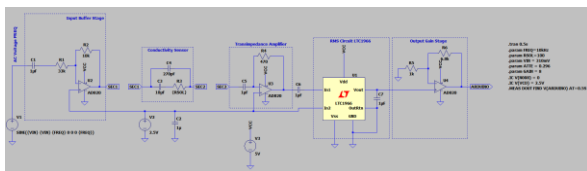


Figure 2. Conductivity meter Circuit Simulate in LTSpice.

Figure 3 show conductivity meter use breadboard after simulate circuit. Amplitude of Sinewave is generated from AD9833 module have value 620mV and Frequency is adjusted by

Arduino Nano use 10kHz value. Rail to rail opamp AD820 is used on all board. DC voltage output is read by ADC 10 bits of arduino nano.

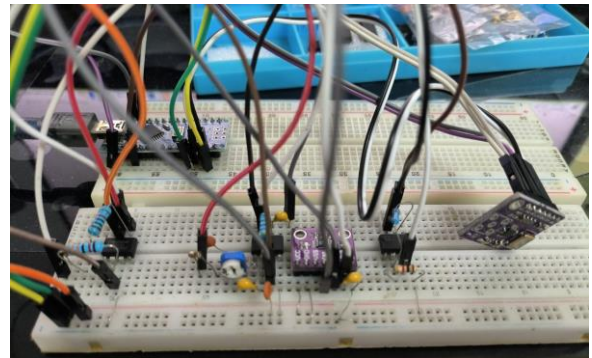


Figure 3. Conductivity meter test on breadboard

Figure 4 show schematic diagram of conductivity meter designed on Altium, laying the groundwork for design PCB. This schematic is based on the simulated circuit and breadboard that has been implemented and yielded the expected simulation results.

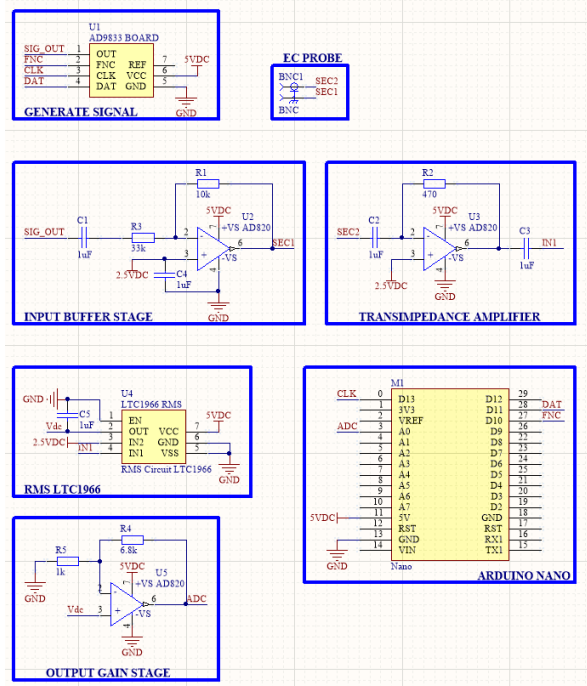


Figure 4. Schematic diagram of Conductivity meter designed on Altium

RESULTS AND DISCUSSION

After designing the circuit schematic using simulation software like LTSpice, you can proceed to assign component values, simulation parameters, and other relevant values to obtain simulation results as follows.

Figure 5 show sinewave voltage signal is used as input of conductivity meter. Amplitude of signal is 620mV and frequency is 10kHz. Figure 6 show DC voltage will be read out by ADC of Arduino. If Conductivity increase, this value will increase too.

The Voltage of ADC 10 bits is 5VDC so the smallest share is approximate 5mV, it conform for measure conductivity in large range.

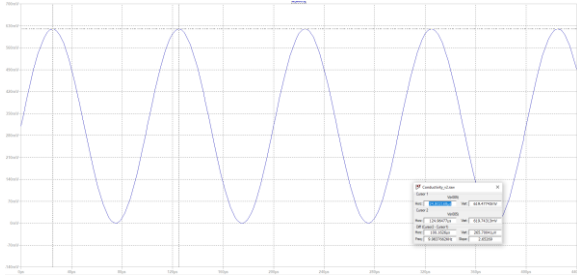


Figure 5. The simulated sine signal provides voltage to the module

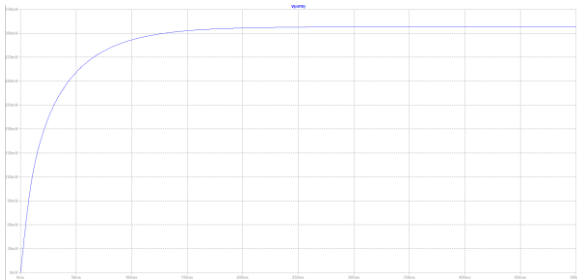


Figure 6. DC voltage signal after current to voltage transfer

With the desired simulation results achieved, redesign the schematic diagram using Altium Designer circuit design software. Export the designed components through the circuit design interface, arrange the components, and route the connections to create a complete conductance reading circuit.

Figure 7 show board PCB is designed base on schematic designed (include top layer, bottom layer, top overlay). After this step, the conductivity sensor reading circuit is essentially completed. Figure 8 is model 3D of conductivity meter board.

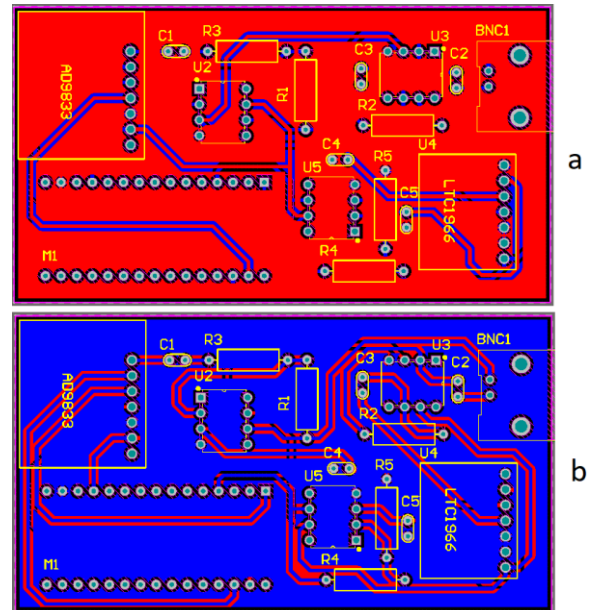


Figure 7. PCB board of conductivity meter is designed on Altium with top layer – red color (a) and bottom layer – blue color (b)

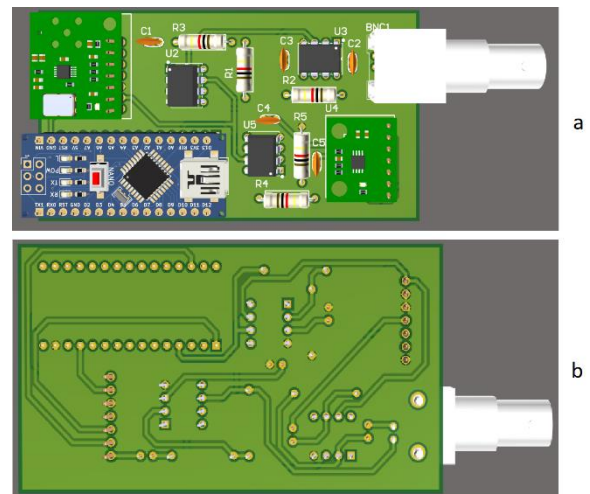


Figure 8. 3D model of conductivity meter board with top view include many electric component (a) and bottom view (b)

CONCLUSION

We have achieved good simulation results, from simulating the circuit using a sine wave input signal to converting current into voltage and obtaining the DC output. In the real conductance reading circuit, the SPI control results match the waveform pattern programmed by the waveform generation module. Additionally, the functional blocks within the circuit perform their intended functions correctly, aligning with the theoretical expectations and simulation results. However, during the practical implementation, certain difficulties were encountered, leading to less-

than-optimal results. Improvements to the conductivity measurement circuit will be pursued in the future.

Acknowledgment

The research was sponsored by the Department of Science and Technology Ben Tre province under Research Project Contract Number: 1642/HĐ-SKHCN.

References

- [1] J. P. J. H. G. P. S. Albert Liddicoat, Development and assessment of a pcb layout and manufacturing laboratory module in introductory electric circuits for ee and non-ee majors, American Society for Engineering Education, (2012).
- [2] K. Chan, Innovative school-level quantitative chemistry experimental technique (iii) a conductivity meter designed for micro-scale use in schools, AJCE (2021).
- [3] P. H. Rieger, ElectroChemistry, London: Chapman & Hall One Penn Plaza New York, (1994).
- [4] F. S. I. Rafael L. Alfonso, Low-cost experiments on electrolytic conductivity, KIMIKA 9 (1993) 73-76.
- [5] A. A. W. S. Randika M.A., Development of an arduino-based low-cost turbidity and electric conductivity meter for wastewater characterization, Larhyss Journal, (2022) 115-127.
- [6] J. C. S. M. H. K. J. D. A. T. Stephanie G. FultonID, Laboratory evaluation of open source and commercial electrical conductivity sensor precision and accuracy: How do they compare?, PLOS ONE, (2023).

MINIMIZING EFFECTIVE MODE AREA OF HEXAGONAL-SHAPED PHOTONIC CRYSTAL FIBERS FILLED BY $C_6H_5NO_2$ AND $C_2H_4Br_2$ LIQUIDS

Trong Dang Van¹, Bao Tran Le Tran¹, Ngoan Le Thi¹, Duy Pham Dinh¹, Thuy Do Thanh¹, Anh Ta Tram², Luu Mai Van³, Vinh Nguyen Thanh¹, Lanh Chu Van^{1*}

¹ Department of Physics, Vinh University, 182 Le Duan, Truong Thi Ward, Vinh City, Vietnam;

² Vinh Medical University, 161 Nguyen Phong Sac, Hung Dung Ward, Vinh City, Vietnam;

³ Hanoi Open University, B101 Nguyen Hien, Bach Khoa Ward, Hai Ba Trung District, Ha Noi City, Vietnam

Email: chuvanlanh@vinhuni.edu.vn

ABSTRACT

In this paper, we propose two new hexagonal photonic crystal fibers (PCFs) with core-filled nitrobenzene ($C_6H_5NO_2$) and 1,2-dibromoethane ($C_2H_4Br_2$) with small effective mode areas. The small effective mode area is achieved by selecting PCFs with five lattice rings and the size of the two air holes on the x-axis of the first ring is larger than the other air holes in the cladding. We numerically analyze and compare the effective area of PCFs with these two different liquid permeation structures, in which the influence of lattice constant and filling factor on the effective mode area properties of PCFs is noted. $C_6H_5NO_2$ -core PCF possesses a smaller effective mode area than the $C_2H_4Br_2$ -core PCF at 1550 nm. The proposed fibers with this small effective mode area open up good application opportunities for PCFs in supercontinuum generation.

Keywords: Photonic crystal fiber, $C_6H_5NO_2$ -core, $C_2H_4Br_2$ -core, hexagonal lattice, nonlinear optics

INTRODUCTION

Photonic crystal fibers (PCFs) [1] have drawn our attention in many commercial realms including telecommunication applications, high-power signal transmission, sensing, high-power fiber lasers [2], and amplifiers [2], fiber-to-the-home (FTTH) applications [3], supercontinuum generation [4], terahertz applications [5] etc. due to being equipped with a number of unique and novel properties that conventional optical fibers cannot achieve. With design flexibility, PCF achieves endlessly single-mode features, large effective mode area, management of chromatic dispersion, high nonlinearity, and high birefringence. Fiber-based supercontinuum (SC) sources have become a strong research focus in the past years. Supercontinuum generation (SCG) is a well-known process that involves the production of broadband light through the interaction of short pulses, divided by narrow sources, with various nonlinear materials. The interest in this type of ultra-broadband source is due to its potential applications in various fields such as sensing, characterization of optical components, interferometry, or optical coherence tomography. Normally, to have a high-

performance SCG, it is necessary to have a PCF with nearly zero flat dispersion, small loss, and a small effective mode area leading to high nonlinear coefficients.

Effective mode area is an important characteristic directly related to the applications of fiber optic technology. A large effective mode area alleviates nonlinear effects such as stimulated Brillouin scattering, self-phase modulation, and Raman scattering. These effects reduce the power density factor in the core region of the fiber to maintain high beam quality for applications such as fiber lasers, amplifiers, and high-power signal transmission systems. Meanwhile, PCF with a small effective mode area increases the nonlinearity of the fiber suitable for SCG.

This paper introduces a new PCF design with a small effective mode area. PCF with five rings of air holes arranged in a hexagonal lattice and the core is filled with two liquids 1,2-dibromoethane ($C_2H_4Br_2$) and nitrobenzene ($C_6H_5NO_2$). We analyze and compare the effective mode areas of PCFs with changes in structural parameters. From there, optimal structures suitable for PCF supercontinuum generation are proposed. The structures of the

PCF are modeled using the finite difference eigenmode (FDE) method. The boundary condition for the simulation herein is perfectly matched layer (PML) boundaries. This boundary condition allows the radiation to propagate out of the computational area without either an interferometer with the field inside or boundaries absorbing incident light upon them.

NUMERICAL MODELING

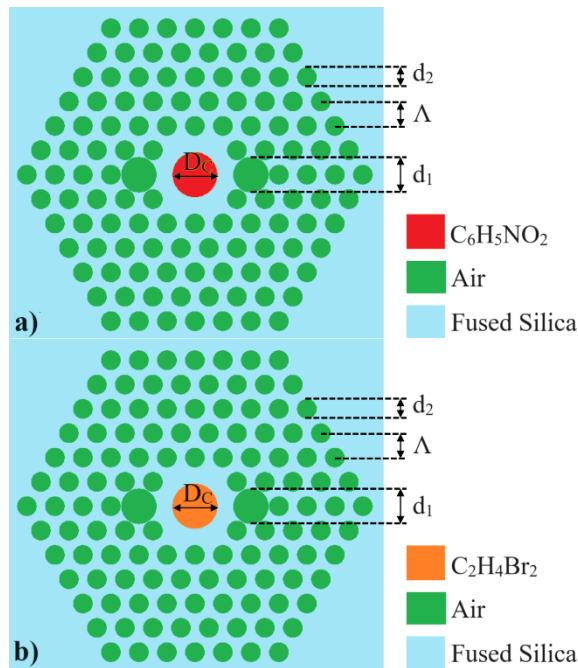


Figure 1. Geometric structure of hollow core hexagonal lattice PCF filled with: a) $C_6H_5NO_2$ and b) $C_2H_4Br_2$

The geometrical structure diagram of PCFs made of silica fused glass, with a core filled with

Table 1. Sellmeier Coefficients of the Materials Used

Sellmeier coefficients	$C_6H_5NO_2$	$C_2H_4Br_2$	Fused silica
A_0	1	1	1
A_1	1.30628	1.3163728	0.6694226
A_2	0.00502	0.4013224	0.4345839
A_3	-	-	0.8716947
B_1	$0.02268 \mu m^2$	$0.01616122 \mu m^2$	$4.4801 \times 10^{-3} \mu m^2$
B_2	$0.18487 \mu m^2$	$142.2298902 \mu m^2$	$1.3285 \times 10^{-2} \mu m^2$
B_3	-	-	$95.341482 \mu m^2$

The effective mode area is determined by the formula (2) [1]:

$C_2H_4Br_2$ and $C_6H_5NO_2$, is shown in Figure 1. The fiber consists of 5 rings of air holes arranged in a hexagonal lattice defined by the lattice constant and air-hole diameter d_1, d_2 . d_1 is the diameter of 2 air holes located on the x-axis near the core and d_2 is the diameter of the remaining air holes ($d_1 = 1.8d_2$). The filling factor (f) of the fiber is determined as $f = d_2 / \Lambda$. The diameter of the core is determined according to the formula $D_c = 4\Lambda - 1.9d_1$ to ensure the technical feasibility of the proposed structure after the manufacturing process. The base material is fused silica which creates a refractive index difference between the core and cladding to improve light confinement in the core. The difference between the size of the two air holes on the x-axis near the core compared to the other air holes in the cladding is the highlight of this structure. This results in diverse fiber optical characteristics.

We investigate and analyze the effective mode area of the fibers with changes in the lattice constant and the filling factor. In which, Λ is chosen to be $1.0 \mu m$ and $1.5 \mu m$, and f changes from 0.3 to 0.7 with a step of 0.05.

The nonlinear refractive index of the materials used in the construction is calculated according to the Sellmeier equation as follows [6]:

$$n(\lambda) = \sqrt{A_0 + \frac{A_1\lambda^2}{\lambda^2 - B_1} + \frac{A_2\lambda^2}{\lambda^2 - B_2} + \frac{A_3\lambda^2}{\lambda^2 - B_3}} \quad (1)$$

The values of the coefficients are listed in Table 1 and λ is the wavelength in micrometers.

$$A_{eff} = \frac{\left(\int_{-\infty}^{\infty} \int_{-\infty}^{\infty} |E(x, y)|^2 dx dy \right)^2}{\int_{-\infty}^{\infty} \int_{-\infty}^{\infty} |E(x, y)|^4 dx dy} \quad (2)$$

Where E is the electric field amplitude.

RESULTS AND DISCUSSION

Figures 2 and 3 show the effective mode area characteristics of $C_6H_5NO_2$ and $C_2H_4Br_2$ core PCFs with different lattice constants and filling factors. Based on the graph, it can be seen that the

effective mode area of the PCF is proportional to the wavelength λ and inversely proportional to the filling factor f . This is because light is absorbed more strongly at large wavelength ranges and is lost more as the filling factor increases. Furthermore, the air hole diameter decreases, so the liquid core diameter increases. Compared with the $C_2H_4Br_2$ permeation PCF structure, the effective mode area of the $C_6H_5NO_2$ permeation PCF structure is smaller because the nonlinear refractive index of $C_6H_5NO_2$ is larger than the nonlinear refractive index of $C_2H_4Br_2$.

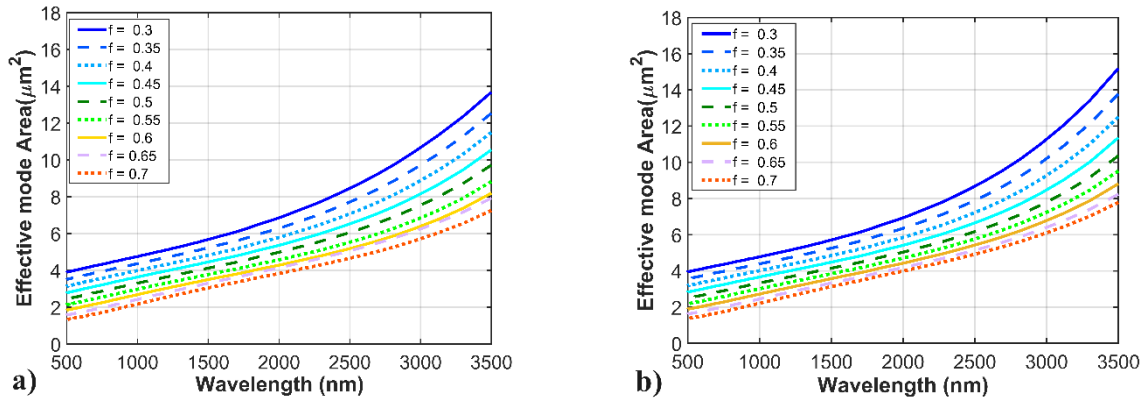


Figure 2. The effective mode areas as a function of the wavelength of the fiber with $\Lambda = 1.0 \mu\text{m}$ (a) $C_6H_5NO_2$ -core; (b) $C_2H_4Br_2$ -core

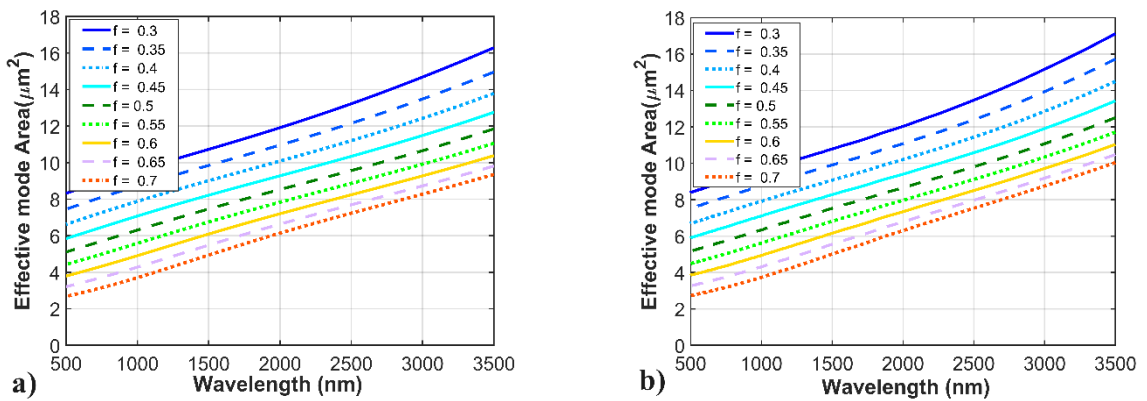


Figure 3. The effective mode areas as a function of the wavelength of the fiber with $\Lambda = 1.5 \mu\text{m}$ (a) $C_6H_5NO_2$ -core; (b) $C_2H_4Br_2$ -core

Table 2 shows the comparison of the effective mode areas of two PCFs at $1.55 \mu\text{m}$ wavelength with different lattice constants and filling factors. Under the same lattice constant, the effective mode area gradually decreases as the filling factor increases from 0.3 to 0.7 at 1500 nm . The effective mode area value of $C_2H_4Br_2$ -core PCF is always larger than that of $C_6H_5NO_2$ -core PCF at each certain lattice constant. Specifically, for the lattice constant $\Lambda = 1.0 \mu\text{m}$, the largest effective mode areas of the $C_6H_5NO_2$ and $C_2H_4Br_2$ -core PCFs are

$5.76 \mu\text{m}^2$ and $5.79 \mu\text{m}^2$, respectively. Similarly, for $\Lambda = 1.5 \mu\text{m}$, this value is $10.82 \mu\text{m}^2$ for $C_6H_5NO_2$ -core PCF and $10.88 \mu\text{m}^2$ for $C_2H_4Br_2$ -core PCF. However, in this work, we aim to choose a structure with a small effective mode area to apply to supercontinuum generation. $C_6H_5NO_2$ -core PCF with $f = 0.7$, $\Lambda = 1.0 \mu\text{m}$ has the smallest effective mode area among the studied fibers. At wavelength 1550 nm , this value is achieved as $3.11 \mu\text{m}^2$. We propose that this structure can be applied to effective SCG. It can

be seen that the proposed fiber has a smaller effective mode area than the previously announced wide-core fibers [7, 8]. A small

effective mode area is always sought for supercontinuum generation efficiency.

Table 2. Effective mode area values of PCF at wavelength 1550 nm with different structural parameters

λ (nm)	d_1/A	A_{eff} (μm^2)			
		$A = 1.0$ (μm)		$A = 1.5$ (μm)	
		$\text{C}_6\text{H}_5\text{NO}_2$	$\text{C}_2\text{H}_4\text{Br}_2$	$\text{C}_6\text{H}_5\text{NO}_2$	$\text{C}_2\text{H}_4\text{Br}_2$
1550	0.3	5.76	5.79	10.82	10.88
	0.35	5.3	5.33	9.93	10.0
	0.4	4.89	4.92	9.1	9.16
	0.45	4.52	4.55	8.3	8.37
	0.5	4.18	4.21	7.55	7.62
	0.55	3.84	3.91	6.84	6.91
	0.6	3.56	3.64	6.19	6.26
	0.65	3.37	3.4	5.58	5.65
	0.7	3.11	3.2	5.04	5.12

CONCLUSION

In this paper, we design two hollow-core photonic crystal fiber structures filled with nitrobenzene ($\text{C}_6\text{H}_5\text{NO}_2$) and 1,2-dibromoethane ($\text{C}_2\text{H}_4\text{Br}_2$). We analyze and compare the effective mode area of PCF with cores filled with different liquids, thereby seeing the influence of lattice constant and filling factor on the effective mode area characteristics of PCF. The $\text{C}_6\text{H}_5\text{NO}_2$ -core PCF structure has a smaller effective mode area than the $\text{C}_2\text{H}_4\text{Br}_2$ -core PCF. Fibers with small effective mode areas are well applied for supercontinuum generation. Our results show that our PCF designs are promising for optical fiber technology applications.

Acknowledgment

This research is funded by Vietnam’s Ministry of Education and Training (B2023-TDV-07).

Le Tran Bao Tran was funded by the Master, PhD Scholarship Programme of Vingroup Innovation Foundation (VINIF), code VINIF.2023.TS.133.

Dang Van Trong was funded by the Master, PhD Scholarship Programme of Vingroup Innovation Foundation (VINIF), code [VINIF.2022.TS136].

References

[1] P. Russell, *Photonic crystal fibers*, Science, **299** (2003) 358–362.
 [2] C. Jauregui, J. Limpert, and A. Tunnermann, *High-power fibre lasers*, Nature photonics, **7** (2013) 861–867.
 [3] M.-J. Li, P. Tandon, D. C. Bookbinder, S. R. Bickham, M. A. McDermott, R. B. Desorcie, D. A. Nolan, J. J. Johnson, K. A. Lewis, and J. J. Englebert, *Ultra-low bending loss single-*

mode fiber for fth, Journal of Lightwave Technology **27** (2009) 376–382.

[4] T. D. Van, L. C. Van, *Supercontinuum generation in $\text{C}_6\text{H}_5\text{NO}_2$ -core photonic crystal fibers with various air-hole size*, Modern Physics Letters B **37** (2023) 2350063.
 [5] H. Han, H. Park, M. Cho, and J. Kim, *Terahertz pulse propagation in a plastic photonic crystal fiber*, Applied Physics Letters **8** (2002) 2634–2636.
 [6] T. A. Birks, J. C. Knight, and P. S. J. Russell, *Endlessly single-mode photonic crystal fiber*, Optics letters **22** (1997) 961–963.
 [7] C. V. Lanh, H. V. Thuy, K. Borzycki, D. X. Khoa, T. Q. Vu, M. Trippenbach, R. Buczyn’ski and J. Pniewski, *Supercontinuum generation in photonic crystal fibers infiltrated with nitrobenzene*, Laser Physics. **30** (2020) 035105.
 [8] L. V. Hieu, H. V. Thuy, N. T. Hue, C. L. Van, R. Buczyn’ski and R. Kasztelanic, *Supercontinuum generation in photonic crystal fibers infiltrated with tetrachloroethylene*, Optical Quantum Electronic **53** (2021) 187.

A HIGHLY BRIEFRINGENT PHOTONIC CRYSTAL FIBER INFILTRATED WITH 1,2-DIBROMOETHANE FOR APPLICATIONS IN OPTICAL TECHNOLOGY

Bao Tran Le Tran¹, Trong Dang Van^{1*}, Linh Cao Khanh¹, Thuy Le Thi¹, Thuy Tu Thi¹, Thien Nguyen Minh¹, Anh Ta Tram², Lanh Chu Van¹

¹ Department of Physics, Vinh University, 182 Le Duan, Truong Thi Ward, Vinh City, Vietnam;

² Vinh Medical University, 161 Nguyen Phong Sac, Hung Dung Ward, Vinh City, Vietnam;

Email: dangvantrong0602@gmail.com

ABSTRACT

A highly birefringent photonic crystal fiber (PCF) with a core infiltrated with 1,2-dibromoethane ($C_2H_4Br_2$) is proposed in this article. The guiding properties of the proposed PCF are numerically investigated using the finite element method. This fiber exhibits high birefringence in the order of 10^{-3} in the wavelength range of 500 – 3500 nm. It is one or two orders of magnitude higher than that of standard birefringence fibers (around 6×10^{-4}). The proposed simple cladding structure is easy to fabricate with the two air holes in the x-axis having a larger size than the others to make a high contrast of refractive index between the x and the y-axis for high birefringence, and also for decrease of confinement loss. The proposed fiber can prove its applications in optical technologies, especially supercontinuum generation.

Keywords: telecommunication applications; photonic crystal fiber; hollow-core; 1,2-dibromoethane; highly birefringence

INTRODUCTION

The birth of photonic crystal fiber (PCF) is an outstanding breakthrough in the field of fiber optic communication technology [1]. In the past, fiber optic technology was chosen as the backbone of modern telecommunications systems because it provides a more flexible and reliable optical communication channel than free space medium [2]. The lack of design flexibility of conventional fiber optics has limited its expansion in various fields such as spectroscopy [3], measurement, sensing applications [4], high-power technology [5], nonlinear optical [6], optical coherence tomography [7], quantum dots [8], supercontinuum generation [9-11]. PCF provides a high degree of freedom in varying structural parameters, thus demonstrating excellent design flexibility. This design freedom provides outstanding features not possible with conventional fibers. Additionally, their compactness, lightness, minimal cost, and insensitivity to hazardous environments make PCF-based devices practical to operate in a variety of environments.

PCF exhibits many unique properties such as low confinement loss, high birefringence, high nonlinearity and flat dispersion, which are highly dependent on the structural parameters. Highly

birefringent PCFs are prominent in many practical applications including laser technology, sensor systems, and telecommunications. To achieve high birefringence, it is necessary to alternate the symmetry of the fiber core structure, which is done using air holes of different radii. However, it reduces the structural complexity in PCF fabrication.

In this paper, a highly birefringent PCF with a high refractive index $C_2H_4Br_2$ permeable core with low confinement loss is designed. Through optimization of the fiber structure, the optimized structure exhibits high birefringence at 10^{-3} . The proposed structure with two air holes on the x-axis is larger in size than the remaining holes, creating a high refractive index contrast between the x axis and y axis for high birefringence. The proposed structure can be fabricated using the conventional stack and draw method [12].

NUMERICAL MODELING

The schematic of the structure has been presented in Fig. 1 with five numbers of rings in the cladding surrounded by an anisotropic perfect match layer (PML). Here, PML is the absolute boundary condition for the waveguide to estimate the confinement loss of optical fiber and absorb the scattered energy of incident light without reflection of electromagnetic waves. Fused silica

(SiO₂) was chosen as the base material and the core was filled with C₂H₄Br₂ which has a higher nonlinear refractive index than SiO₂. This creates a refractive index difference between the core and cladding in the PCF, so light transmitted in the PCF follows the total reflection mechanism like a conventional optical fiber.

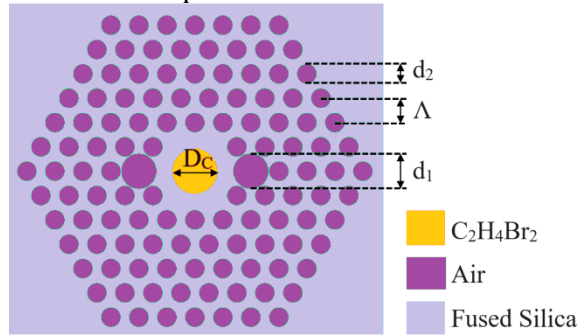


Figure 1. Cross section of the designed C₂H₄Br₂-core PCF with a hexagonal lattice.

The refractive index of SiO₂ glass and C₂H₄Br₂ as a function of wavelength λ is described by the Sellmeier relation [13]:

$$n^2(\lambda) = 1 + \frac{A_1\lambda^2}{\lambda^2 - B_1} + \frac{A_2\lambda^2}{\lambda^2 - B_2} + \frac{A_3\lambda^2}{\lambda^2 - B_3} \quad (1)$$

where the coefficients Sellmeier for SiO₂ are $A_1 = 0.6694226$, $A_2 = 0.434584$, $A_3 = 0.8716947$, $B_1 = 0.004801 \mu\text{m}^2$, $B_2 = 0.0132.85 \mu\text{m}^2$, $B_3 = 95.341482 \text{ nm}^2$. The figures for C₂H₄Br₂ are $A_1 = 1.3163728$, $A_2 = 0.4013224$, $B_1 = 0.01616122 \mu\text{m}^2$, $B_2 = 142.2298902 \mu\text{m}^2$.

In the structure, d_1 is the diameter of two symmetrical air holes on the horizontal axis that are 1.8 times larger than the remaining air holes d_2 . The lattice constants (Λ) selected for investigation vary from 1.0 μm to 2.5 μm with a step of 0.5 μm and the filling factor d_2/Λ changed from 0.3 to 0.7 with a step of 0.05. The PCF structures are simulated with a limited wavelength range from 500 nm to 3500 nm because data is probably only available in this wavelength range. The diameter of the core satisfies the equation $D_c = 4\Lambda - 1.9d_1$, where D_c is the diameter of the core.

The polarization maintaining (PM) ability is usually an important factor that people consider when they investigate chemical sensors. PM PCF can eliminate the polarization modal dispersion, preserve the polarization state of the input THz wave, and increase the stability of optical devices. The birefringence (B) of a fiber is the parameter

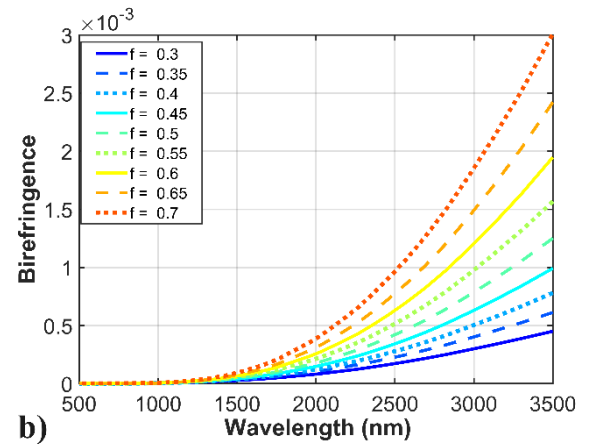
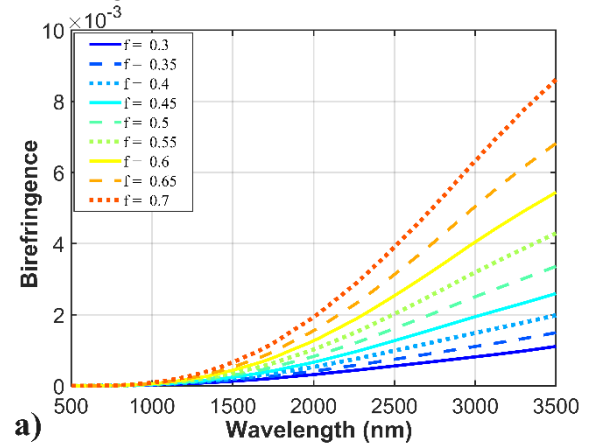
used to evaluate its PM ability. It can be obtained from [14].

$$B = |n_x - n_y| \quad (2)$$

where n_x and n_y are the effective modal refractive indices for the X-polarized and Y-polarized modes, respectively.

RESULTS AND DISCUSSION

The birefringence of PCF depends heavily on the asymmetry of the core region. Figure 2 illustrates the variation of birefringence of the proposed PCF for structural parameters at different wavelengths. It can be seen that the birefringence phenomenon increases with increasing wavelength and increases significantly at wavelengths up to 2500 nm. At the same structural parameters, the birefringence varies with wavelength and has the same shape. Specifically, as the wavelength increases, the birefringence rises. For PCF structures with the same lattice constant, the birefringence increases rapidly with wavelength with a large filling factor (f) and slowly increases with a small filling factor (f). Furthermore, the birefringence decreases with increasing lattice constant.



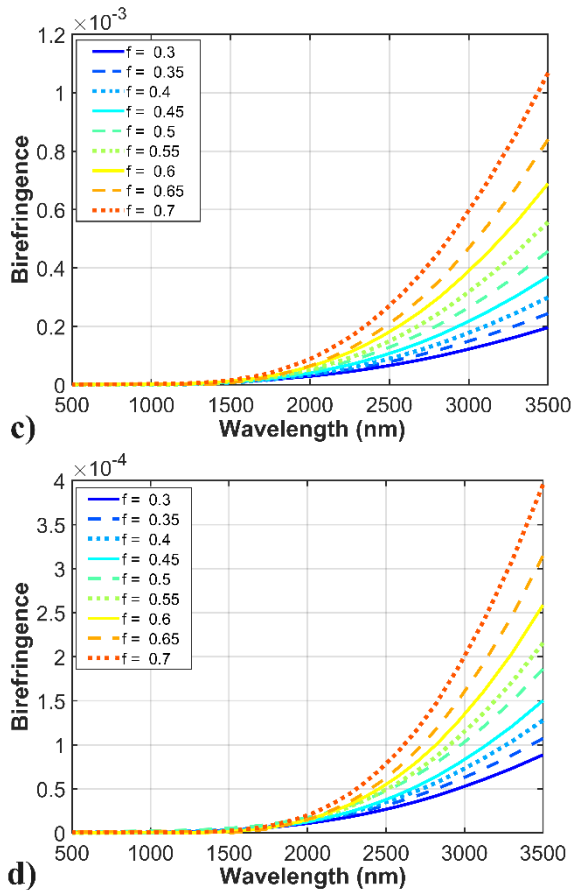


Figure 2. A highly birefringent of PCFs for $f = 0.3 \div 0.7$ and various lattice constants: a) $A = 1.0 \mu\text{m}$; b) $A = 1.5 \mu\text{m}$; c) $A = 2.0 \mu\text{m}$; d) $A = 2.5 \mu\text{m}$.

The asymmetrical nature of the cladding due to the air holes having different diameters enhances the birefringence of the design. It can be confirmed that the birefringence increases as the air hole diameter d_2 increases.

The proposed PCF exhibits high birefringence in the order of 10^{-3} which is recommended for sensing applications. Highly birefringent fibers are significantly used in fiber ring mirrors, which are a key factor in sensing applications and also to reduce the effects of polarization mode dispersion in communication systems.

CONCLUSION

A $\text{C}_2\text{H}_4\text{Br}_2$ -core PCF structure with little structural complexity was designed to provide high birefringence. Additionally, we study the influence of structural parameters on the birefringence of the proposed PCF structure for a wider wavelength range from 500 nm to 3500 nm. The proposed PCF exhibits birefringence as high as 10^{-3} . The proposed PCF can be applied in

sensor systems, non-linear applications and telecommunications.

Acknowledgment

This research is funded by Vietnam’s Ministry of Education and Training (B2023-TDV-07).

Le Tran Bao Tran was funded by the Master, PhD Scholarship Programme of Vingroup Innovation Foundation (VINIF), code VINIF.2023.TS.133.

Dang Van Trong was funded by the Master, PhD Scholarship Programme of Vingroup Innovation Foundation (VINIF), code [VINIF.2022.TS136].

References

- [1] P. Russell, *Photonic crystal fibers*, Science, **299** (2003) 358–362.
- [2] J. Knight, T. Birks, P. S. J Russell, D. Atkin, *All-silica single-mode optical fiber with photonic crystal cladding*, Optics Letters **21** (1996) 1547-1549.
- [3] R. Holzwarth, T. Udem, T.W. Hänsch, J. Knight, W. Wadsworth, P.S.J. Russell, *Optical frequency synthesizer for precision spectroscopy*, Physical Review Letters **85** (2000) 2264–2267.
- [4] O. Frazao, J.L. Santos, F.M. Araújo, L.A. Ferreira, *Optical sensing with photonic crystal fibers*, Laser Photonics Review **2** (2008) 449–459.
- [5] J.S. Feehan, J.H.V. Price, *Efficient high-harmonic generation from a stable and compact ultrafast Yb-fiber laser producing 100 μJ, 350 fs pulses based on bendable photonic crystal fiber*, Applied Physics B **123** (2017) 43.
- [6] H. Ebendorff-Heidepriem, P. Petropoulos, S. Asimakis, V. Finazzi, R. Moore, K. Frampton, F. Koizumi, D. Richardson, T. Monro, *Bismuth glass holey fibers with high nonlinearity*, Optics Express **12** (2004) 5082–5087.
- [7] G. Humbert, W. Wadsworth, S. Leon-Saval, J. Knight, T. Birks, P.S.J. Russell, M. Lederer, D. Kopf, K. Wiesauer, E. Breuer, D. Stifter, *Supercontinuum generation system for optical coherence tomography based on tapered photonic crystal fibre*, Optics Express **14** (2006) 1596–1603.
- [8] Anastasiya A. Chibrova, et al., *The red shift of the semiconductor quantum dots luminescence maximum in the hollow core photonic crystal fibers*, Optical Material **73** (2017) 423–427.

- [9] T. D. Van, L. C. Van, *Supercontinuum generation in $C_6H_5NO_2$ -core photonic crystal fibers with various air-hole size*, Modern Physics Letters B **37** (2023) 2350063.
- [10] T. D. Van, L. C. Van, *Design and optimization of $C_6H_5NO_2$ -core photonic crystal fibers of broadband supercontinuum generation with low peak power*, Crystal Research and Technology, **58** (2023) 2300085.
- [11] T. D. Van, L. C. Van, *Broadband supercontinuum generation with low peak power in a circular lattice nitrobenzene-core photonic crystal fiber*, Bulletin of the Lebedev Physics Institute **50** (2023) 318-331.
- [12] D. Pysz, I. Kujawa, R. Stepien, M. Klimczak, A. Filipkowski, M. Franczyk, L. Kociszewski, J. Buzniak, K. Harasny, Ryszard Buczynski, *Stack and draw fabrication of soft glass microstructured fiber optics*, Bulletin of the Polish Academy of Sciences, Technical Sciences **62** (2014) 667-682.
- [13] S. Kedenburg, A. Steinmann, R. Hegenbarth, T. Steinle, and H. Giessen, *Nonlinear refractive indices of nonlinear liquids: wavelength dependence and influence of retarded response*, Applied Physics B **117** (2014) 803–816
- [14] T. Yang, C. Ding, R. W. Ziolkowski, Y. J. Guo, *A scalable THz photonic crystal fiber with partially-slotted core that exhibits improved birefringence and reduced loss*. Journal of Lightwave Technology **36** (2018) 3408–3417.

SYNTHESIS OF MAGNETIC REDUCED GRAPHENE OXIDE-CHITOSAN FOR REMOVAL OF AQUEOUS Cu (II) AND Pb (II)

Diep Ngoc Le, Dong Duy Tran, Ngan Nguyen Le, Tin Chanh Duc Doan, Chien Mau Dang

Institute for Nanotechnology, Community 6, Linh Trung Ward, Thu Duc City, Ho Chi Minh City, Vietnam;
Vietnam National University Ho Chi Minh City, Ho Chi Minh City, Vietnam

Email: Indiep@vnuhcm.edu.vn

ABSTRACT

This paper presents the results of synthesizing composite materials of reduced graphene oxide with chitosan attached to Fe₃O₄ ferromagnetic nanoparticles and evaluates the ability of this material to adsorb Pb²⁺ and Cu²⁺ ions in water. The process begins with the oxidation of graphite oxide using the Hummer method. The resulting graphite oxide is reduced to reduced graphene oxide, then modified with chitosan, and ferromagnetic nanoparticles are attached to its surface. The modification with chitosan and the attachment of ferromagnetic nanoparticles help to increase the material's metal ion adsorption capacity. The analysis employs various techniques such as field emission scanning electron microscope (FESEM), Fourier transform infrared spectroscopy (FTIR), micro-Raman spectroscopy, atomic absorption spectroscopy (AAS). The fabricated materials are well dispersed in water, easily recovered by magnets, and have a maximum adsorption capacity of 71.15 for Pb²⁺ ions and 70.28 mg/g for Cu²⁺ ions, with a content of 1 g/L adsorbent material.

Keywords: reduced graphene oxide, modified reduced graphene oxide, ferromagnetic, chitosan, removed metal ion.

INTRODUCTION

Graphene and graphene-based materials such as graphene oxide (GO), reduced graphene oxide (rGO), graphene quantum dots (GQDs), are highly versatile materials that have garnered significant attention from researchers today. Among these materials, their application in the environmental field, particularly in the removal of heavy metal ions from water through adsorption, is highly appreciated due to their good removal capabilities [1].

With good conductivity, stability, and a high surface area, rGO is widely used in current adsorbent materials. Examples include rGO aerogel with a Pb(II) adsorption capacity of 58.04 mg/g [2], rGO/Fe₃O₄ with an adsorption amount of 48 mg/g for Pb(II) [3]. Despite its potential for heavy metal adsorption, the adsorption capacity of rGO still needs improvement. One common approach to achieve this is by modifying rGO with other materials, such as amino groups, sodium dodecyl sulfate, or polydopamine.

Recently, chitosan has become an effective material for removing heavy metals due to its numerous functional groups, mechanical strength, flexible polymeric chain structure, high chemical reactivity, low cost, and environmental

friendliness [4]. In addition, Fe₃O₄ material is also used in combination with many other materials for heavy metal ion adsorption applications, providing enhanced adsorption capacity, easy recovery, and durability [5].

In this paper, graphite, after being oxidized to graphite oxide using the Hummer method, will be modified with chitosan, simultaneously reduced to reduced graphene oxide, and finally attached with Fe₃O₄ to form the material reduced graphene oxide - chitosan - magnetic iron (MCrGO). MCrGO material was evaluated for its properties and ability to adsorb Pb²⁺ and Cu²⁺ ions in water.

EXPERIMENTAL

Synthesis of CrGO: 0.1 g of graphite oxide (synthesized by the Hummer process) was dispersed in 100 mL of DI water by sonication for 1 h into a graphene oxide solution. Then, 5 g of chitosan (CS) powder was added and 2 g of sodium borohydride (NaBH₄) was added to reduce graphene oxide to reduced graphene oxide (rGO). The mixture was stirred and heated at 100°C for 4 hours with a circulation system. Subsequently, the reaction mixture was filtered, washed with DI water, and dried at 40°C for 12 h to obtain reduced graphene oxide - chitosan.

Synthesis of MCrGO: In a round-bottomed glass flask, 1,350 g CrGO, 2,030 g FeCl₃·6H₂O, and 0.700 g FeCl₂·4H₂O were combined. The solution was continuously stirred and heated at 50°C for several minutes. 2M NaOH heated to the same temperature was added slowly (with continuous stirring) until the mixture reached pH 10, resulting in the formation of a black precipitate. The reaction was allowed to continue for 15 minutes before cooling to room temperature. The precipitate was then separated magnetically and washed with DI water to remove residual pH, and finally dried at 40°C for 12 h to obtain MCrGO.

Evaluate the adsorption capacity of MCrGO: Weigh 50 mg of MCrGO and add it to 50 ml of Pb²⁺/Cu²⁺ ion solution with a concentration of 20-250 mg/L. The pH of the solution is adjusted to 6-7 with a 0.5 M NaOH solution and a 0.5 M HNO₃ solution. Ultrasound the mixture for 5 seconds so that MCrGO is evenly dispersed in the metal ion solution. Stir the mixture at a speed of 100 rpm during the investigated adsorption time (0.13–24 hours). After adsorption, use a magnet to recover MCrGO and analyze the post-adsorption metal ion solution using atomic absorption spectroscopy (AAS). Each experiment was repeated three times to evaluate the errors. The adsorption amount of Q_e (mg/g) of MCrGO was calculated using the formula:

$$Q_e = (C_0 - C_e)W/w \quad (1)$$

where C₀, C_e, W, and w are the initial ion concentration (mg/L), post-adsorption ion concentration (mg/L), heavy metal ion solution volume (L), and substance mass adsorption (g), respectively.

RESULTS AND DISCUSSION

Characterization of MCrGO material.

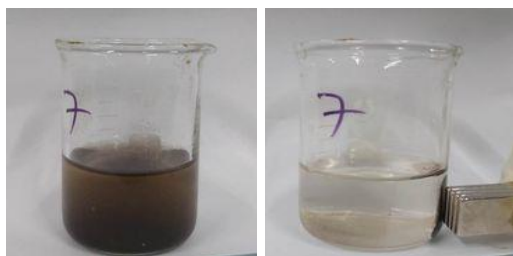


Figure 1. MCrGO dispersion in water before (a) and after being attracted by a magnet (b).

The synthesized MCrGO material can be easily dispersed in water and easily recovered by magnet due to its magnetism (Figure 1).

Figure 2 shows FESEM images of chitosan, nano Fe₃O₄, CrGO and MCrGO. The surface of chitosan is shown in Figure 2(b) to be relatively smooth and glossy. The FESEM images of the CrGO material shown in Figures 2(c, d) show graphene oxide layers stacked on the smooth, glossy surface of chitosan, forming many flakes, folds, and wrinkles more than the surface of the chitosan material. The spherical iron oxide nanoparticles have a size of around 50 nm and tend to aggregate together, which may be due to the magnetic properties of the material, as shown in Figure 2(a). Figures 2(e) and (f) are FESEM images of the MCrGO material surface, where the iron oxide nanoparticles can be seen completely coating the surface of CrGO. The coating is dense, and it is difficult to determine the size of the iron oxide nanoparticles.

Based on the FESEM results, the structure of the MCrGO material can be predicted: chitosan acts as the main core with rGO coating the chitosan, and the outermost layer of iron oxide nanoparticles coats the rGO layer, giving the material magnetic properties and ease of attraction by magnets.

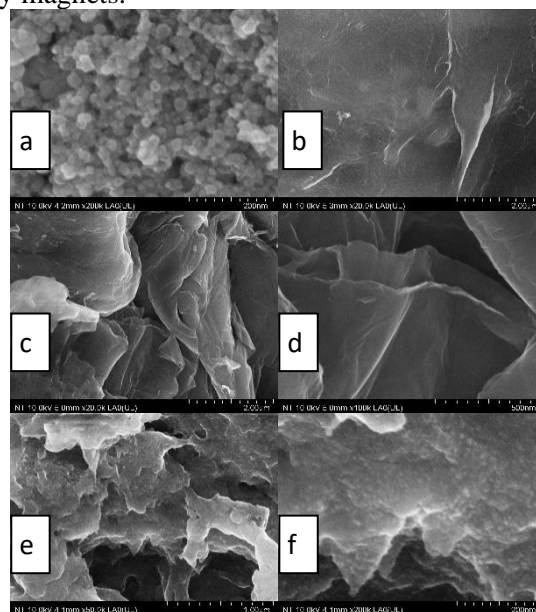


Figure 2. FESEM images of (a) nano Fe₃O₄, (b) chitosan, (c, d) CrGO, (e, f) MCrGO.

The FTIR spectra of nano Fe₃O₄, chitosan, rGO, CrGO, MCrGO are shown in Figure 3. In the FTIR spectra of CrGO and MCrGO, distinct peaks corresponding to chitosan and rGO are evident. These include the peak at 1035 and 1623 cm⁻¹ characteristic of the C-O-C and C=C bonds of graphene oxide, peaks at 1029, 1593, and 3300 cm⁻¹ corresponding to glucosidic bonds, the C=O

stretching vibration of the -NHCO- group, and the NH bending vibration of chitosan [6]. Additionally, the peak at 610 cm^{-1} corresponding to the Fe-O bond in Fe_3O_4 can also be observed.

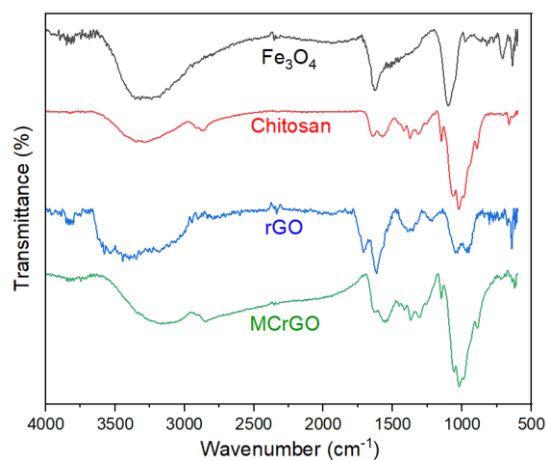


Figure 3. FTIR spectra of nano Fe_3O_4 , chitosan, rGO, CrGO and MCrGO.

Figure 4 presents the XRD spectra of chitosan, Fe_3O_4 , CrGO and MCrGO. In the XRD spectrum of MCrGO, the peaks at $2\theta = 20^\circ$ can be seen, which is characteristic of the (200) lattice plane of chitosan, and peaks at $2\theta = 35.6, 57.3$ and 62.8 , corresponding to the (311), (511) and (440) lattice planes of Fe_3O_4 [7].

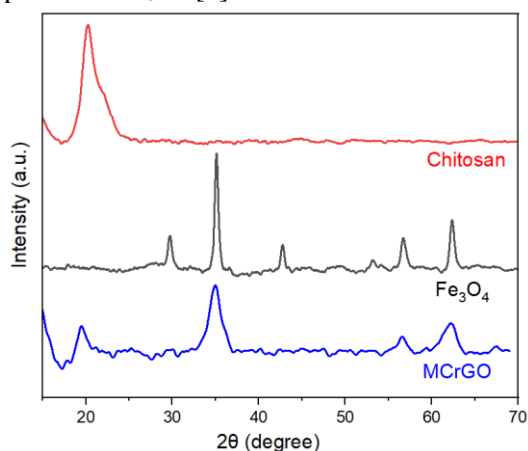


Figure 4. X-ray diffraction spectra of Fe_3O_4 , chitosan, CrGO and MCrGO.

The results of Raman spectral analysis confirm the presence of reduced graphene oxide layers in the MCrGO structure. The Raman spectrum of MCrGO shows the characteristic D and G peaks at 1330 and 1602 cm^{-1} respectively, mirroring the Raman spectrum of reduced graphene oxide [8]. The G peak represents the vibration of carbon atoms bonded together through sp^2 hybridization, while the D peak represents the vibration of carbon atoms with sp^3 hybridization.

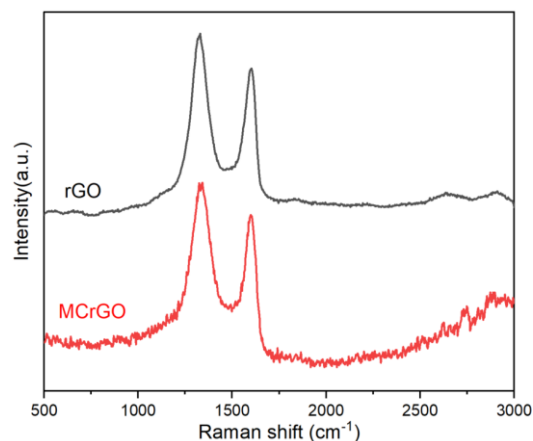


Figure 5. Raman spectra of rGO and MCrGO. Evaluation of Pb^{2+} and Cu^{2+} ion adsorption capacity of MCrGO

When the adsorption time was increased from 10 minutes to 4 hours, the adsorption capacity rose from 18.23 to 51.44 mg/g for Pb^{2+} ions and from 21.12 to 54.07 mg/g for Cu^{2+} ions. However, extending the adsorption time from 3 hours to 24 hours did not significantly alter the adsorption capacity of Pb^{2+} and Cu^{2+} ions. This lack of change might be due to the material having reached adsorption equilibrium, where Pb^{2+} and Cu^{2+} ions were maximally adsorbed. Consequently, despite the increased adsorption time, the adsorption amount remained nearly unchanged.

Figure 7 shows the adsorption capacity of MCrGO when changing the initial Pb^{2+} and Cu^{2+} ion concentrations. When the Pb^{2+} concentration increased from 20 mg/L to 250 mg/L , the adsorption capacity increased from 28.2 to 73.05 mg/g for Pb^{2+} ions and from 29.79 to 72.11 mg/g for Cu^{2+} ions.

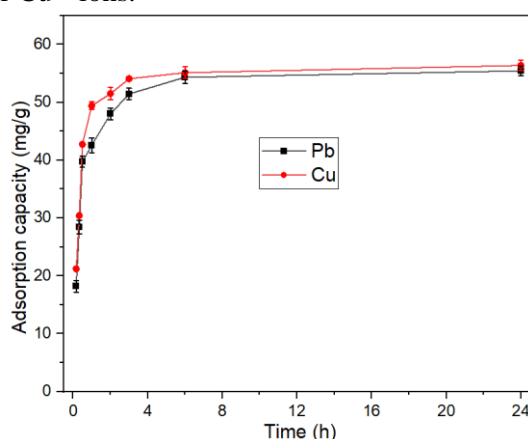


Figure 6. Effect of contact time on the adsorption capacity of Pb^{2+} and Cu^{2+} by MCrGO (experimental conditions: 1 mg/mL adsorbent, $100\text{ mg/L Pb}^{2+}/\text{Cu}^{2+}$, $\text{pH } 6$, a contact

time of 0.13-24 hour and a temperature of $25 \pm 1^\circ\text{C}$).

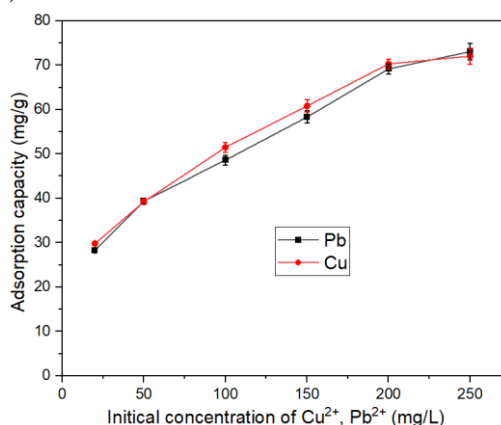


Figure 7. Effect of initial ion concentration on the adsorption capacity of Pb^{2+} and Cu^{2+} by MCrGO (experimental conditions: 1 mg/mL adsorbent, ion concentration ranging from 20-250 mg/L for $\text{Pb}^{2+}/\text{Cu}^{2+}$, pH 6, contact time of 2 hours, and a temperature of $25 \pm 1^\circ\text{C}$).

The observed effect occurs because when the initial ion concentration increases, the diffusion of heavy metal ions from the solution to the adsorbent surface increases, thereby increasing the adsorption rate and saturating the adsorption sites on the surface. However, the number of adsorption sites for a given amount of adsorbent is fixed and can only adsorb a limited amount of heavy metal ions. Therefore, as heavy metal ions gradually occupy the surface adsorption sites, reaching near saturation, the material's adsorption capacity plateaus. This explains the marginal increase in MCrGO's adsorption capacity when the ion concentration was raised from 200 mg/L to 250 mg/L.

CONCLUSION

The reduced graphene oxide - chitosan - magnetic iron oxide composite material has been successfully synthesized, displaying strong magnetism and easy recoverability with a magnet. It also exhibits significant potential for removing Pb^{2+} and Cu^{2+} ions from water. MCrGO has a maximum adsorption capacity of 73.05 and 72.11 mg/g for Pb^{2+} and Cu^{2+} ions, respectively. The influence of initial heavy metal ion concentration and adsorption time on the adsorption capacity of MCrGO was also studied, indicating a positive correlation with increasing initial ion concentration and adsorption duration. Finally, MCrGO composite materials demonstrate promise for further research on the adsorption capacity of other heavy metal ions. There is potential for

further development to improve the material's adsorption capacity in future studies.

Acknowledgment

The authors highly appreciate the financial support of Vietnam National University Ho Chi Minh City for this research under the grant number TX2023-32-01.

References

- [1] H.-L. Liu, J. Zhou, M. Li, Y. Hu, X. Liu, J. Zhou, *Study of the bioavailability of heavy metals from atmospheric deposition on the soil-pakchoi (Brassica chinensis L.) system*, J Hazard Mater. **362** (2019) 9–16.
- [2] X. Mi, G. Huang, W. Xie, W. Wang, Y. Liu, J. Gao, *Preparation of graphene oxide aerogel and its adsorption for Cu^{2+} ions*, Carbon N Y. **50** (2012) 4856–4864.
- [3] C. Prasad, H. Tang, W. Liu, *Magnetic Fe 3 O 4 based layered double hydroxides (LDHs) nanocomposites ($\text{Fe}_3\text{O}_4/\text{LDHs}$): recent review of progress in synthesis, properties and applications*, J Nanostructure Chem. **8** (2018) 393–412.
- [4] N. Ahmad, S. Sultana, M.Z. Khan, S. Sabir, *Chitosan based nanocomposites as efficient adsorbents for water treatment*, Modern Age Waste Water Problems: Solutions Using Applied Nanotechnology. (2020) 69–83.
- [5] N. Subedi, A. Lähde, E. Abu-Danso, J. Iqbal, A. Bhatnagar, *A comparative study of magnetic chitosan ($\text{Chi}@ \text{Fe}_3\text{O}_4$) and graphene oxide modified magnetic chitosan ($\text{Chi}@ \text{Fe}_3\text{O}_4\text{GO}$) nanocomposites for efficient removal of Cr (VI) from water*, Int J Biol Macromol. **137** (2019) 948–959.
- [6] C. Lustriane, F.M. Dwivany, V. Suendo, M. Reza, *Effect of chitosan and chitosan-nanoparticles on post harvest quality of banana fruits*, J Plant Biotechnol. **45** (2018) 36–44.
- [7] J. Zhang, S. Lin, M. Han, Q. Su, L. Xia, Z. Hui, *Adsorption properties of magnetic magnetite nanoparticle for coexistent Cr (VI) and Cu (II) in mixed solution*, Water (Basel). **12** (2020) 446.
- [8] G. Surekha, K.V. Krishnaiah, N. Ravi, R. Padma Suvarna, *FTIR, Raman and XRD analysis of graphene oxide films prepared by modified Hummers method*, J Phys Conf Ser. **1495** (2020) 12012.

ADSORPTION OF HEAVY METAL IONS IN WATER BY POLYVINYLPIRROLIDONE MODIFIED THERMALLY REDUCED GRAPHENE

Diep Ngoc Le, Chien Mau Dang, Tin Chanh Duc Doan

Institute for Nanotechnology, Community 6, Linh Trung Ward, Thu Duc City, Ho Chi Minh City, Vietnam;
Vietnam National University Ho Chi Minh City, Ho Chi Minh City, Vietnam

Email: Indiep@vnuhcm.edu.vn

ABSTRACT

This paper presents the adsorption capacity of Cu^{2+} and Cd^{2+} ions in water of the modified polyvinylpyrrolidone (PVP)/graphene mixture. Graphene is obtained through the thermal separation of graphite oxide (GO), which is synthesized from graphite by the Hummer method. Graphene-PVP composites were prepared by dispersing graphene into PVP solutions at different concentrations and then crosslinking to prevent water washout. This cross-linking ensures that the graphene-PVP mixture is well dispersed and stable. The maximum adsorption capacity of graphene-PVP for Cu^{2+} and Cd^{2+} ions was 172 mg/g and 153 mg/g, respectively, at pH 7, and the contact time was 30 minutes. The experimental results are consistent with the Langmuir kinetic and quadratic pseudo-kinetic models. The study shows that the adsorption mechanism of Cu^{2+} and Cd^{2+} ions on graphene-PVP follows an ion exchange mechanism, which is promoted by the strong interaction between PVP and metal ions. Furthermore, the presence of PVP in the composite enhances the stability and dispersibility of graphene, allowing for efficient ion adsorption. This study provides an easy, low-cost, and environmentally friendly method to produce graphene-PVP materials with high adsorption capacity.

Keywords: thermally reduced graphene, modified graphene, polyvinylpyrrolidone, removed metal ion

INTRODUCTION

Water supplies are currently severely contaminated as a result of the accelerated industry, urbanization, and agricultural activities [1]. Precipitation, membrane separation, ion exchange, and evaporation are just a few of the techniques that have been devised and put to use to remove heavy metal ions from water [2]. Regarding effectiveness, sensitivity, selectivity, and specificity, each of these techniques has pros and cons [3]. Adsorption is the most recommended technique among them because to its low cost, simplicity, and high removal effectiveness from diluted solutions [4].

Activated carbon, clay, zeolite, and carbon nanotubes are a few of the numerous adsorbent materials that have recently been studied [5,6]. Materials made of carbon have a number of benefits, including wide use, high temperature resistance, and resistance to corrosion in a range of pH solutions. Among these materials, graphene stands out due to its much larger surface area. Additionally, polyvinylpyrrolidone (PVP) is a non-toxic, ecologically benign substance that can combine with metal ions to form complexes.

In order to produce a modified material that can successfully absorb metal cations in water, graphene and PVP can be combined. Utilizing the benefits of both materials, the combination of graphene and PVP is a viable material for collecting metal ions [7].

In this study, PVP will be added to graphene after it has been produced through the thermal separation of graphite oxide. After being modified, graphene can be used to filter both domestic and drinking water and to capture Cu^{2+} and Cd^{2+} metal ions from water. Atomic absorption spectroscopy (AAS) was used to evaluate the sample solution both before and after adsorption in order to precisely calculate the concentration of deposited metal ions..

EXPERIMENTAL

Fabrication of graphene by thermal reduction and exfoliation of graphite oxide (rG-H)

Firstly, the furnace was heated to a temperature of 1100 °C. 1 g of Hummer-process-produced graphite oxide powder was placed in a quartz tube and heated in the furnace [8]. The tube was then sealed with a stopper attached to an

exhaust pipe and nitrogen gas cylinder. The quartz tube was then heated for five minutes in the furnace. The tube was taken out of the furnace after five minutes and let to cool to room temperature in the outside air. The sample of graphene powder in the tube was then taken out and the nitrogen cylinder was shut.

Modified graphene with PVP (mG)

1 gram of graphene powder was mixed with 100 grams of PVP solution at concentrations ranging from 1 to 20% in order to create graphene-PVP. 30 minutes were spent stirring the mixture. An ultrasonic vibrator was then used to sonicate the mixture for 30 minutes. The mixture was vacuum-filtered and then washed with DI water to remove any unattached PVP fractions from the graphene after the ultrasonic vibration. The polymer was then cross-linked using a 200°C calcination of the modified graphene powder.

Evaluation of the heavy metal adsorption capacity of graphene-PVP

Weigh 50 mg of mG samples into 100 mL of 100 mg/L Cu^{2+} and Cd^{2+} ion solutions individually at pH 3 (adjusted with 0.5 M NaOH and HNO_3 solution). The mixture was sonicated for 5 s so that the mG was evenly dispersed in the metal ion solution, then stirred at 100 rpm for a contact time of 30 min. After the adsorption period, the solution was filtered, and the concentration was analyzed by atomic absorption spectroscopy. Each batch was repeated three times to evaluate the experimental error.

After the adsorption process, the concentrations of Cu^{2+} and Cd^{2+} ions remaining in the solution were determined using an Atomic Absorption Spectrometer at wavelengths $\lambda_{\text{Cu}} = 324.7$ nm and $\lambda_{\text{Cd}} = 228.8$ nm, respectively. The individual adsorption capacity of graphene-PVP for Cu^{2+} and Cd^{2+} ions Q_e (mg/g) was calculated using equation (1):

$$q_e = (C_o - C_e)W/w \quad (1)$$

Where C_o , C_e , W , and w represent the initial ion concentrations (mg/g), equilibrium ion concentrations (mg/g), solvent mass (g), and adsorbent mass (g), respectively.

RESULTS AND DISCUSSION

Characterization of MCrGO material.

Figure 1 is a FESEM image of rG and graphene after modification with PVP solutions with increasing concentrations from 1-20%. For graphene samples modified with 1-5% PVP solution, the layer structure of the post-modified

graphene is still no different from the pre-modified graphene. The mG-5% sample has a slight change in graphene layer thickness when the graphene sheet thickness is larger than the rG, mG-1%, and mG-2% samples. The reason for this change may be due to the increase in the concentration of modified PVP, leading to more PVP molecules attached to the PVP surface, making the graphene layer thicker. When increasing the concentration of the modified PVP solution to 10%, the thickness of the Graphene sheet increased significantly, but when increasing the PVP concentration to 20%, the thickness of the modified graphene sheet was not much different from the mG-10% sample.

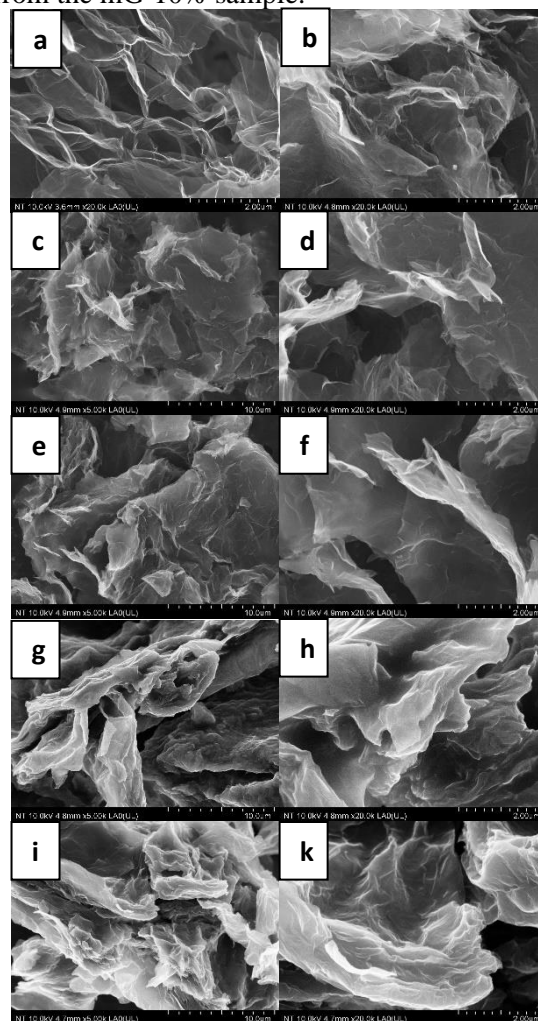


Figure 1. FESEM images of (a) rG, (b) mG-1%, (c, d) mG-2%, (e, f) mG-5%, (g, h) mG-10%, (i, k) mG-20%.

Figure 2 shows the TGA diagrams of samples mG-1%, mG-2%, mG-5%, mG-10%, and mG-20% in nitrogen gas. The TGA curve of rG has a mass loss of 16.5% observed after temperatures up to 800 °C. The TGA diagram of the modified

graphene samples shows a greater weight loss than rG in the temperature range from 500 °C to 800 °C, which is due to the decomposition of PVP attached to the surface of the graphene layers after modification. Samples with higher amounts of PVP have a larger mass loss in the TGA curve.

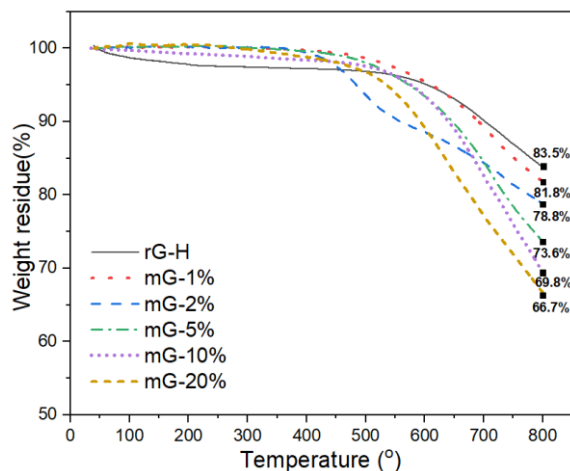


Figure 2. TGA diagram of samples mG-1%, mG-2%, mG-5%, mG-10%, mG-20%.

Figure 3 is the FTIR spectrum of rG-H and mG-1-20%. FTIR analysis results show the presence of PVP in the modified graphene structure, as evidenced by the appearance of characteristic peaks of PVP at 3300 cm^{-1} (OH bond), 2955 and 1420 cm^{-1} (CH bond), 1643 cm^{-1} (C=O bond), and 1291 cm^{-1} (CN bond). The characteristic peaks of graphene were observed at 1571 cm^{-1} (C=C bond) and 1208 cm^{-1} (CO bond) [9,10]. However, when increasing the amount of modified PVP, it can be seen that the peak intensity at 1643 cm^{-1} characteristic of PVP gradually becomes larger than the peak intensity at 1571 cm^{-1} characteristic of graphene. From there, it can be concluded that the amount of PVP attached to graphene increases when the concentration of the modified PVP solution increases.

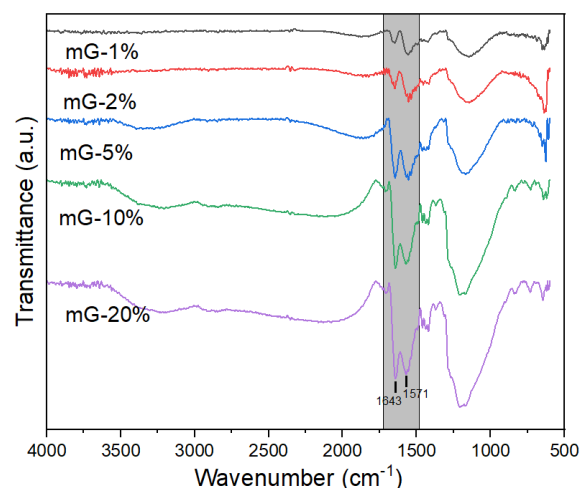


Figure 3. The FTIR spectra of mG-1%, mG-2%, mG-5%, mG-10%, mG-20%.

Figure 4 shows the ion adsorption capacity of different mG samples with an initial ion concentration of 100 mg/L, a contact time of 60 minutes, and a pH of 3. It can be seen that when increasing the amount of denatured PVP, the ion adsorption capacity of mG increases. The adsorption capacities of unmodified graphene were 20.31 and 18.04 mg/g for Cu^{2+} and Cd^{2+} ions, respectively. The ability to adsorb Cu^{2+} and Cd^{2+} ions increased slightly to 44.82 and 39.15 mg/g with the mG-2% sample, then increased sharply to 151.67 and 134.25 mg/g when using the mG-10% sample for adsorption. When using a mG-20% sample for investigation, the adsorption capacity only slightly increased to 165.32 and 146.42 mg/g, respectively. The adsorption capacity of the mG-20% sample increased slightly because the amount of PVP attached to the graphene surface is not much different between the mG-10% and mG-20% samples.

Main adsorption mechanism of heavy metal ion adsorption on the graphene-PVP surface: Strong interaction between functional groups (such as C=O and C-N) of PVP and metal ions provides multiple adsorption sites to remove Cu^{2+} and Cd^{2+} ions [11].

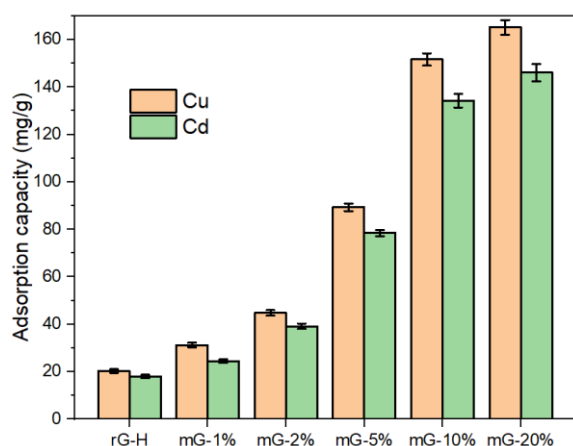


Figure 4. Cu²⁺ and Cd²⁺ ion adsorption capacity of samples rG-H, mG-1%, mG-2%, mG-5%, mG-10%, mG-20% (experimental conditions: 0.5 mg/mL adsorbent, 100 mg/L Cu²⁺/Cd²⁺, pH 3, contact time of 60 min and a temperature of 25 ± 1°C).

CONCLUSION

The study shows the effective adsorption capacity of graphene-PVP in removing Cu²⁺ and Cd²⁺ ions, thanks to the functional groups of PVP attached to graphene. The adsorption capacity improved when increasing the amount of PVP attached to the graphene surface. Experimental results show that the maximum adsorption capacity of graphene-PVP is 158 mg/g for Cu²⁺ and 134 mg/g for Cd²⁺. The study's findings may contribute to the development of more effective graphene-based materials for removing heavy metal ions from wastewater.

Acknowledgment

The authors highly appreciate the financial support of Vietnam National University Ho Chi Minh City for this research under the grant number TX2023-32-01.

References

- [1] J. Briffa, E. Sinagra, R. Blundell, *Heavy metal pollution in the environment and their toxicological effects on humans*, Heliyon. **6** (2020) e04691.
- [2] H. Ma, K.E. Waters, H. Wang, *A Review of Copper and Nickel Extraction from Wastewater by Emulsion Liquid Membrane (ELM)*, Min Metall Explor. (2023) 1-27.
- [3] C. Zamora-Ledezma, D. Negrete-Bolagay, F. Figueroa, E. Zamora-Ledezma, M. Ni, F. Alexis, V.H. Guerrero, *Heavy metal water pollution: A fresh look about hazards, novel*

- and conventional remediation methods*, Environ Technol Innov. **22** (2021) 101504.
- [4] I.O. Saheed, W. Da Oh, F.B.M. Suah, *Chitosan modifications for adsorption of pollutants-A review*, J Hazard Mater. **408** (2021) 124889.
 - [5] P. Hao, X. Ma, J. Xie, F. Lei, L. Li, W. Zhu, X. Cheng, G. Cui, B. Tang, *Removal of toxic metal ions using chitosan coated carbon nanotube composites for supercapacitors*, Sci China Chem. **61** (2018) 797-805.
 - [6] J. Xu, Z. Cao, Y. Zhang, Z. Yuan, Z. Lou, X. Xu, X. Wang, *A review of functionalized carbon nanotubes and graphene for heavy metal adsorption from water: Preparation, application, and mechanism*, Chemosphere. **195** (2018) 351-364.
 - [7] C. Christou, K. Philippou, T. Krasia-Christoforou, I. Pashalidis, *Uranium adsorption by polyvinylpyrrolidone /chitosan blended nanofibers*, Carbohydr Polym. **219** (2019) 298-305.
 - [8] S.N. Alam, N. Sharma, L. Kumar, *Synthesis of Graphene Oxide (GO) by Modified Hummers Method and Its Thermal Reduction to Obtain Reduced Graphene Oxide (rGO)**, Graphene. **06** (2017) 1-18.
 - [9] J. Zhang, B. Yuan, H. Ren, *Synthesis and characterization of PVP/Tb₄/3L•7H₂O luminescent complex*, IOP Conference Series: Earth and Environmental Science **170** (2018) 032-043.
 - [10] S. V. Tkachev, E.Y. Buslaev, A. V. Naumkin, S.L. Kotova, I. V. Laure, S.P. Gubin, *Reduced graphene oxide*, Inorganic Materials. **48** (2012) 796-802.
 - [11] J. Zhao, W.Z. Yuan, A. Xu, F. Ai, Y. Lu, Y. Zhang, *Perfluorinated sulfonic acid ionomer/poly (N-vinylpyrrolidone) nanofiber membranes: Electrospinning fabrication, water stability, and metal ion removal applications*, React Funct Polym. **71** (2011) 1102-1109.

MULTILAYER METAMATERIAL ABSORBER FOR INFRARED EMITTER APPLICATION

Ngo Nhu Viet^{1,3}, Bui Xuan Khuyen^{1,2}, Vu Dinh Lam¹ and Bui Son Tung^{1,2,*}

¹ Graduate University of Science and Technology, Vietnam Academy of Science and Technology,
18 Hoang Quoc Viet, Cau Giay, Hanoi, Vietnam;

² Institute of Materials Science, Vietnam Academy of Science and Technology,
18 Hoang Quoc Viet, Cau Giay, Hanoi, Vietnam;

³ People's Police Academy, Co Nhue 2, Bac Tu Liem, Hanoi, Vietnam.

ABSTRACT

In recent years, there has been a growing global interest in terahertz and infrared metamaterials and their applications. One of the emerging topics is research on emitters utilizing metamaterials [1,2,3]. This article proposes a multilayer metamaterial absorber (MA) structure consisting of hexagonally shaped aluminum (Al) metal and dielectric aluminum oxide (Al_2O_3). The structure exhibits absorption exceeding 90% within the frequency range spanning from 56.9 to 67.9 THz, with two near-perfect absorption peaks at frequencies of 58.6 THz and 64.8 THz. It is postulated that the absorption mechanism is attributed to induced magnetic resonances in the multilayer structure. Furthermore, the study analyzes the spectral emissivity of MA, which demonstrates high and selective emission. Our research may contribute to the development of simple and efficient multilayer THz MAs, which have potential applications in infrared stealth [3], gas sensors [4], and various other domains.

Keywords: metamaterial absorber, multilayer, emission

INTRODUCTION

Metamaterials, which are synthetic materials with artificial structures designed with many special substances. Because of their applications in life, have received increasing research attention over the years. Nowadays, there is much research related to the design and fabrication of multilayer metamaterials for application in many fields such as electromagnetic wave absorption [3,5,14], negative refractive index [6], sensors [4,7]. Among them, the electromagnetic wave absorption property has potential applications in infrared emitter [2,3], harvesters [8], bolometers [9].

In industrial development and civil applications, gas sensors play an increasingly important role. Many recent studies have shown advances in the design and manufacture of optical gas sensors with small size and high response speed [10-12]. For gas sensing applications, infrared emitters show thermoelectric properties using a microelectromechanical system (MEMS) microheater, due to its low thermal mass [13]. It uses conventional blackbody thermal emission in the IR wavelength range, providing a broadband IR emission spectrum.

In this study, we propose a multilayer metamaterial absorber (MA) for application in infrared emitter. It consists of hexagonal metal blocks aluminum (Al) metal and dielectric aluminum oxide (Al_2O_3).

DESIGN AND SIMULATION

Figure 1 shows the unit cell structure of a broadband absorbing multilayer MA operating in the THz frequency region. The unit cell of the proposed multilayer MA has size a and has a two-layers structure. At the top is the first resonance structure made of a hexagonals-shape metal with a thickness t_m and the size l . The second resonance layer has the same size and is located inside a dielectric layer with thickness t_2 . The distance from the second resonance layer to the bottom layer is t_1 . At the bottom is a continuous metal layer of thickness t_b . The structural parameters of the unit cell are optimized with values of $a = 1500$ nm, $t_b = 200$ nm, $t_1 = 100$ nm, $t_m = 100$ nm, $t_2 = 240$ nm, $l = 300$ nm. In this study, the two resonant structures and the continuous metal layer on the bottom surface are made from Al, the dielectric used is Al_2O_3 . In this study, the single-layer MA structures (metal-dielectric-metal), with the top Al layer as a single hexagonal-shaped structure, are also

investigated for different dielectric thicknesses, $t_1 = 100$ nm (denoted as AL1) and $t_2 = 240$ nm (denoted as AL2).

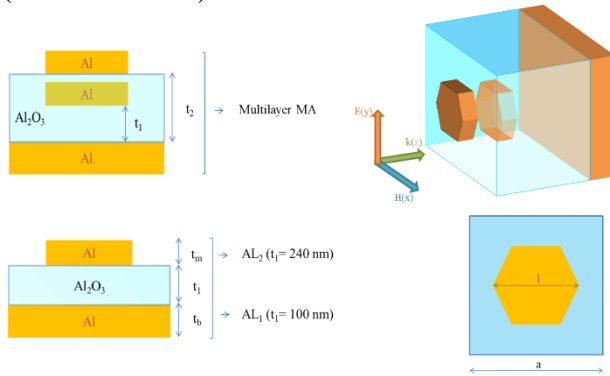


Figure 1. Illustration of the unit-cell structures of a single hexagonal-shaped MA (bottom) and a multilayer MA (top) operating in the THz frequency region.

Characteristics of the structure's electromagnetic properties are simulated using specialized software CST Microwave Studio, in which the Maxwell equations describing the interaction between electromagnetic waves and materials are solved using the finite integration method. In the simulation, the incident wave was a plane wave with the wave vector \mathbf{k} set perpendicular to the MA surface, and the $\mathbf{E-H}$ plane was parallel to the structural surface. Periodic boundary conditions were established for the unit cells in the x and y axes ($\mathbf{E-H}$ plane) and an opening in the z direction. The main simulation results include scattering parameters S_{11} and S_{21} . Absorption, denoted $A(\omega)$, is calculated using the formula:

$$A(\omega) = 1 - R(\omega) - T(\omega), \quad (1)$$

where $R(\omega) = |S_{11}|^2$ is reflection and $T(\omega) = |S_{21}|^2$ is transmission.

RESULTS AND DISCUSSION

Figure 2 presents absorption spectrum of the proposed multilayer MA and the single hexagonal-shaped MAs. The results show that the structures AL1 ($t_1=100\text{nm}$) and AL2 ($t_1=240\text{nm}$) have two absorption peaks at 41.3 THz and 69.5 THz with absorption magnitudes of 94% and 40%, respectively. The AL1+AL2 structure gives better absorption spectrum simulation results with absorption greater than 90% in the frequency range 56.9 - 67.9 THz. It has two maximum absorption peaks at frequencies of 58.6 THz and 64.8 THz with an absorption of 99%. From the absorption spectrum, we predict that Al metal structures have certain contributions in forming the wide-

broadband absorption spectrum for the multilayer metamaterial structure. The formation of broadband absorption may be caused by interactions between metal layers in the structure. Therefore, we continue to investigate the distribution of magnetic fields on the proposed multilayer MA.

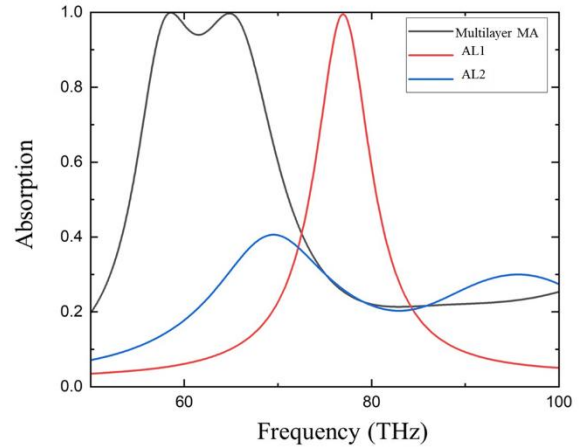


Figure 2. Absorption spectra of single hexagonal-shaped MAs with different thickness and multilayer MA.

To understand the origin of the two absorption peaks of the multilayer MA, the magnetic field distribution at the absorption frequencies of 58.6 and 64.8 THz was investigated and the simulation results are presented in Fig. 3. Results shows that magnetic resonance has appeared between the resonant metal layers and the continuous metal plate below, which is the cause of the absorption peaks. However, the resonances of each pair of layers occurs at different phases. In Fig. 3(a), at phase of 30° , magnetic resonance appears between the middle resonance layer and the bottom metal plate and appears between the two hexagonal resonance layers at phase 100 at frequency 58.6 THz. A similar phase shift at 64.8 THz is shown in Fig. 3(b). The phenomena can be explained by the multilayer structure of the proposed metamaterial. Because the incidence wave is transmitted in the z direction, when passing through and interacting with each metal layer, there is a retardation of phase in z direction, leading to the phase difference of magnetic resonance in each pair of layers. It is noteworthy that the proposed multilayer MA shows two absorption peaks with a wide band absorption band in the infrared region (56.9 - 67.9 THz), which makes this MA potentially useful in enhancing the efficiency of infrared emitter.

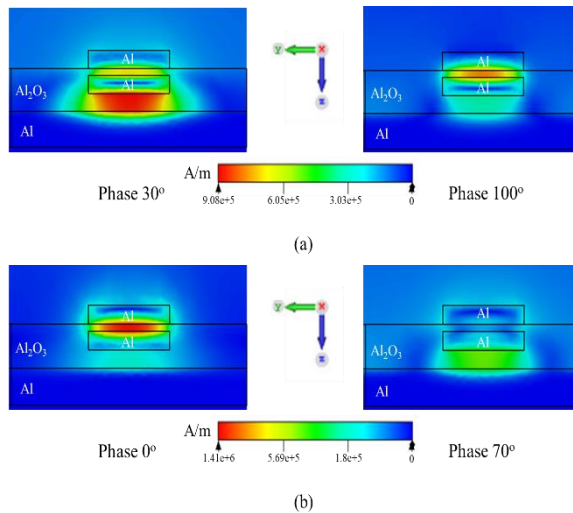


Figure 3. The magnetic field distribution at the absorption frequencies of 58.6(a) and 64.8THz(b) The emission intensity of the MA structure under different temperatures is calculated and the results are presented as shown in Fig. 4.

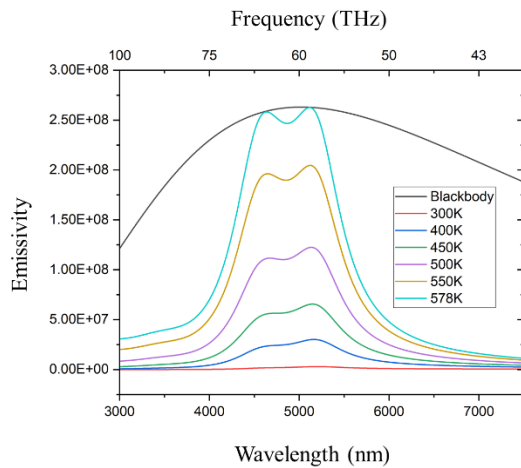


Figure 4. Compare the emission intensities of MA at different temperatures with that of a blackbody

It can be observed that the emission intensity of the multilayer MA sheet increases as the temperature increases. At a temperature of 300 K, the emission intensity is almost zero. When the temperature increases to 400K, the emission intensity begins to increase, and a wider emission band appears. Continuing to increase the temperature, the emission intensity gradually increases and the position of the emission peaks does not change. When $T = 578$ K, the emission intensity at two wavelengths 4632 nm and 5115 nm increases to values corresponding to blackbody.

CONCLUSIONS

We have designed and simulated the electromagnetic characteristics of a multilayer MA

for infrared emitter. The proposed structure consists of two pairs of layers, metal - dielectric - metal. Studied results show that the proposed MA has two absorption peaks at frequencies of 58.6 THz and 64.8 THz with almost absolute absorption, and an absorption greater than 90% is maintained in the frequency range from 56.9 to 67.9 THz. Additionally, the emission intensity of MA is calculated for potential application as emitter. The results show that the multilayer MA has two emission peaks at two wavelengths of 4632 nm and 5115 nm. The intensity of the emission peaks increases with increasing temperature. At 578 K, these two emission peaks have an intensity almost corresponding to blackbody. The absorption characteristics of the proposed MA have been explained based on the magnetic field distribution of the structure. Our work might contribute to various potential applications such as, infrared stealth and gas sensors.

References

- [1] Andrew Caratenuto, Fangqi Chen, Yanpei Tian, Mauro Antezza, Gang Xiao, and Yi Zheng, *Magnetic field-induced emissivity tuning of InSb-based metamaterials in the terahertz frequency regime*, *Optical Materials Express* **11**(9) (2021) 3141-3153.
- [2] Fabio Alves, Brian Kearney, Dragoslav Grbovic, and Gamani Karunasiri, *Narrowband terahertz emitters using metamaterial films*, *Optics Express* **20**(19) (2012) 21025-21032.
- [3] Cong Quan, Jinglan Zou, Chucai Guo, Wei Xu, Zhihong Zhu, Jianfa Zhang, *High-temperature resistant broadband infrared stealth metamaterial absorber*, *Optics & Laser Technology* **156** (2022) 108579.
- [4] Alexander Lochbaum, Alexander Dorodnyy, Ueli Koch, Stefan M. Koepfli, Sebastian Volk, Yuriy Fedoryshyn, Vanessa Wood, and Juerg Leuthold, *Compact Mid-Infrared Gas Sensing Enabled by an All-Metamaterial Design*, *Nano Letters*, **20**(6) (1020) 4169–4176.
- [5] Hanqing Dong, Chengjing Gao, Li Zeng, Dan Zhang, Haifeng Zhang, *Investigating on the electromagnetically induced absorption metamaterial in the terahertz region realized by the multilayer structure*, *Physica B: Physics of Condensed Matter* **639** (2022) 13936.

- [6] Asri Rasad, Hadi Teguh Yudistira, Fitriah Qalbina, Adhitya Gandaryus Saputro, Amir Faisal, *Multilayer flexible metamaterials based on circular shape with negative refractive index at microwave spectrum*, Sensors and Actuators A: Physical, **332**(2) (2021) 113208.
- [7] Motahhare Farrokhfar, Saughar Jarchi, Asghar Keshtkar, *Multilayer metamaterial graphene sensor with high sensitivity and independent on the incident angle*, Optik, **265** (2022) 169536.
- [8] Almoneef T S, Ramahi O M, *Metamaterial electromagnetic energy harvester with near unity efficiency*, Appl. Phys. Lett. **106** (2015) 153902.
- [9] Kong X-T, Khorashad L K, Wang Z, Govorov A O, *Photothermal Circular Dichroism Induced by Plasmon Resonances in Chiral Metamaterial Absorbers and Bolometers*, Nano Lett. **18** (2018) 2001.
- [10] Stanley, R.; *Plasmonics in the mid-infrared*, Nat. Photon, **6** (2012) 409–411.
- [11] Kumar, P.; Morawska, L.; Martani, C.; Biskos, G.; Neophytou, M.K.-A.; Di Sabatino, S.; Bell, M.; Norford, L.; Britter, R.; *The rise of low-cost sensing for managing air pollution in cities*, Environ. Int.; **75** (2015) 199–205.
- [12] Hodgkinson, J.; Tatam, R.P. *Optical gas sensing: A review*, Meas. Sci. Technol.; **24** (2012) 012004.
- [13] Rao, L.L.R.; Singha, M.K.; Subramaniam, K.M.; Jampana, N.; Asokan, S.; *Molybdenum microheaters for MEMS-based gas sensor applications: Fabrication, electro-thermo-mechanical and response characterization*, IEEE Sens. J.; **17** (2017) 22–29.
- [14] C.Gandhi, P.Ramesh Babu, K.Senthilnathan, *Ultra-thin polarization independent broadband terahertz metamaterial absorber*, Front. Optoelectron.; **14**(3) (2021) 288–297.

METAMATERIAL UTILIZING FeCo/GRAPHITE ALLOY FOR ABSORBING ELECTROMAGNETIC WAVES IN THE GHz FREQUENCY RANGE

Tang Xuan Duong^{1,3}, Do Khanh Tung², Bui Son Tung², Vu Dinh Lam¹, Bui Xuan Khuyen^{2*}

¹ Graduate University of Science and Technology, Vietnam Academy of Science and Technology, 18 Hoang Quoc Viet, Cau Giay, Hanoi, Vietnam;

² Institute of Materials Science, Vietnam Academy of Science and Technology, 18 Hoang Quoc Viet, Cau Giay, Hanoi, Vietnam;

³ Joint Russia-Vietnam Tropical Science and Technology Research Center, 63 Nguyen Van Huyen, Ha Noi, Vietnam.

Email: khuyenbx@ims.vast.ac.vn

ABSTRACT

In this report, we have enhanced the electromagnetic wave absorption capabilities in the GHz frequency range of a nano FeCo/graphite composite material by utilizing the structure of metamaterials. The MPA structure consists of three layers, with the top layer being a sheet of FeCo/graphite (FeCo-C) material containing large circular cutouts at the edges of the unit cells and smaller circular cutouts at the center of the unit cells, as well as horizontal slits. The middle layer is a dielectric FR-4 layer, and the bottom layer is a continuous copper sheet. The absorption capability of this structure has been improved by a factor of two compared to regular FeCo-C material, within the range of 6.8 to 10.6 GHz, with absorption exceeding 90%. The absorption mechanism has also been carefully analyzed through the distribution of induced electric- and magnetic-fields. The results obtained could potentially contribute to the development of devices utilizing metamaterials, such as stealth radar technology, electromagnetic shielding for health and safety, and electromagnetic interference reduction for high-performance electronic and communication devices.

Keywords: Metamaterial, broad-band absorption iron-cobalt alloy, electromagnetic coupling

INTRODUCTION

In contemporary times, there is growing interest in conducting research encompassing both theoretical and experimental aspects regarding the impact of electronic devices on living organisms. These devices have the capability to interact with one another, giving rise to the phenomenon of electromagnetic wave interference, resulting in undesirable consequences like electromagnetic interference, signal weakening, and errors in data transmission. To counteract these undesired effects, individuals employ techniques for electromagnetic shielding. In essence, electromagnetic shielding can be categorized into two primary forms: absorption and reflection. The drawback associated with utilizing the reflective approach in electromagnetic shielding is that it does not completely eliminate electromagnetic waves; some of these waves are reflected back into the environment, affecting other adjacent components or devices. Consequently, the

preference often leans toward employing the absorptive method in electromagnetic shielding, which is more prevalent than the reflective method. The fundamental principle underlying this approach involves utilizing materials (or applying coatings) to absorb onto the surfaces of objects, thereby converting electromagnetic wave energy into thermal energy through various loss mechanisms, contingent upon the specific characteristics of each material [1, 2].

In recent decades, scientists have dedicated extensive efforts to the pursuit and advancement of high-performance absorption materials capable of operating across a broad spectrum of frequencies. This quest has been particularly focused on the radar frequency range spanning from 2 to 18 GHz, with specific applications in the military sector. Numerous research endeavors have yielded a diverse array of absorbing materials, encompassing metallic particles, metal oxides, ferrites, carbon nanotubes (CNTs), reduced graphene oxide (RGO), and conductive

polymers [3-8]. Notably, there has been a growing interest among research groups in exploring composite absorbing materials that harness the combined attributes of dielectric and conductive losses [5]. A distinctive subset of these composite materials incorporates carbon-based components, such as carbon nanotubes (CNTs), reduced graphene oxide (RGO), and carbon fibers. These materials exhibit exceptional characteristics, including low density, high dielectric loss, and electrical conductivity [8-13].

Conventional approaches utilized in the field of MPA typically revolve around the generation of either dielectric resonance or magnetic resonance, achieved by implementing circular or dipole currents on metallic structures. In the context of magnetic resonance, the individual unit cells of metamaterials are intricately designed to establish a robust interaction with specific segments of the incident wave, achieved through the integration of high-permeability materials. Conversely, dielectric resonance hinges on the interaction between the incident wave and the electrical response of structures constructed from materials possessing high electrical conductivity. Researchers have developed strategies to enhance the absorption bandwidth by engineering MPA structures with multiple resonance modes. Recent investigations have placed emphasis on the application of FeCo and carbon nanostructures for microwave absorption purposes. FeCo-based materials exhibit exceptional magnetic permeability and can be readily magnetized, rendering them highly suitable for microwave absorption systems relying on magnetic loss mechanisms [14-16].

In this report, we propose an alternative method to expand the absorption frequency range of MPA by incorporating FeCo-C materials into the metamaterial. The electric field distribution and magnetic field intensity of MPA are simulated to elucidate the mechanism behind the broadening of the absorption frequency range. Additionally, the influence of the real and imaginary parts of the permittivity and permeability constants (ϵ and μ) on the absorption spectrum is also investigated.

STRUCTURAL DESIGN AND METHOD

The MPA structure used in our simulation has a basic unit cell size of $220 \times 220 \text{ mm}^2$ (Figure 1) and is constructed from three layers: the top layer is made of FeCo-C material in the

form of a plate with a thickness of $t_f = 2.5 \text{ mm}$, featuring large circular cutouts with a radius of $r_1 = 4.5 \text{ mm}$ at the edges of the unit cell, small circular cutouts with a radius of $r_2 = 2 \text{ mm}$ at the center of the unit cell, and horizontal slits with a width of $w = 1.4 \text{ mm}$. The middle layer consists of FR-4 dielectric material with a thickness of $q = 0.5 \text{ mm}$, an electrical conductivity of $5.8 \times 10^7 \text{ S/m}$, and a dielectric loss of 0.025 mm . The bottom layer is a continuous copper plate with a thickness of $t_m = 0.036 \text{ mm}$. In the CST simulation, we used FeCo-C material with complex permeability and permittivity that vary with frequency, which was fabricated and experimentally measured by Xiaogang Su *et al.* [17], as presented in Figure 2.

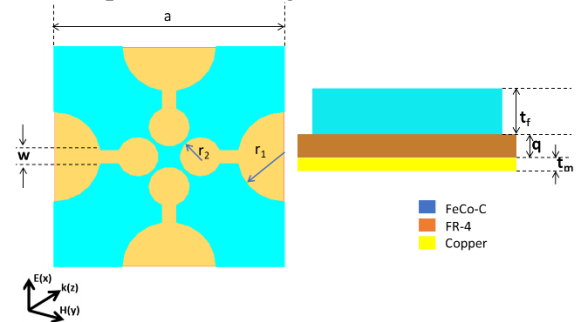


Figure 1. Schematic of MPA unit cell with the optimized geometrical parameters

The simulation was conducted using the CST Microwave Studio commercial simulation software, which was licensed by the Institute of Materials Science/Vietnam Academy of Science and Technology. The simulation was carried out in the frequency range from 1 to 15 GHz. To impose periodic boundary conditions, we employed orientation along the x and y directions. The absorption of the MPA was calculated using the formula $A(\omega) = 1 - R(\omega) - T(\omega)$, where $R(\omega) = |S_{11}(\omega)|^2$ and $T(\omega) = |S_{21}(\omega)|^2$ represent the reflection and transmission coefficients, respectively. In our structure design, the bottom layer is a continuous copper plate, and the transmission coefficient can be considered as 0 in the GHz frequency range. Therefore, the absorption can be simplified as $A(\omega) = 1 - |S_{11}(\omega)|^2$. Due to the asymmetric nature of our proposed MPA structure, the reflected power includes both co-polarization and cross-polarization components.

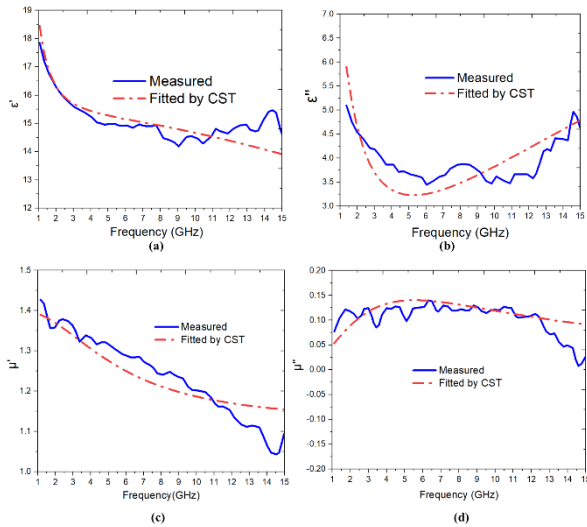


Figure 2. Frequency-dependent variations of the complex permeability and permittivity of FeCo-C material. (a) Real part [ϵ'] and (b) imaginary part [ϵ''] of the permittivity. (c) Real part [μ'] and (d) imaginary part [μ''] of the complex permeability.

RESULTS AND DISCUSSION

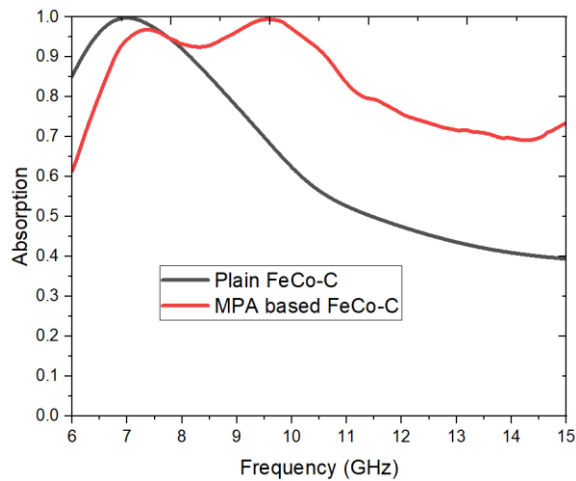


Figure 3. Comparison of absorption spectra for FeCo-C and FeCo-C MPA.

Figure 3 illustrates the absorption spectra in comparison between the FeCo-C MPA and conventional FeCo-C material in the GHz frequency range. The results indicate that integrating FeCo-C material into the metamaterial structure effectively extends both the absorption frequency range and the absorption intensity compared to conventional materials. For conventional FeCo-C material with an equivalent thickness to that of MPA, the electromagnetic wave absorption bandwidth exceeding 90% spans 1.9 GHz (from 6.2 to 8.1 GHz). In contrast, the proposed MPA exhibits a

significantly broader absorption bandwidth, more than doubling at 3.8 GHz (ranging from 6.8 to 10.6 GHz).

To further elucidate the roles of the different layers within the MPA structure, the energy dissipation in each layer is presented in Figure 4. It is evident that over 98% of the energy loss occurs in the FeCo-C layer of the structure, whereas energy loss in the FR-4 dielectric layer is less than 2%. This indicates that the FeCo-C layer within the MPA is the primary contributor to the broad absorption bandwidth capability of the structure.

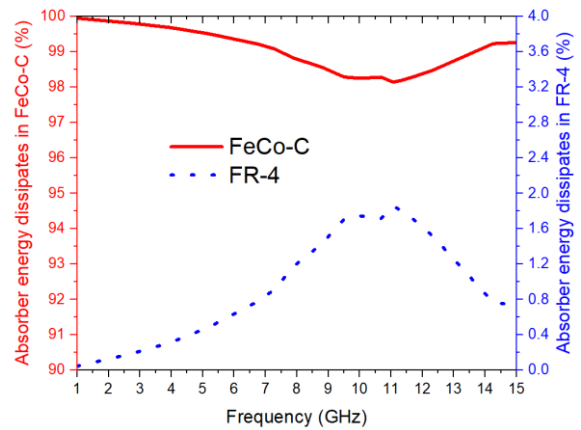


Figure 4. Comparison of the dissipated energy inside the FeCo-C and the FR-4 layers of proposed MPA.

As illustrated in Figure 3, the most prominent absorption peaks of MPA are observed at 7.3 and 9.5 GHz. Therefore, we have selected these two peaks for the observation of electric and magnetic field distributions in order to clarify the absorption mechanism, as shown in Figure 5 and Figure 6.

The strong excitation of the magnetic field is clearly observable at the corners of the structure, where dipole moments align with the direction of the H field, resulting in the formation of electric field spirals at the same locations. This phenomenon, occurring at a frequency of 7.3 GHz, can be attributed to the Mie resonance of dipole moments induced by dielectric resonance [18 - 21]. Likewise, at 9.5 GHz, we observe a similar absorption mechanism driven by Mie resonance of dipole moments, evidenced by the pronounced dipole moments aligned with the H field direction and the half-plane of electric field spirals (E, k). However, it's worth noting that the positions of these dipole moments at 9.5 GHz differ from their positions at 7.3 GHz. As depicted in Figure 6, the dipole moments that

align parallel to the H field are distributed throughout the structure, particularly around the small circular perforations.

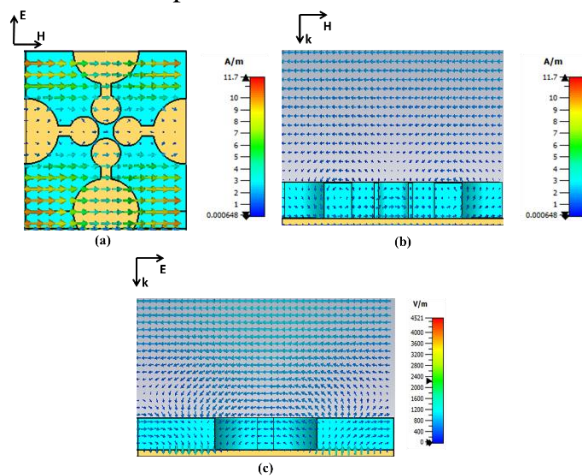


Figure 5. The distributions of induced electric and magnetic fields in the MPA structure at 7.3 GHz: (a) Magnetic field in the (E, H) plane, (b) Magnetic field in the (H, k) plane, and (c) Electric field in the (E, k) plane.

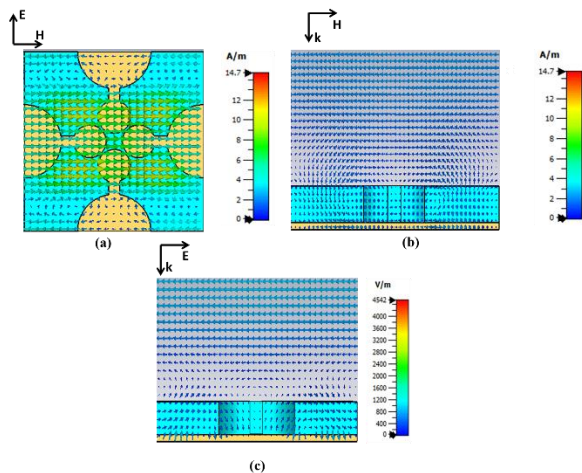


Figure 6. Distributions of the induced electric and magnetic fields of the MPA structure at 9.5 GHz: (a) Electric field in the (E, H) plane, (b) Magnetic field in the (H, k) plane and (c) Electric field in the (E, k) plane

CONCLUSION

In this paper, we proposed an approach to enhance the electromagnetic wave absorption characteristics of FeCo-C materials by incorporating them into a metamaterial structure. The absorption has been doubled in comparison to traditional FeCo-C materials, spanning from 6.8 to 10.6 GHz, with absorption rates over 90%. We have also elucidated that its strong absorption in broad bandwidth can be achieved through the

resonance of dipole moments via Mie resonance and leveraging the inherent electrical properties of FeCo-C materials. The findings of this study contribute to the advancement of tailored materials for use in telecommunications technology and electromagnetic wave shielding, thereby ensuring human safety in near future.

Acknowledgment

This research was supported by the Excellent Research Team Development Program grant funded by the Vietnam Academy of Science and Technology (VAST), Grant No. NCXS02.01/23-24.

References

- [1] Li, Y.; Liu, X. F.; Nie, X. Y.; Yang, W. W.; Wang, Y. D.; Yu, R. H. *Multifunctional Organic-Inorganic Hybrid Aerogel for Self-Cleaning, Heat-Insulating, and Highly Efficient Microwave Absorbing Material*. *Adv. Funct. Mater.* **29** (2018) 1807624.
- [2] Abdulkarim, Y.I.; Mohanty, A.; Acharya, O.P.; Bhargav, A.; Khan, M.S.; Mohapatra, S.K.; Muhammadsharif, F.F; Dong, J. *A Review on Metamaterial Absorbers: Microwave to Optical*. *Front. in Phys.* **10** (2022) 893791.
- [3] Xie, Y.; Yu, Y.; Feng, Y.; Jiang, W.; Zhang, Z. *Fabrication of Stretchable Nanocomposites with High Energy Density and Low Loss from Cross-Linked PVDF Filled with Poly(dopamine) Encapsulated BaTiO₃*. *ACS Appl. Mater. Interfaces*, **9** (2017) 2995-3005.
- [4] Liu, L.; He, N.; Wu, T.; Hu, P. B.; Tong, G. X. *Co/C/Fe/C Hierarchical Flowers with Strawberry-Like Surface as Surface Plasmon for Enhanced Permittivity, Permeability, and Microwave Absorption Properties*. *Chen. Eng. J.* **355** (2019) 103–108.
- [5] Xia, T.; Zhang, C.; Oyler, N. A.; Chen, X. B. *Hydrogenated TiO₂ Nanocrystals: A Novel Microwave Absorbing Material*. *Adv. Mater.* **25** (2013) 6905–6910.
- [6] Chen, Y. H.; Huang, Z. H.; Lu, M. M. *3D Fe₃O₄ Nanocrystals Decorating Carbon Nanotubes to Tune Electromagnetic Properties and Enhance Microwave Absorption Capacity*. *J. Mater. Chem. A* **3** (2015) 12621–12625.
- [7] Zhang, Y. Y.; Huang, T. F.; Zhang, H. C. *Broadband and Tunable High-Performance Microwave Absorption of an*

- Ultralight and Highly Compressible Graphene Foam.* Adv. Mater. **27** (2015) 2049–2053.
- [8] Sun, D.; Zou, Q.; Wang, Y.; Jiang, W.; Li, F. *Controllable Synthesis of Porous Fe₃O₄-ZnO Sphere Decorated Graphene for Extraordinary Electromagnetic Wave Absorption.* Nanoscale, **6**(12) (2014) 6557–6562.
- [9] Liu, Q.; Cao, Q.; Bi, H.; Liang, C.; Yuan, K.; She, W. *CoNi-SiO₂-TiO₂ and CoNi-Air-TiO₂ Microspheres with Strong Wideband Microwave Absorption.* Adv. Mater. **28** (2016) 486–490.
- [10] Wen, B.; Cao, M. S.; Hou, Z. L.; Song, W. L.; Zhang, L.; Lu, M. M. *Temperature Dependent Microwave Attenuation Behavior for Carbon-Nanotube/Silica Composites.* Carbon **65** (2013) 124–139.
- [11] Kim, S. H.; Park, Y. G.; Kim, S. S. *Double-Layered Microwave Absorbers Composed of Ferrite and Carbon Fiber Composite Laminates.* Phys. Status Solidi C **4** (2007) 4602–4605.
- [12] Chen, H.; Ma, W.; Huang, Z.; Zhang, Y.; Huang Y.; Chen, Y. *Graphene-Based Materials toward Microwave and Terahertz Absorbing Stealth Technologies.* Adv. Optical Mater. **7** (2019) 1801318.
- [13] Huang, Z.; Chen, H.; Huang, Y.; Ge, Z.; Zhou, Y.; Yang, Y.; Xiao, P.; Liang, J.; Zhang, T.; Qian, S.; Li, G.; Chen, Y. *Ultra-Broadband Wide-Angle Terahertz Absorption Properties of 3D Graphene Foam,* **28**(2) (2018) 1704363.
- [14] Park, J.H.; Park, C.; Lee, K.S.; Suh, S.J. *Effect of NaOH and precursor concentration on size and magnetic properties of FeCo nanoparticles synthesized using the polyol method.* AIP Adv. **10**(11) (2020) 115220.
- [15] Liu, X.G.; Geng, D.Y.; Meng, H.; Li, B.; Zhang, Q.; Kang, D.J.; Zhang, Z.D. *Electromagnetic-wave-absorption properties of wire-like structures self-assembled by FeCo nanocapsules.* J. Phys. D. Appl. Phys. **41** (2008) 175001.
- [16] Cheng, Y.; Ji, G.; Li, Z.; Lv, H; Liu, W.; Zhao, Y.; Cao, J.; Du, Y. *Facile synthesis of FeCo alloys with excellent microwave absorption in the whole Ku-band: Effect of Fe/Co atomic ratio.* J. Alloys Compd. **704** (2017) 289–295.
- [17] Su, X.G.; Wang, J.; Zhang, X.X.; Huo, S.Q.; Dai, W.; Zhang, B. *Synergistic effect of polyhedral iron-cobalt alloys and graphite nanosheets with excellent microwave absorption performance.* J. Alloys Compd. **829** (2020) 154426.
- [18] Wang, Q.; Zhang, F.; Xiong, Y.J.; Wang, Y.; Tang, X.Z.; Jiang, C. Abrahams, I.; Huang X Z. *Dual-band binary metamaterial absorber based on low-permittivity all-dielectric resonance surface.* J. Electron. Mat. **48** (2019) 787–793.
- [19] Zhang, F.; Jiang, C.; Wang, Q.; Zhao, Z.; Wang, Y.; Du, Z.; Wang, C.; Huang, X. *A multi-band closed-cell metamaterial absorber based on a low-permittivity all-dielectric structure.* Appl. Phys. Express, **13** (2020) 084001.
- [20] Guo, M.Ch.; Wang, X.K.; Zhuang, H.Y.; Tang, D.M.; Zhang, B.S.; Yang, Y. *3D printed low-permittivity all-dielectric metamaterial for dual-band microwave absorption based on surface lattice resonances.* Phys. Scrip. **97** (2022) 075504.
- [21] Zhu, Y.Q.; Tian, X.; Fang, J.K.; Shi, Y.P.; Shi, S.N.; Zhang, S.; Song, J.M.; Li, M.P.; Liu, X.Y.; Wang, X.D.; Yang, F.H. *Independently tunable all-dielectric synthetic multi-spectral metamaterials based on Mie resonance.* RSC Adv. **12** (2022) 20765–20770.

DEVELOPMENT OF HYDROXYAPATITE ON 45S5 BIOGLASS/POLYCAPROLACTONE COMPOSITE FOR ENHANCED BONE TISSUE ENGINEERING APPLICATIONS

Mai Ngoc Trieu Ngo^{1,2,3}, Ni Ni Thi Phan^{1,2}, Dao Quynh Nguyen Le^{1,2}, Linh Thuy Ba Nguyen⁴,
Thuy Thanh Doan Nguyen^{1,2*}, Phuong Tuyet Nguyen^{1,2,3*}

¹ Faculty of Chemistry, University of Science, Nguyen Van Cu Street, Ho Chi Minh City, Vietnam

² Vietnam National University Ho Chi Minh City, Vietnam

³ Faculty of Interdisciplinary Science, University of Science, Nguyen Van Cu Street,
Ho Chi Minh City, Vietnam

⁴ Division of Biomaterials and Tissue Engineering, Eastman Dental Institute, University College London,
Royal Free Hospital, London, United Kingdom.

Email: ntphuong@hcmus.edu.vn (Phuong Tuyet Nguyen)

ndtthuy@hcmus.edu.vn (Thuy Thanh Doan Nguyen)

ABSTRACT

In this study, we investigated Hydroxyapatite (HA) formation on material substrate 45S5 bio glass (BG)/polycaprolactone (PCL), with a focus on its potential applications in bone tissue engineering. BG 45S5 prepared by sol-gel method at a pH of 2 was mixed with PCL at a 1:1 weight ratio. HA formed by immersing the BG/PCL membranes in the simulated body fluid (SBF) solution for different time intervals of 7, 14, 21, and 28 days. The BG/PCL/HA membranes were then characterized by X-ray diffraction (XRD), Fourier-transform infrared spectroscopy (FT-IR), and Scanning Electron Microscopy (SEM). The membranes' biocompatibility was investigated by following its weight loss and pH shift of phosphate-buffered saline solution when the bioglass membranes were soaked in the solution as a function of time. Furthermore, BG/PCL/HA-x (x days immersion) samples were implemented in cell viability tests using MC3T3-E1 (Pre-osteoblast cells) compared to the control sample, thereby analyzing the association between live cell proliferation and SBF immersion durations. The results indicated that HA was generated significantly with porous and amorphous structures on the BG/PCL/HA-28 membrane. Simultaneously, BG/PCL/HA-28 also demonstrated a substantial increase in the number of viable cells, exceeding 75 %, while the count of non-viable cells was significantly lower than that observed in the control sample after 3 days of culture. This research not only clarifies on the development of HA formation but also emphasizes their significant potential in advancing bone tissue engineering and related biomedical applications. Keyword: Bioactive glass, Hydroxyapatite, Polycaprolactone (PCL), Biocompatibility, Biodegradability

INTRODUCTION

Bone plays a vital role in the human body, but it is vulnerable due to multiple factors. Conventional methods used for bone treatment and shaping have limitations. Hence, artificial bone grafting techniques have been researched to provide more optimized solutions for bone healing. To enhance the bone repairing process, materials are required to meet essential properties such as compatibility, biodegradability, ease of synthesis, and cost-effectiveness [1].

Back in the early 1970s, Professor L. L. Hench and his colleagues discovered a remarkable material known as Bioglass (BG). It is a typical bioactive inorganic material which

can connect with soft tissues without being rejected by the body. Additionally, BG demonstrates compatibility and non-toxicity [2]. Bioglass 45S5 not only bonds with bone effectively but also stimulates bone growth through the interaction between the material surface and the bone. When implanted into the human body, BG releases silicon through interacting reactions with body fluids and forms a biologically active hydroxyapatite (HA) layer on its surface [3]. This HA layer has a chemical composition similar to the mineral phase of natural bone. HA formation is a crucial condition to prove that BG has bioactivity when applied in bone repairment. However, BG still has drawbacks such as brittleness and poor

antimicrobial properties, which hinder its widespread application [1].

Currently, the development of new-generation biomaterials like mixing BG with polymers is a special focus in bone tissue engineering strategies [4]. The outstanding features of natural polymers or synthetic polymers when applied in biomaterials are biodegradability and biocompatibility. In addition, the advantages of synthetic polymers and their copolymers include their appropriate mechanical strength and stability for bone tissue [5]. Polycaprolactone (PCL) which is a synthetic polymer has attracted much attention due to its controllable degradation, compatibility with other polymers, biocompatibility, and cost-effectiveness [6]. However, their drawbacks include the lack of osteo-conduction and direct bonds with bone.

Therefore, in this study, we combined BG and PCL to harness the advantages of both materials and overcome their individual drawbacks. We synthesized BG 45S5 using the sol-gel method and then blended it with PCL to create BG/PCL membranes. Then, the bioactivity of materials was investigated through the formation of hydroxyapatite (HA) when immersed in simulated body fluid (SBF). Furthermore, BG/PCL/HA-x samples (x - day: immersion time in SBF) were tested for cell viability using MC3T3-E1 (pre-osteoblast cells) compared to the control sample, to analyze the correlation between cell proliferation and SBF immersion time.

EXPERIMENTAL

Preparation of Bioactive glass

The bioactive glass 45S5 was synthesized using the sol-gel method, with the precursors including TEOS, H₃PO₄, NaNO₃, Ca(NO₃)₂. HNO₃ was used as a catalyst for the reaction and to adjust the pH of the solution. First, TEOS (4.15 mL) was dissolved in distilled water. Then, H₃PO₄ (0.055 mL) was added, and HNO₃ was used to adjust the pH of the solution. NaNO₃ (1.675 g) and Ca(NO₃)₂ (1.800 g) were added to the solution, respectively. It is important to note that Ca(NO₃)₂ was added after NaNO₃ had completely dissolved. The solution was then stirred for about 1 hour to form a sol and this sol was aged after that to form a gel. The gel was dried at 100 °C in 2.5 hours and then heated at 200 °C in 5 hours and 700 °C in 2 hours to obtain the bioactive glass.

Preparation of PCL/BG membrane

PCL (1.00 g) was dissolved in DCM solvent, and then the bioglass (1.00 g) was added (the ratio of PCL and bioglass is 1:1 wt%). After about 3 hours of stirring, the solution looked like glue form. To create PCL/BG membranes, this glue solution was poured into molds with dimensions of 1 cm x 1 cm x 0.6 mm. Then PCL/BG membranes were soaked in SBF solution (the solution was prepared same as the research of Hench and colluagues) [7] for 7, 14, 21 and 28 days to evaluate the formation and bioactivity of HA.

RESULTS AND DISCUSSION

1. Characterization of bioactive glass

FT-IR spectra of bioactive glass synthesized by the sol-gel method are presented in Fig.1. The results show that the peak at 920 cm⁻¹ is attributed to Si-O-Ca bending vibration or Si-O-Si symmetric stretching vibration [8]. The absorption peak at 1006 cm⁻¹ is related to Si-O-Si stretching vibration, which is characteristic of BG. Both Si-O-Si and P-O-P bonds appear at wavenumbers of 1000 - 1100 cm⁻¹, so it is difficult to determine which vibration this signal belongs to [9]. At 690 cm⁻¹, two small peaks relate to the vibrations of the Si-O bonds in the silicate tetrahedron, and peak at 769 cm⁻¹ is Si-O stretching and asymmetric vibration [8]. The appearance of small peaks in the range 1400 - 1500 cm⁻¹ corresponds to the PO₄³⁻ group [10]. The signal observed at 1406 cm⁻¹ is related to P-O-P in the structures of the PO₄³⁻ group, and at 1477 cm⁻¹ is related to P-O-Ca in BG [10]. The ATR-FTIR results of bioactive glass 45S5 are consistent with previous studies [8-10].

The XRD pattern of BG is presented in Fig.2. The baseline is rough indicating low crystallization which is evidence for amorphous state of BG powder. In addition, the result reveals the presence of small amounts of crystalline Na₂Ca₂Si₃O₉ and Na₂Ca₄(PO₄)₂SiO₄ phases [11, 12]. However, the formation of two crystalline phases does not affect the bioactivity of the material.

2. Characterization of BG/PCL membrane

Fig.1 shows the ATR-FTIR spectra of BG/PCL/HA-0, BG, and PCL. Both BG/PCL/HA-0 and PCL FT-IR spectra demonstrate absorption peaks at 2943 cm⁻¹ and 2862 cm⁻¹, corresponding to the vibration in the

methylene group. The peak at 1720 cm^{-1} relates to the $\text{C}=\text{O}$ stretching vibration of the carboxyl group. In addition, symmetric and asymmetric stretching vibration of the $\text{C}-\text{O}-\text{C}$ bond in amorphous PCL can be observed at 1240 cm^{-1} and 1159 cm^{-1} , respectively [13]. Besides, the FT-IR spectrum of BG/PCL/HA-0 shows characteristic absorption peaks of BG, including the peak at 1556 cm^{-1} and the increase in intensity of the peak at 1467 cm^{-1} due to the phosphate group in BG. The peak at 1122 cm^{-1} increases in intensity because of the $\text{Si}-\text{O}-\text{Si}$ bond at 1006 cm^{-1} in BG [8]. Moreover, there are two peaks at 837 cm^{-1} and 873 cm^{-1} in BG/PCL/HA-0 spectrum compared to one peak at 838 cm^{-1} in PCL spectrum, which can be attributed to the effect of $\text{Si}-\text{O}$ bond at 690 cm^{-1} and 769 cm^{-1} in BG [8].

Fig.2 shows the XRD patterns of BG, PCL and BG mixing with PCL (BG/PCL/HA-0). In both PCL and BG cases, they all appear peak at $2\theta = 21.13^\circ$, 22.1° , 23.77° , which are characteristic signals of PCL [14]. However, the result of BG/PCL/HA-0 has a signal at $2\theta = 23.77^\circ$ is higher than PCL. The reason for this phenomenon is that BG has also a signal at $2\theta = 23.77^\circ$ [11], so the intensity is added by two samples. In addition, the baseline of BG/PCL/HA-0 is rough, and this is a good condition to promote the HA formation. From these XRD results, it can be observed that BG is dispersed within the PCL matrix.

3. Characterization of HA formed on BG/PCL membranes

Fig.1 illustrates the ATR-FTIR spectra of BG, PCL, BG/PCL membranes before and after soaking in SBF solution with different days. As can be seen, samples immersed in SBF solution have no characteristic absorption peaks of PCL in the range $600 - 1500\text{ cm}^{-1}$. The ion exchange between samples and SBF solution and the biodegradation of PCL can be reasons for the disappearance of PCL's signals [15]. Especially, all samples after immersing in SBF show the bands ranging from 3200 cm^{-1} to 3400 cm^{-1} which relates to the absorbed water and the hydroxyl group [16]. The peak at 1016 cm^{-1} represents the $\text{Si}-\text{O}-\text{Si}$ bond characterized by BG [8], while the two peaks at 1640 cm^{-1} and 1407 cm^{-1} are due to the asymmetric stretching vibration of the

carbonate group in HA [16]. Besides, in BG/PCL/HA-21, the peak at 872 cm^{-1} is also due to the vibration of the carbonate group [17].

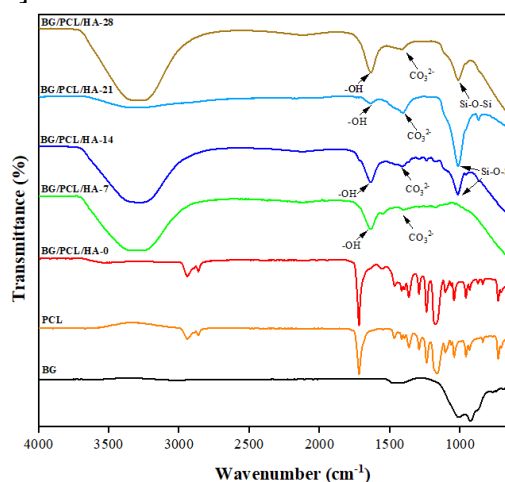


Figure 1. FT-IR spectra of BG, PCL and BG/PCL/HA-x membranes (x: immersion days in SBF solution)

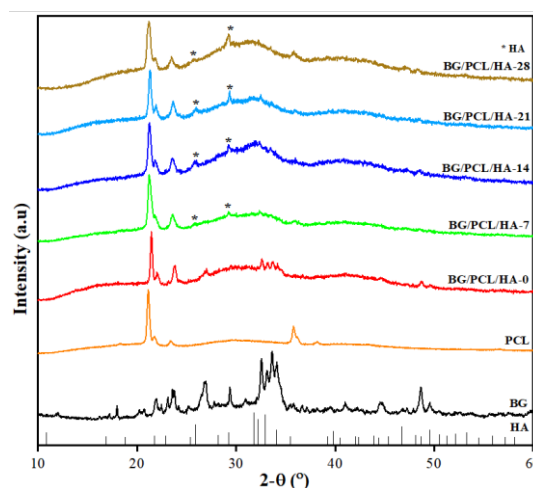


Figure 2. XRD pattern of BG, PCL, and BG/PCL/HA-x membranes

The XRD patterns of the BG/PCL/HA-0 membrane before and after soaking in SBF for 7, 14, 21, and 28 days are illustrated on Fig.2. The membrane after immersing in SBF solution shows the characteristics of HA with diffraction peaks at $2\theta = 25.7^\circ$ and 29.25° , corresponding to the (002) and (210) crystalline planes [18]. The baseline is rough and exhibits the elevation at 2θ from 24.7° to 34.7° , which is evidence proving for the amorphous HA formation. Based on the XRD pattern, it is easily seen that BG/PCL/HA-28 sample is the best membrane for HA development.

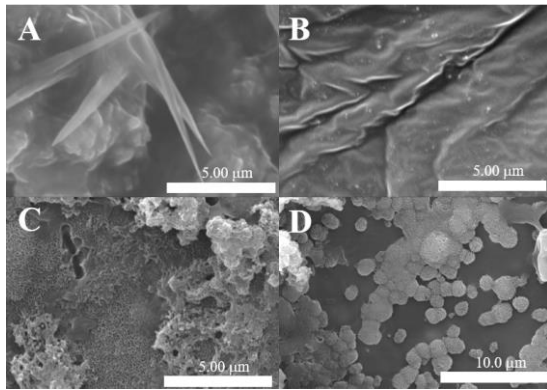


Figure 3. SEM images of A) BG/PCL/HA-0, B) BG/PCL/HA-14, C-D) BG/PCL/HA-28 with different scale bars to show the porous structure (C) and spherical shape (D) of HA

Fig.3 represents SEM images of BG/PCL/HA-0, BG/PCL/HA-14, and BG/PCL/HA-28. It can be seen that BG/PCL/HA-14's surface is flattened and appears defects which are suitable conditions for the formation of hydroxyapatite according to previous reports. In addition, HA seed crystals grow into clusters on the surface of BG/PCL/HA-14 (Fig.3.B). Especially, the longer the soaking time is, the better the HA's structure forms. With SEM image of BG/PCL/HA-28 membrane (Fig.3.C-D), HA forms on the surface with a porous and amorphous structure. However, EDS analysis is needed further to conclude that HA formed has a desired Ca/P ratio.

CONCLUSION

The calcination process at 700 °C resulted in the formation of crystalline phases $\text{Na}_2\text{Ca}_2\text{Si}_3\text{O}_9$ and $\text{Na}_2\text{Ca}_4(\text{PO}_4)_2\text{SiO}_4$ of bioactive glass 45S5, at a pH of 2. On the surface of BG/PCL, an amorphous and porous structure, HA, was formed. The BG/PCL membranes, when immersed in an SBF solution for 21 or 28 days, exhibited the highest production of HA.

Acknowledgements

This research is funded by the University of Science, VNU-HCM under grant number T2023-120.

References

[1] Tang, G., Liu, Z., Liu, Y., Yu, J., Wang, X., Tan, Z., & Ye, X., *Recent trends in the development of bone regenerative biomaterials*, *Frontiers in Cell and Developmental Biology*, **9** (2021) 665813.

[2] L. L. Hench, *Bioceramics: From Concept to Clinic*, *Journal of the American Ceramic Society*, **74**(7), (1991) 1487-1510.

[3] Loh, Z. W., Zaid, M. H. M., Kechik, M. M. A., Fen, Y. W., Amin, K. M., & Cheong, W. M., *New formulation calcium-based 45S5 bioactive glass: In vitro assessment in PBS solution for potential dental applications*, *Journal of Materials Research and Technology*, **24** (2023) 3815-3825.

[4] Arcos, D., & Vallet-Regí, M, *Sol-gel silica-based biomaterials and bone tissue regeneration*, *Acta biomaterialia*, **6**(8) (2010) 2874-2888.

[5] Gloria, Antonio, Roberto De Santis, and Luigi Ambrosio, *Polymer-based composite scaffolds for tissue engineering*, *Journal of Applied Biomaterials and Biomechanics*, **8**(2) (2010) 57-67.

[6] Lee, H., Yeo, M., Ahn, S., Kang, D. O., Jang, C. H., Lee, H., ... & Kim, G. H., *Designed hybrid scaffolds consisting of polycaprolactone microstrands and electrospun collagen-nanofibers for bone tissue regeneration*, *J Biomed Mater Res B Appl Biomater*, **97**(2) (2011) 263-270.

[7] Kokubo, T., & Yamaguchi, S, *Simulated body fluid and the novel bioactive materials derived from it*, *Journal of Biomedical Materials Research Part A*, **107**(5) (2019) 968-977.

[8] Ji, L., Wang, W., Jin, D., Zhou, S., & Song, X., *In vitro bioactivity and mechanical properties of bioactive glass nanoparticles/polycaprolactone composites*, *Materials Science and Engineering: C*, **46** (2015) 1-9.

[9] Goh, Y. F., Alshemary, A. Z., Akram, M., Kadir, M. R. A., & Hussain, R., *In vitro study of nano-sized zinc doped bioactive glass*, *Materials Chemistry and Physics*, **30**, (2017) 1-8.

[10] Adams, L. A., Essien, E. R., Adesalu, A. T., & Julius, M. L., *Bioactive glass 45S5 from diatom biosilica*, *Journal of Science: Advanced Materials and Devices*, **2**(4) (2017) 476-482.

[11] Faure, J., Drevet, R., Lemelle, A., Jaber, N. B., Tara, A., El Btaouri, H., & Benhayoune, H, *A new sol-gel synthesis of 45S5 bioactive glass using an organic acid as catalyst*, *Materials Science and Engineering: C*, **47** (2015) 407-412.

- [12] Lombardi, M., Gremillard, L., Chevalier, J., Lefebvre, L., Cacciotti, I., Bianco, A., & Montanaro, L, *A comparative study between melt-derived and sol-gel synthesized 45S5 bioactive glasses*, Key Engineering Materials, **541** (2013) 15-30.
- [13] N. Singh, U. Batra, K. Kumar, A. Mahapatro, *Investigating TiO₂-HA-PCL hybrid coating as an efficient corrosion resistant barrier of ZM21 Mg alloy*, Journal of Magnesium and Alloys, **9**(2) (2021) 627-646.
- [14] Balu, R., Kumar, T. S., Ramalingam, M., & Ramakrishna, S., *Electrospun Polycaprolactone/Poly (L, 4-butylene adipate-co-polycaprolactam) blends: Potential biodegradable scaffold for bone tissue regeneration*, Journal of Biomaterials and Tissue Engineering, **1**(1) (2011) 30-39.
- [15] Labet, Marianne, and Wim Thielemans, *Synthesis of polycaprolactone: a review*,” Chemical society reviews, **38**(12) (2009) 3484-3504.
- [16] Mujahid, M., Sarfraz, S., & Amin, S., *On the formation of hydroxyapatite nano crystals prepared using cationic surfactant*, Materials Research, **18** (2015) 468-472.
- [17] Chandrasekar, A., Sagadevan, S., & Dakshnamoorthy, A., *Synthesis and characterization of nano-hydroxyapatite (n-HAP) using the wet chemical technique*, Int. J. Phys. Sci, **8**(32) (2013) 1639-1645.
- [18] Moerbeck-Filho, Pio, et al., *Evaluation of the In Vivo Biocompatibility of Amorphous Calcium Phosphate-Containing Metals*, Journal of Functional Biomaterials, **11**(2) (2020) 45.

DEVELOPMENT OF NANOFORMULATION CONTAINING FLUCONAZOLE AND IBUPROFEN TO TACKLE THE *CANDIDIASIS*'S FLUCONAZOLE-RESISTANCE PHENOMENON

Tu Nguyen-Anh Ha¹, Phuong Thi-Xuan Ngo¹ Du-Thien Nguyen¹, Thanh-Hoa Vo¹, Minh-Tri Le^{1,2}, Bac Vu-Giang Nguyen² and Phuoc-Vinh Nguyen^{1,3}

¹ School of Medicine, Vietnam National University Ho Chi Minh City, Hai Thuong Lan Ong Street, Dong Hoa Ward, Di An City, Binh Duong Province, Vietnam;

² Faculty of Pharmacy, University of Medicine and Pharmacy at Ho Chi Minh City, 41 Dinh Tien Hoang, Ho Chi Minh City, Vietnam;

³ Research center for infectious diseases, International University, Vietnam National University Ho Chi Minh City, Quarter 6, Linh Trung Ward, Thu Duc City, Ho Chi Minh City, Vietnam;

Email: npvinh@medvnu.edu.vn

ABSTRACT

The emergence of the drug-resistance phenomenon in fungal infections, particularly fluconazole in candidiasis, poses a real threat to the public health. Several studies have demonstrated the potential of the synergistic effect of fluconazole and ibuprofen to address this issue. However, the poor solubility of ibuprofen as well as a formulation containing these two active pharmaceutical ingredients remain a gap for the use of this combination in reality. This research aims to construct a nano-formulation to co-deliver these active ingredients and develop an in-situ gel recipe to facilitate the use of these drugs in oral candidiasis.

Keywords: Candidiasis, fluconazole-resistance, ibuprofen, nano-formulation.

INTRODUCTION

Oropharyngeal candidiasis is a common opportunistic infection in the oral cavity as a result of *Candida* overgrowth [1,2]. However, as the discovery and development of antifungal drugs are slowing down, the risk of antifungal drug resistance, especially to fluconazole, is increasing across most drug classes [3,4].

Recent studies have explored combinations of non-toxic drugs with antifungal agents to address antifungal resistance, particularly through the synergistic effect of fluconazole and ibuprofen [5-9]. This co-administration presents a potential approach improve oropharyngeal *Candida* treatment. However, gel products combining these two drugs have not yet received approval for use.

In this study, a topical dosage form was developed using nanotechnology. Employing nanotechnology in gel preparation offers several advantages, including enhanced drug solubility, improved storage stability, and increased skin permeability.

METHODS

Materials

Active pharmaceutical ingredients (APIs) (fluconazole & ibuprofen) and excipients (tween 80, tween 20, CapTex 355, soybean oil, Labrasol, propylene glycol, PEG 400, ethanol, poloxamer 407, strawberry & orange flavor, aspartame, acesulfame K, and Sodium Saccharin) were obtained from Boston Vietnam Pharmaceutical Joint Stock Company and quality checked to have a purity level of $\geq 99.99\%$

API solubility

Solubility of 10 mg of APIs in various solvents was determined and the solvent quantity required for complete dissolution was recorded (visually observed).

Solvent-surfactant ratio screening

Determine the solubility of a mixture containing 0.05 g of fluconazole and 0.0125 g of ibuprofen in solvents with varying solvent-surfactant ratios. Select the formula with the lowest solvent-surfactant ratio and proceed to evaluate its particle size.

Screening for excipients

Evaluating multiple excipients for gel dosage forms at varying concentrations based on quality criteria, including taste, texture, adhesion, and ease of cleaning.

Quality control of gel

Evaluating the Nanoparticle and Microemulsion Gel Formulation based on visual appearance, particle size, particle size stability, pH, centrifugal instability and spreadability.

Antifungal susceptibility test

The antifungal activity was determined on two *C. albicans* strains, ATCC and 8XL, using the agar disk diffusion method.

RESULTS AND DISCUSSION

Solubility of APIs

Table 1. Solubility of APIs in various solvents

Solvent	Fluconazole (10 mg)	Ibuprofen (10 mg)
Captex 355	Insoluble	2,5 g
Soybean oil	Insoluble	2 g
Lipoid	Insoluble	Insoluble
Labrasol	3 g	1.5 g
Propylen glycol	0.5 g	0.1 g
Isopropanol	0.35 g	0.1 g
Ethanol	0.1 g	0.05 g

Fluconazole exhibited minimal solubility in oil phases (Captex 355, soybean oil, and lipoid) and limited solubility in water, while it readily dissolved in alcohol (ethanol, isopropanol, propylene glycol). Similarly, ibuprofen showed poor solubility in oils, particularly Labrasol, soybean oil, and CAPTEX 355, but had good solubility in alcohol. Consequently, a nanoformulation containing both fluconazole and ibuprofen was best achieved using an alcohol-based solution.

Solvent-surfactant ratio

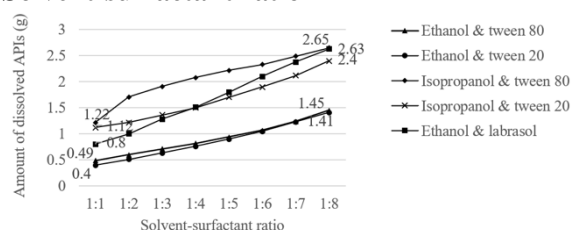


Figure 1. Solvent-surfactant ratio for dissolving fluconazole and ibuprofen mixture

By assessing the solubility of APIs at different solvent-to-surfactant ratios (in the range from 1:1 to 1:8), as the surfactant ratio increased, the solubility of APIs decreased. To ensure a palatable taste and minimize the surfactant concentration in dosage forms, the formulations with a 1:1 solvent-

to-surfactant ratio were selected for further particle size analysis.

Particle size of nanoparticle formulation

Table 2. Particle size of nanoformulation

F	Particle Size (nm)	PDI
M1	11.7±0.2	0.124±0.025
M2	8.8±0.4; 1488±1439 (10%)	0.24±0.06
M3	12,6±1,3	0,22±0.03
M4	9.2±0.7; 1500±1437 (10%)	0,194±0.04
M5	25.3±0.6	0.16±0.04
M6	11.1±0,7; 4558±149 (5%)	0.18±0.03

The six nanoformulations (M1: Ethanol-tween80, M2: Ethanol-tween20, M3: Isopropanol-tween80, M4: Isopropanol-tween20, M5: Ethanol-labrasol, and M6: Ethanol-tween80) were examined for their particle sizes using a granular meter (Nanosizer Malvern, England). Smaller particle size indicates greater stability, with a PDI < 0.2 reflecting uniform particle size distribution and was considered a stable system [10]. Therefore, formulations M2, M3, M4 and M6 did not meet the criteria.

Both M1 and M5 met the particle size and particle distribution requirements. However, this research aimed to select a formula with the lowest ratio of surfactant to solvent for gel formation to treat *Candida* infections in the mouth and throat. Therefore, M1 was chosen as the optimal formula for further evaluation.

Evaluating Quality Criteria for Nanoparticle Formulation

Table 3. Stability results for M1 formula

Time	Particle Size	PDI
W0	11.7±0.2	0.124±0.025
W1	11.7±0.08	0.128±0.013
W2	12.2±0.4	0.175±0.04
W4	11.9±0.25	0.125±0.05
W8	12.1±0.4	0.152±0.04

After a 2-month stability assessment in a controlled microclimate cabinet, the prepared formulation remained transparent and colorless, with no separation and signs of precipitation. The Polydispersity Index (PDI) Values were constantly measured to be < 0.2, indicating a uniform particle size distribution and a stable system. Furthermore, the nanoformulation met

quality criteria for visual appearance, particle size, pH, centrifugal instability, and particle size stability. In comparison to other nanoformulations containing fluconazole, such as the novasome system (110 nm) [11], Nano-Chitosan system (82 nm) [12], niosome system (151.1 nm and 392 nm) [13], and solid lipid granules (138 nm) [14], the nanoformulation in this study exhibited significantly smaller particle size. Additionally, the use of excipients and formulation methods were simplified and cost-effective.

Concentration of Gel Excipients

The different concentrations of Poloxamer 407 in the gel formula (10-18%) were evaluated. The results indicated that Poloxamer 407 concentrations below 14% did not yield a well-concentrated gel. Formulas with 15% Poloxamer 407 exhibited the best sensory characteristics, featuring transparent, thick, soft, easy-to-apply, and easy-to-clean gel. Therefore, a concentration of 15% poloxamer 407 was selected for the final gel formulation. The spreadability of the nanoformulation was slightly less than that of the control placebo. This difference was probably attributed to the active ingredients being integrated into the polymer network of excipients to form a gel, which enhanced adhesion but limited spreadability. However, this variation was less than 10%, indicating that both the product and the placebo met the requirements for topical products. Additionally, the gel product containing nanoformulation of fluconazole and ibuprofen, complied with the predefined criteria for visual appearance, pH, thermal cycling, and spreadability according to Vietnamese Pharmacopoeia V.

Table 3. Spreadability of gel formulation containing 15% Poloxamer 407

Time to read results	Area (cm)		RSD
	Product	Placebo	
1 min	8.55	9.35	6.3%
2 mins after placing the 50 g weight	10.27	11.04	5.1%
2 mins after placing the 100 g weight	11	12.67	10.0%
2 mins after placing the 200 g weight	12.25	13.85	8.7%
2 mins after placing the 500 g weight	16.02	17.85	7.6%

Ratio of flavoring excipients and sweeteners

Table 4. Sweetener screening

Sweetener	Percentage		
Sodium saccharin	0.10%	-	-
Aspartame	-	0.10%	-
Acesulfame K	-	-	0.10%
Evaluation	++*	++	+

++* harshly sweet, bitter aftertaste; ++ sweet; + sweet, bitter aftertaste

When using sweeteners such as 0.05% sodium saccharin, aspartame, and acesulfame K, the product retained a bitter taste and did not mask the tween odor. Increasing the sodium saccharin ratio to 0.1% resulted in a product with both sweetness and a bitter aftertaste. This remained unable to mask the tween odor. Acesulfame K at 0.1% provided a less sweet taste with a lingering bitterness. In contrast, aspartame at 0.1% yielded a sweet and pleasant taste. Consequently, the study selected 0.1% aspartame as the optimal flavoring excipient for the microemulsion gel formulation.

Table 5. Screening for flavoring excipients

Flavor	Percentage			
Strawberry	0,2%	0,3%	-	-
Orange	-	-	0,25%	0,5%
Evaluation	*	*	+	++

Note: * cannot cover the smell; + light orange flavor; ++ just enough orange flavor

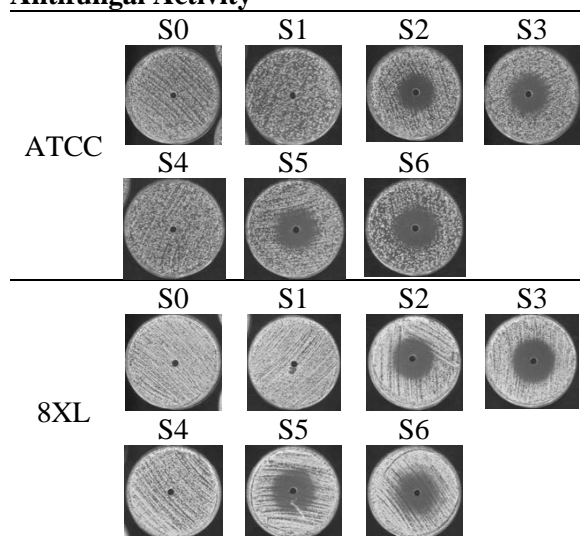
When using strawberry flavoring agents at concentrations of 0.1%, 0.2%, and 0.3%, the product was unable to mask the tween odor due to the poor water solubility of the strawberry flavor. Therefore, the 0.5% orange flavor was selected as the optimal flavoring excipient for the gel formula. Based on these results, the optimal formula for the microemulsion gel containing fluconazole and ibuprofen simultaneously was presented in Table 6.

Table 6. Microemulsion gel formulation

No.	Component	Percentage
1	Fluconazole	0.50%
2	Ibuprofen	0.13%
3	Ethanol	2.50%
4	Tween 80	2.50%
5	Poloxamer 407	15.00%
6	Glycerin	1.00%
7	Orange flavor	0.50%

8	Aspartame	0.10%
9	Water	77.78%
Total		100%

Antifungal Activity



S0: placebo; S1: ibuprofen 125 µg/mL in nanoformulation; S2: fluconazole 500 µg/mL in nanoformulation; S3: combination of fluconazole 500 µg/mL and ibuprofen 125 µg/mL in nanoformulation; S4: ibuprofen 125 µg/mL in pH 6.8 buffer; S5: fluconazole 500 µg/mL in pH 6.8 buffer; S6: combine fluconazole 500 µg/mL and ibuprofen 125 µg/mL in pH 6.8 buffer.

Figure 2. Results of Antifungal Activity Assessment on ATCC and 8XL strain

For the fluconazole-sensitive *C. albicans* ATCC, samples S0 and S1 exhibited no antifungal activity. Sample S2, containing fluconazole alone, had an antifungal ring diameter of 4.01 cm. When combined with ibuprofen (sample S3), the antifungal ring diameter of fluconazole was reduced 3.80 cm. T-test was used to compare the differences between samples. All p-values for these comparisons were greater than 0.05, indicating that the difference in antifungal ring diameter between samples was not statistically significant. This suggests that, for fluconazole-sensitive *C. albicans*, ibuprofen did not enhance the antifungal efficacy of fluconazole when used in combination.

For the fluconazole-resistant fungal strain *C. albicans* 8XL, samples S0 and S1 exhibited no antifungal activity. Sample S2 had an antifungal ring diameter of 4.21 cm, while sample S3, a combination of fluconazole and ibuprofen, showed an increased diameter of 4.67 cm. This

difference was statistically pronounced (p-value = 0.03 < 0.05), indicating a synergistic effect between fluconazole and ibuprofen against fluconazole-resistant *C. albicans*. Furthermore, T-test analysis revealed no statistically significant difference between sample S3 and sample S6 (p-value = 0.21 > 0.05). Therefore, the nanoformulation containing fluconazole and ibuprofen demonstrated antifungal activity equivalent to the combination dissolved in a pH 6.8 environment. However, the nano-sized particle dosage form remained the preferred choice due to its enhanced solubility and increased skin permeability.

CONCLUSION

This study presents the successful development of a microemulsion gel formulation containing fluconazole and ibuprofen that meets quality standards. This lays a foundation for further *in vitro* and *in vivo* research of combinatory formulations containing ibuprofen and fluconazole to counteract antifungal drug resistance. *In vitro* assessments indicate a synergistic effect between fluconazole and ibuprofen against fluconazole-resistant fungal strains, specifically *C. albicans* 8XL. However, no enhancement in antifungal activity was observed when ibuprofen was added to non-fluconazole-resistant fungal strains, such as *C. albicans* ATCC. These findings offer essential insights into potential mechanisms underlying the use of ibuprofen as an adjunct to fluconazole in antifungal therapy.

Acknowledgment

References

- [1] Nucci M, Anaissie E. *Revisiting the source of candidemia: skin or gut*, Clinical Infectious Diseases **33** (2001) 1959-1967.
- [2] Akpan A, Morgan R. *Oral candidiasis*. Postgraduate medical journal **78** (2002) 455-9.
- [3] Morschhäuser J. *The development of fluconazole resistance in Candida albicans— an example of microevolution of a fungal pathogen*, Journal of microbiology **54** (2016) 192-201.
- [4] Tsay SV, Mu Y, Williams S, Epton E, Nadle J, Bamberg WM, Barter DM, Johnston HL, Farley MM, Harb S, Thomas S. *Burden of candidemia in the United States, 2017*,

- Clinical Infectious Diseases **71** (2020) e449-53.
- [5] Liu S, Hou Y, Chen X, Gao Y, Li H, Sun S. *Combination of fluconazole with non-antifungal agents: a promising approach to cope with resistant Candida albicans infections and insight into new antifungal agent discovery*, International journal of antimicrobial agents **43** (2014) 395-402.
- [6] Shi W, Chen Z, Chen X, Cao L, Liu P, Sun S. *The combination of minocycline and fluconazole causes synergistic growth inhibition against Candida albicans: an in vitro interaction of antifungal and antibacterial agents*, FEMS yeast research **10** (2010) 885-93.
- [7] Hill JA, Ammar R, Torti D, Nislow C, Cowen LE. *Genetic and genomic architecture of the evolution of resistance to antifungal drug combinations*, PLoS genetics **9** (2013) e1003390.
- [8] Gamarra S, Rocha EM, Zhang YQ, Park S, Rao R, Perlin DS. *Mechanism of the synergistic effect of amiodarone and fluconazole in Candida albicans*, Antimicrobia agents and chemotherapy **54** (2010) 1753-61.
- [9] Quan H, Cao YY, Xu Z, Zhao JX, Gao PH, Qin XF, Jiang YY. *Potent in vitro synergism of fluconazole and berberine chloride against clinical isolates of Candida albicans resistant to fluconazole*, Antimicrobial Agents and Chemotherapy **50** (2006) 1096-9.
- [10] Danaei M, Dehghankhold M, Ataei S, Hasanzadeh Davarani F, Javanmard R, Dokhani A, Khorasani S, Mozafari MR. *Impact of particle size and polydispersity index on the clinical applications of lipidic nanocarrier systems*, Pharmaceutics **10** (2018) 57.
- [11] Fatima I, Rasul A, Shah S, Saadullah M, Islam N, Khames A, Salawi A, Ahmed MM, Almoshari Y, Abbas G, Abourehab MA. *Novasomes as nano-vesicular carriers to enhance topical delivery of fluconazole: A new approach to treat fungal infections*, Molecules **27** (2022) 2936.
- [12] El Rabey HA, Almutairi FM, Alalawy AI, Al-Duais MA, Sakran MI, Zidan NS, Tayel AA. *Augmented control of drug-resistant Candida spp. via fluconazole loading into fungal chitosan nanoparticles*, International Journal of Biological Macromolecules **141** (2019) 511-6.
- [13] Elmotasem H, Awad GE. *A stepwise optimization strategy to formulate in situ gelling formulations comprising fluconazole-hydroxypropyl-beta-cyclodextrin complex loaded niosomal vesicles and Eudragit nanoparticles for enhanced antifungal activity and prolonged ocular delivery*, Asian journal of pharmaceutical sciences **15** (2020) 617-36.
- [14] Kakkar S, Singh M, Mohan Karuppaiyl S, Raut JS, Giansanti F, Papucci L, Schiavone N, Nag TC, Gao N, Yu FS, Ramzan M. *Lipo-PEG nano-ocular formulation successfully encapsulates hydrophilic fluconazole and traverses corneal and non-corneal path to reach posterior eye segment*, Journal of Drug Targeting **29** (2021) 631-50.

WATER CONDENSATION ON HYBRID SAMPLES WITH CONTROLLED HYDROPHOBICITY

Thuy Chi Do, Hanh Vu Thi Hong, Thuy Nguyen Thi Minh, Thu Hien Nguyen, T-B Nguyen*

Thai Nguyen University of Education, Thai Nguyen University, Vietnam

Email: binhnt@tnue.edu.vn

ABSTRACT

This study introduces an appropriate surface morphology for water-harvesting performance using the hybrid concept. Bio-inspired surfaces which comprise hydrophobic areas and hydrophilic spots with different initial wettability were investigated and demonstrated their superiority in water collection. The advantage can be explained by the enhancement in coalescence possibility which might be induced by the relevant combination of nucleation rate and water-driven ability. The surrounding area and hydrophilic size were chosen to mimic the Namib desert beetle's back morphology. The experiments were conducted inside an environmental chamber for several hours to mimic long-term practical applications. The best combination was found on a hydrophobic – moderately hydrophilic sample that improved water collection efficiency by up to 20% compared to bare Al and supported by the calculation of critical droplet size.

Keywords: water collection, hybrid, superhydrophobic, hydrophilic.

INTRODUCTION

Water harvesting from the atmosphere is an interesting and valuable concept for various problems such as water shortage in arid regions, energy consumption in HVAC (heating, ventilation, and air-conditioning) systems, or industrial applications [1-3]. The surface properties mostly control water collection efficiency [4]. Recently, numerous surface morphologies with different approaches have been introduced to improve collection performance [2,5-8]. The superhydrophobic surface has been named as the potential solution for water collection owing to its unique characteristics in water-driven ability [9-11]. However, the relatively high value in nucleation energy possessed the barrier to enhancing the condensation rate. On the opposite side, the hydrophilic surfaces facilitate the water nucleation compared to superhydrophobic. However, this will block the heat transfer for consecutive nucleation and hinder water collection. Inspired by the fog-basking behavior of Namib Desert beetles [12], various types of hybrid approach have been introduced to demonstrate their advantages over untreated surfaces [13-15]. Recently, Kim et al. proposed water harvesting via dew in a saturated environment and found that hybrid surfaces had the lowest collection mass when almost all water

collected resulted from the superhydrophobic area [9].

In this work, we experimentally investigate the water condensation on hybrid samples with different spot wettability. The results were compared with uniform wettability surfaces and revealed the importance of an appropriate combination of nucleation behavior and water-repellent properties. The results will be supported by a model calculation of critical droplets and a proposed model for further investigation.

EXPERIMENTAL

Al plates were sandblasted and followed by a wet etching step using hydrochloride acid (Merck, Sigma Aldrich, Germany) to generate a hierarchical structure [16]. (Figure 1). Samples were thereafter cleaned with acetone, IPA, and ethanol, followed by rinsed in deionized (DI). The superhydrophobic surface (SP) was carried out by dipping etched samples inside the FOTS (Perfluorooctyltriethoxysilane) solution.

The UVO exposure process was carried out with metal masks to generate hybrid samples by degrading the SAM layer on the exposed areas. The mask pattern contains a square array of different sizes to mimic the *Stenocara* beetle's back morphology.

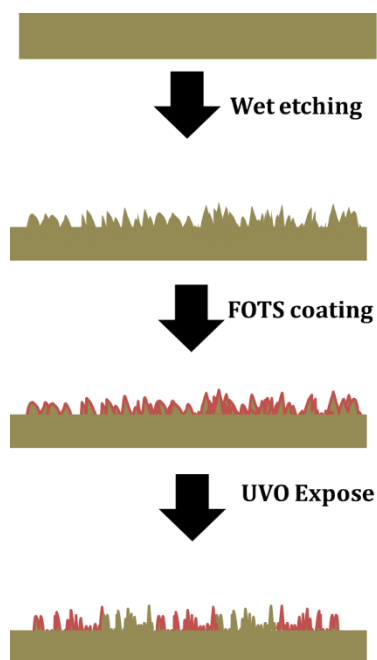


Figure 1. The fabrication process of the hybrid sample

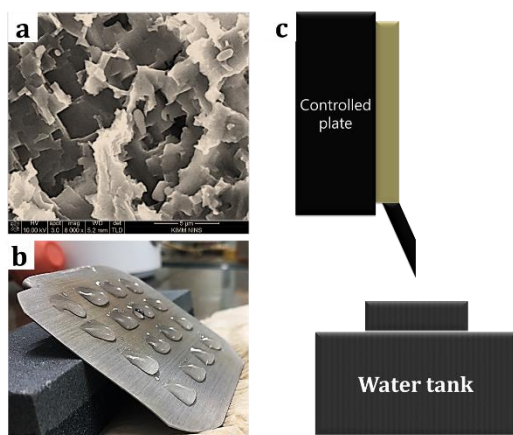


Figure 2. SEM image (a), the water selected deposited on the hybrid sample (b), and set up for water collection experiment (c)

The Hybrid samples with different dot's morphology have been controlled by expose time. Hybrid 1, Hybrid 2, Hybrid 3, and Hybrid 4 correspond to 120°-10°, 120°-30°, 120°-50°, and 120°-70° in contact angle, respectively. Advancing and receding contact angles were measured using a contact angle apparatus to support a theoretical calculation. Functional samples were tiled vertically to the Peltier stage for the water collection test. A balance was used to measure the collected weight. The experiment was carried out inside the controlled chamber at

27° C and 60% humidity for at least 2 hours to facilitate the practical applications.

Table 1. Fabricated surface information

Sample	CA			V _c	Amount (L.m ² /h)
AR Al	80	112	65	3.8	0.52
S.Philic	11	--	--	--	0.48
Philic	50	78	44	5.5	0.53
S.Phobic	155	8	162	5.5	0.50
H 1	118	144	88	4.02	0.63
H 2	121	139	79	3.92	0.66
H 3	119	128	71	3.51	0.72
H 4	120	151	75	4.27	0.55

RESULTS AND DISCUSSIONS

Water harvesting performance was investigated on different combinations with the spot's wettability ranging from super hydrophilic to moderate hydrophilic to generate different contrasts. Interestingly, the condensation rate was maintained on the bare surface (Table 1). After 2 hours of exposure to humid air, the condensation rate on the bare surface was maintained at around 0.35g/h.

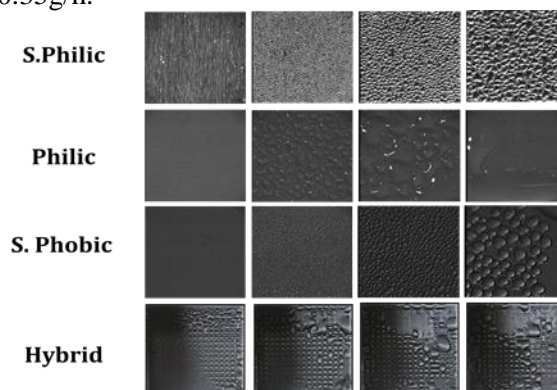


Figure 3. The condensation process on surfaces with different morphology

However, the low hydrophobicity might not facilitate the consecutive collection of water. Therefore, a hydrophobic surface or hydrophobic parts should be considered owing to the support of water-surface friction ability.

An effective water collection surface needs to have a small nucleation rate and low friction for water conduction. Water droplets generated from hydrophilic areas grow rapidly due to low nucleation energy, combining with nearby particles to form a "hybrid droplet" corresponding to the amount of water covering both that spot and around the area.

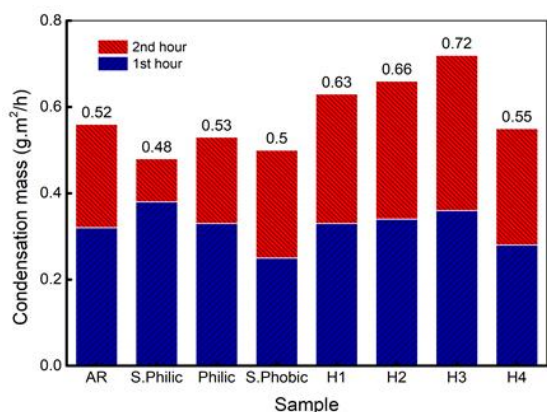


Figure 4. Condensation efficiency on investigated surfaces

This study will focus on investigating hybrid samples with different contrasts to find an optimal combination of water collection ability in comparison to samples with uniform wet adhesion. Table I shows the water weight obtained for samples with different surface morphologies after the experiment. The values of samples with extremely low hydrophobicity (S.Philic) are unrealistic due to the high nucleation rate and the formation of a rapid water film on the hydrophilic areas. Meanwhile, on the opposite side, water droplets form and float sparsely in samples with higher hydrophobicity. This is something that has been mentioned by many scientists in previous studies and shows the weakness of both completely wet and completely non-wet surfaces. If a completely wet surface presents a layer of water to inhibit further nucleation, a completely non-wet surface forms water droplets too independently and requires a lot of time due to the high nucleation energy.

Comparative correlations between hybrid samples are shown in Figure 4 with different wet-stickiness contrasts. This is of great significance in the investigation because different wet-adhesion relationships will determine the morphology of condensed water on wet-adhesive dots. The results show that the highest value belongs to the combination Hydrophobic – moderate Hydrophilic with corresponding contact angles of 120-50. It is also important to reiterate that these hydrophilic dots are square-shaped, 400um in size to simulate the back morphology of the *Stenocara* beetle.

The results show a large contribution of wet adhesion at the wet adhesion areas when the surrounding area is kept in a superhydrophobic state for all samples—the best combination found

on Hydrophobic - Hydrophilic surfaces enhance up to 38% compared to bare surfaces. This result shows good agreement with calculations as the hybrid droplets accumulated on Hydrophobic - Hydrophilic has the lowest critical size. Calculated based on the lowest contact angle hysteresis, receding angle, and advancing angle, the tension force on the droplets shows the importance of reducing the critical volume for falling water and sequential nucleation.

The order of water collected is also consistent with the critical size calculation as the higher the wettability, the better the collection capacity [17]. This shows the importance of wettability for water accumulation. In addition, the change in wetness means changing the wetness relationship between the two areas, which means determining the critical volume of water before falling from the hybrid area. It is worth noting here that the hysteresis may differ with other materials or surface roughness so the most important thing to be considered in hybrid samples is to minimize the wetting hysteresis to minimize capillary forces to enhance drainage ability. This result shows the great contribution of hydrophobicity in water condensation performance and can be explained by lower friction for water driving ability.

CONCLUSION

In this work, we proposed the water harvesting effectiveness investigation on uniform and hybrid samples with different contrasts. The results demonstrated the superiority of hydrophobicity in improving collection performance due to its low adhesion with water which might lead to easier water drainage in both uniform and hybrid surfaces. An appropriate wettability contrast between textured spots and hydrophobic presented their advantage in enhancing condensation efficiency via dewing. The results showed good agreement with hybrid droplet critical size calculation, which was strongly dependent on the wettability hysteresis of hydrophilic spots. Our findings offer a facile and effective strategy for water harvesting approaches.

Acknowledgment

This research has been solely funded by Thai Nguyen University of Education under the grant number TNUE-2023-09. Authors declares our sincere thanks to TNUE for the support.

References

- [1] S. Danilo, C. Dominique, P. Frédéric, *Experimental dropwise condensation of unsaturated humid air – Influence of humidity level on latent and convective heat transfer for fully developed turbulent flow*, Int J Heat Mass Transf. **102** (2016) 846–855.
- [2] H. Li, Z. You, H. Zhang, *Experimental investigation on the heat transfer enhancement of steam condensation on tube with hydrophilic-hydrophobic hybrid surface*, J Phys Conf Ser. **2280** (2022) 12059.
- [3] K.-S. Yang, K.-H. Lin, C.-W. Tu, Y.-Z. He, C.-C. Wang, *Experimental investigation of moist air condensation on hydrophilic, hydrophobic, superhydrophilic, and hybrid hydrophobic-hydrophilic surfaces*, Int J Heat Mass Transf. **115** (2017) 1032–1041.
- [4] C.-W. Yao, J.L. Alvarado, C.P. Marsh, B.G. Jones, M.K. Collins, *Wetting behavior on hybrid surfaces with hydrophobic and hydrophilic properties*, Appl Surf Sci. **290** (2014) 59–65.
- [5] S. Zarei, H.R. Talesh Bahrami, H. Saffari, *Effects of geometry and dimension of micro/nano-structures on the heat transfer in dropwise condensation: A theoretical study*, Appl Therm Eng. **137** (2018) 440–450.
- [6] S. Baba, K. Sawada, K. Tanaka, A. Okamoto, *Dropwise Condensation on a Hierarchical Nanopillar Structured Surface*, Langmuir. **36** (2020) 10033–10042.
- [7] M.M. Garimella, S. Koppu, S.S. Kadlaskar, V. Pillutla, Abhijeet, W. Choi, *Difference in growth and coalescing patterns of droplets on bi-philic surfaces with varying spatial distribution*, J Colloid Interface Sci. **505** (2017) 1065–1073.
- [8] E.K. Her, T.-J. Ko, K.-R. Lee, K.H. Oh, M.-W. Moon, *Bioinspired steel surfaces with extreme wettability contrast*, Nanoscale. **4** (2012) 2900–2905.
- [9] S. Kim, K.J. Kim, *Dropwise Condensation Modeling Suitable for Superhydrophobic Surfaces*, J Heat Transfer. **133** (2011).
- [10] S. Chung, K. Kadala, H. Taylor, *Stable dropwise condensation observed on a hierarchically structured superhydrophobic surface incorporating micro-domes*, Microelectron Eng. **225** (2020) 111252.
- [11] A. Starostin, V. Valtsifer, Z. Barkay, I. Legchenkova, V. Danchuk, E. Bormashenko, *Drop-wise and film-wise water condensation processes occurring on metallic micro-scaled surfaces*, Appl Surf Sci. **444** (2018) 604–609.
- [12] A.R. Parker, C.R. Lawrence, *Water capture by a desert beetle*, Nature. **414** (2001) 33–34.
- [13] T. Nørgaard, M. Dacke, *Fog-basking behaviour and water collection efficiency in Namib Desert Darkling beetles*, Front Zool. **7** (2010) 23.
- [14] R.A. Pinheiro, A.A. Silva, V.J. Trava-Airoldi, E.J. Corat, *Water vapor condensation and collection by super-hydrophilic and super-hydrophobic VACNTs*, Diam Relat Mater. **87** (2018) 43–49.
- [15] Z. Chen, Z. Zhang, *Recent progress in beetle-inspired superhydrophilic-superhydrophobic micropatterned water-collection materials*, Water Sci Technol. **82** (2020) 207–226.
- [16] T.-B. Nguyen, S. Park, Y. Jung, H. Lim, *Effects of hydrophobicity and lubricant characteristics on anti-icing performance of slippery lubricant-infused porous surfaces*, J Ind Eng Chem. **69** (2019).
- [17] C.G.L. Fumidge, *Studies at phase interfaces. I. The sliding of liquid drops on solid surfaces and a theory for spray retention*, J Colloid Sci. **17** (1962) 309–324.

